CYSENI

The 16th International Conference of Young Scientists on Energy Issues

(CYSENI 2019)

23-24 May 2019

Kaunas, Lithuania

Organized by

LITHUANIAN
ENERGY
INSTITUTE

Chair of the Scientific Committee dr. Sigitas Rimkevičius

Chair of the Organizing Committee dr. Vytautas Akstinas

Sponsors:

GVT

A Member of The Linde Group | AGA

EUROfusion

In cooperation with:

KAUNAS

C-Energy2020

H I A

BEA

INTERNATIONAL SCIENTIFIC COMMITTEE

Aleksandrs Ļvovs	Latvia	Mantas Marčiukaitis	Lithuania
Andres Siirde	Estonia	Namejs Zeltins	Latvia
Andris Kreslins	Latvia	Pierre-Etienne Labeau	Belgium
Anton Brin	Belarus	Panos M. Pardalos	USA
Alessandro Petruzzi	Italy	Ralf Ebinghaus	Germany
Bernhard Peters	Luxemburg	Sten Bergstrom	Sweden
Bjørn C. Hauback	Norway	Sigitas Rimkevičius	Lithuania
Darius Milčius	Lithuania	Sergej Zhdanok	Belarus
Enn Mellikov	Estonia	Svetlana Danilova-Tretiak	Belarus
Eugenijus Ušpuras	Lithuania	Victor A. Zhovyansky	Ukraine
Finn Ravndal	Norway	Vaclovas Miškinis	Lithuania
Florentin Paladi	Moldova	Virginijus Radziukynas	Lithuania
Luis E. Herranz	Spain	Vytautas Martinaitis	Lithuania
Myriam Lazard	France		

Board of Reviewers

Akvilė Čibinskienė	Lithuania	Kristina Bočkutė	Lithuania
Aleksandras Iljinas	Lithuania	Kristina Ukvalbergienė	Lithuania
Alessandro Petruzzi	Italy	Lina Ragelienė	Lithuania
Algirdas Gulbinas	Lithuania	Linas Miknius	Lithuania
Algirdas Jasinskas	Lithuania	Linas Paukštaitis	Lithuania
Algirdas Maknickas	Lithuania	Liudvikas Pranevičius	Lithuania
Algis Džiugys	Lithuania	Liutauras Marcinauskas	Lithuania
Alvyra Šlepetienė	Lithuania	Luis E. Herranz	Spain
Andres Siirde	Estonia	Mantas Marčiukaitis	Lithuania
Andrius Jonaitis	Lithuania	Marija Eidukevičiūtė	Lithuania
Andrius Tamošiūnas	Lithuania	Marijus Šeporaitis	Lithuania
Andris Kreslins	Latvia	Marius Urbonavičius	Lithuania
Anupras Šlančiauskas	Lithuania	Martynas Lelis	Lithuania
Artur Rogoža	Lithuania	Martynas Maciulevičius	Lithuania
Antanas Kavolynas	Lithuania	Mindaugas Jakubčionis	Lithuania
Antanas Markevičius	Lithuania	Mindaugas Krakauskas	Lithuania
Anton Brin	Belarus	Mindaugas Milieška	Lithuania
Arturas Klementavičius	Lithuania	Mindaugas Vaišnoras	Lithuania
Artūras Šmaižys	Lithuania	Mindaugas Valinčius	Lithuania
Artjoms Obushevs	Switzerland	Myriam Lazard	France
Arvaidas Galdikas	Lithuania	Namejs Zeltins	Latvia
Arvydas Adomavičius	Lithuania	Narimantas Listopadskis	Lithuania
Arvydas Galinis	Lithuania	Nerijus Pedišius	Lithuania
Asta Malakauskaitė	Lithuania	Nerijus Striūgas	Lithuania
Asta Narkūnienė	Lithuania	Panos M. Pardalos	USA
Audrius Dėdelė	Lithuania	Pierre-Etienne Labeau	Belgium
Audrius Jonaitis	Lithuania	Povilas Krasauskas	Lithuania
Aurimas Lisauskas	Lithuania	Pranas Kuzas	Lithuania
Aurimas Tonkūnas	Lithuania	Pranas Mierauskas	Lithuania
Aušra Pažėraitė	Lithuania	Raimondas Bliūdžius	Lithuania
Benediktas Čėsna	Lithuania	Raimondas Pabarčius	Lithuania
Bernhard Peters	Luxemburg	Ralf Ebinghaus	Germany
Bjørn C. Hauback	Norway	Raminta Skvorčinskienė	Lithuania
Brigita Abakevičienė	Lithuania	Ramūnas Gatautis	Lithuania
Dainius Martuzevičius	Lithuania	Rasa Paleckienė	Lithuania
Dainius Vaičiulis	Lithuania	Reda Čerapaitė-Trušinskienė	Lithuania
Dalia Grigaliūnienė	Lithuania	Regina Kalpokaitė-Dičkuvienė	Lithuania
Dalia Jankūnaitė	Lithuania	Renaldas Raišutis	Lithuania
Dalia Štreimikienė	Lithuania	Ričardas Krikštolaitis	Lithuania

Dalius Tarvydas	Lithuania	Rimantas Pranas Deksnys	Lithuania
Danas Ridikas	Lithuania	Rimantas Levinskas	Lithuania
Danutė Vaičiukynienė	Lithuania	Rita Plukienė	Lithuania
Darius Albrektas	Lithuania	Robertas Alzbutas	Lithuania
Darius Biekša	Lithuania	Robertas Mikalauskas	Lithuania
Darius Milčius	Lithuania	Robertas Navakas	Lithuania
Darius Virbukas	Lithuania	Robertas Poškas	Lithuania
Diana Adlienė	Lithuania	Rolandas Jonynas	Lithuania
Diana Meilutytė-Lukauskienė	Lithuania	Rolandas Paulauskas	Lithuania
Diana Šarauskienė	Lithuania	Rolandas Urbonas	Lithuania
Edgaras Misiulis	Lithuania	Romualdas Kėželis	Lithuania
Egidijus Norvaiša	Lithuania	Romualdas Škėma	Lithuania
Egidijus Saulius Juodis	Lithuania	Saulė Milčiuvienė	Lithuania
Egidijus Urbonavičius	Lithuania	Sergej Zhdanok	Belarus
Eglė Biekšienė	Lithuania	Sigitas Kadiša	Lithuania
Eglė Jaraminienė	Lithuania	Sigitas Masaitis	Lithuania
Enn Mellikov	Estonia	Sigitas Rimkevičius	Lithuania
Ernestas Narkūnas	Lithuania	Simona Tučkutė	Lithuania
Eugenija Farida Dzenajavičienė	Lithuania	Stanislovas Vrubliauskas	Lithuania
Eugenijus Perednis	Lithuania	Stasys Gasiūnas	Lithuania
Eugenijus Ušpuras	Lithuania	Stasys Šinkūnas	Lithuania
Farida Dzenajavičienė	Lithuania	Sten Bergstrom	Sweden
Feliksas Zinevičius	Lithuania	Svetlana Danilova Tretiak	Belarus
Finn Ravndal	Norway	Šarūnas Varnagiris	Lithuania
Florentin Paladi	Moldova	Tadas Kaliatka	Lithuania
Gediminas Stankūnas	Lithuania	Tomas Deveikis	Lithuania
Gediminas Vasiliauskas	Lithuania	Tomas Sabonis	Lithuania
Gediminas Vilkevičius	Lithuania	Vaclovas Kveselis	Lithuania
Giedrė Streckienė	Lithuania	Vaclovas Miškinis	Lithuania
Giedrius Gecevičius	Lithuania	Vaidas Matuzas	Lithuania
Giedrius Laukaitis	Lithuania	Valdas Girdauskas	Lithuania
Giedrius Šiupšinskas	Lithuania	Valdas Ragaišis	Lithuania
Gintautas Dundulis	Lithuania	Valentinas Klevas	Lithuania
Gintautas Miliauskas	Lithuania	Victor A. Zhovyansky	Ukraine
Gvidonas Labeckas	Lithuania	Vidas Lekavičius	Lithuania
Grigorijus Duškesas	Lithuania	Viktorija Bobinaitė	Lithuania
Inga Konstantinavičiūtė	Lithuania	Viktorija Grigaitienė	Lithuania
Inga Radžiūnienė	Lithuania	Viktorija Mimaitė	Lithuania
Inga Stasiulaitienė	Lithuania	Vilma Čipinytė	Lithuania
Inga Valuntienė	Lithuania	Violeta Makarevičienė	Lithuania
Irina Kliopova	Lithuania	Violeta Pukelienė	Lithuania

Iveta Varnagirytė-Kabašinskienė	Lithuania	Violeta Vaitkevičienė	Lithuania
Jolanta Dvarionienė	Lithuania	Virginijus Radziukynas	Lithuania
Jonas Baltrušaitis	USA	Virginijus Vileiniškis	Lithuania
Juozas Gudzinskas	Lithuania	Vitas Valinčius	Lithuania
Jūratė Karbauskaitė	Lithuania	Vykintas Šuksteris	Lithuania
Jūratė Kriaučiūnienė	Lithuania	Vytautas Abromaitis	Lithuania
Jūratė Žaltauskaitė	Lithuania	Vytautas Liesionis	Lithuania
Jurij Tonkonogij	Lithuania	Vytautas Grigas	Lithuania
Justas Kažys	Lithuania	Vytautas Martinaitis	Lithuania
Karolina Čepurnienė	Lithuania	Vytautas Stankus	Lithuania
Karolis Gedvilas	Lithuania	Vytis Kopustinskas	Lithuania
Kęstutis Buinevičius	Lithuania	Vladislovas Algirdas Katinas	Lithuania
Kęstutis Čiuprinskas	Lithuania	Žaneta Simanavičienė	Lithuania
Kęstutis Navickas	Lithuania	Žaneta Stasiškienė	Lithuania
Kęstutis Valančius	Lithuania	Žilvinas Nakutis	Lithuania
Kęstutis Venslauskas	Lithuania	Živilė Rutkūnienė	Lithuania
Kristina Brinkienė	Lithuania	Žydrė Kadžiulienė	Lithuania

The Board of Reviewers was formed from the experts in the field of the Conference topics.

Dear Colleagues,

We are delighted to see you here in the 16th anniversary CYSENI 2019 conference. Series of this annual conference are focused on energy issues and its wide interpretation. Providing good solutions to our energy sector and sustainable usage of natural resources require interdisciplinary approach, hence this criterion is well fulfilled in this conference. The conference once again has brought together young researchers and scientists to discuss recent trends in energy sector worldwide. Findings of cost-effective and acceptable methods to improve energy sector in Europe and worldwide are key future targets. Generally, energy covers a wide spectrum of scientific directions with their certain problems and unsolved issues. This calls for high-quality researches and deeper knowledge.

The Conference CYSENI 2019 provides a setting for discussing recent developments in a wide-variety of topics including over fifteen scientific sessions covering the conference main theme on energy issues. In total 70 research papers were submitted from 14 countries. This year conference is a good opportunity for participants coming from Belarus, Estonia, Germany, Hungary, Israel, Jordan, Latvia, Russia, Sakartvelo (Georgia), Spain, Thailand, Turkey and Ukraine to present and discuss topics in their respective research areas.

We thank all the contributors who made this conference possible. This includes all persons from scientific and organising committees. We would like to thank all participants for their contributions to the Conference program and submission their research papers. Moreover, special thanks go to two keynote speakers – Christopher S. Kulander (USA) and Marco Binotti (Italy). The funding from all the sponsors is well acknowledged and appreciated, therefore once more we would like to thank our main sponsors: Soil Remediation Technologies, AGA, EUROfusion; and cooperation partners Kaunas City Municipality and public enterprise “Kaunas IN”.

We are looking forward to the CYSENI 2020 that will be held on May 21-22, 2020 at the same location. We hope that it will be an interesting and enjoying as its sixteenth predecessors.

Sigitas Rimkevičius
Chair of the scientific committee
Lithuanian Energy Institute

Vytautas Akstinas
Chair of the organizing committee
Lithuanian Energy Institute

CONTENT

KEYNOTE SESSION (2)

I. RENEWABLE ENERGY SOURCES (8)

II ENERGY EFFICIENCY AND RELIABILITY (9)

III SMART ENERGY NETWORKS (3)

IV ENERGY ECONOMICS AND POLICY (9)

V HYDROGEN ENERGY AND FUEL CELL TECHNOLOGIES (0)

VI FUSION ENERGY (1)

VII NUCLEAR FISSION AND RADIATION PROTECTION (6)

VIII COMBUSTION AND PLASMA PROCESSES (9)

IX THERMAL PHYSICS, FLUID MECHANICS AND METROLOGY (10)

X MATERIALS SCIENCES AND TECHNOLOGY (7)

XI GLOBAL CHANGE AND ECOSYSTEMS (2)

XII CROSS-CUTTING ENERGY ISSUES (3)

CYSENI 2019, May 23-24, Kaunas, Lithuania
ISSN 1822-7554, www.cyseni.com

SHALE GAS AND LNG IN THE USA – LESSONS FOR EUROPE

Christopher S. Kulander
South Texas College of Law Houston,
Harry L. Reed Oil & Gas Law Institute
1303 San Jacinto St, Houston, Texas 77002, USA
Email: ckulander@stcl.edu

ABSTRACT

Technological advances in hydrocarbon extraction, such as modern directional drilling and hydraulic fracturing, have sparked a boom in North America. This surge has helped to keep commodity prices down worldwide and heighted interest and investment in expanding the capacity of the worldwide LNG market. A locus of this wave of investment is Louisiana and Texas, United States, resulting in that region providing 17% of worldwide exporting capacity.

This presentation describes the recent phenomena of oil and natural gas development from shale and similar sources in North America and the resultant opportunities for LNG development and export, both with an eye towards making suggestions for Europe. This presentation first covers what "shale gas" is and the various developments in technology and processes that promise to reduce the environmental footprint of shale development while promoting its efficiency. Second, the benefits of unconventional shale development are discussed. Third, several concerns and responses are described, including acquisition of water, fracturing fluid ingredient disclosure, surface use issues, fracturing fluid disposal, and trespass.

The shale gas boom in North America will permit more American LNG exports and Europe will be an important destination. This presentation discusses how the energy security of Europe, especially Eastern Europe, can be enhanced with American LNG to provide political and economic security. North American-sourced LNG and, possibly, locally-derived sources of unconventional natural gas as alternatives to coal and Russian natural gas provides a means of curtailing CO_2 emissions while restraining Russia. The presentation finishes with predictions about the future of LNG exports from North America and the response of demand worldwide.

Keywords: energy security, hydraulic fracturing, LNG, natural gas, oil, shale gas, unconventional energy

CYSENI 2019, May 23-24, Kaunas, Lithuania
ISSN 1822-7554, www.cyseni.com

CONCENTRATING SOLAR POWER: RENEWABLE AND DISPATCHABLE ENERGY FOR THE FUTURE

Marco Binotti
Politecnico di Milano
Via Lambruschini 4, 20156 – Italy
Email: marco.binotti@polimi.it

ABSTRACT

Concentrating Solar Power (CSP) can play an important role in the near future energy scenario thanks to its capability of providing dispatchable, carbon-free, renewable electric energy. CSP systems use a series of mirrors or lenses to concentrate the direct solar radiation and convert it into high temperature heat then used to run a conventional power cycle. The introduction of a cost-effective thermal energy storage decouples thermal energy collection from its conversion into electricity allowing for night production or seeking for high electricity prices. Currently there are about 5 GW of installed CSP plants mainly based on parabolic trough collectors (3.7 GW) and solar tower technology (0.6 GW). The average Levelized Cost of Electricity (LCOE) of CSP plants is currently of about 150-190 $/kWh, far from being competitive with other renewables such as PV and wind, but it is characterized by strong potential cost reductions. Solar towers are currently recognized as the most promising CSP technology in terms of potential LCOE reduction, thanks to the possibility of achieving higher concentration ratios in the solar field (500-100 vs 80 for parabolic trough) and thus improving the thermodynamic conversion efficiency.

The main research programs in the CSP field (SunShot, ASTRI, etc.) are focusing on further developing the solar tower technology in order to increase performance and lower costs. Solar Salts currently used as heat transfer fluid (HTF) in solar tower receivers, allow achieving 565 °C, while research is focusing on new receiver technologies able to achieve temperatures > 700 °C. High temperature receivers technologies under investigation are based on either high temperature liquid HTF (e.g. new molten salts mixtures, sodium), gaseous HTF or solid heat transfer media (i.e. falling particles). With maximum temperatures above 700 °C, conventional steam cycles are outclassed by supercritical CO2 cycles, which are currently under investigation for different high temperature applications and should guarantee efficiencies > 50%.

Keywords: Concentrating Solar Power, Dispatchability, solar receivers, supercritical CO2

CYSENI 2019, May 23-24, Kaunas, Lithuania
ISSN 1822-7554, www.cyseni.com

MICROWAVE PRETREATMENT OF OLIVE MILL SOLID WASTE FOR BIOETHANOL AND BIOSORBENT PRODUCTION

H. N. Abu Tayeh, Y. Gerchman
University of Haifa
199 Aba Khoushy Avenue, 3498838 – Israel
Email: hebaabutayeh@yahoo.com

H. Azaizeh
Tel Hai college,
Department of Environmental Sciences
Upper Galilee 12208 – Israel
&
Institute of Applied, Research The Galilee Society
Shefa-Amr, 20200, Israel

ABSTRACT

In the last decade there is much interest in bio-based fuel production such as ethanol, especially as transportation fuel replacements. To-date, ethanol is produced mainly from corn and sugarcane, raising issues of competition with food crops and the use of land, water and nutrients. One solution is the utilization of agriculture lignocellulose waste as a feedstock for ethanol production.

An interesting waste is the Olive Mill Solid Waste (OMSW). Olives are an important agro-industrial sector in the Mediterranean region, mainly for olive oil production where during the milling process more than 6 million tons/year of OMSW produced worldwide. This waste is rich in cellulose and polyphenols, and is considered as an environmental nuisance without proper economical solution. Converting the cellulolytic fraction of OMSW into ethanol was suggested, but the presences of lignin make the enzymatic hydrolysis a complex process, bringing up the need for an effective pretreatment process.

We have tested two pretreatment processes for OMSW - mild conductive heat with added weak acids and microwave heating with weak acids. After either pretreatment, the biomass was enzymatically saccharified, and the hydrolysate was fermented using commercial yeasts. Finally, the use of the remnants of the process was tested as heavy metal sorbent.

The microwave pretreatment followed by enzymatic hydrolysis resulted in ca 100% conversion of cellulose to glucose, while the conductive-heat pretreatment showed only 41% conversion. The fermentation of the microwave treated OMSW resulted in 85% theoretical yield of ethanol in comparison to the conductive heating pretreatment which resulted only in 37%. Microwave treatment resulted in the production of the best heavy metal absorbent. These results could facilitate the conversion of lignocellulosic biomass into ethanol, which was our major goal.

Keywords: Olive mill solid waste, lignocelluolose, microwave pretreatment, bioethanol

1. INTRODUCTION

Recently there is much interest in bio-based fuels such as ethanol [1]. To-date, ethanol is produced mainly from corn and sugarcane,, raising issues of competition with food crops on land, water and nutrient use [2]. One solution is the utilization of agricultural lignocellulose waste as a feedstock [3]. Such waste is rich in cellulose, hemi-cellulose and lignin [4-6]. The cellulose could be converted into simple sugars and fermented into ethanol. One such interesting waste in the Mediterranean region is olive mill solid waste (OMSW). More than 97% of the global olive production is concentrated in the Mediterranean region, where Spain being the main world producer

(7,870,000 tons), followed by Italy, Greece, Turkey, Morocco and Tunisia. On a global scale, olive production in 2013 exceeded 20,000,000 tons [7].

The olive oil production is an important agro-industrial sector in the Mediterranean, with ~ 2.5 million olive growers (one-third of EU farmers) and an average production of 2.8 million metric tons per a year [8]. Olive oil production result in large amount of organic rich waste, where the production of one metric ton of olive oil using three-phase process result in an average of ca 0.6 ton of OMSW. The OMSW is considered as an environmental pollutant when disposed into lands. Different solutions have been suggested to treat OMSW, but so far no viable solution was found [9-12].

Some attempts were made to use OMSW as feedstock for ethanol production but saccharification of the cellulose and hemicelluloses was complicated due to the high content of lignin (up to 40% w/w), resulting in the need for effective pretreatment. Many chemical-physical pretreatments were suggested to solve this problem, but most of them were either energetically expensive or produce toxic by-products that could hamper downstream ethanol production process [13-15].

Microwave heating is a well-established pretreatment of biomass and it should be investigated in depth for OMSW biomass. Recently, microwave pretreatment was re-used by several research groups, most of them focusing on enhancing enzymatic digestibility of the biomass [16]. We have tested the use of microwave pretreatment on OMSW as biomass for ethanol production.

2. MATERIAL & METHODS

2.1. Raw material

The OMSW was collected from a nearby olive mill (Iksal, Israel) during the olive season of 2016. The OMSW was air dried in the shade, grinded, and sieved where particles from 0.25 mm to 1 mm were collected and kept in a sealed container at room temperature until use.

2.2. Biomass treatment and Biosorbent production

OMSW was suspended in water and aqueous acids were added. Heating was done using laboratory microwave with temperature setting of 140 °C and different residence time, or were autoclaved at 120 °C. Final acid concentration was 0.6 M for formic acid (FA), 2% (w/v) for sulfuric acid (SA) and distilled water (DW) as control. Produced sugar and fermentation inhibitors were determined using High Pressure Liquid Chromatography (HPLC) and the pre-treated biomass (after the liquid solid seperation) was subject to enzymatic hydrolysis using commercial cellulase (CTec2, Novozyme or Accelerase 1500, Dupont). Sugars and fermentation inhibitors in the hydrolysate were quantified as described above, and the solid remnants were tested for their ability to absorb heavy metals from water, as described by Abdelhadi et al. 2017 [17]. A mix stock solution of Cd + 2, Cu + 2, Ni + 2, Pb + 2, Se + 2 and Zn + 2 was prepared by dissolving their respective salts [$Pb(NO_3)_2 \cdot 6H_2O$, $Ni(NO_3)_2 \cdot 6H_2O$, $ZnSO_4 \cdot 7H_2O$, Na_2SeO_4, $3CdSO_4 \cdot 8H_2O$, $CuCl_2 \cdot 2H_2O$] in deionized water at a final concentration of 50 ppm of each tested heavy metal. The initial pH of the prepared mix stock solution was 5.2.

2.3. Bioethanol production

The hydrolysate was subject to fermentation process using commercial yeasts Ethanol red® (Fermentis) yeast strain. The yeast was grown at 35 °C on YPG agar (2% glucose, 1% yeast extract, 2% peptone, and 2% agar), and a single colony was transferred into a sterile liquid YPG medium for overnight cultivation. The cell suspension was added to the hydrolysate. The mixture was incubated at 35 °C, shaked at 120 rpm for 120 hours, and samples were taken at the designated time points for analysis of sugars and ethanol production using HPLC.

3. RESULTS

Fig. 1 & Fig. 2 show that the use of heating method caused highly significant effect on sugars loss as well as the production of inhibitors during the pre-treatment process. Microwave (MW) with either acids gave the highest sugar loss and fermentation inhibitors formation followed by MW with water, where the inhibitors included mixture of acetic and FA, furfural and Hydroxymethylefurfural (HMF). Autoclave with acids gave similar levels of FA but very little amounts of the other inhibitors. Given that FA levels higher than 1.5 g/L are considered inhibitory for the fermentation process [18], especially in the presence of HMF and Furfural [19] where a detoxification step [20, 21] or separation of the solids from the pretreatment liquor before enzymatic hydrolysis (as done here) is required.

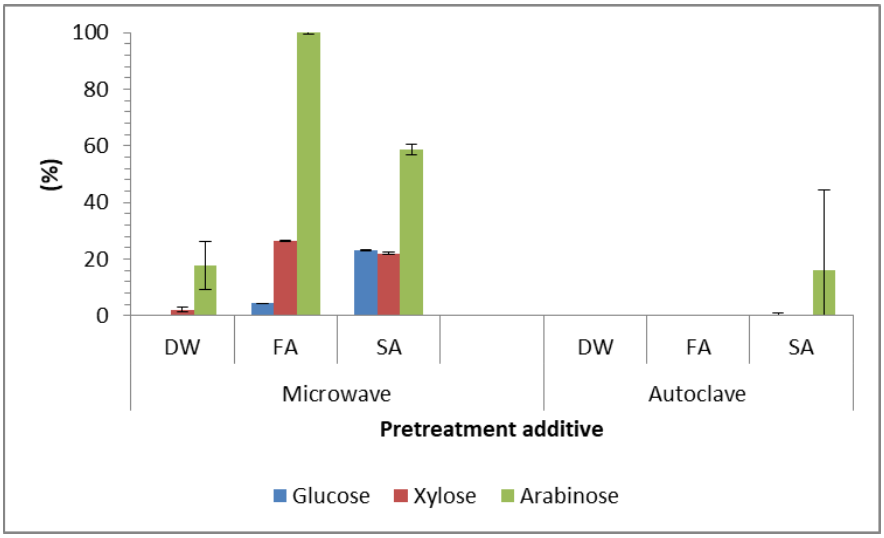

Fig. 1. Percentages of sugar lose into the liquor of microwave or autoclave pretreatment. Bars represent average ± SD of three replicates

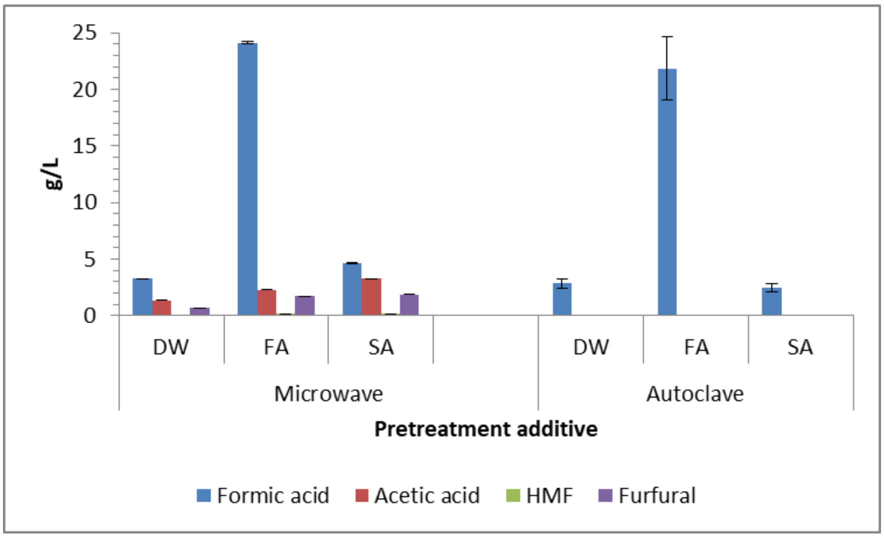

Fig. 2. Fermentation inhibitors content in the liquor of microwave or autoclave pretreatment. Bars represent average ± SD of three replicates

Fig. 3 presents the hydrolysate that was tested, in most cases microwave treatment resulted in the best enzymatic saccharification, especially when combined with FA, yielding 100% to 90%

saccharification of the cellulose fraction, using the CTec2 or Accellerase, respectively. MW with SA resulted in dramatic decrease in sugar release (27% and 17%), while addition of water only resulted in intermediate values (70% and 53%). Autoclave treatment resulted in much lower glucose release, with FA resulting in 41% and 31%, SA 32% and 16%, and water 28% and 8%, for the two enzymes, respectively. Table 1 summarizes the ethanol production when the fermentation was tested, where maximum ethanol production was obtained from MW with FA, resulting in 12.8 g/L, which is 85% of the maximum theoretical ethanol yield, and equivalent to 7.3 g ethanol per 100 g of OMSW (7.3%). Herreo et al. (2016) used acid pretreatment of the two-phase OMSW followed by enzymatic hydrolysis; the concentration of the produced ethanol was 3.15 g/L (7.34g ethanol/kg OMSW) [22]. Senkevich et al. (2012) investigated the effect of thermochemical pretreatment on ethanol production. The highest yield was 49.59 ± 1.79 ml ethanol per kg of OMSW residue [23].

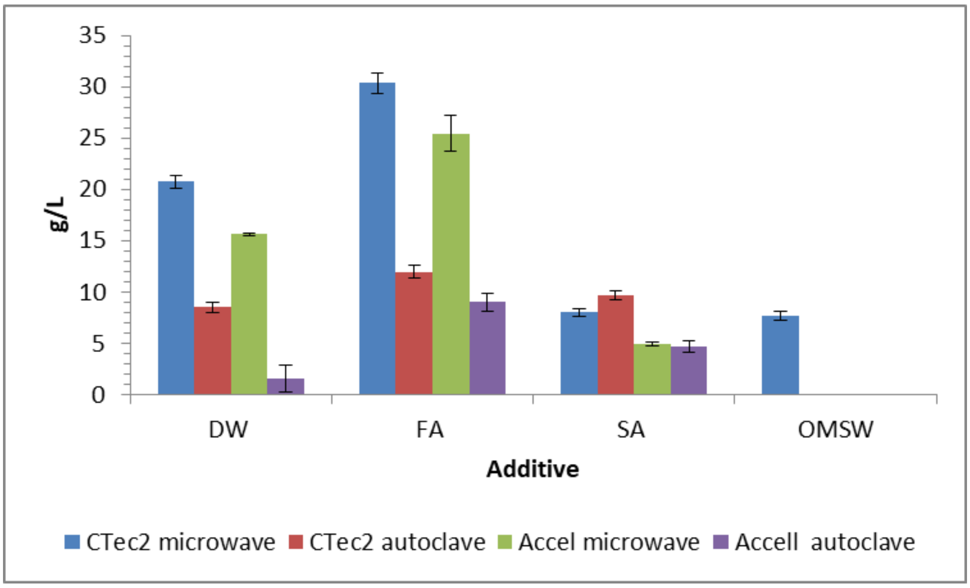

Fig. 3. Glucose released from the OMSW after the different pre- and enzymatic treatments as g/L of cellulose released as glucose. Bars represent average ± SD of three replicates

Table 1. The ethanol concentration produced in different combination of pretreatment, additive, and enzyme saccharification

Enzyme	**Treatment**	**Additive**	**Experimental EtOH (g/L)**
Cellic CTec2	**MW**	**DW**	9.6 ± 2.22
		FA	12.8 ± 0.67
		SA	3.45 ± 0.77
	Autoclave	**DW**	0.6 ± 0.04
		FA	5.6 ± 0.57
		SA	2.7 ± 0.3
Accellerase	**MW**	**DW**	5.1 ± 1.84
		FA	11.37 ± 1.06
		SA	1.01 ± 0.3
	Autoclave	**DW**	0.6 ± 0.5
		FA	2.2 ± 0.4
		SA	1.8 ± 0.8

Finally, to facilitate the economic potential of OMSW, we have tested the utilization of the remnant biomass as a heavy metal sorbent to treat contaminated water. The results showed effective removal of lead and copper ions, 88% and 83%, respectively, from the contaminated water, especially the remnant biomass of MW + DW + CTec2 treatment.

4. CONCLUSIONS

Microwave heating of OMSW biomass showed a potential pretreatment for bioethanol production and biosorbent compared with a conductive heat treatment. Formic acid as an additive enhanced the saccharification yeild and the ethanol production compared to sulfuric acid as additive and with no additive. Enzyme choice also had an effect, with the Cellic CTec2 resulting in a much better sorbent but only mildly better for ethanol production.

REFERENCES

1. BERHE, T., SAHU, O. Chemically Synthesized Biofuels From Agricultural Waste: Optimizimation Operating Parameters With Surface Response Methodology (CCD). *MethodsX*, 2017, Vol. 4, p. 391-403.
2. PANTI, N., PILLAI, S.G., DWIVEDI, A.H. Wheat as a Promising Substitute of Corn for Bioethanol Production. *Procedia Engineering*, 2013, Vol. 51, p. 355-362.
3. LIN, T.H., HUANG, C.F., GUO, G.L., HWANG, W.S., HUANG, S.L. Pilot-scale ethanol production from rice straw hydrolysates using xylose-fermenting *Pichia stipitis*. *Bioresource Technology*, 2012, Vol. 116, p. 314-319.
4. KUMAR, S., SINGH, S.P., MISHRA, I.M. Review- Recent Advances in Production of Bioethanol from Lignocellulosic Biomass, *Chemical Engineering Technology*, 2009, Vol. 32, No. 4, p. 517-526.
5. OLSSON, L., HAHN-HÄGERDAL, B. Fermentation of lignocellulosic hydrolysates for ethanol production. *Enzyme and Microbial Technology*, 1996, Vol. 18, No. 5, p. 312-331.
6. WYMAN, C. E. Ethanol from lignocellulosic biomass: technology, economics, and opportunities. *Bioresource Technology*, 1994, Vol. 50, p. 3-16.
7. *Food and Agriculture Organization of the United Nations* – Statistics Division. 2015, [referred on the 13th of February in 2015]. <http://faostat3.fao.org>
8. *International Olive Council production data*, [referred on the 20th of May in 2018]. <http://www.internationaloliveoil.org/estaticos/view/131-world-olive-oil-figures>
9. KAVDIR, Y., KILLI, D. Influence of olive oil solid waste applications on soil pH, electrical conductivity, soil nitrogen transformations, carbon content and aggregate stability. *Bioresource Technology*, 2008, Vol. 99, p. 2326-2332.
10. MORILLO, J.A., ANTIZA-LADISLAO, B., MONTEOLIVA-SÁNCHEZ, M., RAMOS-CORMENZANA, A., RUSSELL, N.J. Bioremediation and biovalorisation of olive-mill wastes. *Applied Microbiology and Biotechnology*, 2009, Vol. 82, p. 25-39.
11. AZAIZEH, H., JADOUN, J. Co-digestion of olive mill wastewater and swine manure using UASB bioreactors for biogas production. *Journal of Water Resource and Protection*, 2010, Vol. 2, p. 314-321.
12. SHABTAY, A., HADAR, Y., EITAM, H., BROSH, A., ORLOV, A., TADMOR, Y., IZHAKI, I., KEREM, Z. The potential of Pleurotus-treated olive mill solid waste as cattle feed. *Bioresource Technology*, 2009, Vol. 100, p. 6457-6464.
13. ABU TAYEH, H., NAJAMI, DOSORETZ, C., TAFESH, A., AZAIZEH, H. Potential of bioethanol production from olive mill solid wastes. *Bioresource Technology*, 2014, Vol. 152, p. 24-30.

14. BALLESTEROS, I., OLIVA, J. M., SAEZ, F., BALLESTEROS, M. Ethanol production from lignocellulosic byproducts of olive oil extraction. *Applied Biochemistry and Biotechnology*, 2001, Vol. 91-93, p. 237-252.
15. CARA, C., ROMERO, I., OLIVA, J. M., SAEZ, F., CASTRO, E. Liquid hot water pretreatment olive tree pruning residues. *Applied Biochemistry and Biotechnology*, 2007, Vol. 137-140, p. 379-394.
16. XU, J., CHEN, H., KÁDÁR, Z., THOMSEN, A. B., EJBYE, J., PENG, H. Optimization of microwave pretreatment on wheat straw for ethanol production. *Biomass and Bioenergy*, 2011, Vol. 35, p. 3859-3864.
17. ABDELHADI, S.O., DOSORETZ, C.G., RYTWOC, G., GERCHMAN, Y., AZAIZEH, H. Production of biochar from olive mill solid waste for heavy metal removal. *Bioresource Technology*, 2017, Vol. 244, p. 759-767.
18. MAIORELLA, B., BLANCH, H.W., WILKE, CR. By-product inhibition effects on ethanolic fermentation by *Saccharomyces cerevisiae*. *Biotechnology and Bioengineering*, 1983, Vol. 25, p. 103-121.
19. LARSSON, S., HAHN-HÄGERDAL, B., TENGBORG, C., STENBERG, K., ZACCHI, G., NILVEBRANT, N-O. The generation of fermentation inhibitors during dilute acid hydrolysis of softwood. *Enzyme and Microbial Technology*, 1999, Vol. 24, No. 3-4, p.151-159.
20. JÖNSSON, L.J., ALRIKSSON, B., NILVEBRANT, N-O. Bioconversion of lignocellulose: inhibitors and detoxification. *Biotechnology for Biofuels*, 2013, Vol. 6, p.16.
21. JÖNSSON, L.J., MARTÍN, C. Pretreatment of lignocellulose: Formation of inhibitory by-products and strategies for minimizing their effects. *Bioresource Technology*, 2016, Vol. 199, p. 103-112.
22. HERREO, M.L., SARDELLA, M.F., RODRIGUEZ, L., MAMANI, A., MONTORO, M.L., DEIANA, C. Congress Brasileiro de Engenharia Química (COBEQ) 2016, Encontro Brasileiro sobre o Ensino de Engenharia Química (ENBEQ 2016). Second generation bioethanol from waste of the manufacturing of olive oil. 2016 September 25-29.
23. SENKEVICH, S., NTAIKOU, I., LYBERATOS, G. Bioethanol Production from thermochemically pre-treated olive mill solid residues using the yeast *Pachysolen tannophilus*. *Global NEST Journal*, 2012, Vol. 14, No. 2, p. 118-124.

CYSENI 2019, May 23-24, Kaunas, Lithuania
ISSN 1822-7554, www.cyseni.com

MINERALOGICAL CHANGES IN ASH OF HEMP AND WHEAT STRAW AT DIFFERENT ASHING TEMPERATURES

D. Čepauskienė, N. Pedišius
Lithuanian Energy Institute
Breslaujos str. 3, LT-44403 Kaunas – Lithuania
Email: Deimante.Cepauskiene@lei.lt

ABSTRACT

A growing demand for energy and increasing environmental pollution induce search for alternatives of fossil fuel. Currently the interest in using biofuels is growing rapidly, as a result this leads to the introduction of non-woody biomass fuels into the market such as herbaceous plants and agricultural waste. However, the use of such fuel is still limited due to technical problems associated with corrosion of equipment, ash agglomeration, fouling and slagging. In this study, two types of agromass, hemp and wheat straws, were burned at nine different temperatures: 550 °C, 600 °C, 650 °C, 700 °C, 750 °C, 800 °C, 900 °C, 1000 °C, 1500 °C. The crystalline phase of the ash was analysed by X-ray diffraction (XRD), investigation of surface morphology characteristics was performed using scanning electron microscopy-energy dispersive X-ray spectometry (SEM – EDX). Ash fusion characteristics (AFC) were identified using Carbolite. The results showed that increasing ashing temperature leads to decreasing content of ashes. Hemp ash content decreased by 1.45%, while wheat straw ash decreased only by 0.89% comparing ashes at 550 °C and 1000 °C. The X-ray results indicated that increasing temperature leads to the decreasing amount of alkali salts and promotes formation of silicates. Furthermore, potassium compounds (KCl, K_2SO_4, KPO_3) have been identified in wheat straw ash which leads to a lower ash melting temperature.

Keywords: Hemp, wheat straw, ash, ash melting, morphology, mineral composition

1. INTRODUCTION

In recent decades, there has been an increased importance placed on fuels and power generation methods that emit reduced amounts of CO_2, a key contributor to anthropogenic changes to the atmosphere [1]. Latterly much attention has been focused on identifying suitable biomass species, which can provide high-energy outputs, to replace conventional fossil fuel energy sources [2].

The cultivation of hemp was legalized since 1 January 2014 after the Law of the Republic of Lithuania on Hemp came into force. According to the law, the species of hemp with a tetrahydrocannabinol content not exceeding 0.2% can be cultivated. Areas of the land where hemp is cultivated are expanding every year: nearly 2500 ha of hemp were declared in 2017, and this is twice as much as in 2014 (1060 ha). The expanding areas of the land where hemp is cultivated produce a considerable quantities of waste material (hemp stems) that can be used for agrofuel production. Wheat is the most widely grown grain crop in Lithuania. It occupies the area of more than 210 thousand ha. Annual amount of wheat straw is about 3 million tons and only a small part of it is used according to its original purpose (animal litter, feed) [3].

The chemical composition of biomass fuels and especially the content of ash forming elements influence the choise of an appropriate combustion and process control technology [4]. Woody biomass composition is quite stable, and contains large quantities of calcium (Ca) and silicon (Si), yet less phosphorus (P) and potassium (K). On the contrary, agromass composition varies greatly. Both grasses and straws contain large quanitites of Si and K. Smaller amounts of Ca and magnesium (Mg) are found in grasses, the same goes for aliuminium (Al) and sodium (Na) in straw [5]. Moreover, the composition of agromass depends on the soil type, harvesting season [6], climate, type of fertilizer, its concentration and frequency of fertilization [7] and impurities that fall in during preparation and transportation of agromass [8]. However, burning of such fuels is still limited due to technical problems associated with corrosion of equipment, ash agglomeration, fouling and slagging of partially fused deposits on furnace walls and convection heat surfaces.

It is essential to know the concentrations of the main ash forming elements in agromass and the ways they are structured and assembled in the fuel as part of different salts and minerals. Potassium content is important because it indicates potential ash fusion and deposition by vaporization and condensation. In biomass combustion K and Cl can be released in gas such as HCl, KCl and potassium exists as potassium silicate, aluminosilicate and sulphate. During the cooling process the gaseous potassium may condense on the coarse fly ash as KCl and K_2SO_4. The K, sulphur (S) and chlorine (Cl) enrichments in ash are very harmful because of corrosion risk [9].

This study focuses on determination of chemical composition and mineralogical effects on ash by burning fuel at temperatures from within the ashing range to near complete melting. Although there are a few studies on the effects of ashing temperature on the characteristics of biomass ash, but is still needed more knowledge on agromass types which are less investigated and analyzed.

2. METHODOLOGY

Wheat straw and hemp agromass were used in this research. Both samples were dried in low temperature laboratory furnace under temperature of 105 °C and were grinded to a particle size of < 1 mm. The ash content of samples were determined using a muffle furnace (Nabertherm) at all temperatures (550 °C, 600 °C, 650 °C, 700 °C, 750 °C, 800 °C, 900 °C, 1000 °C) according to ISO 18122:2016. The ashing ration is obtained by weight the mass of raw materials and the corresponding ash. Ash melting behaviour was conducted in a muffle furnaces with the monochromatic video camera CAF DIGITAL 380–415V with reference to CEN/TS 15370-1. Ashes were grinded with a pestle to obtain particles with a size of less than 0.075 mm. Using a mould with a defined pressure, a moistened (with ethanol) ash powder was used to form cylindrical ash samples with a size of 5 × 5 mm. Samples were heated in ash fusion furnace under reducing atmosphere. A furnace temperature was raised up to 550 °C. Then temperature was gradually raised 5 °C min^{-1} and photos were automatically made every interval of 2 °C till temperature has reached 1500 °C. The temperature at which the phase of the sample changed was recorded. The main four ash melting phases are: SST – shrinkage starting temperature or softening temperature, DT – deformation temperatute, HT – hemisphere temperature, FT – fusibility temperature.

The calorific value of the samples was determined according to ISO 18125:2017 using calorimeter IKA C 5000. Determination of total carbon (C), hydrogen (H) and nitrogen (N) was conducted using a Flash 2000 elemental analyser. The Cl and S concentration was obtained with a Dionex ICS-5000 ion chromatography system according to ISO 16994:2015.

The crystalline phase analysis of ash was conducted with an X-ray diffractometer (XRD) type D8Bruker. Each sample was scanned for 45 minutes using Θ–2Θ modification in the interval 20°–70°. A source of X-ray – CuKα1. Compounds were identified using EVA Search-Match program from PDF-2 database.

The morphology and microchemistry of the wheat straw and hemp ash were examined by scanning electron microscopy (SEM) Hitachi S-3400N equipped with energy dispersive X-ray spectroscopy (EDX) Bruker Quad 5040.

3. RESULTS AND DISSCUTIONS

Table 1 presents the main wheat straw and hemp agromass and their ash characteristics. As the results show, the ash content of wheat straw is 7.74% and is twice as high as that of hemp (3.22%). Increased ash content results in lower calorific value. The results show that a calorific value of hemp is nearly 1 MG/kg higher compared to wheat straw. The content of N in the agromass was determined to be higher compared to other main elements, such as C, H and O . The content of N in wheat straw is 0.40% higher than in the agromass of hemp. N contents of agricultural residues is higher than those of woody biomass due to the large amounts of N fertiliser applied during crop growth. During combustion N is almost entirely converted to gaseous N_2 and oxides of nitrogen. The tested samples of agromass contained very little of Cl, its content does not exceed 0.05%. These are relatively low values that can be explained by the fact that both the wheat and hemp agromass were kept outdoors after harvesting, they were exposed to precipitation and therefore Cl could be washed out from them (natural leaching by rainfall).

Table 1. Characteristics of the selected agromass types

	Wheat straw (agromass/ash)	**Hemp (agromass/ash)**
Ash, %	7.74/-	3.22/-
Heating Value, MJ/kg	18.57/-	19.40/-
C, %	46.02/1.76	48.53/8.17
N, %	0.90/-	0.50/-
H, %	5.40/0.88	5.62/0.22
S, %	0.07/1.25	-/1.14
O, %	39.87/n.d	42.13/n.d
Cl, %	0.04/0.30	0.02/0.14

Table 2 presents melting temperatures of wheat straw and hemp ash. There is a significant difference in melting points of ash. The primary melting SST phase of wheat straw ash is observed at 783 °C, while the hemp ash starts to melt when temperature reaches 1079 °C. The final melting phase of the ash FT is when the ash sample is completely melted. In case of hemp, FT temperature is 1496 °C, wheat straw finally melts at the temperature of 1175 °C. The data obtained show that SST temperature of hemp ash is similar to FT temperature of wheat straw ash. It means that at the temperature at which hemp ash begins to melt, wheat straw ash approaches the full melting phase.

Table 2. Ash melting temperatures of wheat straw and hemp

Sample	**SST (°C)**	**DT (°C)**	**HT (°C)**	**FT (°C)**
Wheat straw	783	869	1099	1175
Hemp	1079	1418	1490	1496

The ash content of agromass at different temperatures (550 °C, 600 °C, 650 °C, 700 °C, 750 °C, 800 °C, 900 °C, 1000 °C) are listed in Table 3. As is apparent from the results, increasing ashing temperature leads in declining content of ashes. This is due to volatile inorganic elements in organic compounds. The decrease in ash content is observed throughout the temperature range. The content of hemp ash decreases significantly at 600 °C and 650 °C, and the change in both cases is about 0.4%. In the case of wheat straw, a more significant ash content variation can be observed at 600 °C and it continues to change slightly.

Table 3. Ash content of agromass at different temperatures (± SD)

T (ºC)	**Ash (%)**	
	Wheat straw	**Hemp**
550	7.74 ± 0.07	3.22 ± 0.10
600	7.53 ± 0.01	2.81 ± 0.09
650	7.54 ± 0.01	2.35 ± 0.06
700	7.56 ± 0.19	2.31 ± 0.07
750	7.58 ± 0.21	2.15 ± 0.14
800	7.55 ± 0.19	2.02 ± 0.19
900	7.40 ± 0.17	1.90 ± 0.11
1000	7.32 ± 0.10	1.77 ± 0.07

Figure 1 present the results of elemental composition analysis distinguishing the key elements that forms ashes. Hemp ash throughout the temperature range has higher levels of Ca and Mg, wheat straw contains higher levels of K, S, P and Si. Both hemp and wheat ash contain a similar amount of Al and Na that does not exceed 1%. Cl has been identified in the hemp ashes only at 550 °C and was below 0.5%. While wheat straw ash contains more than three times the amount of Cl at the same temperature. The total content, however, does not exceed 1%. The content of Cl decreases in the temperature range from 550 to 750°C, and is no longer identified when temperature reaches 800 °C.

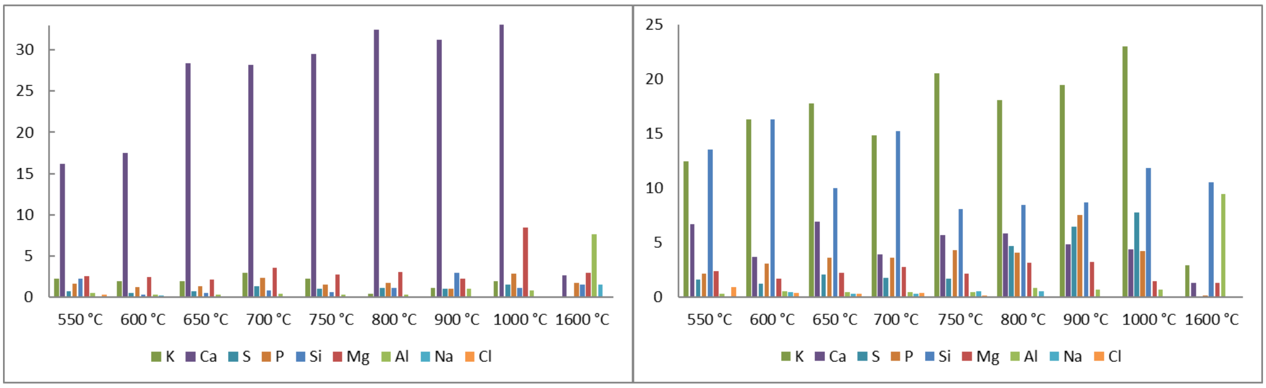

Fig. 1. Composition analysis of hemp and wheat straw ash at different ashing temperatures (%)

Figure 2 presents changes in surface morphology of wheat ash depending on temperature. Wheat ash is loose at 550 °C–600 °C, its particles are layered on top of each other, but no signs of ash melting have been determined. However, molten ash areas with loose particles attached to them can be noticed at 650 °C–800 °C. The particles are completely melted at 900 °C. The surface of accumulations of molten particles is smooth, but they differ by their shape. Completely molten areas of ash with a smooth surface develop at 1000 °C. Smaller structures of the molten particles form larger structures as they connect with each other and then evolve into large accumulations of agglomerate.

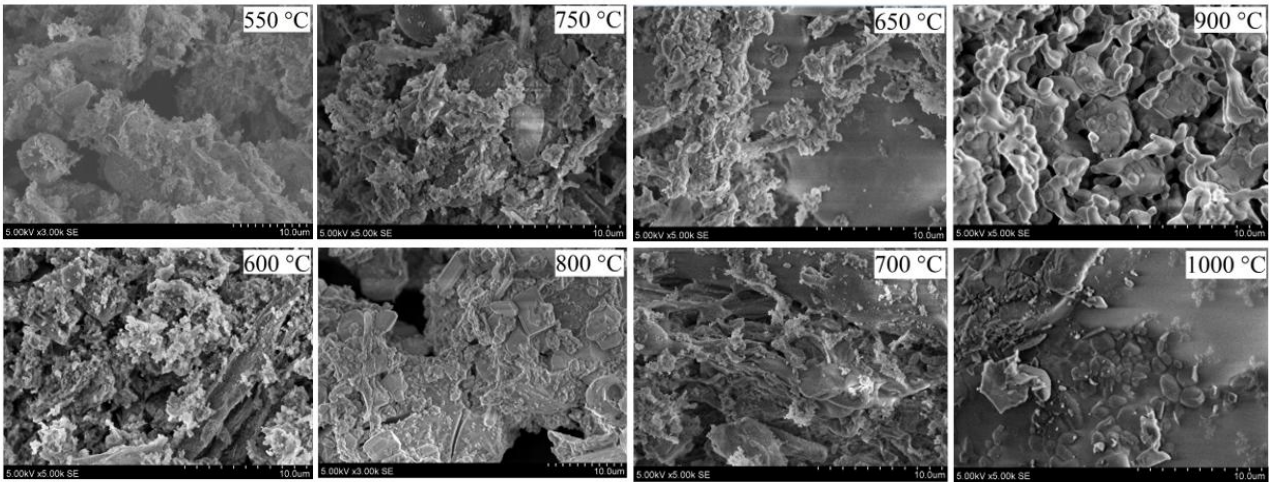

Fig. 2. SEM of wheat straw ash at different temperatures

Figure 3 presents changes in the surface morphology of hemp ash at varying temperatures. The morphology of hemp ash remains unchanged at 550 °C to 800 °C. The ash is loose, the particles are of different sizes and vary by their shape, layered, but no signs of agglomeration can be seen. A slight melting of fine particles can be noticed at 800 °C–900 °C. Melting is the most prominent at 1000 °C. Small, round-shaped ash agglomerates start to develop on the surface of the ash.

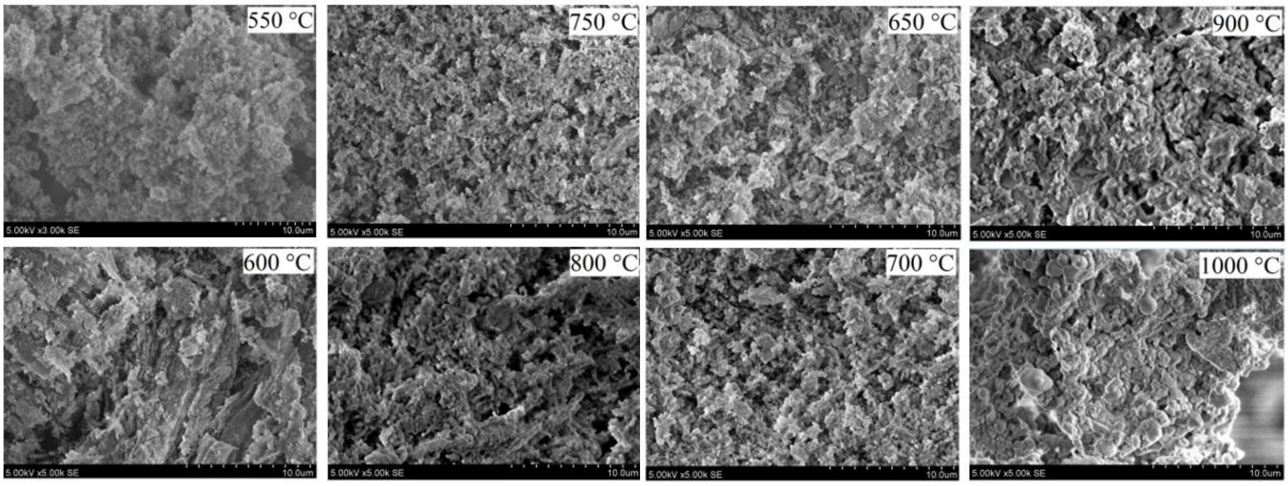

Fig. 3. SEM of hemp ash at different temperatures

Table 4 presents the results of analysis of XRD ash mineral composition variation at different temperatures. Predominantly elemental compounds are one of the most prominent differences in the mineral composition of the test samples. Wheat ash throughout the temperature range is dominated by K compounds, hemp ash is dominated by Ca compounds.

The mineral composition of wheat ash in the temperature range 550 °C–900 °C varies slightly. However, four major compounds can be distinguished: SiO, K_2SO_4, KO_2, KPO_3. In addition to these compounds, K_2CO_3 is also detected at temperatures of 600 °C and 650 °C which is not subsequently identifiable. K_2CO_3 decomposes during the endothermic reaction to form K_2O and CO_2. KO_2 can be identified in ashes until the temperature reaches 1000 °C. $KCaPO_4$ develops when the temperature reaches 800°C, and it then remains at 1000°C. KCl is determined only at a temperature of 550 °C and is not subsequently identified.

Table 4. X-ray diffraction analysis of wheat and hemp ash at different temperatures

Temperature, °C	**Wheat straw ash**	**Hemp ash**
550 °C	KCl, K_2SO_4, $KCaPO_4$, SiO_2	$CaCO_3$, SiO_2, $Ca_4O(PO_4)_2$
600 °C	SiO_2, K_2SO_4, KO_2, KPO_3, $K_2CaP_4O_{12}$, K_2CO_3	$CaCO_3$, CaO, SiO_2, $Ca_{10}(PO_4)_6O$, $Ca_3(PO_4)_2$
650 °C	SiO_2, K_2SO_4, KO_2, KPO_3, K_2CO_3	$CaCO_3$, CaO, SiO_2, $Ca_{10}(PO_4)_6O$, $Ca_3(PO_4)_2$
700 °C	SiO_2, K_2SO_4, KO_2, KPO_3, $K_2CaP_4O_{12}$	$CaCO_3$, CaO, SiO_2, $Ca_{10}(PO_4)_6O$, $Ca_3(PO_4)_2$
750 °C	SiO_2, K_2SO_4, KO_2, KPO_3, $K_2CaP_4O_{12}$	$CaCO_3$, CaO, SiO_2, $Ca_{10}(PO_4)_6O$, $Ca_3(PO_4)_2$
800 °C	SiO_2, K_2SO_4, KO_2, KPO_3, $KCaPO_4$	$CaCO_3$, CaO, $CaSO_4$, SiO_2, $Ca_{10}(PO_4)_6O$, $Ca_3(PO_4)_2$, MgO, K_2O_2, KPO_3
900 °C	SiO_2, K_2SO_4, KO_2, KPO_3, $KCaPO_4$, MgO	$CaCO_3$, CaO, $CaSO_4$, SiO_2, $Ca_{10}(PO_4)_6O$, $Ca_3(PO_4)_2$, MgO, K_2O_2, KPO_3
1000 °C	K_2SO_4, KPO_3, $KCaPO_4$	CaO, $Ca_{10}(PO_4)_6O$, $Ca_3(PO_4)_2$, MgO, K_2O, $Ca(CO_3)$, $CaSO_4$
1600 °C	Al_2O_3, Si, $MgAl_2O_4$, $KAlSi_2O_6$	$MgAl_2O_4$, $Ca_2Al_2SiO_7$, $CaMg_2Al_6O_{12}$, $CaNa_3Al(P_2O_7)_2$, $CaAl_4O_7$

As mentioned above, a mineral composition of hemp is dominated by compounds containing Ca. In this case, no significant structural changes were observed in the temperature range of 550 °C–750 °C, and the same five compounds $CaCO_3$, CaO, SiO_2, $Ca_{10}(PO_4)_6O$ and $Ca_3(PO_4)_2$ have been identified in all cases. All these compounds can be identified until the temperature reaches

1000 °C. But several additional compounds can be identified when the temperature reaches 800 °C and 900 °C. The composition of ash is complemented by $CaSO_4$, MgO, K_2O_2, KPO_3. SiO_2, K_2O_2 and KPO_3 can no longer be identified at 1000 °C, but a K_2O compound appears. It can be said that significant changes in mineral structure occur twice in the case of hemp ash and the selected temperature range. The first change in mineral composition occurs at temperatures between 750 °C and 800 °C, while the second is observed at temperatures between 900 °C and 1000 °C. Changes in mineral composition have been identified at the same temperatures at which the morphology of the ash surface changes.

4. CONCLUSIONS

1. Increasing ashing temperature leads in declining content of ashes. This is due to volatilisation of inorganic elements such as K, Cl, S.
2. Hemp ash throughout the temperature range has higher levels of Ca and Mg, wheat straw contains higher levels of K, S, P and Si.
3. Changes in mineral composition have been identified at the same temperatures at which the morphology of the ash surface changes.
4. Predominantly elemental compounds are one of the most prominent differences in the mineral composition of the test samples. Wheat ash throughout the temperature range (550 °C, 600 °C, 650 °C, 700 °C, 750 °C, 800 °C, 900 °C, 1000 °C) is dominated by K compounds, hemp ash is dominated by Ca compounds. The predominant elements have a significant impact on ash melting. A higher amount of K in wheat straw ash results in a lower ash melting point, therefore at the temperature at which hemp ash begins to melt, wheat straw ash approaches the full melting phase.

REFERENCES

1. MORRIS, J. D., DAOOD, S. S., CHILTON, S., NIMMO, W. Mechanisms and mitingation of agglomeration during fluidized bed combustion of biomass: A review. *Fuel*, 2018, Vol. 230, p. 452-473.
2. MCKENDRY, P. Energy production from biomass (part 1): overview of biomass. *Bioresource Technology*, 2002, Vol. 83, p. 37-46.
3. Agricultural information and rural business center. *Statistical information*. (2019 February 22) https://www.vic.lt/ppis/statistika/
4. BIEDERMANN, F., OBERNBERGER, I. Ash-related problems during biomass combustion and possibilities for a sustainable ash utilisation. Proceedings of international conference „World Renewable Energy Congress“. Oxford: Elsevier B. V. 2005.
5. VASSILEV, S. V., BAXTER, D., ANDERSEN, L. K., VASSILEVA, C. G. An overview of the composition and application of biomass ash. Part 1. Phase-mineral and chemical composition and classification. *Fuel*, 2013, Vol. 105, p. 40-76.
6. NIU, Y., ZHU, Y., TAN, H., HUI, S., JING, S., XU, W. Investigations on biomass slagging in utility boiler: Criterion numbers and slagging growth mechanisms. *Fuel Processing Technology*, 2014, Vol. 128, p. 499-508.
7. SCHIEMENZ, K., EICHLER-LOBERMANN, B. Biomass ashes and their phosphorus fertilizing effect on different crops. *Nutrient Cycling in Agroecosystems*, 2010, Vol. 87, No. 3, p. 471-482.
8. WANG, L., HUSTAD, J. E., SKREIBERG, O., SKJEVRAK, G., GRONLI, M. A critical review on additives to reduce ash related operation problems in biomass combustion applications. *Energy Procedia*, 2012, Vol. 20, p. 20-29.
9. MAGDZIARZ, A., DALAI, A. K., KOZINSKI, J. A. Chemical composition, character and reactivity of renewable fuel ashes. *Fuel*, 2016, Vol. 176, p. 135-145.

CYSENI 2019, May 23-24, Kaunas, Lithuania
ISSN 1822-7554, www.cyseni.com

TECHNICAL ASSESSMENT OF A THERMAL NEUTRALIZATION SYSTEM OF MUNICIPAL SOLID WASTE IN THE CITY OF LAGOS, NIGERIA

O. C. Emem, G. N. Gorbunov, Y. A. Rakhmanov, O. I. Sergienko
St. Petersburg National Research University of Information Technologies,
Mechanics and Optics
Kronverkskiy Prospekt, 49, 197101 – Russia
Email: emem.c.onis@gmail.com

ABSTRACT

As the population of African cities grow exponentially, there is an increase in urbanization and industrialization. This growth rate brings an increase in waste generation and energy consumption. The current waste management techniques employed in these cities are unacceptable, as it is evident from large unregulated dumps and open burning practice observed around the cities. These practices result into serious health and environmental challenges. Also, efforts to overcome the power issues in Nigeria have not yielded the expected results as residents still experience recurrent power outages and must rely on other not sustainable energy sources for their homes and businesses like diesel and fuel generators.

The paper considers the case of the city of Lagos, Nigeria, with a population of 21 million people, generating 13,000 tons of Municipal Solid Waste (MSW) per day. Currently, there is no integrated MSW management system in the city, and the purpose of this study is to perform initial technical evaluation of such system that is sustainable itself, reduces waste disposal and produces energy. The energy from the system could be used in addition to the energy mix in the city, through the development of a thermal neutralization system. The recovered energy from this system could be used for either hot water supply or central air-cooling systems for residents. The incinerator system could contribute to the energy mix in African cities as a source of energy that satisfies the global energy trends. The results of assessment of ecological and energy efficiency of the proposed system confirm its vital role in the country's transition from a fossil fuel dominated energy mix to clean and affordable energy system.

Keywords: Municipal solid waste, thermal neutralization system, energy mix, energy efficiency, waste disposal

1. INTRODUCTION

1.1. The waste situation

Waste is an inevitable consequence of today's life styles and economic activities [1]. Municipal Solid Waste (MSW) is inextricably linked to urbanization and economic development. As countries urbanize their economic wealth increases and as the standards of living and disposable incomes increase, consumption of goods and services increases as well. This results in a corresponding increase of the amount of waste generated [2]. This is the case in most of African cities. According to the 2017 Drivers of Migration and Urbanization in Africa report by the United Nations, more than half of the global population now lives in urban areas [3]. Over the decades, the population of most major cities in Nigeria have increased substantially. Lagos, Kano, Port Harcourt, Maiduguri, Kaduna, Ilorin, and Jos are examples of cities that have had such growth over the past 5 decades. For instance, Kano's population rose from 5.8 million people in 1991 to 9.4 million in 2006. Enugu had 174 thous. in 1965 and 712 thous. in 2006 while over the same period, Lagos had a population of less than one million, 4 million, and over 10 million, respectively [4]. The World Bank reports the Nigerian population to be over 190 million as at 2017, with a growing rate of 2.6% and MSW of over 27 million tons annually [5], [6]. Currently, Lagos alone has a massive population of 21 million people which makes it the most populated city in Nigeria, with MSW generation of 13,000 tons per day [7]. Generally, MSW in Nigeria is plagued with inefficient collection methods, insufficient coverage of the collection system, improper disposal, insufficient financial resources, absence of bylaws and standards, and inappropriate waste management technology [8]. These indicate an urgent need of sustainable MSW management and treatment technologies in Lagos.

1.2. The energy situation

The Nigeria's Federal Ministry of Power (FMP) reports that Nigeria has a peak demand of 12,800 MW with an installed electricity generation capacity of 13,308 MW [9]. Out of this, only 6,158 MW were operational in 2014 and only between 3,000 MW to 4,500 MW were generating due to unavailability of gas, equipment malfunction, water shortage or grid constraints. The poor performance of the power plants has led to acute shortage of power across the country [9], [10]. Nigeria's electricity consumption per capita tends to have had no major increase over a decade from the commissioning of its first power station in 1990, which is not a commensurate power supply for the growing population over the same period (see Fig. 1) [10], [11].

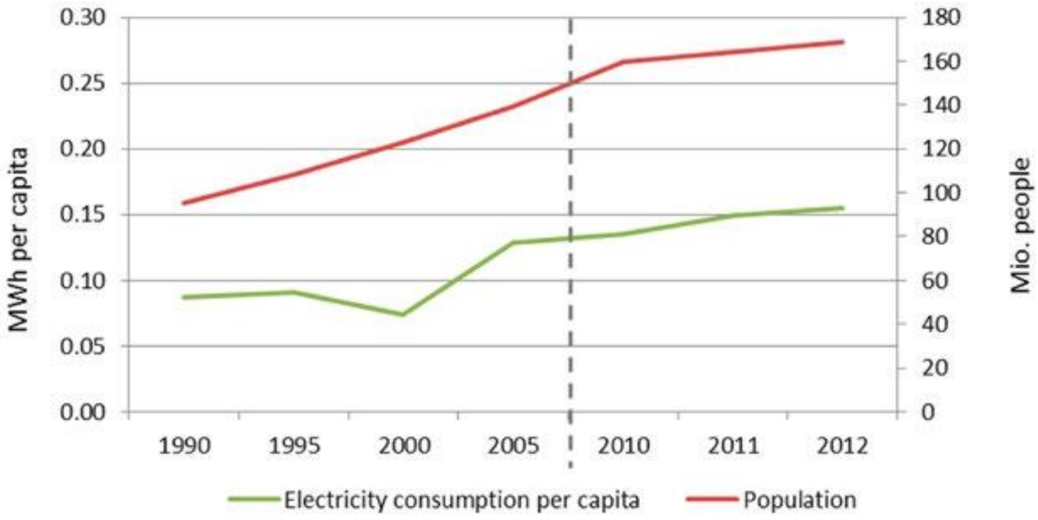

Fig. 1. Historic development of population and electricity consumption per capita in Nigeria 1990–2012 [10], [12]

The absence of on-grid energy capacities or unreliable power supply from the grid has led households and industry consumers to install their own power generation equipment. The majority of these generators use diesel or petrol as fuel while about 23% of consumers use renewable sources like solar inverters [8], [10], [13], [14]. According to Power poll results released by NOIPolls Limited for the second quarter of 2015, it was revealed that as a direct effect of the poor state of power supply in Nigeria, almost 8 of 10 Nigerian households rely on alternative sources of power. This data was collected over a 27-month period (April 2013 – June 2015) [15].

The energy demand of a given country is determined by its population and industry. The available data on Nigeria for electricity consumption by sector reveals that, it is the residential sector that consumes the highest share of total energy (Fig. 2) [10], [14].

The composition of household appliances influences the total energy consumed by customers. In Nigeria, energy is commonly needed in households for appliances like water heaters, lighting, fridges, freezers, air conditioners, televisions, radios sets and computers [14].

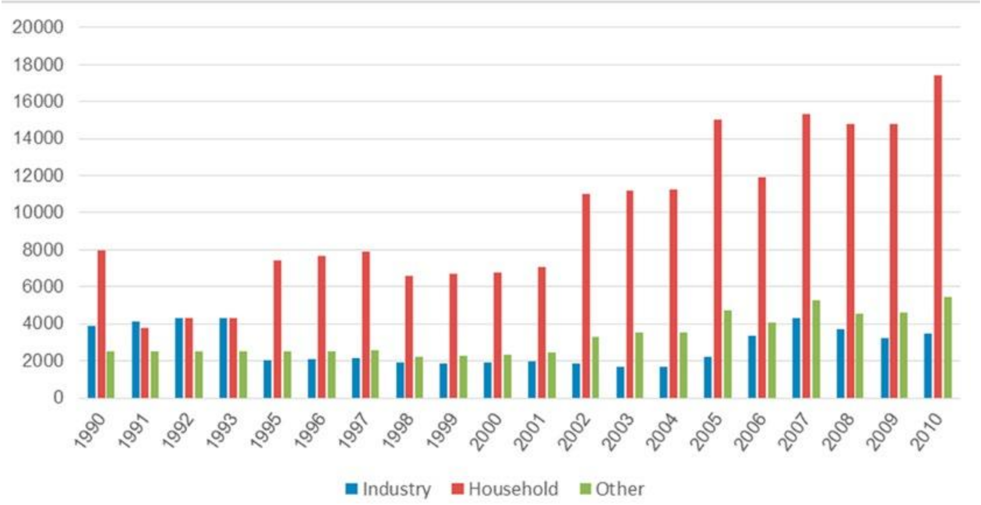

Fig. 2. Historical electricity consumption in Nigeria by economic sectors (GWh) [16], [17]

An analysis of the energy saving potentials of Nigeria's residential buildings reveal that hot water heating, air cooling and lighting have the largest saving potential at the household level [18]. An autonomous hot water heating system could possibly reduce the demand on the power plants in Lagos.

1.3. Waste to energy

Waste-to-energy (WTE) is a process which recovers energy from waste materials and is the preferred option of solid waste management disposal, based on the concept known as the waste hierarchy [1]. In 2008, European member states have agreed on this concept and adopted it as the basis for all legislative measures in the waste sector in addition to other guiding principles (Fig. 3).The Integrated Solid Waste Management (ISWM) hierarchy stipulates that source reduction and reuse are the most desirable solid waste management practices since they are the most effective options to ensure that hazardous contents are removed. In reducing the waste, the consumption of resources is reduced considerably. The next step is to recycle the waste. However, after waste is reduced, reused and recycled, the remaining waste must be managed further. Combustion to recover energy becomes necessary and only what remains after all possibilities have been exhausted could be safely disposed [1], [13], [19]. The average calorific value of Nigerian waste is about 9.6 MJ/kg. Based on Nigeria's waste profile obtained, if all the waste generated could be successfully collected and incinerated in a modern waste-to-energy facility, as much as 3000 MW of electricity could be obtained by 2020 [13], [19].

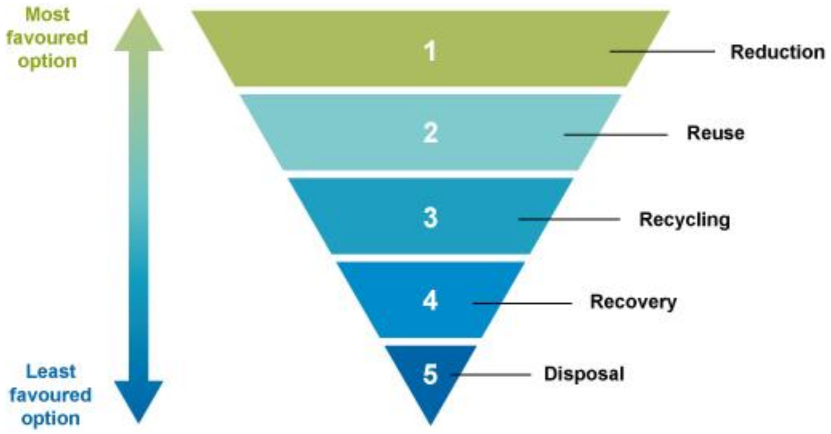

Fig. 3. Integrated Solid Waste Management [13], [20]

1.4. Aim of Study

Due to the increasing importance of sustainable resources and above-mentioned reasons the need to add WTE to the energy mix in Lagos becomes obvious. The proposed system will utilize the massive amount of MSW generated in the city of Lagos for energy recovery. In this case the energy could be used either for hot water or cold air supply to residential buildings. This system will support the city's existing power generation plants to facilitate saving of resources and sustainable living patterns.

The main aim of the paper, therefore, is to determine the technical efficiency of the thermal neutralization system of waste in Lagos by using existing literature on waste composition: (1) to find the specific net calorific value of the waste; (2) to calculate the values of the coefficient of excess air in the furnace as well as recommend a furnace type to use; (3) develop possible scenarios of waste-to-energy utilization.

2. METHODOLOGY

The chosen methodology is based on the known elemental composition of waste, its physicochemical characteristics. Knowing the specific net calorific value of fuel, the amount of air required for complete combustion of 1 kg of waste, composition and amount of combustion products produced are determined. The theoretical combustion temperature and the specific amount of additional fuel are determined to maintain the required combustion temperature, and if it is higher than the theoretical combustion temperature, the process technology is developed.

According to Salami et al [21], the structure of solid waste of the Lagos State is comprised mostly of organic matter (62%), plastic (15%) and paper (10%) while the lowest component is ash which accounts for 2% (see Table 1). This characterisation is used as the bases for finding the working efficiency of the system.

Table 1. Characterization of waste structure in Lagos, Nigeria [21]

Category	Tonnage	Percentage
Organic	8060	62
Plastic	1950	15
Paper	1300	10
Glass	520	4
Silts	910	7
Ashes	260	2
Total	13,000	100

Using the values from the table 1 the theoretically necessary amount of air V^0 (under normal conditions) for complete combustion of a unit amount of fuel can be found:

$$V^0 = 0.0889C^p + 0.265H^p + 0.033(S^p - O^p), \tag{1}$$

where C^p, H^p, S^p are the mass contents of combustible components, and O^p is the percentage of oxygen in the working mass of the waste.

Using equation 1 and values of Table 2 [22], the volume of air (V^0) in the organic matter, plastic, paper and glass can be calculated.

Table 2. Characterization of waste, the percentage of combustible components and the volume of air per one kilogram of waste (V^0)

Component	**C**	**H_2**	**O_2**	**S**	**N_2**	**Total weight, %**	**$V^0 \frac{m^3}{kg}$**
Organic matter	50.321	0.583	44.35	0.806	3.94	100	3.191
Plastics	68.186	0.789	28.79	0.909	1.326	100	5.351
Paper	44.204	0.495	54.648	0.311	0.341	100	2.268
Glass	50.293	0.559	45.823	0	3.325	100	3.107

The theoretically necessary amount of air for waste incineration (V_w^0) can be obtained as follows:

$$V_w^0 = \sum(v_i g_i), \tag{2}$$

where v_i is the summation of V^0 for all waste composition and g_i is the percentage of combustible components of the waste.

$$\mathrm{V_w^0} = 3.191 \times 0.62 + 5.351 \times 0.15 + 2.268 \times 0.10 + 3.107 \times 0.04;$$

$$\mathrm{V_w^0} = 3.1321 \frac{\mathrm{m^3}}{\mathrm{kg}}.$$

The volume of triatomic gases – O_2, N_2, H_2O in the waste component is needed to find the actual amount of flue gasses generated during the combustion (Table 3).

Table 3. The volume of flue gases by waste components

Component	**$V_{R_{O_2}} \frac{m^3}{kg}$**	**$V^0_{N_2} \frac{m^3}{kg}$**	**$V^0_{H_2O} \frac{m^3}{kg}$**	**Percentage % (g_i)**
Organic matter	0.9446	2.5524	1.0478	62
Plastics	1.2787	4.2379	0.1737	15
Paper	0.827	1.7944	0.0915	10
Glass	0.9385	2.4811	0.1121	4
$\sum(v_i g_i)$	0.8977	2.4969	0.6893	

From Table 3 the theoretical volume of flue gases can be obtained:

$$V_{g_w}^0 = 4.0839 \frac{m^3}{kg}.$$

Depending on the capacity of the plant for incinerated waste, their preparation before being fed for incineration, based on the known recommendations and characteristics of the technologies and quality of the incineration process, the type of fuel device (furnace) is selected for which the flow characteristics, heat output, additional fuel, air, and flue expenses are calculated, gases and ashes, which are subsequently needed to determine the main dimensions of the furnace, afterburner, gas cleaning systems and the gas-air duct.

Considering the local difficulties of high-quality waste preparation for incineration in Lagos, a rotary kiln is proposed as it is not responsive to the quality of waste, allowing for increased heat and mass exchange during the combustion of waste as a furnace for the installation [23]. At the exit of the furnace, the temperature is maintained at 900 °C below the melting point of the removed ash. The final afterburning of products of incomplete combustion is carried out in the afterburning chamber at a temperature of 1200 °C. To improve the thermal efficiency of the installation, a heat recovery system is installed after the afterburner, in which the heating water is heated by afterburning gases. After the system of gas cleaning through a chimney the gases are removed to the environment.

A two-stage combustion system has been suggested: the first stage is carried out at a temperature of 900 ° C, and the second one – at 1200 °C [22].

Then the actual amount of flue gases from waste incineration will be found:

$$V_{g_w}^{kc} = 4.0839 + (\alpha - 1) \times 3.1321; \tag{3}$$

$$V_{g_w}^{kc} = 7.216 \frac{m^3}{kg}.$$

Shares of O_2, N_2, H_2O and excess air in the flue gas:

$$r_i = \frac{V_i}{V_{g_w}^{kc}} \tag{4}$$

$$\mathrm{r}_{ea} = (\alpha - 1) \frac{V_w^0}{V_{g_w}^{kc}}.$$

Share of O_2 amounts to 0.1244; N_2 – 0.346; H_2O – 0.0955 and excess air – 0.434.

Full Heat Capacity of flue gases (C_g) at 900 °C for waste:

$$C_g = \sum (v_i r_i). \tag{5}$$

Table 4. Share of O_2, N_2, H_2O and excess air in the flue gas and their heat values at 900 °C [22]

Content	**O_2**	**N_2**	**H_2O**	**CB**
Heat Values	1.4657	1.3806	1.6969	1.4259
r	0.1218	0.6685	0.1251	0.0846

$$C_g = C_{O_2} \times \mathrm{r}_{O_2} + C_{N_2} \times \mathrm{r}_{N_2} + C_{H_2O} \times \mathrm{r}_{H_2O} + CB \times \mathrm{r}_{ea};$$

$$C_g^{kc} = 1.4344.$$

The total energy used to heat 1kg of mixed waste $\boldsymbol{Q_{H_w}^F}$;

$$Q_{H_w}^F = \sum (g_i Q_{H_i}^P). \tag{6}$$

Table 5. The waste components, their percentage and heat values [20]

Component	**% of Waste (g_i)**	**Heating value $Q_{H_i}^P \frac{kJ}{kg}$**
Organic matter	62	4230
Plastic	15	46150
Paper	10	17920

Using equation (6),

$$Q_{H_w}^F = 11337.1\frac{kJ}{kg}.$$

The burning temperature of waste t^{kc} in the combustion chamber is given by the equation (7), where $\alpha = 2$ and $q = 0.05$:

$$t^{kc} = \frac{Q_{H_w}^F(1-q)}{\left(V_{g_w}^{kc} + (\alpha - 1)V_w^0\right)C_g}; \tag{7}$$

$$t^{kc} = 708\ ℃.$$

For complete combustion the value of burning temperature of 900 $^{\circ}$C minimum is needed, hence, an additional diesel fuel is required.

3. RESULTS AND DISCUSSION OF POSSIBLE SCENARIOUS OF WASTE-TO-ENERGY UTILIZATION

The calculations of the heat balance of the waste incineration process showed that heat generation from waste incineration is not enough to maintain the required combustion temperature. Therefore, it is required to burn additional fuel in the amount of 415 kg/h. Flue gases after the second burner can be sent to a gas-water heater, in which, by cooling gases from 1200 °C to 400 °C or 300 °C, it is possible to heat water for the heating system. The resulting amount of heat will be:

when cooled to 300 $^{\circ}$C $\bar{Q}_{300}$ = 1.6983 × 10^{7} kJ/h;

when cooled to 400 $^{\circ}$C $\bar{Q}_{400}$ = 1.5211 × 10^{7}kJ/h.

Due to this, it is possible to heat the water to temperatures in the range of 95–70 $^{\circ}$C. If $t_{g1} = 70\ ℃$ and $t_{g2} = 90\ ℃$.

$$G_g = \frac{\bar{Q}}{C_g(t_{g2} - t_{g1})}; \tag{8}$$

$$G_g\ at\ 300℃\ = 2.0266 \times 10^5 \frac{kg}{h};$$

$$G_g\ at\ 400℃\ = 1.8151 \times 10^5 \frac{kg}{h}.$$

To estimate the degree of useful usage of the heat of combustion of waste and additional fuel in the installation the coefficient of utilization of heat can be used. The coefficient is calculated at flue gas temperatures of 300 $^{\circ}$C and 400 $^{\circ}$C.

The coefficient of utilization of the heat of fire disposal of waste at 300 $^{\circ}$C and 400 $^{\circ}$C can be obtained as follows:

$$\eta = \frac{\bar{Q}_X}{B \times Q_{H_{Dsl}}^F + G_w \times Q_{H_w}^F}; \tag{9}$$

$$\eta_{300} = 0.5853;$$

$$\eta_{400} = 0.5242;$$

It is possible to get hot water at a temperature of 115-110 °C. Such water, in addition to the system of hot heat supply and heating, can be used in heat-using absorption lithium bromide chillers for obtaining cold, as well as for generating electrical energy.

The produced hot water can be used in the absorption lithium bromide chiller, such as, for example, ABKHM-8-10 [23] to obtain about 800 kW of cooling capacity in the form of cold water at a temperature of +7 °C for an air conditioning system. Also, one can get about 500 kW of electrical energy by heating a heat exchanger- an evaporator of a steam microturbine installation, for example, the TGX-100 type, manufactured by CALNETIX company [24].

When using the heat of hot water, fuel and gas emissions are saved in the heat power station being replaced, which supplies the same quantity and quality of heat. The savings of fuel can be estimated as following:

$$\Delta B = \frac{\bar{Q}_{300}}{Q \times 0.9}; \tag{10}$$

$$\frac{1.6983 \times 10^7}{42620} = 442.8 \frac{m^3}{h},$$

where, Q – specific lower calorific value of fuel, kJ/kg and 0.9 is efficiency coefficient of the replaced boiler room.

A corresponding reduction in flue gas emissions can be found as follows:

$$\Delta V = \Delta B \times V_g = 442.8 \times 14.36 = 6358 \ \frac{m^3}{h}, \tag{11}$$

$V_g -$ the volume of flue gases during complete combustion of a unit amount of fuel, m^3/h.

This environmental result can be used to further feasibility study of the proposed thermal neutralization system of waste.

4. CONCLUSION

If installed, the thermal neutralization system of municipal solid waste of the city of Lagos will play a vital role in the country’s transition from a fossil fuel dominated energy mix to clean and affordable energy systems. The system could be effective in plummeting the waste volume in the city as the waste is utilized for power generation. With the addition of diesel fuel, the system can generate enough heat for the hot water supply. The technical assessment of thermal neutralization system of waste showed that recovered energy from the system can be also used for either central air-cooling system for residents or electric energy supply. However, the further study of environmental and economic results of the system and costs-benefits analysis is needed to compare the options of the produced heat utilization and choose the most efficient one.

The use of heat from the flue gases when burning solid municipal waste could reduce fuel consumption in replaceable power plants and, accordingly, reduce the formation of flue gas emissions.

The results of the assessment of ecological and energy efficiency of the proposed system can be utilized for further research in modelling the material and energy flows through the system. Life cycle assessment of MSW treatment plants technologies and examination of possibilities of adding waste from the oil and gas industry, which have higher calorific values, will be also considered in the further research.

REFERENCES

1. R. J. Bilitewski B., Wagner J, “Best Practice Municipal Waste Management,” pp. 1-6, 2015.
2. H. Daniel and B.-T. Perinaz, “WHAT A WASTE: A Global Review of Solid Waste Management,” 2012.
3. M. Awumbila, “Drivers of Migration and Urbanization in Africa,” in *UNITED NATIONS EXPERT GROUP MEETING ON SUSTAINABLE CITIES, HUMAN MOBILITY AND INTERNATIONAL MIGRATION*, 2017, No. September.
4. A. Aliyu and L. Amadu, “Urbanization, cities, and health: The challenges to Nigeria – A review,” *Ann. Afr. Med.*, Vol. 16, No. 4, p. 149, 2017.

5. The World Bank, "What A Waste Global Database," 2017. [Online]. Available: https://datacatalog.worldbank.org/dataset/what-waste-global-database. [Accessed: 05-Apr-2019].
6. The World Bank, "The Woldbank Data Nigeria," 2017. [Online]. Available: https://data.worldbank.org/country/nigeria.
7. S. Mukaila, "LAGOS, WASTE MANAGEMENT AND THE ENVIRONMENT," *Lagos State Government*, 2018. [Online]. Available: https://lagosstate.gov.ng/blog/2018/02/03/lagos-waste-management-and-the-environment/.
8. B. Onu, T. Price Dr., S. S. Surendran, and S. Ebie, "Solid waste management: A critique of Nigeria's waste management policy," *Int. J. Knowledge, Cult. Chang. Manag.*, Vol. 11, No. 4, pp. 373-399, 2012.
9. Federal Ministry of Power, "Power Statistics," *Federal ministry of power website*, 2016. [Online]. Available: http://www.power.gov.ng/index.php/component/content/article/78-featured/140-power- statistics Power Statistic. [Accessed: 11-Jan-2019].
10. K. Ley, J. Gaines, and A. Ghatikar, "The Nigerian Energy Sector- An Overview with a Special Emphasis on Renewable Energy, Energy Efficiency and Rural Electrification," No. June, pp. 1-152, 2015.
11. W. S. Ebhota and P. Y. Tabakov, "The place of small hydropower electrification scheme in socioeconomic stimulation of Nigeria," *Int. J. Low-Carbon Technol.*, Vol. 13, No. 4, pp. 311-319, 2018.
12. IEA, "Electricity Statistics," 2012. [Online]. Available: https://www.iea.org/statistics/electricity/. [Accessed: 11-Jan-2019].
13. E. Akhator, A. Obanor, and L. Ezemonye, "Electricity Generation in Nigeria from Municipal Solid Waste using the Swedish Waste- to-Energy Model," No. April 2013, 2016.
14. W. S. Ebhota and P. Y. Tabakov, "Power Inadequacy , the Thorn in Economic Growth of Nigeria," Vol. 13, No. 16, pp. 12602-12610, 2018.
15. NOIPolls, "Almost 8 in 10 Nigerian Households Rely on Alternative Sources of Power As Erratic Power Supply Persist." [Online]. Available: https://www.noi-polls.com/root/index.php?pid=341&parentid=13&ptid=1. [Accessed: 12-Jan-2019].
16. United Nations, "Energy Statistics Database." [Online]. Available: https://unstats.un.org/unsd/energy edbase.htm. [Accessed: 13-Jan-2019].
17. Africa-EU Renewable Energy Cooperation Programme, "Energy Sector." [Online]. Available: https://www.africa-eu-renewables.org/market-information/nigeria/energy-sector/. [Accessed: 13-Jan-2019].
18. S. Geissler, D. Österreicher, and E. Macharm, "Transition towards energy efficiency: Developing the Nigerian Building Energy Efficiency Code," *Sustain.*, Vol. 10, No. 8, pp. 1-21, 2018.
19. A. Atta, A. M, N. Yusuf, Z. Sani Gano, O. Ahmed, and O. Fasanya, "Potentials of Waste to Energy in Nigeria," *J. Appl. Sci. Res.*, Vol. 12, No. March, pp. 1-6, 2016.
20. Open Learn Create, "The Waste Hierarchy." [Online]. Available: http://www.open.edu/openlearncreate/mod/oucontent/view.php?id=80577&printable=1&extra=thumbnail_idm28307072. [Accessed: 15-Dec-2018].
21. L. Salami, A. Susu, R. Patinvoh, and O. Olafadehan, "Characterisation Study of Solid Wastes: A Case of Lagos State," *Int. J. Appl. Sci. Technol.*, Vol. 1, No. 3, pp. 47-52, 2011.
22. D. Wilson, "Utilization of solid waste (Under the editorship of D. Wilson; Y84 Short translation from English by ed. A.P. Tsygankov, M . Stroyizdat)," p. 336, 1985.
23. Verantis, "Rotary Kiln Incineration." [Online]. Available: http://www.verantis.com/products/incineration-systems/rotary-kiln-incineration/index.html. [Accessed: 09-Apr-2019].
24. D. Lew, "Rotary Kiln Incinerator." [Online]. Available: https://www.drdarrinlew.us/industrial-ecology/rotary-kiln-incinerator.html. [Accessed: 09-Apr-2019].
25. *Absorption machine ABKHM-8-10*.
26. CALNETIX, "Steam turbine power plant of the TGHX 100 type."

CYSENI 2019, May 23-24, Kaunas, Lithuania
ISSN 1822-7554, www.cyseni.com

GEOTHERMAL ENERGY UTILIZATION STATUS FOR TURKEY

M. Koc
Applied Science University of Isparta,
Cunur, 32260 – Turkey
Email: muratkoc@isparta.edu.tr

Y. E. Yuksel
Afyon Kocatepe University
Gazligol Street, 03200 – Turkey

M. Ozturk
Applied Science University of Isparta,
Cunur, 32260 – Turkey

ABSTRACT

In this paper, the geothermal energy sources and its present and possible applications for Turkey are investigated in detail. Additionally, the geothermal power based useful production options (thermal, electricity, alternative fuels, fresh and hot water, other commodities and health options) are analysed, and the other beneficial technologies with geothermal energy are given for preferable geothermal plant design. Generally, in Turkey, the single flash steam power generation systems have been utilized for power generation. Multi-generation systems may be able to offer more effective results when compared to the single generation systems.

Keywords: Renewable energy, geothermal energy, Turkey

1. INTRODUCTION

As energy needs of human increase rapidly, new alternatives for current energy infrastructure will be necessary. Existing energy infrastructure is not sustainable because it is harmfull to the environment and also fossil energy sources are decreasing as well. Therefore, new solutions should be found having feautures such as clean, environmental friendly, cheap and sustainable. With this view of perspective renewable energy sources come into the forefront. Recent studies show that there is a huge trend to transition to the renewable energy sources such as solar, geothermal, hydro power, wind, etc.

In this study, geothermal energy utilization in Turkey is discussed due to high potential of Turkey in terms of geothermal sources. Researches on geothermal sources in Turkey initially started in 1960s by MTA (General Directorate of Mineral Research and Exploration), until now 227 geothermal fields were discovered. Geothermal potential of Turkey has been calculated as 31500 MW [1]. In the last 50 years, there has been a striking development in geothermal energy usage in Turkey.

2. GEOTHERMAL ENERGY UTILIZATION

2.1. Geothermal energy status in Turkey

Turkey, due to its geographic position and lying on the active techtonic belt, is one of the richest countries in terms of geothermal sources. Almost 1000 geothermal sources are widely spread in Turkey with different source temperatures as seen from Fig. 1. As demonstrated in the figure, geothermal fields are found in mostly west Anatolian part of Turkey. Geothermal sources are utilized for electricity production, heating (buildings and greenhouses), thermal and health tourisms, gaining industrial minerals and drying in Turkey.

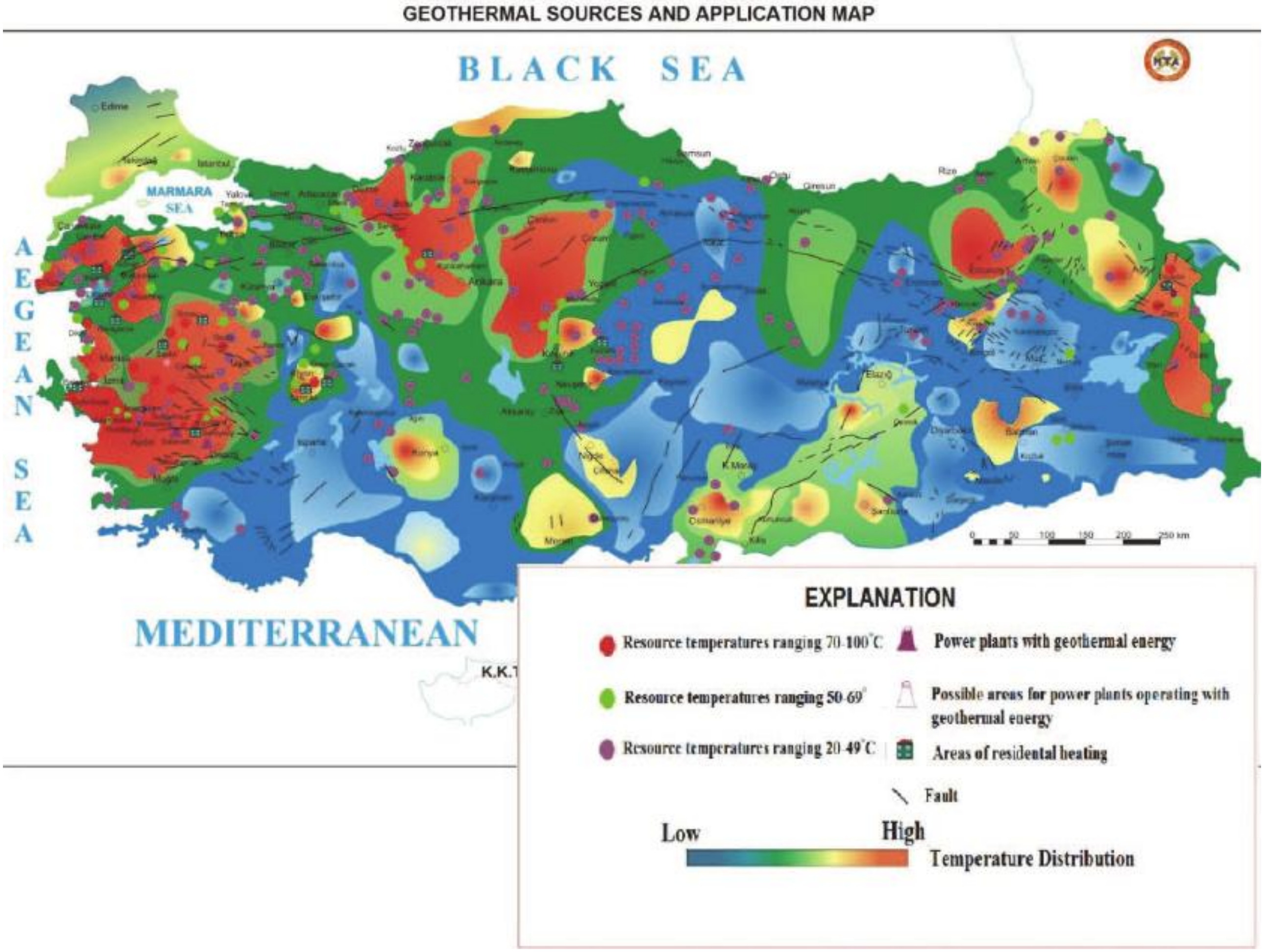

Fig. 1. Map of geothermal sources utilization in Turkey [1]

Electricity generation from geothermal was initially applied in 1975 in Kızıldere, Turkey. The capacity of the first plant of Turkey was only 0.5 MW. Today, according to the June 2018 data from Ministry of Energy and Natural Sources total installed power capacity is 1144 MW [2]. Between 2010 and 2015, Turkey has been the first country in terms of increasing rate of installed capacity of electricity generation from geothermal sources [3]. While heating from geothermal was 3100 MW in 2004, the heating capacity went up to the 5000 MW at the end of November, 2017. In 2002, there was 16 electricity generation plant from geothermal and this number increased to 25 in 2017. The capacity of electricity plants was about 15 MW in 2002, it was 1052 MW in 2017. There has been a 686% increment in greenhouse heating from 2002 to 2017. Also when considered house heating there has been a 281% increment rate such that in 2002 there was 30000 house heated by geothermal sources, at the end of 2017 114567 house heated by geothermal energy. This striking increment rate of geothermal usage in Turkey has brought the country to the second place in the top 5 countries using geothermal energy as seen in Table 1.

Table 1. Distribution of geothermal heat energy among the top 5 countries [4]

Countries	**Installed Capacity, thermal (MWt)**	**Countries**	**Annual produced energy (TJ/year)**
China	6,089	China	74,041
Turkey	2,894	Turkey	44,932
Japan	2,086	Iceland	26,700
Iceland	2,035	Japan	25,630
India	986	Hungary	9,573

2.2. Geothermal energy status in the World

Geothermal energy has been searching and improving rapidly as alternative energy source in many countries having rich geothermal sources. According to Bertani [3], total installed capacity for electricity generation from geothermal has reached to 12635 MWe and direct utilization of geothermal for house heating has reached to 70329 MWt as seen from Fig. 2. in total in the world ?

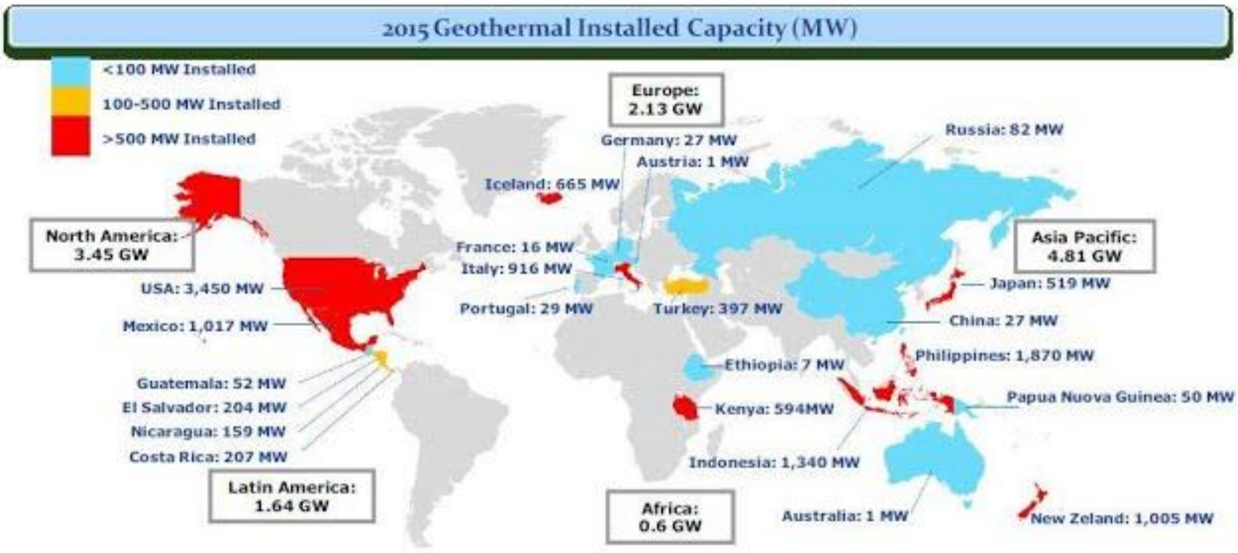

Fig. 2. Map of geothermal installed capacity in World (Adapted from [3])

From 1950 to 2015, total installed capacity and generated power has raisen sharply after 1980s as seen from Fig. 3. As seen from the figure installed capacity has increased 1.7 GW (about 16%) from 1980s to 2015.

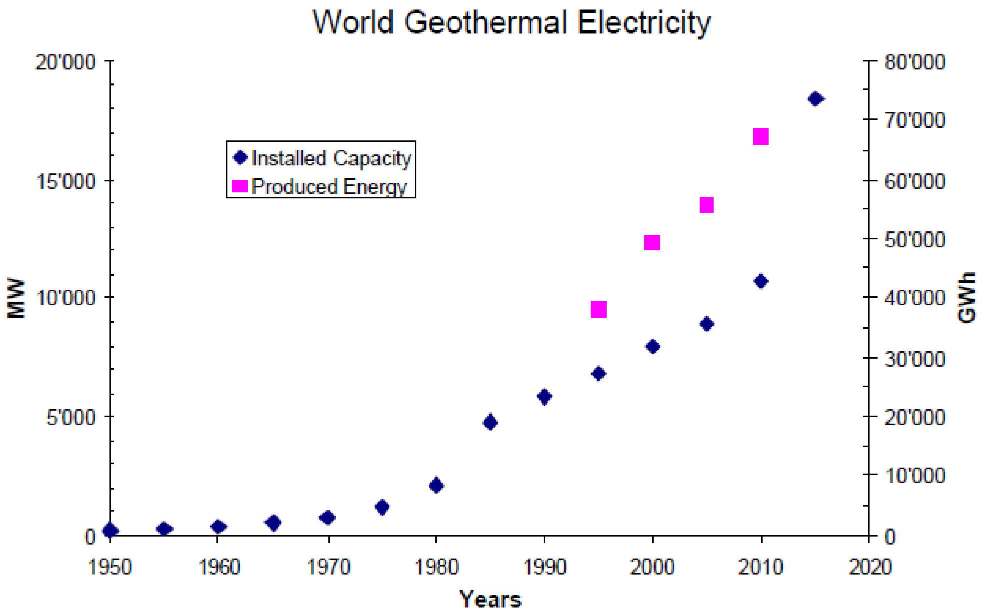

Fig. 3. Total installed capacity and produced energy from geothermal between 1950-2015 [3]

Fig. 4 illustrates the worldwide thermal utilization of geothermal energy in 2015. As seen from the figure the biggest share of thermal usage of geothermal energy belongs to the geothermal heat pump technology with 55.30%.

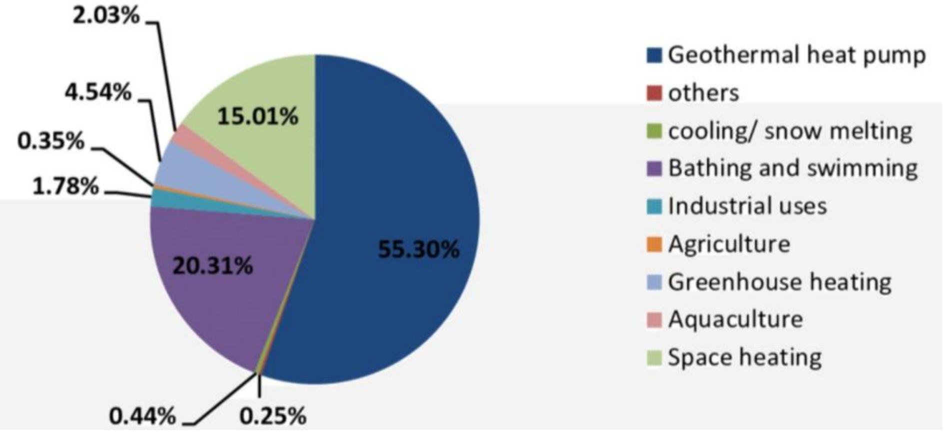

Fig. 4. World wide utilization of geothermal energy, TJ/yr [5]

Table 2 demonstrates geothermal power plants and which technology is used in different countries. As seen from the table, still single flash technology is the ranked 1 when compared to other technologies.

Table 2. Geothermal power plants for each technology per country (installed capacity MW) [6]

Country	**Back pressure**	**Dry steam**	**1-flash**	**2-flash**	**3-flash**	**Binary**	**Hybrid**	**Total**
Australia	-	-	-	-	-	1	-	1
Austria	-	-	-	-	-	1	-	1
China	-	-	1	24	-	3	-	28
Costa Rica	5	-	140	-	-	63	-	208
El Salvador	-	-	160	35	-	9	-	204
Ethiopia	-	-	-	-	-	7	-	7
France	-	-	10	5	-	2	-	17
Germany	-	-	-	-	-	27	-	27
Guatemala	-	-	-	-	-	52	-	52
Iceland	-	-	564	90	-	10	-	664
Indonesia	-	460	873	-	-	8	-	1341
Italy	-	795	120	-	-	1	-	916
Japan	-	24	355	135	-	7	-	521
Kenya	48	-	543	-	-	4	-	595
Mexico	75	-	466	475	-	3	-	1019
New Zealand	44	-	209	356	132	265	-	1006
Nicaragua	10	-	142	-	-	8	-	160
Papua New Guinea	-	-	50	-	-	-	-	50
Philippines	-	-	1286	365	-	219	-	1870
Portugal	-	-	-	-	-	29	-	29
Russia	-	-	82	-	-	-	-	82
Turkey	-	-	20	178	-	198	-	396
USA	-	1584	60	881	50	873	2	3450
Totals	182	2863	5081	2544	182	1790	2	12644
Percent of total	1.44	22.64	40.19	20.12	1.44	14.16	0.016	100.00

Due to advantages of geothermal energy such as clean, cheap and feasible, there are many plants to be installed in the future. Fig. 5 shows that operating capacities and future additions of geothermal plants with respect to countries. As seen from the figure, Indonesia, Kenya, Turkey and USA are planning to build new plants for geothermal energy.

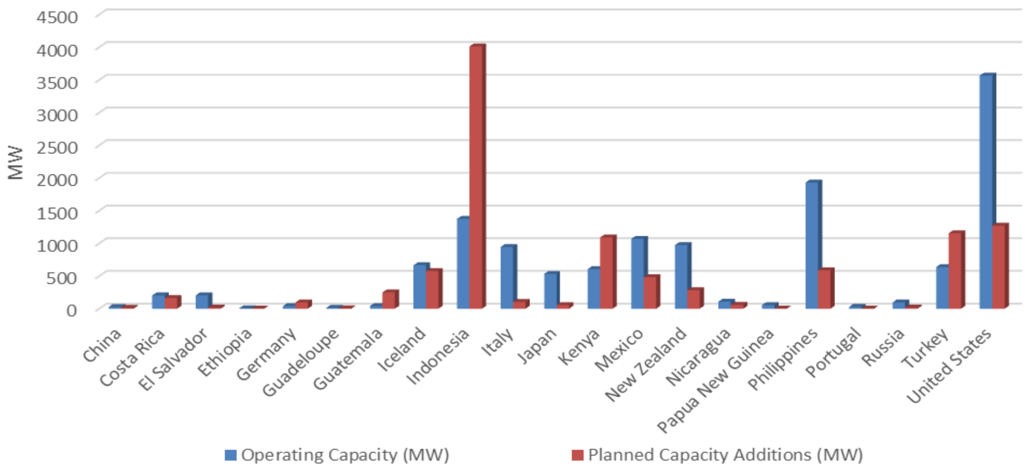

Fig. 5. Geothermal power operating and planned capacity by country (Adapted from [6])

3. GEOTHERMAL POTENTIAL OF TURKEY

There are about 2000 hot and mineral water reserves of which their temperatures range between 20-287 °C and there are 227 geothermal field which are economically feasible [1]. Main geothermal fields are in West Anatolia part of Turkey and on Nort Anatolia fault line. MTA has launched total 332000 m geothermal drilling. The depth of drilling to search for geothermal is more than 4000 m. According to previous studies and literature, geothermal heat capacity of Turkey is about 60000 MWt [7], [8].

4. CURRENT APPLICATIONS OF GEOTHERMAL ENERGY IN TURKEY

There are 25 geothermal electricity production plants in 14 different geothermal fields in Turkey at the end of 2015 which are shown in Table 3 [9].

Table 3. Geothermal electricity plants in Turkey (Adopted from [9])

Region	**Plants-Firm**	**Year of foundation**	**Number of units**	**Type**	**Total installed capacity (MWe)**
Denizli	Kızıldere (Zorlu)	1984/2003	2	1F, 2F+B	80+15
Aydın	Salavatlı Dora 1,2,3 (MeGe)	2006/2013	3	B	50,86
Aydın	Germencik(Gürmat)	2009	1	2F	47,4
Çanakkale	Tuzla (Enda)	2010	1	B	7,5
Aydın	Hıdırbeyli (Maren)	2011/2013	3	B	92
Aydın	Pamukören (Çelikler)	2013	1	B	45
Denizli	Kızıldere (Bereket)	2007	1	B	6,85
Manisa	Alaşehir (Türkerler)	2014	1	B	24
Aydın	Gümüşköy (BM)	2014	1	B	6,6+6.6
Denizli	Gerali (Değirmenci)	2014	1	B	2,52
Aydın	Germencik(Gürmat)	2014	1	B	22,5
Denizli	Tosunlar (Akça)	2015	1	B	3,5
Aydın	Pamukören (Çelikler)	2015	1	B	22,5
Aydın	Germencik (Gürmat)	2015	3	2(B)+2F	22.5+22.5+47.4
Manisa	Alaşehir (Zorlu)	2015	1	B	45
Aydın	Umurlu (Kar-Key)	2015	1	B	12
Denizli	Tekkehamam (Greeneco)	2015	1	B	12,8
Manisa	Alaşehir –Kemaliye (Enerjeo)	2015	1	B	25
Total					**620.03**
1F*= Single flash*, ***2F****=Double flash*, ***B****= Binary*					

Kızıldere – Denizli was the first geothermal field which was discovered as suitable for electricity generation from geothermal source in Turkey in 1968. Kızıldere is in the West part of the Turkey as many other geothermal fields. West part of Turkey, rich in terms of geothermal sources, were researched by MTA and UNDP (United Nations Development Program) [1]. Beside electricity generation, geothermal source is utilized for house heating in Sarayköy and for 100000 m^2 greenhouse heating. In addition, there is a dry ice plant on that site with the capacity of 12×10^7 kg/yr.

Other economically feasible geothermal field in Turkey is Germencik geothermal field which was discovered in 1982. The first plant was founded in 2009 as double flash. Then in 2014-2015 years 3 binary plants (3 × 22.5 MWe) and a 47.4 MWe double flash plant were started to generate power [2].

4.1. Possible applications for geothermal sources

Because of the diversity of geothermal fluid temperature there are different geothermal energy utilizations such as house heating, greenhouse heating, electricity production, health and agricultural utilizations etc. In Turkey, most of the geothermal energy systems are single flash steam power generation. The number of cogeneration plants are still limited. In literature, there are many novel applications are offered for multiple product from geothermal source in more effective way than traditional systems. Yuksel et. al [10] have proposed a novel multigeneration system based geothermal energy with four sub-systems which are double flash geothermal system, organic Rankine cycle, proton exchange membrane electrolyzer and hydrogen liquefaction system. Beside thermodynamic analysis, some parameters have also been investigated to reveal the effects of parameters on system performance. According to the parametric analysis, geothermal fluid temperature is the most effective parameter on system performance. Khalid et. al [11] have also made an assessment of solar-geothermal based multigeneration system in terms of thermodynamic and thermoeconomic. According to the their results, levelized cost of produced electricity is 0.089 $/kWh. According to Republic of Turkey Energy Market Regulatory Authority the price of 1 kWh electricity is 0.093 $ by February 2019 [12]. In Denmark having the most expensive electricty prices in Europe, 1 kWh electricity is 0.35 $/kWh in the first half of 2018 [13]. Therefore comparing these prices, it can be said that geothermal based multigeneration systems can challenge with fossil based plants in terms of electricity prices.

5. RESULTS AND DISCUSSION

In this study current applications of geothermal energy and its potential for Turkey is presented. In addition geothermal applications such as electricity generation and heat production in world is shared as well. Turkey is one of the richest country in terms of geothermal energy. From 2008 after some legal regulations have been implemented, capacity of installed plants have increased too. At the end of the 2017, installed capacity for electricity generation from geothermal energy has reached up to 1052 MWe. Thermal capacity of geothermal energy has raisen to about 15500 MWt at the end of 2017. As a conclusion, the following suggestions can be made:

- New research techniques should be adapted for searching geothermal fields.
- New electricity production options such as tri-generation or multi-generation should be used because their efficiencies are much higher than single generation plants.
- New cooperations among universities, private firms and MTA should be set.
- Due to most geothermal fields having temperature below than desired for electricity generation, those geothermal sources should be used for space heating and green house heating.

REFERENCES

1. Turkey geothermal potential and research studies. General Directorate of Mineral Research and Exploration. 2017 – [referred on the 12th of February in 2019 y.]. Link to the internet http://www.mta.gov.tr/v3.0/arastirmalar/jeotermal-enerji-arastirmalari.
2. Geothermal. Ministry of Energy and Natural Resources. 2018 – [referred on the 12th of February in 2019 y.]. Link to the internet https://www.enerji.gov.tr/tr-tr/sayfalar/jeotermal
3. BERTANI, R. Geothermal Power Generation in the World-2010-2015 Update Report. World Geothermal Congress 2015 (WGC2015). Proceedings number: 01001, Australia. 2015 April 24.
4. JOHN, W.L.; TONYA, L.B. Direct utilization of geothermal energy 2015 worldwide review *Geothermics*, 2016, Vol. 60, p. 66-93.

5. LUND, J.; BOYD, T. Direct utilization of geothermal energy 2015 worldwide review, World Geothermal Congress 2015 (WGC2015). Proceedings number: 01046, Australia. 2015 April 24.
6. BERTANI, R. Geothermal power generation in the world 2010–2014 update report, *Geothermics*, 2016, Vol. 60, p. 31–43.
7. YILMAZER, S. Determining the potential of geothermal potential of Western Anatolia, 11th Turkey Energy Congress 2009, Izmir, Turkey (in Turkish).
8. Geothermal Energy Development Report, Turkish Geothermal Association (TJD), 2015, Ankara (Unpublished).
9. ŞIMŞEK, Ş. Geothermal developments in the World and Turkey. III. Geothermal Resources Symposium, 2015. proceedings, p. 1-17 (in Turkish).
10. YUKSEL, Y. E., OZTURK, M., DINCER, I. Analysis and performance assessment of a combined geothermal power-based hydrogen production and liquefaction system. *International Journal of Hydrogen Energy*, 2018, Vol. 43, No. 22, p. 10268-10280.
11. KHALID, F., DINCER, I., ROSEN, M. A. Techno-economic assessment of a solar-geothermal multigeneration system for buildings. *International Journal of Hydrogen Energy*, 2017, Vol. 42, No. 33, p. 21454-21462.
12. Electricity Tariff Lists. Republic of Turkey Energy Market Regulatory Authority . 2019 – [referred on 3rd of April in 2019 y.]. Link to the internet https://www.epdk.org.tr/detay/icerik/3-0-1/tarifeler
13. Electricity price statistics. Eurostat. 2018 – [referred on 3th of April in 2019 y.]. Link to the internet https://ec.europa.eu/eurostat/statistics-explained/index.php/Electricity_price_statistics

CYSENI 2019, May 23-24, Kaunas, Lithuania
ISSN 1822-7554, www.cyseni.com

INVESTIGATION OF REDUCTION OF FLY ASH EMISSIONS FROM BIOMASS COMBUSTION EQUIPMENT USING ACOUSTIC AGGLOMERATION

M. Kulokas, N. Pedišius
Lithuanian Energy Institute
Breslaujos 3, LT-44403 – Lithuania
Email: Mindaugas.Kulokas@lei.lt

ABSTRACT

Currently, various methods are used to reduce emissions of fly ashes emitted with flue gases. However, their efficiency no longer meets increasingly stringent requirements for ambient air quality. In order to fulfill the tightened emission requirements, investigation studies on the modification of filtering methods and equipment are being expanded. Particular importance is given to investigations focused on reducing the emission of fly ash particles by acoustic, dynamic, chemical, electrical and magnetic effects, which creates relative movement between particles forcing them to collide more frequently and agglomerate into larger particles.

Acoustic agglomeration is considered to be the most promising pretreatment technology to reduce fly ash particles emissions. Previous studies already identified the main factors affecting agglomeration of particles: radiation frequency, exposure time, sound pressure level, initial concentration of particles and their size distribution. It has also been confirmed that the agglomeration process is essentially determined by orthokinetic and hydrodynamic particle interaction mechanisms, although other interactions cannot be completely ignored.

Experimental setup for testing the properties of fly ash particles from biofuel-powered plants and their agglomeration in the acoustic field, which provides control over flow yield in the range of 16–510 m^3/h, particle concentrations of 20–1000 mg/m^3 as well as acoustic field frequency, pressure and transmitted particle exposure time up to 31000 Hz, 135 dB and 3–7 s respectively, has been constructed. All experimental investigations were carried out in the cold fly ashes flow, at the temperature of 20 ± 5 ºC. During the investigation of acoustic agglomeration, the effects caused by the main influencing factors such as initial particle size distribution, its concentration and acoustic parameters were analyzed and compared. The agglomeration efficiency of 0.1–5 μm particles was determined to be as much as 40% at a flow rate 190 m^3/h and fly ash concentration 300 mg/m^3.

Keywords: acoustic agglomeration, emitted frequency, sound pressure level (SPL), residence time, fly ash, particulate matter (PM, $PM_{2.5}$ and PM_{10})

1. INTRODUCTION

Fly ash, which are removed from the combustion chamber with exhaust fumes, are solid particles of 0.01–100 μm diameter [1]. $PM_{2.5}$, i.e. particles < 2.5 μm [2] is the main subject in focus of precipitation, as most particles of > 5 μm, are deposited in currently used flue gas treatment plants [3]. $PM_{2.5}$ is very dangerous to human health due to its small size as well as heavy metals and other hazardous substances incorporated into ash flow [4, 5]. In addition, $PM_{2.5}$ and PM_{10} are considered as a dangerous source of environmental pollution in many countries, e.g. [4, 5]. Therefore, particulate matter (PM) emissions into the atmosphere are constantly monitored and controlled.

Currently used flue gas treatment plants do not appropriately meet the requirements of a new standard for particulate emissions [6] and therefore methods and measurements to improve their performance [7] are being explored.

Acoustic agglomeration is considered to be one of the most efficient and practically applicable $PM_{2.5}$ precipitation methods [8, 9], operation principle of which is based on high intensity sound waves to move small particles with the media and form agglomerates during collisions [9]. Studies of $PM_{2.5}$ precipitation using the acoustic agglomeration method were performed at different baseline conditions (radiation frequency, exposure time and sound pressure level (SPL)) using particles from coal plants [9-11]. In these studies, the resonant frequencies of 1400–2400 Hz and 1400–2200 Hz were determined, respectively, to increase the efficiency of the sleeve-type filter and electrostatic precipitator (ESP) at 148 dB of SPL [9]. Since the frequency is < 20000 Hz, i.e. audible, it produces acoustic noise, thus limiting its practical application [12]. For this purpose, the practical applications of the deposition of $PM_{2.5}$ precipitated in ESP from coal-powered plant by ultrasound were performed [13, 14].

This article discusses the test results obtained during the experimental study of $PM_{2.5}$ agglomeration using high-intensity acoustic effects and an analysis of its key control factors to determine the most effective acoustic agglomeration conditions for the $PM_{2.5}$ agglomeration from the burned biofuel as opposed to coal particles, which were usually used in other studies.

2. METHODS AND MEASURING INSTRUMENTS

The experimental agglomeration chamber (Fig. 1) was made of 0.22 m internal diameter and 2.0 m long vertical stainless steel tube. The top of the chamber was equipped with a Piezoelectric plate-transducer, which was controlled by the SFG-1013 signal generator and the YM-401/4-1 power amplifier.

Piezoelectric plate-transducer consists of a piezoelectric element of transduction in a sandwich configuration and a solid horn that acts as a mechanical vibration amplifier for extensive area stepped-grooved profile radiating plate. During the experiments, it generated 120 W 16000 Hz (f_{rez1}) and 31000 Hz (f_{rez2}) frequencies with SPL up to 135 dB in the center of the agglomeration chamber.

An agglomeration chamber is fitted with a removable reflector made of stainless steel to provide a relatively standing acoustic wave throughout the whole volume of the chamber.

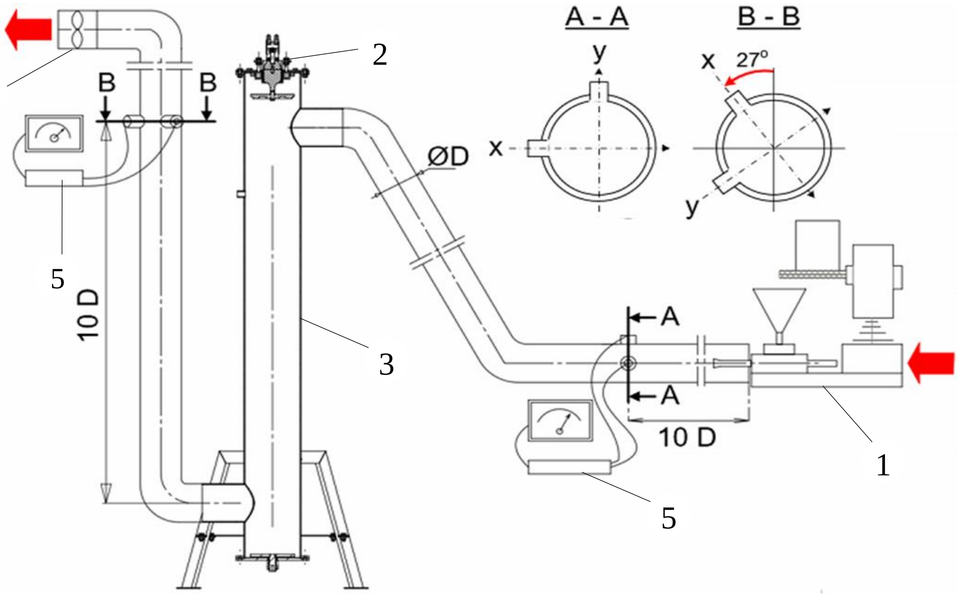

Fig. 1. Composition of experimental acoustic agglomeration device: 1 – aerosolizer; 2 – Piezoelectric ultrasonic plate-transducer; 3 – agglomeration chamber; 4 – fan; 5 – measurement and sampling equipment

The SPL in the chamber was measured with a noise level meter (ROBOTRON 00023) with a measuring range of 10–130 dB using a MV201 condenser microphone connected via a pre-amplifier to the acoustic level indicator. The axial changes in the measured SPL at three agglomeration cell measuring points were < 3 dB.

In order to achieve the required exposure time of 3 to 7 s (τ), the air flow rate was controlled within the range of 16–510 m^3/h, with known and adjustable initial particle concentrations in the range of 20–1000 mg/m^3. All experiments were performed at a particle flow temperature of 20 ± 0.5 °C, i.e. cold fly ashes flow, and measurements were made under isokinetic conditions.

For experimental studies, the fly ash collected from the wood chip incinerator ESP were used. The concentrations of the collected solid PM are known and they have been regulated by the use of an aerosolizer to continuously inject it into the air stream (Fig. 2).

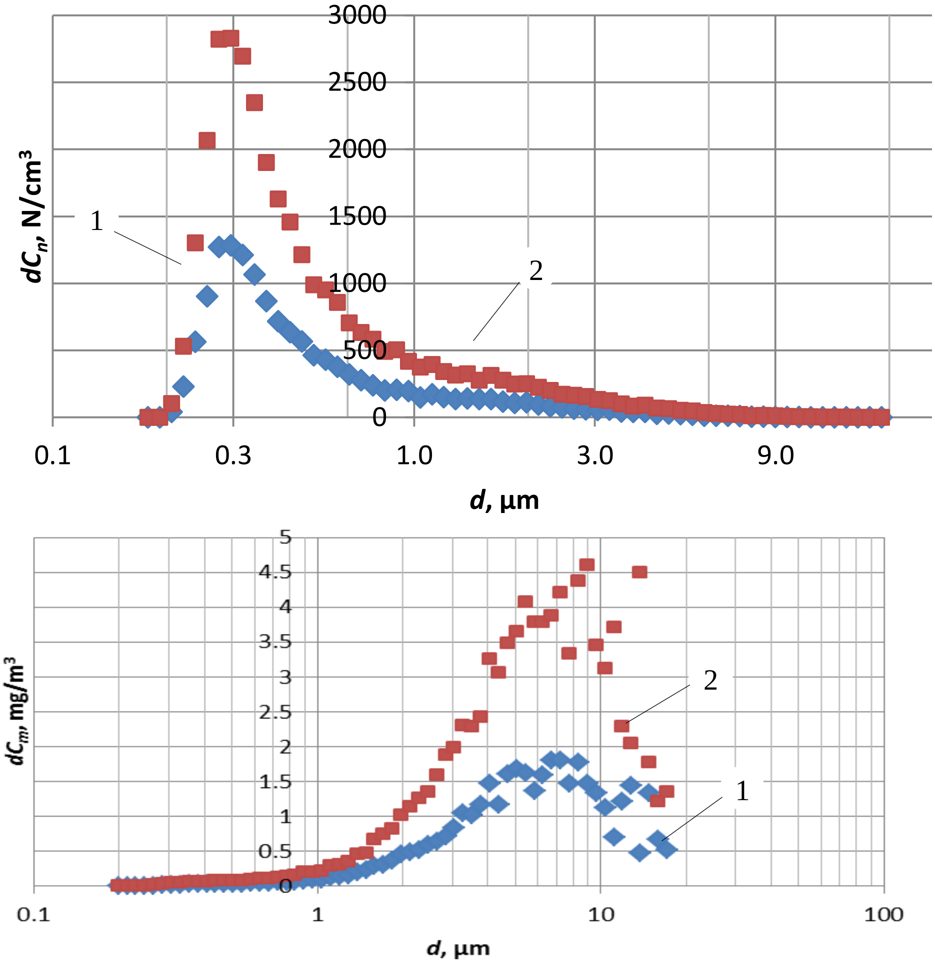

Fig. 2. Particle number and mass distributions were determined before agglomeration chamber (plane "A") at the corresponding initial mass concentrations: 1 – 175 mg/m^3 and 2 – 350 mg/m^3

Optical spectrometers were used to measure particle size distributions and number concentrations of particle flow in the experimental chamber.

The gravimetric analyzer was used under isokinetic conditions for the sampling of solid microparticles and the assessment of the acoustic agglomeration using an electronic microscope.

3. RESULTS AND DISCUSSION

During the analysis of the formed agglomerates significant difference in the mean particle number and mass concentration in the range of 0.2–10.0 µm was determined (Table 1). Average number particle concentrations dC_{n1} and dC_{n2} as well as mass concentrations dC_{m1} and dC_{m2} were determined for frequencies f_{rez1} and f_{rez2} respectively. Meanwhile, the change in dC_n and dC_m was calculated according to equatons 1-2 and 3-4, respectively, when the average values of dC_n and dC_m, determined in plane "B", with acoustic effect were compared to the average dC_{n0} and dC_{m0}

values measured without the accustic effect. The uncertainty of dC_n and dC_m measurements was ± 10 % and ± 10 mg/m^3, respectively.

Change in the number concentration of PM (ΔdC_n):

$$\Delta\left[N/cm^3\right] = dC_{ni} - dC_{n0} \tag{1}$$

$$\Delta[\%] = 100\left(dC_{ni} - dC_{n0}\right)/dC_{n0}\ , \tag{2}$$

where dC_{n0} – average particle number concentration without acoustic effect in plane "B", and dC_{ni} – average particle number concentration with acoustic effect in plane "B".

Change in mass concentration of PM (ΔdC_m):

$$\Delta\left[mg/m^3\right] = dC_{mi} - dC_{m0} \tag{3}$$

$$\Delta[\%] = 100\left(dC_{mi} - dC_{m0}\right)/dC_{m0}\ , \tag{4}$$

where dC_{m0} – average particle mass concentration without acoustic effect in plane "B", and dC_{mi} – average particle mass concentration with acoustic effect in plane "B".

Table 1. Comparison of average number and mass concentrations determined for f_{rez1} and f_{rez2} with the corresponding concentrations measured without the acoustic effect at the initial concentartion of 175 mg/m^3

f_{rez}, Hz	**dC_n, N/cm^3**	**ΔdC_n, N/cm^3**	**ΔdC_n, %**	**dC_m, mg/m^3**	**ΔdC_m, mg/m^3**	**ΔdC_m, %**
0	50984	-	-	76.35	-	-
16000	56108	5124	10	91.63	15.27	20
31000	65204	14220	28	106.90	30.54	40

In the agglomeration chamber, the effect of the sound frequency and SPL was analyzed during the exposure on PM for 3 to 7 seconds (Fig. 3). In this case, dC_n decreases monotonically when exposure duration increases and relative number concentration dC_n/C_n ranges from 0.68–0.3 and 0.75–0.35 at 120 dB and 135 dB SPL. It is clear from the analysis of the results that the acoustic effect on the particles occurs within a split part of second and slowly decreases with increasing exposure time, which is important to know, because too long exposure time (> 7 s) in the chamber can be the potential cause of the increase in fine particle concentration. Therefore, an effective and properly selected exposure time is required for an efficient agglomeration process.

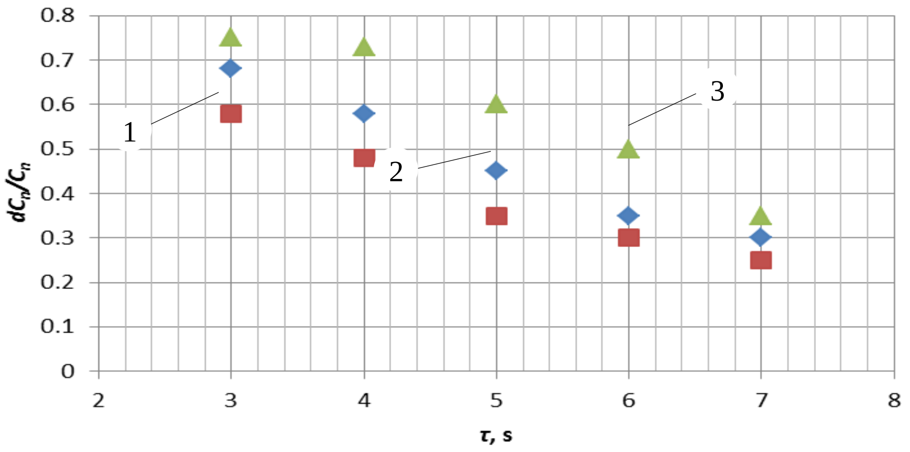

Fig. 3. Influence of exposure time on acoustic agglomeration of PM by changing SPL: 1 – 110 dB, 2 – 120 dB, 3 – 135 dB

Results of exposure time and SPL analysis correlate well with the literature data, which present similar sensitivity of acoustic effect to an increase of SPL and consistent change of the exposure time influence. Figure 3 shows the increased efficiency of $PM_{2.5}$ agglomeration by increasing SPL over the same exposure time. Therefore, an effective agglomeration process requires high SPL and sufficient exposure time.

Samples of solid microparticles taken under isokinetic conditions using a gravimetric sampler and were analyzed using an electronic microscope (Fig. 4). The average diameter of PM increases at least 4 times, when the SPL increases from 110 dB to 135 dB.

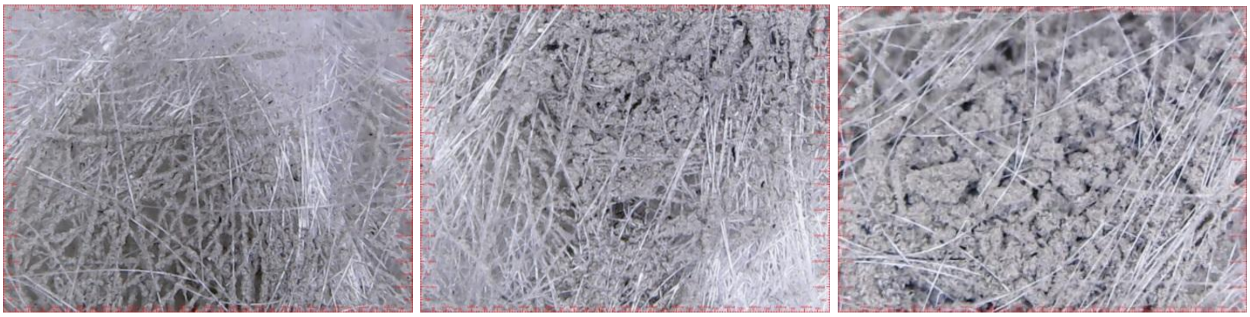

Fig. 4. The influence of change in the initial concentration of PM on the development of acoustic agglomeration

The influence of PM initial mass concentration was determined in the range of 175–700 mg/m^3 according to the change in particle concentration. However, 10–160 mg/m^3 of PM mass concentration was determined prior to the agglomeration chamber and 10–40 % change in particle mass concentration after a agglomeration chamber. Obviously, the acoustic agglomeration is more effective in solving the fly-ash problem, if the initial concentration of $PM_{2.5}$ is increased, but at 300 mg/m^3 the maximum effect was achieved, while the flow was 190 m^3/h and in the range of 300–700 mg/m^3 acoustic agglomeration have been found to have a constant 40% effect.

The determined mass concentration of PM overlapping with [13] and the [7, 9, 10, 12] results can be achieved by using acoustic and water drops effect [7, 12]. Acoustic agglomeration methods were compared according to the change in PM size, because the chemical composition of the particles does not affect the acoustic impact. Therefore this method can be applied for ESP and cyclone efficiency increase in solid biomass as well as coal plants even though the composition and size of volatile ash of coal and biomass are different.

4. CONCLUSIONS

The most important 0.1–5 μm agglomeration control factors (such as radiation frequency, SPL, and exposure time and initial particle concentration change) were evaluated experimentally. The increase of $PM_{2.5}$ deposition can be seen from Table 1 and Fig. 3 when the radiation frequency and SPL have been increased. The optimum exposure time was determined to be equal to 3–7 s according to Fig. 3, above which the efficiency of the acoustic agglomeration significantly decreases. The minimal initial particle concentration was found to be about of 175 mg/m^3 when apparent acoustic agglomeration of the fly-ash particles was observed.

The agglomeration efficiency of 0.1–5 μm particles was determined to be 40% at a flow rate of 190 m^3/h and fly ash concentration 300 mg/m^3. The change of dC_n and dC_m remained essentially the same after increase of flow rate 16–510 m^3/h.

The analysis of the microparticles using a gravimetric analyzer leads to the conclusion that the reduction in mass concentration of 10–20 % $PM_{2.5}$ can be achieved regardless of other exposure factors, when the initial concentration of PM was 300–700 mg/m^3.

REFERENCES

1. FLAGAN, Richard C.; SEINFELD, John H. *Fundamentals of air pollution engineering*. New Jersey: Prentice-Hall Englewood Cliffs, 1988. 537 p. ISBN 0-13-332537-7.
2. KATARZYNA, J.-R., KOWALCZYK, D. Size distribution and trace elements contents of coal fly ash from pulverized boilers. *Polish Journal of Environmental Studies*, 2013, Vol. 22, No. 1, p. 25–40.
3. JAWOREK, A., KRUPA, A., CZECH, T. Modern electrostatic devices and methods for exhaust gas cleaning: a brief review. *Journal of Electrostatics*, 2007, Vol. 65, No. 3, p. 133–155.
4. GUTTIKUNDA, S.K., GOEL, R. Health impacts of particulate pollution in a megacity—Delhi, India. *Environmental Development*, 2013, Vol. 6, No. 1, p. 8–20.
5. CAO C., JIANG W., WANG B., FANG J., LANG J., TIAN G., JIANG J., ZHU T.F. Inhalable Microorganisms in Beijing’s PM2.5 and PM10 Pollutants during a Severe Smog Event. *Environmental Science & Technology*, 2014, Vol. 48, No. 3, p. 1499–1507.
6. NEVERS, N. *Air Pollution Control Engineering*. Illinois: Waveland Press, 2010. 582 p. ISBN 1577666747.
7. LUO, Z., CHEN, H., WANG, T., ZHOU, D. LU, M., HE, M., FANG, M., CEN, K. Agglomeration and capture of fine particles in the coupling effect of pulsed corona discharge and acoustic wave enhanced by spray droplets. *Powder Technology*, 2017, Vol. 312, No. 1, p. 11–20.
8. CHEN, H., LIU, W., LI, J., XUN, X., SHEN, X. Experimental study on acoustic agglomeration of fine particles from coal combustion. International Conference on Digital Manufacturing & Automation 2010. Proceedings of annual conference on digital manufacturing & automation, 2010, Changsha, China. 2010 December 18-20.
9. ZHOU, D., LUO, Z., JIANG, J., CHEN, H., LU, M., FANG, M. Experimental study on improving the efficiency of dust removers by using acoustic agglomeration as pretreatment, *Powder Technology*, 2016, Vol. 289, p. 52–59.
10. LIU, J., WANG, J., ZHANG, G., ZHOU, J., CEN, K., Frequency comparative study of coal-fired fly ash acoustic agglomeration, *Journal of Environmental Sciences*, 2011, Vol. 23, No. 11, p. 1845–1851.
11. Zhao, Y., Zeng, X., Tian, Z. Acoustic agglomeration of fine particles based on a high intensity acoustical resonator. *AIP Conference Proceedings*, 2015, p. 1–5.
12. ZHANG, G., ZHANG, L., WANG, J., HU, E. Improving acoustic agglomeration efficiency by addition of sprayed liquid droplets. *Powder Technology*, 2017, Vol. 317, No. 15, p. 181–188.
13. GALLEGO-Juárez, J. A., De SARABIA, E. R.-F., RODRÍGUEZ-Corral, G., HOFFMANN, T. L., and GÁLVEZ-Moraleda, J. C., RODRÍGUEZ-Maroto, J. J., GÓMEZ-Moreno, F. J., BAHILLO-Ruiz, A., MARTÍN-Espigares M. Application of acoustic agglomeration to reduce fine particle emissions from coal combustion plants. *Environmental Science & Technology*, 1999, Vol. 33, No. 21, p. 3843–3849.
14. OZAROVSKIS, D. *The research of acoustic cyclone*: doctoral dissertation. Vilnius: Technika, 2012. 118 p. ISBN 978-609-457-422-1.

CYSENI 2019, May 23-24, Kaunas, Lithuania
ISSN 1822-7554, www.cyseni.com

DESIGN AND EVALUATION OF A CONCENTRATING SOLAR COLLECTOR BASED INTEGRATED PLANT WITH THERMAL ENERGY STORAGE

M. Koc
Isparta University of Applied Sciences
Cunur, 32260 – Turkey
Email: muratkoc@isparta.edu.tr

Y. E. Yuksel
Afyon Kocatepe University
Gazligol Street, 03200 – Turkey

M. Oztruk
Isparta University of Applied Sciences
Cunur, 32260 – Turkey

ABSTRACT

Nowadays, to generate the power, heating-cooling, drying, hot-fresh water, hydrogen and other synthetic fuels, the multigeneration systems have important role in the developing and under-developing countries. In this paper, the energetic and exergetic evaluations of a concentrating solar collector based integrated system for multigeneration with thermal energy storage are given. The investigated solar plant consists of parabolic dish collector to produce useful heat, Rankine cycle to produce power, high temperature steam electrolyzer to produce hydrogen, quadruple effect absorption cooling system to produce cooling effect, thermal energy storage system to storage thermal energy, hot water production system to produce hot water for residential applications. Finally, the effect of environmental condition and some design conditions on the solar plant performance is investigated.

Keywords: Thermodynamic analysis, concentrating collector, thermal energy storage

1. INTRODUCTION

Nowadays, meeting energy need is very important for rapidly increasing consumption rate. Also, energy consumption is increasing day by day with the increase of population and industrial development. But current energy resources, especially fossil fuels, are gradually decreasing. One of the most significant solution for this problem is to find new, environmentally, economical, reliable and secure energy sources [1]. The world’s largest energy source is Sunlight. Solar energy is free, clean and renewable [2]. It isn't also technologically complex. So, we need to use the sunlight to produce energy. The parabolic dish collectors are one of the most appealing ways of energy production because of the high concentrations ratios which can be achieved [3]. In this study, authors have presented design and evaluation of a concentrating solar collector based integrated plant with thermal energy storage.

2. SYSTEM DESCRIPTION

The hot fluid obtained from solar energy is transferred to the hot water storage tank by flowing at point 2 on the 3-way valve 1 with flow 1. Likewise, the flow through flowing 1 and 3-way valve 2 is also sent to pump 1 to increase the low hot fluid pressure. Subsequently, the increasing

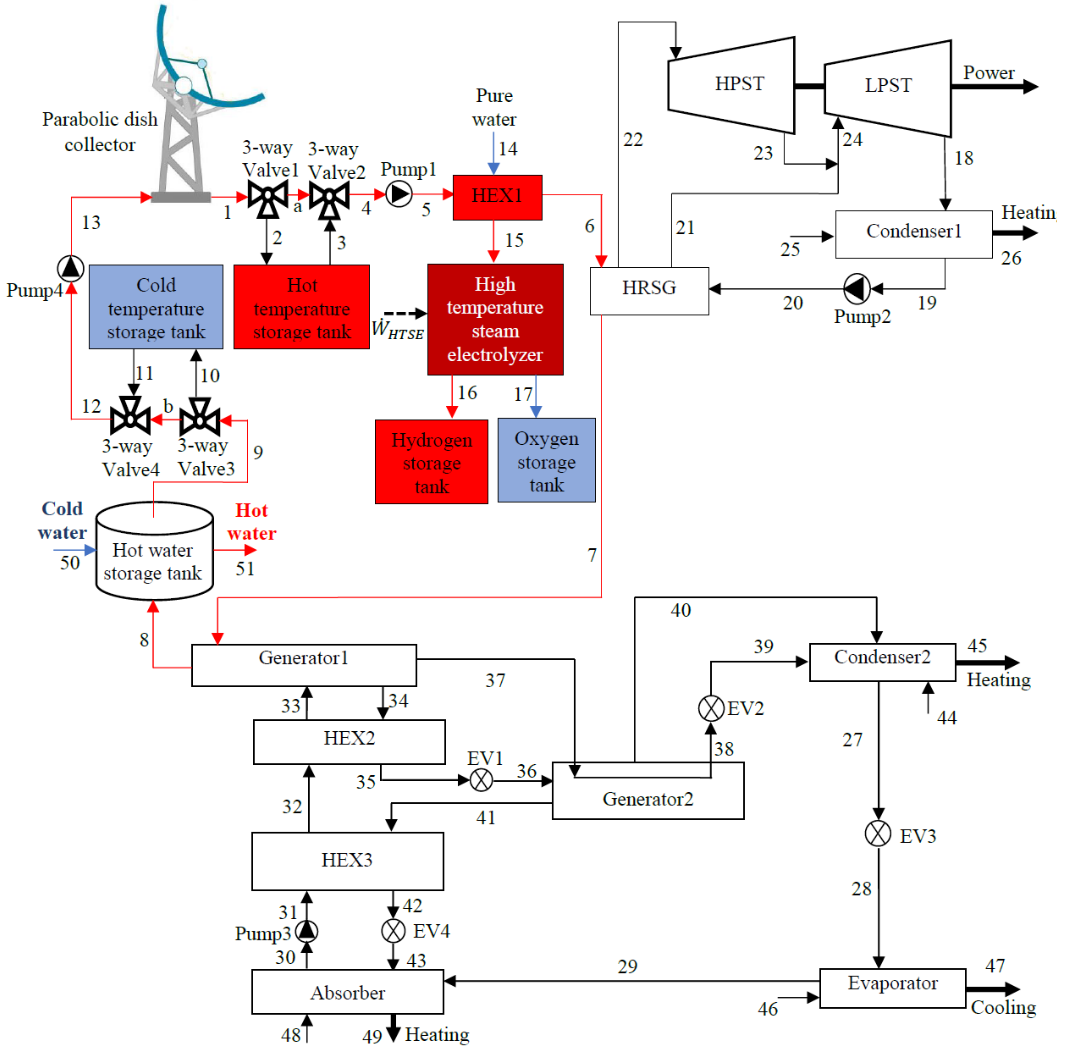

Fig. 1. Schematic diagram of solar energy based integrated plant

pressure of hot water, and the pure water are sent to HEX 1 by flows 5 and 14, respectively. The high-temperature steam electrolyzer (HTSE) is used to produce hydrogen from this energy system. The pure water required for HTSE is heated up to the operating temperature of electrolyzer in the heat exchanger and then flow to the HTSE through flow 15. The hydrogen and oxygen produced are then stored for later use. The part of hot fluid also enters the heat recovery steam generator (HRSG) to provide high and low pressure steam. The low pressure fluid is delivered to the generator 1 and the low pressure steam turbine by flow 7 and 21, respectively. High pressure steam is sent to high pressure steam turbine (HPST) by flow 22. At the same time, the pressure drop in HPST is sent to low pressure steam turbine (LPST) by flow 23. The power is generated by steam at low pressure, which enters the LPST with flow 24. In order to obtain heating output, the fluid is sent to condenser 1 by flow 18. The heating output is obtained from the condenser 1 with flow 26. The low enthalpy fluid from turbine with flow 18 is sent to pump 2 by flow 19 to increase the pressure value after passing through the condenser 1. The high pressure fluid from pump is sent to HRSG with flow 20. Thus, the Rankine cycle is completed. To achieve the cooling requirement, the exhaust gas enters the generator of the 7-line flow-through double-acting absorption cooling system. The weak fluid solution in stream 30 is pumped with pump 3 to reach the generator of the absorption refrigeration cycle by passing HEX 3 and HEX 2, respectively, by flowing at 31. At 34, water is cleared away from the fluid solution and the strong fluid solution returns to the absorber of cooling system through path 43 through passing HEX 2, low temperature generator (generator 2) and HEX 3 and expansion valve 4, respectively. On the other hand, water vapor comes out of generator 1 with flow

37, after entering the low-temperature generator, it enters the condenser 2. The fluid vapor flows into the expansion valve with flow 27, reducing the pressure and entering the evaporator through flow 28. The saturated steam from evaporator returns to the absorber with flow 29 and completes the cycle. As the enthalpy of exhaust gas from generator 1 is usable, the exhaust gas can provide enough energy to provide domestic hot water to be stored in the hot water tank.

3. THERMODYNAMIC ASSESSMENT

In order to analyze the energy systems, four balance equalities (mass, energy, entropy and exergy) must be investigated. By defining these equalities for plant, sub-plants and components, the thermodynamic equalities should be analyzed completely [4]. The mass balance is

$$\sum_{in} \dot{m} = \sum_{out} \dot{m} \tag{1}$$

here, $\dot{m}$ shows the inlet or outlet mass flow rate. The energetic balance is

$$\sum_{in} \dot{m}h + \sum_{in} \dot{Q} + \sum_{in} \dot{W} = \sum_{out} \dot{m}h + \sum_{out} \dot{Q} + \sum_{out} \dot{W} \tag{2}$$

here, $\dot{Q}$ and $\dot{W}$ show the heat transfer and power rate, h denotes the specific enthalpy. The entropy balance is

$$\sum_{in} \dot{m}s + \sum_{in} \frac{\dot{Q}}{T} + \dot{S}_{gen} = \sum_{out} \dot{m}s + \sum_{out} \frac{\dot{Q}}{T} \tag{3}$$

where, s is the specific entropy, $\dot{S}_{gen}$ denotes the entropy generation rate. The exergetic balance is

$$\sum_{in} \dot{m}ex + \sum_{in} \dot{E}x^{Q} + \sum_{in} \dot{E}x^{W} = \sum_{out} \dot{m}ex + \sum_{out} \dot{E}x^{Q} + \sum_{out} \dot{E}x^{W} + \dot{E}x_{D} \tag{4}$$

here, ex is the specific exergy.

$$ex = ex_{ph} + ex_{ch} \tag{5}$$

where ex_{ph} and ex_{ch} shows flow and chemical exergy.

$$ex_{ph} = (h - h_o) - T_o(s - s_o) \tag{6}$$

$$ex_{ch} = \sum n_i(u_i^0 - u_i^{00}) \tag{7}$$

where u_i^0 and u_i^{00} show the chemical potential of i^{th} part in the thermomechanical equilibrium and chemical equilibrium, respectively [5]. The other exergetic terms given in Eq. (4) are

$$\dot{E}x_Q = \left(1 - \frac{T_o}{T}\right)\dot{Q} \tag{8}$$

$$\dot{E}x_W = \dot{W} \tag{9}$$

$$\dot{E}x_D = T_0 \dot{S}_{gen} \tag{10}$$

here, $\dot{E}x^{Q}$ and $\dot{E}x_{W}$ show the exergy rate of heat energy and associated with shaft work, respectively, and also $\dot{E}x_D$ denotes the exergy destruction rate. The balance equalities of integrated plant components are defined in Table 1.

3.1. Efficiencies of integrated plant

The energetic and exergetic performance terms for single production are:

For power generation;

$$\eta_{sgen}=\frac{Energy\ in\ exit\ useful\ products}{Energy\ in\ inputs}=\frac{\dot{W}_{HPST}+\dot{W}_{LPST}}{\dot{Q}_{solar}+\dot{W}_{P1}+\dot{W}_{P2}+\dot{W}_{P4}} \tag{11}$$

$$\psi_{sgen}=\frac{Exergy\ in\ exit\ products}{Exergy\ in\ inputs}=\frac{\dot{W}_{HPST}+\dot{W}_{LPST}}{\dot{E}x^{Q}_{solar}+\dot{W}_{P1}+\dot{W}_{P2}+\dot{W}_{P4}} \tag{12}$$

The energetic and exergetic performance terms for double production are:

For power and cooling production;

$$\eta_{cgen1}=\frac{\dot{W}_{HPST}+\dot{W}_{LPST}+\dot{Q}_{Cooling}}{\dot{Q}_{solar}+\dot{W}_{P1}+\dot{W}_{P2}+\dot{W}_{P3}+\dot{W}_{P4}} \tag{13}$$

$$\psi_{cgen1}=\frac{\dot{W}_{HPST}+\dot{W}_{LPST}+\dot{E}x^{Q}_{Cooling}}{\dot{E}x^{Q}_{solar}+\dot{W}_{P1}+\dot{W}_{P2}+\dot{W}_{P3}+\dot{W}_{P4}} \tag{14}$$

For power and heating production;

$$\eta_{cgen2}=\frac{\dot{W}_{HPST}+\dot{W}_{LPST}+\dot{Q}_{Heating}}{\dot{Q}_{solar}+\dot{W}_{P1}+\dot{W}_{P2}+\dot{W}_{P3}+\dot{W}_{P4}} \tag{15}$$

$$\psi_{cgen2}=\frac{\dot{W}_{HPST}+\dot{W}_{LPST}+\dot{E}x^{Q}_{Heating}}{\dot{E}x^{Q}_{solar}+\dot{W}_{P1}+\dot{W}_{P2}+\dot{W}_{P3}+\dot{W}_{P4}} \tag{16}$$

For power and hydrogen production;

$$\eta_{cgen3}=\frac{\dot{W}_{HPST}+\dot{W}_{LPST}+\dot{m}_{H_2}LHV_{H_2}}{\dot{Q}_{solar}+\dot{W}_{P1}+\dot{W}_{P2}+\dot{W}_{P4}+\dot{W}_{HTSE}} \tag{17}$$

$$\psi_{cgen3}=\frac{\dot{W}_{HPST}+\dot{W}_{LPST}+\dot{m}_{H_2}ex_{H_2}}{\dot{E}x^{Q}_{solar}+\dot{W}_{P1}+\dot{W}_{P2}+\dot{W}_{P4}+\dot{W}_{HTSE}} \tag{18}$$

The energetic and exergetic performance terms for triple production are:

For power, cooling and heating production;

$$\eta_{tgen1}=\frac{\dot{W}_{HPST}+\dot{W}_{LPST}+\dot{Q}_{Cooling}+\dot{Q}_{Heating}}{\dot{Q}_{solar}+\dot{W}_{P1}+\dot{W}_{P2}+\dot{W}_{P3}+\dot{W}_{P4}} \tag{19}$$

$$\psi_{tgen1}=\frac{\dot{W}_{HPST}+\dot{W}_{LPST}+\dot{E}x^{Q}_{Cooling}+\dot{E}x^{Q}_{Heating}}{\dot{E}x^{Q}_{solar}+\dot{W}_{P1}+\dot{W}_{P2}+\dot{W}_{P3}+\dot{W}_{P4}} \tag{20}$$

For power, cooling and hydrogen production;

$$\eta_{tgen2}=\frac{\dot{W}_{HPST}+\dot{W}_{LPST}+\dot{Q}_{Cooling}+\dot{m}_{H_2}LHV_{H_2}}{\dot{Q}_{solar}+\dot{W}_{P1}+\dot{W}_{P2}+\dot{W}_{P3}+\dot{W}_{P4}} \tag{21}$$

$$\psi_{tgen2}=\frac{\dot{W}_{HPST}+\dot{W}_{LPST}+\dot{E}x^{Q}_{Cooling}+\dot{m}_{H_2}ex_{H_2}}{\dot{E}x^{Q}_{solar}+\dot{W}_{P1}+\dot{W}_{P2}+\dot{W}_{P3}+\dot{W}_{P4}+\dot{W}_{HTSE}} \tag{22}$$

The energetic and exergetic performance terms for multigeneration are:

For power, cooling, heating, hydrogen and hot water production;

$$\eta_{mgen}=\frac{\dot{W}_{HPST}+\dot{W}_{LPST}+\dot{Q}_{Cooling}+\dot{Q}_{Heating}+\dot{m}_{H_2}LHV_{H_2}+\dot{Q}_{Hot\_water}}{\dot{Q}_{solar}+\dot{W}_{P1}+\dot{W}_{P2}+\dot{W}_{P3}+\dot{W}_{P4}+\dot{W}_{HTSE}} \tag{23}$$

$$\psi_{mgen}=\frac{\dot{W}_{HPST}+\dot{W}_{LPST}+\dot{E}x^{Q}_{Cooling}+\dot{E}x^{Q}_{Heating}+\dot{m}_{H_2}ex_{H_2}+\dot{E}x^{Q}_{Hot\_water}}{\dot{E}x^{Q}_{solar}+\dot{W}_{P1}+\dot{W}_{P2}+\dot{W}_{P3}+\dot{W}_{P4}+\dot{W}_{HTSE}} \tag{24}$$

In addition to that, to investigate the thermodynamic analysis for integrated sub-plants, the energetic and exergetic performance equalities are given as:

For parabolic dish solar collector process;

$$\eta_{PDC} = \frac{\dot{m}_1(h_1 - h_{13})}{\dot{Q}_{solar} + \dot{W}_{P1} + \dot{W}_{P4}} \tag{25}$$

$$\psi_{PDC} = \frac{\dot{m}_1(ex_1 - ex_{13})}{\dot{E}x^Q_{solar} + \dot{W}_{P1} + \dot{W}_{P4}} \tag{26}$$

For high temperature steam electrolyzer;

$$\eta_{HTSE} = \frac{\dot{m}_{17} LHV_{H_2}}{\dot{m}_{14} h_{14} + \dot{W}_{HTSE}} \tag{27}$$

$$\psi_{HTSE} = \frac{\dot{m}_{17} ex_{H_2}}{\dot{m}_{14} ex_{14} + \dot{W}_{HTSE}} \tag{28}$$

For Rankine cycle process;

$$\eta_{RC} = \frac{\dot{W}_{HPST} + \dot{W}_{LPST} + \dot{Q}_{Heating}}{\dot{m}_6(h_6 - h_7) + \dot{W}_{P2}} \tag{29}$$

$$\psi_{RC} = \frac{\dot{W}_{HPST} + \dot{W}_{LPST} + \dot{E}x^Q_{Heating}}{\dot{m}_6(ex_7 - ex_6) + \dot{W}_{P2}} \tag{30}$$

For double effect absorption cooling cycle;

$$\eta_{DEAC} = \frac{\dot{Q}_{Cooling}}{\dot{m}_7(h_7 - h_8) + \dot{W}_{P3}} \tag{31}$$

$$\psi_{DEAC} = \frac{\dot{E}x^Q_{cooling}}{\dot{m}_7(ex_7 - ex_8) + \dot{W}_{P3}} \tag{32}$$

For hot water storage system;

$$\eta_{HWSS} = \frac{\dot{Q}_{Hot\_water}}{\dot{m}_8(h_8 - h_9)} \tag{33}$$

$$\psi_{HWSS} = \frac{\dot{E}x^Q_{hot\_water}}{\dot{m}_8(ex_8 - ex_9)} \tag{34}$$

The absorption cycle performance should be usually defined through the energetic and exergetic coefficient of performance. The COP_{en} and COP_{ex} of DEAC cycle can be given as:

$$COP_{en,DEAC} = \frac{\dot{Q}_{Eva}}{\dot{W}_{P3} + \dot{Q}_{Gen1} + \dot{Q}_{Gen2}} \tag{35}$$

$$COP_{ex,DEAC} = \frac{\dot{E}x^Q_{Eva}}{\dot{W}_{P3} + \dot{E}x^Q_{Gen1} + \dot{E}x^Q_{Gen2}} \tag{36}$$

4. RESULT AND DISCUSSION

Thermodynamic analysis of this proposed system has been performed via Engineering Equation Solver (EES) software. The results of thermodynamic analysis of system and its subsystems are given in Table 1. As given in this table, the hot water storage system and double effect absorption cooling have the maximum and minimum energetic and exergetic efficiencies, respectively. The power, heating-cooling, hot water and hydrogen production rates from the integrated solar energy-based system are given in Table 2. The effects of changing environmental temperature on the energy efficiency, exergy efficiency and system outputs of subsystems and the whole system are investigated. As shown in Fig. 2, when the ambient temperature increased from 0 to 40 ° C, the highest increase in the energy efficiency is realized in HWSS system.

Table 1. Thermodynamic analysis results for whole plant and its sub-plants

Sub-plants	**Energy efficiency (%)**	**Exergy efficiency (%)**	**Exergy destruction rate (kW)**	**Exergy destruction ratio (%)**
Parabolic dish collector	58.17	54.36	18850	35.65
High temperature steam electrolyzer	56.24	51.08	12570	23.77
Rankine cycle	41.62	38.74	11250	21.28
Double effect absorption cooling	16.35	13.16	8780	16.61
Hot water storage system	78.48	74.49	1425	2.69
Overall system	54.59	50.27	52875	100

Table 2. Integrated solar energy based plant outputs

Outputs	**Values**
High pressure steam turbine power, $\dot{W}_{HPST}$, (kW)	3548
Low pressure steam turbine power, $\dot{W}_{LPST}$, (kW)	1421
Cooling capacity, $\dot{Q}_{Cooling}$, (kW)	1564
Heating capacity, $\dot{Q}_{Heating}$, (kW)	2873
Hot water production capacity, $\dot{Q}_{Hot\_water}$, (kW)	3182
Hydrogen production rate, $\dot{m}_{Hydrogen}$, (kg/s)	0.00824

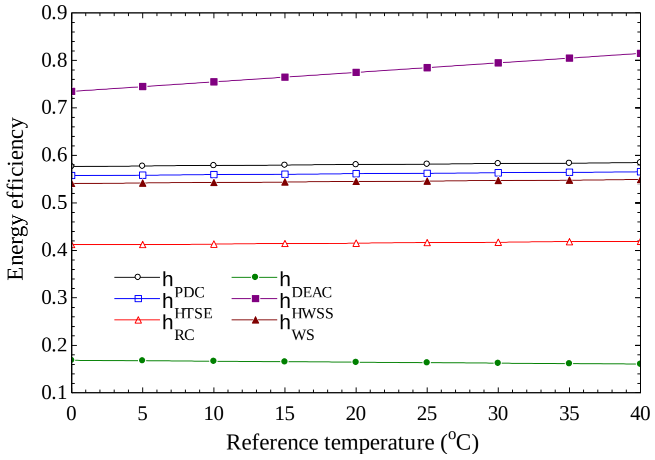

Fig. 2. Effect of reference temperature on whole plant and its sub-plants energy efficiencies

The effect of increasing ambient temperature on the exergy efficiency of the integrated system and sub-systems is shown in Fig. 3. As it can be seen from this figure, the exergy efficiency of all the sub-systems except the cooling system and the whole system are increasing with the increasing ambient temperature. This reduction in the exergy efficiency of refrigeration cycle is due to the increased ambient temperature increasing the cooling load. At the same time, the effect of changing ambient temperature on system outputs is shown in Fig. 4.

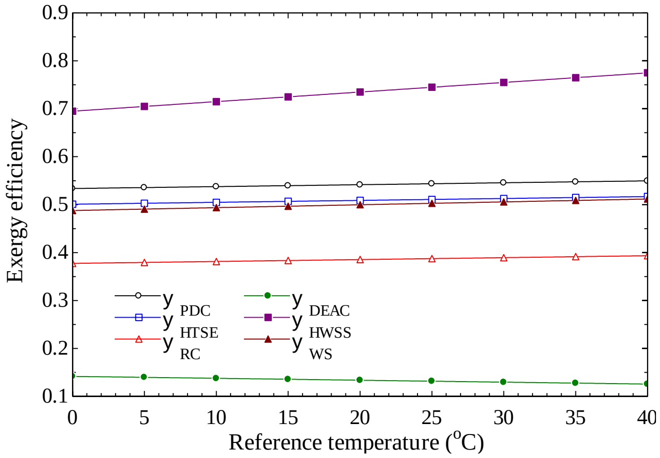

Fig. 3. Effect of reference temperature on whole plant and its sub-plants exergy efficiencies

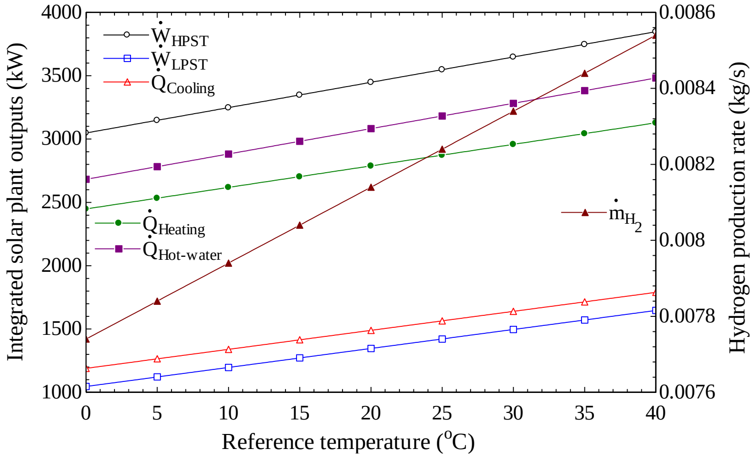

Fig. 4. Effect of reference temperature on power, cooling, heating and hydrogen production rate

The effects of changing solar radiation on the energy efficiency, exergy efficiency and system outputs of subsystems and the whole system were investigated. As shown in Fig. 5, when the solar radiation is increased from 500 to 1000 W/m^2, the energy efficiency of all sub-systems and the whole system is increasing with the increasing solar radiation.

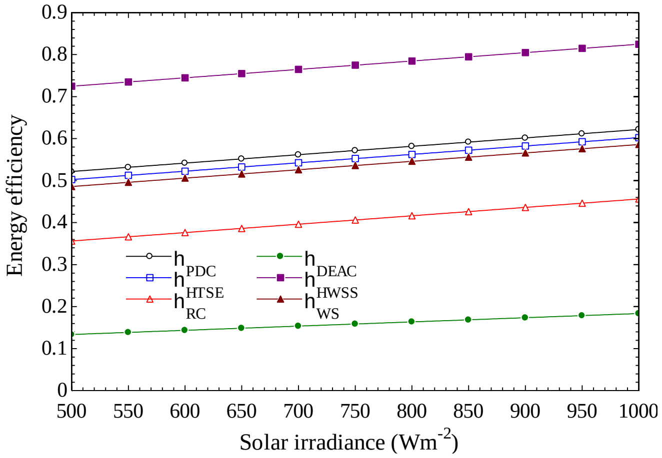

Fig. 5. Effect of solar irradiance on whole plant and its sub-plants energy efficiencies

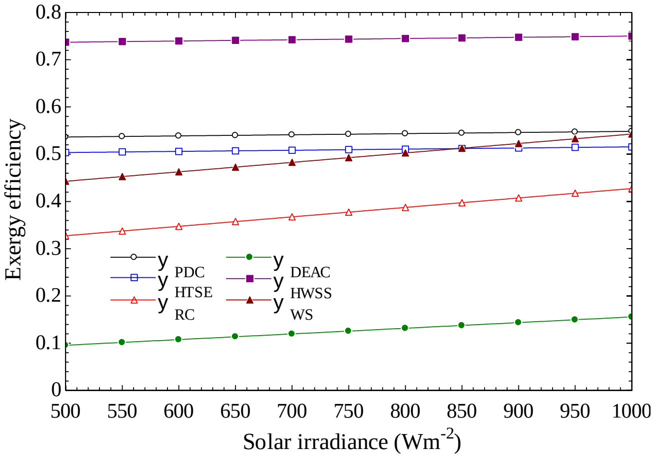

Fig. 6. Effect of solar irradiance on whole plant and its sub-plants exergy efficiencies

The effect of increasing solar radiation on the exergy efficiency of the integrated system and sub-systems is shown in Fig. 6. As seen from the figure, the exergy efficiency of all sub-systems and integrated system increases with increasing solar radiation.

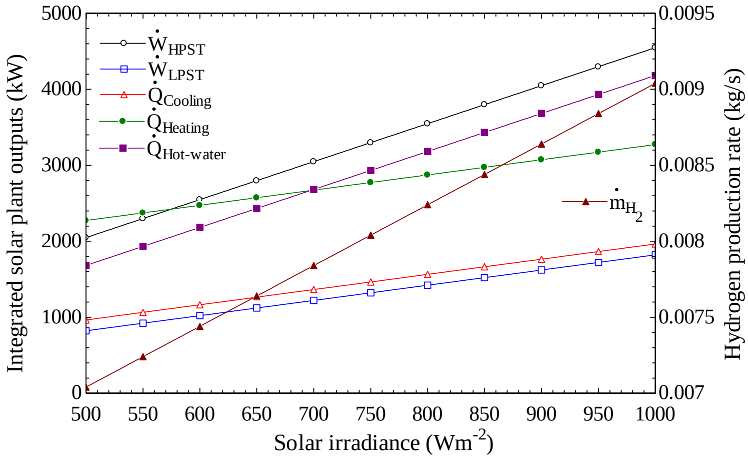

Fig. 7. Effect of solar irradiance on power, cooling, heating and hydrogen production rate

At the same time, the effect of changing solar radiation on system outputs is shown in Fig. 7. As given in this figure, the hydrogen production rate increase from 0.0072 to 0.0091 kg/s with increasing solar radiation.

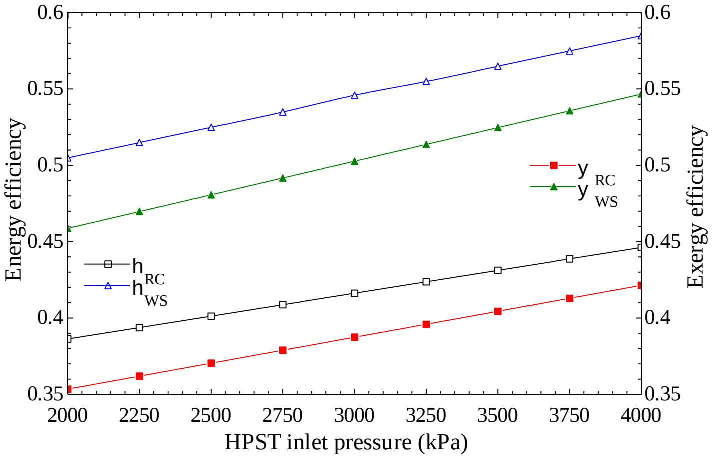

Fig. 8. Effect of HPST on energy and exergy efficiencies of Rankine cycle and whole plant

The effects of the changing high-pressure steam turbine inlet pressure on the energy efficiency and system outputs of the sub-systems and the whole system were investigated. As shown in Fig. 8, when the inlet pressure increases from 2000 to 4000 kPa, the energy efficiency of all sub-systems and the whole system increases with increasing inlet pressure.

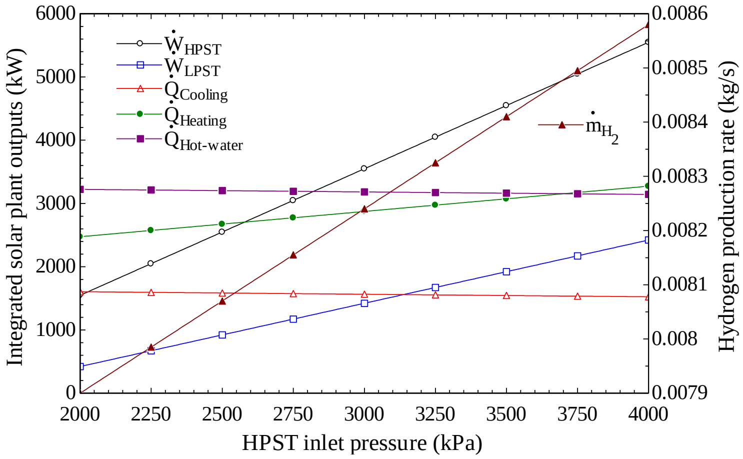

Fig. 9. Effect of HPST inlet pressure on power, cooling, heating and hydrogen production rate

The effect of the changing high-pressure steam turbine inlet pressure on the system outputs is shown in Fig. 9. As seen from the figure, as HPST inlet pressure increases, produced hydrogen increases from 0.0079 to 0.0086 kg/s.

5. CONCLUSIONS

In this study, authors have designed and evaluated of a concentrating solar collector based integrated plant with thermal energy storage. Power, heating, cooling, hot water, hydrogen and oxygen are obtained from this system. To investigate the system performance, the thermodynamic analysis and also some parametric studies are given. The energy and exergy efficiencies of the solar based integrated system are calculated as 54.59% and 50.27%, respectively.

REFERENCES

1. YUKSEL, Emre Y.; OZTURK, M.; DINCER, I. *Thermodynamic analysis and assessment of a novel integrated geothermal energy-based system for hydrogen production and storage.* International Journal of Hydrogen Energy, 2018, Vol. 43, p. 4233-4243.
2. WU, S.; XIAO, L.; CAO, Y.; LI, Y. *A parabolic dish/AMTEC solar thermal power system and its performance evaluation.* Applied Energy, 2010, Vol. 87, p. 452-462.
3. STEFANOVIC, Velimir P.; PAVLOVIC, Sasa R.; BELLOS, E.; TZIVANIDIS, C. *A detailed parametric analysis of a solar dish collector.* Sustainable Energy Technologies and Assessments, 2018, Vol. 25, p. 99-110.
4. DINCER, I; ROSEN, M. *Energy, Environment, and Sustainable Development*. Oxford: Elsevier, 2013. 459 p. ISBN 9780080445298.
5. BEJAN, A.; MORAN, M. *Thermal Design and Optimization.* New York: John Wiley & Sons, 1996. 281 p. ISBN 978-0-471-58467-4.

CYSENI 2019, May 23-24, Kaunas, Lithuania
ISSN 1822-7554, www.cyseni.com

RESEARCH OF RENEWABLE ENERGY RESOURCES' EFFECTS TO THE ENERGY MIX OF EU WITH OPTIMAL POWER FLOW CALCULATION

D. Kertesz, I. Vokony
Budapest University of Technology and Economics
Nap street 1082 – Hungary
Email: kertesz.david@eszk.org

ABSTRACT

The aim of this paper is to take a closer look on the challenges caused by weather dependent energy production while using optimal power flow (OPF) simulations. The importance, complexity and the different types of optimal power flow was analyzed during the optimal power flow calculations with a software of DIgSILENT Power Factory. This software can only be used for static simulations therefore, the paper shows a dynamic method to visualize the effects of renewable energy source production on three busses network. The dynamic method was also used on a grid model, which represents the energy mix of EU-28. Economic OPF simulations with different RES production scenarios were carried out which concluded that the significant underlying costs of using renewable energy sources are paid mostly by conventional power plants as these plants are tasked to control the power balance of the grid.

Keywords: optimal power flow, OPF, renewable energy sources, grid, DIgSILENT Power Factory, energy mix of EU-28

1. INTRODUCTION

The current composition of electricity generation is undergoing a massive transformation. Small-scale household power plants will become more widespread instead of high-capacity power plants. In addition to this, more high-capacity solar power plants and wind parks are being built. The extension of this development is well illustrated by that the installed wind and solar capacities of the EU-28 have dramatically increased.

The explosive growth is influenced by various favorable factors. Energy technologies are evolving at a rapid space, which is why solar panels and wind turbines are competing with conventional power generation solutions in terms of cost. Since 2008, the prices of photovoltaic systems on the roof have shrunk to a quarter. On the top of all, incentives to meet climate targets, high state subsidies have also contributed to the solar investments.

Thousands MWs of new renewable capacities have a strong market distorting effect thanks to the state subsidies. These production units can produce at very low variable costs, "almost free", thus changing the supply-demand connection. This makes increasingly difficult the operation of fossil fueled power plants, as well as making gas-fired units inoperable.

Nowadays, especially in the absence of sufficient amount of energy storage, the weather-dependent production of renewable energy sources (RES) are balanced by conventional power plants. Continuous up and down load affect the physical parameters and efficiency of these conventional power generation units. This paper determines the cost of this balancing, which is actually a kind of underlying cost of renewable energy (wind and solar) production. These tests were performed with Optimal Power Flow calculation. [1]

2. OPTIMAL POWER FLOW CALCULATION

2.1. The main task of Optimal Power Flow

A special type of load flow calculations is Optimal Power Flow (OPF) calculations. System-level optimal load balancing can be classified as operational control task.

The main task of OPF is to determine the load of the power plant units and the power flow through the transmission system according to the requirements of the electricity supply (keeping the voltage and frequency at consumer points) based on a predetermined optimization goals. Optimization can be done to minimize costs, system losses, or import balance. [2], [3]

Regardless of the goal of optimization, the quality and quantity requirements of electricity supply must always be met. One of the prerequisites for this is that the system-level load balance has to be fulfilled at any time:

$$P_G + P_I = P_C \tag{1}$$

where: P_G – total power supplied to the system [MW]; P_I – export-import balance, where imports are considered positive [MW]; P_C – total system consumption [MW].

Performing OPF calculations is a very complex task, mainly due to the complexity of the modelled network. Often, thousands of busbars and cables need to be optimized for which we need to know network parameters (e.g. voltage levels, impedances, nominal values, etc.). Optimization is further complicated by system requirements, goals and standards. Moreover, it is essential to care about the pre-cast power plant schedule, the units' resilience, and the standby capacity, which the fast shortages sudden be provided. [4], [5]

2.2. Cost minimization

According to today's money-based management system, OPF calculations that support cost reduction are most often used. If we look at the operation of a power plant from an economic point of view, the total cost of its life cycle can be broken down into fixed and variable costs. Permanent expenditures mean depreciation of investments that are independent from operating conditions, so we cannot change them. Conversely, variable costs depend mainly on the used technology, the type of fuel, the annual operating time. Therefore, in optimization, it is usually enough to minimize the cost of total primary energy carriers per unit ($C_{fuel,R}$ [EUR/s]). Of course, the sum of the fuel inputs of each power plant unit ($C_{fuel,i}$ [EUR/s]) determine the total cost of the system.

The power plant's equipment produce optimally on a given load or in its narrow range, but the actual power demand changes from moment to moment. For this reason, the load of the given block will change, which also change the fuel cost in time. (4), [6]

Based on these reviews to determine the optimal redispatch is a mathematical optimization problem where the objective function (OF) want to be minimized observing the extension functions (EF):

$$OF: C_{fuel,R}\left(P_{g1}, P_{g2}, \dots, P_{gi}, \dots P_{gn}\right) = \sum_{i=1}^{n} C_{fuel,i}\left(P_{gi}\right) = min \tag{2}$$

$$EF_1: P_C - P_I - \sum_{i=1}^{n} P_{gi} = 0 \tag{3}$$

$$EF_2: P_{gi,min} \le P_{gi} \le P_{gi,max} \tag{4}$$

In all cases, calculations were made for the system cost-optimal in this paper.

2.3. Power Factory description

By the end of the 1960s, mathematical models of OPF calculations were evolved and in the 70s, the development of related software began. For example, the DIgSILENT Power Factory, which was used in version 14.1 to make the calculations.

The optimal load flow simulations can use three mathematical methods in Power Factory:

- AC optimization
- DC optimization
- Contingency Constrained DC optimization

There are a number of configuration options available in the software under OPF menu. In addition to the optimization aspect, the calculation method, its equality constraints, and control variables are adjustable. Moreover, the type of load flow calculation method, the maximum number of iteration and convergence criteria can be determined. [7]

3. TEST METHOD

3.1. Process of development

When designing the test method, the primary consideration was to transform OPF calculations from static to dynamic, since the weather-dependent production of renewable sources can thus be best modeled. Steps to design the test method:

- Testing static OPF calculation options
- Making the calculations dynamic
- Testing the developed method
- Perform sharp tests on modelled networks

To develop and test this method, a three-buses network was used (coal fired power station, gas turbine block and consumer district). During the simulations, the compliance of the equality constraints of the test network (bus voltage, load capacity of power lines, operating ranges of power plants) must be checked.

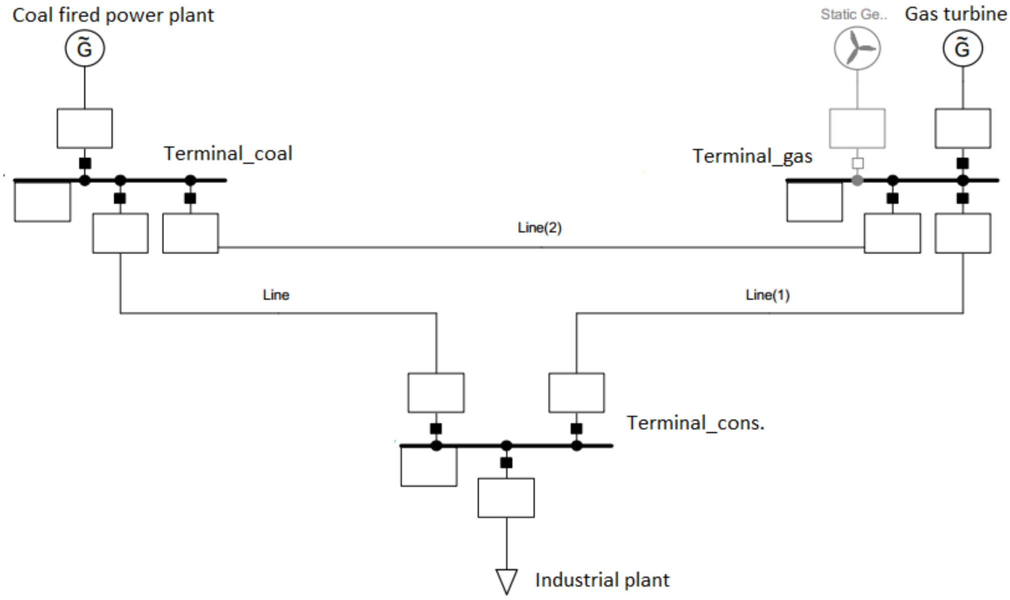

Fig. 1. Model of the test network in Power Factory

3.2. Converting calculations to dynamic

In order to make the Power factory calculation methods dynamic, two main conditions must be met. The first is that the test not only for a given status can be done, but also for a longer period. Another important step is to integrate the volatile production of RESs into the test models.

To satisfy the first condition, Power Factory's built-in programming language was used. In the program, pre-prepared scripts are found; one of them is called *Timesweep.pfd*. This allows us to run 15-minute load flow calculations. This script also calls another program code that can be used to draw the obtained results graphically.

None of the built-in available scripts can be used to run OPF simulations, so a new script was created to run optimal power flow calculations by converting *Timesweep.pfd*.

In the second aspect, the test method should be suitable for the treatment of volatile production of renewables. Fortunately, there is a solution in Power Factory. Consumers can provide consumption characteristics in many ways. As a result, the capability of managing these producing profiles were examined.

Initially, solar cells were modelled as a regenerative consumer, but the software could not handle the negative consumption. The modelling of wind turbines was implemented by synchronous generators, but the Power Factory did not correctly interpret the input characteristics. Finally, static generators (equipment without rotating masses) managed to properly model renewable energy sources.

Each of the later used daily characteristics were generated with relative values in a quarter-hour breakdown. The advantage of this process is that it is enough to use one profile for consumers/producers with different rated, nominal inputs/outputs.

3.3. Testing the developed method

The function of the fictional test method was analyzed on the test network. First, a consumption characteristic was set for the consumer, then a dynamic AC based OPF was run using the written script.

The test can be considered a success because the consumption needs were met at every time and conformed the previously defined equality limits. The latter shows that the load of gas turbines did not fall below the minimum dispatch, and in the case of peak consumption, the output of gas turbines increased, while the coal power plant fell slightly to avoid overloading the transmission lines.

It was also checked whether the characteristics associated with a static generator were properly handled by the software and whether the script displayed the input profile well.

Based on these, the described test method was suitable for performing real simulations.

4. ENERGY MIX OF EUROPE

4.1. Modelling the European network

The European network is a very complex system, so it is difficult to model. The aim of the research is to build a model network based on the energy mix of the European Union, which can be used to analyze the effect of photovoltaic and wind-based volatile energy production next to normal operating conditions.

The EU-28 Member States had approximately 958 GW of built-in capacity in 2013, with a peak network capacity of 529 GW. Oil-based units have been neglected when modelling the production site, as they do not operate due to their high production costs in the normal operation of the system. In addition, the model does not consider biomass and biogas fueled blocks. This is because the fuel composition of biomass-fired power plants is very difficult to model during the calculations and they are often only competitive with the inclusion of secondary heat production. (Table 1).

Table 1. The European Union's energy mix modelling based on built in capacities [8]

Type	Capacity [MW]
Coal	95
Lignite	80
Hydro	150
Nuclear	123
Wind	118
Photovoltaic	80
Gas	128
Total	774

The network was created to minimize costs by running DC-based OPF, so that reactive power was not modelled due to the complexity of the European network.

4.2. Parameters of power plant types

Each power plant can be characterized by its maximum load, its operating range, the fuel used, the emissions, its up and down loading speed and its efficiency. When looking for a system cost-optimal, the operating costs of each block need to be known. A cost minimization method was mentioned in chapter 2.2, the article examines a more complex cost system during the simulations. These costs consist of three parts: fuel costs, maintenance and operating costs and CO_2 quota prices.

$$C_{var} = C_{fuel} + C_{O\&M} + C_{CO2} \tag{5}$$

where: C_{var} – Power plant specific variable cost [EUR / MWh]; C_{fuel} – Power plant specific fuel specific fuel cost [EUR / MWh]; $C_{O\&M}$ – Power plant specific operating and maintenance costs [EUR / MWh]; C_{CO2} – CO_2 quota price [EUR / MWh].

The efficiency of conventional power plants is highly dependent on external factors such as temperature or current load. Therefore, the change in efficiency also changes the specific fuel costs, so they are calculated as follows:

$$C_{fuel} = \frac{3{,}6 \cdot C_{fuel}}{\eta} \tag{6}$$

where: C_{fuel} – Power plant specific fuel specific fuel cost [EUR / kWh]; $C_{fuel.x}$ – Specific cost of used fuel [EUR / GJ]; η – Power plant efficiency [%].

O&M (Operations and Maintenance) costs include the salary of the plant's employees and operation-related maintenance costs. For the calculations, the annual O&M costs in \$ / kW were available in units, so they were converted:

$$C_{O\&M} = \frac{C_{O\&M,P} \cdot P_{capacity}}{8760 \cdot \ P_{actual}} \tag{7}$$

where: $C_{O\&M}$ – Power plant specific operating and maintenance costs [EUR / MWh]; $C_{O\&M,P}$ – Power plant specific operating and maintenance costs [EUR / MW]; $P_{capacity}$ – Power plant installed capacity [MW]; P_{actual} – Current power plant load [MW].

Fossil-based blocks have CO_2 emissions after which they are required to pay CO_2 tax to compensate for the damage caused to the environment. They also lose competitiveness with renewable energy sources. The amount to be paid for the quantity issued is calculated as follows:

$$C_{CO2} = \frac{3{,}6 \cdot x_{CO2} \cdot C_{CO2,y}}{1000 \cdot \eta} \tag{8}$$

where: C_{CO2} – Power plant specific CO$_2$ quota price [EUR / kWh]; x_{CO2} – Fuel-specific CO$_2$ emissions [t / GJ]; $C_{CO2,an}$ – Annual average price for CO$_2$ quota [EUR / t]; η – Power plant efficiency [%].

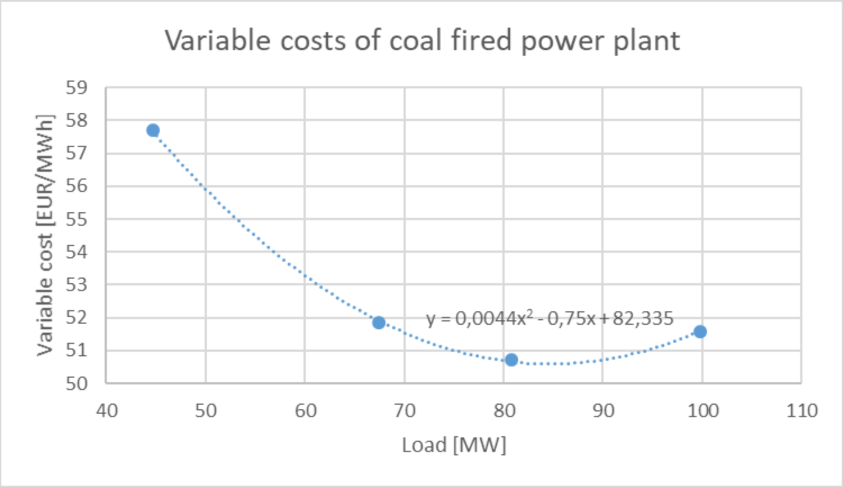

Fig. 3. Variable costs of coal fired power plant

The variable costs are determined by the proportional P-η function of Hungarian power plants, considering the cost of fuel and their operating range [9], so that the P-C$_{var}$ function of the given power plant type can be specified. P-C$_{var}$ equations are displayed to fit the measurement points by adding a polynomial-based trend line [10], [11], [12]. In Table 2 shows the range of variable costs based on power plant types.

Table 2. Efficiency-dependent variable costs of power plant types

Type	Variable costs [EUR/MWh]
Coal	50,7-57,7
Lignite	32,3-38
Hydro	4,63
Nuclear	37,1
Wind	4,6
Photovoltaic	2,5
CCGT	75,3-97,7

4.3. Network structure

The requirements for the modern electricity system have been considered in the design of the looped network (Figure 4). The system is based on 20, 120, and 220 kV transmission lines, which have been parameterized with the data of the Hungarian system (Table 3). In the model, the individual production units and consumption points are dispersed. The individual production units were modelled using the models built into Power Factory. The hydropower plant was set up as a slack on the network.

Table 3. Grid parameters

Voltage level [KV]	Resistivity [Ω/km]	Reactivity [Ω/km]	Capacity [nF/km]
20	0.677	0.394	9
120	0.117	0.4	9
220	0.1173	0.44	1

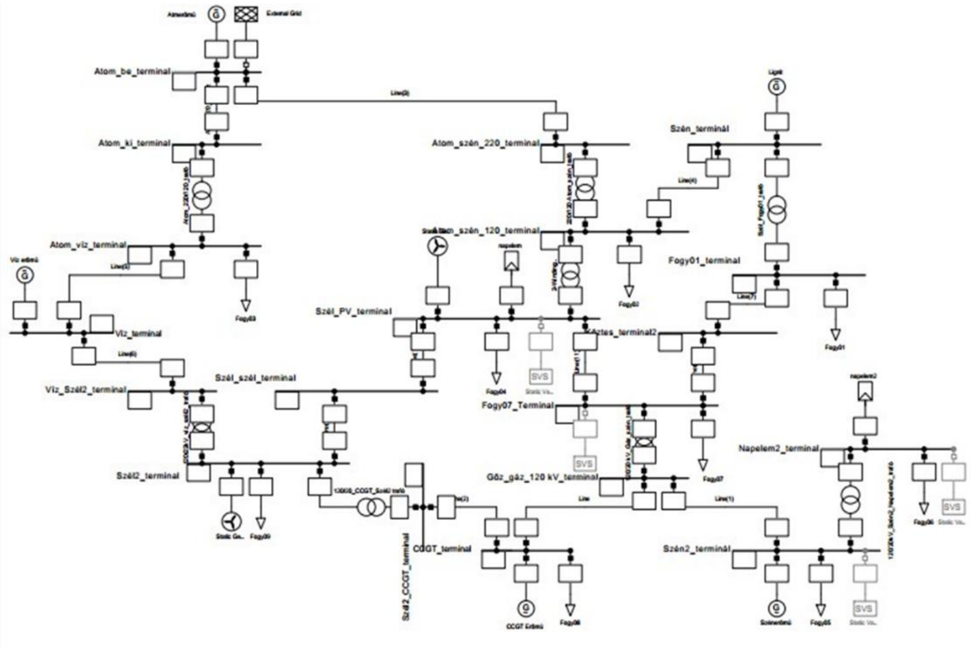

Fig. 4. The modelled energy of the European Union mix with simplified network

4.4. Applied scenarios

The simulations have been performed under different scenarios, in order to compare the weather-dependent production of RESs in some special cases. Thus, the relative profiles for three unique options are based on MAVIR (Hungarian Transmission System Operator) wind power production data and photovoltaic energy production data from “ Livable Future Park”. Wind power and solar power plants installed on the grid have different characteristics for each scenario. In addition to fix these profiles, the other power-generating units have automatically changed the effective output during DC-based OPF calculation.

In the first case, it was investigated when there is stable and large production of both solar and wind generation. The second scenario examines a case when wind is not blowing during the day, but the production of solar panels can compensate to some extent. The last case uses relative profiles when there is relatively little wind production, and the amount of photovoltaic energy is highly dependent on the weather conditions. (Figure 5.)

The characteristics of the consumers are aggregated and adjusted based on MAVIR daily load data. During the simulations, the operating range of the power plants has been defined as the load limit.

A fourth scenario was also launched to evaluate the results when solar and wind power plants were not connected to the grid. The results of this test can be used to show the underlying costs of weather-dependent production of RESs.

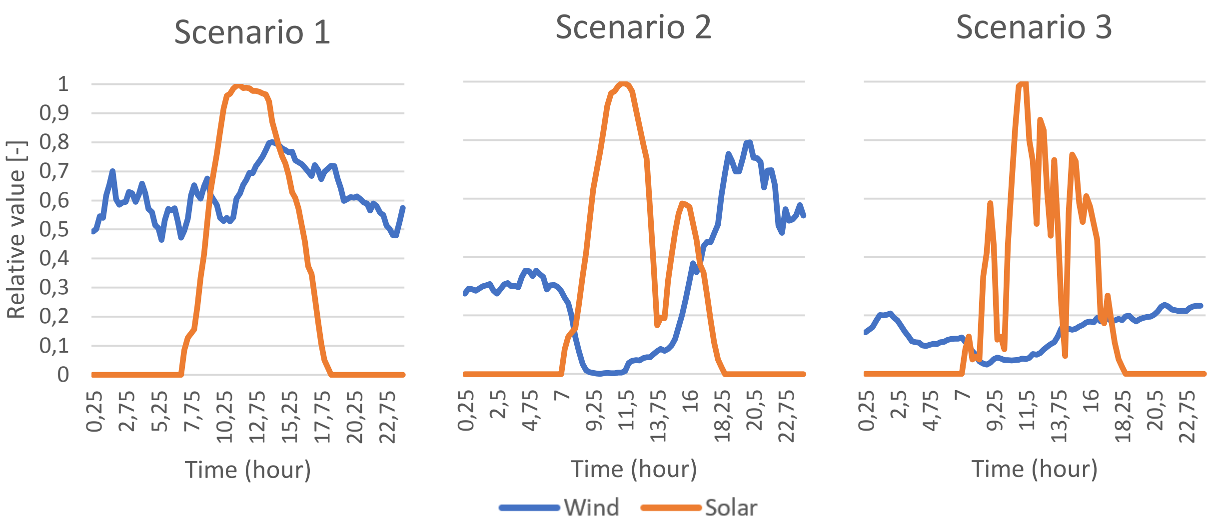

Fig. 5. Daily production - Scenario 1

4.5. Results

As described in Equation 1, the total consumption requirement of the system must be compensated at every moment. In the energy mix of EU-28, balancing the volatile production of renewable energy can be achieved when using the test model by changing the load of conventional blocks . As a result, our fossil units do not work in the economically optimal operation shown in Scenario 4, so the unit variable costs also increase.

The cost difference resulting from this change is the underlying cost which caused by the weather-dependent production of renewables. The calculation of this for each state of operation was made using the following equation:

$$C_{underlying,i} = E_{g,i} \cdot (C_{var,j,i} - C_{var,4,i}) \tag{9}$$

where: $C_{underlying,i}$ – The underlying cost of RESs at time segment i. [EUR]; $E_{g,i}$ – Produced energy by a given power plant at time segment i [MWh]; $C_{var,4,i}$ – Variable cost of the given power plant at time segment i in Scenario 4 [EUR/MWh]; $C_{var,j,i}$ – Variable cost of the given power plant at time segment i in scenario j [EUR/MWh].

For each of the scenarios examined, we managed to satisfy the consumption needs at any time.

In Scenario 1, coal, lignite and hydro generation were also operated under partial load, so there was an enough revolving reserves in case wind power production dropped drastically. In the morning, production increased in all three sub-load units due to increasing load. The high share of renewable production forced the CCGT power plant to shut down during the day, so it operated only in the evening, when solar energy was no longer available, but consumption was still significant (Figure 6).

The proportion of each power plant type represented by production and production costs was examined. The results thus obtained correspond to the significant price differences experienced in the production of cost functions.

During the day between 13:45 and 14:00, the production cost of the system was the lowest, since wind production was the most significant at that time, so the lignite-based unit was also heavily controlled and the CCGT power plant was not in operation at that time. The most expensive period was between 23:45 and 24:00, as consumer demand dropped significantly by then, but the CCGT power plant continued to operate as it had enough turnaround in the system.

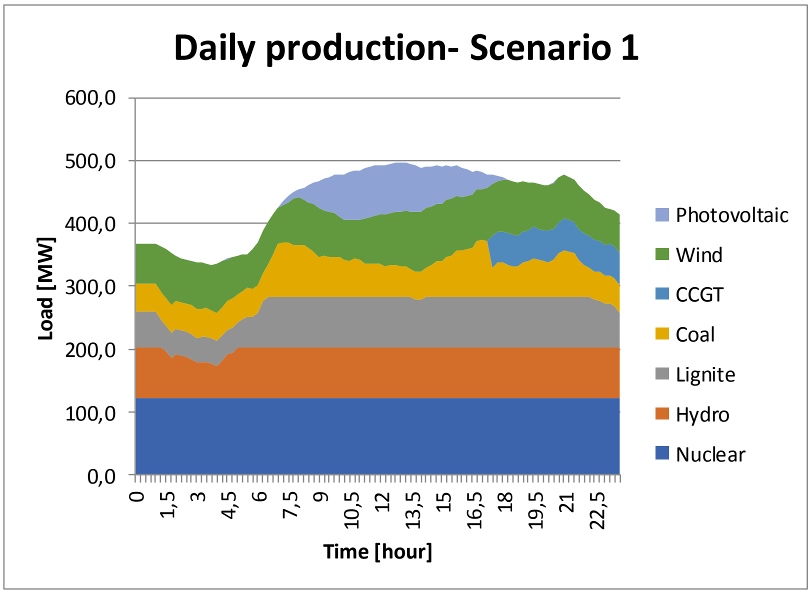

Fig. 6. Daily production - Scenario 1

In the analysis of Scenario 1, the underlying costs of the volatile production of RESs can be calculated with the above described (9) correlation. The daily production cost of the system in the model was 287,500 EUR of which 8,370 EUR can be written at the expense of weather-dependent solar and wind production.

Table 4 clearly shows that at higher share of renewables in production, the total daily production cost is less. However, the daily specific cost is the most difficult to estimate at this point, as there is a difference of more than 60% between the minimum and maximum unit costs. Despite these observations, the total cost of production is lower if the share of wind and solar energy is higher.

Table 4. Summary of results

	Scenario 1	**Scenario 2**	**Scenario 3**
Produced energy [MWh]	10500,9	10500,9	10500,9
Total cost of production [EUR]	287.500	379.800	398.420
Specific unit costs [EUR/MWh]	27,42	36,17	37,94
Share of wind and solar energy [%]	22	12	8
Underlying costs of RESs [EUR]	8.370	17.450	13.530
Underlying costs of RESs/total cost of production [%]	2,9	4,6	3,4

The underlying costs of renewables differ significantly in each scenario. The difference of thousands of EURs between Scenario 1 and Scenarios 2, 3 derives from the fact that in the first case, the CCGT block did not operate all day, only in the evening. In this respect, it gives a more realistic picture if we compare the underlying costs of renewables to the total cost of production. From this point of view, it is also important to consider when it comes that it is worthwhile to shut down a large power plant and thus keep a smaller rotating reserve in operation. If a wrong redispatch decision is made, the small amount of reserves in the system can also endanger security of supply.

Finally, the daily specific costs were compared with the average electricity prices of the 2013 energy exchange. This year was an annual average of 39.1 EUR/MWh, which is close to the results of the calculations [13].

5. CONCLUSION

The rapid expansion of RESs has a clear impact on the current electricity system. Weather-dependent production causes controlling difficulties that are challenging for operators.

After getting to know the optimal power flow calculations, the paper has presented a test method that can be used to analyze the effects of renewables on the system. This method can quantify the underlying costs of volatile production, which fell between 2.9% and 4.6% in the model. It represents billion-euro competitive disadvantage for conventional power plants in the European Union annually.

I trust that the article will draw attention to the importance of properly dimensioned and thoughtful network development and provide a basis for energy agencies to develop a regulation that would reduce the market distorting effects of volatile production and support for renewables.

For the further development of the topic, it would be worthwhile to make calculations with annual production data sets. The cost functions created for the simulations and the EU network can be easily reset so the modelling of future energy mixes can be easily solved. Furthermore, it would be useful to carry out the test on the Hungarian network with the actual parameters and cost functions of each production unit, the result of this test could support the system development plans.

REFERENCES

1. GERSE Á. “*Piactorzító hatások II.: Megújuló energiaforrások rendszerintegrációja”,* lecture at the Student Association of Energy, 2017.03.28.
2. DÁN A., RAISZ D. “*Kisfeszültségű hálózatok veszteségeinek tudásalapú modellezése*”, lecture, 2008.09.11.
3. FAZEKAS A. I. *A villamosenergia-rendszerek rendszerszintű tervezési feladatai*, Magyar energetika, 2004/2, 17-22 p.
4. FALUDI A., SZABÓ L. *Villamosenergia-rendszer üzeme és irányítása*, Budapest, 2011.
5. KIRSCHEN, D. *Optimal power flow*, lecture at the University of Washington, 2011.
6. FAZEKAS A. I. *Rendszerszintű optimális teherelosztás és termeléselosztás*, Magyar energetika, 2003/3, 7-10 p.
7. DIgSILENT Power Factory 14.1., Technical Reference.
8. Statistical pocketbook:EU energy in figures, 2015, 86-104.
9. BIHARI P., GÁCS I., GRÓF Gy., STRÓBL A. *Power plant efficieny data for an electrical energy market model – Hungarian Power Plant Data sheets*, Budapest, 2008.
10. Budapest University of Technology and Economics: Energetikai gazdaságtan, lesson 5, 2014.
11. https://www.eex.com/en/market-data/environmental-markets/auction-market/european-emission-allowances-auction#!/2013/12/10, checked: 2017.05.10.
12. http://www.power-technology.com/features/featurepower-plant-om-how-does-the-industry-stack-up-on-cost-4417756/, checked: 2017.05.10.
13. STRÓBL A. “*Merre tart a világ energetikája? Számokkal és irányzatokkal”*, lecture at the Student Association of Energy, 2017.02.21.

CYSENI 2019, May 23-24, Kaunas, Lithuania
ISSN 1822-7554, www.cyseni.com

RENEWABLE ENERGY STATUS AND SMART SOLUTIONS FOR TURKEY

Y. E. Yuksel
Afyon Kocatepe University
Gazligol Street, 03200 – Turkey
Email: yeyuksel@aku.edu.tr

M. Koc, M. Ozturk
Applied Science University of Isparta,
Cunur, 32260 – Turkey

ABSTRACT

Due to increasing energy demand of humankind in the World, the green energy production technologies based on the intelligent, clean and cheap options are required. Current energy infrastructure is not sustainable because most of energy needs for World and also Turkey has been met by using the fossil sources and unsmart technologies. In recent years, Turkey starts to change its energy substructure with new investments on the renewable energy sources and technologies, and also with new plans to meet its energy need including nuclear energy plants. In this study, existing energy situation and energy sources of Turkey are presented. In addition, smart solutions for new energy infrastructure are presented. On the other hand, the potential of renewable energy is supplied as solar, wind, geothermal, hydro energy, biomass, and wave energy. This study shows that Turkey has great potential in renewable energy sources, mainly hydropower, solar and wind energies that can be used as primary energy source of the country in the near future.

Keywords: Renewable energy, smart solutions, Turkey

1. INTRODUCTION

As fossil energy sources decrease, trends for transition to renewables have started to rise. Turkey, as many developed and developing countries do, have made investments on renewable energy usages in the last ten years. In literature, there are many studies showing that Turkey is rich in terms of renewable energy sources that can be developed and used in future [1]. According to Yuksel [2], from 1993 to 2003 electricity demand in Turkey has increased more than 8% per year due to economic development. Because of energy demand and increasing of it, Turkey has imported energy especially as natural gas in order to meet the needs [3]. However, that situation is not sustainable for future development and there are also some disadvantages of fossil energy sources such as emissions, external dependence and depletion of resources. Figure 1 illustrates the sources of electricity generation used in Turkey. As clearly seen from that figure, fossil fuel sources are the major part of the supplies for electricity generation.

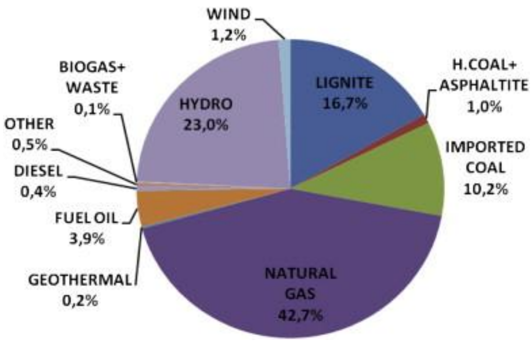

Fig. 1. Share of sources in electricity generation in Turkey [2]

Renewable energy sources are important factor for a development of a country, although there are some limitations to improve and increase the renewable energy usage.

2. RENEWABLE ENERGY STATUS OF TURKEY

2.1. Wind Energy Status of Turkey

Wind energy is clean, natural, renewable and unlimited source of energy of which source is Sun. 1-2% of solar energy converts to wind energy. Heat energy absorbed by earth surfaces is not homogenous and therefore this heat difference causes wind. Wind has two parameters as speed and direction. Wind speed increases with increasing height and maximum theoretical power increases as wind speed rises. Wind energy systems have some disadvantages like high initial investment cost and low capacity factor. However, there are many advantages of wind energy as follows:

- Wind is available in atmosphere bountiful and freely.
- It is a renewable and clean energy option.
- Source of wind energy is reliable. There is no risk of exhaustion.
- It has cost which is able to challenge to other energy production options.
- Cost of operation and maintenance is low.
- It decreases external dependence.

Because of its geographic position, Turkey has great wind energy potential in Marmara, South East Anatolian and Aegean regions. Table 1 shows the annual average wind speed and density with respect to regions in Turkey. These wind speed values have been measured 10 m above the surface between 1989-1998 and the values present in the table are average values. Obviously, at higher elevations and in some places these values will be higher than current numbers.

Table 1. Wind energy potential of Turkey with respect to regions at 10 m elevation [4]

Region	**Annual average wind speed (m/s)**	**Annual average wind density (W/m^2)**
South-Eastern Anatolia region	2.69	29.33
Mediterranean region	2.45	21.36
Aegean region	2.65	23.47
Middle Anatolia region	2.46	20.14
Eastern Anatolia region	2.12	13.19
Marmara region	3.29	51.91
Black Sea region	2.38	21.31
Average	2.58	25.82

Figure 2 demonstrates the wind map of Turkey. The wind speed is 5.0-6.0 m/s, 4.5-5.0 m/s and 3.5-4.0 m/s in red, yellow and green areas, respectively. In Marmara region, which is the North-West part of the Turkey, wind speed is higher than other regions because Marmara is a coastal region with different altitudes of area. This elevation difference and sea-coast effect causes wind. The same situation is seen also in Aegean region which is the West part of Turkey.

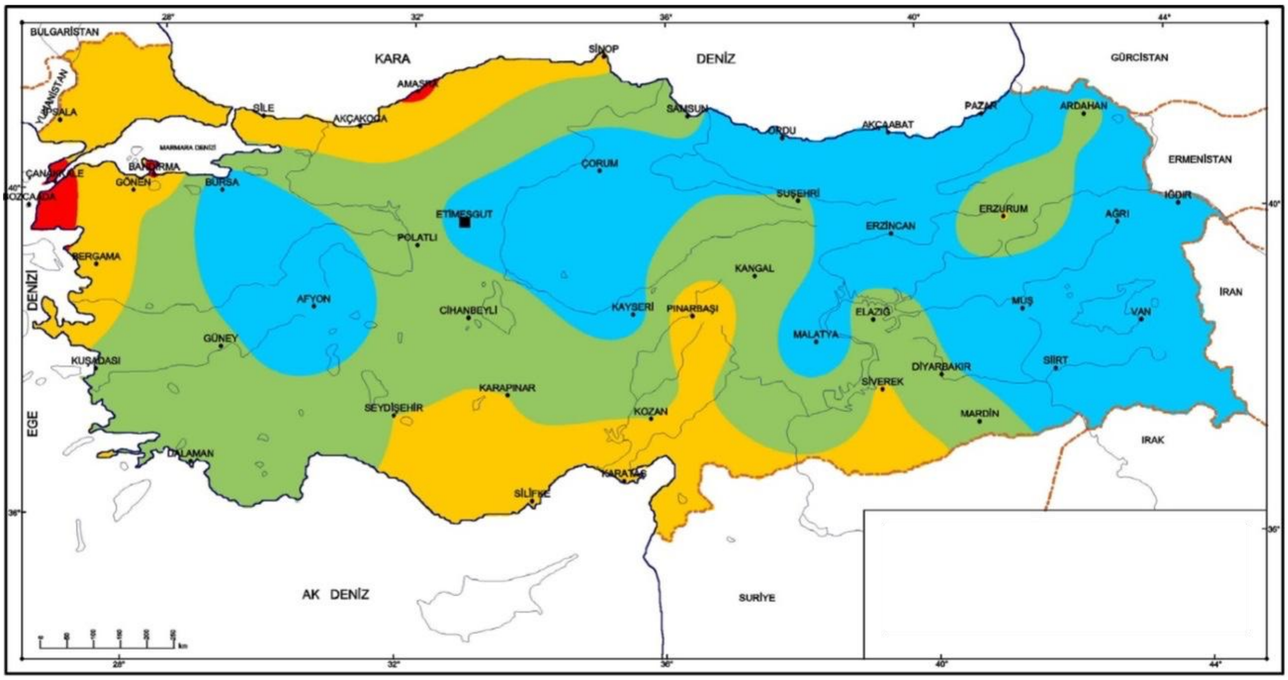

Fig. 2. The wind map of Turkey at 10 m above the surface [1]

In 2018, 19882 TWh electricity was produced via wind energy in Turkey. Total capacity of wind plants at the end of 2018 is about 7005 MW.

2.2. Solar Energy Status of Turkey

Solar energy is caused by fusion reaction in Sun core. Solar radiation is about 1370 W/m^2 out of atmosphere however due to atmosphere 0-1100 W/m^2 solar radiation is able to reach earth surface. After 1970s, studies to produce electricity from Solar energy have been increasing rapidly. There are different technologies to use solar energy such as photovoltaic, thermal and photovoltaic-thermal, concentrating collectors, solar towers and solar ponds. Turkey has rich solar energy sources as shown in Fig. 3.

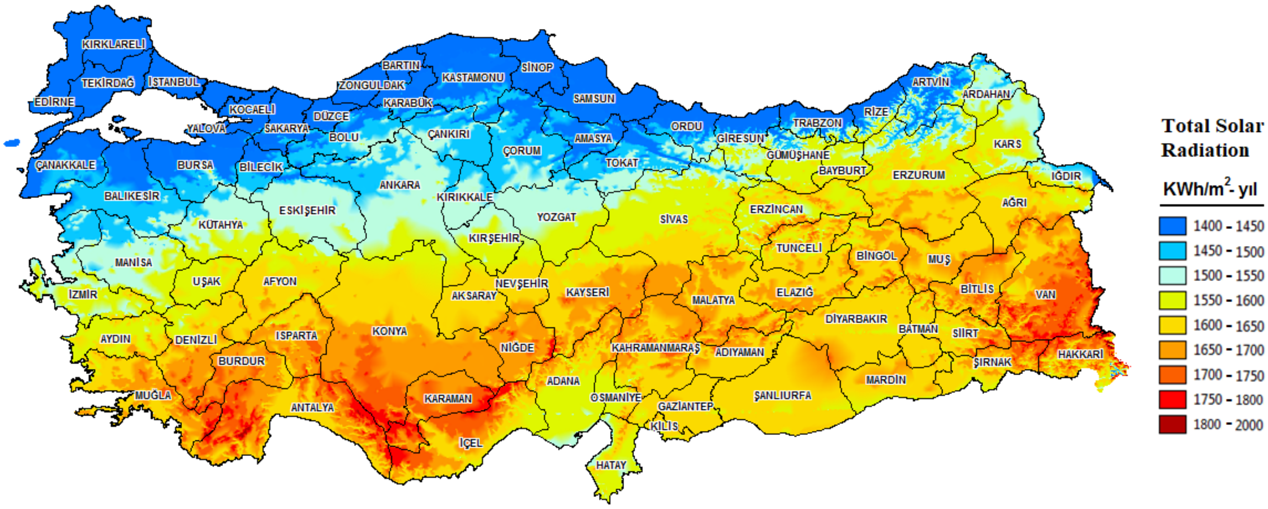

Fig. 3. Map of solar radiation in Turkey [5]

According to the map of solar radiation in Turkey, total annual sunshine duration is 2741 hours (daily average 7.5 hours), and total annual solar radiation is about 1527 kWh/m^2 [6]. In Turkey, total solar collector area has reached 20,200,000 m^2 at the end of 2018, and total heat production is about 10.2 TWh. In 2018, there are 5868 solar energy plants of which capacity is about 5063 MW. According to the Ministry of Energy of Turkey [6], share of solar energy of total electricity production has reached up to 2.5%.

2.3. Geothermal Energy Status of Turkey

Because of the location which is on the active tectonic line, Turkey has rich geothermal sources. There are about 1000 natural geothermal sources in different places of Turkey with different temperatures. Especially West Anatolian part of Turkey is rich in terms of geothermal potential in which 78% of geothermal sources locate in this region. 90% of geothermal sources are low grade sources and they are suitable for heating (space and green house), thermal and health tourism and industrial mineral gaining. Only 10% of geothermal sources are convenient for electricity generation. Fig. 4 illustrates the distribution of geothermal sources in Turkey with different temperatures. Turkey has increased its electricity production from geothermal with new investments and legal regulations. As a result of these investments and regulations, during the years between 2010 and 2015, Turkey has been the first country in terms of increasing rate of installed capacity of electricity generation from geothermal sources [7]. In Turkey, during the year of 2017 total electricity energy production is about 6.1 TWh.

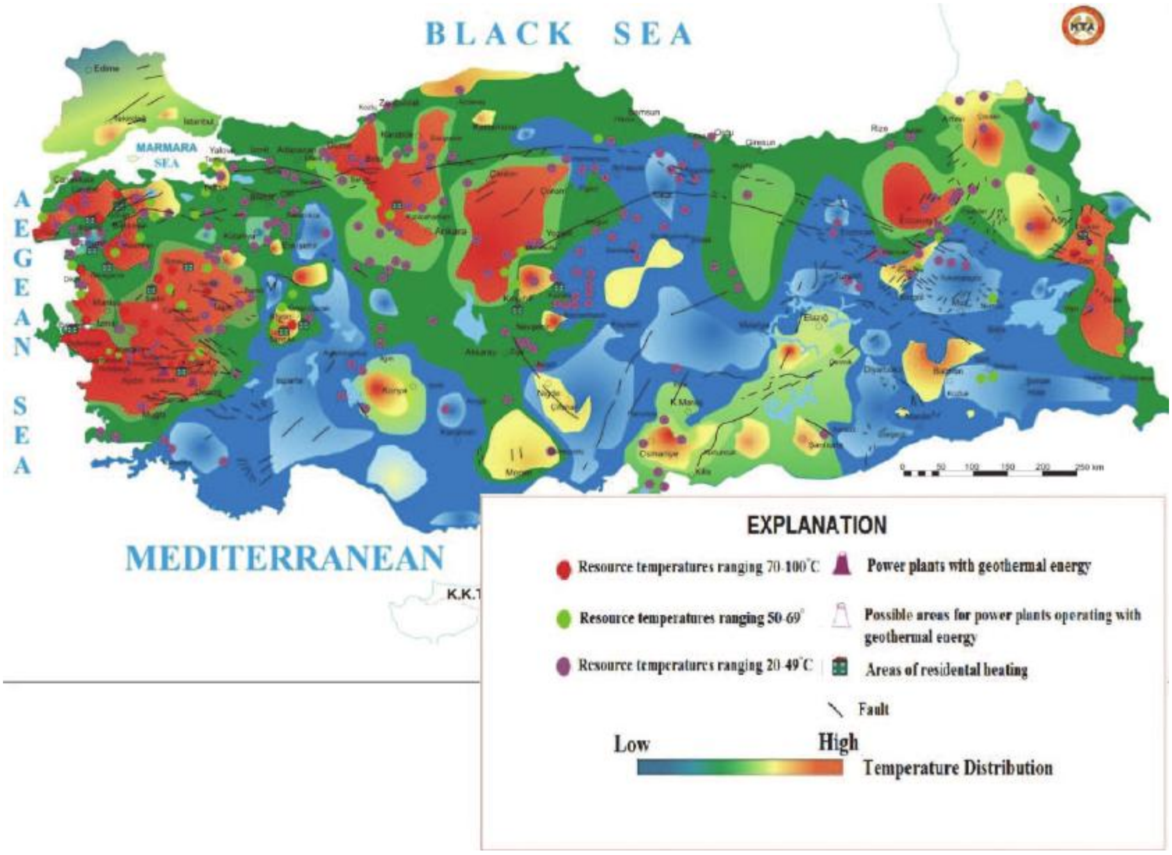

Fig. 4. Geothermal map of Turkey [8]

2.4. Hydropower Energy Status of Turkey

Hydropower plants are environmental friendly, clean, renewable, efficient, long lived, non-external dependent source of energy [9]. Theoretical hydropower potential of Turkey is 1% of World theoretical hydropower potential and economic potential of hydropower of Turkey is 16% of economic potential of Europe [10]. Theoretical potential of hydropower sources in Turkey which are the main part of renewable energy systems in Turkey is 433 TWh of which 216 TWh is assessable potential. In addition, economic hydropower potential of Turkey is 140 TWh/yr. In 2017, 58.2 TWh electricity was produced from hydroelectric sources in Turkey. At the end of June 2018, there are 636 hydropower plants of which capacities are 27912 MW. This rate of electricity production is 32% of total installed power plants in Turkey. Fig. 5 demonstrates the major rivers in Turkey, some of which is currently used for hydropower plants are some of which is potential for future use. Some of the important dams are Keban, Özlüce and Atatürk dams on Euphrate River, Arpaçay dam on Aras River, Seyhan and Çatalan dams on Seyhan, and Sır, Aslantaş and Kartalkaya dams on Ceyhan River. There were 150 dams in 1991 in Turkey and this number increased to 727 in 2017.

Fig. 5. Major rivers in Turkey [11]

Also Fig. 6 shows that the share of electricity production in Turkey. As it can be clearly seen, hydropower share in renewables are higher than other renewables by 2013. As seen from this figure, the share of hydropower among other renewables is 86.2% in Turkey by year of 2013.

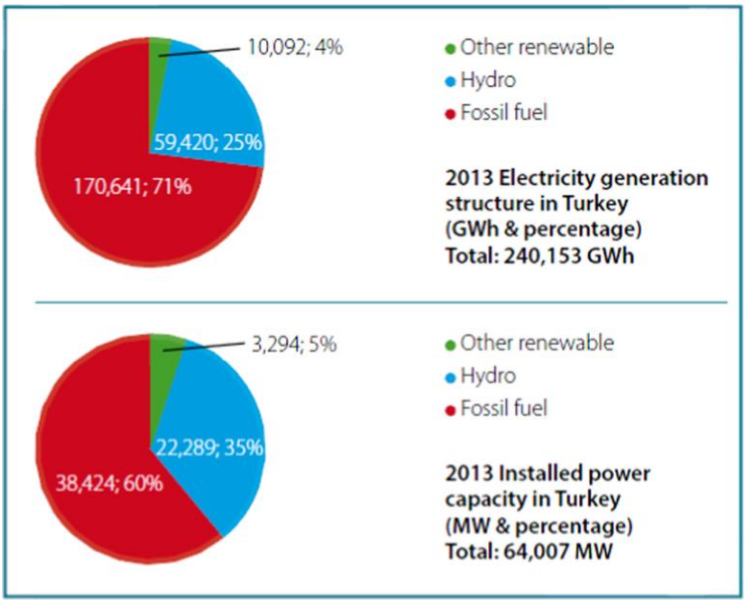

Fig. 6. The share of electricity production and installed power capacity in Turkey in 2013 [12]

2.5. Biomass Energy Status of Turkey

Biomass is the most widely used renewable energy source in the world. Biomass is utilized mostly in solid form, in lesser amount in the form of liquid and gas [13]. Main biomass sources are vegetable wastes and seeds, forestry products, animal wastes, organic wastes and industrial wastes. Bioenergy can be used either as centralized or district energy systems with the traditional use of biomass energy. Fig. 7 demonstrates the share of energy and biomass share in the world. As seen from that figure, the share of renewables is 13% and 77% of this share belongs to the bioenergy sources.

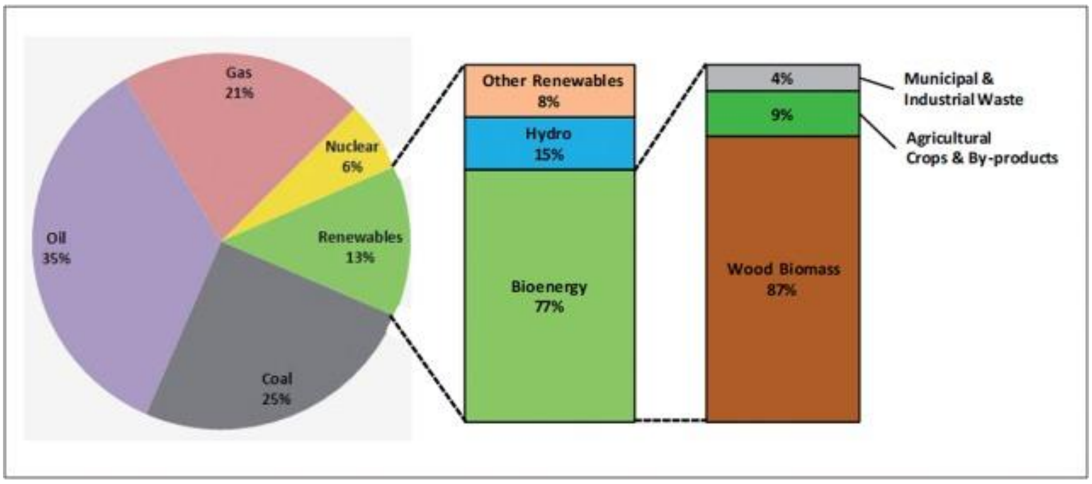

Fig. 7. Share of bioenergy in the world, 2006 [14]

In 2009, in the World electricity production capacity from biomass especially wood was about 10 GW. For future prediction, it is expected that this number will be reached up to 50 GW in 2030. For this increment and growth rate, it is calculated that the economic benefits will be 6.4 billion USD and will supply job opportunities to 250000 people [15], [16]. According to the Ministry of Energy of Turkey [17], the potential of biomass is about 100 TWh and it is estimated that biogas potential of Turkey is about 17.4-23.3 TWh. There are biomass plants in Turkey with 811 MW capacity and in 2018 3216 GWh electricity was produced from biomass in those plants.

3. SMART SOLUTIONS FOR TURKEY

Turkey is located in the northern hemisphere between 36-42° northern parallel and the 26-45° eastern meridians. Due to its location, Turkey is like a bridge between Asia and Europe. Current population of Turkey is about 80 million which is the second highest population after Germany in Europe [18]. Most of current energy production systems are not renewable, hazardous to the environment and they are not economically viable. One of the disadvantages of the current energy production systems is that they are utilizing sources for one product which are called as single generation. The trend to increase the efficiency is to renew current energy infrastructure with higher efficient options such as co-generation, tri-generation or multigeneration energy production systems [19]. Single generation systems do not recover waste heat of the system. However, multigeneration energy production systems offer more than three useful products by utilizing waste heat again and again [20]. Multigeneration systems can either utilize one source of energy or two. For example, if solar radiation is enough for electricity production in one location, a multigeneration system producing electricity, heating and cooling, hydrogen, drying or freshwater can be set there. Because of the intermittency of solar energy, this plant can be supported by secondary source such as biomass, geothermal or wind energy. These types of multigeneration systems can be planted either in district areas or as a centralized plant according to the needs. In Turkey, there are some studies to integrate current energy infrastructure to more efficient systems. Another smart solution for Turkey and also for the World is hydrogen energy. Due to advantages of hydrogen, it is thought that hydrogen will be very important role in future energy sectors. Therefore, there are some studies for green hydrogen production and hydrogen storage as well.

4. CONCLUSIONS

In this study, the general situation and future plans of energy issue in Turkey is briefly discussed. Although, the most of the electricity production is met by fossil sources in Turkey, there are huge potential in terms of renewable energy sources especially hydroelectric and geothermal. After regulating law related to energy production, Turkey has started to pass to produce more electricity from renewable energy sources. Finally, following remarks can be drawn as a conclusion:

- Turkey is very rich country in terms of renewable energy sources. Share of renewable energy use to produce electricity is increasing.
- Geothermal sources having high grades should be utilized for multigeneration purposes in order to increase the efficiency.
- Regions having high solar radiation should be supported to install new solar plants.
- Biomass wastes should be put to good use both to produce electricity and decrease the wastes.

REFERENCES

1. HEPBASLI, A., OZDAMAR, A., OZALP, N. Present status and potential of renewable energy sources in Turkey. *Energy Sources*, 2001, Vol. 23, No. 7, p. 631-648.
2. YUKSEL, I. Renewable energy status of electricity generation and future prospect hydropower in Turkey. *Renewable Energy*, 2013, Vol. 50, p. 1037-1043.
3. DEMIRBAS, A., BAKIS, R. Energy from renewable sources in Turkey: Status and future direction. *Energy Sources*, 2004, Vol. 26, No. 5, p. 473-484.
4. Turkey wind map. Turkish State Meteorological Services. 2019- [referred on the 12th of February in 2019 y.]. Link to the internet https://www.mgm.gov.tr/genel/ruzgar-atlasi.aspx
5. Solar energy potential map of Turkey. Renewable Energy General Directorate. 2019- [referred on the 12th of February in 2019 y.]. Link to the internet http://www.yegm.gov.tr/MyCalculator/Default.aspx
6. Solar energy. Turkish Republic Ministry of Energy. 2019- [referred on the 16th of February in 2019 y.]. Link to the internet https://www.enerji.gov.tr/tr-TR/Sayfalar/Gunes
7. BERTANI, R. Geothermal Power Generation in the World-2010-2015 Update Report. World Geothermal Congress 2015 (WGC2015). Proceedings number: 01001, Australia. 2015 April 24.
8. Turkey geothermal potential and research studies. General Directorate of Mineral Research and Exploration. 2017 – [referred on the 12th of February in 2019 y.]. Link to the internet http://www.mta.gov.tr/v3.0/arastirmalar/jeotermal-enerji-arastirmalari
9. KAYGUSUZ, K. Hydropower potential in Turkey. *Energy Sources*, 1999, Vol. 21, No. 7, p. 581-588.
10. DURSUN, B., GOKCOL, C. The role of hydroelectric power and contribution of small hydropower plants for sustainable development in Turkey. *Renewable Energy*, 2011, Vol. 36, No. 4, p. 1227-1235.
11. KEMAL OZTURK, H. Present status and future prospects of hydroelectric energy in Turkey. *Energy sources*, 2004, Vol. 26, No. 9, p. 829-840.
12. YOUSEFİ-SAHZABİ, A., UNLU-YUCESOY, E., SASAKİ, K., YUOSEFİ, H., WİDİATMOJO, A., & SUGAİ, Y. Turkish challenges for low-carbon society: current status, government policies and social acceptance. *Renewable and Sustainable Energy Reviews*, 2017, Vol. 68, p. 596-608.

13. TOKLU, E. Biomass energy potential and utilization in Turkey. *Renewable Energy*, 2017, Vol. 107, p. 235-244.
14. WEC, World Energy Council Survey of Energy Resources 2010: Bioenergy WEC. 2010 - [referred on the 10th of January in 2011 y.]. Link to the internet www.worldenergy.org/publications
15. ERDEM, Z.B. The contribution of renewable resources in meeting Turkey's energy-related challenges. *Renewable and Sustainable Energy Reviews*, 2010, Vol. 14, pp. 2710-2722.
16. TOKLU, E., KAYGUSUZ, K. Present situation and future prospect of energy utilization in Turkey. *Journal of Engineering and Applied Sciences*, 2012, Vol. 1, No. 2, p. 73-86.
17. Biomass energy. Turkish Republic Ministry of Energy. 2019- [referred on the 16th of February in 2019 y.]. Link to the internet https://www.enerji.gov.tr/tr-TR/Sayfalar/Biyokutle
18. OZTURK, M., YUKSEL, Y.E., OZEK, N. A bridge between East and West: Turkey's natural gas policy. *Renewable and Sustainable Energy Reviews*, 2011, Vol. 11, No. 9, p. 4286-4294.
19. YÜKSEL, Y. E. Thermodynamic assessment of modified Organic Rankine Cycle integrated with parabolic trough collector for hydrogen production. *International Journal of Hydrogen Energy*, 2018, Vol. 43, No. 11, p. 5832-5841.
20. YUKSEL, Y. E., OZTURK, M., DINCER, I. Thermodynamic analysis and assessment of a novel integrated geothermal energy-based system for hydrogen production and storage. *International Journal of Hydrogen Energy*, 2018, Vol. 43, No. 9, p. 4233-4243.

CYSENI 2019, May 23-24, Kaunas, Lithuania
ISSN 1822-7554, www.cyseni.com

ENVIRONMENTAL ASPECTS ANALYSIS OF CRYPTOCURRENCY MINING

M. A. Daniliuk, A. S. Pavlova, O. I. Sergienko, A. S. Pavlov
St. Petersburg National Research University of Information Technologies,
Mechanics and Optics, ITMO University
Lomonosova str. 9, St. Petersburg, 191002 – Russia
Email: maria-a-d@yandex.ru

ABSTRACT

The rapid growth of cryptocurrency in the global market drew attention to the environmental aspects of its production. Cryptocurrency production or mining is a process aimed at creating new digital coins and confirming transactions, which requires solving complex mathematical equations. This process is based on the use of significant computing power, which consumes a large amount of electricity. In most cases, traditional non-renewable energy sources are used, which leads to the depletion of natural resources.

The mining process of cryptocurrency has remained unchanged, but with increasing popularity, the scale of operations has increased dramatically. The environmental aspects analysis is significant element in designing of new product or service which could be affecting to decision making process. The paper summarized the results of research provided by experts of ITMO University. As methodology of environmental aspects analysis, the consequence/probability matrix was chosen. The following environmental aspects of cryptocurrency were identified and ranked: energy consumption for mining, computer using for mining, energy consumption for cooling of the computers, critical raw materials consumption for computer production, hazardous electronic waste generation from computer using in the end of life cycle. One of the most significant environmental aspects is energy consumption. To maintain the competitiveness of cryptocurrency in the global market, it is necessary to develop an alternative development strategy using renewable energy sources. The need for a transition to a new economic course in the development of a “green” or “low-carbon” economy in the field of cryptocurrency mining determines the relevance of the chosen research topic.

The paper investigates the following key points: trends in the cryptocurrency market; the matrix for environmental risks analysis; identification of significant environmental aspects of cryptocurrency mining in accordance with ISO 14001 requirements, and environmental-friendly methods of mining (hydro mining). As a conclusion, possible development of green cryptocurrency in Russia is considered.

Keywords: environmental aspect, energy efficiency, blockchain technologies, cryptocurrency mining, digital coins, green cryptocurrency.

1. INTRODUCTION

Mining for crypto or digital currency is the process of confirming and verifying transactions on a blockchain or public ledger [1]. A blockchain is made of several blocks and solving a block through this process is the means by which new coins are released as a reward to the miners. This process involves high computational power and along with cryptography and decentralization is what makes digital currency so secure and attractive.

Blockchain technologies to date are a serious innovation breakthrough both abroad, where the first blocks were developed to implement the idea of Bitcoin, and in Russia, where the blockchain is just beginning to develop. The creation of the blockchain was the impetus for a revolution in data storage. Technology will change the world at a rapid pace, and not only in the financial sector, but also in government, medicine, logistics, education, and business. Blockchain technology is relevant in the area of protecting people from fraudulent schemes and in other areas where work with big data is required. Certainly, this system has advantages and disadvantages.

The blockchain makes data transfer faster, safer and cheaper, since it eliminates the participation of intermediaries, ensures the safety of information, operates automatically, and reduces the risk of human error. In this transparent database, information is protected from illegal manipulations, changes, or breakdowns of parts of the blockchain, because it is virtually impossible to control all the computers that work on the Web to create blocks and chains [2].

The government of the Russian Federation has officially announced a policy of completely reforming the state apparatus and reorienting the country's priority tasks towards the digital economy [3]. Coverage of the upcoming and recent changes in the legislative framework, the effectiveness of experimental implementations of the blockchain will make it possible to understand how far-reaching changes and reforms will be.

The areas of application of technology in the banking and commercial sectors are placement of private shares of small and medium-sized enterprises in the sphere of money circulation or sale on IPO; trade and settlement of large collateral loans; settlements by mutual monetary and pension funds; delivery documentation; various payments; mortgage lending and more.

The most successful global project using blockchain technology is still a cryptocurrency. A work is currently proceeding on the issue of special IPO and ICO shares, and more recently, trading in cryptocurrency futures began in the world.

However, it is necessary to take into account that this process is based on the use of significant computing power that consumes a large amount of electricity. In most cases, traditional, non-renewable energy sources are used, which leads to the depletion of natural resources.

On this basis, the paper examines the environmental aspects analysis and the challenges with development of “green” cryptocurrency.

2. TRENDS OF CRYPTOCURRENCY MARKET DEVELOPMENT

New types of cryptocurrency appear almost every day. The total number of cryptocurrencies in the world is more than 1,300 and is constantly growing [4].

All cryptocurrencies have a common feature: they are built on the basis of the blockchain technology, which stores all information on transactions encrypted using cryptography. But each cryptocurrency has its own characteristics. Cryptocurrencies differ in cost, network consensus, cryptography algorithm, and core functions [4]. The main type and the most expensive digital currency today is Bitcoin. It is isolated in a separate form, because it all started with it and the rest of the cryptocurrencies are built on its modified code.

Bitcoin is actively used in different countries of the world, first of all – in the most developed countries: Japan, Luxembourg, Singapore, Qatar and Scandinavian countries.

In Japan, bitcoins are legal tender, but organizations that accept them need to get a special license. The world's largest companies, such as Dell, Microsoft and Paypal, have already started accepting Bitcoins for payment, and the list of such organizations is actively growing.

The beginning of the active promotion of the blockchain technology in the Russian Federation can rightly be called 2016. It was in January of that year at a business meeting with President of Russia Vladimir Putin, Chairman of Sberbank of Russia, German Gref, a statement was made that the blockchain could significantly update the mechanisms of state regulation and schemes financial management. As a result, a working group was formed to study the blockchain technology. [6].

Russia has its own type of cryptocurrency, which is called Ethereum. This financial unit was offered by Vitalik Buterin in 2013, but finally the currency entered the market in 2015. Ethereum is not only a cryptocurrency, but also a platform created to implement blockchain-based decentralized online services [2].

Ethereum is included in the list of the main types of cryptocurrency, which is in stable demand. It occupies the second or third position in the list of the most popular digital coins, which is a very good indicator, given the short history of the coin [4].

Throughout the existence of cryptocurrency, the process of their production has remained unchanged, but with increasing popularity the scale of operations has increased dramatically. According to research by Power Compare, at the end of 2017, the amount of electricity spent on mining exceeded 29 terawatts per hour. This figure exceeds the level of energy consumption in countries such as Moldova, Iceland, Ireland, the Baltic States, almost all of Eastern Europe and African countries on an annualized basis. Russia occupies a third place in terms of energy consumption for cryptocurrency production in relation to annual electricity consumption with an indicator of 2.73%. According to this indicator, Russia is inferior to China and the United States (0.49% and 0.74%, respectively). Researchers estimate that if this trend continues, by 2020 the power consumption per mining will exceed global electricity consumption per year.

The famous farm called Genesis Mining is located in Iceland. Its creators have relied on a cold climate, because it is natural cooling that significantly reduces the cost of Bitcoin during production. In addition, the country is famous for cheap electricity and fast internet.

The creator of a Bitcoin farm in Switzerland, Guido Rudolfi, is confident that the world needs cryptocurrencies, just as the Internet was once needed. Rudolfi has long been engaged in the study of the new phenomenon, tried to create several farms and eventually settled on the village of Lynthal. The largest Bitcoin farm in the country, naturally, is located in the area with the cheapest electricity.

But despite the fact that at least two European cities have impressive farms, more than half of the capacity of the entire Bitcoin network is concentrated in China.

3. METHODOLOGY FOR ENVIRONMETAL ASPECTS ANALISYS OF CRYPTOCURRENVY MINING

3.1. Consequence/probability matrix methodology

Risk matrix or consequence/probability matrix are probably one of the most widespread tools for risk evaluation. In according with IEC 31010:2009 “Risk management - Risk assessment techniques”, the consequence/probability matrix is a means of combining qualitative or semi-quantitative ratings of consequence and probability to produce a level of risk or risk rating [7, 8]. Inputs to the process are customized scales for consequence and probability and a matrix which combines the two.

Probability is not a mathematical certainty. It is consideration of likelihood that a loss risk event may occur in the future, based upon historical data, the nature of the neighborhood, immidiate vicinity, overal geographical location, political and social conditions, and changes in the economy, as well as other factors that may affect probability. The Table 1 presents the description of probability.

Table 1. Probability description

Descriptor	Description
Very High	The Risk event is expected to occur in most circumstances and/or it's happening now
High	The Risk Event will propably occur in most circumstances. A direct credible threat has been received and/or it has happened, or would have happened if not activly prevented, a number of times before.
Medium	The Risk Event might occur at some time but generally only under specific circumstances. Indirect Threats have been received. The conditions could be favorable for ot to occur.
Low	The Risk Event could occur at some time but is unlikely. No direct credible threats have been received. Conditions are not favorable for it to occur.
Very Low	The Risk Event is very unlikely to occur

As Table 2 shows, the consequence scale covers the range of different types of consequence to be considered (for example: financial loss; direct and indirect costs; safety; environment or other parameters, depending on context) and extend from the maximum credible consequence to the lowest consequence of concern. Even if the probability of loss is low, but the impact costs are high, security solutions are still are necessary to manage the risk.

Table 2. Consequence description

Descriptor	Description
Critical	Very significant environmental impact. Very significant financial loss. Very significant harm to image and reputation that leads to significant and sustained fall in price and significant loss of sales over the long term. Long term loss of competitive advantage. Very significant, sustained negative international media coverage.
High	Significant environmental impact. Significant financial loss. Major embarrassment/harm to reputation leading to significant fall in share price and loss of sales over medium term. Significant loss of competitive advantage. Negative international media coverage
Medium	Environmental impact in line with limit and legislation requirements. Significant financial loss. Moderate embarrassment or harm to image and reputation that impacts on sales over short term. Possibility of some minor loss of competitive advantage. Negative media coverage at a national level.
Low	Environmental impact without negative trends. Minor financial loss. Minor embarrassment but no harm to image and reputation. Minor impact on sales in short term. Some local media coverage unlikely to be of interest at the national level
Very Low	No impact to the environment. Very minor financial loss, etc.

Table 3 shows matrix which is drawn with consequence on one axis and probability on the other. The risk levels assigned to the cells depend on the definitions for the probability/ consequence scales.

Table 3. Probability criteria matrix

	CONSEQUENCE RATING				
PROBABILITY RATING	Very Low	Low	Medium	High	Critical
Very High	Very Low Risk	Low	Medium	High	Critical
High	Very Low	Low	Medium	High	Critical
Medium	Very Low	Low	Medium	High	High
Low	Very Low	Very Low	Low	Medium	Medium
Very Low	Very Low	Very Low	Low	Medium	Low

4. ENVIRONMENTAL ASPECTS ANALYSIS

Mining farm – is a data center, technically equipped to mine bitcoins or other cryptocurrencies. Physically, crypto mining farm mining farms are rooms with a large number of computers and servers that take on tasks for mining.

In accordance with ISO 14001 environmental aspect is “an element of an organization’s activities or products or services that can interact with the environment.” An environmental impact is defined as “any change to the environment, whether adverse or beneficial, wholly or partly resulting from an organization’s environmental aspects.” [9]

ITMO University is as a one of the leading higher education institutions in Russia, providing the research in information technologies and computer science. The group of researchers works on blockchain technologies challenges. The working goup conducted the multicriteria analysis in frame of which the environmnetal risks of criptocurrency mining were evaluated.

Such environmental aspects was identified for cryptocurrency mining as computer using, energy consumption for mining, energy consumption for cooling of the computers, critical raw materials using for computer production, hazardous electronic waste generation from computer using in the end of life cycle.

According to experts’ assessment shown in the Table 4, all identified environmental aspects are significant which means that have or can have a significant environmental impact. The description of each environmental aspect is presented below.

Table 4. Environmental aspects analysis

#	Environmental Aspect	Impact to environmental	Probability	Impact level	Risk
1	Energy consumption for mining	Depletion of nature resources	Very high	Critical	Critical
		Air pollution (Carbon footprint)	High	High	High
2	Computer using for mining	Air pollution by evolution of heat	Very high	Critical	Critical
3	Energy consumption for cooling of the computers	Depletion of nature resources	Very high	High	High
4	Critical raw materials consumption for computer production	Depletion of nature resources	High	High	High
5	Hazardous electronic waste generation from computer using in the end of life cycle	Pollution of land with hazardous waste	High	Medium	High

4.1. Energy consumption for mining

4.1.1. Depletion of nature resources

In China, the world's largest producer of mining systems, many farms receive energy from “dirty” coal-fired power plants, while the government has legally restricted harmful emissions into the atmosphere and is considering the possibility of introducing new taxes designed to control the domestic electricity market and cryptocurrency operations.

The founder of many projects, mathematician Moritz Strube from Berlin, considered the consumption of electricity throughout the network. The mathematician estimated that mining equipment consumes 1.17 terawatt-hours of electricity per month throughout the world. For example, Slovenia consumes 1.08 terawatt-hours of electricity per month [10].

4.1.2. Air pollution (Carbon footprint)

Analysis of Australian businessman Nick Gogerty shows that that miners will spend up to 90% of the bitcoin price on electricity with which it may mine. This price for electricity will vary depending on the Bitcoin price. The research assumes that 50% of all mining takes place in China or the USA. It uses the latest estimates from the International Energy Agency (IEA) on carbon emissions per kilowatt of power lines in each country, and averages them. As a result, for every megawatt of electricity spent for mining bitcoins, 0.65 tons of CO2 is emitted into the atmosphere. The method chosen by the researcher projects these figures on average electricity prices and gives an average emission rate of about 6.98 kg of CO2 per dollar spent on electricity for Bitcoin mining [11]. Bitcoin is mined everywhere from data centers, distributed locations, pools, mining farms in garages. This makes the assessment of this "carbon footprint" very difficult, as there are a lot of different types of equipment used for mining.

4.2. Air pollution by evolution of heat and energy consumption for cooling of the computers

Mining equipment, while in permanent operation, emits a large amount of heat, can overheat or burn under loads without conditioning. For proper operation of this equipment requires certain ambient temperatures, respectively, it must be cooled. To create a cooling system for mining farms, additional refrigeration equipment or fans are required.

4.3. Critical raw materials using for computer production

Critical Raw Materials (CRMs) are used for electronic equipment production. CRMs are those raw materials which are economically and strategically important for the European economy, but have a high-risk associated with their supply [12]. The EU's industry and economy are reliant on international markets to provide access to many important raw materials since they are produced and supplied by third countries. Although the domestic production of certain critical raw materials exists in the EU in most cases the EU is dependent on imports from non-EU countries. The risks associated with the concentration of production are in many cases compounded by low substitution and low recycling rates [13].

4.4. Hazardous electronic waste generation from computer using in the end of life cycle

The large amount of the computers and electronic equipment are used for mining. The cryptocurrency development is required modernization and constant updating of the mining farms. Thus significant amount of electronic waste are generated. Electronic waste (WEEE, e-waste) is one of the types of waste containing electronic and other electrical devices, as well as their parts. Electronic waste may have high hazard classes due to the substances contained in them, such as lead, mercury, polychl orinated biphenyls, polyvinyl chloride (due to the appearance of dioxins during combustion).

5. RESULTS AND DISCUSSIONS

Due to the increase in cryptocurrency production in recent years, the consumption of electricity by mining farms has also increased significantly. If the industry continues to use the energy produced by burning fuel, it will cause great harm to the environment in the form of pollution and greenhouse gas emissions. An example of generating capacity using renewable energy sources is hydroelectric power stations, which have been built around the world for more than a century. Wind, tidal, solar, geothermal and other renewable energy power plants were also developed many decades ago, and such solutions can be based on a variety of technological approaches.

Today green or environmental friendly cryptocurrency has been created. The main goal of it is to take care of our environment. The example of green cryptocurrency is BitSeeds which collaborate with the Rainforest Foundation. 10% of the released units of BitSeeds go to the organization of planting new trees, as well as the restoration of forests [14].

The main goal of SolarCoin is to encourage people who are engaged in the process of developing the method of energy production using solar panels. Thus, the author of this project motivates investors to develop alternative methods for the extraction of electricity, so that in a few years people will only use it. According to [15], today one unit of this cryptocurrency corresponds to one megawatt of electricity.

Hydro-mining is a specific method of mining cryptocurrencies based on the use of electricity from hydroelectric power plants and water cooling systems. It allows you to make the process of mining coins more economical and profitable.

6. CONCLUSIONS

The blockchain is proving to be a promising technology, and every year it spreads more and more confidently in various directions.

Cryptocurrency is one of the example the application of blockchain technology. The trend of digital coins development reflects the interest of government to cryptocurrency. Although it is necessary to pay attention to possible threats and weaknesses of the system and, based on this analysis, to make informed decisions about the cryptocurrency dissemination on the national level and the use of blockchain technology in Russia.

The environmental aspects analysis is significant element in designing of new product or service. Also it is applicable to assessment the environmental impact of new technologies.

The environmental aspects analysis is based on risk assessment methodologies, one of which is consequence/probability matrix.

The consequence/probability matrix was chosen as methodology for environmental aspects analysis due to following reason: relatively easy to use; provides a rapid ranking of risks into different significance levels, involves the wide range of experts, takes into account the expertise of working group.

Risk assessment which was provided by experts of ITMO University identified and ranking the following environmental aspects: energy consumption for mining, computer using for mining, energy consumption for cooling of the computers, critical raw materials consumption for computer production, hazardous electronic waste generation from computer using in the end of life cycle.

The output of environmental aspects analysis can be an input to the decision-making processes.

Taking into account that mining companies have their farms in countries with low electricity costs, mining complexity continues to grow, increasing the need for electricity, so the cryptocurrency industry needs alternative solutions - and it is likely that renewable energy sources may play a big role in the near future.

REFERENCES

1. Pilkington, Marc, Blockchain Technology: Principles and Applications. Research Handbook on Digital Transformations, edited by F. Xavier Olleros and MajlindaZhegu. USA, Edward Elgar, 2016, p. 225-254. ISBN: 9781784717759. Link to the internet <SSRN: https://ssrn.com/abstract=2662660>
2. Babkin A. V., Burkaltseva D. D., Pshenichnicov V. V., Tyulin A. C. Cryptocurrency and technology in digital economy: development genesis, St. Petersburg State Poliytecnical University Journal. Economics, 10 (5) (2017) 9-22. DOI: 10.18721/JE.10501.
3. Site of Financial Ministry of Russian Federation. Link to the internet <https://www.minfin.ru/ru/>
4. KuoChuen, D. L. HandBook of Digital Currency Bitcoin, Innovation, Financial Instruments, and Big Data, USA, Elsevier, 2015, 588 p., ISBN 978-0-12-802117-0.

5. Petuhova L. RBK, Shopping for Bitcoin: how to exchange cryptocurrency for rubles and where to spend it [referred on the 11th of August in 2017 y.]. Link to the internet <https://www.rbc.ru/money/11/08/2017/5989d59e9a794728aa3bd573>
6. Tadviser: State. Business. IT. Link to the internet <http://www.tadviser.ru>
7. IEC 31010:2009 “Risk management - Risk assessment techniques”.
8. BS ISO 31000:2018 Risk management – Guidelines.
9. ISO International Organization for Standardization Environmental management system, standard ISO 14001:2015, edition 3, 2015, p. 35, ICS 13.020.10, Link to the internet <https://www.iso.org/standard/60857.html>
10. Palacio, N. S. Blockchain: A technological tool for sustainable development or a massive energy consumption network, Bionatura 2018, Vol. 3, No. 4, Link to the internet <http://revistabionatura.com/2018.03.04.11.html >
11. Karl J. O., Malone,D. Bitcoin Mining and its Energy Footprint, Limerick, June 26-27 In: Proceedings of the 25th Joint IET Irish Signals & Systems Conference 2014 and 2014 China-Ireland International Conference on Information and Communications Technologies (ISSC 2014/CIICT 2014). IET, pp. 280-285.
12. Site of Critical Raw Materials. Link to the internet <http://criticalrawmaterials.org/critical-raw-materials/>
13. Site of European Commission. Link to the internet <http://ec.europa.eu/growth/sectors/raw-materials/specific-interest/critical_en>
14. Lia, J., Lia, N., Peng, J., Cuia, H., Wua, Z. Energy consumption of cryptocurrency mining: A study of electricity consumption in mining cryptocurrencies, Energy, 2019, Vol. 168, p. 160-168.
15. Andonia, M., Robua,V., Flynna, D., Abramb, S., Geachc, D., Jenkinsd, D., McCallumd, P., Peacock, A. Blockchain technology in the energy sector: A systematic review of challenges and opportunities, Renewable and Sustainable Energy Reviews, 2019, Vol. 100, p. 143-174.

CYSENI 2019, May 23-24, Kaunas, Lithuania
ISSN 1822-7554, www.cyseni.com

PREDESIGN SIMULATION OF SUPERCAPACITORS BASED ON SIMPLIFIED EQUIVALENT CIRCUIT MODEL

M. E. Şahin,
Department of Electrical and Electronics Engineering, RTE University,
53100 Rize – Turkey
Email: mustafaerginsahin@yahoo.com

F. Blaabjerg, A. Sangwongwanich
Department of Energy Technology, Aalborg University
Pontoppidantstraede 9220 Aalborg East – Denmark

ABSTRACT

The need for energy storage devices especially in renewable energy applications has increased the use of supercapacitors. Accordingly, several supercapacitor models have been proposed in the previous researches. Nevertheless, most of them require an intensive test in order to obtain the model parameters. This may not be suitable for an early simulation study, where a simple model based on the datasheet is required to evaluate the system performance before building the hardware prototype. To address this issue, a simplified electrical circuit model for supercapacitor based on the voltage-current equation is proposed in this paper. The parameters of the proposed model can be obtained from the datasheets value with a minimum test requirement. The experimental method to obtain the parameters of the supercapacitor equivalent circuit is described. Based on the proposed method, the supercapacitor model is built in MATLAB/Simulink and the characteristics of ESR measurement and cycle life are compared with data sheets. The simulation results have verified that the proposed model can be applied to simulate the behavior of the supercapacitor in several energy and power applications.

Keywords: Supercapacitors, Energy storage systems, Supercapacitor modelling, MATLAB/Simulink

1. INTRODUCTION

There is a strong demand to reduce the use of fossil fuel and move toward more sustainable energy sources. Accordingly, several efforts have been made to increase the penetration level of Renewable Energy Sources (RES) such as photovoltaics and wind turbines [1]. Nevertheless, the intermittency nature of the power production from RES have risen a concern regarding the grid-integration. In order to ensure high power quality and stability of the electrical network, energy storage systems are one of the promising solutions to this problem.

Traditional energy storage devices such as batteries have some disadvantages such as slow charging and limited lifetime. Some other storage technologies, such as; mechanical, electrochemical and electromagnetic, which store the energy in another form, are more expensive and complex [2]. The fluctuation in the power production of renewable energy sources raises some requirement for the stability of the energy network. The need for instantaneous energy storage devices increases the use of supercapacitors (SCs) as an alternating storage device, especially in renewable energy applications. By employing the SCs, it is possible to smooth out a certain power fluctuation in the renewable energy systems. On the other side, energy storage systems play an important role in a diverse range of industrial applications [2, 3].

For instance, the increased installation of grid-connected Photovoltaic (PV) systems and building integrated PV systems have made rapid progress around the world over the last years. Photovoltaic panels are intermittent sustainable energy sources whose power generation capability varies with the environmental conditions. Thus, energy storage such as SCs can be used to smooth out the power fluctuation due to its high power density [4].

In general, rechargeable batteries and SCs have a similar chemical structure and work process to store and convert through diffusion and migration of ions. However, the SCs present some advantages which will be useful for the storage systems. An SC is a double-layer electrochemical capacitor that can store thousands of times more energy than a typical capacitor. Moreover, they have almost negligible losses and long lifespan [5]. They can process a large number of charge and discharge cycles compared to only a few thousand cycles for lead-acid batteries and can supply much higher currents than batteries [6, 7].

It is possible to find some basic studies in the literature that chemical, mathematical and electrical characteristic and dynamic structure of SCs were simulated and investigated [8-15]. Also, a simple electrical model of SCs has been designed to describe the behavior of SCs as a function of frequency, voltage, and temperature [16]. This makes them inadequate to demonstrate the SCs dynamics under different conditions sometimes. However, the structural simplicity and decent modelling accuracy make the equivalent electrical circuit model designed by Zubieta and Faranda for simulations very suitable for power electronic applications and real-time energy management simulations [22, 23]. The SCs module simulation was based on two branches electrical circuit model which included the module structure and its mathematical equation simulation in some studies [5, 15, 16]. An experimental method used to determine some of the parameters of the SC equivalent circuit has in the literature [15, 17]. Therefore, a simplified SC module model to be used in real time simulations and to adjust and modified for some parameters is required.

In this paper, the chemical structure of SCs, physical and electrical characteristics, working principle, advantages, and drawbacks are investigated in detailed. The chemical, mathematical and electrical and the other developed models in literature are investigated. Using the equivalent circuit model of the SCs which is suitable for power electronic applications the mathematical equation of SCs was derived. How to obtain of SCs coefficients experimentally are given. Using this equation and coefficients of the SCs the MATLAB/Simulink model was simulated and the characteristics of ESR measurement and cycle life are simulated and compared with data sheets for different supercapacitors. Also, charge and discharge characteristics of SCs for different values were simulated to compare the power and energy density of SCs different values.

2. OVERVIEW OF SUPERCAPACITORS TECHNOLOGY

In this section, an overview of SCs technology including the chemical structure, the physical and electrical characteristics will be discussed in detailed. The performance comparison of SCs with the other energy storage technologies will also be provided.

2.1. Chemical structure

A typical SC is shown in Fig. 1 (a) where the chemical structure is illustrated in Fig. 1 (b) [19, 20]. The SCs, which called as ultra-capacitors or double layer capacitors and have a very light and small size, capacity values are reached more than thousand Farads, although the voltage value is only 2.7 V in most products.

Unlike the ceramic or electrolytic capacitors, SCs do not have dielectric material between positive and negative electrodes. Instead of an electrolyte which has positive ions and negative ions is filled between the two electrodes, it uses the electrical double layer (EDL) that is formed at the interface of the solid electrode and liquid electrolyte. A typical SC is composed of solid electrodes and liquid electrolytes which including electrolyte salt, and a separator to prevent direct contact between the positive and negative electrodes. The electrodes are positioned on the electricity collectors and coated with activated carbon powder. An electrical double layer is formed at each interface where the active carbon powder contacts the electrolyte as shown in Fig. 1 (b) [20]. The Stern layer accounts for the specific absorption of the ions on the electrode surface. The diffuse layer incorporates the Gouy-Chapman model and their combination is called a Gouy - Chapman - Stern model [22].

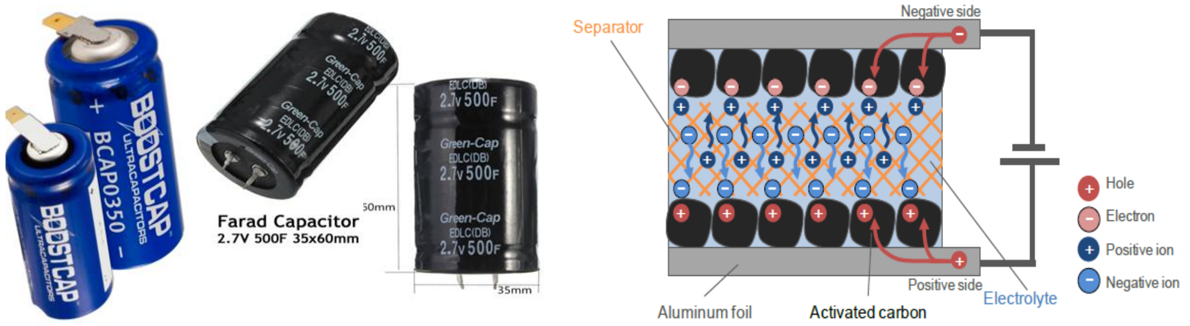

(a) (b)

Fig. 1. (a) Some SCs to be obtained in the market, (b) The structure of SCs [19, 20]

When the SC is charged, the negative ions and vacancies on the positive electrode side and the positive ions and the electrons on the negative electrode side are aligned across the interface as shown in Fig. 2 (a). This state of alignment of ions and electrons is called an electrical double layer capacitor (EDLC) [20]. The capacitance value of SCs is depended on the surface area and large surface area have powdered activated carbons which are used as an electrode material [21]. The SCs are charged by ions moving through the carbon surface and discharged by reverse moving away of ions as shown in Fig. 2 (a, b) respectively [20].

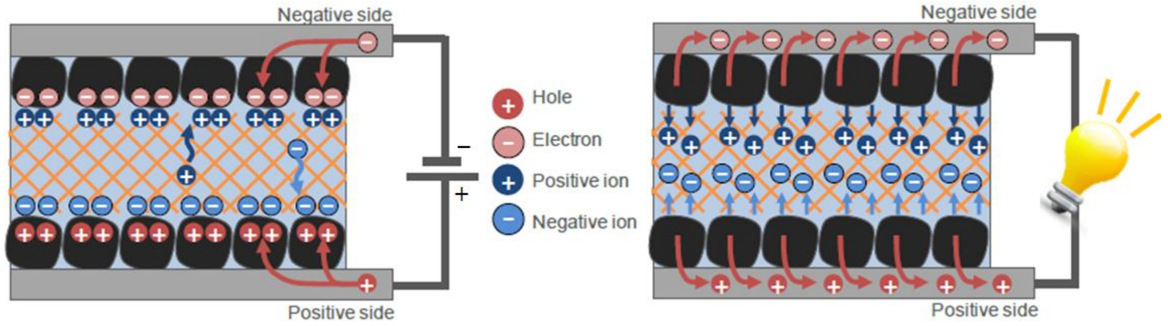

Fig. 2. (a) Charge, (b) discharge state in SCs [20]

2.2. Performance comparison with other energy storage technologies

The main advantages and drawbacks of SCs are given in this section. The SCs have a high power density, but low energy density. The SCs are quick charging and discharging but they have a very high self - discharge rate. Does not blow up in case of accidental direct short connection, and stops accepting energy when it becomes fully charged. SCs has extended the lifetime and long shelf life and them environmentally safe and no gas emissions [4]. Table 1 presents a numerical comparison between battery, SC and electrolytic capacitor characteristics. Compared with the other commercially available energy storage technologies, the SCs usually offer a high power density, high efficiency, fast charging and discharging speed, and long cycle lifetime [16]. On the other hand, the energy density of SC is limited compared to batteries. Accordingly, a combination of SC and battery may be required in some application.

Table 1. Comparison between the battery, SC and electrolytic capacitor performances [16]

Storage devises characteristics	**Battery**	**Supercapacitor**	**Electrolytic capacitor**
Charging time	1< *t* <5 h	1-30 s	$10^{-3}< t <10^{-6}$
Discharging time	*t* > 0.3 h	1-30 s	$10^{-3}< t <10^{-6}$
Energy density (Wh/kg)	10-100	1-10	< 0.1
Lifetime (cycle number)	1000	10^6	10^6
Power density (W/kg)	< 1000	10,000	> 1,000,000
Charge/discharge efficiency	0.7-0.85	0.85-0.98	> 0.95

3. LITERATURE REVIEW FOCUS ON SUPERCAPACITOR CIRCUIT MODELS

For SCs systems, modeling is essential for the system dimensioning, condition monitoring, and controller design. Several SC models are available in the literature based on; chemical, mathematical and electrical characteristic, aging, artificially intelligent, and dynamic structure of SCs models [8-15, 22]. A simple electrical model of SCs to describe the behavior of SCs as a function of frequency, voltage, and temperature has also been discussed in [16]. Electro-chemical models offer high accuracy but increase the calculation complexity. As an alternative, an equivalent circuit model derived from empirical and experimental data can also be used. This makes them inadequate to demonstrate the SCs dynamics under different conditions sometimes. However, structural simplicity and decent modeling accuracy make the equivalent electrical circuit model suitable for real-time energy management simulations [22, 23].

The electrochemical model is basically known as a double layer model since the structure of the SC has a double layer at the junction of a metal with an electrolyte solution, and the layer has two elements as shown in Figure 1 (b). The inner element, known as the ‘‘compact layer’’ or ‘‘Helmholtz layer’’ discover by Helmholtz [24] and described the EDL phenomenon it using a model where all the charges were assumed to be absorbed in the electrode surface. The outer element, the ‘‘diffuse layer’’ or ‘‘Gouy–Chapman layer’’, is semi-infinite in extent and contains anions and cations distributed unequally. Gouy [25] and Chapman [26] further modified the Helmholtz model to account for the ion mobility in the electrolyte solutions as a result of diffusion and electrostatic forces. The model to describe the (metal)/(electrolyte solution) double layer modified by Stern [27, 28].

Several circuit models have been proposed for SCs. The most often applied being the classical capacitor model [31, 32] where the simplified equivalent circuit is considered as actual capacitor behavior in a slow discharge application as illustrated in Fig. 3 (a). This circuit consists of a capacitance (C_d), the equivalent series resistance (R_s) which occurs during charging and discharging internal resistance, and an equivalent parallel resistance (R_p) to represent the path of leakage charge of SCs in a long-term effect [30]. In addition, Nelms et al. described another approach where the SC characteristics are modeled using a Debye polarization cell which is shown in Fig. 3 (b) [33].

(a) (b)

Fig. 3. (a) Classical SC model, (b) SC model using a Debye polarization

Conventional equivalent circuit model employs basic electrical circuit elements to represent the SC dynamics as shown in Fig. 4 (a) [23]. The basic model has limitation due to the fact that the capacitance of an SC is in general strongly dependent on terminal voltage [16, 34]. Therefore, a more effective model for SCs has been proposed in [34] based on the circuit diagram in Fig. 4 (b). In fact, a more complex equivalent circuit model that represent the physical mechanisms in the SC has also been discussed in the literature. Such a model is known as a transmission line network model where the resistances and non-linear capacitances represent the distributed ESRs and electrostatic double-layer capacitance intrinsic to each pore in the electrode material. There are also additional resistances in the electrode material and a diffusion resistance in the membrane [35, 36].

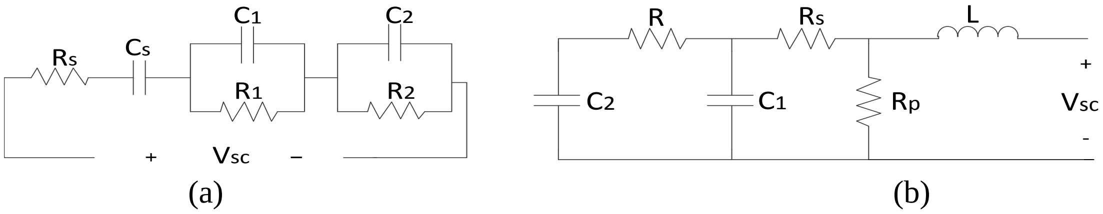

Fig. 4. (a) Conventional equivalent circuit model, (b) a dynamic model for SCs [34]

Unfortunately, the equivalent circuits used in the detailed modeling of SCs mentioned above are not very suitable for a power electronic simulation environment. Therefore, a simplified equivalent circuit that can capture the characteristic behavior of SCs under different operating conditions has been developed. Such a model implementing the variable capacitance feature is described by Zubieta et al. [15]. The model uses three separate RC time constants in three parallel branch networks and a high resistance element to model cell leakage as illustrated in Fig. 5 (a). The thirty or delayed branch parameters are R_d and C_d. An improved version of the Zubieta model was proposed by Rafik [16] where the frequency dependent parameters in the capacitor are taken into consideration. Faranda [10] proposes a simplified version of the Zubieta model [15] with one RC-branch less as shown in Fig. 5 (b). According to [10], this model simplifies the estimation of parameters and reduces the number and complexity of measurements and decreases the possibility of errors. Faranda also proposes a method of determining the parameters in the model based on measurements. The complexity of the parameters determined in the Zubieta model makes it difficult to be implemented. Therefore, using the simplified Faranda model gives adequate relevance with the measurements besides good accuracy.

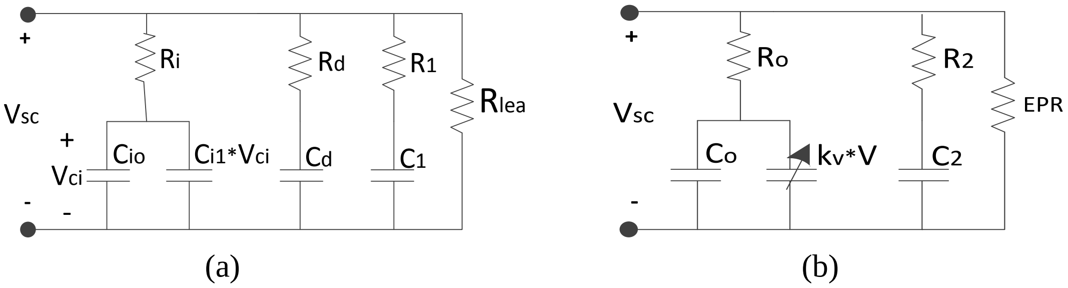

Fig. 5. The equivalent circuits of SCs; (a) Zubieta model, (b) Faranda model

Fractional order equivalent circuit's model of SCs has also been developed in the previous research [23]. In order to further improve the model accuracy, a fractional-order calculus has been introduced for SC modeling applications [22]. When the SCs operate under high rate cycling, they may generate high heat depend on low internal resistance. This operation affects the performance and lifetime of SCs which are very sensitive to temperature change. Therefore, several studies focused on the temperature model of SCs [16, 37-40]. Intelligent modeling techniques such as an artificial neural network (ANN) and fuzzy logic have been successfully utilized to predict the performance of energy storage systems including batteries and SCs [41, 42]. Temperature, voltage, and current are the parameters of the accelerating aging of SCs and define the lifetime. A simplified thermal model of the SC to estimate the core temperature and the case temperature of the components are proposed [43, 44].

Although all these models include more details and different applications, in this paper focused on the equivalent circuit model designed by Zubieta and Faranda for simulations which will be very suitable for power electronic applications.

4. PROPOSED SUPERCAPACITOR CIRCUIT MODEL

There are several studies in the literature that investigate the chemical, mathematical and electrical stimulation of SCs [8-15]. The SCs module simulation was based on two RC branches electrical circuit model as shown in Fig. 6 which included the module structure and its mathematical equation simulation in this study [5, 15, 16]. This circuit is simplified by neglecting the leakage current of SC as given in Eq. 1. The U_{SC} and I_{SC} are the SC module voltage and currents respectively. The v_{sc}, i_{sc}, N_{S_SC} , and N_{P_SC} are the SC primary voltage and current, series elements and parallel branches respectively. The main capacitance C_1 depends on the voltage v_1 and consists of a constant capacity C_0 and a constant parameter C_V and it is written as $C_1 = C_0 + C_V.v1$. The R_1C_1 branch determines the immediate behavior of the SC during rapid charge and discharge cycles in a few seconds. The R_2C_2 cell is the slow branch and completes the first cell in the longtime range and describes the internal energy distribution at the end of the charge. The equivalent parallel resistance R_f represents the leakage current and can be neglected during fast charge/discharge [5].

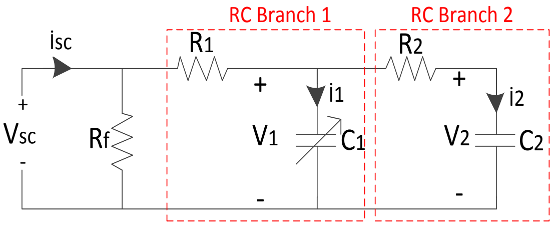

Fig. 6. SC two branches circuit model

$$U_{SC} = N_{S\_SC} v_{SC} = N_{S\_SC}(v_1 + R_1.i_{SC}) = N_{S\_SC}(v_1 + R_1 \frac{I_{sc}}{N_{P\_SC}}) \tag{1}$$

The relationship between quick charge (Q_1) and voltage (v_1) is shown in Eq. 2 depend on current (i_1). The charge (Q_1) is shown in Eq. 3. The inverse relationship between v_1 and Q_1 the equation obtained as in Eq. 4. Considered the equivalent electric circuit with two RC branches proposed by Zubieta and Bonert [36], Rafik et al. [37] to obtain this equation.

$$i_1 = C_1.\frac{dv_1}{dt} = \frac{dQ_1}{dt} = (C_0 + C_V.v_1)\frac{dv_1}{dt} \tag{2}$$

$$Q_1 = C_0 v_1 + \frac{1}{2} C_v.v_1^2 \tag{3}$$

$$v_1 = \frac{-C_0 + \sqrt{C_0^2 + 2C_V Q_1}}{C_V} \tag{4}$$

Eq. 1 and 4 are combined as in Eq. 5.

$$U_{SC} = N_{S\_SC} v_{SC} = N_{S\_SC}(v_1 + R_1.i_{SC}) = N_{S\_SC}\left(\frac{-C_0 + \sqrt{C_0^2 + 2C_V Q_1}}{C_V} + R_1 \frac{I_{sc}}{N_{P\_SC}}\right) \tag{5}$$

The voltage (v_2) in the secondary capacity (C_2) is described in Eq. 6.

$$v_2 = \frac{Q_2}{C_2} = \frac{1}{C_2}\int i_2 dt = \frac{1}{C_2}\int \frac{1}{R_2}(v_1 - v_2)dt \tag{6}$$

These equations are designed in MATLAB/Simulink as an SC module model as shown in Fig. 7 (a). The Eq. 5 and 6 is modified for 310 F capacitor coefficients in the simulation. These coefficients are obtained and calculated in previous studies experimental values and datasheets [45]. This values are R_1 = 5.5 mΩ, R_2 = 6 Ω, C_0 = 210 F, C_V = 80 F/V, C_2 = 39 F for 310 F SCs. Identification of coefficients of different capacitors is given in the next section more detailed. An SC electrical model for simulations of power systems is shown in Fig. 7 (b).

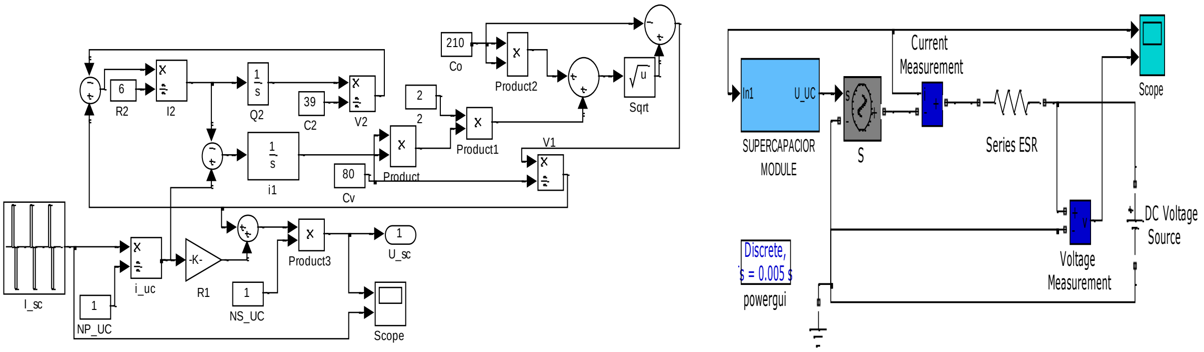

(a) (b)

Fig. 7. (a) Module model, (b) Electrical model of an SC in MATLAB/Simulink

To identify the parameters of the proposed model a charge and discharge test at constant current have been carried out. The experimental method which determines the coefficient of the SC equivalent circuit is described firstly by Zubieta and Bonert [5]. In the proposed model, the parameters are identified by charging the DLC from zero to rated voltage and by observing the terminal voltage during the internal charge redistribution over the time of 30 min. The process to identify the parameters assumes that this condition of zero charges is present at the beginning. The approach to determine the different equivalent circuit model parameters is based on the fact that the three equivalent branches: the immediate branch, delayed branch, and long-term branch have distinctly different time constants considering the coefficient identifications. Table II shows the average of the equivalent model parameter values measured for the two types of double-layer capacitors. [15].

The other experimental method to define the coefficients is described in [10]. At the first step, the values of the parameters of the immediate branch are determined. The R_0 resistance is calculated by measuring the potential difference ΔV between the two terminals during the first charge moment and subdividing it for the total charge current, assuming all the capacitances still discharged. The two components of the total capacitance of the short term branch are determined through a unique procedure. In order to validate the proposed model, seven models of SCs and their coefficients are tested as shown in Table 2. According to the results, it can be noticed that capacitors of the same type and size can have different parameters values of the equivalent circuit [10].

Table 2. The parameters and their coefficients for different SC measurements [5, 10]

Parameters	**Zubieta and Bonert**		**Faranda et all**			
Capacitor Value	470F	1500F	110F	200F	350F	600F
R_i, R_o (mΩ)	2.5	1.5	10	8.8	4.8	2.8
C_{io}, C_o (F)	270	900	89	158	232	454
C_{i1} (F/V)	190	600	29	56	90	176
R_d, R_2 (Ω)	0.9	0.4	17.5	8.8	5.5	3.1
C_d, C_2 (F)	100	200	13.7	27.5	43.2	77.4
R_1 (Ω)	5.2	3.2	-	-	-	-
C_1 (F)	220	330	-	-	-	-
R_{lea}, EPR (kΩ)	9	4	5	5	2.5	2.5

5. THE TEST OF SUPERCAPACITOR MODEL AND SIMULATIONS IN MATLAB/SIMULINK

The SC model is simulated and compared with the capacitance/ESR measurements and cycle life waveforms from the datasheet of 310 F SCs [46]. The ideal Capacitance/ESR measurements waveforms for data sheets are given in Fig. 8 (a) and cycle life waveform measurements for data sheets are given in Fig. 8 (b).

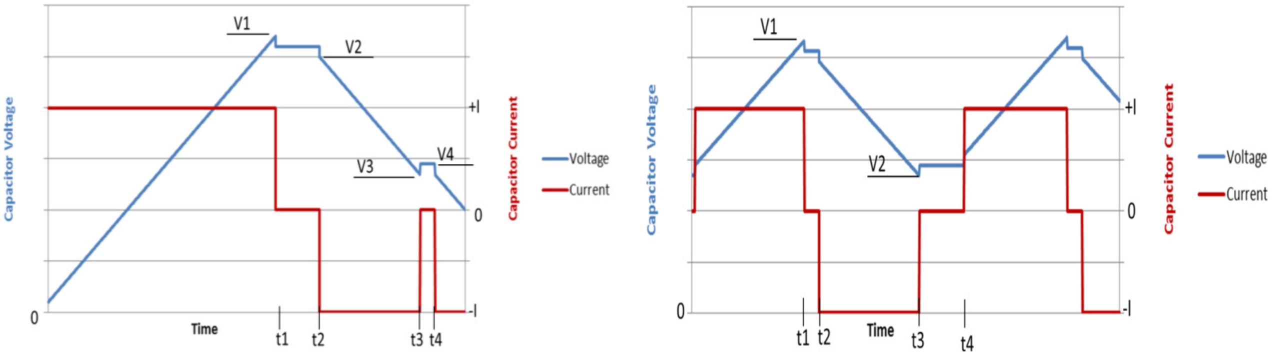

Fig. 8. (a) Capacitance/ESR, (b) cycle life waveform measurements in datasheet [46]

In data sheet $V_1 = V_{rated} = 2.7$ V, $V_3 = 0.5\ V_{rated} = 1.35$ V, $t_2 - t_1 = 15$ seconds, $t_4 - t_3 = 5$ seconds are given for Fig. 8 (a). The $t_3 - t_2$ value is calculated from capacitance Eq. 7. T_{charge} is calculated as a 26 second for 0 to t_1.

$$\text{Capacitance} = I\frac{\Delta t}{\Delta V} \rightarrow \Delta t = \frac{CV}{I} \rightarrow t_3 - t_2 = \frac{C(V_2 - V_3)}{I} = \frac{310(2.7-1.3)}{31} = 14 \text{ second} \tag{7}$$

where $V_1 = V_{rated} = 2.7$ V, $V_2 = 0.5V_{rated} = 1.35$ V, $t_2 - t_1 = 5$ seconds, $t_4 - t_3 = 15$ seconds are given for Fig. 8 (b) in data sheets.

For these tests used a constant current source in charge, discharge and zero current mode, and voltage variations are observed. The simulation result for capacitor/ESR measurement waveform is shown in Fig. 9 (a) and cycle life waveform is shown in Fig. 9 (b) for 310 F SCs. The simulation results are seen suitable with the experimental results and calculations in Fig. 8 manufacturer data sheets and this shows the SC model works correctly. The simulation result for capacitor/ESR measurement waveform is shown in Fig. 10 (a) and cycle life waveform is shown in Fig. 10 (b) for 1500 F SCs. The charge and discharge cycle time of this SC is longer than the first one as expected. Also, the charge and discharge times are compared with data sheet values quantitatively.

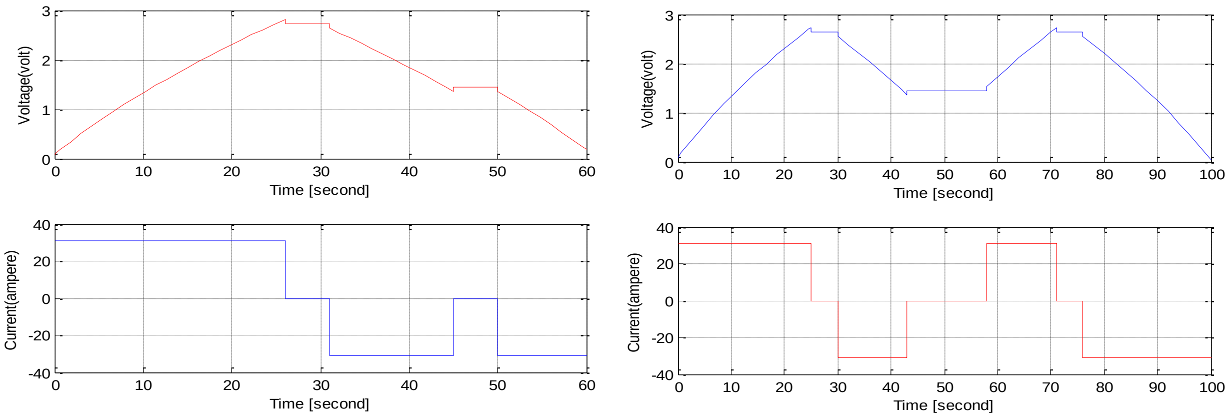

(a) (b)

Fig. 9. (a) CAP/ESR, (b) cycle life waveforms simulation results for 310 F SCs

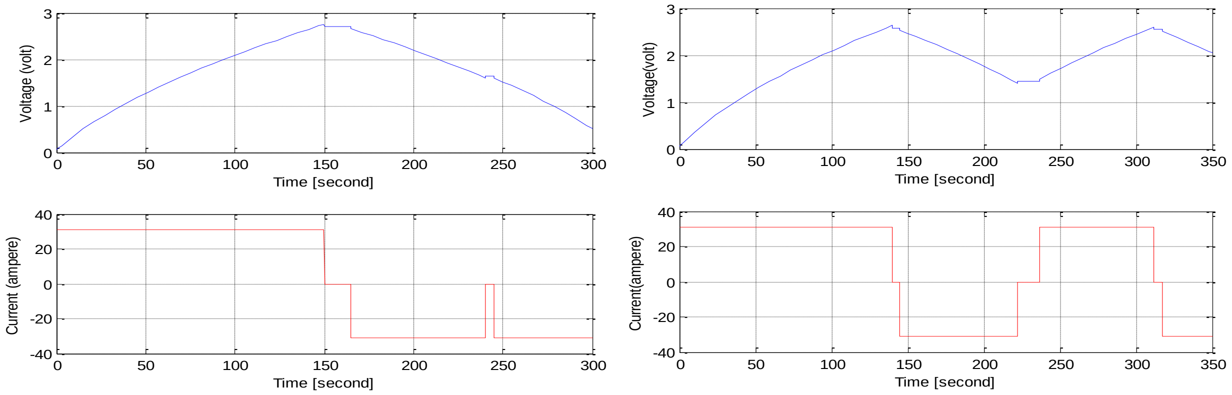

(a) (b)

Fig. 10. (a) CAP/ESR, (b) cycle life waveforms simulation results for 1500 F SCs

The SC charge and discharge circuit simulation results are shown in Fig. 11 (a, b) for a specific series charge ESR and discharge load resistance. The charge and discharge simulation results of a 310 F SC model are shown in Fig. 11 (a). The SC voltage reaches 2.7 V and fixed their charge mode. The current and power go to zero with time. Adversely in the discharge mode, the SC voltage and current and power go to zero with time. The SCs charged in 300 seconds and discharged 100 seconds depending on resistances. The charge and discharge simulation results of the 1500 F SC model are shown in Fig. 11 (b). The SCs charged in 1000 second and discharged 500 seconds depending on resistance. The maximum power in charge mode reaches 20W and in discharge mode reaches 70 W depend on ESR resistance and discharge load resistance. The ESR resistance is select 0.1 Ω and the load resistance is selected 0.01 Ω for the simulation set up. These results are seen suitable with theoretical and experimental results in data sheets.

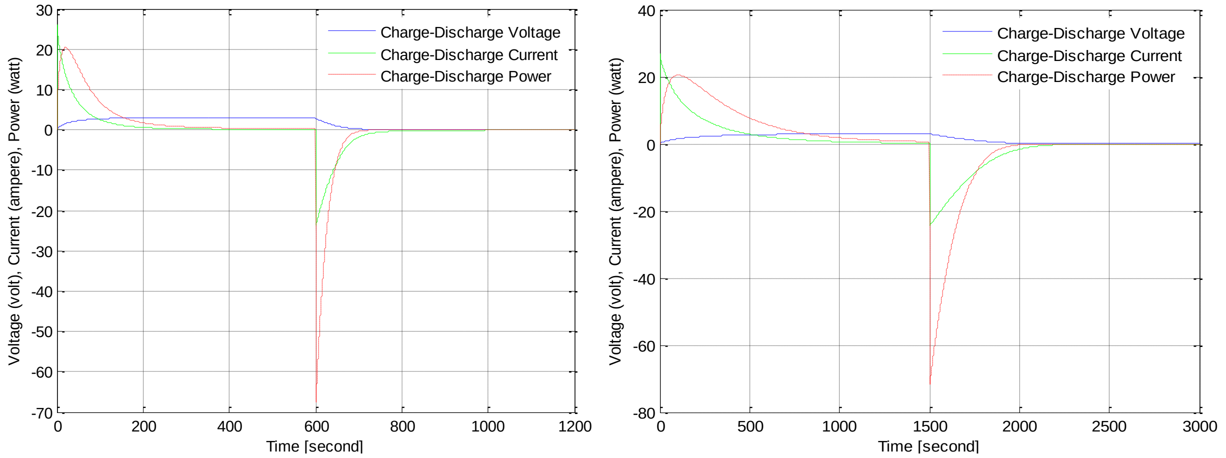

(a) (b)

Fig. 11. The SC charge and discharge circuit simulation results for 310 F (a), and 3000 F (b)

6. CONCLUSIONS

In this paper, the principle of SCs and their chemical structure, the advantages, and disadvantages of SCs, basic specifications, and performance comparison of SCs with the batteries and electrolytic capacitors are given. The different SC models in the literature, their specifications and design aims are investigated. The voltage-current equation of the SC module using the SC simplified circuit model is given in this study. The experimental methods which determine the parameters of the SC equivalent circuit are mentioned, and for different capacitors the obtained coefficients with this methods are presented. Using this parameter and voltage-current equations the SC MATLAB/Simulink model was designed and simulated. The characteristics curves of Capacitance-ESR measurement and cycle life are obtained and compared with data sheets. Also, charge and discharge characteristics of SCs for different capacitor values are simulated to compare the power and energy density of SC modules. The results are seen suitable with theory and data sheets, and the designed models can be used for different electrical applications as a storage system.

7. ACKNOWLEDGMENT

This study was supported through The Scientific & Technological Research Council of Turkey (TUBITAK), 2219 postdoctoral research program with a 1059B191700997 application number. The authors wish to thank for the support of TUBITAK.

REFERENCES

1. PALACÍN, M., GUIBERT, A. D. Why do batteries fail? *Science*, 2016, vol. 351, p. 6273.
2. DÍAZ-GONZÁLEZ, F., SUMPER, A., GOMIS-BELLMUNT, O., VILLAFÁFILA-ROBLES, R. A review of energy storage technologies for wind power applications. *Renew Sustain Energy Rev*, 2012, Vol. 16, No. 4, p. 2154-71.
3. ZOU, Y., HU, X., MA, H., LI, SE. Combined state of charge and state of health estimation over lithium-ion battery cell cycle lifespan for electric vehicles. *J. Power Sources*, 2015, vol. 273, p. 793–803.
4. GLAVIN, M. E., HURLEY, W. G. Optimizations of a photovoltaic battery ultracapacitor hybrid energy storage system. *Solar Energy*, 2012, Vol. 86, No. 10, p. 3009-3020.
5. LAHYANI, A., VENET, P., GUERMAZI, A., TROUDI, A. Battery/supercapacitors combination in uninterruptible power supply (UPS), *IEEE transactions on power electronics*, 2013, Vol. 28, No. 4, p. 1509-1522.
6. RUFER, A., BARRADE, P. A. Supercapacitor-based energy-storage system for elevators with soft commutated interface. *IEEE Trans. Ind. Appl*., 2002, Vol. 38, No. 5, pp. 1151-59.
7. MALLIKA, S., KUMA, R. S. Review on ultracapacitor-battery interface for energy management system. *Int. J. Eng. Technol*., 2011, Vol. 3, No. 1, pp. 37-43.
8. JOHANSSON, P., ANDERSSON, B. *Comparison of simulation programs for supercapacitor modelling.* Master of Science Thesis, Chalmers University of Technology, Sweden, 2008.
9. MICHALCZUK, M., GRZESIAK, L., UFNALSKI, M. B. Experimental parameter identification of battery-ultracapacitor energy storage system. In Industrial Electronics (ISIE), 24th International Symposium on IEEE, 1260-1265, June, 2015.
10. FARANDA, R., GALLINA, M., SON, D. T., A new simplified model of double-layer capacitors, International Conference on in IEEE Clean Electrical Power, 706-710, 2007 May.
11. SHAH, V. A., KUNDU, P., MAHESHWARI, R. Improved method for characterization of ultracapacitor by constant current charging. *International Journal of modeling and optimization*, 2012, Vol. 2, No. 3, p. 290.
12. BULLER, S., KARDEN, E., KOK, D., DE DONCKER, R. W. Modeling the dynamic behaviour of SCs using impedance spectroscopy, In Industry Applications Conference, Thirty-Sixth IAS Annual Meeting. *Conference Record of the 2001 IEEE*, 2001, Vol. 4, p. 2500-2504.
13. CHENG, Z. L., CHEN, W. R., Li, Q., JIANG, Z. L., YANG, Z. H. Modeling and dynamic simulation of an efficient energy storage component-supercapacitor. In Power and Energy Engineering Conference (APPEEC), 2010 Asia-Pacific, 2010 March 1-4.
14. ISLAM, M. S., HOSSAIN, M. B., HOSSAIN, M. N., ALAM, S. B., ENAMUL, M., CHOWDHURY, H. Modeling of a Double-Layer Capacitor with Individual Branch Response, In Proceedings of the World Congress on Engineering and Computer Science, Vol. 2, 2010.

15. ZUBIETA, L. B. Characterization of double-layer capacitors for power electronics applications, *IEEE Transactions on industry applications*, 2000, Vol. 36, No. 1, p. 199-205.
16. RAFIK, F., GUALOUS, H., GALLAY, R., CRAUSAZ, A., BERTHON, A. Frequency, thermal and voltage supercapacitor characterization and modeling. *Journal of power sources*, 2007, Vol. 165, No. 2, p. 928-934.
17. ZUBIETA, L.B. Characterization of double-layer capacitors for power electronics applications. 1997, Ph.D. Thesis, National Library of Canada.
18. BURKE, A., Ultracapacitor: why, how, and where is the technology. *J. Power Sources*, 2000, Vol. 91, pp. 37-50.
19. BC series ultra-capac. , Data Sheet, Doc. *No: 1017105.2,* 2013, [Re*ferred to 20.11.20*18], Link to the internet <http://www.maxwell.com/images/documents/bcseries_ds_1017105-4.pdf>.
20. Supercapacitor (EDLC) Basics (Part 1): What Is a Supercapacitor (EDLC)?, Murata Manufacturing Co., Ltd., [referred on to 20.11.2018], Link to the internet <https://www.murata.com/products/emiconfun/capacitor/2015/03/24/20150324-p1>.
21. ZHANG, Y., FENG, H., WU, X., WANG, L., ZHANG, A., XIA, T., et al. Progress of electrochemical capacitor electrode materials: a review. *Int. J. Hydrogen Energy*, 2009, Vol. 34, No. 11, p. 4889-99.
22. ZHANG, L., HU, X., WANG, Z., SUN, F., DORRELL, D. G. A review of supercapacitor modelling, estimation, and applications: A control/management perspective. *Renewable and Sustainable Energy Reviews*, 2018, Vol. 81, p. 1868-1878.
23. ZOU, C., ZHANG, L., HU, X., WANG, Z., WIK, T., PECHT, M. A review of fractional-order techniques applied to lithium-ion batteries, lead-acid batteries, and supercapacitors. *Journal of Power Sources*, 2018, Vol. 390, p. 286-296.
24. HELMHOLTZ, H. Studien suber electrische grenzschichten. *Ann Phys*, 1879, Vol, 243, p. 337-82.
25. GOUY, G. Constitution of the electric charge at the surface of an electrolyte. J Phys Theor Appl, 1910, Vol. 9, No. 4, p. 457–67.
26. CHAPMAN, D. L. A contribution to the theory of electro capillarity. *Philos Mag Ser 6*, 1913, Vol. 25, No. 148, p. 475-81.
27. STERN, O. The theory of the electrolytic double shift. *Z Elektrochem and Angew Phys Chem*, 1924, Vol. 30, p. 508-16.
28. OLDHAM, K. B. A Gouy–Chapman–Stern model of the double layer at a (metal)/ (ionic liquid) interface. *Journal of Electroanalytical Chemistry*, 2008, Vol. 613, No. 2, p. 131-138.
29. SEIM, L. H. Modeling, control and experimental testing of a SC/battery hybrid system: passive and semi-active topologies, Master's thesis, Norwegian University of Life Sciences, 2012.
30. JARUSHI, A. M. Analysis and modelling of energy source combinations for electric vehicles, Doctoral dissertation, University of Manchester, 2010.
31. SPYKER, L., NELMS, R. M. Classical Equivalent Circuit Parameters for a double layer capacitor. *IEEE transactions on aerospace and electronic systems*, 2000, Vol. 36, No. 3.
32. PAGANO, M. PIEGARI, L. Hybrid Electrochemical Power Sources for On-board Applications, *Energy Conversion, IEEE Transactions*, 2007, Vol. 22, pp. 450-456.
33. NELMS, R. M., CAHELA, D. R., TATARCHUK, B. J. Using a Debye polarization cell to predict double-layer capacitor performance. *Indus. Applic, IEEE Trans.*, 2001, Vol. 37, p. 4-9.
34. VURAL, B., UZUNOGLU, M., ERDINC, O., ONAR, O. C. A dynamic ultracapacitor model for vehicular applications. International Conference on Clean Electrical Power, 2009.
35. YAO Y., ZHANG D., and XU D. A study of supercapacitor parameters and characteristics. IEEE Conferences, 2006.
36. ATCITTY, S., Electrochemical capacitor characterization for electric utility applications. Ph.D. dissertation, Virginia Polytechnic Institute and State University, USA, 2006.
37. GUALOUS, H., LOUAHLIA, H., GALLAY, R. Supercapacitor characterization and thermal modelling with reversible and irreversible heat effect. *IEEE Trans Power Electron*, 2011, Vol. 26 No. 11, p. 3402-9.

38. WANG, K., ZHANG, L., JI, B., YUAN, J. The thermal analysis on the stackable supercapacitors. *Energy*, 2013, Vol. 59, p. 440-4.
39. D'ENTREMONT, A., PILON, L. First-principles thermal modelling of electric double layer capacitors under constant-current cycling. *J Power Sources*, 2014, Vol. 246, p. 887–98.
40. SAKKA, M., GUALOUS, H., MIERLO, J., CULCU, H., Thermal modelling and heat management of supercapacitor modules for vehicle applications. *J Power Sources*, 2009, Vol. 194, No. 2, p. 581-7.
41. SOUALHI, A., SARI, A., RAZIK, H., VENET, P., CLERC, G., GERMAN, R., BRIAT, O., VINASSA, JM. Supercapacitors ageing prediction by neural networks. In: Proceedings of the 39th IEEE industrial electronics society annual conference, 2013, p. 6812-8.
42. FARSI, H., GOBAL, F. Artificial neural network simulator for supercapacitors performance prediction. *Computational material science*, 2007, Vol. 39, No.3, p. 678-83.
43. HIJAZI, A., KRECZANIK, P., BIDEAUX, E., VENET, P., CLERC, G., DI LORETO, M. Thermal network model of SC stack. *IEEE Trans Ind Electron*, 2012, Vol. 59, No. 2, p. 979-87.
44. KRECZANIK, P., VENET, P., HIJAZI, A., CLERC, G. Study of supercapacitor aging and lifetime estimation according to voltage, temperature, and RMS current. *IEEE Transactions on industrial electronics*, 2014, Vol. 61, No. 9, p. 4895-4902.
45. CHIA, Y. Y., Integrating SCs into a hybrid energy system to costs using the genetic algorithm (GA) and support vector machine, Doctoral dissertation, University of Nottingham, 2014.
46. Maxwell Technologies, BC Series supercapacitors, Datasheet, Document number: 1017105.4, [referred to 30 November 2018], Link to the internet <http://www.maxwell.com/images/documents/bcseries_ds_1017105-4.pdf >

CYSENI 2019, May 23-24, Kaunas, Lithuania
ISSN 1822-7554, www.cyseni.com

RELIABILITY IMPROVEMENT OF DISTRIBUTION SYSTEM USING AUTO RECLOSER IN LAO PEOPLE'S DEMOCRATIC REPUBLIC

V. Thepmahavong, P. Khunkitti, A. Siritaratiwat and
R. Chatthaworn[*]
Department of Electrical Engineering, Faculty of Engineering
Khon Kaen University,
Khon Kaen, 40002 – Thailand
Email: visanousanhth@kkumail.com

Ch. Surawanitkun
Faculty of Applied Science and Engineering
Khon Kaen University, Nong Khai Campus,
Nong Khai, 43000 -Thailand

ABSTRACT

This paper presents the reliability assessment of distribution system using Monte Carlo simulation. A reliability evaluation model is created by using MATLAB software. The simulation method generates time to failure (TTF) and time to repair (TTR) of each component in distribution system which are modelled by using exponential distribution function. The operations of each component in distribution system including circuit breaker, load break switch, disconnecting switch, fuses and automatic protective device are used to calculate the reliability indices of the distribution system. The considered indices are the system average interruption frequency index (SAIFI), the system average interruption duration index (SAIDI) and the energy not supplied (ENS). Moreover, the benefit-cost analysis is conducted to find the optimal location of an auto recloser. The objective function includes the benefit of reliability improvement obtained from the installing of an auto recloser minus the investment cost and the operation-maintenance cost of an auto recloser. Finally, the proposed simulation method is tested on a 22 kV distribution system from Electricite Du Laos network in Attapeu province, Lao People's Democratic Republic. The simulation results show that the proposed method can find the optimal location of an auto recloser which maximizes the benefit of distribution utility.

Keywords: auto recloser, benefit-cost analysis, Monte Carlo simulation, reliability evaluation, reliability indices

1. INTRODUCTION

A conventional electric power system can be separated into four sections including generation system, transmission system, distribution system, and load or customer. The distribution system is a considerable section of the electric power system because it is the final link between the customers and transmission system. It has been reported that 80% of all outages occurs because of failures in the distribution system [1]. The radial distribution system in Attapeu province, Laos PDR has one major defect that in case of any transmission line failure, the associated customers would not get any power because there is no alternative path to feed the power to the customers. In case of transformer or substation failure also, the power supply is interrupted. The customers in the distribution system are not supplied until the feeder or substation is restored. The most interruptions of the distribution system are the "line to line fault", "the line to ground fault" and lightning.

For the review of reliability assessment, research works [2]-[6] present the basic principle of reliability assessment of the distribution system. There are two kinds of the assessment techniques consisting of the analytical method and the simulation method. The analytical method is widely used, [5]-[8], but it cannot be used to establish the model for the complex distribution system. For the simulation method, it is also known as Monte Carlo simulation. This method is more suitable for the complex distribution system and it can predict the failure event of distribution components that is likely the random event, while the other methods cannot predict [9]-[13]. The utilization of Monte Carlo simulation technique in reliability assessment has enhanced considerably during the last few decades. Consequently, the Monte Carlo simulation method uses the simplified assumption that failure rate and repair time of the components in the distribution system are exponentially distributed. For the works related to the protective devices, the research work [14] proposes the optimal placement of an auto recloser to improve system reliability. The Monte Carlo simulation method is used to evaluate the system reliability of the distribution system. In research work [15], the auto reclosers are used to enhance the system stability and reliability of the distribution system by dividing the zone of interruption.

Consequently, this paper proposes the method to solving the optimal placement of an auto recloser in order to improve the reliability of the Attapeu distribution system, Lao People's Democratic Republic. The Monte Carlo technique is used to evaluate the system reliability. Moreover, the benefit-cost analysis is conducted to find the optimal placement of an auto recloser. The objective function includes the benefit of reliability improvement obtained from the installing of an auto recloser minus the investment cost and the operation-maintenance cost of an auto recloser.

2. METHODOLOGY

2.1. Reliability indices

In distribution system reliability assessment, there are three basic reliability parameters consisting of the failure rate λ (interruptions/year), the interruption duration r (hours/interruption), and the annual unavailability U (hours/year), [16] - [17] as shown below.

$$\lambda = \sum_{i=1}^{N} \lambda_i \tag{1}$$

$$r = \frac{U_i}{\lambda_i} \tag{2}$$

$$U = \sum_{i=1}^{N} \lambda_i U_i \tag{3}$$

where, N is the total number of the components in the distribution system.

These parameters are calculated based on the historical failure data of each component. This research considers three significant reliability indices consisting of SAIFI, SAIDI and ENS. These indices can be described by the following:

1) System average interruption frequency index: SAIFI (interruptions/customer/year), it can be expressed in each simulation according to the equations presented in, [16] - [17].

$$SAIFI = \frac{\sum_i \lambda_i N_i}{\sum N_i} \tag{4}$$

where N_i is the number of consumers at load point i.

2) System average interruption duration index: SAIDI (hours/customer/year) can be calculated in equation (5) in, [16] - [17].

$$SAIFI = \frac{\sum_i U_i N_i}{\sum N_i} \tag{5}$$

3) Energy not supplied: ENS (kWh/yr.) [16] - [17]. It can be calculated by equation (6).

$$ENS = \sum L_{a(i)} U_i \tag{6}$$

where $L_{a(i)}$ is the average load (kW) at each load point i that is one of the important parameters required in the evaluation of load point and energy orientated indices in, [16] - [17]. The average load can be calculated in equation (7). On the other hand, the average load can be calculated in equation (8).

$$L_a = L_p f \tag{7}$$

$$L_a = \frac{E_d}{t} \tag{8}$$

where, t is the number of hours of a year, E_d is the energy demand in a period of interest (kWh), L_p is the peak load (kW) and f is a load factor.

2.2. Reliability worth

The yearly energy not supplied cost (ENSC) for each feeder in distribution system is estimated by the equation (9), [16] - [17].

$$ENSC = \sum_{i=1}^{M} C_{ij} \times ENS_{ij} \tag{9}$$

where C_{ij} is the cost of interruption of load point i due to event j. M is the number of load points in the system.

The costs of auto recloser are divided into two types consisting of investment and maintenance costs. Investment cost is a one-time cost that includes installation, monitoring device, construction costs, etc, [18]. The investment and maintenance costs calculation can be written as shown in equation (10) and equation (11), respectively.

$$INVC = C_{RE-INV} \times N_{RE} \tag{10}$$

where, $INVC$ is the total investment cost of auto recloser ($). N_{RE} is the number of auto reclosers. C_{RE-INV} is the purchase and installation cost ($) of an auto recloser.

The yearly maintenance cost consisiting of annual electrical restoration, mechanical and renovation costs can be calculated by equation (11) in, [18]:

$$MAINC = C_{RE-MAIN} \times N_{RE} \tag{11}$$

where, $MAINC$ is the total maintenance cost of an auto recloser ($/year). $C_{RE-MAIN}$ is the annual maintenance cost of an auto recloser ($/year).

The purpose of the auto recloser installation is to obtain the highest profit during its life time in, [18]. The life time that considered in this paper is 20 years. Thus, the objective function considering the benefits and costs of auto recloser can be explained by the following equation:

$$CF = ENSC - MAINC - INVC \tag{12}$$

where, CF is the profit of distribution system company ($) obtained from the installation of auto recloser.

2.3. Monte Carlo simulation

Because the reality that the fault occurrence in distribution systems are random, the fault occurrence is simulated by Monte Carlo simulation method. This method is a probabilistic technique that can be used to forecast the behavior of the distribution system components. The time sequential simulation is one of the Monte Carlo simulation types used when the system behavior depends on past events. An artificial operation of distribution system component is required in time sequential simulation, and Monte Carlo simulation can provide it by producing the up and down operation status of each component in the distribution system. The time to (before) failure (TTF) is the time period that takes the component to failure as explained in [16], [19], and [20]. It is randomly forecasted by the following equation (13).

$$TTF = -\frac{1}{\lambda}\ln(n) \tag{13}$$

where, n is a random number (range from 0 to 1).

The time to repair (TTR) is the time required to repair or replace a failed component. Also, it is forecasted randomly by the following equation (14).

$$TTR = -\frac{1}{\mu}\ln(n) \tag{14}$$

where, μ is the repair rate of system component.

It is clears from equations (13) and (14) that TTF and TTR follow exponential distributions. To forecast the artificial history of system components, TTF and TTR are established for the whole simulation times (e.g. 1 year) in chronological order. A sample of component operation history is presented in Fig. 1. In order to obtain an accurate result, Monte Carlo simulation has to be operated for a large number of scenarios and the simulation time can be expanded to be a very long time (e.g. 1,000 years or more) depending on the desired accuracy. In this research, the simulation time is defined to be 50,000 years which is obtained by the test. In the test, the simulation time is firstly defined to be 1,000 years and the tolerance will be calculated. After that, the simulation time is increased with the step of 1,000 years until the tolerance is acceptable which is defined to be 10^{-6}. Finally, from the test, the suitable simulation time is equal to 50,000 years.

The flow chart of simulation process by Monte Carlo method is presented in Fig. 2.

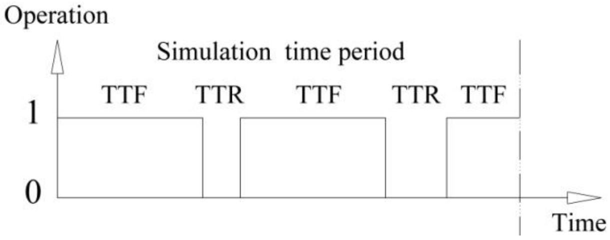

Fig. 1. TTF and TTR of the component

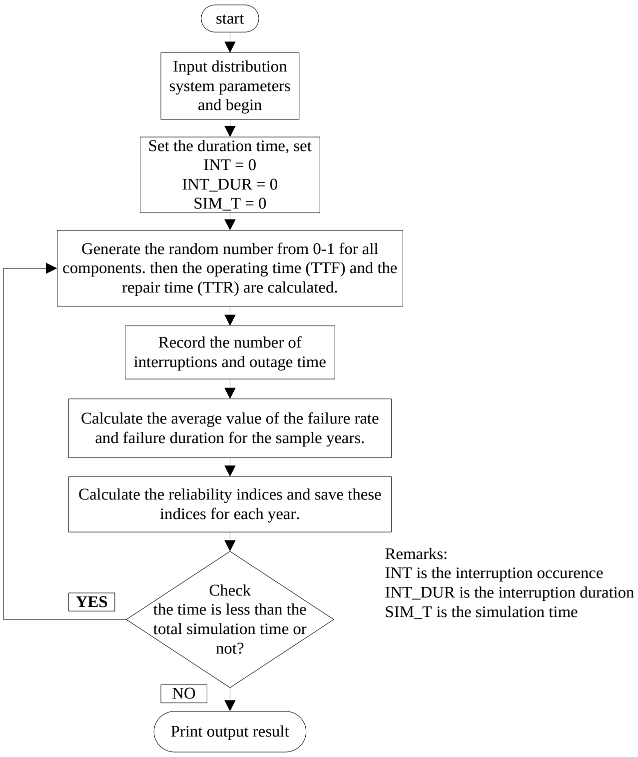

Fig. 2. Flow chat of Monte Carlo simulation process

2.4. Proposed method for solving the optimal placement of an auto recloser

This section presents the proposed method to find the optimal placement of an auto recloser in the distribution system considering reliability indices. The process is to find the minimum values of ENS, SAIFI, and SAIDI when changing the location of an auto recloser as shown in Fig. 3.

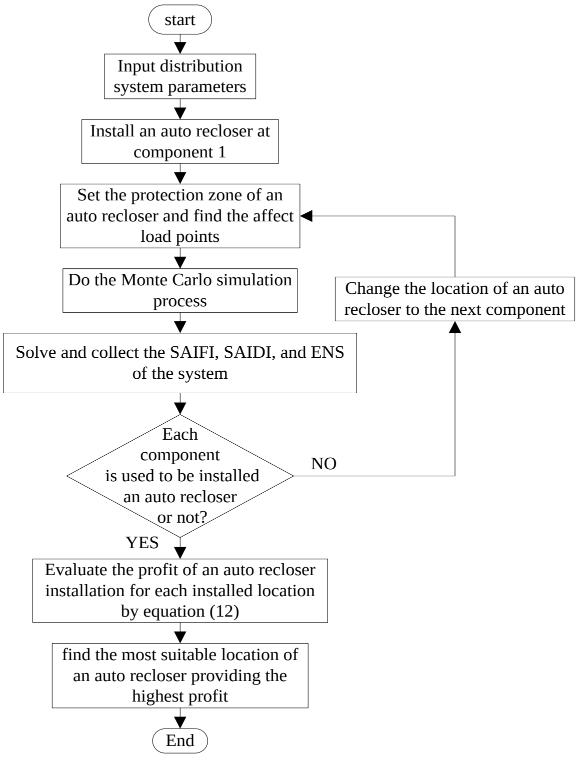

Fig. 3. The flowchart for solving the optimal placement of an auto recloser

3. NUMERICAL RESULTS AND DISCUSSION

3.1. Test systems

The selected systems for testing is the Institute of Electrical and Electronics Engineers Roy Billinton Test System (IEEE RBTS BUS-2) (Fig. 4) and the distrubition system of Attapeu province, Lao PDR on Feeder 03. The IEEE RBTS BUS-2 consists of 4 feeders, 22 load points, 36 lines, 2 switches, 10 disconnecting switches and 22 fuses [6]. This system widely used for reliability assessment in distribution systems because it provides completely detailed data such as interruption rate and average maintenance time for each component as shown in Fig. 4. Moreover, in this research, the Feeder 03 of distribution system in Attapeu province, Lao PDR is selected for testing. The number of customer in Feeder 03 is 3,877 and the total line length is 79.44 km, the failure rate is 0.176 interuptions/yr.km and the repair time is 0.76 hr./km. The system consists of 30 load points, 60 lines, 1 load break switch, 30 fuses as shown in Fig. 5.

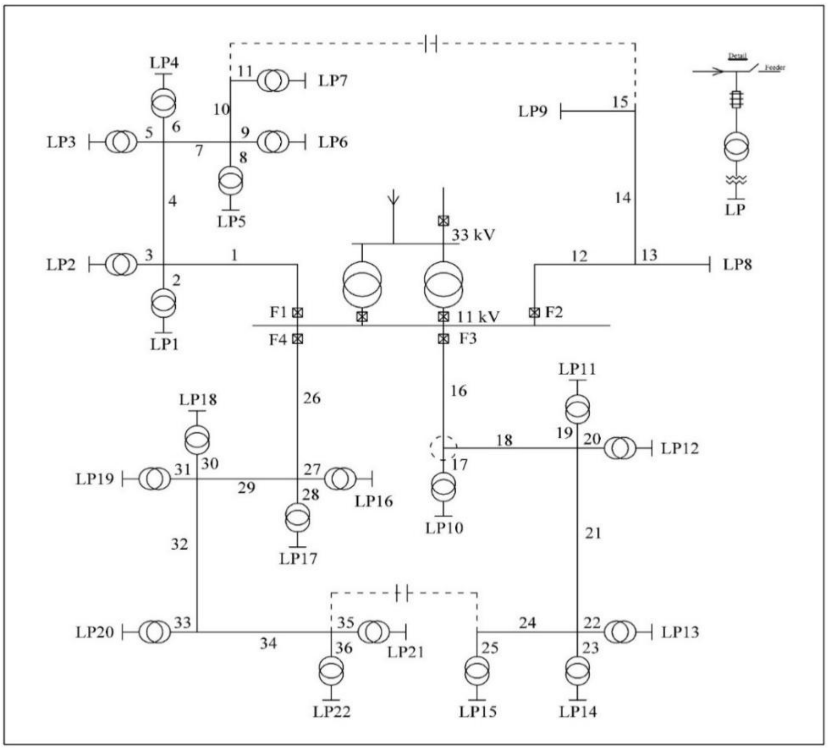

Fig. 4. The IEEE RBTS BUS-2

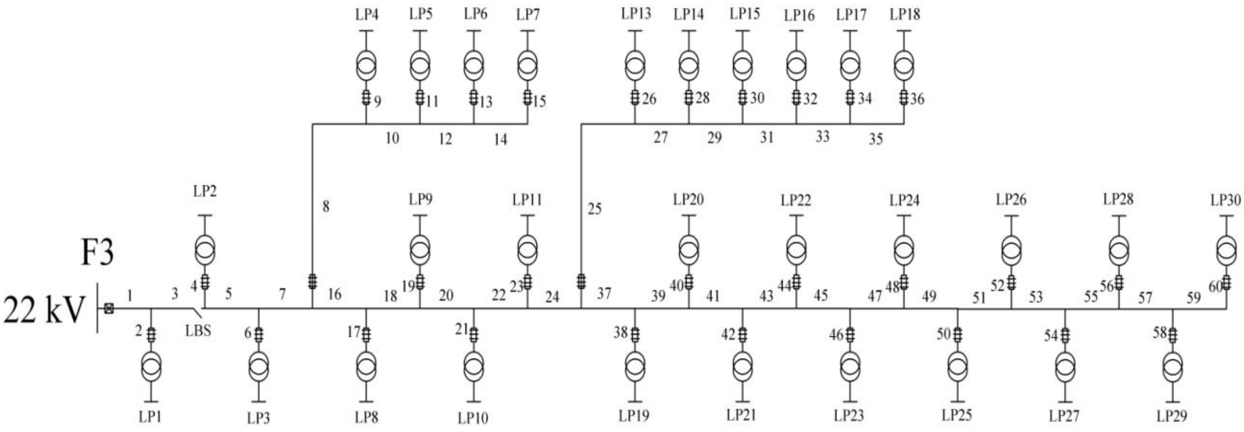

Fig. 5. Feeder 03 distribution system of Attapeu province, Lao PDR

In this paper, the life time of an auto recloser is defined to 20 years, the purchase and installation cost are 8,000 $/unit, and the annual maintenance is 5% of auto recloser purchase and installation cost. The electricity tariff rate in 22 kV distribution system of Electricite Du Laos network is 0.0857 $/kWh by using the currency exchanged rate on January 2019 which is 8,562 KIP per 1 $.

In order to analyze the system reliability considering with the auto recloser, the test cases are divided into three cases as explained below.

Case A: considering only repair of transformers without alternative supply, fuses and disconnecting switch.

Case B: considering repair of transformers with alternative supply, fuses and disconnecting switch.

Case C: same as Case B but including an auto recloser installation in the distribution system.

For the IEEE RBTS BUS-2, firstly, in order to check the accuracy of the results from the Monte Carlo simulation method that is used in this work comparing with the analytical method, the Case A and B are selected as the case for this comparison. The comparison results of system reliability obtained from the analytical and simulation methods are presented in Table 1.

Table 1. The comparison results of system reliability obtained from the analytical (A) and simulation (S) methods for IEEE RBTS BUS-2

Index	**Case A in overhead line of BUS 2**			**Case B in overhead line of BUS 2**		
	(A) [6]	**(S)**	**Difference (%)**	**(A)** [6]	**(S)**	**Difference (%)**
SAIFI (Int/cus.yr)	0.602	0.602	0.00	0.248	0.249	0.55
SAIDI (hrs/cus.yr)	22.50	22.45	0.21	3.61	3.60	0.38
ENS (kWh)	231,263	230,869	0.17	37,746	37,799	0.14

To find the optimal placement of an auto recloser considering the system reliability in the feeder number 01 of the IEEE RBTS overhead line on BUS 2, the simulation model and simulation process are produced by using Monte Carlo simulation method. The difference of reliability indices between before and after installation of auto recloser is presented in Table 2. The system reliability indices are depended on the placement of auto recloser. The optimal location of an auto recloser that can provide the best reliability is shown in Case C of Table 2.

Table 2. The comparison of system reliability indices in Feeder 1 of the IEEE RBTS BUS-02 (overhead line case)

Case	**Optimal location of an auto recloser**	**Index**	**Results**		
			(A) [6]	**(S)**	**Difference (%)**
Case A in Feeder 1 on overhead line of BUS 2	-	SAIFI (Int/cus/yr)	0.626	0.625	0.12
	-	SAIDI (hrs/cus/yr)	23.61	22.83	3.40
	-	ENS (kWh)	86,040	83,228	3.38
Case B in Feeder 1 on overhead line of BUS 2	-	SAIFI (Int/cus/yr)	0.248	0.246	0.45
	-	SAIDI (hrs/cus/yr)	3.62	3.47	4.10
	-	ENS (kWh)	13,172	12,658	4.06
Case C in Feeder 1 on overhead line of BUS 2	Component 4	SAIFI (Int/cus/yr)	-	0.272	-
	Component 4	SAIDI (hrs/cus/yr)	-	1.363	-
	Component 7	ENS (kWh)	-	6,789	-

The simulation results in the Feeder 3 distribution system of Attapeu province, Lao PDR (Fig. 5) are presented in Table 3. The suitable location of an auto recloser considering only the number of interruptions is component 24 because it provides the minimum SAIFI. While, the suitable location of an auto recloser when considering the interruption time and energy not supplied is component 45. The bar chart of SAIFI index and SAIDI index are presented in Fig. 6 and Fig. 7, respectively.

Table 3. The result of Feeder 03 (F3) distribution system at Attapeu province

Test	**Optimal location of auto recloser**	**Index**	**Result** (S)
Case B	-	SAIFI (Int/cus/yr)	13.927
	-	SAIDI (hrs/cus/yr)	38.89
	-	ENS (kWh)	72,277
Case C	Component 24	SAIFI (Int/cus/yr)	9.383
	Component 45	SAIDI (hrs/cus/yr)	25.40
	Component 45	ENS (kWh)	48,366

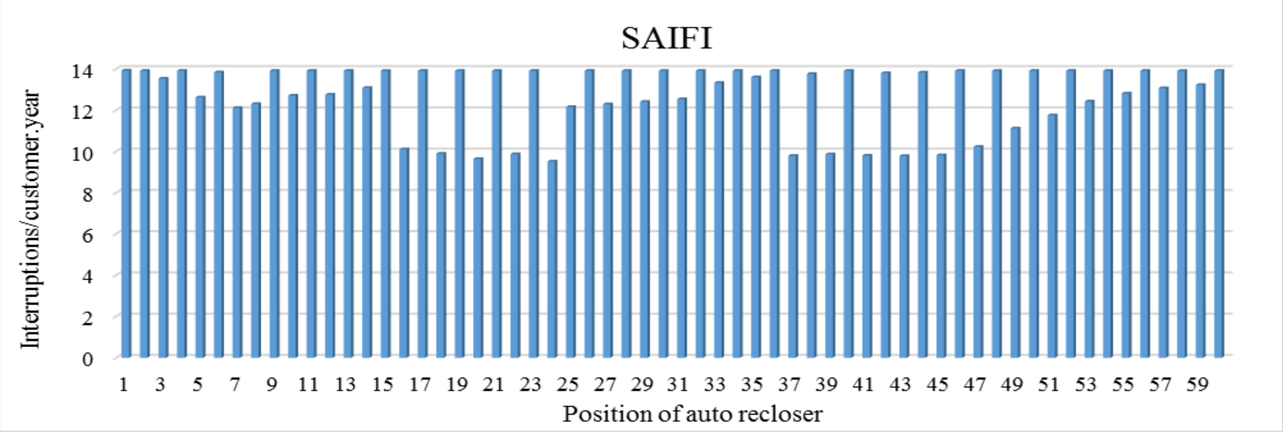

Fig. 6. The calculated SAIFI when installing an auto recloser for each location in feeder 03 distribution system, Attapeu province

Fig. 7. The calculated SAIDI when installing an auto recloser for each location in feeder 03 distribution system, Attapeu province

It can be seen from Fig. 8 that the minimized of the energy not supplied of Feeder 3 is occurred when an auto recloser is installed at component 45.

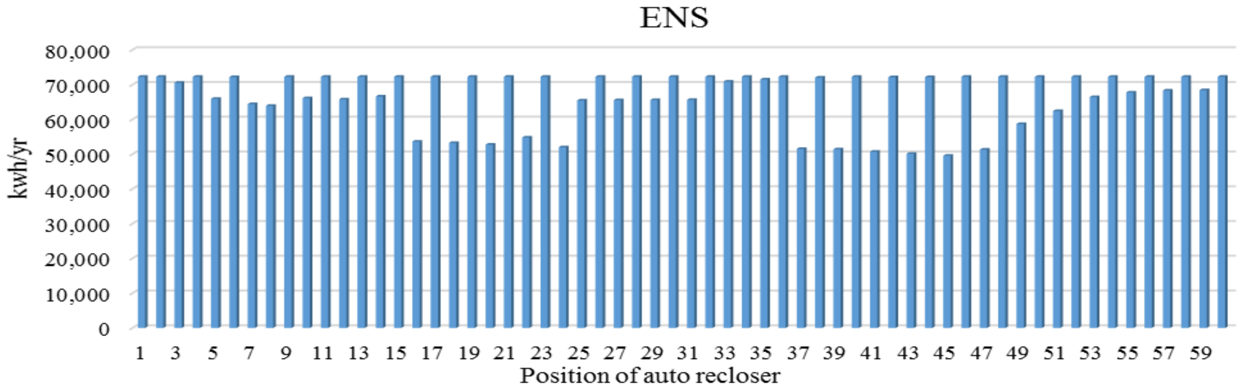

Fig. 8. The calculated ENS when installing an auto recloser for each location in feeder 03 distribution system, Attapeu province

The profit of distribution system utility from the optimal placement of auto recloser considering its lifetime which is 20 years is presented in Table 4. It can be seen that, the utility of Attapeu province, Lao PDR can make a profit obtained from equation (12) by an auto recloser investment about 24,983$ when considering throughout the auto recloser lifetime.

Table 4. The benefit of distribution system at Attapeu province

Detail	**Quantity**	**Unit**
ENS without auto recloser	72,277	kWh/yr
ENS after installing auto recloser	48,366	kWh/yr
Difference	23,911	kWh/yr
Difference in the 20 years	478,220	kWh/yr
ENS cost in the 20 years	40,983	$
The investment cost of an auto recloser	8,000	$
Maintenance cost 5% of investment cost in the 20 years	8,000	$
The profit of distribution system company	**24,983**	$

4. CONCLUSIONS

This paper presents the reliability improvement of distribution system using auto recloser. The Monte Carlo simulation method is used to evaluate the reliability of distribution system. The simulation results show that the proposed method can calculate the reliability of the distribution system. From the testing results, the reliability of distribution system can be maximized by installing an auto recloser at proper location which can maximize the utility profit. For the case study of distribution system of Attapeu province, Lao PDR, the selected location for installing an auto recloser is component 45 because it can reduce most energy not supplied which can maximize the profit of the distribution system utility of Attapeu province, Lao PDR. After the installation of an auto recloser, SAIFI, SAIDI, and ENS of the system were improved by 32.63%, 34.69%, and 33.08%, respectively. In addition, from the research results, it can be concluded that the optimal placement of an auto recloser should be around the center of the system. This conclusion can help the decision of the system planner to select the optimal placement of an auto recloser in order to improve the system reliability.

ACKNOWLEDGEMENTS

This research was supported by Electricity Generating Authority of Thailand (EGAT) and Electricite Due Laos (EDL).

REFERENCES

1. X. LIANG and L. GOEL, “Distribution system reliability evaluation using the Monte Carlo simulation method,” *Electr. Power Syst. Res.*, 1997, Vol. 40, No. 2, pp. 75-83.
2. G. R.N ALLAN, R. BILLINTON, A.M BREIPOHL, “Bibliography on the application of probability methods in power system reliability evaluation- 1987-1991,” IEEE Trans. Power Syst, Febr. 1994, Vol. 9, No. 1, pp. 41-49.
3. R. N. ALLAN and S. MEMBER, “The IEEE reliability test system - extensions to and evaluation of the generating system,” IEEE Trans. 1986, Vol. PWRS-1, No. 4, pp. 1-7,
4. C. FONG, S. HADDAD, and D. PATTON, “A report prepared by the Reliability test tystem task force* of the application of probability methods subcommittee,” IEEE Reliab. Test Syst. - 1996, Augus - 1999, Vol. 14, No. 3, pp 1010-1020.
5. R. Billinton, “A test system for teaching overall power system reliability assessment,” IEEE Trans. Power Syst. 1996, Vol. 11, No. 4, pp. 1670-1676.
6. R. N. ALLAN, R. BILLINTON, I. SJARIEF, L. GOEL, and K. S. SO, “A reliability test system for educational purposes-basic distribution system data and results,” IEEE Trans. Power Syst., 1991, Vol. 6, No. 2, pp. 813-820.
7. R. BILLINTON, P. WANG, “Reliability network equivalent approach to distribution system reliability evaluation,” IEE Proc.- Gener. Transm. Distrib., 1998, Vol. 145, No. 2, pp. 149-153.
8. L. GOEL, R. BILLINTON, R. GUPTA, “Basic data and evaluation of distribution system reliability worth,” WESCANEX ’91 ’IEEE West. Canada Conf. Comput. Power Commun. Syst. a Rural Environ., 1991, Vol. -, No. -, pp. 271-277.
9. H. CHEN, “A sequential simulation technique for adequacy evaluation of generating systems including wind energy”, 1996, Vol. 11, No. 4, pp. 728-734.
10. R. BILLINTON, A. SANKARAKRISHNAN, “A comparison of Monte Carlo simulation on techniques for composite power system reliability assessment”,1995,Vol.-, No. 95, pp.145-150.
11. A. SANKARAKRISHNAN, R. BILLINTON, “Effective techniques for reliability worth assessment in composite power system networks using Monte Carlo simulation,”, 1996, Vol. 11, No. 3, pp.1255-1261.
12. R. BILLINTON and P. WANG, “Teaching Distribution System Reliability Evaluation Using Monte Carlo Simulation,” IEEES Trans. Power Syst. , 1999, Vol. 14, No. 2, pp. 397-403.
13. L. GOEL, “Monte Carlo simulation based reliability studies of a distribution test system,” Electr. Power Syst. Res., 2000, Vol. 54, No. 1, pp. 55-65.
14. T. M. ALJOHANI and M. J. BESHIR, “Matlab code to assess the reliability of the smart power distribution system using monte carlo simulation,” , 2017, Vol. 5, No. -, pp. 30-44.
15. A. ALAM, V. PANT, and B. DAS, “Switch and recloser placement in distribution system considering uncertainties in loads , failure rates and repair rates,” Electr. Power Syst. Res., 2016, Vol. 140, pp. 619-630.
16. R. Billinton, R. N. ALLAN, “*Reliability Evaluation of Power Systems*”, Second Edi. Plenum Press, New York: Book, 1996.
17. R. Billinton, R. N. ALLAN, “*Reliability Assessment of Large Electric Power Systems*”, 1987.
18. S. ABDI, K. AFSHAR, S. AHMADI, N. BIGDELI, M. ABDI, “Optimal recloser and autosectionalizer allocation in distribution networks using IPSO – Monte Carlo approach,” Int. J. Electr. Power Energy Syst., 2014, Vol. 55, pp. 602-611.
19. V. MOLLICK, “*The Monte Carlo Simulation Method for System Reliability and Risk Analysis*”, Book, 2003.
20. W. LI. R. BILLINTON, “*Reliability Assessment of Electric Power Systems Using Monte Carlo Methods*”, Vol. 91, 1994.

CYSENI 2019, May 23-24, Kaunas, Lithuania
ISSN 1822-7554, www.cyseni.com

REDUCTION OF SUPPLY TEMPERATURES AND ITS IMPACT ON THE COMPONENT PARAMETERS OF THE DISTRICT HEATING SYSTEM. CASE STUDY: TOWN OF MAARDU, ESTONIA

A. Volkova, E. Latõšov
Tallinn University of Technology, Department of Energy Technology,
Ehitajate tee 5, 19086 Tallinn – Estonia

A. Hlebnikov, V. Mašatin
AS Utilitas Tallinn, Punane 36, 13619 Tallinn – Estonia

ABSTRACT

In the frame of the research the potential to implement low temperature district heating for Maardu town (Estonia) was evaluated, using simulation software NetSim. The goal was to determine the lowest supply temperature that can be achieved without changing any other conditions, such as consumer substations and return temperature. Through this approach, it was possible to determine the key obstacles to reducing supply temperature. Parameters, such as pressure, flow rate, and heat losses were calculated for various temperature schedules, taking into account the pressure and flow rate limitations established by consumer heating facilities, pipelines, etc. Two supply temperature strategies were analysed: reducing the supply temperature by the same number of degrees for each case of outdoor temperature (in parallel)., and reducing the maximum supply temperature, while not changing the minimum supply temperature. The results show that due to temperature reduction it is possible to get the heat losses saving up to 5.7%

Keywords: pipes, district heating networks, low-temperature DH, heat loss reduction

1. INTRODUCTION

For many years, district heating (DH) has been widely used for space heating and domestic hot water supply [1]. The total number of district heating systems in the world is approximately 80 thousand, with about 6 thousand DH systems located in Europe[2]. The main benefits of DH include reliable heat supply, lower heat production costs, the possibility of using heat produced by combined heat and power units, as well as integrating large thermal energy storage units and heat pumps into the system [3]-[5]. One of the main conditions, that should satisfied by the DH system as a heat supply technology for it to be considered an energy-efficient and environmentally friendly solution is possibility to use low-temperature heat carrier [6]. Lower supply and return temperatures reduce heat loss and increase the utilisation of renewable and waste heat energy sources, such as solar heat, seawater heat, and low-grade industrial waste heat. Numerous studies have discussed the possibility to reduce heat loss through the use of low-temperature heat carriers in the DH systems. Network heat loss is a very important factor associated with supply and return temperatures of the system's heat carrier [7]. The methodology for determining steady-state heat loss for various pipe types and configurations with a particular focus on low-temperature appliances was described in [8]. Some researchers have provided case studies on the transition of the existing DH towards low-temperature systems. Most of them are focused on supply temperature reduction down to low temperatures (50-65ºC) coupled with renovation of pipes and consumer substations. The results of the research on low-temperature district heating implementation in existing DH in Norway showed that the heat losses can be reduced by 25% annualy while decreasing the supply temperature from 80 °C to 55 °C with no change in pipe diameters[9]. In other research modelling results have shown, that supply temperature reduction from 115 °C to 105 °C will reduce heat losses from 28 W/m to 25 W/m [10]. Case-study simulation results showed that supply temperature lowering from 90 to 50 ºC leads to annual heat loss reduction from 18% to 8.3% [12]. The conditions for above-mentioned case studies are related with complex improvements, including both renovation of network pipes and consumer substations. The idea of current research is developing the methodology for possible supply temperature reduction, taking into account restrictions, related to current state of DH system. The goal of the analysis is to determine the lowest supply temperature that can be achieved without changing any other conditions, such as consumer substations and return temperature. This approach reflects the situation, when district heating operator prefer to reduce heat losses without cooperation with consumer and large investments into renovation of distribution pipes. Analysing various supply temperature reducing strategies, both possible heat loss reduction and key obstacles to reducing supply temperature can be determined.

Although the concept of low-temperature DH has already been implemented in some European DH systems, the DH networks in Estonia can still be classified as high-temperature DH. The supply temperature in Estonian DH systems varies from 75 to 120 ºC and DH companies are very interested in reducing temperature due to the aforementioned advantages. Reducing the temperature leads to changes in the DH network operation and affects the operation of its components, such as pipes, pumps, heat exchangers, regulating valves, and flow meters. The impact is particularly significant if the heat source is located quite far from the consumers. In the result of this study, the analysis of the possibility for reducing the DH network's supply temperature is conducted for the town of Maardu (Estonia) using NetSim simulation software.

The second section of this paper offers the description of the analysed DH network; the third provides the overview of the analysis methodology; and the fourth section reports the results, focusing on the main obstacles to temperature reduction identified during the calculations. The closing section of the paper presents conclusions and discussion.

2. BACKGROUND

The DH network of Maardu is connected to the Tallinn DH network. The Tallinn-Maardu DH network is very large and complex: over 426 km in length, with the maximum heat load going up to 750 MW in winter. The amount of heat supplied into the network is ~2048 GWh per normalized year, consumption ~1766 GWh, network heat loss ~283 GWh (13.8%). The Tallinn DH network has undergone significant renovation in the last 20 years [13]-[15]. In 2017, the share of the renovated pipeline in operation was 43% and the share of the pre-insulated pipeline − 38% [16]. Seven heat sources supply the network, three of which are combined heat and power (CHP) plants, operating on wood chips and waste, and the rest are boiler houses running on natural gas. Maardu, a satellite town of Tallinn, is located east of Tallinn. The abovementioned DH network provides heat to Maardu, which has a separate mainline of over 12 km in length. The maximum load of the Maardu network is 28-30 MW. The amount of heat supplied into the network is ~89 GWh per normalized year, consumption ~63 GWh, network heat loss ~26 GWh (28.9%).

Early in the network's operation (since 1959), extremely high-temperature schedules were in use at the Tallinn DH network, with 150 ºC supply and 70 ºC return temperature used until 70-ies, and 130 ºC supply and 70 ºC return temperature used until 90-ies. Currently, the temperature schedule has been set to 120 ºC supply and 65 ºC return temperature. The possibility of reducing supply temperature in the Maardu network was evaluated as a pilot project.

Fig. 1 shows how the town of Maardu is connected to the Tallinn DH network.

Maardu's heat supply comes from the waste incineration plant and biomass-based CHP located 11 km from the town limit in Iru district. The heat is transferred from Iru to Maardu through mainly DN500 and DN600 mm insulated pipes. The structure of the connection pipelines and district heating network is shown in Fig. 2. It can be seen, that newly insulated above ground pipelines constitute over 70% of the network.

The diagram in Fig. 3 is based on the 2017 data on the dependence of the heat load on outdoor temperature.

Fig.1. Tallinn-Maardu district heating network

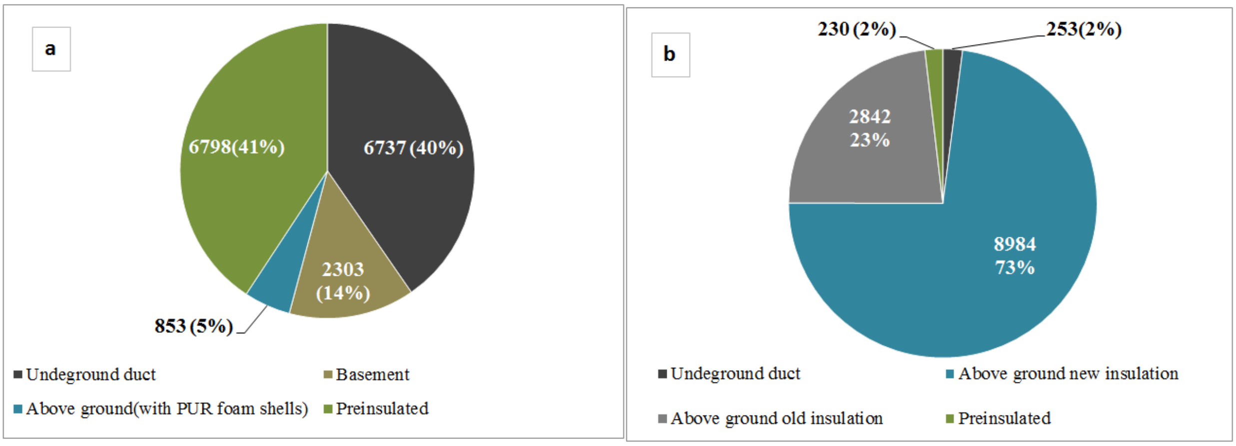

Fig. 2. The structure of and Maardu DH network pipes (a) and Maardu connection pipeline (b)

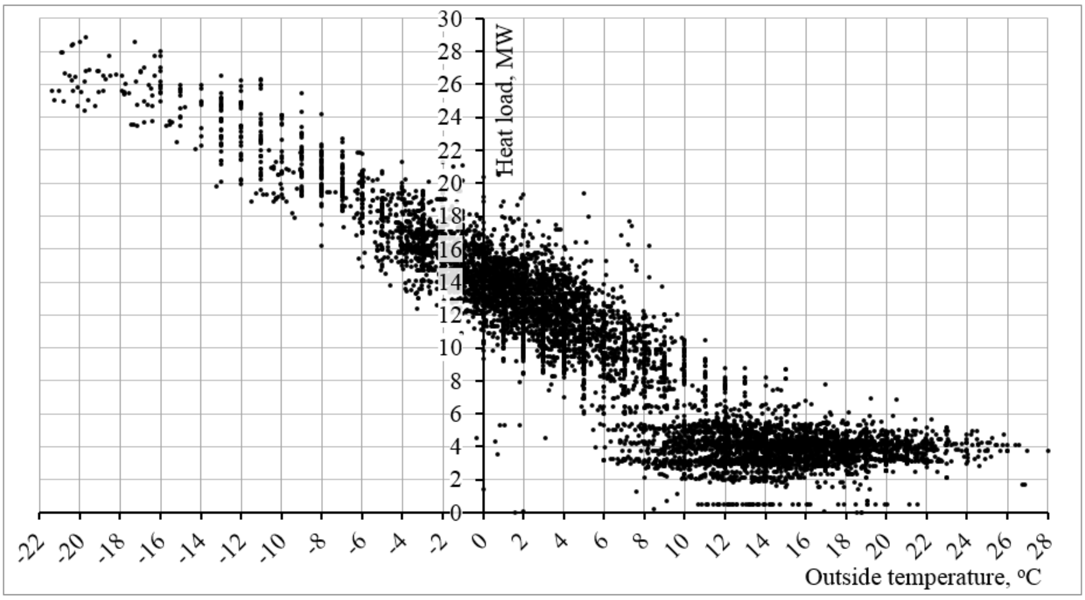

Fig. 3. Hourly heat load depending on outdoor temperature (in 2017)

According to previous evaluations, transmission pipes are oversized, providing the possibility to reduce the temperature and increase heat flow without extreme pressure surges in pipelines.

3. METHOD

The methodology includes an analysis of changes in system parameters in the event of supply temperature reduction. The scenarios for supply temperatures of 120, 115, 110, 105, 90, and 75 ºC have been compared with the baseline scenario for the supply temperature of 120 ºC.

Reducing supply temperature leads to an increase in pressure and flow rate, which affects other DH network components. That is why pressure (bar) and flow rate (t/h) were chosen as evaluation parameters for scenario comparison. As already mentioned, the main benefit of reducing the temperature is the reduction of heat loss, so annual heat loss (MWh) was selected as another comparison parameter.

As part of the analysis, we evaluated two strategies to reduce the DH network supply temperature. With Strategy A, it is planned to reduce the supply temperature by the same number of degrees for each case of outdoor temperature (Fig. 4). This strategy describes the case, where supply temperature is continuously reduced throughout the year. Only three scenarios have been analysed for Strategy A: scenarios for supply temperatures of 115 ºC, 110 ºC, and 105 ºC. If scenarios for 95 ºC and 75 ºC supply temperature are implemented as part of Strategy A, there will be too small difference between supply and return temperatures in the summer season.

Strategy B suggests that supply temperature is reduced only during the heating season (with the outside temperature below +5 ºC) linearly to the pre-defined maximum supply temperature (with the outside temperature -22 ºC) (Fig. 5). Supply temperature of +5 ºC and above is the same as for the baseline scenario (current operating regime). The main input parameters for both strategies are shown in Table 1.

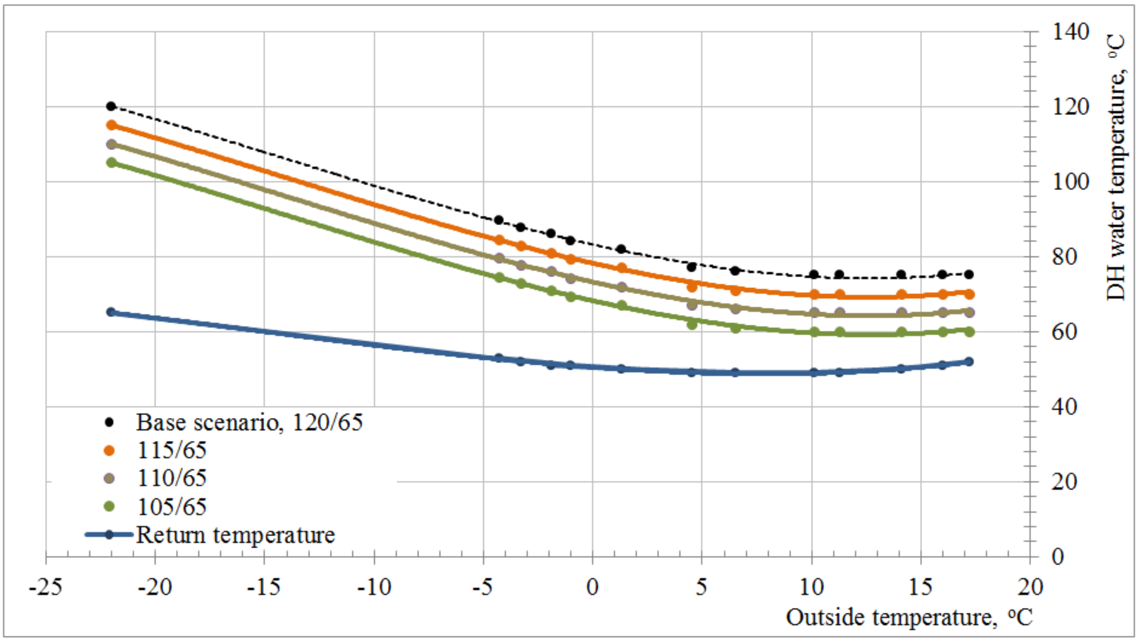

Fig. 4. Supply temperature reduction for Strategy A

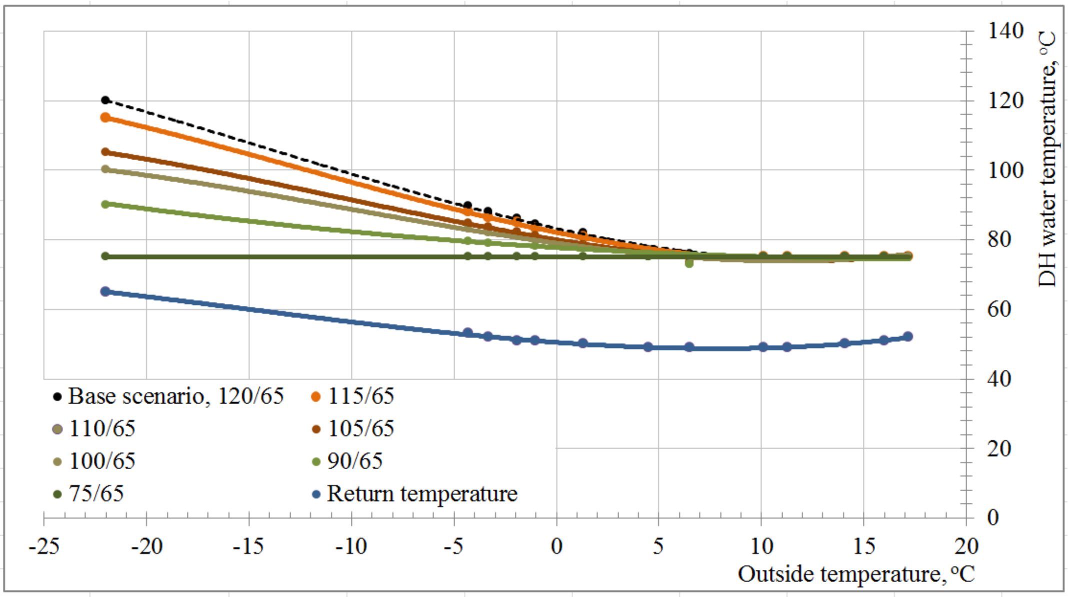

Fig. 5. Supply temperature reduction for Strategy B

Table 1. Input parameters for scenarios

Scenarios		**Baseline**	**1**	**2**	**3**	**4**	**5**
Supply/return temperature for min. outdoor temperature (-22ºC), ºC		120/65	115/65	110/65	105/65	90/65	75 /65
Strategy A	Maximum supply tºC	120	115	110	105	-	-
	Average supply tºC	79.8	74.8	69.8	64.8	-	-
	Minimum supply tºC	75	70	65	60		
Strategy B	Maximum supply tºC	120	115	110	105	90	75
	Average supply tºC	79.8	79.1	78.4	77.8	77.6	76
	Minimum supply tºC	75	75	75	75	75	75

Hydraulic and thermal calculations were performed to determine pressure and flow rate parameters for different supply temperatures. The model of the DH network was built using NetSim, a DH network modelling software by Vitec Energy. The model is based on actual data on production, consumption, and heating carrier temperatures; outdoor temperatures in recent years; actual GIS maps of the DH network. It should be noted that the model was calibrated in accordance with the actual operation data from 2017: heat sources load, consumers heat consumption, network heat losses, pressures, flow rates and temperatures

Flow rates and pressure were calculated for outdoor temperature varying from -22 to +15 ºC for both strategies. Annual system heat loss has also been calculated.

Reducing the supply temperature will lead to an increase in pressure and flow rate in the DH network. The key obstacles related to pressure and flow rate are associated with inlet valves, flow measurement equipment, and old pipes. Moreover, if the consumer’s internal system has a hydraulic connection to the DH networks, the heat is supplied directly through the heat carrier without a heat exchanger; there are also pressure limits. Limitations established by the specified conditions are given in Table 2.

Table 2. Limiting factors

Limiting factor	Limitation
Direct connection without heat exchangers	Maximum pressure is 7.5 bar
Old pipelines	Maximum pressure is 6 bar
Pumps	Maximum pressure is 7 bar

4. RESULTS

First, changes in pressure were calculated for different outdoor temperatures. The results for Strategy A are shown in Fig. 6. Limitations imposed by the old pipes and the open system are shown with bold black lines. As can be seen, supply temperature can only be reduced by 5 degrees without overcoming the limitations related with the old pipelines. If these limitations are removed through pipe renovation or replacement, it will be possible to reduce supply temperature by 10 ºC (down to 110 ºC). Flow rate limitations were calculated based on pressure limitations (Fig. 7), and the results show that with Strategy A it is possible to reduce supply temperature by 5 degrees.

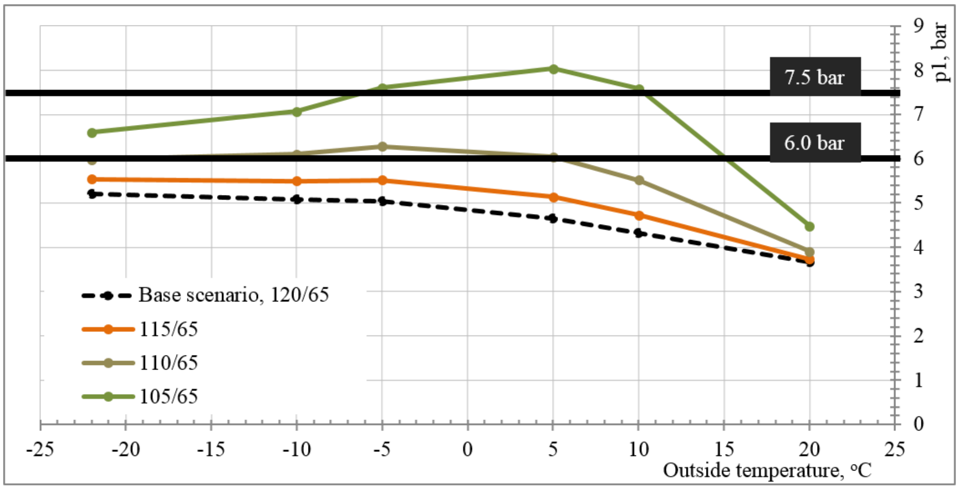

Fig. 6. Pressure calculations for Strategy A

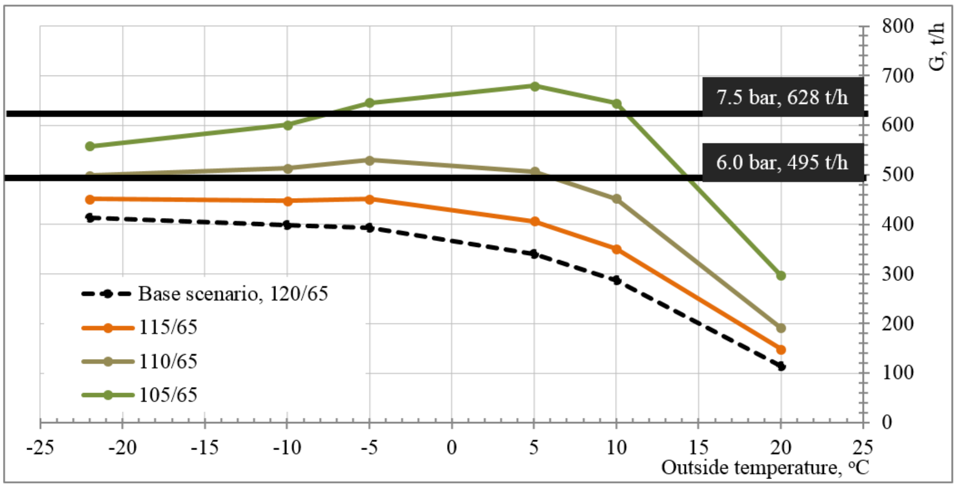

Fig. 7. Flow rate calculations for Strategy A

The same parameters were calculated for Strategy B. Considering pressure and flow rate limitations, with Strategy B it is possible to reduce supply temperature by 10 degrees (down to 110 ºC) (Fig. 8 and Fig. 9).

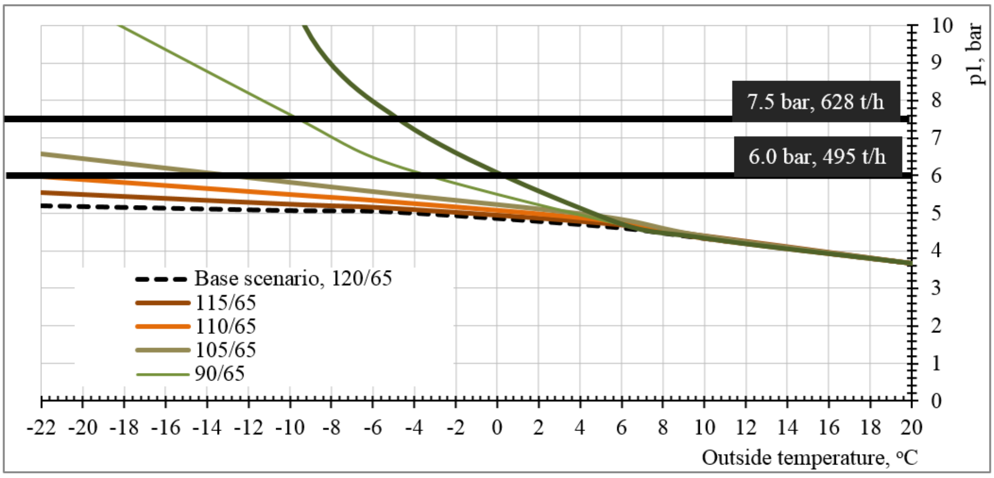

Fig. 8. Pressure calculations for Strategy B

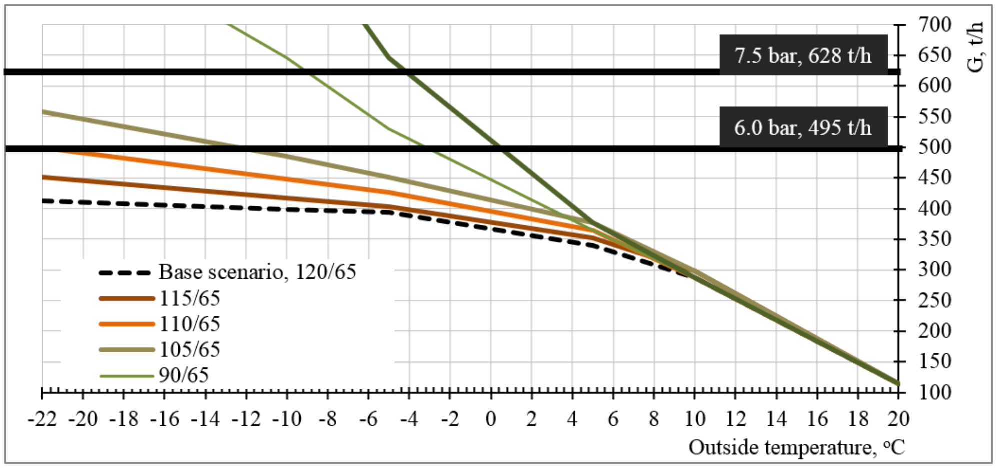

Fig. 9. Flow rate calculations for Strategy B

Based on the points where scenario lines cross the limitation line (old pipes, 6 ℃), two pressure limit-dependent temperature schedules were determined for Strategy A and Strategy B. These temperature schedules are shown in Fig. 10.

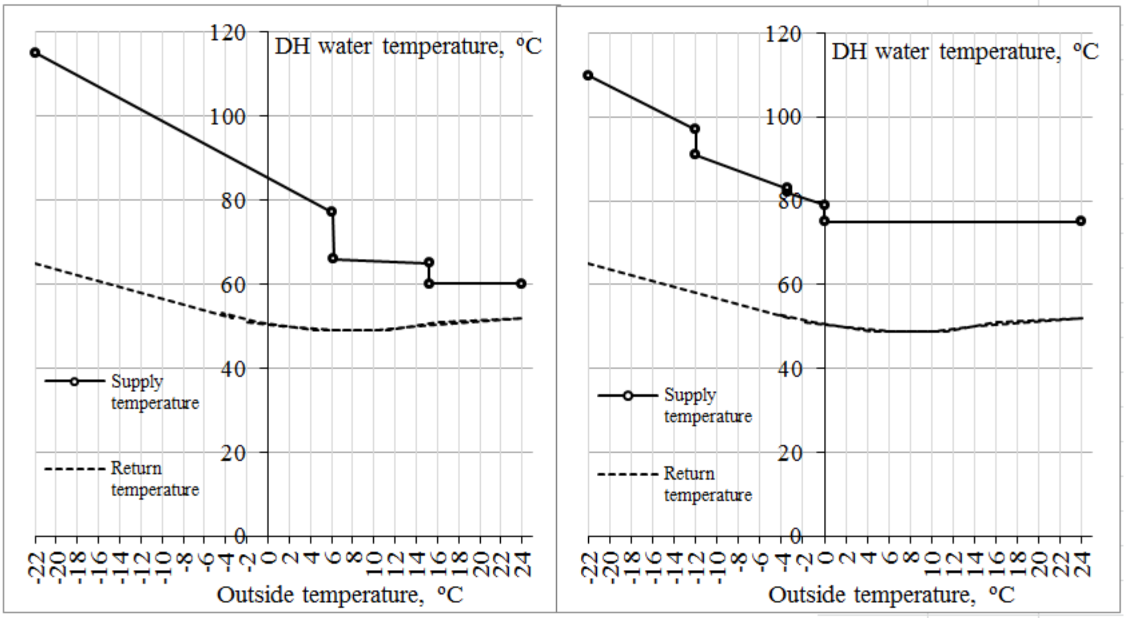

Fig. 10. Pressure limit-dependent temperature schedule for Maardu DH network

The proposed temperature schedule allows the DH system to operate at the lowest possible supply temperature, switching to a higher supply temperature only when it is needed.

The main advantage of reducing supply temperature is heat loss reduction. This parameter was calculated for all scenarios, as well as for the pressure limit-dependent temperature schedule, and is presented in Fig. 11.

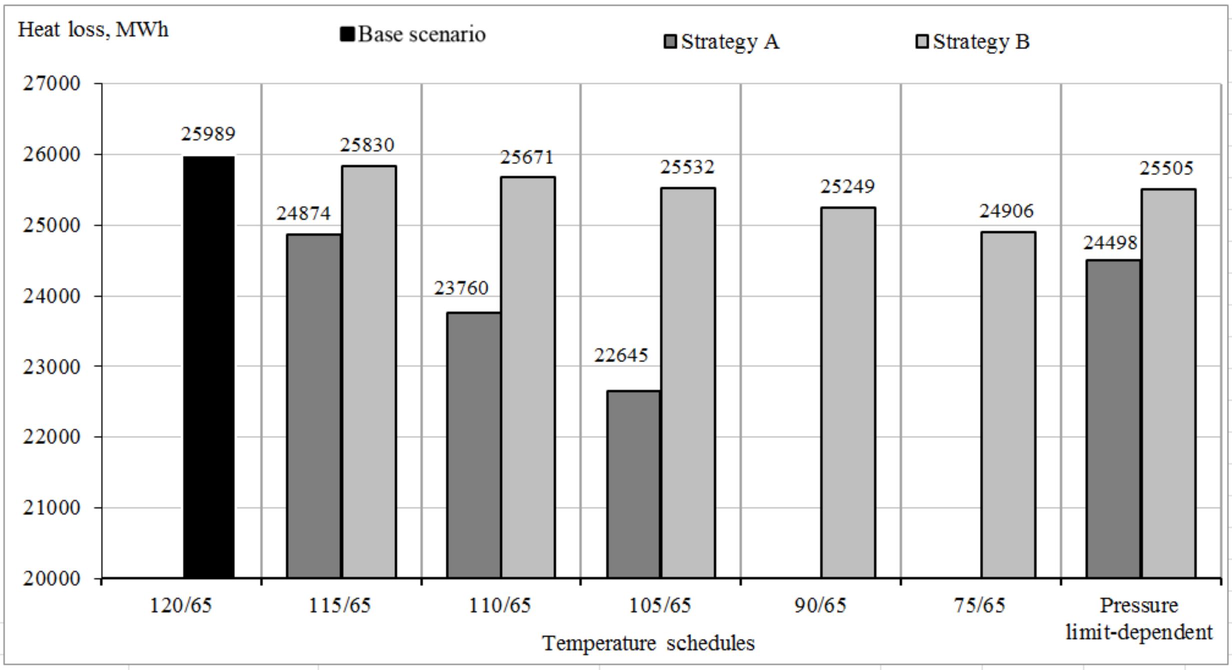

Fig. 11. Heat losses for supply temperature reduction strategies

Relative heat loss reduction is shown in Fig. 12. It can be seen that in the scenarios implemented in accordance with Strategy A, heat loss reduction is more significant compared to Strategy B.

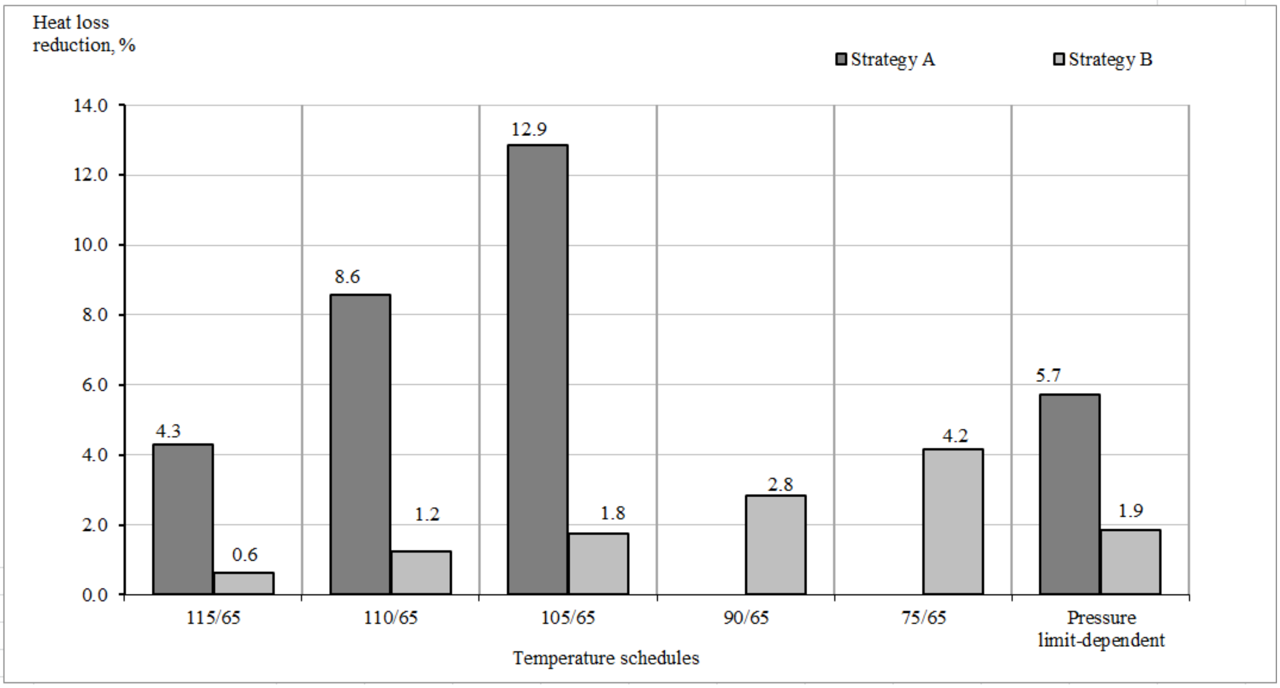

Fig. 12. Relative heat loss for supply temperature reduction strategies

If all limitations are taken into account, and supply temperature is reduced by 5 degrees using Strategy A, heat loss will be reduced by 4.3% (1115 MWh). Taking into account, that heat production cost is 35.6 eur, heat loss reduction saves up to 40 thousand EUR per year. Reducing the maximum supply temperature by 10 degrees to 110ºC, during the heating period (Strategy B), will reduce heat loss by only 1.2%, or 318 MWh, saving about 10 thousands EUR. In the case of the pressure limit-dependent temperature schedule based on Strategy A, heat loss will be reduced by 5.7% (1448 MWh). If the system operates in accordance with the pressure limit-dependent temperature schedule based on Strategy B, heat loss will be reduced by 1.9 % (484). MWh.

5. DISCUSSION AND CONCLUSIONS

Reducing heat carrier temperature provides advantages, such as heat loss reduction and the ability to utilise renewable energy sources. If the DH network is designed for a high-temperature heating carrier, it is possible to lower the temperature. One of the main obstacles associated with temperature reduction originates from consumer heating facilities that determine the return temperature. The DH operator cannot influence the return temperature, but even if the return temperature does not decrease, there is a possibility to reduce supply temperature. As part of this study, the possibility of reducing supply temperature was evaluated for the Maardu district heating network, which gets its heat supply from the Tallinn district heating system. Parameters, such as pressure, flow rate, and heat losses were calculated for various temperature schedules, taking into account the pressure and flow rate limitations established by consumer heating facilities, pipelines, etc. Two supply temperature strategies were analysed in this paper. Strategy A suggests reducing the supply temperature by the same number of degrees for each case of outdoor temperature (in parallel). Strategy B assumes that only the maximum supply temperature will be reduced, while the minimum supply temperature remains the same.

The main conclusion is that it is possible to reduce supply temperature from 120 to 115 ºC (up to 5 degrees throughout the year) using Strategy A, without any pressure and flow rate restrictions. This reduction will lead to heat savings of 1115 MWh (4.3% of the current 25989 MWh). With Strategy B, it is possible to reduce the supply temperature from 120 ºC to 110 ºC without any pressure and flow restrictions, leading to heat savings of 318 MWh (1.2% of the current 25989 MWh). Further reduction of temperature will be restricted by pressure limits: 6 bar for old pipes and 7.5 bar for consumer substations, in addition to heat exchanger capacity limits.

In addition, based on the calculations for both strategies, pressure limit-dependent temperature schedules were determined and heat losses for these schedules were calculated. Heat loss reduction for Strategy A is 5.7% (1491 MWh), and for Strategy B – 1.8% (484 MWh).

It should be noted that this study focused on the obstacles set by network components. There are significant flow rate obstructions associated with consumer substation heat exchangers that are designed for the baseline temperature schedule of 120/65. Usually, there is a 10-20% power reserve in the substation heat exchangers. This aspect requires further research.

AKNOWLEDGEMENT

This work was supported by Estonian Ministry of Education and Research (base funding project B55) and TalTech University R&D project SS429.

REFERENCES

[1] A. Lake, B. Rezaie, and S. Beyerlein, “Review of district heating and cooling systems for a sustainable future,” *Renew. Sustain. Energy Rev.*, Vol. 67, pp. 417–425, 2017.

[2] S. Werner, “International review of district heating and cooling,” *Energy*, pp. 1–15, 2017.

[3] I. Dimoulkas and M. Amelin, “Monte Carlo simulation of district heating system short-term

operation in electricity markets," *Energetika*, No. 3, pp. 93–104, 2017.
[4] H. Pieper, T. Ommen, F. Buhler, B. Lava Paaske, B. Elmegaard, and W. Brix Markussen, "Allocation of investment costs for large-scale heat pumps supplying district heating," *Energy Procedia*, Vol. 147, pp. 358–367, 2018.
[5] I. Pakere, D. Purina, D. Blumberga, and A. Bolonina, "Evaluation of Thermal Energy Storage Capacity by Heat Load Analyses," *Energy Procedia*, Vol. 95, pp. 377–384, 2016.
[6] H. Lund, S. Werner, R. Wiltshire, S. Svendsen, J. E. Thorsen, F. Hvelplund, and B. V. Mathiesen, "4th Generation District Heating (4GDH). Integrating smart thermal grids into future sustainable energy systems.," *Energy*, Vol. 68, pp. 1–11, 2014.
[7] J. I. B.Elmegaard, T.S.Ommen, M.Markussen, "Integration of space heating and hot water supply in low temperature district heating," *Energy Build.*, Vol. 124, pp. 255–264, 2016.
[8] A. Dalla Rosa, H. Li, and S. Svendsen, "Method for optimal design of pipes for low-energy district heating, with focus on heat losses," *Energy*, Vol. 36, No. 5, pp. 2407–2418, 2011.
[9] N. Nord, E. K. Løve Nielsen, H. Kauko, and T. Tereshchenko, "Challenges and potentials for low-temperature district heating implementation in Norway," *Energy*, Vol. 151, pp. 889–902, 2018.
[10] M. Rämä and K. Sipilä, "Transition to low temperature distribution in existing systems," *Energy Procedia*, Vol. 116, pp. 58–68, 2017.
[11] S. Paiho and F. Reda, "Towards next generation district heating in Finland," *Renew. Sustain. Energy Rev.*, Vol. 65, pp. 915–924, 2016.
[12] F. Neirotti, M. Noussan, S. Riverso, and G. Manganini, "Analysis of Different Strategies for Lowering the Operation Temperature in Existing District Heating Networks," *Energies*, Vol. 12, No. 2, p. 321, 2019.
[13] A. Hlebnikov and A. Siirde, "The major characteristic parameters of the Estonian district heating networks and their efficiency increasing potential," *Energetika*, No. 4, pp. 67–74, 2008.
[14] A. Hlebnikov, A. Volkova, O. Džuba, A. Poobus, and U. Kask, "Damages of the Tallinn district heating networks and indicative parameters for an estimation of the networks general condition," *Environ. Clim. Technol.*, Vol. 5, pp. 49–55, 2010.
[15] V. Masatin, A. Volkova, A. Hlebnikov, and E. Latosov, "Improvement of District Heating Network Energy Efficiency by Pipe Insulation Renovation with PUR Foam Shells," in *Energy Procedia*, 2017, Vol. 113.
[16] E. Latõšov, A. Volkova, A. Hlebnikov, and A. Siirde, "Technical improvement potential of large district heating network: Application to the Case of Tallinn, Estonia," in *Energy Procedia*, 2018.

CYSENI 2019, May 23-24, Kaunas, Lithuania
ISSN 1822-7554, www.cyseni.com

EXERGOECONOMIC ANALYSIS OF AN AIR SOURCE HEAT PUMP FOR SPACE HEATING

V. Voloshchuk, M. Polishchuk, I. Polishchuk
National Technical University of Ukraine "Igor Sikorsky Kyiv Polytechnic Institute"
Politehnichna str. 56, 03056 Kyiv – Ukraine
Email: Vl.Volodya@gmail.com

A. Nikiforovich
Chernihiv National University of Technology
Shevchenka str. 95, 14027, Cernihiv – Ukraine

ABSTRACT

In addition to conventional exergoeconomic evaluation, advanced exergoeconomic analysis considers the interactions among components of the energy-conversion system and the real potential for improving each system component. The aim of the paper is to demonstrate the application of the advanced exergetic and economic analysis of an air source heat pump providing space heating and to find possible ways of improving this energy-conversion system from the thermodynamic and economic viewpoints. In order to determine thermodynamic parameters of the refrigeration vapor compresion cycle in different operating modes during a heating season, a mathematical model is used which is based on quasi-steady state approach. The analysis includes splitting the exergy destruction costs and investment costs within each component of a heat pump into unavoidable, avoidable, endogenous and exogenous parts. Taking into account values of avoidable costs, the heat pump components can be sorted in descending order as: compressor, evaporator, condenser and throttling valve. Almost all these total avoidable costs, except for the throttling valve, are endogenous i.e. are associated with the internal operating conditions of the mentioned components. For the purpose of decreasing total costs of the system the thermodynamic efficiency of the evaporator and condenser should be improved. This is confirmed with the modified exergoeconomic factor based on avoidable endogenous costs. On the other hand the value of the same modified exergoeconomic factor for the compressor illustrates that the capital investments of this component should be reduced. This is possible due to increasing irreversibilities within the compressor. The negative value of exogenous avoidable part of the investments cost for the compressor shows that decreasing thermodynamic inefficiencies within the evaporator and condenser can make the total cost for the compressor a little lower.

Keywords: advanced exergetic and exergoeconomic analysis; air source heat pump; space heating

1. INTRODUCTION

Combination of thermodynamics with economics (exergoeconomics) is a more powerful and convenient tool for investigation and improvement of energy conversion systems without the need of additional analysis and iterations. The exergoeconomics assigns monetary costs (associated with capital investment, operating maintenance and exergy destructions) to the interactions that a system experiences with its surroundings and to the sources of thermodynamic inefficiencies within it [1-6]. The exergoeconomic analysis identifies the relative cost importance of each component of the system and options for improving the overall cost effectiveness of it – i.e. reducing the cost of the product which is generated by energy conversion systems (electricity, heat, cold, etc.).

The conclusions provided from the exergoeconomic assessment can be substantially enhanced if the investment costs associated with system components and costs of exergy destructions within these components are split into unavoidable/avoidable and endogenous/exogenous parts. The evaluation based on these procedures is called as advanced exergoeconomic analysis which has been proposed and developed at the Institute for Energy Engineering of Technische Universität (TU) Berlin [1-5, 7].

According to the current knowledge of the author, advanced exergoeconomic analysis has been applied mostly to refrigeration machines and industrial heat pump systems where only single modes (design or nominal ones) were investigated it [1-6]. A distinguish feature of the heat pump systems providing thermal comfort in buildings is variation of operational regimes. This variation is mainly affected by climate and weather conditions (temperatures, solar radiation, wind velocity, pressure, humidity, etc.). All those factors change randomly over time. This feature should be taken into account when applying exergy-based methods to heat pump systems providing space heating [8].

So, the scope of the paper is to apply exergoeconomic analyses (both conventional and advanced ones) to an air-source heat pump providing space heating when operational modes vary within a heating season. The obtained results are used for finding possible ways of improving this energy-conversion system from the thermodynamic and economic viewpoints. This is continuation of an ongoing research dedicated to application of exergy-based analysis for heat pump units [8, 9].

2. METHODOLOGY

The methodology of advanced exergoeconomic analysis splits the total exergy destruction and total investments costs in each system component into endogenous/exogenous parts ($\dot{E}_{D,k} = \dot{E}_{D,k}^{EN} + \dot{E}_{D,k}^{EX}$ and $\dot{Z}_k = \dot{Z}_k^{EN} + \dot{Z}_k^{EX}$), unavoidable/avoidable parts ($\dot{E}_{D,k} = \dot{E}_{D,k}^{AV} + \dot{E}_{D,k}^{UN}$ and $\dot{Z}_{D,k} = \dot{Z}_k^{AV} + \dot{Z}_k^{UN}$), and combined to identify options for improving the system ($\dot{E}_{D,k} = \dot{E}_{D,k}^{UN,EN} + \dot{E}_{D,k}^{UN,EX} + \dot{E}_{D,k}^{AV,EN} + \dot{E}_{D,k}^{AV,EX}$ and $\dot{Z}_{D,k} = \dot{Z}_{D,k}^{UN,EN} + \dot{Z}_{D,k}^{UN,EX} + \dot{Z}_{D,k}^{AV,EN} + \dot{Z}_{D,k}^{AV,EX}$) [1-4, 10, 11].

During the improvement procedure only the avoidable part of exergy destruction and investments cost ($\dot{E}_{D,k}^{AV}$, $\dot{E}_{D,k}^{AV,EN}$, $\dot{E}_{D,k}^{AV,EX}$, $\dot{Z}_k^{AV}$, $\dot{Z}_{D,k}^{AV,EN}$, $\dot{Z}_{D,k}^{AV,EX}$) should be considered as having real potential for system improvement.

To split exergy destructions and investment costs into the above-mentioned parts the thermodynamic-cycle-based approach can be used [1, 10, 11] taking into account that the product of the heat pump in all analysed cycles remains unchanged.

The sum of cost rates associated with investment costs consists of two contributions: costs due to capital investments ($\dot{Z}_k^{CI}$) and operating and maintanance expenses ($\dot{Z}_k^{OM}$) [1]

$$\dot{Z}_k = \dot{Z}_k^{CI} + \dot{Z}_k^{OM}. \tag{1}$$

To figure out these cost rates, the capital recovery factor should be calculated and yearly time of operation for the system, cost of the purchased equipment (PEC) and the factor of the operating and maintenance cost should be stated.

For estimation of the equipment costs the following functions based and adapted from [1] are used

$$PEC_{CM} = \frac{k_{CM} \cdot \dot{m}_{CM}}{\eta_{CM}^{UN} - \eta_{CM}} \left(\frac{p_2}{p_1} \right) ln \left(\frac{p_2}{p_1} \right) \text{ – for compressor} \tag{2}$$

$$PEC_{CD} = k_{CD} \left(A_{CD} \right)^{0.6} \text{ – for condenser} \tag{3}$$

$$PEC_{EV} = k_{EV} \left(A_{EV} \right)^{0.6} \text{ – for evaporator} \tag{4}$$

where k_{CM}, k_{CD}, k_{EV} are constants; $\dot{m}_{CM}$ is mass flow rate of the working fluid through the compressor; p_2 / p_1 - pressure ratio in the compressor; η_{CM} and η_{CM}^{UN} are isentropic efficiencies of the compressor in real cycle and corresponding to unavoidable exergy destruction in the compressor respectively (the latter is assumed to be equal to 96 %); A_{CD} and A_{EV} are areas of heat-transfer surfaces of the condenser and evaporator respectively. All these values are estimated for the design operating conditions (nominal mode) of the system.

The purchased equipment costs for the throttling valve are neglected in the analysis as being vary small [2, 3].

In every case the cost functions and constants can be different compared to ones proposed in Eq. (2)-(4) [1, 12, 13].

The total costs are calculated as sum of costs due to investment and exergy destruction, $\dot{Z}_k + c_{F,k} \cdot \dot{E}_{D,k} = \dot{Z}_k + \dot{C}_{D,k}$, where $c_{F,k}$ presents the cost per unit of exergy for fuel of the k-th component and $\dot{C}_{D,k}$ is cost rate associated with the exergy destruction within the k-th component. The values of $c_{F,k}$ are estimated by specific exergy costing method (SPECO-method)) using cost balance and auxiliary equations for the components of the investigated heat pump [5].

The contribution of the investments cost, $\dot{C}_{D,k}$, to the total costs associated with investments and exergy destruction in conventional exergoeconomic assessment is expressed by the exergoeconomic factor [1-3]:

$$f_k = \frac{\dot{Z}_k}{\dot{Z}_k + c_{F,k} \cdot \dot{E}_{D,k}}. \tag{5}$$

To better characterize the component being considered the exergoeconomic factor of the conventional exergoeconomic analysis can be adjusted by the help of the modified exergeoconomic factor ($f_k^{AV,EN}$) calculated exclusively on the avoidable endogenous costs as follows [1, 4]:

$$f_k^{AV,EN} = \frac{\dot{Z}_k^{AV,EN}}{\dot{Z}_k^{AV,EN} + c_{F,k} \cdot \dot{E}_{D,k}^{AV,EN}}. \tag{6}$$

The analysis is performed for a typical Ukrainian house. The dwelling has two floors with a gross floor area of 170 m^2 and a volume of 470 m^3. The weighted average insulation value of non-glazed external surfaces is 0.5 $W/(m^2 \cdot K)$. U-value of windows including frames is 1.67 $W/(m^2 \cdot K)$. Internal heat gains are defined with a constant value of 5 W/m^2. Setpoint for the indoor temperature is 18 ^oC. The fraction of east and west oriented glazing is 30%, of the south one – 50%, of the north one – 20%. Natural ventilation is used in the dwelling. The design heating capacity of the house is 25 kW. Hydronic system is used for space heating. The heat pump is a basic heater covering 12 kW of heating demand in the design mode and uses outside air as a low temperature heat source. R134a is chosen as a working fluid in the heat pump.

In the design operating conditions (nominal mode) of the heat pump the following parameter values are set: the low temperature heat source medium is cooled in the evaporator from -10 ^oC to -15 ^oC; the minimal temperature differences in the evaporator is 12 K and in the condenser is equal to 5 K. The calculated value of the real isentropic efficiency of the compressor in the nominal mode is equal to 70%. For evaluating unavoidable exergy destructions in nominal mode the following parameter values are assumed: the unavoidable temperature differences in the evaporator and the condenser are equal to 3 K and 1 K respectively. The unavoidable compressor efficiency is equal to 96%. For creating the theoretical cycle of the heat pump the following assumptions are used: the minimal temperature differences in the evaporator and the condenser are equal to 0 K; the efficiency of the working fluid compression is equal to 100%; the throttling process is replaced by an ideal expansion process [5].

In order to determine thermodynamic parameters of the refrigeration vapor compresion cycle in off-design modes, which is typical for such kind of heat pumps, the mathematical model has been used. The model is based on quasi-steady state approach [14]. A set of nonlinear equations, involving heat, mass balances, heat transfer and equations for calculation of thermodynamic properties of working fluids, has been utilized. The equations, solved simultaneously with a gradient numerical method, has been established to describe the behaviour of each component and of the system as a whole. During the simulation the temperature of heat source (outdoor air) in off-design modes varies in a range from +10 ^oC to -16 ^oC.

Daily weather data within a heating season for the city of Rivne located in the western part of Ukraine are used for the analyses. The data includes daily mean outdoor temperature and wind velocity. Cumulative daily solar radiation is also included in the investigations. So, 24-hour time steps are assumed for quasi-steady state modelling.

A heating season for the city of Rivne usually lasts for 180 days. The mean outdoor temperature of the heating season is equal to 0.1 °C. Heating degree days are equal to 3300 °C·day.

For exergetic and exergoeconomic assesment of the heat pump providing space heating it is proposed to take into account annual (seasonal) values (denoted with superscript yr). Within a heating season the investigated parameters are different for different operational modes. And it is not sufficient to analyze only single operational mode (for example, design mode).

3. RESULTS AND DISCUSSIONS

The results of advanced exergetic analysis of the investigated vapor-compression heat pump are presented in Table 1.

Using results obtained from the conventional (without splitting the exergy destruction) exergetic analysis (see the first column of the Table 1), the following conclusions can be formulated. The most important component from the thermodynamic viewpoint is the compressor ($E_{D,CM}^{yr} = 1752$ kW·hr/year). The throttling valve has the second position ($E_{D,TV}^{yr} = 1632$ kW·hr/year). The third position is associated with the evaporator ($E_{D,EV}^{yr} = 1144$ kW·hr/year). And the condenser is the last important component from the thermodynamic viewpoint ($E_{D,CD}^{yr} = 726$ kW·hr/year). So, the components should be improved in the following order: compressor, throttling valve, evaporator and condenser.

Table 1. Advanced exergetic analysis of the vapor-compression heat pump (splitting the exergy destructions)

Component	*Unit*	$E_{D,k}^{yr}$	$E_{D,k}^{UN,yr}$	$E_{D,k}^{AV,yr}$	$E_{D,k}^{EN,yr}$	$E_{D,k}^{EX,yr}$	$E_{D,k}^{UN,yr}$		$E_{D,k}^{AV,yr}$	
							$E_{D,k}^{UN,EN,yr}$	$E_{D,k}^{UN,EX,yr}$	$E_{D,k}^{AV,EN,yr}$	$E_{D,k}^{AV,EX,yr}$
Compressor	kW·hr/yr	1752	469	1282	834	918	385	84	448	834
	%	100	27	73	48	52	22	5	26	48
Condenser	kW·hr/yr	726	409	317	630	96	396	13	234	83
	%	100	56	44	87	13	55	2	32	11
Throtling valve	kW·hr/yr	1632	1108	524	968	664	968	140	0	524
	%	100	68	32	59	41	59	9	0	32
Evaporator	kW·hr/yr	1144	637	507	1267	-123	702	-65	565	-58
	%	100	56	44	111	-11	61	-6	49	-5

These results are misleading to some extent. Among others it can be concluded that in order to reduce the exergy destruction within the compressor and the throttling valve an investigator should try improve these component first of all. But thermodynamic inefficiency in the compressor increases when the pressure ratio in it is also increased which can take place due to bigger temperature differences in the condenser and evaporator. So, exergy destruction within the compressor can be eliminated with the help of thermodynamic improving condenser and evaporator but not the compressor itself. The same conclusion is refferd to the throtling valve. Moreover the throttling process is completely irreversible and there are no ways of improving this process with the help of decreasing irreversibilities in it.

Taking into account the above-mentioned information we need more precise, detailed and additional information about irreversibilities within the system. This can be provided by advanced exergy-based analysis [1-4, 6, 10, 11].

As can be seen from the Table 1 it is possible to decrease 73%, 44%, 32% and 44% of the total exergy destruction in the compressor, condenser, throtling valve and evaporator respectively.

The throtling valve and the evaporator have almost the same values of exergy destruction which can be really removed ($E_{D,TV}^{AV,yr} = 524$ kW·hr/year and $E_{D,EV}^{AV,yr} = 507$ kW·hr/year).

The results obtained from the advanced exergetic analysis indicate that the endogenous avoidable exergy destruction in the throttling valve is zero. This means that the exergy destruction within this component can be reduced through changes in the remaining components or in the structure of the overall system. Only 448 kW·hr/year of exergy destruction in the compressor can be avoided by improving this component. The endogenous avoidable exergy destructions in the evaporator and condenser are equal 565 kW·hr/year and 234 kW·hr/year respectivetly).

The biggest part of exergy destruction that can be avoided in the compressor is exogenous, i.e. can be eliminated through changes in the remaining components or in the structure of the overall system, and is equal $E_{D,CM}^{AV,EX,yr} = 834$ kW·hr/year. All thermodynamic inefficiency which can be avoided in the throttling valve is due to the remaining components or in the structure of the analyzed heat pump. Very small values of avoided exogenous exergy destruction belong to the condenser and the evaporator. Yet, interesting information is provided by the avoidable exogenous exergy destruction within the evaporator. It is egative $E_{D,EV}^{AV,EX,yr} = -58$ kW·hr/year. This means that the exergy destruction within this component can be decreased by increasing irreversibilities within the other components of the analyzed heat pump. The similar information is obtained in [8, 10, 11].

The results from splitting the investments cost are presented in Table 2. The investments cost of the throtling valve are neglected because of the small value. The unavoidable investment costs, $Z_k^{UN,yr}$, of the components are higher than their avoidable ones, $Z_k^{AV,yr}$, and constitute 65%, 81% and 70% for the compressor, condenser and evaporator respectively. Meanwhile, the avoidable investment costs indicate that priority should be given to the compressor. The highest values of the investments cost in the components of the heat pump are endogenous, $Z_k^{EN,yr}$, which shows that component interactions are not of high priority as their internal operation. The results presented in Table 2 show that the largest part of the avoidable endogenous investment cost, $Z_k^{AV,EN,yr}$, is associated with the compressor and is equal to 689 Euro/year. The highest value of the avoidable exogenous investment cost (but with negative value), $Z_k^{AV,EX,yr}$, is also found for the compressor (-63 Euro/year). The latter means that it is possible to decrease to some value the investment costs of the compressor due to decrease exergy destruction within the other components.

Table 2. Splitting the investment costs for components of the vapor-compression heat pump

Component	*Unit*	Z_k^{yr}	$Z_k^{UN,yr}$	$Z_k^{AV,yr}$	$Z_k^{EN,yr}$	$Z_k^{EX,yr}$	$Z_k^{UN,yr}$		$Z_k^{AV,yr}$	
							$Z_k^{UN,EN,yr}$	$Z_k^{UN,EX,yr}$	$Z_k^{AV,EN,yr}$	$Z_k^{AV,EX,yr}$
Compressor	Euro/yr	1771	1145	626	1308	463	620	526	689	-63
	%	100	65	35	74	26	35	30	39	-4
Condenser	Euro/yr	137	111	27	125	12	96	15	29	-2
	%	100	81	19	91	9	70	11	21	-2
Evaporator	Euro/yr	141	99	41	165	-24	136	-37	29	13
	%	100	70	30	117	-17	97	-26	21	9

The results of splitting the total costs, $Z_k^{yr} + c_{F,k} \cdot E_{D,k}^{yr} = Z_k^{yr} + C_{D,k}^{yr}$, for components of the investigated heat pump are presented in Table 3. As seen the compressor presents the highest total costs (1832 Euro/year). The total costs for the condenser, throtling valve and evaporator are characterized with lower values (356, 359 and 910 Euro/year respectively). Table 3 shows that for the system analyzed here, the compressor and the evaporator are the components with the highest potential for reducing the total costs of the overall system. This is due to the relatively high avoidable total costs, $Z_k^{AV,yr} + c_{F,k} \cdot E_{D,k}^{AV,yr}$, associated with both components (671 and 382 Euro/year respectively). It is found that for the condenser and the throttling valve the avoidable total costs are lower compared with the compressor or the evaporator and are equal to 122 and 115 Euro/year respectively. Exogenous parts of the total costs, $Z_k^{EX,yr} + c_{F,k} \cdot E_{D,k}^{EX,yr}$ or $Z_k^{AV,EX,yr} + c_{F,k} \cdot E_{D,k}^{AV,EX,yr}$, are not high for the components of the analyzed heat pump. But it is observed that for the compressor exogenous parts of the total costs which can be avoided is negative.

Table 3. Splitting the total costs for components of the vapor-compression heat pump

Component	*Unit*	$Z_k^{yr} + C_{D,k}^{yr}$	$Z_k^{UN,yr} + C_{D,k}^{UN,yr}$	$Z_k^{AV,yr} + C_{D,k}^{AV,yr}$	$Z_k^{EN,yr} + C_{D,k}^{EN,yr}$	$Z_k^{EX,yr} + C_{D,k}^{EX,yr}$	$Z_k^{UN,yr} + C_{D,k}^{UN,yr}$		$Z_k^{AV,yr} + C_{D,k}^{AV,yr}$	
							$Z_k^{UN,EN,yr} + C_{D,k}^{UN,EN,yr}$	$Z_k^{UN,EX,yr} + C_{D,k}^{UN,EX,yr}$	$Z_k^{AV,EN,yr} + C_{D,k}^{AV,EN,yr}$	$Z_k^{AV,EX,yr} + C_{D,k}^{AV,EX,yr}$
Compressor	Euro/yr	1832	1161	671	1337	495	633	529	705	-34
	%	100	63	37	73	27	35	29	38	-2
Condenser	Euro/yr	356	234	122	315	41	125	19	99	23
	%	100	66	34	88	12	35	5	28	6
Throttling valve	Euro/yr	359	244	115	213	146	213	31	0	115
	%	100	68	32	59	41	59	9	0	32
Evaporator	Euro/yr	910	527	382	1017	-107	608	-81	409	-26
	%	100	58	42	112	-12	67	-9	45	-3

Figure 1 presents values of the modified exergoeconomic factor, $f_k^{AV,EN}$, based on avoidable endogenous costs. The parameter of the throtling valve $f_{TV}^{AV,EN}$ is not taken into account because of investments costs being negligible.

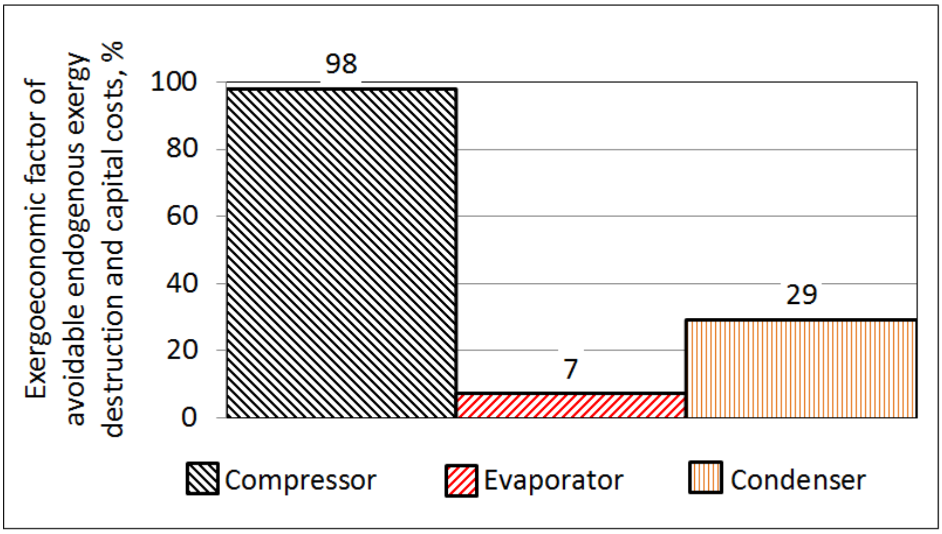

Fig. 1. Values of the modified exergoeconomic factor, $f_k^{AV,EN}$, based on avoidable endogenous costs

As seen from the Fig. 1, the values of the $f_k^{AV,EN}$ for the evaporator and condenser mean that the cost effectiveness of the heat pump might be improved by improvement of the exergy efficiency of these components (at the expense of increasing investment costs). Moreover, it should be mentioned that inreasing thermodynamic efficiencies within the evaporator and condenser can make the total cost for the compressor lower due to decrease of the investments cost of this component (negative value of exogenous avoidable part of the investments cost illustrate this in Table 2).

Additional information concerning this case can be gained after additional splitting the exogenous avoidable total cost for the compressor which is planned to do in further investigations. The high value of the same modified exergoeconomic factor for the compressor means that reducing the investment cost for this component (at the expense of its efficiency) can substantially decrease the total cost of the investigated heat pump.

The validity of these conclusions will be verified in further investigations. It is also important to include combination of exergy and ecological evaluation.

4. CONCLUSIONS

1. The advanced exergy-based evaluation provides information about location, magnitude, causes of avoidable inefficiencies and avoidable costs of thermodynamic inefficiencies in an energy-conversion system which is valuable for system improvement.
2. The advanced exergy estimation has shown that in the investigated air-source heat pump for space heating the compressor, the throttling valve and the evaporator are the components causing the biggest values of exergy destructions (1282, 524 and 507 kW·hr/year respectively) which can be removed. The avoidable exergy destructions of the compressor and the throttling valve mostly depend on irreversebilies within other components. On the contrary the avoidable exergy destruction in the evaporator is caused by thermodynamic efficiency within this component.
3. The biggest part of the heat pump avoidable investment expenditures are due to the compressor (626 Euro/year). This cost can be decreased substantially with the help of increasing thermodynamic inefficiencies within the compressor itself. But, according to the results obtained it is possible to make lower the investment cost of the compressor due to decrease of thermodynamic inefficiencies within the other components (negative value of exogenous investment cost demonstrates this).
4. According to the results received, the compressor and the evaporator are the components with the highest potential for reducing the total costs of the overall system. This potential is due to the relatively high avoidable total costs, $Z_k^{AV,yr} + c_{F,k} \cdot E_{D,k}^{AV,yr}$, associated with both components (671 and 382 Euro/year respectively). Almost all these costs are endogenous e.i. caused by the same components. For the condenser and the throttling valve the avoidable total costs are lower compared with the compressor or the evaporator and are equal to 122 and 115 Euro/year respectively.
5. The values of the modified exergoeconomic factor, $f_k^{AV,EN}$, based on avoidable endogenous costs for the evaporator and condenser indicate that the cost effectiveness of the heat pump might be improved by improvement of the exergy efficiency of these components. The high value of the same modified exergoeconomic factor for the compressor means that reducing the investment cost for this component can decrease the total cost of the investigated heat pump. Meanwhile, further splitting exogenous avoidable total cost for the compressor can provide information concerning how increasing thermodynamic efficiencies within the evaporator and condenser can make the total cost for the compressor lower due to decrease of the investments cost of this component (negative value of exogenous avoidable part of the investment cost illustrate this).

5. ABBREVIATIONS

A	heat transfer area (m^2);
c	cost per unit of exergy (€·kWh^{-1});
C	cost associated with an exergy stream (€);
E	exergy (kW·h);
f	exergoeconomic factor (%);
m	mass (kg);

p	pressure (Pa);
τ	time step (day);
Z	cost associated with capital investment (€).

Greek symbols

η	isentropic efficiency (-).

Subscripts and superscripts

·	time rate;
AV	avoidable;
UN	unavoidable;
EX	exogenous;
EN	endogenous;
UN, EN	unavoidable endogenous;
UN, EX	unavoidable exogenous;
AV, EN	avoidable endogenous;
AV, EX	avoidable exogenous;
D	exergy destruction;
F	exergy of fuel;
k	k-th component;
yr	annual.

Abbreviations

CM	compressor;
CD	condenser;
PEC	purchase equipment costs;
CI	capital investment;
OM	operating and maintanance expenses;
EV	evaporator;
TV	throttling valve.

REFERENCES

1. TSATSARONIS, G., MOROSUK T. Advanced exergy-based methods used to understand and improve energy-conversion systems. CPOTE-2016. Proceedings of the 4th International Conference on Contemporary Problems of Thermal Engineering. Gliwice – Katowice: The Silesian University of Technology Institute of Thermal Technology. 2016 September 14-16.
2. TSATSARONIS, G. Exergetic and Economic Performance – Strategies for Optimizing Energy Systems. The LowEx Symposium. Program and Proceedings, Kassel, Germany, October 28-29, 2009. Kassel, Germany, 2009. – P. 18-27.
3. TSATSARONIS, G. Minimization of Costs and Environmental Impact Using Exergy-Based Methods. The Future for Sustainable Built Environments with High Performance Energy Systems. Program and Proceedings, Munich, Germany, October 19-21, 2010. – P. 185-198.
4. TSATSARONIS, G., MOROSUK T. Exergoeconomic evaluation of refrigeration machines based on avoidable endogenous and exogenous costs. The 20th International Conference on Efficiency, Cost, Optimization, Simulation and Environmental Impact of Energy Systems. Program and Proceedings, Vol 3, Padova, Italy, June 25–28, 2007. – P .1459-1467.
5. MOROSUK, T. Elements of exergoeconomics for the analysis of compressor heat pumps. VI Minsk International Seminar “Heat Pipes, Heat Pumps, Refrigerators”. Program and Proceedings, Minsk, Belarus, September 12-15, 2005 – P. 403-409.
6. ERBAY, Z., HEPBASLI, A. Advanced exergoeconomic evaluation of a heat pump food dryer Biosystems engineering. – 2014. – Vol. 124. – P. 29-39.

7. TSATSARONIS G. Strengths and limitations of exergy analysis. Proceedings of the NATO Advanced Study Institute on Thermodynamics and the Optimization of Complex Energy Systems. Neptun, Romania. 1998 July 13-24: Kluwer Academic Publishers. p. 93-100.
8. VOLOSHCHUK V. Advanced exergetic analysis of a heat pump providing space heating in built environment. Energetika, 2017, Vol 63 (3), p. 83-92.
9. VOLOSHCHUK, V., NIKIFOROVICH, A., Features and results of advanced exergoeconomic evaluation of a heat pump providing space heating. CYSENI 2018. Proceedings the 15th International Conference of Young Scientists on Energy Issues. Kaunas: Lithuania. 2018 May, 23-25.
10. MOROSUK, T., TSATSARONIS, G. Advanced exergetic evaluation of refrigeration machines using different working fluids. Energy, 2009, Vol. 34, p. 2248-2258.
11. MOROSUK, T., TSATSARONIS, G. New approach to the exergy analysis of absorption refrigeration machines. Energy, 2008, Vol. 33, p. 890-907.
12. WALL, G. Optimization of refrigeration machinery. Int. Journal of Refrigeration. – 1991. – № 7 – P. 336-340.
13. D’ACCADIA, M. D., De Rossi, F. Thermoeconomic Optimization of Refrigeration Plant Int. Journal of Refrigeration. – 1998. – № 21 – P. 42-45.
14. HERBAS, T. B., BERLINCK, E. C., URIU, C. A. T., MARQUES, R. P., PARISE, J. A. R. Steady-state simulation of vapor-compression heat pump. International Journal of Energy Research, 1993, Vol. 17, p. 801-816.

CYSENI 2019, May 23-24, Kaunas, Lithuania
ISSN 1822-7554, www.cyseni.com

OPTIMIZATION ALGORITHMS FOR VOLTAGE CONTROL IN MEDIUM VOLTAGE DISTRIBUTION SYSTEMS

S. Šantaras
Lithuanian Energy Institute
Breslaujos g. 3, LT-44403 Kaunas
Email: simonas.santaras@lei.lt

ABSTRACT

More and more distributed generators (DGs) will penetrate into the distribution power system in the future. Therefore, due to generated reactive power, voltage fluctuation becomes a challenging essential issue distribution systems. To addresses the problem of reactive power control of DG units in the medium voltage (MV) distribution systems in order to maintain the system voltages within the predefined limits. It is formulated as an optimization problem which aims to minimize the reactive power changes of DG units while returning the voltage of the violated buses inside the permitted limits with taking into account the available reactive power capacity of DGs.

To control multiple DG smart grids are employed. Smart grids aim at evolving the traditional electrical grid system by making increasing use of sophisticated control and communication network technology, to properly deal with the high penetration of controllable assets, such as DG and flexible loads, and their associated challenges. Since electrical grids are critical infrastructures, control strategies regulating their operation need to face both efficiency and cost aspects, as well as resilience related ones in order to assure reliable service.

The problem of DGs active and reactive powers control is formulated using different load and generation algorithms as an optimization problem that uses the sensitivity analysis for linearizing the system around its operating points. The optimal reactive power changes are obtained by implementing mathematical or heuristic solving methods. Used control algorithms makes it possible to provide a balanced voltage at the point of common coupling resulting in the generated power of high quality from DG.

Main objective of this work is to evaluate different optimization algorithms used for reactive power control and therefore voltage control in medium voltage distribution systems.

Keywords: optimization, algorithm, medium voltage

CYSENI 2019, May 23-24, Kaunas, Lithuania
ISSN 1822-7554, www.cyseni.com

EVALUATION OF POTENTIAL BIOGAS PRODUCTION FROM CONSTRUCTION OF ANAEROBIC DIGESTION FROM WWTP IN JORDAN

A. Albatayneh
German Jordanian University
Amman Madaba Street
P.O. Box 35247, Amman 11180 Jordan
Email: Aiman.Albatayneh@gju.edu.jo

G. Halaweh
German Jordanian University
Amman Madaba Street

M. N. Assaf
German Jordanian University
Amman Madaba Street
P.O. Box 35247, Amman 11180 Jordan

ABSTRACT

Biogas is a viable renewable energy source that provides much needed energy, in addition to helping to reduce greenhouse gases (GHG) emissions. In modern waste water treatment plants (WWTPs), anaerobic digestion is more common. This process reduces the volume of sludge and produces biogas, to supply the WWTP site with electricity.

This research evaluates the biogas production potential via the construction of anaerobic digestion plant in South Amman WWTPs. The feasibility study is performed using the volume of biogas and potential energy production.

The results show that anaerobic digestion installation will produce 6,942,869 kWh/a through biogas generation, which covers 66% of energy demand in South Amman WWTPs. In addition, anaerobic digestion unit will reduce 29662 ton CO_{2e} of WWTPs' greenhouse gas (GHG) annually.

Keywords: Anaerobic digestion; Biogas; Energy efficiency

1. INTRODUCTION

In the past five years, the Hashemite Kingdom of Jordan faced a rapid growth of population, in addition to improved living conditions, developments in industry and agricultural sectors, and the adoption of higher environmental rules by authorities.

Since Jordan is one of the most impoverished countries in regard to fresh water in the world, this expansion has placed enormous pressure on the water resources – especially in urban areas where approximately three-quarters of the population is located.

The global trend is moving toward the treatment of wastewater and sludge – the thick material that is left after the treatment of wastewater; and, as a result, treated wastewater is now an integral component of Jordan's water resources. Since the 1930s wastewater treatment has been carried out in Jordan and this sector continues to develop.

Jordan now has 31 wastewater treatment plants, that use processes and technologies, consuming a great deal of energy, so it is wise to find new opportunities for improvement of energy efficiency and energy savings in wastewater treatment plants. One of these methods which investigated in this report is the anaerobic digestion (AD) of wastewater sludge.

Wastewater sludge is a byproduct of chemical, physical and biological processes, performed in WWTP. This sludge contains significant hazardous pathogens to be removed before disposal. There are different methods to achieve this purpose. One such method is anaerobic digestion [1].

AD has been used in many WWTPs for more than 20 years. The US EPA (2006) defines anaerobic digestion (AD) as a natural biological process in which the absence of oxygen and a large number of anaerobic bacteria convert organic matter into biogas - a mixture of methane (CH_4) and carbon dioxide (CO_2) [2].

The end product is a useful renewable energy source (biogas). The result is combined with a stabilized solid matter rich with nutrient materials, such as ammonia and nitrogen, which is commonly used as fertilizer.

Methane production from waste is currently receiving renewed attention as it can potentially reduce CO_2 emissions through renewable energy production. The purpose of this paper is to review and evaluate anaerobic digestion technologies to determine their methane production potential.

Sewage sludge is a wastewater byproduct. It consists of organic and inorganic materials, a large concentration of plant nutrients, organic chemicals, as well as pathogens. It is, therefore, extremely important that sludge is properly treated to minimize environmental impacts [3].

The integration of anaerobic digestion in wastewater plants has several barriers. Costs and local regulations are the main obstacles to the application of this technology. Additionally, wastewater plant facilities are unlikely to change their sludge digestion systems and there is a lack of support programs [4, 5]. A hybrid system consists of anaerobic biogas digestion plant with solar photovoltaic capable of minimizing the Levelized Energy Cost (LCOE) in Kenya, Africa. Compared to current technology, the system shows efficient costs [6]. The generation of electricity using anaerobic biogas is considered a feasible technology to increase the mix of renewable energy sources in Argentina. Efficient anaerobic digestion systems produce energy with cost-effective potential [7].

The technology of solid oxide fuel cells fed by biogas from AD can cover 25 percent of Italy's energy demand for wastewater plants. By integrating a concentrated solar thermal system into this wastewater plant, Levelized electricity costs can be reduced and the energy required from the grid can be reduced by 25 percent [8]. In the European case, the fact that biogas from different available resources, such as municipal solid waste, waste water, sewage sludge and agriculture residues?, is increasingly dependent on anaerobic digestion technology, which has an enormous capacity to efficiently generate energy and treat waste at the same time [9]. Improving the energy efficiency of WWTPs was investigated in several studies. A comprehensive study review investigated several multi-technological ways to improve the autonomy of wastewater treatment plants. The result shows that an efficient conversion of biogas is a key step in achieving efficient energy demand covering for self-sufficiency in wastewater treatment plants [10].

Developed mono-digestion methods provide a significant yield of biogas in a wastewater treatment plant. This technology has used algal species grown in municipal wastewater as substrates for biogas production. These technologies show higher capacity in covering the energy demands of wastewater treatment plants comparing to conventional technology [11].

Analysis of the economic feasibility for biogas production in anaerobic WWTP is recommended. This way any generated municipal solid waste (MSW) per capita could be replicated. The findings indicate economic feasibility of mentioned technology? for cities with population larger than 300,000 and with assumption that it's energy potential could supply 0.25% of the residual fuels [12].

A multi-step approach for the assessment of the energy aspects of wastewater treatment, was applied at the largest wastewater facility in Italy (2.7 M population equivalents as organic load), and the thermal energy demand of the plant was estimated (49.15 GWh/year, more than 93% from sludge line) [13].

The use of bio digesters to produce biogas through anaerobic digestion can play an important role in local economies because of the possibility of producing renewable fuel from organic waste and also as an alternative to waste treatment [14].

Currently, in Jordan, there is only one WWTP provided with biogas generation technology, which is the AS-SAMRA WWTP. In addition, there are plans to provide other two WWTP's, Wadi Al Arab and Irbid Center, with biogas technology [15]. The scientific novelty of this work is the complex approach in assess of technological, economic and environmental aspects in evaluating of installation of AD units in WWTP in Jordan.

The South Amman WWTP (see Fig. 1), which is using the activated sludge process, is located in the south of Amman in Aljiza. The location of the facility was carefully selected to ensure it is located at a safe distance from residential areas. This treatment plant was built to serve residents of Sahab, Khribet Al Souq, Al- Qweismeh, Al-Nuzha, RajmuAlShami, Dheiban, Jwaideh, Abu Alanda, al-Yadoudeh, Theibeh, Feisaleyeh, and Jawa.

It is designed to handle wastewater flow rate of 52,000m^3/day. The calculated quantities depend on the population forecast, which is estimated to be 831,000 in 2035.

Fig. 1. Aerial photo of South Amman WWTP

The South Amman WWTP consists of: three bioreactor tanks, five settling tanks, two thickener grit chambers, grease removal installations, splitter boxes & chambers, sludge drying beds, headwork structure, irrigation pumping station, sludge dewatering building, chlorination building, return activated sludge (RAS) and waste activated sludge (WAS) was pumping stations A and B, thickener sludge pumping station, influent pumping station, headwork structure and outlet structures [15].

The wastewater treatment process of South Amman WWTP consists of primary and secondary treatments (see Fig. 2). The primary treatment consists of screens, an aerated grit chamber and rectangular primary sedimentation basin.

The secondary treatment consists of rectangular basins, where Ferrous Sulphate is added to precipitate phosphorus and the sludge settles to the bottom of the tanks. Treated wastewater is discharged to irrigate 15,000,000 m^2. The settled sludge is treated in various stages.

The first stage of sludge treatment in South Amman WWTP is gravity thickening. Sludge dewatering with three centrifugal dehydrators is the second stage. The dewatered sludge is then transported to the sludge drying bed, an open area in which moist sludge is left to dry. Finally, the dry sludge is transported to an area near the Dead Sea to be disposed of, at a cost of 15 USD per 1 ton. The electricity demand of WWTP reaches to 10500 MWh/a.

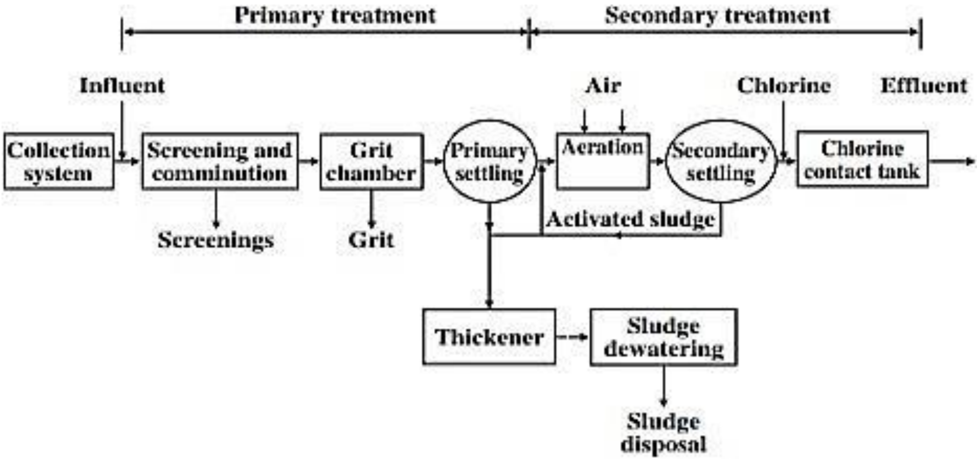

Fig. 2. Current treatment process of South Amman WWTP

WWTPs are an ongoing part of urban development infrastructure. Several environmental standards require the treatment of sludge produced during wastewater treatment process. Different treatment processes are used to solve this problem. Anaerobic digestion is more common in modern WWTPs. This process reduces the volume of sludge and produces biogas, which can be used to supply electricity generation to the WWTP site.

The current situation of this WWTP is lack of a digestion stage, so a digestion unit should be constructed to produce biogas in South Amman WWTP.

2. METHODOLOGY

A field visit was made to south Amman WWTP, and data collected from various resources, including the Water Authority of Jordan (WAJ) [16], Wastewater Engineering book by Eddy and Metcalf [17] and the operator of the South Amman WWTP, such as design parameter as shown below in Table 1.

Table 1. Design parameters

		Source
Population	831,000 cap	The Kingdom wide bio solids management plant 2014 USAID/Table 3-2 [18]
Dry Solid mass	499 kg/10^3.m^3	The kingdom-wide bio solids management plant 2014 USAID
Total dry solid (%)	0.8%	Wastewater engineering/Metcalf and eddy/Table 13-8 [17]
Solids loading	50 kg/m^2.d	Wastewater engineering/Metcalf and eddy/Table 13-19 [17]
Wastewater generation (80%)	100L/cap.day	Ministry of water and irrigation
Chemical Oxygen Demand (COD)	1125 mg/L	Ministry of water and irrigation
Biochemical Oxygen Demand (BOD)	750 mg/L	Ministry of water and irrigation
Total Suspended Solids (TSS)	750 mg/L	Ministry of water and irrigation
Design average flow	52000 m^3/day	The Kingdom wide bio solids management plant 2014 USAID
Flow rate	125L/cap/day	Ministry of water and irrigation

The potential biogas production of the AD system if installed in the South Amman WWTP is calculated to use the sludge at flow rate discharged from the thickening stage. Due to a lack of information, in this report, the thickener in South Amman WWTP will be redesigned using information collected from WAJ and others to attain the sludge flow rate that will enter the digester. Thus, we can find the volume and numbers needed to evaluate the potential biogas production in addition to the amount of stabilized solid matter that will be used as fertilizer.

To increase the efficiency of primary sludge, the Circular tanks are used for sedimentation purpose. Where the feed stream enters the thickener from the middle and is distributed radially. Settlement and compaction of the sludge is then able to take place. Clarified liquor overflows to the top and the settled sludge underflow is removed from the bottom, and then sent to the digesters.

Table 2. New design assumptions of South Amman WWTP

Parameter	**Specification**
BOD removal	35%
TSS removal	50%
Solids retention time in the digester	15 Days
Hydraulic retention time in the digester	15 Days
Temperature of sludge in the digester	35 °C
Yield Coefficient ($\boldsymbol{\gamma}$)	0.08 (g VSS/ g bCOD)
Endogenous Coefficient (K_d)	0.03
COD in effluent	20475 kg /d
Heat transfer coefficient of the dry earth embanked	0.68 W/ m^2.°C
Heat transfer coefficient of the floor of digester in moist earth	2.85 W/ m^2.°C
Heat transfer coefficient of the fixed concrete insulated roof exposed to air	1.5 W/ m^2.°C
Assumed temperature of air	-5 °C
Assumed temperature of the walls of digester	0 °C
Assumed temperature of the incoming sludge	10 °C
Assumed temperature of earth below	5 °C

Finding the specific gravity of the sludge (SG): If 1/3 of the solid matter in sludge containing 90% water is composed of fixed mineral solids with SG = 2.5, and 2/3 is composed of volatile solids with SG = 1, the specific gravity of all solids Ss = 1.25 [18]. The thickener is already constructed at the South Amman WWTP, but due to a lack of information, investigations need to be performed to find the sludge flow rate that will enter the digester.

The design parameters of a gravity thickener for combined primary and waste activated sludge as well as the specifications and the result of the thickener design are summarized in table 3.

Table 3. Specification of thickened wastewater sludge

Parameter	**Quantity**
Total volume of thickened sludge	3,179.9 m^3/ d
Total quantity of thickened sludge	25,948 kgTS/d
Total dry solid	0.80%
Dry solid mass	499 kg/10^3.m^3

2.1. The potential of methane production estimated using the following equations [17]:

$$V_{CH4} = (0.4)[(S_o - S)(Q)(10^{-3} - 1.42Px], \quad (1)$$

where V_{CH4} is the volume of produced methane (m^3/d), Q is the wastewater sludge flow (m^3/d), S_0 is COD in influent of Digester (mg/L), S is COD in effluent of Digester (mg/L) and Px is net mass of cell tissue produced per day (kg/d). So the net mass of biological solids produced daily, Px can be estimated as:

$$P_x = \frac{\gamma Q(S_0 - S)x\ 10^{-3}}{1 + K_d(SRT)}, \tag{2}$$

where γ is yield coefficient, g is VSS/g COD , K_d is Endogenous coefficient per day and SRT is Solid Retention Time.

Depending on the assumption that 65% of biogas is methane [19], the total of biogas will be estimated

3. RESULTS AND DISCUSSION

3.1. Anaerobic Digestion Design and Biogas energy production

Considering the total volume of AD that founds 45,791 m^3 and assuming that one digester volume is 7,686 m^3, the number of required digester estimated to be six.

To calculate the biogas generation, the design parameters applied to Equations 1 and 2, were found that methane production is 5,283.85 m^3 /d. Thus biogas production is around 8,129 m^3/d.

Using AD led to decreasing the mass of treated sludge at the dewatering stage, which results in a reduction of Centrifugal dehydrator use. Data related to a centrifugal dehydrator at South Amman WWTP is shown in Table 4.

Table 4. Centrifugal dehydrator data

Parameter	Quantity
Power	90 kW
Capacity	61 m^3/ day
Number of centrifuges	3 units

The Influent Sludge to the centrifuge should recalculation to detect the number of needed centrifuge after AD installation, which found as following:

Influent Sludge to the centrifuge = Volume of digested sludge = 8,303.36/(1.05*1,000*3.5/100) = 2,259.4 m^3/d.

Influent Sludge to the centrifuge = 225.94 m3/d / 24 hour = 94.14 m^3/h.

Centrifugal dehydrator of capacity 61 m^3/h as shown in Table 4, so using of 2 centrifuges can cover the WWTP demand.

There are many installations using biogas produced; gas engines are the most common in many countries, especially European ones. The electricity bill is the main cost of a wastewater treatment plant in operation. It would therefore be useful to find a way to cover part of this electricity consumption.

With biogas in hand, it would be more feasible to use the biogas in a gas engine to produce electricity. In addition, the engine's co-product heat content of effluent gas can be used to heat digesters in winter.

According to the Swedish Gas Centre a typical normal cubic meter of methane has a calorific (heat) value of around 10 kWh, while carbon dioxide has zero [20]. Therefore, the energy content of biogas is directly related to the methane concentration. In other words, assuming a biogas composition with 65% methane, the energy content would be around 6.5 kWh per cubic meter.

Considering the total volume of biogas to be equal to 8,129 m^3/d, the total energy content will be: 8,129 m^3/d * 6.5 kWh/m^3 = 52,838.5 kWh/d.

Considering an electrical efficiency of a gas engine to be 36%, the generated electrical energy is: electrical power production = 52,838.5 kWh/d * 36% = 19,021.56 kWh/d.

The thermal efficiency of a gas engine is assumed 45%, so the total heat generated is: heat power production = 52,838.5 kWh/d * 45% = 23,777.325 kWh/d and this will cover heat consumption to maintain required digester temperature, which is 17,333.33 kWh /day.

3.2. Feasibility analysis

The investment costs of facilities and buildings required for anaerobic digestion are calculated, using the price of reduced electricity demand, savings from the use of the digested sludge as a fertilizer, savings from dry sludge disposal cost and other costs, which are used to economically justify the utilization of anaerobic digestion.

Approximated costs of biogas utilization are shown in Table 5. These costs include costs related to the construction of buildings and installation of equipment. It should be noted that biogas has a small content of H_2S. Concentrations of H_2S exceeding 100 ppm (part per million) require H_2S removal facilities. Costs associated with these facilities are also included in Table 4. It should be noted that these are approximated costs from another WWTP that produced 6,913.73 m^3/day of methane.

Table 5. Costs of anaerobic digestion facilities

Unit	**Cost ($)**
Digester	984,848
Sludge Holding Tank	146,061
H_2S Removal	248,485
Biogas Holding	242,424
Gas Engine	1,242,424
Gas Flare	40,909
Pipes and Cables	136,364
Sum in $	3,041,515
Operation and Maintenance cost	84,972 $/ year

Volume of digested sludge = 2,259.4 m^3/d is to be used as a fertilizer, assuming each 1$m^3$of this digested sludge will save 1 USD, then:

Total annual saving = (2,259.4 m^3/day) * (1 USD/ m^3) *(30 days / month) *(12 months /a) = 813,384 USD/a.

Using two centrifugal dehydrators instead of three can save in electrical consumption; it can save in operation and maintenance costs for 1 centrifugal dehydrator. The electricity savings are estimated to be 259,200 kWh / year.

Depending on Jordanian electrical tariff, the kWh charged 0.165 cents for the WWTPs.

The investment cost and the potential of saving money after AD unit installation illustrated in Table 6.

Table 6. The potential of saving after installing AD

Saving in disposal cost	197,351 $/year
Fertilizer production	1,145,611 $/year
Saving of use 2 centrifugal dehydrator instead of 3 at dewatering process	42,582 $/year
Saving in electricity	1,140,614 $/year
Total of saving	2,526,159 $/year

3.3. Environmental benefits of AD

WWTP emitted GHG directly from the biological process and indirectly through electricity generation. The biological emission included methane and Nitrous oxide which have high global warming potential reach 25 and 298 times CO_{2e} [21]. The AD unit has the capacities to capture of methane – 5,283.85 m^3/day (2,927.2 kg/day), and reduce carbon dioxide – 73,181 CO_{2e}/day. The biogas combustion released around 100 to 40o g CO_{2e}/kWh [22-24], which assumed to be 250 g CO_{2e}/kWh. Thus, the GHG produced from biogas is reduced 425 g CO_{2e}/kWh of GHG emission caused by current energy max in Jordan, which found 675 g CO_{2e}/kWh. The total GHG reduction through using AD unit reach 81,265 kg CO_{2e}/day.

After the thickening stage the sludge flows to six anaerobic digesters, each with a capacity of 7,686.5 m^3/d. The sludge is kept in the digester for 15 days at 35°C. The main product of this process is biogas providing the amount of 8,129 m^3/d and by product – the digested sludge which is dewatered by two centrifuge dehydrators, each one having a capacity equal to 61 m^3/h.

There are many devices capable of using biogas, while the most common being the gas engine. Cogeneration cycle used to produce power and useful heat at some time, biogas can be used in a gas engine to produce electricity, the heat content of which can be used to warm digesters in the winter months.

Biogas is a viable renewable energy source that can supply much needed energy, in addition to reducing GHG emissions. The results are shown in Table 7.

Table 7. Final result

Result	**Value**
Volume of each Digester	7,686.5 m^3
Number of Digester	6
Volume of produced methane	5,283.85 m^3/day
Volume of digested sludge	225.94 m^3/day
Volume of produced Biogas	8,129 m^3/day
Electricity generation	6,942,869 kWh/a
GHG reduction	29,662 tons CO_{2e}/a
Payback Period	Approximately 1.3 years

4. CONCLUSIONS

There are many environmental and economic advantages to an anaerobic digester. It reduces the deposit of sludge and odour. Biogas can also be used for production of electricity to cover part of the plant's generated energy consumption. Having specification of influent wastewater to the South Amman WWTP and its treatment process, it is estimated that there is the possibility to produce around 8,129 m^3/d biogas. Generation of electricity using this volume of biogas could lead to annual savings of 1,140,614 USD.

In addition, the use of anaerobic digesters in the WWTP in South Amman will reduce CO_2 emissions. Finally, we conclude in this research that the costs of using the AD system in South Amman WWTP are feasible and will be repaid in less than two years.

REFERENCES

1. M. Ameri A. Bafandeh A Feasibility Study for Electricity Generation by Anaerobic Digestion. ICEM CM2015. 2nd International Conference on Electrical, Computer, Mechanical and Mechatronics Engineering. Istanbul, Turkey. 2015 August 27-28.
2. PuchaUSDa, B. and Oleszkiewicz, J. Impact of sludge thickening on energy recovery from anaerobic digestion. *Water Science and Technology*, 2008, Vol. 57, No. 3, p. 395-401.

3. Step Wastewater Sludge Treatment Process. (n.d.). [referred on the 5th of February in 2019] https://www.wateronline.com/doc/step-wastewater-sludge-treatment-process-0001.
4. Pfluger, A., Coontz, J., Zhiteneva, V., Gulliver, T., Cherry, L., Cavanaugh, L. and Figueroa, L. Anaerobic digestion and biogas beneficial use at municipal wastewater treatment facilities in Colorado: A case study examining barriers to widespread implementation. *Journal of Cleaner Production,* 2019, Vol. 206, p. 97-107.
5. Edwards, J., Othman, M. and Burn, S. A review of policy drivers and barriers for the use of anaerobic digestion in Europe, the United States and Australia. *Renewable and Sustainable Energy Reviews,* 2015, Vol. 52, p. 815-828.
6. Lai, C.S. and McCulloch, M.D. Sizing of stand-alone solar PV and storage system with anaerobic digestion biogas power plants. *IEEE Transactions on Industrial Electronics,* 2017, Vol. 64, No. 3, p. 2112-2121.
7. Caruana, M.E.C. Organizational and economic modeling of an anaerobic digestion system to treat cattle manure and produce electrical energy in Argentina's feedlot sector. *Journal of Cleaner Production*, 2019, Vol. 208, pp. 1613-1621.
8. Mehr, A.S., Gandiglio, M., MosayebNezhad, M., Lanzini, A., Mahmoudi, S.M.S., Yari, M. and Santarelli, M. Solar-assisted integrated biogas solid oxide fuel cell (SOFC) installation in wastewater treatment plant: energy and economic analysis. *Applied energy,* 2017, Vol. 191, p. 620-638.
9. Grando, R.L., de Souza Antune, A.M., Da Fonseca, F.V., Sánchez, A., Barrena, R. and Font, X. Technology overview of biogas production in anaerobic digestion plants: A European evaluation of research and development. *Renewable and Sustainable Energy Reviews*, 2017, Vol. 80, p. 44-53.
10. Gandiglio, M., Lanzini, A., Soto, A., Leone, P. and Santarelli, M. Enhancing the energy efficiency of wastewater treatment plants through co-digestion and fuel cell systems. *Frontiers in Environmental Science,* 2017, Vol. 5, p.70.
11. Tsapekos, P., Kougias, P.G., Alvarado-Morales, M., Kovalovszki, A., Corbière, M. and Angelidaki, I. Energy recovery from wastewater microalgae through anaerobic digestion process: Methane potential, continuous reactor operation and modelling aspects. *Biochemical engineering journal,* 2018, Vol. 139, p. 1-7.
12. Guimarães, C.D.S., Maia, D.R.D.S. and Serra, E.G. Construction of Biodigesters to Optimize the Production of Biogas from Anaerobic Co-Digestion of Food Waste and Sewage. *Energies,* 2018, Vol. 11, No. 4, p. 870.
13. Panepinto, D., Fiore, S., Zappone, M., Genon, G. and Meucci, L. Evaluation of the energy efficiency of a large wastewater treatment plant in Italy. *Applied Energy,* 2016, Vol. 161, p. 404-411.
14. dos Santos, I.F.S., Barros, R.M. and Tiago Filho, G.L. Electricity generation from biogas of anaerobic wastewater treatment plants in Brazil: an assessment of feasibility and potential. *Journal of Cleaner Production*, 2016, Vol. 126, p. 504-514.
15. Climate Change Mitigation Measures in the Wastewater Sector in Jordan. .).[referred on the 5th of April in 2019] http://www.waj.gov.jo/sites/ar-jo/Documents/KfW_Retender_Climate%20Protections%20Wastewater_Jordan_20170331_Final.pdf
16. Annual report 2016. Water Authority- Jordan Valley Authority.
17. Eddy, I.S.M., 1986. Wastewater engineering: treatment disposal reuse.
18. South Amman Waste Water Treatment Plant and Trunk line. (n.d.).[referred on the 5th of February in 2019] http://www.atcco.com.jo/project.php?id=22&cat=7
19. Tsagarakis, K.P. Optimal number of energy generators for biogas utilization in wastewater treatment facility. *Energy Conversion and Management*, 2007, Vol. 48, No. 10, p. 2694-2698.

20. Basic data on biogas. (2012). Malmö: Svenskt gastekniskt center.
21. Pachauri, R.K. and Reisinger, A. IPCC fourth assessment report. *IPCC, Geneva, 2007*.
22. Meyer-Aurich, A., Schattauer, A., Hellebrand, H.J., Klauss, H., Plöchl, M. and Berg, W. Impact of uncertainties on greenhouse gas mitigation potential of biogas production from agricultural resources. *Renewable Energy*, 2012, Vol. 37, No. 1, p. 277-284.
23. Paolini, V., Petracchini, F., Segreto, M., Tomassetti, L., Naja, N. and Cecinato, A. Environmental impact of biogas: A short review of current knowledge. *Journal of Environmental Science and Health, Part A*, 2018, Vol. 53, No. 10, p. 899-906.
24. Campos, J.L., Valenzuela-Heredia, D., Pedrouso, A., Val del Rio, A., Belmonte, M. and Mosquera-Corral, A. Greenhouse gases emissions from wastewater treatment plants: minimization, treatment, and prevention. *Journal of Chemistry*, 2016.
25. Hussein, N. Greenhouse Gas Emissions Reduction Potential of Jordan's Utility Scale Wind and Solar Projects. *Jordan Journal of Mechanical & Industrial Engineering*, 2016, Vol. 10, No. 3.

FEATURES OF THE INFLUENCE OF TECHNOLOGICAL FACILITY OF REDUCTION THE NITROGEN OXIDES EMISSIONS BY THE BOILER-FURNACE EQUIPMENT

M. Z. Abdulin, O. A. Siryi, O. V. Baranyuk, K. S. Horban
Igor Sikorsky Kyiv Polytechnic Institute
Polytechnichna str. 6, 03056 Kyiv – Ukraine
Email: o.siryi@kpi.ua

ABSTRACT

Burning processes of organic fuels generate polluting emissions the most toxic of which are nitrogen oxides (generally NO and NO_2). The main process of formation of these components is complicated due to the simultaneous existence of several mechanisms of their formation.

The forecasting and mutual analysis of emission toxic NO_x by the combustion of hydrocarbon fuels is significantly complicated due to ambiguous views on the patterns of their formation. It does not allow to develop unambiguous recommendations for reducing the amount of oxides.

The main purpose of the article is researching the results of the influence technological facility of reduction nitrogen oxides by the boiler-furnace equipment that modernized with the jet-niche fuel combustion technology (JNT). The principles of energy-environmental audit, energy diagnostics and industrial testing of burning devices in real operation conditions were used for the processing and presentation of experimental results. Conditions of stable combustion and emission characteristics NO_x by excess-air factor are described. The main technological features of the equipment are taking into account: the excess-air factor, the heat load of the combustion space, the temperature of the oxidizer and fuel, the concentration of oxygen in the oxidizer and pressure in the combustion chamber.

As a technological facility of reducing NO_x has been accepted a scheme of self-recycling of lew gases into the combustion space. At the nominal operating conditions has been achieved 2.5 multiple reduction of nitrogen oxide concentrations up to 25–35 ppm conditions at 12% volumetric gas recirculation. Thus, a reduction NO_x emissions in the range of 3.4–4.8% per 1% of the recirculation gases has been achieved. The effect is increased with the power set. The similar reducing of NO_x achieved with humidifieng of blow air. The results are presented for water boiler units with a capacity up to 6.5 gcal.

Keywords: jet-niche technology, fuel consuming equipment, burner devices, emission characteristics, nitrogen oxides

1. INTRODUCTION

Ukraine has a national plan for reducing atmospheric emissions. Power engineering is known as one of the main sources of pollution of the ambient air. According to Directive 2010/75/EC, operators of large (> 50 MW) fuel combustion plants are obliged to reduce emissions of sulfur dioxide and nitrogen oxides, and to achieve the emission limit values of these pollutants. The plan is scheduled for 2018–2033.

Among the negative factors of the impact of energy objects on the environment, one of the most dangerous emissions is the nitrogen oxide, the relative toxicity of which far exceeds than toxicity of carbon monoxide and sulfur. It should be noted quite high value of gross emissions and the multivariable of their negative manifestations [1]. Reducing NOx concentrations can be achieved in two ways. The first of them is connected with the direct improvement of the combustion process so-called technological methods. The second method is the chemical cleaning the waste gases.

The main issue of this paper is researching technological methods for nitrogen oxides reducing in natural gas combustion systems.

There are certain technical difficulties associated with the developing effective methods for reducing NOx emissions:

- presence of various mechanisms of formation of nitrogen oxides (thermal, fuel, fast and catalytic);
- insufficient level of research of mechanisms, except for the thermal mechanism of NO formation;
- the possibility of partial transformation of monoxide (NO) into dioxide (NO_2) and other emissions;
- the presence of factors whose influence on emissions of the nitrogen oxides is ambiguous.

The main technological factors affect to the nitrogen emission level are the following: the excess air factor, the load of fuel consuming equipment (FCE), the flue gas recirculation, the afterburning, the water or steam supplying to the combustion space, the fuel and air redistribution through the burner channels, the fuel and air redistribution over the burner stages, the partial desactivation of burners devices (BD), the change of twist intensity (for burners with a twist flux of combustible mixture), the application the micro-torch combustion mechanism (a lot of BD power-generating boilers and the combustion chambers of the gas-turbine units – GTU). In the GTU combustion chambers is using excessive amount of the air for suppressing the formation of nitrogen oxides.

The application of catalytic combustion technologies relates to the second method and depending the technical conditions of FCE. There are divided into selective catalytic and selective non-catalytic reduction of nitrogen oxides.

One of the effective primary methods of reducing NOx emissions is the method of *reburning*. The main idea of this method is in the distribution of fuel and oxidant streams with the aim of minimizing high-temperature zones. At the previous stage, the main part of the fuel is burned, with about 80% of energy released. The excess of air in this zone is maintained at 1.05–1.2. Nitrogen oxides in this area depend on the combustion conditions and the content of nitrogen in the fuel. The remaining fuel is fed to the second zone, the reduction zone, with an excess air factor of 0.7–0.9. This technology for combustion of fuel oil provides up to 50% reduction of emissions of the nitrogen oxide. It is also efficient to apply this approach to combustion of solid and gaseous fuels. The main disadvantage should be the need to stop the boiler unit for reconstruction [2].

The staged air supply method is used on the power-generating boilers. This method involves the division of combustion space into enriched and depleted zone. In the first zone there is combustion of fuel with insufficient amount of oxygen and long time of the products in the reaction zone. The slightly cooled incomplete combustion products are burnt in the second zone of excessive air. Time spent in the second area should be much smaller compared to the first one. This method is most effective for fuels with a constant content of nitrogen [3].

The most inexpensive and simple in terms of implementation is the method of recirculating of exhaust gases. It is widely used in small and medium power-generating boilers. The main idea of this method is to supply the inert medium (combustion products) to the combustion space at a temperature lower than the temperature of the flame. The temperature of the recirculation flue gases determines the efficiency of reducing the concentration of NOx – the efficiency increases with a decrease of temperature. This method is most effective when burning gaseous fuels. For coal combustion the emission of oxides of nitrogen does not exceed 10–15% [4, 5].

A certain result regarding the improvement of environmental performance can be achieved by replacing the burner equipment with low-emission burners. In burners of this type, the length of the torch is delayed to increase the combustion time and reduce the maximum temperature of the process. Therefore, it is possible to lower the temperature of nitrogen oxides. This variant is the most suitable for gaseous fuels for most types of boiler equipment [6, 7].

Water and steam injection is often used in combustion chambers of GTU. Also, this method is considered promising for boiler equipment, because it achieves lower temperature of the flame and thus reduce the thermal NOx. In some cases, the reducing of the NOx concentration reaches 80%.

The amount of water or steam is limited by the condensation conditions. It should be noted that there is a decrease in the boiler efficiency by 3–10%. A widespread scheme of the implementation of this method is used in a combination with the recirculating of flue gases and installation low-emission burners [8, 9].

Selective non-catalytic reduction is a method of injection of ammonia or urea in flue gases of the boiler unit at temperatures 750–900 °C. Reagents convert nitrogen oxides into molecular nitrogen and water. The NOx reduction can reach 70% [10].

A selective catalytic reduction is also a reagent injection but with the presence of a catalyst. The presence of a cautalyst reduces the concentration of NOx at a lower temperature. This method can be used at temperatures of 260–600 °C. Reducing NOx concentration reaches 90%. The disadvantages include a fairly high cost of the method [11, 12].

In general, each of the methods alone or in combination significantly improves the environmental performance of the equipment. Nevertheless, one of the significant factors of improvement ecological characteristics of existing equipment is changing the swirling flow to the direct-flow scheme for supply the combustible mixture into the fire-chamber of FCE. Thereby, the canonical principles of minimizing NOx concentrations are: preliminary mixing, staged combustion and direct-flow aerodynamic structur. The burner devices that are correspond the main canonical principles developed in Igor Sikorsky Kyiv Polytechnic Institute. One of such perspective tecnilogies is Jet-niche combustion technology (JNT) [13]. The basic principles of the technology are: rational distribution of fuel in the stream of oxidant; stable regulated flow of fuel, oxidant and combustion products; self-regulation of the blend composition of the fuel mixture in the flame stabilization zone.

All the principles mentioned above are achieved due to the successful construction location of the jet-niche system (JNS) [14] on the autonomous module (Fig. 1, a), of which a burner is formed (Fig. 1, b).

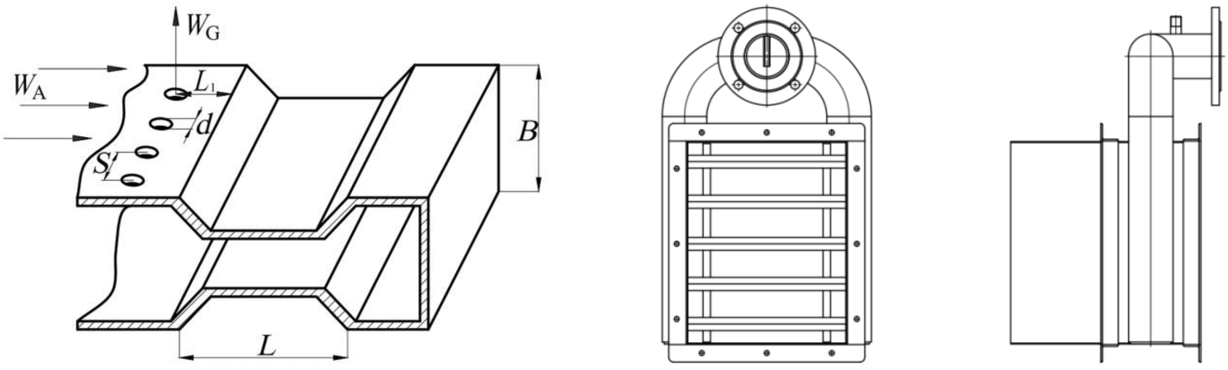

a)

b)

Fig. 1. Schematic of location of JNS on a stabilizer a) the jet-niche type burner b): W_A – air velocity, W_G – fuel velocity, L_1 – distance of fuel openings from detachment edge of the niche, S – step of openings location, d – diameters of openings, L – length of niche cavity, B – thickness of stabilizer

The practical value of the work is definition the influence of the operation factors and the geometric parameters of the JNS on the emission of nitrogen and carbon oxides. The second stage of the research was to determine the technological facility of reduction the nitrogen oxides emissions by the boiler-furnace equipment, which was modernized on the basis of JNT.

To accomplish the issue of the paper, the following tasks have been set:

- to study the emission characteristics of the JNS in the form of relation of nitrogen oxides $NO_x = f(\alpha)$ and carbon oxides $CO = f(\alpha)$ when the mode and geometrical parameters of fuel distribution are changed, as well as to determine the critical limits of the operating range of the JNS by the excess air factor;

- to take into account of forecasting concentrations of nitrogen oxides by fire equipment the influence of the main technological factors: the excess air factor, the effect of vitiated air, the temperature of the oxidizer, the working volume pressure and the range of high-beat volume of the working space of the FCE;
- to explore the efficiency the recirculation of flue gases into the hot-water furnace in terms of reducing harmful emissions into the environment, the boiler is modernized on the basis of the JNT;
- to determine the influence of moistening of blast air on the boiler equipment emission characteristics.

2. METHODOLOGY

The results of experimental and industrial research are presented on the basis on the generalizations arising from the thermal theory of formation of NO_X [15], as well as works performed in the problem combustion laboratory Igor Sikorsky Kyiv Polytechnic Institute [16] and based on the approach [17].

The main advantage for such an approach is explained taking into account the influence of interdependent factors on the formation of nitrogen oxides such as: temperature and oxygen content in oxidizer, specific heat stress and pressure in the combustion zone, and also the excess air factor. Thereby, such reduces units are more convenience of processing and analysis of experimental results compared with the analysis of direct NOx emission dependencies.

The following dependence is used for processing experimental data:

$$NO_X^{red} = \frac{NO_X}{\prod K_i^{0,5}} = k_0 \exp\left[\frac{-E_{eff}}{RT}\right], \tag{1}$$

where NO_X^{red} – total concentration of nitrogen oxides (NO та NO_2) that reduced to nitrogen dioxide; $\prod \cdot K_i$ – the product of the coefficients of influence K_i, k_0 – the preexposing factor, E – the activation energy of the resulting formation reaction NO, R та T – the gas constant and the combustion temperature, respectively.

$$K_1 = (1-\psi)^2 \cdot \psi\,; \qquad K_2 = \sqrt{\frac{P}{P_{n.c.}}}\,; \qquad K_3 = \sqrt{\frac{T_{n.c.}}{T_0}}\,; \qquad K_4 = \sqrt{\frac{(\alpha-1)}{\alpha}}\,. \tag{2}$$

The coefficient K_1 reduces the oxygen concentration in the air, with the help of the coefficients K_2 and K_3 take account of the pressure and the initial temperature; the coefficient K_4 allow an excess of air.

The coefficient of fuel residence time in the combustion zone $K_5 = K_\tau$ gives a reduction in the time of residance $\tau_{res.}$ It depends on the heating power of fuel (Q_{hp}, MJ/kg), the air excess factor (α), the ambient temperature (T) and the blast air (T_0), the specific heat density q_v, W/(m^3·Pa), the stoichiometric coefficient L_0, kg/kg, and the technical gas constant R = 287 kJ/(kg·K). This parameter is determined from the ratio:

$$K_\tau = q_v^{-n}. \tag{3}$$

3. RESULTS AND DISCISSION

3.1. General characteristics of CO and NOx emissions in the JNS

The series of laboratory experiments was carried out on a specially equipped fire stand for the analysis of the influence of the main mode parameter – excess air (α) on the emission characteristics of the JNS (NOx and CO). It should be noted that the critical values of this parameter are the main criterion for choosing the BD according to the technological conditions of the combustion process on the FCE. The influence of α on the emission level depends mainly on the design of the BD, the method of mixing and the intensity of heat and mass transfer processes in the combustion space.

Construction of the characteristics of the species NOx = f (α) and CO = f (α) can be realized in two ways. The first is the change of the air flow at constant fuel consumption and other operating parameters. The second method is realized by changing fuel consumption at constant air velocity.

In Fig. 2 shows the individual emission characteristics of the JNS with the location of the step of the openings 4.5 and the diameter of 3.0 mm. As can be seen from the Fig. 2, the given dependencies have an extreme look. Thus, the characteristic for nitric oxide has an extremum in the region of α → 1, while in the same region, products of incomplete combustion of carbon are reduced to almost zero and take their minimum at α = 1.48.

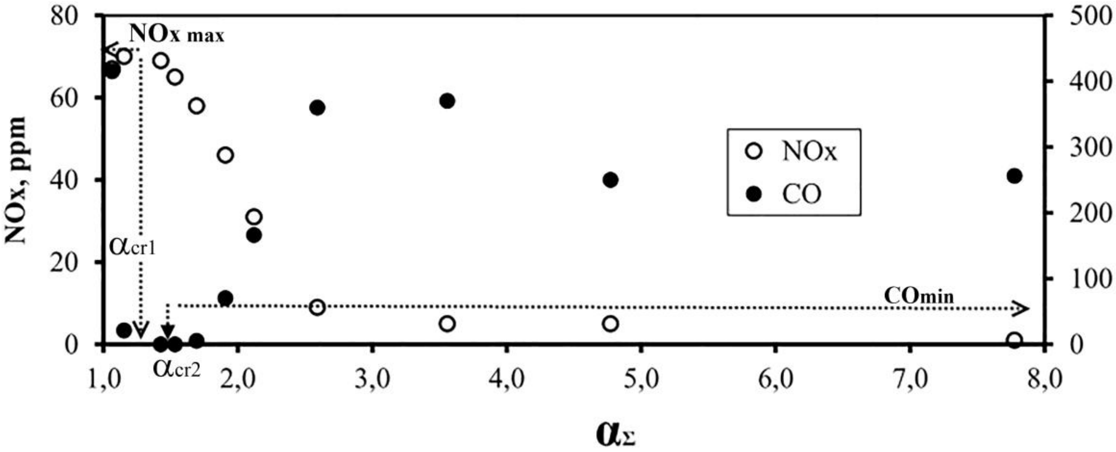

Fig. 2. Effect of excess air factor on the concentration of nitrogen oxides and carbon monoxide in the combustion of liquefied gas in the JNS

The alignment of two characteristics allows to analyze the presence of two characteristic critical points corresponding to the extremums of the corresponding curves. Taking into account the location of α_{cr1} and α_{cr2}, for the general analysis of domains in the range of researched modes, three regions can be distinguished. The first of them corresponds to the gap ($\alpha < \alpha_{cr1}$) in which the emission of nitrogen oxides is reduced, and the emission of carbon monoxide, on the contrary, is extremely high. In the second zone, which corresponds to $\alpha_{cr1} \leq \alpha \leq \alpha_{cr2}$, in the direction of reducing the excess air there is a unique increase in the studied emission characteristics.

In the third region ($\alpha > \alpha_{cr2}$) there is an ambiguous behavior of the characteristics as in the first region, but the curves behave the opposite in comparison with ($\alpha < \alpha_{cr1}$).

Thus, the second critical point α_{cr2} is a peculiar indicator of the quality of the organization of the mixing process. The closer the condition $\alpha_{cr2} \rightarrow 1{,}0$ is fulfilled, the better the energy potential of the fuel can be realized. It should be noted, the determination of emission characteristics for a single JNS stabilizer does not fully reflect the maximum effective range of SNT burners, where $\alpha_{cr2} = 1.01–1.05$.

3.2. Influence of geometrical parameters of fuel supplying to the emission characteristics of JNS

The results of gas analysis of combustion products the liquefied gas in JNS are presented in Fig. 3. The research was carried out at atmospheric pressure, as an oxidizer, cold air was used at a temperature of 15–20 °C. Air velocity was maintained constant Wa = 20 m/s.

Characteristics are similar in the figure, but it should be noted that the step and diameter have some effect on the concentration of carbon monoxide. It can be seen that α_{cr2} is within the limits of α = 1.6–1.4 and depends on the geometry. The minimum values of the underburning correspond to the relative step $\overline{S}$ = 5.0 (on the mode α_{cr2} the value of the underburning was C_{CO} =0 ppm). With a decrease the number of fuel openings, the underburning increased and the greatest concentration value corresponds to the geometry of the fuel distribution with $\overline{S}$ = 5.0 and d = 2.0 mm. At the same time, it was not possible to enter the operating mode ($\alpha \rightarrow 1.0$) with the maximum possible depth of fuel burn-out. In the operating modes of the system in the region $\alpha < 1.5$ there is a flame die-out from the stabilizer and the torch is stabilized in the fireproof area. In these conditions, the steady vortex structure in the fire stabilization zone is disturbed that severe connected with the flameout in JNS.

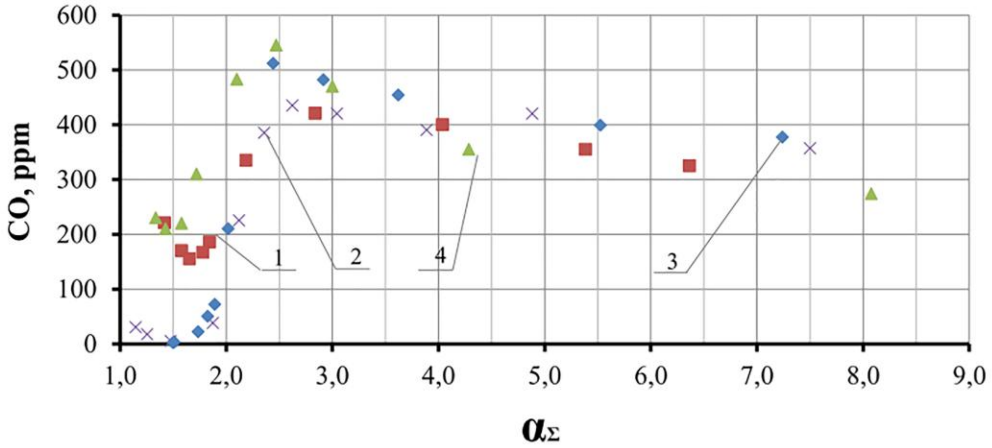

Fig. 3. Effect of excess air factor on the concentration of carbon monoxide in flue gases of combustion the liquified propane-butane mixture in the JNS with different relative steps of the location of fuel openings: 1 – $\overline{S}$ = 3.0, d = 3 mm; 2 – $\overline{S}$ = 4.5, d = 3 mm; 3 – $\overline{S}$ = 5.0, d = 3 mm; 4 – $\overline{S}$ = 3.0, d = 2 mm

Reducing the parameter $\overline{S}$ to the values of 4.5 allows to arrange the necessary flow structure, with the flame torch reliably stabilized at $\alpha = 1.15$ without the die-out processes and flow pulsation. A further reduction of the step of openings location leads to a local oversaturation of the fuel mixture with fuel and does not allow minimizing the underburning to the sampling point. It should be noted, that the “rich” flameout did not arise during the passage of α_{cr2} in all other studied modules.

Thereby, from the obtained results it should be concluded that for reliability burning process more important is the hydrodynamic structure of the stream than the stoichiometry of mixture in stabilization area. All this aims reached by the correction of the step of openings.

Increasing the diameter value within the ranges of the studied values provides a deeper burningout of fuel (in the region of $\alpha < 3.0$). The reverse results are observed on the starting conditions. The researched modules with a larger diameter values reduce the completeness of carbon burning.

The results of measurements of nitrogen oxides in the geometric conditions described above are presented on Fig. 4.

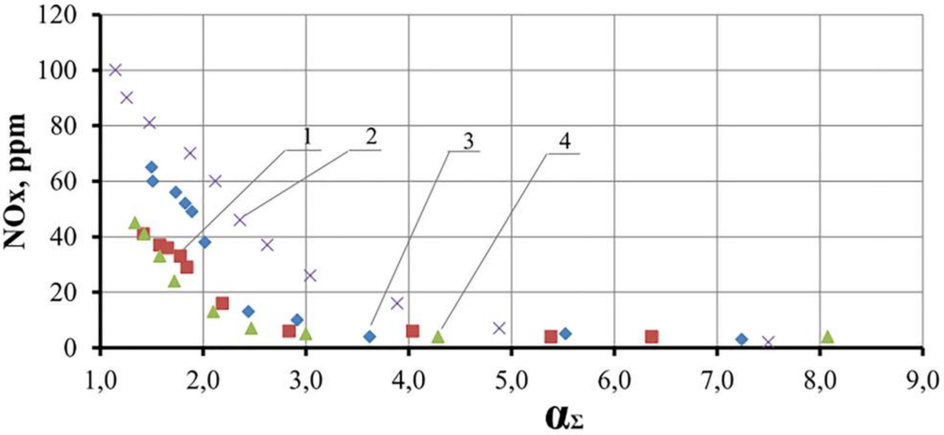

Fig. 4. Effect of excess air factor on the concentration of nitric oxide in flue gases of combustion the liquified propane-butane mixture in the JNS with different relative steps of the location of fuel openings: 1 – $\overline{S}$ = 3.0, d = 3 mm; 2 – $\overline{S}$ = 4.5, d = 3 mm; 3 – $\overline{S}$ = 5.0, d = 3 mm; 4 – $\overline{S}$ = 3.0, d = 2 mm

Characteristics of NOx = f(α) are physically similar and consistent with the general notions with NOx emissions by burning hydrocarbon fuels. The emission of nitrogen oxides is maximum and reaches values of about 100 ppm at operating conditions for work modules, in which the minimum values of CO concentrations have been reached. It's indicate the full burnout of the carbon and maximals temperatures of working process. The indicators in the corresponding modes of excess air are 2 times smaller for modules with the parameter $\overline{S}$ = 3.0, and is no more than 46 ppm. Such levels of oxides in the conditions of modern ecological standards require using of special methods for reducing emissions.

The geometry charasteristics of fuel supply has a negligible impact on the emission quality of the JNS in the range of starting conditions, which correspond to the value of excess air α > 4.0.

3.3. Application the technological facilities for NOx reduction by the boiler-furnace equipment

Full-scale industrial tests of the effect of recirculated exhaust gases were made on a water heating boiler KV-G-6,5 (thermal capacity is 6.5 Gcal). The regulation of the percentage of gases was carried out with the help of a valve shutter. Technologically the scheme represents a way of self-recirculation.

The number of recirculation gases is determined by the ratio:

$$K_{rec} = \frac{V_{rg}}{V_a}, \tag{4}$$

where V_{rg} – the volume of the recirculated exhaust gases, m^3/s, V_a – the volume of blast air, m^3/s.

The concentration of oxygen in the air with adding recirculation gases can be estimated by the following dependence [18]:

$$C_{O_2} = \frac{0,209 \cdot \left[\left(1 + \alpha_F \cdot L_0\right) + \left(\alpha_F - 1\right) \cdot L_0 \cdot 0,01 \cdot K_{rec} \right]}{\left(1 + \alpha_F \cdot L_0\right) \cdot \left(1 + 0,01 \cdot K_{rec}\right)} \cdot 100, \tag{5}$$

where α_F – the excess air factor in boiler furnace.

The assessment of the oxygen concentration in the diluted air can be estimated with a fractional accuracy of no more than 2.0% for the for the object of study.

It is noted, the emission factors are almost independent of the boiler's thermal load. This is especially evident in the supply of recirculation gas to the burner. At the maximum load during the tests (87.5% of the nominal) emissions were 18.5% higher than the partial (37% of the nominal load). This difference is minimized with mixing flue gases, even at 12% volumetric flew gases recycle does not depend on the load of the boiler unit (Fig. 5). The penetration of 12% of combustion products into the boiler's space reduces the nitrogen oxide almost in 2.5 times. At the facility under study, the NOx emission reduction was achieved within the range of 3.4–4.8% for 1% of the recirculation gases. The effect increases with the power set and allows to reduce the total concentration to 100 mg/m^3. The values of CO do not exceed the maximum allowable norms (C_{CO} < 100 mg/m^3).

The effect of recirculation flue gases on the emission of carbon monoxide is given on fig. 6. The obtained results correlate with the physical representations of the incomplete combustion products formation of hydrocarbons. The main reason is the reduction of the oxygen content in the air, which is fed into the furnace. The maximum values of the underburning correspond to the maximum recirculation flue gases.

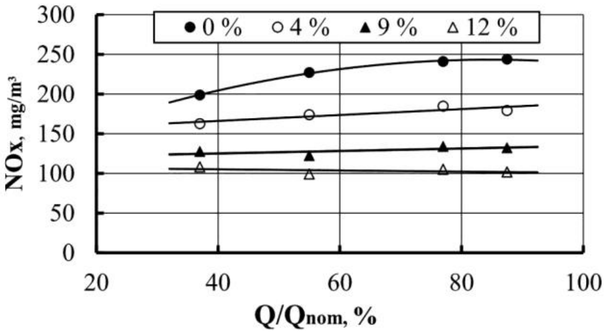

Fig. 5. NOx relation of the heat load of the boiler KV-G-6,5 and the volume of the flue gas recirculation

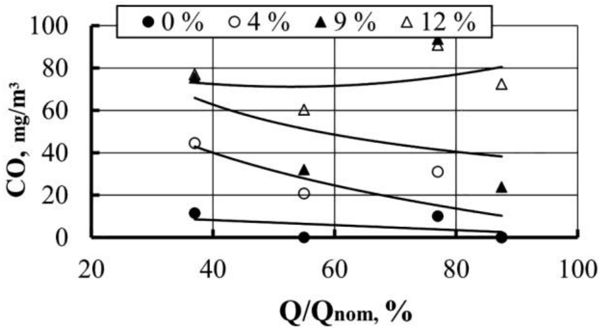

Fig. 6. CO relation of the heat load of the boiler KV-G-6,5 and the volume of the flue gas recirculation

As shown on Fig. 7, the addition resrculated gases does not affect the temperature of the products of combustion. There is a slight increase of temperature within 4.0 °C at low loads. At the maximum load during the tests changes in the temperature of the waste gases were within the measurement error of the device.

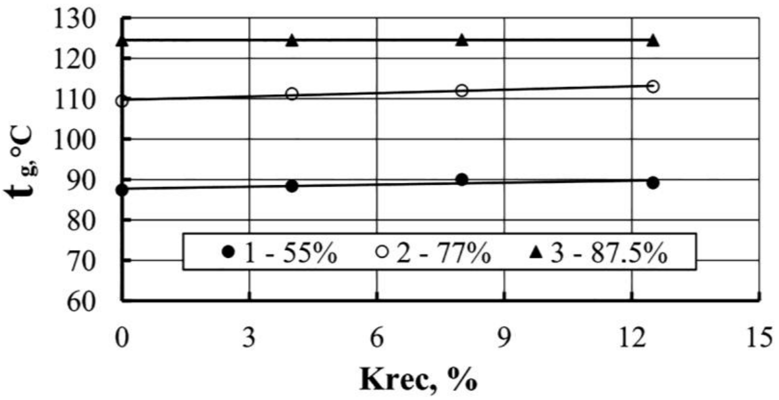

Fig. 7. The temperature relation of the flue gases on the volume of gas recirculation when changing the boiler load

Estimation of the NOx concentration in the flue gases is possible by the dependence:

$$NO_x = A_{NO_x} \cdot e^{a \cdot r} \cdot K_P \cdot K_T \cdot K_\alpha \cdot K_\tau \cdot K_\psi , \qquad (6)$$

where A_{NOx} = 4091 – a preexposing empirical value, mg/(m^3·s^{0,5}); a = -0.052. The obtained dependence can be used as an estimate for boilers, equipped with burners of the JNT type, specific heat load of the fire space to 0.5 MW/m^3, temperature of blast air 2–20 °C and excess air factor α = 1.25–1.5; depression in the furnace ΔP = 10–100 Pa, the amount of gas recirculation r = 0–0.12, which corresponds to the concentration of oxygen in the air C_{O_2}=20.9–18.9%.

3.4. Research of moistening of air on emission characteristics JNT industrial gas burners

The effect of the blast air humidifying on the NOx emission level was carried out on contact water heaters (CWH) and a water boiler NIISTU-5 type, modernized on the basis of JNT.

Dampening was carried out by return water from the heating network system. Thus, 100% hydration is achieved and air is heat to a temperature of 40–45 °C. In comparison with "dry" combustion it is achieved more than twofold reduction of the emission level by installations to the values of $C_{NOx} \approx 50$ mg/m^3.

The air humidifying by the saturated steam is carried out on a NIISTU-5 boiler, which also resulted in nearly twofold reduction of nitrogen oxide concentrations, with maximum concentrations at 80–90 mg/m^3 for moisture content $d_0 \approx 25$ g/kg.

The following dependence should be used to predict the emission level of FCE with the humidification of the blast air:

$$\mathrm{NO_X} = A_{\mathrm{NO_x}} \cdot \left(N \big/ N_0 \right)^a \cdot \left(\frac{d}{d_0} \right)^b \cdot \prod_{i=1}^{n} K_i^{0,5}, \tag{7}$$

where A_{NOx} – empirical value, mg·s/m^3; N/N_0 – the ratio of the current power to the nominal power of the installation; d_0 – the natural moisture content of blast air, g/kg; d – artificial humidification, g/kg.

Table 1. Results of statistical analysis of emission characteristics of JNT burners on FCE

Type FCE	**A_{NOx}, mg·s/m^3**	**a**	**b**	**d_0, g/kg**	**d, g/kg**
CWH (KVN-2,5)	$9.55 \cdot 10^4$	–0.55	–0.25	1.0–10.0	10–55
NIISTU-5	$1.75 \cdot 10^3$	1.25	–0.6	1.0–3.0	10–22

Usage of vaporizers in the composition of industrial boilers due to the heat of waste gases for the organization "wet" combustion is considered a promising way to reduce emissions of nitrogen oxides on equipment of the objects of heat networks.

4. CONCLUSIONS

1. The paper presents the results of reducing the concentration of nitrogen oxides in combustion products by improving the combustion technology. The results were obtained during industrial tests of FCE, which was modernized on the basis of the JNT. There are, water boilers with capacity of 0.5 and 6.5 Gcal and contact water heater with capacity of 2.9 Gcal. Apart from widely used burners with mixture rotation, JNT is direct flow burner devices. It has several significant advantages. They are following, high-quality of mixture formation, reduced hydraulic resistance of the burner, a wide range of power control of the object (10–100%). These qualities provide high generality of technology. At present, it is implemented on many types of fuel consumption equipment – boilers, furnaces and dryers. At present, the necessary direction of technology development is improving its environmental performance.

2. The possibility of constructing a universal methodology of ecological analysis was determined. The prediction of nitrogen oxides emission by FCE based on consideration of the set of

operational factors is presented. This approach is considered promising from the point of view of the possibility of reliable forecasting of emission characteristics for a wide range of FCE.

3. Proved the ability of implementing the principles of universalize in the design of industrial burners. Thermal power is obtained by setting the required number of base (single) flame modules. Also, proved the possibility of physical modeling of a work process in the single fuel propagation modules with the subsequent adequate application of the received dependences to industrial gas burning equipment on the basis of JNT.

4. The application of the flue gas recirculation into the fire space of a water boiler with the flow of the main air allows determine the main capability of nitrogen oxides suppression on the objects of the cities heating networks. Reduction of nitrogen oxide content in products of combustion was more than twofold. The reduction of NOx by 1% of the recirculation gases was reduced by 3.4–4.8%, that exceeds the similar indicators of burners with the swirling flow of fuel and oxidizer by 10–30%. The effect increases with the thermal power. Estimation of the impact of recirculation on the boiler efficiency showed a slight decrease – within 1.0%.

5. The humidifying of the blast air in the contact water heaters allows decrease the concentration of nitrogen oxides by more than 2 times. In this case C_{NOx} = 80–100 mg/m^3. The preservation of carbon monoxide emissions within the normative limits – C_{CO} = 30–55 mg/m^3. Similar indicators for the reduction of nitrogen oxides are achieved during humidifying the air with saturated steam in a water heating boiler NIISTU-5.

REFERENCES

1. *Clean tecnnology center*, Nitrogen oxides (NOx), why and how they are controlled. epa-456/f-99-006r, November 1999. Link to the internet, <http://www.epa.gov/ttn/catc>.
2. HOU, J., MA, Y., SHUYUAN, L., SHANG, W. A comparative study on characteristics of sulfur and nitrogen transformation and gaseous emission for combustion of bituminous coal and char. *Carbon Resources Conversion*, 2018, Vol. 1, No. 1, p. 86–93.
3. ELBAZAB, A.M., MONEIBB, H.A., SHEBILB, K.M., ROBERTSA, W.L. Low NO_X – LPG staged combustion double swirl flames. *Renewable Energy*, 2019, Vol. 138, p. 303–315.
4. FREDERICK, N., AGRAWAL, R.K., WOOD, P.E., WOOD, S.C. Induced Flue Gas Recirculation for NOx Control: Application on Boilers and Process Heaters. *Energy Texas Industries press.* Report 03 ETEC, 2004, 24 p.
5. KOBZAR, S.G., HALATOV, A.A. Reducing Nitrogen Oxides in Gasboiler Equipment with Flue Gases Recirculation. *Thermalingeneering.* 2009, Vol. 31, No. 4, p. 5–11.
6. KOTLER, V.R., Gas Turbine Installation and Current Problem of Harmful Pollution. *Thermalingeneering.* 2003, No. 8. p. 73–78.
7. DUTKA, M., DITARANTO, M., LOVAS, T. Application of a Central Composite Design for the Study of NOx Emission Performance of a Low NOx Burner. *Energies.* 2015, No. 8, p. 3606–3627.
8. LANDMAN, M.J., DERKSEN, M.A.F., KOK, J.B.W. Effect of Combustion Air Dilution by Water Vapor on Nitrogen by NOx Emission in a Premixed Turbulent Natural Gas Flame: an Experimental Study. *Combustion Science and Technology*. Pittsburgh, USA. 2006, Vol. 178, p. 623.
9. ZHAO, D., YAMASHITA, H., KITAGAVA, K., ARAI, N., FURUHATA, T. Behavior and Effect on NOx Formation of OH Radical in Methane-air Diffusion Flame with Steam Addition. *Combustion and Flame*. 2002, Vol. 130, p. 352.
10. BLEJCHAŘ, T. KONVIČKA, J., HEIDE, B, MALÝ, R., MAIER, M. High Temperature Modification of SNCR Technology and its Impact on NOx Removal Process. *EPJ Web of Conferences*. *EFM 2017*. 2018, <https://doi.org/10.1051/epjconf/201818002009 EFM 2017>.

11. BYEONG, J.L., HO-CHUL, K., JIN, O.J., YOUNG, S.M. Consideration of the Role of Plasma in a Plasma-Coupled Selective Catalytic Reduction of Nitrogen Oxides with a Hydrocarbon Reducing Agent. *MDPI. Catalysts*. 2017, No. 7, p. 325–339.
12. WANG, R., WU, X., CHUNLEI, Z., XIAOJIAN, L., YALI, D. NOx Removal by Selective Catalytic Reduction with Ammonia over a Hydrotalcite Derived NiFe Mixed Oxide. *MDPI. Catalysts*. 2017, No. 7, p. 61–70.
13. ABDULIN, M.Z., PETRENKO, V.N. The Experience of the Implementation of Jet-niche Technology of Fuel Combustion in the Industrial and Municipal Power Facilities. A comprehensive solution the problems of energy saving in industrial and municipal energetics. The Crimea, Yalta, May 23–25, 2009. p. 28–30.
14. ABDULIN, M.Z., SIRYI, O.A. Research of hydrodynamic flame stabilizer with cross fuel feed characteristics. *Scientific Journal of Riga Technical University. Series: Power and Electrical Engineering.* 2014. No. 32. p. 12–18.
15. ZELDOVICH YA.B. *Physics of Shock Waves and High-temperature Hydrodynamic Phenomena.* Moscow: Publishing house physics and maths lit., 1963. 632 p.
16. LYUBCHIK, G.N, GOVDYAK, R.M., MIKULIN, G.A., SHELKOVSKY, B.I., ZARITSKY, A.A. Environmental audit of gas-burning devices based on the application of the method of basic characteristics of NOx and CO. *Ecotechnologies and resource saving*. 2007, No. 4. p. 64–70.
17. SULLIVAN, D.A. A simple gas turbine combustor NOx correlation including the effect of vitiated air. *Journal of Engineering for Power.* Transactions of the ASME, 1977, p. 145–152.
18. SIGAL I.YA. *Air protection urban-industrial environment during fuel combustion*. Leningrad: Nedra, 1988, 310 p.

CYSENI 2019, May 23-24, Kaunas, Lithuania
ISSN 1822-7554, www.cyseni.com

EVALUATION OF WOOD FUEL FLUE GAS COMPONENT CONCENTRATIONS DEPENDING ON TEMPERATURE, AIR EXCESS VALUE AND FUEL MOISTURE

Z. Uldinskas, V. Dagilis
Kaunas University of Technology
Studentų g. 56, 51424, Kaunas – Lithuania
Email: zilvinas.uldinskas@ktu.edu

ABSTRACT

Increasing global awareness regarding climate change, results in renewable energy sources promotion in global energy sector with overall energy production efficiency magnification. However, green energy (i.e. commonly wind and solar power) is greatly dependable on weather conditions which tend to generate feasibility problems using aforementioned sources all year round. Biomass (wood fuel), also regarded as green energy source, has developed significantly over the last two decades due to its availability, calorific value and even greater efficiency when economizers are implemented. Flue gases after the main heat transfer process in boiler are then used in economizers, where flue gases are cooled to lower temperatures and condensed (extracting additional heat) only up to a certain degree- not reaching dew point temperatures. In this paper the algorithm of predicting the flue gas component concentrations is presented, which would allow to accurately calculate the energetic parameters of cooled flue gases (below the dew point), potentially leading to greater heat value recovery and improving overall energy production efficiency. In order to evaluate the possibility of further flue gas usage after economizer system, component (water vapour – H_2O, carbon dioxide – CO_2, oxygen – O_2 and nitrogen – N_2), molar concentrations flue gas mixture were calculated which depend on biofuel wetness factor (w) values from 0.45 to 0.60 and excess air supply (λ) values of 1.2; 1.5 and 1.8 in combustion process. It was constituted that water vapour molar concentration depends only on gas mixture temperature (when fluid is below dew point) while other gas component concentrations change gradually with temperature, wetness of the fuel and air excess value. Molar component concentrations are crucial in gas enthalpy calculations and will be used in further studies in heat transfer and energy evaluation. Flue gas dew point dependency was also evaluated (according to different cases of w and λ values), ranging from 54.9 °C up to 70.4 °C in different cases.

Keywords: Biomass, flue gas components, fuel moisture, economizer, calculation

1. PROBLEM ANALYSIS

The current energy policy of the European Union as well as world climate change policy encourage usage and development of renewable energy sources. Biomass (especially wood), arguably considered as carbon neutral energy source, is well integrating in Europe’s energy sector. However, in comparison with fossil fuels, biomass (especially freshly cut wood) has a major disadvantage- it burns significantly worse and therefore does not ensure stable combustion process in furnaces, making heat generation less effective, however it could be argued that with proper boiler plant regulation, stable combustion process can be achieved. Nevertheless, there is a large part of water in wood beside the flammable composites – carbon and hydrogen, thus it requires a lot of energy for water evaporation subsequently resulting in large quantity of energy losses. Even though a condensing economizer is usually used, it could be argued that the flue gas could still be used to further increase the overall efficiency of the plant. (major part of which could be called latent heat) [7]. The temperature of the ejected flue gas is relatively low – around 50 °C, therefore this low-grade heat can be utilized by exploiting additional equipment such as heat pumps.

Low grade heat recovery is related to capital investments as well as to additional energy use. For example, an implementation of chemical heat pumps [1, 2] requires additional heat energy – primary and cheap energy source. The cooling capacity of the heat pumps can also be used like a solitary instance [3, 4]. The mechanical heat pumps [5, 6] need electrical or mechanical energy source. In the article [7] other type of low-grade heat potential utilization is discussed; water vapour of the flue gas could be regenerated in a mass transfer regenerator, i.e. transferred from flue gases to air which is blown towards a burning chamber. In all instances, the low-grade utilization requires additional effective means, be that economic, energetic or both.

The transformation of all waste heat of the plant is arguably not rational, mainly because the heat capacity is gradually decreasing while the flue gas temperature is lowering. Because of this, more detailed calculations of the low-grade heat amount must be developed. In previously mentioned articles, only Hebenstreit et al. [5, 6] provides some graphics of wood fuel waste heat calculations. Nonetheless, the authors do not present mathematical algorithm which is crucial to analyse the flue gas heat and mass flow in additional heat exchanger.

The aforementioned algorithm must evaluate a number of essential parameters, such as the flue gas dew point temperature (derived from partial water vapour pressure – volumetric parameter) and enthalpy (derived from component mass concentrations) of the flue gas mixture.

Therefore, the first step is to evaluate volumetric and mass component concentrations, parameters which are to be used in future calculations regarding gas mixture enthalpies and heat and mass transfer afterwards.

Main equations, suitable for aforementioned volumetric and mass parameter evaluation are presented in this article as well as general dependencies between flue gas mixture components and air excess value (1.2; 1.5; 1.8) and also with an increasing wood fuel moisture from 45 to 60%.

2. FUEL AND FLUE GAS COMPOSITION

T. Nussbaumer [8] proposes reduced wood fuel chemical formula expressed as $CH_{1.44}O_{0.66}$. Therefore, the equation of combustion chemical reaction can be shown as:

$$\begin{gathered} CH_{1.44}O_{0.66} + (24/\mu^{H2O})w/(1-w) + 1.03\lambda[O_2 + (3.76 - \varphi/0.21)]N_2 \rightarrow \\ \rightarrow CO_2 + 0.72H_2O + 24/\mu^{H2O})w/(1-w) + 1.03(\lambda - 1)O_2 + \\ +1.03\lambda[(3.76 - \varphi/0.21)N_2 + (\varphi/0.21)H_2O], \end{gathered} \tag{1}$$

where w – moisture of the wood, i.e. water mass part in moist wood mass unit, λ – excess air ratio, $24/\mu^{H2O}$ wood and water kilo mole mass ratio, φ – air moisture volumetric part; water like nitrogen does not bear part in combustion reaction, so it is accepted that φ decreases the nitrogen proportion 3.76 by value of $\varphi/21$. Major part of water vapour in flue gas comes from hydrogen reaction and physical presence of water in wood. When wood moisture w becomes greater than 0.35 (35%), part of physical water overbalances the part of hydrogen reaction in generating water vapour [7].

Relative partial water vapour pressure $\bar{p}^{H2O}$ is calculated as volumetric water proportion in flue gas. This proportion is obtained by dividing the mole quantity of water vapour by the mole quantity of flue gas when one mole of wood is burned. It is known that in uniform circumstances, the various gas mole occupies the same volume, thus it can be said that relative partial water vapour pressure $\bar{p}^{H2O}$ is determined by ratio of water vapour volume υ^{H2O} with flue gas mixture volume υ^{W}. Therefore, the physical water constitutes $1.33w(1-w)$ moles or volumetric parts in wood. Using (3), relative water vapour pressure can be calculated as:

$$\begin{gathered} \bar{p}^{H2O} = p^{H2O}/P = \upsilon^{H2O}/\upsilon^{W} = [0.72 + (24/\mu^{H2O} + 1.03\lambda\varphi/0.21]/ \\ /[1 + 0.72 + (24/\mu^{H2O})w/(1-w) + 1.03(\lambda-1) + 1.03\lambda(3.76 - \varphi/0.21) + 1.03\lambda\varphi/0.21], \end{gathered} \tag{2}$$

where flue gas volume is:

$$\begin{gathered} \upsilon^{W} = 1 + 0.72 + (24/18)w/(1-w) + 1.03(\lambda - 1) + \\ +1.03\lambda(3.76 - \varphi/0.21) + 1.03\lambda\varphi/0.21. \end{gathered} \tag{3}$$

Relative partial pressure of the component is a proportional dimension, which indicates the component pressure raised at the particular mixture pressure P. When mixture pressure P is known, partial pressure of each component p^n can be calculated by multiplying the P by the $\bar{p}^n$ or $\bar{v}^n$.

The condensation starting point temperature of vapour on vapour partial pressure p^{H2O} and not on its proportion value $\bar{p}^{H2O}$. Consequently, the said temperature (or the dew point temperature t_s), can vary even when the vapour concentration in mixture is constant. For example, when atmospheric pressure rises, vapour condensation starting point t_s becomes greater.

The temperature of the dew point t_s can be calculated via mathematical function $t_s = f(p^{H2O})$, the expression of which depends on mathematical approximation method. If logarithmic approximation is used, the expression is:

$$t_s = 243.5 \times ln(p^{H2O}/6.11 \times 10^{-3})/[17.67 - ln(p^{H2O}/6.11 \times 10^{-3})]. \tag{4}$$

The pressure and temperature dimensions are bar and °C, respectively.

Using (1) expression, partial pressures p^n and volumetric proportions of other flue gas components with the mixture pressure P of flue gas flow.

On the other hand, for calculation of an energy parameters of the flue gas (enthalpy, heat capacity, condensing heat) and fuel (its caloric value and supply quantity), mass proportions of components are needed but not the volumetric ones. Therefore, it is more usable to have calculation methodology based on mass proportions. In addition, since the mass parts of the components must include the physical water amount, the formulae have to be expressed considering the mass of wet wood, but not of its dry part. The wood moister changes the calorific value of the fuel, so the mass quantity of its demand for the same heat capacity changes as well.

The molar parts in chemical reaction (1) is changing by the ratio of $(1 - w)\mu^n/24$, where μ^n are the kilomole mass of each (n) component (nitrogen, oxygen, carbon dioxide or water vapour), the number 24 means the kilomole mass of reduced chemical formula of the wood. Applying the correctional ratio, the equation of combustion chemical reaction, based on mass unit of wet wood, is:

$$\begin{gathered}(1 - w) + w + 1.03\lambda(1 - w)[(\mu^{O2}/24) + (3.76 - \varphi/0.21)(\mu^{N2}/24) + (\varphi/0.21)(\mu^{H2O}/24)] \rightarrow \\ \rightarrow (1 - w)(\mu^{CO2}/24) + 0.72(1 - w)(\mu^{H2O}/24) + w + 1.03(\lambda - 1)(1 - w)(\mu^{O2}/24) + \\ +1.03\lambda(1 - w)[(3.76 - \varphi/0.21)(\mu^{N2}/24) + \varphi/0.21(\mu^{H2O}/24)]. \end{gathered} \tag{5}$$

Using the equation (5), the following equations can be written for mass m^ncalculation of each components n, as well as for relative mass $\bar{m}^n$calculation, based on the flue gas mass, in case when one-kilogram wet woodfuel is burned. For example, when one kilogram of wood with w moisture is burned using air excess ratio λ, water vapour mass in flue gas is calculated by the equation:

$$m^{H2O} = 0.72(1 - w)(\mu^{H2O}/24) + w + 1.03\lambda(1 - w)(\varphi/0.21)(\mu^{H2O}/24). \tag{6}$$

The mass of flue gas when one kilogram of wet wood is burned:

$$\begin{gathered} m^W = (1 - w)(\mu^{CO2}/24) + 0.72(1 - w)(\mu^{H2O}/24) + w + 1.03(\lambda - 1)(1 - w)(\mu^{O2}/24) + \\ +1.03\lambda(1 - w)[(3.76 - \varphi/0.21)(\mu^{N2}/24) + (\varphi/0.21)(\mu^{H2O}/24)]. \end{gathered} \tag{7}$$

Water vapour mass concentration (or relative mass) in mixture of flue gas is the following ratio of the two former parameters:

.

$$\bar{m}^{H2O} = m^{H2O}/m^W. \tag{8}$$

Consequently, other components mass concentrations can be calculated as follows:

$$\bar{m}^{CO2} = (1 - w)(\mu^{CO2}/24)/m^W. \tag{9}$$

$$\bar{m}^{O2} = 1.03(\lambda - 1)(1 - w)(\mu^{O2}/24)/m^W. \tag{10}$$

$$\bar{m}^{N2} = 1.03\lambda(1-w)[(3.76-\varphi/0.21)(\mu^{N2}/24)]/m^{W}. \tag{11}$$

Expressions of volumetric concentrations of components $\bar{\upsilon}^{n}$ can be evaluated using the equation of chemical reaction (1). The relation of the vapour volumetric concentration $\bar{\upsilon}^{H2O}$ (see eq. (4) is derived from eq. (3). According to (3) equation it is possible to write down the following equations:

$$\bar{\upsilon}^{CO2} = 1/\upsilon^{W}. \tag{12}$$

$$\bar{\upsilon}^{O2} = 1.03(1-\lambda)/\upsilon^{W}. \tag{13}$$

.

$$\bar{\upsilon}^{N2} = 1.03\lambda(3.76-\varphi/0.21)/\upsilon^{W}. \tag{14}$$

3. CALCULATION ALGORITHM FOR THE FLUE GAS MIXTURE PROPERTIES

Primary results are calculated using air excess ratio (λ) values as 1.2 1.5 and 1.8 and fuel moisture values (w) 45%, 50%, 55% and 60% (seen as the starting parameters of the mixture). The calculations are carried out via the algorithm shown below.

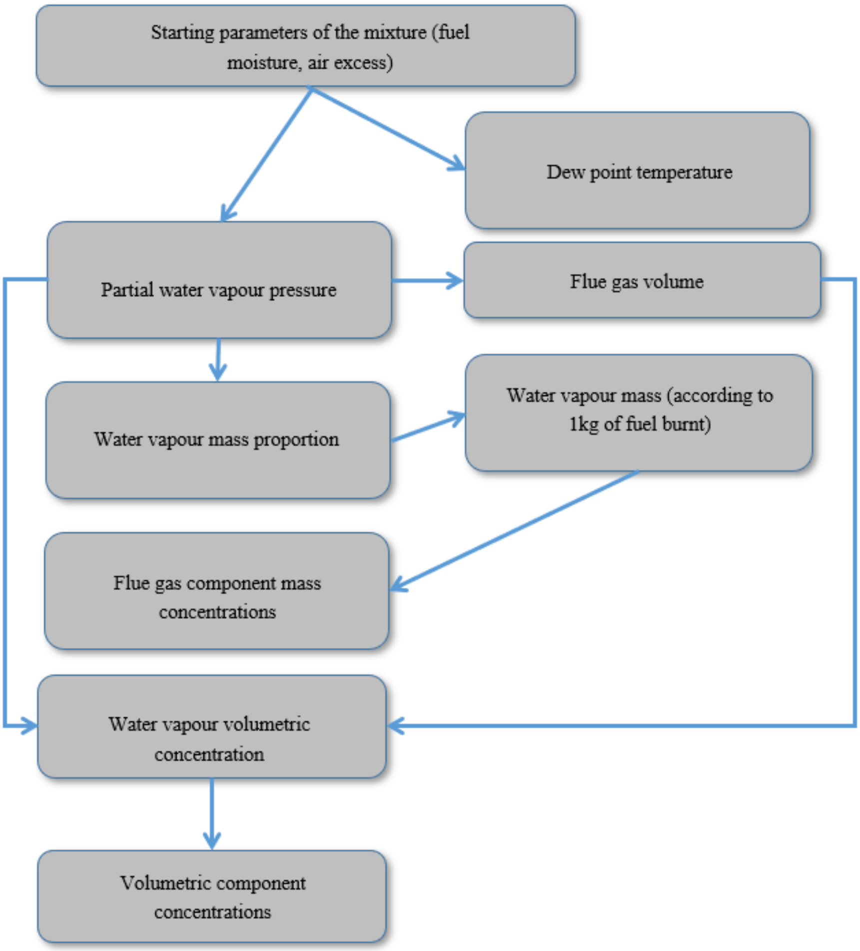

Fig. 1. Calculation algorithm

With starting parameters, first step is to predict the dew point temperature of the flue gas mixture, firstly calculating relative water vapour pressure eq. (2) and flue gas volume eq. (3), which are both derived from equation (1). Water vapour volumetric concentration is calculated with relative water vapour pressure multiplied by flue gas volume (2).

In order to calculate mass component concentrations, equation (5) has to be used, which allows to derive relative water vapour mass concentration (6). Mass concentrations then have to be calculated when 1kg of fuel is combusted, by using (7) equation (in order to have mass proportion).

Mass component concentrations are calculated using (9) (10) and (11) equations, additionally, volumetric concentrations are calculated with (12) (13) and (14) equations.

The algorithm process diagram is shown in Fig. 1, calculations were carried out using MS Excel and PTC Mathcad software.

4. PRIMARY CALCULATION RESULTS AND DISCUSSION

The algorithm has significant value in predicting the flue gas constituents as mass and volumetric parts of the flue gas mixture. The major problem is that the similar studies tend to account for wood-fuel burning emissions [8, 9], or concentrates solely on the connection between wood fuel moisture levels and heat recovery [5–7] and technological approaches [1–4, 7]. The issue is that it is difficult to describe the low grade heat value only using emissions, making heat transfer hardly predictable.

The aim of this study is to present the algorithm for crude flue gas mixture component evaluation, which will lead to further calculations of flue gas heat values and will give the possibility to approach the issue in a way that could allow greater waste heat management. The results of the calculation algorithm (prediction of crude CO_2, H_2O, N_2, O_2 components) is shown in the table below.

According to data in Table 1, water vapour concentration in flue gasses increases with increasing fuel moisture. Higher air excess ratio impacts contrarily: the more air is blown to burning chamber, the lower water vapour proportion is. At the same time, the concentration of O_2 and N_2 gases increases, that is quite naturally, because air excess ratio is valuated under mass unit of the dry woodfuel part.

Table 1. Flue gas mixture component volumetric and mass concentrations

part	Air excess ratio	Volumetric concentration, $\overline{\upsilon}$				Mass concentration, $\overline{m}$				t_s
		Water vapour	Carbon dioxide	Oxygen	Nitrogen	Water vapour	Carbon dioxide	Oxygen	Nitrogen	Dew point temperat. oC
0.4	1.2	0.219	0.134	0.028	0.620	0.140	0.210	0.031	0.619	61.8
	1.5	0.185	0.112	0.058	0.646	0.117	0.175	0.065	0.643	58.2
	1.8	0.159	0.096	0.079	0.667	0.100	0.150	0.090	0.661	54.9
0.45	1.2	0.241	0.131	0.027	0.602	0.155	0.206	0.031	0.608	63.9
	1.5	0.203	0.110	0.056	0.632	0.129	0.172	0.064	0.634	60.1
	1.8	0.175	0.094	0.078	0.653	0.111	0.148	0.089	0.653	57.1
0.5	1.2	0.264	0.127	0.026	0.584	0.172	0.202	0.030	0.596	65.9
	1.5	0. 223	0.107	0.055	0.615	0.145	0.169	0.063	0.623	62.2
	1.8	0.194	0.092	0.076	0.640	0.124	0.146	0.087	0.643	59.1
0.55	1.2	0.291	0.122	0.025	0.563	0.191	0.197	0.030	0.582	68.1
	1.5	0.247	0.103	0.053	0.596	0.161	0.166	0.062	0.611	64.5
	1.8	0.215	0.090	0.074	0.621	0.139	0.143	0.086	0.632	61.5
0.6	1.2	0.321	0.117	0.024	0.538	0.214	0.192	0.029	0.565	70.4
	1.5	0.275	0.100	0.051	0.574	0.182	0.162	0.061	0.596	66.9
	1.8	0.241	0.087	0.072	0.601	0.157	0.140	0.084	0.619	63.9

Using the results seen in the Table 1, component concentration changes and dew point temperatures are drawn in graphs.

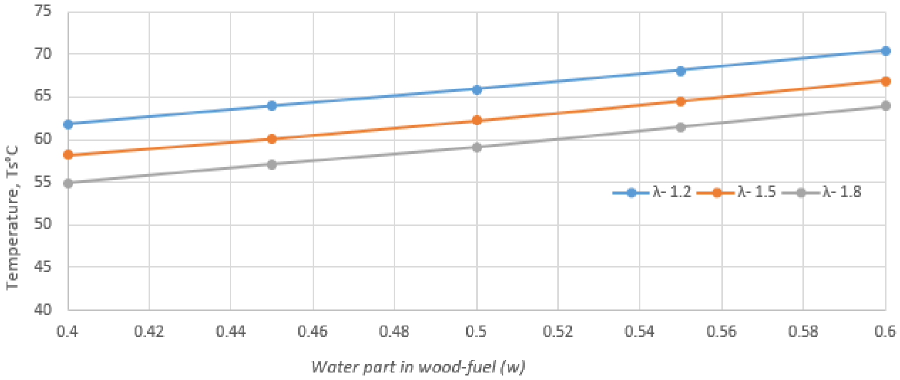

Fig. 2. Dew point temperature

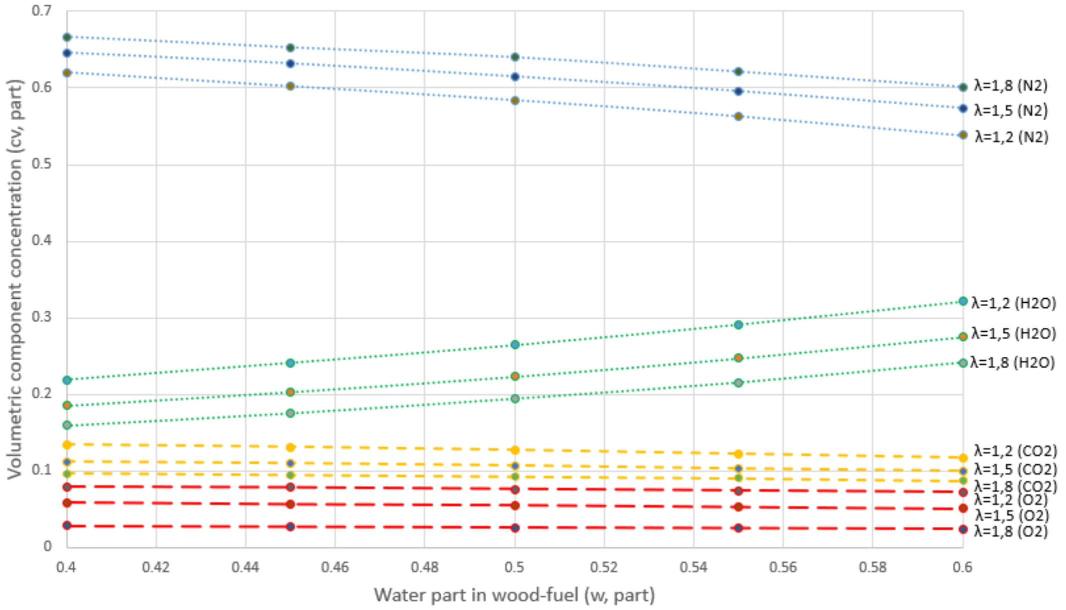

Fig. 3. Volumetric component concentrations

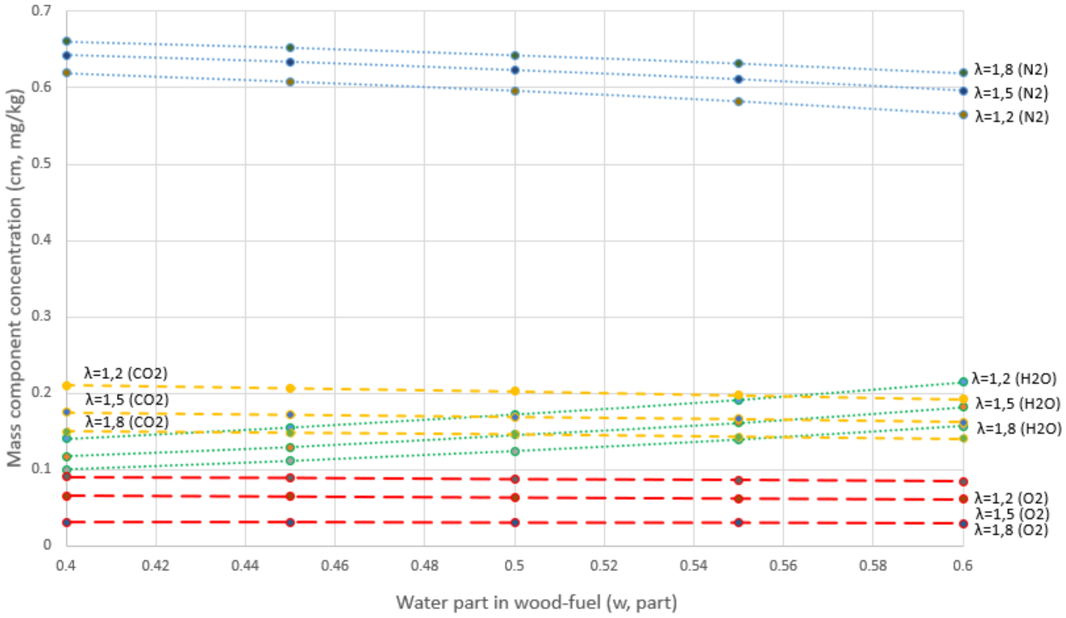

Fig. 4. Mass component concentrations

Fig. 2 shows the nature of the dew point temperature of the flue gas. It is visible that with increasing air excess value dew point temperature decreases (i.e. increasing air excess from 1.2 up to 1.8, dew point temperature drops by approx. 7 °C in every case). However, dew point temperatures tend to increase with more moisture in the biofuel. For example fuel moisture being at 40% and air excess at 1.2, determine dew point temperature at 61.8 °C, therefore if fuel moisture level rises up to 60% (air excess const.) dew point temperature of the flue gas becomes 70.4 °C. The same characteristics can be observed with additional parameters.

Figs. 3 and 4 displays the characteristics of flue gas component concentrations (both mass and volumetric) regarding the fuel moisture and air excess values. Volumetric value ranges are visible in Fig. 3, most notable changes are of nitrogen, which volumetric part increases with increasing air excess value and water vapour which volumetric part decreases with increasing air excess value. However with an increase of fuel moisture, nitrogen tends to drop down, while water vapour volumetric concentration rises. Other component volumetric and mass parts (CO_2, O_2) changes appears to be not significant. Mass concentration changes (Fig. 4) maintain same attributions.

5. CONCLUSIONS

The main studies regarding the issue of harnessing the low-grade heat energy from the low temperature flue gas do not provide enough information on the subject of calculation. Provided studies show only emission values or concentrate solely on technological process (incorporating heat pumps) of flue gas waste heat management. There is little to no information about flue gas component concentrations calculation, which is crucial in evaluating the possibility of predicting flue gas low-grade heat energy recovery and design required heat exchanging equipment. This study focused on calculation algorithm which gives out the required parameters for further low-grade heat capacity evaluation.

The calculation algorithm was produced in order to evaluate flue gas component concentrations from wood fuel using several cases of different primary parameters: wood fuel moisture (40, 45, 50, 55 and 60%) and air excess value (varying from 1.2, 1.5 and 1.8). The concentration (mass and volumetric) values of H_2O, CO_2, N_2 and O_2 were examined at each starting parameter instance.

The provided results in the study, assist in finding that dew point temperature, greatly depend on fuel moisture part and air excess value. It was observed that dew point temperature rises together with higher moisture level and bigger air excess value, both instances provide characteristic of linear form: when fuel moisture is at 40% ($\lambda = 1.2$), the dew point temperature is 61.8.°C, and with fuel moisture of 60% ($\lambda = 1.2$) dew point temperature reaches 70.4.°C. Similarly taking bigger air excess values (1.5 and 1.8) the smallest dew point temperatures becomes 58.2 °C and 54.9 °C respectively, and the biggest 66.9 °C and 63.9 °C respectively within starting point boundaries.

Component mass and volumetric concentration values both follow similar scale trends. Water vapour part grows with bigger moisture level (from 0.219 volumetric parts to 0.321 at 40% and 60% (when $\lambda = 1.2$) respectively), and bigger air excess value leads to smaller water vapour part in flue gases – decreasing from 0.219 to 0.159 volumetric parts at 40% fuel moisture and λ values of 1.2 and 1.8 respectively (same trends are visible at different fuel moisture points). Nitrogen reacts oppositely to water vapour – it decreases with bigger fuel moisture (0.620 to 0.538 at 40% and 60% moisture) and greater air excess value tends to increase Nitrogen part in flue gas mixture (from 0.620 to 0.667 volumetric parts at 40% moisture and λ values from 1.2 to 1.8, similar trends emerge with other starting point parameters). O_2 and CO_2 gases remain relatively unaffected. All obtained numerical values of flue gas components will be used in further studies for gas energetic parameters- enthalpy and heat transfer calculations.

REFERENCES

1. LU Y., BAO H., YUAN Y., WANG Y., WANG L., ROSKILLY A.P. Optimization of a novel resorption cogeneration using mass and heat recovery. *Energy Procedia*, No. 61, 2014, p. 1103-1106.
2. DONNELLAN Ph., CRONIN K., BYME E. Recycling waste heat energy using vapour absorption heat transformers: A review. *Renewable and Sustainable energy*, No. 42, 2015, p. 1290-1304.
3. WANG L., ZIEGLER F., ROSKILLY A.P., WANG R., WANG Y. A resorption cycle for cogeneration of electricity and refrigeration. *Applied Energy*, No. 106, 2013, p. 56-64.
4. KUMAR M., DAS R.K. Experimental analysis of absorption refrigeration system driven by waste heat of diesel engine exhaust. Thermal Science, 2017, p. 3-3.
5. HEBENSTREIT B., SCHENTZINGER R., OHNMACHT R., HOFTBERGER E., LUNGREN J., HASLINGER W., TOFFOLO A. Techno-economic study of a heat pump enhanced flue gas heat recovery for biomass boilers. *Biomass and bioenergy*, No. 71, 2014, p. 12-22.
6. HEBENSTREIT B., SCHENTZINGER R., OHNMACHT R., HOFTBERGER E., HASLINGER W. Efficiency optimization of biomass boilers by a combined condensation-heat pump-system. Proceedings of ECOS, 2011, Novi Sad, Serbia, July 4-7.
7. DAGILIS V., VAITKUS L., BALČIUS A., GUDZINSKAS J., LUKOŠEVIČIUS V. Low grade heat recovery system for woodfuel cogeneration plant using water vapour regeneration. *Thermal Science*, 2018, p. 81-81. https://doi.org/10.2298/TSCI171020081D
8. NUSSBAUMER T. Combustion and Co-combustion of biomass: Fundamentals, Technologies, and Primary Measures for Emission Reduction. *Energy and Fuels*, No. 17 2003: pp. 1510-1521.
9. MYLLÄRI F., KARJALAINEN P., TAIPALE R, AALTO P., HÄYRINEN A., RAUTIAINEN J., PIRJOLA L., HILLAMO R., KESKINEN J., RÖNKKÖ T,. Physical and chemical characteristics of flue-gas particles in a large pulverized fuel-fired power plant boiler during co-combustion of coal and wood pellets. *Combustion and Flame*, Vol. 176, 2017, p 554-566. https://doi.org/10.1016/j.combustflame.2016.10.027

CYSENI 2019, May 23-24, Kaunas, Lithuania
ISSN 1822-7554, www.cyseni.com

LOAD FREQUENCY CONTROL IN POWER SYSTEM USING ADVANCED CONTROL SCHEMES

P. Cicėnas
Lithuanian Energy Institute
Breslaujos str. 3, LT-44403 – Lithuania
Email: paulius.cicenas@lei.lt

ABSTRACT

The power system is changing and inertia of the power system constantly decreasing due to growing power electronics devices in Transmission System. Frequency stability is difficult to be maintained. Transmission System Operator (TSO) shall use different solution to improve frequency control and ensure stability of the power system. It can be done by increasing the spinning reserve capacity, short circuit of the system by installing synchronous condensers and improving Load Frequency Control (LFC). Advanced LFC help stabilize frequency deviations in power system. Two control loops are used stabilize the frequency. They are primary frequency control loop and secondary, called Load Frequency Control. This Paper is overview of the classical and advanced control schemes of Load Frequency Controllers and demonstrate the ability of the different LFC control schemes in damping the frequency oscillations. Approaches are compared against different controllers and control methods in the literature; Proportional – Integral (PI), Proportional – Integral – derivative (PID), fuzzy PID, adaptive and self-tuning control, optimal control, variable structure control, etc. LFC methods are presented in the text.

Keywords: Load Frequency Control, PID Control, sliding mode controller, Area control error, Fuzzy systems, Power systems

1. INTRODUCTION

Load Frequency Control (LFC) system is designed to maintain the frequency in acceptable range defined by each synchronous zone and restore the active power interchange on tie-lines between different Power Systems. In order to understand design of the control system two variables needs to be explained - control area and area control error.

1. Control area (CA): “A power system, a part of a system, or a combination of systems to which a common generation control scheme is applied.”(IEEE Standards Committee 1991 def. 103)

2. Area control error (ACE): “The frequency deviation of an isolated power system consisting of a single control area is the area control error. The area control error of a control area on an interconnected system is the net interchange minus the biased scheduled net interchange.” (IEEE Standards Committee 1991 def. 124)

Two control loops are used stabilize the frequency. They are primary frequency control loop controls the speed of the governor and secondary control loop eleminates the error in frequency and regulates active power balance between interconnected Power Systems.

Figure 1 shows that this paper highlights tree main LFC control topics: Classical Control, Adaptive Control and Variable Structure methods.

Classical and advanced control schemes of Load Frequency Controllers and demonstrate the ability of the different LFC control schemes in damping the frequency oscillations will be presented further in this paper.

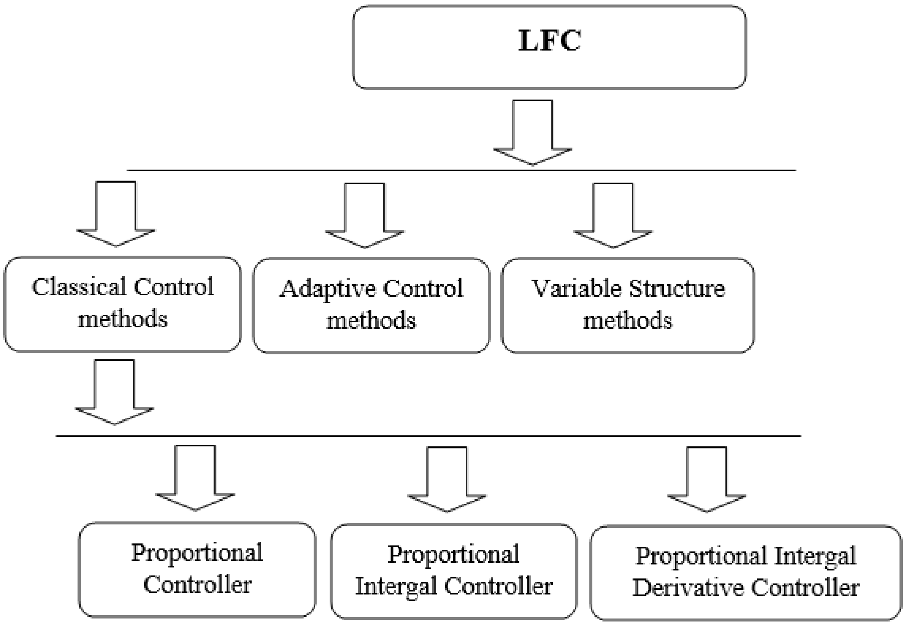

Fig. 1. Classification of LFC control methods

2. CLASSICAL CONTROL METHODS

Conventional controllers are linear controller, as they work on the fixed parameters values. These controllers are the Proportional (P), the Proportional Integral (PI) and the Proportional Integral Derivative (PID) controllers.

2.1. Proportional controller

Proportional (P) controller output is proportional to the error signal, which is the difference between the setpoint and the process variable. In other words, the output of a proportional controller is the multiplication product of the error signal and the proportional gain.

This can be mathematically expressed [1]:

$$P_{out} = K_p e(t) + p0\,, \tag{1}$$

where: p0 – controller output with zero error; P_{out} – output of the proportional controller; K_p – proportional gain; e(t) – process error at time t.

2.2. Proportional Integral controller

Proportional Integral (PI) controller is a feedback controller based on weighted sum of the error and the integral of that error. The inputs to the PI controller for the two-area bilateral market structure are the ACE of the respective areas. Equation (2) expresses the controller output [2]

$$U_{PI} = K_p ACE_i + K_i \int_0^t ACE_i dt\,, \tag{2}$$

where: K_p – the proportional gain; K_i – the integral gain.

2.3. Proportional Integral Derivative controller

Proportional Integral Derivative (PID) control scheme is named after its three correcting terms, whose sum conclude the controlled variable (MV). The proportional, integral, and derivative terms are summed to calculate the output of the PID controller, defining u(t) as the controller output. The derivative part can also be interpreted as prediction by linear extrapolation. In practical terms it applies accurate and responsive correction to a control function.

The overall control function can be expressed [3] mathematically as

$$u(t) = MV(t) = K_p e(t) + K_i \int_0^t e(\tau) d\tau + K_d \frac{de(t)}{dt}, \tag{3}$$

where: K_p – is the proportional gain; K_i – is the integral gain; K_d – is the derivative gain; e(t) – process error at time t; t – is the time (the present); τ – is the variable of integration.

Traditional LFC control approaches are based on classical controllers applied to the governor to minimize ACE in Power Systems and stabilize the frequency deviations. Classical methods was proposed for LFC [4–10]. PI controllers are widely used for LFC due to their ease of operation, performance and simplicity in execution.

The described method in [11] shows ability of each controller to control frequency in each area of its own load variation by related area control center in which no interaction between frequency and tie-line power is considered.

In order to control the frequency and tie-line power flow using communication links, decentralized proportional-integral control design for power system load – frequency regulation with communication delays. In this methodology, the PI-based LFC problem is reduced to a static output feedback control synthesis for a multiple-delay system [10].

Dual mode control is applied in the proportional-integral (PI) controller [8]. Proportional mode is made active when the rate of change of the error is larger than a specified limit otherwise switched to the integral mode. PI control for hydropower system [9] have been proposed. LFC distribution algorithm based on two independent distribution criteria: economical and technical. Economical part is based on cost-efficiency power redistribution taking into account plants efficiency curves and their regulating ranges. Technical part is considering the actual operating point and regulating limits.

PI control for micro-grid systems, which can operate in two systems states: connected to the grid and island mode is presented in [12]. This paper introduced a novel LFC control scheme for micro-grid wehre PI control was introduced into control flow and first-order inertia link have been added into proposed LFC control strategy.

Unified PID tuning method [7] is used for LFC. The author presented a unified method to desing and tune PID load frequency controller for Power Systems with non-reheat, reheat and hydro turbines. This method is based on internal model control method and adapted for the closed-loop systems. The method have been extended to multi-area Power Systems.

The classical control methods are well-investigated for LFC in Power Systems. However, there are several drawbacks that need to be handled:

- robustness against parametric and nonparametric uncertainties need to be clearly-solved;
- approaches are not suitable for large-scale power systems where the total number of state variables is large;
- the integral of the control error are used as the control signal;
- poor dynamic performance.

3. ADAPTIVE AND VARIABLE STRUCTURE METHODS

The power system is changing and inertia of the power system constantly decreasing due to growing power electronics devices and renewable energy in Transmission System. This requires on-line regulation to interact with the changing energy in real time. The task of the adaptive control technique is to make the process under control less sensitive to changes in plant parameters and not modelled plant dynamics due to the nonlinearity of the power system elements.

Adaptive frequency regulation strategy based integral sliding mode control described in the paper [13]. Presented simulation results shows competitive performance and adaptive ability of the smart frequency control in the non-linear power system. Adaptive learning control method and adaptive dynamic programing have been used in order to maintain the frequency within the limits and solve the problems from the point of the nonlinear control scheme. The nonlinear sliding mode regulator [10] can be derived as

$$u(t) = -(c_1 B)^{-1}(c_1 Ax(t) + c_2 x(t) + \eta sat(s)), \tag{4}$$

where: x(t) is the state vector; u(t) is the control vector; A, B matrixes derived from the frequency dynamic equations of the grid; η – sliding mode gain value; c_1 and c_2 are the appropriate vectors matched to x(t); η sat(s) – depresse the power fluctuations in the grid.

Variable structure control (VSC) is the controller design such that the state trajectory is trapped on a switching surface and remains on it. In this case, the system is called in the sliding mode. The main mode of VSC operation is sliding mode control (SMC). During the sliding mode, the system behavior has invariance property which is independent of matched uncertainty [14, 15].

In the paper [15] considered a class of uncertain power system to show that designed variable structure controller is robust and capable of effectively controlling frequency in such power system.

Intelligent load frequency control approach for a power system with three thermal-thermal-hydro control areas using adaptive neuro fuzzy (ANFIS) technique have been introdused in the paper [16]. Where PID, Fuzzy and ANFIS based controller for Load frequency control has been discussed. As the input for ANFIS is the error and derivative of error in the frequency. Therefore ANFIS is capable to generate the parameters to be used in the FIS controller of type-sugeno. Simulations presented in the [16] shows that controller (Fig. 2) based on neuro-fuzzy control methodology is faster and accurate as compared to conventionally used PI and PID controllers. Controller scheme of the power plant system with three control (thermal-thermal-hydro) areas are presented in Figure 2. It implies that the each one of the controlling areas shall contribute to frequency control and should take care of their own their exchange [16]. In this control, the error of each area is kept a linear function frequency error and tie line power error [17].

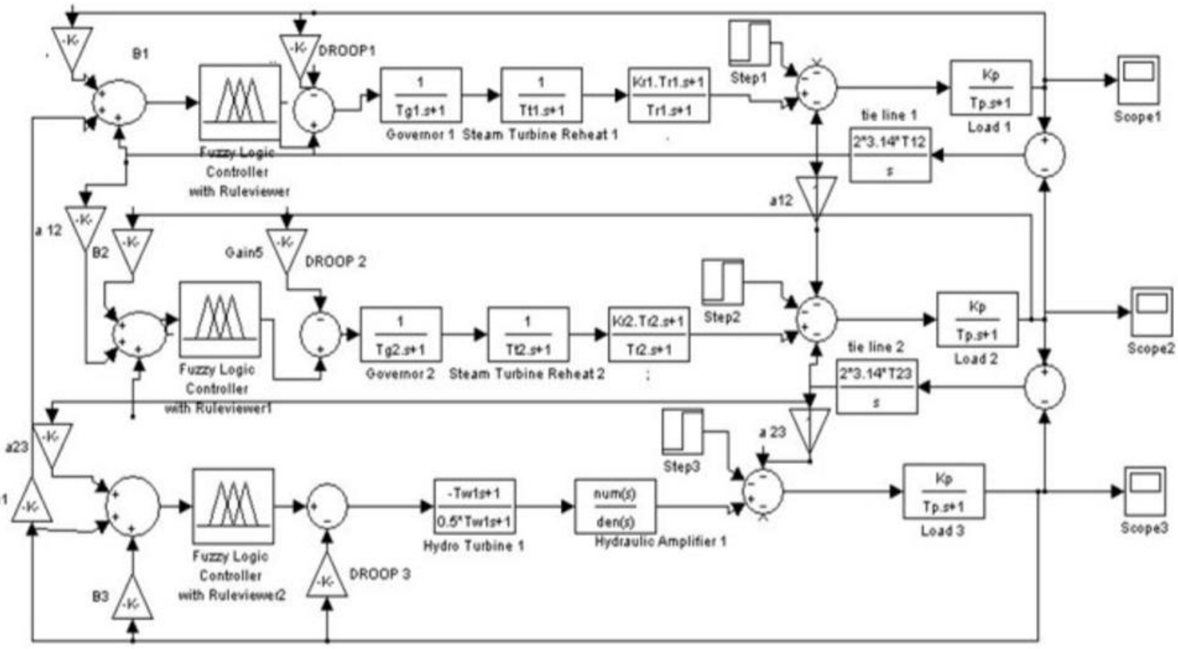

Fig. 2. Model for three area power system using ANFIS based controller [16]

L1 adaptive controller has been implemented and tested in LFC in order to recover frequency deviation to its balance at zero [18]. Simulation results prove that L1 adaptive controller is able deal with adaptation and estimation of uncertainties. The method ensure the stable transient performance and control frequency oscillations without frequency deviation after transient period. L1 Adaptive control desing used in simulation [18] presented in Figure 3.

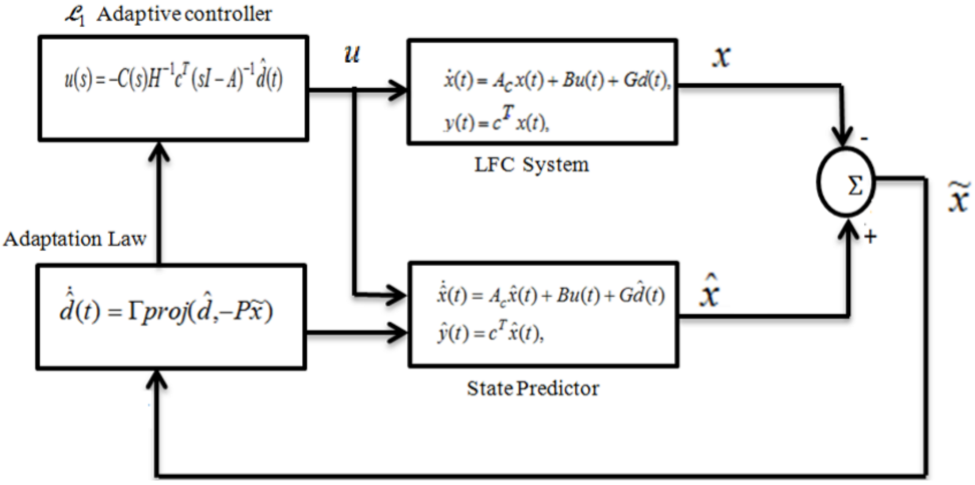

Fig. 3. Close-loop L1 Adaptive scheme

Control scheme shown in Figure 3 consist of four main control blocks: 1. Uncertain System in L1 adaptive form, 2. State Predictor; 3. Low-Pass Filter and Control Law, 4. Adaptive Law.

This method has two main advantages: the methos does not depend on gain scheduling on control parameters; it does not depend on high gain feedback [19].

An adaptive fuzzy controller for LFC have been proposed in the paper [20]. This controller has improved lerning loop with FCL rules tuned online for different operating conditions. This controll logic has two inputs (ACE and ΔACE) and one output (U_f). This method is capible to run self-ajustment. This function alows to reach better frequency control in compare with traditionall controllers, like integral or adaptive.

However, there are several drawbacks and advantiges:

- variable structure control is robust for the uncertainty;
- maximum overshoot and the settling time of ANFIS based controller are lesser when compared to the conventional controllers;
- faster than the conventional controller and have improved dynamic response;
- conventional fuzzy controllers are not able to perform self-tuning;
- LFC controllers using fuzzy logic are capable to provide better performance of controlling the frequency.

4. CONCLUSIONS

This paper presented various LFC methods focused on the recent researches and intends to be useful reference of control techniques in the LFC problem. The paper is focused on various LFC strategies reported in the literature and their features and disadvantages. In conclution, I can say that there are no rules as to when a particular controll method is better to use in order to solve LFC problems.

Currently in practice most TSO in CE and IPS/UPS does not require advanced control logic of LFC. Most generators are equipped with LFC sytems using PI or PID controllers. These LFC with traditional inertia ensure of the system frequency within acceptable range. Taking into account that renewable energy sources (RES) going to increase more and more in the Power system. As the result of RES increase, an inertia of the power system drastically decrese as well as an ability of the Power System to restore the frequency. Countermeasures including advanced LFC systems will be needed to increase the relliabillity of the Power System.

REFERENCES

[1] Bela G. Liptak, Instrumental engineers handbook: process cntrol. United State of America, 1999, 0-8019-8242-1.

[2] K. Smiriti Rao, Ravi Mishra, Comparative study of P, PI and PID controler for speed control of VSI-fed induction motor. IJEDR, 2014.

[3] K.J. Åström and T. Hägglund, PID Controllers: Theory, Design, and Tuning. Research Triangle Park, NC: Instrum. Soc. Amer., 1995.

[4] Jagatheesan, K.; Anand, B.; Dey, N.; Ashour, A.S. Artificial intelligence in performance analysis of load frequency control in thermal-wind-hydro power systems. *Int. J. Adv. Comput. Sci. Appl,*. 2015, 6, p. 203–212.

[5] Jagatheesan, K.; Anand, B.; Dey, N. Evolutionary algorithm based LFC of single area thermal power system with different steam configurations and non-linearity. *Information Systems Design and Intelligent Applications*; Berlin/Heidelberg, Germany, 2016; p. 185–194.

[6] Khooban, M.H.; Niknam, T. A new intelligent online fuzzy tuning approach for multi-area load frequency control: Self Adaptive Modified Bat Algorithm. *Int. J. Electr. Power Energy Syst.* 2015, p. 254–261.

[7] Tan, W. Unified tuning of PID load frequency controller for power systems via IMC. *IEEETrans. Power Syst*. 2010, p. 341–350.

[8] Chatterjee, K. Design of dual mode PI controller for load frequency control. *Int.J.Emerg. Electr. Power Syst.* 2011, 11.

[9] Vrdoljak, K.; Peric´, N.; Šepac, D. Optimal distribution of load-frequency control signal to hydro power plants. *In Proceedings of the 2010 IEEE International Symposium on Industrial Electronics (ISIE)*, Bari, Italy, 4–7 July 2010, p. 286–291.

[10] Bevrani, H.; Hiyama, T. On load-frequency regulation with time delays: Design and real-time implementation. *IEEE Trans. Energy Convers*. 2009, p. 292–300.

[11] Quazza, G. Noninteracting controls of interconnected electric power systems. *IEEE Trans. Power Appar. Syst.* 1966, p. 727–741.

[12] Zhao, H.; Zhu, G.; Xu, C. A novel frequency control strategy of micro-source based on the secondary frequency regulation of power system. *In Proceedings of the 2012 China International Conference on Electricity Distribution (CICED)*, Shanghai, China, 10–14 September 2012; p. 1–6.

[13] Chao Xu Mu, Jian Xun Jin, Wei Xu. Adaptive Frequency Regulation Strategy Based Integral Sliding Mode Control for Smart Grid with Renewable Energy Sources. *Proceedings of 2015 IEEE International Conference on Applied Superconductivity and Electromagnetic Devices*, Shanghai, China, November 20–23, 2015, p. 391–392.

[14] Z.M.Al-Hamouz,H.N.Al-Duwaish. A New Load Frequency Variable Structure Controller Using Genetic Algorithms. *Electric Power Systems Research*, Vol. 55, 2000, p.1–6.

[15] Mi Yang, Pan Da, Wu Xiao, Jing yuanwei. The design of load frequency variable structure controller for power systems. *24th Chinese Control and Decision Conference (CCDC)*, Taiyuan, China, 23–25 May 2012, p. 1–3.

[16] Varsha Kusfuzzy Kushwaha, Kamlesh Pandey, Sumeet Sehrawar, Devashish Sharma. Adaptive Neuro – Fuzzy based Load Frequency Controller for Three Area Inter – Connected Hydro – Thermal Power System. *2016 Second International Innovative Applications of Computational Intelligence on Power, Energy and Controls with their Impact on Humanity (CIPECH)*, Ghaziabad, India, 18–19 Nov. 2016,

[17] Kothari, D.P. and Nagrath (2012), Modern Power System Analysis, Tata Macgraw Hiil, Fourth Edition.

[18] Ayman Alhejji, L1 Adaptive Load Frequency Control of Single-Area Electrical Power System. *2017 4th International Conference on Control, Decision and Information Technologies (CoDIT)*, Barcelona, Spain, 5–7 April 2017, p. 595–598.

[19] N. Hovakimyan, C. Cao, L1 Adaptive Control Theory: Guaranteed Robustness with Fast Adaptation, SIAM, 2010.

[20] A.Anil Kumar, Dr.N.V.Srikanth, Load frequency control for diverse sources of interconnected two area power system: an adaptive fuzzy approach, International Conference on Control, Computing, Communication and Materials (ICCCCM) IEEE, 2016.

CYSENI 2019, May 23-24, Kaunas, Lithuania
ISSN 1822-7554, www.cyseni.com

INDUCTANCE SELECTION CRITERIA AND DESIGN STEPS FOR POWER ELECTRONICS APPLICATIONS

M. E. Şahin
Department of Electrical and Electronics Engineering, RTE University,
53100 Rize – Turkey
Email: mustafaerginsahin@yahoo.com

H. I. Okumuş
Department of Electrical and Electronics Engineering, Karadeniz Technical University,
61080, Ortahisar, Trabzon – Turkey

ABSTRACT

The power electronics circuits are indispensable devices today for renewable energy applications and for storing energy. One of the main components of this power electronic circuits is the inductance. The inductance working as a live heart, store the energy and pumps the energy from the source to the load in converters, and supply continuously the current of the circuit to the load. The energy efficiency in the system depends on the inductance efficiency. So, a well-designed inductance is very important in order to operate the converter in continuous mode so the current flow is uninterruptible. In this paper, a suitable inductance selection criteria for the converters are investigated from the literature and solved with electromagnetics equations. Also, the design steps of an inductance including necessary calculations are shown with an example application. The cores and wires effect to the inductance efficiency is also investigated in this paper. An inductance using Ferrite core and Litz wire is proposed and designed experimentally for a converter circuit. Measurements to determine the inductance value was shown. Also, the inductance current variations for higher frequencies are investigated, and used in the converter is shown.

Keywords: Inductance selection and design, Ferrite cores, Litz wire, Inductance measurement, Skin effect in inductance, Inductance efficiency, Power electronics converters

1. INTRODUCTION

The energy harvesting from renewables, and also using it more efficient is an important topic for the scientific researchers today. The power electronics circuits and devices are the main parts for renewable energy applications and also to be storable the energy efficiently. The scientific researchers are focused on design and control of the converters, and also increases the efficiency of the power electronic circuit's components.

One of the main components of the power electronics circuits is inductances. The electrical energy is stored in the inductance temporarily in switch mode power converters. The inductance, which is like the heart in a human which storage and pump the blood, the storage the energy temporarily and pumps the energy from the source to load in switch mode converters, and supply continuously and the circuit current on the load [1, 2].

The energy efficiency of converters depends of course on the inductance efficiency. So a well-designed inductance is very important for the converter in continuous mode operation and continues the current to flow uninterrupted. The inductance value determines how to operate the converter under load condition. There is a limit value for the converter to work in continuous and non-continuous mode. The inductance limit value is calculated for this criterion [3–5]. On the other hand, the switching frequency of the converter is related directly to the inductance size. To reduce the inductance size the switching frequency can be selected to be more than 1 MHz in some applications.

Inductance design is an important research matter. It is possible to find more documents and papers about the calculation process and most of them are belong MAGNETICS Trade Company and the other corporations [6, 8, 12, 13]. Also, it is possible to find software tools to calculate and give inductance values [18]. These studies are trying to generalize the method in a simple way. The first step in the design is to select a core for a suitable geometry and also materials [14]. An inductance with powder, sheet and ferrite cores made from different materials and Litz wire for winding are proposed and designed experimentally for a converter circuit [15, 17]. These special designs aim to reduce all the losses in the inductance [4]. The hysteresis curves of this inductance define the energy density, volume and wire turn [7]. Some differently designed inductances are found in literature such as a printed circuit board (PCB) design. This inductance design is aiming towards a compact and small system and also to solve the mutual inductance problem [9–11, 16].

The winding area, winding resistance, and air gap length is the other main topics for inductance design. The calculation and details of these matters are important for the design of the inductance. The correct winding area calculation reduces the winding resistance, and air gap length which affects the inductance design. [15, 17].

In this paper, suitable inductance selection criteria for power converters are investigated in detail and solved by using electromagnetics equations. Also, the design steps of inductance, necessary calculations, and information are shown with an example application. The cores and wires effect on the inductance efficiency are also investigated. An inductance with a Ferrite core and a special manufactured Litz wire is proposed, and designed experimentally for a converter circuit. Measurement for determination of an inductance value is shown. Also, the inductance current variations for different frequencies are studied and to be used in the converter safely.

2. INDUCTANCE EFFECT AND SELECTION CRITERIA FOR POWER CONVERTERS

The energy efficiency of converters depends a lot on the inductance efficiency and a well-designed inductance is very important for the converter in continuous mode. The inductance value is determining how to work the converter under different load conditions. There is a limit value for the converter where it works in continuous and discontinuous mode. The inductance limit value is typically calculated for this criterion. Inductance current and voltage variation for the limit of continuous and discontinuous mode are given in Fig. 1 for a buck-boost converter circuit. The critical inductance value is calculated using this figure. If the inductance current is above zero all in time the converter works in continuous conduction mode, else the converter works in discontinuous conduction mode. In this mode, the inductance voltage is going to zero and do not supply the load in a short time and the capacitor could also supply the load.

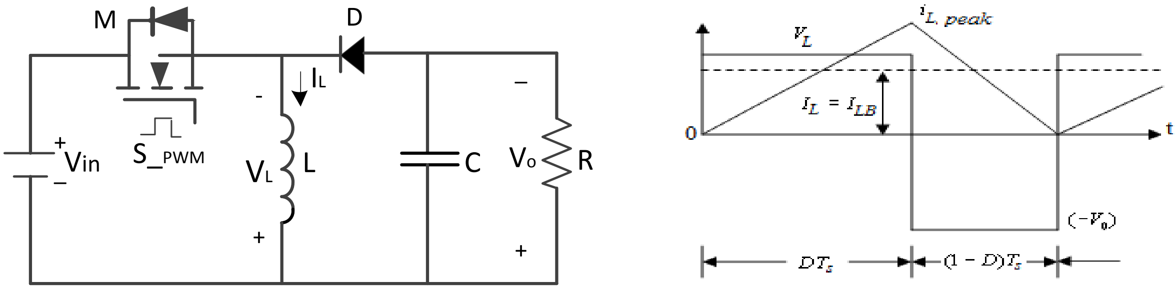

(a) (b)

Fig. 1. Buck-boost converter circuit (a), Inductance current and voltage variation at the limit value between continuous and discontinuous mode (b)

Equation 1 can be written in Fig. 1 (b) geometry for the limit value.

$$I_{LB} = \frac{1}{2} i_{L,peak} = \frac{T_s V_{in}}{2L} D. \tag{1}$$

If the capacitor current in Fig. 1 (a) is accepted zero the inductance current is equal to input and output current sum for the converter. Using these equations the inductance current average value and the output current depends on the output voltage for the limit values given in Equation 2 and 3 respectively.

$$I_{LB} = \frac{T_s V_o}{2L}(1-D)\,. \tag{2}$$

$$I_{OB} = \frac{T_s V_o}{2L}(1-D)^2\,. \tag{3}$$

The maximum values of I_{LB} and I_{OB} for the buck-boost converter have reached this value when the duty ratio is zero and this is given in Equation 4. This equation gives the minimum inductance value for the limit of continuous mode operation.

$$I_{LB,\max} = I_{OB,\max} = \frac{T_s V_o}{2L}\,. \tag{4}$$

3. DESIGN STEPS OF INDUCTANCE

The necessary calculations for inductance design will be given more detailed in this section with an example using the related documents and studies [6–8, 11–13, 17]. Some of these studies only include general information's and technical data's without more details and power electronics application examples [6–8 11]. The others are case studies and include general or specific information's about this matter [12, 13]. Not includes all the variable of core design in a study. The electromagnetic equations of inductance, core structures, and necessary calculations for wire effect as well as power loses relation are also investigated in this study.

The main component in inductance design is the core structure where to be used for magnetic flux flow is provided. Air cores, iron cores, ferrite and powder cores are known inductance cores. Ferrite and powder cores are preferred for high switching frequency power converters having less loses and saturation. Ferrite cores are cheaper and have low power losses at higher switching frequencies but the flux level is lower. These cores are obtained from Mn-Zn and Ni-Zn alloys and have F, P, R, K types depending on the alloy's ratios [12]. Also, the air gap in cores makes it preferable against the saturation. Powder cores have an air gap dispersed in the material due to the nature of the material from which they are produced, and this feature is ideal for switching rectifiers. In addition to a soft saturation characteristic, this feature provides a lot of design convenience, such as small core volume, overcurrent protection, low heat, and powder cores provide high levels of direct current (DA) magnetic force characteristics without saturation [4, 12].

The other matter for core selection is core geometry and it is possible to find pot, E shape, toroid cores and the others in manufacturer catalogs depending on their applications. Pot cores, when assembled are nearly surrounded the wound bobbin and this aids in shielding the coil from picking up electromagnetic interference (EMI) from outside sources. Double slab and RM cores are also similar to pot cores but are designed to minimize board space, providing at least a 40% savings in the mounting area. EP Cores are round center-post cubical shapes which enclose the coil completely except for the printed circuit board terminals. PQ cores are designed especially for switched mode power supplies. The design provides an optimized ratio of volume to the winding area and surface area. E cores are less expensive than pot cores and have the advantages of simple bobbin winding plus easy to assemble. Also, E cores can be mounted in different directions, and if desired, they provide a low profile. EC, ETD, EER and ER shapes are a cross between E cores and pot cores. Like E cores, they provide a wide opening on each side. Toroids are economical to manufacture; hence, they are the least costly of all comparable core shapes. Since no bobbin is required, accessory and assembly costs are nil, but winding is done on toroidal winding machines.

Ferrite geometries offer a wide selection in shapes and sizes. To choose a core for power applications the parameters in Table 1 can be used and evaluated [8, 11, 13, 20].

Table 1. Comparison of ferrite core geometry types [8]

Core Type	**POT CORES**	**DOUBLE SLAB, RM CORES**	**EP CORES**	**PQ CORES**	**E CORES**	**EC, ETD, EER, ER CORES**	**TOROIDS**
Core Cost	High	High	Medium	High	Low	Medium	Very Low
Bobin Cost	Low	Low	High	High	Low	Medium	None
Winding Cost	Low	Low	Low	Low	Low	Low	High
Winding Flexibility	Good	Good	Good	Good	Excellent	Excellent	Fair
Assembly	Simple	Simple	Simple	Simple	Simple	Medium	None
Mounting Flexibility	Good	Good	Good	Fair	Good	Fair	Poor
Heat Dissipation	Poor	Poor	Poor	Good	Excellent	Good	Good
Shielding	Excellent	Good	Excellent	Fair	Poor	Poor	Good

E cores are more advantageous in terms of core, coil and winding prices and easy to use, also with cross-sectional area and window spacing of different sizes. E cores have a double flux path which reduces their dimensions and this allows for small footprint and easy installation on printed circuits. E cores air gap can be adjusted, but the fringe fluxes formed in cores with air gap lead to flow losses and eddy current (Eddy) losses on winding wires as shown in Fig. 2 (a). Therefore, Kool Mμ E powder cores with an equal air gap as shown in Fig. 2 (b) are more preferred. The 10.500 gauss saturation level of the Kool Mμ E powder cores provides higher energy storage capability that they can be achieved with the air gap ferrite E-cores, which means a smaller core size [19, 20].

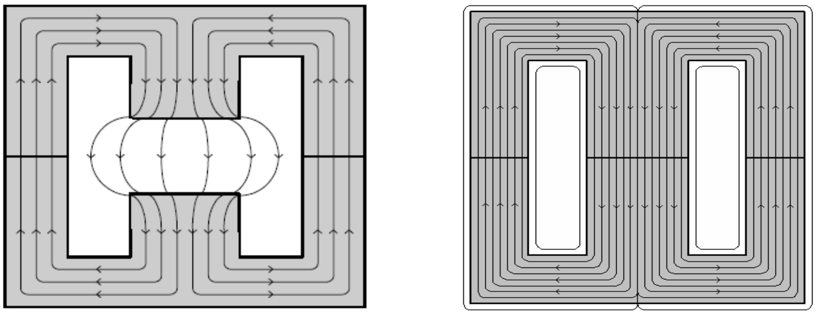

(a) (b)

Fig. 2. E cores and flux way; gapped Ferrite (a), Kool Mμ (b)

The basic principles of the inductance calculation are based on Faraday's laws. The B-H hysteresis curve between the magnetic flux density (B) and the magnetic field strength (H) for the inductance is given in Fig. 3 (a). The relation between B and H are given in Equation 5 according to Fig. 3 and magnetic permeability, which is equal to the product of the magnetic permeability of air and core. The magnetic permeability of the air $\mu_0 = 1.26x10^{-6} H/m$, the magnetic permeability of the material μ varies between 2000–4000 for Ferrite materials [7]. As the μ value increases, the B-H curve will reach a linear saturation as shown in Fig. 3 (b). Therefore, the magnetic flux density must be selected small.

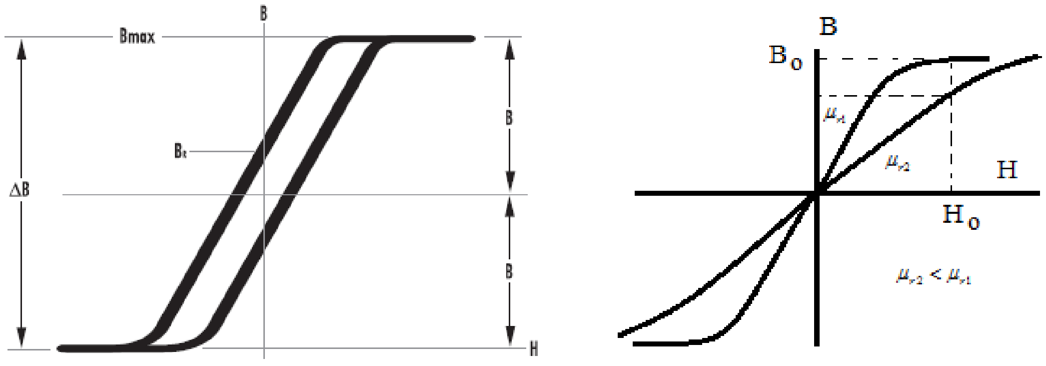

(a) (b)

Fig. 3. B-H hysteresis curve (a), the change of the B-H curve with different μ values (b)

The relationship between the magnetic flux density (B) and the magnetic field strength (H) is given in Equation 5 and gives the permeability of the core.

$$\mu = \frac{\Delta B}{\Delta H} \Rightarrow B = \mu \times H = \mu \times \mu_o \times H\,. \tag{5}$$

The inductance value is calculated using Equation 4 and the inductance value is calculated as a 0.72 mH for the maximum power current which is given as an 8.5 A and for the switching frequency. The maximum energy can be stored on the inductance is calculated for this maximum current in Equation 6.

$$LI^2 = (0.72 \times 10^{-3}) \times (8.5)^2 \ = 52.02 \times 10^{-3}\, Joule\,. \tag{6}$$

The Hanna curve obtained from the relation between B and H in Equation 6 is given in Fig. 4 (a). V_e is defined as the volume in this equation.

$$H = \frac{LI^2}{V_e B_{\max}}\,. \tag{7}$$

If the center of the scale on the Hanna curve is selected as seen in Fig. 4 (a) the volume value (V_e) can be calculated as in Equation 8.

$$\frac{LI^2}{Volume} = 5 \times 10^{-4} \Rightarrow Volume = \frac{52.02 \times 10^{-3}}{5 \times 10^{-4}} = 104.04\ cm^3\,. \tag{8}$$

The nearest volume value from the E-type core catalog of the manufacturer is 120 cm³ for the coded DMR40-EE70. The catalog data for this core is given in Fig. 4 (b).

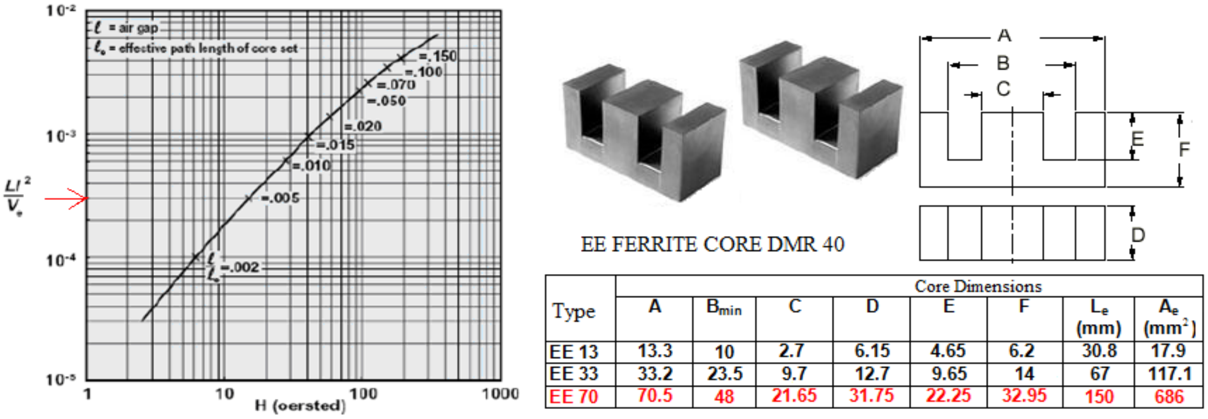

Type	Core Dimensions							
	A	Bmin	C	D	E	F	Le (mm)	Ae (mm²)
EE 13	13.3	10	2.7	6.15	4.65	6.2	30.8	17.9
EE 33	33.2	23.5	9.7	12.7	9.65	14	67	117.1
EE 70	70.5	48	21.65	31.75	22.25	32.95	150	686

(a) (b)

Fig. 4. Hanna curve (a), catalog data (b) of E-type ferrite core

For this volume value, the flux path, L_e = 150 mm and the flux path cross-sectional area is given as A_e = 686 mm². For new volume value selected is given in Equation 9.

$$\frac{LI^2}{Volume} = \frac{52.02\times10^{-3}}{102} = 0.51\times10^{-3} cm^3 . \tag{9}$$

If we look again at the Hanna curve in Figure 4 (a), it is found for the $\frac{LI^2}{Volume}$ corresponds to value $\frac{l}{l_e} = 0.005$ and H = 20. The winding number of the magnetic force from the Oersted expression in Equation 10 is found as:

$$H = \frac{0.4\pi NI}{l_e} \Rightarrow N = \frac{Hl_e}{0.4\pi I} = \frac{20\times14.9}{0.4\times\pi\times8.5} = 27.91 \cong 28 \text{ winding} . \tag{10}$$

The cable cross-section to be used for the winding of the current $I_{LB\_\max} = 13.8\,A$ is selected from the standard table as 1.5 mm².

The next step is the selection of the type of wire to be used. The effect of the skin phenomenon at high frequencies and the proximity effect of the cables adversely affect the uniform distribution of the current in the conductive wire as seen in Fig. 5 (a) and (b) [15, 21].

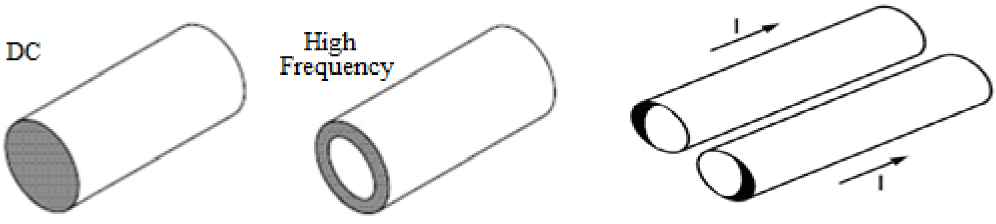

(a) (b)

Fig. 5. Skin effect with high frequency (a), and the effect of closure effect of the wire (b)

Various solutions have been proposed to eliminate the effects of skin phenomenon. The major ones are the use of multi-stranded Litz wires, the use of multi-core winding cables or the use of ribbon cables [21]. The cross sections of this type of wires are shown in Fig. 6.

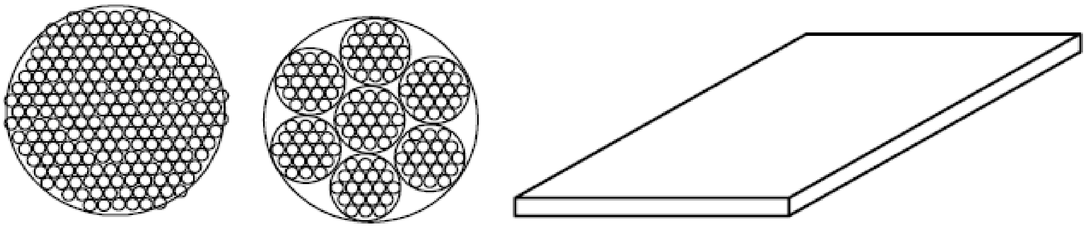

(a) (b) (c)

Fig. 6. Various vires cross sections; (a) Litz wire, (b) multi-core wire, (c) strip wire

According to the catalog data for Litz wire, the cable cross section is taken as two times for the same load flow capacity and the cross-section area for a single wire and required window spacing is calculated as given in Equation 11, 12.

$$A_w = 2\times1.5\times10^{-2} = 3\times10^{-2} cm^2 . \tag{11}$$

$$W_A = 3\times10^{-2}\times(42\div0.4) = 263\times10^{-2} = 2.63\ cm^2 . \tag{12}$$

The window spacing for the DMR40-EE70 coded E core can be calculated as in Equation 13 using Fig. 4 (b) catalog data. This value is greater than the calculated value for wire winding and the core window spacing is sufficient.

$$W_A = E(B - C) = 5.86\ cm^2 . \tag{13}$$

There is no need for an air gap calculation for Kool powder core materials with an equal air gap as mentioned before. Air gap for the Ferit cores can be calculated as in Equation 14.

$$\frac{l}{l_e} = 0.005 \Rightarrow l = 14.9 \times 0.005 = 0.0745\ cm . \tag{14}$$

4. EXPERIMENTAL DESIGN FOR AN APPLICATION

Realization of the inductance experimentally, measurements of inductance value, and study condition under current are given in this section. In accordance with the calculations, the required inductances are designed by using Litz wire, which is specially wrapped with the appropriate coil supplied from the market. The E cores are combined together with a frame where the windings wound are as shown in Fig. 7 (a). So, the electromagnetic flux will be flow in this core without any leakage. The last appearance of the designed inductance with Litz wire wound and fixed on a frame is shown in Fig. 7 (b). Considering the unexpected situations in use, losses and sudden loadings, the winding numbers and therefore the inductance values were selected a little too large.

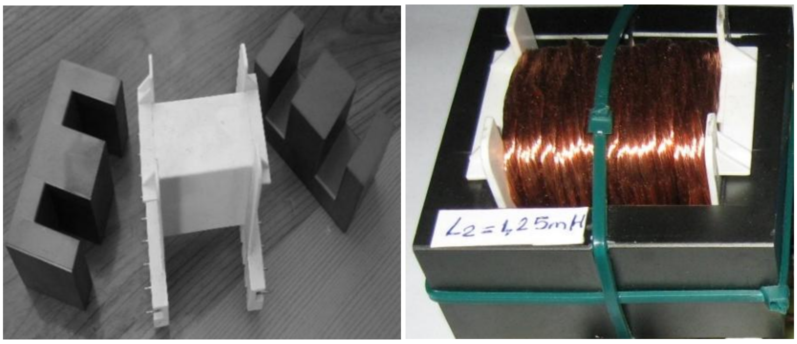

Fig. 7. The used E cores with a frame (a), designed inductance with Litz wire wound and fixed on a frame (b)

The next step is the measurement or to determine the inductance value. Using an LCR meter and measure the inductance value is an easy method. Alternatively, an LC resonance circuit can be used to estimate the inductance value by applying different frequencies. The value of the designed inductance is measured to be 1.2 mH depend on the winding values which are a few spins more.

The study of the inductance on a switch mode power converter is shown in Fig. 8. The inductance current measured with a current probe which is rated 50 mV/A. Also, the inductance current and voltage are shown in Fig. 8 for a duty cycle of 0.5. When the voltage is applied to the inductance the current increases linearly and when the voltage is not applied the current is continuous to flow through the inductance and the inductance behaves as a voltage source. This cycle is called a continuous mode. For the circuit, the switching frequency is 29.2 kHz and inductance maximum current is 5 A for this application. These results are suitable for the theoretical results in Fig. 1 (b) when they are compared. Also, it is seen that the inductance is stored the necessary energy for the continuous mode study of the converter.

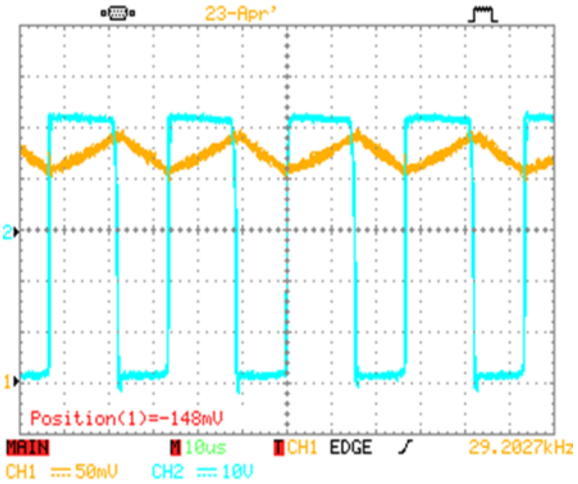

Fig. 8. Inductance voltage variation with current for a buck-boost converter circuit. CH1 (Inductance current 50 mV/1A), CH2 (Inductance voltage)

5. CONCLUSION

The inductance selection criteria and design steps for power electronics applications which are scattered and rarely found in the literature and manufacturer catalogs are investigated in this paper in more detailed. Different studies and applications in literature are used and expanded with an example and application as a fundamental study for researchers who will study inductance design. Inductance operation principle and selection criteria for power converters are firstly given in this paper. The novelty of this study is mainly this. The calculations and the design steps of inductance related to this criterion are also given more detailed. The importance of core and wire selection and the important points for this selection are given. In the experimental and in the application part, measurement of the inductance value and behavior for power converters are given. This study will be a reference study for the researchers who will study in this area. The losses, efficiency, heat increase of designed inductance and electromagnetic interference for electromagnetic compatibility can be investigated in the future.

ACKNOWLEDGMENT

This study was supported through The Scientific & Technological Research Council of Turkey (TUBITAK), project number, 111E292. The authors wish to thank for the support of TUBITAK. Also, the authors wish to thank Prof. Frede Blaabjerg from Aalborg University/Danmark for the contributions also TUBITAK, 2219 postdoctoral research program with a 1059B191700997 application number.

REFERENCES

[1] MOHAN, N.; UNDULAND, T. M.; ROBBINS, W. P., *Power Electronics*, John Wiley, 1995.

[2] EMADI, A.; KHALIGH, Z.; NIE, Y. J. Lee., *Integrated Power Electronic Converters and Digital Control*, CRC Press, 2009.

[3] SHIAU, J. K., CHENG, C. J., Design of a non-inverting synchronous buck-boost DC/DC power converter with moderate power level, *Robotics, and Computer-Integrated Manufacturing*, June 2010, Vol. 26, No. 3, p. 263-267.

[4] YOU, B. G., KIM, J. S., LEE, B. K., CHOI, G. B. and YOO, D. W., Optimization of Powder Core Inductors of Buck-Boost Converters for Hybrid Electric Vehicles, *Journal of Electrical Engineering & Technology*, 2011, Vol. 6, No. 4, p. 527-534.

[5] RYLKO, M. S., LYONS, B. J., HAYES, J. G., EGAN, M. G., Revised Magnetics Performance Factors and Experimental Comparison of High-Flux Material for High-Current DC-DC Inductors, *IEEE Transactions on Power Electronics*, Vol. 26. No. 8, August 2011, p. 2112-2126.

[6] Fair-Rite Products Corp., The Effect of Direct Current on the Inductance of a Ferrite Core, *Technical Information*, 14th Edition, pp: 165-169.

[7] GARY L. J., Inductors and Transformers, *Solid State Tesla Coil*, Chapter 4, October 29, 2001.

[8] Magnetics Corperation, General Core Selection Data Sheet, Section 4, 2006.

[9] ORENCHAK, G., Boost Material Improves Inductor Characteristics Under DC Bias Conditions, *PCIM Article*, November 1999.

[10] SONNTAG, C. L. W., LOMONOVA, E. A., DUARTE, J. L., Implementation of the Neumann formula for calculating the mutual inductance between planar PCB inductors. In Electrical Machines, 2008, ICEM 2008, 18th International Conference on (pp. 1-6). IEEE.

[11] MACRELLI, E., ROMANI, A., WANG, N., ROY, S., HAYES, M., PAGANELLI, R. P., TARTAGNI, M., Modeling, design, and fabrication of high-inductance bond wire micro transformers with a toroidal ferrite core, *IEEE Transactions on Power Electronics*, 2014, Vol. 30, No. 10, p. 5724-5737.

[12] MCLYMAN, C. W. T., Transformer and inductor design handbook, CRC Press., 2016.

[13] LOSSOUARN, B., AUCEJO, M., DEÜ, J. F., MULTON, B., Design of inductors with high inductance values for resonant piezoelectric damping, *Sensors, and Actuators A: Physical*, 2017, Vol. 259, p. 68-76.

[14] GRANDI, G., KAZIMIERCZUK, M. K., MASSARINI, A., REGGIANI, U., SANCINETO, G., Model of laminated iron-core inductors for high frequencies. *IEEE Transactions on Magnetics*, 2004, Vol. 40, No. 4, p. 1839-1845.

[15] WILLIAMS, A. (2011). Fundamentals of Magnetics Design: Inductors and Transformers. Lecturer Notes.

[16] GALA, K., ZOLOTOV, V., PANDA, R., YOUNG, B., WANG, J., BLAAUW, D., On-chip inductance modeling and analysis, In Proceedings of the 37th Annual Design Automation Conference, June 2000, p. 63-68.

[17] SAHIN, M. E, Design and Control of Parallel Connected Buck-Boost Converter for Hybrid Energy System, Ph.D. Dissertation, Karadeniz Technical University, 2014.

[18] Coilcraft Inc, Power Inductor Finder, (2019), https://www.coilcraft.com/apps/power_tools/power/.

[19] Magnetics Kool, Mμ E-Cores, Technical Bulletin, Bulletin No: KMC-E1, Magnetics, 2005.

[20] Fair-Rite Products Corp., The Effect of Direct Current on the Inductance of a Ferrite Core, Technical Information, 14th Edition, 2005, p. 165-169.

[21] BEN-YAAKOV S., Magnetic design, Switch mode DC-DC converters, Part 3, Lecturer slides (2019), http://www.ee.bgu.ac.il/~dcdc/slides/index.html.

CYSENI 2018, May 23-25, Kaunas, Lithuania
ISSN 1822-7554, www.cyseni.com

ELECTRICITY NETWORK MANAGEMENT ALGORITMS ANALYSIS

D. Stanelytė
Lithuanian Energy Institute
Breslaujos str. 3, LT-44403 Kaunas – Lithuania
Email: d.stanelyte@gmail.com

ABSTRACT

A rapid development of modern electric power systems with the objective to move towards smart grids depends on the widely applied generation of the distributed electric power introduced in the medium voltage distribution networks. One of the main issues related with the development of smart grids is the automatic distributed voltage control (ADVC). The devices controlled with a controllable power (e.g. in capacitor batteries that have programmable logic controllers installed) may be coordinated to control the voltage of distributed electricity networks in order to meet the high demand of distributed generation. Leaving cost and environmental impact aside, Battery Energy Storage (BES) is perhaps the most efficient method to stabilize power grids that access important quantities of renewable energy (e.g., >10%).

The task of reactive power optimisation contains the continuous and discrete variables that must be determined by the optimisation algorithm. The variables are the voltage on generator terminals, the position of the branch switch of an overloaded transformer that is adjusted in a feasible space area restricted by parameters. That way, an electric system is created that conditions the least losses of the active and reactive power. On one hand, discrete variables are the parameters to determine the transformer branch and capacitor compensation power. On the other hand, continuous variables are the reactive output powers of generators and synchronous compensators.

The drawbacks common to the classical methods may be overcome with the recent calculation methods based on artificial intelligence.

In general, the classical optimisation algorithms become invalid when the reactive power is practically optimised in large-scale power systems. On the other hand, an exceptional effectiveness of nature-based optimisation algorithms has been proven in solving optimisation tasks that contain many variables, including discrete and continuous variables, as well as local optimum points.

Keywords: electric power systems, smart grids, automatic distributed voltage control, controllable power, Battery Energy Storage, optimisation algorithms

CYSENI 2019, May 23-24, Kaunas, Lithuania
ISSN 1822-7554, www.cyseni.com

THE CONTRIBUTION OF ENERGY TAXES TO CLIMATE CHANGE POLICY IN THE EU

G. Liobikienė
Department of Environmental Sciences, Vytautas Magnus University
Vileikos 8, LT-40444 Kaunas – Lithuania
Email: genute77@gmail.com

ABSTRACT

Energy taxes are one of the main market-based tools directed to mitigate climate change in the European Union (EU). Therefore, the aim of this article is to analyse whether energy taxes really contribute to the reduction of greenhouse gas (GHG) emissions and successful implementation of climate change policy. Thus, applying the Granger causality test on time series and using panel data analysis, the direct and indirect (via the reduction of fossil energy consumption and energy intensity as well as the increase of the share of renewable energy consumption) impact of energy taxes on GHG emissions in EU countries was analysed in the present study. The results showed that energy taxes did not Granger cause fossil energy consumption, energy intensity, renewable energy consumption, and GHG emissions in almost all EU countries. Referring to panel data analysis, the results showed that energy taxes did not directly and indirectly influence GHG emissions. These findings reveal that the demand of fossil energy in EU is inelastic and energy tax policy in the EU is ineffective. Thus, tax policy should be reformed and matched with emission trading system seeking climate change mitigation.

Keywords: energy taxes; climate change policy; energy efficiency; renewable energy; tax reform.

1. INTRODUCTION

In recent decades, particular attention is paid to the climate change mitigation. However, the main question is how to achieve the reduction of greenhouse gas (GHG) emission between 80 and 95 % by 2050. The main policy tools for emission control are market-based. The environmental taxes are the mostly used tools in environmental policy, which the main aim is to change market prices to internalize environmental harms [1, 2]. The prices are increased by the tax, consumers should be motivated to change their buying behaviours and consequentely to reduce pollution [3].

In order to mitigate the climate change, the energy or carbon taxes are the most applied market-based tools. Economists and international organizations highly recommended these tools as the most efficient market-based mitigation instruments [4, 5]. The EU has favoured these instruments to reach environmental policy objectives as well [6, 7]. However, it is very important to guarantee that the taxes do not hinder the welfare and economic growth [8, 9]. The carbon taxes are directly assigned to GHG reduction [4, 10-12] by taxes imposed on the carbon-content of fossil fuels. However, considering that energy taxes can be found in most EU countries, meanwhile carbon taxes with many exemptions have been introduced in EU countries it is necessary to analyse the impact of energy taxes on climate change policy.

Energy taxes are only indirect GHG emission taxes [13]. The main target of energy tax is to levy tax on fossil fuels, which are the main source of GHG emissions [14-16]. Energy taxes contribute to the reduction of GHG emissions in two ways: 1) *by improving energy efficiency* [14, 17, 18]. The energy efficiency is one of the main determinants, which is related to mitigation of climate change policy [19]. Energy tax has the advantage of generating revenue that could be used for investment in more environmentally friendly economic activities and abatement technologies [13, 20]. 2) *Energy tax by using fuel with a lower carbon content could contribute to the reduction of GHG emissions* [14, 17, 18]. Placing a tax on fossil fuels may make alternative fuels more attractive and initiate the consumers to choose more fuel-efficient products [21]. The consumption of renewable energy is also one of the most important tool to reduce GHG emissions. The price increase of fuel should motivate a substitution effect that leads to a decreased demand for polluted energy sources [2, 18]. Moreover, revenues could be used to subside the environmental protection projects or the technological development of emission reduction [4, 9, 21].

The impact of energy taxes on GHG emissions has been scarcely analysed. The main question has been raised: whether energy taxes really contribute to the reduction of GHG emissions. Therefore, the aim of this study is to analyse the direct and indirect impact of carbon energy taxes on GHG emissions in EU countries.

2. DATA AND DESCRIPTIVE STATISTICS

For the analysis of energy taxation impact on climate change policy the data was collected over the period 1995-2012 for 28 EU member states. The data was provided by Eurostat and World bank database. Energy taxes were used (TAX) EUR per energy (except renewable and nuclear) tone (of oil equivalent TOE) consumed; fossil energy consumption (FEC) – final energy (except renewable and nuclear) consumption per capita (tonnes of oil equivalent TOE); energy intensity (EI) – gross inland consumption of energy divided by GDP (kg of oil equivalent per 1 000 EUR); share of renewable energy (REN) – share of renewable energy in gross inland consumption of energy (%); GHG emissions (GHG) – total greenhouse gas emissions per capita (tones of CO_2 equivalent).

Figure 1 shows that during the period 1995-2012 the relative taxation on energy grew in all EU countries. The most intensive growth was observed in Estonia. Meanwhile, the lowest growth of taxes was found in Croatia, Portugal and Germany by 2%, 3% and 10% a year, respectively. Furthermore, the results reveal that relative taxation on energy increased more in the countries where initially carbon energy was not so heavily taxed. It suggests that the convergence of energy taxation level between EU countries was observed. The EU countries fastly catched up with the countries characterised by high energy tax rates.

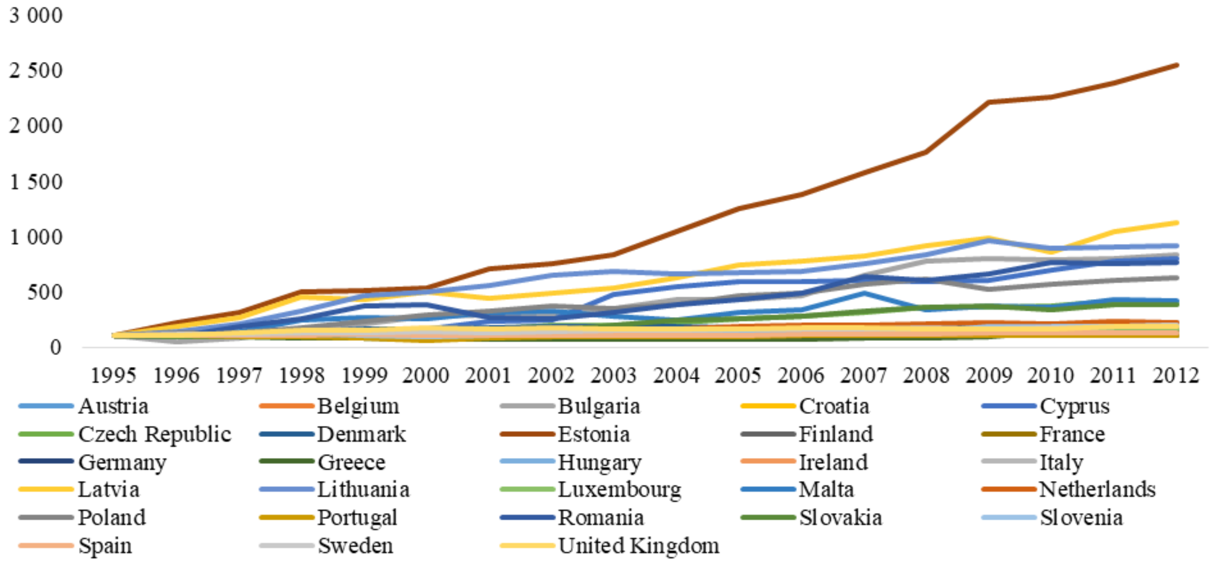

Fig. 1 Change in relative taxation on carbon energy use over 1995-2012.
Level of 1995 is equal to 100%

3. MODEL AND ESTIMATION METHOD

In order to examine the impact of energy taxes (TAX) on fossil energy consumption (FEC), energy intensity (EI), renewable energy (REN) as well as on greenhouse gas emissions (GHG) at country level, the Granger causality test via ADLM or ECM to time series data was applied. T-tests once lagged values of carbon energy taxes provide statistically significant results about future values of energy consumption, intensity, renewable energy consumption, and GHG emissions. In order to detect whether variables are cointegrated, also known as having a long-run stochastic trend by standard unit root testing such as Augmented Dickey-Fuller test following Engel-Granger 4-step procedure was performed. The general ADLM takes a form of:

$$y_t = \gamma + \delta y_{t-1} + \varphi x_{t-1} + \varepsilon_t, \tag{1}$$

where y_t and x_t are stationary variables, and ε_t is a white noise.

Applying equation (1) to our case we have:

$$FEC_t = \gamma_1 + \delta_1 FEC_{t-1} + \varphi_1 TAX_{t-1} + \varepsilon_t, \tag{2}$$

$$EI_t = \gamma_2 + \delta_2 EI_{t-1} + \varphi_2 TAX_{t-1} + \varepsilon_t, \tag{3}$$

$$REN_t = \gamma_3 + \delta_3 REN_{t-1} + \varphi_3 TAX_{t-1} + \varepsilon_t, \tag{4}$$

$$GHG_t = \gamma_4 + \delta_4 GHG_{t-1} + \varphi_4 TAX_{t-1} + \varepsilon_t. \tag{5}$$

ECM will be used in cases where cointegrated relationships will be detected. ECM directly estimates the speed at which energy consumption, intensity, renewable energy consumption, or GHG emissions return to equilibrium after a change in energy taxes. Given that many time series appear to be stationary in first differences, in order to use the Box-Jenkins approach, we could difference the series and then estimate models such as ARIMA, however, any information about long-run adjustments that the data in levels may contain is omitted. This leads us to use the ECM methodology developed by Sargan [22], which retains the level information.

Thus, if both variables appear to be integrated and co-integrated by the Engle-Granger theorem, nexus between fossil energy consumption, energy intensity, share of renewable energy consumption, GHG emissions, and energy taxes will be analyzed using equation:

$$\Delta y_t = \gamma + \delta \Delta y_{t-1} + \varphi \Delta x_{t-1} + \alpha (y_{t-1} - \beta_0 - \beta_1 x_{t-1}) + \varepsilon_t, \tag{6}$$

where α is the speed at which *y* returns to equilibrium after a change in *x*. Presence of long-run effect can then be tested using a standard t-statistic on α.

While this approach is easy to apply, there are, however, numerous problems that were summarized by Vance et al. [23]. Applying equation (6) to our case we have:

$$\Delta FEC_t = \gamma_1 + \delta_1 \Delta FEC_{t-1} + \varphi_1 \Delta TAX_{t-1} + \alpha_1 EC_1 + \varepsilon_t, \tag{7}$$

$$\Delta EI_t = \gamma_2 + \delta_2 \Delta EI_{t-1} + \varphi_2 \Delta TAX_{t-1} + \alpha_2 EC_2 + \varepsilon_t, \tag{8}$$

$$\Delta REN_t = \gamma_3 + \delta_3 \Delta REN_{t-1} + \varphi_3 \Delta TAX_{t-1} + \alpha_3 EC_3 + \varepsilon_t, \tag{9}$$

$$\Delta GHG_t = \gamma_4 + \delta_4 \Delta GHG_{t-1} + \varphi_4 \Delta TAX_{t-1} + \alpha_4 EC_4 + \varepsilon_t, \tag{10}$$

where *EC* is the error correction term.

To examine energy tax impact on reduction of GHG emissions at EU level, we alternatively apply panel data analysis. Ascertaining the fact that panel data contain two complementary dimensions of cross section and time, this data typically provide more information and variability compared to one-dimensional time series data and thus allow to include more variables. Thereby, analyses conducted by using panel data provide the increased degree of freedom and the decreased degree in potential collinearity problems among the variables. As this research intends to investigate the effect of energy taxes on GHG emissions, besides direct effect we will model potential indirect effect through lowering energy intensity, fossil energy consumption or promoting renewable energy.

Our proposed dynamic panel data model (in the form of unobserved effects) that, so far, captures just direct effect of carbon energy taxes on GHG emissions with a time lag, takes the following general form:

$$GHG_{i,t} = \delta GHG_{i,t-1} + \beta_0 + \beta_1 FEC_{i,t} + \beta_2 EI_{i,t} + \beta_3 REN_{i,t} + \beta_4 TAX_{i,t-1} + \varphi_t + \mu_i + \varepsilon_{i,t}, \quad (11)$$

where $i = 1, \ldots, N$ for each country in the panel and $t = 1, \ldots, T$ refers to the time period. The given variables are in natural log form. μ represents unobserved country fixed-effects; η represents time-specific effects that are time-variant and common to all countries. The parameters $\beta_1, \ldots, \beta_4$ represent the long-run elasticity estimates of GHG emissions with respect to corresponding factor. ε is the classical error term which is assumed to be independent and identically distributed.

Indirect effect of carbon energy taxes on GHG emissions through fossil energy consumption, energy intensity, and share of renewable energy consumption will be modelled by adding to the base equations corresponding interaction terms $FEC_t \times TAX_{t-1}$, $EI_t \times TAX_{t-1}$ and $REN_t \times TAX_{t-1}$.

Classical estimation methods like OLS, fixed or random effects for panel regression models do not seriously address issue regarding endogeneity in the dynamic framework. Theoretically, however, it is plausible, and also very likely, that higher GHG emissions are increasing incentives to reduce energy consumption, intensity and to increase renewable energy consumption and energy taxes. This would lead to an understatement or overstatement (i.e. biasness) of the effect of variables on GHG emissions.

The generalized method of moments (GMM) is used for estimating the equation (11) because it enables us to deal with potential endogeneity problem of right-hand side variables. According to the GMM technique, equation must be differentiated, next, lagged observations of the first difference of the independent variables are used as instruments for estimation. Taking into account time-specific effects, we obtain:

$$GHG_{i,t} - GHG_{i,t-1} = \delta\left(GHG_{i,t-1} - GHG_{i,t-2}\right) + \beta\left(X_{i,t} - X_{i,t-1}\right) + \left(\varepsilon_{i,t} - \varepsilon_{i,t-1}\right), \quad (12)$$

where $X_{i,t}$ is now the set of explanatory variables, also including energy taxes and the interaction term.

Combining equation in differences with equation in levels into one system, the estimators are called system GMM estimators (SGMM). As Bond et al. [24] and Hauk and Wacziarg (2009) pointed out, the SGMM estimators should be used for panel data regressions to estimate more consistent and efficient parameters. To examine the overall validity of the SGMM estimation, following Arellano and Bond [25] and Blundell and Bond [26], two tests are to be carried out: (1) the Sargan test which tests the null hypothesis that the instruments are valid; and (2) the AR(2) test which tests null hypothesis that there is no second-order auto-correlation. The SGMM estimation results are valid only after passing two tests mentioned above.

4. RESULTS AND DISCUSSION

4.1. Time series data analysis

Considering that energy taxes contribute to the reduction of GHG emissions in two ways: 1) by reduction of energy intensity and 2) by increase of renewable energy consumption, the Granger causalities between these variables were analysed in separate EU countries. The direct effect of energy taxes on GHG emissions was estimated as well. Analysing Granger causality between energy taxes and fossil energy consumption, we found statistical evidence for the Netherlands, Spain and Lithuania, which reveals that higher energy taxes contribute to the reduction in fossil energy consumption. These countries, due to the increase of energy taxes, invested and developed abatement technologies. Meanwhile it was observed that higher level of energy taxes corresponds to energy consumption growth in the United Kingdom (UK). It can be related to the fact that the level of energy taxes is rather low in the UK and producers are not motivated to implement new technologies. In the rest of EU countries no statistically significant Granger causalities between energy taxes and fossil energy consumption were observed. It can be related to inelastic energy demand and oil monopoly energy taxes have no impact on current energy production [27].

Granger causality between energy taxes and energy intensity level showed the statistical evidence of negative relationship between these variables in Cyprus and Italy. Thus, in these countries due to the increase in carbon energy taxes energy efficiency programmes were successfully implemented. The statistical evidence of significant correlation between energy taxes and energy intensity was observed in Lithuania. This result shows that in the case of energy taxes growth, the energy intensity increases as well. In other EU countries there was observed insignificant Granger causality between energy taxes and energy intensity. Therefore, despite growing energy taxes producers are not motivated to develop technologies.

Granger causality between energy taxes and a share of renewable energy showed a statistical evidence of a negative correlation between these variables in Hungary. Thus, whileenergy taxes reduced, the share of renewable energy consumption increased. Meanwhile, in Lithuania and France we found a positive relationship, which shows that in these countries, the increase in energy taxes Granger causes the growth in a share of renewable energy consumption. Therefore, in these countries carbon energy taxes created incentives to develop and use alternative low-carbon fuels and technologies. In the rest of EU countries no Granger causality between analysed variables was observed. Thus, taxes on energy sources did not motivate fuel substitution effect.

Analyzing the Granger causality between energy taxes and GHG emissions, we found statistical evidence in Malta, Lithuania and Sweden. These results showed that higher energy tax is associated with lower GHG emissions in these countries, therefore, energy taxes could directly contribute to effectiveness of climate policy. However, the contrary result was observed in Italy where the statistical evidence of positive correlation between energy taxes and GHG emissions was observed. In the rest of EU countries the relationship between these variables was insignificant. Thus, these results show (with some minor exceptions) that energy taxes did not reduce the GHG emissions and did not contribute much to the implementation of climate change policy in EU countries. Therefore, almost all EU countries should initiate and implement energy tax reform by promoting the growth of energy efficiency and renewable energy consumption, and the decrease of energy consumption and GHG emissions.

4.2. Panel data analysis

The impact of direct carbon energy taxes on GHG emissions is presented in Table 1. Estimation (I) corresponds to the equation (11) but with omitted carbon energy taxes variable. It was done in order to estimated the effects of control variables, the ones that are broadly used in the studies examining relationship between economic activity and environmental degradation in terms of GHG emissions. Therefore, estimation (I) shows a positive and statistically significant correlation between fossil energy consumption, energy intensity and GHG emissions and negative between the share of renewable energy and GHG emissions. Therefore, the growth of fossil energy consumption by 1% corresponds to increase in GHG emissions by 0.14-0.15% and respectively for energy intensity the effect on GHG emissions is about 0.1-0.11%. In case of renewable energy consumption – growth by 1 % leads to reduction of greenhouse gas emissions by 0.02%.

Table 1. Estimation results of direct energy taxes effect on GHG emissions

Variables	**(I)**	**(II)**	**(III)**	**(IV)**
Y(-1)	0.7999*** (13.2505)	0.7469*** (10.7328)	0.7455*** (11.1713)	0.7201*** (10.6530)
Const.	0.0670 (0.5521)	−0.2181 (−0.7935)	−0.3092 (−1.1728)	−0.2335 (−0.9707)
Fossil **E**nergy **C**onsumption	0.1396** (2.2714)	0.1400*** (2.7330)	0.1454*** (2.9286)	0.1593*** (3.1568)
Energy **I**ntensity	0.0963** (2.0435)	0.1013** (2.1963)	0.1110** (2.4624)	0.1131*** (2.7101)
RENewable energy	−0.0194** (−2.1374)	−0.0196** (−2.1042)	−0.0190** (−2.0397)	−0.0203** (−2.0209)
relative **TAX**ation on energy		0.0431 (1.4287)		
(-1)			0.0533* (1.9444)	
(-2)				0.0459* (1.9205)
Sample size	435	411	408	405
Number of countries	28	28	28	28
Error AR(2) test (p-value)	0.3390 (0.7346)	0.3391 (0.7345)	0.3292 (0.7420)	0.5268 (0.5984)
Sargan test (p-value)	27.281 (0.5151)	32.846 (0.8020)	45.465 (0.7402)	32.413 (0.8207)

Note: All estimations are 1-step SGMM including equations in levels and all of them include time dummies. The statistics given in the parentheses under the coefficients of explanatory variables are Z-values using robust (Windmeijer-corrected) standard errors. *,**,*** indicate statistically significant at the 10%, 5% and 1% levels, respectively.

Estimation (III) directly corresponds to equation (11), i.e. examines the one-year lagged effect of energy taxes on GHG emissions, estimation (II) tests instant effect of change in taxation policy on GHG emissions and estimation (IV) examines the two-year lagged effect. However, in all these estimations any negative or statistically significant correlation between carbon energy taxes and GHG emissions was not observed (Table 1).

The estimation of augmented equation (11) where indirect energy tax effect on GHG emissions is modelled using interactions is presented in Table 2.

Estimation (V) shows the results of indirect carbon energy tax effect via fossil energy consumption, estimation (VII) via energy intensity and estimation (IX) via renewable energy consumption on GHG emissions. Adding interaction terms to the base equation markedly changes estimated effect as well as its significance on separate variables involved in interactions compared with those we had without interaction term in Table 1. This suggests that interaction term correlates with separate variables that are interacted and since the standard errors are usually wide in the presence of multicollinearity, this in our estimations will mean that it is hard to obtain small standard errors due to insufficient separate information between the collinear variables. To overcome that problem, we alternatively estimated equation (11) with interactions, but omitted separate variables that are involved in interactions (see estimations VI, VII and X in Table 2). All interaction terms do not show negative or statistically significant relationship with GHG emissions, providing no evidence of indirect carbon energy tax effect on GHG emissions.

Table 2. Estimation results of indirect energy taxes effect on GHG emissions

Variables	**(V)**	**(VI)**	**(VII)**	**(VIII)**	**(IX)**	**(X)**
Y(-1)	0.6367*** (9.2912)	0.8450*** (15.5058)	0.6884*** (11.2957)	0.8164*** (16.3240)	0.7708*** (11.2318)	0.8322*** (16.0842)
Const.	−0.4274 (−1.5066)	0.0603 (0.6627)	0.8665 (1.1760)	0.1856** (1.9928)	−0.2775 (−0.9927)	0.0993 (1.0229)
Fossil **E**nergy **C**onsumption	0.7623 (0.7673)		0.1491*** (3.8035)	0.1562*** (2.8163)	0.1312*** (2.6379)	0.1485** (2.3817)
Energy **I**ntensity	0.1152*** (2.6747)	0.12084* (1.8876)	0.0701 (0.5940)		0.1012** (2.2909)	0.1138** (2.0399)
RENewable energy	−0.0207** (−1.9927)	−0.0181** (−2.0021)	−0.0225** (−2.0089)	−0.0199** (−2.1413)	−0.0272 (−0.4062)	
relative **TAX**ation on energy (-1)	0.1058*** (3.8149)		−0.1687 (−1.2961)		0.0462 (1.2746)	
FEC^{x}TAX(-1)	−0.1102*** (−3.0753)	0.0156 (1.1610)				
EI^{x}TAX(-1)			0.0387* (1.9534)	0.0090* (1.8908)		
REN^{x}TAX(-1)					0.0021 (1.2746)	0.0420 (0.6607)
Sample size	408	408	408	408	408	408
Number of countries	28	28	28	28	28	28
Error AR(2) test (p-value)	0.4682 (0.6396)	0.3203 (0.7487)	0.3566 (0.7214)	0.2654 (0.7907)	0.3190 (0.7497)	0.3349 (0.7377)
Sargan test (p-value)	49.6031 (0.7695)	32.8467 (0.6020)	26.7601 (0.5645)	26.0443 (0.5451)	29.5715 (0.5738)	35.3894 (0.6709)

Note: All estimations are 1-step SGMM including equations in levels and all of them include time dummies. The statistics given in the parentheses under the coefficients of explanatory variables are Z-values using robust (Windmeijer-corrected) standard errors[7]. *,**,*** indicate statistically significant at the 10%, 5% and 1% levels, respectively.

Referring to panel analysis the results showed that in all EU countries higher energy tax rate did not directly or via energy consumption, intensity, and renewable energy consumption correspond to lower GHG emissions. Meanwhile, the main determinants of lower level of GHG emissions are higher share of renewable energy consumption and decrease of energy consumption and intensity. These findings are in line with a lot of studies [see 28-31 and etc.]. Therefore, seeking the reduction of GHG emissions, the improvement of technological progress and the promotion of the renewable energy consumption are essential tools in the climate policy. The tax policy should be combined with other market-based instrument as subsidies for renewable energy sources and technology installation.

5. CONCLUSIONS

Taxes are the most applied market-based initiatives in order to solve environmental problems. This article analysed direct and indirect (via reduction of energy consumption and energy intensity, and increase in a share of renewable energy) impacts of energy tax on GHG emissions in EU countries. Analysing the Granger causality between energy taxes and GHG emissions we found that (with some minor exceptions as Lithuania, Malta and Sweden) energy taxes did not reduce the GHG emissions at all. Moreover, energy taxes in majority of cases did not Granger cause fossil energy consumption, energy intensity, and increase in a share of renewable energy consumption. Referring to panel data analysis, the results revealed that in EU the higher tax rate did not directly or indirectly correspond to lower GHG emissions. These findings reveal that energy taxes are ineffective and almost do not contribute to reduction of GHG emissions in the EU. Therefore, EU countries should initiate and implement the environmental taxes reform. Moreover, the energy taxes should be combined with other market or normative based tools in order to implement more successfully the climate change policy.

REFERENCES

1. PIGOU, A.C., 1932. The Economics of Welfare. Macmillan and Co.
2. DONGA, H., DAIB, H., GENGA, Y., FUJITAD, T., LIUE, Z., XIED, Y., WUF, R., FUJIF, M., MASUID, T., TANGG, L. Exploring impact of carbon tax on China’s CO2 reductions and provincial disparities. *Renewable and Sustainable Energy Reviews*, 2017, Vol. 77, p. 596-603.
3. FREEDMAN, M., FREEDMAN, O., STAGLIANO, A. J. Greenhouse gas disclosures. Evidence from the EU response to Kyoto. *International Journal of Critical Accounting*, 2012, Vol. 4, No. 3, p. 237-264.
4. LIN B. and LI X. The effect of carbon tax on per capita CO2 emissions. *Energy Policy*, 2011, Vol. 39, p. 5137-46.
5. LIANG, Q.M., WEI, Y.M. Distributional impacts of taxing carbon in China: results from the CEEPA model. *Appl. Energy*, 2012, Vol. 92, p. 545-551.
6. Eurostat. 2010. Environmental statistics and accounts in Europe. Luxembourg: Publications Office of the European Union.
7. GOULDER, L. H. 2009. Working paper. Carbon taxes vs. cap and trade. Stanford University.
8. HWANG, J. J. Policy review of greenhouse gas emission reduction in Taiwan. *Renewable and Sustainable Energy Reviews*, 2011, Vol. 15, P. 1392-1402.
9. KUO, T.C, HONG, I.H, LIN, S.C. Do carbon taxes work? Analysis of government policies and enterprise strategies in equilibrium. *Journal of Cleaner Production* 2016, Vol. 139, p. 337-346.
10. ZHANG, Z., ZHANG, A., WANG, D., LI, A., SONG, H. How to improve the performance of carbon tax in China? *Journal of Cleaner Production*, 2017, Vol. 142, p. 2060-2072.
11. WESSEH, P.K., LIN, B., ATSAGLI, P. Carbon taxes, industrial production, welfare and the environment. *Energy*, 2017, Vol. 123, p. 305-313.
12. VERA, S. and SAUMA, E. Does a carbon tax make sense in countries with still a high potential for energy efficiency? Comparison between the reducing-emissions effects of carbon tax and energy efficiency measures in the Chilean case. *Energy*, 2015, Vol. 88, p. 478-486.
13. OIKONOMOU, V., JEMTA, C., BECCHIS, F., RUSSOLILLO, D. White certificates for energy efficiency improvement with energy taxes: A theoretical economic model. *Energy Economics*, 2008, Vol. 30, p. 3044-3062.
14. VOLLEBERGH, H.R.J. Lessons from the polder: Energy tax design in the Netherlands from a climate change perspective. *Ecological Economics*, 2008, Vol. 64, p. 660-672.
15. EISEMACK, K., EDENHOFTER, O., KALKUHL, M. 2012. Resource rents: The effects of energy taxes and quantity instruments for climate protection. *Energy Policy*, 2012, Vol. 48, p. 159-166.

16. ANTANASIJEVIC, D., POCAJT, V., RISTIC, M., PERIS-GRUJIC, A. Modeling of energy consumption and related GHG (greenhouse gas) intensity and emissions in Europe using general regression neural networks. *Energy*, 2015, Vol. 84, p. 816-824.
17. JEFFREY, C., PERKINS, J.D. The association between energy taxation, participation in an emissions trading system, and the intensity of carbon dioxide emissions in the European Union. *The International Journal of Accounting*, 2015, Vol. 50, No. 4, p. 397-417.
18. BHANDARIA, V., GIACONIC, A.M., WOLLENBERGA, B.F., WILSONA, E.J. Interacting policies in power systems: Renewable subsidies and a carbon tax. *The Electricity Journal*, 2017, Vol. 30, No. 6, p. 80-84.
19. CABALU, H., KOSHY, P., CORONG, E., RODRIGEUZ, U-P. E., ENDRIGA, B.A. Modelling the impact of energy policy on the Philippine economy: Caron tax, energy efficiency, and changes in the energy mix. *Economic Analysis and Policy*, 2015, Vol. 48, p. 222-237.
20. MARKANYA, A., ORTIZ, R.A., MUDGAL, S., TINETTI, B. Analysis of tax incentives for energy-efficiency durables in the EU. *Energy Policy*, 2009, Vol. 37, p. 5662-5674.
21. CHOI, J-K., BAKSHI, B.R., HUBACEK, K., NADER, J. A sequential input-output framework to analyze the economic and environmental implications of energy policies: Gas taxes and fuel subsidies. *Applied Energy*, 2016, Vol. 384, p. 830-839.
22. SARGAN J. D. 1964. Wages and Prices in the United Kingdom: A Study in Econometric Methodology, 16, 25–54. in Econometric Analysis for National Economic Planning, ed. by P. E. Hart, G. Mills, and J. N. Whittaker. London: Butterworths.
23. VANCE, M., STAN, H., DAVID, H. Econometric Modelling with Time Series. New York: Cambridge University Press. 2013. pp. 662-11. ISBN 978-0-521-13981-6.
24. BOMD, S., BOWSHER, C., WINDMEIJER, F. Criterion-based Inference for GMM in Autoregressive Panel Data Models. *Economic Letters*, 2001, Vol. 73, No. 3, p. 379-388.
25. ARELLANO, M. and BOND, S. Some tests of specification for panel data: Monte Carlo evidence and an application to employment equations. *The Review of Economic Studies*, 1991, Vol. 58, No. 2, p. 277-297.
26. BLUNDELL, R. and BOND, S. Initial conditions and moment restrictions in dynamic panel-data models. *Journal of Econometrics*, 1998, Vol. 87, No. 1, p. 115-143.
27. de Sá, S.A. and DAUBANES, J. Limit pricing and the (in)effectiveness of the carbon tax. *Journal of Public Economics*, 2016, Vol. 139, p. 28-39.
28. KANG Y-Q, ZHAO T, YANG Y-Y. Environmental Kuznets curve for CO2emissions in China: a spatial panel data approach. *Ecol Indic*, 2016, Vol. 63, p. 231-239.
29. SEBRI, M. and BEN-SALHA, O. On the causal dynamics between economic growth, renewable energy consumption, CO2 emissions and trade openness: fresh evidence from BRICS countries. *Renew Sustain Energy Rev*., 2014, Vol. 39, p. 4-23.
30. WANG, S, LI, Q, FANG, C, ZHOU, C. The relationship between economic growth, energy consumption, and CO2 emissions: empirical evidence from China. *Sci Total Environ*, 2016, Vol. 542, p. 360-371.
31. PACESILA, M, BURCEA, SG, COLESCA, S-E. Analysis of renewable energies in European Union. Renew Sustain Energy Rev, 2016, Vol. 56, p. 156-1570.

CYSENI 2019, May 23-24, Kaunas, Lithuania
ISSN 1822-7554, www.cyseni.com

ELECTRIC VEHICLES AND THEIR CHARGING PATTERNS IN ENERGY PLANNING MODELS

E. Neniškis
Lithuanian Energy Institute
Breslaujos str. 3, LT-44403 Kaunas – Lithuania
Email: eimantas.neniskis@lei.lt

ABSTRACT

Latest studies estimate that global temperatures will increase by 2,9-3,4°C in 2100 even with agreed measures in Paris climate agreement. Therefore, more ambitious actions are necessary to achieve climate targets. Energy planning models like MESSAGE, TIMES, Balmorel are well suited and widely used to estimate least-cost energy sector development pathways to meet set environmental goals. However, many sectors are interconnected and often complex multisectoral models are needed to find best solutions how to decarbonize the economy.

A significant share of greenhouse gas emissions is from transport sector. It is apparent that changes in this sector are necessary in order to limit global temperature increase to 2%. Carbon emissions in this sector potentially could be reduced by electric vehicles. However, it is important to assess how high penetration of electric vehicles will affect not only greenhouse gas emissions, but also other sectors, primarily energy sector. Emission reduction by switching to electric vehicles could be undermined by increased power production in fossil power plants to satisfy additional electricity demand to power them. On the other hand, flexible charging could be used to balance peak generation from variable renewable sources, which could result in higher penetration of renewable sources. For this reason, there is a benefit to include electric vehicles in energy planning models, especially in ones, which are used to estimate possible decarbonisation pathways. The aim of this paper is to present a methodology on how electric vehicles can be modelled in energy planning models.

In described methodology an optimization problem is defined to distinguish vehicle departure and arrival patterns from hourly traffic volume data. Departure and arrival patterns allows to determine vehicle state - on the road, parked at home, parked somewhere else. It is important because electric vehicle charging capabilities depend on its state, i.e. all vehicles that are parked at home can be charged, only part of vehicles parked somewhere else can be charged and vehicles on the road cannot be charged at all. In energy planning models if all electric vehicles are represented by a single technology, then it is as if everyone could share these vehicles, because the same capacity can be used for different travel patterns, so total installed capacity (vehicle count) required to satisfy travel demands can be much lower than in real life. Since total charging capacity is related to electric vehicle count, it can also be lower than it should be. Furthermore, this “car sharing” decreases the time when electric vehicles can be charged, resulting in distorted charging patterns. To reduce this affect, traffic patterns are divided into components based on vehicle arrival and departure patterns. Each component is set as a separate demand in an energy planning model, which is satisfied by a separate electric vehicle technology. Each electric vehicle technology has its own energy storage (battery) and charging technology modelled. This separation of components does not eliminate “car sharing” problem but it helps to reduce it. It still exists within the components but not between them.

Methodology was tested by incorporating explained electric vehicles model into isolated Lithuanian energy and heat sectors model. From modelling results it was noticed that electric vehicle charging patterns reacted to power availability and partially absorbed electricity production variability from wind resulting in higher wind power penetration (53,2% vs 48,7% in 2050), compared to scenario without electric vehicles.

Keywords: electric vehicle, MESSAGE, energy planning, model, charging pattern

CYSENI 2019, May 23-24, Kaunas, Lithuania
ISSN 1822-7554, www.cyseni.com

ENERGY STORAGE MANAGEMENT SYSTEM FOR VILLAGE NETWORK WITH HIGH PENETRATION OF ROOFTOP SOLAR PV: A CASE STUDY OF THAILAND

C. Srithapon, A. Siritaratiwat, R. Chatthaworn
Electrical Engineering Department, Faculty of Engineering
Khon Kaen University
Khon Kaen, 40002 – Thailand
Email: chitchai.sr@kkumail.com

P. Fuangfoo
Provincial Electricity Authority (PEA)
Bangkok, 10900 – Thailand

ABSTRACT

The increasing of rooftop solar photovoltaic (PV) in residential building can help to gain the portion of clean energy generation in power network. However, electricity energy from solar PV is available only in daylight and its output power depends on solar radiation intensity. Where, these characteristics of solar PV cause to negative impacts on village network such as load factor decrease and overvoltage and, in many researches, an energy storage system is essentially required to deal with these problems. Accordingly, the energy storage management system for mitigating the impacts from high penetration of rooftop solar PVs in a village network is proposed in this study. The aim of this paper is to optimize the size, operation and location of battery energy storage system (BESS). In addition, the objective function is to maximize economic benefit from the investment of BESS that includes battery price arbitrage, peak demand reduction, energy losses reduction and carbon emission reduction, while system load factor improvement is considered. The newly optimal power flow techniques developed by using the following control method of load factor correction curve combination with energy price arbitrage pattern. First, the size and operation of BESS are optimized by using genetic algorithm (GA) and then its optimal location is finding by using search method. To verify the effectiveness of the proposed system, a case study of real village network in Udon Thani, Thailand is selected. The proposed approach has been developed and simulated in MATLAB. By using this methodology, the numerical results show that load factor of village network with high penetration of solar PVs is improved and reach to a desired value, that is not lower than the load factor in the case without solar PV integration in the network. In addition, economic benefit which is a net present value (NPV) of BESS investment is maximized. Furthermore, network energy losses are decreased during the peak load time, and all buses voltages operate within theirs limits.

Keywords: battery, economic benefit, genetic algorithm, net present value, optimization, residential network

1. INTRODUCTION

Climate change and global warming problem due to greenhouse effect are pressing issue of the world. Hence, to reduce greenhouse gas (GHG) emission such as CO_2 is very concerned in power production. Indeed, Thailand also pay attention on this role by setting a target of renewable energy generation portion to 30% of all energy consumption within 2036 in alternative energy development plan (AEDP) 2015 [1]. In fact, Thailand is a country that locates in tropical zone which has high potential of solar energy [2]. In addition, the installation costs of solar photovoltaic (PV) system for residential is continuously reduced [3]. Therefore, Thailand government tried to promote the using of solar PV especially rooftop solar PV installed in buildings. However, the increasing of rooftop solar PV in households can impact to power network especially in low voltage network such as village network. For the negative impacts on power network, there are various impacts such as power quality issue due to high harmonic generation from DC-AC converter [4], power fluctuation due to the uncertainty of solar irradiation and overvoltage in the duration of solar

PV generation exceeds the demand [5]. This is the challenge of the distribution system operator (DSO) of Provincial Electricity Authority (PEA), who is a state-owned enterprise responsible for power distribution and electricity retailing for 74 provinces except Bangkok metropolis and its suburbs [6], to deal with this situation.

Several researches studied about how to deal with the negative impacts of renewable energy sources (RES) integration in network. Research works [7]-[9] and [10] proposed the use of energy storage system (ESS), because its technology and price will be commercialized for utility and residential applications in a near future [11]. For example, a study in [12], optimal locating, sizing and operating ESS, in residential system with rooftop solar PVs is proposed for flattening the daily power demand curve by considering a target of desired load factor. Moreover, the voltage profile is enhanced by optimal dispatching reactive power in ESS. However, they did not evaluate the cost of ESS that is very important for project investment. Specifically, in [13], authors have applied ESS to do economic optimal power flow in microgrid with RES integration. Nevertheless, they did not consider some benefits related to ESS installation, such as transmission access fee reduction and energy losses reduction. Instead, most possible benefits and costs from ESS deployment to a utility is presented in [14], for example, peak power generation reduction, energy price arbitrage, reduction of energy loss, transmission and distribution (T&D) systems upgrade deferral, reduction of CO_2 emission and reactive power support are evaluated. However, optimal strategy of ESS is only proposed for locating and sizing ESS while optimal ESS operation is not presented. Indeed, only upgrade deferral of T&D benefit is significant to gain a high net present value (NPV) of ESS investment because cost of ESS deployment is still high. Also, a study in [15] is presented the optimal operation, size and location for battery energy storage system (BESS) in low voltage distribution system with high integration of solar PVs. Indeed, BESS optimal operation strategy uses the following control method of solar PV generation profile combination with economic benefit pattern that is consisted of energy price arbitrage, reduction of CO_2 emission cost and reduction of transmission access fee. However, improving system load factor is not considered in that work.

In order to fulfill the previous research works, this paper proposed the energy storage management system to enhance efficiency of village network with high penetration of rooftop solar PVs. The approach strategy is using a battery energy storage system (BESS) for optimal power flow in low voltage distribution system. In addition, sizing, operating and locating of BESS are optimized to improve network load factor and the economic benefits from BESS investment which are considered as NPV. The considered economic benefits of BESS investment in this paper are battery prices arbitrage, power demand peak reduction, energy losses reduction and CO_2 emission reduction. Finally, load, PV, BESS and village network of a study case are modeled, and the power flow calculation is simulated in MATPOWER 6.0 [16] while, an optimization problem is solved by genetic algorithm (GA) implemented in MATLAB (Natick, Massachusetts, USA).

The remainder of this paper is organized as follows: Section 2 explains a methodology that describes modeling of load, PV and BESS including a proposed optimal strategy. Section 3 presents results and discussions from the simulation of the proposed strategy performing on a village network. Finally, Section 4 is a conclusion that highlights the major contribution of this work.

2. METHODOLOGY

This section describes a proposed methodology of energy storage management system (ESMS) for village network that is shown its framework method in Fig. 1. In addition, the aim of this work is to optimize size, operation and location of BESS in a low voltage distribution system with rooftop solar PVs. As shown in Fig. 1, village network, historical load curve, solar PV generation profile, battery model and electricity tariffs are used as input data for optimal power flow (OPF) that is based on technical-economical technique. Consequently, optimization problem is formulated, and a proposed optimal strategy is used for finding an optimal size, operation schedule and location of BESS.

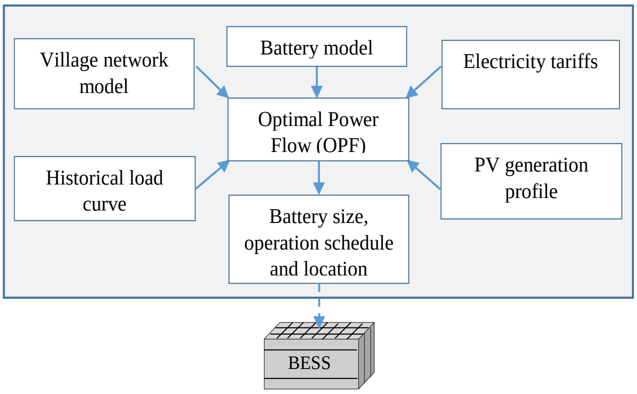

Fig. 1. Energy storage management system (ESMS) framework

2.1. Load, PV and BESS modeling

Firstly, village load is modeled as a residential load curve for 24 hours of a day, that is collected from load research data of PEA [17]. Indeed, daily load curve is generated from last two years of historical data and then is constructed to be the averaged model for 24 hours of a day which is selected as a representative load model for planning years. Secondly, solar PV model is assumed by the following; all rooftop solar PV units were already installed in the network and operated at unity power factor. In fact, historical data of hourly solar PV outputs for two years are collected from the real installation place in Udon Thani, Thailand. In addition, all installed solar PV modules are obtained the same solar irradiance. For the daily generation profile of solar PV, its 24-hour interval is defined same as the load profile and then hourly solar PV curve is normalized by dividing its daily peak value. While, vanadium redox battery (VRB) is selected for this study, because it has high efficiency, long life cycle [18]. Moreover, it can be applied for a long time charging and discharging. Therefore, the employment of VRB in residential network with solar PV integration is cost effective. Because of very small self-discharge in VRB [19], it is neglected in this work. Finally, the efficiency of both solar PV and battery inverter are assumed to be 100% and operate only in real power supply mode.

2.2. Problem formulation

As mentioned before, the optimal power flow by using BESS can mitigate negative impacts of RES in network, such as load factor improvement and voltage control. On the other hand, due to high cost of BESS investment, the economic benefit from its deployment should be considered. In this study, there are four possible economic benefits that can be occurred as following:

1) The direct economic benefit of BESS is buying energy from the main grid to charge battery with a low price in off peak rates and then selling the stored energy back to the main grid with higher price during on peak rates that is called battery arbitrage (BA).

2) Same as battery arbitrage, the energy is charged with a low CO_2 emission rate in off peak period and then the energy is discharged back to network during on peak period which the CO_2 emission rate is high. Moreover, it can be said that, BESS can help to reduce CO_2 emission from the generation of fossil power plant by storing energy from surplus solar PV generation during day time and then discharge back to network during night time. Consequently, CO_2 emission reduction (CR) can be evaluated to be an economic benefit term by using the damage cost of CO_2 emission saving.

3) In order to reduce energy losses, flattening substation transformers load curve by using BESS allocation is presented to improve system load factor [12] which can reduce power demand in the peak time. Therefore, the highest power losses occurring in the peak time can be reduced which can consequently benefit to the total energy losses reduction (LR).

4) Use of BESS to discharge some power into the network during peak period can shave peak demand. As a result, the cost of peak reduction (PR) can be converted to an economic benefit as transmission access fee saving.

Therefore, an objective function in this paper is proposed based on NPV as shown below:

$$F_{obj} = \sum_{n=1}^{N} \left((BA + CR + LR + PR - BESS_{O\&M}) \times \left(\frac{1+i_f}{1+d_r} \right)^n \right) - BESS_{inv} \tag{1}$$

where *BA*, *CR*, *LR*, and *PR* are the benefits of battery arbitrage, CO_2 emissions reduction, energy losses reduction and peak reduction, respectively. While, $BESS_{O\&M}$ is an operation and maintenance cost of BESS deployment. Indeed, these benefits and cost are evaluated for all project period of *N* years that is usually equal to a battery life time. In addition, i_f , d_r and *n* are inflation rates, discount rates and year of evaluation, respectively that are used as a multiplier for NPV calculation. Lastly, $BESS_{inv}$ is a first time investment cost of BESS installation. Accordingly, the all benefits in this paper are formulated as shown in (Eq. 2)-(Eq. 5):

$$BA = 365 \times \sum_{i=1}^{24} \left[(P_i^b - P_i^{rev}) \times E_i^{pr} \right] \tag{2}$$

$$CR = 365 \times \sum_{i=1}^{24} \left[(P_i^b - P_i^{rev}) \times co_i^{cdm} \right] \tag{3}$$

$$LR = 365 \times \sum_{i=1}^{24} (P_i^{LR} \times E_i^{pr}) \tag{4}$$

$$PR = 12 \times c_{dr} P_m^{DR} \tag{5}$$

where P_i^b and E_i^{pr} are battery dispatching power (kW) and electricity price rates ($/kWh) at hour *i*, respectively. While, P_i^{rev} is the reverse power flow (kW) from the village network to the main grid that is occurred when rooftop solar PVs power generation exceeds network power demand. The reverse power flow in this paper is defined as negative value. In addition, in case of no policy for the utility to pay the surplus energy from residential solar PV, using BESS to store this surplus energy not only can protect voltage rise issue in network, but also make a profit by selling this no cost energy back to village. Consequence, co_i^{cdm} parameter in the (Eq. 3) is a CO_2 emission cost damage rates ($/kWh) at hour *i*. The third of benefit term is an energy losses reduction (Eq. 4), where P_i^{LR} is power losses reduction (kW) at hour *i*. The last of all benefits is a peak reduction (Eq. 5), where c_{dr} and P_m^{DR} are montly peak demand charged ($/kW) and reduction of peak demand (kW), respectively. In addition, the costs related to BESS deployment can be expressed as follows:

$$BESS_{inv} = C_p P_{rate}^B + C_e E_{rate}^B \tag{6}$$

$$BESS_{O\&M} = C_{Mp} P_{rate}^B + C_{Me} E_{rate}^B \tag{7}$$

from (Eq. 6) and (Eq. 7), C_p ($/kW) and C_e ($/kWh) are the first time investment costs of BESS related to inverter power rating (P_{rate}^B; kW) and enegy capacity rating (E_{rate}^B; kWh), respectively. While, C_{Mp} ($/kW) and C_{Me} ($/kWh) are the operation and maintenance costs of BESS related to power rating and enegy capacity rating, respectively.

2.3. Proposed optimal strategy

To improve system load factor by using BESS, the status of BESS operation could be “charged” at low power demand and “discharged” at high power demand. In fact, the BESS daily operation pattern can be constructed by using the load factor correction (LFC) curve. That the equation of load factor (LF) and LFC curve are expressed as following:

$$LF = \frac{P_{avg}^D}{P_{peak}^D} \tag{8}$$

$$LFC_i = \frac{P_i^D - P_{avg}^D}{P_{peak}^D - P_{avg}^D} \tag{9}$$

where P_i^D, P_{avg}^D and P_{peak}^D are power demand (kW) at hour i, average value of daily power demand (kW) and peak of power demand (kW), respectively. However, the project deployment must consider the maximum benefit of investment, therefore, BESS could store energy at low energy prices period and supply back to network at the high energy price period. Consequently, the operation pattern of the BESS can be constructed by using the price arbitrage pattern (PAB) that is expressed as follows:

$$PAB_i = \frac{E_i^{pr} - E_{avg}^{pr}}{E_{peak}^{pr} - E_{avg}^{pr}} \tag{10}$$

where E_i^{pr}, E_{avg}^{pr} and E_{peak}^{pr} are electricity energy price rates ($/kWh) at hour i, average value of daily electricity energy price rates ($/kWh) and peak of electricity energy price rates ($/kWh), respectively.

According to the proposed method of this study, the optimization objective is to improve system load factor with the maximum benefit of BESS investment (maximized NPV). Therefore, the scheduling of battery operation using load factor correction (LFC) curve combining with energy price arbitrage (PAB) pattern via following control method is proposed. Consequently, a new proposed objective function for daily optimal power flow by using BESS can be expressed as follows:

$$P_i^b = \beta P_{max} \tag{11}$$

where P_i^b is the battery dispatced power (kW) at hour i (positive value when BESS discharges power and negative value when the power is charged in to the BESS). Secondly, P_{max} is the maximum dispatched power (kW) of the battery that could not be higher than substation transformer rating (S_{rate}^{tr}; kVA). Finally, β and α are weighting factor for BESS optimal size and operation, respectively.

To schedule BESS operation following LFC curve, BESS will be charged at low power demand perirod and BESS discharges at high power demand period. Thus, when α = 1, only load factor is improved. While, when α = 0, the weighting factor for load factor improvement is equal to zero; therefore, BESS operates following only PAB curve to maximize benefit of energy price arbitrage. In addition, β and α parameters are tuned by the genetic algorithm (GA) optimization and their values is varied between 0-1 based on the objective functions (Eq. 1) and optimization constraints.

For the maximum life cycle time of BESS, the 24 hours operation of charging and discharging energy could be balanced by considering roundtrip efficiency which is considered as constrains and can be writen as shown (Eq.12).

$$\sum_{i=1}^{24}(P_i^{bd}) = \sum_{i=1}^{24}\eta(P_i^{bc}) \tag{12}$$

where P_i^{bd} and P_i^{bc} are the discharged power (kW) from the BESS and charged power (kW) to the BESS at hour i, respectively. These two parameters could not exceed maximum limit (P_{max}; kW), while η is the battery round trip efficiency of BESS. As a result, the sizing of BESS power rating and energy capacity rating can be calculated as shown below:

$$P_{rate}^B = max(P_i^b) \tag{13}$$

$$E_{rate}^B = \frac{max(\sum_{i=1}^{h} E_i^b)}{\gamma} \tag{14}$$

where E_i^b is the stored energy (kWh) of BESS at hour that cumalates from hour i to hour h, while, γ is the battery depth of discharge (DoD) that represents a range of its operation between the highest and the lowest allowable battery state of discharge (SoC).

Because a typical village network is a small scale network consisting of one feeder or two feeders. Thus, in this work, the strategy for solving the optimal location of BESS focuses only one BESS installation because the operation and maintenance costs will be more economical. However, to protect overvoltage issue, the optimal operation do not allow reverse power flow in the network and the voltage of each bus has to be within lower and upper limits. According to PEA grid code standard, system voltage could be between 200 V and 240 V. Moreover, power flow of each line in the network could not exceed its thermal limitation. Therefore, inequality constraints for the technical term in this study are epressed as following:

$$P_i^{grid} \geq 0 \text{ and } V_{low} \leq V_{bus,i} \leq V_{up} \;\; ; i \in n_{bus} \tag{15}$$

$$I_{brance,i} \leq Icon_{max} \;\; ; i \in n_{branch} \tag{16}$$

where P_i^{grid} and $V_{bus,i}$ are grid supplied power (kW) and bus voltage (V) at hour i, respectively. Thus, V_{min} and V_{max} are lower and upper limits of voltage level, respectively. While, $I_{branch,i}$ is the current (A) of branch i, while $Icon_{max}$ is the maximum current (A) limit of branch corressponding to its thermal limit, respectively. While, n_{bus} and n_{branch} are number of bus and number of branch for village network.

The proposed procedure for solving optimal size, operation and location of BESS is presented in Fig. 2. At the first step, daily dispatch pattern of BESS is constructed by using the load factor correction curve (LFCc) combining with energy price arbitrage pattern (PAB) following control method. Secondly, the population of weighting factor such as β and α are generated by GA function implemented in MATLAB. Then, network power flow is performed via MATPOWER by varying BESS location to find a place that provides the minimum system energy losses. After that, the objective function and optimization constraints are evaluated. While, GA continually tunes β and α until the objective function meets the desired load factor and maximized NPV while all technical constraints are not violated.

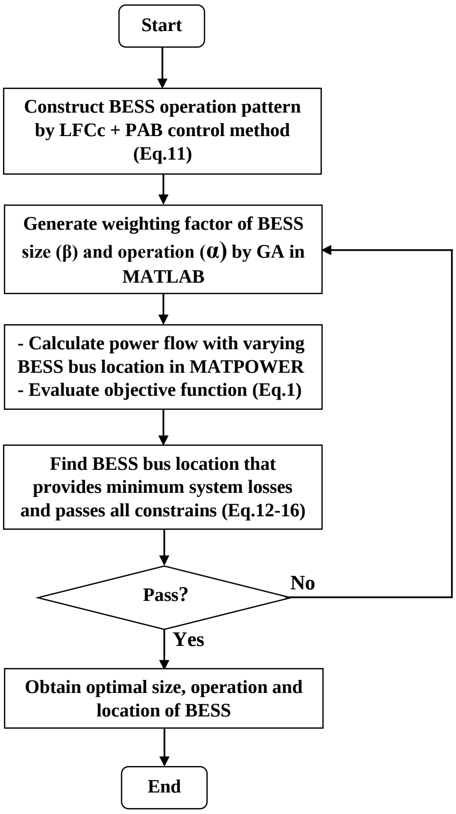

Fig. 2. Flow chart of proposed procedure

2.4. Case study

A case study for verifying capability of this proposed method uses the real village network that locates in Udon Thani, Thailand as shown in Fig. 3. The 43 buses radial system is connected with a medium voltage distribuition system at 22 kV through a 250 kVA substation transformer that steps down voltage to 230/400 V for 99 households. In this network, it is assumed to be a balance load sytem. Distributed solar PVs representing rooftop solar PVs in a village network that are placed at bus number 25, 28, 31, 40 and 43 to present the worst case of solar PVs impacts both voltage rise and power losses increase. In addition, solar PV power capacity of all units are varied for study the effect of high solar PV penetration in each scenario. Solar PV penetration level is defined as the ratio of total solar PV rated power to peak apparent power demand of a village. Infact, the daily peak load is 184.5 kVA that is calculated from the historical electricity bill of all households. In addition, the system power factor is set to be a constant at 0.90 lagging. Consequently, daily power demand curve and solar PV generation profile are collected from the two years historical data. Then, both curves are generated to an averaged model and then are normalized by its peak value for 24 hours of a day. Finally, the electricity energy price rates is defined by using the time of use (TOU) rates of Thailand electricity tariffs [20]. Moreover, the environment assessment is considered to model the saving of the damage cost of CO_2 emission ($/kWh) that relate to the damage cost of CO_2 emission ($/kg) and the CO_2 emission rate (kg/kWh). The damage cost of CO_2 emission is assumed to be 0.0257 $/kg and the CO_2 emission rate from fossil power plants varying by each hour of a day is refered from the study in [15]. Therefore, the damage cost of CO2 emission are varying by each hour of a day. The relationship of village load curve and solar PV output profile is presented in Fig. 4 (a) and the electricity TOU price rates and the damage cost of CO2 emission rates are shown in Fig. 4 (b).

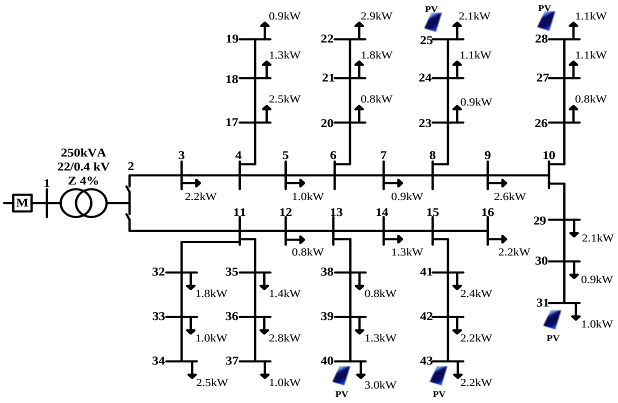

Fig. 3. A village network for case study in Udon Thani, Thailand

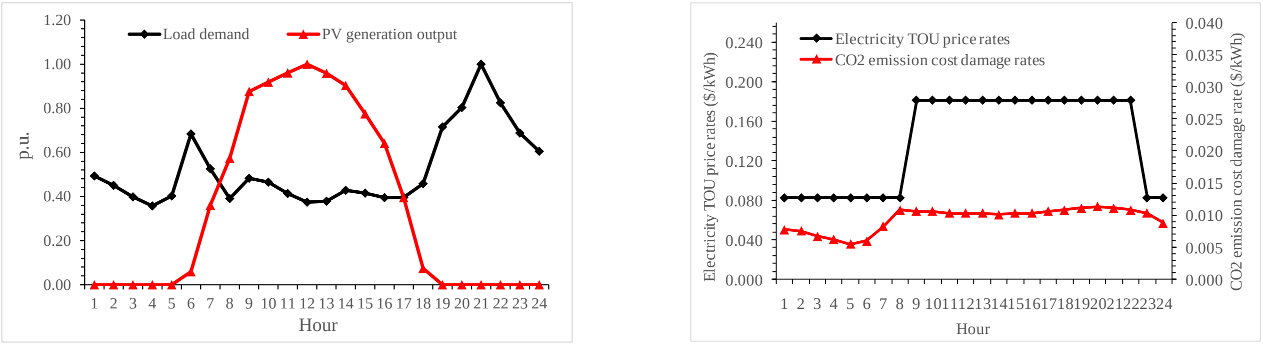

(a) (b)

Fig. 4. (a) The relationship of village load curve and PV generation output profile
(b) The electricity TOU price rates and the damage cost of CO_2 emission rates

3. RESULTS AND DISCUSSIONS

This section presents the success of the energy storage management system (ESMS) in this study. Firstly, power flow of a village case has been simulated by MATPOWER to perform the effect of PV for each penetration level. The proposed method has been evaluated in MATLAB to proof its effectiveness that is consisted of both technical issue mitigation and economic benefit from BESS deployment.

3.1. Effect of varying solar PV penetration

In this study, the increment of solar PV penetration is assumed to be increased from 0% to 100% with 20% for each step. Fig. 5 (a) shows the effect of each solar PV penetration level to power demand profile. While, system load factor, energy losses and maximum bus voltage versus solar PV penetration level are presented in Fig. 5 (b). As a result, there is a reduction of load factor when solar PV penetration level is increased becauase of non-matching between the increment of solar PV generation and power demand during the intraday. For the energy losses, the losses seem to be decreased at low level of solar PV penetration; however, at the higher level of penetration, the losses are continuously increasing as same as the increasing of reverse power which is the power that flow back into the main grid because the power from solar PV is higher than power demand in the network. For the system voltage, it will rise following the solar PV penetration and the maximum voltage (Vmax) is occurred at bus number 31 which solar PV is installed.

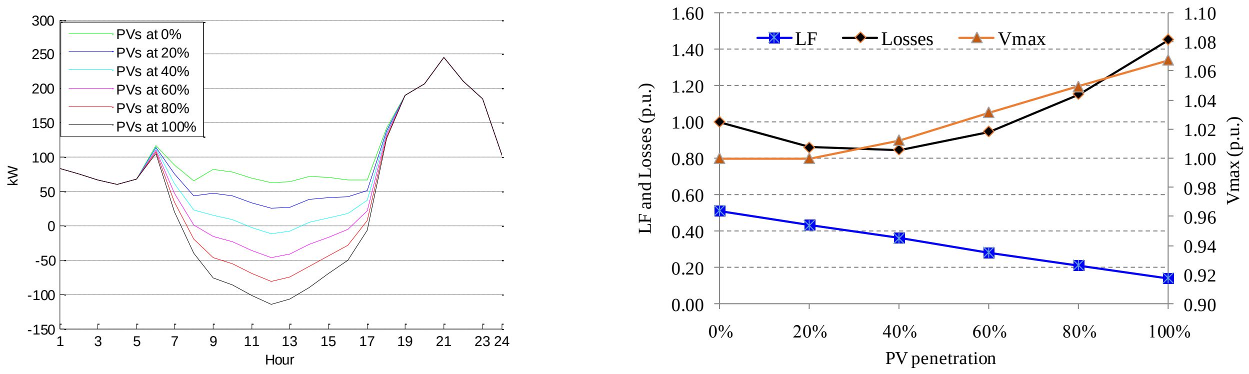

(a) (b)

Fig. 5. (a) Effect of each solar PV penetration level to load profile, (b) Load factor (LF), energy losses (Losses) and maximum voltage (Vmax) versus PV penetration level

3.2. Proposed method evaluation

As a result of negative effects from each solar PV penetration level in Fig. 5, load factor (LF), energy losses and system voltage simultaneously confront the negative effects when solar PV penetration level reaches 40%. Therefore, the ESMS is proposed to mitigate these effects with solar PV penetration level at 40%, 60%, 80% and 100%, respectively. By these assumptions, the at least load factor could be not lower than the case of no integration of solar PV in network (base case LF is 0.51). Consequently, the desired LF of the test is defined to 0.52. The effectiveness of the proposed system for the technical enhancement is shown in Table 1. Accordingly, the evaluation results of daily load factor, daily energy losses, daily reverse energy and maximum/minimum (Max/Min) of system voltage are improved by the proposed optimal strategy for all solar PV penetration levels.

Table 1. Technical evaluation result

Solar PV penetration	Case	Daily load factor	Daily energy losses (kWh)	Daily reverse energy (kWh)	Max/Min of system voltage (Volt)
40%	Without ESMS	0.36	62.57	21.20	232.8/ 211.4
	With ESMS	0.52	60.16	-	232.4/213.7
60%	Without ESMS	0.28	69.96	213.65	237.2/211.4
	With ESMS	0.52	55.44	-	231.8/215.7
80%	Without ESMS	0.21	85.14	477.43	241.5/ 211.4
	With ESMS	0.52	56.61	-	233.6/216.3
100%	Without ESMS	0.14	107.52	742.71	245.5/211.4
	With ESMS	0.52	64.53	-	235.5/216.7

Finally, based on economic parameter for NPV calculation as shown in Table 2, the evaluation results of BESS location, size and its cost-benefit for each solar PV penetration level are shown in Table 3.

Table 2. Economic parameter

Parameter	Value (unit)	Parameter [15]	Value (unit)
i_f	1.5%	c_{Mp}	9$/kWh
d_r	7.0%	c_{Me}	0
N	25 years	c_p	426 $/kW
C_{dr}	4.2 $/kW	c_e	100 $/kWh
γ	0.8	η	75%

Table 3. Economic evaluation result (Eq. 1)

Solar PV penetration	BESS location	BESS size (kW/kWh)	Investment cost ($)	O&M ($)	BA ($)	PR ($)	LR ($)	CR ($)	NPV ($)
40%	Bus#2	64/321	59,364	8,135	112,105	36,198	5,218	3,038	89,060
60%	Bus#8	86/503	86,936	10,963	178,459	51,174	15,713	8,662	156,109
80%	Bus#8	105/703	115,030	13,322	292,660	65,499	25,185	17,620	272,612
100%	Bus#8	120/870	138,120	15,281	398,162	79,667	36,053	26,455	386,936

Data in Table 3, shows the optimal size and location of BESS and economic benefit related its deployment versus varying PV penetration level. The numerical results of all economic evaluation values are increased following the increment of solar PV penetration level. Consequently, a net present value (NPV) from BESS investment is positive for all penetration levels which means that the BESS installation is worth for investment. By a comparison between the proposed ESMS method with previous method from the literature reviews in [14] and [15], it shows that the proposed ESMS method can effectively improve load factor and maximize NPV together, whereas those studies can not provide. In addition, the proposed strategy can gain village network capability for integration of high solar PV penetration.

4. CONCUSSION

This paper proposes the energy storage management system for mitigating the negative impacts from high penetration of rooftop solar PVs in a village network. Indeed, the aim of this work is to optimize size, operation and location of BESS unit. In addition, the contribution of this work is developing a novelty technical-economic optimal power flow by using the following control method of load factor correction curve combining with energy price arbitrage pattern. In this proposed framework, input data consisting of village network parameter, load model, solar PV model, vanadium redox flow battery model and electricity price rates (TOU) are used for optimal power flow calculation. Consequently, the optimization problem is formulated based on the objective of maximizing NPV while system load factor is considered to meet the desired value. Then BESS size and operation scheduling are optimized by using genetic algorithm (GA) function in MATLAB. In fact, a case study from a village network, power demand and solar PV generation profiles from real system at Udon Thani, Thailand are used to verify effectiveness of the proposed ESMS. Accordingly, the study result from power flow simulation in MATPOWER shows that the low of system load factor due to high penetration of solar PV in the network can be mitigated. The load factor can be reach to 0.52 that is higher than the load factor in the case without solar PV integration. The economic benefit based on net present value (NPV) of BESS investment is maximized which can reach to 386,936$ for a case of 100% of solar PV penetration. Thus, this proposed method can make the profits from BESS investment. Furthermore, network energy losses are decreased, especially during the peak load time while all technical constraints are not violated.

ACKNOWLEDGEMENTS

This research publication was supported by grants of Khon Kaen University, Thailand.

REFERENCES

1. INTERNATIONAL RENEWABLE ENERGY AGENCY. *Renewable Energy Outlook: Thailand 2017,* 2017. Link to the internet <https://irena.org/publications >.
2. Department of Alternative Energy Development and Efficiency, Ministry of Energy, Thailand. Areas with solar power potential, 2013. Link to the internet < http://weben.dede.go.th/webmax/content/areas-solar-power-potential>.
3. Fu, R., FELDMAN, D., MARGOLIS, R. *U.S. Solar Photovoltaic System Cost Benchmark: Q1 2018*, 2018. Link to the internet <https://nrel.gov/docs/fy19osti/72399.pdf>.
4. SHEVCHENKO, S.Y., VOLOKHIN, V.V., DIAHOVCHENKO, I. M. Power quality issues in smart grids with photovoltaic power stations. *Journal Energetika*, 2017, Vol. 63, p. 146-53.
5. NGUYEN, A. T., CHAITUSANEY, S., YOKOYAMA, A. Optimal Strategies of Siting, Sizing, and Scheduling of BESS: Voltage Management Solution for Future LV Network. *IEEJ Trans*., 2019, Vol. 22, p. 1-11.
6. Provincial Electricity Authority, Thailand. Link to the internet < https://www.pea.co.th/en>.
7. YANG, Y., BREMNER, S., MENICTAS, C., KAY M. Battery energy storage system size determination in renewable energy systems: A review. *Renew. Sustain. Energy*, 2018, Vol. 91, p. 109-125.
8. MAY, G. J., DAVISON, A., MONAHOV, B. Lead batteries for utility energy storage : A review. *J. Energy Storage*, 2018, Vol. 15, p. 145-157.
9. HESSE, H.C., MARTINS, R., MUSILEK, P., NAUMANN, M., TRUONG, C.N., JOSSEN, A. Economic optimization of component sizing for residential battery storage systems. *Energies*, 2017, Vol. 10, p. 1-19.
10. BARAI, G.R., VENKATESH, B., AWADALLAH, M.A. Optimization of Hybrid Energy Storage Systems for Power Curve Smoothening at Grid Scale. *Canadian.J. Elec. & Com. Eng.*, 2018, Vol. 41, p. 87-94.
11. INTERNATIONAL RENEWABLE ENERGY AGENCY. *Electricity storage and renewables: Costs and markets to 2030,* 2017. Link to the internet <https://irena.org/publications>
12. SARDI, J., MITHULANANTHAN, N., HUNG, D.Q. Strategic allocation of community energy storage in a residential system with rooftop PV units. *Appl. Energy*, 2017, Vol. 206, p.159-171.
13. EL-HENDAWI, M., GABBAR, H. A., EL-SAADY, G., EL-NOBI, A. I. Control and EMS of a grid-connected microgrid with economical analysis. *Energies*, 2018, Vol. 11, p. 1-20.
14. SARDI, J., MITHULANANTHAN, N., GALLAGHER, M., HUNG, D.Q. Multiple community energy storage planning in distribution networks using a cost-benefit analysis. *Appl. Energy*, 2017, Vol. 190, p. 453-463.

15. JANNESAR, M.R., SEDIGHI, A., SAVAGHEBI, M., GUERRERO, J.M. Optimal placement, sizing, and daily charge/discharge of battery energy storage in low voltage distribution network with high photovoltaic penetration. *Appl. Energy*, 2018, Vol. 226, p. 957-966.
16. ZIMMERMAN, R.D., MURILLO-SANCHEZ, C.E., THOMAS, R. J. M. MATPOWER : Steady-State Operations, *Systems Research and Education*, 2011, Vol. 26, p. 12-19.
17. Provincial Electricity Authority, Thailand, *Load Research of PEA*, 2018. Link to the internet < http://peaoc.pea.co.th/loadprofile/en/>.
18. CHOI, C., NOH, H., KIM, S., KIM, R., LEE, J., HEO, J., KIM H.T. Understanding the redox reaction mechanism of vanadium electrolytes in all-vanadium redox flow batteries. *J. Energy Storage*, 2019, Vol. 41, No. 2, p. 87-94.
19. ZHANG, X., LI, Y., SKYLLAS-KAZACOS, M., BAO, J. Optimal sizing of vanadium redox flow battery systems for residential applications based on battery electrochemical characteristics. *Energies*, 2016, Vol. 9, p. 1-20.
20. Provincial Electricity Authority, Thailand. *Electricity Tariffs (November 2018)*, 2018. Link to the internet <https://www.pea.co.th/en/electricity-tariffs>.

CONSUMER PREFERENCES IN ELECTRIC VEHICLE PROMOTION SYSTEM: THE CASE OF LITHUANIA

P. Mačiulis
Lithuanian Energy Institute
Breslaujos str. 3, LT-44403 Kaunas – Lithuania
Email: povilas.maciulis@gmail.com

ABSTRACT

The transport sector is one of the major polluter of greenhouse gases and other pollutants. Electric vehicles are considered as one of the most effective technologies for decrease greenhouse gas emissions from the transport sector, reduce dependence on oil and improve air quality. Although electric vehicles can significantly contribute to energy consumption efficiency, reduction of carbon dioxide emissions and independence from petroleum imports, numerous technical and economic challenges burden electric vehicle mass-market adoption. Having faced the problems of air quality decrease, a number of countries worldwide are striving to promote electric vehicle usage. One of the reasons why natural market entry for electric vehicles is relatively slow can be linked to their prices, which are higher than the prices of traditional fossil fuel-driven vehicles. Trying to improve the situation, national and local authorities develop promotive policy instruments which enhance competitiveness of electric vehicles and increase their popularity among consumers. This article examines the effects of such policy measures, including tax iniciatives, grants, traffic regulations and investments in charging infrastructure. Consumer choices were assessed using willingnes to pay method. This article also employs a discrete choice model, expert evaluation and Simple Additive Weighing (SAW) methods. The results may serve as initial guidance for policymakers and investors in improving promoting measures for electric vehicles adoption.

Keywords: renewable energy in transport, electric vehicle, willingness to pay

1. INTRODUCTION

In the eyes of the public, electric vehicle technologies are treated as ones providing the following benefits: responding to the detrimental environmental effects caused by the transportation system, reducing national energy dependency and easing the pressure society puts on the energy sector (Windisch, 2013). The development of the electric-vehicle market offers the advantages related to human health, air and environment quality, grid resilience and economic growth (Daina et al. 2017, Malmgren, 2016). Due to the environmental impact and growing popularity of electric vehicles, the problems of their use and development raise increasing scientific interest. One of the reasons why natural market entry for electric vehicles is relatively slow can be linked to their prices, which are higher than the prices of traditional fossil fuel-driven vehicles. Trying to improve the situation, national and local authorities develop promotive policy instruments which enhance competitiveness of electric vehicles and increase their popularity among consumers (Yang et al., 2016). Electric vehicle promotion measures and efficiency of these measures have become relevant issues of scientific research.

Promotion systems as well as economic evaluations of individual incentives can be found in the studies introduced by Yan (2018), Jenna et al. (2018), Kester et al. (2018), Hardman et al. (2017), Zhang el al. (2017), Hall et al. (2017), Hall and Lutsey (2017), Jin and Slowik (2017), Yang et al. (2016), Langbroek et al. (2016), Mock and Yang (2014),Windisch 2013, Kampman (2011), etc. Along with all other benefits, electric vehicles serve as a convenient alternative to traditional means of transportation, and the changes in the transportation market are caused by the changes in consumer needs and expectations (Hardman et al., 2017). Namely for this reason the studies in the area of electric vehicle promotion must consider consumer preferences. The issues of consumer preferences in respect of electric vehicles were analysed in the studies conducted by Ramos-Real el al. (2018), Cecere et al. (2018), Hackbarth and Madlener (2016), Helveston et al. (2015), Chorus et al. (2013), Hackbarth and Madlener (2013), Ewing and Sarigöllü (2000) and other authors.

The main purpose of this article is to identify the most efficient electric vehicle promotion measures in Lithuania with consideration of consumer preferences and assessment of the efficiency, feasibility and annual implementation costs of particular measures. This article employs a discrete choice model which is estimated by a logit regression. Measure efficiency and feasibility were assessed by employing the method of expert evaluation. The results were summarised by applying SAW (Simple Additive Weighing) method for multiple criteria decision-making problems.

2. THEORETICAL BACKGROUND

The variety of electric vehicle promotion measures is really wide. Scientific publications propose different classifications of these measures. For instance, electric vehicle promotion measures can be classified by their character, volume or administrative level (Mačiulis et al., 2018). IEA-RETD (2015) proposes segmentation by administrative levels and separation by three dimensions: vehicles, energy infrastructure and energy carries. Electric vehicle promotion measures can also be attributed to such categories as traffic regulation, charging infrastructure and monetary incentives, which are often limited in time and are only available to a limited number of eligible consumers (Tyrrell and Dernbach, 2011). Having analysed different categories of electric vehicle promotion measures, the authors of this article selected the most commonly used ones that, with consideration of their specifics and implementation practices, can be adapted in Lithuanian context. The selected electric vehicle promotion measures are presented in the Table below.

Table 1. Policy measures analysed in this article (compiled by the authors)

Category	**Promotion measure**
Monetary	Value added tax exemptions
	Direct subsidies for a vehicle purchase
	Vehicle tax exemptions
Traffic regulations	Free city centre parking
	Free use of bus lanes
Charging infrastructure	Free charging at public areas
	Financial support for charging stations near homes
	Financial support for charging stations near work

Unlike all other measures, value added tax exemptions and direct subsidies for a vehicle purchase were assessed together, leaning on Lieven's (2015) methodology. The sizes of these two measures were estimated with reference to the most common examples in Europe (Tsakalidis and Thiel, 2018). The options of the sizes used for this research are presented in the Table 2.

Table 2. The combinations of value added tax exemptions and direct subsidies (compiled by the authors)

No.	**Value added tax rate, %**	**Direct subsidies for a vehicle purchase, Eur**
1.	21	-
2.	14	12.000
3.	7	8.000
4.	0	4.000

Much marketing effort is wasted for assessment of consumers' willingness to pay (WTP). If the real price of a product is lower or equal to the WTP level, a consumer needs one item of this product (Varian, 1992). But the problem is that not all WTP-related studies are able to reflect real values and a real consumer decision to buy. The direct methods, which ask consumers to clearly define their WTP in open-ended questions, help to easily obtain and understand the survey data. Nevertheless, it should be noted that respondents are not always able to objectively assess their WTP when they are trying to compare competing products or services, especially if the hypothetical nature of surveys is borne in mind (Blatter el al., 2009).

Individual preferences play a key role in stimulating the demand for eco-friendly vehicles. Generally, when assessing consumers' WTP, the attributes of different technology vehicles, for instance, maintenance costs, vehicle performance, purchase tax exemption, fuel costs and driving range, are compared (Potoglou and Kanaroglou, 2007). In this article, we analyse consumers' WTP for an electric vehicle, and each electric vehicle promotion measure is treated as an attribute which generates higher value added compared with the one generated by traditional vehicles with internal combustion engines. The similar assessment of electric vehicle promotion measures (the estimations are based on the method of conjoint analysis) can be found in Lieven's (2015) study that explores two financial measures, two traffic control measures and three electric vehicle charging measures.

In this article, for estimation of WTP, we employ a discrete choice model which describes, explains and forecasts the choice of two or more discrete alternatives. In other words, discrete choice models are employed in the situations, when the possible result is a discrete size. For assessment of the situation in the transportation sector, discrete choice models were previously employed by Tanaka et al. (2014), Hoen and Koetse (2014), Hackbarth and Madlener (2013), Ziegler (2012), Higgins et al. (2012), Ewing and Sarigöllü (2000), Axsen et al. (2009), Mau et al. (2008), Potoglou and Kanaroglou (2007), Bunch (1993) and others.

To solve similar problems, the techniques of logistic regression and probit regression are commonly applied. These techniques estimate the probability that a person will choose a particular alternative. Models are commonly used to forecast how a personal choice will change along with the changes in the attributes of alternatives. A set of possible choices, comprising all possible alternatives, must meet three basic requirements (Train, 2002):

1. The set of alternatives must be exhaustive, and a person must choose one alternative from the set.
2. A person may choose only one alternative from the set, which means that by choosing one alternative, he/she refuses other alternatives.
3. The set must comprise a finite number of alternatives.

3. METHODOLOGY

The description of the methodology is structured into three parts: the first part describes the consumer preference survey, the second part characterises the expert evaluation, while the third part explains cost estimation and multi-criteria assessment.

As in practice it is impossible to know all the factors that may determine a personal choice, consumer preferences were researched by employing discrete choice models based on the stochastic presumptions and specifications that helped to assess unobtrusive factors. Discrete choice models define the probability that a person will choose a particular alternative. Here the probability is expressed as a function of obtrusive (marked x) and unobtrusive (marked γ) variables (factors). Human-choice related factors are expressed as the following function (Train, 2002, Fosgerau and Bierlaire, 2009):

$$y = h(x, \gamma). \tag{1}$$

Endogenous variable y can acquire values {0,1}, where, for instance, y = 0 denotes that the event under research will not occur, while y = 1 denotes that the even under research will occur.

Depending on different presumptions about the function of the distribution of unobtrusive factors, different discrete choice models are developed. Presuming that the distribution is of 'extreme value' (also known as double exponential Weibull distribution), a logit model is developed, while presuming that the distribution is normal, a probit model is developed.

Logit model thus far has been the most widely used model. The situation, when a person needs to choose one of two alternatives, is called a binary choice. While analysing a binary logistic regression, the probability ratio $P(y \leq j)/P(y > j)$, also known as odds, is commonly estimated. For instance, the odds $P(y \leq j)/P(y > j)$ indicates to which extent variable y is more likely to acquire higher rather than lower value.

Odds ratio indicates how odds are going to change if the corresponding variable increases by 1, but the values of other variables remain fixed. Odds ratio depends only on model coefficients. Suppose we are dealing with P(y > j)/P(y ≤ j). In this case, if variable x_1 increases by 1, the odds ratio changes by $e^{\hat{b}_1}$. Multiplier $e^{\hat{b}_1}$, namely odds ratio, is a quantitative estimate of the impact of variable x_1 in the model. If $\hat{b}_1 > 0$, it indicates that when x_1 is increasing, the probability that y will gain higher values is also increasing. This is a qualitative characteristic. To answer the question to which extent this probability is going to increase is impossible without knowing the very initial probability. Odds ratio is a compromise solution which indicates the plausible changes in the probability ratio (Čekanavičius, 2011).

Thus, the model of binary logistic regression is developed not for a dependent variable, but for the logarithm of its probability ratio, i.e. for the logit function:

$$ln\frac{P(y=1)}{P(y=0)} = b_0 + b_1x_1 + b_2x_2 + b_3x_3 + \cdots \tag{2}$$

An equivalent expression of the model is as follows:

$$P(y=1) = \frac{e^z}{1+e^z} = \frac{1}{1+e^{-z}}, \tag{3}$$
$$P(y=0) = 1 - P(y=1)$$

here $P(y=1)$ denotes the probability that event y = 1 will occur, while *z* is called a probability ratio logit function:

$$z = b_0 + b_1x_1 + b_2x_2 + b_3x_3 + \cdots, \tag{4}$$

where x_1, x_2, etc. denote obtrusive factors, while b_1, b_2, etc. stand for model parameter estimates. The logistic transformation of values *y* into values *z* is estimated by adjusting the logit function for forecasted values of variable y (Mazzocchi, 2008). Logit transformation is a logarithm of the probability ratio indicating that events y = 1 and y = 0 will occur. Logit relation allows to transform binary variable y into continuous variable z. Parameters β are estimated by employing the maximum likelihood estimation method. The difference between logistic regression and logit models is that logistic regression incorporates at least one independent variable which is continuous, whereas in logit models all independent variables are binary or categorical. Despite the above-mentioned difference, the names of these two models are often used as synonyms (Mazzocchi, 2008). The data collected during the survey were analysed by employing model (2). The main characteristic, which indicates if a logistic regression model matches the data, is classification table. While assessing the data, value y is forecasted for particular observations, and later it is checked whether the forecast overlaps with the real value y. The larger is the number of the overlaps, the more reliable is the model (Čekanavičius, 2011).

In the second part of the research, the method of expert evaluation was employed. For data collection, a questionnaire survey was conducted. The expert evaluation was arranged following the requirements of the social research ethics stipulating that (Kardelis, 2007): experts must possess sufficient competence to answer the questions, a researcher cannot affect respondents, experts give their agreement to participate in the survey. The authors of this article attribute the experts, who are most concerned with the issues under research and have directly or indirectly faced the problems of electric vehicle use and development in Lithuania, to the following groups:

- business (companies and associate business structures) representatives;
- scientists (personnel of higher education institutions);
- representatives of non-governmental organisations dealing with the issues of electric vehicles;
- representatives of public authorities.

The experts for the survey were selected by considering their competence and professional specifics, also by assessing the links between their institutions or organisations and/or the issues of electric vehicle infrastructure development in the public, business and non-governmental sectors. The questionnaire was distributed to 42 respondents by e-mail; 36 completed questionnaires were received.

The third part of the research is devoted to evaluation of the costs borne while implementing electric vehicle promotion measures. This article is not intended to estimate any specific costs for 2020 and 2030; it is aimed at estimation of the ratios that would allow to identify relative differences observed while implementing particular measures. Thus, although the estimations are based on the projected number of cars, costs are assessed leaning on the current cost level. The main reason for this is that it is impossible to estimate the exact value of particular cost components (for instance, annual permission for city centre parking or charging station technologies) in 2020 and 2030.

The principles, leaning on which we assessed VAT exemption and non-refundable subsidy costs, are provided in more detail. Subsidisation means direct costs to the state budget, whereas VAT exemptions are related to missed state budget revenue. These two different measures are assessed together, but the costs are calculated in three different proportions: (1) a 0% VAT tariff and a 4000 Eur subsidy, (2) a 7% VAT tariff and an 8000 Eur subsidy, (3) a 14% VAT tariff and a 12000 Eur subsidy. Since VAT tariff is a relative size depending on a product's price, it is necessary to estimate the average price of an electric vehicle; the size of the average price will be used for estimation of implementation costs. Table 3 presents the information about the most popular models and prices of electric vehicles in Europe in 2017 (Tsakalidis and Thiel, 2018).

Table 3. Most popular electric vehicles and their prices in Europe in 2017 (compiled by the authors with reference to the data presented in car manufacturers' websites)

Electric vehicle	**The number of M1 electric vehicles sold in Europe over 2017, units**	**Price (without VAT) 2018-12**	**Price (including 21% VAT) 2018-12**
Renault Zoe	30.628	19.274	24.398
Nissan Leaf	17.454	28.361	35.900
Tesla Model S	15.553	75.880	91.814
BMW i3	14.493	33.698	42.656
Volkswagen e-Golf	12.895	31.613	40.017

The average price of an electric vehicle was calculated based on the prices of the five new best-selling electric vehicles in Europe. As previously mentioned, VAT exemption is related to missed state budget revenue. Therefore, annual implementation costs for particular measures are estimated by multiplying this missed revenue (NP) by the projected number of newly sold electric vehicles under different development scenarios. The costs of subsidisation (SK) are estimated in the same way: the projected number of newly purchased electric vehicles is multiplied by the size of subsidies. Total annual implementation costs (A) are estimated by the following formula:

$$A = (NP_{(1,2,3)} + SK_{(1,2,3)}) \text{ x } S_{(\text{electric vehicle sales})} ,$$

here: A – annual implementation costs of a measure, NP – missed state budget revenue with granting of VAT exemptions estimated based on the average price of most popular electric vehicles in Europe, SK – the size of a non-refundable subsidy granted for electric vehicle purchasers, $S_{(\text{electric vehicle sales})}$ – the projected number of newly sold electric vehicles under one of the development scenarios.

Annual implementation costs of the six remaining electric vehicle promotion measures are estimated following the same principle.

Further in the research, the multi-criteria assessment is conducted. The core of quantitative methods comprises the statistical data (or expert evaluation) matrix $R = \|r_{ij}\|$, developed for the indicators characterising the comparable objects, and indicator significance (weight) values $\omega_{\square\square}$, $i = 1,\ldots,m$; $j = 1,\ldots,n$, where m denotes the number of the indicators, and n – the number of comparable objects (alternatives). This research incorporates 9 objects, i.e. 9 electric vehicle promotion measures (n = 9), and 4 indicators, i.e. WTP, measure feasibility, efficiency and implementation costs (m = 4). Quantitative multi-criteria research methods help to find out which format – maximised or minimised – each indicator has. The best values of maximised indicators are maximal, while the best values of minimised indicators are minimal. The criteria in quantitative multi-criteria research methods commonly integrate non-dimensional (normalised) values r_{ij} and indicator weights into a single size – a method criterion. Most methods lean on different specific normalisation of initial data (indicator values) or data transformation (Pollescha, Daleb 2016; Jain et al. 2018; Ginevičius and Podvezko 2008).

In this research, we apply SAW (Simple Additive Weighing) method. Criterion S_j in this method clearly reflects the essence of multi-criteria assessment, i.e. integration of different criteria and weights into a single size (Hwang and Yoon 1981, Ginevičius and Podvezko 2007). The sum of the weighted normalised values of all indicators S_j is calculated for each jth object. The sum is expressed by the formula (Ginevičius and Podvezko 2007):

$$S_j = \sum_{i=1}^{m} \omega_i \tilde{r}_{ij}, \qquad \sum_{i=1}^{m} \omega_i = 1,$$

here ω_i – weight of the ith indicator; $\tilde{r}_{ij}$ – normalised value of the ith indicator for the j the object. The best value of criterion S_j is maximum.

For data normalisation, different functions can be applied. In this research, we use the formula that was applied by Maxim (2014) for assessment of the sustainability of electric power generation. The formula can be written in two ways, depending on the interpretation of an indicator. In case a higher value of an indicator is treated as better, the following data normalization formula is applied (Pollescha, Daleb 2016):

$$\tilde{r}_{ij} = \frac{r_{ij} - min_i \{r_{ij}\}}{max_i \{r_{ij}\} - min_i \{r_{ij}\}}.$$

In case a lower value of an indicator is treated as better, the reverse data normalisation formula is applied:

$$\tilde{r}_{ij} = 1 - \frac{r_{ij} - min_i \{r_{ij}\}}{max_i \{r_{ij}\} - min_i \{r_{ij}\}}.$$

4. RESEARCH RESULTS

Below we present the car market forecast, necessary for the estimation of particular implementation costs. With reference to the data of the International Energy Agency (IEA), in 2017, 1.4 million electric vehicles were sold worldwide. In the same year, the global fleet of electric vehicles reached 3.7 million (IEA, 2018). In 2017, Lithuanians registered 29044 new passenger cars, and this number was 26% larger than in 2016. The number of newly registered electric vehicles in the country in the same year amounted to 956, and in comparison to 2016 this number increased by 54% (in 2016, it amounted to 620). With reference to the data of the Ministry of Transport and Communications of the Republic of Lithuania (2018), 47 new electric vehicles were purchased over 2017.

Estimation of the value of promotion measures to a large extent depends on the size of the market. For instance, VAT exemption or subsidy estimations require the forecast of how many consumers may use these promotion measures, while estimating the value of free parking or free charging initiatives, we need to know the total number of potential beneficiaries in the country. As thus far Lithuania has not had any comprehensive electric vehicle market analysis or electric vehicle promotion scenarios, below we introduce the scenario, leaning on which we estimate annual costs of particular electric vehicle promotion measures.

New Policies Scenario (2030). The New Policies Scenario (NPS) is the fundamental scenario introduced by International Energy Agency (IEA). It combines market-oriented political actions and sets of promotional measures already implemented by administrations of different countries. At the same time, the scenario assesses national plans and objectives that may affect the market of electric vehicles. In order to reveal to which extent implementation costs depend on the number of electric vehicles, in this article we will consider the forecasts for 2020 and 2030. With reference to IEA forecasts, the global market of electric vehicles in 2020 will cover 13 million vehicles. The sales of electric vehicles in the same year are expected to reach 4 million transactions (IEA, 2018). Thus, by the above-described scenario, the global fleet of electric vehicles will increase by 351.4%, while the sales of new electric vehicles will grow by 285.7% over the period from 2017 to 2020. The forecasts for Lithuania are as follows: in 2020, the country will have 3359 electric vehicles, and their sales will reach 134 vehicles per year. IEA’s scenario for 2030 provides that the global fleet of electric vehicles will cover 130 million vehicles, while the sales will amount to 21.5 million vehicles, i.e. over the period between 2017 and 2030, annual sales of electric vehicles will grow by 24% (IEA, 2018). The sales of electric vehicles in Lithuania grew by 54% (comparing the data for 2017 and 2016) (The Ministry of Transport and Communications of the Republic of Lithuania, 2018). By applying the New Policies Scenario, it can be forecasted that over the period from 2017 to 2030, the total number of electric vehicles worldwide will increase by 3513.5%, while the sales will grow by 1535.7%. By applying the same scenario for Lithuanian market, it can be forecasted that in 2030 the fleet of electric vehicles in the country will cover 33589 vehicles, while the sales will reach 722 vehicles per year.

In this study, consumer preferences were researched by employing the questionnaire survey, conducted in November-December, 2018. The total number of the respondents amounted to 104; the majority of the respondents represented the population of three largest Lithuanian cities. By following Lieven's (2015) methodology, 12 datasets were compiled. Each dataset comprised alternatives A, B and C that could be chosen by a respondent. Alternatives B and C covered different attributes (in this case, electric vehicle promotion measures). The total amount of the attributes in each dataset was the same. Scientific literature proposes the choices 'none' and 'no-choice' as highly relevant for choice-based research since they ensure result objectivity and allow to avoid putting pressure on respondents to choose an unwanted compromise (Batsell and Louviere, 1991; Louviere, 1988). In this research, this function is attributed to alternative A which serves the respondents who do not want to choose an electric vehicle as an alternative or who do not need any promotion measures. VAT tariff in alternative A is 21%. This tariff is currently charged on all goods, including vehicles.

Calculated probabilities indicate that all the parameters are significant (i.e. the values of all of them statistically significantly differ from 0). Since all regression scales are the same, odds ratios can be used to determine the significance of the regressors. It can be presumed that the variance of a more significant regressor changes (i.e. increases or decreases) the odds ratio more times. A positive coefficient indicates that when the value of a corresponding variable is growing, probability P(Y = 1) is also increasing, and vice versa – a negative coefficient indicates the growth of probability P(Y = 0). Column EXP(B) presents the odds ratios, while graph '95% EXP(B) confidence intervals' depicts upper and lower bounds of the odds ratio 95% confidence intervals. The results propose that consumer choice is critically affected by virtually all attributes. Free use of bus lanes is the only attribute that reduces the probability of the alternative, i.e. if free use of bus lanes is provided, the probability of the alternative (the odds ratio $P(y = 1)/P(y = 0)$ decreases by 22.2 percent (see column Exp(B)). Meanwhile, all other attributes increase the probability of the alternative:

- The probability of the alternative is to the largest extent increased by financial support for charging stations near homes. Inclusion of this attribute into a measure set increases the probability of the alternative by 5.12 times.
- A 14% VAT tariff and a 12000 Eur subsidy increase the probability of the alternative by 2.41 time.
- Financial support for charging stations near works/educational institutions increases the probability of the alternative by 2.37 times.
- A 7% VAT tariff and an 8000 Eur subsidy increase the probability of the alternative by 2.36 times.
- Free city centre parking increases the probability of alternative by 2.09 times.
- A 0% VAT tariff and a 4000 Eur subsidy increase the probability of the alternative by 1.71 times.
- Free charging at public areas increases the probability of the alternative by 1.37 times.
- Vehicle tax exemption increases the probability of the alternative by 1.25 times.

In the second part of the research, the expert evaluation was conducted. According to the European Foresight Monitoring Network (2008), the method of expert evaluation is one of the most widely used methods of insight. The expert evaluation for this research was conducted between August 10 and October 14, 2018. It was based on a pre-designed questionnaire aimed at:

1. Assessment of the effectiveness of electric vehicle promotion measures.
2. Assessment of the feasibility of electric vehicle promotion measures.
3. Attribution of the weights for the components of the promotion measure assessment model.

The questionnaire comprised an introduction and three question groups. The introduction presented the information about the research purpose and authors. The first part was designed to determine experts' work experience and institutions they represent. The majority of the experts (77.8% of the respondents) represented public institutions and business organisations. 75% of the respondents indicated having work experience longer than 10 years. The second part of the questionnaire was designed to find out expert opinions about the values of electric vehicle promotion measures. The results of this part allowed to form the sets of consumer preferences with inclusion of the values of particular electric vehicle promotion measures: the value of VAT exemptions, the value of subsidies and the value of vehicle tax. The third part of the expert evaluation was designed to identify the indicators that would allow to assess the effectiveness and feasibility of electric vehicle promotion measures. These indicators were previously researched by Bakker and Trip

(2013) who, employing the method of expert evaluation, were attempting to identify the alternatives of electric vehicle promotion policies that would allow to reduce urban pollution.

The respondents were asked to indicate whether it is easy or difficult to implement particular electric vehicle promotion measures in Lithuania at political and administrative levels (1 point – implementation is very difficult, 10 points – implementation is very easy).

The measures, indicated by the experts as most easily implemented, included: free city centre parking (mean rank 8.92), free use of bus lanes (mean rank 8.72) and free charging (mean rank 7.58). It should be noted that most of these measures are already implemented in major cities of Lithuania. Introduction of vehicle tax and exemption of electric vehicles from this tax was indicated as the measure that is most difficult to implement at political and administrative levels (mean rank 4.83).

The experts were also asked to assess what impact implementation of particular promotion measures could have on the sales of electric vehicles in Lithuania, i.e. they were asked to indicate how effective a particular measure is (1 point – the measure is completely ineffective, 10 points – the measure is extremely effective). The measures, indicated by the experts as most effective (influential), included: VAT exemption and subsides (mean rank 8.24), free city centre parking (mean rank 7.14) and financial support for charging stations near homes (mean rank 7.11). Free use of bus lanes was indicated as least effective. The summary of the effectiveness and feasibility of electric vehicle promotion measures is presented below.

Table 4. The indicators of the feasibility and effectiveness of electric vehicle promotion measures identified on the basis of the expert evaluation (compiled by the authors)

	Indicator of feasibility	**Indicator of efficiency**
0% VAT and 4000 Eur subsidy	5.88	8.24
7% VAT and 8000 Eur subsidy	5.88	8.24
14% VAT and 12000 Eur subsidy	5.88	8.24
Vehicle tax exemptions	4.83	6.78
Free city centre parking	8.92	7.14
Free use of bus lanes	8.72	6.67
Free charging at public areas	7.58	6.92
Financial support for charging stations near homes	5.81	7.11
Financial support for charging stations near work	6.47	7.08

The value of Kendall's coefficient of concordance W = 0.26 shows a slight overlap of the expert opinions on the feasibility of electric vehicle promotion measures, although the fact that the probability is lower than the significance level proposes that the expert opinions are not entirely random. Meanwhile, the value of Kendall's coefficient of concordance W = 0.06 points to even greater divergence of the expert opinions on the effectiveness of electric vehicle promotion measures, although the fact that the probability is lower than the significance level proposes that the expert opinions are not entirely random.

While assessing the similarities in the expert opinions on the feasibility of electric vehicle promotion measures, it can be seen that the value of Friedman's $\chi 2$ criterion is equal to 82.26, while its probability is lower than α. Meanwhile, while assessing the similarities in the expert opinions on the effectiveness of electric vehicle promotion measures, it can be seen that the value of Friedman's $\chi 2$ criterion is equal to 27.40, while its probability is also lower than α. It means that the feasibility and effectiveness of eight electric vehicle promotion measures under consideration is, according to the experts, quite different.

The third part of the questionnaire was designed to find out to which extent each of the criteria under consideration (listed below) is important when assessing electric vehicle promotion measures:

I. Consumer opinion on a particular measure (i.e. how a consumer decision to buy an electric vehicle is affected by implementation of a certain measure);
II. Implementation costs (i.e. how much implementation of a certain measure costs);
III. Feasibility of a particular measure (i.e. how difficult/easy it is to implement a certain measure at political and administrative levels);
IV. Effectiveness of a particular measure (i.e. what impact implementation of a certain measure may have on the sales of electric vehicles).

According to the experts, the effectiveness of a promotion measure is most weighty factor (relative weight is equal to 7.96). Consumer opinion on a particular promotion measure is at the second position (relative weight is equal to 6.162).

The smallest number of the experts favoured such criteria as feasibility of a particular measure and implementation costs, which, in its turn, proposes that the experts focus on the impact of the promotion system rather than on administrative and financial resources that might be required for implementation of promotion measures. The summary of criteria weights is presented in the Table 5.

Table 5. Relative weights of the criteria employed for assessment of electric vehicle promotion measures (compiled by the authors)

Description of the criterion	**Relative weight**
Consumer opinion on a particular measure	6.16
Implementation costs	5.53
Feasibility of a particular measure	5.70
Effectiveness of a particular measure	7.96

Following the principles described in the methodology section, annual implementation costs of nine electric vehicle promotion measures were estimated. The results of these estimations are depicted in Table 6. It should be noted that free use of bus lanes is the only measure that does not involve any direct costs and is not related to missed state budget revenue.

The results of the research were summarised by employing the method of multi-criteria analysis. After recalculations, the normalised values of the indicators fell into the interval [0,1] (Pollescha, Dale 2016), i.e. the best value of an indicator was set to 1, while the worst value was set to 0.

Table 6. Annual implementation costs of electric vehicles promoting measures (compiled by the authors)

	Measure annual implementation costs (by the NPS 2020 forecast), Eur	**Measure annual implementation costs (by the NPS 2030 forecast), Eur**
0% VAT and 4000 Eur subsidy	1.767.693	9.524.437
7% VAT and 8000 Eur subsidy	1.780.479	9.593.328
14% VAT and 12000 Eur subsidy	1.962.239	10.572.664
Vehicle tax exemptions	806.160	8.061.360
Free city centre parking	2.266.205	22.661.378
Free use of bus lanes	0	0
Free charging at public areas	2.771.175	27.710.925
Financial support for charging stations near homes	227.964	1.228.288
Financial support for charging stations near work	289.237	1.558.431

Summarised results of the three parts of the research are presented in Table 7, which depicts consumer preferences, measure feasibility, effectiveness and annual implementation costs. The results also reveal the relative weights of the criteria estimated after the expert evaluation. In this case, the higher is an indicator value, the more effective is a promotion measure.

Table 7. Summary of the research results by SAW multi-criteria assessment method (compiled by the authors)

	Measure effectiveness indicator (by the NPS 2020 forecast)	**Measure effectiveness indicator (by the NPS 2030 forecast)**
0% VAT and 4000 Eur subsidy	0.44	0.50
7% VAT and 8000 Eur subsidy	0.47	0.54
14% VAT and 12000 Eur subsidy	0.46	0.53
Vehicle tax exemptions	0.20	0.20
Free city centre parking	0.49	0.49
Free use of bus lanes	0.52	0.52
Free charging at public areas	0.28	0.28
Financial support for charging stations near homes	0.58	0.59
Financial support for charging stations near work	0.47	0.48

5. CONCLUSIONS

The majority of consumers favoured financial support for charging stations near their homes. Inclusion of this attribute into the set of electric vehicle promotion measures increases the probability of the alternative by 5.12 times. Regardless of relatively low implementation costs, this measure could also help consumers feel safe knowing that they will always be able to charge their vehicles. Free use of bus lanes was rated as worst measure that reduces the probabily of the alternative by 22.2% (this was the only measure rated negatively). In the category of VAT tariffs and direct subsidies, the largest part of consumers favoured a 14% VAT tariff and a 12000 Eur subsidy (this attribute was found to increase the probability of the alternative by 2.41 times). Meanwhile, the smallest part of consumers favoured a 0% VAT tariff and a 4000 Eur subsidy (this attribute was found to increase the probability of the alternative by 1.71 times). The results lead to the conclusion that consumers find direct subsidies much more tangible and easier to understand than VAT exemptions, which relatively depend on the price of a vehicle.

The expert survey revealed that free city centre parking (mean rank 8.92) and free use of bus lanes (mean rank 8.72) are most significant electric vehicle promotion measures by their feasibility which shows how difficult/easy it is to implement a certain measure at political and administrative levels. This can be explained by the fact that the above-mentioned promotion measures are popular in many countries, including Lithuania, and are easily implemented under a municipal decision. What is more, implementation of these measures does not require any additional administrative resources. Exemption of electric vehicles from vehicle tax (mean rank 4.83) was rated as hardly feasible. In Lithuania, vehicle taxation poses a great public opposition, and, despite many political discussions, none of the country's governments has thus far legitimized this measure to avoid a negative public reaction.

VAT exemptions and subsidies (mean rank 8.24) were ranked as most efficient electric vehicle promotion measures, while exemption of electric vehicles from an annual vehicle tax (mean rank 6.78) and free use of bus lanes (mean rank 6.67) were recognised as least efficient. During the expert survey, the weights of the four components (criteria) of electric vehicle promotion assessment were also obtained: effectiveness of a particular measure was indicated as weightiest (mean rank 7.96), while implementation costs were recognised as least weighty (mean rank 5.53).

After estimation of the annual implementation costs for all promotion measures under consideration (by NPS for the years 2020 and 2030) and summarisation of the research indicators based on multi-criteria assessment, the most effective electric vehicle promotion measures in the case of Lithuania were identified. Under the NPS 2020 electric vehicle fleet and sales development scenario, three most effective promotion measures are as follows: financial support for charging stations near homes (mean rank 0.58), free use of bus lanes (mean rank 0.52) and free city centre parking (mean rank 0.49). Under the NPS 2030 scenario, three most effective promotion measures include financial support for charging stations near homes (mean rank 0.59), a 7% VAT tariff and a 8000 Eur subsidy, and a 14% VAT tariff and a 12000 Eur subsidy for purchase of an electric vehicle. The results propose that financial support for charging stations near homes is absolutely effective in Lithuania. This measure is favoured by consumers and can have the greatest impact on promotion of the purchase of electric vehicles. In addition, this measure has relatively low implementation costs. Nevertheless, the experience of other countries shows that there is no single measure that could lead to major changes, so a comprehensive promotion system has to be developed. Despite that, it should be noted that the results of this research identified a clear outsider: exemption of electric vehicles from an annual vehicle tax (mean rank 0.20) is least effective of all measures. One of the reasons for this is public opposition to introduction of a new tax, which severely complicates implementation of this measure.

REFERENCES

1. Jenna, A., Springel, K., & Gopa, A. R. (2018). Effectiveness of Electric Vehicle Incentives in the United States, *Energy Policy*, 119, 349–356.
2. Axsen, J., Mountain, D. C., Jaccard, M. (2009). Combining Stated and Revealed Choice Research to Simulate the Neighbour Effect: The Case of Hybrid-electric Vehicles, *Resource and Energy Economics*, 31, 221–238.
3. Bakker, S., & Trip, J. J. (2013). Policy options to support the adoption of electric vehicles in the urban environment, *Transportation Research Part D*, 25, 18–23.
4. Batsell, R.R., & Louviere, J.J. (1991). Experimental Analysis of Choice, Market. Lett. 2(3), 199–214.
5. Blatter, D., Miller, K., Hofstetter, R., & Krohmer, H. (2009). Improving the Direct Estimation of Demand.
6. Bunch, D. S., Bradley, M., Golob, T. F., Kitamura, R., & Occhiuzzo, G. P. (1993). Demand for Clean-fuel Vehicles in California: a Discrete-choice Stated Preference Pilot Project. *Transportation Research Part A: Policy and Practice* 27(3), 237–253.
7. by Adjusting for Incorrect Price-Statements, *Proceedings of the 38th EMAC Conference*, Nantes, France.
8. Cecere, G., Corrocher, N., & Guerzoni, M. (2018). Price or Performance? A Probabilistic Choice Analysis of the Intention to Buy Electric Vehicles in European Countries, *Energy Policy*, 118, 19–32.
9. Čekanavičius, V. (2011). Taikomoji Regresinė Analizė Socialiniuose Tyrimuose. Projektas „Lietuvos HSM duomenų archyvo LiDA plėtra“ SFMIS Nr. VP1-3.1-ŠMM-02-V-02-001.
10. Chorus, C. G., Koetse, M. J., & Hoen, A. (2013). Consumer Preferences for Alternative Fuel Vehicles: Comparing a Utility Maximization and a Regret Minimization Model, *Energy polic*, 61, 901–908.
11. Daina, N., Sivakumar, A., & Polak, J. W. (2017). Modelling Electric Vehicles Use: a Survey on the Methods, *Renewable and Sustainable Energy Reviews*, 68, 447–460.
12. Ewing, G., & Sarigöllü, E. (2000). Assessing Consumer Preferences for Clean-fuel Vehicles: a Discrete Choice Experiment.” *Journal of public policy & marketing* 19(1), 106–118.
13. Fosgerau, M., & Bierlaire, M. (2009). Discrete choice models with multiplicative error terms. *Transportation Research Part B*, 43(5), 494–505.
14. Ginevičius, R., & Podvezko, V. (2007). Complex Assessment of Sustainable Development of State Regions with Emphasis on Ecological and Dwelling Conditions, *Ekologija [Ecology]*, 53, 41–48.
15. Ginevičius, R., & Podvezko, V. (2008). Daugiakriterinio Vertinimo Būdų Suderinamumas. *Verslas:teorija ir praktika [Business: theory and practice*, 9, 73–80.
16. Hackbarth, A., & Madlener, R. (2013). Consumer Preferences for Alternative Fuel Vehicles: a Discrete Choice Analysis, *Transportation Research Part D: Transport and Environment*, 25, 5–17.
17. Hackbarth, A., & Madlener, R. (2016). Willingness-to-pay for Alternative Fuel Vehicle Characteristics: A Stated Choice Study for Germany, *Transportation Research Part A: Policy and Practice*, 85, 89–111.
18. Hardman, S., Chandan, A., Tala, G., & Turrentinea, T. (2017). The Effectiveness of Financial Purchase Incentives for Battery Electric Vehicles – A Review of the Evidence, *Renewable and Sustainable Energy Reviews*, 80, 1100–1111.
19. Helveston, J. P., Liu, Y., Feit, E. M., Fuchs, E., Klampfl, E., & Michalek, J. J. (2015). Will Subsidies Drive Electric Vehicle Adoption? Measuring Consumer Preferences in the US and China, *Transportation Research Part A: Policy and Practice*, 73, 96–112.
20. Higgins, A., Paevere, P., Gardner, J., & Quezada, G. (2012). Combining Choice Modelling and Multi-criteria Analysis for Technology Diffusion: An Application to the Uptake of Electric Vehicles, *Technological Forecasting & Social Change*, 79, 1399–1412.

21. Hoen, A., & Koetse, M. J. (2014). A Choice Experiment on Alternative Fuel Vehicle Preferences of Private Car Owners in the Netherlands, *Transportation Research Part A: Policy and Practice*, 61, 199–215.
22. Hwang, C. L., & Yoon, K. (1981). Multiple Attribute Decision Making: Methods and Applications. Springer-Verlag, New York.
23. IEA (2018). Global EV Outlook 2018: Towards Cross-modal Electrification. International Energy Agency. Available from internet: https://webstore.iea.org/global-ev-outlook-2018
24. IEA-RETD (2015). Driving Renewable Energy for Transport – Next Generation Policy Instruments for Renewable transport (RES-T-NEXT). IEA Implementing Agreement for Renewable Energy Technology Deployment (IEA-RETD). Utrecht. Available from internet: http://iea-retd.org/wp-content/uploads/2015/12/IEA-RETD-RES-T-NEXT-201511.pdf
25. Jain, S., Shukla, S., & Wadhvani, R. (2018). Dynamic Selection of Normalization Techniques Using Data Complexity Measures, *Expert systems with application*, 106, 252–262.
26. Kampman, B., Essen, H., Braat, W., & Gopalakrishnan, D. (2011). Impacts of Electric Vehicles - Deliverable 4 Economic Analysis and Business Models Delft, CE Delft.
27. Kardelis, K. (2007). Mokslinių tyrimų metodologija ir metodai: vadovėlis. Šiauliai: Lucilijus.
28. Kester, J., Noel, L., Rubens, G. Z., & Sovacool, B. K. (2018). Policy Mechanisms to Accelerate Electric Vehicle Adoption: A Qualitative Review From the Nordic Region, *Renewable and Sustainable Energy Reviews*, 94, 719–731.
29. Langbroek, J. H. M., Franklin, J. P., & Susilo, Y. O. (2016). The Effect of Policy Incentives on Electric Vehicle Adoption, *Energy Policy*, 94, 94–103.
30. Lieven, T. (2015). Policy measures to promote electric mobility – A global Perspective, *Transportation Research Part A*, 82, 78–93.
31. Louviere, J.J. (1988). Conjoint Analysis Modelling of Stated Preferences: a Review of Theory, Methods, Recent Developments, and External Validity, *Journal of Transport Economics and Policy*, 22(1), 93–119.
32. Mačiulis, P., Konstantinavičiūtė, I., & Pilinkienė, V. (2018). Assessment of Electric Vehicles Promotion Measures at the National and Local Administrative Levels, *Engineering Economics*, 29(4), 434–445.
33. Malmgren, I. (2016). Quantifying the Societal Benefits of Electric Vehicles, *World Electric Vehicle Journal*, 8, 2032–6653.
34. Mau, P., Eyzaguirre, J., Jaccard, M., Collins-Dodd, C., & Tiedemann, K. (2008). The ‘Neighbour Effect’: Simulating Dynamics in Consumer Preferences for New Vehicle Technologies, *Ecological economics*, 68, 504–516.
35. Mazzocchi, M. (2008). Statistics for Marketing and Consumer Research. SAGE Publications Ltd., 432.
36. Mock, P., & Yang, Z. (2014). Driving Electrification: a Global Comparison of Fiscal Incntive Policy for Electric Vehicles. International Council on Clean Transportation.
37. Pollescha, N. L., & Daleb, V. H. (2016). Normalization in Sustainability Assessment: Methods and Implications, *Ecological Economics*, 130, 195–208.
38. Potoglou, D., & Kanaroglou, P.S. (2007). Household demand and willingness to pay for clean vehicles, *Transportation Research Part D*, 12, 264–274.
39. *Practice*, 46(8), 1372–1385.
40. PUKĖNAS, K. (2009). Kokybinių duomenų analizė SPSS programa: mokomoji knyga, Lietuvos kūno kultūros akademija, Kaunas.
41. Ramos-Real, F. J., Ramírez-Díazb, A., Gustavo A., Marrerob, G. A., & Perez, Y. (2018). Willingness to Pay for Electric Vehicles in Island Regions: The Case of Tenerife (Canary Islands), *Renewable and Sustainable Energy Reviews*, 98, 140–149.
42. Tanaka, M., T. Murakami, I. K., & Friedman, L. (2014). Consumers’ Willingness to Pay for Alternative Fuel Vehicles: A Comparative Discrete Choice Analysis Between the US and Japan, *Transportation Research Part A: Policy and Practice* 70, 194–209.
43. Train, K. (2002). Discrete Choice Methods with Simulation, Cambridge University Press, Available from internet: https://eml.berkeley.edu/books/train1201.pdf
44. Train, K. (2002). Discrete Choice Methods with Simulation. Cambridge University Press.

45. Tsakalidis, A., & Thiel, C. (2018). Electric Vehicles in Europe from 2010 to 2017: is Full-scale Commercialisation Beginning? An Overview of the Evolution of Electric Vehicles in Europe, EUR 29401 EN, Publications Office of the European Union, Luxembourg, 2018, ISBN 978-92-79-96719-1.
46. Tyrrell, M., & Dernbach, J.C. (2011). The ‘‘Cash for Clunkers” Program: a Sustainability Evaluation., *University of Toledo Law Review*, 42, 467–492.
47. Varian, H. R. (1992). *Microeconomic Analysis*, 3rd ed., Norton: New York et al., NY.
48. Windisch, E. (2013). Driving electric? A nancial analysis of electric vehicle policies in France, Statistical Finance, Ecole des Ponts ParisTech.
49. Yan, S. (2018). The Economic and Environmental Impacts of Tax Incentives for Battery Electric Vehicles in Europe, *Energy Policy*, 123, 53-63.
50. Yang, Z., Slowik, P., Lutsey, N., & Searle, S. (2016). Principles for Effective Electric Vehicle Incentive Design. International Council on Clean Transportation. Washington, DC. Available from internet: https://www.theicct.org/sites/default/files/publications/ICCT_IZEV-incentives-comp_201606.pdf
51. Zhang, X., Lianga Enhai, Y., Rao, Y. R., & Xiea, J. (2017). Review of Electric Vehicle Policies in China: Content Summary and Effect Analysis, *Renewable and Sustainable Energy Reviews*, 70, 698–714.
52. Ziegler, A. (2012). Individual Characteristics and Stated Preferences for Alternative Energy Sources and Propulsion Technologies in Vehicles: a Discrete Choice Analysis for Germany, *Transportation Research Part A: Policy and...*

CYSENI 2019, May 23-24, Kaunas, Lithuania
ISSN 1822-7554, www.cyseni.com

THE ROLE OF SOCIALLY RESPONSIBLE BUSINESS IN SUSTAINABLE ECONOMY

D. Silakalne–Arāja
Riga Technical University
Kalnciema str. 6, LV-1048 Riga – Latvia
Email: danha@inbox.lv

ABSTRACT

The concept of socially responsible business has evolved in the context of the paradigm of sustainable development, a development that satisfies today's needs without endangering the needs of the next generation. Sustainable development is characterized by three interconnected dimensions: environmental, economic and social. Building on the principle of sustainable development, development must be done with careful handling of the planet's resources and ensuring that biodiversity is preserved on Earth. In the age of globalization, with the growing internationalization and interconnectedness of production processes, the extent to which the company follows good governance practices socially responsible throughout the company's. A company that declares responsibility values at the management level, but produces ingredients that are manufactured in violation of human rights and degradation of the environment, is actually causing a negative impact in environment and human. Development is ultimately about people and improving their lives.The aim of the research is to develop social entrepreneurship in a sustainable economy. The key result is to protect the environment with the help of the social entrepreneurship support mechanism. In research the theoretical research methods, analysis of literature, documents, legislation, information obtained on the internet and graphic analysis were used.

Keywords: sustainable development, responsible business, globalization, human rights, degradation, environment

1. INTRODUCTION

The Rio Declaration on Environment and Development and the Action Program for the 21st Century (Agenda 21) were adopted.

The documents adopted in Rio de Janeiro, including the Action Program for 21st Century, which contains descriptions of the necessary actions to deal with global environmental problems. “Think Global, act in the specific place” – this strategy states that no global action can be imagined without deliberate action at the local level. In many states around the world, it was recognized, that states have to develop their own development strategy in such way, so as to preserve not only pace and opportunities of economic development and the quality of life, but also to prevent environmental degradation and resource overrun. Thereby, the concept of sustainable development became a set of views capable to influence the behavior of the present society and to establish future society. In order to achieve sustainable development, environmental protection must become an integrated part of the development but they both bound together by the social field. It plays an essential role in eradicating poverty in the world and in meeting the needs of the majority of the world’s population. Since much of the required people get from nature, care must be taken to ensure the integrity and viability of the Earth’s ecosystems.

1.1. Insufficient sustainable development in economics

Sustainable development is one of the key objectives of the European Union Treaty, which defines EU policies and actions. Sustainable development, which provides the Earth with the ability to maintain life in all its diversity, must be based on the principles of democracy, gender equality, solidarity and principles of the rule of law, as well as respect for fundamental rights, freedom and equal opportunities. It is oriented towards improving the quality of life and prosperity for this and all future generations. Sustainable development promotes a dynamic economy, full employment, a high level of education, good medical care, social and territorial cohesion and environmental protection in a peaceful and secure world, while respecting cultural diversity.[14]

The concept of sustainable development is based on the need to optimize economic development and social system, as well as the impact on the environment and usage of the resources. This development model should ensure the sustainability in time and space of the economy, the environment and the social field.

The three basic fields without which the existence of mankind is impossible are the economy, the harmonious society and the healthy environment, which at the same time are the preferred external conditions for the development of the individual.[19]

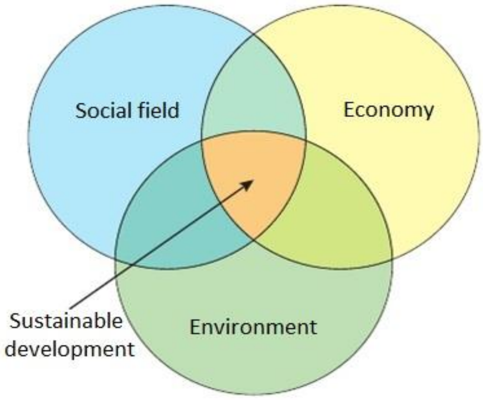

Fig. 1: Interactions between the environment, the economy and the social field that provides sustainable development [8]

Sustainable development means that any issue of the economy, society or the environment must be addressed in such a way that the decision taken is favorable or least unfavorable to the development of the other fields.

The goals and principles of sustainable development have become guidelines for adoption of appropriate economic and political as well as environmental protection decisions aimed at:

- limiting the impact of mankind on the surrounding natural environment and preventing further exceeding of the self-renewal abilities of the environment;
- minimizing the consumption of non-renewable resources and ensuring the expansion of the use of renewable resources;
- preserving and protecting nature by preserving biodiversity;
- promoting economic development to meet human needs, to increase quality of life and to ensure a fair distribution of world wealth;
- developing a decision-making and management system that promotes public participation in the decision-making process.[8]

In order to ensure sustainable development, the public must meet several key challenges**.** Preservation of resources, namely, the availability of resources for human development not only for present but also for future generations. Therefore, it is necessary to implement an action program and policies aimed at increasing the efficiency of the use of non-renewable resources, their replacement with renewable resources, while preserving biodiversity and protecting the genetic potential of species. Approaches to this task include the development of alternative energy sources, the reuse of production and other waste, the development of environmentally friendly technologies.

The balanced development of man-made (anthropogenic) and natural environment, linked, for example, to the need to maintain agricultural land productivity, optimize the use of urban areas and transport flows.

Ensuring acceptable environmental quality for society development by stopping or limiting processes that degrade the environment, has a negative impact on the self-regeneration capacity of ecosystems and preventing processes that can adversely affect human health and reduce quality of life. At the same time, the need to restore the degraded environment must be kept in mind.[8]

Ensuring social equality. Sustainable development is unthinkable without ensuring social equality, both nationally and internationally, avoiding an increase in income inequality and providing development that reduces the social divide between rich and poor.

Public participation in state and environmental administration to support and sustain sustainable development across the nation, as it cannot be achieved without a change in public attitudes towards consumption and use of resources. The public has an important political commitment to building a system based on the equal sharing of existing and acquired benefits, social equality, careful use of resources and efficient management.

The process of implementing sustainable development requires changes in attitudes towards values which must be initiated and supported by lower layers, involving increasing proportion of the public in political decision-making and governance. At the same time, it is clear that such changes in society cannot be achieved through administrative reforms.

Sustainable development can be achieved by finding solutions to all six of these challenges - implementing public planning in a market economy according to an optimal political system. Sustainable development exists when common land capital stocks remain unchanged or continue to grow. It means three main forms of capital:

- Economic (man-made) capital, which traditionally includes equipment, machinery, buildings and infrastructure and is used in the production of goods and services;
- Social capital, which is linked to the well-being of people in both public and individual ways. It consists of social norms, of formal and informal structures which provides access to resources, helps to solve common problems and promotes social unity, but is based on people's mental and physical health, education, motivation, talent, skills and skills;
- Natural capital – all ecosystems and natural resources (renewable and non-renewable). In addition to traditional natural resources (wood, water, energy, minerals), natural capital also includes natural values difficult to express in monetary units – biodiversity.

Sustainable development foresees constant development and preservation of all forms of capital, as on them depends the existence and well-being of mankind, both now and in future. Since the total capital of the Earth consists of the sum of these capitals, there is a possibility that the total capital stock may increase even if one form of capital decreases and other increases. For example, natural capital is being reduced, but economic growth is high enough to ensure total capital growth.[15]

2. EUROPEAN CLIMATE POLICY AND ITS OBJECTIVES

The climate on Earth is changing. The average global temperature on Earth is rising because of the increase in greenhouse gas emissions from human activities. These gases allow the solar energy to enter the atmosphere but slows down heat reflection from the planet. The rise in temperature associated with that has unprecedented consequences worldwide – glaciers melt and sea level rises, floods and droughts are found in regions that were not previously affected by such extreme weather. These unusual weather conditions are increasingly affecting the economy, the environment, health and our daily lives. Greenhouse gases have gained their name due to the fact that they hold the sun in the atmosphere, just as glass holds heat in the greenhouse. The main greenhouse gas concentration of carbon dioxide (CO_2) in the atmosphere is currently the highest in the last 800 000 years.

The global scale agreement, known as the Kyoto Protocol, currently limits the emissions of the following seven greenhouse gases in industrialized countries: – carbon dioxide ($_{CO2}$): resulting from the combustion of fossil fuels, wood or carbonaceous materials, but also absorbed by plants and trees; – methane (CH_4): emissions from a wide range of natural sources and human activities, including fossil fuel extraction, livestock farming, rice cultivation and waste management; – nitrogen oxide (N_2O): Emission sources include fertilizer, fossil fuel burning and the chemical industry using nitrogen; – four types of fluorinated gases specifically designed for industrial purposes: hydrofluorocarbons (HFCs), perfluorocarbons (PFCs), sulfur hexafluoride (SF6) and nitrogen trifluoride.

A new global treaty is currently under negotiation. This agreement is expected to be adopted in 2015. The European Union wants a new protocol that is ambitious and comprehensive for all legally binding. Some Consequences of Climate Change: – Rising sea levels, threatening low-lying island states and coastal populations. – Extreme weather, threatening food production, especially in the poorest developing countries. – Heat waves have caused thousands of premature deaths in Europe over the last decade. – Water and food shortages can lead to regional conflicts, hunger and refugee flows. – The risk of extinction of some plant and animal species is increasing. – It is estimated that if we won't adapt to climate changes, the costs will amount to € 100 billion per year by 2020 in the European Union as a whole.

2.1. The role of science in climate change

The role of science in climate change is a sensitive issue. Some deny its existence and emphasize that there is no need for policy change and behavior to reduce greenhouse gas emissions. This thesis does not take into account the conclusions of the vast majority of climatologists in the world: 97% agree with the statement that climate change is a reality and that people are causing it with activities that cause greenhouse gases such as burning fossil fuels – coal, oil and natural gas – burning and deforestation. This conclusion is reflected in the internationally recognized scientific assessments carried out by the Intergovernmental Panel on Climate Change, which brings together the world's leading atmospheric science experts. The Intergovernmental Panel on Climate Change (IPCC), established in 1988 by the United Nations Environment Program and the World Meteorological Organization, is a leading international body that assesses climate change and its potential ecological and socio-economic impact. This council bases its assessments on hundreds of specialized studies conducted by climate experts around the world. The average surface temperature has risen by almost 0.8 °C since 1880, but it has risen further in Europe by about 1.4 °C. Scientific evidence suggests that there is a growing likelihood of irreversible and potentially catastrophic changes in the environment if global warming would exceed pre-industrial temperature levels by an average of 2 °C (or current temperature levels by average 1.2 °C). Thirteen of the 14 warmest years registered have been experienced in this century. New research shows that current global government action is not enough to prevent global warming of more than 3 °C by the end of this century, and a 4 °C or even 6 °C increase in temperature is not excluded. The EU has been insisting for a long time that global warming should be limited to 2 °C growth. The international community has now recognized that this goal must be achieved. EU policy is based on scientific knowledge. The EU believes that global action is needed to tackle climate change, such as binding aims for Member States and initiatives such as the Emissions Trading Scheme (ETS). Between 1990 and 2012, the EU has reduced its greenhouse gas emissions by 19% while its economy has grown by 45%. As a result, during this period, the EU's greenhouse gas intensity (the ratio between emissions and gross domestic product) was cut by almost half in the EU. In all Member States, the link between increasing emissions and economic growth has been overcome and is no longer valid. Timely measures strengthen the economy. It is technically and economically possible to prevent the planet from rising by more than 2 °C. The sooner the measures are implemented, the more effective and cost-effective they are. Therefore, while the economic crisis and public finances are limited, the

EU continues to pursue its climate policy. The structural policies in the field of climate and energy have made a significant contribution to the EU emission reductions since 2005. Almost half of the 2008-2012 observed decrease is attributable to the economic crisis. Timely measures to develop a low-carbon emission economy will stimulate growth and employment by stimulating innovation in cleaner technologies such as renewable energy and energy efficiency. This "green economy" is not only one of the most promising areas for job creation, it also improves Europe's energy security and our foreign trade balance by reducing dependence on imported oil and gas. Adapting to Climate Change, the effects of climate change are already making themselves felt. Even if greenhouse gas emissions were drastically reduced, the warming of the Earth would continue for decades, and for centuries the effects of former emissions through inertia would be felt. Adaptation and mitigation measures are therefore complementary. The European Commission has developed an adaptation strategy for the European Union aimed at strengthening the EU's resilience to the effects of climate change.[17]

3. QUALITY OF LIFE OF THE POPULATION

According to economic theory, quality of life means meeting needs. From the very beginning, human needs are perceived as a necessity, which means that the main thing is to satisfy the most necessary – nutrition, health services and education.

Besides meeting the basic needs, there is also a nation's development based on the idea of improving the quality of life that is realized through economic growth and at the same time sharing the benefits of this growth among the people. The main goal of the country is to get every individual above the level of all primary needs to achieve potential equality. When everyone is across this level, the population can choose other goals.

Tasks of raising the quality of life	**Criteria**	**Assessment indicators**
Achieving sustained economic growth	Efficiency of economic development	• GDP per capita at current prices, in line with purchasing power parity; • inflation rate (in consumer prices); • unemployment rate (%) of the working population; • compulsory deductions % of GDP for workers' social protection;
Increase in population welfare	Living standard	• per capita income; • dynamics of the decline in income disparities; • the income part of the richest of the whole population income; • estimation of one household with medium assets (with private cars, housing and other real estate), taking into account the average annual exchange rate of the local currency and purchasing power parity;

4. POVERTY IN EUROPE

Overall, almost one in four Europeans is at risk of poverty and more than half of these people are women. One of the biggest risk groups is single parents, most of whom are women. Researcher from the European Institute for Gender Equality emphasizes that at risk of poverty are 48% of single mothers and only 32% of single fathers. The second group is large families. Statistics show that 17% of couples with one child live in poverty. However, if the number of children reaches three, this risk almost doubles. This is due not only to higher spending on raising children but also to the fact that large family mothers are more likely to stay at home or work part-time. As a result, the total family income is shrinking. Therefore, large families are largely dependent on their father's income. If the father loses his job, 70% of large families' risk falling into poverty. This shows that families have to pay a very high price for each child's birth. If national policies are not designed to support families, we can face very serious problems in the future, the researcher explains. Some researchers think that society is basically punishing women for childbirth. In working age, they are forced to work less or part-time, but receive a low pension in old age because they have not paid enough social contributions. Overall, in Europe, the number of underprivileged people has increased by four million over the last five years. This is largely due to unemployment caused by the financial crisis. In Latvia, the risk of poverty is higher than the European average. 33% of the population are exposed to it, compared with 24% on average in the EU. People with special needs and people with very low education are also particularly vulnerable. Economists of the European Bank for Reconstruction and Development, encourages thinking more about the quality of education. The target set by the EU is to have 20 million fewer poor people in our block of states by 2020. Although the situation is gradually improving, it does not seem that this target could be met in the next two years [16].

4.1. Solution to the problem

The concept of socially responsible business has evolved in the context of the paradigm of sustainable development, a development that ensures meeting today's needs without compromising the needs of the next generation. Sustainable development is characterized by three interrelated dimensions: environmental, economic and social. Building on the principle of sustainable development, development must be based on careful management of the planet's resources and on the maintenance of biodiversity on Earth [7].

What is the (true) impact of business? It is the awareness of how and to what extent the impact of business on society and the environment as a whole is the basis for the development of the concept of socially responsible business. Contaminated rivers, burnt forests, brownfields, chemical pollution disasters - these are often the consequences of under-responsible business. They have to be paid by the whole society, and each of us is a loser as a result of such a business. Understanding the true impact of business on society has led to the spread of socially responsible business in the world.

In an era of globalization, where economic manufacturing processes are becoming more international and interrelated, the extent to which a company follows good governance practices throughout the company's supply chain is crucial. A company that preaches responsibility values at the management level but during the production process uses components produced in violation of human rights and degradation of the environment, has a negative impact. This business practice is often based on the fact that the laws of the countries in question where such violations occur do not require change. However, it is the business social responsibility to promote responsible business practices rather than the ones accepted by national governments. Development cooperation policy makers have also recognized the role of the private sector in development, and more and more attention is being paid to the development of the business environment worldwide to ensure that the stages of the production supply chain do not contribute to the existence of irresponsible business practices.

The Organization for Economic Co-operation and Development (OECD) in cooperation with the governments of forty-four countries, the OECD has developed guidelines for multinational businesses on voluntary principles and standards for responsible business management.[12]

Corporate Social Responsibility (CSR) in the European Union

What is Corporate Social Responsibility (CSR)?

Corporate or business social responsibility means that business do more than their law requires in their day-to-day operations, and voluntarily fulfill social and environmental protection goals. It covers several areas:

- Europe 2020" (especially new skills and jobs, youth, local development);
- business and human rights;
- CSR reporting;
- social responsibility in public procurement.

Corporate Social Responsibility (CSR) as a good business practice and organized movement has been developing since the 1990s and is gaining more and more support not only among businesses but also among consumers, by choosing products and services from companies with high reputation and from businesses that implementing well-established business ethical principles daily. Business competitiveness and productivity are not possible without engaging in international and global processes, so CSR has become a part of businesses strategies over the last 10 years. CSR is a topic that is increasingly mentioned in the business conversations also in Latvia. However, according to the latest reputation and CSR studies conducted in Latvia, there are few representatives of businesses, state institutions and society in Latvia who understand the essence of CSR and support its forms of expression. Most often, opinions expressed by different people and in different situations also differ in content. With CSR tends to understand both voluntary initiatives by private entities and the ability of businesses to improve the socio-economic conditions of their employees. The International Organization of Employers (IOE), with CSR, means voluntary business initiatives that have a positive impact on the social conditions of society, the national economy and the environment. CSR programs that extend beyond the requirements of regulatory enactments can be implemented independently by the businesses, as well as in cooperation with interest groups affecting the business, especially customers, suppliers, consumers. However, corporate social responsibility is not limited to the labor market or labor law. It is also not a classic model of social dialogue, but rather encourages society and businesses to socially responsible business, including participation in working and living conditions for both employees and society at large.

Development trends in the European Union and the world

Every citizen of the European Union (EU) is associated with corporate social responsibility whether he is an employer or employee in the private or public sector.

The development of CSR at global level is influenced by two main factors:

1) demand for a sorted out corporate structure and socially responsible business environment, clear principles and good reputation by becoming a supplier to foreign companies or their partners;

2) the need to enter the global market and be equal player by offering quality services and products in accordance with responsible business principles.

Business is the driving force behind the development of society and the creator of its prosperity. Understanding this role of business is the basis for the debate at European and international level on the voluntary or compulsory implementation of CSR programs in business. Undoubtedly, global development trends have made today's business international network actions more visible as they have a direct impact on national economies, social stability and environmental sustainability. Being aware of this impact, businesses, as well as demonstrating the best corporate business principles (business governance and financial policy) to their investors and shareholders, demonstrate their attitude towards the society within CSR programs. The role of government is to develop and implement laws that create and maintain stable and predictable political and social progress. It is the government's responsibility to invest in education and the social well-being of its people to create the right conditions for business growth and competitiveness. Businesses can implement support programs and demonstrate specific social standards in their activities to encourage similar action by surrounding businesses. The role of government is to develop and implement laws that create and maintain stable and predictable political and social progress. It is the government's responsibility to invest in education and the social well-being of its people to create the right conditions for business growth and competitiveness. Businesses can implement support programs and demonstrate specific social standards in their activities to encourage similar action by surrounding businesses.

Businesses can find several support points for CSR implementation:

- Intergovernmental Initiatives: The United Nations (UN) Global Treaty Movement, promoted by the Latvian Employers' Confederation of State of Latvia, invites companies to ratify and inform the public of the fundamental principles of human rights, labor law, environmental protection respect for the basic principles of anti-corruption; entrepreneurs are called upon to respect the International Labour Organizations (ILO) Tripartite declaration on principles governing multinational companies and social policy; Organization for Economic Co-operation and Development (OECD) guidelines for multinational businesses on voluntary principles and standards for responsible business - employment, industrial relations, human rights, environment and transparency of information;
- Initiatives of international business organizations: International Labour Organizations, International Chamber of Commerce Sustainable Development Principles show examples of companies implementing CSR programs;
- Initiatives by non-governmental organizations, governments, commercial structures and businesses lead to compliance with certain standards and compliance with the needs of certain interest groups [20].

The Baltic needs effective, responsible and sustainable social entrepreneurship

Social entrepreneurship is relatively new and not yet well known. The first understanding of social entrepreneurship as a special method of solving social problems occurred in the late 1980s in Italy, when the society had to look for solutions to the problem of unusually high unemployment. Currently, social businesses create jobs for people with disabilities, print books and stage theaters, and offer opportunities for young people with addictions to acquire a profession or supplement their knowledge. To put it simply, social entrepreneurship helps to solve social problems with business tools – the company produces goods or services as a traditional entrepreneurship, only with the aim of solving the social problem, not with the aim of gaining financial benefit for business owners. In this way, both more social problems are solved, and the number of people who benefit from it increases as well. Social entrepreneurship areas and their impacts vary widely, but primarily depend on the overall social and economic situation, available education and health care, environmental factors and other relevant aspects of a particular region, country or city. Such business fields in Europe is mainly focused on the areas of social services, employment, trade, environment, education and society. However, it has to be said that there are many free slots in this form of entrepreneurship. It is recognized in the world that countries do not always have the capacity to solve all the problems of the social sector themselves, while the private sector is not doing it because of financial disadvantage. Social entrepreneurs in Latvia are currently either registered as a merchant governed by the Commercial Law, or if the amount of cash flow is not higher than regulated by the Law on Associations and Foundations – as a non-governmental organization

(NGO). Although both of these legal forms exist in Latvia, none of them is suitable for the development of a sustainable social business environment. Because social entrepreneurship as an NGO cannot be a core business, but as a merchant, it is not really defined, as is the case when the profit is to be invested in the achievement of the social purpose of the statute.

5. SUCCESSFUL SOCIAL ENTREPRENEURSHIP REQUIRES INNOVATION

The role of innovations in our economics is constantly growing: it promotes the development of certain companies, as well as the growth of national economy and social welfare. The creation and implementation of new ideas is important for all businessmen – whatever the type and amount of their activity is. Innovation process gives profits not only to businesspeople, but also to its participants – scientists, national institutions, educational establishments – and to the society in general. Innovations in business play an important role in the promotion of Latvian businessmen competitiveness, especially after Latvia has joined the European Union. However, the statistics shows that in Latvia only one fifth of companies introduce innovations. The state financing granted to science and research in Latvia considerably falls behind the level of the advanced EU countries. One of the fundamental barriers for the development of innovative activity in Latvia is insufficient cooperation between businessmen and scientists.

Businessmen in Latvia lack information (and wherewith interest) about the possible cooperation with scientists and introduction of innovations. Nevertheless, a large part of scientists work on fundamental research, which certainly is important for their academic career, but still does not promote the emergence of innovative products in the market. In Latvia there have been developed a number of documents and strategies connected with the improvement of innovation policy, however the introduction mechanisms of these documents do not function in practice and thus the situation is improving slowly. The model of cooperation has been built on the report about the situation of innovation policy in Latvia, innovation support programmes and structures, for example, the cooperation of businessmen with Latvian and foreign scientists, and the conclusions given by Science and Business Partnership Council. The model of cooperation consists of three parts:

1) summary of cooperation obstacles;
2) strategy of cooperation model;
3) necessary actions to be taken.

The National Innovation Initiative identified three vital elements of this ecosystem—talent; investment for both knowledge creation and risking taking; and infrastructure, including the actions of government to create an innovation-friendly environment. Networks that connect these elements, and a national orientation toward innovation and risk-taking, enhance this ecosystem. First, talent. People are the source of new ideas and creativity. High-value innovation requires not just the best scientists, engineers, and information technology workers. We must also be concerned with developing the best at creating new business models, the best market researchers and marketers, creative financiers, and the best designers and artists – all to fuel an explosion of ideas to meet the [27].

6. CONCLUSIONS

1. EU Member States need to consider changes in all systems, not just in specific sectors. The system includes all processes and infrastructures that are resource or activity related and are important to human activity. For example, the power system includes the use of usable energy resources (coal, wind, sun, oil, natural gas and other forms of energy), the use of energy production or obtaining (wind turbines, oil boreholes, shale gas mills and other types) applications (industry, transport, housing heating and other applications) and

distribution. It would also help address the problems of land and water resources affected by the use and production of energy resources.

2. The term "circular economy" provides for the creation of a system of production and consumption that minimizes losses. Ideally, almost all goods would be reused, recycled or used in the production of other goods. By transforming products and production processes, you can help reduce waste and use unused parts as resources.
3. Water scarcity can become a global issue of the earth's ecosystem. Unfortunately, the facts show that there are places that are already affected by the water crisis. The facts show that less than 1% of ground water resources can be used for human consumption. At least 20 to 50 liters of clean water is needed daily for human to meet his basic needs. Over the last century, water consumption has risen six fold. It grows much faster than the Earth's population. Over 1.2 billion people on the planet do not have access to clean and safe drinking water.
4. Corporate social responsibility is not limited to the labor market or labor law. It is also not a classic model of social dialogue, but rather encourages society and businesses to socially responsible entrepreneurship, including participation in working and living conditions for both employees and society at large.
5. Global energy demand is expected to grow by more than half over the next two decades. America is growing more, not less dependent on foreign oil. Half the world’s known oil reserves are in the Persian Gulf, and the Middle East oil supply is increasingly unstable. There are growing worries about global warming from fossil fuels, and pressure on advanced nations to do something about it. Many facets of the energy problem are international. But there are major opportunities to answer the energy challenge domestically. Japan offers an example. Endowed with few natural resources, Japan has long embraced business philosophies and methods that focus on energy and material efficiency, economy of design, saving resources by achieving zero-defects, and eliminating many forms of waste in production.

REFERENCES

1. Innovateamerica (2005) *Innovateamerica.* National innovation initiative summit and Report. Council on Competitiveness.
2. Latvijas ilgtspējīgas attīstības stratēģija līdz 2030.gadam. (2010) Rīga: LR Saeima.
3. Martin, R., Kitson, M., Tyler, P. (2006) *Regional Competitiveness.* United Kingdom: Routledge.
4. OECD (2011) *Better policies for Development. Recommendations for Policy Coherence.* OECD and Eurostat.
5. *Open Innovation 2012*. European Commision report.
6. Sener, S., Saridogan, E. (2011) *The Effects of Science-Technology-Innovation on Competitiveness and Economic Growth.* Published by Elsevier Ltd. Selection and/or peer-review under responsibility of 7th International Strategic Management Conference.
7. Climate Policy, European Commission Directorate-General for Communication, Citizens' Information Service, Brussels BELGIUM, Manuscript, November 2014
8. Rompczyk E. *We want sustainable development.* 2007
9. http://www.varam.gov.lv/files/text/darb_jomas/book_gribamia.pdf
10. http://europa.eu/pol/rd/index_lv.htm
11. http://unesdoc.unesco.org/images/0023/002354/235407e.pdf
12. http://ec.europa.eu/environment/sustainable-development/index_en.htm
13. http://ec.europa.eu/environment/action-programme/
14. http://www.varam.gov.lv/lat/darbibas_veidi/ilgtspejiga_attistiba
15. https://www.eesc.europa.eu/lv/policies/policy-areas/sustainable-development

16. https://m.likumi.lv/doc.php?id=65563
17. https://www.un.org/sustainabledevelopment/economic-growth
18. https://www.pkc.gov.lv/lv/valsts-attistibas-planosana/ano-ilgtspejigas-attistibas-merki
19. http://profizgl.lu.lv/mod/book/view.php?id=19966&chapterid=4471
20. https://ec.europa.eu/info/sites/info/files/2018-european-semester-country-report-latvia-lv.pdf
21. https://www.lsm.lv/raksts/zinas/arzemes/petijums-nabadzibai-eiropa-ir-sievietes-seja.a216156/
22. http://lv.wikipedia.org/wiki/Ilgtspējīga_attīstība
23 http://lapas.lv/wp-content/uploads/2012/02/Fact-sheet-soc.atbild.uznemejdarb.
24. http://ec.europa.eu/social/main.jsp?catId=331&langId=lv
25. https://www.lm.gov.lv/text/753
26. https://skolas.lu.lv/mod/book/tool/print/index.php?id=40180
27. http://www.jst.go.jp/crds/sympo/gies2007/en/symposium/materials/summary/Summary_DWS.pdf

CYSENI 2019, May 23-24, Kaunas, Lithuania
ISSN 1822-7554, www.cyseni.com

TIME OF USE ELECTRICITY RATES EVALUATION FOR RESIDENTIAL CUSTOMERS IN THAILAND

A. Sukawattanapornkul, S. Khunkitti,
P. Khunkitti, A. Siritaratiwat, R. Chatthaworn
Khon Kaen University
40002, Khon Kaen – Thailand
Email: atitep.suk@kkumail.com

A. Sukawattanapornkul
[2]*Provincial Electricity Authority (PEA), Northeast region 1,*
42000, Loei – Thailand

C. Surawanitkun
Khon Kaen University
Nong Khai Campus,
43000, Nong Khai – Thailand

ABSTRACT

At present, solar energy plays an important role in electrical grid. Due to its simple installation and reasonable cost of devices, trend of electricity generation by utilizing solar photovoltaic (PV) considerably increases leading to reduction of electric energy consumption from utility grid. Moreover, in Thailand, the government has an incentive to support electricity generation from solar PV by price adder to reduce dependence of fossil fuel. For these reasons, power demand in daytime and electric energy consumption seem to be reduced while power demand in night time still grows. The time-of-use (TOU) rate is one of the price-based demand response programs that widely used to offer electricity price rate for each time period in order to persuade customers to shift their power usage at peak demand period to off-peak demand period. This paper proposes a method for optimizing TOU rate and electricity consumption to minimize peak load, load variation and total customer's energy cost. The genetic algorithm (GA) is employed to solve this optimization problem. The proposed TOU rate are classified into three rates based on time period consisting of peak load, mid-peak load, and off-peak load while the probability of customers to change their electricity consumption behavior is modeled by using the economic price elasticity of demand model. The numerical case studies will be performed on residential customers of provincial electricity authority (PEA) of Thailand. The TOU rate from the proposed method can reduce peak load, load variation, and total customer's energy cost which may convince the customers to change their electricity consumption behavior.

Keywords: Customer's energy cost, Load variation reduction, Multi-objective optimization, Peak load reduction, Retail customers, Time-of-use (TOU) rate

1. INTRODUCTION

Nowadays, the trend of using renewable energy especially solar photovoltaic (PV) rapidly grows because of its simple installation and reasonable cost of devices. Moreover, government has the incentive to support electricity generation from solar PV by price adder to reduce the dependence of fossil fuel. In 2015, an alternative energy development plan (AEDP) of Thailand aims to increase the percentage of renewable energy usage for electricity generation to 18% within 2036 [1]. For these reasons, power demand in daytime and electric energy consumption seem to be reduced while power demand in night time still grows up. This situation leads to the decrease of system load factor which causes the over investment costs of infrastructure form the utility. To deal with situation, the TOU rate is one of the price-based demand response programs that is widely used to offer an electricity price rate for each time period in order to persuade customers to shift their power usage at peak demand period to off-peak demand period which can improve the system load factor. At present in China, TOU rate is determined to encourage the customers to change their energy consumption. The aim of the TOU rate determination is to decrease customer electricity expenditure and system peak load. The solving method uses the numerical simulation to optimize multi-objective function consisting of maximizing load shifting and minimizing customer electricity expenditure. The three rates of TOU comprising off-peak, mid-peak and peak rates are evaluated based on typical load data. The multi-objective optimization model shows that TOU rate can shift peak load to valley load and reduce customer electricity expenditure [2]-[4]. There are studies of load characteristics clustering by seasonal and typical loads to find the optimal TOU rate for different seasons. The price demand elasticity coefficient is adopted to model the TOU rate. The result shows that an incentive price can motivate the customers to change the consumption which cause the peak load decrease; however, the load is still high in some durations [5]. In Denmark, the electricity market characteristic is one day ahead spot market price, there are the studies of TOU rate optimization for the industrial load, residential load and commercial load to reduce total electric consumption cost of the customers. There are two constraints considered in this work. Firstly, the total energy consumption after using optimal TOU rate must be equal to the total energy consumption before using optimal TOU rate. Secondly, the power demand changes of each TOU period must not be higher than 20% of its original power demand. That is to say, the power demand in peak load period must stay in the range of 0% to -20% of its original power demand. For the mid- peak load and off-peak load periods, the power demand must stay in the range of -10% to 10% and 0% to 20% of its original power demand, respectively. The result from sequential quadratic programming optimization indicates that the peak loads of three customer types are decreased and the system peak load is significantly reduced [6]. In Cyprus, a method to obtain the optimal TOU rate for residential prosumers is presented. The target of the optimization is to maximize load factor (LF) and electricity cost of prosumers. The derived TOU rate was implemented in pilot three hundred prosumers which can reduce the peak load by changing the prosumers behavior to use more electricity in the off-peak period [7]. In Malaysia, the TOU application instead of the flat tariff for residential customers is studied. The target is to minimize the variation of the actual and the average demands that aims to reduce the peak load. The result presents the difference of the peak and off-peak prices which can urge the customers to shift their electricity usage [8]. In Iran, demand response program by using TOU method is used to maximize the benefits of both utility and customer. The objective is to reduce peak demand by using the optimal TOU price and incentive price to motivate customers to change the rate of electricity from flat rate to TOU rate. To obtain the change of power demand after use the new TOU rate, the scenario considering single period (self elasticity) and multi period (self and cross elasticity) is used [12].

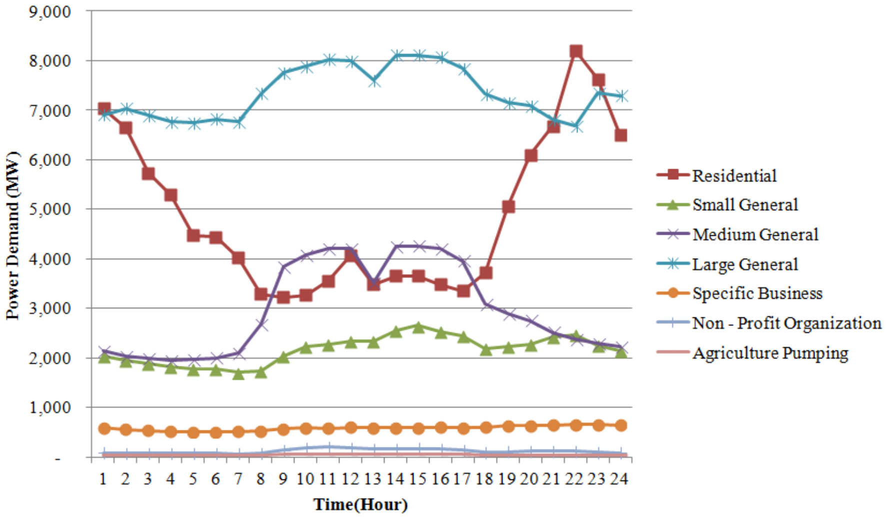

Fig. 1. Power demand of PEA, Thailand on peak day in 2017 separated by the types of customers

From Fig. 1, in Thailand, the peak power demand of PEA occurs on Wednesday 3rd May 2017 at 21:45 and the high consumption comes from residential customers. Moreover, the load variation of residential customers is higher than the other customer types. At present, the durations of TOU rate for residential customers consist of off-peak load duration defined from 22:00-9:00 and peak load duration defined from 9:00-22:00. The two rates have been used since 2000 but they are not suitable with the Thailand load characteristic at present because the high load period at night time is longer than that in the past and the high load at day time is reduced due to the supply from renewable energy generation [11]. Therefore, the TOU rate for residential should be adjusted to suit the current situation.

Consequently, this paper proposes a method to define the optimal TOU rate to reduce the peak load, load variation and total customer's energy cost with constraints consisting of peak demand limit, load variation limit, the difference of price between peak demand and off-peak demand periods limit and the total customer's energy cost limit. Economic elasticity demand price is adopted to find the optimal TOU rate according to the residential load characteristics. For the optimization algorithm, the genetic algorithm (GA) is used and the weighted sum approach is used to combine each objective together.

2. METHODOLOGY

2.1. TOU demand response

TOU is one of the price-based demand response programs that widely used to offer the electricity price rate for each time period in order to persuade customers to shift their power usage at peak demand period to off peak demand period. It can be said that the electricity price in peak demand period will be higher than the electricity price in low demand period. Normally, TOU provides 2 to 3 rates according to power demand characteristic which can be written as shown in equations (1).

$$T_{O-Pk} + T_{M-Pk} + T_{Pk} = 24 \tag{1}$$

where $T_{O-Pk}, T_{M-Pk}, T_{Pk}$ are the time (hour) of off-peak demand, mid-peak demand and peak demand periods, respectively.

The energy consumption is power that used in a period of time which the total energy consumption derived power demand in each TOU periods as shown in equations (2).

$$E = \int d(t)dt = \int_{T_{O-Pk}} d(t)dt + \int_{T_{M-Pk}} d(t)dt + \int_{T_{Pk}} d(t)dt = E_{O-Pk} + E_{M-Pk} + E_{Pk} \tag{2}$$

where E is the total energy consumption (kWh), E_{O-Pk}, E_{M-Pk}, E_{Pk} are the total energy consumption (kWh) of off-peak demand, mid-peak demand and peak demand periods, respectively. Lastly, the power demand (MW) at the time *t* in a day is denoted by $d(t)$.

2.2. Economic demand response model

In economic term, the ratio between demand change and change of goods price is called the price elasticity of demand that can be expressed as the following equation.

$$\varepsilon_d = \frac{\frac{\Delta d}{d_O} \times 100}{\frac{\Delta p}{p_O} \times 100} = \frac{\Delta d}{\Delta p} \times \frac{p_O}{d_O} \tag{3}$$

where ε_d is price elasticity of demand. d_O and p_O are the initial demand and price, respectively. Δd and Δp are the demand and price changes, respectively. The price elasticity of demand consists of self and cross price elasticity of demand which can be explained as follows.

1) Self price elasticity of demand is the proportion between demand change and change of the price at the time t which normally less than zero due to inverse relationship between quantity demand and prices. The equations can be written as follows.

$$\varepsilon_d(t,t) = \frac{\Delta d(t)}{\Delta p(t)} \times \frac{p_O(t)}{d_O(t)} \leq 0 \tag{4}$$

where $\varepsilon_d(t,t)$ is the price elasticity of demand at the time *t*. $d_O(t)$ and $p_O(t)$ are the initial demand (kW) and price (Baht) at the time *t*, respectively. $\Delta d(t)$ and $\Delta p(t)$ are the demand(kW) and price (Baht) changes at the time *t*, respectively.

When adopting elasticity of demand to evaluate TOU rate, the demand is namely electricity power demand and price is namely electricity price. From equation (4) the power demand can be expressed as shown below.

$$d(t) = d_O(t) + \varepsilon_d(t,t) * d_O(t) \left[\frac{p(t) - p_O(t)}{p_O(t)} \right] \tag{5}$$

where $d(t)$ is the power demand (kW) at the time t. $p(t)$ is the electricity prices (Baht) at the time t that differed from the initial price.

2) Cross price elasticity of demand presents the ratio between the change of good quantity and the change of prices of the other goods. If there are two goods that can substitute each other, cross price elasticity will be more than zero. Therefore, the customers can change their consumptions from peak, mid-peak or off-peak demand periods to other periods. The cross-price elasticity can be expressed as the following equation (6).

$$\varepsilon_d(t,u) = \frac{\Delta d(t)}{\Delta p(u)} \times \frac{p_O(u)}{d_O(t)} \geq 0 \tag{6}$$

Therefore, the power demand at the time t is affected by the electricity prices change at another time within 24 hours. This relationship can be written as follow.

$$d(t) = d_O(t) + d_O(t) \sum_{u=1, t \neq u}^{24} \varepsilon_d(t,u) \left[\frac{p(u) - p_O(u)}{p_O(u)} \right] \tag{7}$$

When the self and cross price elasticities are considered together in a day, the power demand is changed from the initial demand due to the adjustment of prices. This relationship can be expressed as shown below.

$$d(t) = d_O(t) \left\{ 1 + \varepsilon_d(t,t) \left[\frac{p(t) - p_O(t)}{p_O(t)} \right] + \sum_{u=1, t \neq j}^{24} \varepsilon_d(t,u) \left[\frac{p(\mathrm{j}) - p_O(u)}{p_O(u)} \right] \right\} \tag{8}$$

2.3. Proposed problem formulation

2.3.1. Objective function

The proposed TOU rate after implementation can benefit to utility by reducing peak demand and load variation. Moreover, it can also benefit to the customers by reducing customer’s energy cost. The objective function can be written as shown below.

1) Minimizing peak demand

$$Min\left\{d(t, p_{N\_O-Pk}, p_{N\_M-Pk,}, p_{N\_Pk})\right\} \tag{9}$$

where $p_{N\_O\text{-}Pk,}$ $p_{N\_M\text{-}Pk,}$ p_{N_Pk} are electricity prices at off-peak demand period, mid-peak demand period and peak demand period after using a new TOU rate (Baht/kWh).

2) Minimizing variation of load

$$Min\left\{Max\left\{d(t, p_{N\_O-Pk}, p_{N\_M-Pk,}, p_{N\_Pk})\right\} - Min\left\{d(t, p_{N\_O-Pk}, p_{N\_M-Pk,}, p_{N\_Pk})\right\}\right\} \tag{10}$$

3) Minimizing total customer's energy cost

$$totalp_N = E_{N\_O-Pk} * p_{N\_O-Pk} + E_{N\_M-Pk} * p_{N\_O-Pk} + E_{N\_Pk} * p_{N\_Pk} \tag{11}$$

where $totalp_N$ is the total customer's energy cost after use a new TOU rate (Baht/kWh). $E_{N\_O\text{-}Pk,}$ $E_{N\_M\text{-}Pk,}$ E_{N_Pk} are total energy consumption (kWh) of off-peak demand, mid-peak demand and peak demand after used a new TOU rate and.

The weighted sum approach is used to combine the multi-objective functions together because the unit of total customer's energy cost is different from the units of others. To merge these objectives together, each objective must be normalized by its original value. The weighted coefficient can be defined equal to 0.25 for minimizing peak demand and variation of demand and 0.5 for minimizing total customer's energy cost. After that, genetic algorithm (GA) is used to simulate this optimization problem.

2.3.2. Constraints

All constraints can be explained as follow.

1) The new peak demand is not higher than original peak demand.

$$Max\left\{d(t, p_{N\_O-Pk}, p_{N\_M-Pk,}, p_{N\_Pk})\right\} \leq Max\left\{d_O(t, p_{O\_O-Pk}, p_{O\_Pk})\right\} \tag{12}$$

where $p_{O\_O\text{-}Pk,}$ p_{O_Pk} are the original electricity prices at off peak demand period and peak demand period before using a new TOU rate, respectively (Baht/kWh).

2) The load variation is not higher than original load variation.

$$Delta_{N\_Max-Min}\left\{d(t, p_{N\_O-Pk}, p_{N\_M-Pk,}, p_{N\_Pk})\right\} \leq Delta_{O\_Max-Min}\left\{d_O(t, p_{O\_O-Pk}, p_{O\_Pk})\right\} \tag{13}$$

where $Delta_{N\_Max\text{-}Min}$ is the difference between maximum and minimum demand (kW) after using a new TOU rate and $Delta_{O\_Max\text{-}Min}$ is the difference between maximum and minimum demand (kW) before using a new TOU rate.

3) The difference of price between peak demand and off-peak demand periods should be determined to prevent the price at of-peak demand higher than the price at peak demand.

$$2 < \frac{p_{\mathrm{N}\_Pk}}{p_{\mathrm{N}\_O-Pk}} < 7 \tag{14}$$

4) The mid-peak demand price must not less than the original average price.

$$p_{N\_M-Pk} \geq p_{O\_avg} \tag{15}$$

where p_{O_avg} is the average electricity prices before using a new TOU rate (Baht/kWh).

5) The total customer's energy cost after use a new TOU rate must not higher than the original total customer's energy cost to persuade customers to shift their time of power usage.

$$totalp_N \le totalp_O \tag{16}$$

where $totalp_O$ is the original total customer's energy cost (Baht/kWh).

3. RESULT AND DISCUSSION

The numerical case study is performed on residential customers of provincial electricity authority (PEA) of Thailand because these customers have the highest peak demand at night time as mentioned in the introduction.

3.1. Data parameter before using a new TOU rate

From load research of PEA [8], the peak power demand in 2017 is on Wednesday 3rd May 2017 at 21:45. The maximum power demand is 20,328,465.32 kW whereas the highest consumption comes from the residential customers. The residential demand data are shown in Table 1.

Table 1. Residential demand data at peak day of 2017

Time (Hour)	**Load (×10^3 MW)**	**Time (Hour)**	**Load (×10^3 MW)**	**Time (Hour)**	**Load (×10^3 MW)**
1	7.0299	9	3.2598	17	3.3467
2	6.6404	10	3.5577	18	3.7133
3	5.7245	11	4.0713	19	5.0557
4	5.2897	12	3.4771	20	6.0922
5	4.4656	13	3.6563	21	6.6763
6	4.4333	14	3.6486	22	8.2050
7	4.0219	15	3.4745	23	7.6200
8	3.2829	16	3.2598	24	6.4933

The original TOU rate for residential customers based on PEA data is defined to be the initial electricity price as shown in Table 2.

Table 2. The original TOU rate for residential customer [10].

TOU Period	**Time Period**	**Price (USD/kWh)**
Peak	09:00-22:00	0.18244
Off-Peak	22:00-24:00	0.08297

Electricity is necessity goods especially for residential customers. Although, electricity price is increased, residential customers still need to use electricity. In Thailand, demand response program for industrial customers has been studied. The data of industrial customers who join this pilot project in May 2015 can be used to calculate self elasticity equal to -0.272 and cross elasticity equal to 0.16 [7]. From the referenced paper which studies on residential customers, the self elasticity is equal to -0.1 and cross elasticity is equal to 0.008-0.01 [3]. Generally, the change of electricity usage of residential customers is more difficult than the change of industrial customers. Therefore, in this paper, both self and cross elasticity are defined by using the lowest values mentioned in [7] as presented in Table 3.

Table 3. The price elasticity of electricity demand

	Self Elasticity	Cross Elasticity
Price elasticity of electricity demand	-0.1	0.008

In order to motivate the residential customers to change their behavior of electricity consumption, the electricity price of each period in a day should be different according to the power demand level and the production cost. Several TOU rates in many countries were separated into 2-3 periods that depend on load characteristic. From the power demand of peak day in 2017 as shown in Fig. 1, the variation of residential power demand in each time is very high. To determine the TOU period, the residential power demand data is used to plot their distribution data for indicating the density of each power demand in a day as shown in Fig. 2.

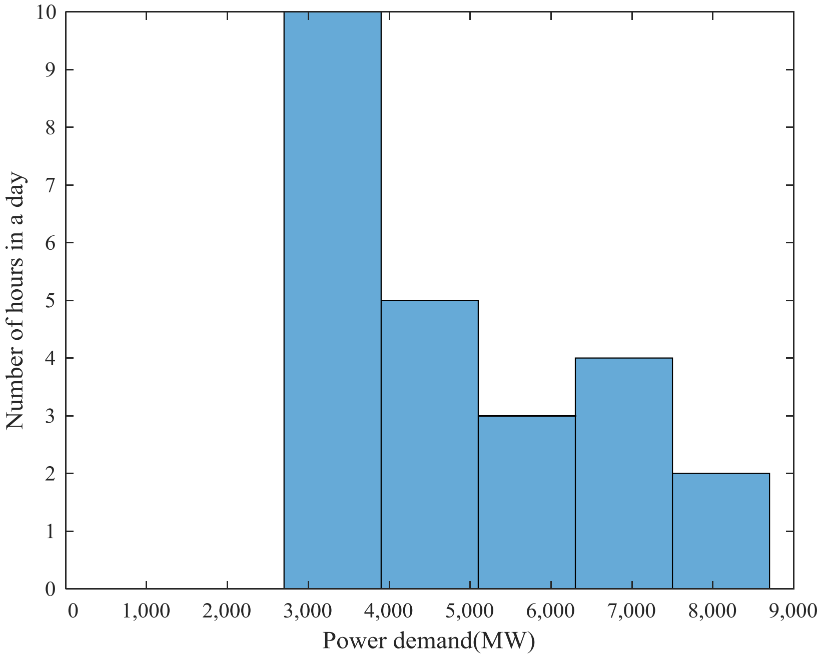

Fig. 2. Distribution of original daily residential power demand

From Fig. 2, the distribution data show that the number of hours of power demand which is less than 4,000 MW are the highest. While, the number of hours of power demand between 4,000-6,000 MW are the second highest and the number of hours of power demand which is higher than 6,000 MW are the lowest. Therefore, the TOU period can be separated into three periods according to the distribution data. The new TOU period is presented in Table 4.

Table 4. New TOU period

TOU period	Time Period
Peak	00:00-02:00, 20:00-24:00
Mid-Peak	02:00-08:00, 18:00-20:00
Off-Peak	08:00-18:00

3.2. Simulation result

After using an elasticity price model under the constraints that are described in the subsection 2, the three new optimal TOU rates are obtained as demonstrated in Table 5 presenting the comparison of the interesting values when using the original TOU rate and using the optimal TOU rate.

Table 5. Comparison of the interesting values when using the original TOU rate and using the optimal TOU rate

Interesting values	**Using original TOU rate**	**Using optimal TOU rate**	**% difference**
Customer's energy cost (×10^6 USD)	15.207	15.156	-0.33%
Peak price (USD/kWh)	0.18244	0.23358	28.03%
Mid-peak price (USD/kWh)	0.00000	0.13058	- *
Off-peak price (USD/kWh)	0.08297	0.03337	-59.78%
Peak price/ Off peak price	2.199	7.000	218.35%
Maximum power demand (×10^3 MW)	8.205	8.137	-0.83%
Minimum power demand (×10^3 MW)	3.215	3.151	-1.97%
(Max-Min) power demand (×10^3 MW)	4.990	4.985	-0.10%
Total energy consumption (×10^3 MWh)	116.451	114.815	-1.40%

*Note: it cannot be evaluated because there is no mid-peak price in the original TOU rate

From the optimal TOU rate, the peak demand price increases 28.03% from the original peak demand price and the off-peak demand price decreases 59.78% from the original off-peak demand price. These cause the peak demand, the difference of peak and off-peak demands and the customer's energy cost reduce to 0.83%, 0.1% and 0.33%, respectively. The difference of demand profile between using the optimal TOU rate and the original rate can be investigated in Fig. 3.

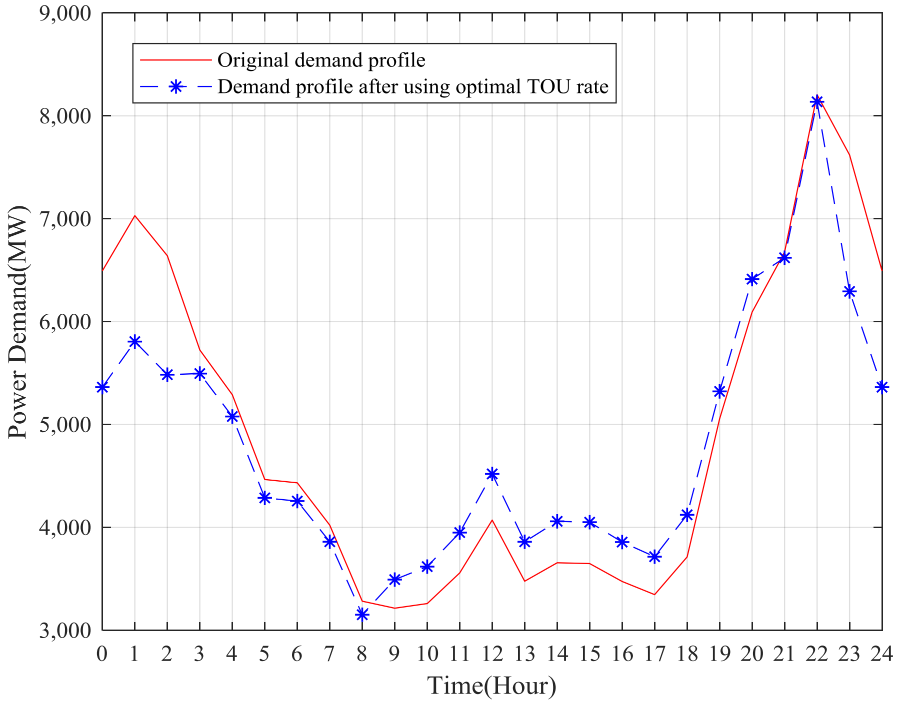

Fig. 3. The residential demand profile before and after using optimal TOU rate

From Fig. 3, the change of TOU rate during 9:00-18:00 from the original peak price to the new off-peak price can increase the power demand at this period comparing with the power demand when using the original TOU rate. Therefore, this increased power demand can match up with the generation of solar photovoltaic (PV) which generates electricity during daytime. Whereas, during 8:00-9:00 is still defined to be the off-peak period because the change of price is the lowest comparing with the price changes in other periods. Then the power demand in this period is decreased because residential customers change the consumption to the other periods which have the lower price.

During 02:00-08:00, a small increase of price from off-peak period to mid-peak period cause the small power demand decrease. Conversely, during 18:00-20:00, a small decrease from of price from peak period to mid-peak period cause the small power demand increase. Moreover, during 23:00-2:00, the period is changed from off-peak period to peak period. The significant increase of price causes the significant decrease of power demand by shifting the consumption to the other periods. However, during 21:00-23:00, this period is still defined as the peak period; although, the new price is increased but the power demand slightly decreases.

Because the presented elasticity model not only considers the price change in a self period which is defined as a self elasticity but also the price change in other period which is defined as a cross elasticity. The price increase during 21:00-23:00 is lower than the price increase of other periods; therefore, the power demand of this period is slightly decreased. As a result of the evaluation, the change of TOU period from 2 periods to 3 periods by using GA optimization subject to the mentioned constraints (subsection 2.3.2) can provide the optimal TOU rate which can reduce the load variation and peak demand by shifting the original peak demand to the other periods.

4. CONCLUSION

This research proposes a method for optimizing TOU rate to minimize peak demand, load variation and total customer's energy cost based on economic price elasticity of demand model. The optimal TOU rate can be classified into three rates consisting of peak demand, mid-peak demand and off-peak demand periods which are suitable for present residential demand characteristic of PEA. The genetic algorithm (GA) is employed to solve this optimization problem. Unlike previous studies, this paper uses residential load characteristic of Thailand and presents the method to change the TOU period from 2 periods to 3 periods in order to decrease the impact from solar PV generation. For the price elasticity, the price change is not only considered during its period but also the other periods in a day. The evaluation result after optimization process shows that power demand is increased at the old TOU peak period which is defined at day time. It means that the power demand increase will be matched with the generation from solar PV; consequently, the battery investment for gathering the surplus energy from solar PV during day time is decreased.

The new mid-peak TOU rate changing the price slightly changes the power demand slightly as well. The power demand at the new peak period changed from the old off-peak period is highly decreased because the change of price is very high. Although, during 21:00-23:00 which is fixed to be the peak period same as old peak period, the price is increased, the power demand slightly decreases because the impact of the change of price in other periods is higher. Finally, the optimal TOU rate from the proposed method can convince the customers to change their behaviors of power usage which can benefit to the peak load and load variation reductions and total customer's energy cost without any constraints violation.

ACKNOWLEDGE

This paper was supported by Provincial Electricity Authority of Thailand (PEA).

REFERENCES

1. Energy Policy and Planning Office, Ministry of Energy, Thailand. *Alternative Energy Development Plan, 2016*. Link to the internet < http://www.eppo.go.th/index.php/en/policy-and-plan/en-tieb/tieb-aedp>.
2. Qiuwei Wu, Lei Wang, and Haozhong Cheng, "Research of TOU power price based on multi-objective optimization of DSM and costs of power consumers," *2004 IEEE Int. Conf. Electr. Util. Deregulation, Restruct. Power Technol. Proc.*, 2004, Vol. 1, no. April, p. 343–348.

3. N. Yu and J. Yu, "Optimal TOU Decision Considering Demand Response Model," 2006 International Conference on Power System Technology, Chongqing, 2006, pp. 1–5.
4. T. A. N. Zhong-fu, W. Mian-bin, Q. I. Jian-xun, H. O. U. Jian-chao, and L. I. Xue, “Time-of-use Price Optimizing Model And Fuzzy Solving Method,” Syst. Eng. - Theory Pract. 2008, Vol. 28, No. 9, pp. 145–151,.
5. C. Taihua, L. Hong, H. Yang, and G. Junlin, “Research on seasonal power load characteristics and modeling of TOU price,” *Proc. 29th Chinese Control Decis. Conf. CCDC 2017*, 2017, pp. 1415–1420.
6. Z. Chen and B. Bak-jensen, “Optimal Load Res sponse to Time-of-Use Power Price for Demand S Side Management in Denmark,”, 2010, pp. 10–13.
7. V. Venizelou, N. Philippou, M. Hadjipanayi, G. Makrides, V. Efthymiou, and G. E. Georghiou, “Development of a novel time-of-use tariff algorithm for residential prosumer price-based demand side management,” *Energy*, 2018, Vol. 142, pp. 633–646.
8. M. A. R. Muzmar, M. P. Abdullah, M. Y. Hassan, and F. Hussin, “Time of Use pricing for residential customers case of Malaysia,” *2015 IEEE Student Conf. Res. Dev. SCOReD 2015*, 2015, pp. 589–593.
9. Energy Regulatory Commission of Thailand. *Demand Response and Rates*(*28 September 2016*),2016 Link to the internet < http://www.erc.or.th/ERCWeb2/Upload/Document/%E0%B9%81%E0%B8%99%E0%B8%9A%202%20%E0%B9%80%E0%B8%AD%E0%B8%81%E0%B8%AA%E0%B8%B2%E0%B8%A3%E0%B8%A1%E0%B8%B2%E0%B8%95%E0%B8%A3%E0%B8%81%E0%B8%B2%E0%B8%A3%20(Final).pdf >.
10. Provincial Electricity Authority, Thailand. *Electricity Tariffs (November 2018)*, 2018. Link to the internet <https://www.pea.co.th/en/electricity-tariffs>.
11. Provincial Electricity Authority, Thailand, *Load Research of PEA*, 2017. Link to the internet < http://peaoc.pea.co.th/loadprofile/en/>.
12. H. Aalami, G. R. Yousefi and M. Parsa Moghadam, "Demand Response model considering EDRP and TOU programs," 2008 IEEE/PES Transmission and Distribution Conference and Exposition, Chicago, IL, 2008, pp. 1–6.

CYSENI 2019, May 23-24, Kaunas, Lithuania
ISSN 1822-7554, www.cyseni.com

ELECTRICITY PRICE INFLUENCING FACTORS IN A LONG-TERM ELECTRICITY PRICE FORECASTING MODELS

M. Česnavičius
Lithuanian Energy Institute
Breslaujos str. 3, LT-44403 Kaunas – Lithuania
Email: mindaugas.cesnavicius@lei.lt

ABSTRACT

Electricity market liberalization created a meaningful electricity price fluctuation not only in a short-term but also in a long-term perspective. Environmental awareness dramatically increased the installed power of the renewable energy power stations, safety issues put nuclear energy into a question and pollution regulations made fossil fuel power plant less attractive for the investment. Previous mentioned factors can heavily affect electricity price in a long-term and extend the foreseen investment payback time. Changes in electricity market create a possibility and demand for an accurate long-term electricity price forecasting model. Companies in a heavy industry, electricity power plants and government officials can benefit from long-term electricity price forecast while planning future strategy and expenses.

Electricity price forecasting from the long-term perspective is a challenging task for several reasons. Predictions made for a period which is longer than a year could be very inaccurate due to many forecast affecting factors. Part of the considered factors might have a significantly weaker effect on the forecasted value in a year and unconsidered factor's importance might significantly grow. Essentially, each of the selected factors will include a separate long-term forecast for itself. If those forecasts will lack precision overall accuracy of the model will decrease. Accurate long-term electricity price forecasting model require a careful selection of factors according to their possible relevance in the future and precise forecast possibilities.

Up to date academic literature heavily focus on short-term electricity price forecasting models with few exceptions presenting a methodology for long-term forecasting models. In total, ten articles presenting methods for a long-term electricity price forecasting model were selected for analysis. Each of the selected articles present a methodology for one year or longer forecast period. Articles have been divided into three main groups according to the used method: quantitative, qualitative and combination of both. Each article was reviewed, and factors used in each method were registered. Mentioned factors were: historical electricity price, seasonal component, oil price, wind generation, electricity exchange, electricity supply and demand price, expert judgment and others. Finally, used methods and picked factors were rated according to the final model accuracy and occurrence in all selected material.

Selected articles review revealed that purely quantitative methods for long-term electricity price forecasting have less accuracy than qualitative or a combination of two. The primary reason for that is long forecasting period with many uncertainties which statistically are hardly predicted and can be better evaluated through the expert's opinion. Electricity supply and demand price is the most commonly evaluated factor. Long-term electricity supply and demand forecast tend to have higher accuracy since electricity production and consumption have a smaller change over a long period.

Keywords: long-term, forecasting models, electricity price influencing factors

CYSENI 2019, May 23-24, Kaunas, Lithuania
ISSN 1822-7554, www.cyseni.com

PERSPECTIVES OF DIFFERENT CHP PLANTS IN THE CONTEXT OF LATVIAN TODAY'S ENERGY POLICY

T. Odineca
Riga Technical University
Kalku 1, LV-1658 Riga − Latvia
Email: tatjana.odineca@rtu.lv

A. Borodinecs
Riga Technical University
Ķīpsalas iela 6B, LV-1048 Riga – Latvia

ABSTRACT

The paper gives an insight into the Latvian Energy long-term policy towards the CHP plants in a period 2006–2019. The subject of analysis is the steps made to stimulate the development of CHP plants, with the focus on the mandatory procurement component (MPC) as an important instrument of CHP support.

The aim of the research is to make the conclusions about the effectiveness of policy in a period by using comparative analysis, to look through the problems the existing CHP plants meet, to weight the perspectives of solutions and to suggest the variants of policy appropriate in future.

According to the latest statistical data (2017), the progress in development of Latvian CHP plants in Latvia looks obvious. At the moment the development of CHP (both using renewable or fossil fuels) stopped because of suspending the MPC support system due to concerns about corruption and a lack of transparency.

The first offered new support mechanisms included the implementation of green certificates and was rejected because the prices of certificates would be fluctuating. The second was “feed-in premium” model.

The rapid abolition of MPC support system would have negative consequences: – increase of electricity and heat prices; – bankrupts of CHP plants burdened by loans followed by a shortage in the energy market and, therefore, necessity to import electricity; – potential litigation with the support recipients; – failure to gain the targets for promoting the use of renewable energy resources and fine from the European Commission. The existing MPC support system needs to be improved and developed rather than abolished. The problem of existing system was the lack of control of support recipients, which resulted in the situation when several companies have fraudulently kept the licences having not completed the CHP projects in time. In this case the decisions to avoid the overcompensation of all MPC power plants and to reduce support for non-commissioned CHP plants are completely reasonable. For those MPC recipient who comply with the law, a fair solution should be found.

The experts of Foreign Investors’ Council in Latvia suggest to implement a tax reform along with the reform of the MPC as well as to introduce the “polluters pay” principle where the energy producer pays the costs of environmental pollution [13]. Either the newly developed or modified existing CHP support mechanism should provide a predictable legal and business environment for entrepreneurs and investors.

Keywords: cogeneration, RES, energy efficiency and reliability, energy economics and policy

1. INTRODUCTION

The possible principles of modern Energy Policy for Europe were firstly elaborated in the European Commission's paper A European Strategy for Sustainable, Competitive and Secure Energy in 2006. In 2007, in its Renewable Energy Roadmap 21 [4] the European Commission has proposed a binding target of increasing the level of renewable energy in the European Union's overall mix to 20% by 2020.

According to the European Climate and Energy package, Latvia, as EU member, had to increase energy efficiency, to reduce the greenhouse gas emissions and to increase the renewable energy part in a gross final energy consumption from 35% in 2005 to 42% by 2020. The combination of combined heat and power (CHP) and usage of renewable energy sources (RES) were named among other ways to reach these ambitious climate protection targets [3].

The paper gives an insight into the Latvian Energy long-term policy towards the CHP plants (working on both renewable and fossil fuels) during the last two decades. The subject of analysis are the steps made to stimulate the development of CHP plants, with the focus on the mandatory procurement component (MPC) as an important instrument of CHP support. The aim of the research is to make the conclusions about the effectiveness of policy in a period 2006–2018 by using comparative analysis, to look through the problems the existing CHP plants meet, and to weight the perspectives of solutions. Although the idea is not new, the novelty, or, better to say, the interest of this research is in observing the unstable period in energy politics when the farther situation is not clear.

2. CHP PLANTS IN LATVIA IN A PERIOD 2007–2018

2.1. Development of Latvian energy long-term policy towards the CHP plants

Reaching the long-term goals of Latvia’s energy sector is a complex process that demanded finalizing a long-term strategy, defining and justifying feasible goals and tasks, as well as establishing concrete political, legal and institutional frameworks and tools.

The key strategic document, defining the fundamental principles of the Latvian government policy, as well as long-term goals and course of action in the energy sector, was the Principles of Energy Sector Development 2007-2016, adopted in 2006. The goals spelled in the document are identical to those defined by the EU, namely: 1) secure supply, 2) encouraged competition and competitiveness, and 3) use of renewable resources.

In 2016, the Cabinet of Ministers of the Republic of Latvia approved the Guidelines for Energy Sector Development 2016–2020 [5] that defining the key objectives of the Latvian energy policy: 1) enhancing the competitiveness of the national economy, 2) the formation of prices on energy resources and energy under the free market and competition, 3) sustainable energy production and consumption. To contribute to the sustainability of the energy sector, it was planned to implement activities aimed at increasing the proportion of “green energy”, reducing GHG emissions and contributing to efficient energy use, which needed revising and developing of new support mechanisms for RES use. The set objective – increase the proportion of RES in the total consumption of energy, focusing on competitive energy prices – seemed to be rather contradictory and needed wisely developed support system.

In a period 2006–2018, electricity generation in cogeneration and renewable electricity generation was stimulated through a complex support system in a form of a feed-in tariff, which also included elements of a quota system and tenders. Despite many changes made in the relevant documents during the described period, the main idea remained unchanged.

The documents, regulating support mechanisms in 2006–2018 (Electricity Market Law [9], Electricity Tax Law [10], “Regulations regarding electricity production and price determination upon the production of electricity in cogeneration”[8]), have been amended a total of 36 times during the period of their actuality.

The first document regarding the MPC support of CHP plants was Minister Cabinet’s Regulation No. 921 “Regulations on electricity generation in cogeneration”, 06.11.2006. [7], establishing that a CHP plant which simultaneously produces electricity and useful thermal energy with an appropriate efficiency coefficient may acquire the right to sell the produced electricity within the framework of mandatory procurement. The Regulation specified the measures for the control and deduction of the applicants as well as established the price calculation formula for CHP plants with electrical power < 4 MW for the amount of electricity that could be sell within the framework of mandatory procurement. The prices depended on the fuel used by CHP plant (for

RES – 25% higher than for natural gas). There was a strict price synchronisation with the end-of-trade tariff for natural gas approved by the regulator, even if using RES.

On 10.03.2009. the previous document was replaced by Minister Cabinet's Regulation No. 221 "Regulations on electricity generation and pricing while producing the electricity in cogeneration" [8]:

- the energy producers can use the mandatory procurement support within a maximum period of 15 years. The rules for the actions of producers, their control and submission of reports were specified.
- a support recipient who has obtained the right to receive a guaranteed fee for the electrical capacity installed in a CHP plant shall ensure that the capacity installed in the cogeneration unit is put into operation not later than 3 years after the decision (license) of Ministry of Economics enters into force.
- the Regulation defined the formulas for the calculation of the fee for the installed electrical capacity < 4 MW. The fee for CHP plants with electrical capacity > 4 MW is determined by the regulator.

The amendments to Minister Cabinet's Regulation No. 221, 22.12.2009. defined the formulas for the calculation of the fee for the installed electrical capacity > 4 MW. The working CHP plants can choose between the previous system and the formulas. A period during which the CHP plant should be put into operation following the coming into force of the license, was extended from 3 to 5 years.

The amendments to Minister Cabinet's Regulation No. 221, 07.09.2010. Only those energy producers who use or plan to use the RES for electricity generation may apply for the MPC licence. Gas CHP plants which have already acquired MPC licence by 31 October 2010 shall maintain the previous conditions for the sale of electricity and the same principles for price calculation.

The amendments to Minister Cabinet's Regulation 221, 28.08.2012. For existing support recipients, the duration of the support is limited to 10 years for CHP plants with an electric capacity < 4 MW and 15 years for plants with an electric capacity > 4 MW. These deadlines shall be counted from the date the CHP plant is put into operation. From 10.09.2012 to 01.01.2016, an entrepreneur is not entitled to apply for the right to sell the generated electricity within the scope of mandatory procurement, as well as to receive a guaranteed fee for the electrical capacity installed in a CHP plant (*moratorium*).

The amendments to Minister Cabinet's Regulation 221, 30.07.2013 specified that the extension of time limits for the implementation of supported projects is no longer allowed and the energy producer who has obtained the licence must be able to put a CHP plant into operation in the time period defined by the regulation.

The amendments to Minister Cabinet's Regulation 221, 06.11.2013 reduced the support intensity for CHP plants with installed electric capacity > 4 MW. They would no longer be able to obtain the right to sell electricity within the mandatory procurement, but only to obtain a guaranteed fee for the capacity installed at the CHP station under the existing conditions for operating arrangements, time limits and calculation of the power component. The previous regulatory framework remained for CHP plants with a capacity of < 4 MW.

The amendments to Minister Cabinet's Regulation 221, 22.04.2014 limited the variability of the natural gas price included in MPC pricing formulas by setting its ceiling at the level of the natural gas trade tariff in March 2014.

The amendments to Minister Cabinet's Regulation 221, 15.12.2015 extended the *moratorium* until 2020.

The amendments to Minister Cabinet's Regulation 221, 05.07.2016 intended a mechanism to eliminate the risks of overcompensation for operators producing electricity from AER or high-efficiency cogeneration. When a project overcompensation is found, a reducing factor – a price differentiation coefficient – is applied to future aid, ensuring that the overall level of the project IRR at the end of the aid period does not exceed 9%. In order to ensure that mandatory procurement prices do not fall below the level required to ensure the operation of supported CHP plants as a result of the fall of the natural gas trade tariff, the natural gas trade price included in the MPC pricing formula shall be fixed at the level which was average in a period from August 2007.

The amendments to Minister Cabinet's Regulation 221, 20.06.2017: In order to adapt the functioning of the MPC system to a liberalised natural gas market, the tariffs on the commercial service, transmission, storage and distribution service included in the calculation formula for electricity shall be fixed at the level they were before the liberalisation of the natural gas market.

The amendments to Minister Cabinet's Regulation 221, 03.10.2017 intended that in 2017 energy producers who received a guaranteed fee for the capacity installed in the cogeneration unit with electric capacity of > 100 MW may apply for a lump-sum payment consisting of 75% of the guaranteed fee to be received during the remainder of the support period.

The amendments to Minister Cabinet's Regulation 221, 10.04.2018 reinforced the control mechanism for CHP plants and established additional operational measures for support receiving.

The described support scheme is temporarily suspended and is planned to be closed for new installations until the new support scheme is worked out.

2.2. Development of CHP plants

The changes made in regulations regarding electricity generation while producing the electricity in cogeneration are reflected in the data compiled by the Central Statistical Bureau [6]. Figure 1 shows the rapid increase of installed electrical capacity of CHP plants in 2009, when the first new CHP plants were put in operation (in 3 years after the MPC license enters into force) and 2013, when the second part of the new CHP plants were put in operation (in 5 years, according to the amendments to Minister Cabinet's Regulation No 221, 22.12.2009). The amendments of 07.09.2010 ("only those energy producers who use or plan to use the RES for electricity generation may apply for the MPC licence") are also reflected on Figure 1 by the increase of installed electrical capacity of CHP plants using RES. The last insignificant increase of capacity is seen on 2016 (5 years after the *moratorium* was established).

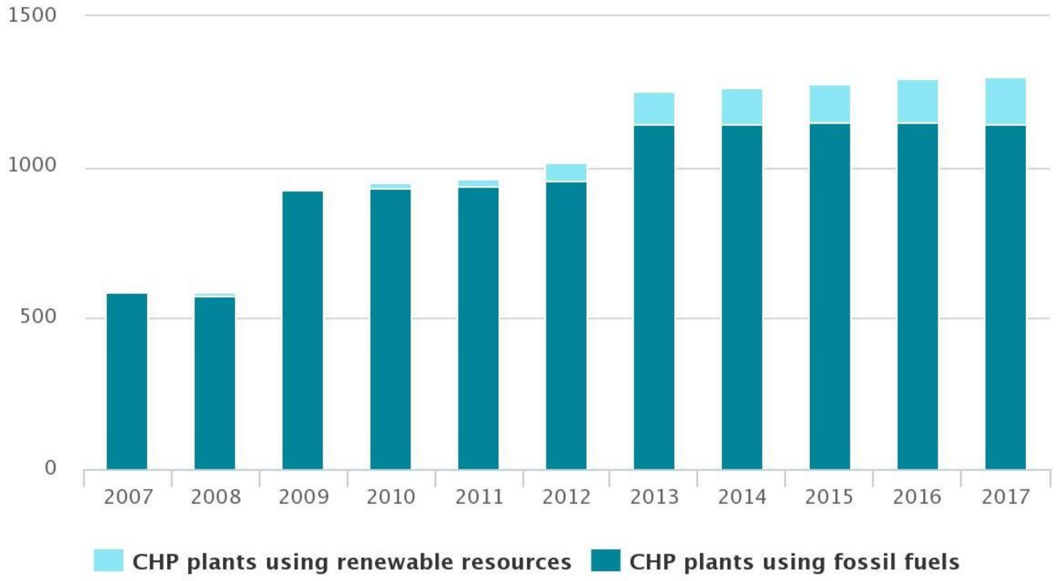

Fig. 1. Installed electrical capacity of CHP plants (MW) [6]

Figure 2 shows that in end of 2016 the amount of electricity produced in CHP plants reached its peak – 3700 GWh. Unfortunately, the most recent data (after the strict inspections started) is not available yet.

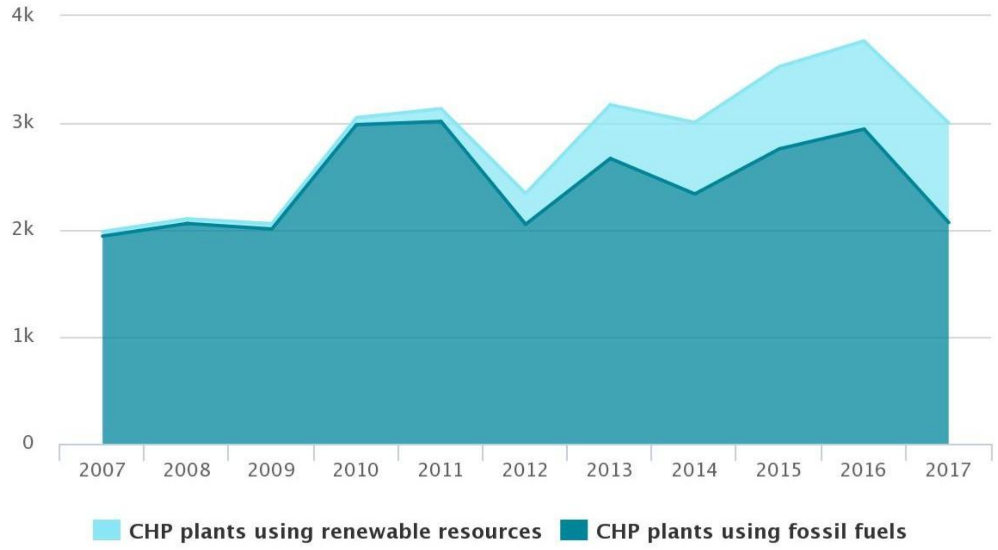

Fig. 2. Electricity produced in CHP plants (GWh) [6]

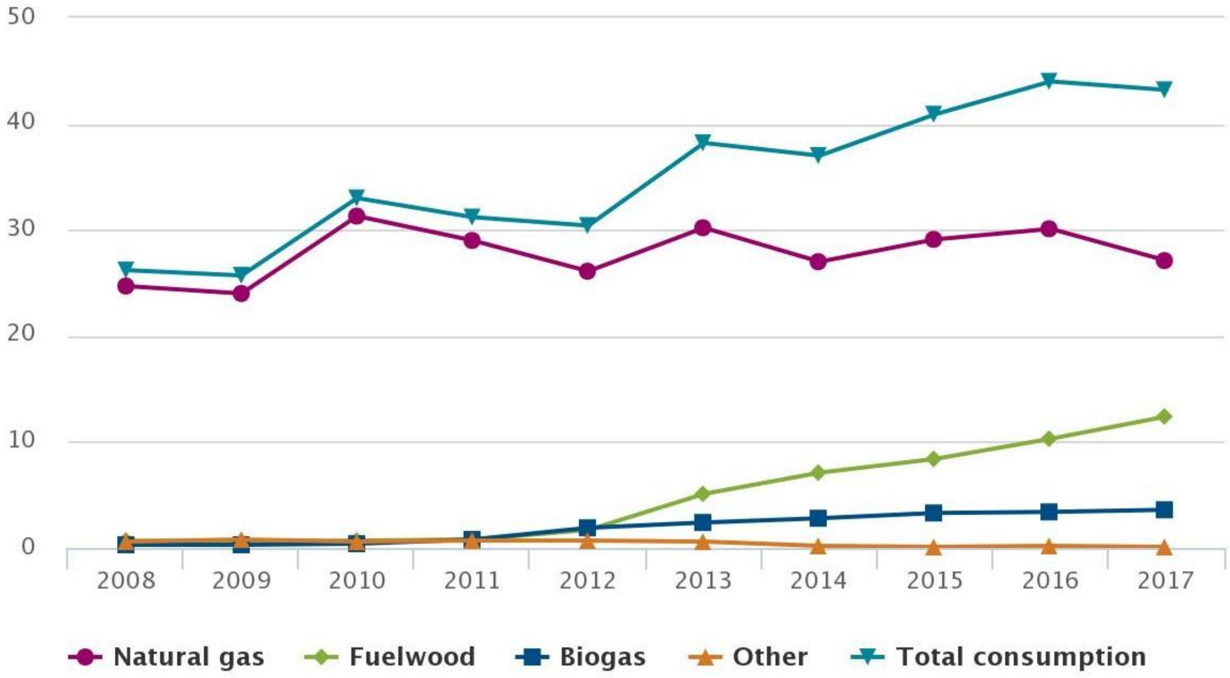

Fig. 3. Fuel consumed in CHP plants (PJ) [6]

As it is seen on Figure 3, by 2017 Latvian CHP plants mainly consumed natural gas (27.1 petajoules (PJ)) and fuelwood (12.4 PJ). During the examined period (2008–2017), the share of natural gas consumed in CHP plants fell from 94% to almost 63%, while the share of electricity produced in RES-fuelled CHP plants has increased by 29%. By 2017 930 GWh of electricity were produced from RES, constituting 31% of the total amount of electricity produced in CHP plants. The biggest relative increase of RES consumption was observed for fuelwood, and the second one - for biogas.

Despite the financial and organizational difficulties caused by changes in support system, the gain of CHP plants in Latvia looks obvious (Table 1).

Table 1. Number of CHP plants, installed electrical capacity and produced heat energy (MW) in 2010 and 2017 [6]

xxx	**Number of public CHP plants**		**Installed electrical capacity, MW**		**Electricity produced, GWh**		**Heat energy produced, GWh**	
Year	2010	2017	2010	2017	2010	2017	2010	2017
TOTAL	**56**	**204**	**932.8**	**1299.1**	**2984.8**	**3000.1**	**4603.4**	6301.7
≤ 0.2 MW	8	28	1.3	4.1	7.2	22.2	20.2	48.2
0.2 < P ≤ 0.5 MW	14	39	5.7	14.8	23.5	77.8	99.1	255.8
0.5 < P ≤ 1 MW	9	71	6.2	58.3	23.9	368.8	197.6	750
1 < P ≤ 5 MW	21	59	54.3	144.2	323.3	861.3	867.4	2016.7
5 < P ≤ 20 MW	1	3	11.8	27.9	35.7	102.8	36.9	156.3
> 20 MW	3	4	853.5	1049.8	2571.2	1567.2	3382.2	3074.7

3. THE PROBLEMS AND PERSPECTIVES OF CHP PLANTS

3.1. The fuels: renewable VS fossil

As one of the weak points of CHP support policy of the last 20 years is mentioned the support not only for RES using CHP plants, but also for those using fossil fuels (meaning natural gas). This decision is justified by the fact that usage of natural gas allows to apply highly effective (with high α-ratio) CHP technologies. Besides, gas combustion is more ‘environment-friendly’ from the point of de-carbonization.

One of Latvia’s advantages, which serves as a (short-term) guarantee of continual supply, is its underground gas storage facilities. The amount of active gas in currently functional Incukalns underground storage may reach 2.3 billion cubic meters, and there are plans to increase this amount to 3.2 billion cubic meters. The expansion of these storage facilities may bring about several significant advantages, such as strategic reserves, economic benefits and improvement of regional energy supply. Nevertheless, it may also boost local energy and production companies’ inclination to use imported gas instead of exploring sustainable local options by means of increasing energy efficiency and using renewable energy sources.

Anyway, gas distribution system does not cover all Latvian territories, including the ones with big forest density. In 2017 the largest share of electricity produced from RES in CHP plants was registered in Vidzeme and Zemgale regions – 89% and 82%, respectively, while the smallest share was observed in Riga – 3% of the total electricity produced in the region (Fig. 4). As mentioned before, the most popular RES consumed by Latvian CHP plants is fuelwood. Usage of wood fuels is considered perspective: it not only helps to increase the part of renewable energy in gross final energy consumption, but also gives relative independence from importing of fossil fuel resources.

The problem of CHP technologies applying common combustion of wood is low α-ratio, which means much heat and little electricity. Trying to achieve the wishful electrical energy production causes over-production of heat energy. In many new CHP plants the realization of heat, which is the main success factor in the cogeneration project, was not properly considered. When the heat production exceeds the demand, it can be accumulated by the thermal energy storage system, however, the necessary analysis of heat load variations for calculation of the accumulation system capacity is a complicated process.

Wood gasification (a thermo-dynamical process that converts wood to a gaseous fuel) is more effective in CHP than common combustion of wood, for the reason that generated gas can be a fuel for such effective CHP technologies as gas-steam turbines and internal combustion sets. Wood gasification is more environment-friendly comparing to common combustion, because of less CO_2 emissions during gasification process. Though the advantages of wood gasification in cogeneration seem to be self-evident, as it allows high efficiency combined with an increase of renewables' share, this technology is not widely spread and implemented [2].

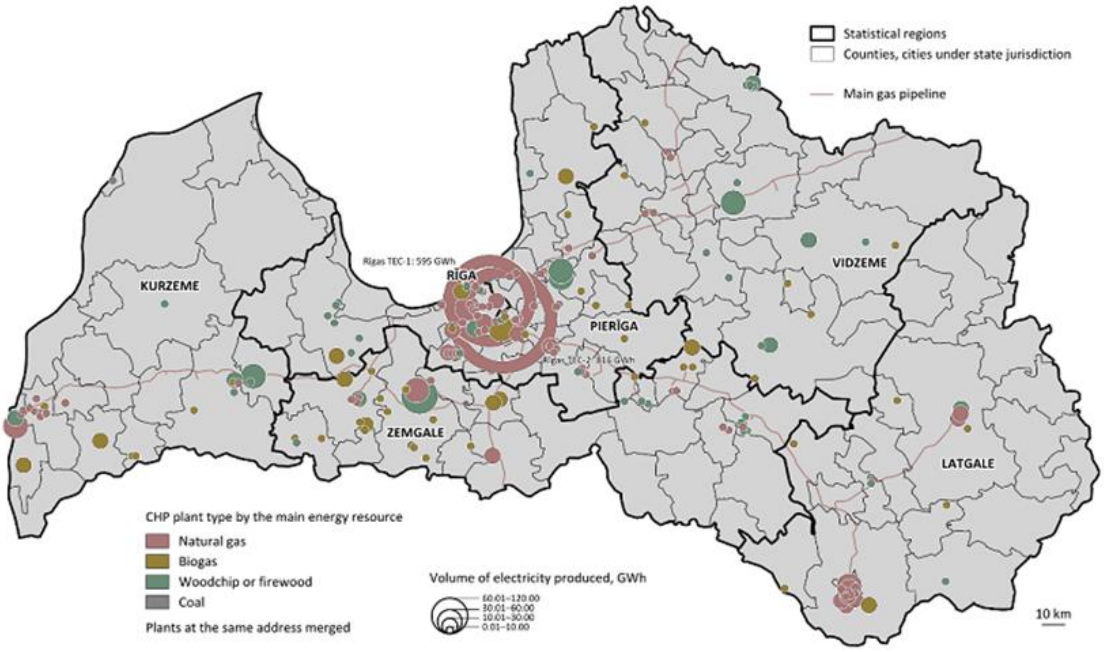

Fig. 4. CHP plants in Latvian territory (by volume of electricity produced and the main fuel consumed) [6]

Producing electrical energy in the internal combustion engine demands special quality of gasifier and gas. World's experience of exploitation of this kind of systems shows that they are sensitive towards the changes of fuel parameters and the load of equipment, quality of service, and environmental conditions. Necessity of cleaning, cooling and mixing of gas makes technology difficult and expensive.

3.2. The new CHP (including consumed by RES) support mechanisms

As mentioned before, the support scheme existing in a period 2007–2018 is temporarily suspended. By now, the existing feed-tariff is on hold until 01.01.2020 due to concerns about corruption and a lack of transparency in the way it was carried out since 2007.

The increase of electricity bills caused by the change in the MPC system, forcing electricity consumers to pay "green energy" components for installed capacity, led to sharp discussions. The existing state support mechanisms for energy production from RES were assessed and revised.

In August 2018, the working group of the Ministry of Economics worked out a proposal about a refusal of the MPC payment over a period of three years. It was proposed to reinstate the subsidized electricity tax, to include the MPC capacity payment in the transmission tariff and to limit the profits of MPC recipients, thereby reducing the amount of mandatory procurement, as well as to set the new requirements for biogas plants by setting a minimum proportion of organic waste. Three years later, the reform of the MPC system provides for one of the models, based on the market principles: either introduction of "green certificates" or implementation of the market price efficiency model.

Some of the proposals were opposed by energy producers and other organisations, including the Latvian Renewable Energy Federation). According to Janis Bethers, the chairman of the board of company "Enefit", the company's experience on the Polish and Swedish markets showed that the implementation of "green certificates" does not reduce consumer payments for electricity, besides, it is likely that the prices of certificates would be fluctuating [11]. After discussions, the proposal concerning the “green certificates” was removed from the MPC reform plan.

Stringent supervision of subsidised electricity producers, stricter controls and a limited timeframe for the implementation of RES projects have been introduced. In December 2018, the Ministry of Economics drew up a legislative proposal regarding the organisation of supervision and control of the mandatory procurement mechanism, to eliminate the overcompensation and to recover unduly paid state aid. “Overcompensation” is defined as the amount of aid received by the electricity producer, which results in an excess of the norm of total internal rate of return on capital investment.

The redrafted list of measures proposed by the Ministry of Economy in January 2019 included the following support measures for electricity producers:

- to avoid the overcompensation of all MPC power plants in 2019;
- to reduce support for non-commissioned CHP plants in 2019;
- to introduce stricter requirements for raw materials for biogas plants in 2022;
- in 2022 to quit MPC support of gas CHP plants, except Riga TEC-2 as this power plant is strategically important for Latvia's energy independence and security of energy supply.

The new plan no longer offered to renew the subsidized energy tax on MPC recipient. At the same time, the Ministry proposed a solution for the transition to a market-based support mechanism for electricity producers. The market model would be applied to the existing fairly working power plants contributing to the renewable energy targets. As for the new CHP plants, no support was planned for them.

The proposed “feed-in premium” model means that green electricity producers participate in the electricity market, like all other producers, but receive a premium at the wholesale market price of electricity sold. The main difference from the existing compulsory procurement system is that no profit will be guaranteed for stations. In the MPC model the state buys electricity from the support recipients at a fixed price, while in the “feed-in premium” model the CHP plants themselves should sell electricity at times when the price is the highest. The “feed-in premium” model is simpler and easier to implement than the “green certificates” proposed above.

The total amount of green energy aid was projected to not exceed 0.3% of gross domestic product (GDP), compared to 1.0% of GDP in 2017.

The electricity producers were opposed to the offered plan. Gas CHP plants did not agree with reducing their profit margins, and biogas CHP plants also with new quality criteria for the raw materials.

As the process of MPC system abolition obviously has many risks, in March 2019 the Ministry of Economics set up two working groups in order to receive an independent assessment of the possibilities and consequences of this decision. The first group consists of representatives of the Ministry, Latvenergo and the High Voltage Network, the second one shall represent the recipients and payers of MPC support. One more working group – the lawyers – assessed the legal part of abolishing the MPC.

Finally, on 26.03.2019. the government has decided not to advance solutions for lifting the MPC from 31.03.2019 (as it was planned before).

The rapid abolition of MPC support system would have negative consequences.

First of all, it's driving up electricity and heat prices. According to the information provided by the suppliers of thermal energy [12], in some municipalities heating rates could become 10%-40% higher. This is explain by the fact that the MPC aid currently received is used to subsidise heat energy: the revenues from electricity are directed to reduce the heat rates.

Secondly, a big part of producers have received loans, with total commitment amount of €200 million. Stopping the MPC support could lead to difficulties with loan repayment. As a result, several CHP plants will go bankrupt, followed by a shortage in the energy market, and electricity should be imported.

Another risk is potential litigation. The contracts with energy producers have been made for long periods (many years), creating legitimate expectations.

Finally, the national targets for promoting the use of renewable energy resources cannot be achieved without the state support. In this case that the European Commission would start the infringement procedure and impose the fine.

The Ministry of Economics is working on a number of scenarios, the main aim of which is to decrease the electricity bills. Though the development of a new support mechanism was expected to be completed by the end of 2018 (according to Energy Development Guidelines 2016–2020), it is more likely to be implemented after the completion of the new Latvian National Energy and Climate Plan 2021–2030.

4. CONCLUSIONS

During the period from 2008 to 2017, the share of natural gas consumed in CHP plants fell from 94 % to almost 63 %, while the share of electricity produced in RES-fuelled CHP plants has increased by 29% [6] that corresponds with Latvian target to increase the renewable energy part in a gross final energy consumption to 42% by 2020. Despite the financial and organizational difficulties caused by changes in support system, the progress in development of Latvian CHP plants in Latvia looks obvious. Unfortunately, the more recent data, which could demonstrate the results of suspending the MPC support system, are not yet available.

Without changing and improving existing energy policy, the use of cogeneration using RES cannot be efficiently stimulated. The sustainability of RES in Latvia is going to be ensured if the government finds ways how to limit the support effect on the price on electricity for final consumers. The high costs would force the society to choose cheaper energy produced from fossil energy resources. Such scenario would significantly restrict the ability of Latvia to facilitate the potential of production of local energy and the use of local energy resources.

The rapid abolition of MPC support system was found undesirable due to its many negative consequences. Talking of trials to reduce the consumers’ electricity bills, the share of MPC in final payments is around 15% while a large part is made up of electricity transmission and distribution payments, therefore the abolition of MPC would be not be significantly reflected in bills.

The existing MPC support system needs to be improved and developed rather than abolished. The problem of existing system was the lack of control of support recipients, which resulted in the situation when several companies may have cheated – having not completed the CHP projects in time, they have fraudulently kept the licences. In this case the decisions to avoid the overcompensation of all MPC power plants in 2019 and to reduce support for non-commissioned CHP plants sound completely reasonable. For those MPC recipient who comply with the law, an acceptable solution should be found.

The experts of Foreign Investors’ Council in Latvia (FICIL) suggest to implement a tax reform along with the reform of the MPC. FICIL either believes that the use of renewable energy resources in Latvia could be promoted by implementing the “polluters pay” principle where the energy producer pays the costs of environmental pollution [13].

In order to decide on one or the other future support system model in Latvia (modification of the existing system, "green certificates", feed-in premium, etc.), it is necessary to have an in-depth analysis of how these systems will work, what will be the impact on economy, what the risks are and how to control them.

In any case, to meet the goals by Latvian National Energy and Climate Plan 2021-2030, the new developed CHP support mechanisms should provide a predictable legal and business environment for entrepreneurs and investors. Stability and transparency are a key factors for crediting of new projects, which is impossible when the support scheme constantly change.

This study was supported by European Regional Development Fund project Nr.1.1.1.1/16/A/048 “Nearly zero energy solutions for unclassified buildings”.

REFERENCES

1. RUBINS, M., PILVERE, I. Development of renewable energy policy in Latvia. Proceedings of the 2017 International Conference “ECONOMIC SCIENCE FOR RURAL DEVELOPMENT” No 44 Jelgava, LLU ESAF, 27-28 April 2017, pp. 281-291.
2. ODINECA, T. Wood gasification in Latvia: today and in future. CYSENI 2009. Proceedings of annual conference of young scientists on energy issues. [CD]. Kaunas: Lithuanian Energy Institute. 2009 May 28-29.
3. Energy Efficiency Policies and Programmes of Latvia 2007 - In-depth Review. Link to the internet:https://energycharter.org/fileadmin/DocumentsMedia/IDEER/IDEER-Latvia_2008_en.pdf
4. Communication from the Commission to the Council and the European Parliament - Renewable energy road map - Renewable energies in the 21st century: building a more sustainable future. Link to the internet: https://eur-lex.europa.eu/legal-content/EN/ALL/?uri=celex:52006DC0848
5. Par Enerģētikas attīstības pamatnostādnēm 2016.-2020. gadam. LR likums (About Energy Development Guidelines 2016-2020). Link to the internet: https://likumi.lv/ta/id/280236-par-energetikas-attistibas-pamatnostadnem-2016-2020-gadam
6. Central Statistical Bureau (2017). Rise in electricity produced in CHP plants from renewable energy sources. Link to the internet: https://www.csb.gov.lv/en/statistics/statistics-by-theme/environment-energy/energy/search-in-theme/2401-activities-chp-plants-2017
7. MK noteikumi Nr. 921. Noteikumi par elektroenerģijas ražošanu koģenerācijā. LR likums (Regulations on electricity generation in cogeneration). Link to the internet: https://m.likumi.lv/doc.php?id=147673
8. MK noteikumi Nr. 221. Noteikumi par elektroenerģijas ražošanu un cenu noteikšanu, ražojot elektroenerģiju koģenerācijā. LR likums (Regulations Regarding Electricity Production and Price Determination upon Production of Electricity in Cogeneration). Link to the internet: https://likumi.lv/ta/en/id/189260-regulations-regarding-electricity-production-and-price-determination-upon-production-of-electricity-in-cogeneration
9. Elektroenerģijas tirgus likums. LR likums (Electricity Market Law). Link to the internet: https://likumi.lv/doc.php?id=108834
10. Elektroenerģijas nodokļa likums. LR likums (Electricity Tax Law). Link to the internet: https://likumi.lv/doc.php?id=150692
11. «Enefit»: Jācenšas uzlabot, nevis mainīt OIK sistēmu. LSM.lv ziņu redakcija. (“Enefit”: The MPC system should be to improved, not changed.) Link to the internet: https://www.lsm.lv/raksts/zinas/ekonomika/enefit-jacensas-uzlabot-nevis-mainit-oik-sistemu.a287696/
12. FRIDRIHSONE, M. Plānotās OIK atcelšanas dēļ 15 vietvarās siltuma tarifi varētu augt par 10-40%. (The planned abolition of MPC could lead to a 10-40% increase of heat rates in 15 municipalities) Link to the internet: https://www.lsm.lv/raksts/zinas/ekonomika/planotas-oik-atcelsanas-del-15-vietvaras-siltuma-tarifi-varetu-augt-par-10-40.a312460/
13. The FICIL’s Position Regarding Cancelation of Mandatory Procurement Component (OIK). 1st of August, 2018. Link to the internet: https://www.ficil.lv/wp-content/uploads/2018/08/01_08_2018_FICIL_position_OIK_ENG-1.pdf

CYSENI 2019, May 23-24, Kaunas, Lithuania
ISSN 1822-7554, www.cyseni.com

ENERGY CONSUMPTION, CAPITAL EXPENDITURES RESEARCH AND DEVELOPMENT COST AND PROFITABILITY OF THE COMPANY IN PAPER INDUSTRY

A. Zuoza
Lithuanian Energy Institute
Breslaujos st. 3, LT-44403 Kaunas – Lithuania
Email: andrius.zuoza@lei.lt

V. Pilinkienė
Kaunas University of Technology
Gedimino g. 50-334, LT-44029 Kaunas – Lithuania
Email: vaida.pilinkiene@ktu.lt

ABSTRACT

The interest in energy efficiency and economic development of the country has been developed in the last couple of years. However, there is still a gap in the literature regarding the influence of the consumed energy to the company financial performance and especially profitability of the company. To evaluate a company's profitability a ratio of the earnings before interest, taxes, depreciation and amortisation and total revenue (EBITDA margin) was used. This paper aims to empirically examine the relations between energy consumption, R&D costs and capital expenditures on the profitability of the manufacture companies. The main focus in this article dedicated to the companies, which are operating in the manufacture of pulp from wood and paper production industry. In this paper two null hypotheses were tested: H_1: a higher level of energy consumption reduces the profitability of the company; H_2: a higher level of energy consumption, R&D costs and capital expenditures reduce the profitability of the company. The data sample consists of 104 records from 44 companies; time period cover 2002 to 2016. Positive and statistically significant correlation was found between energy consumption and profitability of the company (r = 0.249, p.val = 0.01) and between profitability and R&D costs (r = 0.43, p.val < 0.01). In the studied data the true correlation between profitability and capital expenditures was equal to 0. The performed regression analysis shows that energy consumption has a significant contribution to the profitability of the company. The results of the regression indicated the energy consumption explained 5.3% of the variance (adj. $R^2 = 0.053$, F(1,102) = 6.769, p.val = 0.01). For this reason, we rejected hypothesis H_1. The β coefficient for energy consumption in a regression model shows that profitability will increase by abt. $2.3*10^{-7}$% for each 1000 GJ energy consumed. Multiple regression analysis was used to test if the energy consumption, R&D costs and capital expenditures significantly predict profitability. The results of the regression indicated the three predictors explained 25.4% of the variance (adj. $R^2 = 0.254$, F(3,84) = 10.86, $p < 0.01$). The positive and statistically significant value of the β coefficient for energy consumption and R&D costs points out the positive relationship between them and the company's profitability. For this reason, we rejected hypothesis H_2. The results of complex regression analysis also show that capital expenditures have no significant influence on the profitability of the company. The findings of this paper can be updated by testing for energy intensity or adding other independent variables and expended to other manufacture industries.

Keywords: energy consumption, profitability, pulps and paper industry

EFFECT OF ELECTRIC FIELD IN DEUTERIUM PERMEATION IN ALUMINA COATINGS

P. Muñoz, I. García-Cortés, A. Moroño, F. J. Sánchez, T. Hernandez
Laboratorio Nacional de Fusión, CIEMAT
Avda, Complutense, 40, 28040 Madrid – Spain
Email: patricia.munoz@ciemat.es

ABSTRACT

Effective permeation barriers are needed for fusion reactors to prevent hydrogen embrittlement and tritium inventory control. The use of Al_2O_3 coatings over the structural material, is an efficacious way to reduce hydrogen isotopes permeation through the steel walls, due to the chemical stability and low solubility for hydrogen of Al_2O_3 layers.

The samples studied were 1-µm alumina coatings deposited on Eurofer steel discs by reactive sputtering. Samples were subjected to an electric field (1V and -1 V) during permeation from room temperature up to 450 ºC (at a rate of 10 ºC/min) with and without irradiation.

Permeation was clearly reduced by irradiation but no clear effects have been observed by the electric field. Permeation was reduced compared to bare material in the temperature range 25 ºC-450 ºC demonstrating alumina coatings are good candidates as barriers to reduce hydrogen isotopes permeation in fusion reactors.

Keywords: permeation barriers, coatings, electrical conductivity

Highlights: RIPER facility is an adequate facility to measure permeation with an electric field applied.
Permeation is not influenced by an applied electrical field (even during irradiation)

1. INTRODUCTION

In self-cooled liquid metal blanket concepts, including lead–lithium (PbLi) fusion blankets, an induced electric current will be produced by magnetohydrodynamic (MHD) effects... A magnetic field induces currents in a moving conductive fluid. A current passing through a conductive fluid can create forces on the fluid and affect the magnetic field. Therefore it is necessary to develop an electrical insulating coating to insulate this electric current from the conducting walls [1].

An MHD flow confined by electrical conducting walls provokes an increase in pressure drop (MHD pressure drop). As for MHD thermofluid research, an electrical insulating coating is extremely important from the viewpoint of the safe electrical insulating wall condition in fusion reactors [2]. There are some studies of Al_2O_3 as an electrical insulating coating in terms of the Al_2O_3 compatibility with PbLi [3, 4], considering alumina (Al_2O_3) as a candidate for the electrical insulating coating against PbLi flows for a blanket concept [5].

The dual-functional lead–lithium (DFLL) and the water-cooled PbLi breeder (WCLL) concepts with ferritic steel structures [6] can adopt an Al_2O_3 coating as tritium permeation barrier (TPB) in order to reduce the tritium permeation. Many researches in the development of fusion reactors have been focused on the development of coatings that avoid permeation [7, 8]. However, as described above, it is also necessary that these coatings be electrical insulators.

Controlling the tritium permeation is a very important aspect in these reactors, and it has been seen that it can be affected by various factors, such as ionizing radiation, temperature or coating thickness. [9, 10]. The alumina conductivity can be affected by different factors, mainly temperature and ionizating irradiation. [11, 12]. Due to irradiation, hydrogen isotopes diffusion increases [13, 14] and also due to an electric field [15]. Therefore, permeation has to be evaluated in both conditions at the same time.

Nevertheless, there is no research on electrical insulating performance of the coatings during permeation. In this sense, RIPER facility was developed at CIEMAT, firstly to measure permeation during irradiation in order to test permeation in the similar condition of reactors. Secondly it was modified to measure the permeation while applying an electric field, making also possible to measure permeation during irradiation and under an electric field simultaneously. The same facility allows conductivity measurements of the coatings.

There are previous studies where it is observed that the electric field can have an effect on the desorption of deuterium, which can then affect the permeation [15-17]. The objective of this work is to verify the effects of an applied electric field on deuterium permeation. In this sense, a modification was made in the RIPER installation in order to apply electric field and conduct conductivity measurements. Other objective was to check if the sign of the electric field has an influence on permeation.

2. EXPERIMENTAL

The RIPER facility (Fig. 1) consists of three main systems, a Van de Graaff electrostatic generator, the permeation system attached to the electron accelerator and the detection system connected to the vacuum cell of the permeation chamber. The oven used to heat is held by the sample (Fig. 2).

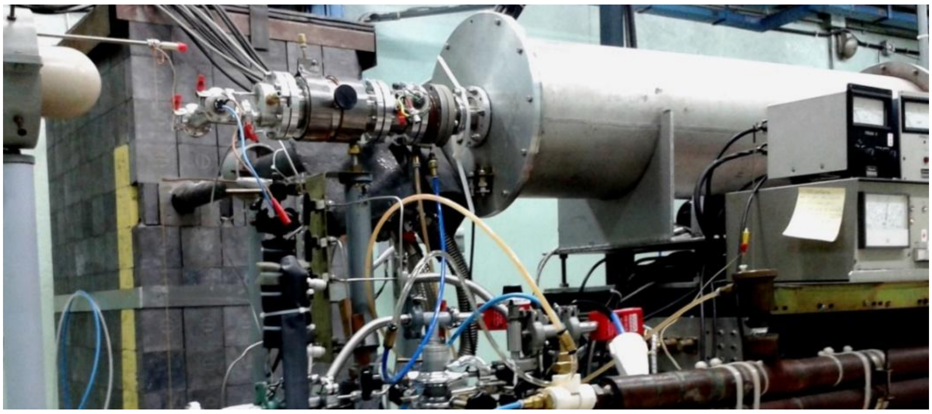

Fig. 1. RIPER facility

Fig. 2. Resistor oven

An electric field can be applied to the sample through the polarization of the oven by applying voltage to it. The oven is insulated and the other side of the sample is metallic and grounded, so the ceramic coating is exposed to an electric field. In the control room there is an electrometer interposed between the insulated oven and the power supply (Fig. 3) which allows voltage application to the sample while the conductivity is measured. This equipment allows to apply a potential difference in the range of mV-kV, and there is a sensitivity in the measurement of current in a range of mA to pA.

Due to high radiation levels the execution of the experiments has to be made from the control room. In this installation, where it is generally desired to measure very large resistances, triaxial cables are used, with greater shielding against noise than the usual coaxial cables.

Fig. 3. Conductivity system

At the same time from the control room it is possible to control the permeation tests and perform irradiations [9].

In this way an alumina coating manufactured by sputtering was mounted as presented in Figure 4. An aluminum plate is placed on the cathode and a small concentration of oxygen is established in the tube in order to make the reaction: $2Al + 3/2O_2 \rightarrow Al_2O_3$ possible.

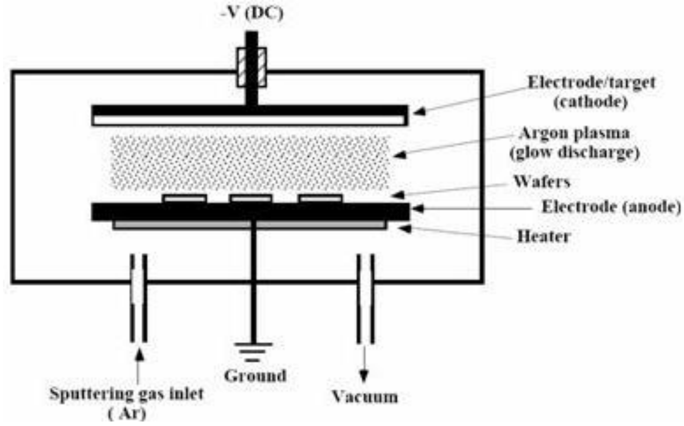

Fig. 4. Sputter system schema

In the cathode an ionic bombardment occurs, which results in an erosion of the aluminum with the consequent deposition of the atoms forming the coating on the surface of the steel. The desired operation pressure is obtained by means of a pump (usually a two-stage rotary vacuum pump or a turbomolecular pump), with an inert gas such as argon injected into the chamber through an intake valve. The presence of argon as an inert gas is very desirable since it will not decompose in the luminescent discharge. It also has a relatively high atomic weight and provides an adequate ion source for effective bombardment of the target material. The sputter coater used and the Eurofer sample before and after the deposition of alumina is shown in Figure 5 and 6 respectively.

Fig. 5. Sputter coater

Fig. 6. Eurofer coated with alumina (left) and bare Eurofer sample (right)

The sample was mounted in the RIPER system (Fig. 7) to check the coating was insulating before measurements. More details in reference [9]. The experimental procedure is as follows, the sample is mounted in the permeation chamber. After the sample chamber is closed it is pumped down to 10^{-5} bar, then the chamber is filled with the test gas, for example D_2, to a pressure between 10^{-4} and 1 bar. The sample can be heated and exposed to an electric field. The electron beam irradiates the sample while the amount of gas permeating through the sample is measured.

First a deuterium permeation test was performed as follow. Sample is heated from 25 ºC to 450 °C at 10 °C/min while permeation is measuring with a leak detector. Temperature is kept at 450 °C during one hour and cooled with the same temperature rate.

Next, the same permeation test was carried out, but applying an electric field of + 1 V. To see the effect of the sign of the field, the same experiment was carried out in the same way by changing the sign to -1 V.

Deuterium permeation in alumina coatings is influenced by electron irradiation, as measured previously, decreasing permeation. Permeation is also influenced by the temperature. In this sense, an experiment was carried out heating up the sample to 450 ºC and measuring the permeation when the temperature was stable. After that 1 V was applied measuring permeation at the same time. The same procedure was done later applying -1 V. The process was repeated, but applying electric field and irradiation at the same time. In addition, as previously mentioned, the system allows measuring conductivity in the same assembly, so the conductivity of the sample was measured.

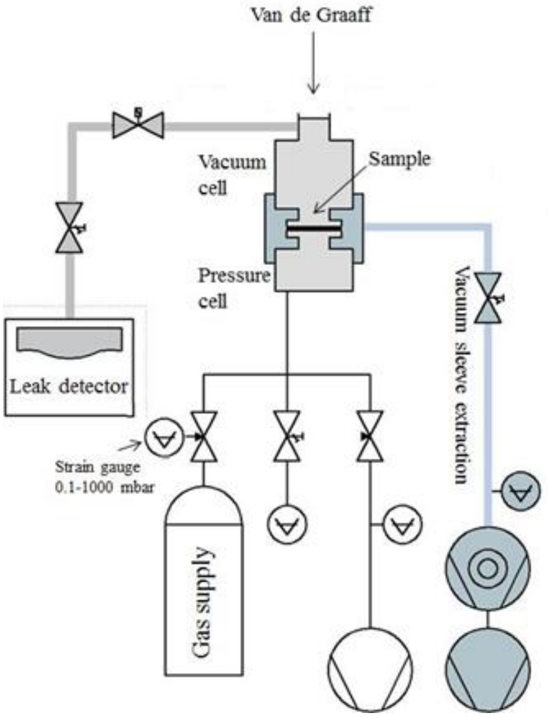

Fig. 7. Schema of the RIPER system

3. RESULTS

RIPER facility system has been used for measurements of permeation under an applied electric field. Figure 8 presents permeation measurements without field, and with an applied field of +1 V and -1 V respectively, where it is observed that there is no difference between the measurements.

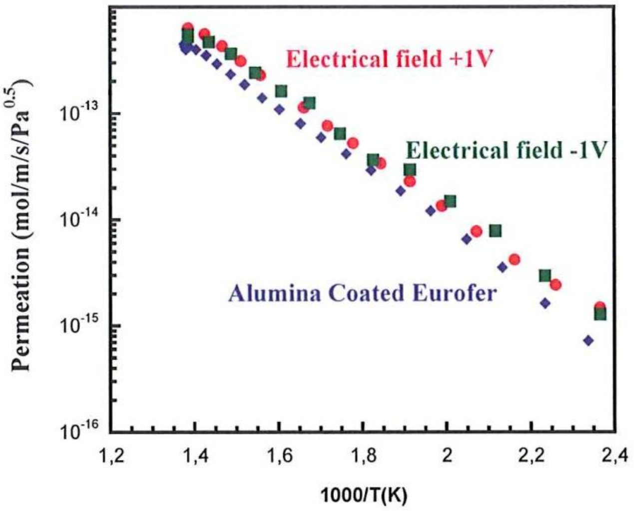

Fig. 8. Permeation vs permeation under electrical field (positive and negative)

The following Figures 9 and 10, show the values of deuterium release rate as a function of time at a temperature of 450 ºC. The moments at which the positive and negative fields are applied are shown in Fig. 9 and Fig. 10, respectively, as well as the moment in which irradiation starts (for both positive and negative field value). The application of the electric field has no effect on deuterium permeation even if the electron irradiation is present.

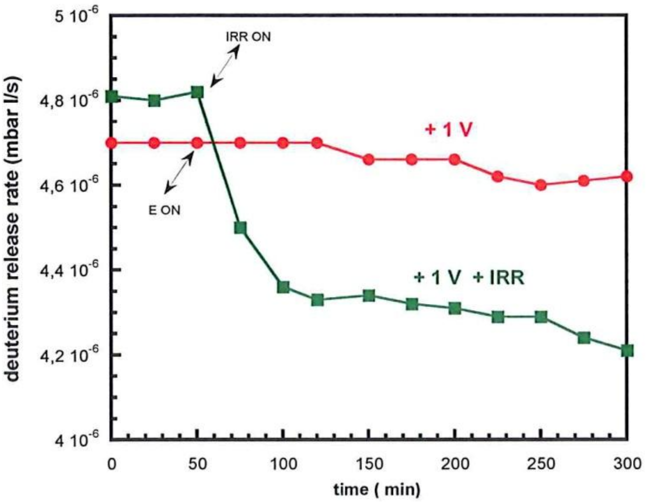

Fig. 9. Deuterium release rate during application of an +1V electrical field (red line) vs, Deuterium release rate during application of an +1 V electrical field during irradiation (green line)

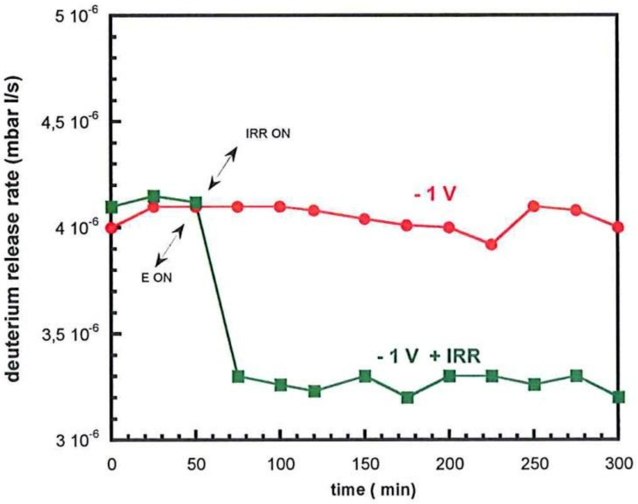

Fig. 10. Deuterium release rate during application of an -1V electrical field (red line) vs, Deuterium release rate during application of an -1V electrical field during irradiation (green line)

RIPER facility system for in-situ characterization of the electrical conductivity has been checked for alumina coatings (beam off, no irradiation), as shown in Figure 11. The conductivity values obtained for Eurofer coated with alumina are compared with electrical conductivity of α-Al_2O_3 (Wesgo AL995) reported in reference [18], showing similar values and identical behaviour with temperature (Fig. 11).

An ATR-FTIR spectrum was performed in order to characterize the coating (Fig. 12). The infrared spectroscopy (IR) characterization was carried out employing a Nicolet 5700 IR spectrometer in the range of 4000-400 cm^{-1}, coupled with a smart performer single-reflection ATR (attenuated total reflectance) accessory.

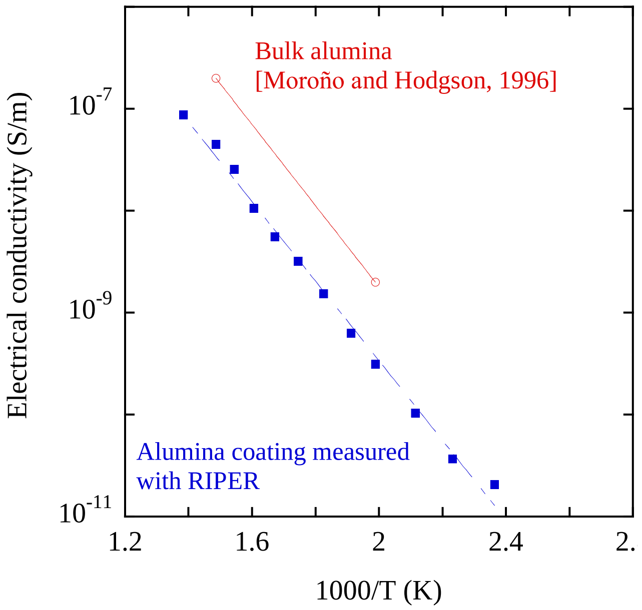

Fig. 11. Electrical conductivity for alumina coated Eurofer measured in RIPER and electrical conductivity for bulk alumina taken from a previous work [18]

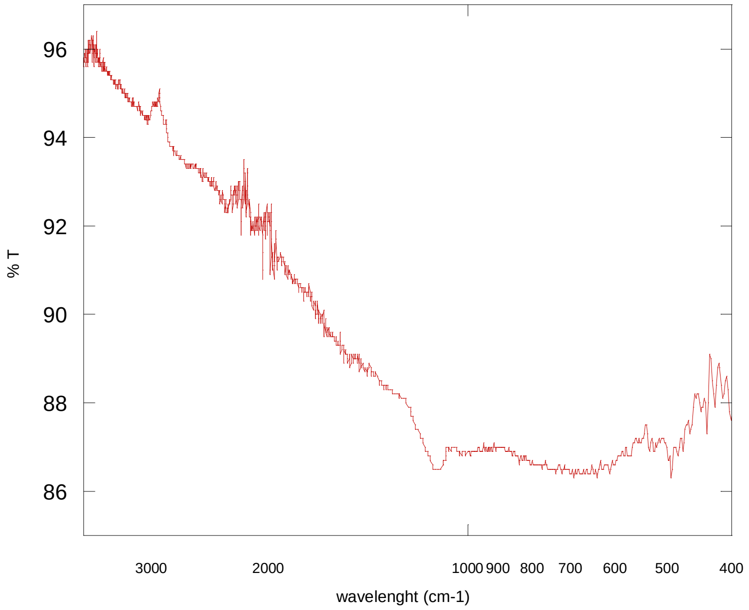

Fig. 12. ATR-FTIR spectrum of the CIEMAT coating

3. DISCUSSION

The objective of this study was to verify if the electric field applied on the alumina coating has effect on deuterium permeation. Results while an electrical field is applied do not show any effect on the deuterium permeation. It has been measured with two polarities (+/-) and it has been proved no effect on the permeation. This situation is also shown under irradiation.

Although these studies point to the mobility of D^+ and H^+ species under an electric field, these studies have been carried out on alumina single crystals. According to references [15, 17] these species move along the crystallographic axes. In the case of coatings manufactured as described in this work (reactive sputtering) there are no crystalline phases being mainly an amorphous phase.

In the ATR-FTIR spectrum it can be observed there are no discrete bands. There is a poorly defined band between 450 and 1100 cm^{-1} corresponding to Al-O vibrations. The coating is formed by clusters of different compositions, Al_2O_3, but also Al_2O_4 and Al_2O_5 as presented in the reference [19].

Accordingly, the mobility of the species under an electric field is reduced, since there are no preferential directions to move, therefore not affecting the permeation.

The work presented in reference [9], concludes that the radiation affects the permeation due to ionizing radiation that enhances desorption of deuterium from the alumina surface. This fact causes the permeation reduction in the coating under irradiation. On the other hand, it has been studied how the conductivity of alumina is affected by irradiation [12], thus it was also necessary to measure the permeation during electric field application and during irradiation.

In this case, the observed effect is the same as that observed when performing the permeation only with irradiation, so that no effect on the permeation is observed in the case of applying the electric field even with irradiation Fig. 9 and 10.

The RIC (Radiation-Induce-Conductivity) effect is dependent on the radiation dose [12], and the dose used in this test is not very high, so perhaps a higher dose is necessary to observe some effects of the joint application of electric field and irradiation.

The system also allows measuring the conductivity of the coatings in situ. One alumina coating sample was mounted in the facility and then was electrically characterized. The conductivity measurement made in them shows that they are electrical insulators and the value in the order of 10^{-7} S/m at 450 ºC is similar to values found in bibliography [18].

It is possible to conclude that for this value of applied field, the coatings of alumina present a good insulating behaviour that makes it a good option for use in fusion reactors. The possibility of surface degradation in insulators for a higher electrical field and dose rate of irradiation for ITER and future fusion reactors needs to be fully assessed.

4. CONCLUSIONS

In this article it was studied if the electric field has any influence on the permeability of deuterium in alumina coatings. Results of permeation measurements show no effects on permeation for the voltage applied here (+1 V / -1 V). Even when the electric field has been applied with radiation, the effect observed in this case is due to the irradiation with electrons but not due to the application of the electric field. The RIPER facility has been consolidated as a system for measuring permeation under electric field application.

ACKNOWLEDGMENT

The authors are indebted to J. Valle, F. Jimenez and Ms. Martín Laso for their help with the experiments. P. Munoz also acknowledges a pre-PhD contract from the Spanish MEIC. This work has been also partially supported by Spanish ‘Ministry of Economy and Competitiveness’ and the ‘European Regional Development Fund’ under the grant number ENE2016-76755-R (AEI/FEDER, EU).

REFERENCES

[1] D.L. SMITH, J.-H. PARK, I. LYUBLINSKI, V. EVTIKHIN, A. PERUJO, H. GLASSBRENNEr, et al., Progress in coating development for fusion systems, Fusion Eng. Des. 2002. 61–62 p. 629–641.

[2] L. BUHLEr, S. MOLOKOV, Magnetohydrodynamic flow in ducts with insulating coatings, Report KfK 5103, Forschungzentrum Karlsruhe, 1993.

[3] J. KONYZ, W. KRAUSS, Z. VOSS, O. WEDEMEYER, Comparison of corrosion behavior of bare and hot-dip coated EUROFER steel in flowing Pb–17Li, J. Nucl. Mater. 367–370 (2007) 1144–1149.

[4] H. GLASBRENNER, J. KONYS, Z. VOSS, O. WEDEMEYER, Corrosion behavior of Al based permeation barriers in flowing Pb–17Li, J. Nucl. Mater. 307–311 (2002) 1360–1363.

[5] M. NAKAMICHI, H. KAWAMURA, Out-of-pile characterization of Al2O3 coating as electrical insulator, Fusion Eng. Des. 58–59 (2001) 719–723.

[6] L. GIANCARLI, L. BARAER, B. BIELAK, M. EID, M. FUTTERER, E. PROUST, et al., European reference design of the water-cooled lithium–lead blanket for a demonstration reactor, Fusion Technol. 26 (1994) 1079–1085.

[7] D.L. SMITH, J. KONEYS, T. MUROGA, V. EVITKHIN, Development of coatings for fusion power applications, J. Nucl. Mater. 307–311 (2002) 1314–1322.

[8] A. PERUJO, T. SAMPLE, E. SERRA, H. KOLBE, Low aluminum content permeation barrier coatings for din 1.4914 martensitic steel (Manet), Fusion Technol. 28 (1995) 1256–1261.

[9] P. MUÑOZ et al. Radiation effects on deuterium permeation for PLD alumina coated Eurofer steel measured during 1.8 MeV electron irradiation. J. Nucl. Mater., 512 (2018) 118–125.

[10] YAO, Z., LIU, C., & JUNG, P. Diffusion and Permeation of Deuterium in EUROFER97: Effect of Irradiation and of Implanted Helium. Fusion Science and Technology, 48 (2005), 1285–1291.

[11] E.R. HODGSON, M. MALO, J. MANZANO, A. MOROÑO, T. HERNANDEZ, Radiation induced modification of electrical conductivity for three types of SiC, J. Nucl. Mater. 417 (2011) 421–424.

[12] C. PATUWATHAVITHANE, W.Y. WU, R.H. ZEE, Radiation induced conductivity in alumina. Journal of Nuclear Materials 225 (1995) 328-335

[13] S.J. ZINKLE, V.A. SKURATOV, D.T. HOELZER, On the conflicting roles of ionizing radiation in ceramics, Nucl. Instrum. Methods B 191 (2002) 758e766.

[14] P. MUÑOZ, A. MOROÑO, F.J. SANCHEZ, A. MAIRA, I. GARCÍA-CORTES Ionizing radiation effects on the thermal stability of deuterium trapping in reaction bonded SiC. J. Nucl. Mater 508 (2018) 219–225.

[15] RAMÍREZ, R., COLERA, I., GONZALEZ, R., SAVOINI, B., CHEN, Y. Hydrogen-deuterium exchange induced by an electric field in α-Al2O3 single crystals Radiation Effects and Defects in Solids 155(1) (2001) 415–419.

[16] R. GONZÁLEZ and Y. CHEN, Transport of hydrogenic species in crystalline oxides: Radiation and electric-field-enhanced diffusion, Journal of Physics Condensed matter, 14 (45) R1143 (2002).

[17] RAMÍREZ, R., COLERA I., GONZALEZ, CHEN, Y., KOKTA, M.R., Hydrogen-isotope transport induced by an electric field in α-Al2O3 single crystals. 2004. Physical Review B 69(1).

[18] A. MOROÑO and E. R. HODGSON, Surface and volume electrical degradation in Wesgo AL995. J. Nucl. Mater. 233, 1299 (1996).

[19] S. R. DESAI, H. WU, C. M. ROHLFING, L.WANG, A study of the structure and bonding of small aluminum oxide clusters by photoelectron spectroscopy: AlxOy 2 (x51–2, y51–5), J. Chem. Phys., 106, No. 4, (1997).

CYSENI 2019, May 23-24, Kaunas, Lithuania
ISSN 1822-7554, www.cyseni.com

NUMERICAL INVESTIGATION OF HYDROGEN INFLUENCE ON J-INTEGRAL OF ZIRCONIUM ALLOY

R. Janulionis
Breslaujos str. 3, LT-44403 Kaunas – Lithuania
Email: remigijus.janulionis@lei.lt

ABSTRACT

Zirconium alloy is used for manufacturing of claddings and fuel channels for nuclear power plants. The fuel cladding is the second and the most significant barrier preventing the release of fission products into the reactor coolant while the fuel channel is the part of the third barrier. Therefore, these components have to meet strict requirements in terms of operational reliability. The structural integrity of claddings are also important during decommissioning when the spent fuel with claddings are stored in short and intermediate term spent fuel storage and dry storage casks. Therefore, the ageing mechanisms of zirconium alloys that can weaken the strength of the components should be carefully evaluated. One of the degradation mechanisms acting on claddings and fuel channels is hydrogen absorption. Under certain conditions absorbed hydrogen can form brittle metal hydride inclusions what can lead to crack formation and even component failure, i.e. fracture. Therefore the evaluation of zirconium alloy resistance to fracture due to hydrogen absorption is important.

J-integral is one of the parameters used to estimate the materials resistance to fracture. Usually J-integral for materials is determined experimentally. However, it is not always possible to conduct the experiment. Therefore, alternative methods to predict J-integral should be used. Determined J-integral values later can be used for evaluation of cracks and prediction of residual lifetime in components made of Zr alloy.

Numerical modelling of J-integral using finite element method was performed in this work. J-integral was predicted by numerically simulating actual tension of compact tension specimen. Numerical prediction was performed for Zr alloy with and without hydrogen. The influence of hydrogen was evaluated by applying actual material properties of Zr alloy with hydrogen. Obtained numerical simulation results were verified with experimental data.

Keywords: hydride, hydrogen, zirconium alloy, finite element method, numerical modelling, J-integral

1. INTRODUCTION

Zirconium alloy is used for manufacturing of fuel channels and fuel cladding used in NPP. The ageing mechanisms of zirconium alloys are irradiation, thermal creep, embrittlement under exposure of irradiation and hydrogen absorption. Hydrogen absorption by zirconium alloy during corrosion process is one of the main factors determining lifetime of Zr-2.5Nb fuel channels (FC). When hydrogen concentration in FC exceeds solubility limit, formation of hydrides occurs. The hydride is a brittle phase. The source of the embrittlement is hydride precipitates that formed as platelets. The formation of hydrides in the matrix of zirconium alloy degrades the mechanical properties of zirconium alloys: reduces ductility and resistance to fracture [1–4]. Critical J-integral is one of the parameters used to estimate the materials resistance to fracture [5]. It is used as a fracture parameter for ductile materials. Calculated J-integral value of the component with crack is compared with critical J-integral value of the material. And then it can be decided if construction with cracks is safe to be in operation. J-integral depends on the size and location of the crack, geometry, the magnitude of load. The critical J-integral is the material property and as all material properties it depends on temperature, surrounding environment and etc. Usually critical J-integral is determined by an experiment, whereas the procedures are described in standards such as ASTM, ISO, etc. However, experimental testings are destructive test methods, where actual material samples have to be cut and brought to the laboratory. As the Zr alloy is used for NPP reactor components materials are also irradiated and that makes the experimental testing even more complicated. There are existing non-destructive technologies to measure flaws (cracks) and hydrogen concentration in zirconium alloy. Therefore alternative non-destructive methods for prediction of fracture toughness are necessary. The residual lifetime of NPP components made of Zr alloys can be determined by knowing the actual values of fracture toughness and existing flaws. Finite element method (FEM) and boundary element method (BEM) are the most widely used techniques for evaluating J-integral.

A number of papers can be found on fracture parameters calculation using FEM [6, 7]. Jun-Young and all [8] present sophisticated crack extension modelling technique which is used for critical J-integral determination. However this technique requires damage analysis to be added in the model and another three material constants (α, β, γ) have to be found. To determine these constants additional notched bar tensile experiments have to be conducted and analysed. Also calculation results appear to be sensitive to mesh size. Overall it makes this technique complicated. To determine critical J-integral Mahler and Aktaa [9] suggest using cohesive element layer for crack extension. However, to describe cohesive elements also the additional tension tests of notched specimens are necessary.

The aim of this work is numerical determination of J-integral of zirconium alloy with and without hydrogen using finite element method and comparison with experiment.

2. METHODOLOGY

The idea of numerical investigation of J-integral is to numerically simulate the experiment according to actual procedures/instructions used for experiment conduction. Instructions described in ASTM E1820 standard [10] for J-integral determination were chosen. For this purpose finite element model of compact tension specimen has to be created and tension of specimen has to be simulated. As results J-integral, tension force, crack mouth opening displacement and crack extension should be obtained. Having these results and following ASTM E1820 instructions critical J-integral can be determined. More detailed explanation on ASTM instruction, model preparation and crack extension determination is presented in following sections. ABAQUS/Standard v6.11 [11] has been chosen as computer code for model preparation and numerical simulation. ABAQUS uses finite element method (FEM) for numerical simulation.

2.1. Instructions for critical J-integral determination

According to ASTM E1820, to determine the value of J-integral it is necessary to develop so called J-R curve which consist of J-integral values at a series of measured specimen crack extensions. The actual result after the experiment is data points which later are used for J-R curve construction. However not all points are good to be used for J-R curve but the points which are in the area limited by 0.15 mm and 1.5 mm exclusion lines and by J_{limit} line. To draw an exclusion line in the first place it is necessary to determine a construction line which is calculated by the following equation:

$$J = 2\sigma_Y \Delta a, \tag{1}$$

where σ_Y – effective yield strength (the average of yield strength R_p and ultimate strength R_m) of the material, MPa; Δa – crack extension, mm.

The exclusion lines are just the parallel lines to the construction line with offset of 0.15 mm and 1.5 mm. J_{limit} is calculated by equation:

$$J_{limit} = b_0 \sigma_Y / 7.5, \tag{2}$$

where b_0 – uncracked ligament of the specimen, mm.

Using selected data points power law regression line can be constructed using a method of least squares. Also the offset line has to be determined. The offset line, the same as exclusion lines, is the line parallel to the construction line with offset of 0.2 mm. This line is used to determine the conditional J_Q value which is determined at the intersection of regression line with offset line. After J_Q is determined and if effective yield strength, specimen size and J_Q meet ASTM E1820 conditions it is possible to state that $J_Q = J_{IC}$.

2.2. Material and specimen

The effect of hydrogen influence on zirconium alloy was evaluated by applying material properties with different hydrogen concentration. Material properties of Zr-2.5Nb alloy which were used in the model were found in the paper [12] and are presented in Table 1. Here $R_{p0.2}$ is yield strength and R_m is tensile strength.

Table 1. Mechanical properties of Zr-2.5Nb alloy

Hydrogen concentration, ppm	**$R_{p0.2}$, MPa**	**R_m, MPa**
0	411	492
52	368	480
100	470	545
140	470	555

Modulus of elasticity was calculated according to the following equation [13]:

$$E = 97.928 - 0.0647T \quad (3)$$

where: E – modulus of elasticity, GPa; T – temperature, °C.

The true stress-strain curves that were used in the analysis are presented in Fig. 1.

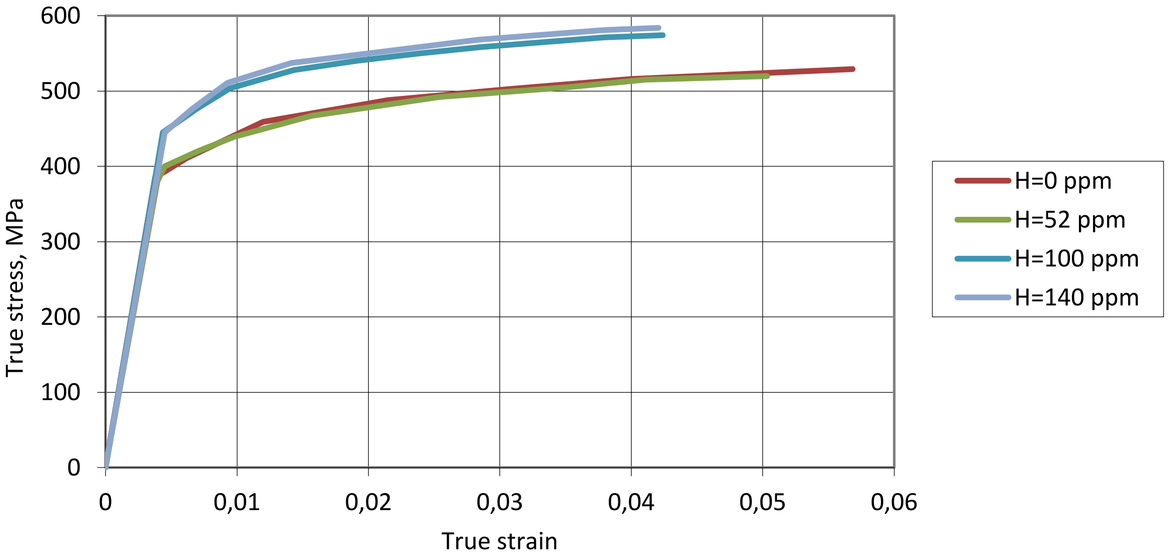

Fig. 1. True stress-strain curves of Zr-2.5Nb alloy with and without hydrogen

2.3. Finite element model

Finite element model of compact tension (C(T)) specimen was prepared for modelling of J-integral. The finite element model is shown in Fig. 2. As the C(T) specimen geometry, loading and boundary conditions are symmetric about XZ plane only half of the specimen was modelled. The cutting plane (red coloured surface) and applied symmetry boundary conditions are shown in Fig. 2 a). The small surface at the same plane was left unrestrained as that area represents front surface of crack. The load and other boundary conditions in the model were applied to the Reference Points (RP) placed at the center of the hole, i.e. on axis of cylindrical hole and in the middle of the thickness of specimen. The holes of C(T) specimen in experimental test is used for pin placement of testing equipment and application of loading. In the FE model RP point was connected with the half of cylindrical surface of the hole by coupling constrain. Constrain that connect RP point and cylindrical hole (red coloured surface) is presented in Fig. 2 b). A coupling constraint allows to constrain the motion of a surface to the motion of a single point. It means that forces, moments, displacements and rotations can be transferred from the point to the surface and vice versa.

The displacement of RP was restricted in two directions, i.e. along the X and Z axes, and rotation was restricted around Y axis. The displacement along Y axis was added to RP and used as load. To take into account large strains and displacements the option for nonlinear geometric effects, Nlgeom [11], was used. Nonlinear geometric effects are important when loads on a model result in large displacements.

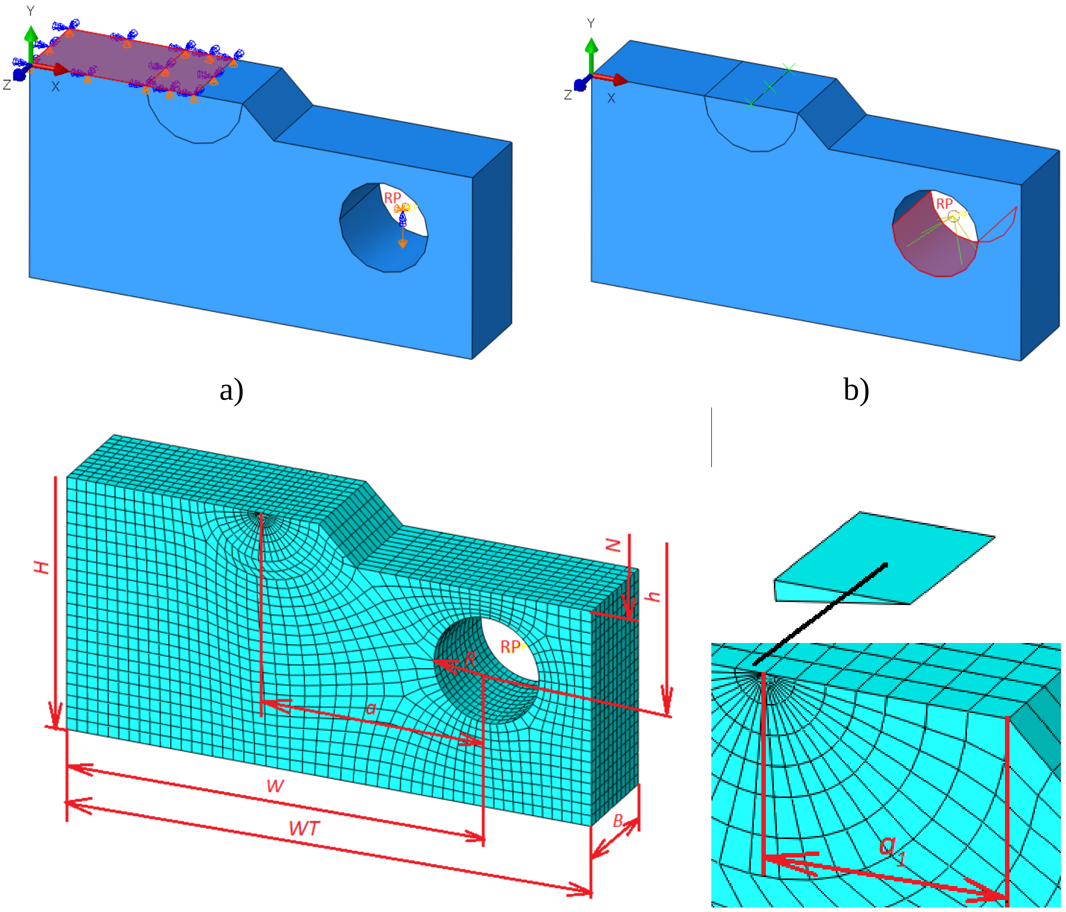

a) b)

c) d)

Fig. 2. Finite element model of C(T) specimen: a) boundary conditions; b) constrains; c) finite element mesh; d) enlarged view of mesh around crack tip

The dimensions of 3D FE model (see Fig. 2 c) and d)) were the same as dimension of C(T) specimen found in the experimental testing [12] where $W = 17$ mm, $B = 4.2$ mm, $a = 6.7$ mm, $a_1 = 2.2$ mm, $H = 20.4$ mm, $WT = 21.25$ mm, $R = 2.125$ mm, $h = 9.35$ mm and $N = 6.7$ mm. Whole 3D FE model was meshed with C3D20R elements [11]. These elements are quadratic brick shape and have 20 nodes. In general the size of the mesh was around 0.4 mm in all directions and the shape of FE were close to the cube. Only the volume around crack front was meshed differently. It is recommended [11] to perform the analysis using brick shape elements created in circular pattern around crack front. To create such mesh the nodes of one face of elements closest to the crack tip have to be collapsed to a single line. Collapsing the nodes of one face to the sing line creates the elements which still have 20 nodes but have shape of prism (see Fig. 2 d)).

The analysis was done by running non-linear analysis were elastic-plastic material properties were used (see Fig. 1). As calculation results the following parameters were received: reaction force at the RP, crack opening displacement, which was determined by tracking the displacement of point RP in Y direction and J-integral at crack tip.

3. RESULTS AND DISCUSSION

To check if load is transferred properly and boundary conditions are working correctly von Mises stress distribution in model without hydrogen is shown in Fig. 3. The figure show stress distribution at crack mouth opening displacement (CMOD) of 1 mm. As it was expected the highest stress values are around crack tip. Also figure shows the stress distribution inside pin hole, what means that displacement of RP point is transferred to the surface of the cylinder.

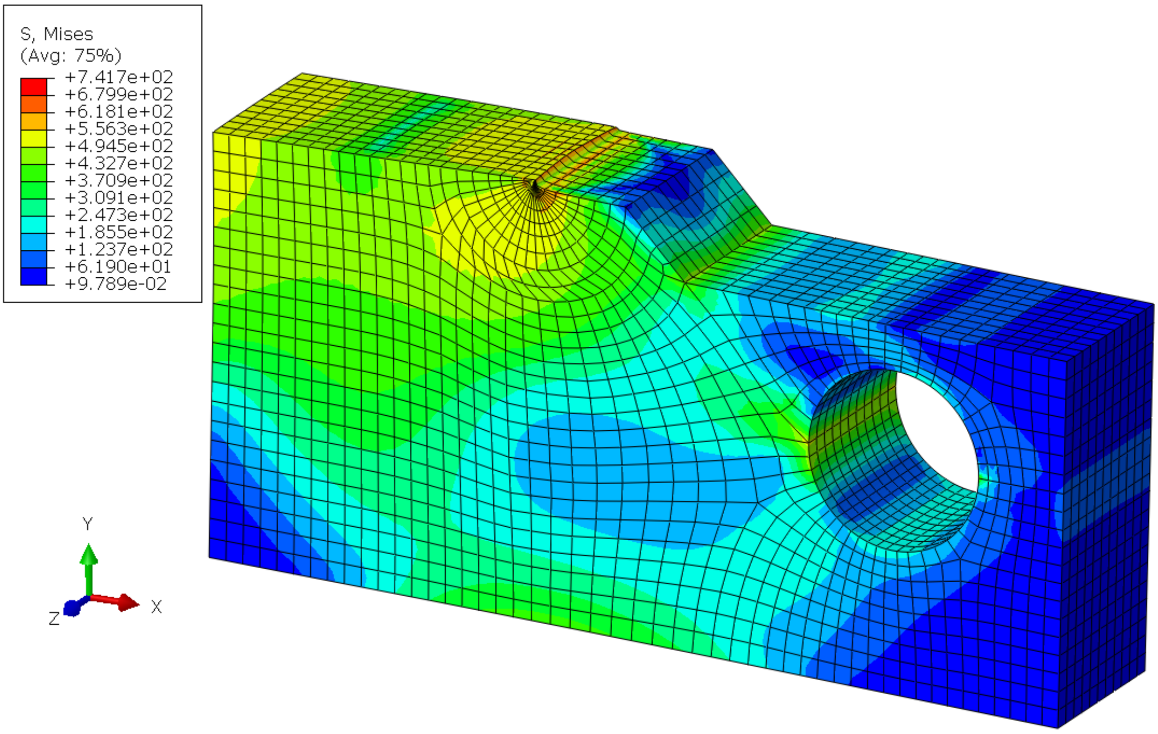

Fig. 3. Von Mises stress distribution in FE model without hydrogen

Simulation of CT specimen tension results are compared with experiment and presented in Fig. 4. Figure presents load versus crack mouth opening displacement curves for Zr-2.5Nb alloy without and with hydrogen up to 140 ppm. As figure shows simulation results have good coincidence with experimental for Zr alloy without hydrogen (Fig. 4, a)). However, simulation results for Zr alloy cases with hydrogen start to deviate from experimental data, especially from the peak of experimental curve. This deviation occurs due to the fact that the drop of the load appears due to the growth of the crack and the actual crack growth is not directly modelled in numerical simulation. Despite the fact that drop of load was not simulated accurately the peak value of load is close to experiment, where the highest deviation of load is up to 5 %.

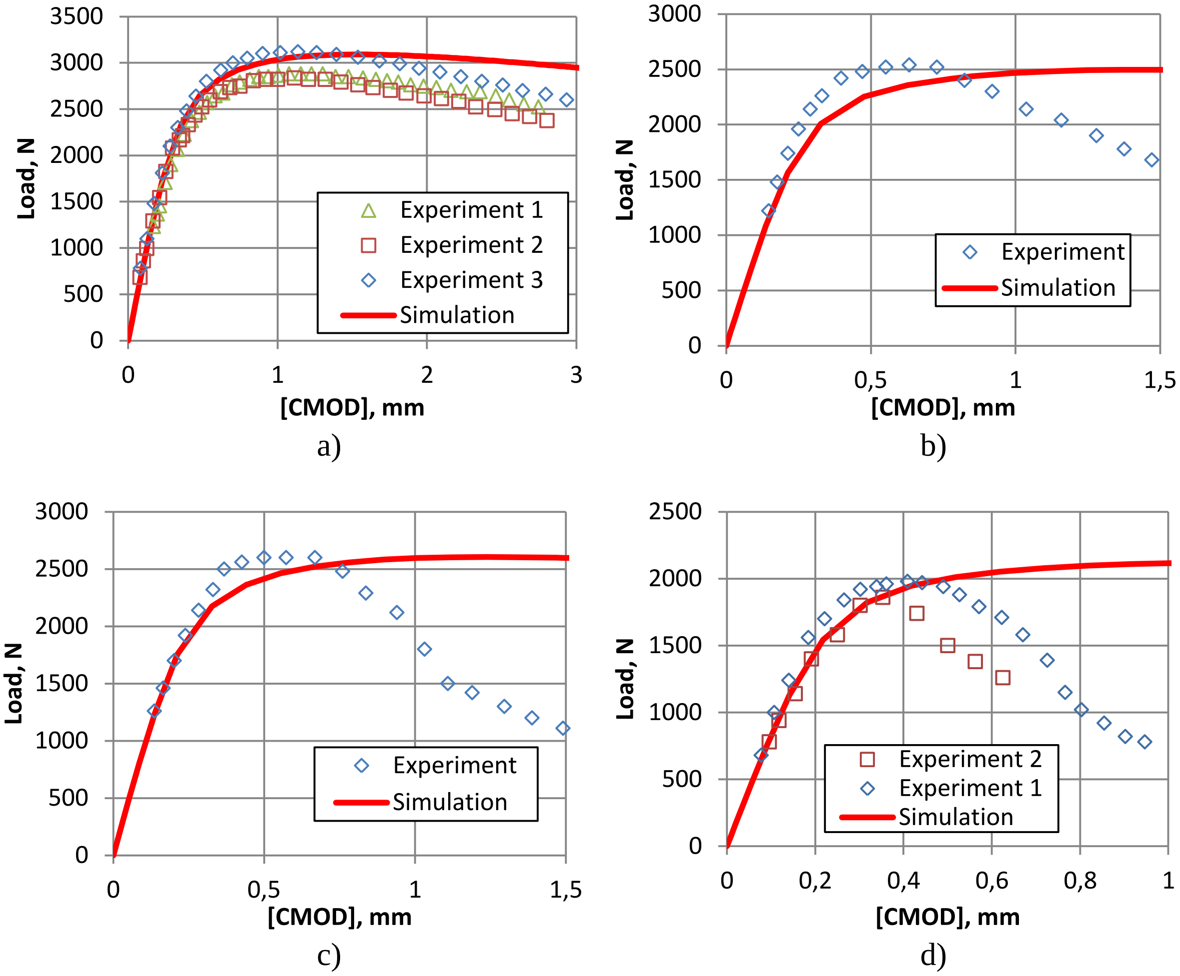

a) b) c) d)

Fig. 4. Simulation results of load vs CMOD compared with experiment at different hydrogen concentration: a) 0 ppm; b) 52 ppm; c) 100 ppm; d) 140 ppm

According to methodology presented in section 2.1 it is necessary to construct J-R curve for J-integral determination. For this reason the crack extension should be measured during the tension of CT specimen. However, for the FE models presented in the section 2.3 the direct crack extension is not simulated. Therefore neither direct crack length measurement nor the elastic compliance measurement method suggested in ASTM code can be used. Earlier research have shown that crack extension of numerically simulated tension of CT specimen can be calculated using quadratic polynomial expression derived from experimentally determined $EB_N[COD]/P$ versus $\Delta a/W$ curves. Three curves constructed from experimental test data and an averaged curve, which was used for determination of polynomial expression for crack length extension, are shown in Fig. 5. Quadratic polynomial expression determined from averaged curve is presented below:

$$\frac{EB_N[COD]}{P} = 15719\left(\frac{\Delta a}{w}\right)^2 + 2401.5\left(\frac{\Delta a}{w}\right) + 45.155\,. \tag{4}$$

The same expression (4) was used for all numerical simulation cases.

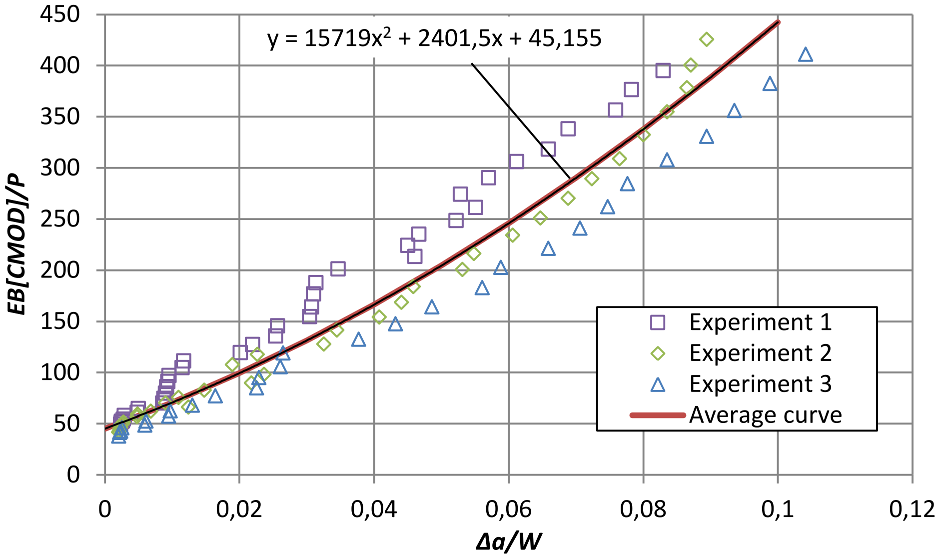

Fig. 5. *EB[COD]/P* versus *Δa/W*

Numerically calculated J-R curve for Zr alloy without hydrogen and comparison with experimental results [12] is shown in Fig. 6. Simulated J-R curve lies between experimental points up to crack extension Δa = 1.2 mm what shows good coincidence with experiment. According to methodology described in section 2.1 J-integral value J_{IC} is found at the cross section of 0.2 mm offset line and J-R curve. For the Zr-2.5Nb alloy without hydrogen numerically determined J_{IC} = 104 kN/m.

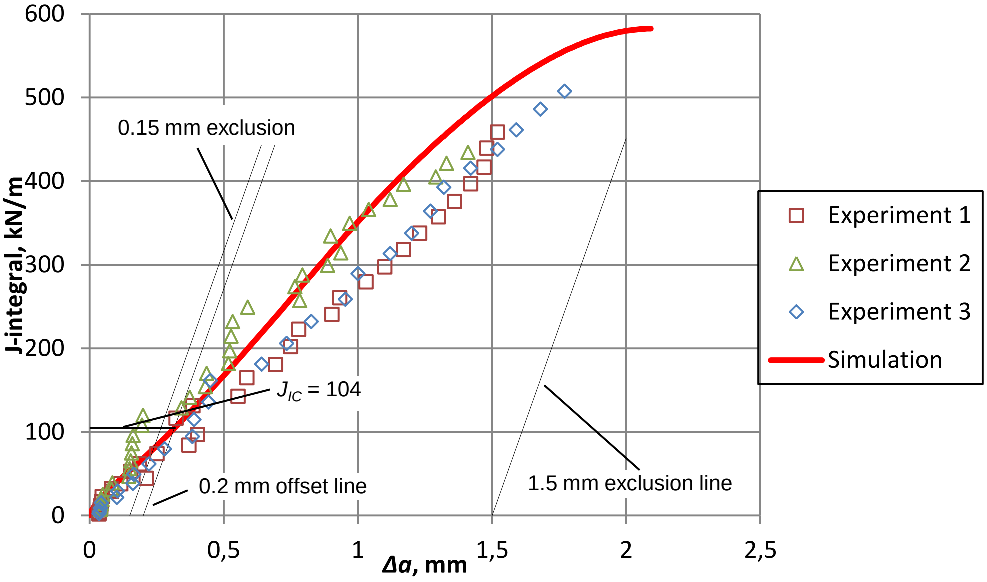

Fig. 6. Simulation results of J-R curve comparison with experiment on specimen without hydrogen

Simulation results of hydrogen concentration influence on critical J-integral value are presented in Fig. 7. This figure also shows experimental results [12]. According to the figure hydrogen has a significant influence on critical J-integral value. Increased hydrogen concentration from 0 ppm up to 140 mm makes the critical J-integral to decrease by 68% (from 104 kN/m to 33 kN/m) determined numerically. Found experimental results show critical J-integral decrease by 84% (from 95 kN/m to 15 kN/m).

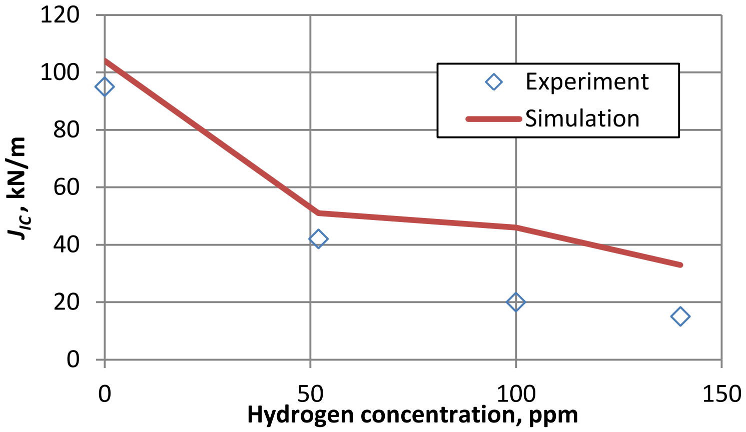

Fig. 7. Simulation and experiment results of J_{IC} vs hydrogen concentration

4. CONCLUSIONS

The numerical investigations of the Compact Tension (CT) specimen were carried out for the estimation of J-R curve for the Zr-2.5Nb. Critical J-integral values have been determined for specimen with different hydrogen concentrations. For this purpose finite element method was used. The values of J-integral were determined using finite element analysis simulating the experiment according to instructions described in ASTM E1820 standard. The numerical investigation results have been compared with the experimental test.

For crack extension calculation of CT specimen of Zr-2.5Nb was done by suggested quadratic polynomial expression.

Current research has showed that suggested numerical method for J-integral determination can be used to predict J_{IC} for Zr alloy with and without hydrogen. However, J-integral prediction for Zr alloy with higher hydrogen concentration has to be improved. It can be achieved by conducting higher number of experimental tests of mechanical properties and J-integral experiments of Zr-2.5Nb alloy with and without hydrogen.

REFERENCES

1. COLEMAN, C. E., HARDIE, D. The hydrogen embrittlement of α-zirconium – A review. *Journal of the Less-Common Metals*. 1966, Vol. 11, p. 168.
2. KURODA, M., YAMANAKA, S., SETOYAMA, D., UNO, M., TAKEDA, K., ANADA, H., NAGASE, F., UETSUKA, H. Tensile test of hydrided Zircaloy. *Journal of Alloys and Compounds*. 2002, Vol. 330, p. 404-407.
3. BERTOLINO, G., MEYER, G., PERREZ IPINA, J. Mechanical Properties at Room Temperature in ZRY-4 by Hydro-gen Brittleness. *Materials Research*, 2002, Vol. 5, No. 2, p. 125-129.
4. BIND, A. K., SUNIL, S., SINGH, R. N. Effect of hydrogen isotope content on tensile flow behavior of Zr-2.5Nb pressure tube material between 25 and 300 °C. *Journal of Nuclear Materials*, 2016, Vol. 476, p. 5-12.
5. ANDERSEN, T. L. *Fracture Mechanics. Fundamentals and Applications*. Boca Raton, Ann Arbor, Boston: CRC Press Inc, 1991. 793 p. ISBN 0-8493-4277-5.
6. ZARE, A., KOSARI, E. S. M., ASADI, I., BIGHAM, A., BIGHAM, Y. Finite Element Method Analysis of Stress Intensity Factor in Different Edge Crack Positions, and Predicting their Correlation using Neural Network method. *Research Journal of Recent Sciences*, 2014, Vol. 3(2), pp. 69-73.

7. LIKEB, A., GUBELJAK, N., MATVIENKO, Y. Stress Intensity Factor and Limit Load Solutions for New Pipe-Ring Specimen with Axial Cracks. *Procedia Material Science*, 2014, Vol. 3, pp. 1941-1946.
8. JUN-YOUNG, J., YUN-JAE, K., SA-YONG, L., JIN-WEON, K. Extracting ductile fracture toughness from small punch test data using numerical modeling. *International Journal of Pressure Vessels and Piping*, 2016, pp. 1-16.
9. MAHLER, M., AKTAA, J. Approach for J-R curve determination based on sub-size specimens using a triaxiality dependent cohesive zone model on a (ferritic–martensitic) steel. *Engineering Fracture Mechanics*, 2015, Vol. 144, pp. 222-237.
10. ASTM E1820-15a. Standard Test Method for Measurement of Fracture Toughness. ASTM International, West Conshohocken, PA, 2014. www.astm.org
11. ABAQUS/Standard User’s Manual, Version 6.11.
12. DAUNYS, M., DUNDULIS, R., GRYBĖNAS, A., KRASAUSKAS, P. Hydrogen influence on mechanical and fracture mechanics characteristics of zirconium Zr-2.5Nb alloy at ambient and elevated temperatures. *Nuclear engineering and design*, 2008, Vol. 238, Iss. 10, pp. 2536-2545.
13. PAN, Z. L., WANG, N., HE, Z. Measurements of elastic modulus in Zr alloys for CANDU applications. *11th International Conference on CANDU Fuel*, Niagara Falls, Ontario, Canada, 2010 October 17-20.

SELECTION OF THE OPTIMAL GEOMETRICAL PARAMETERS OF VENTILATION TRACT OF STORAGE CONTAINER WITH SPENT NUCLEAR FUEL

D. Lunov, S. Alyokhina
V. N. Karazin Kharkiv National University
Svobody Sq. 4, UA-61022 Kharkiv – Ukraine
Email: d.lunev21@gmail.com

ABSTRACT

Safe thermal storage conditions for spent fuel assemblies (SFA) are a key safety issue for the storage facility. The numerical estimation of the SFA thermal state was carried out using the methodology of the conjugate heat transfer problems solving.

Each container includes a hermetic storage cask, which contains 24 WWER-1000 SFA. Cooling occurs due to the movement of air through the ventilation ducts. The speed of the cooling air and the intensity of heat transfer depend on the hydraulic resistance of the ventilation ducts. Thus, a change in the geometric characteristics of the ventilation ducts of the storage container leads to a change in their hydraulic resistance and, as a result, a change in the thermal conditions of the cask with SFA.

The choice of optimal values of the geometric characteristics of the ventilation system of the spent fuel storage container was carried out according to two criteria: the maximum temperature of the concrete and the maximum temperature in the storage cask.

Analysis of the results showed that it is possible to reduce the temperature level in the container with spent fuel assemblies by reducing the geometric characteristics of the ventilation ducts. However, the decision must be made with taking into account the container loading technology.

Keywords: SNF; thermal simulation; conjugate heat transfer problems; dry storage; WWER-1000 SFA

1. INTRODUCTION

The nuclear industry is one of the main sources of electricity. In 2017, about 50 percent of all electricity received in Ukraine is produced at nuclear power plants [1]. But while focusing on atomic energy, we are faced with one of the main problems in the future – spent nuclear fuel (SNF). Currently, the problem of SNF is temporary solved by long-term storage in dry-type containers. The question of improving storage safety is a major one.

After 3-4 years of working in reactor, the fuel assembly is removed and placed into spent nuclear fuel pools at least for 5 years. During this time, the decay heat of each assembly is reduced. Since 2001 in Ukraine at the Zaporizhzhya Nuclear Power Plant spent nuclear assemblies has been stored in dry-type containers. The storage area is designed for 380 containers, each with 24 assemblies. Therefore, the storage of spent fuel in dry-type containers remains relevant for a long time.

The safety of spend nuclear fuel storage includes radiation and thermal investigations. In this paper, only thermal part was considered. Improving thermal conditions is the main task of thermal safety. It could be done through changing the geometrical parameters of the storage containers. These investigations were not done under containers design and the search of ways how to improve thermal state of containers is a purpose of this work.

2. GEOMETRY OF CASKS

In Ukraine SNF of six reactor WWER-1000 of Zaporizhzhya NPP is placed in a sealed metal cask filled with inert gas, which is placed in a ventilated concrete container. The storage cask is cooled by air convection due to natural traction in the vent ducts of the container (Fig. 1).

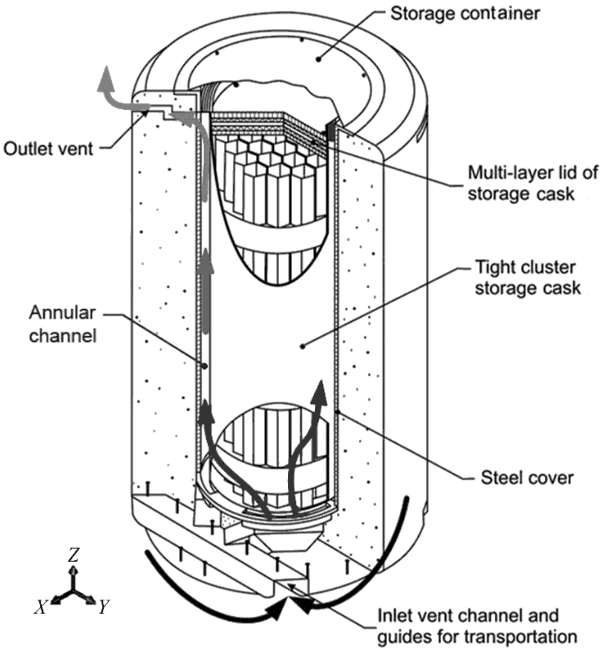

Fig. 1. Structure of storage cask

Inside the cask are 24 assemblies (Fig. 2) (the heat generation of each fuel assembly should not be more than 1 kW) in individual guide tubes. Each spent fuel assembly (SFA) consists of 3 parts: head, fuel rods, tail. Heat is released in the middle part.

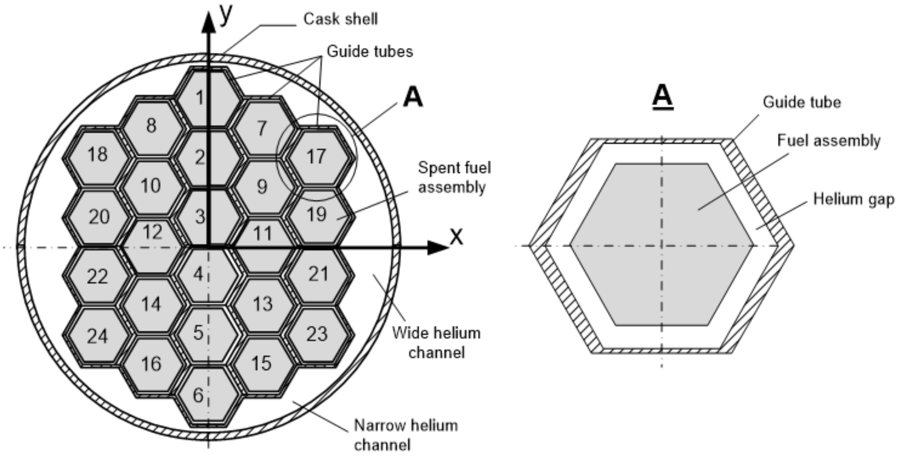

Fig. 2. Structure of storage cask (horizontal section)

3. WORK DESCRIPTION

This work was done to improve the thermal conditions of spent nuclear fuel in the dry storage of spent fuel at Zaporizhzhya NPP by changing the geometric characteristics of the storage container.

The constructive parameters of the container are one of the factors influencing the thermal state of containers with Spent Nuclear Fuel (SNF). The geometric dimensions of the storage cask cannot be changed because it is determined by the layout of the Spent Fuel Assembly (SFA). So, in order to reduce the temperature in the storage container, it is necessary to find optimal dimensions of the geometric parameters of the ventilate ducts.

The task of determining the geometric dimensions of the ducts of the storage container, based on the best cooling conditions of the SFA. The minimum temperature in the storage cask was chosen as a criterion of the optimal condition.

The ventilating tract of the container with SNF include the input ducts, the circular channel and the z-shaped output ducts. The lower input ducts have a dual purpose: the supply of ventilation air and the guides to transport the container to the storage platform. The change in the geometric shape and size of the input ducts cannot be carried out because the dimensions of the guides must correspond to the size of the transporter lifts. Thus, the parameters that may vary are the diameter of the circular channel (r), which is determined by the inner diameter of the sidewall of the container, and the height of the z-shaped output ducts (h) (Fig. 3). The task of minimizing the temperature in the SNF storage cask is considered at the beginning of storage. Weather factors such as wind were not taken into account.

Earlier calculations were carried out for a simplified two-dimensional model. The lower ducts geometry was not taken into account [2].

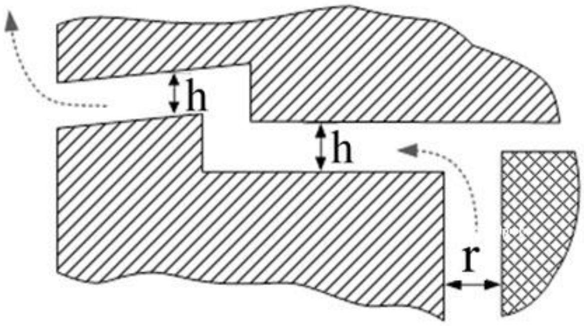

Fig. 3. Parameters of the container that were changing

4. METHODOLOGY

Due to specific of the investigated object, only numerical simulation was carried out. The effective methodology in this situation is conjugate heat transfer problems, which allow modelling mutual heat transfer in solid and fluid media. Mathematical model includes [3]:

- continuity equation;
- equation of motion of viscous gas;
- energy equation for fluids;
- heat conduction equation for solids;
- equations of k-ε turbulent flow model;
- ideal gas law for calculation of cooling air density;
- equations for calculating thermal properties of helium as a function of temperature;
- equations which describe the radiative heat transfer.

Equations are solved by standard program complexes, which are used methodology based on finite-elements methods.

Two models were used in the simulation. In the first model, the cask was a solid object with equivalent thermal properties. The power of the SFA is uniformly distributed inside cask. With this model, the boundary conditions (the temperature of the ventilation air and the heat transfer coefficient at the cask surface) were obtained. In the second model, a cask with complex geometry inside (assemblies were simplified as a solid body) and with boundary conditions, which were found in the first model.

The calculations could be done by any commercial or open-source CFD-complexes like OpenFOAM, ANSYS CFx, PHOENICS, STAR-CD etc.) but it usage must be validated and results are verified.

5. RESULTS AND DISCUSSIONS

Let's consider the influence of each of the geometric parameters on the level of maximum temperatures in a cask with spent fuel. At a fixed height z-shaped output duct h = 70 mm, the values of the maximum temperature in the cask with SNF are shown in Table. 1.

Table 1. Maximum SNF temperatures inside storage cask depending on the width of the circular channel (h is constant, h = 70 mm)

r, mm	100	90	80	70	60	55	50	45	40	30	25	20	15
Tmax, °C	347,8	344	339,8	335,0	331,7	326,7	326,7	323,9	320,6	314,0	313,0	320,0	348,7

As a result of minimization, the value of the optimal width of the circular channel h = 25.378 mm was obtained. The graphic dependence of the maximum temperature on the width of the ventilation channel r is shown in Fig. 4.

Data are approximated by the dependence:

$$T_{\max} = 415{,}998 - 11416{,}127 / h + 614198{,}674 / h^2 - 18099086{,}17/h^3 + \\ + 263897884{,}6 / h^4 - 1432261435 / h^5. \qquad (1)$$

With a decrease of the width of the circular channel to 25 mm the maximum temperature of the cask with SNF decrease to 313 °C, with further decrease of r the level of maximum temperature increases, which is due to a significant increase in hydraulic resistance due to the reduction of the passage of the channel.

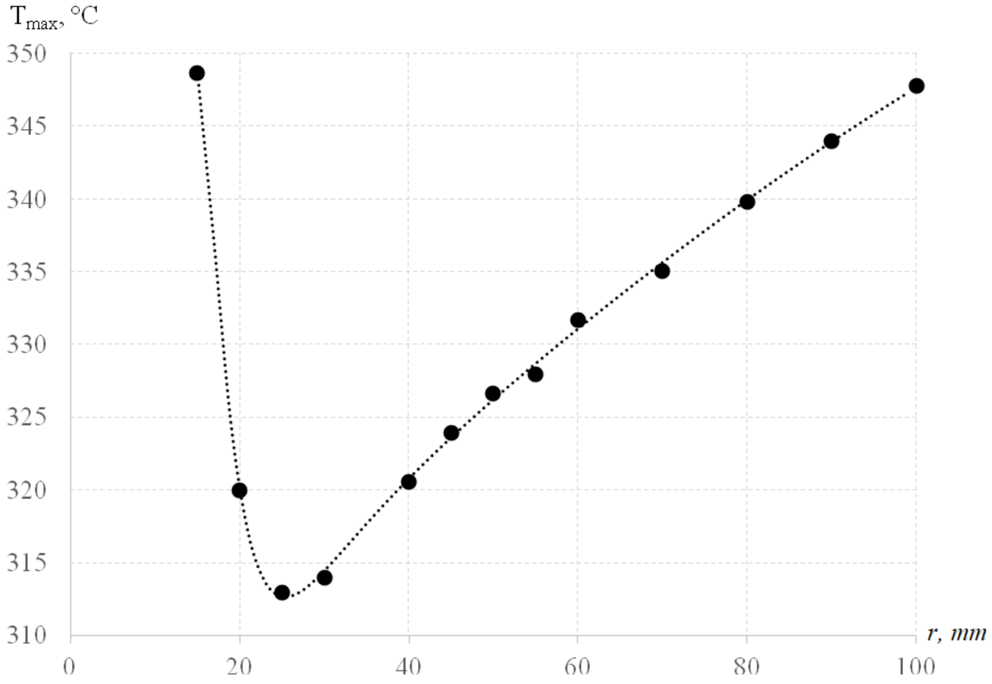

Fig. 4. Dependence of maximum temperature in storage cask from the width of the circular canal

When a value r = 70 mm fixed, the values of the maximum temperature in the cask with SNF are shown in Table. 2.

Table 2. Maximum SNF temperatures depending on the height of the z-shaped output ducts (r is constant, r = 70 mm)

h, mm	110	100	90	80	70	60	50
Tmax, °C	331,6	332,4	333,3	334,8	335,1	337,6	340,9

Data are approximated by the dependence:

$$T_{\max} = 330{,}859 - 0{,}011779 \cdot r + 26509{,}55892/r^2 \tag{2}$$

The graphic dependence of the maximum temperature on the height of the z-shaped output canal shown in Fig. 5.

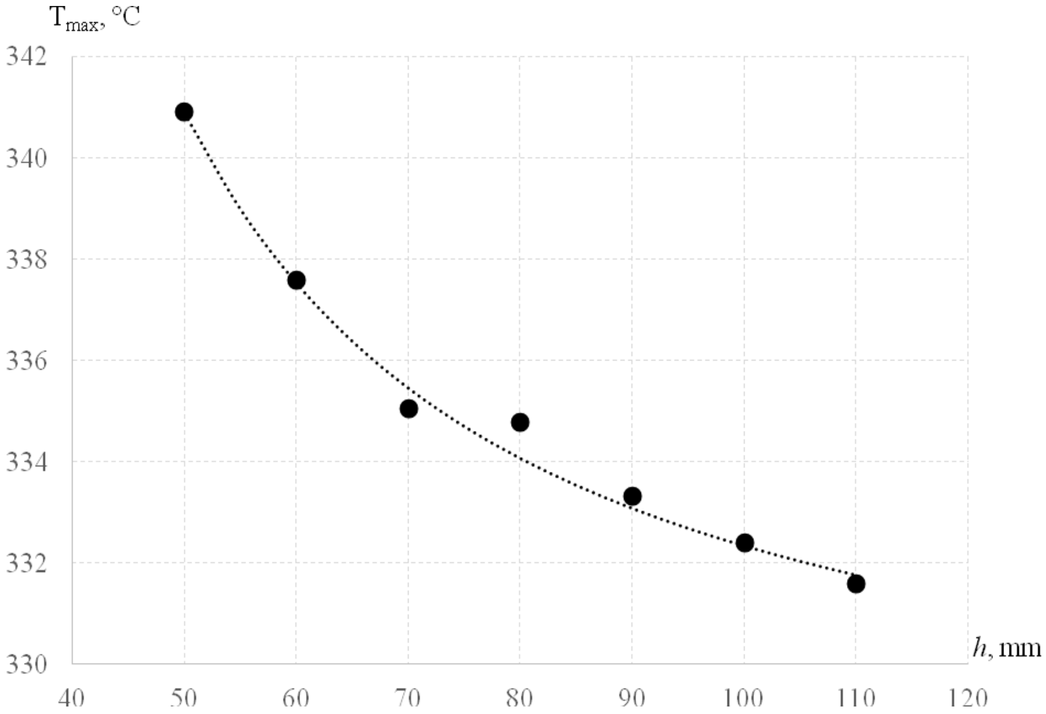

Fig. 5. Dependence of the maximum temperature of spent fuel from the height of the z-shaped output channel

Follows from the figure that an increase in the height of the output ducts leads to a decrease in temperature in the storage cask, because the hydraulic resistance decreases and the ventilation air leaves the container more freely.

6. CONCLUSION

So, based on the data and the approximation dependencies, to reduce the temperature level in the cask of spent nuclear fuel, it is advisable to reduce the width of the circular ventilation channel and increase the height of the output ducts. However, it should be noted that the final decision on the values of the parameters r and h must be made taking into account the limitations caused by technological processes. For example, with a significant reduction in the size of the ventilation ducts, difficulties may arise when placing the cask in a concrete container and a significant increase in the height of the output ducts, the strength requirements of the container may be violated.

REFERENCES

1. The results of performance of the ENERGOATOM in 2018 <http://energoatom.com.ua/ru/press_centr-19/infografika-28/p/rezultaty_deatelnosti_energoatoma_v_2018_godu-44708>.
2. Алёхина С. В. Оптимизация ширины вентиляционного тракта контейнера с отработанным ядерным топливом / С. В. Алёхина, В. Н. Голощапов, А. О. Костиков // Проблемы машиностроения – 2011. Т. 14, № 6. – С. 23–29.
3. Alyokhina S. Simulation of thermal state of containers with spent nuclear fuel: multistage approach / S. Alyokhina, V. Goloshchapov, A. Kostikov, Yu. Matsevity // International Journal of Energy Research. – 2015. – V. 39, Iss. 14, Nov. – P. 1917–1924, DOI: 10.1002/er.3387.

CYSENI 2019, May 23-24, Kaunas, Lithuania
ISSN 1822-7554, www.cyseni.com

THE MOLECULAR DYNAMICS STUDYON WATER PROPERTIES AT LIQUID-VAPOUR EQUILIBRIUM

G. Skarbalius, A. Džiugys
Lithuanian Energy Institute
Breslaujos str. 3, 44403 Kaunas – Lithuania
Email: gediminas.skarbalius@ktu.edu

ABSTRACT

In this paper, we present the results of molecular dynamics simulations of water liquid-vapour phase equilibrium at four different temperatures 373 K, 423 K, 473 K and 523 K using the flexible fixed-point charge molecular model, which includes the OH bond stretching and HOH angle vibrations. It was found that the model slightly overestimates the liquid density and underestimates the vapour density and also contradicts the results obtained by model developers. The interphase thickness increases as the temperature rises and is a linear function of temperature at given temperature range. The examination of liquid, interphase and vapour temperatures at 423 K case showed that the vapour temperature is 7 K higher than in liquid temperature and there exists an interphase temperature jump. Furthermore, the simulation results show that the translational velocity distribution of molecules leaving the liquid surface and condensing molecules agree with the Maxwellian velocity distribution.

Keywords: molecular dynamics simulation, liquid-vapour equilibrium, interphase thickness, velocity distribution function

1. INTRODUCTION

The evaporation and condensation of water are non-equilibrium processes in which molecules cross the interphase region from liquid to gas phase and vice versa. The rates of water evaporation and condensation have an influence to the rate of natural water cycle in the nature and evaluation of evaporation rate has great importance in many fields of science and engineering, such as physics, chemistry, biology, climatology, astronomy, hydrology and nanotechnology just to name a few [1], [2], [3]. Therefore, it is essential to develop accurate and efficient models for evaluating evaporation and condensation rates.

The widely used relation for evaluating the evaporation rate of fluids is the Hertz-Knudsen (HK) relation in which the phase change rate is proportional to the difference in vapour pressure and vapour saturation pressure. The numerical values obtained from the HK relation is greater than the experimentally determined phase change rates for many fluids and, therefore, the concept of the empirical evaporation coefficient was introduced to account for the discrepancies. However, the evaporation coefficients do not entirely solve the problem because the reported values of the coefficients for many fluids are inconsistent with each other, especially for the case of water where evaporation coefficient has been reported to vary by three orders of magnitude from 0.001 to 1 [4].

The reasons for the large scattering of the values of evaporation coefficient can be attributed to the uncertainty of the available experimental method. Firstly, it is impossible to experimentally measure velocity distributions of evaporating and condensing molecules. Therefore, in order to apply HK relation, researchers assume that the evaporating and condensing molecules are distributed by the Maxwellian distribution during the evaporation, whereas the evaporation is a non-equilibrium process and the Maxwellian distribution holds only for equilibrium states [5]. Secondly, there exists few molecular diameters thick temperature and pressure discontinuities in the liquid-vapour interphase layers of the evaporating liquid which are challenging to measure experimentally [4], [6]. Therefore, the boundary conditions for HK relation obtained by measuring the temperature of liquid and vapour phases might not correspond to the real boundary conditions in the interphase layers at molecular scale.

The method which provides possibility to investigate phase change properties of water and other fluids at liquid-vapour phase equilibria conditions without any experimental uncertainties is molecular dynamics (MD) simulation. In the work [7], authors investigated water condensation using SPC/E water model and showed that just like in the case of monoatomic molecules the condensation coefficient of polyatomic molecules can be expressed as a function of the translational energy of molecular motion in surface normal direction and the liquid surface temperature. Evaporation coefficient of water was investigated via TIP4P molecular model in the work [6]. Authors derived a relation to evaluate the evaporation coefficient by combining Hertz-Knudsen-Schrage relation and the molecular dynamics simulations. However, authors had to assume that evaporation coefficient is equal to the condensation coefficient. Furthermore, the derived relation suggests that the evaporation coefficient might be dependent on the dimensions of the simulation domain, but the system size sensitivity analysis was not performed. In their work [8], authors presented MD study of liquid-vapour equilibrium and evaporation into the virtual vacuum study for polyatomic molecules, including water. From their results, they concluded that the evaporation coefficient of water is a function of bulk liquid temperature, which decreases with the increase of the temperature. They also obtained the distribution functions of translational and rotational velocities and internal energies for water molecules evaporating into virtual vacuum which agree with the Maxwellian distribution.

In the reviewed and other available papers concerning molecular dynamics simulations of water, the rigid models are used with fixed lengths of OH bonds. The rigid molecular models are designed to accurately reproduce bulk liquid and liquid-vapour coexisting properties of water at ambient temperatures. However, the evaluation of the flexibility of the molecule might be important for predicting the behaviour of evaporation, condensation and other processes of water, especially, at higher temperatures. The reason for this is that the real molecules have more intramolecular degrees of freedom than the rigid models, which can be exited, namely the vibrational motion of molecule. Thus, the behaviour of the processes including molecular collisions changes as the molecular collisions are inelastic in terms of the energy of translational and rotational motion. This point can be illustrated by the work [9], in which the authors investigated the dynamics of water cluster formation via molecular collisions using both rigid and flexible models. They showed that additional flexibility has the impact on process dynamics as the lifetime of the cluster increases due to the stabilization effect, which is caused by the energy transfer between translational and vibrational motion.

The aim of the present work was to test the flexible water molecular model with MD simulations at liquid-vapour equilibrium in temperature range from 373 K to 523 K and measure some of the water properties. Firstly, the water density profiles are studied by dividing the simulation domain into thin layers and counting densities of each layer. These profiles allow us to evaluate the interphase thickness at various temperatures. Then, the temperature of liquid and vapour phases was examined. Finally, the velocity distribution functions were calculated by measuring the velocities of all molecules that leave the liquid surface and impinge on it (condense).

2. SIMULATION METHOD

The MD method is based on solving the classical equations of motion for every atom in the modelling system. The Newtonian equations of motion of the system atoms are

$$m_i \frac{d^2}{dt^2}\boldsymbol{r}_i(t) = \sum_{j=1,j\neq i}^{N} -\frac{d}{dr}U\left(r_{ij}\right)\frac{r_{ij}}{r_{ij}} \; , \; i = \overline{1;N} \; , \tag{1}$$

where m_i and $\boldsymbol{r}_i$ are the mass and the position vector of the i-th atom, U is the potential between the i-th and j-th atoms and $\boldsymbol{r}_{ij} = \boldsymbol{r}_i - \boldsymbol{r}_j$ is the vector connecting the centre of i-th atom to centre of the j-th atom.

The molecular model of water in this work is flexible fixed-point charge (flex-FPC) model, which was developed by [10]. In this model, the total potential of the system is given as the sum of the intermolecular and the intramolecular potentials:

$$U_{system} = U_{intermolecular} + U_{intramolecular}\ . \tag{2}$$

The intermolecular pair-wise potential of two atoms is described as the sum of the Lennard-Jones (LJ) potential and the Coulombic interaction potential:

$$U_{intermolecular}(r_{ij}) = 4\varepsilon_{ij}\left[\left(\frac{\sigma_{ij}}{r_{ij}}\right)^{12} - \left(\frac{\sigma_{ij}}{r_{ij}}\right)^{6}\right] + \frac{q_i q_j}{4\pi\varepsilon_0 r_{ij}}\,, \tag{3}$$

ε_{ij}, σ_{ij}, $q_{i,j}$ and ε_0 are the depth of the LJ potential well, σ_{ij} is the distance at which the strong repulsion force starts to act on the atoms (radius of the atom), q_i is the charge of the atom and ε_0 is the vacuum permeability. The combination rule to obtain the LJ parameters for unlike interaction is the Lorenz-Berthelot (LB) rule:

$$\sigma_{ij} = \frac{\sigma_i + \sigma_j}{2}\,. \tag{4}$$

$$\varepsilon_{ij} = \sqrt{\varepsilon_i \varepsilon_j}\,. \tag{5}$$

The intramolecular term of the potential consists of harmonic OH bond and HOH angle vibrations as given in the Eq. (6:

$$U_{inramolecular}(r_{ij}) = \frac{1}{2}K_r(r - r_0)^2 + \frac{1}{2}K_\theta(\theta - \theta_0)^2\,, \tag{6}$$

where K_r is the stiffness of the OH bond, K_θ is the stiffness of the HOH angle vibrations, r_0 is the distance at which the OH bond is at equilibrium, θ_0 is the angle at which the HOH angle is at equilibrium. The parameter values of the model are given in Table 1. The cut-of distance for both short range and long-range interactions used in the simulations was 11 Å.

Table 1. Flex-FPC molecular model parameter values

r_{OH}, Å	0.9611	$K_r, kJ/(mol\cdot \text{Å}^2)$	1480
θ_{HOH}, º	109.4712	$\theta_r, kJ/(mol\cdot rad^2)$	353
q_H, e	0.4238	$\varepsilon_H, kJ/mol$	0.0324
q_O, e	-0.8476	$\varepsilon_O, kJ/mol$	0.6284
σ_O, Å	3.1169	σ_H, Å	0.98

In order to form sufficient regions for both the liquid and the vapour phases, the simulation geometry used for this was the 90 × 93 × 200 Å box with periodic with boundary condition applied in all axis. The liquid water film 90 × 93 × 45 Å made from 12000 molecules was placed in the middle of z axis of the simulation box. The initial positions of the molecules were chosen accordingly to the fcc lattice. The visualisation of the box and the initial positions of the molecules is given in Fig. 1. The initial velocities of atoms were given with the normal distribution to match the simulation temperatures: 373 K, 423 K, 473 K and 523 K. The equations of motion given by Eq. (1), were solved using Verlet-velocity integration algorithm with timestep value $\Delta t = 0.35 \cdot 10^{-15}$ s. All simulations were carried out using classical molecular dynamics simulation code LAMMPS.

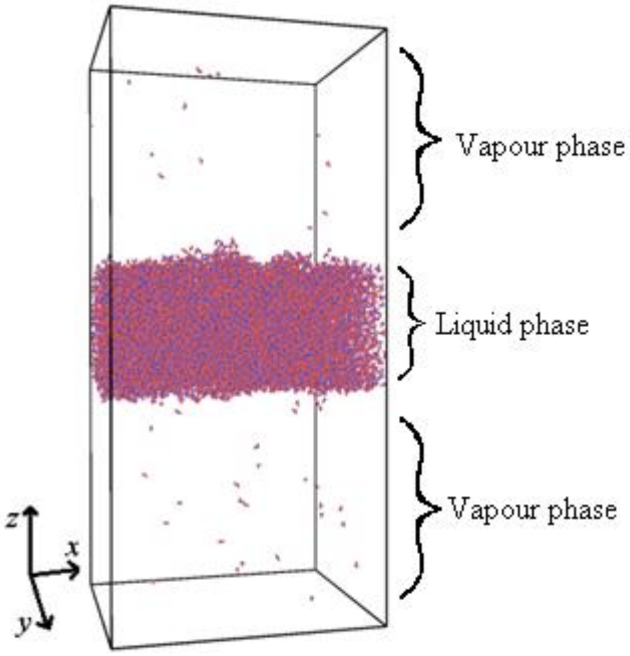

Fig. 1. Water system visualization with marked liquid and vapour regions

After the initialization of the system parameters, the equilibration runs were performed in canonical (*NVT*) ensemble for about 100 ps (290000 timesteps) with temperature control using the Nosé–Hoover thermostat. Temperature control was done every 100 timesteps. Then, system was set to run for another 100 ps in the microcanonical (*NVE*) ensemble. During the first 200 ps, the system reaches liquid-vapour dynamic equilibrium state at which the vapour phase is fully saturated, and the evaporation rate is same as the condensation rate. Finally, the sampling run was performed in the microcanonical (*NVE*) ensemble for about 1.4 ns (4000000 timesteps) during which the information of the atoms in the system is sampled for the analysis. The 2000 data sets were sampled as sampling was done every 2000 timesteps.

3. RESULSTS AND DISCUSION

In order to obtain information about the thickness of the interphase layers and system density distributions, the density profiles along the z axis was acquired from the modelling data. The density profiles for each data set were calculated by dividing the simulation box into layers (the layer thickness is $\Delta z = 0.75$ Å) and counting the mass of atoms which are located within the layer at given time. Then, the layer densities were obtained by dividing the mass of atoms by the volume of the layer. Obtained 2000 profiles were averaged. Finally, calculated density profiles were averaged over 2000 datasets to reduce the density fluctuations occurring due to a finite size of modelling system. The density profiles at four different temperatures are given in Fig. 2. From here, we can see that there are three distinct regions in the system: the vapour phase region with the density of saturated vapour; the liquid phase region with the density of bulk liquid and the interphase region, where the density continuously decreases form the liquid phase density to the vapour phase density.

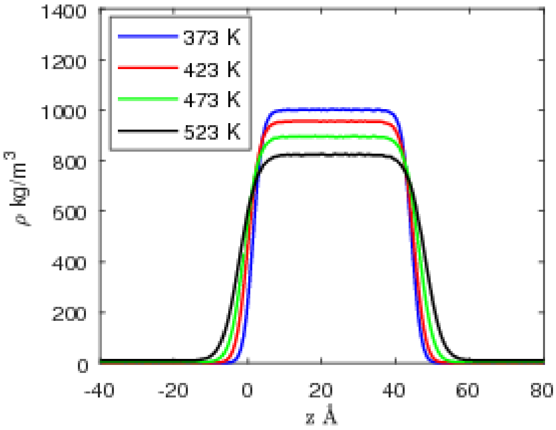

Fig. 2. Density profiles of the system at four different temperatures

As suggested in [8], the interphase region density can be accurately approximated using hyperbolic tangent function:

$$\rho(z) = \frac{1}{2}(\rho_v + \rho_l) + \frac{1}{2}(\rho_v - \rho_l)\tanh\left(\frac{z-z_0}{\delta}\right), \tag{7}$$

where ρ_l is the liquid phase density, ρ_v is the vapour phase density, z_0 is the middle point of the interphase and δ is the meassure of the interphase thickness. The example of density at the interphase region at 373 K with the fitted function is given in Fig. 3.

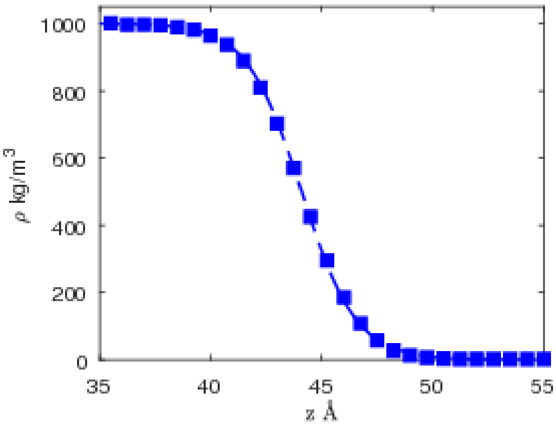

Fig. 3. The density at the interphase at 373K. Filled squares represent modelling results and the dotted line represent the fitting function given by the Eq. (7)

The “10-90” thickness of the interphase or the interphase thickness d is related to the measure of interphase thickness by the $d = 2.1972\delta$. We can observe from Fig. 4 that the interphase thickness varies from 5.38 Å to 9.57 Å and is the linear function of temperature in range from 373 K to 573 K. Furthermore, Fig. 4 shows that values of the interphase thickness obtained in the work [6] using the TIP4P molecular model agree with our calculations in temperature range from 423 K to 463 K. However, the interphase thickness obtained with the TIP4P model does not follow the linear trend obtained in this work at temperatures below 423 K as the values of the thickness are significantly lower than our results. The disagreement can be explained by different geometries of the molecular models as the angle HOH of the TIP4P model is 104 ° while equilibrium angle of the flex-FPC model is approx. 109 °.

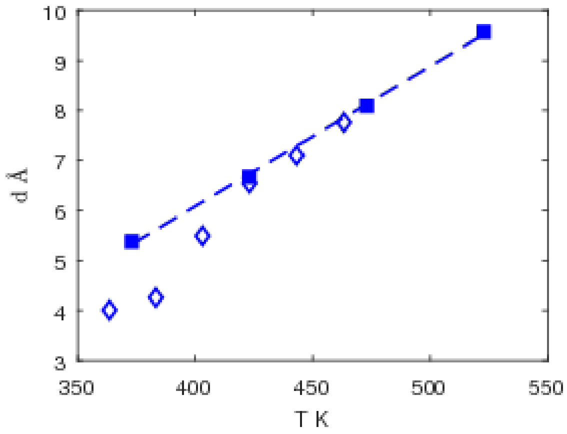

Fig. 4. The interphase thickness as a function of temperature. Filled squares represent present work results and empty diamonds represent TIP4P model results from [6]

The comparison of liquid and vapour phase densities obtained with different molecular models and experimental values are in Fig. 5. The value of liquid phase density was obtained by averaging profile density function values over liquid region. The same was done with the vapour density. The calculated densities follow the experimental, however, the liquid densities are overestimated, and the vapour densities are slightly lower. Furthermore, the densities obtained in [10] with the same molecular model as used in present work deviate from our results and give better agreement with the experimental data. The explanation for this can be the effect of finite size of the system and different density calculation methods as the authors used NVT-Gibbs ensemble Monte Carlo (GEMC) technique and the coupled-decoupled configurational-bias Monte Carlo (CBMC) algorithm with 350-450 molecules for the phase equilibrium simulations. The SPC/E molecular model shows also good agreement with the experiments while the density values obtained with TIP4P model are underestimated for liquid and overestimates vapour phases.

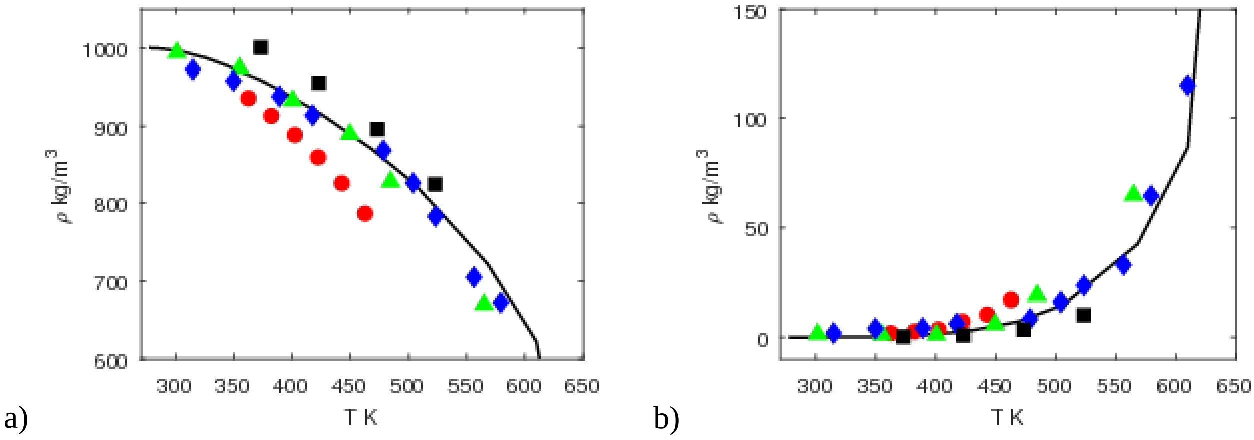

Fig. 5. The density as a function of temperature for: a) liquid phase; b) vapour phase. The solid line represent experimental values [11], the black squares represent present work results, green triangles represent SPC/E model results [12], blue diamonds represent results using same model as in the present work [10], red circles represent TIP4P model results [6]

The value of temperature is related with the kinetic energy of atoms as Eq. (8) suggests [13]:

$$T(t) \equiv \frac{1}{N_f k_B} \sum_{i=1}^{N} m_i v_i(t)^2 \,, \tag{8}$$

where N_f is the number of degrees of freedom ($N_f = 3N - 3$ for a system of N atoms with fixed total momentum), $k_B = 1.38 \cdot 10^{-23}\ J/K$ is the Boltzmann constant, m_i is the mass of the i-th atom and v_i is the velocity of the i-th atom. Then, the temperature of the process is obtained by averaging the temperature values over time of the process.

The time evolutions of temperature obtained in 423 K case by Eq. (8) for liquid, vapour and interphase regions are given Fig. 6. The more violent temperature fluctuations are observed in the vapour and the interphase regions as the number of atoms in those regions is significantly lower than in the liquid, namely, the vapour phase contains around 150 atoms (50 molecules) on average while liquid phase contains over 33000 atoms (11000 molecules) on average. Furthermore, the average liquid and interphase temperatures are the same as the simulation temperature (423 K) but the temperature value of the vapour phase is higher by 7 K. This indicates that temperature jump between liquid and vapour phases exits at the interphase. More information about temperature jump starting and ending points could be acquired from temperature profile along the z axis, however, it cannot be done from our simulation results as there are not enough molecules in vapour phase to evaluate temperature of each layer as in density calculations.

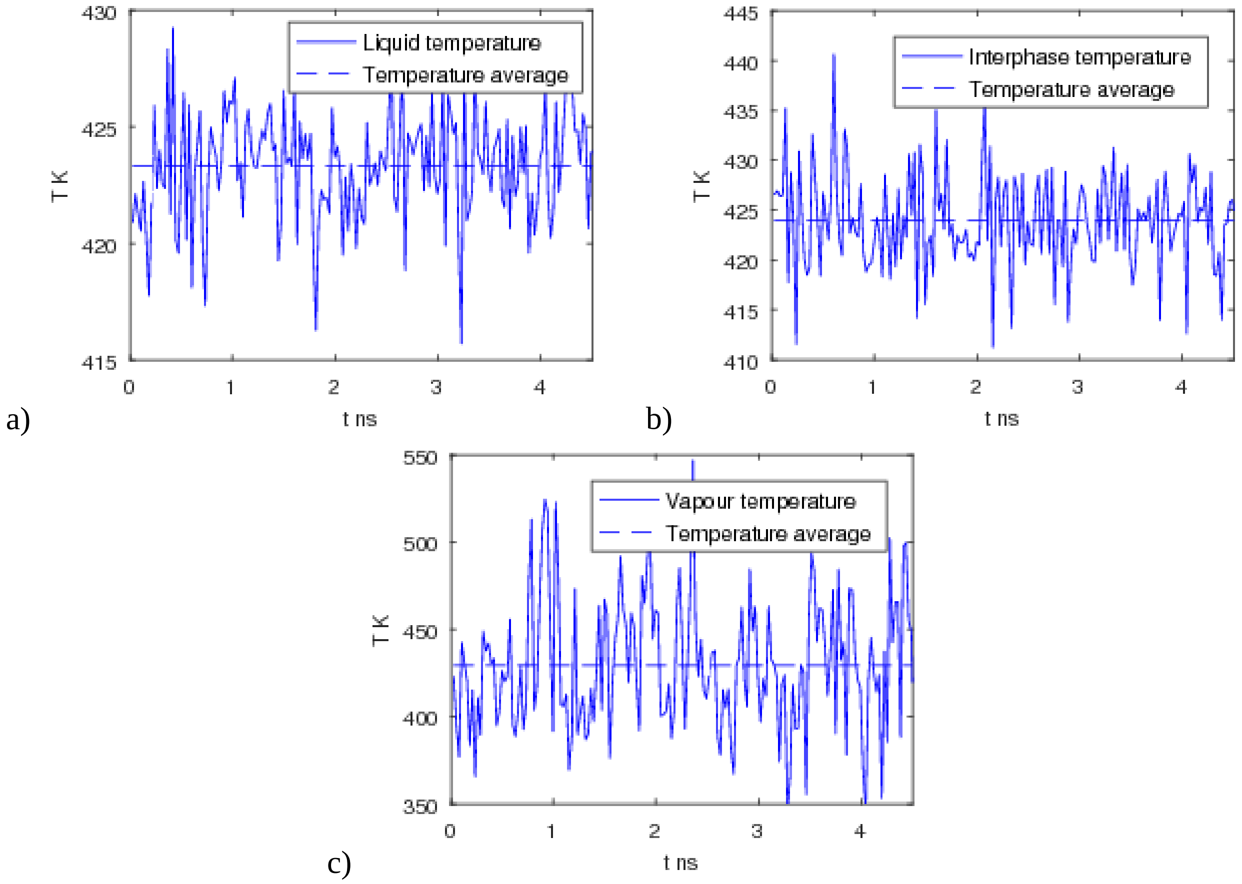

Fig. 6. The time evolutions of: a) liquid temperature; b) vapour temperature and c) interphase temperature for 423 K case

In order to obtain sufficient number of events for molecular velocity distribution evaluations during evaporation and condensation, the simulation with same equilibration time but longer sampling period (4 ps) was performed at 423 K temperature. The Fig. **7** shows the translational velocity distribution functions of all leaving molecules from the liquid surface (including evaporating and reflecting from the surface molecules), condensing molecules and normalized Maxwellian velocity distribution given by the

$$F_{x,y}\left(v_{x,y}\right) = \left(\frac{m}{2\pi k_B T}\right)^{\frac{1}{2}} \exp\left(-\frac{m v_{x,y}^2}{2k_B T}\right), \qquad (9)$$

for the x and y axis and

$$F_z(v_z) = \left(\frac{m}{k_B T}\right) v_z \exp\left(-\frac{m v_z^2}{2 k_B T}\right), \tag{10}$$

for the z axis. For the tangential components v_x and v_y, and the surface normal component v_z, the distribution functions obtained from simulation results are consistent with the Maxwellian distribution at 423 K for both the liquid surface leaving and condensing molecules. However, in order to determine the impact of molecular flexibility on the phase change phenomena, a further investigation have to be done.

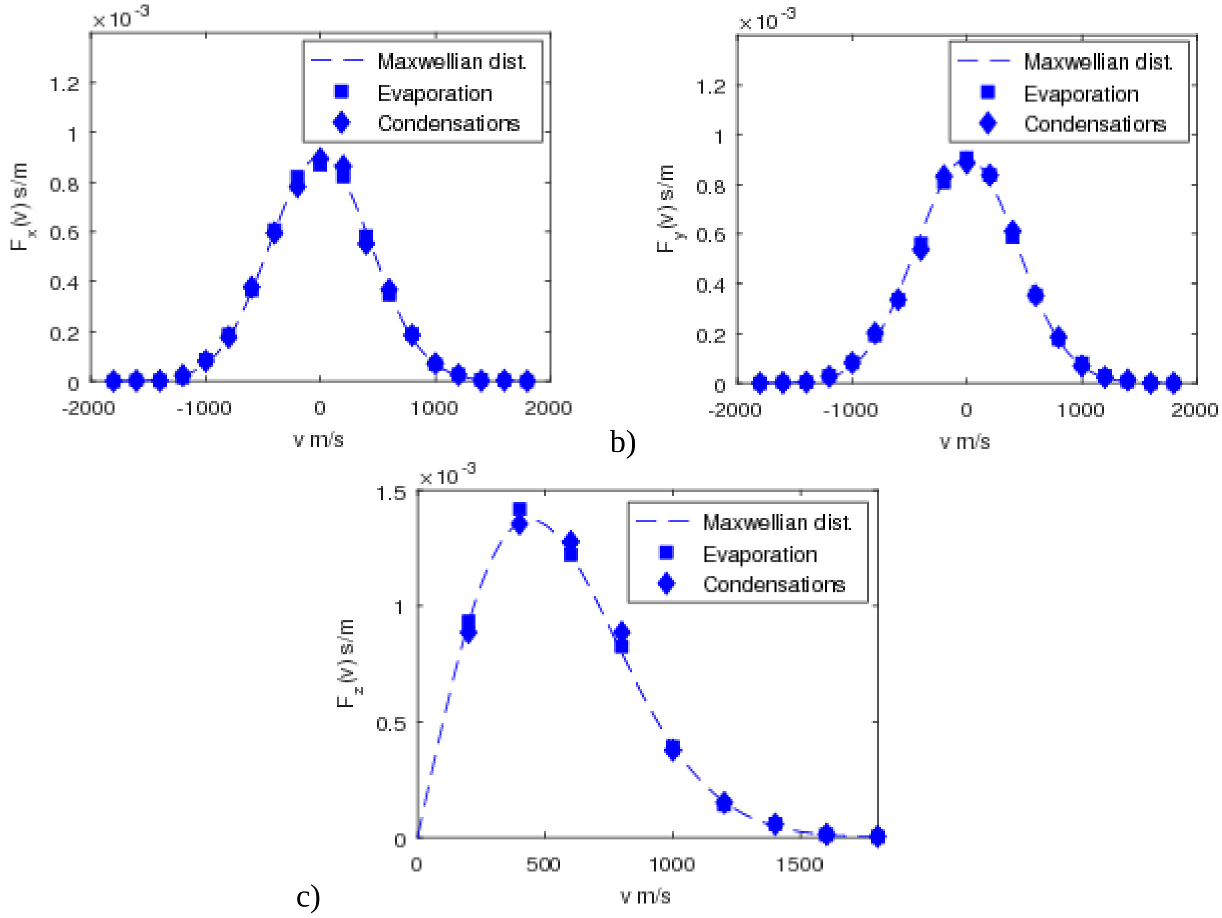

a) b) c)

Fig. 7. The translational velocity distribution functions of all leaving molecules from the liquid surface and condensing molecules for 423 K case: a) in *x* axis; b) in *y* axis and c) in *z* axis

4. CONCLUSIONS

The molecular dynamics simulations of liquid-vapour phase equilibrium state were performed using flexible fixed-point charge molecular model for water at four different temperatures: 373 K, 423 K, 473 K and 523 K. From the simulation results following conclusions can be drawn for used molecular model at the temperature interval from 373 K to 523 K:

- The molecular model slightly overestimates the liquid phase density and underestimates vapour phase density. This result contradicts the results obtained in [10]. The disagreement is attributed to the different methods for density calculations;
- the interphase thickness increases with the increasing temperature and is a linear function of temperature;
- there is a temperature jump at equilibrium state where the value of temperature increases during the transition from liquid to the vapour phase. For the 423 K simulation case, the temperature difference is 7 K. More information could be

attained from temperature profile along the system, however, it could not be done in current work as the simulated system size was too small.

- the translational velocity distribution functions of molecules leaving the liquid surface and condensing molecules agree with the Maxwellian distribution. However, in order to determine the impact of flexibility, the further investigation on intramolecular energy distributions has to be done.

ACKNOWLEDGEMENTS

This research is funded by the Research Council of Lithuania under the project P-MIP-17-108 "ComDetect" (Agreement No. S-MIP-17-69), 2017-2020 and project Nr. DOTSUT-598 (09.3.3-LMT-K-712-10-0041).

-

REFERENCES

[1] V.P. Singh, C.-Y. Xu, Evaluation and Generalization of 13 Mass-Transfer Equations for Determining Free Water Evaporation, Hydrol. Process. 11 (1997) 311–323. doi:10.1002/(SICI)1099-1085(19970315)11:3<311::AID-HYP446>3.3.CO;2-P.

[2] J. Of, T.H.E. Atmospheric, Temperature Dependence of Evaporation Coefficient for Water Measured in Droplets, J. Atmos. Sci. 64 (2006) 996–1004. doi:10.1175/JAS3860.1.

[3] G. Xue, Y. Xu, T. Ding, J. Li, J. Yin, W. Fei, Y. Cao, J. Yu, L. Yuan, L. Gong, J. Chen, S. Deng, J. Zhou, W. Guo, Water-evaporation-induced electricity with nanostructured carbon materials, Nat. Nanotechnol. 12 (2017) 317–321. doi:10.1038/nnano.2016.300.

[4] A.H. Persad, C.A. Ward, Expressions for the Evaporation and Condensation Coefficients in the Hertz-Knudsen Relation, Chem. Rev. 116 (2016) 7727–7767. doi:10.1021/acs.chemrev.5b00511.

[5] K. Almenas, Evaporation / Condensation of Water. Unresolved Issues, Vytautas Magnus University, 2015. https://www.vdu.lt/wp-content/uploads/2015/05/2015_Evaporation-condensation_K.Almenas_11p.pdf.

[6] T.H. Yang, C. Pan, Molecular dynamics simulation of a thin water layer evaporation and evaporation coefficient, Int. J. Heat Mass Transf. 48 (2005) 3516–3526. doi:10.1016/j.ijheatmasstransfer.2005.03.015.

[7] T. Tsuruta, G. Nagayama, Molecular Dynamics Studies on the Condensation Coefficient of Water, J. Phys. Chem. B. 108 (2004) 1736–1743. doi:10.1021/jp035885q.

[8] T. Ishiyama, T. Yano, S. Fujikawa, Molecular dynamics study of kinetic boundary condition at an interface between a polyatomic vapor and its condensed phase, Phys. Fluids. 16 (2004) 4713–4727. doi:10.1063/1.1811674.

[9] I. Napari, H. Vehkamäki, A comparison of rigid and flexible water models in collisions of monomers and small clusters, J. Chem. Phys. (2006) 1–7. doi:10.1063/1.2346674.

[10] X.B. Zhang, Q.L. Liu, A.M. Zhu, An improved fully flexible fixed-point charges model for water from ambient to supercritical condition, Fluid Phase Equilib. 262 (2007) 210–216. doi:10.1016/j.fluid.2007.09.005.

[11] W.C. Reynolds, Thermodynamic Properties in SI, Department of Mechanical Engineering, Standford, 1979.

[12] B. Shi, S. Sinha, V.K. Dhir, Molecular dynamics simulation of the density and surface tension of water by particle- particle particle-mesh method Molecular dynamics simulation of the density and surface tension of water by particle-particle particle-mesh method, J. Chem. Phys. 124 (2012) 2006. doi:10.1063/1.2199849.

[13] D. Frenkel, B. Smit, Understanding Molecular Simulation - From Algorithms to Applications, Academic Press, 2002.

CYSENI 2019, May 23-24, Kaunas, Lithuania
ISSN 1822-7554, www.cyseni.com

NEUTRON FLUX SIMULATION OF A ONE DIMENSIONAL REACTOR ZONE

Zs. Tóth, D. P. Kis
Budapest University of Technology and Economics – Institute of Nuclear Techniques
Budapest Műegyetem rakpart 3. – 1111 Hungary
Email: zsofiatoth412@gmail.com

ABSTRACT

In nuclear power plants the energy is produced by thermal fission. It is extremely important to be able to monitor the processes in the reactor to ensure the safety and the reliability of the power plant. One of the main traits of the reactor zone is the neutron flux. It changes in time and space, therefore it is crucial to be able to simulate its changes with computer codes. In the research work a program code was established in Matlab software with which the neutron flux of a one dimensional zone can be simulated with homogenic and heterogenic zone parameters as well. The code is written using the one-group one dimensional time and space dependent diffusion equation. The equation of an average delayed neutron group was also included in the system to give a more precise look on the problem. The main innovation in the code is that numerical methods were used to solve the problem: finite differences approach was applied for the place dependent and for the time dependent solution. The advantage of this code compared to other ones is that one-dimensional zones can be simulated in a really short time and it still gives a precise solution because of the complex numerical methods used.

Keywords: nuclear power plant, neutron flux, simulation, finite differences

CYSENI 2019, May 23-24, Kaunas, Lithuania
ISSN 1822-7554, www.cyseni.com

NUMERICAL INVESTIGATION OF TWO-PHASE NATURAL CONVECTION AND THERMAL STRATIFICATION PHENOMENA IN ROD BUNDLE

A. Graževičius, A. Kaliatka
Lithuanian Energy Institute
Breslaujos st. 3, LT-44403 Kaunas – Lithuania
Email: audrius.grazevicius@lei.lt

ABSTRACT

Two-phase natural convection and thermal stratification phenomena in rod bundle with axially distributed heat flux were numerically investigated using ANSYS Fluent code in relation to the safety of nuclear reactors. These phenomena were simulated for a rod bundle, where the part of the heater rods are heated and the lower part of the heater rods are unheated. Numerical results shows a drastic temperature change at the interface of thermal stratification. In the heated region, upward flow occurred in the rod bundle center and downward flow occurred at the peripheral region of the rod bundle. The CFD results proves that the methodology and the heat-up model created (by Lithuanian Energy Institute) for CFD simulations of two-phase natural convection and thermal stratification phenomena works well. This methodology and heat-up model can be used for CFD investigations of mentioned phenomena in the nuclear spent fuel bundles, spent nuclear fuel pools or passive condensate cooling tanks.

Keywords: natural convection, thermal stratification, computational fluid dynamics (CFD), ANSYS Fluent

1. INTRODUCTION

In the event of station blackout (SBO), such as that which occurred in Fukushima Dai-ichi nuclear power plant, or loss of the residual heat removal system during shutdown of the pressurized water reactor (PWR) plant, reactor core cooling has to occur through natural convection. Decay heat distribution in the nuclear fuel assembly is distorted where the upper part of fuel rod has more thermal power, while lower part has less. Under this condition, thermal stratification is considered to occur and natural circulation flow is limited to the upper part of the pressure vessel, spent fuel pool, passive condensate cooling tanks, etc.

The present study focuses on a numerical investigation of the experiment of two-phase natural convection and thermal stratification phenomena in rod bundle with axially distributed heat [1]. The main goal of this study is a continuation of the previous investigations [2-4] and supplementation of CFD methodology used for simulations of two-phase natural convection and thermal stratification phenomena in complex geometries.

2. DESCRIPTION OF THE EXPERIMENTAL FACILITY AND CONDITIONS

The experimental facility is depicted in Figs. 1, 2. It consist of a vessel with an attached pipe to simulate the pressure vessel and the hot leg of a nuclear reactor. Experiment were carried out at atmospheric pressure. The vessel has a 120 mm × 120 mm square bottom and a height of 550 mm. The pipe simulating the hot leg is round with an inner diameter of 30 mm and a length of 250 mm. It is attached 45 mm from the top of the vessel, and its far end is closed. The 25 heaters were installed in the vessel. Each heater has a 100 mm heated section, while the rest section was unheated. The heat flux of each heater was 4.4 kW/m^2. The vessel was filled up with deionized water until 155 mm altitude, that corresponds half pipe of its diameter. The initial temperature of the water was around 9 °C. In the vessel, 16 thermocouples were located in the center sub-channel and 10 thermocouples were located in the peripheral sub-channel. 11 thermocouples were located in the pipe section. Details of thermocouple locations are presented in Fig. 2.

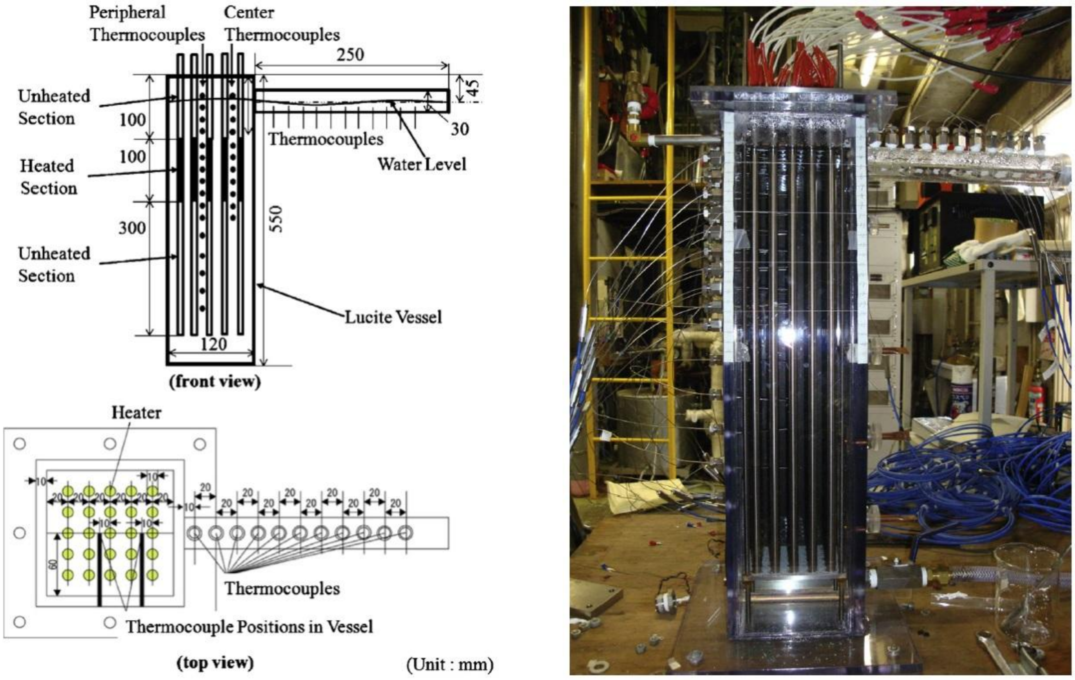

a) b)

Fig. 1. Experimental facility [1]: a) a schematic view; b) photograph

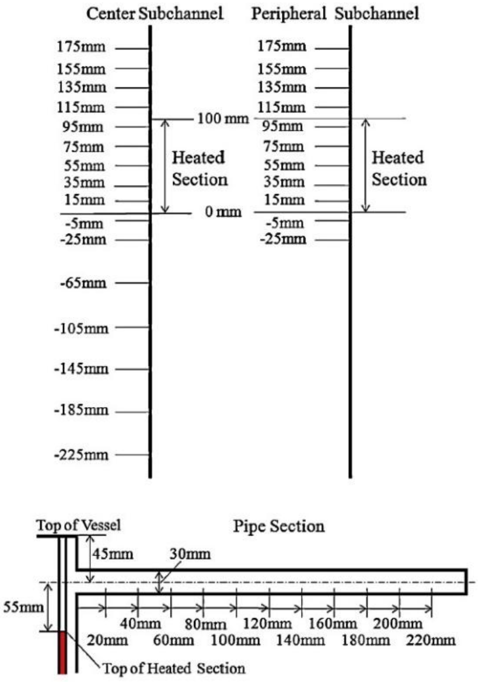

Fig. 2. Locations of thermocouples for water temperature measurement [1]

3. DESCRIPTION OF CFD COMPUTATIONAL MODEL

The ANSYS Fluent 17.2 code [5-6] and high performance computing cluster SGI Altix ICE 8400 were used for numerical investigations.

3.1. Geometry and mesh generation

Geometry and hexahedral mesh of a vessel with an attached pipe were created using ICEM CFD, taking into account OECD/NEA Best Practice Guidelines [7-8], ECORA [9], ERCOFTAC [10] and ANSYS [11] recommendations. In order to simplify computational domain symmetry plane was used.

3.2. Numerical setup

The same numerical set-up of ANSYS Fluent, as in the 3 chapter of the 2018 CYSENI manuscript [4], were chosen.

3.3. Boundary and initial conditions

The initial water temperature is 9 ℃, ambient air is 14 ℃, and initial walls temperature is approximately 12 ℃, respectively. Thermal power of the heater rods is 4.4 kW/m^2. The convection boundary condition with heat transfer coefficient 19 W/m^2·K was chosen. The heat transfer coefficient was applied for all walls (vessel and pipe), except for the top surface. Because the top surface is open. The experiment was performed under atmospheric pressure conditions. Experimental facility is not isolated. Due to the lack of information regarding the structure of walls, especially around the pipe, solid walls was not considered in calculation. Water was simulated as incompressible fluid with all thermal-physical properties of real water. Air was simulated as ideal-gas. Special heat-up model has been developed by Lithuanian Energy Institute and incorporated in the CFD model by means of User-Defined Functions. The term “two-phase” means water and air fluids.

3.4. Mesh independence study

The mesh independence was investigated by considering five different mesh sizes: (a) 249’077; (b) 433’772, (c) 598’034, (d) 809’020 and (e) 1’005’212 cells. The results of the monitoring points, which represents all thermocouples in the experimental facility, for all mesh sizes were compared. The mesh size (d) 809’020 was chosen for further simulations, because the temperature values of the monitoring points was the same magnitude as (e) mesh. Fig. 4 shows the CFD model.

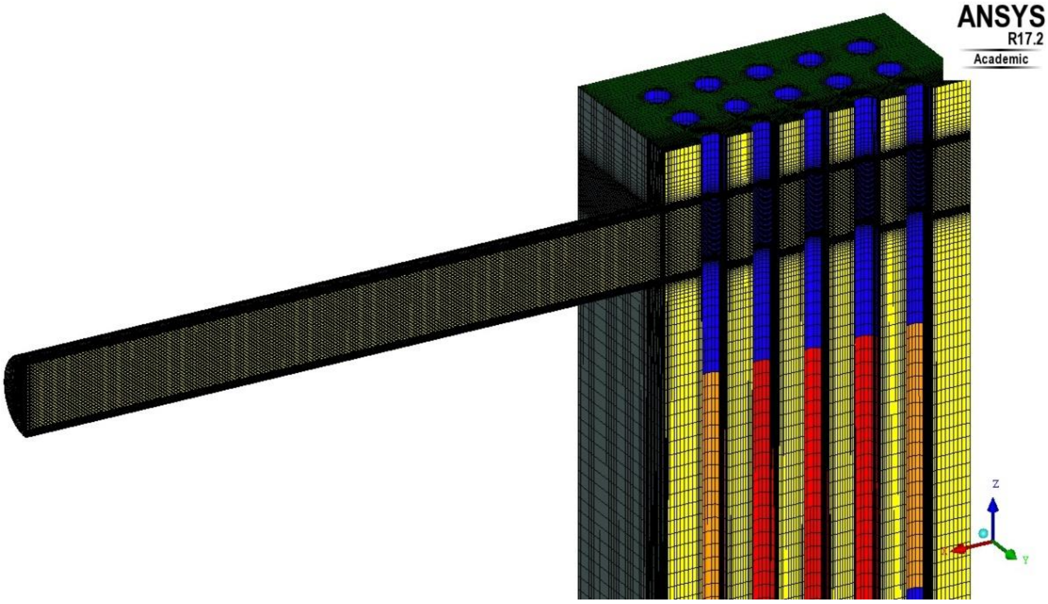

Fig. 4. The CFD model

4. RESULTS AND DISCUSSION

Figs. 5-10 shows comparison of experiment and CFD temperature variation in various vertical positions of center and peripheral sub-channel. Thermal stratification is clearly observed: temperature below heated section remain low, while at the heated section and above the heated section increase over time. The water at the heated section and above the heated section is well mixed due to natural convection, while where is no natural convection below the heated section. As shown in Figs. 8, 9, temperature at location below the heated section, but still near (-5 and -25) increase slightly. However, these temperatures increases only due to heat conduction from the hot water above from the heated section and no natural convection occuried. The interface of thermal stratification is fixed at the bottom of the heated section. The temperature variantion at different peripheral positions was almost the same as center positions, indicating that water is well mixed in the peripheral directions. Figs. 11, 12 shows temperature and density fields at the symmetry plane.

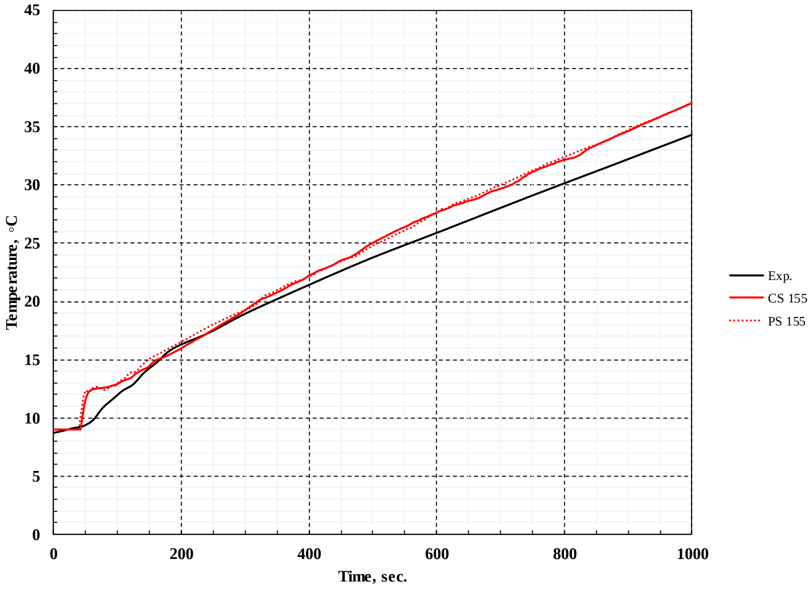

Fig. 5. Temperature variation of the monitoring points CS 155 and PS 155

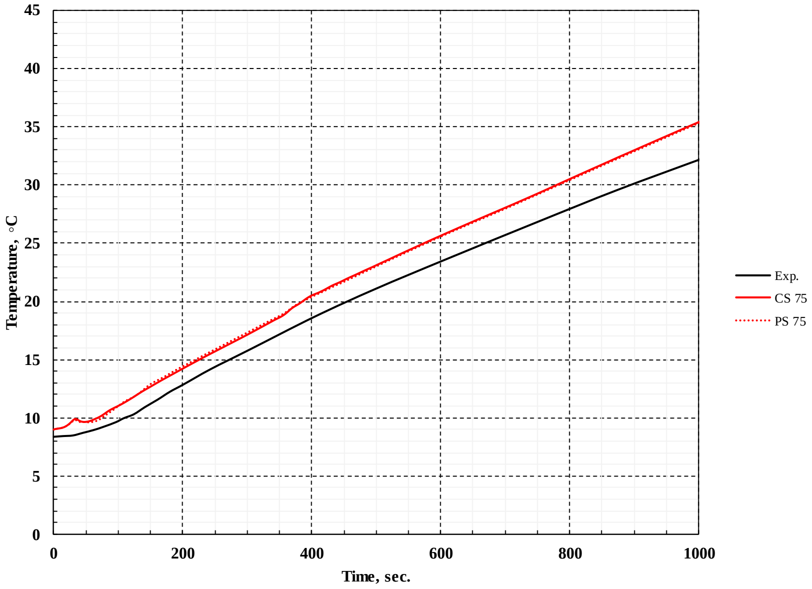

Fig. 6. Temperature variation of the monitoring points CS 75 and PS 75

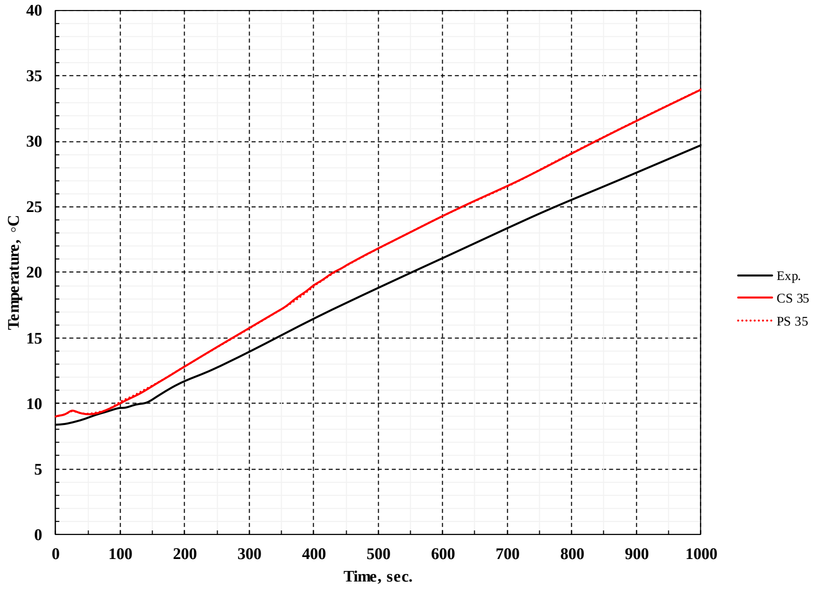

Fig. 7. Temperature variation of the monitoring points CS 35 and PS 35

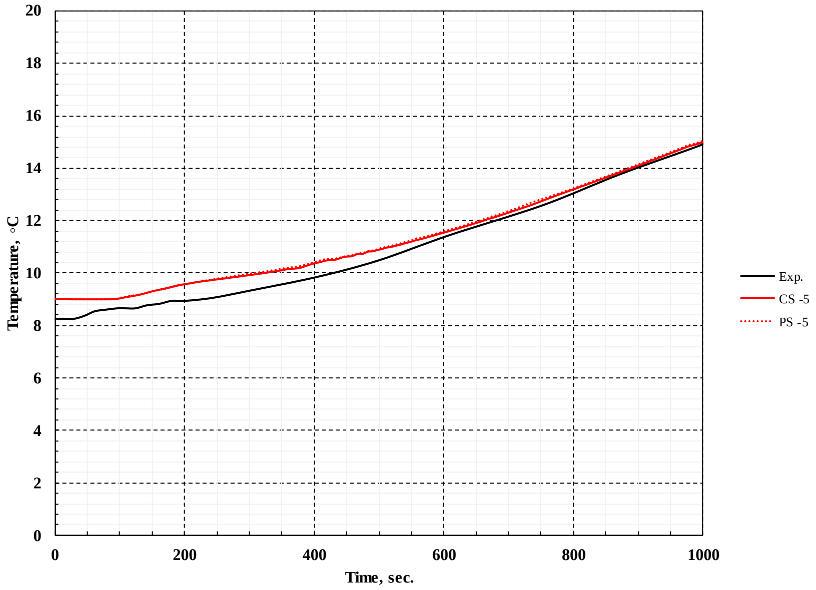

Fig. 8. Temperature variation of the monitoring points CS -5 and PS -5

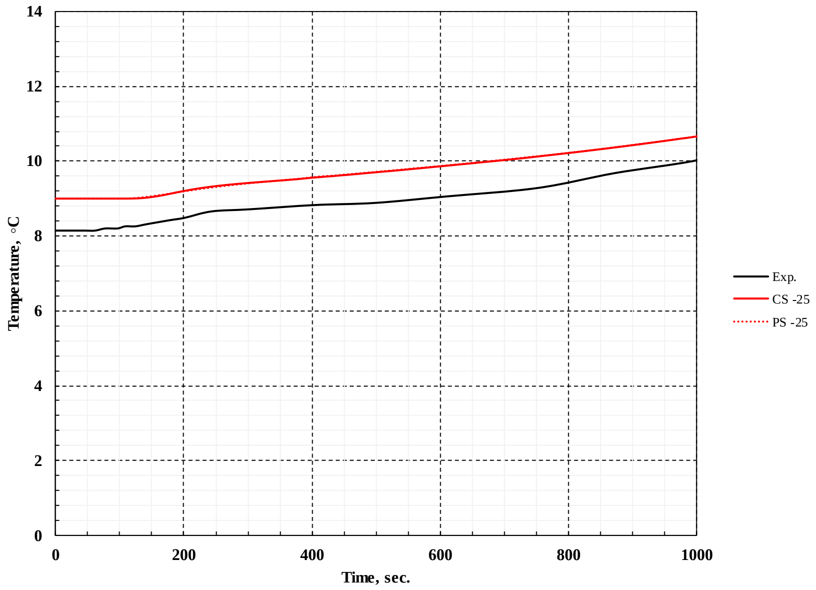

Fig. 9. Temperature variation of the monitoring points CS -25 and PS -25

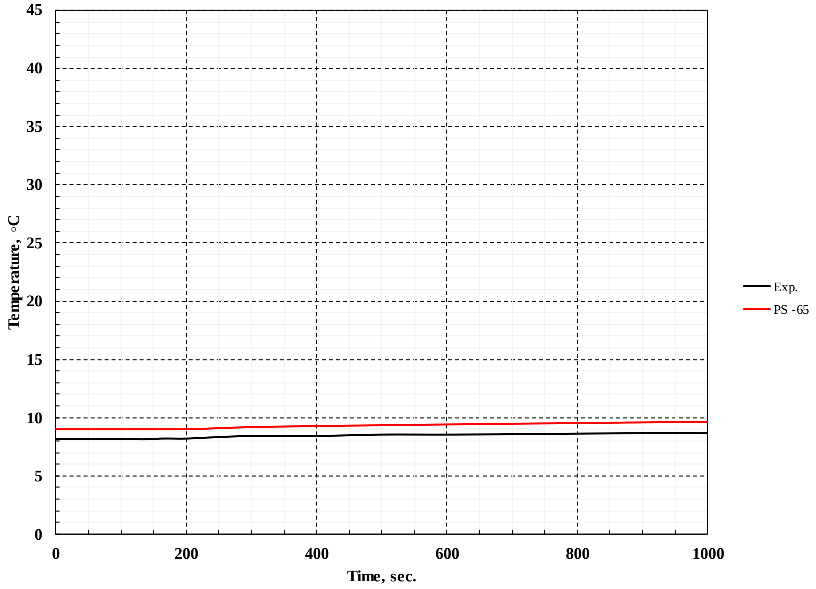

Fig. 10. Temperature variation of the monitoring points CS -65

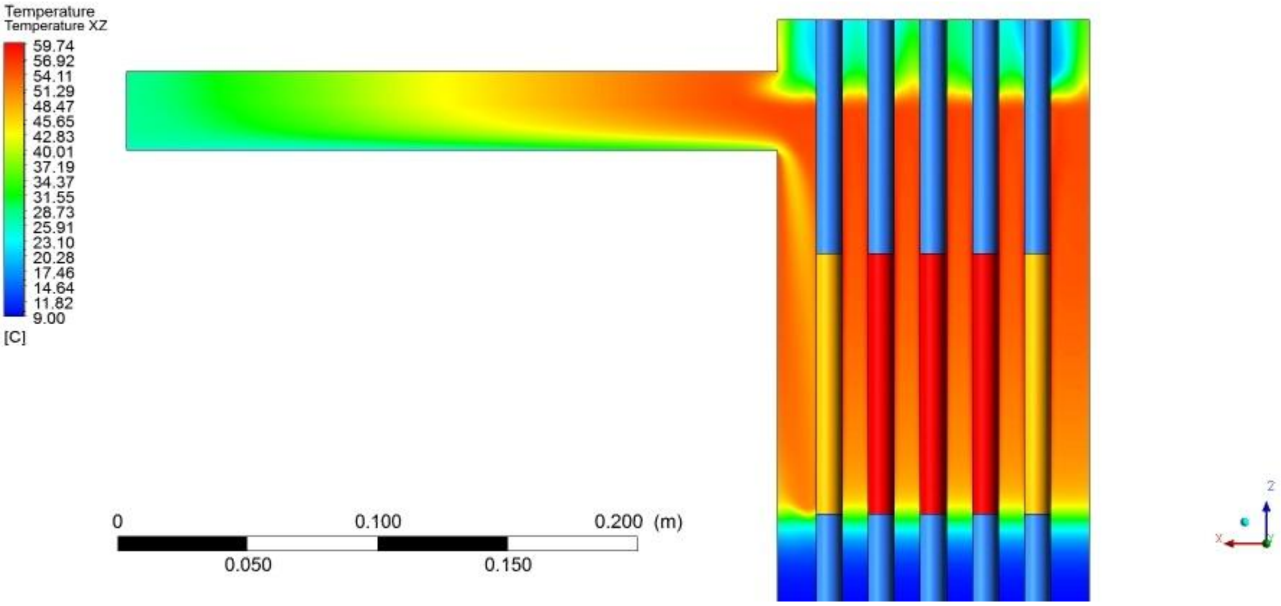

Fig. 11. Temperature field at the symmetry plane

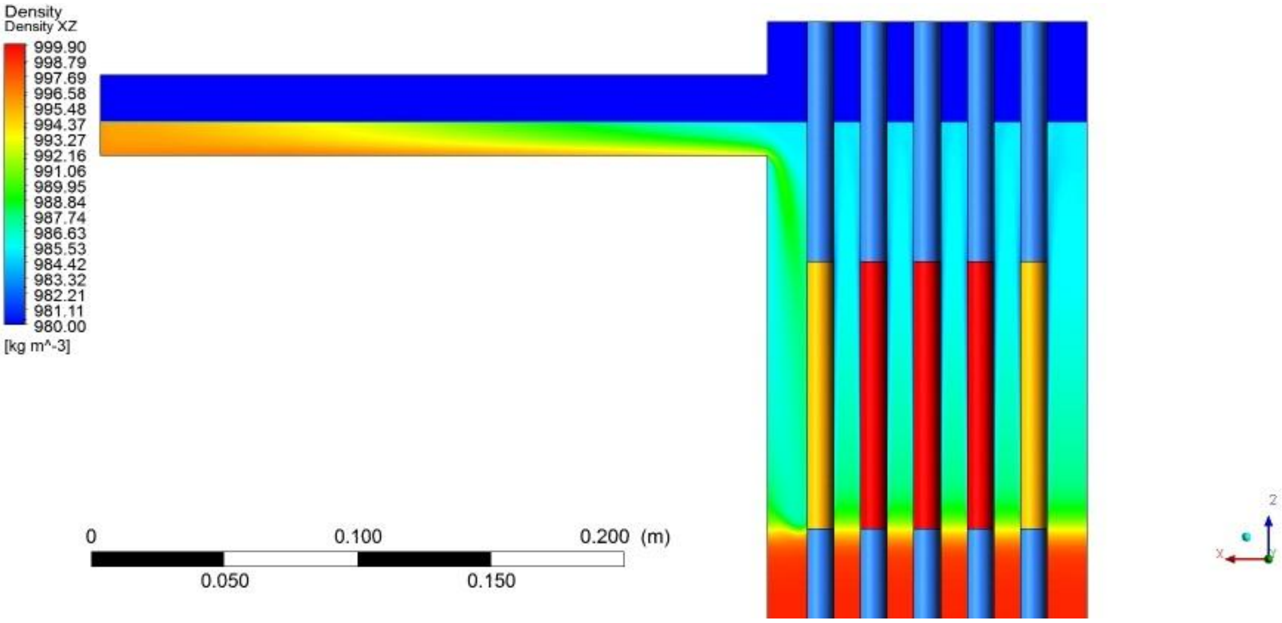

Fig. 12. Density field at the symmetry plane

5. CONCLUSIONS

Two-phase natural convection and thermal stratification phenomena in rod bundle with axially distributed heat flux were numerically investigated using ANSYS Fluent code in relation to the safety of nuclear reactors. Natural convection and thermal stratification were clearly observed. It proves, that the methodology and the heat-up model created (by Lithuanian Energy Institute) for CFD simulations of two-phase natural convection and thermal stratification phenomena works well. This methodology and heat-up model can be used for CFD investigations of mentioned phenomena in the nuclear spent fuel bundles, spent nuclear fuel pools or passive condensate cooling tanks.

REFERENCES

1. KODAMA, S., YOSHIDA, K., KATAOKA, I. Thermal stratification and mixing under single- and two-phase flow in rod bundle with axially distributed heat flux in vessel without forced convection. Nuclear Engineering and Design, 2014, Vol. 268, p. 164-172.
2. GRAŽEVIČIUS, A., KALIATKA, A. Modelling of the spent fuel heat-up in the spent fuel pools using one-dimensional system codes and CFD codes. Kerntechnik, 2017, Vol. 82, 316-333 p.
3. GRAŽEVIČIUS, A. Modelling of pool heat-up experiment using ANSYS Fluent. Conference of Young Scientists on Energy Issues 2017, 2017, p. 216-224.
4. GRAŽEVIČIUS, A. Numerical investigation of the thermal hydraulic phenomena in a rectangular enclosure. Conference of Young Scientists on Energy Issues 2018, 2018, p. 269-276.
5. ANSYS, August 2016. ANSYS Fluent User's Guide. 17.2 Release.
6. ANSYS, August 2016. ANSYS Fluent Theory Guide. 17.2 Release.
7. MAHAFFY, J., et al. Best Practice Guidelines for the use of CFD in Nuclear Reactor Safety Applications. NEA/CSNI/R(2007)5.
8. MAHAFFY, J., et al. Best Practice Guidelines for the use of CFD in Nuclear Reactor Safety Applications – Revision. NEA/CSNI/R(2014)11.
9. MENTER, F., et al. CFD Best Practice Guidelines for CFD Code Validation for Reactor - Safety Applications. EU project Evaluation of Computational Fluid Dynamic Methods for Reactor Safety Analysis (ECORA) under Contract No: FIKS-CT-2001-00154.
10. CASEY, M., WINTERGERSTE, T. ERCOFTAC Special Interest Group on Quality and Trust in Industrial CFD. Fluid Dynamics Laboratory, Sulzer Innotec, Version 1.0, January 2000.
11. ANSYS, 12 April 2016. Module 09: Best Practice Guidelines. Introduction to ANSYS Fluent, 17.0 Release.

CYSENI 2019, May 23-24, Kaunas, Lithuania
ISSN 1822-7554, www.cyseni.com

CALCULATION OF BOUNDARY CONDITIONS USING CFD MODELING AS PART OF A COMPREHENSIVE APPROACH TO IMPACT ASSESSMENT OF MODIFICATIONS ON THE SERVICE LIFE OF CRITICAL ELEMENTS OF A NUCLEAR POWER PLANT TURBINE

T. V. Nikulenkova
Igor Sikorsky Kyiv Polytechnic Institute
Polytechnichna str. 6, 03056 Kyiv – Ukraine
Email: tetyana.nikulenkova@gmail.com

A. G. Nikulenkov
Separated Subdivision «Scientific and Technical Center» of
the State Enterprise «National Nuclear Energy Generating Company «Energoatom»
B. Khmelnitskogo str. 63a, 01054 Kyiv – Ukraine

ABSTRACT

The approaching end of the scheduled operating lifetime of nuclear power plant (NPP) power units in Ukraine, as well as a need to increase power generation due to constantly increasing demand from consumers, formulate two global tasks for nuclear industry: 1) to carry out a set of works and modifications to ensure operation of NPPs beyond the design period while maintaining the required safety level; 2) to increase the installed capacity of operating NPPs while maintaining the required safety level using designed engineering margins combined with the latest developments in science and technology. Within the framework of the specified tasks one of critical elements – is turbine. Its critical elements include rotors and high- and low-pressure cylinder shells. Ensuring continued operation of NPP turbines envisages carrying out a set of works to assess technical conditions of the turbine, in particular, to detect and analyze damages, defects, identify causes and mechanisms for their occurrence and possible development. Further, the residual service life is assessed and recommendations in aging management are developed to ensure robust and safe operation of the turbine beyond the design period.

One of the ways to assess and predict the residual service life is by using software based on a finite element method. It is well-known that increasing the installed capacity of a power unit requires modernization of the flow section of the turbine high pressure cylinder, which, accordingly, will affect the service life of the rotor of the high-pressure cylinder. Therefore, the one of purposes of this paper is to investigate some impact on the service life of the high-pressure cylinder rotor of a typical high-speed turbine K-1000-60/3000, which is installed and operated at Khmelnitsky NPP Units No. 1, 2, South-Ukraine NPP Unit No. 3, Rivne NPP Units No. 3, 4.

The paper provides approaches to assessment and analysis of modifications having impact on the service life of critical elements of the NPP turbine. In order to test main steps of proposed approaches a spatial 3-D model of the high pressure cylinder of K-1000-60/3000 high-speed turbine was developed, as well as boundary conditions were calculated to determine a non-stationary temperature loads and subsequently assess the service life of the critical elements of K-1000-60/3000 turbine using software based on the finite element method.

Keywords: boundary conditions, cylinder, rotor, service life, temperature loads, turbine

1. INTRODUCTION

Nuclear power in Ukraine is represented by four nuclear sites (Zaporizhzhya NPP, Rivne NPP, South Ukraine NPP and Khmelnitsky NPP) that house fifteeen operating power units with total installed capacity of 13 835 MW.

The approaching end of the design service life of NPP equipment encourages to seek for solutions on how to replace and increase power generation. One of the ways is by increasing thermal output of existing power units using design margins with due consideration of operating experience and achievements of science and technology. A thermal power uprate of existing NPP units would allow increasing amount of generated electricity without significant costs [1-2]. Further, the specified modification would require carrying out a comprehensive research to ensure safe operation of power units while maintaining the required safety level. One of research areas is impact assessment of the modification on turbine’s critical elements.

Ukrainian NPPs with 1000 MW installed capacity operate two types of turbines running on dry saturated steam: a high speed K-1000-60/3000 turbine and a low speed K-1000-60-1500 turbine designed in three modifications.

This paper examines a standard high speed K-1000-60/3000 turbine, that is installed and operated at Rivne NPP Units 3, 4, Khmelnitsky NPP Units No. 1, 2, South Ukraine NPP Unit No. 3.

The objective of this paper is to describe a comprehensive approach to impact assessment of NPP thermal power uprate on the service life of critical elements of the high-pressure cylinder of a high-speed turbine, as well as to determine boundary conditions using CFD modeling for futher strength problems.

2. METHODOLOGY

2.1. Overview of research object

A K-1000-60/3000 turbine is a condensing steam turbine without controlled steam bleeding with intermediate separation and single-stage steam superheating designed to operate in the VVER-1000 power unit.

A throttling steam distribution is performed by means of four high pressure and four low pressure control valves. A high-pressure cylinder (HPC) is located in the middle of the turbine, low pressure cylinders (LPC) are symmetrically located on both sides of an HPC. The HPC is a double flow cylinder comprised of inner and outer shells. Steam is supplied to the HPC from the side through two nozzles located in the bottom half of the vessel. An HPC rotor is a single forged rotor with constant root diameter of all stages.

High pressure cylinders are double flow cylinders with five pressure stages per each flow. The LPC consists of inner and outer welded shells. The rotor exit points from the LPC shells are equipped with end seals to prevent an air inflow into the turbine vacuum system in all operation conditions. The principal diagram is shown on Fig. 1.

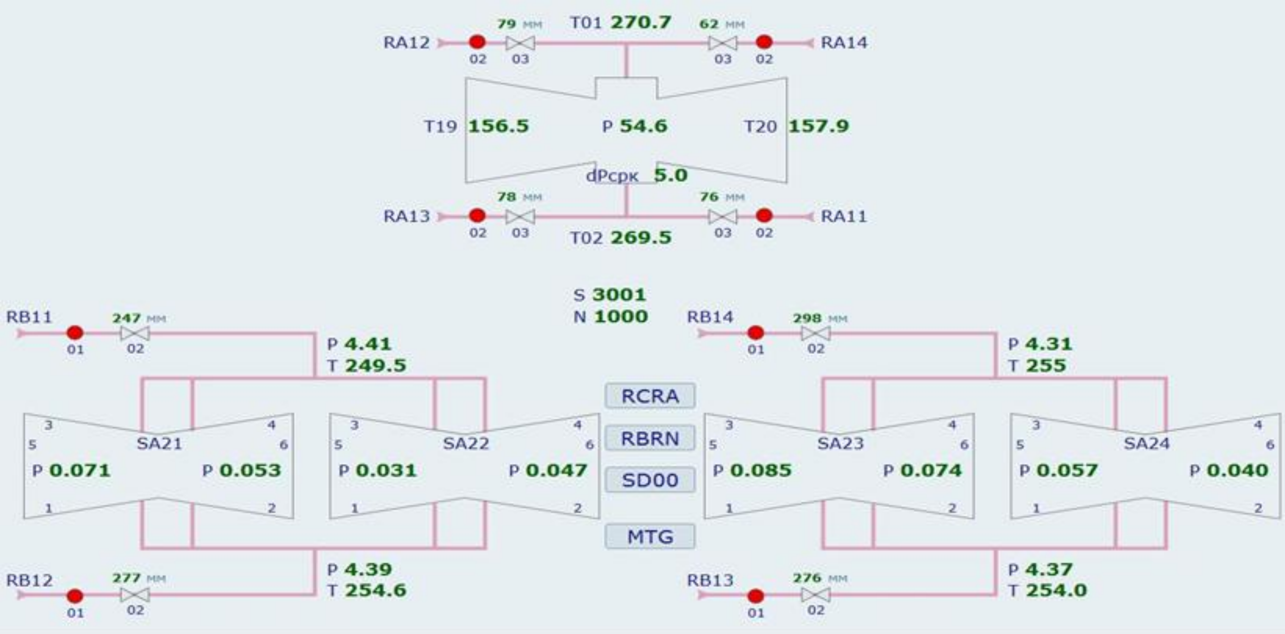

Fig. 1. Principal diagram of the K-1000-60/3000 turbine

This paper examines a high-pressure cylinder, since it is the main contributor to conversion of the kinetic energy of the steam into the mechanic rotation energy.

Examining low-pressure cylinders in terms of analysis of cavitation processes emerging in the last stages is a separate problem which is not considered herein.

2.2. Comprehensive approach to impact assessment of modifications on critical elements of the turbine

When assessing impact of the modification on the service life of critical elements of the examined turbine it is suggested to use the pattern as follows:

1) Assessment of a current service life:
   - building a 3-D model;
   - calculation of initial and boundary conditions (using CFD-codes or criterial equations as specified in [3]);
   - determining a nonstationary temperature field in the solid critical element for further calculation of thermal load;
   - strengh calculations (low-cycle fatigue, static loading, etc.) to determine a strengh deformed state (the calculations are permormed following recommendations provided in [4]);
   - assessment of remaining service life (the remaining service life of a rotor is determined by assessing its accumulated damage and design service life, and the design remaining service life is a remainder between the design service life and its operating life at the time of carrying out the works, to be done pursuant to [5]).
2) Service life assessment with account of the modification:
   - adjustment of a 3-D model (if needed);
   - recalculation of boundary conditions;
   - determining the strengh deformed state;
   - impact assessment on remaining service life.

This paper provides for a developed 3-D model of the high-pressure cylinder, as well as CFD modelling to identify boundary conditions for subsequent determining of low-cycle loads for with and without modification cases.

2.3. Description of a 3-D model of the turbine's critical element

As previously specified in the 2.2 section of the paper, building a 3-D model is the first step in examining impact of the modification on the service life of the turbine's critical element. The critical element examined in this paper is the high-pressure cylinder as mentioned above. Figure 2 provides a 3-D model of the high-pressure cylinder with steam inlet nozzles, steam bleeds, exhaust of waste steam, nozzle rings, diaphragms, inner shell, rotor with impeller. Figure 3 provides a 3-D model of the high-pressure cylinder with cam mechanism of a turning gear. The presented 3-D models were developed based on design and engineering documentation.

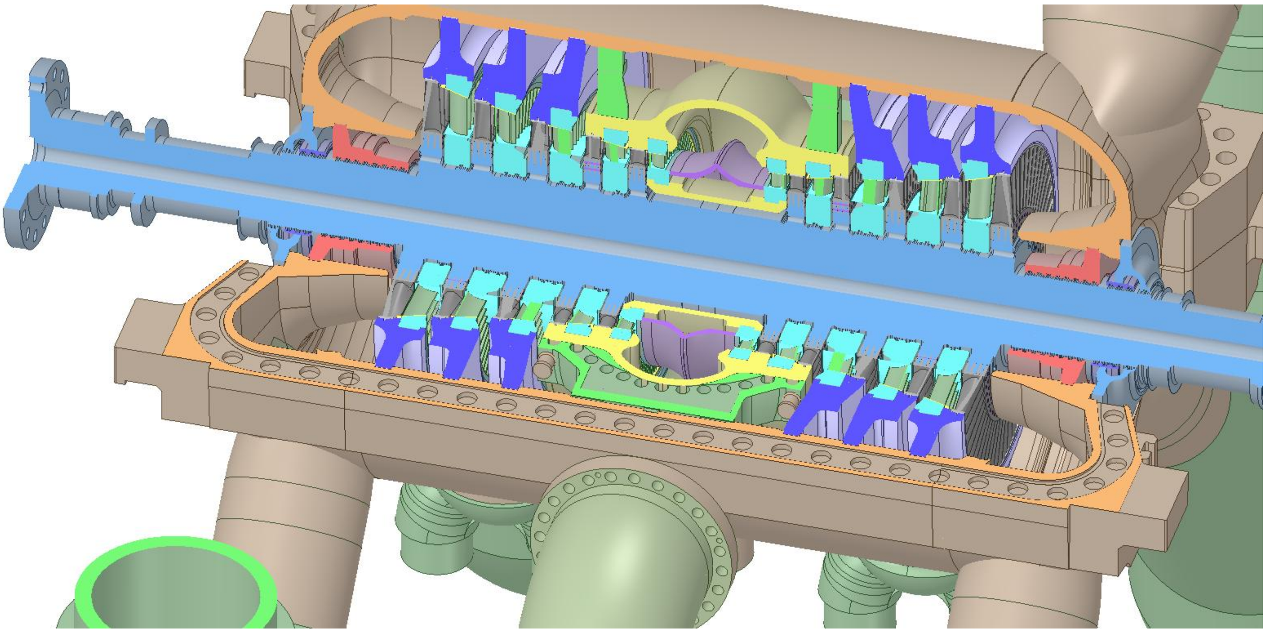

Fig. 2. 3-D model of a high-pressure cylinder of the K-1000-60/3000 turbine

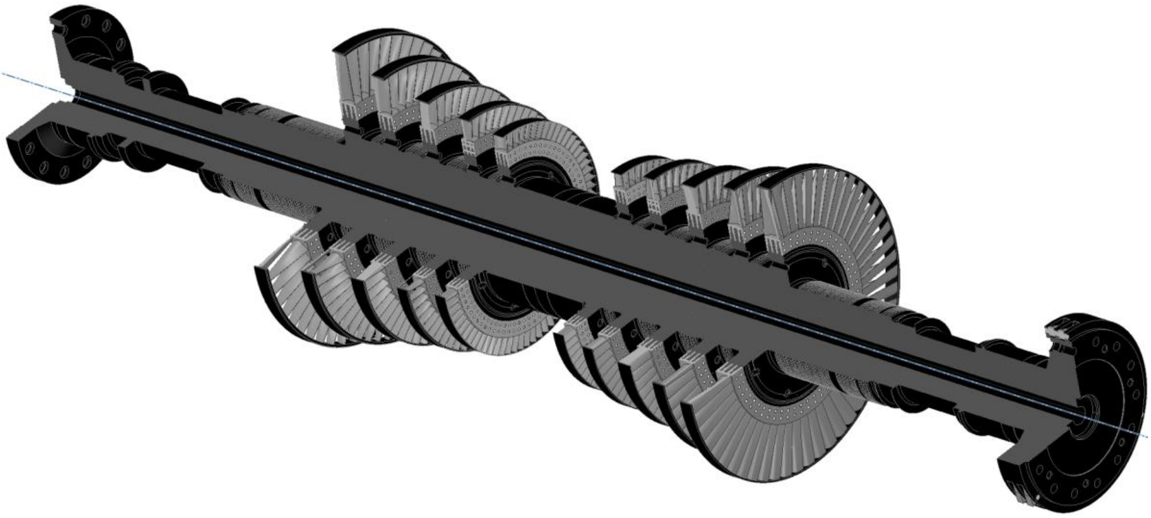

Fig. 3. 3-D model of the high-pressure rotor of the K-1000-60/3000 turbine

2.4. Computational fluid dynamics modelling

The main attention of the paper is focused on a subsequent stage of the described comprehensive approach that is to identify boundary conditions and determine temperature field in one of HPC critical elements, namely its rotor (see Fig. 3). Heat transfer in a rotor is described by a differential thermal conductivity equation of the following type [6]:

$$div[\lambda(T) gradT] = c(T)\gamma(T)\frac{\partial T}{\partial \tau} \tag{1}$$

$$\underbrace{-\lambda \left.\frac{\partial T}{\partial n}\right|_{w}}_{\text{Fourier's law}} = \alpha\left(T_f - T_w\right) \tag{2}$$

where $c(T)$ – specific heat; $\gamma(T)$ – density; λ – coefficient of thermal conductivity; α – heat transfer coefficient.

It should be noted that calculation of boundary conditions of the third kind (2) to solve a differential thermal conductivity equation (1) in the works related with extension of service life of rotors, e.g. in [7], was performed primarily using criterion equations obtained by summarizing experimental data. One of the shortcomings of this approach used to determined boundary conditions is its nonuniversality and a built-in excessive conservatism. Having sufficient calculation means an alternative method would be using CFD modeling.

To test this method the paper considers nominal operation mode of the turbine set in a stationary position for the 1st stage of the HPC flow section. To reduce application of calculation means, taking into account axial symmetry that decreases twofold the calculation field owing to entry of only one steam flow, the considered flow section of the HPC 1st stage is replaced by a 3-D model as 30^0 sector. The calculation field also includes a balance opening. (see Fig. 4).

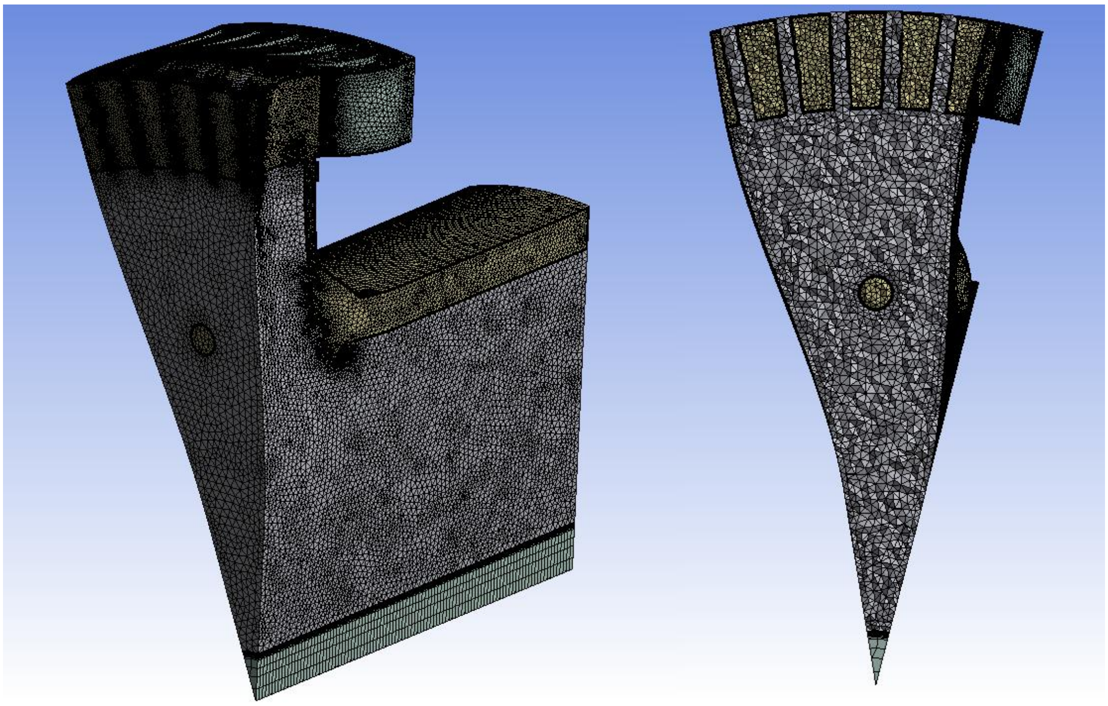

Fig. 4. Calculation model of a 300 sector of the HPC 1st stage

The geometry dimensions of the calculation field are: 0.368 × 0.746 × 0.536 m. The computational mesh was build using standard ANSYS tools. The computational mesh contains 1210111 nodes and 3690243 elements.

Other modeling features are described in the relevant subsections below.

2.4.1. Description of a mathematical model

The statement of problem provides that flow and heat exchange processes are described by the system of energy and Navier-Stokes stationary equations in a 3D setup. A mathematical model, which was used, is embedded in the ANSYS CFX code. It is represented by equations of continuity (3), variation of momentum (4) and total energy (5) [8].

$$\frac{\partial \rho}{\partial t} + \nabla \cdot (\partial \boldsymbol{U}) = 0 \tag{3}$$

$$\frac{\partial (\rho \boldsymbol{U})}{\partial t} + \nabla \cdot (\rho \boldsymbol{U} \otimes \boldsymbol{U}) = -\nabla p + \nabla \cdot \tau + \boldsymbol{S}_M \tag{4}$$

$$\frac{\partial (\rho h_{tot})}{\partial t} - \frac{\partial p}{\partial t} + \nabla \cdot (\rho \boldsymbol{U} h_{tot}) =$$
$$= \nabla \cdot (\lambda \nabla T) + \nabla \cdot (\boldsymbol{U} \cdot \tau) + \boldsymbol{U} \cdot \boldsymbol{S}_M + \boldsymbol{S}_E \tag{5}$$

$$\tau = \mu\left(\nabla \boldsymbol{U} + (\nabla \boldsymbol{U})^T - \frac{2}{3}\delta\nabla \cdot \boldsymbol{U}\right) \tag{6}$$

$$h_{tot} = h + \frac{1}{2}\boldsymbol{U}^2 \tag{7}$$

where, the stress tensor, τ in (4), is related to the strain rate by (6); h_{tot} is the total enthalpy, related to the static enthalpy h(T,p) by (7); the term $\nabla \cdot (\boldsymbol{U} \cdot \tau)$ represents the work due to viscous stresses and is called the viscous work term; the term $\boldsymbol{U} \cdot \boldsymbol{S}_M$ represents the work due to external momentum sources and is currently neglected.

Discretization of spatial operators is performed using the end volume method (discretization scheme of the second order).

2.4.2. Choosing a turbulence model

Up until now two equation turbulence models are most widely used to solve a great variety of engineering problems and are, definitely, the most representative group of differential models. This model class envisages solving independent equations for two characteristics of turbulence that as a whole allow to determine the turbulent viscosity using algebraic relations. The first characteristic is a kinetic energy of turbulent fluctuations k. There is a large flexibility in selection of the characteristic for which the second equation is built. The most widely used are two groups of models, specifically: k-ε and k-ω models. The $\varepsilon \sim k^{3/2}/l$ represents the dissipation velocity of the turbulence kinetic energy, and $\omega \sim k^{1/2}/l$ describes the frequency of energy-containing eddies fluctuations. The turbulent viscosity is estimated, accordingly, as $\nu_t \sim k^2/\varepsilon$ or $\nu_t \sim k/\omega$.

The different versions of k-ω model are widely applied in practice. One of the models, which should be specifically mentioned among the range of models that received rather high ratings during testing and practical application recently, is a Menter's shear stress transport turbulence model [9], that represents a combination of k-ε and k-ω models using the strengths of both models. The Menter's shear stress transport model has following features: the standard k-ω model and the transformed k-ε model are blended using a so called F1 filter function that is equal to one near the wall surface (applying the k-ω model), and decreases to a value of zero away from the wall (applying the transformed k-ε model). The relevant equations for k-ω models are multiplied by F1 function, and equations for k-ε model – by (1-F1) function, and then summed. As a result, the following equations are formed:

$$\frac{\partial \rho k}{\partial t} + \frac{\partial \rho U_j k}{\partial x_j} = \tilde{P}_k - \beta^* \rho \omega k + \frac{\partial}{\partial x_j}\left(\Gamma_k \frac{\partial k}{\partial x_j}\right) \tag{8}$$

$$\frac{\partial \rho \omega}{\partial t} + \frac{\partial \rho U_j \omega}{\partial x_j} = \frac{\alpha}{\nu_t} P_k - \beta \rho \omega^2 + \frac{\partial}{\partial x_j}\left(\Gamma_\omega \frac{\partial \omega}{\partial x_j}\right) + (1 - F_1) 2\rho\sigma_{\omega 2} \frac{1}{\omega}\frac{\partial k}{\partial x_j}\frac{\partial \omega}{\partial x_j} \tag{9}$$

The Menter's model underwent extensive testing when solving problems related to flows in the turbomachines [10-12].

In view of the abovementioned, the SST turbulence model was selected for the purpose of this paper. However, a sensitivity analysis was performed to determine the effect of different turbulence models on the key parameter – temperature of rotor wall. The results of this analysis are provided in Section 3.

2.4.3. Description of initial and boundary conditions

The computational model (see Fig. 4.) consists from one solid and three fluid domains. The first stationary fluid domain models the flow of wet steam through nozzle blades, the second rotating fluid domain models the flow of wet steam through working baldes of the turbine, the third rotating fluid domain models air flow in the central opening of the rotor designed for handling operations related with package inspection. Wet steam is modeled as a homogeneous binary mixture based on IAPWS IF97 condition data for water and water steam.

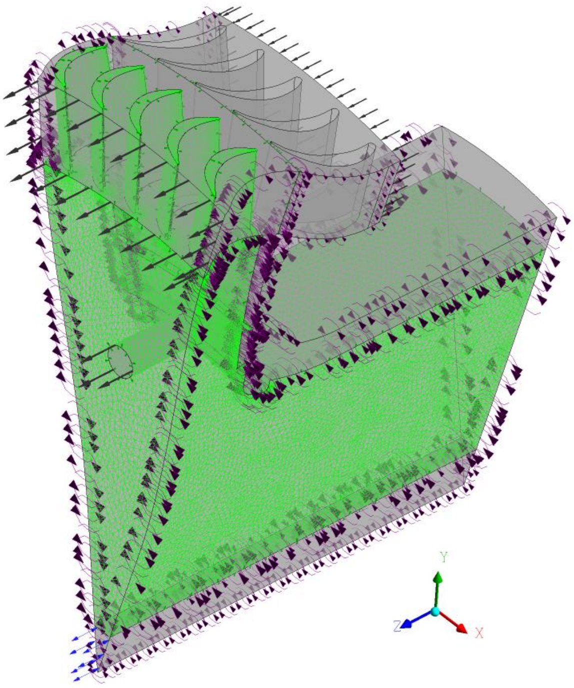

Fig. 5. Schematic diagram of the assigned boundary conditions in the ANSYS CFX computer environment

The boundary conditions at the inlet and outlet of the fluid domains were assigned as specified in Table 1. The outlet flow rate was recalculated using the modeled part.

Table 1. Initial calculation parameters

Parameter	**Nominal value**	**Nominal value with modification**
Mass steam flow rate per turbine, kg/s [13]	1622	1706
Inlet static pressure, MPa	5.839	5.839
Inlet static temperature, K	546.96	546.96
Modelled medium (fluid 1 and fluid 2)	wet steam	wet steam
Steam moisture content at the inlet	0,002	0.002
Modelled medium (fluid 3)	air	air
Material of solid domain	steel	steel
Rotor speed, rpm	3000	3000

A boundary condition permitting flow reverse circulation is applied at the outlet of the domain modeling air flow. The side edges with Z as rotation axis received periodical boundary conditions. Selection of turbulence model is descibed in Subsection 2.4.2. The convergence criteria: 1) root mean square errors are not more than 10^{-5}; 2) the global imbalance level is less than 0.01.

3. RESULTS AND DISCUSSION

The results in this section are provided based on the objective of calculation that is obtaining boundary conditions of the third kind (2) and 3-D temperature field in the rotor. Exporting temperature field of the rotor from ANSYS CFX into Structural mechanical is less preferred that exporting boundary conditions of the third kind (2) due to principal differences in the structure of computational meshes. Hence, calculations were performed according to the following sequence:

1) Calculation of turbine's nominal condition in the stationary position (see Figs. 6-8) to define the adequacy of the received results by comparing characteristic parameters (average-weighted by flow rate, outlet pressure, available heat drop of the stage, outlet moisture, flow rate through balance opening).

2) Determining impact of turbulence models (see Fig. 9) on the characteristic parameters: on distribution of wall temperature along the flow section in the zone of impeller.

3) Calculation of boundary conditions of the third kind (2) for modification case (increase of nominal flow rate through turbine) and comparison with basic nominal mode (see Figs. 10-12).

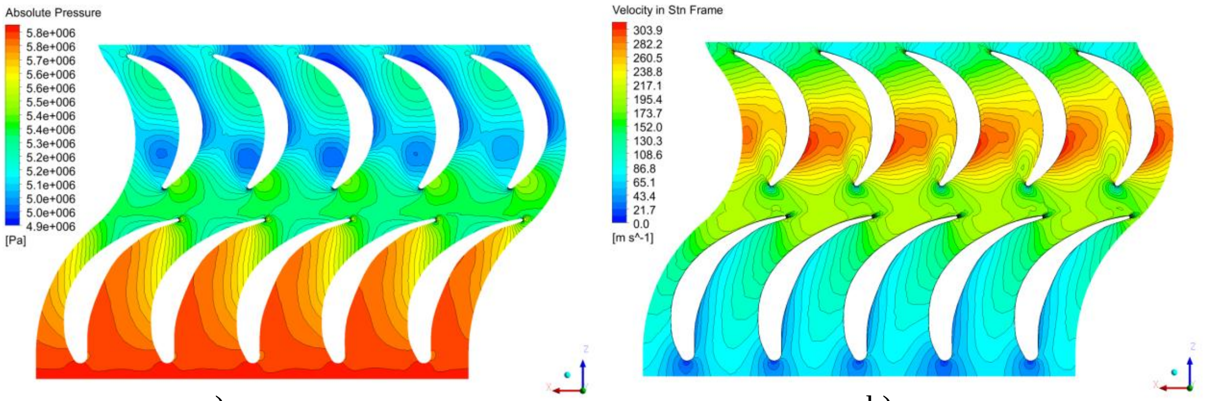

a) b)

Fig. 6. Change in steam parameters in XZ section of the HPC 1st stage: a) pressure field; b) velocity field

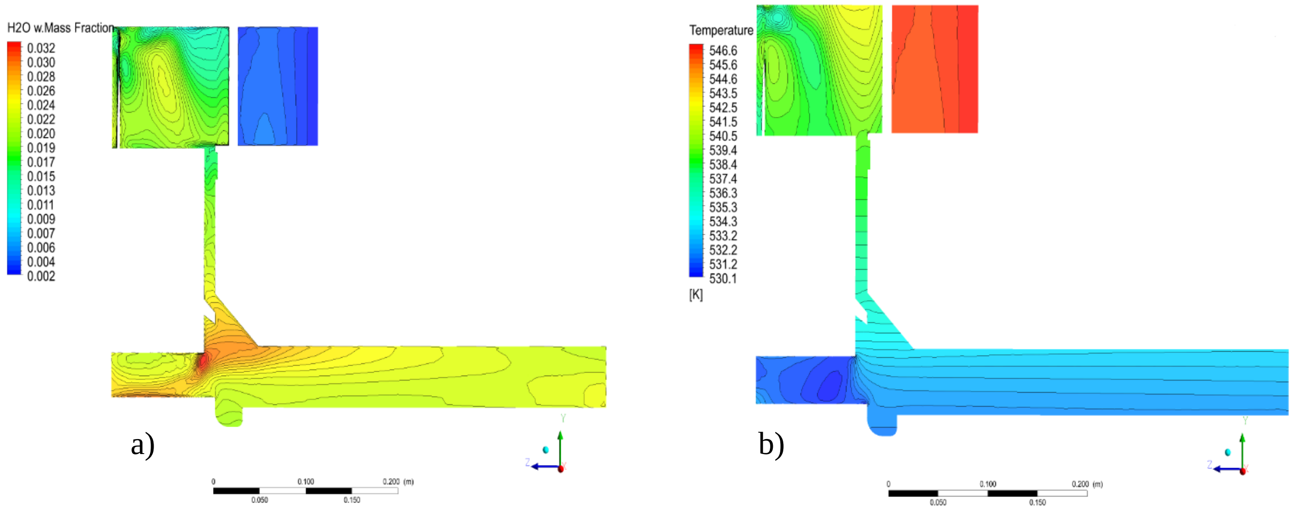

a) b)

Fig. 7. Change in moisture parameters in YZ section of the HPC 1st stage: a) temperature field; b) water mass fraction field

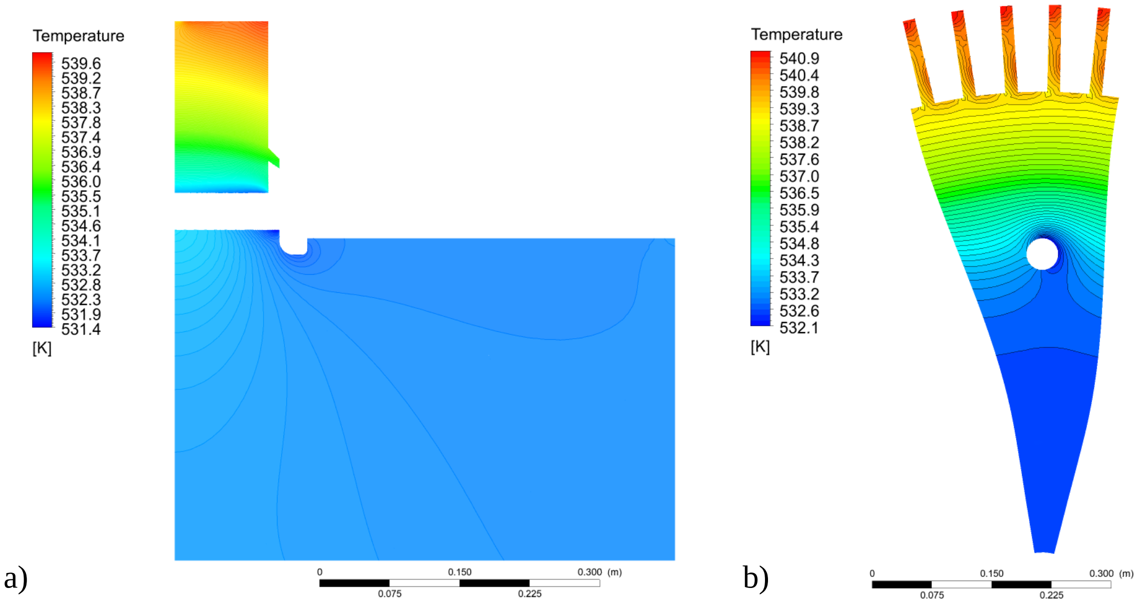

Fig. 8. Temperature field in the rotor section: a) temperature field in YZ section without working blades; b) temperature field in YX section with working blades

The results of calculation show that according to it. 1) of Section 3, overwatering of steam can be observed in the field of balance opening (↑ of water content) due to its excessive cooling (↓ of temperature of wet steam) (see Fig. 7). Significant increase of temperature difference can be observed in the field of impeller due to being washed by the main steam-flow (see Fig. 8). Distribution of pressure and temperature field is typical for field with rotating motion (see Fig. 6). The average-weighted flow parameters specified in it 1) of Section 3 are provide in Table 2.

Table 2. Average flow-weighted parameters

Outlet pressure	**Outlet temperature**	**Available heat drop of the stage**	**Flow rate through balance opening**	**Moisture level**
5 MPa	537.26 K	24.5 kJ/kg	2.03 kg/s	0.978

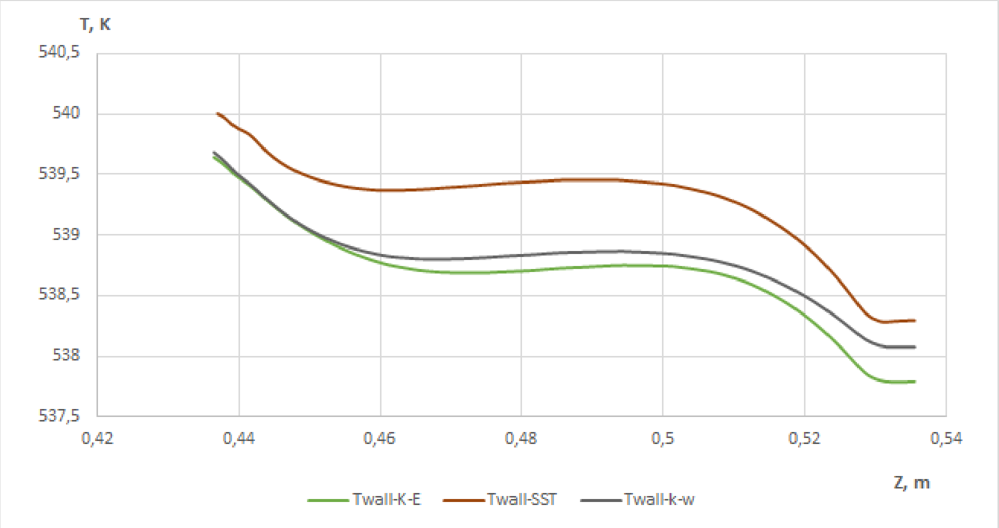

Fig. 9. Effect of turbulence models on change of wall temperature in the zone of impeller along the flow section

As the results of the calculation show, according to it. 2) of Section 3, Fig. 9 illustrates the effect of turbulence models on the average-weighted wall temperature by elemental area along the flow section of the impeller area. The k-ε and k-ω models underrate the wall temperature compared to SST model that leads to increase of wall heat flux and wall heat transfer coefficient. Thus, selection of SST model in this paper is justified and corresponds to the recommendations [10-12].

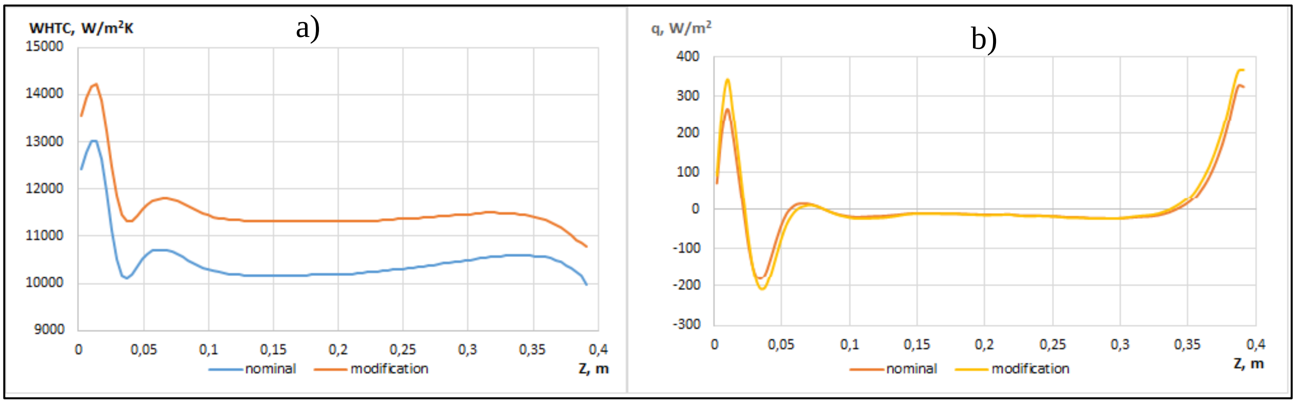

Fig. 10. Change in parameters along the flow section:
a) wall heat transfer coefficient; b) wall heat flux

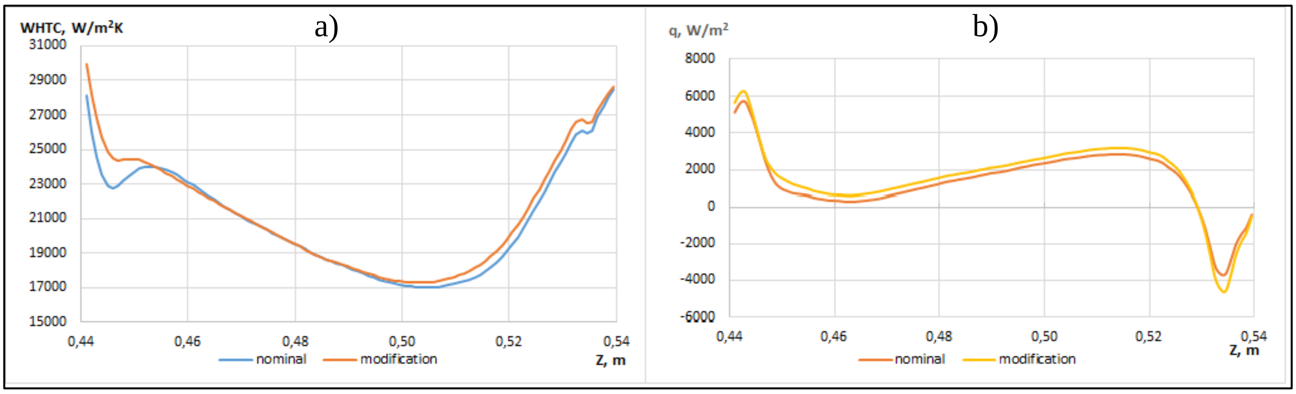

Fig. 11. Change in parameters along the flow section (impeller area):
a) wall heat transfer coefficient; b) wall heat flux

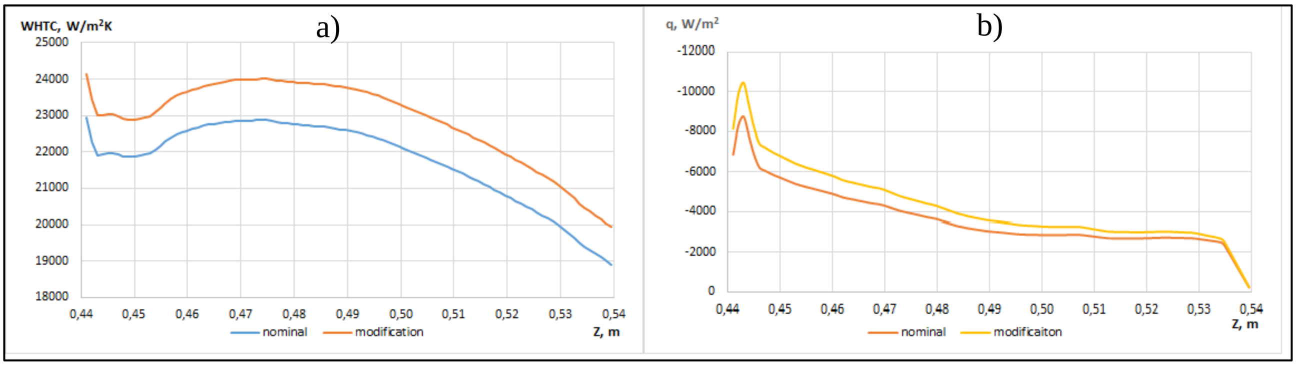

Fig. 12. Change in parameters along the flow section (balance opening zone):
a) wall heat transfer coefficient; b) wall heat flux

Figures 10-12 demostrate the results as specified in it 3) of Section 3. The provided results show that increase in steam flow rate leads to increase of wall heat flux and wall heat transfer coefficient, and, consequently, to decrease of rotor wall temperature. The wall heat transfer coefficient is normed to the temperature difference between T_{wall} and $T_{adjacent}$, where $T_{adjacent}$ is an average temperature in the nearest cell of the fluid domain. It should be noted that a negative sign of the heat flux means that heat is transferred from solid to fluid, while positive sign – from fluid to solid. Figure 10 shows stagnation of the flow at the origin that results in the heat transfer velocity due to heat conductivity being more that heat transfer due to forced convection. This can be explained by the zero-point motion in this section. The impeller zone (see Fig. 11) illustrates forced convection with heat transfer from fluid to rotor subject to change along the flow section depending on the generated eddies. The balance opening zone illustrates domination of heat transfer velocity due to heat conductivity over heat transfer due to forced convection owing to low flow rate 2.03 kg/s.

4. CONCLUSIONS

This paper describes a comprehensive approach to impact assessment of modifications on the critical elements of turbine.

Based on design and engineering documentation a 3-D model of the HPC of the K-1000-60/3000 high-speed was developed which can be subsequently used for CFD modeling and strength calculations.

The results of CFD modeling are provided for the 1st stage of the HPC at nominal operation parameters of the turbine in stationary position. The obtained results specified in Table 2 correspond with controlled paramenters during nominal operation mode.

A sensetivity analysis was performed to deteremine the effect of turbulence model on the temperature of rotor wall along the flow section. The recommendations are confired as specified in [10-12] regarding selection of SST model for modeling of turbomaniches.

The results are provided for the effect of modification related with increase of nominal flow rate to the values specified in [13] on the boundary conditions of the third kind (2). An insignificant increase of wall heat flux and cooling of rotor wall temperature in the 1st stage area can be observed. The change pattern of wall heat transfer coefficient along the flow section of the turbine calculated pursuant to criterion equations in the paper [6] correspond to the results of this research.

Futher it is necessary to perform CFD modeling for all stages of the turbine in transient loads from cold, warm and cold shutdown to ensure possibility of strength calculations with subsequent impact assessment of the modification on the service life.

REFERENCES

1. Chernousenko, O. Yu., Nikulenkova, T. V., Nikulenkov, A. H. *Analysis of the opportunity for an increase in the thermal power of power generating units of nuclear power plants (Part 1).* Bulletin of NTU "KhPI". Series: Power and heat engineering processes and equipment, no. 10(1232), pp. 6–12, ISSN 2078-774X, doi: 10.20998/2078-774X.2017.10.01.
2. Nikulenkov A. H., Chernousenko O. Yu., Nikulenkova T. V. *Analyzing the influence of an increase in the thermal power of energy generating unit at the nuclear power plant on the behavior of beyond the design basis accident*. Bulletin of NTU "KhPI". Series: Power and heat engineering processes and equipment, no. 13(1289), pp. 37–4, ISSN 2078-774X, doi: 10.20998/2078-774X.2018.13.07.
3. RTM 108.020.16-83. *Calculating the Temperature Fields of Steam Turbine Rotors and Housings* – M., 1985 – 115 p.
4. RTM108.021.103, *Details of stationary steam turbines. Low cycle fatigue calculation*. – M., 1985. – № AZ-002/7382. – 49 p.
5. RD34.17.440-96, *Methodological guidelines to perform works within assessment of individual service life of steam turbines and its extension beyond the fleet service life*. – M., 1996. – 47 p.

6. Chernousenko, O., Nikulenkov, A., Nikulenkova, T., Butovsky, L., and others. *Calculating boundary conditions to determine the heat state of high pressure rotor of the turbine NPP K-1000-60/3000.* Bulletin of NTU "KhPI". Series: Power and heat engineering processes and equipment, no. 12(1288) 2018, pp. 51–56, ISSN 2078-774X, doi: 10.20998/2078-774X.2018.12.09.
7. Bakhmutskaya, Y., Goloshchapov, V. *К-325-23,5 Steam Turbine High-Pressure Rotor Thermal and Thermo-structural State during cold start-up*. Journal of Mechanical Engineering, Vol. 20, No. 2 (2017), pp. 3–11.
8. Alyokhina, S. *Simulation of thermal state of containers with spent nuclear fuel: multistage approach* / S. Alyokhina, V. Goloshchapov, A. Kostikov, Yu. Matsevity // International Journal of Energy Research. – 2015. – V. 39, Iss. 14, Nov. – P. 1917–1924, DOI: 10.1002/er.3387.
9. Menter, F., Carregal Ferreira, J., Esch, Th., Konno, B. *The SST Turbulence Model with Improved Wall Treatment for Heat Transfer Predictions in Gas Turbines*. Proceedings of International Gas Turbine Congress, Tokio, November 2-7, 2003, pp. 1–7, IGTC-TS-059.
10. Menter, F.R. Two-equation Eddy-Viscosity Turbulence Models for Engineering Applications. AIAA J., Vol. 32, No. 8 (1994), pp. 1598–1605.
11. Kirillov, A. I., Galaev, S. A. Some results of numerical simulation of turbulent flow in turbomachine grids. Proceedings of the XV school-seminar for young scientists and specialists under the leadership of Acad. RAS A.I. Leontieva, Vol. 2 (2005), pp. 7–12.
12. Bukov, Y. A. Numerical modeling of aeroelasticity in the cooled blades grids. Aerospace Engineering and Technology, No. 5 (2010), pp. 59–63.
13. Nikulenkov A., Samoilenko D., Nikulenkova T. *Study of the impact of NPP rated thermal power uprate on process behaviour at different transient conditions*. Nuclear & Radiation safety, No. 4(80). 2018, pp. 09–13, ISSN 2073-6231.

CYSENI 2019, May 23-24, Kaunas, Lithuania
ISSN 1822-7554, www.cyseni.com

REMEDIATION OF ORGANOCHLORINE PESTICIDES CONTAMINATED SOIL USING THERMAL PLASMA

D. Gimžauskaitė, A. Tamošiūnas, S. Tučkutė, M. Aikas, R. Uscila
Lithuanian Energy Institute
Breslaujos str. 3, LT-44403 Kaunas – Lithuania
Email: Dovile.Gimzauskaite@lei.lt

J. Samosionokas
Public Agency "Soil remediation technologies"
Antakalnio str. 42, LT-10304 Vilnius – Lithuania

ABSTRACT

Organochlorine pesticides have been used widely in agriculture for effective pest, weed control. Also, pesticides have been utilised to control and prevent diseases, e.g. malaria, yellow fever. Dichloro-diphenyl-trichloroethane (DDT) was the best-known, widely produced and used organochlorine pesticide. However, organochlorine pesticides such as DDT contaminate soil, groundwater and causes carcinogenic effects, reproductive and endocrine system disorders for living beings. Also, organochlorine pesticides have low water solubility, low volatility and long persistence in the environment (e.g. half-life of DDT in the soil is estimated to be approximately 36 years). Such pesticides are classified as persistent organic pollutants (POPs) and are listed in the Stockholm Convention on POPs. Although the use of these priority pollutants has been banned for a while, its residues still exist in the environment. Soil is the primary environmental reservoir for organochlorine pesticides in the terrestrial environment — furthermore, soil act as the secondary source of persistent organic pollutants. The pesticides desorption from the soil causes secondary pollution of the atmosphere and water. Hence, it is necessary to find a remediation method which allows to remove organochlorine pesticides from the soil entirely and to avoid secondary pollution of the biosphere. Thus, numerous soil remediation methods based on biological, physical, chemical, thermal processes exist. Nevertheless, these methods had drawbacks such as limited penetration of reagents within the soil matrix, incomplete degradation of pesticides, generation of toxic by-products, prolonged treatment time, strong dependence on environmental conditions. It is evident that the treatment of pesticides polluted soil requires the development of new strategies and measures. Consequently, application of plasma technologies for soil remediation has a great interest because there are no special requirements for the pre-treatment of the raw soils, the remediation process is fast in time and any additional materials are not needed. Notwithstanding, more detailed experimental research on pesticides contaminated soil remediation with plasma is still required. Thus, this experimental research aimed to investigate thermal air and water vapor plasmas suitability to remediate soil contaminated by organochlorine pesticides (mainly DDT). Hence, parameters of the contaminated soil were studied before and after the treatment with thermal plasma using a scanning electron microscopy (SEM), optical microscopy, an energy dispersive X-ray spectroscopy (EDX) and a gas chromatography-mass spectrometry (GC-MS). Obtained results with SEM revealed that interaction of contaminated soil with thermal air plasma or water vapor plasma led to structural transformations of the soil. EDX data showed complete removal of chlorine after the soil treatment with thermal plasmas. Moreover, the measurements performed with GC-MS confirmed that organochlorine pesticides concentrations in the soil were reduced significantly after the soil remediation with thermal plasmas. Thus, experimental results indicate that contaminated soil treatment using thermal air or water vapor plasma has adequate pesticides degradation capacity.

Keywords: thermal plasma, organochlorine pesticides, soil remediation

CYSENI 2019, May 23-24, Kaunas, Lithuania
ISSN 1822-7554, www.cyseni.com

CARRIER GAS EFFECT ON TYRE PYROLYSIS OIL COMPOSITION

T. M. Henarava, K. A. Viazava, V. V. Sauchyn, A. I. Liavonchyk
A. V. Luikov Heat and Mass Transfer Institute
National Academy of Sciences of Belarus
P. Brovki str. 15, 220072 Minsk – Belarus
Email: tatiana-susliako@mail.ru

E. I. Hapankova, I. A. Latyshevich
Institute of Physical Organic Chemistry
National Academy of Sciences of Belarus
Surganov str. 13, 220072 Minsk – Belarus

ABSTRACT

Pyrolysis oil obtained from tyre pyrolysis process can be used as fuel or a source of fine chemicals. Pyrolysis yields and characteristics of the products obtained depend not only on the feedstock and operating conditions used for the experiments, but also on the specific characteristics of the system used, such as the size and type of reactor, the efficiency of heat transfer, the residence time. The research has been carried out in a laboratory facility of screw thermolysis reactor (STR-10). The pyrolysis process of tyre particles has been carried out at a temperature of 500 °C under nitrogen, water vapour and the mixture of water vapour with nitrogen.

The influence of the carrier gas in the pyrolysis process on the chemical composition of pyrolysis oil was studied. Tyre pyrolysis liquids have been characterized, including elemental analysis, FT-IR spectroscopy and gas chromatography/mass spectroscopy (GC/MS). Pyrolysis oils are a complex mixture of C8-C28 organic compounds with a lot of aromatics (42.2-44.5%), aliphatics (11.6-12.4%), olefins (21.8-22.3), sulfureted (0.65-0.73%), nitrogenated (0.34-0.62%), oxygenated compounds (8.15-9.56%). Quantitative analysis of limonene by absolute calibration method was made.

Keywords: tyre pyrolysis oil, gas chromatography-mass spectrometry, FT-IR spectroscopy, carrier gas

1. INTRODUCTION

The recycling of waste tyres is a major environmental problem in nowadays. Tyre pyrolysis is an interesting and processing area of research because the rubber polymer is decomposed to gases and liquids, which can be useful as fuels or sources of chemicals.

In the recent years, studies of the chemical composition and properties of pyrolysis oil, both for isolation of individual compounds with valuable properties and for improving the consumer properties of pyrolysis oil as fuel, are progressing [1, 2]. Pyrolysis is the thermal fragmentation of solid substances in an airless environment. The products obtained with this process can be easily handled, stored and accessible to transportation that increases the applicability of this method. The chemical composition of pyrolysis oil depends on many factors, the most important of them being the heating rate and the presence and type of an atmosphere, preventing the thermal oxidation of solid and liquid products of pyrolysis. The pyrolysis of tyre has largely been studied in the inert atmosphere. Inert carrier gases such as nitrogen, hydrogen, helium are often used in pyrolysis process for this fragmentation of waste tyre [3-7]. There are some works of pyrolysis process in reactive atmosphere, for example carbon dioxide, nitric oxide and oxygen that are analysed in works [8, 9]. It is known that the pyrolysis atmosphere significantly affects the composition of pyrolysis products. The effects of water vapour on the pyrolysis oil composition remain unclear.

The aim of the paper is to study the composition of the pyrolysis oils depending on carrier gases such as nitrogen, water vapour and the mixture of water vapour with nitrogen.

2. METHODS

2.1. Materials

Analytical grade solvents: distilled water, *n*-hexane (99.5%) and chloroform (99.4%) solvents were used.

2.2. Experimental procedure

2.2.1. Pyrolysis

The research was carried out in a laboratory facility STR-10 (Figure 1) [10]. In contrast to classical pyrolysis technologies, where the hot gas passes through the layer of material lying motionless, the material is continuously moving in the STR-10, providing effective mass transfer and heat of tyre. This method prevents material caking and formation of stable gas channels, reduces the heating time and, consequently, increases the rate of reaction.

Fig. 1. Scheme of the facility: 1 – dozer; 2 – screw pyrolysis reactor; 3 – solid residue bunker; 4 – condensate reactor

According to the scheme (Fig. 1) the tyre particles are loaded into the dozer (1) and then fed into the screw reactor (2). The material is heated in the reactor at 500°C. Due to the heating, material decomposes and an organic vapour condenses in a condensate reactor (4) where pyrolysis oil is formed. In addition, the solid residue is collected in the bunker (3). The pyrolysis of a tyre was carried out with the following carrier gases: water vapour (Sample 1), the mixture nitrogen-water vapour (Sample 2) and nitrogen stream (Sample 3).

2.2.2. Pyrolysis oils characterization

Pyrolysis oils were extracted with chloroform, then extract was evaporated, the precipitate was mixed with KBr after that obtained samples were analysed by Fourier Transform Infrared (FT-IR) spectrometer “Protégé 460” of “Nicolet” (USA). FT-IR spectra were collected at a resolution of 4 cm^{-1}.

Elemental analysis of liquids was determined with a CHNS/O-analyser VarioMicroCube (Elementar, Germany).

On the other hand the pyrolysis oils were analysed in an Agilent Technologies 7890A gas chromatograph, equipped with mass-detector and a capillary column “HP-5MS” (30 m × 0.25 mm

× 0.25 μm). Pyrolysis oils were firstly prepared by treatment of solvent deasphalting with *n*-hexane from 4 to 8 °C and decanting. After that, the analyses were performed by following conditions of GC-MS: the initial oven temperature was maintained at 50 °C for 3 min and then ramped at 10 °C/min to 300 °C, which was held for 22 min.

3. RESULTS AND DISCUSSION

3.1. Chemical composition of pyrolysis oils

The oils obtained from pyrolysis of waste automobile tyre, which are oily organic compounds with dark-brown-colour and strong acrid smell. The pyrolysis oil has many impurities and odour, which causes difficulties in using. Depending on the feedstocks and pyrolysis processes, the composition of pyrolysis oil varies in a large range. Pyrolysis oil is a complex mixture of more than 300 organic compounds that includes alkanes, olefins, aromatics, asphaltenes and heteroatom-compounds [11].

It is known that oil composition from tyre pyrolysis in nitrogen stream is 26.77 wt% alkanes, 42.09 wt% aromatics, 26.64 wt% non-hydrocarbons and 4.05 wt% as asphaltenes [12]. The tyre pyrolysis oil consists of a single ring and polycyclic aromatic compounds and their alkylated derivatives, containing mainly alkylated benzenes, alkanes, and alkenes [13]. There are significant concentrations of naphthalene and methyl, dimethyl and trimethyl naphthalenes [14]. Higher molecular weight compounds included phenanthrene and pyrene [15].

The pyrolysis oils in the present paper were derived from waste tyre pyrolysis with using different carrier gases. Pyrolysis oil is a black, viscous and has a sulphurous/aromatic odour. The pyrolytic oil composition from waste tyre consists of both short and long chain 8-28 carbon molecules, as well as single and multiple ring structures.

3.2. FT-IR spectra analysis

Typically, FT-IR spectroscopy is widely used in the analysis of functional group components of pyrolysis oils. FT-IR spectra (Fig. 2) and results of functional group components are shown in Table 1, where Sample 1 is pyrolysis oil obtained under water vapour; Sample 2 is pyrolysis oil obtained under the mixture of water vapour and nitrogen; Sample 3 is pyrolysis oil obtained under nitrogen stream.

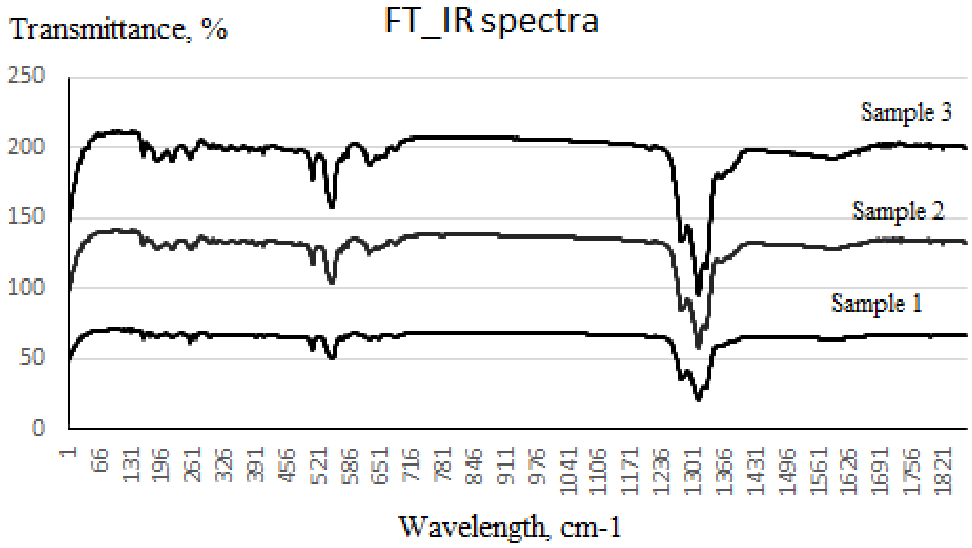

Fig. 2. FT-IR spectra of samples

Table 1. Functional group components of samples

Theoretical frequency range (cm^{-1})	**Actual peak (cm^{-1})**	**Functional group**	**Class of compounds**	**Samples**
900-690	726	C=C (oop)	Aromatic rings	Sample 1, Sample 2, Sample 3
975-780 2720	769.36 2720	C-H st C=O	Aldehyds	Sample 2
1110-1070	1130	S=O st	Sulfoxides	Sample 2
1175-1125 1225-980	1078.32, 1180.46	deformation vibration C-H	Aromatic rings	Sample 2
1310-1290 ~1600	1310.94 1601.21	HRC=CR`H C=C as st	Alkenes	Sample 1
1400-1100	1376.18	C=S st	Thiols	Sample 1, Sample 2, Sample 3
1465-1440	1454.67	C-H st	Aromatic ring	Sample 1, Sample 2, Sample 3
1525-1475	1495.07, 1514.53	C-H st	Aromatic ring	Sample 1
1640-1560	1609.11	N-H bend	Secondary amines	Sample 2, Sample 3
1640-1535 1725-1705	1643.36, 1710.01	C=O st	Ketones	Sample 1
2870-2845	2870	CH_2 sym st	Alkanes	Sample 2, Sample 3
~2900	2900	R-SO-OH	Sulfones	Sample 1
2940-2915	2924.95	CH_2 st asymmetric	Alkanes	Sample 2, Sample 3
2975-2950	2954	CH_3 as st	Alkanes	Sample 1, Sample 2, Sample 3
3095-3010	3023.40	HRC=CH_2 as st	Alkenes	Sample 2
3550-3400	3473.61	O-H bond	Alcohols	Sample 2, Sample 3

There are differences in chemical composition of samples. All samples of pyrolysis oils contain aromatics, olefins, alkanes, sulphur-organic compounds (thiols). It is shown that sample 1 consists of sulfones, sample 2 – sulfoxides. All samples contain oxygenated compounds, but there are ketones in sample 1, aldehyds in sample 2 and alcohols in samples 2, 3. The presence of these compounds may be explained by the thermal degradation of oxygenated components of the tyre, such as stearic acid, extender oils. Nitrogenated compounds are as well present in tyre oils. Some other authors have also detected nitrogenous compounds in tyre pyrolysis oils [12, 14, 15]. Studies of the pyrolysis oils at different temperatures, pyrolysis time and under different atmospheres show different trends in chemical composition of pyrolysis oils obtained [16]. While pyrolysis under inert conditions yields major products comprising alkene, aldehyde and carboxylic acids, under oxidative conditions the main products were alcohol, alkane and aldehyde.

3.3. Results of GC-MS method and elemental analysis

The chemical composition of oils was determined by GC-MS method and elemental analysis. It is important to consider the sulphur-containing components. Sulphur-containing compounds, even in very low concentrations, can result in a foul odour to the oil, thus reducing the quality and economic value of oil (Table 2). Almost coincident results concerning elemental composition of tyre pyrolysis liquids under nitrogen were obtained by [8]. Table 2 shows that there is effect of carrier gas in the elemental composition of the oils.

Table 2. Elemental composition (wt.%) of pyrolysis oils

Sample	**C, %**	**N, %**	**H, %**	**S, %**	**O + others (by difference)**
Sample 1	81.04	0.34	9.82	0.65	8.15
Sample 2	82.01	0.48	7.23	0.72	9.56
Sample 3	82.56	0.62	6.83	0.73	9.26

The GC-MS method is one of the main analytical methods in chemical identification of liquid pyrolysis products due to the high resolution, high sensitivity, good reproducibility, a large number of standard spectra libraries, and the low solvent usage. It is shown that the chemical composition of obtained oils depends on used carrier gas (Fig. 3). It is known that the pyrolysis oils contain valuable monoterpene such as limonene [17]. Limonene has an extremely fast growing and wide industrial applications including formulation of industrial solvents, resins and adhesives, as a dispersing agent for pigments, as a fragrance in cleaning products and as an environmentally acceptable solvent.

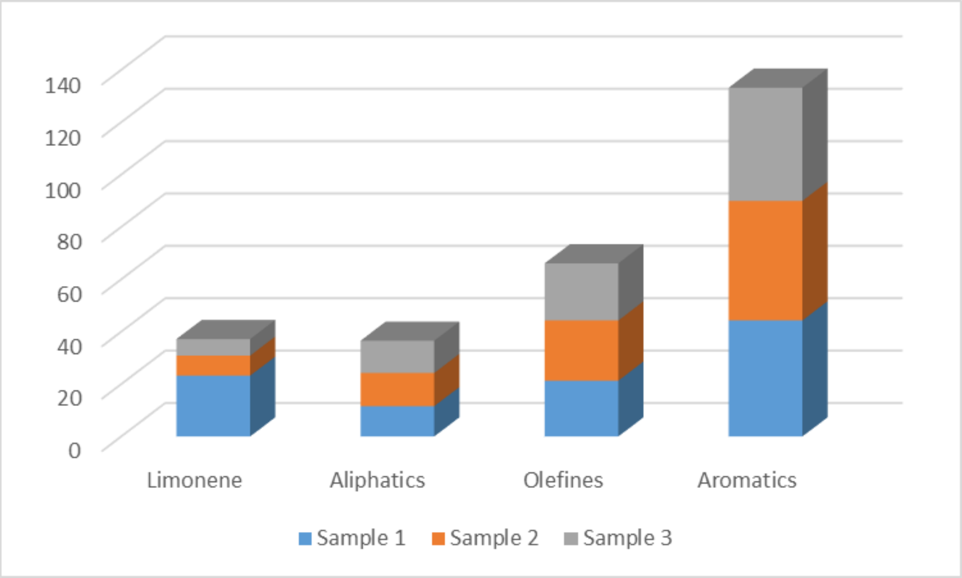

Fig. 3. % content of limonene and different classes of compounds, where Sample 1 is pyrolysis oil obtained under water vapour; Sample 2 is pyrolysis oil obtained under the mixture of water vapour and nitrogen; Sample 3 is pyrolysis oil obtained under nitrogen stream

The tyre pyrolysis oils are a very complex mixture of organic compounds of 8-28 carbons. There are such a great number of compounds in tyre oils that the peak areas are very low. The most abundant product with peak areas around or greater than 6% is limonene. This result is comparables to those obtained by Perondi [12]. For instance they obtained 6.9% limonene under nitrogen.

These concentrations are greater than those obtained by Cunliffe and Williams [3] (3.10% limonene) and those presented by Mastral [15] (4.00% limonene). This volatile hydrocarbon are considered valuable products, which give a potential high value to tyre pyrolysis oils. Limonene is the one present in the highest concentration. Fig. 3 also shows a very important decrease of limonene concentration under water vapour atmosphere (from ≈7 to 23%).

The aromaticity of tyre oils (42.2-44.5%) is due, on the one hand, to the aromatic nature of the source polymeric material, styrene–butadiene rubber, and on the other hand, to ciclation of olefin structures followed by dehydrogenation reactions, which take place during the pyrolysis process.

Pyrolysis process under water vapour results in an oil with more valuable chemical compounds. The results show that lesser content of sulphur-organic compounds was obtained by pyrolysis under water vapour. Moreover, the yield of limonene is increased in oil obtained during pyrolysis under water vapour in comparing with other studied carrier gases. It can be seen that the proportion of aromatics, olefins and aliphatics doesn't significantly depend on carrier gas.

4. CONCLUSIONS

Analysis of the chemical composition of the pyrolysis oil obtained during the pyrolysis of automobile tyre waste under carrier gases such as water vapour, mixture of nitrogen with water vapour and nitrogen was studied. By using different processes and analysing techniques, chemical compounds were detected in the oils. It is found that type of sulphur-containing compounds depends on carrier gas. Aromatic, aliphatic and olefins content was also analysed. Thus, the nitrogen atmosphere leads to the formation of amines. It was established that water vapour as carrier gas gives pyrolysis oil with better characteristics in comparison with other samples such as lower content of sulphur and more content of limonene. Thus, the pyrolysis process under water vapour results in oil with more valuable chemical compounds. Studies of the chemical composition of the waste pyrolysis tyre oils under different atmospheres show different trends in chemical composition of pyrolysis oils obtained. All samples contain aromatic (42.2-44.5%), olefin (21.8-22.3) and aliphatic (11.6-12.4%) fraction, sulfureted (0.65-0.73%), nitrogenated (0.34-0.62%), oxygenated compounds (8.15-9.56%). While pyrolysis under nitrogen conditions the oils contain alcohols, secondary amines and thiols. The pyrolysis under mixture of water vapour and nitrogen leads to formation of aldehydes, sulfoxides and secondary amines. Under water vapour atmosphere ketones and sulfones in pyrolysis oil are formed.

REFERENCES

1. GONZЍALEZ, J. F. Pyrolysis of automobile tyre waste. Influence of operating variables and kinetics study. *Journal of Analytical and Applied Pyrolysis*, 2001, Vol. 58, p. 667-683.
2. KYARI, M. Characterization of oils, gases, and char in relation to the pyrolysis of different brands of scrap automotive tires. *Energy Fuels*, 2005, Vol. 19, p. 1165-1173.
3. CUNLIFFE, A. M., WILLIAMS, P. T. Composition of oils derived from the batch pyrolysis of tyres, *Journal of Analytical and Applied Pyrolysis*, 1998, Vol. 44, p. 131-152.
4. LARESGOITI, M. F. Characterization of the liquid products obtained in tyre pyrolysis. *Journal of Analytical and Applied Pyrolysis*, 2004, Vol. 71, Iss. 2, p. 917-934.
5. BARBOOT, I. M. Optimization of pyrolysis conditions of scrap tyres under inert gas atmosphere. *Journal of Analytical and Applied Pyrolysis*, 2004, Vol. 72, p. 165-170.
6. HYEON, S. H., HYUN, J. P., SUNG, H. P., DONG, J. S. Fast pyrolysis of rice husk under different reaction conditions. *Journal of Industrial and Engineering Chemistry*, 2010, Vol. 16, p. 27–31.
7. GERCEL, F., CITIROGLU, M., SNAPE, C., PUTUN, E., EKINCI, E. Beneficial effects of hydrogen pressure in the pyrolysis of biomass: a study of Euphorbia Rigida. *Fuel Processing Technology*, 1993, Vol. 36, p. 299-305.
8. JAMIL, K., HAYASHI, J. Pyrolysis of a victorian brown coal in helium and CO2 atmosphere. *Journal of Energy & Environment*, 2005, Vol. 4, p. 83-96.
9. COOLEY, S., ANTAL, M. Kinetics of cellulose pyrolysis in the presence of nitric oxide. *Journal of Analytical and Applied Pyrolysis*, 1988, Vol. 14, p. 149-161.
10. LOZHECHNIK, A., SAUCHYN, V. Pyrolysis of rubber in a screw reactor. *Journal of Engineering Physics and Thermophysics*, 2016, Vol. 89, Iss. 6, p. 1482-1486.
11. ISLAM, M. R. Innovation in Pyrolysis Technology for Management of Scrap Tire: a Solution of Energy and Environment. *International Journal of Environmental Science and Development*, 2010, Vol. 1, No. 1, p. 89-96.

12. PERONDI, D. Characteristics of Pyrolysis Products from Waste Tyres and Spent Foundry Sand Co-Pyrolysis Progress in Rubber. *Plastics and Recycling Technology*, 2016, Vol. 32, No. 41, p. 213-240.
13. HRUSHEUSKI, U. U. Determination of polycyclic aromatic hydrocarbons in the pyrolysis products of waste rubber and straw. *Heat and mass transfer-2013*, 2014, p. 113-118. [In Russian].
14. WILLIAMS, P. T. Pyrolysis of waste tyres: A review. *Waste Management*, 2013, Vol. 33, Iss. 8, p. 1714-1728.
15. MASTRAL, A. M. Influence of process variables on oils from tire pyrolysis and hydropyrolysis in a swept fixed bed reactor. *Energy Fuels*, 2000, Vol. 14, p. 739-744.
16. FORTES, C. P., BAUGH, P. J. Pyrolysis–GC/MS studies of vegetable oils from Macauba fruit. *Journal of Analytical and Applied Pyrolysis*, 2004, Vol. 72, p. 103-111.
17. DANON, B. A review of dipentene (DL-limonene) production from waste tyre pyrolysis. *Journal of Analytical and Applied Pyrolysis*, 2015, Vol. 112, p. 1-13.

CYSENI 2019, May 23-24, Kaunas, Lithuania
ISSN 1822-7554, www.cyseni.com

AGING OF THE FAST PYROLYSIS PRODUCTS WITH HIGH WATER CONTENT OBTAINED FROM LIGNOCELLULOSE

N. Iljina, K. Meile, A. Zhurinsh
Latvian State Institute of Wood Chemistry
Dzerbenes 27, Riga, LV-1006 Latvia
Email: n.iljina17@gmail.com

N. Iljina, K. Meile
University of Latvia
Jelgavas 1, Riga, LV-1004 Latvia

ABSTRACT

Fast pyrolysis produces bio-oil, which is well-known for its diverse chemical composition and valuable properties. Bio-oils have several uses for example vehicle fuels or a renewable source of chemicals. However, speaking about the main drawbacks of bio-oil, it is unstable and its instability is characterized by changes in various physico-chemical parameters. When two interlayer insoluble layers are formed, the main products anhydrosaccharides are stable, but there can be observed changes in viscosity, aldehyde and phenol content. In our work, we pay attention to the fast pyrolysis condensate with high water content, which ages creating a precipitate. In the work, we use not only classical analytical methods, but also ultra-high performance liquid chromatography to characterize condensation changes. We did aging experiments at room and elevated temperature conditions, to be able to observe the changes in condensate chemical composition at different temperatures. Among the compounds were identified anhydrosaccharides, aldehydes and acids.

Keywords: Lignocellulose pyrolysis, condensate, liquid chromatography

1. INTRODUCTION

Nowadays, great attention is paid to the use of renewable resources. One such renewable resource is wood from which biomass can be obtained. That biomass can be further transformed during pyrolysis into valuable bio-oil, which has the potential to replace fossil fuels. It should be noted that bio-oil can be widely used not only as a source of energy, but also as a valuable source of chemical compounds, as it contains more than 300 chemicals [1, 2]. The main limitation to the use of bio-oil as an energy source is the need to reduce the oxygen content in them, which is a costly and time-consuming process, while the process of extracting chemicals from bio-oils could be more cost-effective. However, the main difficulties in achieving this goal is the need to develop a strategy to effectively target and separate the target chemical. Highly water-rich bio-oils, which are particularly well suited for the release of chemicals, are often called pyrolysis condensates produced during fast pyrolysis. In contrast, bio-oil compounds, especially sugars and aromatic compounds, are hydrogenated to produce biofuel [3].

Pyrolysis is the thermal decomposition process of biomass without oxygen [4]. This process produces a dark brown, viscous solution. The solution consists of a variety of chemical compounds, mainly due to depolymerization or fragmentation of hemicellulose, cellulose and lignin [5]. However, the potential use of bio-oil is influenced by changes in various physico-chemical properties over time. These changes are particularly important for bio-oils which can potentially be used as biofuels. As is known in bio-oils there are several types of compounds, such as aldehydes, phenols, sugars, alcohols, etc., which have a significant effect on the stability of this solution, as several adverse reactions occur over time [6]. Regardless of the changes in different groups of compounds and physical properties in bio-oils, the elimination of its instability could be one of today's challenges not only in the context of biofuels, but also in the context of the release of chemical compounds.

In the case of pyrolysis solutions, one of the main problems can be the aging of the solution, which results in the formation of two insoluble layers in the solution within 7 days. In previous work, the aging of pyrolysis solutions is characterized by changes in various parameters such as changes in water and viscosity [7], aldehydes [8] or molecular weight [9] distribution. Previous studies made it possible to understand the changes in viscosity and water content over a small period of time, but more precise information could be obtained from gas chromatography/mass spectrometry (GC/MS), gel permeation chromatography (GPC) and Fourier transform infrared spectroscopy (FTIR) data [7, 9-11]. More and more diverse analytical methods are used over time to better characterize ongoing changes, such as the determination of ash content by the thermogravimetric (TGA) method in addition to the methods mentioned in [7], and additional chemical information on bio-oil can be provided by ^{13}C nuclear magnetic resonance (NMR). It should be noted that the composition of bio-oil is very complex, so this method is quite complicated in deciphering directly obtained spectra.

In this work, attention is paid to pyrolysis condensates with a high water content, which are produced in the overheated steam stream, so the condensable products are recovered from the pyrolysis reactor in the form of a diluted water solution. This condensate could potentially be used to produce valuable chemical compounds. In the condensate, changes in aldehydes, dry matter, weak acids and sugars are observed at elevated (80 °C) and room temperature. Mainly using much simpler and more classic analysis methods – potentiometric and iodometric titration and absorption measurements. As well as chromatography methods that allow you to describe in detail the changes in components over time.

2. MATERIALS AND METHODS

Materials. All reagents (acetic acid ≥ 99.8%, sulfuric acid ≥ 95-97%, potassium hydroxide ≥ 85%, potassium iodide ≥ 99.5%, hydroxylammonium chloride ≥ 99.0%, sodium (meta) periodate ≥ 99.8%, sodium thiosulfate from fixanal) were purchased from Sigma and used without further purification

Sample. The condensable pyrolysis products were obtained at LSIWC. Birch chips were treated with diluted sulfuric acid and washed with deionized water. The obtained lignocellulose was ground to particle size < 2 mm. The lignocellulose was pyrolysed in a superheated steam 380-420 °C flow in an entrained flow thermoreactor, after which char was separated in a cyclone, but the liquid products in a condenser.

Bio-Oil Characterizations: The total amount of aldehydes: 2-5 mL of the sample was weighed in a glass weighing bottle with lid, 5 mL of 0.5 M hydroxylamine hydrochloride was added and the solution was stored for 2.5 h, and then titrated with standardised 0.1 M KOH. The titration end point was determined potentiometrically with a glass electrode and an Ag/AgCl reference electrode.

Weak organic acids were determined as acetic acid using potentiometric titration. 2-5 mL of the sample was weighed in a beaker, 25 mL deionized water was added and the solution was titrated with standardised 0.1 M KOH. The titration end points were determined potentiometrically with a glass electrode and an Ag/AgCl reference electrode.

The dry matter of non-volatiles was determined by evaporating the 20-25 mL samples at 103 °C until a constant mass of the dry residue was reached.

Sugars: The sample was weighed 2-3 mL in a 25 mL volumetric flask and diluted with deionized water. 5 mL aliquots were taken and transferred to two 25 mL volumetric flasks. One flask was diluted with deionized water and 5 mL of 15% sulfuric acid was added to the contents of the second flask and placed in a thermostat at 120 °C for 2.5 h. After hydrolysis, the flask was cooled and diluted with deionized water. 2 mL of solution was withdrawn from the flask and transferred to a weighing bottle with a cap. 1 mL of $NaIO_4$ was added to the samples and 0.2 mL of 15% sulfuric acid was added to the non-hydrolyzed sample. The prepared samples were placed in the thermostat at 40 °C for 4 h. Afterwards 5 mL 10% ammonium molybdate was added, after 15 min 1 mL acetic acid and 1 mL 10% KI was added. The released iodine was titrated with standartised 0.1 M $Na_2S_2O_3$ with starch as a visual indicator. The content of sugars was calculated as levoglucosan.

UV absorption: 1 mL sample was weighed into a 25 mL volumetric flask and diluted with deionized water. The absorbance of the prepared solution was measured with a Perkin Elmer Lambda 25 UV/VIS Spectrometer at 275 nm wavelength in a 1 cm cuvette, against deionized water.

Precipitation. 10 mL of cooled pyrolysis condensate was flushed into a pre-weighed dish with a cap and left to stand at room temperature. After a certain period of time, the condensate was poured off and the precipitate formed on the walls of the dish was weighed.

Ultra-high performance liquid chromatography analysis. Waters Acquity UPLC system with a CSH Phenyl-Hexyl column (1.7 µm, 2.1 × 100 mm) at gradient conditions 0.1% formic acid in water:acetonitrile 90:10 0-7 min, 10:90 7-8 min and 90:10. Flow rate 0.4 mL/min. All solutions were filtered through Kinesis syringe filters (0.22 µm pore size) before the injection. Waters photodiode array detector was used for quantitative analysis of the phenols (at 275 nm wavelength) and a Waters quadrupole mass spectrometer in positive ESI with 12 V cone voltage, was used for qualitative analysis.

Size exclusion chromatography analysis. The distribution of the molecular weight of the compounds found in the pyrolysis condensates was analysed by Waters Advanced Polymer Chromatography size exclusion chromatography system – quaternary pump, autosampler, column oven, photodiode array un refractive index detector. The condensates and the precipitates were analysed with Waters Acquity APC XT-series columns: APC XT 45 (4.6 × 150 mm, 1.7 µm), APC XT 200 (4.6 × 150 mm, 2.5 µm), APC XT 450 (4.6×150 mm, 2.5 µm) with tetrahydrofuran as the eluent. The flow rate was 0.6 $mL \cdot min^{-1}$, the column and RI detector temperature was 40 °C, the injection volume was 20 µL. Polystyrene standards were purchased from Sigma-Aldrich (Mw 266-21200 $g \cdot mol^{-1}$) were used for calibration.

3. RESULTS AND DISCUSSIONS

Condensate aging was studied for one year. During this period, the most significant concentration changes are observed in the first 3 months and results are shown in Fig. 1.

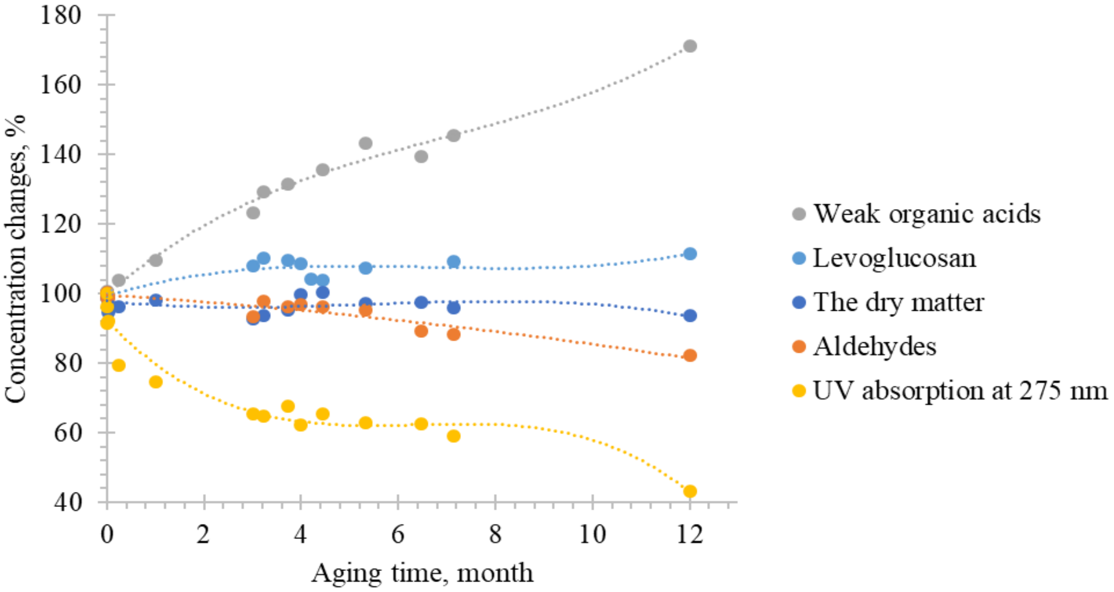

Fig. 1. Pyrolysis condensate aging at room temperature for one year

First 3 months, the dry matter content decreased by 7.4%, while the aldehyde content decreased by 6.6%, UV absorption indicating changes in phenolic compounds decreased by 34.4%. Meanwhile, the weak acid content increased by 23.3 %. However, the acid content increased 1.7 times during the year, while the amount of aldehydes and dry matter decreased by 1.2 and 1.1 times, respectively. Absorption increased 2.3 times. Groups of selected compounds do not change significantly overnight.

Often, the literature also describes aging of bio-oil at elevated temperatures, for example, [13] authors claim that the bio-oil obtained from the change in viscosity of oak at 60 °C after 4 days is the same as bio-oil storage at 37 °C for three months. Hence, the expected change in bio-oil aging at room temperature is expected to be comparable during the accelerated aging of bio-oil at 80 °C. The results obtained are shown in Fig. 2.

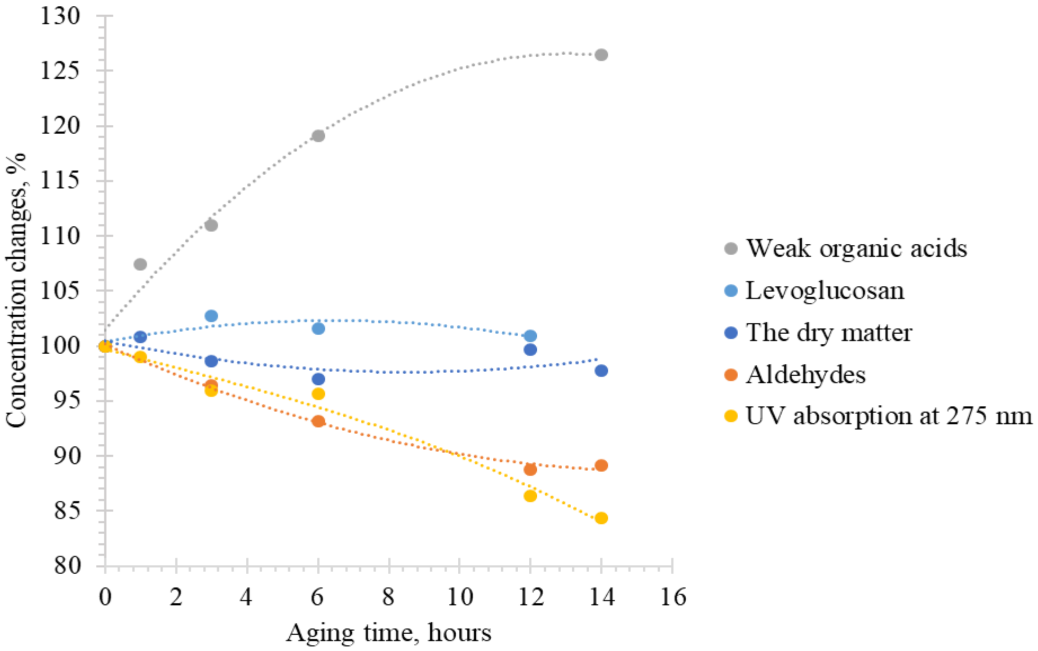

Fig. 2. Pyrolysis condensate aging at 80 °C temperature for 14 hours

In an accelerated aging experiment at elevated temperature (80 °C), the same trend is observed as at room temperature, namely, the aldehyde and dry matter content as well as the UV absorption decreases while the content of weak acids increases. It should also be noted that changes that occurred within 6 hours in the accelerated aging experiment are also observed at room temperature after 3 months of condensation storage. In terms of sugar content change in aging experiments, it can be seen that their content does not change significantly over a longer period of time (small fluctuations in the results can be explained by the dilutions made during the experiment and the transfer of samples), which also corresponds to the information found in [14] literature.

When the condensate is stored at room temperature, precipitation is observed. To check what kind of compounds are precipitated at room temperature over time, the precipitate that falls out of the pyrolysis condensate is stored for 1 year (shown in Fig. 3.).

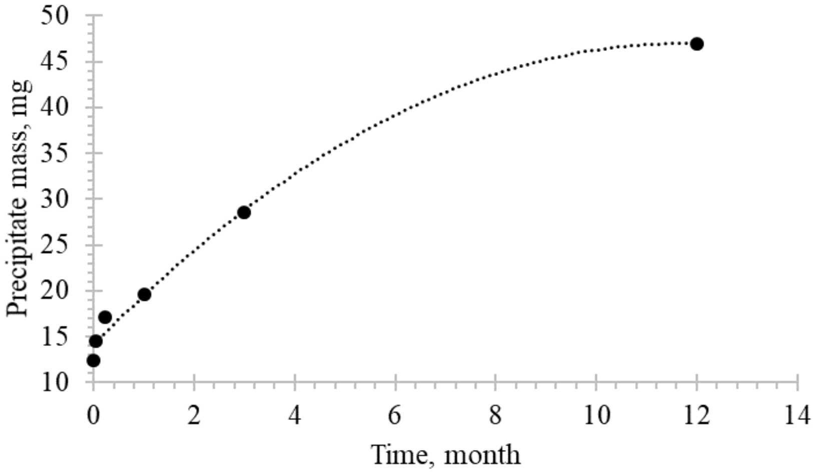

Fig. 3. Formation of precipitate in pyrolysis condensate at room temperature

Within 3 months, 28.6 mg of sediment is observed, of which nearly half falls during the first days. After 3 months, the amount of precipitation decreases and reaches 47 mg per year. According to Ultra-high performance liquid chromatography, there are no significant changes in the phenolic and furan type compounds within 3 months. For example, 5-HMF increases by 7%, while furfural and vanillin decrease by 10% and 5% respectively. It should also be mentioned that after a year vanillin and other phenols have already turned into other compounds (Fig. 4.).

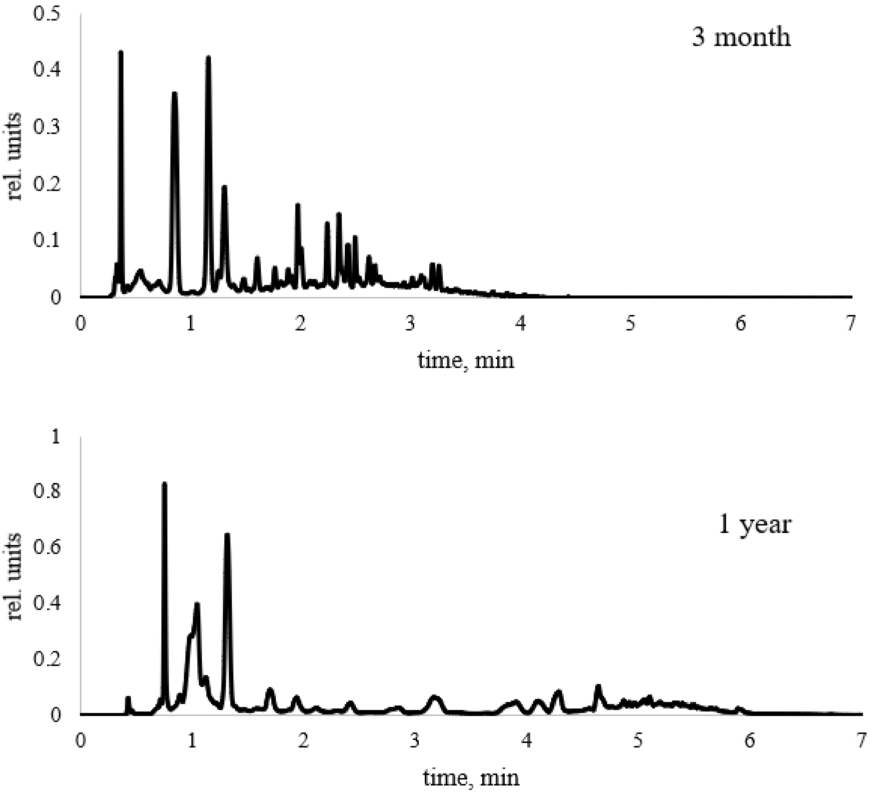

Fig. 4. UHPLC chromatogram by condensation at room temperature for 3 months and a year

Literature [12] shows that acids and various ketones in pyrolysis oils prevent phase separation. However, aldehydes and ketones have a tendency to react or decompose into other products, thereby forming high molecular compounds.

To test this claim, it is weighed during certain time periods established sludge pyrolysis condensate, which is then analyzed by Size Exclusion Chromatography. It should also be noted that the molecular weights of the compounds present in the bio-oils are very different, so they mostly describe the molecular weight ranges. By studying the pyrolysis condensate precipitate with the SEC-RI method, it was found that their molar mass was 200-4500 $g \cdot mol^{-1}$ with a peak at 800 $g \cdot mol^{-1}$. Comparing the solutions stored at the same time as the precipitate formed, it is determined that their molar mass is no greater than 3200 $g \cdot mol^{-1}$ with a peak at 400 $g \cdot mol^{-1}$. Thus, it can be concluded that the compounds whose molar mass can be considered to be medium are precipitated. Both types of samples also show higher molar mass (> 20000 $g \cdot mol^{-1}$), however, they did not exceed 7% of the total lane in the chromatograms. According to the data provided by [10] at work, molecular weights above 1000 $g \cdot mol^{-1}$ are significantly increased during aging.

4. CONCLUSIONS

The instability of bio-oil obtained during pyrolysis can also be explored using classical methods of analysis that do not require expensive hardware and large amounts of reagents. During the aging of bio-oil, the most significant changes are observed in the content of aldehydes and phenols, which only proves the high propensity of these compounds to engage in various polymerization reactions. Thus, increasing the amount of high molecular compounds in pyrolysis condensates. Pyrolysis condensates with increased water content are predominantly medium molar compounds, indicating that molar masses are not the determining factor in their water solubility. It should be concluded that the changes in sugars in condensates are negligible and would not significantly affect the outcome of their release. By contrast, the total amount of acids, aldehydes and phenols depends directly on the condensate storage conditions.

ACKNOWLEDGMENTS

This research was supported by the ERDF project No. 1.1.1.1/16/A/010’’Developing an innovative technology for producing levoglucosenone from lignocellulose’’.

REFERENCES

1. De WILD, P. J., REITH, H., HEERES, H.J., Biomass pyrolysis for chemicals. *Biofuels*, 2011, Vol. 2, No. 2, p. 185-208.
2. LIU, C., WANG, H., KARIM, A. M., SUN, J., WANG, Y. Catalytic fast pyrolysis of lignocellulosic biomass. *Chem. Soc. Rev.*, 2014, Vol. 43, p. 7594-7623.
3. XUN, H., MOURANT, D., GUNAWAN, R., LIPING, W., YI, W., LIEVENS, C., CHUN-ZHU, L. Production of value-added chemicals from bio-oilviaacid catalysiscoupled with liquid–liquid extraction. *RSC Adv*., 2012, Vol. 2, p. 9366-9370.
4. SAFDARI, M., RAHMATI, M., AMINI, E., HOWARTH, J. E., BERRYHILL, J. P., DIETENBERGER, M., WEISE, D. R., FLETCHER, T. H. Characterization of pyrolysis products from fast pyrolysis of live and dead vegetation native to the Southern United States. *Fuel*, 2018, Vol. 229, p. 151-166.
5. CZERNIK, S.; MAGGI, R.; PEACOCKE, G.V.C. in: BRIDGWATER, A. V. (Ed.), Review of Methods for Upgrading Biomass-Derived Fast Pyrolysis Oils, in *Fast Pyrolysis of Biomass: A Handbook*, Vol. 2, Newbury, UK: CPL Press, 2002. 424 p. ISBN 1-872691-47-1
6. CORDELLA, M., BERRUECO, C., SANTARELLI, F., PATERSON, N., KANDIYOTI, R., MILLAN, M. Yields and ageing of the liquids obtained by slow pyrolysis of sorghum, switchgrass and corn stalks. *J. Anal. Appl. Pyrolysis*, 2013, Vol. 104, p. 316-324.
7. ALSBOU, E., HELLEUR, B. Accelerated Aging of Bio-oil from Fast Pyrolysis of Hardwood. *Energy Fuels*, 2014, Vol. 28, No. 5, p. 3224-3235.

8. BLACK, S., FERRELL, J. R. Determination of Carbonyl Groups in Pyrolysis Bio-oils using Potentiometric Titration: Review and Comparison of Methods. *J. Vis. Exp.*, 2017, Vol. 120, p. 1-5.
9. REN, S., Ye, X. P. Stability of crude bio-oil and its water-extracted fractions. *J. Anal. Appl. Pyrolysis*, 2018, Vol. 132, p. 151-162.
10. CHEN, D., ZHOU, J., ZHANG, Q, ZHU, X. Evaluation methods and research progresses in bio-oil storage stability. *Renew. Sust. Energ. Rev.*, 2014, Vol. 40, p. 69-79.
11. MENG, J., MOORE, A., TILOTTA, D. C., KELLEY, S. S., ADHIKARI, S., PARK, S. Thermal and Storage Stability of Bio-Oil from Pyrolysis of Torrefied Wood. *Energy Fuels*, 2015, Vol. 29, No. 8, p. 5117-5126.
12. *ResearchGate*. Siriwardhana (M.): Aging and Stabilization of Pyrolitic Bio-Oils and Model Compounds. Western University, 2018- [referred on the 12th of February in 2019 y.]. Link to the internet < https://www.researchgate.net/publication/322951082_Aging_and_Stabilization_of_Pyrolitic_Bio-Oils_and_Model_Compounds >.
13. CZERNIK, S., JOHNSON, D. K., BLACK, S. Stability of wood fast pyrolysis oil. *Biomass Bioenergy*, 1994, Vol. 7, p. 187-192.
14. JOSEPH, J., RASMUSSEN, M. J., FECTEAU, J. P., KIM, S., LEE, H., TRACY, K. A., JENSEN, B. L., FREDERICK, B. G., STEMMLER, E. A. Compositional Changes to Low Water Content Bio-oils during Aging: An NMR, GC/MS, and LC/MS Study. *Energy Fuels*, 2016, Vol. 30, p. 4825-4840.

MEASUREMENT OF THE PARTICLES VELOCITY AND THERMAL EROSION EFFECT ON INCLINED BARRIER IN A SUPERSONIC HETEROGENEOUS PLASMA FLOW

D. V. Nestsiarovich
A. V. Luikov Heat and Mass Transfer Institute
Brovki str. 220072 Minsk – Belarus
Email: dmitry.nesterovith@gmail.com

ABSTRACT

The Mars study by autonomous descent vehicles is one of the most important tasks of space exploration. It is known that the atmosphere of the Red Planet contains a large amount of suspended particles, which significantly affect the ablation of heat-shielding material. To study the impact on the materials when entering the planet atmosphere at hypersonic speeds is necessary to create a hypersonic heterogeneous flow with constant control of its gas-dynamic parameters over a long time interval. Such high-enthalpy flows are typically created by passing the gas through an arc of a plasma torch and the subsequent output from converging or diverging nozzle.

In this research we used an electric arc gas heater of a linear scheme with gas-dynamic and magnetic stabilization of the jet. As a dispersed phase, SIO_2 particles with a size of 14.2 μm were used. As a test samples of heat-shielding material, flat plates of asbestos-textolite and fluoroplastic, installed at an angle of 30 degrees to the flow axis, were used. The particle velocity vector field was measured using the PIV diagnostic method using a high-speed CCD camera with an image amplifier and a dual-pulse Nd: YAG laser.

The measurement results show the applicability of the proposed method for estimating the flow parameters in a wide range of operating modes of an electric arc gas heater and at the power of the plasma torch of the order of 1.5 kW, the time-averaged velocity of the dispersed phase reaches values of 2000 m/s. It has been established that the addition of dispersed SiO_2 particles with a mass concentration of ≈ 0.1 to a uniform plasma flow leads to a significant increase in the linear destruction rate and heat flux on the surface of the heat-shielding material.

Keywords: two-phase plasma flow visualization, supersonic plasma flows, particle image velocimetry, electric arc gas heater, plasma, heat-shielding material

1. INTRODUCTION

The intensive development of technologies is associated with the growth of the thermodynamic parameters of the working bodies of various devices, in particular, the effect of high-temperature multiphase flows (gas – solid particles, gas – liquid particles, etc.) on the material of the structural elements of turbines, rocket engines, thermal protection of descent vehicles and other power setups operating in high-speed and high-temperature heterogeneous flows. In this regard, the studies related to the organization of such flows with given characteristics of the speeds of the dispersed phase, the concentration of particles in the flow, their size, heat flux, etc. are of great interest for practice.

These issues are especially relevant when assessing the performance of thermal protection of rocket and space technology products both when landing descent objects on other planets, for example, Mars, and when flying in the Earth's atmosphere [1, 2].

Thermal protection of spacecraft for various purposes is mainly based on the use of passive means in the form of entrained thermal protective coatings. The destruction of materials occurs with the absorption of heat when exposed to thermal power loads and is accompanied by complex physicochemical processes on the surface of the material and in the shock layer. Protection of the product from high-temperature plasma exposure is provided as a result of ablation (ablation) from the working surface of the thermal protection of a part of the coating and preservation of subsequent layers of material as thermal insulation. This reliable and effective method of protecting products is widely used in rocket and space technology when the surface temperature of a thermal protective coating (TPC) exceeds 1.300 K [3, 4]. However, for practice in this case, it is especially important to know the behavior of the heat-shielding coating under such heat load and gas flow rates with the presence of a dispersed phase of ~1–5 km/s in velocity, since in this case, ablation of the coating material increases significantly compared with a single-phase plasma jet [5, 6].

2. METHODOLOGY

Electric arc gas heaters are the only way to create high-enthalpy supersonic flows for a long period of time [7]. Such flows are necessary for modeling the conditions of impact on materials when descent vehicles enter the atmosphere at hypersonic speeds. The high-enthalpy flow in the plasma torch is created by the passage of gas through an arc discharge and the subsequent exit through a nozzle. The study of the parameters of high-temperature two-phase velocity flows and their thermal erosion effect on the structural elements of the thermal protection system is of great interest for practice. Diagnostics of such two-phase flows includes measurements of temperature, density, gas velocity, temperature and velocity of various size particles, particle size distribution, mass and volume concentration of particles, determination of their phase composition, etc.

To date, it has been shown that heterogeneous flows affect the ablation of heat-shielding materials, while its value largely depends on the kinetic energy of the dispersed phase. In this regard, one of the main issues is the experimental study of the ablation of heat-shielding materials in conditions close to natural. This, in turn, requires the creation of heterogeneous high-temperature flows given by thermal and aerodynamic parameters and their thorough diagnostics (determination of heat flux, stagnation pressure, gas flow rates and the dispersed phase (particles), their size, temperature, etc.).

The purpose of this work was to experimentally study the interaction of a two-phase supersonic plasma flow with heat-shielding materials. A detailed understanding of the mechanisms of interaction of such flows with heat-shielding materials is possible only on the basis of improved methods for measuring gas and particles velocities, heat flux and temperature of the heat-insulating material.

2.1. Experimental setup

In this paper, we studied a two-phase flow formed by an electric arc gas heater of a linear scheme with gas-dynamic and magnetic stabilization of an arc discharge (Fig. 1, Table 1). This type of plasma torches is characterized by a wide variety of electrode configurations.

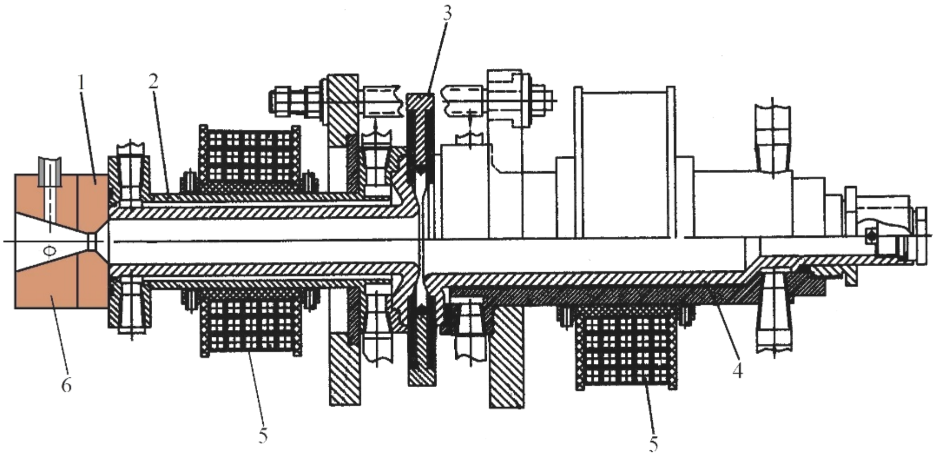

Fig. 1. Diagram of the design of the plasma torch EAGH(Electrical Arc Gas Heater) 1.2: 1 – nozzle, 2 – anode, 3 – gas ring, 4 – cathode, 5 – water-cooled solenoid, 6 – orifice

Table 1. Parameters of the experimental stand

Parameter	Value
Electrical power EDPG, kW	from 200 to 1500
Power supply voltage, kV	up to 2.3
Arc current, kA	up to 1
Mass-average enthalpy of air, MJ / kg	15–20
Pressure in the electric arc chamber, bar.	19

For the operation of the plasma torch almost any gases can be used. The equipment necessary for the operation of the plasma torch includes a high-voltage power source, a gas supply system and a liquid cooling system.

The maximum test duration is 15 seconds. The design of this plasma torch allows to install nozzles of various configurations at the exit from the discharge chamber.

To ensure a supersonic gas outflow rate a separate nozzle unit and orifice for the injection of the dispersed phase were installed. Schematic images of the blocks are presented in Fig. 2.

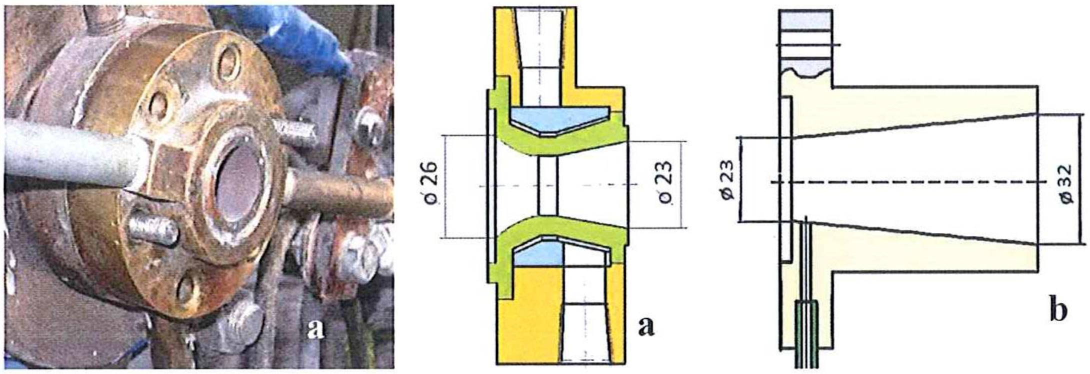

Fig. 2. Schematic representation of the nozzle (a) and nozzles
(b) for the injection of the dispersed phase in a supersonic flow

In the course of the experiment, the dispersed phase was fed through the channels into the supersonic plasma flow from an injector-type metering device specially designed to work with EAGH at elevated pressure in the discharge chamber. As a dispersed phase, SiO_2 particles with a determining size of 14.2 µm were used.

2.2. Measurement of the velocity field of the dispersed phase

To measure the velocity of the dispersed phase, the PIV-method was used. To register the flow, a “laser knife” was created using a two-pulse Lotis Tii LS-2134D laser. The wavelength of the emitted light is 532 nm. The “laser knife” on the plasmatron axis made it possible to obtain data from an area 120 mm wide. The filming was carried out with a high-speed PCO Dicam camera in two-frame mode with external synchronization relative to laser flashes. To suppress the plasma glow an interference filter was installed in front of the camera lens. Fig. 3 shows the experimental design.

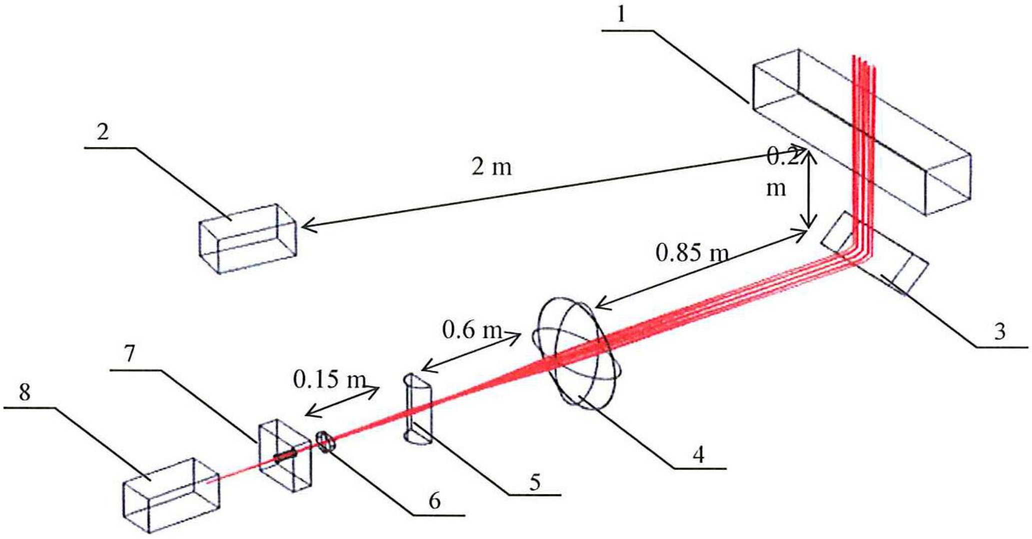

Fig. 3. Experimental scheme: 1 – high-temperature plasma flow, 2 – high-speed camera, 3 – mirror, 4 – spherical collecting lens, 5 – a cylindrical collecting lens, 6 – cylindrical diverging lens, 7 – diaphragm, 8 – laser

2.3. Measurement of heat erozion effect and heat flux

To measure the heat flux, a flat wall was set at a distance of 140 mm from the plasma torch nozzle at an angle of 30° to the jet axis. The motivation for installing such an angle is that in most cases the thermal protection is installed in a similar position. The two-phase flow expires through a nozzle at a pressure in the arc chamber of $10 \cdot 10^5$ Pa and a power output of 1.250 MW on the electric arc. The scheme of the experiment for measuring the thermal discharge effect is shown in Fig. 4.

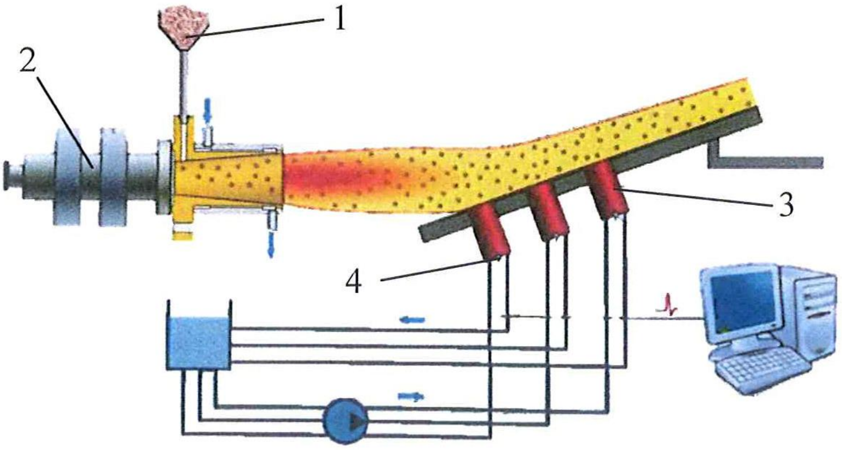

Fig. 4. Experimental diagram: 1 – particle dispenser, 2 – plasma torch, 3 – calorimeter, 4 – thermocouple

The heat flux was measured using uncooled regular mode sensors. The schematic representation and an image of the sensors after testing are shown in Fig. 5 copper calorimeters were used as heat-receiving elements, in which the temperature of the protected end was measured with a chromel-copel thermocouple.

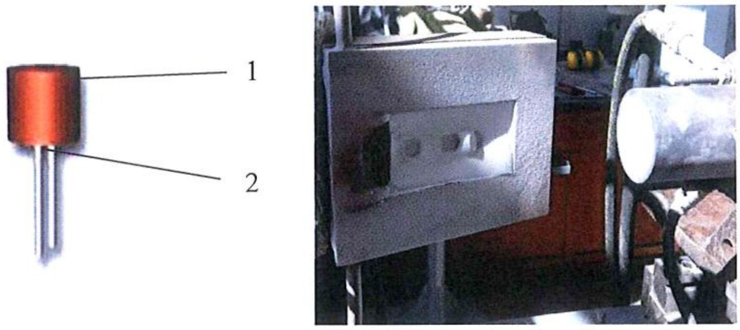

Fig. 5. Schematic representation of the sensor: 1 – a copper “penny”,
2 – chromel-copel thermocouple installed at the end

3. RESULTS

As the result of the experiment 30 pairs of images of the dispersed phase were obtained. The frequency of pairs of images was 10 Hz. The exposure time of each frame was 100 ns, and the time between frames of the pair was 500 ns.

Fig. 6 shows a characteristic pair of photographs of a flow around a plate by a supersonic axisymmetric jet with SiO_2 particles.

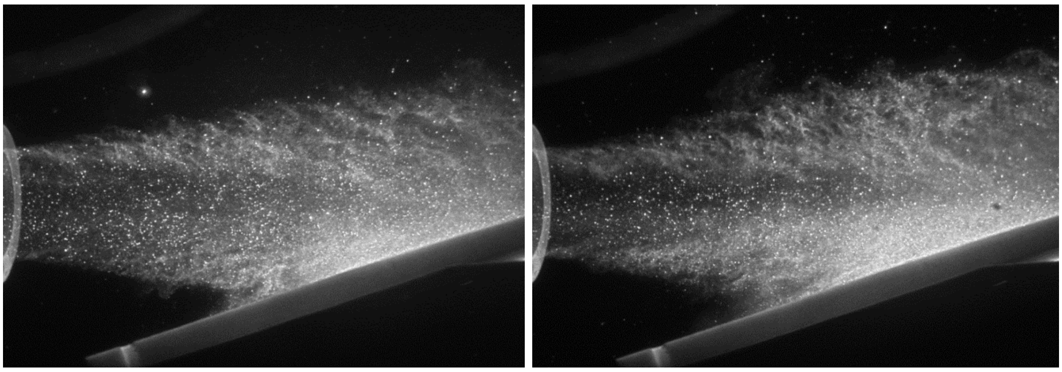

Fig. 6. The flow of a supersonic heterogeneous jet onto an oblique barrier

The averaged vectorial velocity fields obtained by the PIV method presents at Fig. 7, where the abscissa axis is the distance from the nozzle exit.

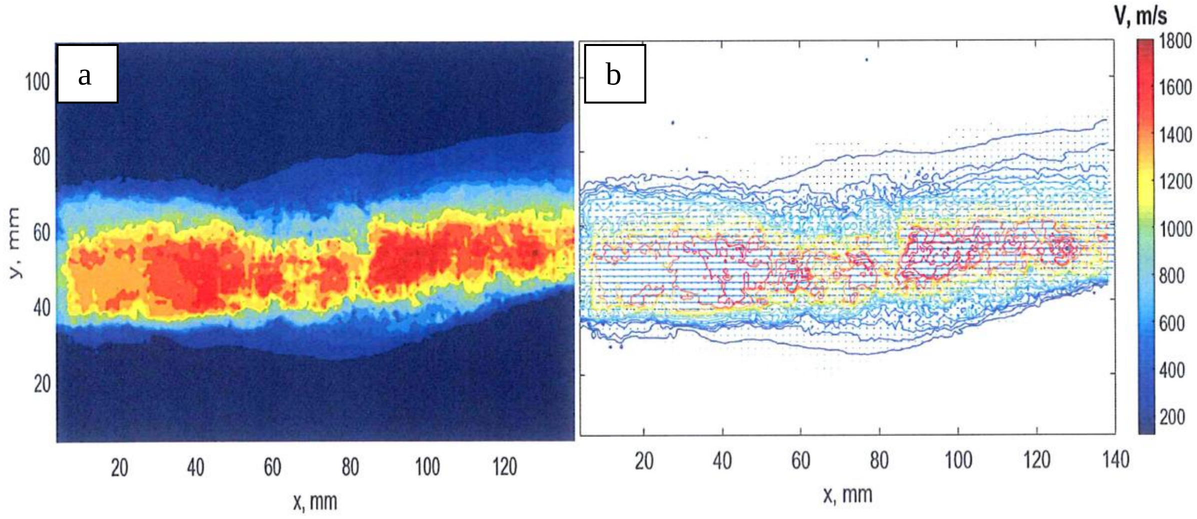

Fig. 7. Averaged vectorial velocity field of particles in a plane passing through the axis of symmetry of the jet with isolines (a) and the velocity modulus field (b), the dotted line is the barrier surface

The results of measuring the heat fluxes in a two-phase high-speed jet are shown in Fig. 8. The heat flux on the fluoroplastic plate in case of a two-phase jet increases by about 40%. In the case of the copper plate, the change is not significant and averages 10%.

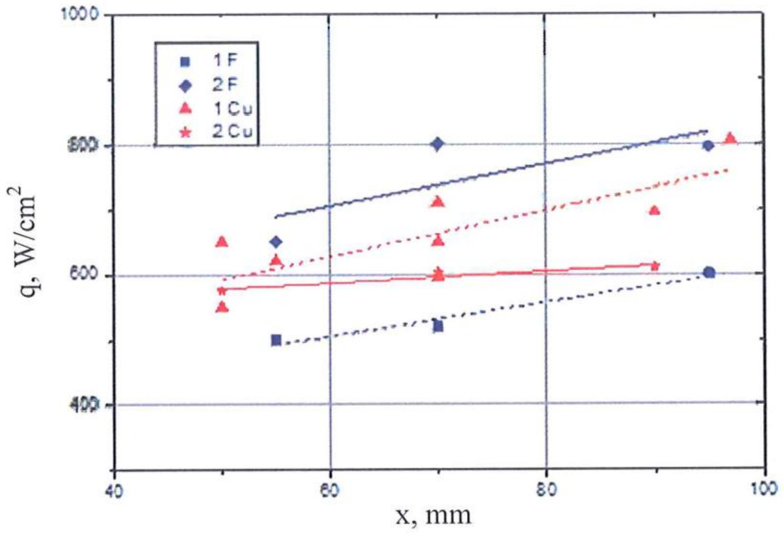

Fig. 8. Heat flow in single (1) and two-phase (2) jet on Fluoroplastic (F) and copper (Cu) plates

Under similar conditions, the destruction of samples from fluoroplast, textolite, asbotextolite in a two-phase high-speed jet was studied. Fig. 9. shows photographs of the samples before and after the experiment.

A charred layer is present on the surface of textolite samples. After testing in a two-phase flow, the charred layer is absent.

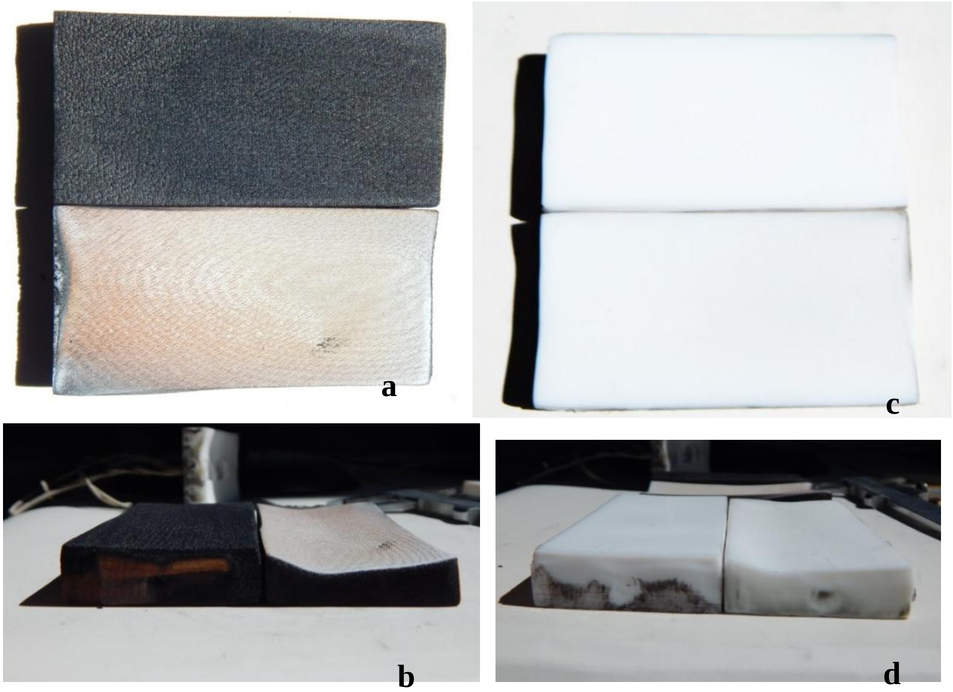

Fig. 9. Textolite sample is **a** (top – flow without particles, bottom – flow with particles),
b (left – flow without particles, right – flow with particles),
fluoroplastic is **c** (top – flow without particles, bottom – flow with particles),
d (left – flow without particles, right – flow with particles)

The obtained value of the linear destruction rate along the sample axis for all materials significantly increases with the injection of dispersed SiO_2 particles into the homogeneous flow. Fig. 10 shows the linear ablation (destruction) rate of materials in different flows. It should be noted that asbestextolite, which has a low linear ablation rate in a single-phase flow, in a two-phase flow was destroyed almost at the same rate as other materials.

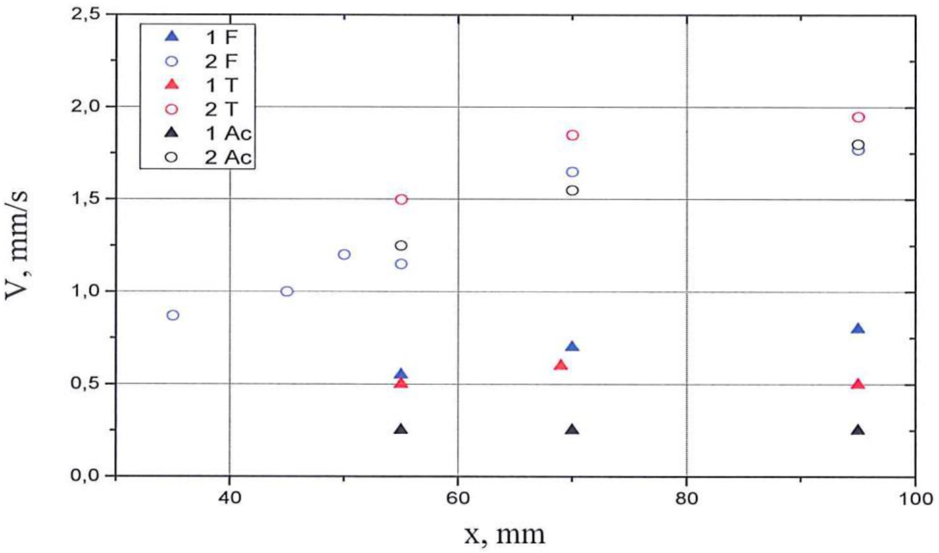

Fig. 10. Linear ablation (destruction) rate of materials in one- (1) and two-phase (2) flows (F – fluoroplastic, T – textolite, Ac – asbestextolite)

In a two-phase flow, the average mass destruction rate of fluoroplastic samples increased 2.1 times, textolite – 3.1, and asbestos textolite 3.3 times.

4. CONCLUSIONS

The experimental testbed was developed for measuring the velocity field of the dispersed phase of the plasma flow of an electric arc gas heater using the PIV diagnostic method. Software algorithms for automatic processing of experimental data based on the use of statistical methods were prepared.

For a stable supersonic mode of operation, heat flux values were measured at an barrier plate set at a distance of 140 mm from the plasma torch nozzle at an angle of 30° to the jet axis in single-phase and two-phase flows. The heat flux on the barrier plate significantly depends on the conditions of interaction of the jet with the barrier and the history of the boundary layer. Its value depends both on the ablation of the heat-shielding material and on the chemical reactions that take place in the boundary layer in front of the sample.

It is shown that in case of supersonic heterogeneous plasma flows with a mass concentration of particles ≈ 0.1, the ablation velocity of the heat-shielding coating as a result of erosion at SiO_2 particles velocities of $\approx$ 1800–2000 m/s can increase by 2–3 times as compared to ablation in a homogeneous jet.

The results of this work will allow us to explore new promising heat-shielding materials for aerospace vehicles under conditions that simulate natural ones. This will allow to obtain reliable data to create a reliable system of thermal protection of spacecraft when operating in a dusty atmosphere.

REFERENCES

1. SAUVAGE, N., TRAN, P., MONTOIS, I., PIROTAIS, D. CEA/CESTA and EADS ST Common Approach of Particles Impact Effect on Ablative Material Application to Mars Reentries. Proceedings of the 5th European Workshop on Thermal Protection Systems and Hot Structures. 17–19 May 2006, Noordwijk, The Netherlands.
2. MARRAFFA, L. Hypersonic technologies and atmospheric entry missions at ESA. Proceedings of 1st international symposium Hypersonic Flight. 30 June 2014, Rome.
3. НИКИТИН, П. В. *Тепловая защита*. М.: Изд-во МАИ, 2006, 512 с.
4. ПОЛЕЖАЕВ, Ю. В., ФРОЛОВ, Г. А. *Тепловое разрушение материалов*. Киев: ИПМ НАНУ, 2005, 288 с.
5. BUGEL, M., REYNIER, P., SMITH, A. Review of European Aerodynamics and Aerothermodynamics Capabilities for Sample Return Missions. Proceedings of the 6th European Symposium on Aerodynamics for Space Vehicles. November 2008, Versailles, France, ESA SP-658.
6. BUGEL, M., REYNIER, P., SMITH, A. Survey of European and Major ISC Facilities for Supporting Mars and Sample Return Mission Aerothermodynamics and Tests Required for Thermal Protection System and Dynamic Stability. *International Journal of Aerospace Engineering*, 2011, V. 2011, Article ID 937629.
7. MOSTAGHIMI, J. Thermal Plasma Sources: How Well are They Adopted to Process Needs? *Plasma Chemistry and Plasma Processing*, 2015, Vol. 35, No. 3, p. 421–436.

CYSENI 2019, May 23-24, Kaunas, Lithuania
ISSN 1822-7554, www.cyseni.com

Na*, K*, Ca* RADICALS EMISSION AND ASH-RELATED ISSUES DURING COMBUSTION OF BIOMASS

M. Sadeckas, N. Striūgas
Lithuanian Energy Institute
Breslaujos str. 3, LT-44403 Kaunas – Lithuania
Email: Marius.Sadeckas@lei.lt

ABSTRACT

Nowadays the demand of biomass extensively grows year by year. Biomass products are beneficial because they often are waste products from forestry and wood industries. Therefore, biomass is often locally available and easy and relatively cheap. Nevertheless, the inorganic constituents of biomass cause several problems during combustion. The biggest challenges occurring during biomass combustion is related with an ash issue. Flame and combustion monitoring using chemiluminescence method has received a lot of attention for combustion sensing and diagnostic applications in various fields. In various reaction zones emission of radicals are different and can be indicated as important combustion parameters. The most important problem is the formation of aerosols during biomass combustion, which might cause slagging, fouling or agglomeration formation on boilers walls. These problems emerge costly shutdowns of power plants for unexpected maintenance. In general, it has been observed that ash deposition and corrosion problems are more common during combustion of biomass fuels with high alkali contents, such as straws and wood. Similarly, woody biomass fuels generally contain lower levels of chlorine, sodium and potassium than most other biomass fuels, corrosion effect also occurs in wood-fired systems. To prevent mentioned problems, early control of alkali release is necessary and online detection techniques might help.

This study focuses on the measurement of selected alkali metals emission during the combustion of single biomass pellets doped with different amounts of Na, Ca, and K using a spectroscopy method. A biomass washing, and soaking procedure was used to demineralize and to dope the biomass samples with different concentrations (0.5%, 2%, 5%) of Na, Ca, and K. The experimental results show that the emission intensity of K* was noticeable strong in higher temperature zones from 1000 °C to 1200 °C in wood case, and 750–900 °C during straw pellet combustion. In Na* wood combustion case, the highest radiated intensity was shown near 400–500 °C and 900–1000 °C. Calcium keeps stable and does not evaporate under given conditions and shows extra stability during wood and straw combustion.

Keywords: biomass, combustion, spectroscopy, alkali-induced slagging, agglomeration

1. INTRODUCTION

Biomass is an widely spread future fuel and is used in innumerable applications as a renewable energy source. As this waste comes from forest residues, agriculture organic matter, its environmental and economic feasibility have made it a competitive alternative to traditional solid fossil fuels. Accordingly, biomass is a renewable energy with immense potential. Used every day by more and more companies, it aims to cover the high demand for energy that society demands day after day presenting a solution to energy problems, although it also is inconvenient due to ash production when thermochemical processes are applied to produce energy. Lately, the use of biomass for heat and power production became very meaningful [1]. With the growth of the biomass usage, the quality of the feedstock for energy production becomes an issue when the feedstock variety increases. During the thermal degradation of biomass, a number of chemical or physical transformations occur, and it is not easy to forecast the whole combustion process when the change of fuel composition varies. The combustion of agro-biofuels poses a significant challenge due to the typically high amount of ash, specifically alkali chlorides, which may lead to the corrosion of the boiler’s surfaces. The characteristics of biofuels influence directly the combustion process and ash slagging problems can occur [2].

Likewise, the fly ash deposited on the heat transfer surfaces, economizers, super-heaters cuts down the efficiency of the boilers. The ash content, moisture content and particle size are some of the primary biomass characteristics that afect the quality of combustion process [2]. Especially, the potassium amount in the biomass fuel is an indicator of chances to form the deposits in the surface of the boiler [3].

Burning crummy quality featuring biofuels leads to ash slagging problems [4]. Fly ash deposited on the heat transfer surfaces of the boiler, furnace brick walls. These things negatively effect the performance of the boilers.

Also, the combustion of biomass mixtures with straw or other agricultural crops, where is more ash contains, many alkali chloride which causes corrosion of boiler surfaces. Humidity, mineral impurities, biomass particle size – it is one of the main characteristics of biofuels which determines the quality of combustion and combustion equipment work. The potassium content in biofuels is one of the main characteristics that determine the ash and plaque formation. Therefore, chemiluminescence method was used to determine the straw, wood, sludge during combustion emissions of potassium, sodium, calcium elements ion intensities [5].

For instance, potassium biggest radiating intensity seen at the beginning of combustion, then in later combustion stages this quantity proportionally decreasing [6]. Potassium is not the only challenging inorganic, others include sodium and calcium are important too [2]. Biomass thermal decomposition occurring regularities lack of data encourages researchers to engage in the global experimental and numerical studies.

The main goal of this work is to investigate the emissions of three important alkali radicals K*, Na* and Ca* of wood and straw pellets during combustion under selected temperatures.

In this work, wood and straw biomass pellets were used. The main properties of raw wood and straw is presented in previuos work [7]. Two types of biomass that are wood and straw were used to a „washing“ procedure to remove the origin minerals and impurities. Later washed and dryed biomass was impregnated with different quantities (0.5 wt %, 2.0 wt. %, 5.0 wt. %) of K, Na and Ca. The washing and doping procedure consists of using HNO_3 acid for the washing procedure and adding the required concentration of minerals for doping the samples. The alkali content found in the original samples, and in the samples before and after the washing procedure was mentioned in previuos work [7].

1.1. Experimental setup

The main method for flame emission spectroscopy (FES) used is chemiluminescence analysis. In a chemiluminescent reaction, a part of the released energy is used to excite an electronic state and relaxes through a number of mechanisms, including spontaneous photon emission. In the case of photon emission, species emit at a characteristic wavelength, signaling the presence of the species [8]. Other authors [9], [10] has demonstrated successful application of chemiluminescence method for detection of alkali-metal emissions during combustion and demonstrated successful application of the same method on measuring organic group through combustion proving that it as a highly reliable method. The method extended its success in latest research [7] by measuring spontaneous emission of alkali metal under temperature up to 1000 °C. The experiment setup is shown in Figure 1, the same as the previous one. The ICCD camera was mounted with optical band filters with wavelengths of K, Na and Ca. A thermocouple was inserted in the center of the pellet to measure the central particle temperature (T_p). The combustion fuel, natural gas, was mixed in mixing chamber with primary air supply while there was a secondary air supply controlling the flame temperature.

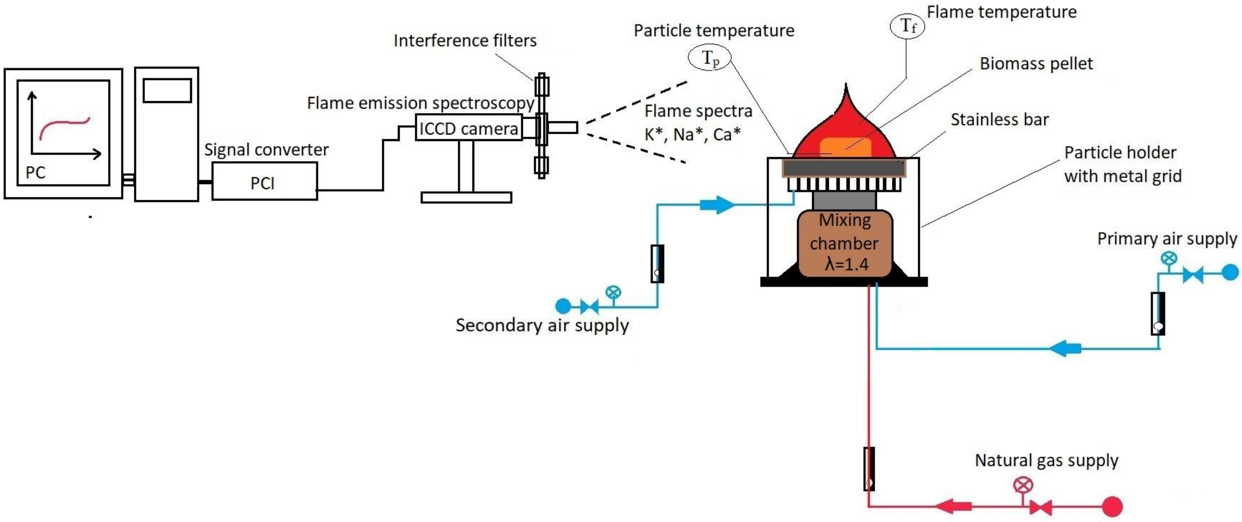

Fig. 1. Experimental setup

2. RESULTS AND DISCUSSION

During the combustion of biofuel particles and the formation of char particles, volatile organo-metallic compounds are first released followed by devolatilization; then, partial alkali and alkali-earth elements and volatile trace elements scattered out of the char [11]. A schematic of ash formation and transformation mechanism in biomass combustion is shown in Fig. 2. As the gas temperature decreases, the volatile components nucleate and condense to form submicronsized particle. Also, some volatile material condenses on residual fly ash. The high concentrations of K and Na (especially K) through nucleation, condensation, and reactions result in a variety of severe ash-related problems such as alkali-induced slagging, silicate melt-induced slagging (ash fusion), and agglomeration. These then condense on the heating surfaces and form a sticky initial slagging layer. Mentioned ash slagging problems occurs in furnaces in different high temperature zones.

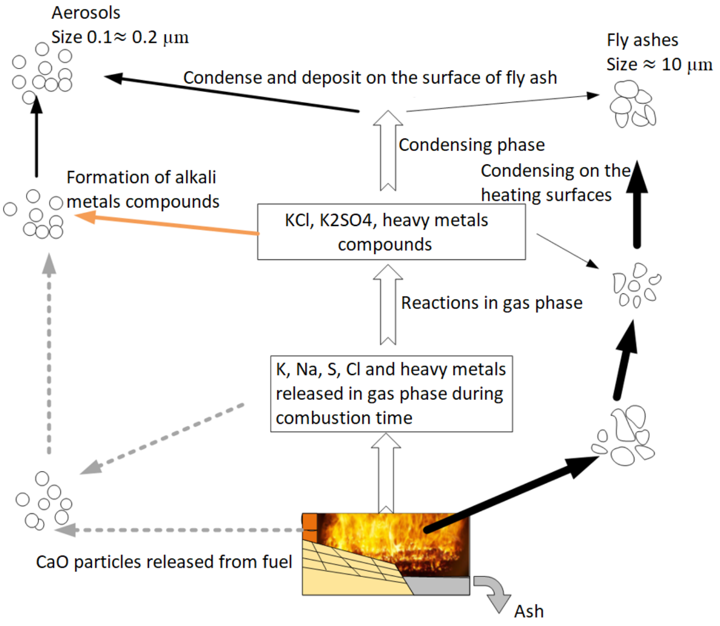

Fig. 2. Schematic of the formation processes of the main ash-related issues in biomass combustion [11], [12]

During the biomass combustion process, the main temperature zones that have a significant influence on the fixation intensity of the alkaline elements K, Na and Ca appear. In the wood pellet we see two temperature zones at all K and concentrations (Fig. 3 a and d), where the highest fixed intensity of radiation is revealed, respectively form 0.8 to 1 a. u (aligned to max value of captured intensity). It is between 400–600 °C and 1000–1200 °C. As for Na (Fig. 3 b and e), the maximum relative intensity 0.8–1 a. u in the temperature zones 400–500 °C and 900–1000 °C is recorded. In the case of calcium in wood pellets (Fig. 3 c) the maximum intensities are fixed in the temperature zones of 300–700 °C, and in case of straw (Fig. 3 e) the Ca exit to the gaseous state is noticeable already at a temperature of 600–900 °C.

The intensities emitted by K and Na are noticeably more pronounced and stronger than the Ca values. Actually at 1200 °C Ca radiation remains constant throughout the combustion period, as most Ca transforms CaO compounds[13] that settle in ash, in the solid state. Only a small portion of Ca is observed in gaseous state [11].

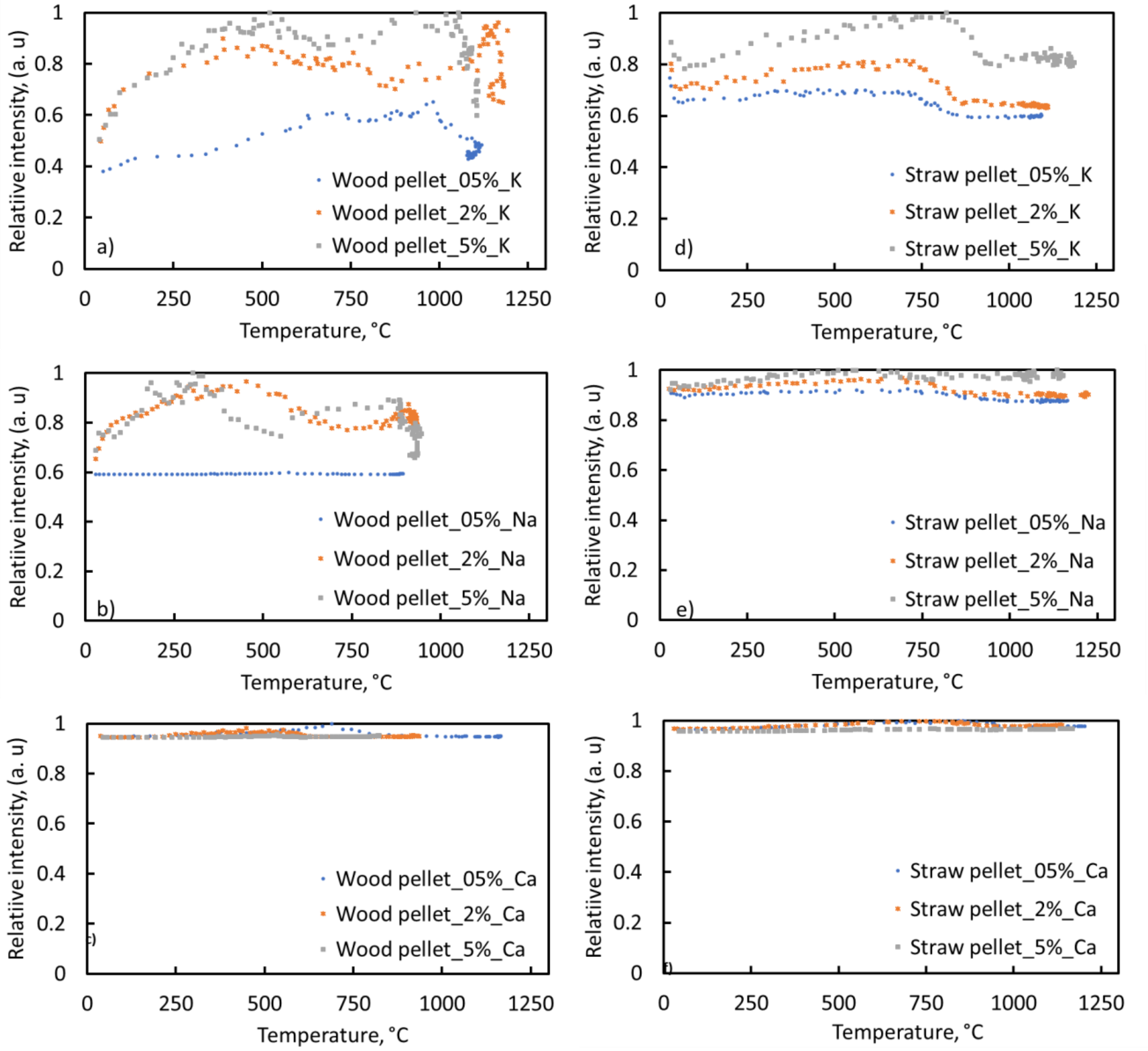

Fig.e 3. Relative intensities (arbitrary unit) dependence on the internal pellet temperature in surrounding gas flame 1200 ^{o}C temperature

3. CONCLUSIONS AND SUMMARY OF RESULTS

The emissions of alkali metal K*, Ca* and Na* from wood and straw biomass pellets under high temperature was studied. The experimental results show that the emission intensity of K* was noticeable bright in higher temperature zones from 1000 °C to 1200 °C in wood case, and 750–900 °C during straw pellet combustion. In Na* wood combustion case, the highest radiated intensity was shown near 400–500 °C and 900–1000 °C. Calcium keeps stable and does not evaporate under given conditions and shows extra stability during wood and straw combustion.

It can be concluded, that chemiluminescence method can be used for monitoring the release of alkali species (mainly potassium) as indicator in biomass furnaces at high temperature zones. This method can be used in conjunction with other boiler auxilary systems to reduce emissions or prevent ash-slagging occurrence.

REFERENCES

[1] L. R. A. Ferreira, R. B. Otto, F. P. Silva, S. N. M. De Souza, S. S. De Souza, and O. H. Ando Junior, "Review of the energy potential of the residual biomass for the distributed generation in Brazil," *Renewable and Sustainable Energy Reviews*, Vol. 94. pp. 440–455, 2018.

[2] A. Demirbas, "Combustion characteristics of different biomass fuels," *Progress in Energy and Combustion Science*, Vol. 30, No. 2. pp. 219–230, 2004.

[3] S. S. Kim, Y. S. Kang, H. D. Lee, J. K. Kim, and S. C. Hong, "Release of potassium and sodium species during combustion of various rank coals, biomass, sludge and peats," *J. Ind. Eng. Chem.*, Vol. 18, No. 6, pp. 2199–2203, 2012.

[4] Kortelainen M., Jokiniemi J., Nuutinen I. Torvela T., Lamberg H., Karhunen T., Tissari J., Sippula O., "Ash behaviour and emission formation in a small-scale reciprocating-grate combustion reactor operated with wood chips, reed canary grass and barley straw," *Fuel*, Vol. 143, pp. 80–88, 2015.

[5] P. E. Mason, L. I. Darvell, J. M. Jones, M. Pourkashanian, and A. Williams, "Single particle flame-combustion studies on solid biomass fuels," *Fuel*, Vol. 151, pp. 21–30, 2015.

[6] P. E. Mason, L. I. Darvell, J. M. Jones, and A. Williams, "Observations on the release of gas-phase potassium during the combustion of single particles of biomass," *Fuel*, Vol. 182, pp. 110–117, 2016.

[7] *Sadeckas M., Striugas N., Andriunas P., Navakas R., Praspaliauskas M., Rabaçal M., Costa M.*,"Spontaneous Emission Measurements of Selected Alkali Radicals during the Combustion of a Single Biomass Pellet," *Energy and Fuels*, Vol. 32, No. 10, pp. 10132–10143, 2018.

[8] S. Karnani and D. Dunn-Rankin, "Visualizing CH* chemiluminescence in sooting flames," *Combust. Flame*, Vol. 160, No. 10, pp. 2275–2278, 2013.

[9] N. Striūgas, M. Sadeckas, and R. Paulauskas, "Investigation of K*, Na* and Ca* flame emission during single biomass particle combustion," *Combustion Science and Technology*, Vol. 191, No. 1, pp. 151–162, 2019.

[10] R. Navakas, A. Saliamonas, N. Striūgas, A. Džiugys, R. Paulauskas, and K. Zakarauskas, "Effect of producer gas addition and air excess ratio on natural gas flame luminescence," *Fuel*, Vol. 217, pp. 478–489, 2018.

[11] Y. Niu, H. Tan, and S. Hui, "Ash-related issues during biomass combustion: Alkali-induced slagging, silicate melt-induced slagging (ash fusion), agglomeration, corrosion, ash utilization, and related countermeasures," *Progress in Energy and Combustion Science*, Vol. 52. pp. 1–61, 2016.

[12] J. Capablo, "Formation of alkali salt deposits in biomass combustion," *Fuel Process. Technol.*, Vol. 153, pp. 58–73, Dec. 2016.

[13] T. Brunner, M. Joeller, I. Obernberger, and F. Frandsen, "Aerosol and fly ash formation in fixed bed biomass using woody biofuels," in *Proceeding of 12th European biomass conference*, 2002, No. June, pp. 17–21.

CYSENI 2019, May 23-24, Kaunas, Lithuania
ISSN 1822-7554, www.cyseni.com

CFD MODELING OF HEAT EXCHANGE AND HYDRODYNAMICS IN A JET-NICHE SYSTEM OF FUEL COMBUSTION

M. Z. Abdulin, A. A. Siryi, A. V. Baranyuk
National Technical University of Ukraine "Igor Sikorsky Kyiv Polytechnic Institute"
Polytechnic street 6, 03134, Kiev – Ukraine
Email: AleksandrW@i.ua

ABSTRACT

Practice of burning gaseous fuel shows, that one of the most important energy equipment element is burner. In case of natural gas burning, one of the most perspective technology is a jet-niche burner system (JNS). Experimental selection of its rational work parameters is a complex and expensive process. This problem could be solved by numerical simulation methods usage, but first the model should be verified. The object of the study was to adopt the hydrodynamic parameters of the flow in JNS. As a subject of research the numerical model of gas distribution was adopted. The gas was distributed by circular jets fed perpendicularly to the incident flow oxidizer through a single-row system of holes. The mathematical model of the process contains system of differential equations of motion, continuity and transfer of the i-th component of the mixture and is solved numerically in the Ansys-Fluent environment. In the simulation the standard method was used for predicting the formation of NOx by means of this software package. The obtained results indicates that a single-row supply is capable of providing the necessary combustible level of concentrations of the fuel mixture and a stable controlled aerodynamic structure of the flow in the field of stabilization of the combustion process in range of the air excess coefficient variations from 1.12 to 2.62. The possibility of qualitative research of the hydrodynamic characteristics of detached flows used to; predict the fields of concentrations and temperatures during combustion of hydrocarbon fuels in the conditions of the JNS by the methods of numerical modelling is shown. An important issue is the possibility of using simulations to predict the harmful emissions into the atmosphere.

Keywords: Jet-niche system, burner, nitrogen oxides, mathematical modelling, concentration, methane

1. INTRODUCTION

It is known that today the problem of maintaining the efficiency of fire technical equipment (FE) on the interchangeable modes of operation is important and relevant. It should be noted that a significant part of Ukrainian FEs are physically and morally outdated. One of the ways to solve this problem is to carry out its modernization with the introduction of modern fuel-using equipment. The main direction in this situation is the orientation to domestic technologies, which differ favourably from the imported analogues due to better adaptation to domestic FEs, as well as more favourable pricing policy of domestic producers.

In addition to the problems associated with the need to search for alternative fuels and to save scarce energy resources, burner units are required to expand their capacity by reducing the starting pressures of fuel, as well as to increase the unit capacity with regard to emissions and efficiency of fuel burn up. Therefore, understanding the regularities of formation of harmful substances and the ability to predict their emission when the ratio of fuel consumption to oxidizer in the mixture changes is one of the main issues of ensuring environmental protection standards.

It is known that in order to reduce the emission of harmful substances it is necessary to develop a burner device (BD) of a complex design with an increase in the number of combustion zones, each of which is optimized for a certain mode of operation. Therefore, for maintenance of perspective norms on emission of harmful substances, it is necessary to create a BD which would allow to simultaneously reduce all kinds of harmful components. It is established that only in a very narrow temperature range (1650-1900 K) it is possible to achieve simultaneously the required levels of NOx and CO emissions [1, 2].

Taking into account the ambiguity of the influence of such main factors as: pressure in the combustion chamber, temperature and oxygen content in the oxidizer, heat load of the working volume and the coefficient of excess air, the behaviour of the emission characteristics of FE requires thorough study and deeper analysis [3]. The use of methods to intensify the process of mixture formation and the implementation of micro diffusion fuel combustion is considered to be one of the effective factors influencing the emission of toxic nitrogen oxides [4].

Implementation of diffusion-kinetic (micro diffusion) mechanism of CO gas combustion is achieved, for example, by introduction of jet-niche technology (JNT), which is developed on the basis of studies conducted in the Laboratory of combustion of TEF of Igor Sikorsky KPI. JNT is a universal technology of gaseous fuel combustion, the introduction of which into the industry and further study of its features is engaged in Production Association «SNT» (Stream-Niche Technology) (Kyiv) [5].

At present day, Production Association «SNT» modernised a large number of FE in Ukraine and abroad. It should be noted that the city heating networks of Zhytomyr, Luhansk, Alchevsk, Ivano-Frankivsk and other cities have been reconstructed due to low cost of modernization.

Fig. 1. Jet niche type burner

The analysis of works of foreign authors shows that since 2000 the majority of scientific-research works are executed by means of computer modelling. The authors prove that computer modelling allows to study correctly the operating modes and optimize both newly designed and reconstructed power equipment. However, it should be remembered that the simultaneous use of computer modelling and physical experimentation makes it possible to obtain the most complete and reliable information about the subject of the study. At the same time, the costs of experimental and research work is significantly reduced [6].

On the subject of the work in the available literature there are articles related to the study of heat and mass exchange during the combustion of coal in the furnaces of the boiler unit. For example, in work [7] numerical modelling of NOx concentration in the boiler furnaces was carried out at variation of burners location. At the same time, it is not said for which specific boiler the simulation was carried out and no comparison with the experimental data is given. The work [8] devoted to the study of furnace processes in the furnace of the boiler BKZ-420-140 of Omsk CHPP-4 at combustion of design and alternative fuel on the basis of mathematical modelling by means of the applied software package FIRE 3D is quite thorough. The authors have analyzed the results in a three-dimensional statement for each type of fuel and compared the data obtained with the results of the calculation of regulatory documents. Ekibastuz and Kuznetsky coal was used as fuel in the work. In works [9, 10] by means of the same program complex the authors investigated influence of tangentially located burners at coal and natural gas combustion. These and many other works are performed using CFD modeling methods without using quality experimental data.

Modelling of working processes in the furnace of steam water tube boiler DE 10/14 with the purpose of ways search to decrease nitrogen oxides is devoted to works [11, 12]. These works show that the formation of harmful emissions is influenced by excess air, pyrometric level in the furnace chamber, time when fuel and oxidizer are in the high-temperature zone. The burner GMG-7 with the capacity of 728 m^3/h of natural gas was used, which realized the vortex structure of the flame with the possibility of changing its length. However, the authors provide data on nitrogen oxide emissions from the boiler furnace and little attention is paid to the processes taking place in the burner.

The paper [13] is the closest to the subject of the paper, where the authors determined the environmental friendliness of burning biogas in the combustion chamber of a 100 kWe MGT gas turbine. The authors provide numerical values of NOx emissions, which can be used as a basis for the analysis of the results of the presented work, especially when burning depleted mixtures.

The analysis of available literature shows that little attention was paid to the prediction of the formation of nitrogen oxides during the combustion of natural gas in the jet-niche flame stabilizer. Availability of a wide industrial implementation and constant increase of requirements to the equipment environmental friendliness requires a more in-depth study of the regularities of the BD environmental characteristics, including the use of methods of mathematical modelling.

2. AIM AND OBJECTIVES

The purpose of the work is to deepen the understanding of the processes of formation of harmful oxides during the combustion of gaseous fuels in the jet niche flame stabilizer. In works [14] numerical research of processes of hydrodynamics and fuel and oxidizer mixing in the JNS at the single- and double-row scheme of gas distribution and research of structure of an air flow at use of specially profiled niche of the trapezoidal form is carried out. The presented work, to a certain extent, is a development of previous studies, the main task of which is to determine the nature of the distribution of nitrogen oxides after the BD in a quantitative ratio and to compare the data obtained with the results of experimental studies [14].

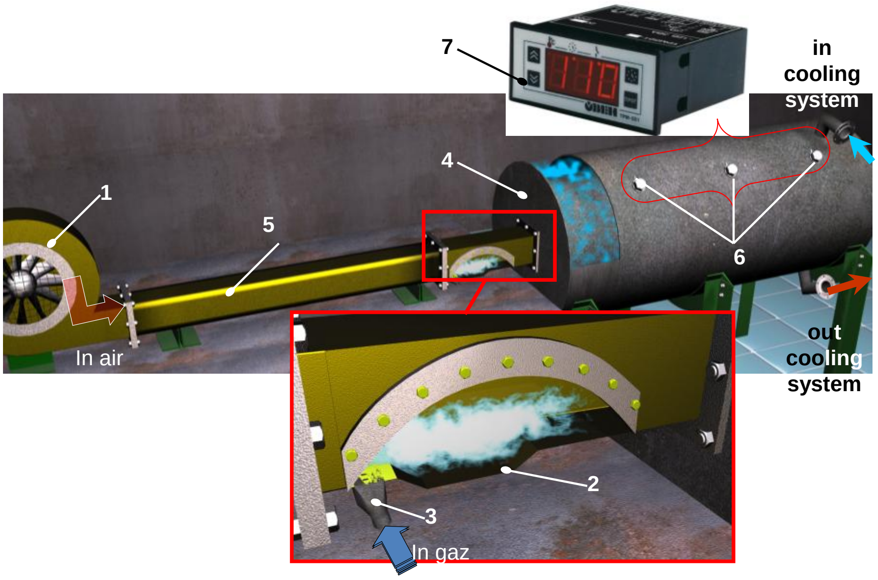

Fig. 2. Model of a laboratory installation for the study of combustion processes in the JNS: 1 – Fan, 2 – JNS, 3 – Fuel distribution system, 4 – Refractory section body, 5 – Static and full pressure withdrawals, 6 – Thermocouples, 7 – Thermocouple signal meter

To calculate NOx emissions, the authors developed a CFD-model of the process occurring in the JNS (Fig. 2). In the general case, it contains the geometrical model of JNS, created on its basis discretized model with boundary conditions and mathematical description of the calculation process, which is implemented by means of ANSYS-Fluent.

3. CFD SIMULATION METHODOLOGY

The mathematical model of the investigated process contains systems of differential equations of motion, continuity and transfer of i-th component of the mixture and is solved by numerical methods in the Ansys-Fluent. The standard method of NOx prediction by means of this program was used for modelling. Thus, the following main mechanisms of nitrogen oxides formation were considered in modelling [15].

3.1. Thermal NOx

Thermal mechanism including oxidation of N_2 along the chain of Zeldovich's mechanism and interaction of N atoms with OH radicals, as well as mechanisms of N_2O, NO_2 and NO; N_2O mechanism is determined by a group of reactions, in which N_2O acts as an intermediate substance in the formation of NO. The NO_2 mechanism results in the formation of NO for the following reactions:

$$NO_2 + CO = NCO + NO;$$

$$NO_2 + OH = HO_2 + NO;$$

$$NO_2 + H = OH + NO;$$

$$NO_2 + O = O_2 + NO;$$

$$NO_2 + M = O + NO + M.$$

3.2. Prompt NOx

The mechanism of NO is determined by the interaction of "fast" nitrogen oxides, which are formed during the combustion of fuel in the flame front as a result of interaction of N_2 with the radicals of CH and CH_2, appearing in the destruction of complex molecules of hydrocarbon fuel.

Prompt NOx is the most prevalent in rich flames. The actual formation involves a complex series of reactions and many possible intermediate species. The route now accepted as follows:

$$CH + N_2 = HCN + N;$$

$$N + O_2 = NO + O;$$

$$HCN + OH = CN + H_2O;$$

$$CN + O_2 = NO + CO.$$

Prompt NOx formation is proportional to carbon atoms number present per unit volume and is independent of the parent hydrocarbon identity. The quantity of HCN formed increases according to concentration of hydrocarbon radicals, which in turn increases with equivalence ratio. As the equivalence ratio increases, prompt NOx production increases at first, then passes a peak, and finally decreases due to a deficiency in oxygen.

ANSYS-Fluent calculates thermal and fast NOx levels. When setting up ANSYS-Fluent to solve the problem, the authors chose a model that considers the turbulent-chemical components interactions and allows levels of NOx calculation taking into account the effect of turbulent pulsations at an average time response rate. Also, to predict radical O concentration, it’s necessary to predict the NOx temperature, the authors use the partial equilibrium model, which developers of ANSYS-Fluent recommended as primary.

The carbon number of fuel (the number of carbon atoms in a fuel molecule) is denoted by 1 (Fig. 3c) and the equivalence factor (determines the fuel-air ratio (stoichiometric conditions)) is 0.76. These parameters are used to calculate the NOx formation rate described in detail User's Guide of Fluent.

The pressure-based algorithm is chosen as the solution algorithm. On the assumption that the burner device in the boiler unit is designed for continuous operation, as an example, for the entire heating season, the calculation is made in a stationary setting (Steady).

The pressure-based solver is traditionally used for incompressible and weakly compressible flows. However, it is currently applicable to a wide range of flows (from incompressible to highly compressible). The choice of such solver was also based on the fact that a model without prior transport mix and gas combustion was used in the work, which was not available on the basis of density. This assumption is made in order to reduce resources and calculations time.

Reactive components of thermophysical properties (in this case air and methane) were set in the form of piecewise-polynomial temperature dependence. In this case, two temperature ranges were used. The first is from 300 K to 1000 K and the second is from 1000 K to 5000 K.

It is known that the Realisable k-ε model of turbulence has a high computational efficiency for the class of tasks under consideration. The authors used this model as a calculation model.

On the outer walls of the burner model, the boundary conditions for temperature constancy were set (T_wall = const), due to their water cooling.

The mass flow rate of fuel and the oxidizer was established by analogy with the physical experiment. As the result, conditions were created for the atmosphere emissions of flue gases.

In order to determine the effect on the combustion process and NOx formation in the calculation using the CFD-model, the excess air ratio was changed. The gas and air flow rates required to calculate this factor are shown in Table 1. The experimental data of NOx values necessary for verification of CFD-model [14] are given there.

Table 1. Experimental NOx values at the flame tube outlet [14]

α	1.12	1.27	1.62	2.00	2.62
w_q, m/s	61.5	56	40.5	32	20
w_n, m/s	13.2	13.7	12.6	12.2	13.9
NOx, ppm	45	43	30	11	1

On the Fig. 4 CFD-model of jet-niche flame stabilizer, which is the object of research, is presented. The model is a computer copy of the laboratory stand, where the experimental studies of hydrodynamics, mixture formation and combustion in the jet-niche system were carried out. On the same stand was carried out the determination of NOx concentration at the outlet of the investigated area with the help of gas analyzer Testo 330-1 LL. The laboratory stand includes a low-pressure fan that supplies air to the isothermal channel of square section with a wall size of 70 mm. The channel is 700 mm long, taking into account the need to form a flow rate profile in front of the burner. Gas distribution is carried out through one row of fuel holes (7 holes with a diameter of 3 mm), through which natural gas is supplied perpendicularly to the oxidizer flow. In the JNS there is a mixture formation and stabilization of the combustion process, afterburning of fuel is completed in the flame tube. The combustion process is characterized by the formation of a spatially developed and extended flare, the length and configuration of which varies depending on the ratio of fuel and oxidizer consumption. At the flame tube outlet, flammable gases are directed to the exhaust duct [14]. Experimental NOx values represented by Table 1.

The mesh of the model takes into account the development of the boundary layer on the surfaces of the walls of the jet and niche flame stabilizer and the flame tube. The area outside the boundary layer was modelled using an uneven tetrahedral grid. The Skewness did not exceed 0.8 and the aspect ratio (AspectRatio) of the elements did not exceed 40.

To increase the calculation speed, the model is divided into two separate calculation areas. One of them contains a previously included stabilizing section (Fig. 3a). The second one contains a jet-niche system and a flame tube (Fig. 3b).

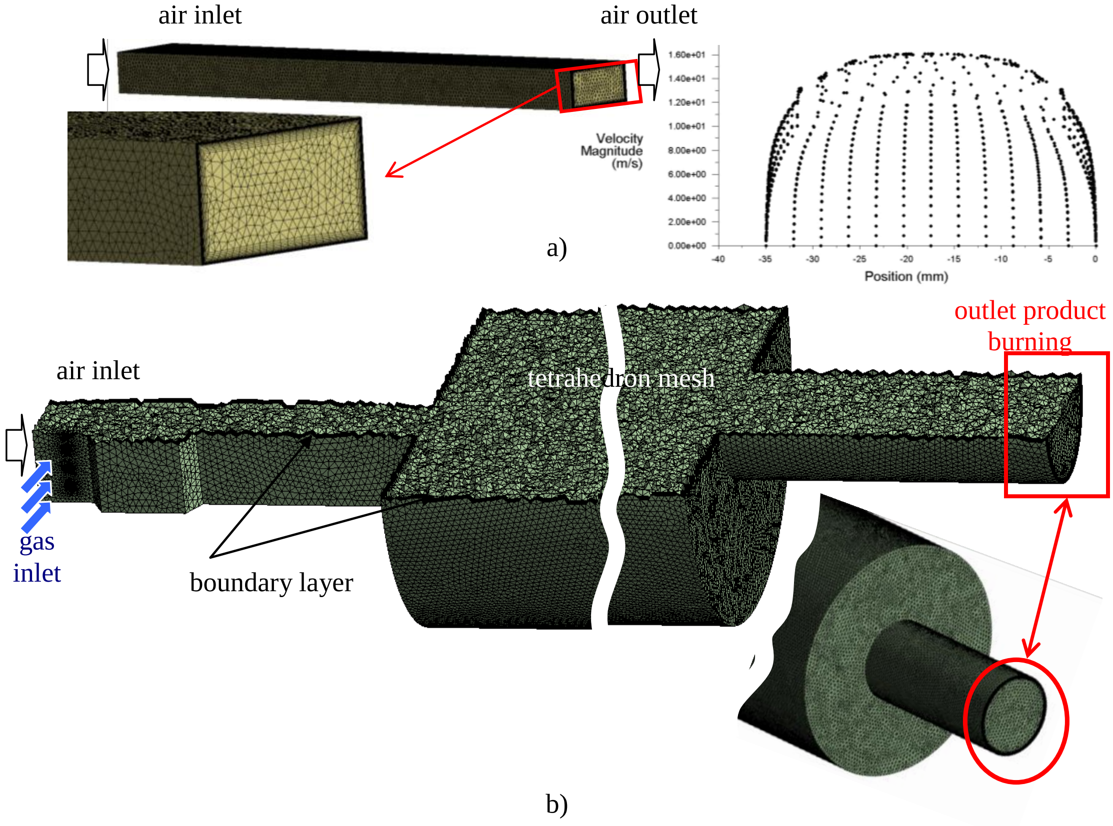

a)

b)

Fig. 3. The mesh of stabilizing section (a) and JNS with refractory section (b)

Given the experimental results, the length of the flare can be determined by the empirical dependence:

$$L_f / d = c \cdot \left(\rho_g W_g^2 / \rho_a W_a^2\right)^m \cdot \alpha^n , \tag{1}$$

where c, m, n – constant and degree index at variables in the equation, d – diameters of gas supply holes, mm; ρ – density, kg/m^3; W – flow rate, m/sec; α – excess air ratio; indices 'a' and 'g' – air and gas, respectively.

$$\begin{cases} C = 115,\ m = 0{,}17,\ n = -1.13; \\ d = 2 \div 6\ mm,\ W_g = 6 \div 70\ m/c; \\ W_a = 3 \div 15\ m/c,\ \alpha = 1.1 \div 3.0 \end{cases} \tag{2}$$

The given results allow to carry out the analysis of emission of nitrogen oxides from the point of view of the thermal mechanism of their formation.

The distribution of NOx in the burner and flame tube is easy to analyze in parts per million (ppm) – NO [ppm]. NO [ppm] in the presented paper was calculated using the following equation:

$$NO\ ppm = \frac{NO\ mole\ \ fraction \times 10^6}{1 - H_2O\ mole\ \ fraction}. \tag{3}$$

Distributions of molar concentrations of nitrogen oxides and water vapour included in the dependence (3) were calculated by means of ANSYS-Fluent.

4. RESEARCH RESULTS

To visualize the results of the combustion process studies, the JNS used the values of average speeds and temperatures of the mixture and the distribution of nitrogen oxides. The visualization of methane distribution in the niche and behind the burner is also given.

The aerodynamic structure of flows in the field of stabilization of the combustion process is shown on (Fig. 4). The increase in the velocity of methane jets leads to intensive mixing of the mixture due to the turbulence of the tear-off layer. In addition, in the niches and caverns, which are washed by the flow at large numbers of Reynolds, an intensive circulation current is observed [16]. Next picture shows a hydrodynamic picture of the flow under the conditions of chemical reaction of combustion components. The results are on the Fig. 4a show that a vortex occupying 1/4 of the niche area can be observed in the course of the flow near the leading edge of the niche. When the methane velocity decreases (Fig. 4b), the mixing intensity of the flow in the niche decreases significantly. As evidenced by the presence of a much smaller vortex near the front flow in comparison with the previous case.

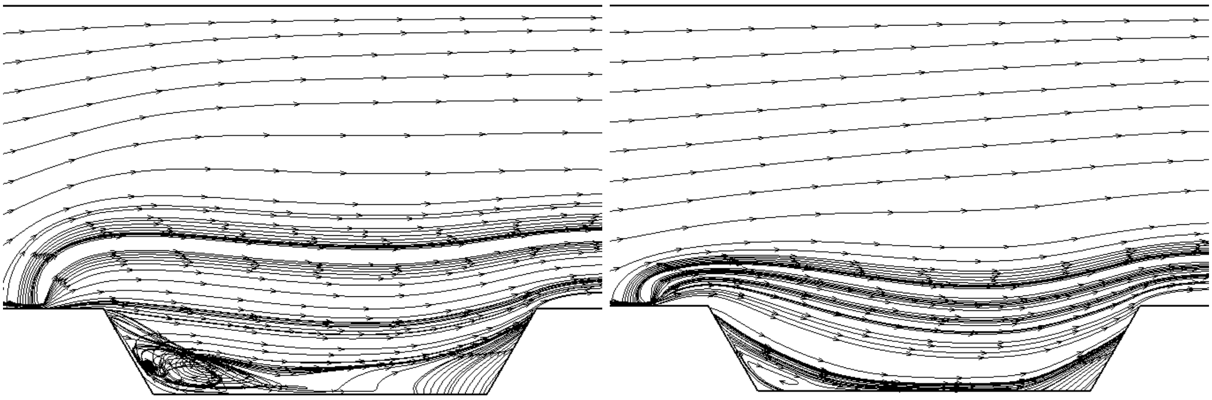

a) b)

Fig. 4. Mixture particle trajectories near niche walls at α = 1.12 (a) and α = 3.62 (b)

The distribution of the components involved in the combustion reaction depends significantly on the aerodynamic structure of the flow. So, as shown in Fig. 6 and 7, the mass fraction of methane in the burner section and in the niche depends on the velocity of the reacting flows. Thus, for the ratio of methane-air velocity, which corresponds to the excess air coefficient α = 3.62 (Table 1), there is the presence of a single vortex in the niche near the leading edge of the niche in the course of the flow. At the same time, the flow "presses" the methane into the niches (Fig. 5a). If the velocity of fuel jets reaches 61.5 m/s at the air flow rate of 13.2 m/s (α = 1.12), the flow pattern changes – the current lines of methane jets practically do not deform (Fig. 5b). The flow of methane runs parallel to the walls of the burner and conditions are created in the niche for intensive mixing of the mixture.

The intensive mixing of the flow near the leading edge of the niche is also shown in Fig. 7. If the excess air ratio is 1.12, there is an area of 1/2 of the niche area near the leading edge of the niche, where there is a presence of 1 to 6% oxygen (Fig. 6a). As the methane velocity decreases, the area in the considered section decreases, and at α = 3.62 degenerates (Fig. 6b).

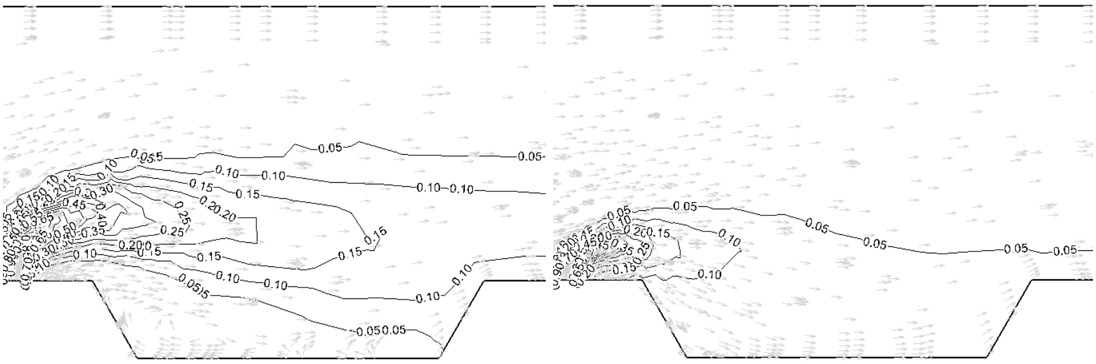

a) b)

Fig. 5. Mass fraction of methane near niche walls at α = 1.12 (a) and α = 3.62 (b)

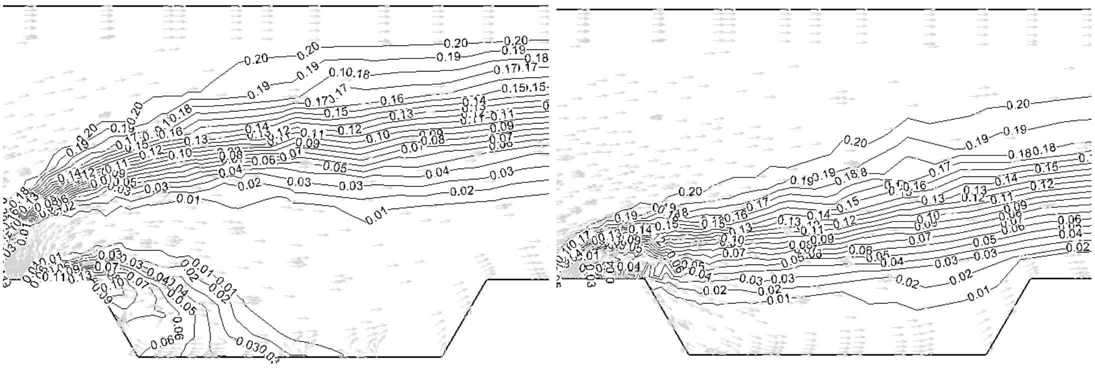

a) b)

Fig. 6. Mass fraction of oxygen near niche walls at α = 1.12 (a) and α = 3.62 (b)

Thus, the results confirm that the niche in the JNS is an active combustion zone. Fuel ignition and flame stabilization are carried out in the niche and the flame spreads further inward through the flow. The flame propagation range depends on the ratio of methane-air velocities (Fig. 7).

As shown in Fig. 7, increasing the excess air ratio significantly reduces the length of the flare.

Experimental measurements of the mixture temperature along the flame tube indicate that the temperature level does not exceed 1220 °C for α = 1.12 and 860 °C for α = 1.12. Calculations using the CFD model show that at α = 1.12 the temperature level in the centre of the flame tube reaches 1320 °C, and for α = 3.62-720 °C. Therefore, deviations of CFD-modelling data from the experimental ones do not exceed 10%.

The distribution of NOx formation obtained through the calculation for (3) is shown in Fig. 8. Fig. 8 shows that with an increase in the excess air ratio, the generation of nitrogen oxide emissions is suppressed. For α = 1.62, 2.00, 3.62, the maximum emissions are observed in high temperature zones, which does not contradict the current understanding of the nature of nitrogen oxides spread. For the investigated cases, when the excess air ratio is in the range of 1.1-1.2 the maximum intensity of nitrogen oxides generation shifts to the end of the flare. This can be explained by the fact that the oxidizer molecules stay in the high-temperature zone longer.

Not the last place in terms of nitrogen oxides formation is taken by the nature of fuel and oxidizer flow in the study area. According to numerous results, the maximum concentration is in the tail area of the flame tube, which is corrected with the peculiarities of fuel distribution in the JNS. Thus, free oxygen in the air, which does not interact with combustible components of fuel, is largely in the transit layer of air above the fuel distribution zone, so directly begins to interact with nitrogen further after the flow of the process and shifts to the tail part of the lined area. For operating modes with α → 1.0 concentration is maximum.

To be able to compare the experimental data with the data of the CFD-model, the latter should be averaged over the area of the output section. The averaging procedure over the area of any thermophysical parameter is organized by standard user function in ANSYS-Fluent.

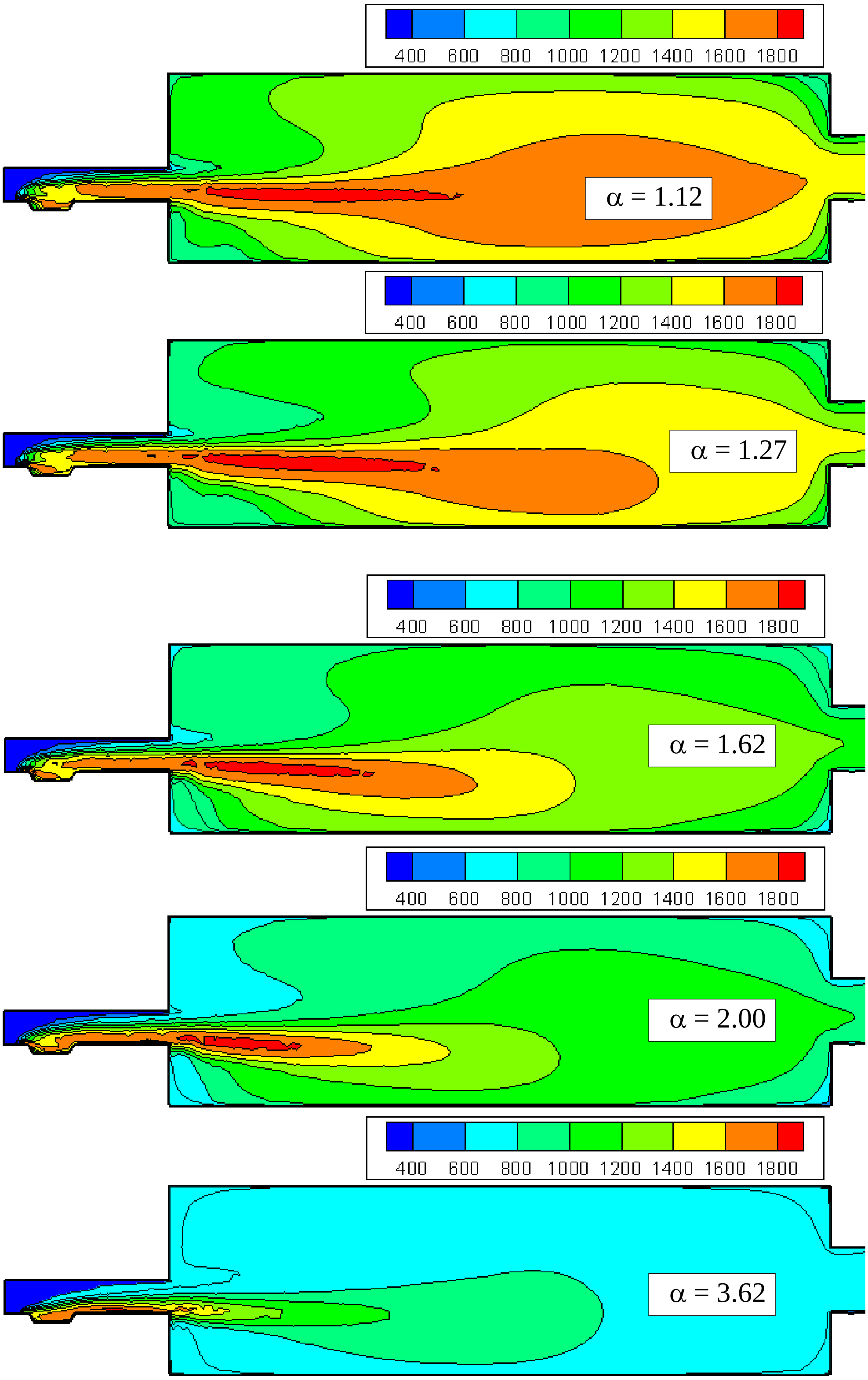

Fig. 7. Flow temperature distribution in the longitudinal section of the model

The CFD-modelling data obtained by calculating the dependence (4) were compared with the experimental data [10] in Fig. 9. Analysis of Fig. 9 shows that in comparison with the experimental data [10] the developed CFD-model accurately predicts the behaviour of nitrogen oxides.

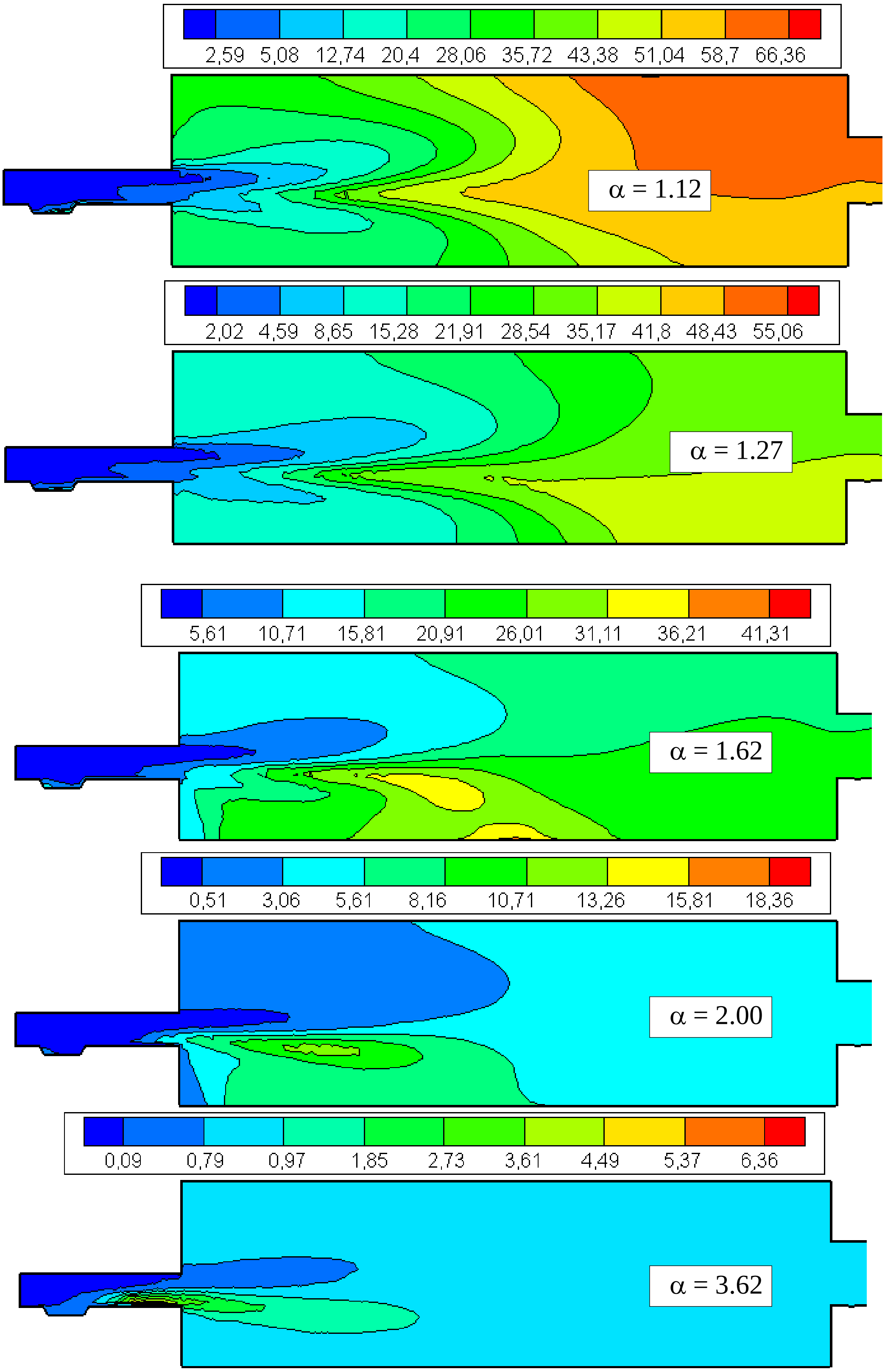

Fig. 8. Distribution of NOx formation in the longitudinal model section

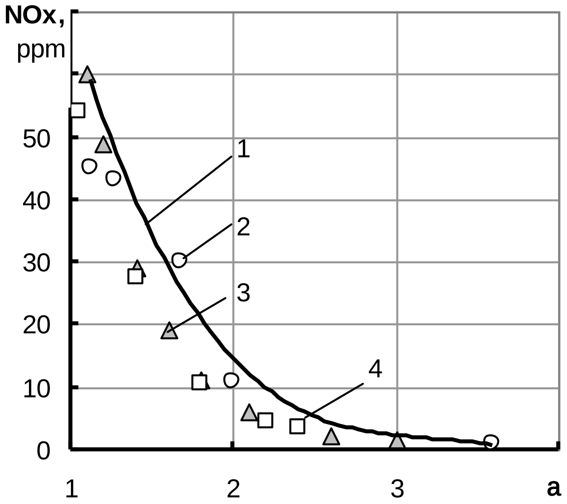

Fig. 9. Verification of the numerical experiment on nitrogen oxides comparison of JNS with the burners of the tubular type of KPI design: 1 – CFD-modeling data, 2 – JNS experimental studies [10], 3 – TMD [13], 4 – TMDN [3]

Fig. 9 also shows the dependence of NOx = $f(\alpha)$ both for experimental data [14] and for CFD-modelling data. Fig. 10b is given for the purpose of comparing the environmental friendliness of the JNS with the burner of the KPI design on the basis of the tubular technology of gas combustion, which was developed by the authors [3]. In general, these types of flame stabilizers are based on a similar principle of flame stabilization, which is implemented by the interaction of combustible mixture with a poorly streamlined body, but with certain differences. The main difference is that in the tubular modules flame stabilization occurs in the toroidal vortex at the air flow outlet into the channel, which expands, and in the JNS – in the cavity on the channel wall. In addition, the results shown in Fig. 10b concern tubular modules in which fuel is introduced directly into the eddy zone, that is, into the zone with an increased level of turbulence of the flow, while in the JNS fuel jets do not interact directly with the eddy structure in the niche cavity.

Figure 9 shows the nitrogen emission level at the outlet of the diffusion module without an internal insert (TMD type) [13] by number (3) and the same data for the diffusion module with an internal insert (TMDN type) by number (4) [13]. Analysis of Fig. 9 shows that the nature of dependence of NOx = $f(\alpha)$ for the JNS in general coincides with the data given in the literature, however, at the boundary of the selected range α the value of NOx for the JNS and TMD coincide completely, and in the middle of the selected range of α the concentration of NOx is almost 40% lower. Such difference is explained by different conditions of measurements, and for tubular burners the volume of the response zone was much smaller in comparison with the combustion zone for JNS.

5. CONCLUSIONS

The analysis of the obtained results allows to draw the following conclusions:

- The conducted data of the CFD-modeling confirmed work [14] assumption that there is a circulation flow in the niche cavity under gas stream jets, which in turn significantly influence the burner flow structure. Thus, with the increase of air excess coefficient from 1.12 to 3.62, the flows hydrodynamic structure in the niche changes as a result of which the torch length is reduced;
- The verification of the CFD-model performed by comparing the experimental measurements of the mixture along the flue tube temperature indicates that the deviation of the data from the CFD-model from the experimental does not exceed 10%. As for the range of air excess coefficient from 1.12 to 3.62, the temperature measured experimentally varies from 1220 °C to 860 °C, while the estimated data vary from 1320 °C to 720 °C;

- Conditions realized in the work, namely for the specified range of NOx, an excess of air α and methane velocities W_g = (61.5-20) *m/s* and air W_a = (13.9-12.2) *m/s*, are determined, the CFD-developed model accurately predicts the behavior of nitrogen oxides. The data deviation from the CFD-modelling from the experimental for α = 1.27-3.62 does not exceed 8%;
- The results of mixing processes modelling in the JNS confirmed combustible concentration field presence in the niche cavity zone when changing the regime parameters of the system in a wide values range;
- The presented numerical results confirm efficiency of the investigated flame stabilizer for ensuring combustion stability without flame failure in a wide range of systems operating loads;
- The data from numerous calculations can be used in the design process of energy-ecological gas burner equipment.

REFERENCES

1. ABDULIN, M.Z. Application of jet niche technology of fuel combustion in power plants. Energy and heat engineering processes and equipment. *Bulletin of NTU "KPI": Collection of scientific works*, 2005, No. 6, p. 130-144.
2. BAUKAL, C. *Industrial Burners Handbook*. New York: Washington DCCRC Press, 2003. 221 p.
3. LYUBCHIK, G.N.; GOVDYAK, R.M.; MIKULIN, A.J.; ZARITSKY, A.A. Ecological audit of gas burners on the basis of application of the method of basic characteristics of NOx and CO emissions. *Ecotechnology and resource saving*, 2007, No. 4, p. 64-70.
4. ZHAO, D.; YAMASHITA, H.; KITAGAVA, K.; ARAI, N.; FURUHATA, T. Behavior and effect on NOx formation of OH radical in methane-air diffusion flame with steam addition. *Combustion and Flame*, 2002, Vol. 130, No. 4, p. 352-360.
5. Abdulin, M.Z.; Dvortsin J.R.; Teplyakov I.B.; Strokin V.H. Burner device based on self-regulating mixing and flame stabilization system. *Proceedings of the IV International Scientific and Technical Conference "Complex Automation of Industry"*, 1990, p. 12-16.
6. KOBZAR, S., KHALATOV, A. Reduction of nitrogen oxides emissions in gas boilers by flue gas recirculation. *Industrial heat engineering*, 2009, Vol. 31, No. 4, P. 5-11.
7. CHERNETSKAYA, N.; CHERNETSKIY, M.; ZHUKOV, A., Effect of the reburning zone stoichiometry on the NOx concentration at the three-Stage combustion of pulverized coal. DOI: 10.1051 / matecconf / 2016727201022.
8. GIL, A.V.; ZAVORIN, A.S.; KRASILNIKOV, S.V.; OBUKHOV, S.V.; STARCHENKO, A.V. Study of aerodynamics and combustion in the furnace of the boiler BKZ-420-140 with reference to the variants of replacement of design fuel. *News from Tomsk Polytechnic University*, 2007, Vol. 310, No. 1, p. 175-181.
9. ZAVORIN, A.S.; BETHER, T.M.; LEBEDEV, B.V. Analysis of furnace environment of BKZ-210-140 boiler on the basis of numerous modelling. *News from Tomsk Polytechnic University*, 2011, Vol. 319, No. 4, p. 50-55.
10. TAILASHEVA, T.S. Modelling of the flue gas medium in a DKVR boiler of natural gas combustion. *News from Tomsk Polytechnic University*, 2009, Vol. 34, No. 4, p. 42-47.
11. REDKO, A.A.; DAVIDENKO, A.V.; PAVLOVSKIY, S.V.; KULIKOVA, N.V.; PAVLOVSKAYA, A.A.; REDKO, I.A. Simulation of Working Processes in the Water-Tube Boiler Furnace with the Purpose of Reducing Emissions of Nitrogen Oxides. *Problemele energeticii regionale*, 2017, Vol. 1, No. 33, p. 54-65.
12. REDKO, A.A.; DAVIDENKO, A.V.; PAVLOVSKY, S.V.; KOSTYUK, V.E.; Modelling of aerodynamic processes water-tube steam boiler DKVR (DE) -10/14. *Bulletin of the National*

Technical University "KhPI", 2016, No. 44(1216), p. 54-65. DOI: 10.20998 / 2411-0558.2016.44.07.

13. LIGUORI, V., Numerical investigation: Performances of a standard biogas in a 100 kWe MGT. *Energy Reports*, 2016, No. 2, p. 99-106.
14. SIRYI, A.A. Influence of the parameters of the jet and niche system on the working process of the burners. Candidate of Technical Sciences: 05.14.14 / NTUU "KPI". Kiev, 2016. 199 p.
15. MATVEEV, S.; LUKACHEVA, S.; ORLOV, M.; CHECHET, I.; KRASOVSKAYA, Yu. *Calculation of the formation of CO and NOX in the combustion chambers of the GTD*. Ministry of Education and Science of the Russian Federation, Samara State Aerospace University named after S.P. Koroleva, 2012. 41 p.
16. ABDULIN M.Z. Jet-niche system of stabilization and fuel combustion: Author's Dissertation for the degree of Candidate of Technical Sciences: 05.04.01 / NTUUU "KPI". Kiev, 1986. 18 c.

DETERMINATION OF DRYING INTENSITY IN STATIONARY AND MOVING LAYER OF WOOD CHIPS

L. Vorotinskienė, N. Striūgas
Lithuanian Energy Institute
Laboratory of Combustion Processes
Breslaujos str. 3, LT-44403 Kaunas – Lithuania
Email: lina.vorotinskiene@lei.lt

ABSTRACT

One of the alternatives to fossil fuels in the production of thermal energy is the combustion of the biomass, which is also used for district heating. In the cold period, in case of a high demand for the heat energy, biofuel furnaces often burn low-quality biofuels, with humidity fluctuating and often reaching 60% on wet basis (w.b.), which results in the unstable furnace operation and the incomplete burning of the fuel. Such a negative effect could be avoided by intensifying the fuel drying on the furnace grates and optimizing the control of the furnace, however, in order to accomplish such goals, firstly, it must be determined how the controllable furnace parameters affects the drying of the wet biofuel.

The aim of this work is to study the processes occurring during the drying of the wet biofuels in the drying zone of the furnace and to determine the influence of the parameters on the fuel drying intensity. To achieve such aims the experiments were carried out at the experimental rig with the operating parameters corresponding to the operational parameters common to 6 MW grate furnace. The experiments were performed by simulating the influence of primary air, exhaust gas recirculation through the grates and the influence of the primary air with the radiation from the inside surfaces of the furnace. Poor quality wet (60%) wood chips of different lineage were used. It was determined that the highest intensity of the moisture loss from the biofuel was when it was dried using infrared lamps, which simulated the radiation from the hot surfaces of the furnace. Within 30 minutes the moisture content decreased by 17% from the initial value when the temperature of the supplied primary air was 200 °C and the infrared lamps were radiating thermal energy. Additional experiments were also carried out to simulate the movement of furnace grates and to determine how the mixing intensity affects the biomass drying. Radiation of the hot surfaces inside the furnace has the largest effect on biofuel drying intensity, whereas injection of recirculating flue gas into the drying zone in the furnace reduces the biofuel drying intensity.

Keywords: biofuel, furnace, moisture content, drying, radiation

1. INTRODUCTION

Widespread and long-term use of fossil fuel resulted in global climate warming, which causes more frequent heat waves, storms and floods [1]. Due to these reasons more stringent environmental regulations were introduced to decrease the emissions of CO_2 and to substitute fossil fuel with renewable energy sources. Biomass is the most prospective alternative to fossil fuel in thermal energy production, therefore, biomass is also used for district heating in small countries such as the ones in North Europe. As an example, in Lithuania two thirds of fossil fuel used to produce heat for district heating has been replaced by biomass [2]. Mostly, fossil fuel has been substituted by building small and medium-scale heating plants, in which reciprocating grate biomass furnaces (5–10 MW) equipped with water boilers and condensing economisers are installed. These systems are designed for high thermal efficiency with low emissions of gaseous pollutants (CO, NOx, etc.) firing good quality biomass with a 30–55% moisture content [3]. However, the continued development of renewable energy source usage for heat production leads to increased demand for biomass (wood chips), resulting in price increase of good quality biofuel. Due to this reason, in order to remain in the market and to stay competitive, heat producers choose to use moist biofuel of lower quality such as stem wood, coniferous bark, with varying moisture content that can reach up to 60% wt. Besides, the lower heating value of such fuel is only 6 MJ/kg, while the lower heating value of biofuel with moisture content of 30% wt. is about 12 MJ/kg [4]. In this case, combustion on the grate of so moist fuel becomes complicated as drying process occupies most of the space in the furnace and combustion heat from lower layer is consumed for drying up the upper fuel layer [5]. Moreover, it could cause burning instability and incomplete combustion, which leads to increased CO emissions.

One of the solutions to avoid these problems is an additional fuel drying before supplying to the furnace. For this purpose, superheated steam dryers, rotary dryers, bed dryers and fluidized bed dryers [6–8] are used. Using these systems, biomass could be dried out to required moisture content resulting in improved energy quality, energy efficiency and reduced negative environmental impacts during combustion. However, these advantages come with certain drawbacks. The drying system must be selected precisely evaluating the energy efficiency, risk of fire and drying emissions in order to reach the desired moisture content of supplied biofuel. Pang and Mujumdar [9] reviewed packed moving bed, rotary and pneumatic drying systems. According to the authors, these systems are suitable for drying of wood chips. The packed moving bed dryer is working with lower drying temperature (80–150 °C) and occupies a larger land area in the heating plant, while the rotary dryer operates at drying temperature from 200 °C to 500 °C resulting in high drying capacity, but it is with higher risk of fire. Myllyma et al. [10] studied the prospect of drying biomass at a municipal CHP plant using excess heat and solar energy by performing drying experiments in a fixed-bed batch-dryer. The results revealed that the drying time for the bed height of 300 mm decreases in half when the drying air temperature increases from 50 °C to 70 °C, whereas the drying time changes only slightly when the temperature increases from 70 °C to 90 °C. The author determined that the temperature of drying air should be over 70 °C. Myllyma et al. [10] also performed the economic evaluation and determined that biomass drying at a municipal CHP plant using excess heat and solar energy could be profitable if the investment costs are reasonable and the price of the wood chips is sufficiently high. Similar drying experiments using different drying air temperatures (120 °C, 140 °C, 160 °C and 180 °C) were performed by Danielsson and Rasmuson [11]. The authors also investigated the release of volatile organic components during the drying process. The results showed that part of the calorific value is lost when drying biofuel with air at the temperature exceeding 100 °C because of evaporation of monoterpenes. Release of these monoterpenes is most intense in the beginning of the drying process during the periof of up to 30 minutes, and the amount depends on the nature of biomass and the temperature of the drying agent. The higher is the temperature of the drying agent, the more intense is evaporation of VOC and therefore the loss of calorific value. It has been also determined that heating biofuel with superheated steam leads to higher VOC release rate compared to the case when using the air as the drying medium.

In summary, additional drying systems require additional costs for installation in the heating plant and equipment, occupy large spaces and lead to release of VOC during biomass drying with medium at a temperature of over 100 °C, resulting in lowered heating value. In order to avoid the loss of VOC and additional expenses for biofuel drying when firing wet biofuel, optimizations of furnaces are necessary, such as corrections of the grate motion regimes using the moisture prediction method [12, 13] or intensification of fuel drying on the grates. For this purpose, biomass drying experiments were performed to determine the influence of the primary air supply and flue gas recirculation products injected through the bottom of the grate and exposure of biofuel bed to radiation from incandescent surfaces of the furnace to biofuel drying in the furnace.

2. MATERIALS AND METHOD

2.1. Equipment

Biofuel drying was analysed in an experimental setup (reactor) equipped with a fixed fuel bed. The scheme of the setup is shown in Fig. 1. The experimental equipment consists of four main components: electrical heater, steam generator, drying chamber and two infrared lamps. Air needed for the experiment is supplied from a compressor through two heating coils to preheat air to the desired temperatures of 50 °C, 100 °C, 150 °C, 200 °C. The temperature of hot air was measured and controlled by means of a K-type thermocouple installed in front of the reactor. The readings of the thermocouples were collected and processed by a PICO TC-08 application. The drying air flow rate was maintained constant at 18 ±1 m3/h. The fuel bed height was 0.23 m, with thermocouples embedded at various heights to determine the drying zone progression through the bed (Fig. 1). Air humidity was measured by a measurement unit Testo 454 with a connected relative humidity (RH) sensor. To simulate the furnace radiation, two infrared lamps were installed above the biofuel bed with power output of 2 kW each. This corresponds to the furnace radiation of 50 kW/m2.

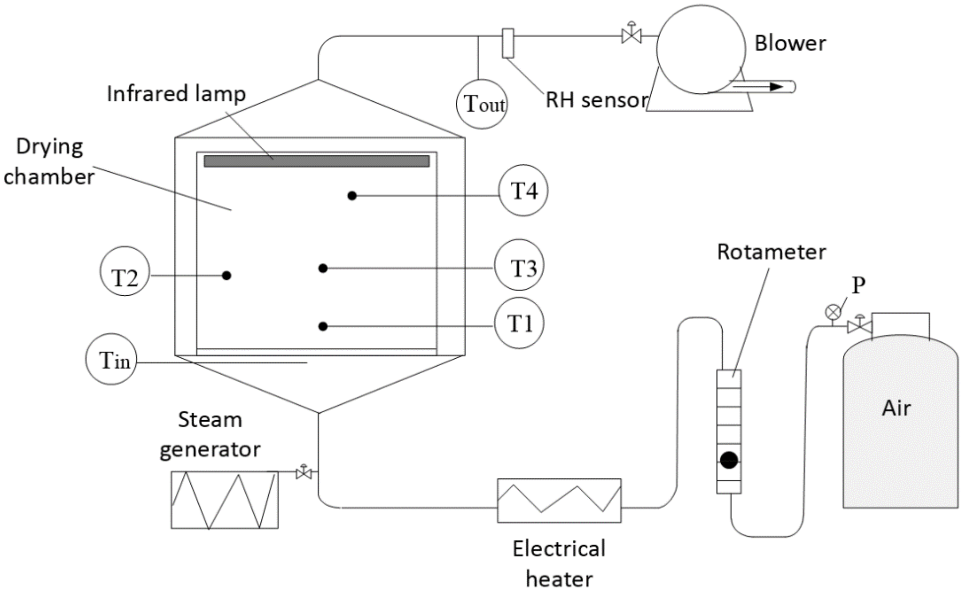

Fig. 1. Scheme of experimental rig for biomass drying

2.2. Procedure

It is known, that biofuel does not stay longer than ten minutes in the drying zone on a grate in a furnace of heating plant. If biofuel with high moisture content (approx. 60% wt.) is supplied into the furnace, it does not dry out completely in 10 minutes, therefore, in largest part of the furnace fuel is drying out rather than burning. The part of a 6 MW furnace that was simulated corresponds to the drying zone. In this furnace, the grate movement velocity is 0.003 m/s. Therefore, the time fuel spends until it burns out in the furnace is approximately 30 minutes. The drying zone occupies 1/3 of the furnace length, therefore, the actual time spent in this zone is approximately 10 minutes. By adjusting the grate movement velocity in the drying zone, the biofuel residence time in this zone can be extended. In order to clarify the influence of residence time to biofuel drying, biofuel was left to dry out for 30 minutes during experiments.

Before performing experiments in the biofuel drying chamber, biofuel was specifically prepared. To imitate the situation when moist biofuel (approx. 60% wt. moisture content) can enter the furnace in certain seasons, it was additionally soaked in water to saturate it sufficiently with humidity in the lab. Wood chips were loaded into a steel crate and submerged to a vessel filled with water together with the crate and left to soak in the vessel for 16 hours. After the crate containing biofuel is lifted out, the sample is left to drain for 2 hours in the temperature of a closed room.

To imitate feeding of wet cold biofuel to a hot furnace, the entire rig was preheated during experiments. The temperature of drying air was selected to replicate the temperatures of primary air supplied to the medium power capacity (6 MW) furnace. After the parameters of the unloaded experimental setup (the specified air flow rate and temperatures) reached the steady state, the drying chamber was loaded with a layer of wood chips for an experiment. The data from thermocouples were collected and processed by the PICO TC-08 software. The loss of moisture content in biofuel samples is estimated by measuring the humidity of outflow air.

Since the initial sample mass was different in all the experiments while maintaining the same height of the bed and the initial moisture content varied (60 ± 3%), the normalized residual moisture content of solid fuel Ym is calculated based on minimum and maximum values by Eq. (1) [14]. The fraction of residual moisture content in biofuel is estimated by measuring the humidity of outflow air and recalculating it into the moisture content of exhaust flow by calculations presented in previous work [12].

$$Y_m = 1 - \left(\frac{Y_{max} - Y_{min}}{Y_{max}}\right), \qquad (1)$$

where: Y_{max} – maximums value ratio of the moisture content in the sample and dry sample mass initial weight of sample (over all during of the study in 30 min.), Y_{min} – ratio of the moisture content in the sample at the time moment *t* and dry sample mass, it is accepted that $Y_{max} \neq 0$ ($m_{initial} > m_{dry}$, $m_{initial}$ – initial mass of the sample g, m_{dry} – dry sample mass g).

These calculations are suitable only for wet biofuel and not fit for dry fuel as a combustion process starts earlier. Thunman and Leckner [15] stated that the combustion of biofuel on grates could start when the moisture content of biofuel is less than 45%.

2.3. Wood chips characteristics

A biomass mix of bark chips with chips of different tree branches were used for the experiment. The main characteristics of the used samples are presented in Table 1. Before feeding the sample into the experimental drying chamber and after the experiment is complete, samples were taken and its moisture content was determined conform the LST EN ISO 18134-1:2015 standard. The proximate analysis of this wood chips sample was performed using an IKA C5000 calorimeter and a Flash 2000 CHNS analyser in accordance with: LST EN 14918 (HHV), LST EN 14775 (ash content), LST EN 15148 (volatile content) and LST EN 15104 (CHNS content).

Table 1. The characteristics and compositions of used samples

Fuel	**HHV, (kJ/kg)**	**MC % wt.**	**A, %**	**C, %**	**H, %**	**N, %**	**S, %**	**O (diff.), %**
Chips of various species of tree branches with bark	18998	36	3.50	48.6	5.80	0.60	< 0.01	49.99

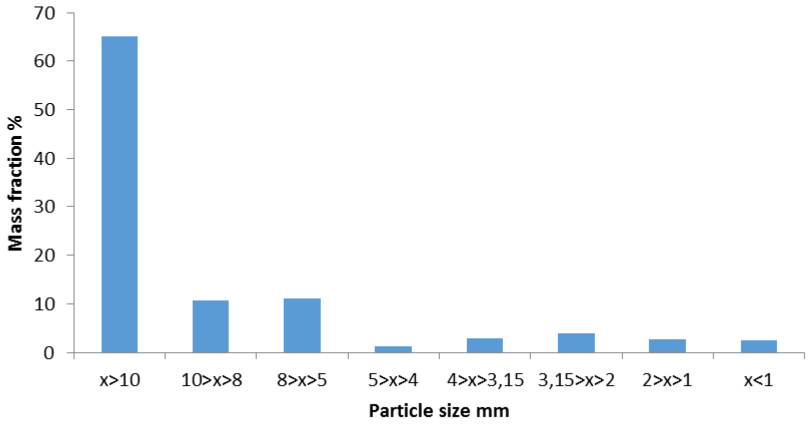

Fig. 2. Distribution of particles of different lengths as cumulative percentages of mass

Granulometric composition of biofuel was determined by using sieves (Fig. 2). The biofuel particle size parameter is important because many particle systems can be homogenized for a simpler heat and mass transfer considerations. The major part (more than 60%) of biofuel samples used in the experiments consisted of particles larger than 10 mm in length.

3. RESULTS AND DISCUSION

3.1. Effect of primary air temperature and radiation on biofuel layer drying intensity

Particle size distribution of the tree bark samples used for experiments can be very different and this might influence significantly the shapes of the drying curves, therefore, each experiment was repeated five times.

Comparison of the residual moisture content in the samples revealed that the trends of biofuel samples drying is very similar during the first 5 minutes (from the beginning of the experiment), regardless of the temperature of air supplied from the bottom of the grate. The resulting moisture loss curves confirmed that the drying process starts immediately after the biofuel sample is placed into the biomass rig. After the biofuel samples are being dried for 5 minutes, the moisture content decreases by up to 1% (Fig. 3). When drying biofuel samples for 10 minutes by preheated air and in presence of radiation from above, intensity of moisture evaporation was observed depending on the temperature of the drying air. When supplying air with the temperature of 50–150 °C, the moisture content reduces by no more than 2% after 10 minutes, and when the drying temperature increases to 200 ^{o}C – by 2.5%. The influence of primary air becomes even more pronounced when drying samples for 30 minutes. When supplying 50 °C air from below and irradiating the biofuel bed by IR lamps from above, the moisture content in the sample reduces by 8%, and when drying with higher air temperatures of 100–150 °C, moisture content in wood chips reduces by 10%. The most intense moisture loss was observed when exposing wood chips to air with the temperature of 200 °C in this case, moisture content in the sample was reduced by approx. 17% in 30 minutes.

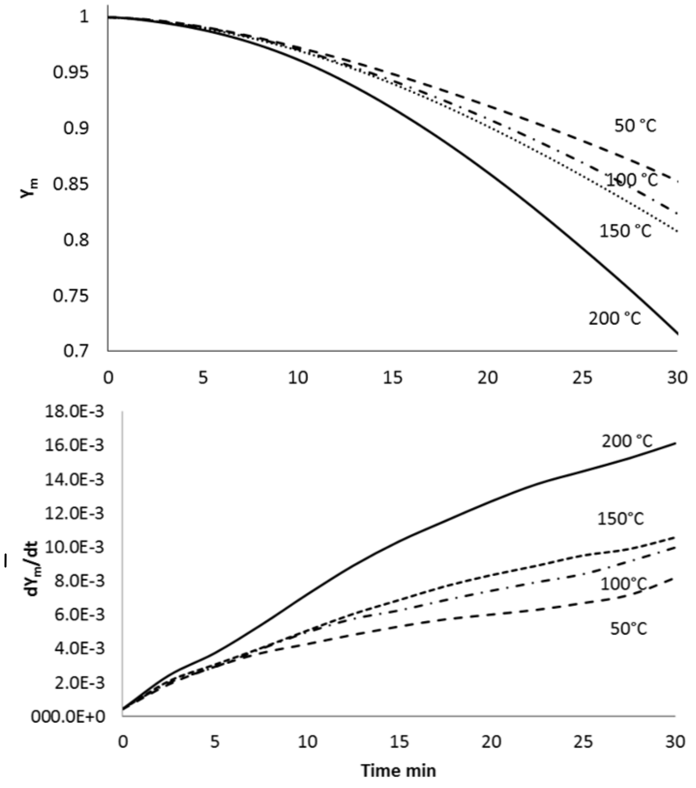

Fig. 3. Normalized of the residual moisture content (Y_m) and moisture lost rate ($-dY_m/dt$): biomass drying with radiation and different air temperatures

Despite the fact that the temperature change in the top layer of biofuel was not observed, due to intense moisture evaporation together with the escaping flue gas, and taking into account the experiments of the previous phase involving only preheated drying air, it was determined that most moisture evaporated from the top layer of the sample due to effect of radiation. Experiments with a stationary layer (fixed bed) of biofuel revealed that fine particles of the biofuel sample at the top of the fuel bed not only dried out, but ignited as well, thereby intensifying the biofuel bed drying even more, therefore, the following experiments were conducted for a moving bed of biofuel.

3.2. Effect of primary air temperature and radiation on drying intensity of nonstationary biofuel bed

Mixing of biofuel is necessary in order to make optimal use of radiation energy for biofuel drying rather than drying out the surface particles only, which leads to low intensity of heat transfer to inner layers, and to speed up the drying process and obtain homogeneous heating in all the layers of the bed. During mixing of biofuel layers, drying process is influenced by both convection and radiation leading to more intense and homogeneous drying. In real furnaces, biofuel is stirred by natural grate motion. In order to imitate the grate motion and mixing of layers in the furnace, a screw mixer was installed in the experimental biofuel drying chamber (Fig. 1). To monitor the drying tendency and influence of mixing, biofuel was selected having the same properties as in previous experiments. During these experiments, mixing periods of 600 s, 300 s and 150 s were selected. The drying results using the samples of wood bark chips in case of mixing were compared to those obtained in experiments with the same operating conditions, but without mixing. Changes in normalized mixture content depending on the primary air temperature and mixing period were determined and the obtained data are presented in Fig. 4.

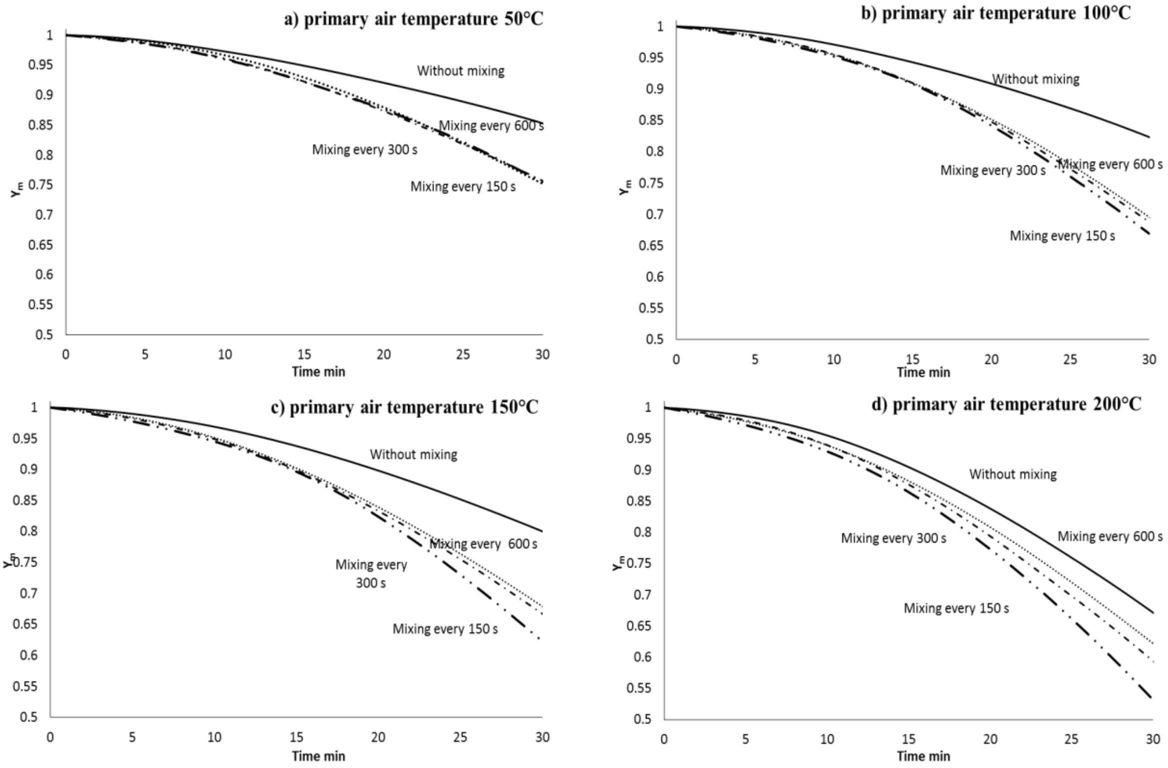

Fig. 4. Residual normalized moisture content (Y_m) in wood chips with bark when drying with different air temperatures, presence of radiation and changing of mixing period

It was noticed from the drying experiments in nonstationary fuel bed and analysis of the results obtained that the mixing period does not influence the biofuel drying rate at the drying air temperature of 50 °C and the moisture content in the sample decreased by approximately 10% after 30 minutes in presence of mixing (Fig. 4a). With the increase of the drying air temperature to 100 °C in presence of mixing, moisture evaporation increased to 13–16% (Fig. 4b), and its increase to 150 °C led to increased moisture evaporation by approximately 12% when mixing every 600 seconds, and up to 18% when mixing every 150 seconds (Fig. 4c). When exposing the biofuel samples to drying air of 200 °C (the highest in these experiments), moisture evaporation is approximately 7% when mixing the layer every 600 seconds, and up to only 16% when mixing every 150 seconds (Fig. 4c). It was determined from the normalized moisture content curves that the mixing period when drying biofuel for approximately 30 minutes becomes significant only when supplying primary air with the temperature not lower than 150 °C (Fig. 4c). After increasing the drying air temperature to 200 °C, the mixing period became less significant. Analysis of the obtained results when drying wood chips, estimating the influence of the mixing rate, revealed that the drying intensity increases already after 20 min when supplying primary air at the temperature of 100–150 °C, and after the primary air temperature is increased to 200°C, influence of mixing to drying intensity decreases, whereas the influence of the mixing period rate increases (by up to 9%).

Experiments conducted in the stationary biofuel bed revealed that high temperature (200 °C) of the primary air influences the highest drying rate, therefore, the mixing process has lower effect to sample drying intensity when comparing the cases of samples dried out using the primary air temperatures of 100–150 °C. When drying wood chips at the primary air temperature of 200 °C, it was determined that the influence of the mixing period (150, 300 and 600 s) to drying process is significant and the change of the normalized moisture content increases linearly with increasing intensity of mixing. This dependence of the drying rate on the mixing rate shows that the influence of radiation to biofuel drying is high when the primary air temperature is high (200 °C).

Despite the fact that the highest drying intensity at the primary air temperature of 200 °C there was established that the most efficient mixing of the fuel bed is in case when wood chips are being dried out for 30 minutes, the drying air temperature is 150°C and the bed mixing is repeated every 150 seconds.

4. CONCLUSIONS

The results of the experimental studies of the stationary and non-stationary biofuel layer can be summarized as follows:

1. Radiation from the hot internal surfaces of the furnace was imitated by infrared lamps of 4000 W power output, corresponding to radiation intensity in the furnace of 50 kW/m^2. High temperature of primary air of 200 °C and radiation from hot surfaces of the furnace can reduce the moisture content in biofuel from 60% to 43% in 30 minutes.

2. Analysis of influence of the mixing period (150, 300 ir 600 s) to the drying intensity depending on the primary air temperature revealed that the mixing period is significant only when drying the samples using the drying agent at the temperature of 200 °C, i.e., dry air, and the change of the normalized moisture content increases linearly with increasing intensity of the bed mixing.

3. Experiments with imitated biofuel mixing determined the optimal conditions when the influence of biofuel bed mixing is highest: i.e., when wood chips are dried using the drying air at the temperature of 150 °C for 30 minutes and the fuel bed mixing is repeated every 150 seconds.

REFERENCES

1. Dhillon, R.S., von Wuehlisch, G.: Mitigation of global warming through renewable biomass. Biomass and Bioenergy. 48, 75–89 (2013). doi:10.1016/j.biombioe.2012.11.005.
2. Ramanauskas, V.: Biokuro naudojimas lietuvos šilumos ūkyje – nauda ir ateitis. (2015).
3. Razmjoo, N., Sefidari, H., Strand, M.: Measurements of temperature and gas composition within the burning bed of wet woody residues in a 4 MW moving grate boiler. Fuel Process. Technol. 152, 438–445 (2016). doi:10.1016/j.fuproc.2016.07.011.
4. Quaak, P., Knoef, H., Stassen, H.: Energy from Biomass: A review of combustion and gasification technologies. World Bank Tech. Pap. 1–78 (1999). doi:ISBN0 -8213-4335.
5. Bauer, R., Gölles, M., Brunner, T., Dourdoumas, N., Obernberger, I.: Modelling of grate combustion in a medium scale biomass furnace for control purposes. Biomass and Bioenergy. 34, 417–427 (2010). doi:10.1016/j.biombioe.2009.12.005.
6. Stenström, S.: Drying of biofuels from the forest–A review. Dry. Technol. 35, 1167–1181 (2017). doi:10.1080/07373937.2016.1258571.
7. Daud, W.R.W.: Fluidized Bed Dryers – Recent Advances. Adv. Powder Technol. 19, 403–418 (2008). doi:10.1016/S0921-8831(08)60909-7.
8. Sai, P.S.T.: Drying of Solids in a Rotary Dryer. Dry. Technol. 31, 213–223 (2013). doi:10.1080/07373937.2012.711406.
9. Pang, S., Mujumdar, A.S.: Drying of Woody Biomass for Bioenergy: Drying Technologies and Optimization for an Integrated Bioenergy Plant. Dry. Technol. 28, 690–701 (2010). doi:10.1080/07373931003799236.
10. Myllymaa, T., Holmberg, H., Hillamo, H., Laajalehto, T., Ahtila, P.: Wood Chip Drying in Fixed Beds: Drying Kinetics and Economics of Drying at a Municipal Combined Heat and Power Plant Site. Dry. Technol. 33, 205–215 (2015). doi:10.1080/07373937.2014.945179.
11. Danielsson, S., Rasmuson, A.: THE INFLUENCE OF DRYING MEDIUM, TEMPERATURE, AND TIME ON THE RELEASE OF MONOTERPENES DURING CONVECTIVE DRYING OF WOOD CHIPS. Dry. Technol. 20, 1427–1444 (2002). doi:10.1081/DRT-120005860.
12. Striūgas, N., Vorotinskienė, L., Paulauskas, R., Navakas, R., Džiugys, A., Narbutas, L.: Estimating the fuel moisture content to control the reciprocating grate furnace firing wet woody biomass. Energy Convers. Manag. 149, 937–949 (2017). doi:10.1016/j.enconman.2017.04.014.
13. Kortela, J., Jämsä-Jounela, S.L.: Fuel moisture soft-sensor and its validation for the industrial BioPower 5 CHP plant. Appl. Energy. 105, 66–74 (2013). doi:10.1016/j.apenergy.2012.12.049.
14. Holmberg, H., Ahtila, P., & Ahtila, O. Experimental study on drying of bark in fixed beds. *Drying Technology*. 2011. Vol. 29(8), P. 953–960.
15. Yin, C., Rosendahl, L. A., & Kær, S. K. Grate-firing of biomass for heat and power production. *Progress in Energy and combustion Science*. 2008. Vol. 34(6). P. 725–754.

CYSENI 2019, May 23-24, Kaunas, Lithuania
ISSN 1822-7554, www.cyseni.com

EXPERIMENTAL INVESTIGATION OF EFFECTS OF THE RATIO OF SWIRLER HUB DIAMETER TO OUTER DIAMETER (d_h/d_o) ON SYNTHETIC GAS FLAMES: PART 1: COMBUSTION AND EMISSION CHARACTERISTICS

H. Yilmaz, O. Cam
Erzincan Binali Yildirim University
Department of Airframes and Powerplants, Civil Aviation College,
Erzincan, 24002, Turkey
Email: hyilmaz@erzincan.edu.tr

I. Yilmaz
Erciyes University
Dept. of Airframes and Powerplants, Fac. of Aeronautics and Astronautics,
Kayseri, 38039 Turkey

ABSTRACT

Swirling flows increase combustion performance via favoring flame stability, pollutant emissions and combustion intensity, and strength of a swirling flow is characterized by a parameter known as swirl number, which is highly related to d_h/d_o ratio. In this study, effects of swirler d_h/d_o ratio on combustion and emission characteristics of premixed 20%CNG-30%H_2-30%CO-20%CO_2 mixture synthetic gas flames were experimentally investigated in a laboratory scale, swirl stabilized combustor. For this purpose, twelve different swirl generators were designed and manufactured. d_h/d_o ratios of these swirlers were set as 0.30 and 0.50, and geometric swirl number was varied between the values of 0.4 and 1.4 (at 0.2 intervals). All experiments were conducted at fuel-lean equivalence ratio (ϕ = 0.6), room temperature and local atmospheric conditions of city of Kayseri, Turkey. A data logger was utilized to plot axial, radial temperatures and NO_x, CO, CO_2 profiles, which were exploited to assess combustion and emission performance. Results showed that d_h/d_o ratio has a non-monotonic effect on combustion and emission behaviour of tested synthetic gas mixture. Depending on the swirl number, increments and decrements were observed in temperature and emission values.

Keywords: Synthetic gas, d_h/d_o ratio, swirler, combustion, emission

CYSENI 2019, May 23-24, Kaunas, Lithuania
ISSN 1822-7554, www.cyseni.com

EXPERIMENTAL INVESTIGATION OF EFFECTS OF THE RATIO OF SWIRLER HUB DIAMETER TO OUTER DIAMETER (d_h/d_o) ON SYNTHETIC GAS FLAMES: PART 2: DYNAMIC FLAME BEHAVIOUR AT EXTERNALLY ALTERED ACOUSTIC CONDITIONS

H. Yilmaz, O. Cam
Erzincan Binali Yildirim University
Department of Airframes and Powerplants, Civil Aviation College,
Erzincan, 24002, Turkey
Email: hyilmaz@erzincan.edu.tr

I. Yilmaz
Erciyes University
Dept. of Airframes and Powerplants, Fac. of Aeronautics and Astronautics,
Kayseri, 38039 Turkey

ABSTRACT

In a combustion device, unsteady heat release causes acoustic energy to increase when acoustic damping (energy loss) is not that effective, and as a result, thermos-acoustic flame instabilities occur. In this study, effects of swirler d_h/d_o ratio (at different swirl numbers) on dynamic flame behaviour of premixed 20%CNG-30%H_2-30%CO-20%CO_2 mixture under externally altered acoustic boundary conditions and stability limits (flashback and blowout equivalence ratios) of such mixture were investigated in a laboratory scale, variable geometric swirl number combustor. Therefore, swirl generators with different dh/do ratio (0.3 and 0.5) and geometric swirl number (0.4, 0.6, 0.8, 1.0 1.2 and 1.4) were designed and manufactured. Acoustic boundary conditions in the combustion chamber were altered using loudspeakers, and flame response to these conditions was perceived using photodiodes and pressure sensors. Dynamic flame behaviour of respective mixture was evaluated using luminous intensity and pressure profiles. Results showed that d_h/d_o ratio has a minor impact on dynamic flame behaviour.

Keywords: Synthetic gas, d_h/d_o ratio, thermo-acoustic, dynamic flame behavior

CYSENI 2019, May 23-24, Kaunas, Lithuania
ISSN 1822-7554, www.cyseni.com

INVESTIGATION OF PRIMARY VORTEX STRUCTURE IN OPEN TYPE CAVITY

P. Vilkinis, N. Pedišius
Lithuanian Energy Institute
Breslaujos str. 3, LT-44403 – Lithuania
Email: paulius.vilkinis@lei.lt

ABSTRACT

The structure of the fluid flow in cavity driven by the interactions of boundary layer is an attractive area of research due to various applications in environmental, industrial and biomedical applications as well as due to huge importance of this kind of flow to the basic study of fluid dynamics. In this study flow visualizations using micro-particle image velocimetry system and numerical simulation using Ansys Fluent software are carried out in open-type cavity located in straight square-cross section channel. The study is conducted by changing Reynolds number in the channel in order to investigate flow structure at different flow regimes. Also, measurements are performed at different measurement planes across the width of the cavity in order to understand the spatial development of velocity components. The main attention is paid to the spatial structure of primary vortex in the cavity. Additionally, three-dimensional simulation is performed and experimental and simulated results are compared. It is learned that flow structure in cavity highly depends on flow regime in the channel. In turbulent flow regimes flow is bifurcated near side walls of the cavity. Scheme of explanation of formation of vortical flow in open-cavity is proposed.

Keywords: cavity flow, open-type cavity, flow structure, vortex structure, micro-particle image velocimetry, CFD

1. INTRODUCTION

Recirculating flow in deep, wall-bounded geometries is a benchmark case for many industrial problems. Many experimental studies investigated flow structure inside both lid-driven and shear layer driven cavities of various shapes [1–6]. The configuration of geometry and flow is relevant to various industrial applications such as heat transfer enhancement [7, 8], mixing process improvement [9] and wide area of biomedical applications [10–12]. These flows also have great scientific interest because of difficult flow structure consisted of corner vortices, longitudinal vortices and instabilities in shear layer occurring in the same geometry.

Open-type cavity is characterized by its length-to-depth ratio $L/h_1 > 8$–6. Open-type cavities can be further classified into “deep” ($L/h_1 \leq 1$) or “shallow” ($L/h_1 > 1$). Flow in these types of cavities exhibits different recirculating flow topology [13].

The three-dimensional structure of flow in open-type cavity has been widely investigated over past decades. Both experimental and numerical studies get a lot of attention. Experimental investigation is mostly performed using particle streak and dye emission techniques giving spatial information on flow structure. Migeon et al. [14] showed that quasi-toroidal corner vortices develops near side walls in square and rectangular cross-section open-type cavities at Re = 1000. These vortices have a centrifugal origin and surround the primary eddy core. Countanceau et al. [15] showed that Taylor-Gortler-like vortices and corner vortices formats in cylindrical semi-circular shell. These vortical structures become blurred after short period of time as Reynolds increases because of onset of turbulence. These authors also proposed a schematic vortical structure in semi-circular geometry.

Faure et al. [16] investigated vortex morphology in open-type cavities with different cavity aspect ratio (L/h_1) and span ratio (b/h_1). Authors found that centrifugal instabilities are generated in open-type cavity flow. The amount of instabilities highly depends on cavity geometry. The amount of Görtler-like type vortices on the floor of the cavity increases as cavity aspect ratio decreases and span ration increases. The Görtler-like type vortices are developing in spanwise row but structures disappear at small span ratio.

Yao et al. [13] numerically showed that the appearance and structure of longitudinal vortices in open-type cavity depends on Re number and boundary layers thickness. Feldman [17] found that in diagonally lid-driven cavity existence of oscillation amplitude peak is the result of centrifugal effects of the flow.

This paper presents experimental and numerical study of velocity distribution across the centre of primary vortex in “deep” open-type cavity. The study is based on measurements of velocity profile at different flow regimes and three-dimensional numerical simulation. Effects of Reynolds number on velocity distribution across the centre of primary vortex are showed. The aim of this study is to investigate primary vortex dynamics in open-type cavity depending on Reynolds number. This study is continuous research, where the previous studies [18, 19] were based on investigation of flow topology in open-type cavity in stationary and pulsatile flow conditions. In this article is presented more detailed analysis of flow structure based on Reynolds number.

2. METHODOLOGY

2.1. The cavity

The cavity used for experimental and numerical investigations is shown in Fig. 1 a. The cavity has length L = 0.5 mm, depth h_1 = 1.0 mm and width b = 0.5 mm. The channel is of square-cross section with h = b = 0.5 mm. Cavity is located at a distance of 40 mm from the channel inlet, therefore flow is fully developed before the cavity. Measurements are performed at different x-y planes across the width of cavity as shown in Fig. 1 b. 7 to 9 measurements are performed for each investigated Re number with distance between successive measurements planes equal to 40 μm. Red line indicates the location where velocity profiles were analysed.

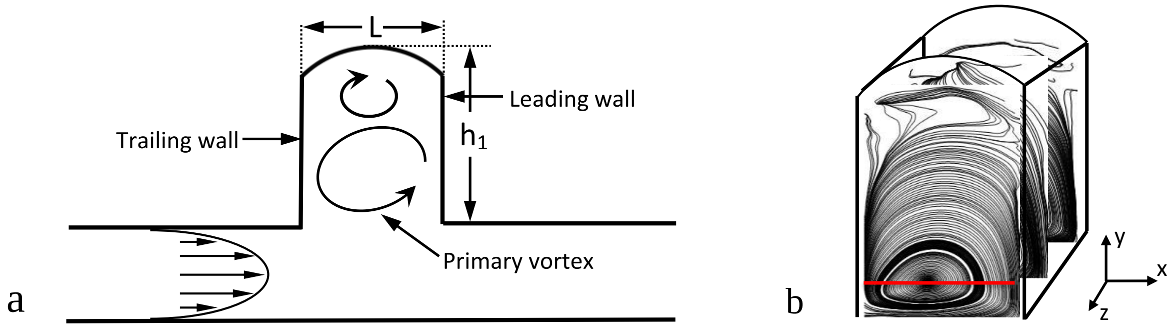

Fig. 1. Geometry of open-type cavity used for investigation (a) and location of measured velocity profiles (b)

2.2. Experimental setup

Flow visualization inside cavity is performed using micro particle image velocimetry (μPIV) system. Fluorescent tracer particles immersed in working fluid (water in our case) is illuminated by laser sheet and generated fluorescence signal is collected by CCD camera. Flow images are processed using DynamicStudio software provided by Dantec Dynamics. Flow velocity is measured calculating particles displacing within know period of time. Images pairs are captured at 15 Hz rate while time period between successive images depends on flow rate and is in the range from 10000 to 50 μs. Particle images are analysed using Adaptive correlation method with interrogation windows size of 16 × 32 pixels. In this case objective lenses of 20× magnification and 0.4 numerical aperture were used achieving spatial resolution of 20.6 × 41.2 μm and depth of correlation 42.4 μm.

The μPIV system provided by Dantec Dynamics consists of double pulsed neodymium-doped yttrium aluminium garnet (Nd:YAG) laser (λ = 532 nm), laser control system LPU 450, FlowSense EO CCD camera providing an image field of 2048 × 2048 pixels mounted on the inverted Leica DM ILM microscope. The microscope is equipped with dichroic mirror used to filter out background noise and only florescent light from excited tracer particles can reach the camera. 1 μm diameter tracer particles (Invitrogen) with a specific gravity of 1.05 were used, particles excitation and emission wavelengths of 535 nm and 575 nm, respectively. Deionized water flow rates from 0.001 μl/h to 7635 ml/h in the microchannel are formed by syringe pump WPI AL4000 (World Precision Instruments).

2.3. Numerical setup

Three-dimensional numerical simulation is performed using commercially available Ansys Fluent package. Reynolds Stress – Baseline model (RSM-BSL) is employed for computation of time-averaged flow parameters. SIMPLEC solution algorithm together with second-order upwind discretization schemes are used in the simulations. A convergence criterion is set to 10^{-6} for all variables.

Grid is generated using Ansys Meshing. Mesh is generated with clustering nodes for 10 cell layers near wall region in order to simulate pressure and velocity gradients in greater accuracy and to ensure y^+ value below 1. Grid with minimum element size of $7\cdot10^{-4}$ mm and maximum face size of $1.5\cdot10^{2}$ consists of $1.13\cdot10^{6}$ nodes and $5.12\cdot10^{6}$ elements leading to average element quality of 0.78 and average orthogonal quality of 0.87. CFD-Post is used for results post processing.

3. RESULTS AND DISCUSSIONS

3.1. Velocity distribution across centre of vortex

Reynolds number considered is this study is based on channel hydraulic diameter D_h and is calculated as follows:

$$Re_{Dh} = \frac{vD_h}{\nu}, \tag{1}$$

here v – mean velocity in channel, *m/s* and ν – kinematic viscosity, *Pa·s*.

It should be noted that measurements were performed in two-dimensional plane. Since v_z velocity component is not measured, total velocity magnitude is sum of two velocity components v_x and v_y:

$$v = \sqrt{v_x^2 + v_y^2}\,. \tag{2}$$

Measured and numerically simulated velocity distribution across the centre of vortex is presented in Fig. 2 and 3 respectively. Here flow direction in channel is from left to right. x/L = 0 corresponds to trailing cavity wall and x/L = 1 – leading cavity wall. Positive values of v_x corresponds to flow direction in channel, also positive values of v_y corresponds to flow direction entering the cavity (from cavity lid to bottom) and negative values of v_y – flow directed from cavity bottom to its lid.

As can be seen from Fig. 2, velocity distribution across centre of primary vortex depends on flow regime. In the case of laminar flow regime (Re_{Dh} = 100) maximum total velocity v is located near the leading wall. Maximum positive v_x velocity component is located in the central part of cavity and near trailing wall while negative velocity zones appear near side walls and are stretched from central part of cavity towards leading wall. v_y velocity component distribution is similar to the case of total velocity since v_y contributes most to the total velocity (note the velocity values). In this case measured velocity scalar maps are in good agreement with simulated ones (Fig. 3).

Re_{Dh}	V	V_x	V_y
100	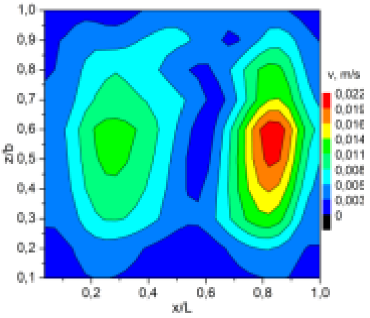	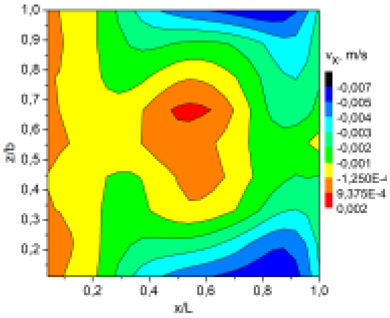	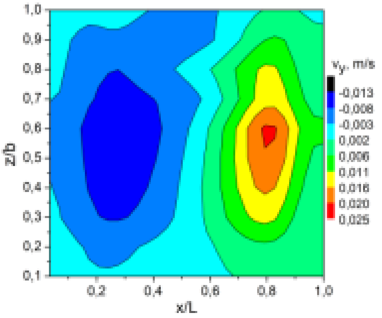
1000	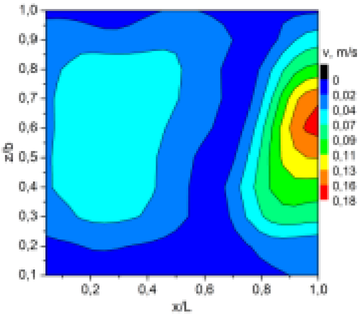	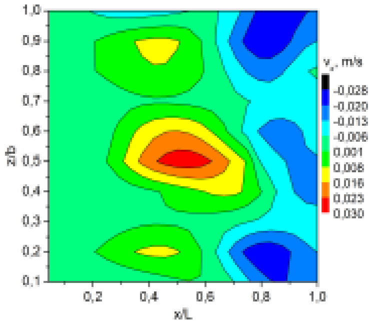	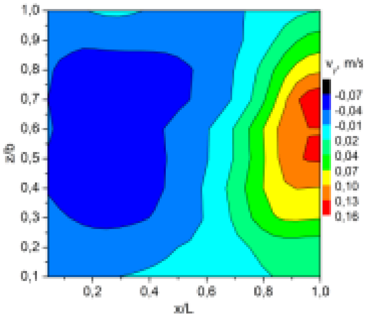
2000	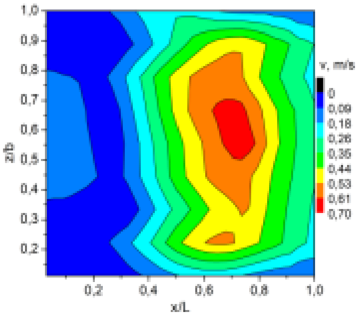	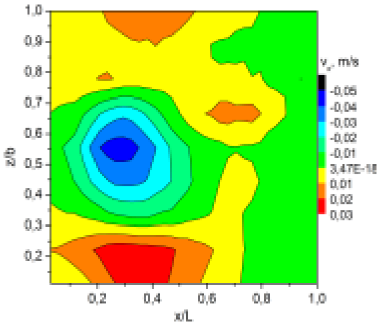	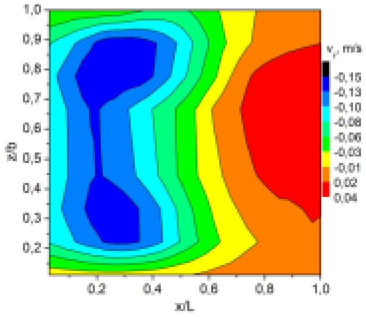
3000	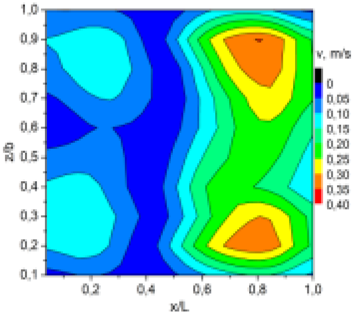	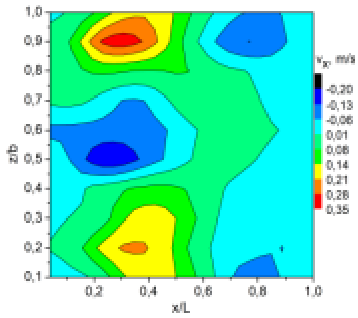	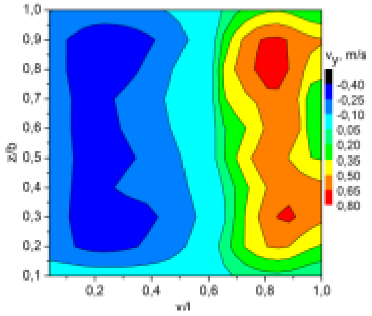

Fig. 2. Measured velocity scalar maps across the centre of primary vortex

Velocity profiles near trailing wall are measured at x/L = 0.2 and at x/L = 0.8 near leading wall for all cases. Flow in cavity is laminar as it can be seen from measured and simulated velocity profiles having parabolic shape in the case of total velocity. (Fig. 4 a, d). Simulated velocity values are higher than measured ones in all cases of v and v_x. Also velocity near leading wall is about 1.8 times higher than near trailing wall, this ratio appears to be about the same for all Re numbers investigated. Velocity differences between measured and simulated profiles can be explained by spatial illumination nature of µPIV system. In present case depth of correlation is 42.4 µm. It means that measured fluorescent signal is the average value coming from volume of fluid which height is 42.4 µm. Therefore measured velocity values are always lower than actual ones.

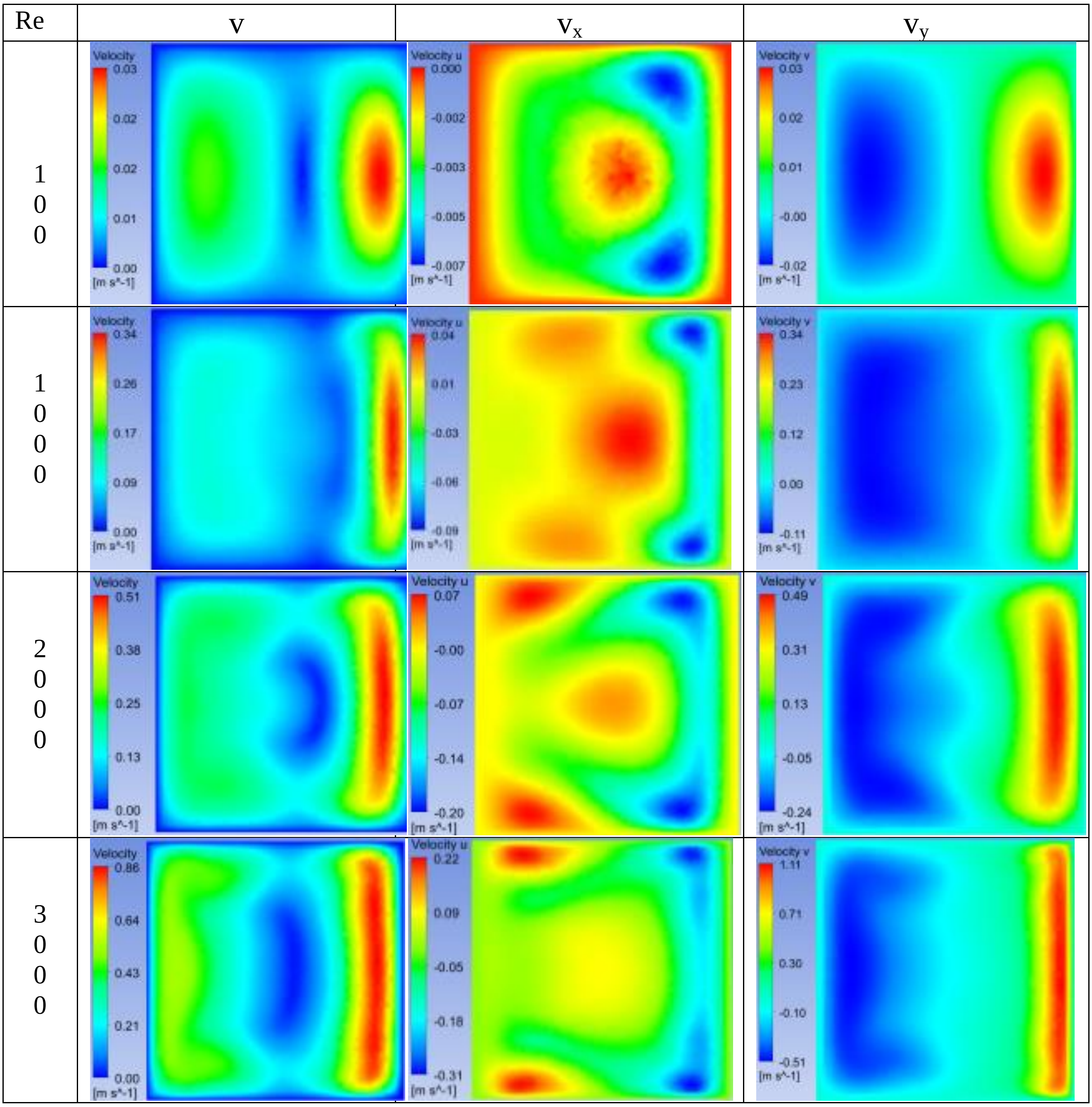

Fig. 3. Simulated velocity scalar maps across the centre of primary vortex

In the case of Re_{Dh} = 1000, total maximum velocity *v* is stretched across leading wall. Velocity profiles are flattened near trailing wall, with slightly higher velocity zones near side walls, (Fig. 5 a, c) but maintain parabolic shape near leading wall for *v* and v_y (Fig. 5 d, f). Also v_x velocity component changes its direction near trailing (Fig. 5 b) wall. Velocity minimum located between higher velocity zones represents the centre of cavity. As can be seen from velocity scalar maps, vortex centre changes its location from x/L = 0.55–0.6 at Re_{Dh} = 100 to x/L = 0.7 at Re_{Dh} = 1000. Also velocity distribution in the centre changes its shape from straight line at Re_{Dh} = 100 to arched at higher Re_{Dh}. It can be explained by changes of velocity distribution at different planes which is presented in previous investigation [18].

At Re_{Dh} = 2000 transition to turbulent flow regime is observed. As can be seen from velocity profiles near trailing wall, total *v* and v_y velocity component have increased values near side walls and velocity minimums in the mid-plane (Fig. 6 a, c). Near leading wall velocity profiles maintain its flattened shape corresponding to the turbulent flow regime (Fig. 6 d, f). In this case maximum positive velocity zones appear in the corner near trailing wall in v_x component scalar map (Fig. 2, 3). Simultaneously, velocity in the centre part of cavity decreases compared to $Re_{Dh} = 1000$.

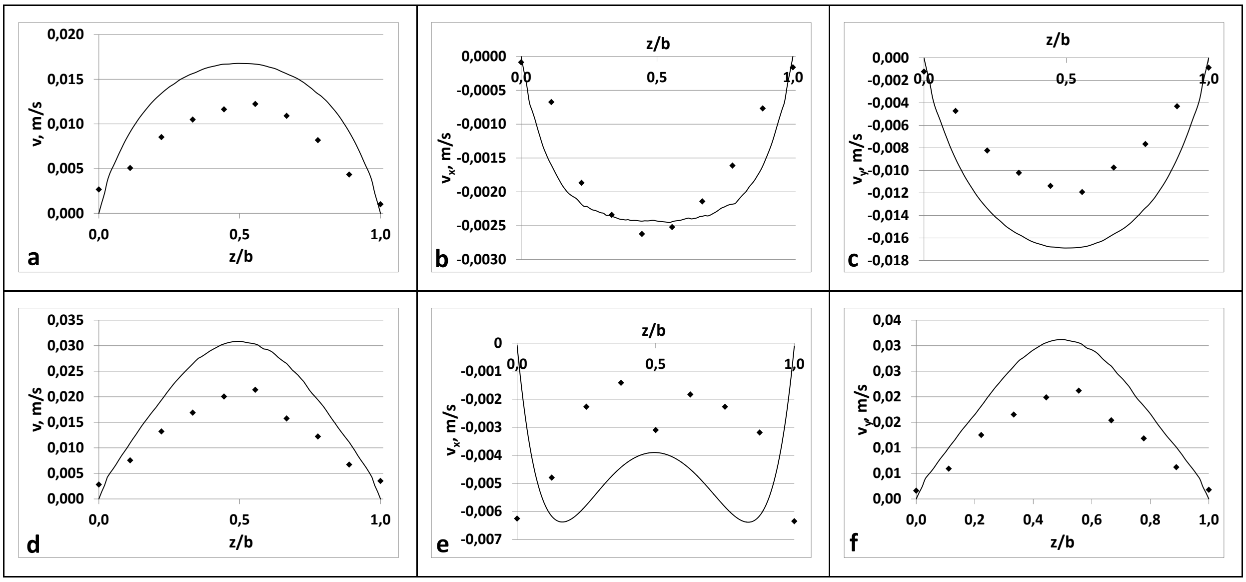

Fig. 4. Comparison of measured (dots) and simulated (lines) velocity profiles near trailing (a, b, c) and leading (d, e, f) walls at $Re_{Dh} = 100$: a and b – total velocity v; d and e – v_x component; c and f – v_y component

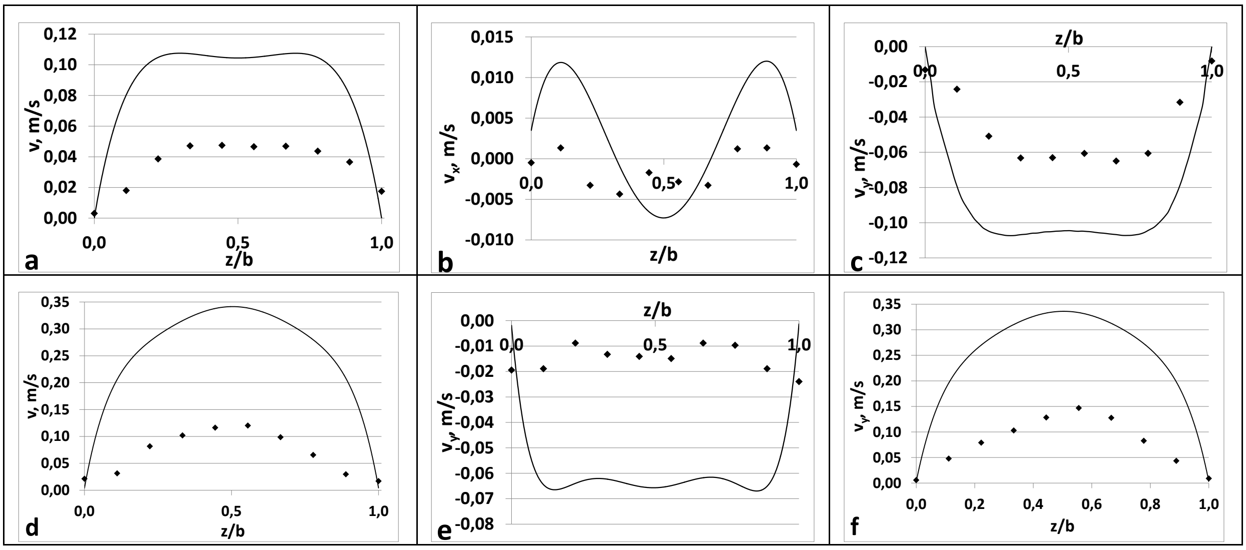

Fig. 5. Comparison of measured (dots) and simulated (lines) velocity profiles near trailing (a, b, c) and leading (d, e, f) walls at $Re_{Dh} = 1000$: a and b – total velocity v; d and e – v_x component; c and f – v_y component

After transition to the turbulent flow regime at $Re_{Dh} = 3000$, experimental velocity scalar maps (Fig. 2) show flow division to two symmetrical structures in respect of cavity mid-plane. This velocity bifurcation is also observed in velocity profiles (Fig. 7 a, c, d and f) and it appears stronger in experimental measurements than in numerical simulation. As can be seen from Fig. 7 a and Fig. 7 d, in the case of experimental measurements two velocity peaks near side walls of cavity appear near trailing and leading walls. These measurements are in good agreement with numerical simulation except one case of total velocity near trailing wall (Fig. 7 a) where additional peak instead of velocity minimum is observed.

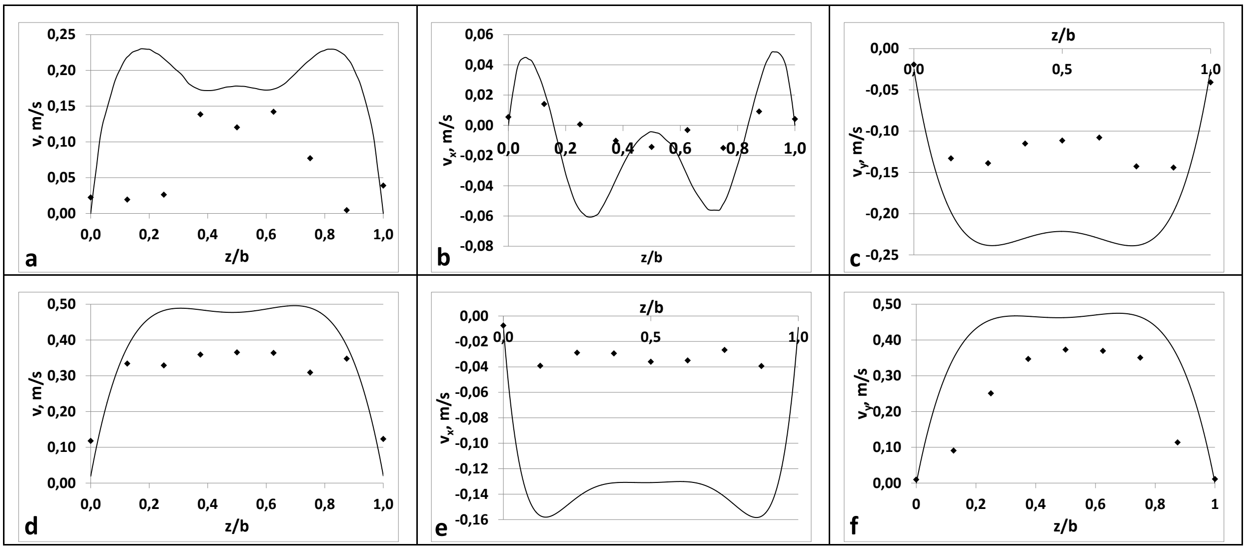

Fig. 6. Comparison of measured (dots) and simulated (lines) velocity profiles near trailing (a, b, c) and leading (d, e, f) walls at Re_{Dh} = 2000: a and b – total velocity *v*; d and e – v_x component; c and f – v_y component

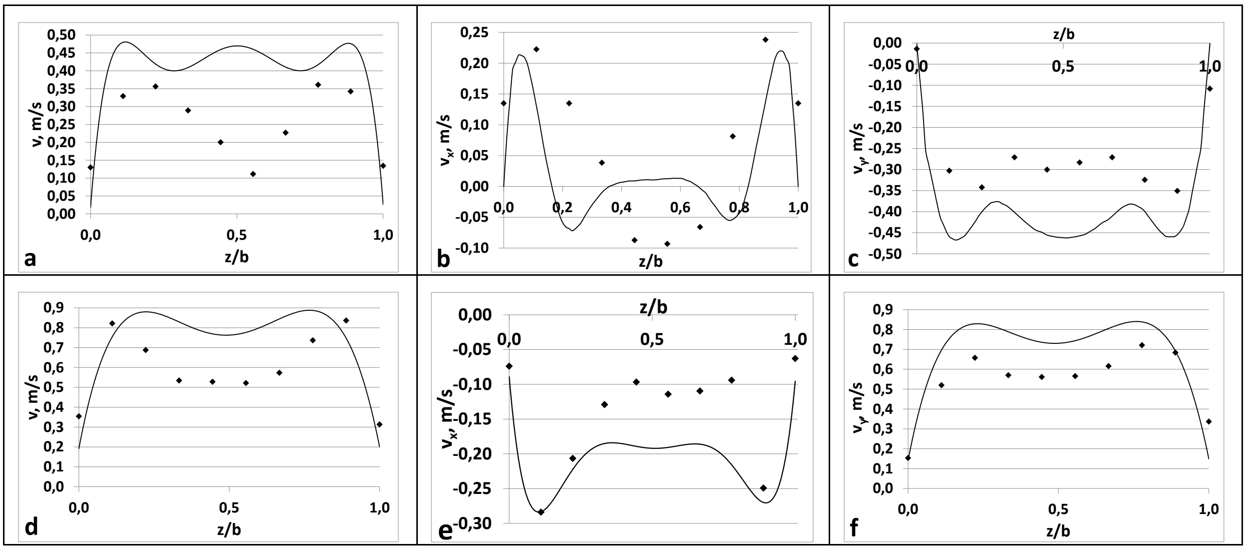

Fig. 7. Comparison of measured (dots) and simulated (lines) velocity profiles near trailing (a, b, c) and leading (d, e, f) walls at Re_{Dh} = 3000: a and b – total velocity *v*; d and e – v_x component; c and f – v_y component

Also it is observed that at $Re_{Dh} > 2000$, scalar maps show total v_y velocity component to have toothed form distribution near trailing wall. Stretched velocity zones near side walls can be related to v_x velocity component values in the same position.

3.2. Flow structure across centre of vortex

Streamlines at the x-z plane across the centre of vortex at different flow regimes are presented in Fig. 8 and velocity vectors at the same planes are presented in Fig. 9. In the case of laminar flow regime (Fig. 8 a and 9 a) flow is two-dimensional. No longitudinal vortices are observed. After flow velocity in channel increases up to Re_{Dh} = 1000 corner vortices near trailing wall is formed. Flow structure is symmetrical with respect to mid-plane of the cavity. Inward out-of-the-plane current formed in the centre part of cavity and directed towards lid of the cavity is observed. Similar inward flow structures are observed in square and rectangular lid-driven cavities at Re = 1000–3200 [14, 20]. While increasing Re_{Dh} this inward flow intensifies. Bigger volume of flow crosses the plane as it can be seen from wider “V” shape structure at the centre of cavity. As a result vortices near the trailing edge are squeezed into the corners. As Re_{Dh} increases the gap of lover velocity flow between vortices also increases. At $Re_{Dh} = 3000$ new velocity peak between vortices occurs as seen in Fig. 7 a.

In general flow structure overcomes drastic changes in the range of $100 < Re_{Dh} < 1000$, where signs of flow three-dimensionality occurs. At $Re_{Dh} > 1000$ changes in flow topology are not such drastic and for further analysis only the case of $Re_{Dh} = 3000$ is investigated. Flow is regime is fully turbulent at this Re_{Dh}.

Streamlines at y-z plane for $Re_{Dh} = 3000$ at different x/L (near trailing wall (a), in the mid-plane of cavity (b) and near the leading wall (c)) planes of cavity are presented in Fig. 10. As can be seen from presented streamlines corner vortices are formed in the main channel. The existence of secondary corner vortices in square-cross section channel is already analysed by other authors [21, 22]. Near trailing wall of cavity corner vortices are formed in all corners but they disappear from upper side of channel while approaching the leading wall of cavity. Nevertheless, corner vortices are observed in the middle plane (Fig. 10 b) just immediately above intersection with cavity.

Flow structure inside the cavity is fully three-dimensional and topology changes rapidly with x/L. In the plane near trailing wall of cavity (Fig. 10 a) intersection between primary and secondary vortices is clearly visible. The direction of flow in the intersection is towards the reader corresponding to direction of primary vortex. Whereas, the direction of secondary vortex in the channel and direction of primary vortex are opposite small vortices just above the main channel are formed near side walls of the cavity. Vortical nature of cavity flow is clearly visible in the mid-plane of cavity (Fig. 10 b). Three vortices pairs located just above main channel, in the intersection between primary and secondary vortices and above secondary vortex are well defined. Since the vortical flow is stronger in the mid-plane, vortices near the lid of the cavity are better defined despite the lack of corner vortices in the channel. Also, inward flow discussed above, directed towards cavity lid is observed. By analogy, flow direction near the leading wall of cavity in the interception between primary and secondary vortices (Fig. 10 c) is directed towards the reader since flow is entering the cavity near leading edge. For the same reason flow direction in the upper corners of channel and lower side of cavity is the same, thus corner vortices are not observed in the intersection.

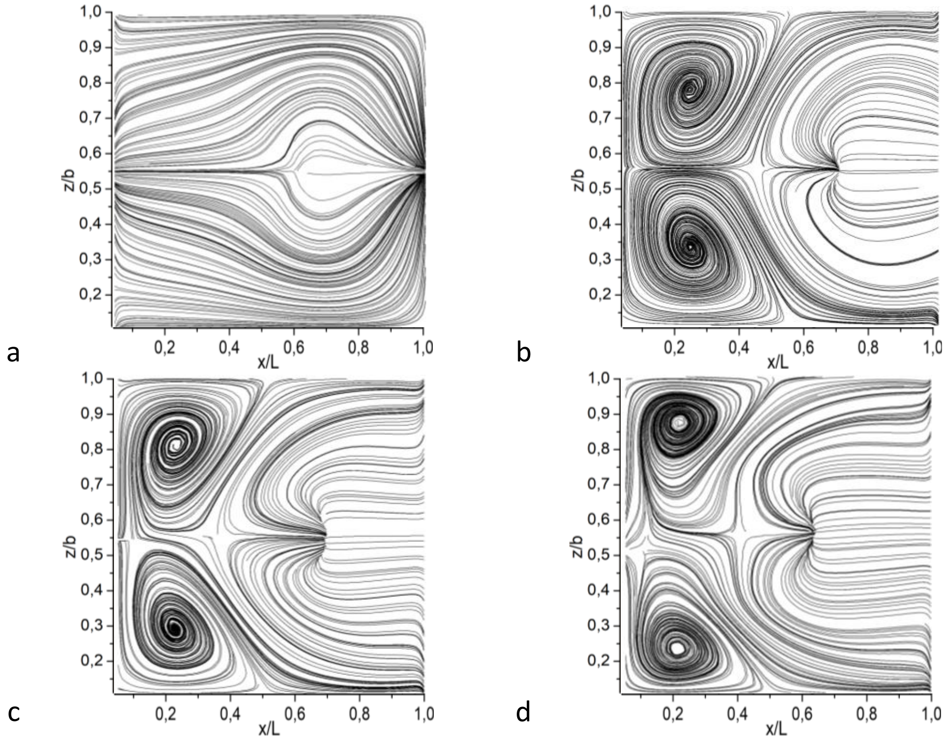

Fig. 8. Streamlines at x-z plane across the centre of vortex at Re_{Dh}: a) 100; b) 1000; c) 2000; d) 3000

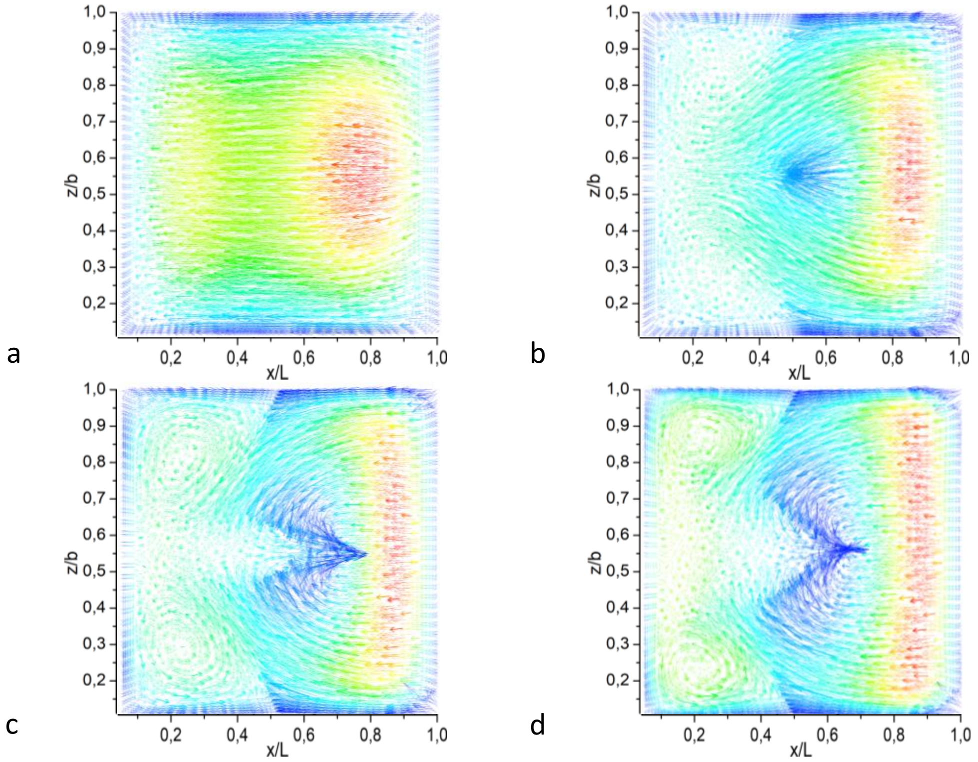

Fig. 9. Velocity vectors at x-z plane across the centre of vortex at Re_{Dh} a) 100; b) 1000; c) 2000; d) 3000

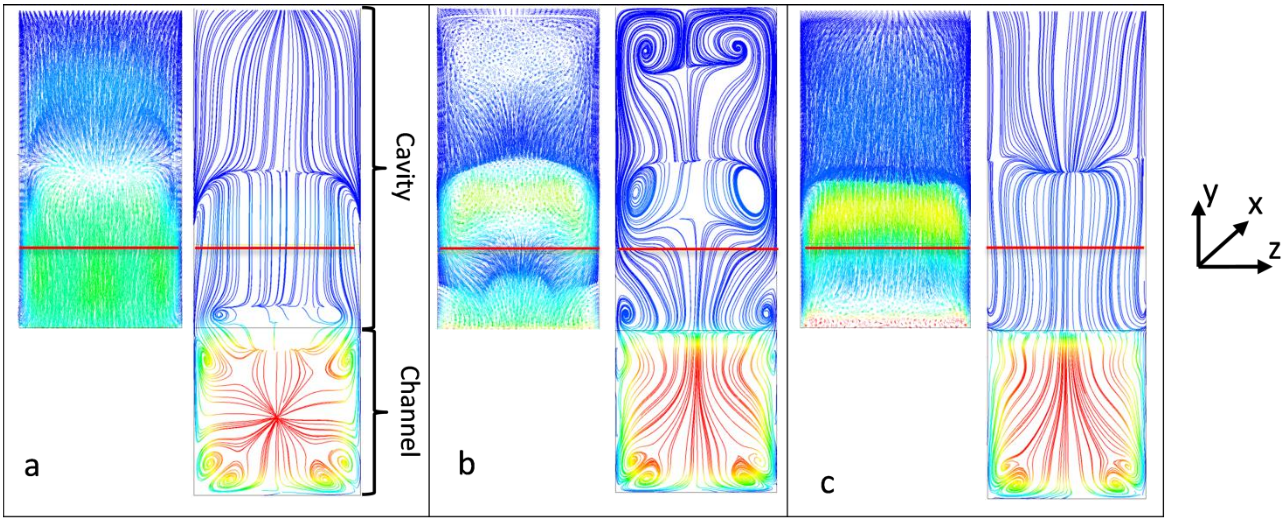

Fig. 10. Velocity vectors and streamlines at y-z plane at different x/L distances for Re_{Dh} = 3000: a) x/L = 0.2 (near trailing wall); b) x/L = 0.5 (mid-plane); x/L = 0.8 (near leading wall). Red lines indicate position of primary vortex centre

Scheme of flow streamlines at different measurement planes of cavity is presented in Fig. 11. All flow fields are obtained by using three-dimensional numerical simulation. Present figure summarises obtained results. Flow structure is symmetrical in respect of cavity axis. Vortical flow in deep open-type cavity at turbulent flow regime (Re_{Dh} > 1000) is a system of counter rotating vortices. Additional vortical structures are formed in the interception between main flow in the main channel and recirculating flow in the cavity and between primary and secondary vortices in the cavity. Unfortunately, in this study experimental measurement results alone are not sufficient enough to present information of three-dimensional flow structure, therefore, numerical three-dimensional simulation must be used.

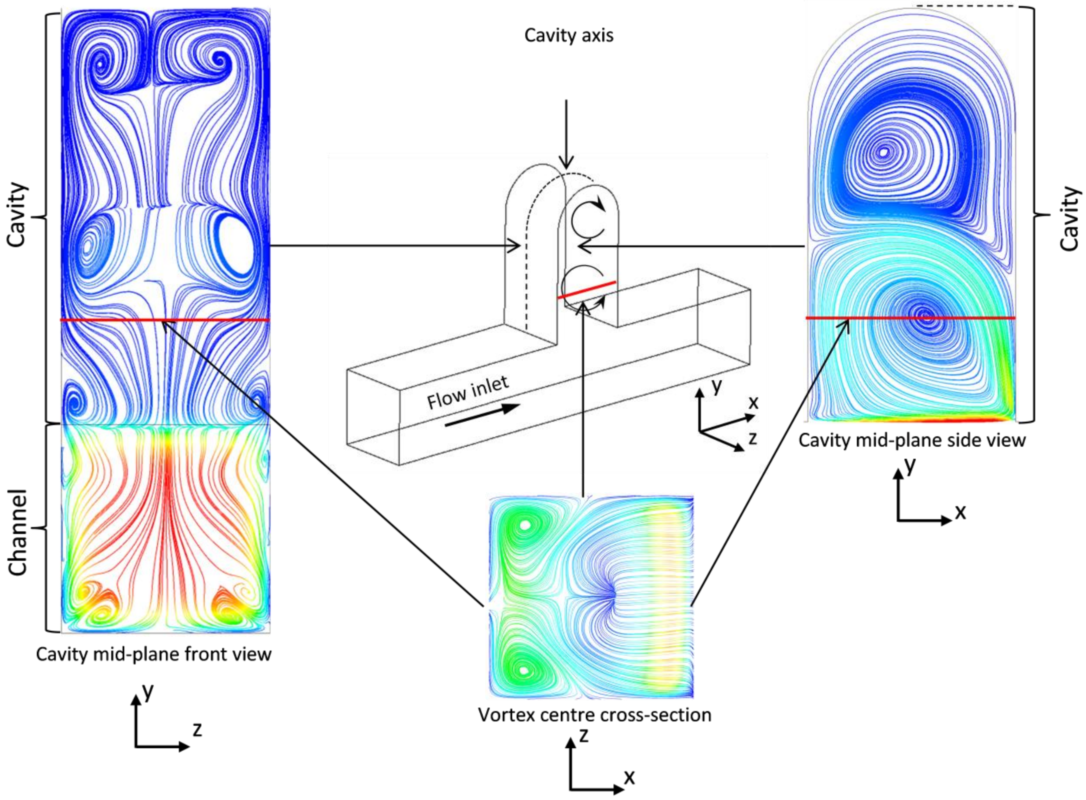

Fig. 11. Streamlines at different planes in open-type cavity

4. CONCLUSIONS

In this article flow structure in open-type cavity was discussed in wide range of Reynolds numbers covering laminar, transitional and turbulent flow regimes. Measured and numerically simulated velocity distribution was analysed in the plane crossing the centre of primary vortex. In the case of laminar flow regime ($Re_{Dh} = 100$) flow in the cavity is two-dimensional consisted of single vortex near the lid of cavity. Vortical structures in the corners near trailing wall of cavity and inward current in the centre of cavity form at $Re_{Dh} \geq 1000$. While further increasing Reynolds number up to $Re_{Dh} = 3000$ vortices are squeezed into the corners and low velocity zone appears between vortices. Vortical flow in cavity bifurcates into two separate symmetrical structures. The volume of inward out-of-the-plane flow also increases with Re_{Dh}.

System of counter-rotating vortices in cavity is observed using three-dimensional numerical simulation. Streamlines at different planes of cavity reveal three-dimensional flow nature in the cavity. Experimental flow-visualization at different cavity planes should be performed to obtain full picture of flow structure in deep open-type cavity.

REFERENCES

1. SHANKAR, P. N.; DESHPANDE, M. D. Fluid mechanics in the driven cavity. *Annual review of fluid mechanics*, 2000, Vol. 32, p. 93-136.
2. FISHLER, R.; MULLIGAN, M.K.; SZNITMAN, J. Mapping low-Reynolds-number microcavity flows using microfluidic screening devices. *Microfluid Nanofluid*, 2013, Vol. 15, p. 491-500.
3. SHEN, F.; XIAO, P.; LIU, Z. Microparticle image velocimetry (μPIV) study of microcavity flow at low Reynolds number. *Microfluid Nanofluid*, 2015, Vol. 15, p. 403-417.
4. CHENG, M.; HUNG, K.C. Vortex structure of steady flow in a rectangular cavity. *Computers & Fluids*, 2006, Vol. 35, p. 1046-1062.

5. CHENG, C.-H.; CHEN, C-L. Buoyancy-induced periodic flow and heat transfer in lid-driven cavities with different cross-sectional shapes. *International Communications in Heat and Mass Transfer*, 2005, Vol. 32, p. 483-490.
6. MERCAN, H.; ATALIK, K. Vortex formation in lid-driven arc-shape cavity flows at high Reynolds numbers. *European Journal of Mechanics B/Fluids*, 2009, Vol. 28, p. 61-71.
7. HERMAN, C.; KANG, E. Heat transfer enhancement in a grooved channel with curved vanes. *International Journal of Heat and Mass Transfer*, 2002, Vol. 45, p. 3741-3757.
8. SELIMEFENDIGIL, F. Numerical analysis of mixed convection in pulsating flow for a horizontal channel with a cavity heated from below. *Thermal Science*, 2016, Vol. 20(1), p. 35-44.
9. ANDERSON, P.D.; GALAKTIONOV, O.S.; PETERS, G.W.M.; VAN DE VOSSE F.N.; MEIJER, H.E.H. Chaotic fluid mixing in non-quasi-static time-periodic cavity flows. *International Journal of Heat and Fluid Flow*, 2000, Vol. 21, p. 176-185.
10. KHABIRY M, CHUNG B.G., HANCOCK M.J., SOUNDARARAJAN H.C., DU Y., CROPEK D., LEE W.G., KHADEMHOSSEINI A. Cell docking in double grooves in a microfluidic channel. *Small*, 2009, Vol. 5, No. 10, p. 1186-1194.
11. JANG, Y.H.; KWON, C.H.; KIM, S.B.; SELIMOVIC, S.; SIM, W.-Y.; BAE, H., KHADEMHOSSEINI, A. Deep wells integrated with microfluidic valves for stable docking and storage of cells. *Biotechnology Journal*, 2011, Vol. 6(2), p. 156-164.
12. MANBACHI, A.; SHIVASTAVA, S.; CIOFFI, M.; CHUNG, B. G.; MORETTI, M.; DEMIRCI, U.; YLIPERTTULA, M.; KHANDEMHOSSEINI, A. Microcirculation within grooved substrates regulates cell positioning and cell docking inside microfluidic channels. *Lab Chip*, 2008, Vol. 8(5), p. 747-754.
13. YAO, H.; COOPER, R.K.; RAGHUNATHAN, S. Numerical simulation of incompressible laminar flow over three-dimensional rectangular cavities. *Journal of Fluids Engineering*, 2004, Vol. 126, p. 919-927.
14. MIGEON, C.; PINEAU, G.; TEXIER, A. Three-dimensionality development inside standard parallelepipedic lid-driven cavities ar Re = 1000. *Journal of Fluids and Structures*, 2003, Vol. 17, p. 717-738.
15. COUTANCEAU, M.; MIGEON, C.; EHRMANN, P. Particulars of the cross- and spanwise near-wake development of a short semicircular-section shell, through the transition Re-range ($60 \leq Re \leq 600$). *Journal of Visualization*, 2000, Vol. 3, p. 9-26.
16. FAURE, T.; PASTUR, L.; LUSSEYRAN, F.; FRAIGNEAU, Y.; BISCH, D. Three-dimensional centrifugal instabilities development inside a parallelepipedic open cavity of various shape. *Experiments in Fluids*, 2009, Vol. 47, No. 3, p. 395-410.
17. FELDMAN, Y., Oscillatory instability of fully 3D flow in a cubic diagonally lid-driven cavity. *arXiv preprint arXiv: 1606.3267*, 2013.
18. VILKINIS, P.; VALANTINAVIČIUS, M.; PEDIŠIUS, N. Investigation of fluid flow structure in open type cavity under stationary and pulsatile flow conditions. *Energetika*, 2016, Vol. 62, p. 37-44.
19. VILKINIS, P.; PEDIŠIUS, N. Investigation of pulsating flow in open-type microcavity. *Proceedings of CYSENI*, 2017. p. IX-308 - IX-315.
20. MIGEON, C. Details on the start-up development of the Taylor-Gortler-like vortices inside a square-section lid-driven cavity for $1,000 \leq Re \leq 3,200$. *Experiments in Fluids*, 2002, Vol. 33, p. 594-602.
21. BAI, J.H.; STOESSR, T. Transport and deposition of fine sediment in open channel with different aspect ratios. *Earth surface processes and landforms*, 2012, Vol. 38, p. 591-600.
22. GALLETTI, B.; BOTTARO, A. large-scale secondary structures in duct flow. *Journal of Fluid mechanics*, 2004, Vol. 512, p. 85-94.

CYSENI 2019, May 23-24, Kaunas, Lithuania
ISSN 1822-7554, www.cyseni.com

RADIATIVE HEAT TRANSFER IN PACKED BED OF SPHERICAL PARTICLES

A. I. Malinouski, O. S. Rabinovich
A. V. Luikov Heat and Mass Transfer Institute
National Academy of Sciences of Belarus
P. Brouka str. 15, 220072 Minsk – Belarus
Email: a_malin@hmti.ac.by

ABSTRACT

A new technique for implementing external (particle-to-wall) and particle-to-particle radiative heat transfer in discrete element method (DEM) simulations is proposed. It is based on view factor calculation. The idea behind the article is to find relevant local bed parameters and establish relations between them and statistically averaged view factors. Calculation of view factors via formula evaluation requires considerably less computational effort then in situ integration, while providing comparable accuracy. The proposed method is more robust than transient direct calculation of instant view factors, but more accurate than simple averaging among neighbours. Both mono- and polydisperse mixtures of spherical particles were considered. It was shown that for dense beds simple linear dependence on particle to wall distance is valid for external radiative heat flux. Also, relation between relative particle size and its view factor to the wall was found for polydisperse beds. Exponential fit was proposed for particle-particle radiative heat flux estimation. Generalisation of obtained formula for various bed porosities is proposed. A DEM implementation of proposed relations is showcased using the simple example of external radiative heat-up of cylindrical particle bed.

Keywords: configuration factor; radiative heat transfer; packed bed; discrete element methods

1. INTRODUCTION

There are a few ways of transmitting thermal energy in gas-solid systems. Radiative heat transfer is one of them. Importance of its effect varies severely depending on situation, due to the fact that radiative heat flux is proportional to temperature in the fourth degree. There are several indicators that radiative transfer matter a lot for current application: if particles are large and temperature is high, or if other ways of heat transfer are suppressed.

Examples of such applications are particle beds that are used for heat transportation, say, in heliothermal stations; combustion of particles (especially when high temperature gradients are expected); and so on.

If we consider specifics of DEM techniques, there are several key targets: computational robustness, parallelisation, accuracy. DEM program codes that are used nowadays (LIGGGHTS, XDEM) are evolving steadily, yet there are many assumptions that would hardly be terminated soon. One of them is homogeneous temperature of particle surface.

There are several approaches commonly used for modelling radiative transfer in dispersed media. Historically the most common way to describe heat transfer in gas-solid systems, such as packed or fluidised beds, is to make use of effective heat conductivity model.

Review of radiation transfer equation can be found [1].

Diffusion-like description of heat transfer in particle systems, especially through radiative and conductive mechanisms, uses several assumptions and empirical coefficients that are hard to validate.

In contrast, Discrete Elements Method (DEM) makes it possible to resolve that issues by natural consideration of system on the particle scale.

It is safe to say that technique of description for both conductive and convective heat transfer in DEM calculations has been firmly established by now and has only slight variations between many modern papers [2].

However, as stated earlier, for a number of processes radiative heat transfer is crucial and should be also taken into consideration. Unlike conduction and convection, there is no widely approved standard in its implementation.

1.1. Overview of existing approaches to modeling radiative heat transfer in particle + gas systems

Heat transfer in beds with large particles (~ 1 cm) is studied usually in context of investigating projects of pebble-bed nuclear reactors. Relations were formulated for effective heat conductivity in particle bed with static gas, taking into account gas conductivity and radiative heat transfer [3].

Though, in this case conductivity through contacts was neglected, that considerably constraints class of problems where it can be used - it is viable only for large, stiff, spherical particles under no convection.

In article [4] it is proposed to use temperature $\mathrm{T_{local}}$, obtained as an average among particles in some neighbourhood of given particle, as an effective ambient temperature in calculation of radiative heat flux from ith particle:

$$\mathrm{Q_{i,rad}} = \sigma\varepsilon_{\mathrm{pi}}\mathrm{A_i}\left(\mathrm{T_{local,i}^4} - \mathrm{T_i^4}\right), \tag{1}$$

where σ is Stefan-Boltzmann constant, $\varepsilon_{\mathrm{pi}}$ – greyness coefficient, $\mathrm{T_i}$ – temperature of ith particle, $\mathrm{A_i}$ – its surface area.

Shortcomings are averaging of temperature and nondirected heat flux. As a result, one can encounter significant errors when calculating temperature in presence of high temperature gradients in bed; moreover, it is hard to establish conservation of integral heat using this approach. Principal advantage of this method is its numerical robustness.

Another approach is presented in work [5]. It is assumed that particles are grey, opaque spheres. Voronoi tesselation is applied, with polyhedra substituted with cones of the same volume. Radiative heat transfer between opaque surfaces is commonly described through view factor, which is defined as the proportion of the radiative flux which leaves surface A that strikes surface B. Formula for view factor between sectors on two spheres are well known, then the equation for radiative heat flux could be obtained:

$$\mathrm{Q_{ij,rad}} = \frac{\sigma\left(\mathrm{T_i^4}-\mathrm{T_j^4}\right)}{\frac{1-\varepsilon_{\mathrm{r,i}}}{\varepsilon_{\mathrm{r,i}}\mathrm{A_i}}+\frac{1}{\mathrm{A_iF_{ij}}+\left[1/\mathrm{A_iF_{iR}}+1/\mathrm{A_jF_{jR}}\right]^{-1}}+\frac{1-\varepsilon_{\mathrm{r,j}}}{\varepsilon_{\mathrm{r,j}}\mathrm{A_j}}}, \tag{2}$$

here $Q_{i,rad}$ – radiative heat flux from ith to jth particle, A_i, A_j – visible surface area of particles, $\varepsilon_{r,i}$ – greyness coefficient, F_{ij} – view factor between hemispheres.

One of the shortcomings of this approach is inability to correctly account for possible effect of other particles, that can reduce visible area. Therefore, method is correct only for calculating flux towards the closest neighbours. Moreover, Voronoi tesselation is relatively computationally costly procedure.

Collaboration working on CFDEMcoupling implemented an approach to calculate view factors between spherical particles during main calculation. Their idea [6] is to substitute view factors between particles with body angles. This method deals with overlaying projections on the surface of ith particle of every jth particle. View factors are proportional to body angles that are seen from the centre of ith particle. This approach allows to account correctly for partial obstruction between different neighbours, but yields substantial error for nearest (and most relevant) neighbours; that problem is partially solved by introducing additional correction factor.

XDEM collaboration [7] has another, simplier but arguably coarser implementation. The view factor between particles $\mathrm{F}_{\mathrm{i}\rightarrow\mathrm{j}}$ is determined as the ratio of the surface of particle i to the sum of the surfaces A_{j} of all neighbouring particles j with

$$\mathrm{F}_{\mathrm{i}\rightarrow\mathrm{j}} = \frac{\mathrm{A}_{\mathrm{i}}}{\sum_{\mathrm{j}} \mathrm{A}_{\mathrm{j}}}. \tag{3}$$

Thus, it is assumed that particle i emits a radiative flux at surface temperature T_s and adsorbs a flux from all neighbouring particles j weighted by the respective view factor $\mathrm{F}_{\mathrm{i}\rightarrow\mathrm{j}}$.

There are also several ways of using ray tracing for calculating view factors for heat transfer calculations. Starting from using well-established hemicube method implemented in standard OpenGL libraries [8]. Another authors [9] implemented a transient variation of ray tracing between the particles in bed. For every (ith) particle in every time step (Δt) a ray is generated that emits from random point on particle surface in random direction, and a certain amount of thermal energy is associated with it that is equal to integral energy emitted from whole particle surface during timestep ($Q_i = 4\pi r_i^2 T_i^4 \Delta t$); this amount of energy now travels with the ray. When ray intersects another particle, it transfers $\epsilon_i Q_i$ to it, and $(1 - \epsilon_i)Q_i$ is reflected as another ray; this procedure is repeated until ray travels to the cut-off distance from the initial particle. If until that ray didn't meet any particle, it is considered to go to ambient space. In that case the first particle gets additional $Q_{ext} = 4\pi r_i^2 T_{ext}^4 \Delta t$ from ambient source.

That way, because timestep for particles is considerably smaller then characteristic time of thermal relaxation for particle bed, in the long run amount of transmitted heat between the particles would be proportional to view factor between them.

In [10] Spherical Nodalization Unit method was proposed. It is based upon finding empirical relation for particle-to-particle view factor in generated particle bed with natural porosity. In many cases – for packed bed, and in emulsive phase of fluidized bed – porosity is virtually the same, as is distances between particles. In that very cases obtained relation can be used. In the same way view factors between particle and external boundary can be found for problems of external radiative heat transfer.

This method has remarkably easy and computationally robust implementation, but it has its weak spots – for example, it would struggle to deal with any inhomogenuities in bed (say bubbles in fluidized bed), and it lacks implementation for polydisperse beds.

The idea of this work is to make radiative heat transfer algorithm similar to conductive heat transfer. In order to do so, we should find relation between statistically expected value of view factor and a set of particle and bed properties. Heat transfer calculation, therefore, would require at minimum, distance between particles and their radii. Optional is accounting for particle size distribution bed-wise, emissivity, local porosity.

2. METHODOLOGY

2.1. Particle bed generation

It is essential to formulate the model system such that it would possess the properties of real particle beds and would be compatible with DEM approach to particle systems. In order to generate packed bed of particles for further investigation, DEM code LIGGGHTS® version 3.8.0 was used. Cylindrical shape of bed was chosen (typical view in Fig. 1), with average particle to bed diameter ratio 30, number of particles in bed 20000. Particle to wall view factors were calculated against the cylinder wall. The bed was big enough to neglect the effects of top and bottom boundaries by considering only particles at least 5 diameters away from them.

To simulate real-world polydisperse beds for investigation of radiation factors, we used empirically obtained Rosin-Rammler distribution for particle size

$$Y = 1 - \mathrm{Exp}\left[-\frac{x}{x_0}\right]^n, \tag{4}$$

where Y is cumulative mass fraction, x is particle radius, x_0 and n are distribution parameters.

Numerically array of particle radii was generated with random.weibull function from numpy library

$$Y = \lambda\left(-\ln(U)\right)^{1/s} \tag{5}$$

using uniform pseudorandom distribution U, with scale parameter λ = 0.0003, and with spread parameter *s* (which essentially inversely related to width of particle size distribution) values 4, 5, 6, 8, 10, 12, 15, 18. Typical distribution curves are presented in Fig. 2.

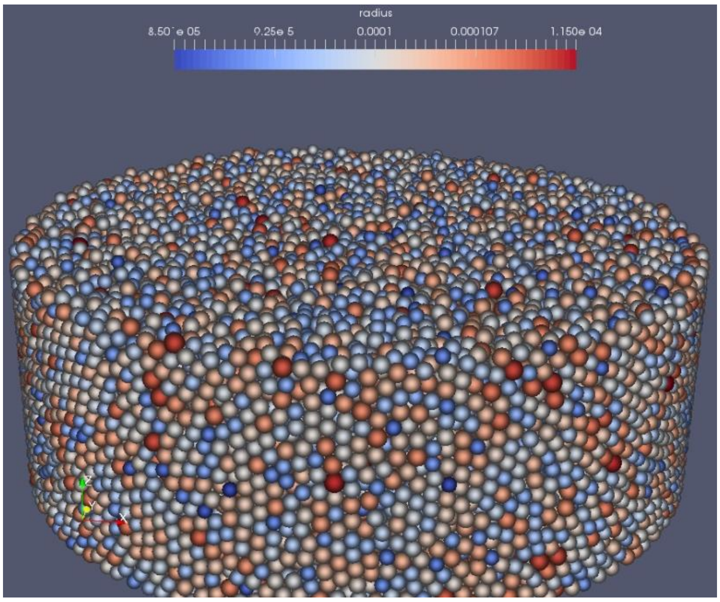

Fig. 1. General view of generated polydisperse particle bed

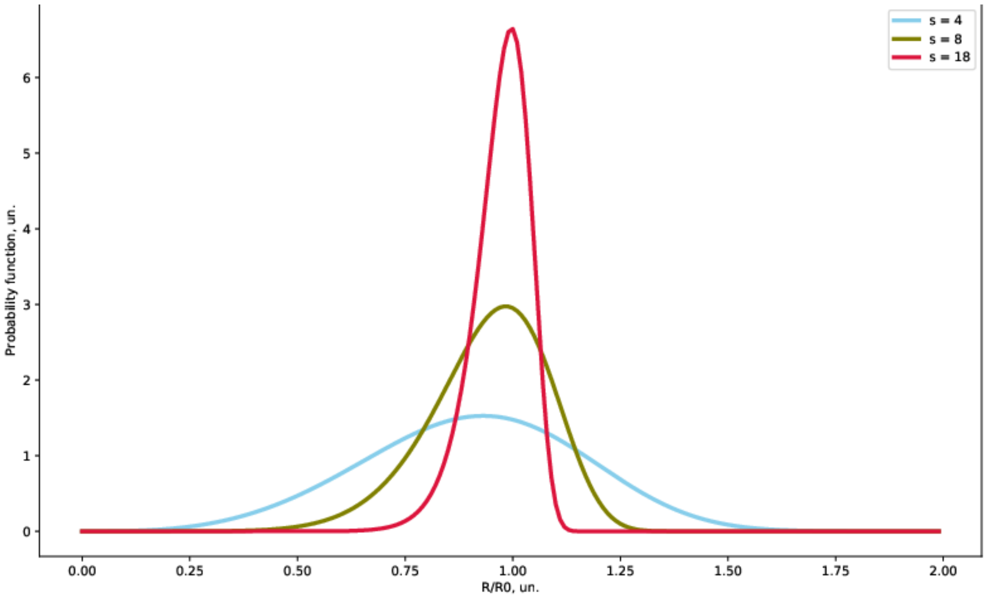

Fig. 2. Typical probability density function of particle radii with Rosin-Rammler distribution for several values of spread parameter *s*

2.1.1. Generation of beds with specific porosity values

Ensuring that packing of particle bed is realistic is generally important for granular applications, and may be even more so for calculation of view factors as they essentially are functions of relative position of particles. Typical case is random close packing of spheres with porosity 0.36-0.39. In fluidized systems there could be regions with higher porosity.

In this work, we used a model of elastic spheres with Hooke law of mechanical interaction and friction. Material properties are listed in Table 1.

Table 1. Properties of generated particles

Parameter	**Value**
Young's modulus	$5.0{\cdot}10^6$ Pa
Poisson's ratio	0.45
Coefficient of restitution	0.9
Friction coefficient	0.5
Particle count	12 000
Particle density	2000 kg/m^3
Bed to average particle diameter ratio	30

After the necessary number of particles were generated inside cylindrical vessel, they were relaxed in gravity field to form a fixed bed. This way the porosity that corresponds to close random packing was naturally obtained.

To reproduce higher porosities, special procedure was implemented. Again, the same number of particles were generated inside cylindrical vessel; but this time the height of the vessel was adjusted to correspond to desired value of porosity. The particles were constrained in cylinder, and their velocity vector was modulated with random function. In this case, no external field (e.g. gravity) was applied. The final particles positions were obtained after the velocity vanished due to energy dissipation at collisions.

As a result, particle beds with natural porosity (0.39) and series of values from 0.45 to 0.62 were generated. Fig. 3 illustrates that porosity is uniform except for the near-wall effects. It is not efficient to consider porosities higher than that with proposed method. The reason for that is characteristic distance of radiative transport that becomes much higher than reasonable distance for calculating mechanical interaction, therefore, it requires separate algorithm for detecting neighbours.

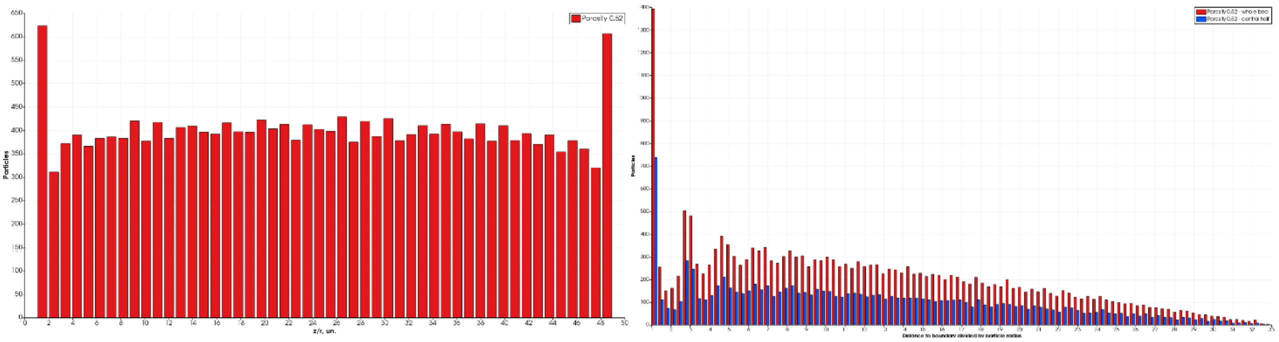

Fig. 3. Histograms of particle's centres distribution for porosity 0.52 in vertical direction (left) and in radial direction (right) for the whole bed (in red) and without ¼ of particles near its top and bottom (blue)

2.2. View factor calculation

Numerical procedure of calculating view factors implies numerical integrating of view factors from elemental patches ΔF_{ij} over surfaces of two objects (spheres) with surfaces A_i and A_j.

$$\Delta F_{ij} = \frac{\cos\theta_1 \cos\theta_2}{\pi s^2} dA_j;\quad F_{ij} = \frac{1}{A_i}\int_{A_i}\int_{A_j} \frac{\cos\theta_1 \cos\theta_2}{\pi s^2} dA_j dA_i\,. \tag{6}$$

This procedure is classical way of view factor calculation, and described in detail, for example, [11]. For calculation in our work simple spherical discretization was implemented, as it is better suited for calculation with arbitrary position of neighbour spheres.

In case of calculating view factors between particle and wall, cylindrical wall was substituted with disk oriented tangentially with center at the point where normal from particle center intersects wall surface (Fig. 4). If spheres are deformed, body angle that corresponds to contact spot is included in view factor.

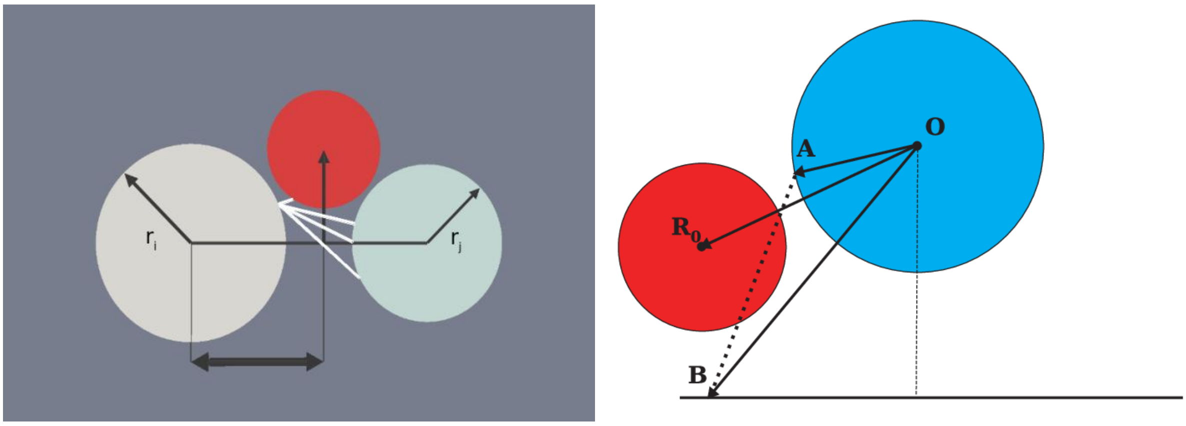

Fig. 4. Sketch of view factor calculation between particles (left) and between particle and wall (right) with respect to obstructing particle (red)

2.3. Verification and accuracy optimization

In order to ensure correct numerical implementation, we checked it results in asymptotic cases where analytical solutions are available. For particle-particle view factor, there is a semi-analytic correlation for two spheres with radius ratio R = r_1/r_2 and nondimensional distance S = s/r_2 [12]:

$$F_{ijsph} = \left(1 - \sqrt{1 - \left(\frac{R}{S+R+1}\right)^2}\right)\left(1 - \sqrt{1 - \left(\frac{1}{S+R+1}\right)^2}\right)\left(\frac{S+R+1}{R}\right)^2. \tag{7}$$

Discrepancy was under 2% for discretization of mutually visible sphere areas into 40 by 40 patches. Higher discretization causes considerable increase in computation time.

For particle to wall view factors, we tested what diameter of disk that imitates wall and dimension of grid discretization of particles would be optimal.

We conducted several calculations with different discretization number and size of boundary disk, as shown in Fig. 5. As a result, serial calculations were made with D = 4L, discretization of 40 for every dimension in spherical coordinates.

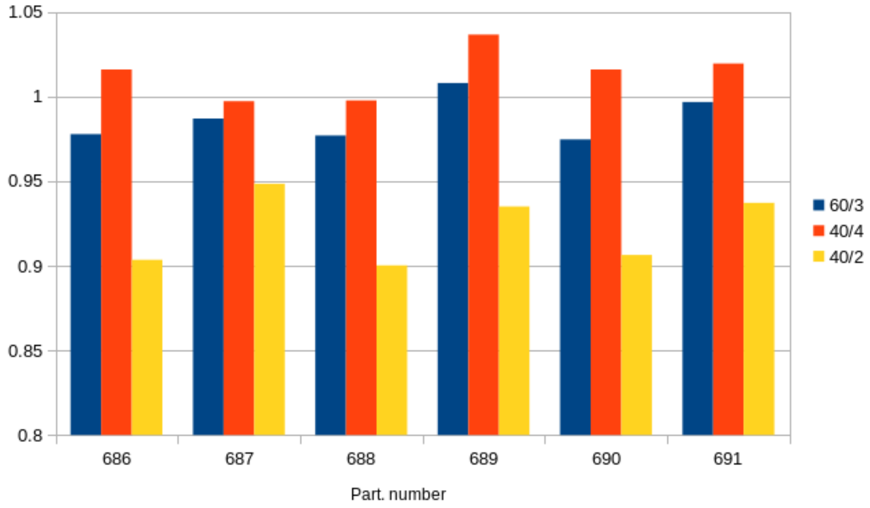

Fig. 5. View factors of selected particles with different discretization number and diameter of boundary disk, normalized by the most accurate obtained value

3. RESULTS AND DISCUSSIONS

The general idea proposed in the article is to find relevant local bed parameters and establish relations between them and statistically averaged view factors. When implemented in DEM code, calculation of view factors via formula evaluation requires considerably less computational effort then in situ integration, while providing comparable accuracy.

3.1. Particle-to-boundary view factors

One can expect view factor between particle and wall to decrease rapidly while increasing the distance between them. Given all the assumptions we implicitly make (and first of all uniform temperature of particle surface), in most actual cases it is safe to neglect radiative heat transfer to the wall if expected corresponding view factor is 0.01 or less. We were able to find out several parameters that make it possible to formulate relatively simple relations for view factor between particle and nearby boundary.

First, we introduce normalized distance $L^* = H/R$, where H is distance from sphere to wall (equals 0 when they touch each other), and R is radius of the particle.

It turns out that for particle bed of uniform spheres with close random packing relation between view factor F_{ex} and distance to the wall is fitted well by linear function in region where $F_{ex} \geq 0.05$. Its accuracy is sufficient for most applications. To even more surprise, this function seems to be the same for every polydisperse system we considered. Linear relation (valid for $L^* < 1.5$)

$$F_{ex1} = 0.31 - 0.19L^*. \tag{8}$$

We recommend for a moderate accuracy use equation (7) for $L^* < 1.5$ or for non-negative function values, and equal to 0 for all other particles.

Another possible fit is simple exponential relation

$$F_{ex2} = 0.31e^{-1.2L^*}. \tag{9}$$

3.1.1. Polydisperse correction

We can further enhance the accuracy of prediction for polydisperse mixtures. It turns out that smaller particles has on average higher view factor with wall, as they centers can be closer to wall. In this situation we can introduce another parameter R^*: size of the current particle R relative to the average particle size of the mixture $< R >$.

$$\mathrm{R}^* = (\mathrm{R} - < \mathrm{R} >)/< R > . \tag{10}$$

We search for the best fit in the following form:

$$F = f_0 + k_L L^* + k_R R^* . \tag{11}$$

Using native linear fitting module from R framework, we found following values (Table 1).

Table 1. Results of fitting data with formula (5)

Parameter	Estimate	Std. Error
f_0	0.306	0.0003
k_L	-0.189	0.0007
k_R	-0.103	0.0012

As fitting is sufficiently accurate (adjusted R-squared 0.962) and simple, we can recommend using following general correlation for view factor between particle and wall in polydisperse bed with close random packing:

$$F = 0.31 - 0.19L^* - 0.10R^* . \tag{12}$$

3.1.2. Variable porosity

Porosity is another parameter that should be considered. We propose to keep the linear dependency in the form of (12) for the sake of simplicity and consistency.

$$F = f_0 + k_L L^* + k_\varepsilon \epsilon + k_{\varepsilon L} \epsilon L^* . \tag{13}$$

Fitting for monosized particles showed that linear approximation becomes rougher for higher porosity. Yet, adjusted R-squared for linear law remains reasonably high ($R^2 > 0.83$) in studied range of porosities to stick with this form of relation.

Table 2. Results of Direct fitting for monodisperse particles with formula (13)

Parameter	Estimate	Std. Error
f_0	0.201641	0.001564
k_L	-0.311920	0.003168
k_ε	0.279812	0.003114
$k_{\varepsilon L}$	0.309267	0.006146

Coefficients are changing steadily with porosity; so, we can generalize them as

$$F = 0.20 - 0.31L^* + 0.28\epsilon + 0.31\epsilon L^* = (0.20 + 0.28\epsilon) - (0.31 - 0.31\epsilon)L^* . \tag{14}$$

3.2. Particle to particle view factor

3.2.1. Parametrisation

In case of particle to particle view factors, the parameters that were chosen for correlation search were ratio of particle radii and distance between them.

There is another aspect to be consider. For the reason of energy conservation correlation should be reversible, e.g. yield the same flux when calculated for any of two particles. Obviously, for monodisperse systems this feature is implemented by default; but to deal with polydisperse mixtures this mean that condition

$$F_{i-j} A_i = F_{j-i} A_j \tag{15}$$

should be met.

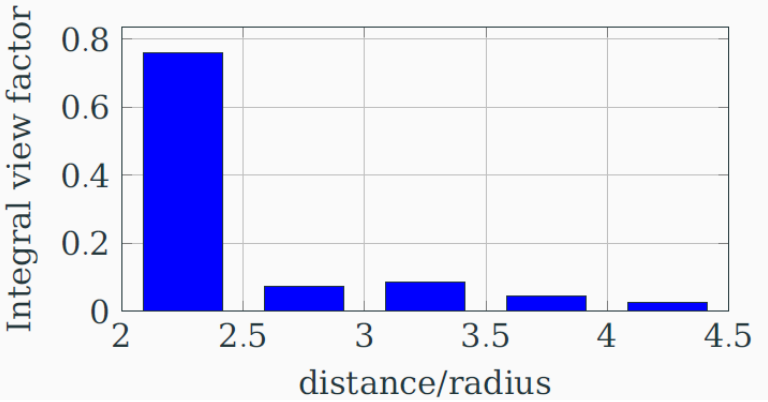

Fig. 6. Histogram of integral view factor between bins of particle neighbours according to their distance

3.2.2. *Correlation*

Average distribution of view factors for the neighbour particles sorted by their distance is illustrated in Fig. 6. One can see that although values are quickly decreasing for larger distances for individual particles, and major part is indeed related to closest neighbours, other particles combined account for more then 20% of view factor and, hence, heat flux. It should also be noted that every further bin consists of more particles (roughly as d^2).

We obtained relation only for close random packing (porosity 0.37). It consists of two cases:

for particle j with radius r_j within direct contact of particle i with radius r_i

$$F_{i-jdir} = 0.23\left(r_i/r_j + 0.8516\right)^{-1.8}, \tag{16}$$

for all other particles

$$F_{i-jind} = exp(1.5 - 1.9d/r). \tag{17}$$

where d is distance between particle centers, r is average particle radius.

For polydisperse mixture (17) is valid if $r_i \leq r_j$, in the opposite direction – it should be adjusted according to (15).

3.2.3. *Comparison to existing calculations*

We compared the correlations that we propose with data from direct calculation of view factors, available from [11] particle to particle view factors. The results shown in Fig. 7 suggest that correlation predicts actual view factors both qualitatively and quantitatively.

4. CONCLUSIONS

In this paper we propose several correlations to calculate view factors in beds both between particles and between particle and boundary wall. The correlations use parameters of particles (radius, distance between them) and collective parameters (average particle radius, porosity). We have found several nondimensional parameters that enable general formulation for particle-wall view factors in polydisperse mixtures and for a certain range of bed porosity.

The correlations were verified against asymptotic cases and data obtained in direct calculations of view factors.

The correlations are formulated in a way that is natural for accounting for radiative heat transfer in DEM.

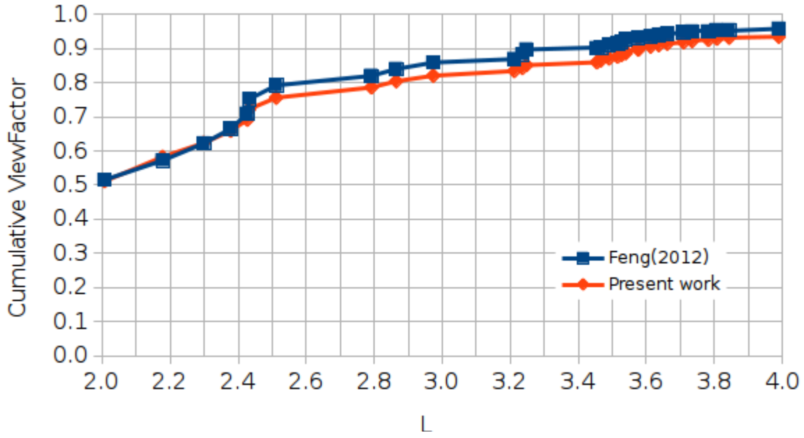

Fig. 7. Cumulative view factors of selected particle to its neighbours laying within sphere of radius L (according to direct calculations in [11]; and using formula proposed in current work)

REFERENCES

1. RANDRIANALISOA, J. & BAILLIS, D. Analytical model of radiative properties of packed beds and dispersed media. *Int. J. Heat Mass Transf.* 2014, Vol. 70, p. 264–275.
2. ZHOU, Z. Y., KUANG, S. B., CHU, K. W. & YU, a. B. Discrete particle simulation of particle–fluid flow: model formulations and their applicability. *J. Fluid Mech.* 2010, Vol. 661, p. 482–510.
3. SLAVIN, A. J., IRVINE, E. & PENSON, S. Analytical model for the thermal conductivity of a binary bed of packed spheroids in the presence of a static gas, with no adjustable parameters provided contact conductance is negligible. *Int. J. Heat Mass Transf.* 2004, Vol. 47, p. 1015–1021.
4. ZHOU, Z. Y., YU, A. B. & ZULLI, P. Particle scale study of heat transfer in packed and bubbling fluidized beds. *AIChE J.* 2009, Vol. 55, p. 868–884.
5. CHENG, G. J. & YU, A. B. Particle Scale Evaluation of the Effective Thermal Conductivity from the Structure of a Packed Bed: Radiation Heat Transfer. *Ind. Eng. Chem. Res.* 2013, Vol. 52, p. 12202–12211.
6. FORGBER, T. & RADL, S. A novel approach to calculate radiative thermal exchange in coupled particle simulations. *Powder Technol.* 2018, Vol. 323, p. 24–44.
7. PETERS, B., DŽIUGYS, A. & NAVAKAS, R. Simulation of thermal conversion of solid fuel by the discrete particle method. *Lith. J. Phys.* 2011, Vol. 51, p. 91–105.
8. KRAMER, S. C., GRITZKI, R., PERSCHK, A., RÖSLER, M. & FELSMANN, C. Fully parallel, OpenGL-based computation of obstructed area-to-area view factors. *J. Build. Perform. Simul.* 2015, Vol. 8, p. 266–281.
9. AMBERGER, S., PIRKER, S. & KLOSS, C. Thermal Radiation Modeling using Ray Tracing in LIGGGHTS. in 6th International Conference on Discrete Element Methods (DEM6), 2013.
10. PITSO, M. L. Characterisation of long range radiation heat transfer in packed pebble beds. Master thesis. Pretoria: North-West University, 2011.
11. FENG, Y. T. & HAN, K. An accurate evaluation of geometric view factors for modelling radiative heat transfer in randomly packed beds of equally sized spheres. *Int. J. Heat Mass Transf.*, 2012, Vol. 55, p. 6374–6383.
12. HOWELL, J. R., MENGUC, M. P. & SIEGEL, R. *Thermal Radiation Heat Transfer*. CRC Press, 2015. 1016 p. ISBN 9781466593268.

THERMODYNAMIC ANALYSIS OF A TRIPLE EFFECT ABSORPTION COOLING SYSTEM INTEGRATED WITH WASTE ENERGY

Y. E. Yuksel
Afyon Kocatepe University
Gazligol Street, 03200 – Turkey
Email: yeyuksel@aku.edu.tr

M. Koc, M. Ozturk
Isparta University of Applied Sciences,
Cunur, 32260 – Turkey

ABSTRACT

In this paper, the energetic and exergetic assessment for triple effect absorption cooling process integrated with waste energy is given to investigate the system performance. Against the vapor compression-based cooling systems, the triple effect absorption cooling process demonstrates an effective solution from the approaches of smart solution and ecological protection. The most important role of absorption cooling process is the utilization of the low-grade or waste energy to generate cooling effect. Nowadays, the single and double effect-based absorption cooling processes are frequently obtainable, although the triple and also quadruple effect-based cooling processes have been examined for effectively system design. The energy and exergy efficiency of triple effect absorption process have computed as 62.37% and 59.03%, respectively.

Keywords: Energy, Exergy, Absorption cooling, waste energy, thermodynamic analysis

1. INTRODUCTION

As standards of life increase, human should find new energy sources to meet their needs. One of the important energy consuming areas is the heating and cooling processes. As alternative to the vapor compression-based cooling cycles, the absorption cooling systems have started to be used. The advantage of absorption cooling (AC) systems is that they are able to use low gradient heat or waste heat [1]. On the other hand, there are some types of absorption cooling processes such as single, double, triple and quadruple effect in accordance with how many times heat is supplied to the system. A double effect AC system is better than the single effect AC system in terms of performance. Similarly, a triple effect AC system performs better than the double effect AC systems in certain temperature conditions [2]. In literature, there are many studies about the absorption cooling processes. According to studies, a coefficient of AC system performance is not directly proportional to the number of effects. Also, as number of effects increase, the complexity of system increases too. Finally, it can be said that the double effect AC cycle is suitable for commercial use [3-5]. In this study, authors have presented an effective triple effect absorption cooling cycle without being too complex to integrate a waste heat source. Also, some parametric analysis results have been shared in order to see the effects of parameters on system performance.

2. TEAC CYCLE

The schematic diagram of triple effect absorption cooling (TEAC) cycle is illustrated in Fig. 1. The waste energy from any external source is provided to the high temperature generator (HT-generator) of triple effect absorption cooling (TEAC) cycle to generate cooling effect. The supplied heat energy is utilized in the HT-generator, where the strong ammonia-water working fluid coming from the high temperature heat exchanger (HT-HEX) at point 12 is heated. After that, the weak solution and ammonia-water vapor leave from the HT-generator at points 18 and 13, respectively.

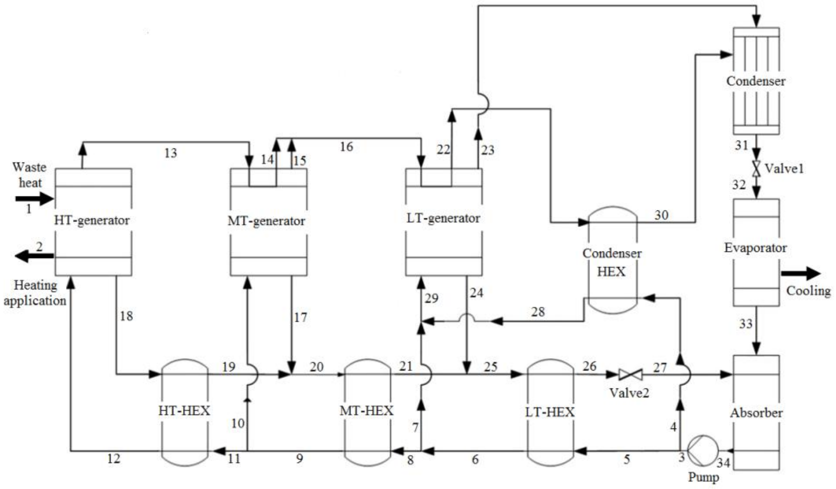

Fig. 1. Schematic diagram of waste heat based triple effect absorption cooling system

The weak working fluid at point 18 releases heat energy in the HT-HEX and integrates with the weak working fluid coming from mid temperature (MT) generator at point 17, providing a weak working fluid at point 20. The weak working fluid at point 20 leaves heat energy in the MT-HEX and integrates with the weak working fluid at point 24 to provide the solution at point 25. The weak working fluid goes into the low temperature heat exchanger (LT-HEX), where this solution heats the strong working fluid joining at point 5. After that, the weak working fluid at point 26 goes into the valve 2, where this solution temperature reduces and goes into the absorber at point 27. The working steam at point 13 goes into the MT-generator, where this steam heats the strong working fluid at point 10, which exists as an NH_3-H_2O vapor solution at points 14 and 15. After that, two NH_3-H_2O vapors are integrated at point 16, and go into the LT-generator, here the integrated vapors heat the strong working fluid, entering at point 29 and leaving as the NH_3-H_2O vapor at points 22 and 23. The working fluid at point 23 goes into the condenser, and also, at point 22, it goes into the condenser-HEX, here heat energy could be transferred to the working fluid entering at point 4 and leaving at point 28. The NH_3-H_2O vapor exiting from the condenser-HEX at point 30 goes into the condenser, releases heat energy, and exits at point 31. After that, the working fluid stream enters the valve1 at point 31, than goes into the evaporator at point 32. In this component, heat energy should be gained by the process and the heated working fluid leaves at point 33 to the absorber, where all three working mixtures, release the heat energy, and go into the pump at point 34 in the liquid phase.

3. ENERGETIC AND EXERGETIC ANALYSES

This sub-chapter is arranged in the following layout; first, the mass, energy, entropy and exergy balance equalities are defined. Next, the balance equalities for all sub-components of TEAC cycle are presented. Finally, the energetic and exergetic performances are defined, and efficiency equalities of sub-components are written [6].

The mass balance is:

$$\sum \dot{m}_{in} = \sum \dot{m}_{out} \tag{1}$$

The energetic balance is:

$$\sum \dot{m}_{in} h_{in} + \dot{W}_{in} + \dot{Q}_{in} = \sum \dot{m}_{out} h_{out} + \dot{W}_{out} + \dot{Q}_{out} \tag{2}$$

The entropy balance is:

$$\sum \dot{m}_{in} s_{in} + \dot{Q}_{in}/T_{in} + \dot{S}_{gen} = \sum \dot{m}_{out} s_{out} + \dot{Q}_{out}/T_{out} \tag{3}$$

The exergetic balance is:

$$\sum \dot{m}_{in} ex_{in} + \dot{E}x_{in}^{Q} + \dot{E}x_{in}^{W} = \sum \dot{m}_{out} ex_{out} + \dot{E}x_{out}^{Q} + \dot{E}x_{out}^{W} + \dot{E}x_{D} \tag{4}$$

The mass, energy, entropy and exergy balance equalities, based on the given above procedures, for sub-parts of TEAC cycle can be defined as given below.

For HT-generator sub-component:

$$\dot{m}_1 = \dot{m}_2 \qquad \dot{m}_{12} = \dot{m}_{13} + \dot{m}_{18} \tag{5}$$

$$\dot{m}_1 h_1 + \dot{m}_{12} h_{12} = \dot{m}_2 h_2 + \dot{m}_{13} h_{13} + \dot{m}_{18} h_{18} \tag{6}$$

$$\dot{m}_1 s_1 + \dot{m}_{12} s_{12} + \dot{S}_{g,HT-generator} = \dot{m}_2 s_2 + \dot{m}_{13} s_{13} + \dot{m}_{18} s_{18} \tag{7}$$

$$\dot{m}_1 ex_1 + \dot{m}_{12} ex_{12} = \dot{m}_2 ex_2 + \dot{m}_{13} ex_{13} + \dot{m}_{18} ex_{18} + \dot{E}x_{D,HT-generator} \tag{8}$$

For MT-generator sub-component:

$$\dot{m}_{13} = \dot{m}_{14} \qquad \dot{m}_{10} = \dot{m}_{15} + \dot{m}_{17} \tag{9}$$

$$\dot{m}_{10} h_{10} + \dot{m}_{13} h_{13} = \dot{m}_{14} h_{14} + \dot{m}_{15} h_{15} + \dot{m}_{17} h_{17} \tag{10}$$

$$\dot{m}_{10} s_{10} + \dot{m}_{13} s_{13} + \dot{S}_{g,MT-generator} = \dot{m}_{14} s_{14} + \dot{m}_{15} s_{15} + \dot{m}_{17} s_{17} \tag{11}$$

$$\dot{m}_{10} ex_{10} + \dot{m}_{13} ex_{13} = \dot{m}_{14} ex_{14} + \dot{m}_{15} ex_{15} + \dot{m}_{17} ex_{17} + \dot{E}x_{D,MT-generator} \tag{12}$$

For LT-generator sub-component:

$$\dot{m}_{16} = \dot{m}_{22} \qquad \dot{m}_{29} = \dot{m}_{23} + \dot{m}_{24} \tag{13}$$

$$\dot{m}_{16} h_{16} + \dot{m}_{29} h_{29} = \dot{m}_{22} h_{22} + \dot{m}_{23} h_{23} + \dot{m}_{24} h_{24} \tag{14}$$

$$\dot{m}_{16} s_{16} + \dot{m}_{29} s_{29} + \dot{S}_{g,LT-generator} = \dot{m}_{22} s_{22} + \dot{m}_{23} s_{23} + \dot{m}_{24} s_{24} \tag{15}$$

$$\dot{m}_{16} ex_{16} + \dot{m}_{29} ex_{29} = \dot{m}_{22} ex_{22} + \dot{m}_{23} ex_{23} + \dot{m}_{24} ex_{24} + \dot{E}x_{D,LT-generator} \tag{16}$$

For condenser-HEX sub-component:

$$\dot{m}_{22} = \dot{m}_{30} \qquad \dot{m}_4 = \dot{m}_{28} \tag{17}$$

$$\dot{m}_4 h_4 + \dot{m}_{22} h_{22} = \dot{m}_{28} h_{28} + \dot{m}_{30} h_{30} \tag{18}$$

$$\dot{m}_4 s_4 + \dot{m}_{22} s_{22} + \dot{S}_{g,Condenser-HEX} = \dot{m}_{28} s_{28} + \dot{m}_{30} s_{30} \tag{19}$$

$$\dot{m}_4 ex_4 + \dot{m}_{22} ex_{22} = \dot{m}_{28} ex_{28} + \dot{m}_{30} ex_{30} + \dot{E}x_{D,Condenser-HEX} \tag{20}$$

For condenser sub-component:

$$\dot{m}_{23} + \dot{m}_{30} = \dot{m}_{31} \tag{21}$$

$$\dot{m}_{23} h_{23} + \dot{m}_{30} h_{30} = \dot{m}_{31} h_{31} + \dot{Q}_{Condenser} \tag{22}$$

$$\dot{m}_{23} s_{23} + \dot{m}_{30} s_{30} + \dot{S}_{g,Condenser} = \dot{m}_{31} s_{31} + \dot{Q}_{Condenser} / T_{Condenser} \tag{23}$$

$$\dot{m}_{23} ex_{23} + \dot{m}_{30} ex_{30} = \dot{m}_{31} ex_{31} + \dot{E}x_{Condenser}^{Q} + \dot{E}x_{D,Condenser} \tag{24}$$

For valve1 sub-component:

$$\dot{m}_{31} = \dot{m}_{32} \tag{25}$$

$$\dot{m}_{31} h_{31} = \dot{m}_{32} h_{32} \tag{26}$$

$$\dot{m}_{31} s_{31} + \dot{S}_{g,Valve1} = \dot{m}_{32} s_{32} \tag{27}$$

$$\dot{m}_{31} ex_{31} = \dot{m}_{32} ex_{32} + \dot{E}x_{D,Valve1} \tag{28}$$

For evaporator sub-component:

$$\dot{m}_{32} = \dot{m}_{33} \tag{29}$$

$$\dot{m}_{32} h_{32} = \dot{m}_{33} h_{33} + \dot{Q}_{Cooling} \tag{30}$$

$$\dot{m}_{32} s_{32} + \dot{S}_{g,Evaporator} = \dot{m}_{33} s_{33} + \dot{Q}_{Cooling} / T_{Evaporator} \tag{31}$$

$$\dot{m}_{32}ex_{32} = \dot{m}_{33}ex_{33} + \dot{E}x^{Q}_{Cooling} + \dot{E}x_{D,Evaporator} \tag{32}$$

For absorber sub-component:

$$\dot{m}_{27} + \dot{m}_{33} = \dot{m}_{34} \tag{33}$$

$$\dot{m}_{27}h_{27} + \dot{m}_{33}h_{33} + \dot{Q}_{Absorber} = \dot{m}_{34}h_{34} \tag{34}$$

$$\dot{m}_{27}s_{27} + \dot{m}_{33}s_{33} + \dot{Q}_{Absorber}/T_{Absorber} + \dot{S}_{g,Absorber} = \dot{m}_{34}s_{34} \tag{35}$$

$$\dot{m}_{27}ex_{27} + \dot{m}_{33}ex_{33} + \dot{E}x^{Q}_{Absorber} = \dot{m}_{34}ex_{34} + \dot{E}x_{D,Absorber} \tag{36}$$

For pump sub-component:

$$\dot{m}_{34} = \dot{m}_{3} \tag{37}$$

$$\dot{m}_{34}h_{34} + \dot{W}_{Pump} = \dot{m}_{3}h_{3} \tag{38}$$

$$\dot{m}_{34}s_{34} + \dot{S}_{g,Pump} = \dot{m}_{3}s_{3} \tag{39}$$

$$\dot{m}_{34}ex_{34} + \dot{E}x^{W}_{Pump} = \dot{m}_{3}ex_{3} + \dot{E}x_{D,Pump} \tag{40}$$

For valve2 sub-component:

$$\dot{m}_{26} = \dot{m}_{27} \tag{41}$$

$$\dot{m}_{26}h_{26} = \dot{m}_{27}h_{27} \tag{42}$$

$$\dot{m}_{26}s_{26} + \dot{S}_{g,Valve2} = \dot{m}_{27}s_{27} \tag{43}$$

$$\dot{m}_{26}ex_{26} = \dot{m}_{27}ex_{27} + \dot{E}x_{D,Valve2} \tag{44}$$

For LT-HEX sub-component:

$$\dot{m}_{25} = \dot{m}_{26} \qquad \dot{m}_{5} = \dot{m}_{6} \tag{45}$$

$$\dot{m}_{6}h_{6} + \dot{m}_{26}h_{26} = \dot{m}_{5}h_{5} + \dot{m}_{25}h_{25} \tag{46}$$

$$\dot{m}_{6}s_{6} + \dot{m}_{26}s_{26} + \dot{S}_{g,LT-HEX} = \dot{m}_{5}s_{5} + \dot{m}_{25}s_{25} \tag{47}$$

$$\dot{m}_{6}ex_{6} + \dot{m}_{26}ex_{26} = \dot{m}_{5}ex_{5} + \dot{m}_{25}ex_{25} + \dot{E}x_{D,LT-HEX} \tag{48}$$

For MT-HEX sub-component:

$$\dot{m}_{20} = \dot{m}_{21} \qquad \dot{m}_{8} = \dot{m}_{9} \tag{49}$$

$$\dot{m}_{9}h_{9} + \dot{m}_{21}h_{21} = \dot{m}_{8}h_{8} + \dot{m}_{20}h_{20} \tag{50}$$

$$\dot{m}_{9}s_{9} + \dot{m}_{21}s_{21} + \dot{S}_{g,MT-HEX} = \dot{m}_{8}s_{8} + \dot{m}_{20}s_{20} \tag{51}$$

$$\dot{m}_{9}ex_{9} + \dot{m}_{21}ex_{21} = \dot{m}_{8}ex_{8} + \dot{m}_{20}ex_{20} + \dot{E}x_{D,MT-HEX} \tag{52}$$

For HT-HEX sub-component:

$$\dot{m}_{11} = \dot{m}_{12} \qquad \dot{m}_{18} = \dot{m}_{19} \tag{53}$$

$$\dot{m}_{12}h_{12} + \dot{m}_{19}h_{19} = \dot{m}_{11}h_{11} + \dot{m}_{18}h_{18} \tag{54}$$

$$\dot{m}_{12}s_{12} + \dot{m}_{19}s_{19} + \dot{S}_{g,HT-HEX} = \dot{m}_{11}s_{11} + \dot{m}_{18}s_{18} \tag{55}$$

$$\dot{m}_{12}ex_{12} + \dot{m}_{19}ex_{19} = \dot{m}_{11}ex_{11} + \dot{m}_{18}ex_{18} + \dot{E}x_{D,HT-HEX} \tag{56}$$

The energetic and exergetic performance equalities are given as [7];

$$\eta = \frac{\sum useful\ output\ energy}{\sum input\ energy} = 1 - \frac{\sum energy\ loss}{\sum input\ energy} \tag{57}$$

$$\psi = \frac{\sum useful\ output\ exergy}{\sum input\ exergy} = 1 - \frac{\sum exergy\ loss}{\sum input\ exergy} \tag{58}$$

The energetic and exergetic performances, based on the given above procedure, for components of TEAC cycle are defined in Table 1.

Table 1. Energy and exergy efficiency equations of TEAC cycle components

Component	**Energy efficiency equation**	**Exergy efficiency equation**
HT-generator	$\eta_{HT-generator} = \frac{\dot{m}_{13}h_{13}+\dot{m}_{18}h_{18}-\dot{m}_{12}h_{12}}{\dot{m}_1(h_1-h_2)}$	$\psi_{HT-generator} = \frac{\dot{m}_{13}ex_{13}+\dot{m}_{18}ex_{18}-\dot{m}_{12}ex_{12}}{\dot{m}_1(ex_1-ex_2)}$
MT-generator	$\eta_{MT-generator} = \frac{\dot{m}_{15}h_{15}+\dot{m}_{17}h_{17}-\dot{m}_{10}h_{10}}{\dot{m}_{13}(h_{13}-h_{14})}$	$\psi_{MT-generator} = \frac{\dot{m}_{15}ex_{15}+\dot{m}_{17}ex_{17}-\dot{m}_{10}ex_{10}}{\dot{m}_{13}(ex_{13}-ex_{14})}$
LT-generator	$\eta_{LT-generator} = \frac{\dot{m}_{23}h_{23}+\dot{m}_{24}h_{24}-\dot{m}_{29}h_{29}}{\dot{m}_{16}(h_{16}-h_{22})}$	$\psi_{HT-generator} = \frac{\dot{m}_{23}ex_{23}+\dot{m}_{24}ex_{24}-\dot{m}_{29}ex_{29}}{\dot{m}_{16}(ex_{16}-ex_{22})}$
Condenser	$\eta_{Condenser} = \frac{\dot{m}_{31}h_{31}}{\dot{m}_{23}h_{23}+\dot{m}_{30}h_{30}}$	$\psi_{Condenser} = \frac{\dot{m}_{31}ex_{31}}{\dot{m}_{23}ex_{23}+\dot{m}_{30}ex_{30}}$
Valve 1	$\eta_{Valve1} = \frac{\dot{m}_{32}h_{32}}{\dot{m}_{31}h_{31}}$	$\psi_{Valve1} = \frac{\dot{m}_{32}ex_{32}}{\dot{m}_{31}ex_{31}}$
Evaporator	$\eta_{Evaporator} = \frac{\dot{m}_{32}h_{32}}{\dot{m}_{33}h_{33}}$	$\psi_{Evaporator} = \frac{\dot{m}_{32}ex_{32}}{\dot{m}_{33}ex_{33}}$
Absorber	$\eta_{Absorber} = \frac{\dot{m}_{34}h_{34}}{\dot{m}_{27}h_{27}+\dot{m}_{33}h_{33}}$	$\psi_{Absorber} = \frac{\dot{m}_{34}ex_{34}}{\dot{m}_{27}ex_{27}+\dot{m}_{33}ex_{33}}$
Pump	$\eta_{Pump} = \frac{\dot{W}_{Pump}}{\dot{m}_3h_3-\dot{m}_{34}h_{34}}$	$\psi_{Absorber} = \frac{\dot{W}_{Pump}}{\dot{m}_3ex_3-\dot{m}_{34}ex_{34}}$
Valve2	$\eta_{Valve2} = \frac{\dot{m}_{27}h_{27}}{\dot{m}_{26}h_{26}}$	$\psi_{Valve2} = \frac{\dot{m}_{27}ex_{27}}{\dot{m}_{26}ex_{26}}$
LT-HEX	$\eta_{LT-HEX} = \frac{\dot{m}_6h_6-\dot{m}_5h_5}{\dot{m}_{25}h_{25}-\dot{m}_{26}h_{26}}$	$\psi_{LT-HEX} = \frac{\dot{m}_6ex_6-\dot{m}_5ex_5}{\dot{m}_{25}ex_{25}-\dot{m}_{26}ex_{26}}$
MT-HEX	$\eta_{MT-HEX} = \frac{\dot{m}_9h_9-\dot{m}_8h_8}{\dot{m}_{20}h_{20}-\dot{m}_{21}h_{21}}$	$\psi_{MT-HEX} = \frac{\dot{m}_9ex_9-\dot{m}_8ex_8}{\dot{m}_{20}ex_{20}-\dot{m}_{21}ex_{21}}$
HT-HEX	$\eta_{HT-HEX} = \frac{\dot{m}_{12}h_{12}-\dot{m}_{11}h_{11}}{\dot{m}_{18}h_{18}-\dot{m}_{19}h_{19}}$	$\psi_{HT-HEX} = \frac{\dot{m}_{12}ex_{12}-\dot{m}_{11}ex_{11}}{\dot{m}_{18}ex_{18}-\dot{m}_{19}ex_{19}}$

4. RESULTS AND DISCUSSION

In this sub-section, the TEAC cycle outputs are submitted and investigated. Table 2 illustrates the thermodynamic inlet indicators for modeling TEAC cycle. The exergy destruction rates of points are calculated by utilizing the Engineering Equation Solver (EES) software program.

Table 2. Thermodynamic properties and exergy contents of TEAC each state

State	**$\dot{m}$ (kg/s)**	**T (°C)**	**P (kPa)**	**h (kJ/kg)**	**s (kJ/kgK)**	**Concentration**	**ex (kW/kg)**	**$\dot{Ex}$ (kW)**
1	0.3386	280	225	3030	7.765	-	770.53	260.9
2	0.3386	135	225	2735	7.146	-	655.64	222
3	1	7.1	400	-197.6	-0.0629	0.6	1181	1181
4	0.2	7.1	400	-197.6	-0.0629	0.6	252.5	50.5
5	0.8	7.1	400	-197.6	-0.0629	0.6	945.2	756.16
6	0.8	54.1	400	535.9	2.329	0.6	974.8	779.84
7	0.16	54.1	400	535.9	2.329	0.6	195	31.2
8	0.64	54.1	400	535.9	2.329	0.6	779.9	499.17
9	0.64	91.1	400	1114	3.991	0.6	840.1	537.66
10	0.128	91.1	400	1114	3.991	0.6	168	21.5
11	0.512	91.1	400	1114	3.991	0.6	672.1	344.11
12	0.512	114.1	400	1916	6.114	0.6	766.3	392.35
13	0.171	224.3	400	1806	6.106	0.999	237.5	40.62
14	0.171	176.4	400	1689	5.857	0.999	229.8	39.3
15	0.04274	344.1	400	1441	5.23	0.999	54.67	2.37

State	$\dot{m}$ (kg/s)	T (°C)	P (kPa)	h (kJ/kg)	s (kJ/kgK)	Concentration	ex (kW/kg)	$\dot{E}x$ (kW)
16	0.2137	155.7	400	1639	5.745	0.999	283.7	60.63
17	0.08526	111.1	400	1186	3.938	0.4	119.4	10.18
18	0.341	134.1	400	2264	6.674	0.4	573.6	195.6
19	0.341	107.3	400	1060	3.608	0.4	467.3	159.35
20	0.4263	108.1	400	1085	3.674	0.4	547.4	233.36
21	0.4263	62.8	400	217.4	1.276	0.4	514.5	219.33
22	0.2137	-0.9	400	1228	4.522	0.999	271.9	58.1
23	0.1202	17.2	400	1313	4.824	0.999	152.5	18.33
24	0.2398	57.2	400	125.3	1	0.4	286.5	68.7
25	0.6661	60.7	400	184.2	1.177	0.4	800.9	533.48
26	0.6661	-88	400	-696.7	-2.248	0.4	878.2	584.97
27	0.6661	-87.9	250	-696.7	-2.247	0.4	878.2	584.97
28	0.2	27.1	400	71.51	0.849	0.6	237	47.4
29	0.36	37.2	400	277.9	1.522	0.6	430.4	154.94
30	0.2137	-1.6	400	976.5	3.599	0.999	275.6	58.89
31	0.3339	-1.7	400	378.7	1.405	0.999	444.2	148.32
32	0.3339	-13.5	250	378.7	1.474	0.999	437.5	146.08
33	0.3339	-13.3	250	1058	4.081	0.999	411	137.23
34	1	6.7	250	-199.5	-0.0683	0.6	1181	1181

The energetic and exergetic efficiencies of TEAC cycle and its sub-components are given in Fig. 2. The last column illustrates the energetic and exergetic performances of TEAC cycle. The energy and exergy performances of LT-HEX and condenser sub-components are higher compared to the other sub-components and TEAC cycle.

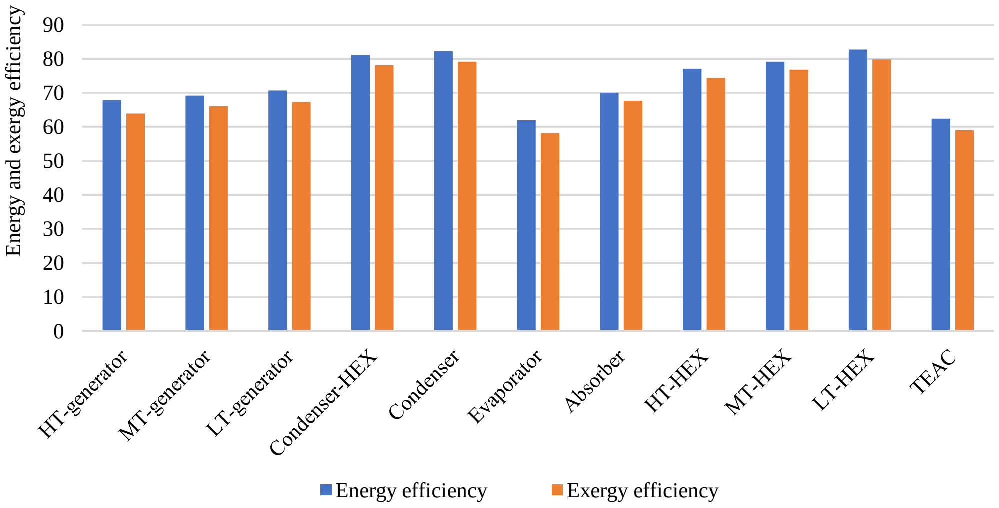

Fig. 2. Energy and exergy efficiency of TEAC cycle and its sub-components

The irreversibility rates for the main parts of TEAC cycle are illustrated in Fig. 3. The highest irreversibility rates occur in the HT-generator and absorber, while the lowest are in the pump and valves. On the other hand, based on the exergy destruction rate, 195.03 and 158.27 kW of power are lost in the HT-generator and absorber, respectively, and 1465 kW is lost in the TEAC cycle. The reason of this high irreversibility occurs because high temperature generator works greater temperature than reference temperature. High temperature difference causes more irreversibility. The graphic and values of irreversibility rates are the beneficial to tool to focus on the sources of exergy destruction rates.

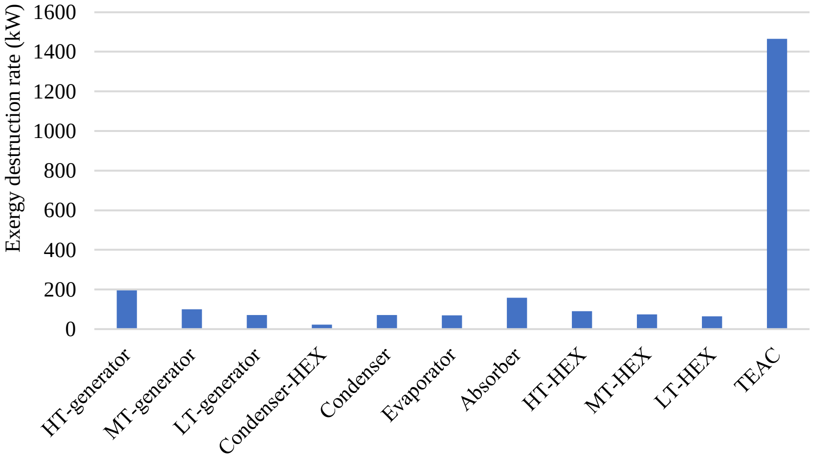

Fig. 3. Exergy destruction rates of TEAC cycle and its sub-components

Fig. 4 illustrates the impact of HT-generator temperature on a number of generator numbers and corresponding the performance levels. The increasing HT-generator temperature affects the TEAC cycle and its sub-components energy performance efficiencies directly in Fig. 4. The energetic efficiencies of HT-generator and TEAC cycle rise from 73.81% to 80.83% and 59.56% and 64.47%, respectively. Supplied heat is firstly utilized in HT-generator therefore increasing HT-generator temperature causes positive impact on the efficiency of the components of TEAC system.

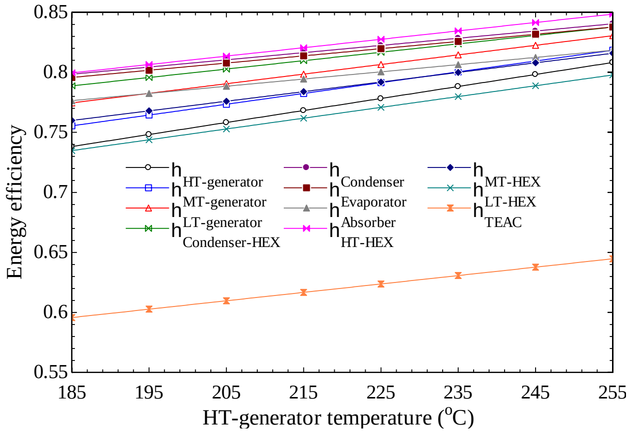

Fig. 4. Effect of HT-generator temperature on energy efficiency of TEAC cycle and its sub-components

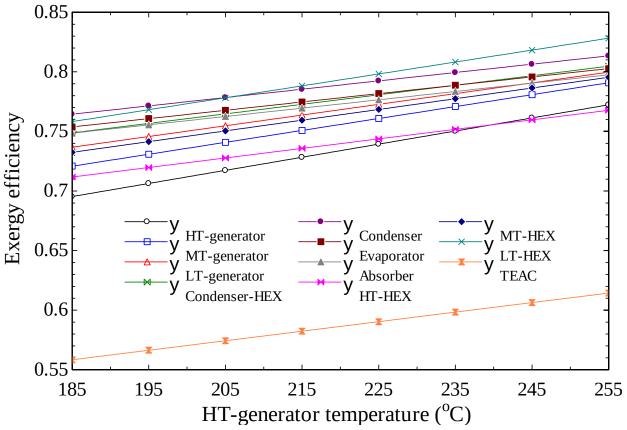

Fig. 5. Effect of HT-generator temperature on exergy efficiency of TEAC cycle and its sub-components

Fig. 5 illustrates that when the HT-generator temperature is increased from 185 to 255 °C, the exergetic performance of TEAC cycle and sub-components increase. The energetic and exergetic performances of TEAC cycle and components are affected positively because heat inlet to the HT-generator component rises. As given in this figure, the exergetic efficiencies of HT-generator and TEAC cycle rise from 69.54% to 77.22% and 55.82% and 61.44%, respectively.

In Fig. 6, the irreversibility rates of TEAC system and its sub-systems versus HT-generator temperature are investigated. All the irreversibility rates rise with the increasing HT-generator temperature of the TEAC system. The most important rise is in the HT-generator, followed by MT-generator irreversibility rate. Also, the irreversibility rate of TEAC cycle rises from 751 to 1453 kW.

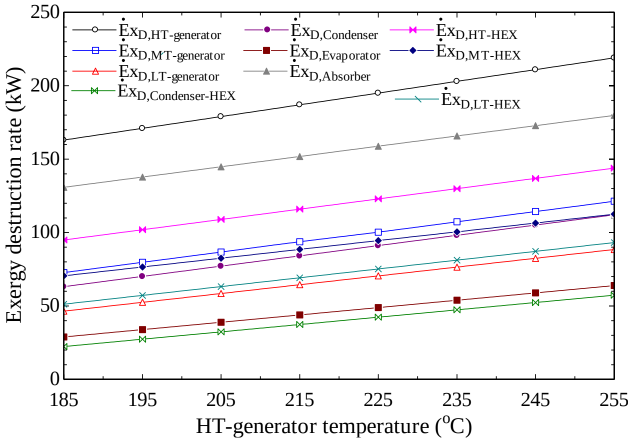

Fig. 6. Effect of HT-generator temperature on exergy destruction rate of sub-components

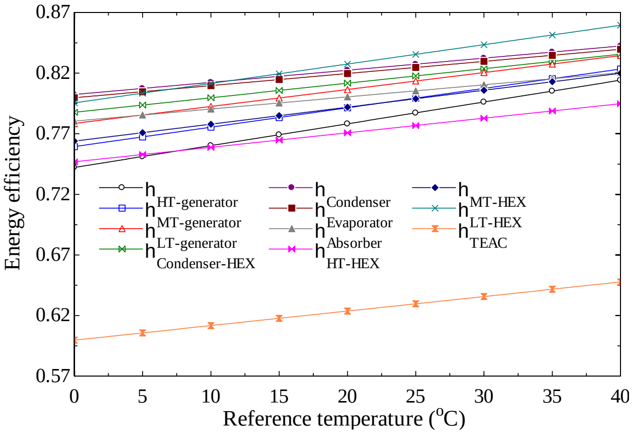

Fig. 7. Effect of reference temperature on energy efficiency of TEAC cycle and its sub-components

Another parametric analysis is performed for the reference temperature in order to see the effects of it on the system performance. The range of reference temperature is chosen as 0-40°C as done in literature. The reference temperature affects the energetic performances of whole cycle and its sub-plants. All the energetic performances rise with the increasing reference temperature as illustrated in Fig. 7, because the heat energy loss from cycle components to the environment decrease with increasing reference temperature. In addition to that, the energetic efficiency of whole cycle rises from 59.96% to 64.78%.

Fig. 8 illustrate that the exergetic performance of cooling cycle and its sub-components rises with the increasing reference temperature. The exergetic performances of HT-generator, Mt-generator and LT-generator rise from 69.92 to 77.91%, 72.47 to 79.69% and 74.26 to 80.28%, respectively. In addition to that, the exergetic performance of whole cooling cycle rises from 56.22% to 61.84% with increasing reference temperature.

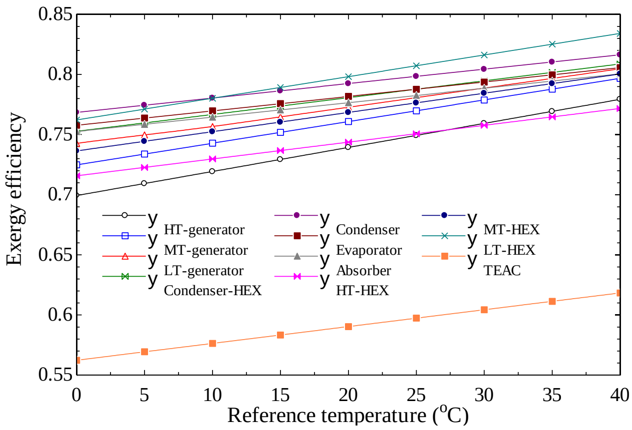

Fig. 8. Effect of reference temperature on exergy efficiency of TEAC cycle and its sub-components

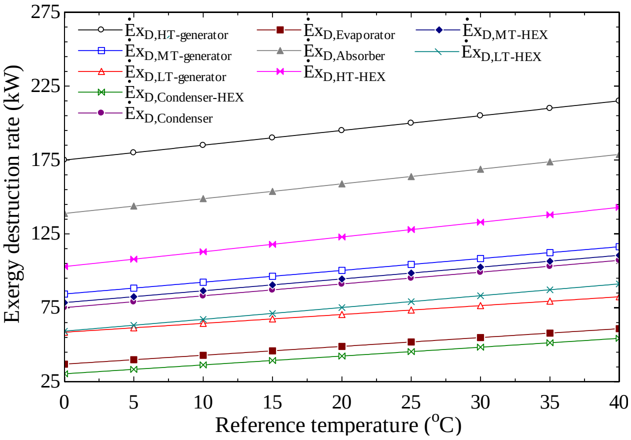

Fig. 9. Effect of reference temperature on exergy destruction rate of sub-components

All the irreversibility rates rise by increasing reference temperature in Fig. 9. The reference temperature range is between 0 and 40 °C. As can be observed from these outputs, the irreversibility rate of HT-generator, absorber and HT-HEX increase from 174 to 216 kW, from 137.6 to 178.5 kW, and from 102.8 to 142.7 kW, respectively. The exergy destruction rates increase because the heat energy transfer rates of whole cycle components increase.

5. CONCLUSIONS

In the TEAC cycle, waste energy is used to generate heating and cooling effect. This TEAC cycle is consisting with high, medium and low temperature generators, high, medium and low temperature heat exchangers, condenser heat exchanger, condenser, evaporator, absorber, pump and two valves. In this paper, to investigate cooling cycle performance, the thermodynamic analysis of TEAC is given. In addition to that, the parametric studies of TEAC cycle are investigated to analyze the effect of increasing HT-generator and reference temperature on the system performance. Lastly, the increasing reference and HT-generator temperature has positive impacts on the TEAC cycle and its sub-parts. But at the same time, the irreversibility rates of these sub-parts rise by the increasing these variable from 0 to 40 °C, and from 185 to 255 °C. Moreover, it can be suggested that other cycles such as single, double and quadruple effect absorption cooling systems can be compared in further studies both thermodynamically and economically in order to find out the feasibility of them.

REFERENCES

1. ASSILZADEH, F., KALOGIROU, S. A., ALI, Y., SOPIAN, K. Simulation and optimization of a LiBr solar absorption cooling system with evacuated tube collectors. *Renewable Energy*, 2005, Vol. 30, No. 8, p. 1143-1159.
2. AZHAR, M., SIDDIQUI, M. A. Exergy analysis of single to triple effect lithium bromide-water vapour absorption cycles and optimization of the operating parameters. *Energy Conversion and Management*, 2019, Vol. 180, p. 1225-1246.
3. ÁLVAREZ, M. E., ESTEVE, X., BOUROUIS, M. Performance analysis of a triple-effect absorption cooling cycle using aqueous (lithium, potassium, sodium) nitrate solution as a working pair. *Applied Thermal Engineering*, 2015, Vol. 79, p. 27-36.
4. GROSSMAN, G., ZALTASH, A., ADCOCK, P.W., DEVAULT, R.C. Simulating a 4-effect absorption chiller. *ASHRAE Journal*, 1995, p. 45-53.
5. ZIEGLER, F., KAHN, R., SUMMERER, F., ALEFELD, G. Multi-effect absorption chillers. *International Journal of Refrigeration*, 1993, Vol. 16, No. 5, p. 301-310.
6. DINCER, I., ROSEN, M.A. Energy, Environment, and Sustainable Development. *Elsevier*: 2nd ed., Oxford, 2013.
7. BEJAN, A., MORAN, M.J. Thermal Design and Optimization, *John Wiley & Sons*, New York; 1996.

CYSENI 2019, May 23-24, Kaunas, Lithuania
ISSN 1822-7554, www.cyseni.com

RESONANCE MODE OF SOUND PROPAGATION IN FLUIDIZED BED OF CNT AGLOMERATES

A. G. Petrovich
A. V. Luikov Heat and Mass Transfer Institute, National Academy of Sciences of Belarus
P. Brovka str. 15, Minsk, 220072 – Belarus
Email: al_petrovich1994@mail.ru

ABSTRACT

Fluidized bed (FB) technology is very promising for the production and processing of nanomaterial powders. However, uniform fluidization and perfect mixing of nanopowders during their synthesis is difficult due to the strong cohesion of nanoparticles and their agglomerates. Acoustic waves contribute to the perfection of nanomaterial fluidized bed. The experimental and theoretical study was aimed at the determination of acoustic parameters that ensure high quality of the FB of carbon nanotubes (CNT).

Recordings of sound in the line of microphones placed along the height of FB of CNT agglomerates were used to determine the speed of sound and the degree of its attenuation. Nitrogen was used as fluidizing gas. Investigation was performed in the frequency range from 50 to 1000 Hz. An acoustic speaker, placed in the upper zone of FB freeboard, has provided the sound intensity up to 140 dB. It was found that the sound speed depends on the gas flow rate and the vertical position, and lies in the range from 20 to 100 m/s. The detailed measuring was performed at the first resonance frequency of the system, which provides maximal acoustic energy input to the FB. The increase in gas flow rate leads to the expansion of the bed and, consequently, to an increase in the speed of sound in it. The value of attenuation coefficient also varies and lies in the range from 7 to 15 np/m.

Axisymmetric 2D numerical model of sound propagation in the system “CNT fluidized bed - freeboard” was investigated within the framework of COMSOL acoustic module. The spectrum of resonance frequencies was determined and the good correlation with experimentally found values was shown.

The obtained results allow us to formulate a strategy for maintaining highest heat and mass transfer rates in a fluidized CNT bed by changing the sound frequency when the height of CNT FB increases during CNT synthesis.

Keywords: Carbon Nanotubes, Fluidized Bed, Sound Waves, Sound Velocity, Attenuation, Resonance, Modelling

1. INTRODUCTION

An important factor determining the development of nanotechnology is availability of high-performance processes for the synthesis and manipulation of nanoparticles, i.e. transportation, dispersion, modification of their surface properties. Fluidized bed technology (FB) is one of the most effective methods for implementing all of these operations. The advantages of this technology are manifested in relation to nanopowders in particular due, first of all, to a record-high contact surface between particles and gas, which allows to significantly intensify the process. It is also necessary to point out the environmental advantages of the fluidized bed technology, in which there are no liquid and hazardous products. A large amount of research is devoted to the fluidized nanopowder systems; a review of the main papers and results on this topic can be found in [1, 2].

At the same time, the fluidization of nanopowders faces the problem of the heterogeneity of the suspended layer of particles, appearing in piston flows, channeling, jets and stagnant zones formation. The reason for this is the dominant role of cohesion forces between nanoparticles in relation to the forces of gravity and hydrodynamic drug force in the gas flow, which is a consequence of the very large ratio of the surface area of a particle to its volume ($S_p/V_p = 6/d_p$). As a result, the structural unit of a fluidized nanomaterial powder is not a single nanoparticle, but a nanoparticle agglomerate, the size of which depends both on the characteristics of the nanoparticles and on the hydrodynamic environment in the layer. In particular, multi-walled carbon nanotubes (MWCNTs), synthesized in a catalytic fluidized bed (see [3, 4]), are a mixture of agglomerates with sizes ranging from 10 to 50 microns. However, for agglomerates of this size, the role of cohesion in their fluidization is still significant. In accordance with the classification of fluidizable systems [5], the parameters of the agglomerates in this case correspond to the lower part of the region “C” of the Geldart diagram, characterized by poor fluidization homogeneity. Thus, for agglomerates of nanoparticles of the specified type, it is necessary to apply special methods of influencing the fluidized bed in order to ensure its homogeneity and good mixing.

Sound-assisted fluidization is an effective technique to achieve a homogeneous fluidized bed of nanoparticle agglomerates. The imposition of acoustic oscillations with frequencies of 100–400 Hz and high intensity (with a sound pressure level of 120–160 dB nanopowder, achieved as a result of resonance) leads to the disappearance of channels and stagnant zones in the fluidized bed of nanopowder; to the increase of fluidized bed hight; to the reduction of the minimum fluidization rate. The first scientific publication on this subject appeared in 1955 [6]. Sufficient information about the state of research related to acoustic effects on powder nanosystems can be found in [1, 7–12]. In a large number of publications on the topic under consideration, the effect of sound waves on the characteristics of fluidization, namely on the minimum fluidization velocity, on the height of the fluidized bed and the terminal velocity of bed solids, was experimentally investigated. The main focus was on the formation and destruction of nanoparticle agglomerates. The model of sound wave attenuation by nonoparticle agglomerates with assumption of elastic forces between cluster and subclasters was proposed in [7]. In accordance with this model, the absorption of sound energy by agglomerates increases with increasing frequency.

The structure of coupled sound waves in the FB of nanoparticle agglomerates and in the freebord was first investigated in [13]. However, the analytical model used in this work did not take into account the waves reflected from the interface between the particle layer and the gas, as well as from of the gas distributor. The values of the speed of sound and the absorption coefficient in the fluidized bed were only estimated.

This paper presents the results of a detailed experimental study of the characteristics and resonance parameters of sound waves in a fluidized-bed reactor of MWCNTs, as well as the results of sophisticated mathematical modeling of acoustic phenomena. The basic idea of the work is that the achievement of the maximum expansion and homogeneity of the fluidized bed of nanoparticles in the bubble-free fluidization mode (Agglomerate particle fluidizatiom, APF) does not provide good mixing of the layer. In this mode, significant gradients of temperature and concentration of gaseous reactants can occur, which will reduce the efficiency of the process. The best mixing of the nanoparticle FB occurs in the bubble fluidization regime (Aglomerate bubling fluidization, ABF), which is achieved with the maximum contribution of acoustic energy to the layer, that is, under the condition of acoustic resonance.

2. EXPERIMENTAL STUDY

2.1. Experimental setup and procedure

An experimental device for studying the effects of acoustic impacts on FB MWCNT (Fig. 1) included two “cold” hydrodynamic models of reactors with transparent walls. The structure of a fluidized bed (5) under sound impact was studied on a rectangular section model with a height of 0.5 m, a width of 0.1 m and a thickness of 0.02 m. The speed of sound waves and their absorption coefficient were determined using a circular section model, a plexiglas tube with an internal diameter of 56 mm and a height of 1 m. The sound source was located at the top of the models (6). The length of the second model was chosen from considerations of minimizing the influence of the sound wave reflected from the gas distribution plate (4), which simplifies the measurement of the specified acoustic characteristics of the fluidized bed of the nanomaterial. Nitrogen was used as a fluidizing agent.

The acoustic part of the device is a sound signal generator GZ-33 (ГЗ-33) (1), to which the sound emitters were connected: the dynamics of model 1 GD-54 (1 ГД-54) (2) for the rectangular reactor and YDT613-01 (2) for the circular one. The sound signal generator allows to reproduce frequencies from 20 Hz to 20 kHz with an error of ± 2 Hz. The generator output power ensured the loudness of sound in the reactor model up to 160 dB due to resonance phenomena. The dynamics 1GD-54 in the rectangular model of the reactor had a frequency band of 125–10000 Hz, and the speaker YDT613 01 ranged from 160 Hz to 18000 Hz. To prevent carbon nanotubes leaking into the room through the speaker cone, it was placed in a Plexiglas box.

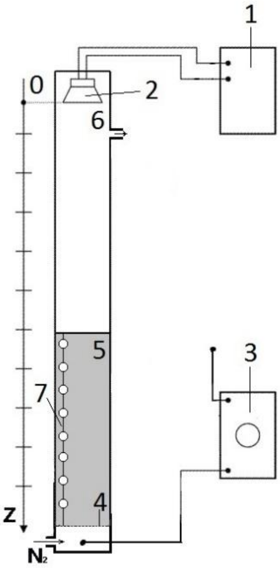

Fig. 1. Experimental setup

To register sound vibrations in the FB MWCNT, SoniCrest's HMO06B electret condenser microphones were used, having uniform characteristics in the range of 50–1600 Hz. Measuring line of microphones (7) consisted of ten sound receivers located at a distance of 5 cm from each other and mounted on a metal rail. All microphones were calibrated by one sound signal. To measure the amplitude and phase of sound vibrations, microphones were connected in pairs using a switch to a two-channel oscilloscope, Hantek DSO 5062B, with the function of recording oscillograms to a file and recording screenshots.

Pressure drops on the reactor and on the nanomaterial layer were measured using an electronic micromanometer (3). Differential pressure sensors Honeywell DUXL01D (measurement range of the constant component -250 Pa – +250 Pa, variable – up to 60 Pa) and Honeywell ASCX01DN (range on the constant component from 0 Pa to 6800 Pa, in a variable – up to 1000 Pa) are used in this micromanometer. The electronic circuit of the micromanometer ensured the sensor sampling frequency of 1 kHz and the recording of data in a file. The relative error in measuring the constant pressure component did not exceed 1%.

Visual observations of the FB MWCNT structure in a rectangular-section reactor model showed that at certain values of the sound frequency, the fluidized bed underwent a strong expansion (up to 30%) and the formation of layered structures in its upper part. At the same time, the lower part of the layer looked denser.

The pressure drop measurements were made in the following order. A layer of carbon nanotubes of a certain height was loaded into the reactor and a certain gas flow rate was set. Then the acoustic emitter was switched on and the sound frequency was selected at which the maximum homogeneity of this layer and its maximum expansion (resonant frequency) were achieved. At this sound frequency, the pressure drop across the bed was measured. At the same sound frequency, the pressure drop across the gas distribution plate (without nanomaterials) was measured.

2.2. Experimental results

2.2.1. Minimum fluidization rate

The pressure drop across the gas distribution plate and the fluidized bed of the nanotubes, determined for this way, is presented in Figure 2 as a function of the gas flow rate through the bed.

After reaching the flow rate that ensures minimal fluidization, as in Figure 2, a homogeneous fluidized bed without bubbles was observed. For the layer of the studied nanocarbon material (multi-walled carbon nanotubes synthesized in a catalytic fluidized bed (HTMI)), the minimum flow rate of fluidization with nitrogen U_{mf} was $3.9 \cdot 10^{-3}$ m/s (under normal conditions). Further increase in gas consumption leads to changes in fluidization regime. The graph shows the specific breaks, after which some reduction in pressure drop occurs. These reductions in pressure drop across the fluidized bed can be associated with changes in fluidization regime, such as bubbling.

The measurements of the minimum flow rate and the calculation of the minimum fluidization velocity for different heights of the fixed bed showed that these parameters do not depend on the initial layer height within the error of their determination.

Figure 3 shows the dependence of the height of the fluidized bed on the flow rate. The initial bed height was 0.36 m (at the presence of sound). Figure 3 also shows that in the investigated range of gas flow rates (from 1 to 3.5 minimum fluidization velocity) the bed height varies linearly with the gas velocity. Obviously, with a further increase in the gas velocity, this dependence ceases to be linear and with ($U/U_{mf} > 5$) the bed height reaches a certain constant value.

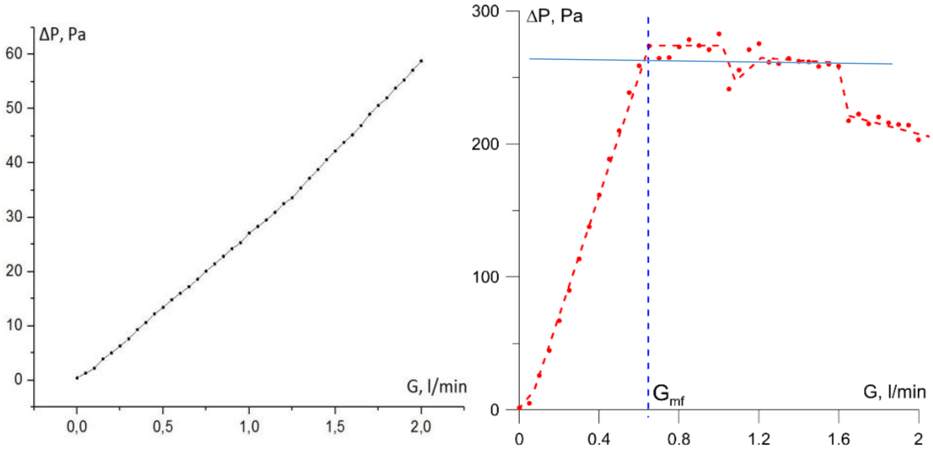

H_0 = 0.36 m, f = 225 Hz

Fig. 2. The dependence of the pressure drop on the gas distribution plate (a) and on the fluidized bed of nanotubes (b) depending on the flow of nitrogen

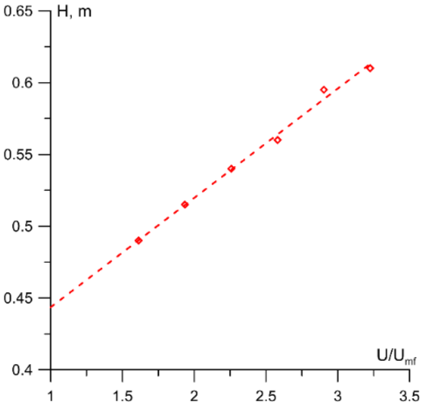

H_0 = 0.36 m, f = 225 Hz

Fig. 3. The dependence of the height of the FB MWCNT on the gas flow

2.2.2. Sound adsorption and sound velocity

The sound absorption coefficient χ in the fluidized bed of the nanotubes was determined by approximating the data on the amplitude of sound using the dependence

$$A = A_0 e^{-\chi z}, \tag{1}$$

where z is the vertical coordinate, which is measured from the upper boundary of the layer.

As the measurements showed, the sound wave passing into the layer with the thickness of 0.5–0.6 m achieved in the experimental model has no time to be absorbed completely; its amplitude at the gas distribution plate is about 5% of the wave amplitude at the upper boundary of the layer. The reflection of the incident sound wave on the gas distribution plate leads to its interference with the reflected wave, which increases the amplitude of sound near the plate and changes its phase. This is clearly seen in Figure 4, which represents the dependence of the sound intencity (in terms of the voltage of a microphone signal) on the distance from the FB boundary. Near the distributor plate (in the region of large z), the decrease in the amplitude of sound with increasing z stops due to the contribution of the reflected wave.

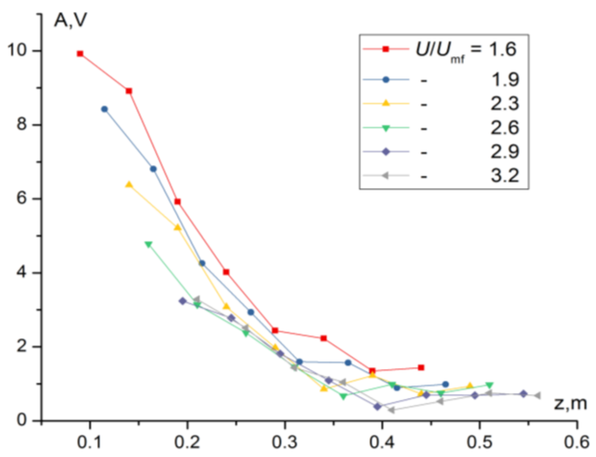

Fig. 4. Sound level (in units of the microphone signal voltage) as a function of the distance from the upper limit of the FB MWCNT

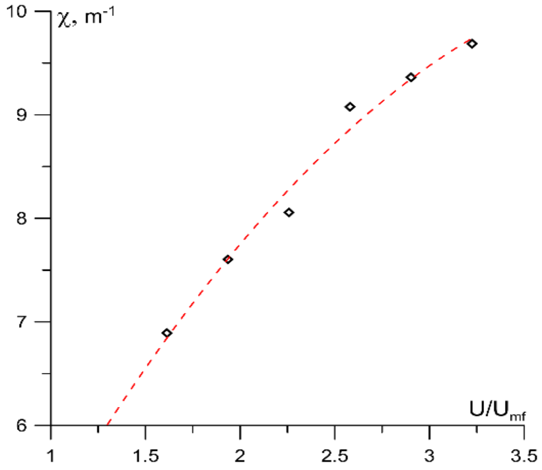

Fig. 5. Dependence of sound absorption coefficient on gas velocity

At the same time, at distances of about 0.2 m above the gas distribution plate, the amplitude of the reflected wave becomes negligible (less than 1% of the initial amplitude of the incident wave). For this reason, the most accurate data on the absorption coefficient and local sound velocity in a layer can be obtained as a result of processing the records of the first 6-7 microphones (counting from the upper boundary of the layer), where the interference of the incident and reflected sound waves is completely absent. The results of such processing are presented in Figure 5 as a dependence of the sound absorption coefficient on the relative velocity of the gas. It should be noted that there is a noticeable increase in the absorption coefficient of sound with increasing gas velocity. In part, this may be due to the expansion of the layer (a decrease in its density) with increasing gas flow. However, apparently, there is also another mechanism underlying the effect under consideration, for example, more efficient transfer of sound energy to nanomaterial agglomerates.

Measurement of the local speed of sound was carried out by comparing the phases of sound vibrations in pair of adjacent microphones located in the microphone line at a minimum distance (5 cm) from each other. The assumption will be used that a flat sound wave propagates in the vertical direction in the nanomaterial layer, and there is no interference with the wave reflected from the gas distribution plate. This assumption is carried out with a sufficient height of the fluidized bed. Then the phase difference of oscillations in two adjacent microphones is defined as

$$\Delta\varphi = \varphi_2 - \varphi_1 = \frac{2\pi\Delta l}{\lambda}, \tag{2}$$

where Δl is the distance between the microphones; λ is the length of the sound wave.

Substituting the expression for λ through the speed of sound and frequency (λ = *c/f*), we get the formula for calculating the speed of sound:

$$c = \frac{2\pi\Delta l}{\Delta\varphi} f \tag{3}$$

The values of the speed of sound in the FB of a nanomaterial obtained as a result of processing experimental data are characterized by a large scatter due to layer density fluctuations, as can be seen from Figure 6.

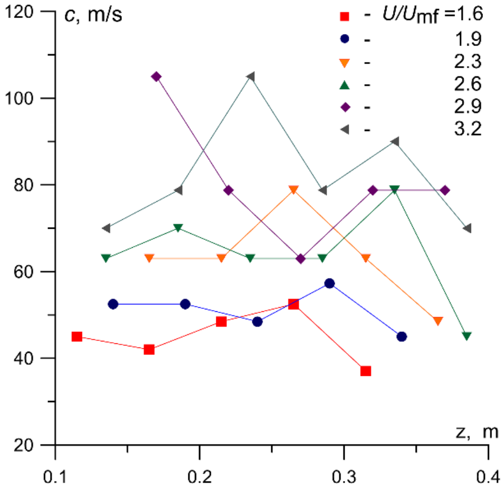

Fig. 6. Dependence of the speed of sound on the distance from the upper limit of the FB MWCNT for various gas velocities

However, they reveal two basic patterns. Firstly, the speed of sound increases with increasing gas flow rate. Secondly, the speed of sound decreases with distance from the upper boundary of the layer of nanometerial. Both these patterns can be understood if we assume that the compressibility of fluidized bed is constant and the speed of sound is inversly proportional to the square root of medium density [14], since an increase in gas flow leads to a decrease in the density of the layer, while this value increases with distance from the upper boundary of the layer.

2.3. Modelling of acoustic resonance phenomena in FB reactor

2.3.1. Statement of the problem

The choice of optimal parameters of the acoustic homogenization of the fluidized bed of the nanomaterial is directly related to finding the resonant frequencies and amplitudes of the stationary sound fields in the reactor. This task was modeled using the COMSOL Multiphysics software package. The purpose of the simulation was to find the distribution of the amplitude of the sound signal over the vertical coordinate depending on the main parameters of the process, i.e., the height of the fluidized bed of carbon nanotubes and the frequency of the sound supplied to the reactor. Acoustics Module of COMSOL package, Pressure Acoustics branch, Frequency Domain was used for calculations.

In the context of this approach, the spatial distribution of the total pressure amplitude is calculated for some harmonic oscillation mode with a frequency f (circular frequency $\omega = 2\pi f$). The total pressure p_t is represented as the sum of the given background pressure p_b and the acoustic pressure p: $p_t = p + p_b$. The distribution of the amplitude of the total pressure obeys the Helmholtz equation [14, 15]:

$$\nabla \cdot \left(-\frac{1}{\rho_c}\nabla p_t\right) - \frac{k_{eq}^2 p_t}{\rho_c} = 0, \tag{4}$$

$$k_{eq}^2 = \left(\frac{\omega}{c_c}\right)^2 - k_z^2, \tag{5}$$

$$c_c = \frac{\omega}{k}, \quad k = \frac{\omega}{c} - i\chi, \quad \rho_c = \frac{\rho c^2}{c_c^2}. \tag{6}$$

To describe the absorption of sound, the complex values of the wave vector (χ is the absorption coefficient), the speed of sound c_c, and density ρ_c are introduced here; k_z is a component of the wave vector that does not coincide with the main direction of plane sound wave propagation in a two-dimensional or one-dimensional formulation of the problem. In our calculations, a two-dimensional axisymmetric model was used, therefore, $k_z$was chosen to be equal to zero.

The simulated domain (Figure 7) was a cylinder divided into three sub-domain: a fluidized bed of nanomaterial (I) with the corresponding density, sound velocity, and absorption coefficient ((ρ_s, c_s and χ); freeboard space (II) (ρ_g, c_g , sound absorption is absent); and a piston (III), which is moving according to a harmonic law with a frequency f and simulating a flat wave radiator. The conditions of reflection from the solid wall were set on the outer boundaries of the regions. On the gas distribution plate at the bottom of the nanomaterial layer, the boundary condition varied, so it was assumed that either a perfect reflection of the sound wave occurs (as from a solid obstacle) or a complete sound absorption on the plate.

The initial data used in the calculations are presented in Table 1.

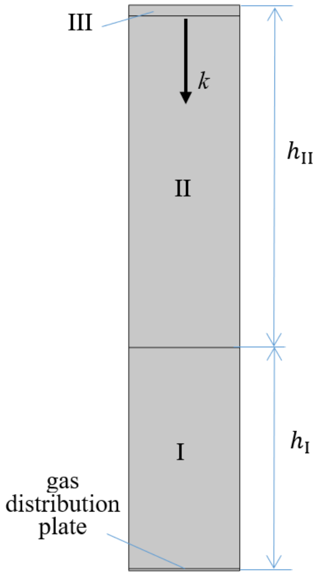

Fig. 7. The scheme of the calculated domain

Table 1. Basic data for reactor calculations in COMSOL Multiphysics

reactor height (h_I+h_{II}), m	0.2 – 1.0
fluidized bed height (h_I), m	0.2 – 0.5
reactor width (D), m	0.06
gas density (ρ_g), kg/m^3	1.2
speed of sound in the gas (c_g), m/s	331
FB density (ρ_s), kg/m^3	50 – 75
speed of sound in FB (c_s), m/s	30 – 80
absorption coefficient in FB (χ),m^{-1}	7 –11

2.3.2. *Results of the modelling and their discussion*

The propagation of sound waves in the system under consideration, which consists of two media with different complex impedances (fluidized bed and freeboard space) leads to a complex patern of the sound pressure distribution over the height of the reactor. The calculation of the structure of a standing wave in such a system is a non-trivial task due to the different speeds of sound propagating in two considered zones and its strong absorption in the fluidized bed. Figure 8 illustrates the evolution of the sound pressure amplitude distribution over the height of the reactor with the frequency of the sound source. Sound pressure is continuous at the interface between the gas and the nanomaterial layer. Because of partial reflection of the wave generated by the sound source, the incident and reflected waves are added at the upper boundary of the fluidized bed, and a maximum of sound pressure is observed at this boundary. Because the speed of sound in the nanomaterial is less than the speed of sound in a gas, the length of the sound wave in the fluidized bed is much shorter and the pattern of interference in this region is more complicated – the number of sound pressure peaks in it is greater. In addition, the strong absorption of sound plays a significant role in the formation of interference in this region makes. At frequencies near 260 and 460 Hz, two resonances are observed, at which one or two wavelengths of sound in gas fit in the freeboard height, respectively.

One would assume that in order to homogenize the fluidized bed of the nanomaterial using sound effects, it is important to achieve the maximum intensity of sound vibrations in the reactor, that is, to ensure resonance modes. Figure 9 presents the results of calculations of the dependence of the maximum amplitude of sound pressure (at the boundary of gas and nanomaterial) on the frequency of sound vibrations for values of the fluidized bed height in the range from 0.2 to 0.6 m in a reactor with a total height of 1 m. The frequency of the sound varied from 10 to 500 Hz. As mentioned above, there are two first resonances in this frequency range. The increase in the amplitude of the second resonance compared with the first is a consequence of carrying out calculations with a constant amplitude of oscillations of the sound source, which was considered as a one-dimensional piston.

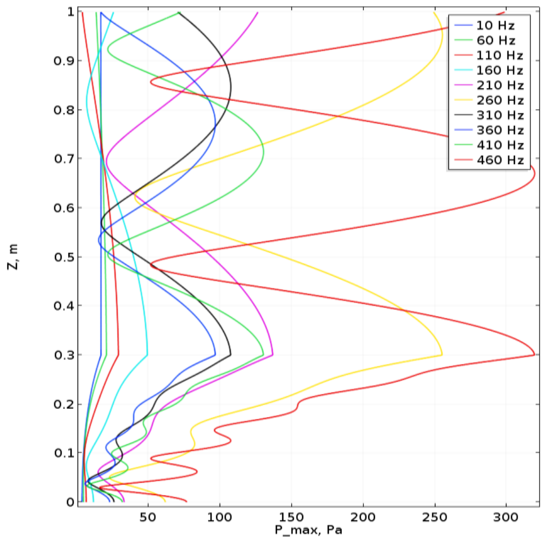

Fig. 8. Summary graph of sound pressure distribution in a fluidized bed reactor of a nanomaterial for sound exposure frequencies ranging from 10 Hz to 460 Hz

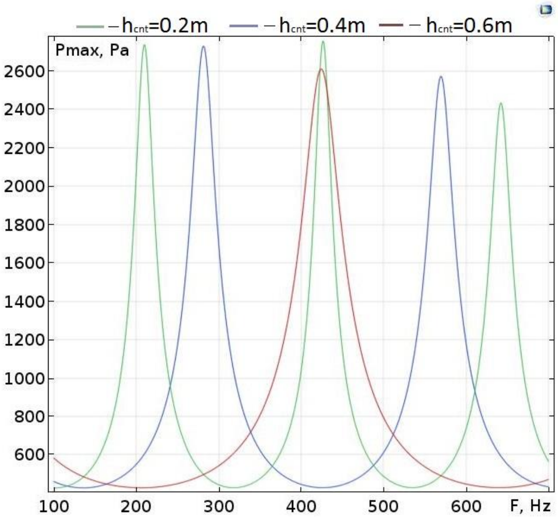

Fig. 9. Resonance curves with resonance peaks for different initial heights of the fluidized bed

It is obvious that the actual conditions in the reactor may not fully comply with the assumptions used in the proposed model. In particular, the model does not take into account the frequency response of the loudspeaker, the existence of radial vibrational modes, the non-uniformity of the nanomaterial bed in height, etc. However, the model accurately predicts the fundamental resonant frequency for the acoustic waves in the reactor. This is illustrated in Figure 10, which compares the calculated resonance curve, adjusted for the loudspeaker frequency response, with the experimental dependence of the sound amplitude on frequency.

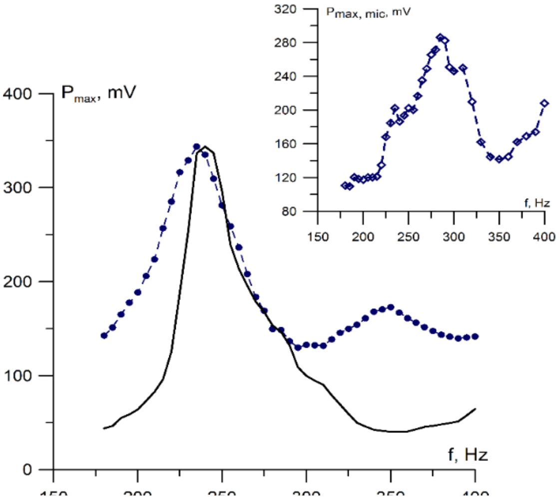

Fig. 10. Comparison of the experimental (blue symbols) and calculated (balck line) resonane curves. The frequency response curve of the loudspeaker is shown on the insert. Experimrntal data were obtained in mV of microphone signal; calculated data are calibrated to ajust the maximum experimental value. The reactor hight is 1 m, the bed hight is 0.3 m

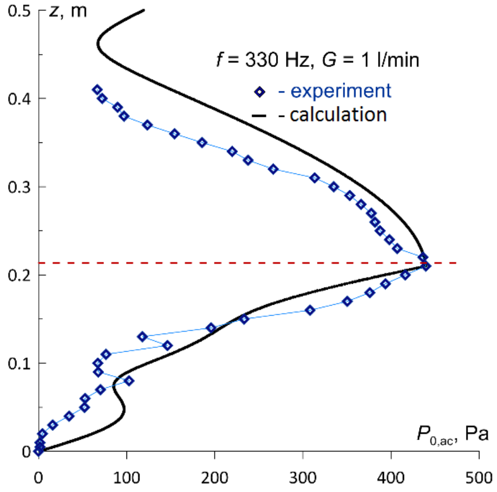

Fig. 11. Comparison of the experimental and calculated sound pressure distribution in the reactor with the maximum expansion of the nanomaterial layer. Experimental data were obtained in mV of microphone signal and then calibrated to cornrenspond to calculated sound pressure

Analysis of the experimental data has shown also that the maximum expansion of the layer and its homogeneity are achieved at approximately half the resonance frequency. Figure 11 shows a comparison of the experimentally obtained distribution of sound pressure over the 0.5 m reactor and a MWCNT (stationary) layer height of 0.21 m, at the sound frequency of 330 Hz, with calculating data. The maximum expansion of the fluidized bed is observed approximately at this frequency in the experiment.

As follows from Figure 11, the calculated and experimental pressure distributions are close to each other, and do not correspond to the pressure antinodes on the sound source surface, but to the node. In the experiments, the antinodes, and, therefore, the resonance are observed at the doubled frequencies. At the moment, the nature of the considered effect , i.e., the mismatch of the sound frequency at which the fluidized bed of the nanomaterial has a minimum density and maximum homogeneity with the resonant frequency, remains unexplained. It can be assumed that the explanation of this fact relates to the presence of characteristic frequencies, determined by the interaction of sound vibrations with domains of the fluidized bed, at which the most intensive destruction of large agglomerates and layer irregularities occurs.

3. CONCLUSIONS

As a result of an experimental study and numerical simulation of the propagation of acoustic oscillations in a fluidized bed of carbon nanotubes, the main regularities of the phenomenon were established and its quantitative characteristics were determined.

During the work, a technique was developed to experimentally study the characteristics of a fluidized MWCNT layer and using it to determine the dependence of the pressure drop on the fluidized bed on the bed parameters and gas flow, the minimum fluidization velocity, sound velocity, acoustic pressure distribution over the bed height, amplitude-frequency response of the reactor.

The experimentally noted heterogeneity of the fluidized bed arises due to the strong absorption of sound in it, which leads to a large vertical gradient of sound pressure in the layer and, as a result, to a change in its density. In the upper part of the layer, its density is the lowest because of the formation of gas-phase bubble interlayers, and at the bottom the density is maximum and almost equal to the density of the fixed layer of particles.

A numerical model has been developed for calculating the propagation of a sound wave in a fluidized bed of a nanomaterial. In general, the developed model and the performed calculations make it possible to predict the distribution of sound pressure in the reactor, its resonant frequencies and to make the choice of optimal conditions for homogenizing the layer.

REFERENCES

1. OMMEN J.R. van., VALVERDE J. M. , PFEFFER R. Fluidization of nanopowders: a review. *J. Nanoparticle Res*., 2012, Vol. 14, No. 3, p. 737.
2. MARTÍN L. de, FABRE F., OMMEN J.R. van. The fractal scaling of fluidized nanoparticle agglomerates. *Chem. Eng. Sci*., 2014, Vol. 112, p. 79–86.
3. RABINOVICH O. S., BORODULYA V. A., BLINOVA A. N., V. L. KUZNETSOV, A. I. DELIDOVICH, KRASNIKOV D. V. Simulation of Transient Processes of the Catalytic Synthesis of Carbon Nanotubes in a Fluidized Bed. *Theoretical Foundations of Chemical Engineering*, 2014, Vol. 48, No. 1, p. 1–12.
4. RABINOVICH J., TSYTSENKA (BLINOVA) A., KUZNETSOV V., MOSEENKOV S, KRASNIKOV D. A model for catalytic synthesis of carbon nanotubes in a fluidized-bed reactor: Effect of reaction heat. *Chem. Eng. J*, 2017, Vol. 329, p. 305–311.
5. GELDART D., Types of gas fluidization . *Powder Technol*, 1973, No. 7, p. 285-292.
6. MORSE R.D. Sonic energy in granular solid fluidization // Ind.Eng. Chem. 1955, Vol. 47, p. 1170–1175.
7. RUSSO P., CHIRONE R., MASSIMILLA L., RUSSO R. The influence of the frequency of acoustic waves on sound-assisted fluidization of beds of fine partixles. *Powder technology*, 1995, Vol. 82, p. 219–230.
8. AMMENDOLA P., CHIRONE R. Aeration and mixing behaviours of nano-sized powders under sound vibration. *Powder Technol*, 2010, Vol. 201, p. 49–56.
9. AMMENDOLA P., CHIRONE R., RAGANATI F. Fluidization of binary mixtures of nanoparticles under the effect of acoustic fields. *Adv. Powder Technol*, 2011, Vol. 22, p. 174–183.
10. AMMENDOLA P., CHIRONE R., RAGANATI F. Effect of mixture composition, nanoparticle density and sound intensity on mixing quality of nanopowders. *Chem. Eng. Process. Process Intensif*., 2011, Vol. 50, p. 885–891.
11. RAGANATI F., AMMENDOLA P., CHIRONE R. Role of acoustic fields in promoting the gas-solid contact in a fluidized bed of fine particles. *KONA Powder Particle J*, 2015, Vol. 32, p. 23–40.
12. RAGANATI F., CHIRONE R., AMMENDOLA P. Gas–solid fluidization of cohesive powders. *Chem. Eng. Research and Design*, 2018, Vol. 133, p. 347–387.
13. HERRERA C.A, LEVY E.K., OCHS J. Characteristics of acoustic standing waves in fluidized bed. *AIChE Jorurnal*, 2012, Vol. 48, No. 3, pp. 503-513.
14. KINSLER L.E., FREY A.R., COPPENS A.B., SANDERS J.V. *Fundamentals of acoustics.* 4th ed. New York: J. Wiley&Sons,. 2000. 568 p.
15. Acoustics Module Application Library Manual, COMSOL 5.3.

PREDICTION OF EFFECTIVE HEAT TRANSFER COEFFICIENTS FOR VAPOUR CONDENSATION INSIDE HORIZONTAL TUBES IN STRATIFIED PHASE FLOW

V. V. Sereda
National University of Water and Environmental Engineering
Soborna 11,
33028 Rivne – Ukraine
Email: v.v.sereda@nuwm.edu.ua

V. G. Rifert, V. V. Gorin, P. A. Barabash
National Technical University of Ukraine "Igor Sikorsky Kyiv Polytechnic Institute"
Politehnichna 6,
03056 Kyiv – Ukraine

ABSTRACT

In modern condensers of air conditioning systems, heat pumps, evaporators of seawater desalination systems and heaters of power plants, the process of vapour condensation is carried out mainly inside the horizontal tubes and channels. Heat transfer processes occurring in condensers have a significant effect on the overall energy efficiency of the mentioned systems. During film condensation in horizontal heat exchangers, annular, intermediate and stratified modes of condensate film flow and phase distribution can occur. The correlations suggested by Thome and others (2003), Cavallini and others (2006), Shah (2009) and Rifert and others (2018) are recommended to be used for the prediction of heat transfer coefficients in case of the annular and intermediate modes of the phases.

In this paper, the experimental investigation of heat transfer was carried out in the case of stratified flow of the phases. Experiments were conducted during condensation of freons R22, R406a and R407c in the plain smooth tube with diameter 17 mm. The range of parameters includes saturated temperature from 35 to 40 ºC, inlet mass velocity from 10 to 100 kg/(m^{2}s), vapour quality from 0.8 to 0.1, heat flux from 5 to 50 kW/m^2 and a difference between saturated temperature and the temperature on the inner tube wall from 4 to 14 K. The unique measurements of circumferential heat fluxes and heat transfer coefficients were carried out with the thick wall method during stratified condensation mode. Circumferential heat flux was varied, while mass velocity and vapour quality were kept constant throughout all experiments. This procedure allows examining the specific impact of heat flux on heat transfer and at the constant value or small changes of other characteristics.

It can be inferred that at the top part of the tube, with the increase of the heat flux, the thickness of the condensate film increases, which leads to the decrease in heat transfer. At the bottom of the tube, the increase in heat flux enhances heat transfer coefficient, that is characteristic of the turbulent liquid flow in the tube. Circumferential heat transfer coefficients in the top tube segment are larger than in the bottom part of the tube due to a large difference in condensate film thickness.

The obtained results allowed us to improve prediction of effective heat transfer coefficients, considering heat transfer in the upper part of the tube and heat transfer in the stream, as well as the angle of tube flooding. Good convergence of a proposed method with the experimental data on condensation various fluids inside horizontal tubes is shown. The data used for the correlation validation includes: freons R22, R134a, R123, R125, R32, R410a, propane, isobutene, propylene, dimethyl ether, carbon dioxide and methane. A total of 213 data points from 5 sources are generalized with an error less than 30%. Using this method for designing heat exchangers, which utilize such types of fluids, will increase the efficiency of thermal energy systems.

Keywords: condensation, heat transfer, heat exchanger, plain tube, stratified flow

CYSENI 2019, May 23-24, Kaunas, Lithuania
ISSN 1822-7554, www.cyseni.com

PRELIMINARY INVESTIGATIONS OF WATER VAPOUR CONDENSATION FROM BIOFUEL FLUE GASES IN A MODEL OF A VERTICAL CONDENSING HEAT EXCHANGER

R. Poškas, A. Sirvydas, V. Kulkovas, P. Poškas
Lithuanian Energy Institute
Breslaujos str. 3, LT-44403 Kaunas – Lithuania
Email: vladislavas.kulkovas@lei.lt

ABSTRACT

Heat recovery from flue gases is very important because it can significantly increase the efficiency of boiler plants. Due to this reason, flue gas condensers (condensing heat exchangers) are used in many boiler plants. But a flue gas condenser is large and costly equipment. Although the general principles for designing of condensing heat exchangers are known rather well, this is not the case for flue gas condensers. Literature review has revealed that there are many investigations related to pure vapour condensation; however, investigations of water vapour condensation from flue gases are mostly oriented to the determination of the average heat transfer. Local parameters of the condensation process are not investigated in detail and due to this it is not possible to perform optimisation of this equipment. Therefore, in this paper, preliminary investigations are presented of water vapour condensation from biofuel flue gases in a model of a vertical condensing heat exchanger for turbulent flow regimes. Temperature measurements have allowed determining temperature distributions along the model of the condensing heat exchanger. For the investigated regimes, the temperature distributions illustrate that condensation of the vapour from the flue gases does not occur in the total length of the model of the condensing heat exchanger. The initial part of the heat exchanger serves as a cooling section of the flue gases until their temperature reaches the dew point temperature at the tube wall. Only after that the condensation of water vapour occurs. Experimental results also show that in long tubes (at x/d larger than 100), the flue gas temperature in the whole cross-section of the tube is below the dew point temperature of the inlet gases.

Keywords: biofuel flue gases, vertical condensing heat exchanger, condensing heat-mass transfer, temperature distribution

1. INTRODUCTION

Since 2003 there was started an operation of the first condensing heat exchanger (economizer) in Lithuania, while the rest biofuel boilers were operating not very efficient – i.e. without condensing economizers [1]. Nowadays the situation in the boiler plants has changed and practically all the boiler plants are equipped with condensing economizers.

In the boiler plants the released flue gases are of relatively high temperature and humidity and in order to efficiently use it, gases usually are directed to the condensing economiser. In the economiser, they release their heat, cool down and the water vapour existing in flue gases starts to condensate. During condensation process, there is an additional amount of heat generated, which can be used to heat the water returning from the heat consumers. So, the condensing economiser allows to increase overall efficiency of the boiler plant.

Although the general principles for designing of condensing heat exchangers are known, but the detailed processes taking place in such type of exchangers and the peculiarities of these processes are almost not investigated. Literature review shows that there are a lot of experimental and theoretical studies devoted to condensation of water vapour in pipes with a high water vapour content (90-100% vol.) and relatively small portion of non-condensing gas [2-7].

The experimental and theoretical investigations of the average condensation heat transfer in the steam-air mixture (2.5-5.5 kg/s) and noncondensable mass fraction 0-10% in short vertical pipe (x/d ≈ 37) [6] demonstrated, that condensation heat transfer decreases with the increase of the noncondensable gas fraction. The analysis of the pressure influence in the system also showed that in case of system pressure increase, the condensation heat transfer also increases.

In the paper [7] heat transfer investigations in the presence of noncondensable gas (nitrogen) in the steam inside a vertical pipe included local bulk steam temperature, pipe wall temperature and cooling water temperature measurements along the test section (x/d ≈ 230). The steam was supplied from the upper part and the cooling water from the lower part of the test section. For the case with pure steam (flow rate 11.2 kg/h), the bulk steam temperature measured in the centre of the pipe up to x/d ≈ 84 was practically constant (100 °C) ant after x/d > 84 up to x/d ≈ 107 a clearly expressed temperature decrease from 100 °C to ≈ 30 °C was observed – this temperature decrease indicated the location of the complete condensation (the location of complete condensation disappeared, when steam flow rate was exceeding 20 kg/h). In case the mass fraction of noncondensable gas was increased to about 10%, the character of the temperatures distribution changed and it was clearly expressed for the bulk steam temperature – the temperature from the beginning of the test section up to x/d ≈ 84 was not constant anymore, but it was negligibly decreasing – from about 100 °C to about 95 °C. From x/d > 84 till the end of the pipe constant decrease (but not so clearly expressed as in case with pure steam) to ≈ 50 °C was observed. The character of the wall temperature in this case was very similar to that for pure steam condensation – it was gradually decreasing along the pipe from about 90 °C to about 20 °C, while the temperature of the cooling water was constantly increasing along the pipe (i.e. from the end till the beginning of the test section) – from ≈ 15 °C to ≈ 38 °C. The analysis of the results of local heat transfer showed the increase when the inlet steam flow rate was increased and the nitrogen fraction was decreased.

So, the papers [6, 7] in general reflect the average and local aspects occurring in the vertical pipes in case of pure steam or steam condensation with small amount of noncondensable gases.

In case of flue gases (smoke) the situation is opposite – the content of water vapour is relatively small (~ 10-25% vol.) and the portion of noncondensable gases is high. Condensation of wet flue gases obtained in case of incineration of natural gas in the boiler was studied experimentally in a vertical pipe of x/d ≈ 79 and in Reynolds number range from 2300 to 5000 [8]. The results have shown that the condensable gas (moisture) existing in the flue gases enhances the total heat transfer up to two times in comparison with dry air. The wall temperature is also an important factor, which has a considerable effect on condensation rate and heat transfer. The increasing wall temperature for about 1.7 times – i.e. from about 30 °C to about 50 °C lead to condensation rate decrease for about four times – from ≈ 0.8 to ≈ 0.2 and total heat transfer decrease almost up to 1.7 times.

Vapour-air mixture was simulated as wet flue gases for the purpose of provision the analysis on thermal fields and heat and mass transfer in the vertical pipe of x/d ≈ 70 and mixture Re numbers from ≈3000 to ≈6000 [9]. The inlet gas mixture temperature was about 60 °C, and the cooling air temperature 20 °C. Volumetric water vapour fraction in the gas mixture was approx. 1% and 17%. It was shown, that the pipe wall temperature in case of vapour condensation remains 10-15 °C higher along the test section in comparison with that without condensation phenomena. Flue gas temperature was also measured in the centre of the test section. In the case without condensation the mixture temperature in the centre of a test section showed a steeper decrease – from inlet temperature of 60 °C to about 45 °C at the outlet from the test section, while in case of vapour condensation at the same inlet temperature the temperature at the outlet of the test section was about 55 °C. Authors also conclude that heat transfer is influenced by water quantity in the gas mixture. During experiments, up to 30% of water vapour was condensed and this lead to substantial increase of the total heat transfer. Other theoretical and experimental investigations also reveal that condensation has a significant impact on heat transfer [10, 11].

Investigation of the simulated flue gas condensation with inlet water vapour mass fraction from 3 to 12% and mixture Reynolds number from 4600 and 14000 in vertical short pipe (x/d ≈ 32) was presented in [12]. The inlet mixture temperature during experiments was in the range of 130-

150 °C and inlet cooling water temperature was about 28-30 °C. The test section was operating in counter flow arrangement – cooling water was supplied from the lower part of test section into the inner pipe and the mixture of hot air and water vapour – in the space between inner and outer pipe. It was concluded, that in case of low inlet water vapour fraction rough and suction effects are the major factors influencing heat transfer. The measured condenser pipe wall temperature was increasing along the pipe for all investigated Re numbers. For the lowest Re numbers (4600, 6400) the less temperature increase was determined along the length of the pipe – about 2.5-3 °C and for the highest Re number (≈ 12300) increase difference along pipe wall temperature was – ~ 4-5 °C. The condensation heat transfer was more influenced when Re number and inlet vapour mass fraction were increased.

Literature review has shown that the condensation phenomena is mostly investigated in rather short test sections and in most cases simulating flue gases at relatively low Reynolds numbers. However, the usual length of the condensing heat exchangers used in boiler plants is from few meters to about 8-9 m or sometimes even more. The condensing heat exchangers are composed of a housing where few hundreds of small diameter thin wall pipes are placed. Flue gases are routed into these pipes, while the cooling water flows around them. Usually counter-current flow scheme is used. The overall design of the condensing heat exchangers depends on the power required [13], but in any case condensing heat exchangers are rather huge and expensive devices and in order to optimise their dimensions and reduce their production costs it is necessary to perform detail heat and mass transfer investigations.

The purpose of this investigation is to analyze the temperature distribution in a model that corresponds to the actual operating conditions, i.e. at high Re number in long channel and then flue gases is flowing. So, in this paper the preliminary experimental results of temperature distribution in various points along the model (to x/d ≈ 171) of the condensing heat exchanger in case of incineration of wood pellets and condensation of low water vapour existing in the flue gases are presented and discussed.

2. METHODOLOGY

2.1. Experimental setup

The experimental setup with the test section – model of the condensing heat exchanger used in the experiments is shown in Fig. 1. During the experiments, wood pellets were incinerated in automatic boiler Kostrzewa (Poland).

According to the EN303-5:2012 standard this boiler is classified as class 3 boiler. Boiler power (max. 50 kW) can be regulated in the range from 50 to 100%. The flue gases from incinerated wood pellets flow via the stack into the test section – i.e. inner pipe of the model of the condensing heat exchanger (condensing economizer). The model of the condensing heat exchanger is composed of one inner calorimetric pipe (inner Ø0.034 m, length x ≈ 5.8 m and x/d ≈ 171) and outer pipe (inner Ø0.108 m, x ≈ 5.8 m). Flue gas flow rate through the test section is regulated by flow control and bypass dampers. After flue gas pass the test section it is routed to the flue gas pipe (chimney) and is released into the environment. The moisture condensed in the calorimetric pipe is drained into the condensate collection tank (0.02 m^3).

For the calorimetric pipe cooling, the cooling water is supplied from the water tank with the pump. The water is supplied into the lower part of the model of the condensing economizer, into the space between inner (calorimetric) and outer pipes. The water flows to the upper part of the test section, leaves it, passes heat exchanger (air-water) where it is cooled down and returns back to the water tank (0.2 m^3).

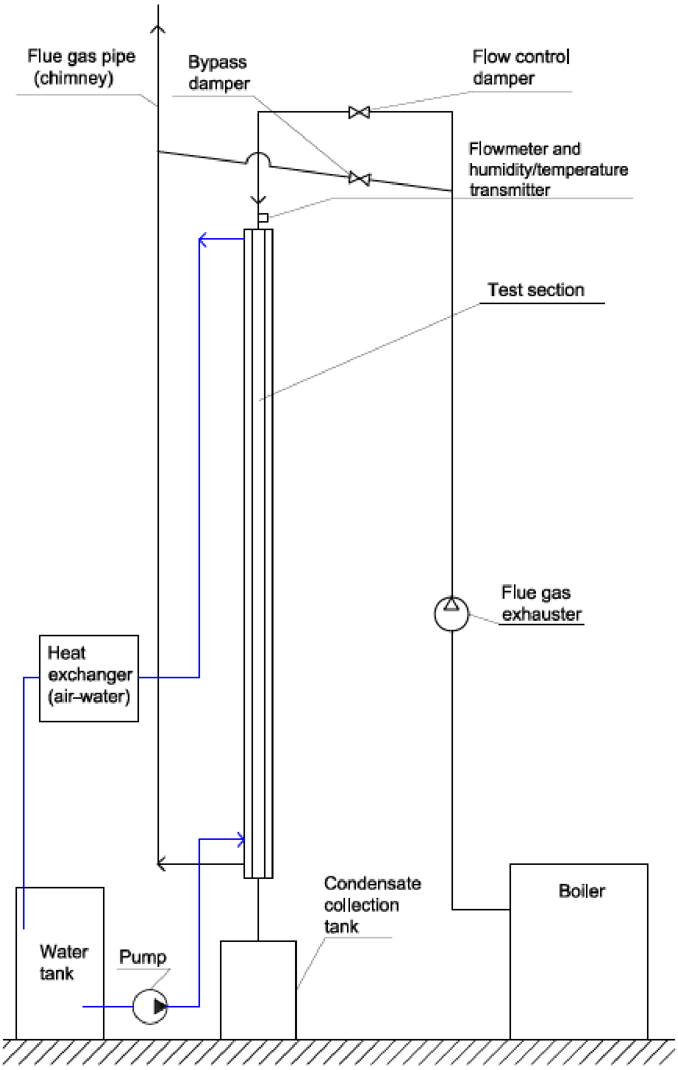

Fig. 1. Experimental setup with the test section (model of the condensing heat exchanger)

2.2. Methodology

Relative humidity (RH_{in}, %) and temperature (t_{in}, °C) of flue gases at the inlet to the calorimetric pipe are measured by using electronic humidity/temperature transmitter (Kimo C310). Flow rate of the flue gases is measured by using bellmouth with installed Pitot-Prandtl tubes, which are connected to the differential micromanometer (measurement point is indicated in Fig. 1).

Cooling water flow rate as well as condensate flow rate were measured by beaker and stopwatch.

Temperature measurements in the model were done by calibrated Chromel Copel thermocouples. Due to this:

- there are 20 thermocouples installed in the centre of the calorimetric pipe along its length for the measurement of the flue gas temperature (Distances between thermocouples are 0.28 m);
- there are 20 thermocouples installed at the inner wall of the calorimetric pipe along its length for the measurement of the pipe temperature (Distances between thermocouples are 0.28 m);
- there are 10 thermocouples installed in the space between inner and outer pipes along its length for the measurement of the cooling water temperature (Distances between thermocouples are 0.56 m).

- there are 3 thermocouples installed for the cooling water inlet and 3 thermocouples installed for the cooling water outlet temperature measurements.

During the experiments, all the thermocouple indications were collected using Keithley automatic data acquisition system. For the registration of the boiler parameters such as flue gas temperature at exit from the boiler, water supply and return temperature, draft – the automatic collection of the mentioned boiler data was done every 5 minutes using KD recorder.

During the experiments inlet cooling water flow rate was almost constant and was equal to 32 l/h.

Flue gas velocity (m/s) in the bellmouth was calculated using the equation:

$$w = \sqrt{\frac{2\Delta p_d}{\rho}}, \tag{1}$$

where Δp_d – dynamic pressure, Pa, ρ – flue gas inlet density, kg/m^3 (based on flue gas inlet temperature t_{in}).

Volumetric inlet flow rate (m^3/s) of the flue gas into the calorimetric pipe is equal to:

$$G_{in} = \mathrm{w} \cdot a, \tag{2}$$

where a – is the minimal cross section area of the bellmouth, m^2.

Inlet flue gas velocity (m/s) in the calorimetric pipe was calculated using the equation:

$$w_{in} = w \cdot \frac{a}{a_{in}}, \tag{3}$$

where a_{in} – is the internal cross section area of the calorimetric pipe, m^2. Other parameters are the same as in equations 1 and 2.

Flue gas Reynolds number at the inlet into the calorimetric pipe was calculated as:

$$Re_{in} = \frac{w_{in} \cdot d}{\nu_{in}}, \tag{4}$$

where d – is the internal diameter of the calorimetric pipe, m, ν_{in} – is the kinematic viscosity of the flue gas, m^2/s. Other parameters are the same as in equations above.

The heat quantity (kW) obtained by the cooling water was calculated as:

$$Q_w = \dot{m} \cdot (c_{pw_{out}} \cdot t_{w_{out}} - c_{pw_{in}} \cdot t_{w_{in}}), \tag{5}$$

where $\dot{m}$ – mass flow cooling water rate of the cooling water, kg/s, $c_{pw\ out,\ in}$ – specific heat of the water at outlet and inlet temperature, respectively, kJ/kg·°C, $t_{w\ in,\ out}$ – cooling water inlet and outlet temperature, respectively, °C.

The heat quantity (kW) release by the flue gases including heat quantity due to condensation process was calculated as:

$$Q_b = \dot{m}_g \cdot (c_{pg_{out}} \cdot t_{g\ out} - c_{pg_{in}} \cdot t_{g\ in}) + r \cdot \dot{m}_c, \tag{6}$$

where $\dot{m}_g$ – mass flow rate of the flue gases, kg/s, $c_{p\ g\ out,\ in}$ – specific heat of the flue gases at outlet and inlet temperature, respectively kJ/kg·°C, $t_{g\ in,\ out}$ – flue gases inlet and outlet temperature, respectively, °C, r – latent heat of condensation, kJ/kg, m_c – condensate flow rate, kg/s.

The error of above mentioned heat quantities was calculated as:

$$\mathrm{Error} = \frac{(Q_b - Q_w)}{Q_b} \times 100\%. \tag{7}$$

3. RESULTS AND THEIR ANALYSIS

In Fig. 2 distribution of temperatures along the test section (model of the condensing heat exchanger) at different Re_{in} numbers is presented. Dew point temperature at the inlet to the calorimetric pipe was calculated based on RH_{in} and t_{in} and using the equations presented in [14]. For the both cases analysed ($Re_{in} \approx 22000$ and $Re_{in} \approx 17000$) the dew point temperature was calculated to be about 46-47 °C.

It is known, that when the wall temperature is lower than dew point temperature, the water vapour starts to condensate on the wall. When the temperature of the flue gases in centre of calorimetric pipe reaches dew point temperature, water vapour should start to condense in all its volume.

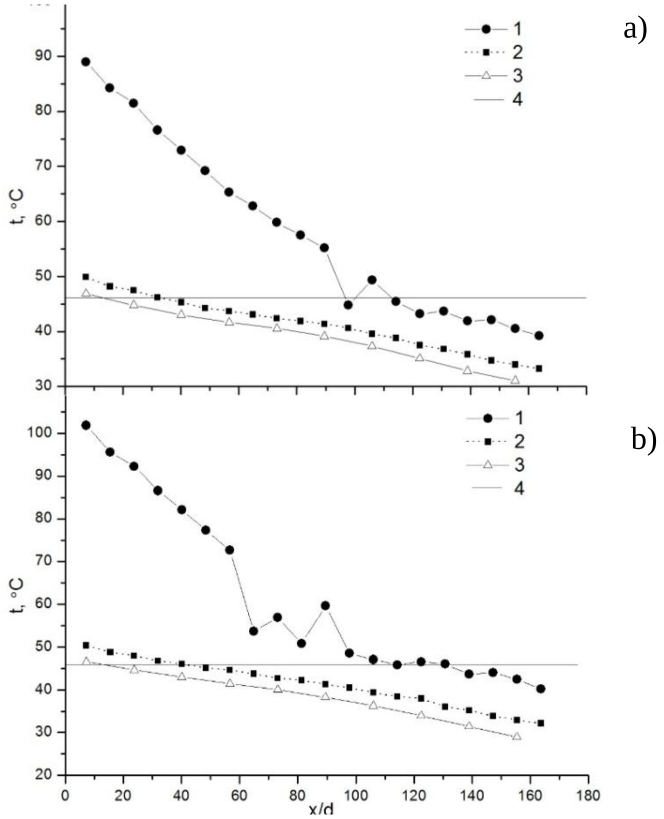

Fig. 2. Temperature distribution along model of the condensing heat exchanger at different Re_{in}. $Re_{in} \approx 22000$ and $RH_{in} \approx 17$ % (a), $Re_{in} \approx 17000$ and $RH_{in} \approx 23$ % (b): 1 – centre of calorimetric pipe, 2 – inner wall of the calorimetric pipe, 3 – cooling water in the space between inner and outer pipes, 4 – dew point temperature

From Fig. 2 it is evident that temperature distributions and tendencies of the inner wall of the calorimetric pipe and the cooling water in both presented cases are very similar (Fig. 2, curves 2 and 3). However, the temperature characters of flue gases in centre of the calorimetric pipe are different in comparison with pipe wall and cooling water temperatures. Initially, flue gases cool down and until the point when the flue gas temperature at the wall of the calorimetric pipe reaches dew point temperature the heat is transferred by single-phase convective heat transfer. For the case with $Re_{in} \approx 22000$ cooling of the flue gases is from $x/d = 0$ till $x/d \approx 30$ and for the case with $Re_{in} \approx 17000$ – from $x/d = 0$ till $x/d \approx 40$. For this reason, flue gas temperature decrease in the mentioned sections of the calorimetric pipe are the highest (Fig. 2, curve 1) – from 90 °C to 75 °C when $Re_{in} \approx 22000$ and from 105 °C to 80 °C when $Re_{in} \approx 17000$.

When the wall temperature is practically equal to the dew point temperature, the character of flue gas temperature changes – less temperature decrease is observed and this is clearly expressed for $Re_{in} \approx 22000$ (Fig. 2 a, curve 1) in the range from $x/d \approx 30$ till $x/d \approx 110$, in comparison with that temperature decrease which was observed from x/d ≈ 0 till x/d ≈ 30. Curve 1 when x/d ≈ 100 (Fig. 2. a) shows temperature fluctuations that may be indication of fog formation, however more investigations are needed to confirm this processes.

In case of lower $Re_{in} \approx 17000$ (Fig. 2 b, curve 1) a noticeable flue gas temperature fluctuation is observed just before the flue gas temperature reaches dew point temperature. It is likely that fluctuation shows fog formation in the total cross-section of the calorimetric pipe, however more investigations are needed to confirm this processes. Also, the flue temperature distribution between x/d ≈ 40 till x/d ≈ 110 obviously shows that condensation process begins and plays an important role on the temperature of flue gases – the temperature decrease is not so significantly expressed in this section of the pipe in comparison with previous section of the pipe.

When the flue gas temperature in a centre of the calorimetric pipe reaches dew point temperature ($Re_{in} \approx 22000$ and $Re_{in} \approx 17000$ from x/d ≈ 110, see Fig. 2) the decrease of flue gas temperature in both analysed cases till the end of the calorimetric pipe is rather small – from about 46 °C to about 42 °C.

Results also show (Fig. 2), that the highest temperature difference between flue gas temperature and calorimetric pipe wall temperature in both analysed cases exists from x/d ≈ 0 till x/d ≈ 110 and the least and almost constant temperature difference remains from x/d ≈ 110 till the end of the calorimetric pipe.

Cooling water temperature (Fig. 2, curve 3) is increasing almost constantly in both analysed cases along the test section (i.e. from x/d ≈ 160 till x/d = 0). However, it can be noticed that water temperature is rising faster in the part of the test section where the heat is transferred by specific and latent heat (i.e. from x/d ≈ 160 till x/d ≈ 90-100) in comparison with the part of the test section where the heat is transferred by single-phase convective heat transfer only.

In Fig. 3 the comparison of heat quantities between flue gases and cooling water at different Re_{in} are presented.

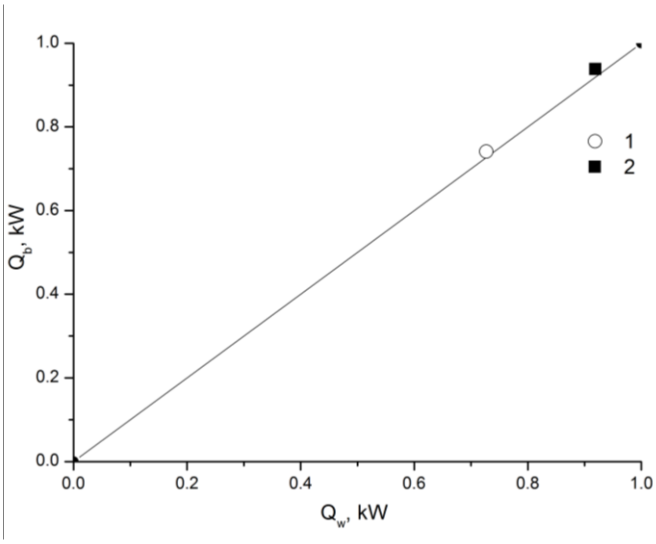

Fig. 3. Heat quantities between flue gases and cooling water at different Re_{in}: 1 – $Re_{in} \approx 22000$, 2 – $Re_{in} \approx 17000$

As the inlet relative humidity of the flue gases at lower Re_{in} ($Re_{in} \approx 17000$) was higher, the data presented in Fig. 3 shows, that this results in higher heat quantity determined during the experiments. So, at $Re_{in} \approx 17000$ heat quantity released from flue gases was about 0.93 kW and the heat quantity obtained by the cooling water – ≈ 0.94 kW. Calculated error between these two heat quantities was close to 2%.

For the case with $Re_{in} \approx 22000$ heat quantity which was released from flue gases was lower than in the case with lower Re_{in} and in this case it was equal to ≈ 0.74 kW. Heat quantity obtained by the cooling water was about 0.72 kW. Calculated error was almost 2.2%.

Calculations also showed, that in case with $Re_{in} \approx 17000$ heat quantity due to latent heat was 0.34 kW and in case with $Re_{in} \approx 22000$-0.17 kW. So, heat quantity obtained from the latent heat composes 36% and 23% of the total heat quantity released from flue gases for analysed cases with $Re_{in} \approx 17000$ and $Re_{in} \approx 22000$, respectively.

4. CONCLUSIONS

After performing temperature distribution measurements along the model of the condensing heat exchanger at different Re_{in} numbers, the following conclusions can be made:

- Condensation of the vapour existing in flue gas does not occur in the total length of the model of the condensing heat exchanger.
- Initial part of the condensing heat exchanger serves as a cooling section of the flue gas until their temperature at the wall reach dew point temperature.
- Flue gas temperature fluctuation in the centre of calorimetric pipe approximately indicate the beginning of the condensation process in the centre of the calorimetric pipe.

During experiments it was determined that inlet relative humidity of the flue gases plays an important role of the condensation heat transfer.

REFERENCES

1. RINKEVIČIUS, N., MILIAUSKAS, G. Heat balance analysis of the shell & tube type biomass flue gas condenser. KTU-LEI 2017. Proceedings of annual conference of Thermal energy and technology. Kaunas: Kaunas University of Technology - Lithuanian Energy Institute. 2017 January 26-27 (In Lithuanian).
2. SIDDIQUE, M., GOLAY, M.W., KAZIMI, M.S. Local heat transfer coefficients for forced-convection condensation of steam in a vertical tube in the presence of a non-condensable gas, *Nuclear technology*, 1993, No. 102, p. 386–402.
3. MAHESHWARI, N.K., SAHA, D., SINHA, R.K., ARITOMI, M. Investigation on condensation in presence of a noncondensable gas for a wide range of Reynolds number. *Nuclear engineering and design*, 2004, No. 227, p. 219–238.
4. CARUSO, G., GIANNETTI, F., NAVIGLIO, A. Experimental investigation on pure steam and steam-air mixture condensation inside tubes. *International journal of heat and technology*, 2012, No. 30, p. 77–84.
5. PARK, I., KIM, S.M, MUDAWAR, I. Experimental measurement and modelling of downflow condensation in a circular tube. *International journal of heat and mass transfer,* 2013, No. 57, p. 567–581.
6. OH, S., REVANKAR S.T. Experimental and theoretical investigation of film condensation with noncondensable gas. *International journal of heat and mass transfer*, 2006, No. 49, p. 2523–2534.
7. LEE, K.Y., KIM, M.H. Experimental and empirical study of steam condensation heat transfer with a noncondensable gas in a small-diameter vertical tube. *Nuclear engineering and design*, 2008, No. 238, p. 207–216.
8. JIA, L., PENG, X.F., YAN, Y., SUN, J.D., LI, X.P. Effects of water vapor condensation on the convection heat transfer of wet flue gas in a vertical tube. *International journal of heat and mass transfer*, 2001, No. 44, p. 4257–4265.
9. DEDALIC, N., DŽAFEROVIC, E., GANIC, E. Experimental and numerical study on vapor condensation of wet flue gas in chimney, 2008, *Defect and Diffusion Forum*, Vol. 273–276, p. 119–125.

10. SHI, X., Che, D., Agnew, B., Gao, J. An investigation of the performance of compact heat exchanger for latent heat recovery from exhaust flue gases. *International journal of heat and mass transfer*, 2011, No. 54, p. 606–615.
11. Li, J.D., Saraireh, M., Thrope, G. Condensation of vapor in the presence of non-condensable gas in condensers. *International journal of heat and mass transfer*, 2011, No. 54, p. 4078–4089.
12. CHANTANA, Ch., KUMAR, S. Experimental and theoretical investigation of air-steam condensation in a vertical tube at low inlet steam fractions. *Applied thermal engineering*, 2013, No. 54, p. 399–412.
13. THULUKKANAM, K. *Heat exchanger design handbook. Second edition.* London-New York: CRS press, 2013. 1186 p. ISBN 978-3-4398-4212-6.
14. *American meteorological society*. 2005-[referred on the 1st of February in 2005 y]. Link to the internet <https://journals.ametsoc.org/doi/pdf/10.1175/BAMS-86-2-225>.

CYSENI 2019, May 23-24, Kaunas, Lithuania
ISSN 1822-7554, www.cyseni.com

IMPROVING THE METHOD OF HEAT TRANSFER CALCULATION DURING CONDENSATION AND EVOPARITION OF A LIQUID FILM IN THE FIELD OF CENTRIFUGAL FORCES

A. S. Solomakha, V. G. Rifert, P. A. Barabash
Igor Sikorsky Kyiv Polytechnic Institute
Polytechnichna str. 6, 03056 Kyiv – Ukraine
Email: a.solomakha@kpi.ua

ABSTRACT

The paper discusses heat and mass transfer apparatus with a rotating surface of various shapes (disk, cone, etc.) for the treatment of liquids for which the residence time in the high-temperature region is critical (fruit juices, pharmacological preparations, etc.). In addition, such devices make it possible to create compact energy-efficient systems, including devices for microgravity conditions.

In most designs of such evaporators, the liquid is supplied to the centre of the rotating surface and spreads out in the form of a thin film under the action of centrifugal forces. The heating medium in most cases is steam, which condenses on the back side of the evaporation surface. In published theoretical papers, the heat transfer coefficient for evaporation and condensation is determined by the Nusselt model, in which gravitational acceleration is substituted with centrifugal.

Experimental studies of heat transfer in the field of centrifugal forces showed that heat transfer coefficients may differ from those calculated by the laminar model by more than 50%. The paper explains this phenomenon and presents more accurate calculation methods, which take into account the possibility of a liquid film flowing into a turbulent mode. This allowed reducing the deviation of the theoretical model from the experimentally obtained results.

The developed technique helps to choose the optimal design and operating parameters of distillation systems based on centrifugal devices for various purposes.

Keywords: centrifugal forces, liquid film, condensation, evaporation

1. TYPES OF CENTRIFUGAL EVAPORATORS

To concentrate heat-sensitive liquids (juices, antibiotics, coffee, tea) it is necessary to minimize the contact time of the liquid with the heating surface. This is achieved in a centrifugal evaporator [1].

Figure 1 shows the design of the heat exchange surface in spinning cone column [2, 3]. It consists of a vertical succession of alternate rotating and stationary cones. Liquid flows as a film down the stationary cone, drains into the base of the rotating cone again as a film by the action of the centrifugal force. Gas flows up the column countercurrent to the flow of the liquid. Mass transfer from the liquid to the vapour phase in a spinning cone column takes place through the large surface area of the film (which may be less than 1 mm thick), and through the liquid spray in the regions between spinning and stationary cones. There may be several dozen cone sets (stages) in a commercial column.

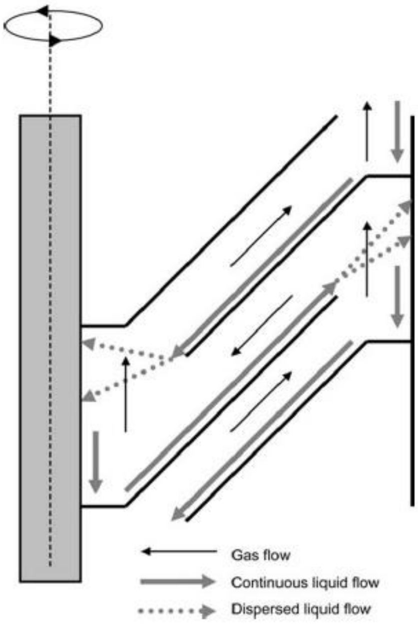

Fig.1. A section through part of a spinning cone column [3]

The Centritherm (CT) evaporator (Flavourtech, Griffith, Australia) is composed of multiple cones (1–12 depending on the evaporative capacity) that form a cone stack (Fig. 2) [4]. The centrifugal force of the rotating cones creates a thin layer and allows effective wettability of the heat exchange surface. As for a falling film evaporator, evaporation is based on indirect heat transfer between steam and the liquid to be concentrated: energy from condensing steam drives vapor from the product, thereby concentrating it. Moreover, concentration is carried out under vacuum. A feed tube distributes the product on the underside of the cone through a feed nozzle (Fig. 2). Steam enters the steam chamber and transfers heat to the product. The steam condensate leaves the steam chamber and the product concentrate is collected by a paring tube. It is claimed that the CT evaporator is able to concentrate dairy products to concentrations unachievable with conventional designs of evaporator while maintaining product functionality. It can process viscous products at low temperature (50 °C). Moreover, the extremely short residence time, claimed to be around one second by the manufacturer, ensures very low thermal impact on the product.

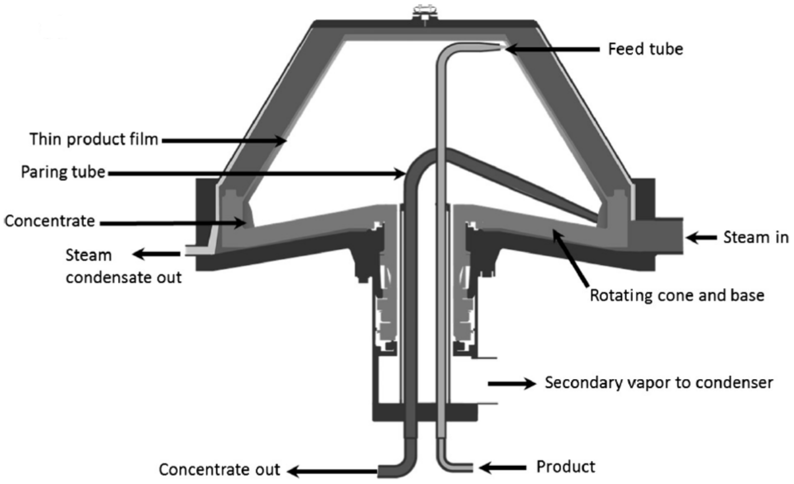

Fig. 2. Operating principle of a single spinning cone evaporator [4]

It is promising to use centrifugal force to create a system for water recovery in a life-support system in microgravity. The design of the vapor compressor vacuum distiller VCD (USA) is shown in Fig. 3 [5]. The distillation unit rotates at 185 rpm to spread the incoming wastewater into a thin film from which water can evaporate easily at ambient temperature and reduced pressure. The water vapor is transferred to the outside of the drum through a compressor, where it condenses as clean water. The demister ensures that only vaporized water is drawn into the compressor by blocking any droplets of wastewater.

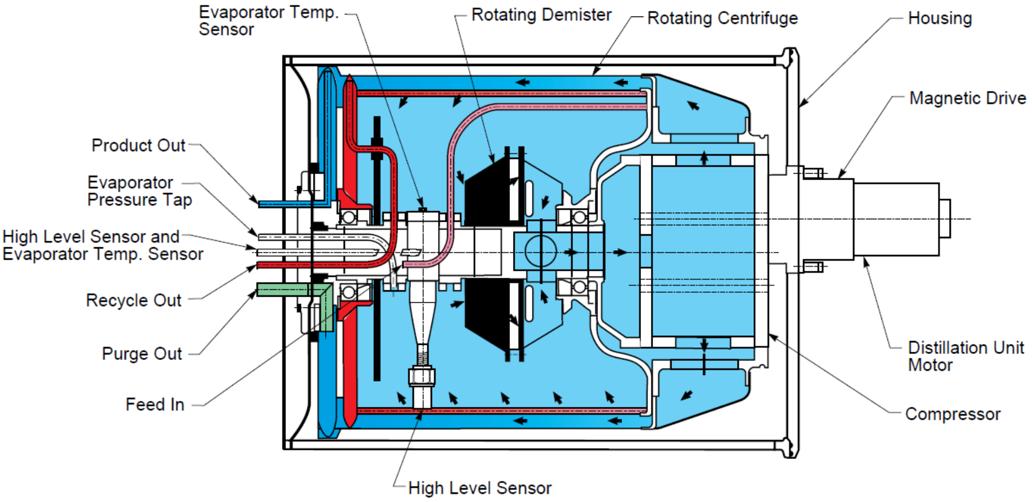

Fig. 3. VCD distillation assembly schematic

In [6–8], the design and test results of a centrifugal multistage vacuum distiller (CMVD) are described. Evaporation occurs in a thin film (less than 0.02 mm) of a liquid (urine or a mixture of urine and water, etc.) inside a rotating rotor (Fig. 4). Condensation of the produced steam occurs on the outer surface. Fig. 4 shows the scheme of CMVD with three stages. CMVD has a sealed housing 1 in which a rotor 2 is placed rotatable through a sealed magnetic coupling. The rotor is divided by partitions into a series of distillation stages and a final condenser. The process solution 3 is fed to the CMVD via channel 4, where it is distributed over the distillation stages. Solution by pitot-tube through channel 5 is fed into the system heater, from which (in an overheated state) through channel 6, it returns to the apparatus, where the superheating of the liquid is removed by self-evaporation. The resulting steam as a heating is used in the previous step. The evaporation of the last stage of evaporation condenses in the final condenser upon contact with the distillate cooled outside the apparatus. The cooled distillate enters the apparatus through channel 7, heats up and is again removed for cooling by the pitot-tube through channel 8. Excess condensate 9 formed in the apparatus is withdrawn by the pitot-tube to the consumer (into the storage tank) via channel 10. Vacuuming is carried out through channel 11.

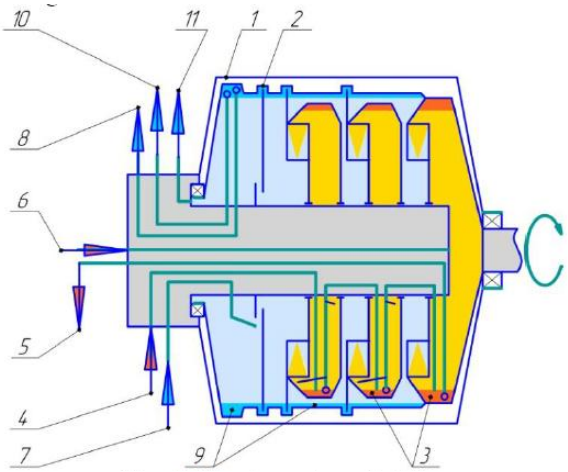

Fig. 4. Three-stage centrifugal multistage vacuum distiller

2. HEAT TRANSFER IN CENTRIFUGAL EVAPORATORS

In most designs of such evaporators, the liquid is supplied to the centre of the rotating surface and spreads out in the form of a thin film under the action of centrifugal forces. The heating medium in most cases is steam, which condenses on the back side of the evaporation surface. In published theoretical papers, the heat transfer coefficient for evaporation and condensation is determined by the Nusselt model, in which gravitational acceleration is substituted with centrifugal.

2.1. Condensation

For the first time, the process of vapor condensation on a rotating surface was theoretically studied by Sparrow [9, 10]. Sparrow and Gregg [9] used a Karman's variable transformation which was applied to the hydrodynamic problem solving for viscous liquid flow on the rotating disk in infinite space. Simultaneous coordinates transformation with accepted assumptions made it possible to reduce partial derivatives equations systems into a simple differential equation. For a number of Pr from 10^{-3}, up to 10 numerical solutions were obtained for the following dimensionless complexes:

$$Nu = \frac{h \cdot \left(\frac{\nu}{\omega}\right)^{0.5}}{\lambda} = 0.904 \left(\frac{\mathrm{Pr}}{c_p \Delta T / r} \right)^{0.25}, \tag{1}$$

where h – heat transfer coefficient, W/(m^{2}K); ν – kinematics viscosity of the liquid m^2/s; ω – angular velocity rad/s; λ – coefficient of thermal conductivity W/(m·K); c_p – specific heat, J/(kg·K); ΔT – temperature difference between a saturated vapour and wall temperature, K; r – latent heat, J/kg; Pr – Prandtl number.

As shown in [1, 11, 12], this equation can be obtained from the Nusselt solution [13] for laminar film condensation, if in the Nusselt formula the gravitational acceleration is substituted with $\omega^2 R$.

Sparrow and Hartnett [10] made a theoretical analysis of the heat transfer at water film condensation on a rotating conic surface. When $\omega^2 R >> g \sin \varphi$ (φ is the taper angle), the hydrodynamics of the film and the heat transfer in case of condensation on both the inner and outer surfaces will not differ from the case of flowing on a rotating disk.

Nandapurkar and Beatty [14] performed experiments on a horizontal water-cooled rotating disk. The experiments were performed at condensation of vapors of organic liquids such as spirits and refrigerants. The surface temperatures were measured at several points along the disk radius; the heat transfer coefficients for total surface were calculated on the basis of these experimental temperatures. The experimental data demonstrated heat transfer coefficients values of 25–30% less in comparison with those predicted by the Sparrow and Greg [9] theory for laminar condensation on the rotation disk. Sparrow and Gregg [15], in a technical brief in February 1960, added the effect of vapor drag to their previous analysis of heat transfer and showed that the effect was quite small. It was claimed that the deviation between theory and experiment must be attributed to other causes.

Heat transfer at water film condensation experiments and film flow parameters was also performed by Astafiev and Baklastov [16, 17]. The tests were performed on rotating horizontal disks with diameters of 80 and 105 mm.

The heat transfer coefficients data were generalized by the equation:

$$Nu = 1.38(\mathrm{Pr} \cdot K)^{0.25}(Ga)^{0.215}, \tag{2}$$

where: $Ga = \frac{\omega R^3}{\nu^2}$.

In a dimensional form, the experimental data [16] were generalized by the equation

$$h = 1.18\left(\frac{\lambda^3 \rho r}{\nu \Delta T}\right)^{0.25} \omega^{0.43}. \tag{3}$$

where h – heat transfer coefficient, W/(m^{2}K); ν – kinematics viscosity of the liquid m^2/s; ω – angular velocity rad/s; λ – coefficient of thermal conductivity W/(m·K); ΔT – temperature difference, K; r – latent heat, J/kg; ρ – density, kg/m^3.

Butuzov and Rifert [11] presented the experimental data on the inversed downwards condensing rotating surface. The vapor steam condensation experiments were performed on a horizontal rotating copper disk with a diameter of 0.3 m. The experimental measurements were performed for the disk angular velocity changes within 10–224 radian/s at heat flux densities from 20 up to 190 kW/m^2.

The experiments demonstrated that, at a constant disk angular velocity, the average heat transfer coefficient at condensation decreased with both heat flux and temperature drop increasing, so for these conditions $h \sim \Delta T^{0.25}$ which were typical of a condensate laminar film flow. At $\omega > 52$ radian/s a condensate film flow, as well as the heat transfer coefficients, were determined mainly by centrifugal forces action and in this case a power index at ω was the same as in the Sparrow and Gregg equation [9].

Yanniotis and Kolokotsa [18] investigated experimentally heat transfer at water film condensation of the steam on the aluminum disk inversed downwards with a smooth surface. The experiments were conducted on the disk with a diameter of 30 cm and thickness of 10 mm. Experimental results show that the local heat transfer coefficient remains almost unchanged across the disk surface. It agreed with the Sparrow and Gregg theory [9].

The theoretical predictions of Sparrow and Gregg [9] were verified by other analytical and numerical studies [19-20] and used by other investigators as a basis for other studies [21–22].

One can conclude that using theoretical predictions of Sparrow and Gregg [9] for the heat transfer coefficient during film condensation and its corresponding temperature difference will give satisfactory results.

2.2. Evaporation

In many works when calculating heat transfer during evaporation, the existence of a laminar film of liquid is assumed (similarly as for condensation) [23–29].

The first studies that provided the formulas for calculating the heat transfer during evaporation of a liquid flowing along a rotating surface, were conducted by Bromley [30]. A well-known dependence is obtained in the dimensionless form:

$$Nu = 1.47\,\mathrm{Re}^{-1/3}. \tag{4}$$

Rahman and Faghri [31], using the well-known theoretical model of heat transfer for laminar condensation and evaporation of thin laminar films, obtained a dimensionless dependence:

$$Nu = Nu^* A\,\mathrm{Re}_{in}^{-1/3} E_{in}^{-2/3} \left(R/R_{in}\right)^{2/3}. \tag{5}$$

Substituting in (5) $Nu^* = h\delta/\lambda$, $A = \left(\nu^2/3gR_{in}^3\right)^{1/3}$, $\mathrm{Re}_{in} = u\delta/\nu$, $u = \omega^2 R\delta^2/3\nu$, $E_{in} = \nu/\omega R^2$ the dependence (4) is obtained (R – radial coordinate, m; δ – film thickness, m).

However, when the liquid evaporates on the rotating surface, its amount may be 10–100 times higher than the amount of condensate on the heating surface. For example, for CMVD the consumption in the hot circuit is 60–80 kg/h (from the side of condensate up to 1.5 kg/h). As a result, the liquid films can have a value substantially greater than Re = 100, which corresponds to the turbulent flow of a liquid film [8].

In most experimental studies of processes in a centrifugal evaporator, the overall heat transfer coefficient was measured [23–28, 32, 33]. The heat transfer coefficient during evaporation was determined in only a few papers [26, 32, 34–35].

The first measurements of the coefficients of heat transfer during the evaporation and boiling of water and NaCl solutions were performed in [34–35].

In the experiments [34] the temperature of the rotating surface was measured by thermocouples through a current collector. Only average heat flux could be measured in the experiments, it was not possible to evaluate experimentally the local (by the radius of the disk) heat transfer coefficient.

Fig. 5 [34] shows the effect of feedwater flow G on the average heat transfer coefficient h. The main feature of these data is the absence of a laminar law of influence of G on h, which contradicts the models of a purely laminar film ($h \sim \mathrm{Re}^{-1/3}$).

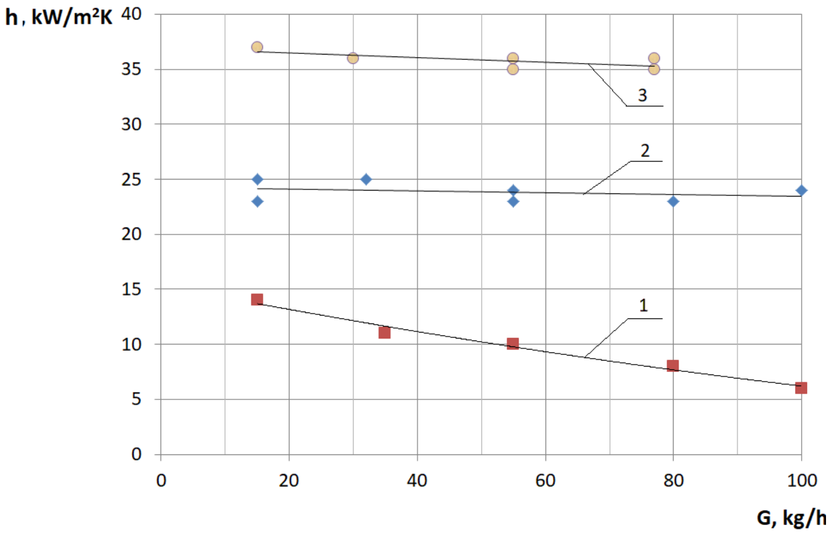

Fig. 5. Influence of the feedwater flow G on the heat transfer during the evaporation of the liquid film on a rotating disk at different rotation speeds ω: 1 – ω = 21 rad/s; 2 – ω = 52 rad/s; $q = 6.6 \cdot 10^4$ W/m^2; 3 – ω = 105 rad/s; $q = 9.6 \cdot 10^4$ W/m^2

This fact was noted in [12]. Using the two-layer model of a turbulent film [36], the author [12] presented a dependence for the average heat transfer during evaporation of a liquid film, which takes into account the effect of turbulence on a disk with a radius of $R < R_{cr}$ (turbulent flow) and laminar flow with a radius of $R > R_{cr}$ (traditional laminar theory).

$$h = h_{lam} \frac{R^2 - R_{cr}^2}{R^2} + h_{turb} \frac{R_{cr}^2 - R_i^2}{R^2}, \tag{6}$$

where R_{cr} – critical radius, m.

The heat transfer coefficients measured by experiments [26–27] during evaporation and condensation for water, solutions of NaCl and sugar solution differed both in the values of h (by 15–30%) and in the character of the effect of the fluid flow. The coefficient of heat transfer did not decrease with an increase in the fluid flow rate, which follows from the laminar theory, but tended to increase (Fig. 6).

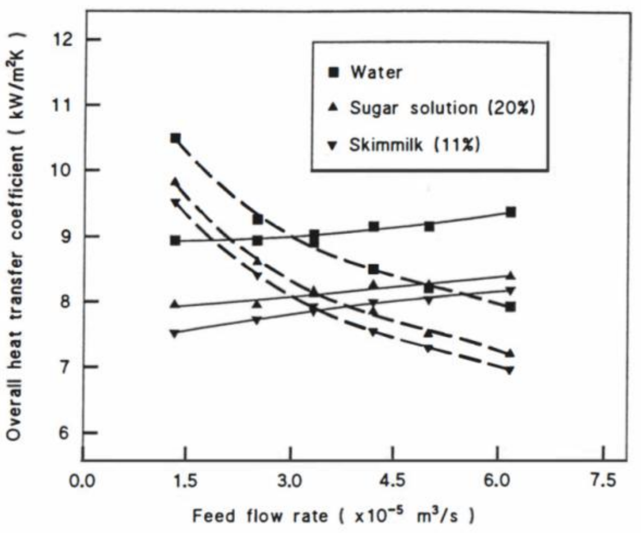

Fig. 6. Effect of the feed flow rate on the overall heat transfer coefficient for water, 20% sugar solution and skimmilk in the Centritherm evaporator. Solid lines are experimental values while dashed lines are theoretical values. Evaporating temperature 60 ºC, rotating speed 146.6 rad/s, temperature difference 10 K

In the paper [37], it was shown that even for small Re numbers there can be an effect of waves on the heat transfer coefficient. This leads to an increase in heat transfer compared with the laminar model.

In [38, 39], an accurate method of checking heat transfer coefficient *h* with a gravitational flow was performed (Re = 1–1000). As a result, it was obtained that already at Re = 1.6 there is a deviation of the experimental *h* from that calculated by the laminar model, and with further growth of Re, the degree of deviation increases (Fig. 7). At Re > 35 first indication for a transititon to turbulence appear. The authors gave corrections to the calculations heat transfer coefficient *h* for different values of the Re number.

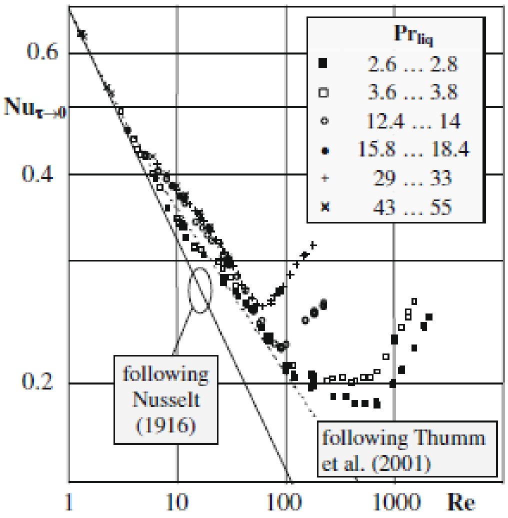

Fig. 7. Heat transfer for the limiting case of zero shear stress [39]

For all experimental studies [26, 32, 34–36], the Re number is more than 100. In this area, the Nusselt laminar model does not work. Thus, for a theoretical calculation of the evaporation process, it is necessary to study the turbulent flow of a liquid film.

3. CONCLUSIONS

The heat transfer during condensation on a rotating surface is well studied. For most cases, the laminar model gives good accuracy. These equations can be obtained from the Nusselt solution for laminar film condensation, if in the Nusselt formula the gravitational acceleration is substituted with $\omega^2 R$.

To date, there is no satisfactory theoretical model for calculating the evaporation process on a rotating surface. For its formulation, first of all it is necessary to clarify the real effect of the Re number on the liquid film flow under the action of centrifugal forces. It is also important to pay attention to the question of justifying the criterion for the transition of a film on a rotating surface to a turbulent flow.

REFERENCES

1. RIFERT, V., BARABASH, P., SOLOMAKHA, A., USENKO, V., SEREDA, V., PETRENKO, V. Hydrodynamics and heat transfer in a centrifugal film evaporator. *Bulgarian Chemical Communications*, 2018, Vol. 50, Special Issue K, p. 49-57.
2. LANGRISH, T., MAKARYTCHEV, S., FLETCHER D., PRINCE, R. Progress in understanding the physical processes inside spinning cone columns. *Chemical engineering research and design*, 2003, Vol. 81, No. 1, p. 122-130.
3. MAKARYTCHEV, S., LANGRISH, T., FLETCHER D. Exploration of spinning cone column capacity and mass transfer performance using CFD. *Chemical engineering research and design*, 2005, Vol. 83 (A12), p. 1372-1380.
4. TANGUY, G., DOLIVET, A., GARNIER-LAMBROUIN, F., MEJEAN, S., COFFEY, D., BIRKS, T., JEANTET, R., SCHUCK, P. Concentration of dairy products using a thin film spinning cone evaporator. *Journal of food engineering*, 2015, Vol. 166, p. 356-363.
5. WIELAND, P., HUTCHENS, C., LONG, D., SALYER, B. Final Report on Life Testing of the Vapor Compression Distillation/Urine Processing Assembly (VCD/UPA) at the Marshall Space Flight Center (1993 to 1997). NASA/TM-1998-208539.
6. RIFERT, V., BARABASH, P., USENKO, V., SOLOMAKHA, A., ANATYCHUK, L., PRYBYLA, A. Improvement the cascade distillation system for long-term space flights. 68th International Astronautical Congress (IAC). Adelaide, Australia. 2017 September 25-29. IAC-17-A1.IP.25.
7. RIFERT, V., RAZUMOVSKIY, V., STRIKUN, A., BARABASH P., USENKO, V., ANATYCHUK, L. Improvement of the distillation methods by using centrifugal forces for water recovery in space flight application. 46th International Conference on Environmental Systems. Vienna, Austria. 2016 July 10-14. ICES-2016-369.
8. LUBMAN, A., MACKNIGHT, A., RIFERT, V., BARABASH, P. Cascade Distillation Subsystem Hardware Development for Verification Testing. SAE International. 2007-01-3177.
9. SPARROW, E., GREGG, J. A Theory of Rotating Condensation. *Journal of Heat Transfer*. 1959, Vol. 81. No. 5. p. 113-120.
10. SPARROW, E., Hartnett, J. The condensation on the rotated cone. *J. Heat Transfer*. 1961. Vol. 83. No. 1, p. 101-102.
11. BUTUZOV, A., RIFERT, V. An experimental study of heat transfer during condensing steam at a rotating disk. *Heat Transfer Soviet Research*. 1972, Vol. 4, No. 6, p. 150-153
12. RIFERT, V. Analysis of the heat transfer during film evaporation from a rotating disk. *Journal of Engineering Physics and Thermophysics*. 1973, Vol. 25, No. 2, p. 970-973.
13. NUSSELT W. Die Oberflachen kondensation des wasserdampfes. *Zeitschrift des Vereunes Deutscher Ingrnieure*. 1916, No. 60, p. 541-569.

14. NUNDUPURKAR, S., BEATTY, K. Condensation on a horizontal rotating disk. *A.J.Ch.E. Chemical Eng. Prog*. 1960, No. 30, p. 129-137.
15. SPARROW, E., GREGG, J. The effect of vapor drag on rotating condensation. *Trans, of ASME J, Heat Transfer*. 1960. Vol. 82, p. 71-72.
16. ASTFIEV, V., BAKLASTOV, A. Vapor condensation on rotating horizontal disk. *Thermal engineering*. 1970. No. 9, p. 55-57.
17. ASTAFIEV, V., BAKLASTOV, A. The film flow and heat transfer by the condensation on the rotated disc. *Thermal engineering*. 1970, No. 10, p. 74-75.
18. YANNIOTIS, S., KOLOKOTSA, D. Experimental Study of Water Vapor Condensation on a Rotating Disc. *Int. Comm. Heat Mass Transfer*. 1996, Vol. 23, No. 5, p. 721-729.
19. WANG, C., GRIEF, R. The Effect of Impingement on Heat Transfer in Rotating Condensation, *Int. J. Heat Mass Transfer*. 1981, Vol. 24, No. 7, p. 1097-1104.
20. CHARY, S., SARMA, P. Condensation on a Rotating Disk with Constant Axial Suction, *J. Heat Tramfer*. 1976, Vol. 98, No. 4, p. 682-684.
21. AI-BAROUDI, H, KLEIN, A. Experimental Simulations and Heat Transfer Parameter Measurements of Film Condensation on a Rotating Flat Plate. *Experimental Thermal and Fluid Science*. 1995, Vol. 10, No. 1, p. 124-135.
22. ALASADI, A., EZZAT, A., MUNEER, A. Investigation of Steam Condensation Process on Rotating Disk Condenser at Different Rotation Speed. *International Journal of Computer Applications*. 2013, Vol. 84, No. 14, p. 10-18.
23. HICKMAN, K. Centrifugal boiler compression still. *Industrial and engineering chemistry*. 1957, Vol. 49, No. 5, p. 786-800.
24. CLARK, R., BROMLEY, L. Saline water conversion by multiple-effect rotating evaporator. *Chemical engineering progress*. 1961, Vol. 57, No. 1, p. 64-70.
25. BROMLEY, L. Multiple-effect rotating evaporator. Desalination. 1966, No. 1, p. 367-393.
26. CHEN, H. Heat transfer and fouling in film evaporators with rotating surfaces. 1997, Thesis PhD.
27. CHEN, H., JEBSON, R., CAMPANELLA, O. Determination of heat transfer coefficients in rotating cone evaporators – Part I. *Food bioprod proc Trans Inst Chem En*. 1997, Vol. 75 (Part C), p. 17-22.
28. CHEN, H., JEBSON, R., CAMPANELLA, O. Heat transfer coefficients for evaporation from the inner surface of a rotating cone – Part II. *Food bioprod proc Trans Inst Chem Eng*. 2003, Vol. 81 (Part C), p. 293-302.
29. SHAH MUHHAMAD. Intensification of heat transfer processes. 2010, Thesis PhD.
30. BROMLEY, L. Prediction of performance characteristics of Hickman–Badger centrifugal boiler compression still. *Ind. Eng. Chem*. 1958, Vol. 50, p. 233.
31. RAHMAN, M., FAGHRI, A. Analysis of heating and evaporation from a liquid film adjacent to a horizontal rotating disk. *Int. J. Heat Mass Transfer*. 1992, Vol. 35, No. 10, p. 2655-2664.
32. WANG, C., GREIF, R., LAIRD, A. Heat transfer in a rotating disk evaporator. *Desilination*. 1980, Vol. 33, p. 259-267.
33. TLEIMUT, B. Performance of a rotating flat-disk wiped-film evaporator. *ASME Publication*. 1971, 71-HT-3.
34. BUTUZOV, A., RIFERT, V. Heat Transfer in Evaporation of Liquid from a Film on a Rotating Disk. *Heat Transfer-Soviet Research*. 1973, Vol. 5, No. 1, p. 1-3.
35. RIFERT, V., PUKHOVOY, I., NIKITENKO, E. Character and Intensity of Heat Exchange at Evaporation of the Fluid Film on the Rotation Disk. Proc. of the 2nd European Thermal-Sciences and the 14th UIT National Heat Transfer Conference. 1996, Rome, Italy, May 29-31, Vol. 1, pp. 249-252.

36. KAPITZA, P. Wave flow of a thin viscous layer. *I. Free flow. J. Exp. Theor. Phys.* 1948, No. 18, pp. 3-20.
37. KUTATELADZE, S. *Fundamentals of Heat Transfer*. London: Verlag E. Arnold, 1963, 307 p.
38. GROSS U., STORCH T., PHILIPP C., DOEG A. Wave frequency of falling liquid films and the effect on reflux condensation in vertical tubes. *Int. J. Multiphase Flow*. 2009, No. 35, pp. 398-409.
39. STORCH, T., PHILIPP, C., DOEG, A., GROSS, U. Near-zero shear stress experiments with heat flux effects on falling film evaporation inside a vertical tube. *International Journal of Thermal Sciences*. 2014, No. 76, pp. 137-146.

CYSENI 2019, May 23-24, Kaunas, Lithuania
ISSN 1822-7554, www.cyseni.com

LATTICE DISTORTION MODEL AND PROBABILISTIC ANALYSIS SIMULATING ELASTIC BEHAVIOR OF CRYSTALLINE MATERIALS

T. Vaitkūnas, A. Jutas
Kaunas University of Technology
Studentų 56, 51424 Kaunas – Lithuania
Email: tomas.vaitkunas@ktu.edu

ABSTRACT

The main aim of our study is to analyze elastic behavior of crystalline materials by simulating one of the elastic characteristics of crystalline material with body-centred cubic lattice – Poisson's ratio of pure Iron. There is still no theory created using which scientists could simulate tensile experiment of crystalline materials without doing any experiment. In different computational methods, especially simulating some individual or complex deformational behavior of solid body, this ratio is taken as constant value obtained after the carrying out of natural experiments and calculating strains. However numerous experimental results allow us to presume that Poisson's ratio taken as an average does not explain quantitatively strain and stress state at the point. The differences in finite element type influence also on the stresses and strains by von Mises. The modern validated softwares use different kind of finite elements adopted for structural and tasks' variety and satisfy experimental results quite good. Nevertheless same finite elements used in statics or dynamics do not describe mechanisms and place of the material break down in cycling loading or in problems of aging. In this study Lattice Distortion Model (LDM) with the sphere of a unit radius is used for the featuring of lattices' groups to simulate a Poisson's ratio value of pure Iron as some evidence of physical reality in crystalline materials. After the lattices' classification there were identified 6 lattices' groups having the total attributes of 266 several lattices. Each group can interact with another group. Then it is possible to superpose 15 pairs of these interacting groups. According this method, the lattices groups' relaxation processes can also be simultaneously observed. The Bayesian equation of hypothetical probability as a proof of LDM was used to simulate the dynamics of superposed lattices. The hypothesis of so called random determinism has allowed us to create mechanisms of quantitative informational transfer from the transformed lattices. This model can be used for the systems with a different number of microstructural groups influenced by the similarities in a spatial orientation of lattices. Leading process such like the lattice groups relaxation, can be simulated according to a selected speed of deformation.

Keywords: crystalline materials, Poisson's ratio, Lattice Distortion Model, lattices' groups, simulation

1. LATTICE DISTORTION MODEL (LDM)

1.1. Introduction and literature review

There is still no theory created using which scientists could calculate the elastic characteristics of crystalline materials without doing any experiment. The method, used in our study, is completely new, nothing similar has been tried and mentioned in any scientific literature by other authors yet. Last decade Lattice Distortion Model (LDM) [2-3] has been created in order to find relations in complex cooperation of atomic systems located in microstructures with the randomly aligned atomic planes. The computational method essence is the deformational evolution of the set of lattices and their random cooperation with the neighbor systems in elastic and plastic states. In literature [4] grain scale polycrystal plasticity behaviour is analysed. Also, sources [6-7] describe possibility to use Lenard-John's potential to find Bulk modulus of material. Formulas relating Bulk modulus with Young modulus enable us to calculate Young modulus of crystalline material by using Poisson's ratio value simulated before and Lenard-John's potential. In this study we analyze elastic behavior of crystalline materials with body-centred cubic lattices. At first, we simulate Poisson's ratio of pure Iron by the method of unit sphere. Then microstructure analysis of chosen crystalline material with body-centred cubic lattice – 99% pure Iron is done. Finally, some assumptions and ideas for calculating Young modulus from Lenard-John's potential are given.

1.2. The Lattice Distortion Model (LDM) with unit sphere

The Lattice Distortion Model (LDM) helps to find relations in complex cooperation of atomic systems located in microstructures with the randomly aligned atomic planes by describing atom-atom interaction physical model which is related with initial atomic planes in material lattices. The idea of this method in our study is based on sphere of chosen crystalline material with radius equal to one. It is predicted that material lattices are located on that sphere homogeneously and symmetrically. The centre of first lattice is on point with coordinates (0; 0; 1). Others lattice's centres coordinates can be calculated according to their centres vector angles α, β and γ with central axis *x*, *y* and *z* of this sphere, increased by a given step. Models with more or less lattices on unit sphere are available (more fine or coarse models). Our model has 266 lattices of Iron with angles α, β and γ with sphere's central axis *x*, *y* and *z* (Figs. 1-2). These angles are equal to Iron lattice's draft angles.

The radius of this sphere is perpendicular to anyone body-centred cubic (BCC) lattice plane which is tangent to sphere's outer face. It is possible to draw tangent plane for each point of the sphere. Plane equation at the point R_0 could be expressed:

$$z = C_x(x - x_0) + C_y(y - y_0) + z_0, \tag{1}$$

where $x^2 + y^2 + z^2 = 1 \Rightarrow z = \pm\sqrt{1 - x^2 - y^2}$ is surface of this sphere equation, $C_x = \left.\frac{\partial z}{\partial x}\right|_{R_0}$ and $C_y = \left.\frac{\partial z}{\partial y}\right|_{R_0}$ coefficients when the coordinates (x_0, y_0, z_0) of point R_0 is known. It is also possible to write normal axis, which intersects tangent plane at point R_0, equation. When microstructure is deformed lattices deformations depend on their orientation angles α, β and γ which now can be expressed:

$$\alpha = \arccos\frac{r_x}{|\vec{i}|}, \quad \beta = \arccos\frac{r_y}{|\vec{j}|}, \quad \gamma = \arccos\frac{r_z}{|\vec{k}|}, \tag{2}$$

where $\vec{i}, \vec{j}, \vec{k}$ unit vectors of global coordinate system axis, $\vec{r}$ (r_x, r_y, r_z) normal vector of sphere at the point R_0.

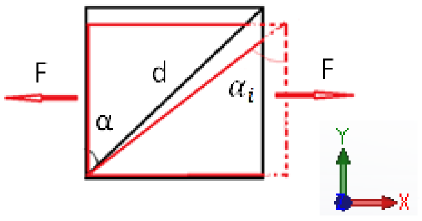

Fig. 1. The scheme for undeformed and deformed lattice states

Due to large number of lattices with different features in microstructure (angles with coordinate axis) it is necessary to find the principles of their recurrence. The recurrence of lattices is a result of sphere symmetry and can be used to classify these lattices into groups. After the lattices' classification there were identified 19 groups with same angle absolute value according to angles with axis *x*, *y* and *z*.

Table 1. 19 groups of lattices

Numbers of lattices (Fig. 1)	**x**	**y**	**z**	**α**	**β**	**γ**	**Part, %**
1, 266, 122, 134, 128, 140	0	0	1	90	90	0	
2, 14, 242, 254, 8, 20, 248, 260, 98, 110, 146, 158, 104, 116, 152, 164,123, 133, 135, 145, 127, 129, 139, 141	0.333	0	0.943	70.53	90	19.47	9.02
3, 13 ,15 ,25, 243, 253, 255, 265, 7, 9, 19, 21, 247, 249, 259, 261	0.314	0.111	0.943	71.68	83.62	19.47	6.02
4, 12, 24, 16, 244, 252, 264, 256, 6, 10, 22, 18, 246, 250, 258, 262	0.289	0.167	0.943	73.22	80.41	19.47	6.02
5, 11, 17, 23, 245, 251, 257, 263	0.236	0.236	0.943	76.37	76.37	19.47	3.01
26, 38, 218, 230, 32, 44, 224, 236, 80, 92, 176, 188, 74, 86, 170, 182, 124, 132, 136, 144, 126, 130, 138, 142	0.5	0	0.866	60	90	30	9.02
27, 37, 39, 49, 219, 229, 231, 241, 31, 33, 43, 45, 223, 225, 235, 237	0.471	0.167	0.866	61.87	80.41	30	6.02
28, 36, 40, 48, 220, 228, 232, 240, 30, 34, 42, 46, 222, 226, 234, 238	0.433	0.25	0.866	64.34	75.52	30	6.02
(29, 35, 41, 47, 221, 227, 233, 239)	0.354	0.354	0.866	69.30	69.30	30	3.01
50, 62, 194, 206, 56, 68, 200, 212, 125, 131, 137, 143	0.707	0	0.707	45	90	45	4.51
51, 61, 63, 73, 195, 205, 207, 217, 55, 57, 67, 69, 199, 201, 211, 213	0.667	0.236	0.707	48.19	76.37	45	6.02
52, 60, 64, 72, 196, 204, 208, 216), 54, 58, 66, 70, 198, 202, 210, 214	0.612	0.354	0.707	52.24	69.30	45	6.02
53, 59, 65, 71, 197, 203, 209, 215	0.5	0.5	0.707	60	60	45	3.01
75, 85, 87, 97, 171, 181, 183, 193, 79, 81, 91, 93, 175, 177, 187, 189	0.816	0.289	0.5	35.26	73.22	60	6.02
76, 84, 88, 96, 172, 180, 184, 192, 78, 82, 90, 94, 174, 178, 186, 190	0.75	0.433	0.5	41.41	64.34	60	6.02
77, 83, 89, 95, 173, 179, 185, 191	0.612	0.612	0.5	52.24	52.24	60	3.01
99, 109, 111, 121, 147, 157, 159, 169, 103, 015, 115, 117, 151, 153, 163, 165	0.889	0.314	0.333	27.27	71.68	70.53	6.02
100, 108, 112, 120, 148, 156, 160, 168, 102, 106, 114, 118, 150, 154, 162, 166	0.816	0.471	0.333	35.26	61.87	70.53	6.02
101,107, 113, 119, 149, 155, 161, 167	0.667	0.667	0.333	48.19	48.19	70.53	3.01
All 266							100%

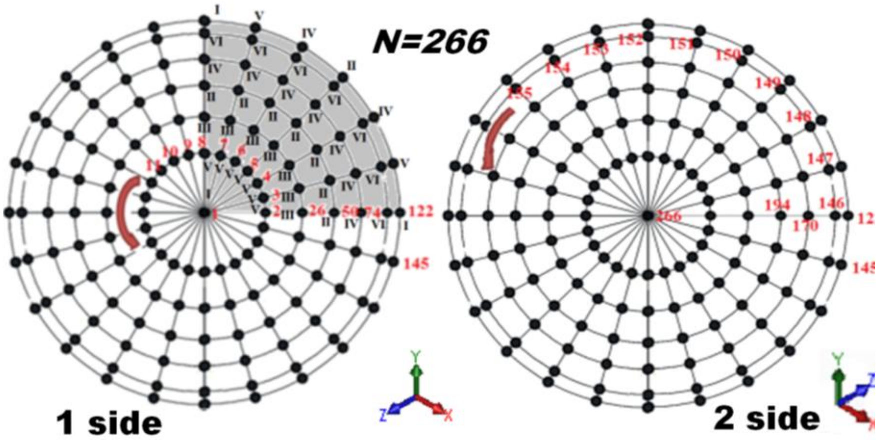

Fig. 2. The sphere with unit radius and lattices location

In case of tensile deformation analysis along *x* axis in plane *xy* and finally can identify 6 groups of lattices according to the angles with *z* axis (Fig. 1-2, Table 1).

Then each lattice's group Poisson's ratio can be calculated:

$$\nu_i = -\frac{\varepsilon_{yi}}{\varepsilon_{xi}}, \tag{3}$$

where $\varepsilon_{xi}(d_{xi}, \alpha_{xi}, C)$ and $\varepsilon_{yi}(d_{yi}, \alpha_{yi})$ – longitudinal and transverse deformation, C – coefficient of deformation intensity $1/\xi \leq C \leq 1/\xi^2$ while ξ – parameter which show one atom inertion to another according to the movement direction and depends on deformation level ($0 < \xi \leq 1$). The experimental measurement of longitudinal and transverse deformation in Poisson's ratio experiment should be done according standard ISO 527 by using extensometers or tensoresistors glued. In our study deformations of the sphere were not measured, they were calculated in simulation by changing angles α_{xi}, α_{yi} with given step 0,002° (Fig. 1). The increment of angles gives the change of longitudinal ε_{xi} and transverse ε_{yi} deformation according to the trigonometrical relations.

Lattices interaction between each of 6 groups is possible. The simplest interaction model predicts that only pair of groups interacts. When each lattice can interact only with another one there are 15 possible pairs [1] of lattices.

$$C_n^k = \frac{n!}{k!(n-k)!} = 15, \tag{4}$$

where [1] *n* = 6 – number groups of lattices, *k* = 2 – number of interacting lattices.

1.3. Simulating the Poisson's ratio

The value of Poisson's ratio of each pair of groups interacting between can be found as average of individual Poisson's ratio values of each group:

$$\nu_{i,j} = \frac{\nu_i + \nu_j}{2}, \tag{5}$$

where *i* and *j* are numbers of interacting groups of lattices (according Fig. 1), *i* and *j* = 1…6 ($i \neq j$).

Simulated Iron Poisson's ratio value is calculated as the average of sums of all peaks which can be seen during simulation (Fig. 2). In this study each group of lattices and overall material Poisson's ratio has peaks which show possible relaxation process. According to this study results the Poisson ratio is different of each pair of lattices group and depends on their orientation in microstructure. The materials Poisson’s ratio value given in literature is average value of all groups’ individual value. Simulated Iron Poisson’s ratio is equal to:

$$v = \frac{1}{n}\left(\frac{1}{n}\sum_{k=1}^{n} v_{\max k} + \frac{1}{n-1}\sum_{k=2}^{n} v_{\max k} + \ldots + v_{\max n}\right) = 0.293, \quad (6)$$

where n is the number of peaks, $v_{\max k}$ – Poisson‘s ratio value at the peak with number k. Given [5] Poisson’s ratio value of Iron is 0.29.

Constant Poisson’s ratio value in all material volume does not explain quantitatively strain and stress state at the point. There might be a reason that Poisson’s ratio value is different in the volume of microstructure as it was simulated in this study. Also, the same finite elements with constant Poisson’s ratio value used in statics or dynamics do not describe mechanisms and place of the material break down in cycling loading or in problems of aging [2, 3]. That may show that our theory with different Poisson’s ratio value of different groups of lattices could be close to real process acting in crystalline materials.

In Fig. 3 lines with points show Poisson’s ratio values of each of 15 pairs of groups and thick line – average value of all groups in microstructure. Deformation interval is chosen elastic and start of plastic deformations.

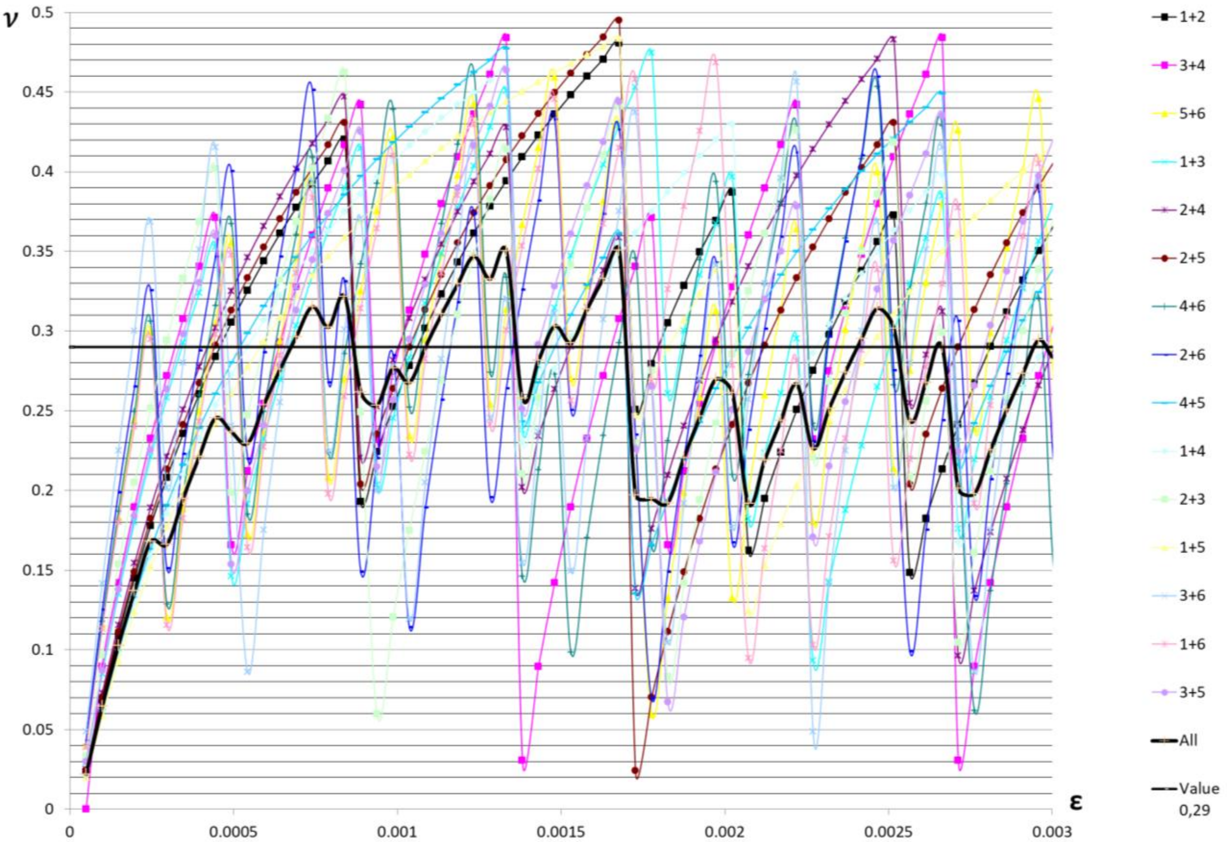

Fig. 3. Poisson’s ratio of each lattices’ group and average (solid line)

According to the simulation results seen on Fig. 2 each pair of interacting lattice’s have different number of relaxation processes during this deformation processes. The influence of each pair of groups to final result can be evaluated in probabilistic analysis.

2. PROBABILISTIC ANALYSIS

Probability of deformation of each pair of group can be calculated by using Bayes equation:

$$P(H_i \mid w_i) = \frac{P(H_{wi})P(w_i \mid H_i)}{\sum P(H_{wi})P(w_i \mid H_i)}, \tag{7}$$

$$P(H_{wi}) = \frac{H_{wi}}{\sum H_{wi}}, \tag{8}$$

$$P(w_i \mid H_i) = \frac{\upsilon_i}{\upsilon}, \text{ if } \upsilon_i < \upsilon, \text{ otherwise } P(w_i \mid H_i) = \frac{\upsilon}{\upsilon_i}. \tag{9}$$

Here H_i is the number of peaks of each pair of groups, H – the sum of all peaks, υ_i – Poisson' s ratio value of each pair of group during the first peak. Different number of peaks shows the different influence of each pair of group to final result. Probabilities of each pairs of groups are calculated and given in Table 2.

Table 2. Probabilities of each pair of lattices deformation

No	$P(H_{Wi})$	$P(w_i \mid H_i)$	$P(H_i \mid w_i)$	Δ_i, %
1	0.07153	0.8376	0.07171	-0.25
2	0.02003	0.8538	0.02047	-2.19
3	0.19313	0.8196	0.18946	1.90
4	0.11445	0.8339	0.11423	0.20
5	0.15737	0.8577	0.16155	-2.66
6	0.05007	0.8580	0.05142	-2.69
7	0.03863	0.8194	0.03788	1.93
8	0.04006	0.8308	0.03983	0.56
9	0.05007	0.8458	0.05069	-1.23
10	0.04292	0.8260	0.04243	1.14
11	0.02861	0.8662	0.02966	-3.68
12	0.08584	0.8262	0.08488	1.11
13	0.04435	0.8271	0.04391	1.00
14	0.03863	0.8010	0.03703	4.13
15	0.02432	0.8541	0.02486	-2.23

The relative errors Δ_i between probability of deformation $P(H_i \mid w_i)$ and probability of pair influence to final result is quite small, no larger than absoliute value of 4.13%. This may show that our model is accurate and realistic enough to real deformation processes of crystalline materials. In order to analyse simulation results some static tension experiments of Iron specimens were made.

3. EXPERIMENT RESULTS

Experiments give possibility to compare simulation results with real deformation of crystalline material. Static tension experiments of Iron specimen with dimensions: length 100 and 200 mm, width 18 and 37 mm, thickness 2 mm, were done. Each specimen dimensions and material properties found from experiment are given in Table 3, stress – strain curves in Fig. 4. Later, the microstructure of specimen was done.

For the specimens' preparation and tensile experiment implementation the standard ISO 6892-84 (GOST 1497-84) was used. The equipment, used for tension experiment, is tension machine equipped with displacement transducer 1-WA/50MM-L connected via signal amplifier HBM Spider 8. The specimen is clamped into two grips of the machine. The speed of deformation is chosen the lowest, 1 mm/min. Measuring data were analyzed using software HBM Catman 4.5, data output frequency was 100 Hz.

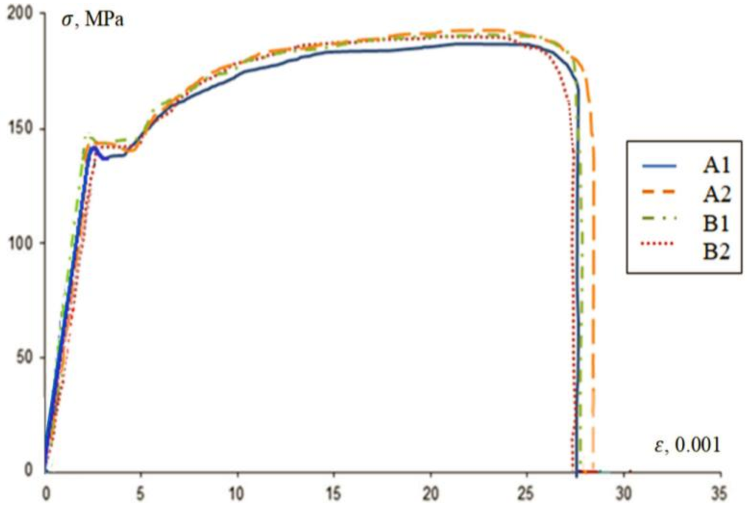

Fig. 4. Tensile experiment stress – strain curves

Table 3. Dimensions and mechanical properties of specimens tested

Specimen	t	h	L	ψ	δ	σ_Y	σ_u	HV
	mm			%		MPa		
A1	2.0	17.85	100	38.6	24	142	190	1703-1725
A2	2.0	17.85	100	35	25	146	193	
B1	2.0	37.15	200	29.8	26	148	191	
B2	2.0	37.05	200	29.3	26	143	188	

The results of tensile experiments presented in Table 3 show that selected and tested Iron specimens' yield limit is about 145 MPa, ultimate strength about 191 MPa. The scale effect of specimen strength can be seen on comparison ultimate strength of $L = 100$ mm, $h = 18$ mm and $L = 200$ mm, $h = 37$ mm specimens. In Fig. 3, elastic limit is about 138 MPa when strain is 0.002 and Young's modulus of these specimens may be calculated from Hooke's law $\sigma = E\varepsilon$ and in this work one has been assumed equal to 210 GPa.

3.1. Microstructure of Iron specimen

Microstructure of Iron specimen on deformation area is shown on Fig. 5. The microstructural analysis was performed using microscope Axio scope, A1 (Carl Zeiss). Different sizes and orientations of microcrystals in microstructure can be used to compare results with our model lattice's group's interactions mechanisms.

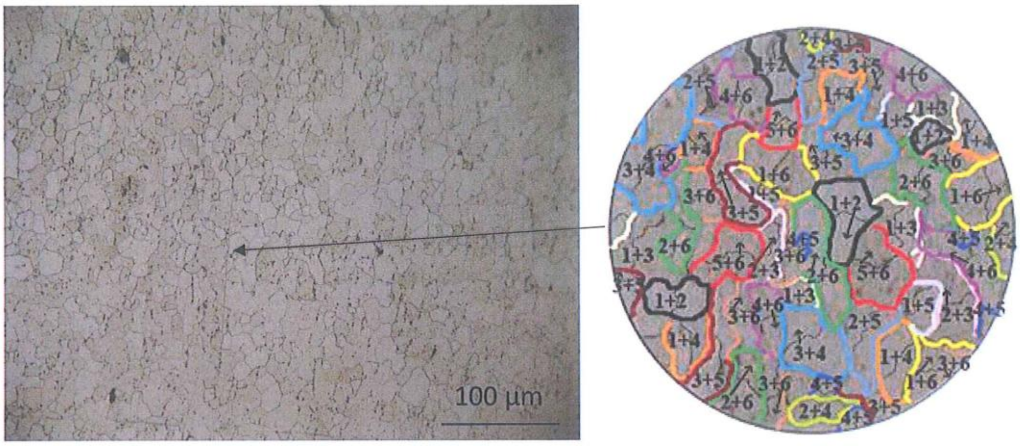

Fig. 5. Microstructure of Iron specimen

In the microstructure shown in Fig. 5 we replace computational scheme with the grain groups used according to the assumptions and principles of this method based on the results presented in Fig. 3. On microstructure we have replaced 15 different groups calculated by Eq. 2. To cover all the area of microstructure we use random repetition of cooperation of these 15 groups. In the microstructure, an average size of microcrystal is about 20 µm: the largest is 50 µm, the smallest is about 10 µm. In the model, averaged diameters of the grains were not taken in to account because of strains that covers and eliminates all inequalities in real groups of microstructure for any basis of the length. According to this procedure, our model has allowed to use lattice's deformation method as an explanation of physical transformations occurring inside the individual microstructure and the results are quite close to Poisson's ratio of Iron [5].

3.2. Discussion

Pressure acting on selected volume of individual microstructural component leads to volumetric deformation related with Bulk modulus of material presented in the equation below [6]:

$$K = -V\frac{dp}{dV}. \tag{10}$$

From the thermodynamic point of view at 0 K an entropy is invariant and contraction of the lattice is led by a change in potential energy

$$dU = -pdV. \tag{11}$$

It's possible to write

$$\frac{dp}{dV} = -\frac{d^2U}{dV^2} \tag{12}$$

and using Eq. 1 we get

$$K = -V\frac{d^2U}{dV^2}. \tag{13}$$

For BCC lattice $V = Na^3/2$, where $a^3/2$ is the volume of one atom in the same lattice consisting of nine atoms, $N = 9$. Using Lenard-John's potential we find a necessity to mention that at some interatomic distance r at absolute temperature (0 K) the potential is equal to the minimal value of total potential energy [8, 9]:

$$U(r) = 4\varepsilon\left[\left(\frac{\sigma}{r}\right)^{12} - \left(\frac{\sigma}{r}\right)^{6}\right] = U_{\min} = \varepsilon, \tag{14}$$

here ε is the strength of potential energy equal 414 kJ/mol [7], σ is a distance when $U(\sigma) = 0$ and $r = 2^{1/6}\sigma$ is the distance at which the energy is minimal. In this case, it is possible to write

$$K = \frac{\varepsilon}{V_{U=0}} \approx \frac{\varepsilon}{N\sigma^3}. \tag{15}$$

Also, having simulated Poisson's ratio and volumetric deformation it is possible to calculate Bulk modulus of a material in the case of quasistatic tensile experiment, where change in pressure is expressed as $\Delta p = 1/3 \cdot \sigma_e$, where σ_e is elastic limit of Iron when microstructure is strained in direction of x axis. Volumetric strain is ratio $\Delta V/V \approx (1-2\upsilon)\varepsilon_x$ influenced by the lattice constant a.

Volumetric deformation could be used in further examination to simulate Young modulus by the equation

$$K = \frac{E}{3(1-2\nu)} \approx \frac{\varepsilon}{N\sigma^3}. \tag{16}$$

From Eq. 14, we now can express Elastic modulus that is obtained using modelled value of Poisson’s ratio and strength of potential energy. The insights based on physics of solid and materials science will be used in further researches to simulate elastic limits of deformation and Young’s modulus in all the featured families of microstructural media.

4. CONCLUSIONS

Our study consists of two main parts. First part is dedicated to the simulation of elastic behaviour of Iron by the use *Lattice Distortion Model* and interaction of selected/grouped lattices in microstructure. In second part, the experimental procedure is explained. According to the simulation results of elastic behaviour in microstructures and tensile experiment done it is possible to notice:

1. The lattice distortion model has been inserted in the microstructure aligned by the spatial angles taken from the tangent plane going at the point on the unit sphere. The simulated behaviour of crystalline materials gave quite accurate results. In the beginning, the model with 266 lattices located on sphere was transformed to fewer numbers of features using the inversion of symmetry. It allowed us to minimize the total number of features from 266 to 6. Simulated Poisson’s ratio was obtained equal to 0.293 that is very close to real Poisson’s ratio of Iron – 0.29 [5].
2. Simulated Poisson’s ratio value is different in all material volumetric elements. This could be used to explain quantitatively strain and stress state at the point and to share all possible natural phenomena as some evidence of physical reality in crystalline materials. Probabilistic analysis of deformation shows high probabilities of each lattices pair group’s simulated by chosen model.
3. Volumetric straining and Bulk modulus obtained by the use simulated Poisson’s ratio of material has explained paths of physical relations with *Lattice Distortion Model (LDM).*

REFERENCES

1. AKSOMAITIS, A. Tikimybių teorija ir statistika, Technologija, Kaunas, 2000: p. 347 (in Lithuanian).
2. OSETSKY, Y. N., BACON, D. J. An atomic-level model for studying the dynamics of edge dislocations in metals Modelling Simul. *Mater. Sci*. Eng. 11 2003: pp. 427-446.
3. KUBIN, L., HIRH, J. P. Dislocations in solids, Volume 15, Elsevier, UK 2009: p.310.
4. RAABE, D., SACHTLEBER, M., ZHAO, Z., ROTERs, F., ZAEFFERER, S. Micromechanical and macromechanical effects in grain scale polycrystal plasticity experimentation and simulation, *Acta Materialia* 17 2001: pp. 3433-3441.
5. *Iron mechanical and physical properties.* Link to the internet https://www.azom.com/properties.aspx?ArticleID=619 (accessed on 2018 12 19)
6. FREDRIKSSON, P., GUDMUNDSON, P. Competition between interface and bulk dominated plastic deformation in strain gradient plasticity Modelling Simul. Mater. Sci. Eng. 15 2007: pp. S61-S69.
7. KITTEL, CH. Introduction to solid state physics, John Wiley and Sons, Inc., New York, 1996: pp. 673.
8. ZEH, H. D. The Problem of Conscious Observation in Quantum Mechanical Description, Found. Phys. Lett. 13 2000 pp. 221-233.

PRIGOGINE, I., STENGERS, I. The end of certainty: time, chaos and the news laws of nature, Simon & Shuter Inc., New York, 1997: p. 228.

CYSENI 2019, May 23-24, Kaunas, Lithuania
ISSN 1822-7554, www.cyseni.com

MODELING OF OBJECTS WITH A LINEAR SPECTRUM FOR PHOTOEMISSION PYROMETER CALIBRATION

K. A. Viazava
A. V. Luikov Heat and Mass Transfer Institute
National Academy of Science of Belarus
P. Brovki 15, 220072 Minsk – Belarus
Email: viazava.kate@gmail.com

ABSTRACT

Temperature measurements of objects with linear spectrum are important for studying of combustion and detonation processes. In this case the measuring device with high time response is needed. However, the most of such devices are non-portable or are very expensive. Photoemission pyrometer is a portable device with low cost and it can be used for measurements of the temperature with a high time response. The main problem of using photoemission pyrometer for temperature measurements of objects with the linear spectra is calibration of the pyrometer. In the present work, calibration method of photoemission pyrometer by modeling of objects with the linear spectra are shown. This method was verified by a comparison of model calibration curve with the experimental curve, which was obtained by using bandpass filters and standard temperature lamp.

Keywords: temperature measurements, linear spectra, photoemission pyrometer

1. INTRODUCTION

There are a lot of noninvasive ways to determine the temperature of objects with a linear spectrum [1]. Such as an absorption and an emission spectroscopy [2-4], a line reversal method [1, 5], a spontaneous Rayleigh and Raman scattering [6, 7], a laser-induced fluorescence [6, 8-9] etc. All these methods have high time response. However, the most devices used in these methods are non-portable or have very high cost [1]. In cases when studying object can't be moved into the laboratory, it can be a problem. A photoemission pyrometer is a portable device with low cost and it can be used for temperature measurements with high time response [10].

The photoemission analysis of radiation is based on the dependence of the energy of a photoelectron on the energy of a photon [10]. Based on this method, a measurement device with photomultiplier tube as a detector can be designed. Such device can be cheap and easily transported to a studying object.

Like all existing pyrometers, the photoemission pyrometer usually is calibrated by using an absolute black body or a temperature lamp. However, such calibration can't be used for temperature measurements of objects with a linear spectrum. It's obvious, that proper standard must be found. In [11] it was shown, that the photoemission pyrometer in a case of continuous spectrum can be calibrated by modeling of a calibration curve. Thus, the aim of this paper is modeling of the calibration curve of photoemission pyrometer in the case of a linear spectrum.

2. METHODOLOGY AND EXPERIMENTAL SETUP

2.1. Calculation of pyrometer calibration

In photoemission method the temperature is determined in the following way. The retarding field in the cathode chamber is created at the time of the negative half-period during modulation of the electron flux by rectangular pulses of a polarity negative relative to the photocathode. The process of measuring the temperature amounts to recording the two-level oscillogram $U(t)$ of the investigated process, when during one period the voltage across the modulating electrode (modulator) at first is equal to the voltage across the photocathode ($U_r = 0$) and then decreases ($U_r < 0$). From the ratio k of the levels of this signal (or modulation factor), the value of k_i can be calculated in each period with number i. The aggregate of ratios of the level of the modulated signal $k(T)$, which are obtained at different temperatures T with respect to the standard temperature radiator, allows plotting the calibration curve of the instrument $k(T) = (\Sigma k_i)/n$, where n is the number of recorded periods. The dynamics of the temperature $T(t)$ of the given process is determined from the calibration curve $k(T)$ and function $k(t)$ recorded in the investigated thermal process [12].

To model such calibration curve, the folowing equation can be used [11]:

$$k(T) = \frac{\int_{\lambda_{min}}^{\lambda_{max}} I(\lambda,T) S_0(\lambda) d\lambda}{\int_{\lambda_{min}}^{\lambda_{max}} I(\lambda,T) S_r(\lambda) d\lambda}, \tag{1}$$

here $I(\lambda,T)$ – Plank function; $S_0(\lambda)$ – spectral characteristic of a pyrometer, when $U_r = 0$; $S_r(\lambda)$ – spectral characteristic of a pyrometer, when $U_r < 0$; (λ_{min}, λ_{max}) – spectral interval determined by spectral characteristic S_0.

In the case of objects with a linear spectrum Plank function can’t be used. Other function which describes a spectral dependence from temperature must be used. To check this assumption the next equation was used to model the calibration curve:

$$k(T) = \frac{\int_{\lambda_{min}}^{\lambda_{max}} \tau(\lambda) I(\lambda,T) S_0(\lambda) d\lambda}{\int_{\lambda_{min}}^{\lambda_{max}} \tau(\lambda) I(\lambda,T) S_r(\lambda) d\lambda} \tag{2}$$

$\tau(\lambda)$ – transmission of a bandpass filter.

2.2. Experimental setup

To verify the model of the calibration curve the following experiments were performed. The bandpass filter (Fig. 1) was placed before the standard tungsten lamp (temperature range – 1200-2800 K) and the flow of radiation passed through the filter was registered by the pyrometer. The calibration curve of a pyrometer was obtained by changing the temperature on the lamp. The obtained experimental calibration curve was compared with the calculated one.

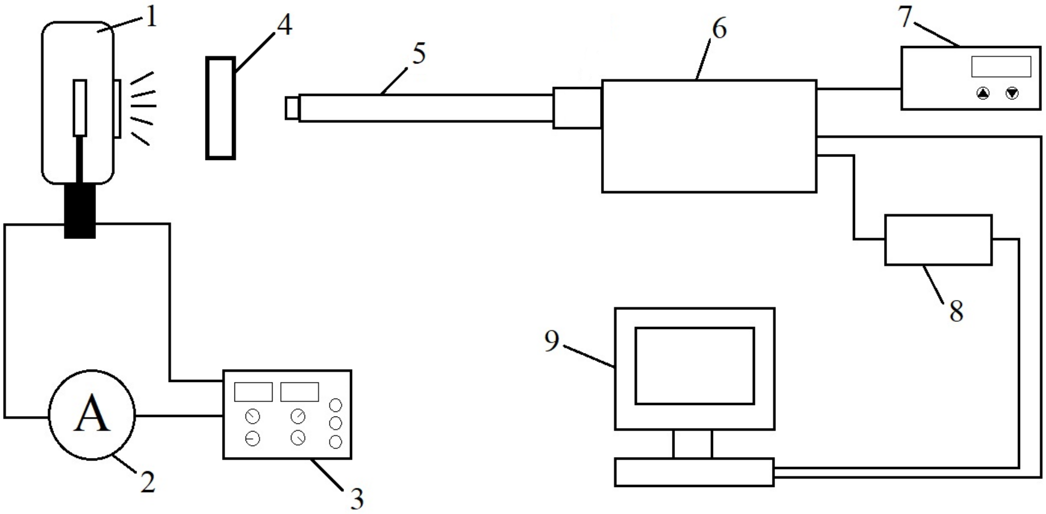

Fig. 1. Scheme of the experimental setup. 1 – tungsten lamp, 2 – ammeter, 3 – lamp power supply, 4 – bandpass filter, 5 – light guide, 6 – pyrometer, 7 – high voltage supply, 8 – digital oscilloscope, 9 – PC

3. RESULTS AND DISCUSSION

To check the possibility of modeling of the calibration curve, two bandpass filters with a different transmission were used (Fig. 2).

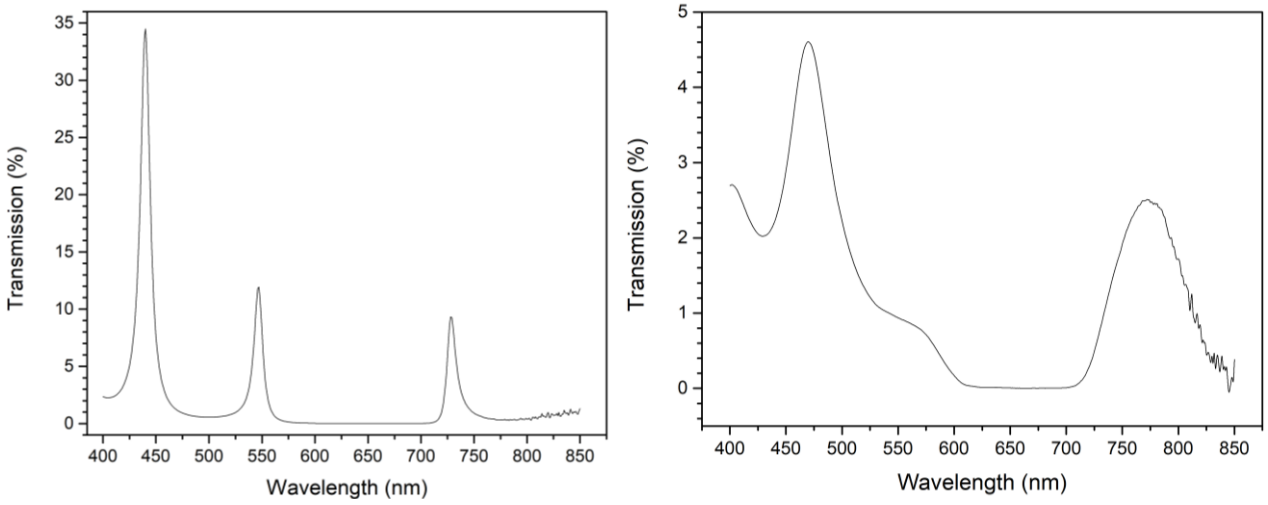

(a) (b)

Fig. 2. Transmission of a bandpass filter “436” (a) and “455” (b)

By using the equation (2), calibration curves were calculated and compared with the experimental ones (Fig. 3).

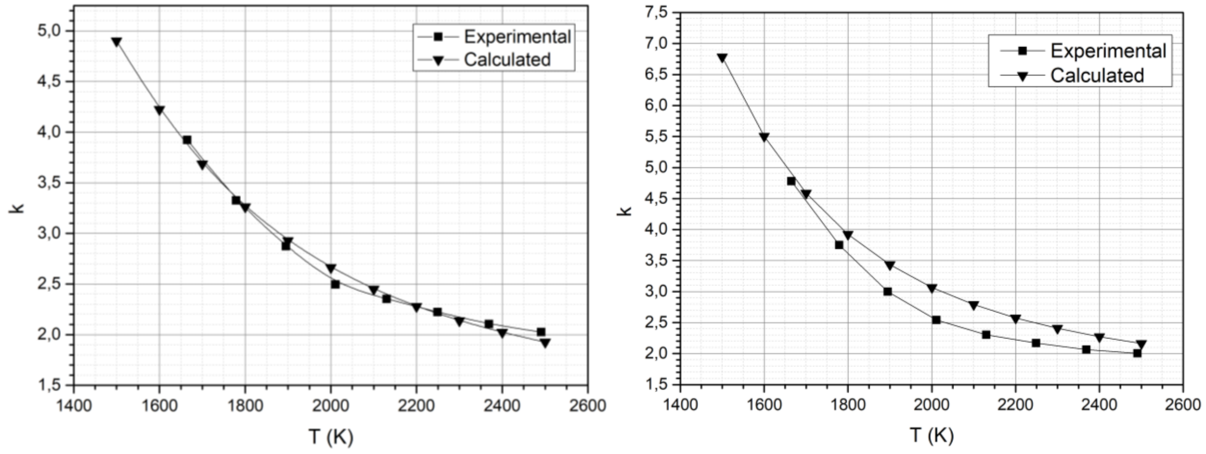

(a) (b)

Fig. 3. Experimental and calculated calibration curves for a bandpass filter “436” (a) and “455” (b)

In the case of using bandpass filter “436” a good match was obtained. Poor matching for bandpass filter “455” can be explaind by a low transmition, a line width and form of transmission line of filter.

Most of calculation errors can be explaind by an inaccuracy of experimental data used in equation (2) such as spectral characteristics and transmission of bandpass filter. In previous work [13] it was shown that the position and slope of the calibration curve depend on accuracy of maximum of spectral characteristic determining.

Also, to avoid experimental errors, an input end of light guide must be parallel to a bandpass filter and to the lamp tungsten filament.

4. CONCLUSIONS

The calibration method of the photoemission pyrometer by modelling of objects with linear spectra was shown. This method was verified by comparison of the model calibration curve with the experimental curve. Based on results were got for filter “436”, it can be concluded that photoemission pyrometer can be used for temperature measurements of objects with line spectra. But still, this method of calibration must be verified on flames or other real objects.

REFERENCES

1. CHILDS, P. R. N., GREENWOOD, J. R., LONG C. A. Review of temperature measurement, *Review of scientific instruments*, 2000, Vol. 71, No. 8, p. 2959-2978.
2. XIANG, L., JEFFRIES, J. B., HANSON, R. K. Measurement of nonuniform temperature distributions using line-of-sight absorption spectroscopy, *AIAA Journal*, 2007, Vol. 45, No. 2, p. 411-419.
3. AIZAWA, T. Diode-laser wavelength-modulation absorption spectroscopy for quantitative *in situ* measurements of temperature and OH radical concentration in combustion gases, *Applied optics*, 2001, Vol. 40, No. 27, p. 4894-4903.
4. HYUN, I.J., Ömer, L. G. Soot formation and temperature field structure in co-flow laminar methane-air diffusion flames at pressures from 10 to 60 atm, *Proceedings of the Combustion Institute*, 2009, Vol. 32, p. 769-775.
5. GAYDON, A. G., WOLFHARD, H.G. Flames: their structure, radiation and temperature, *DA Information Services*, 1979, 400 p.
6. HARTLIEB, A. T., ATAKAN, B., KOHSE-HÖINGHAUS, K. Temperature measurements in fuel-rich non-sooting low-pressure hydrocarbon flames, *Appl. Phys. B*, 2000, Vol. 70, p. 435-445.
7. PFADLER, S., LÖFFLER, M., DINKELACKER, F., LEIPERTZ, A. Measurement of the conditioned turbulence and temperature field of a premixed Bunsen burner by planar laser Rayleigh scattering and stereo particle image velocimetry, *Experiments in Fluids*, 2005, Vol. 39, p. 375-384.
8. BOXX, I., STÖHR, M., CARTER, C., MEIER, W. Temporally resolved planar measurements of transient phenomena in partially pre-mixed swirl flame in a gas turbine model combustor, *Combustion and Flame*, 2010, Vol. 157, p. 1510-1525.
9. LEE, T., BESSLER, W. G., KRONEMAYER, H. [et al.] Quantitative temperature measurements in high-pressure flames with multiline NO-LIF thermometry, *Applied optics*, 2005 Vol. 44, No. 31, p. 6718-6728.
10. KASPAROV, K. N., IVLEV, G. D., BELAZIORAVA, L. I. [et al.] High temperature measurements in fast phenomena by spectrometry of photoelectrons, *High Temperatures – High Pressures*, 2012, Vol. 41, No. 5, p. 325-340.
11. VIAZAVA, K. A., KASPAROV, K.N., MIATSELSKAYA, N.S. [et al.] Calibration of photoemission pyrometer without using standard temperature radiators, *Measurement Techniques*, 2017, Vol. 60, No. 6, p. 578-582.
12. KRASNOV, K. V., OSIPOV G. I., ROSTOVTSEVA V. V. Methods of determining the temperature of by a broadband spectral-ratio optical pyrometer, *Izmeritel’naya Tekhnika*, 1987, No. 3, p. 10-12 (in Russian).
13. VIAZAVA, K. A., KASPAROV, K.N., MIATSELSKAYA, N.S. [et al.] On the possibility of photoemission pyrometer calibration by using spectral characteristics of photodetector, *Teplo- i massoperenos – 2015*, 2016, p. 203-207 (in Russian).

CYSENI 2019, May 23-24, Kaunas, Lithuania
ISSN 1822-7554, www.cyseni.com

INVESTIGATIONS OF DYNAMIC AIR FLOW CHARACTERISTICS IN STRAIGHT PIPE OF WIND TUNNEL USING INNOVATIVE MEASUREMENT SYSTEM

A. Bertašienė, V. Zaleskas
Lithuanian Energy Institute
Breslaujos str. 3, Kaunas, LT-44403 – Lithuania
Email: agne.bertasiene@lei.lt

ABSTRACT

Airflow structure and its development in pipes at the initial stage is still uncertain and disputable. Due to the complexity and limited access different flow regimes has many peculiarities unrevealed. A complex system is presented in the research linking to analyse the flow fluctuations and dynamic features in a wide range of velocities that cover all flow regimes. An improved non-intrusive wave method is proposed to analyse fast processes.

Ultrasonic anemometer as a mean to calculate air velocity values from sound propagation time in the channel enabled to measure highly fluctuating flows. Adapted in the test section of the aerodynamic test rig at initial flow stage it showed reliable and highly comparable results with another non-intrusive method – laser Doppler velocimetry. It also provided comprehensive information about the changes in flow structure according instantaneous time of ultrasound transition. Local vortices identified in the flow may influence the low frequency fluctuations and the scatter in measurement results. Moreover, high frequency fluctuations found in the flow originated from the flow turbulence and the electronic or acoustic noise. Additionally made flow simulation revealed the boundary layer formation and flow recirculation in the cavities of placed ultrasonic transducers and their impact on ultrasound measurements.

Keywords: ultrasonic measurement system, air flow, dynamic characteristics, wind tunnel, flow regimes

CYSENI 2019, May 23-24, Kaunas, Lithuania
ISSN 1822-7554, www.cyseni.com

CHARGE TRANSFER MECHANISMS IN SILICON-GRAPHENE SEMICONDUCTOR FILMS

P. Dolmantas
Kaunas University of Technology
Studentų str. 50, LT-51368 Kaunas – Lithuania
Email: Paulius.Dolmantas@ktu.edu

Š. Meškinis
Institute of Materials Science, Kaunas University of Technology
K. Baršausko str. 59, Kaunas LT-51423 – Lithuania

ABSTRACT

In recent years, the discovery of graphene and its exceptional electrical, mechanical and optical properties initiated intense research on its applications to semiconductor devices. Silicon – graphene Schottky diode utilizes graphene charge mobility ($2.5\cdot10^5$ cm^{2}V^{-1}s^{-1}) and transparency (over 90%) to increase diode sensitivity to wider wavelength intervals. In graphene there is almost no charge scattering, therefore all photogenerated charges reach potential barrier and enter semiconductor. In the present study, directly deposited silicon – graphene Schottky contact electrical characteristics were investigated. Graphene was directly synthesized on silicon substrate using plasma enhanced chemical vapour deposition. It was transfer-less process. Diode ohmic contacts were made using electron beam evaporation. Graphene phase was confirmed using Raman spectroscopy and charge transfer mechanisms were investigated by measuring current – voltage dependence using picoammeter. Effective barrier heights and ideality factors were determined. It was observed that in formed structures for direct and reverse bias, occurring mechanisms were thermionic emission, tunneling and space-charge limited current. From dominating charge transfer mechanisms, it was deduced that a significant layer of insulator (possibly silicon dioxide) remained between graphene – silicon interface. The layer of insulator influenced I-V characteristics as well as charge transfer mechanisms to behave more like a metal-insulator-semiconductor (MIS) device.

Keywords: graphene, Schottky diodes, charge transfer mechanisms, detectors, Raman spectroscopy

1. INTRODUCTION

Graphene, the two-dimensional hexagonal nanocrystal, consisting of sp^2 hybridized carbon atoms, has many applications in solid state devices due to its phenomenal physical properties: large room temperature electron mobility $2.5\cdot10^5$ cm^{2}V^{-1}s^{-1}, Young's modulus of 1 TPa, large thermal conductivity > 3000 WmK^{-1}, optical absorption ~ 2.3%, ability to sustain high electric current densities and more [1]. Graphene does not have a band gap, therefore it is hardly applicable to integrated circuits, however there are a number of fields where graphene properties can be useful in enhancing device performance: high frequency transistors, logic transistors, photodetectors, optical modulators, mode-locked lasers, solar cells and flexible electronics where it could replace indium – tin oxide (ITO) due to its excellent transmittance (97.7%) and sheet ressistance lower than 30 Ω/sq [1], [2].

Silicon-graphene Schottky diodes are potential improvement to conventional Schottky barrier diodes due to negligible charge carrier scattering in high quality defect-free graphene. It has been demonstrated that it is possible to produce graphene Schottky IR photodiode with response larger than 1A/W [3]. However, the main problem is the production of high quality graphene on silicon: large area and uniform graphene films are usually grown by chemical vapour deposition (CVD) process on catalyst (such as copper, nickel, cobalt or other transition metal) films [4]. This method of growing graphene has main disadvantage that it requires transfer step which is complicated and cost-ineffective process. Moreover during transfer step it is not unusual to induce a significant amount of defects and chemical contamination. Therefore there is a large interest in producing graphene on silicon by transferless process. It is possible to produce graphene directly on silicon by CVD process but the quality of graphene often is lacking for application to semiconductor devices and strongly depends on deposition parameters: temperature, hydrocarbon pressure, hydrocarbon concentration, cooling rate [5], [6].

The aim of this work is to produce silicon-graphene Schottky diodes by using transferless chemical vapour deposition on silicon and to investigate its charge tranfer mechanisms by anlysing measured I-V characteristics.

2. METHODOLOGY

Graphene was grown directly on (100) silicon (resistivity 1–10 Ω·cm) by plasma enhanced chemical vapour deposition (PECVD) from the gas phase. Microwave plasma frequency ~ 2.45 GHz. The reactive gases methane (CH_4, purity 99.995%) and hydrogen (H_2, purity 99.999%) were supplied to the camera. The temperature of the process – 850 ^oC, power of the plasma – 1.2 kW and pressure of 2600 Pa. Silicon substrates were cleaned by treating them with hydrogen plasma for 15 minutes (hydrogen flow rate – 200 sccm, pressure – 20 mbar). In total there were 5 graphene films produced on n and p type doped monocrystalline silicon substrates with different H_2 and CH_4 gas fluxes and deposition times (Table 1).

Table 1. Graphene film PECVD deposition parameters

No.	**T, ^oC**	**P, kW**	**H_2, sccm**	**CH_4, sccm**	**p, Pa**	**t, min**	**Si doping type**
1	850	1,2	150	50	2600	20	n
2	850	1,2	170	30	2600	40	n
3	850	1,2	150	50	2600	80	n
4	850	1,2	170	30	2600	80	n
5	850	1,2	170	30	2600	80	p

Carbon films were investigated by using Raman scattering spectrometer (Raman microscope inVia (Renishaw)). Excitation wavelength – 532 nm, maximum laser power – 30 mW. Measurements were performed using 5% of maximum power. Charge coupled device (CCD) camera integration time – 10 s. Copper contacts on the top of the graphene film as well as aluminum contacts on the silicon were deposited using electron beam evaporation. I-V measurements were performed using Keithley 6487 picoammeter with two-wire setup.

There are five main possible charge transfer mechanisms under forward bias in Schottky diodes: thermionic emission, electron tunneling, recombination in space-charge region, electron diffusion in depletion region and hole injection from metal to semiconductor. In metal (or graphene) and silicon devices charge transport is related to majority carriers (that is, electron for n type silicon substrates and holes for p type silicon substrates). No injection of the minor charge carrier (electron for p type substreate and hole for n type substrate) takes place. Dominant charge transfer mechanism in Schottky diodes is thermionic emission, but depending on the strength of the electric field, other mechanisms may also occur [7]. In the case of pure thermionic emission, majority current density J_n is expressed:

$$J_n = \left[A^* T^2 exp\left(-\frac{q\phi_{Bn}}{kT}\right)\right]\left[exp\left(\frac{qV}{kT}-1\right)\right] = J_{TE}\left[exp\left(\frac{qV}{kT}-1\right)\right], \qquad (1)$$

where J_{TE} is saturation current density, $A^* = 112\ A/(cm^2 \cdot K^2)$ – effective Richardson constant for thermionic emission [8], ϕ_{Bn} – barrier height in eV, V – voltage, q – electron charge, k – Boltzman n constant, T – absolute temperature.

Tunnelling in heavily doped semiconductors or at low temperatures is significant. However, exact analytical expressions are complicated due to barrier width dependence on energy. The most often used expression takes into account thermionic emission as well as tunnelling:

$$J = J_0 \left[exp\left(\frac{qV}{\eta kT}\right) - 1 \right], \tag{2}$$

where J_0 is saturation current density, η – ideality factor. When thermionic emission is dominant, η is close to 1. At lower temperatures η is much bigger than 1 and tunnelling occurs. Parameter η also can indicate if recombination current is present if $\eta = 2$. Electron diffusion has similar expression for current density as equation (1), but in this case saturation current density is independent of temperature [7].

During production of Schottky diodes in metal-silicon interface there is possibility of having a natural insulating silicon dioxide layer. This layer of insulator may introduce a range of other current transport mechanisms which are present in dielectric materials, shown in Table 2.

Table 2. Charge transport mechanisms in insulators [8]

Process	**I-V dependence**
Tunneling	$\propto V^2 exp\left(\frac{-b}{V}\right)$
Thermionic emission	$\propto T^2 exp\left[\frac{q}{kT}(a\sqrt{V} - \phi_B)\right]$
Poole-Frenkel emission	$\propto Vexp\left[\frac{q}{kT}(2a\sqrt{V} - \phi_B)\right]$
Ohmic conductivity	$\propto Vexp\left(\frac{-c}{T}\right)$
Space-charge limited current in mobility regime (Mott-Gurtney law)	$\propto V^2$
Space-charge limited current in velocity saturation regime	$\propto V$
Space-charge limited current in ballistic regime (Child – Langmuir law)	$\propto V^{3/2}$

Ideality factor is calculated by using following expression:

$$\eta = \frac{q}{kT}\frac{dV}{d(lnJ)} = \frac{q}{kT}\frac{dV}{d(lnI)} \tag{3}$$

and effective barrier height:

$$\phi_{Bn} = \frac{kT}{q} ln\left(\frac{A^* T^2}{J_0}\right) = \frac{kT}{q} ln\left(\frac{A^* S T^2}{I_0}\right), \tag{4}$$

where I_0 is saturation current, S = 0.2 mm^2 is diode contact area. It was supposed that mechanism is present in given voltage range if corresponding linear fitting correlation coefficient was at least 95%.

3. RESULTS AND DISCUSSION

3.1. Raman spectroscopy

After plasma enhanced chemical vapour deposition on silicon, carbon containing films were investigated using Raman spectroscopy. In Fig. 1 graphene phase is confirmed by characteristic collection of D ~ 1350 cm^{-1}, G ~ 1583 cm^{-1}, 2D ~ 2700 cm^{-1} and D + D' ~ 2940 cm^{-1} peaks. D peak. is due to sp^2 hybridized carbon "breathing" mode in rings, while G peak is due to sp^2 hybridized carbon stretching vibrations [9]. 2D peak is first overtone of D peak and is always observed in graphene [10]. This spectrum indicates that graphene is present on silicon substrate and has defects due to D peak presence [10].

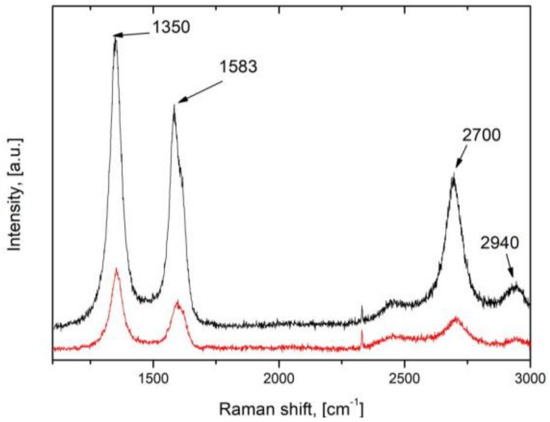

Fig. 1. Raman spectrum of typical graphene film on silicon deposited using PECVD (sample No. 3)

3.2. Charge transfer mechanisms in silicon-graphene structures

After investigation of diode No. 1 I-V characteristics it was obtained that under the forward bias, two charge transfer mechanisms are present: 0–3 V thermionic emission and 3–10 V – tunneling (Fig. 2 a) and b)). Under reverse bias, it appears that I-V characteristic has three linear regions (Fig. 2 c)). It seems that under low reverse voltages, (0–3 V red line) ohmic conduction is present. When the voltage increases to about 8.2 V space-charge limited current kicks in (green line) (velocity saturation). The origin of third blue line is not clear (8.2–9 V). It could be the same space-charge limited current if a "soft" breakdown occurred at about 8.2 V.

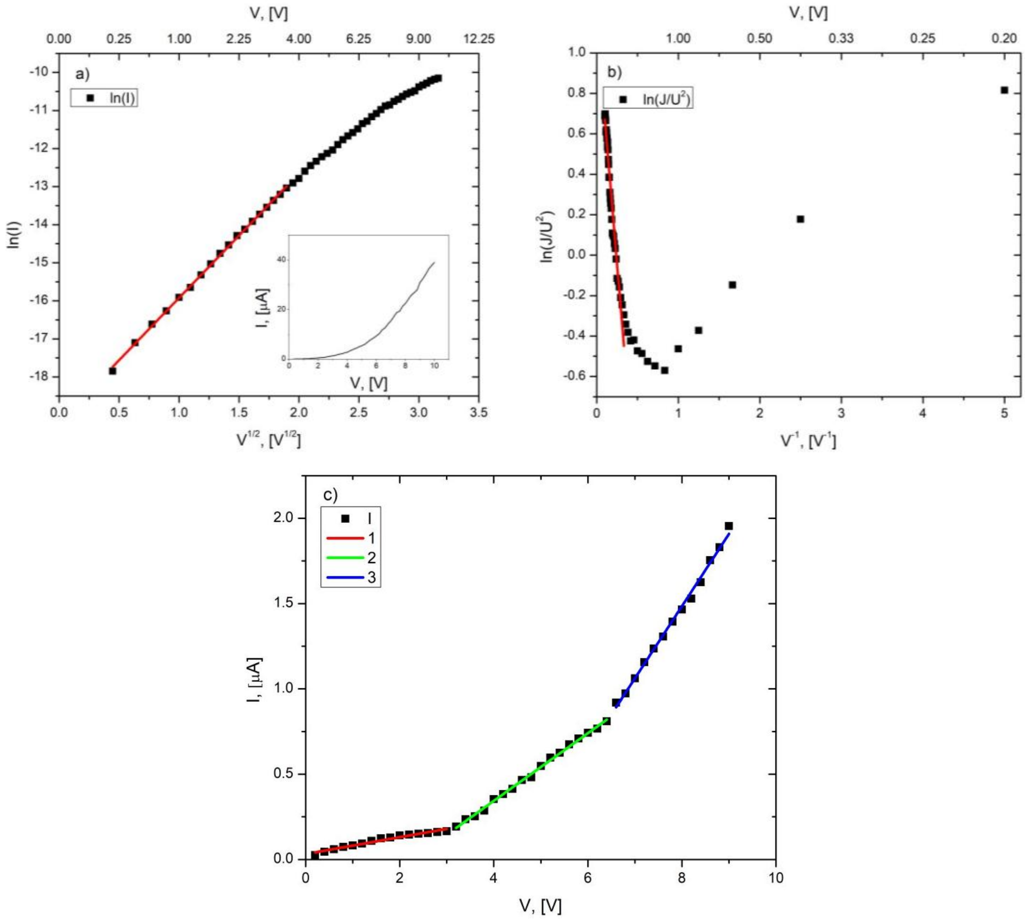

Fig. 2. I-V characteristics of diode No. 1: a) thermionic emission, b) tunneling, c) ohmic conduction and space-charge limited current

In diode No. 2 (Fig. 3 a)) under forward bias from 0 to 2.4 V, I-V characteristic is well described by Mott-Gurtney law (space-charge limited current under mobility regime) [7]. It seems that the thermionic emission in dielectric materials occurs with increase of the voltage (Fig. 3 b)).

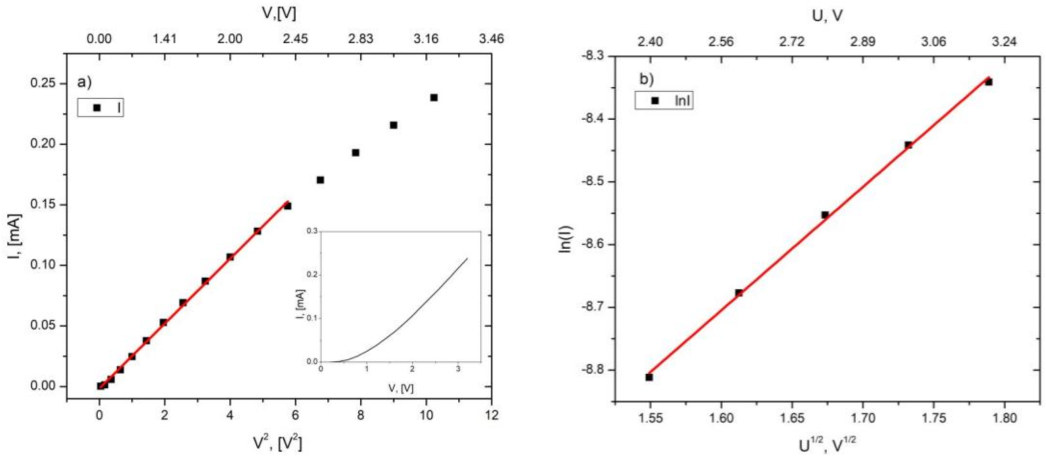

Fig. 3. Diode No. 2 under forward bias: a) space-charge limited current b) thermionic emission

Under reverse bias, when voltage is in 0–4 V range (Fig. 4 a)), experimental results are well described by space charge limited current (mobility regime) and when voltage reaches 4.2–5.2 V range it appears that tunneling is predominant mechanism (Fig. 4 b)).

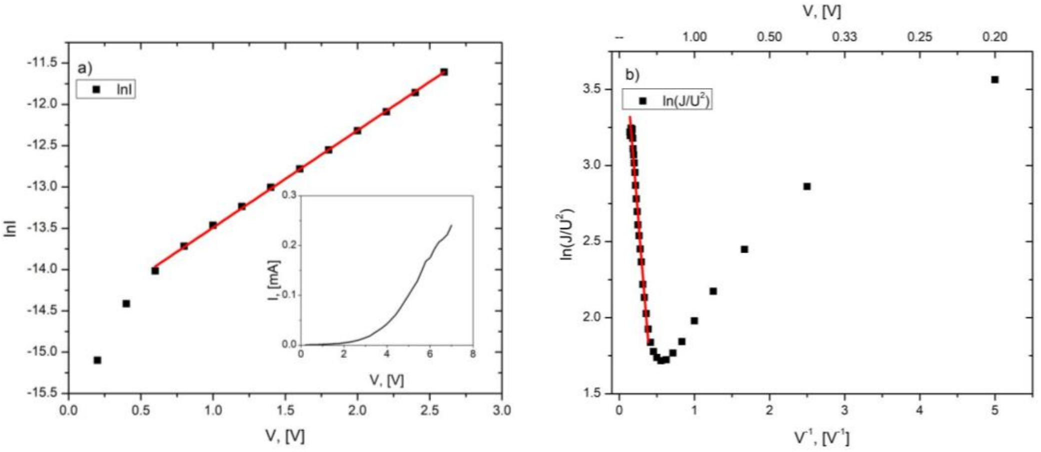

Fig. 4. Diode No. 2 (measured by using reverse bias): a) space-charge limited current b) tunneling

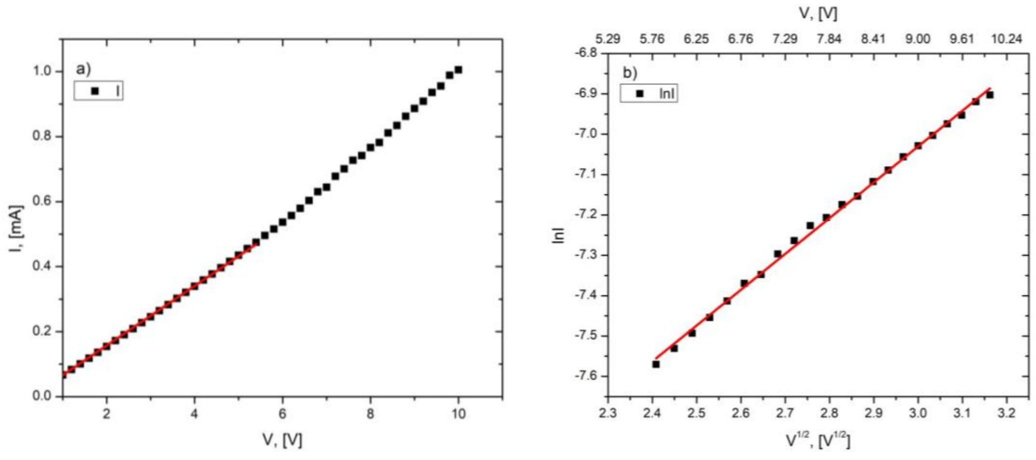

Fig. 5. Diode No. 3 under forward bias: a) ohmic conduction b) thermionic emission

Charge transfer mechanisms in diode No. 3 while using forward bias are presented in Fig. 5. At 0–5.4 V voltages range ohmic conduction occurs (Fig. 5 a)). As the voltage enters 5.4–10 V interval, I-V characteristic is better described as thermionic emission (Fig. 5 b)). Under reverse bias (Fig. 6), it is evident that from 0–4 V space-charge limited current occurs (mobility regime) (Fig. 6 a)) and from 4.2–5.2 V tunneling occurs (Fig. 6 b)).

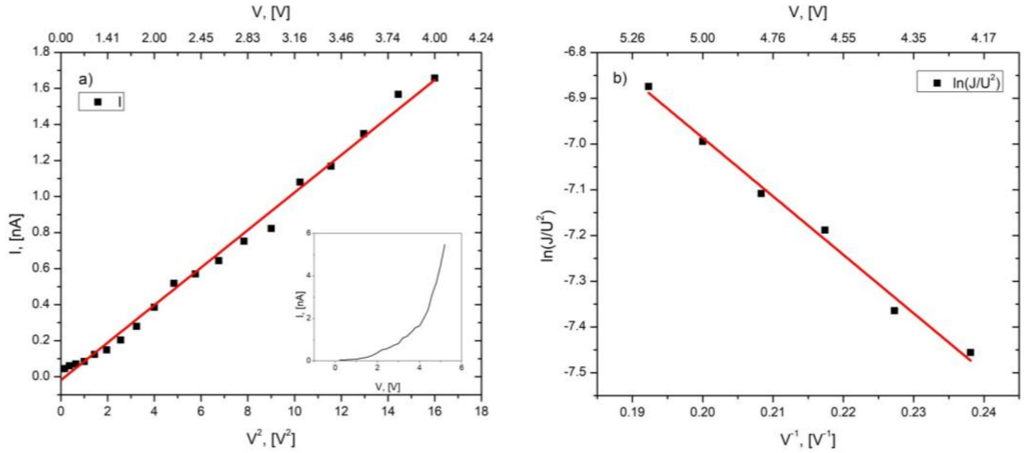

Fig. 6. Diode No. 3 under reverse bias: a) space-charge limited current b) tunneling

Diode No. 4 I-V characteristics are summarized in Fig. 7. This characteristic seems to have two linear dependencies on voltage: two under forward bias (circles) and two under reverse bias (squares). It appears that from 0 to 1.2 V under forward bias and from 0 to 1.8 V under reverse bias ohmic conduction occurs. When the voltage increases from 1.2 to 7.4 V under forward bias and from 1.8 to 8 V under reverse bias, space-charge limited current occurs (velocity saturation regime).

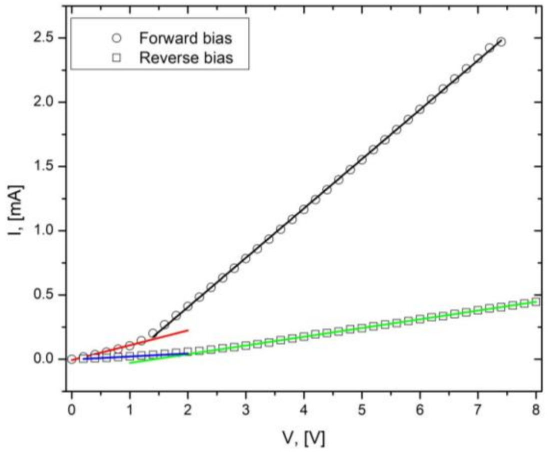

Fig. 7. Diode No. 4 under reverse and forward bias: ohmic conduction (red and blue lines) and space-charge limited current (green and black lines)

For diode No. 5, charge transfer mechanisms in the case of the forward bias are represented in Fig. 8. It appears than in this case, in 0–5.3 V voltages range thermionic emission in dielectrics is predominant mechanism (a) and in 5.3–10 V voltages range space-charge limited current kicks in (Mott – Gurtney law) (b).

In the case of the reverse bias, when voltage is small (0–2.8 V), thermionic emission in dielectric is observed. There is “light” breakdown at 1 V which results a step increase in current, also (Fig. 9 a)). Tunnelling occurs at voltages range 2.8–7.8 V (Fig. 9 b)).

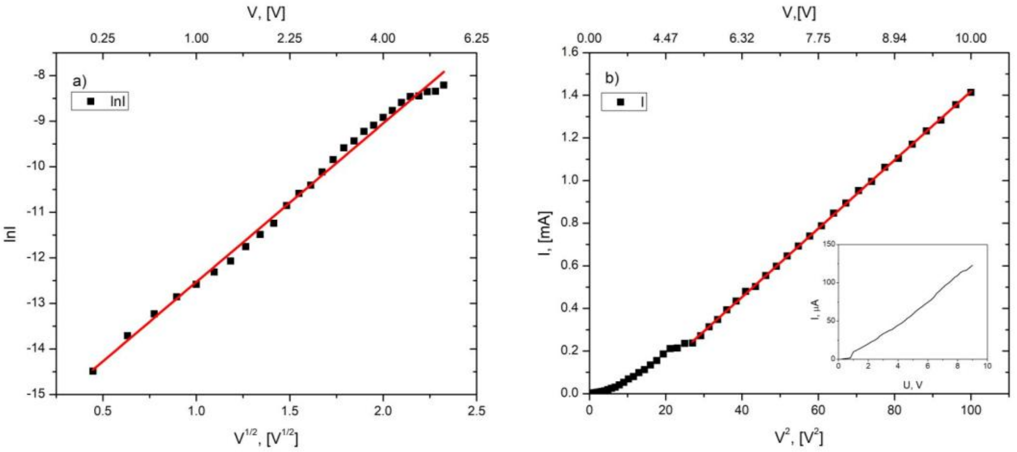

Fig. 8. Diode No. 5 under forward bias: a) thermionic emission b) space-charge limited current

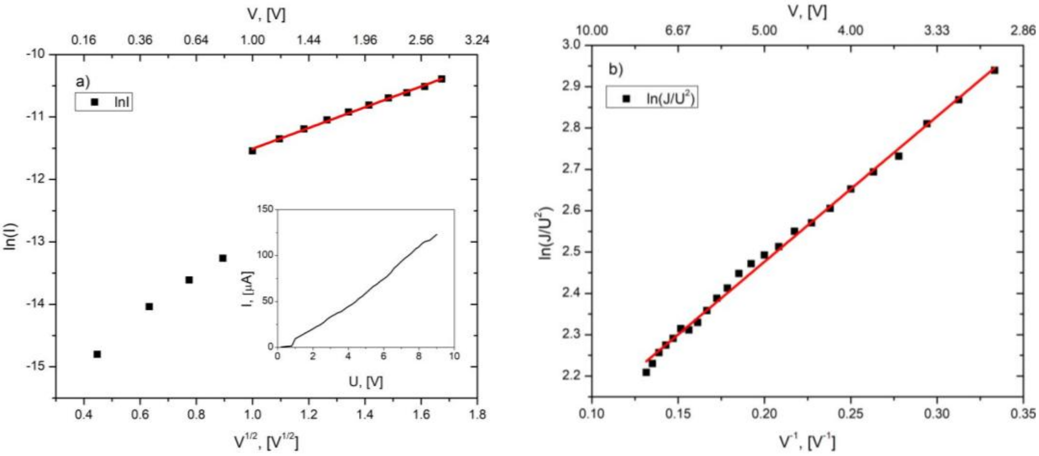

Fig. 9. Diode No. 5 under reverse bias: a) thermionic emission b) tunneling

Ideality factors and effective barrier heights were calculated using equations (3) and (4). Short summary of results and calculated values represented in Table 3.

Table 3. Effective barrier heights, ideality factors and predominant mechanisms of graphene - silicon structures

Diode no.	**Effective barrier height, eV**	**Ideality factor**	**Predominant mechanism**
1	0.69	31.5	Forward bias: 0–3 V thermionic emission (dielectric), 3–10 V tunneling. Reverse bias: 0–3 V ohmic conduction, 3–9 V space-charge limited current (velocity saturation).
2	0.68	5.58	Forward bias: 0–2.45 V space-charge limited current (Mott – Gurtney law), 2.4–3.2 V thermionic emission (dielectric). Reverse bias: 0–2.6 V thermionic emission (Schottky barrier), 2.6–7 V tunneling.
3	0.55	27.6	Forward bias: 0–5.4 V ohmic conduction 5.4–10 thermionic emission (dielectric). Reverse bias: 0–4.2 V space-charge limited current (Mott – Gurtney law), 4.2–5.2 V tunneling.
4	0.54	23.72	Forward bias: 0–1.2 V ohmic conduction, 1.2–7.4 V space-charge limited current (velocity saturation). Reverse bias: 0–1.8 V ohmic conduction, 1.8–8 V – space-charge limited current (velocity saturation).
5	0.61	30.67	Forward bias: 0.2–5.3 V – thermionic emission (dielectric), 5.3–10 V space-charge limited current (Mott – Gurtney law) Reverse bias: 0–2.8 V thermionic emission (dielectric), 2.8–7.8 V – tunneling.

It can be seen in Table 3, that effective barrier height of the diodes was in 0.54–0.69 eV range. Large ideality factors in 5.58–31.5 range were observed.

4. CONCLUSIONS

As seen from Table 3, effective barrier height ranges from 0.54 eV to 0.69 eV. These values are rather close to values obtained by other authors [8], however barrier heigh largely depends on number of graphene layers, growth methods as well as substrate type and doping concentrations. In present work used n type silicon substrate doping concentration is in between $0.45\cdot10^{15}$–$5\cdot10^{15}$ cm^{-3} (for p type silicon, doping concentration is in between $1.4\cdot10^{15}$–$15\cdot10^{15}$ cm^{-3}). The barrier heights are close to values obtained by S. Tongay, M. Lemaitre et. al.: at 2–$6\cdot10^{15}$ cm^{-3} substrate doping concentrations, barrier height was 0.86 eV [11]. However, the ideality factors obtained in this work are 10–15 times larger than presented in A. Bartolomeo review [8]. This rather large difference could be explained by the following argument. As seen from Table 3 most thermionic emissions observed are of the from ~exp($V^{1/2}$) which describes thermionic emission in dielectrics. This expression differs from standard thermionic emission in metal-semiconductor Schottky diodes (of form ~exp(V)). Moreover, another frequently observed mechanism was space-charge limited current which often occurs in dielectrics. Therefore, ideality factor difference and I-V characteristic deviation from typical diode thermionic emission could be explained that in formed semiconductor structures, between silicon and graphene there was natural SiO_2 layer which had big enough thickness to distort I-V characteristics. The diode then behaves more like a metal-dielectric-semiconductor (MIS) structure which typically has lower forward currents, smaller barrier heights and larger ideality factors [7]. More work should be done regarding transferless graphene deposition on silicon to assure that no significant layer of dielectric is present at the graphene-silicon interface.

ACKNOWLEDGEMENTS

Support of the European Space Agency should be acknowledged. Authors would like to thank R. Gudaitis and A. Vasiliauskas (both from Institute of Materials Science of Kaunas University of Technology) for help with samples fabrication.

REFERENCES

[1] K. S. Novoselov, V. I. Fal′ko, L. Colombo, P. R. Gellert, M. G. Schwab, and K. Kim, “A roadmap for graphene,” *Nature*, vol. 490, No. 7419, pp. 192–200, Oct. 2012.

[2] E. P. Randviir, D. A. C. Brownson, and C. E. Banks, “A decade of graphene research: Production, applications and outlook,” *Materials Today*. 2014.

[3] C.-H. Liu, Y.-C. Chang, T. B. Norris, and Z. Zhong, “Graphene photodetectors with ultra-broadband and high responsivity at room temperature,” *Nat. Nanotechnol.*, Vol. 9, No. 4, pp. 273–278, Apr. 2014.

[4] C. M. Seah, S. P. Chai, and A. R. Mohamed, “Mechanisms of graphene growth by chemical vapour deposition on transition metals,” *Carbon*. 2014.

[5] A. Reina and J. Kong, “Graphene growth by CVD methods,” in *Graphene Nanoelectronics: From Materials to Circuits*, 2012.

[6] L. Tai, D. Zhu, X. Liu, T. Yang, L. Wang, R. Wang, S. Jiang, Z. Chen, Z. Xu, and X. Li, “Direct Growth of Graphene on Silicon by Metal-Free Chemical Vapor Deposition,” *Nano-Micro Lett.*, 2018.

[7] S. M. Sze and K. K. Ng, *Physics of Semiconductor Devices*, 3rd ed. Hoboken, NJ, USA: John Wiley & Sons, Inc., 2006.

[8] A. Di Bartolomeo, “Graphene Schottky diodes: An experimental review of the rectifying

graphene/semiconductor heterojunction," *Phys. Rep.*, Vol. 606, p. 1–58a, 2016.

[9] A. C. Ferrari, "Raman spectroscopy of graphene and graphite: Disorder, electron-phonon coupling, doping and nonadiabatic effects," *Solid State Commun.*, Vol. 143, No. 1–2, pp. 47–57, 2007.

[10] A. C. Ferrari and D. M. Basko, "Raman spectroscopy as a versatile tool for studying the properties of graphene," *Nat. Nanotechnol.*, Vol. 8, No. 4, pp. 235–246, 2013.

[11] S. Tongay, M. Lemaitre, X. Miao, B. Gila, B. R. Appleton, and A. F. Hebard, "Rectification at Graphene-Semiconductor Interfaces: Zero-Gap Semiconductor-Based Diodes," *Phys. Rev. X*, Vol. 2, No. 1, p. 011002, Jan. 2012.

CYSENI 2019, May 23-24, Kaunas, Lithuania
ISSN 1822-7554, www.cyseni.com

AN EXPERIMENTAL STUDY OF ELECTROMAGNETICALLY EXCITED LIQUID METAL SURFACE WAVES

A. Gaile, A. Bojarevičs, M. Milgrāvis, V. Geža
University of Latvia
Raiņa bulvāris 19, LV-1586 Rīga – Latvia
Email: antra.gaile@lu.lv

ABSTRACT

The understanding of liquid metal surface waves is beneficial for both their prevention and generation. In various purifying processes the generation of surface waves can enhance the effectiveness of impurity removal by increasing free surface through which the impurities can escape. One of such potential application is Silicon refinement.

A contactless, electromagnetic approach is proposed for the excitation of the surface waves for electrically conductive materials. This paper describes an experimental study of a table-top model using GaInSn alloy. Surface waves were generated by an alternating magnetic field, produced using a Bitter coil. Additional scaling possibility was investigated by externally applied static magnetic field. Cases are compared both quantitatively by analysing acquired photos and qualitatively by determining the wavelength. Both invasive (UDV) and non-invasive measurement techniques were used to characterize the achieved waves.

Experiments demonstrate the possibility to use electromagnetic approach in order to excite intense surface waves. At the same intensity of the alternating magnetic field, the wave patterns. obtained using only a Bitter coil were significantly different from those created by simultaneously applying external static magnetic field. When the static magnetic field is applied, the waves can be excited at much lower alternating field intensity. External static magnetic field leads to power saving for AC field generation. Results demonstrate the potential to scale the technology to industrial size with the aim to increase free surface.

Keywords: electromagnetic field, Galinstan, liquid metal, silicon refinement, surface waves

1. INTRODUCTION

Nowadays the quest to find an alternative energy source to the fossil fuel is still going on. It is motivated by the predictions that fossil fuel is running out and by the concern about the accumulation of greenhouse gases. A desirable alternative is a green power source and more importantly renewable, such as solar, hydro or geothermal energy.

One of the most perspective energy sources is solar energy. Solar panel and battery industry is rapidly developing and seeking for a more efficient product and cheaper production. A common material for both photovoltaic and electronics industry, including solar cells, is silicon, but to enhance the efficiency it must be of high purity – solar grade (SoG-Si). It is both time consuming and expensive to achieve this, therefore cheaper alternatives have been investigated, for example, upgraded metallurgical grade silicon (UMG-Si). Various methods of refinement have been developed to enhance purity [5]. Most of the processes can be sped up by increasing the surface area, more precisely, the surface – volume ratio, through which the impurities can escape.

We propose a method that increases the surface area by exciting surface waves, with a contactless electromagnetic approach, that uses an alternating magnetic field. Since chemical purity is important, the contactless approach is beneficial. Theoretical and experimental studies about electromagnetically excited surface waves have been already presented, but not with similar aim [1]. The use of alternating magnetic fields is common in metallurgy for manipulating the liquid metal, for example, to pump, stir and heat the melt. The alternating magnetic field induces electric currents that interact with the field creating electromagnetic forces. The forces both deform the free surface and create stirring in the bulk.

To show that the proposed method shall work, let us assume that the external electric field is negligible, the Lorentz force density f then can be written as [2]:

$$\vec{f} = \vec{J} \times \vec{B} \tag{1}$$

where J – is the current density, B – external magnetic field density. If an alternating magnetic field is applied, both the induced current and magnetic field density can be described using periodic functions, thus creating:

$$\overrightarrow{f(t)}_{AC} = \frac{1}{2}\sigma\omega r B_0^2 \sin(2\omega t)\,\vec{n} \tag{2}$$

where σ – electric conductivity, ω – frequency of alternating field, r – the radius of the container, B_0 – magnetic field amplitude, $\vec{n}$ – normal, t – time. It can be seen that the force is alternating in time with twice the frequency of the external magnetic field and is proportional to the square of magnetic field amplitude.

Moreover, we propose to investigate the possibility of scaling this method by using a superposition of alternating and a permanent magnetic field. Letting the permanent magnetic field be greater than the alternating, the force density can be written as:

$$\overrightarrow{f(t)_{AC+DC}} = \sigma\omega r B_0 B_{DC} \sin(\omega t)\,\vec{n} \tag{3}$$

where B_{DC} – is the magnitude of the permanent magnetic field that is parallel to the alternating magnetic field. This rough estimate shows that in the case with an applied permanent magnetic field the force density oscillates in the same frequency as the alternating field, yet the amplitude is supposed to be bigger.

2. EXPERIMENTAL APPARATUS

The following table-top model was created in order to investigate electromagnetically excited surface waves in electrically conductive materials. We used GaInSn alloy, also known as Galinstan. It is a eutectic mixture consisting of 68% gallium (Ga), 22% indium (In) and 10% tin (Sn). Galinstan was chosen due to its desired physical properties – it is liquid at room temperature, melting point is around +10 °C and is of low toxicity and low reactivity [3].

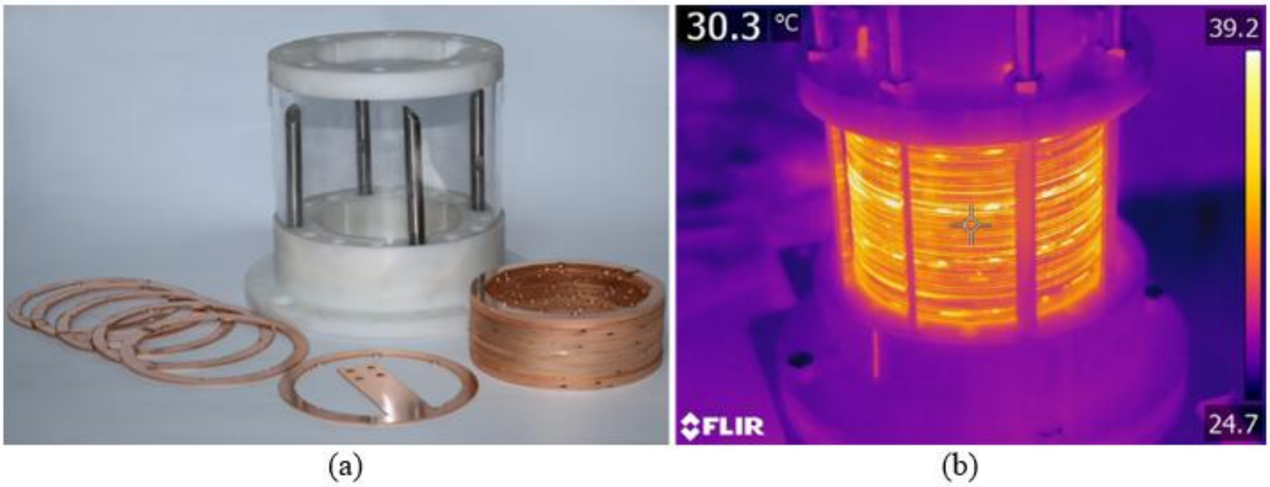

(a) (b)

Fig. 1. The Bitter coil used for the creation of the alternating magnetic field. (a) the copper plates and the outer shell of the cooling system is demonstrated, (b) a thermal picture of the coil (I = 50 A) without the water cooling

To demonstrate the surface waves of various intensities and the possibility of scaling of the technology both alternating and static magnetic field sources are necessary. We used 50 Hz frequency for the alternating magnetic field. To demonstrate the effect of scaling, we chose crucibles that have dimensionless frequency close to 1 and greater than 3. Alternating magnetic field source had to be compact as static magnetic field source was built around it. Therefore, the alternating magnetic field source was created using a Bitter coil principle. This concept provides denser windings with minimum diameter, therefore a stronger magnetic field is achieved if compared to a regular solenoid. The coil consists of 61 circular copper rings of 130 mm inner diameter, 154 mm – outer, and 2 mm – height, see Fig. 1. The coil is held together using eight threaded rods, cooled by maintaining running water over the outside wall. Over the time of the experimental series, electric current strength up to 600 A was used to generate the magnetic field of the strength above 200 mT in the centre of the coil.

The static magnetic field was achieved using a unique permanent magnet system that consists of 192 pieces of magnets. The system is based on Halbach permanent magnet principle. The system has a toroidal shape, the magnets are assembled in layers to create a strong magnetic field along its central axis. The magnet system is placed around the Bitter coil, so the magnetic fields are parallel, see Fig. 2 for the scheme of apparatus.

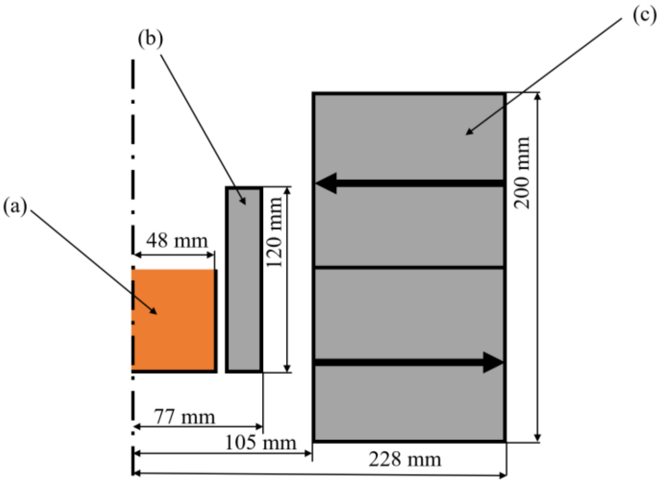

Fig. 2. Apparatus scheme, (a) – liquid metal container, (b) – Bitter coil, (c) – permanent magnet system, the cooling system is not shown

During the experiments the surface was filmed and photographed from above at a slight angle, no greater than 10°, image analysing was performed using ImageJ [4] – image processing program – to measure the characteristic wavelength. Mean velocity measurements were gathered using Doppler ultrasound velocimetry (UDV), performed firstly from above, but later on from below so not to perturb/ invade the flow. Laser sensor was tested for measuring surface profile, yet it was found that the laser could be used only to measure the height of the meniscus, not to map its profile. Therefore, an invasive method of using calibrated needles was used to measure the surface profile.

3. RESULTS AND DISCUSSION

Prior to the main experimental series, the impact of the container form on the results had been tested. Experiments showed that in both slightly conical and cylindrical containers the surface deformations are similar and vary only slightly. Further described experiments are for a cylindrical shaped container $d = 96.6\,mm$, liquid metal level $h = 61\,mm$ henceforth referred as 10 cm container and $d = 60.7\,mm$, liquid metal level $h = 61\,mm$ henceforth referred as 6 cm container.

In the following experiments the container was adjusted in a way that the liquid metal surface was positioned in the middle of the coil where the magnetic field is the strongest.

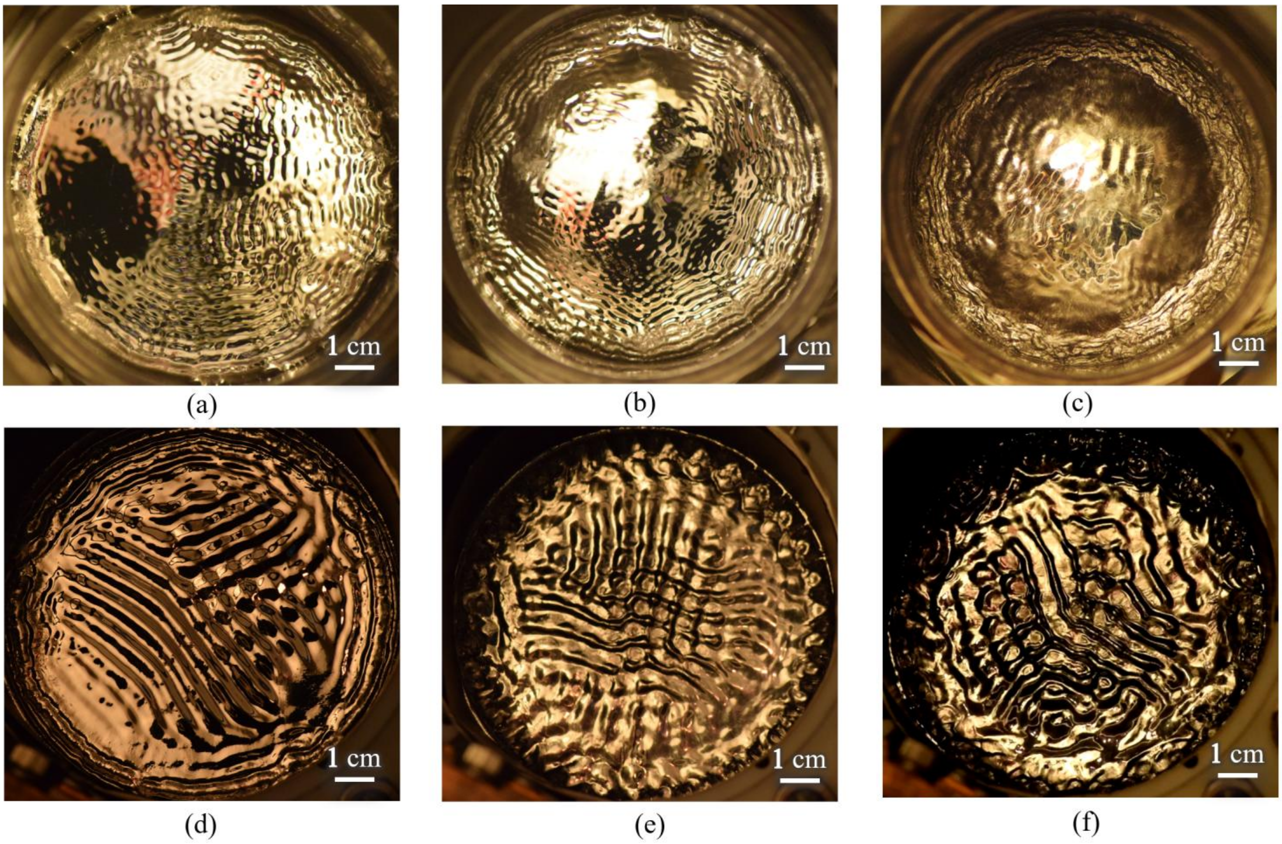

(a) (b) (c)
(d) (e) (f)

Fig. 3. The evolution of waves for a 10 cm container, the magnetic field strength in the centre of the surface is shown for comparison (a) 26 mT, (b) 35 mT, (c) 48 mT, (d) 16 mT with applied external magnetic field, (e) 27 mT with applied external magnetic field, (f) 40 mT with applied external magnetic field

In this study, we compare low magnetic field region, when the alternating magnetic field strength in the centre of the coil is in the range from 20 to 50 mT, the alternating magnetic field has a frequency of 50 Hz. This region was chosen with the aim to show the possibility of scaling – to increase the size while maintaining the energy consumption at the same level.

First, let us discuss the results for 10 cm crucible with a dimensionless frequency approximately 3. In Fig. 3. qualitative differences can be seen for the 10 cm container. An increase of the alternating magnetic field strength, with no static field applied, leads to more intense flows in the bulk, thus creating a convex meniscus. Velocity measurements can be seen in Fig. 4. If the magnetic field strength is increased, an increase in velocity is observed. The asymmetry of the measured vortexes most probably is due to the turbulence and therefore a loss of echo.

Meniscus height measurements in the centre of the container give only partial information about the surface deformation, therefore measuring needles were used to map the profile over the radius of the crucible. It showed up to 5.0 ± 0.2 m height difference for the 48 mT case. For the 10 cm container, the meniscus appears quite soon, it starts to form before 30 mT and is well defined at 50 mT. The small waves cannot climb the height difference and the plateau of meniscus lack small waves but have additional movement created from the movement in the bulk. The needle method's precision was not enough to determine the amplitude of the small waves, but by analysing the photos wavelength was measured. The size of the observed surface wave wavelength ranges from 2.36 ± 0.32 to 2.71 ± 0.21 mm.

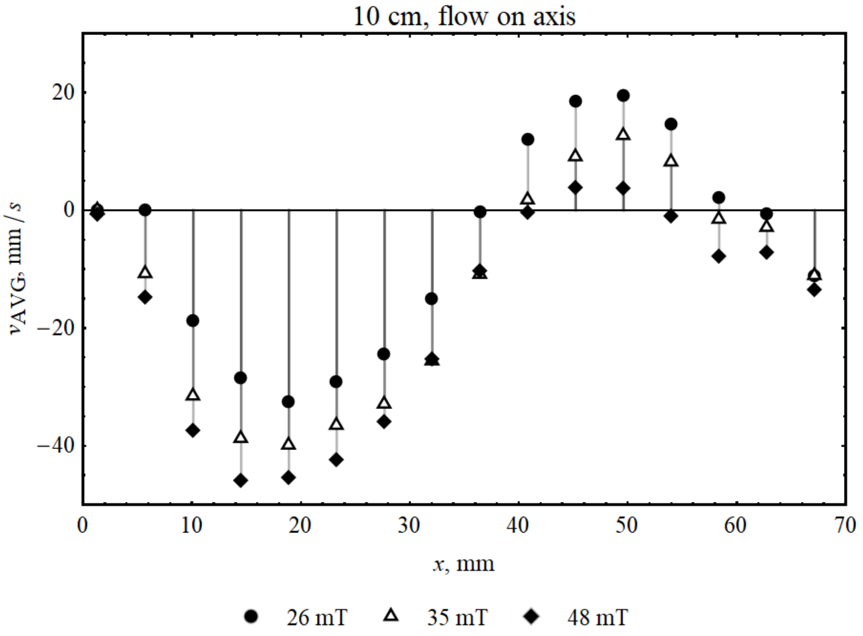

Fig. 4. Velocity profiles from UDV measurements for the 10 cm crucible without additionally applied static magnetic field

In the bottom row of Fig. 3 static magnetic field has been applied. The flow in the bulk is almost totally suppressed, no UDV measurements could be taken and the meniscus is not forming at the investigated alternating magnetic field values. The waves generated are larger (approximately 6.51 ± 0.42 mm for all three cases) and more intense, they are creating a more rigid pattern. The waves were observed steeper, thus their amplitude was larger than in the situation without external magnetic field. The lighting in Fig. 3 e clearly highlights curling around the edge of the container that was not observed previously without the static magnetic field.

Second, let us discuss the results for 6 cm crucible with a dimensionless frequency approximately 1. A similar situation can be seen in Fig 5, where the evolution of waves for a 6 cm container is shown. The meniscus is not present even at the largest field value presented, indicating that the flow in the bulk is not as intense, thus no velocity measurements could be done. The wavelength when no static field is applied is approximately 3.50 ± 0.33 mm for the investigated regimes. If compared to the 10 cm container (Fig. 3 (a)-(c)) the wavelength is greater, and waves are more regular, concentric.

If the static magnetic field is applied, the waves break concentric symmetry and create more complex patterns. Like for the 10 cm container, the wavelength increases, it is in the range of 5.41 ± 0.23 to 6.0 ± 0.41 mm. The curling around the edge is not yet fully observable and will appear only at greater magnetic field strength that is not discussed in this study.

The static magnetic field was applied in order to study the possibility of scaling, and the results show that the addition of a permanent magnetic field significantly changes the wave pattern, especially at higher alternating magnetic field strength. The waves lose the concentricity faster. For 10 cm container and static magnetic field, they are concentric up to 8 mT, and further on become more irregular. For the 6 cm crucible the wave pattern longer stays concentric when no static field is applied, but when the permanent magnetic field is applied, wave concentricity is lost at approximately 16 mT. By increasing the alternating magnetic field strength the wave pattern evolves from concentric to irregular, then becoming so intense to expel small droplets out of the surface.

Both containers showcase greater waves when a static magnetic field is applied, leading to acknowledgeable power saving that is desired in the production process. First and foremost, the power saving is achieved due to the permanent magnetic field being created by a magnet system that does not need electricity for operation. For an effective refinement process, both wavelength and amplitude are of matter. In this study, we have only visually estimated the wave height (amplitude) and can qualitatively say that it increases when the alternating magnetic field is increased and that it is greater when the static field is applied.

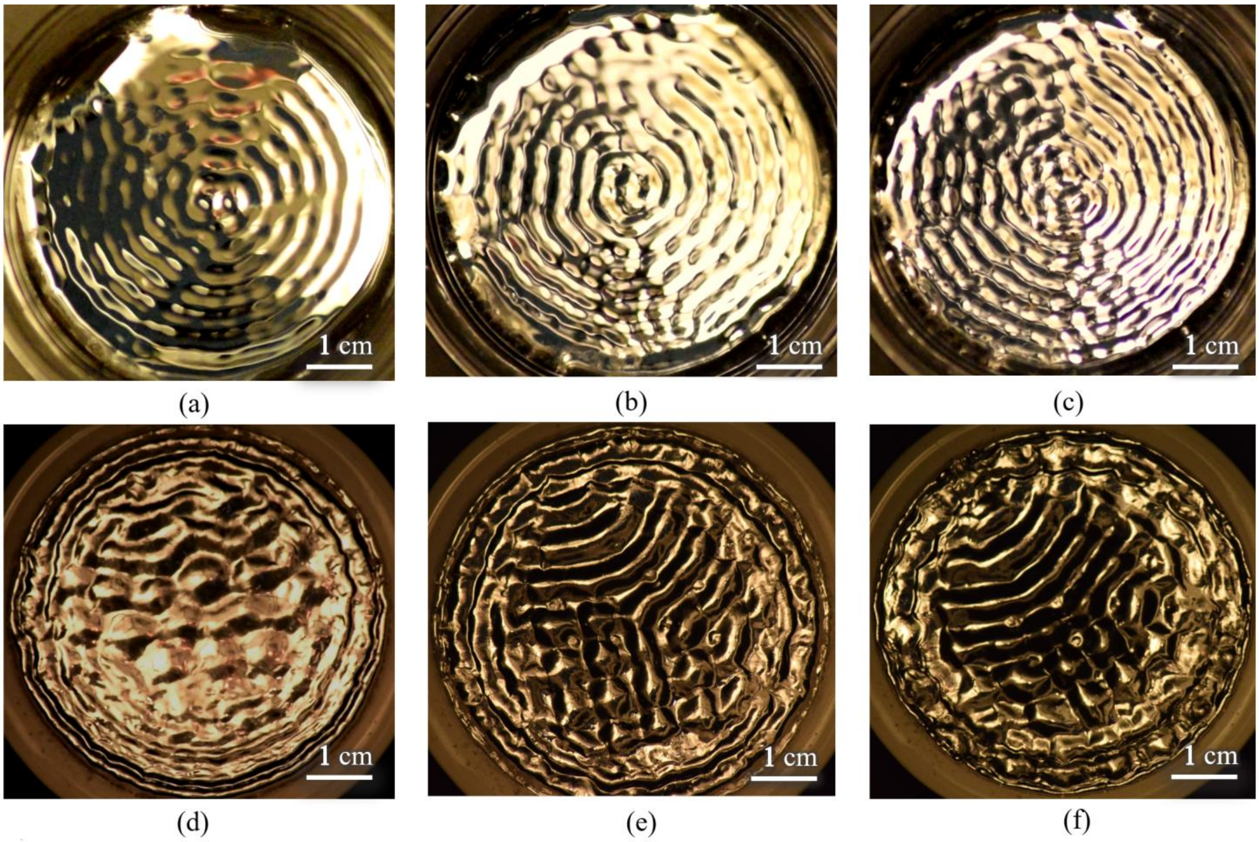

Fig. 5. The evolution of waves for a 6 cm container, the magnetic field strength in the centre of the surface is shown for comparison (a) 26 mT, (b) 35 mT, (c) 48 mT, (d) 17 mT with applied external magnetic field, (e) 28 mT with applied external magnetic field, (f) 45 mT with applied external magnetic field

For the 6 cm crucible similar, well-developed concentric wave patterns and amplitudes were observed when the alternating magnetic field strength was 8 mT, but if a static magnetic field was applied, the waves were observable at 4 mT. Using a simple formula to calculate the power $P = I^2R$, where I – the current and R – the resistance, this would mean that the coil's power consumption can be reduced at least four times, because the magnetic field is proportional to the applied current.

Firstly, the amplitude of waves without the applied magnetic field was significantly smaller than the other case, it was barely visible with a naked eye, secondly, the wavelength was 2.50 ± 0.27 mm when no static magnetic field was applied, and approximately 4.64 ± 0.25 mm with the static field. Thus, the static field case has fewer but greater waves. Yet it is only an estimation and further studies will investigate the amplitude of waves in more detail.

4. CONCLUDING REMARKS

As the results have shown, the aforementioned table-top model demonstrates the possibility of exciting surface waves electromagnetically. Various wave patterns can be achieved by an alternating magnetic field or adding a static magnetic field. The wavelength of the generated waves can be increased to some extent when the static magnetic field is applied. Moreover, the external static magnetic field leads to power saving for AC field generation because longer wavelength waves are generated. Results demonstrate the potential to scale technology to the industrial size, but further experiments must be performed.

ACKNOWLEDGMENT

This work was funded by the European Regional Development Fund under contract “Refinement of metallurgical grade silicon using smart refinement technologies” (No. 1.1.1.1/16/A/097) and supported by Latvian Council of Science under project “Magnetohydrodynamic instability in large scale liquid metal batteries” (No. LZP-2018/1-0017).

REFERENCES

1. GALPIN J.M., FAUTRELLE Y.: Liquid-metal flows induced by low-frequency alternating magnetic fields. *J. Fluid Mech.*, 1992, 239, pp. 383–408.
2. LANDAU L.D., LIFSHITZ E.M.: *Electrodynamics of Continuous Media (Second Edition)*. Pergamon, Amsterdam, 1984, 460 p, ISBN 0-7506-2634-8.
3. MORLEY N.B., BURRIS J., CADWALLADER L.C., NORNBERG M.D., MORLEY N.B., BURRIS J., CADWALLADER L.C., NORNBERG M.D.: GaInSn usage in the research laboratory. *Rev. Sci. Instrum.*, 2008, 79(5) 0561, pp. 8–11.
4. RUEDEN C.T., SCHINDELIN J., HINER M.C., DEZONIA B.E., WALTER A.E., ARENA E.T., ELICEIRI K.W.: ImageJ2: ImageJ for the next generation of scientific image data. *BMC Bioinformatics*, 2017, 18, 529.
5. SAFARIAN J., TRANELL G., TANGSTAD M.: Processes for upgrading metallurgical grade silicon to solar grade silicon. *Energy Procedia*, 2012, 20, pp. 88–97.

CYSENI 2019, May 23-24, Kaunas, Lithuania
ISSN 1822-7554, www.cyseni.com

CONFOCAL SPECTROMETER FOR STUDY OF ORGANIC-INORGANIC PEROVSKITES

N. S. Mahon, O. V. Korolik, A. V. Mazanik
Belarusian State University
Nezavisimosti av. 4, 220030, Minsk – Republic of Belarus
Email: natalimahon@gmail.com

ABSTRACT

Organic-inorganic perovskites (OIPs) are promising photovoltaic materials due to the simplicity of synthesis technique and attractive physical properties. It is known that the power conversion efficiency of solar cells with an OIP photoabsorbing layer has recently reached approximately 23%. Unfortunately, OIPs easily degrade under influence of heat, moisture, oxygen and light soaking. Encapsulation of OIP layers to protect them against moisture and oxygen is necessary, which hampers to use traditional methods of analysis such as electron and probe microscopy, energy-dispersive X-ray analysis, X-ray photoelectron spectroscopy, X-ray diffraction, etc. As a result, significant difficulties in determination of photodegradation mechanisms arise, so, we are forced to look for other techniques of highly informative nondestructive analysis of such structures. For studying photoinduced processes in OIP layers, we applied confocal spectrometer, which allowed to use a laser beam (i) as a source of optical radiation causing photodegradation; (ii) for the local analysis of changes in the structure of the area exposed to optical radiation using Raman and photoluminescence (PL) spectra; (iii) for local measurement of solar cell parameters (short circuit current, open circuit voltage). The presence of a 3D piezoelectric scanner enables one to do the mapping of spectral and photoelectric parameters, which is important for establishing the homogeneity of the objects under study. The proposed approach allows obtaining information on the phase composition and spectrum of electronic states (from the Raman and PL spectra), as well as on the dynamics of charge carriers. By recording PL and Raman spectra, short circuit current and open circuit voltage under laser beam illumination, one can observe the evolution of the system in the online mode, which gives information regard to processes occurring in the OIPs when they are illuminated.

Keywords: confocal spectrometer, nondestructive analysis, organic-inorganic perovskite, photoluminescence

1. INTRODUCTION

Hybrid organic-inorganic perovskite solar cells (SCs) appeared less than 10 years ago [1] and immediately attracted special attention because they combine a high light absorption coefficient, band gap energy close to the optimal value, a long lifetime of charge carriers (up to microsecond range), and the possibility of low temperature (not more than 100 ^{o}C) solution based synthesis [2-5]. It is interesting to note that the efficiency of perovskite SCs (PSCs) increased in a short period of time to more than 23%, which is associated with the possibility of varying the architecture, as well as the chemical composition of the perovskite and transport layers [6-8]. However, there is a problem in the way of commercialization of such solar cells, which is associated with rapid degradation under the influence of light, heat, atmospheric moisture and oxygen [9-13]. The variation of chemical composition of the perovskite structure, electrone and hole acceptor layers, as well as encapsulation made it possible to achieve significant resistance to moisture, oxygen and heat [14]. However, photodegradation still remains an unresolved problem, since regeneration in the dark [15] is too slow to completely restore operating parameters decreased after the light exposure in real operating conditions [14]. Thus photovoltaic researchers focus on identifying the regularities of photodegradation and regeneration of PSCs, establishing the mechanisms responsible for these processes, and also searching for ways to reduce the rate of degradation [4]. The experimental study of PSCs is complicated by difficult access to the active area of device (perovskite and acceptor layers) due to the presence of encapsulation. This makes it problematic to use traditional methods of analysis (X-ray diffraction analysis, scanning electron and probe microscopy, photoelectron spectroscopy) and requires development of techniques based on other non-contact analytical methods, one of which can be the optical confocal spectroscopy.

The aim of our work was the development of a technique for studying photosensitive semiconductor structures using a confocal spectrometer. The objects of research were organic-inorganic PSCs with different chemical composition of perovskite layer. The proposed technique makes it possible to use the laser beam of the spectrometer not only (i) for excitation the Raman and photolumenescence (PL) spectra, but also (ii) for local measurement of photoelectric parameters of SCs (short-circuit current, open-circuit voltage); as well (iii) as a source of local photodegradation for establishing the dynamics of the PSCs properties under illumination. The presence of a 3D-piezoscanner allows mapping of spectral and photoelectric parameters, which is important for unraveling the degree of spatial homogeneity of the samples. So, using of the confocal spectrometer allows obtaining extensive information on photodegradation and recovery processes by analyzing the phase composition and the spectrum of electronic states (from Raman and PL spectra), as well as the generation, transport and recombination of charge carriers. In particular, the registration of PL spectra, short-circuit current and open circuit voltage during illumination with a laser beam for a long period of time enables one to observe the evolution of the system in real time, which gives an information about the processes occurring in solar cells during their illumination.

2. METHODOLOGY

The method of PSC preparation is described in [15]. Briefly, the studied organic-inorganic perovskite SCs contained $MAPbI_3$, $(Cs/FA)Pb(I/Br)_3$ or $(Cs/FA/MA)Pb(I/Br)_3$ as absorbing layer, where MA is methilammonium (CH_3NH_2), and FA is formamidine (CH_4N_2). SnO_2 and Spiro-MeOTAD were used as electron-acceptor and hole-acceptor layers, respectively; ITO and Au were used as front and back contacts.

Nanofinder HE confocal spectrometer (LOTIS TII, Belarus-Japan) was used in the study. As PbI_2 is known as the main product of OIP decomposition, we used a 4 μm thick PbI_2 film as the reference sample. Parameters of Raman spectra measurement were the following: the wavelength of the exciting light λ = 532 nm, the width of the spectrometer pinhole ph = 100 μm, the diffraction grating constant d = 600 mm^{-1} (which provided a spectral resolution of 2.5 cm^{-1}), the exciting radiation power P = 6 μW, the diameter of laser spot on the sample D = 2 μm (10x objective with numerical aperture NA = 0.3), signal accumulation time t = 120 s. These parameters were chosen in such a way as to exert no destructive effect on the objects of investigation. Before and after measurement of Raman spectrum, PL spectra were recorded under the conditions described in the next section. The identity of the shape and position of the obtained Raman and PL spectra made it possible to conclude that the method is non-destructive.

PL spectra were measured in the following conditions: excitation light wavelength λ = 532 nm, width of the spectrometer pinhole ph = 25 μm, grating constant d = 600 mm^{-1} (which provided a spectral resolution better than 0.1 nm), the power of the exciting radiation P = 0.6 μW, the diameter of laser spot on the sample D = 2 μm (10x objective, NA = 0.3), the signal accumulation time t = 5 s. For observation of evolution of PL spectral parameters, exposure time was choosen equal to 250 s (50 PL spectra). Taking into accound the used optical power (0.6 μW), such exposure roughly corresponded to the one day illumination of the solar cell under actual operation conditions. The power of the laser radiation was chosen in such a way as to exert no destructive effect on the sample, but at the same time to provide a slight effect, which makes it possible to detect the behavior of the object under local illumination. For analysis of spatial homogeneity, scanning of samples using a 3D-piezoscanner was carried out with taking PL spectra in each point under the same measurement conditions.

Short-circuit current (SCC) and open-circuit voltage (OCV) were measured when recording PL spectra with a Keithley 2400 source meter.

3. RESULTS AND DISCUSSIONS

3.1. Individual Capabilities of Confocal Spectrometer

Confocal spectrometer is the useful tool for non-destructive analysis, which does not require special sample preparation and allows studying encapsulated samples like perovskites. This section is devoted to the analysis of confocal spectrometer capabilities without any additional devices.

3.1.1. Raman Spectra

Traditionally, confocal Raman spectroscopy is used for local qualitative determination of the phase composition of the samples under study. In the case of OIPs, sharp Raman peaks can be observed only at low temperatures, which is impossible for encapsulated samples due to the risk of encapsulation damage. However, Raman spectroscopy can be used, for example, to identify the presence of the PbI_2 phase as the most common product of perovskite degradation. We investigated weakly and strongly degraded PSCs based on $(Cs/FA)Pb(I/Br)_3$ and $(Cs/MA/FA)Pb(I/Br)_3$ layers.

Figure 1 presents the obtained Raman spectra of reference PbI_2 film and PSCs based on $(Cs/MA/FA)Pb(I/Br)_3$ perovskite previously degraded under the influence of prolonged light exposure and increased temperature in natural condition. The obtained spectra of PbI_2 and perovskite have the shape very similar to that observed in many works [16, 17]. The spectra are given in arbitrary, but in the same units. The absence of Raman lines inherent to PbI_2 in spectrum for perovskite film allows to exclude formation of lead iodide as a process which takes place in our particular case of white light exposure degradation is not accompanied by formation of lead iodide.

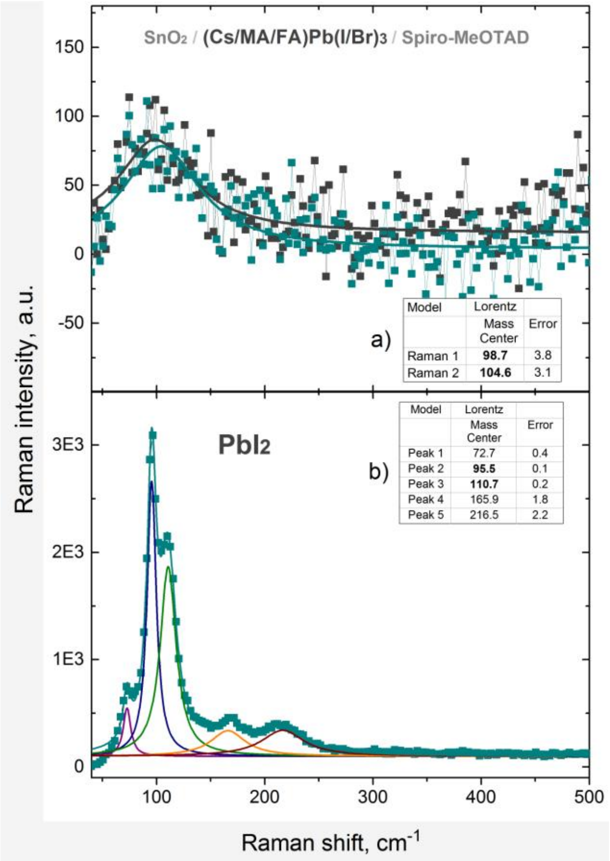

Fig. 1. Raman spectra of degraded $(Cs/MA/FA)Pb(I/Br)_3$ (a) and reference PbI_2 films (b)

3.1.2. Photoluminescence Spectra and Mapping

It is known that hybrid organic-inorganic perovskites can contain more than one species of ions in the cation and anion sublattices for better photovoltaic properties and stability [14]. However, in the case of perovskites with a complex composition, multiphase heterogeneous systems are often formed. Obviously, in this case several peaks corresponding to the individual phases located in the confocal volume will be observed in the PL spectrum. Thus, the registration of PL spectra is a simple method which allows to identify the phase composition of the object under study.

The characteristic PL spectrum of $(Cs/FA)Pb(I/Br)_3$ based PSC is shown in Fig. 2. A single symmetrical peak corresponding to interband radiative recombination in the perovskite layer indicates the presence of a single phase characterized by a definite value of the PL mass center (774 nm) from which the value of the band gap can be approximately estimated (1.60 eV) in the investigated samples. The obtained PL spectra of perovskite have the shape very similar to that observed in other works [18]. The obtained PL spectra not only characterize the quality of the initial sample, but also help to track the possible formation of secondary phases at different stages of the life cycle of the SCs. Determination of the degree of spatial homogeneity is an important stage in the primary characterization of samples, since photodegradation is carried out by illuminating the working surface of the PSCs, whose dimensions are 1000 times larger than the diameter of the laser beam, by which the Raman and PL spectra are recorded. Therefore, without the analysis of spatial homogeneity, the results can be contradictory, and the resulting conclusions are incorrect. The detection of the scattering of the parameters of PL spectra, such as the intensity and center of mass (inset in Fig. 2), allows one to judge the spatial arrangement of the centers of non-radiative recombination, the distribution of regions with the greatest and the least efficiency of charge carrier extraction by transport layers and spatial homogeneity of the chemical composition.

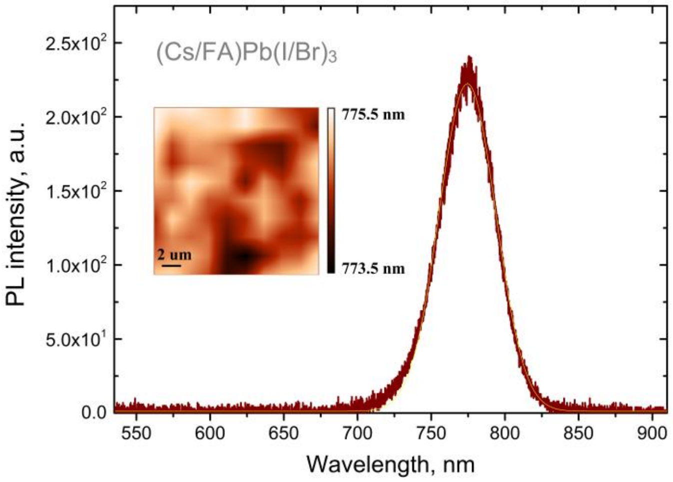

Fig. 2. Typical PL spectrum of $(Cs/FA)Pb(I/Br)_3$ SC and mapping of PL peak position for 20 × 20 μm^2 region (inset)

3.1.3. Kinetics of PL Spectra Parameters

Individual PL spectra do not give a complete information about the processes occurring in the solar cell during its illumination. In addition, at different stages of the life span of the PSCs, certain parameters, for example, the intensity or position of the mass center of the PL band may be identical, while the rates of change of these parameters may differ, since different processes will be responsible for their change. Recording photoluminescence spectra at the equal time intervals, we can observe the evolution of PL parameters during illumination. As one can see from Fig. 3, light-induced processes in general case can lead both to increasing and decreasing PL intensity, which is related to competition of creation and deactivation of recombination centers.

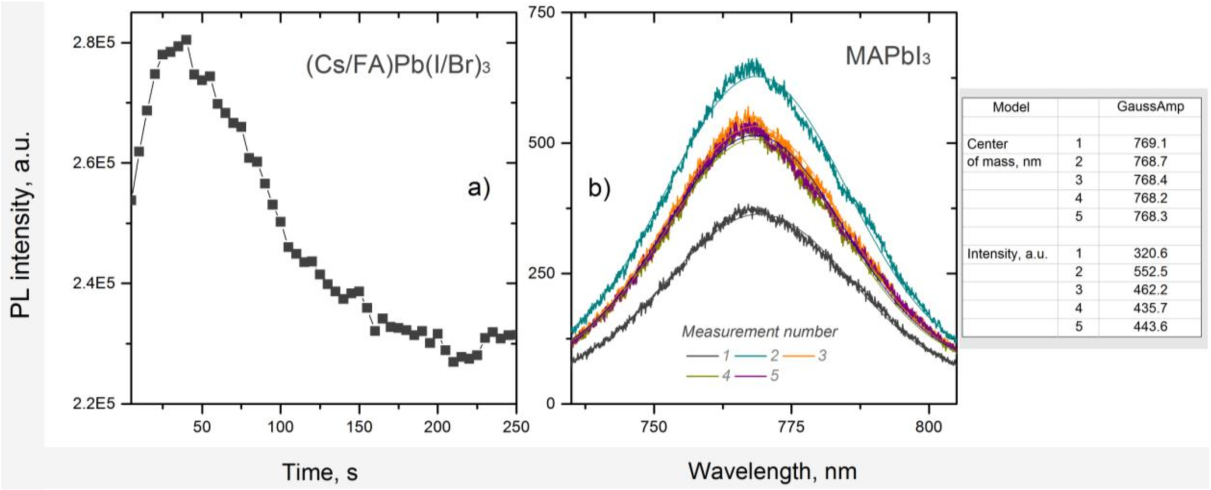

Model		GaussAmp
Center of mass, nm	1	769.1
	2	768.7
	3	768.4
	4	768.2
	5	768.3
Intensity, a.u.	1	320.6
	2	552.5
	3	462.2
	4	435.7
	5	443.6

Fig. 3. PL kinetics for (Cs/FA)Pb(I/Br)$_3$ PSC (a);
PL spectra consequently measured for MAPbI$_3$ PSC (b)

3.2. Capabilities of Confocal Spectrometer with Additional Devices

The consideration given above demonstrates how much information can be obtained using solely confocal spectrometer. However, changes of PL intensity or mass center do not give complete information about the behavior of charge carriers in the sample and, in particular, about peculiarities of their recombination. So, additional devices for measurement of electrical parameters allow to distinguish this processes.

3.2.1. Short-Circuit Current and Open-Circuit Voltage

Advantages of using confocal spectrometer for determination of SCC and OCV are the possibility of simultaneous measurement of PL spectra, which allows to describe the recombination processes in the photoabsorbing layer more accurately. As an example, Fig. 4 shows the kinetics of the change in the OCV, SCC and PL intensity. Approximation of the obtained kinetics by the exponential function (Fig. 4) demonstrates the equality of the characteristic times (~ 16 s) of the processes responsible for the initial decrease in the PL intensity in the short-circuit mode and the increase in the open-circuit voltage, which can be explained by the process of charging the cell capacitance of a locally photogenerated charge carriers. The constancy of the short-circuit current indicates that the processes leading to a decrease in the PL intensity are not associated with the formation of defects at the interfaces.

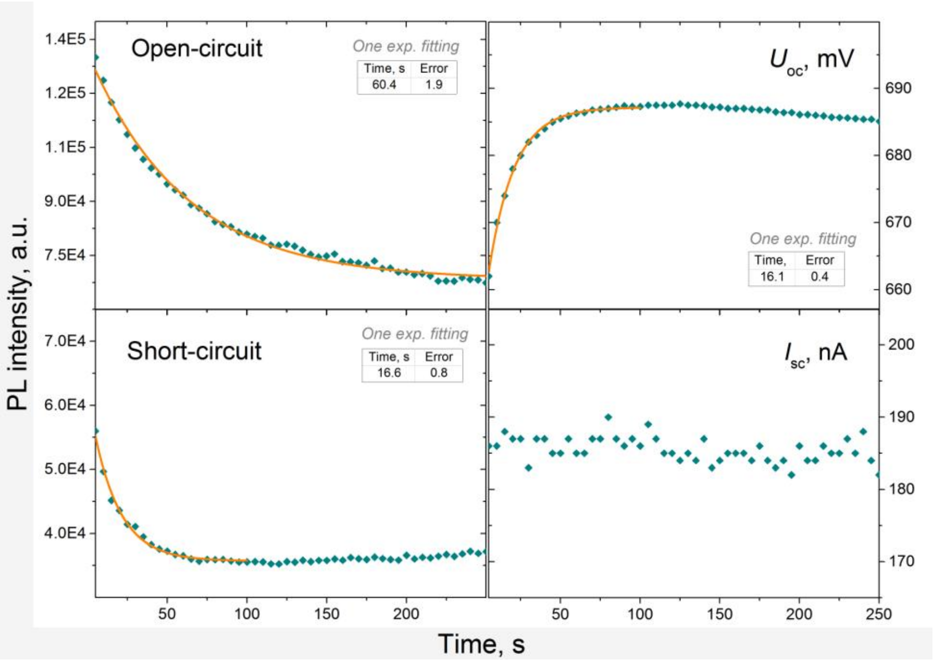

Fig. 4. Kinetics of PL intensity, OCV, SCC for $(Cs/FA)Pb(I/Br)_3$ based SC and their fitting with exponential function

4. CONCLUSIONS

Presented capabilities of confocal spectrometer allow to conclude that the developed and approved method of local investigation of photosensitive structures (by example of organic-inorganic perovskite solar cells) based on the use of a confocal spectrometer and allowing to measure the Raman and PL spectra, kinetics of PL parameters, short-circuit current, open-circuit voltage under the influence of monochromatic radiation can be used for the analysis of photosensitive structures of various types.

The authors thank the Belarusian Republican Foundation for Basic Research for the finantial support (project F16MS-015).

REFERENCES

1. PARK, N.-G., GRÄTZEL, M., MIYASAKA, T. *Organic-Inorganic Halide Perovskite Photovoltaics: From Fundamentals to Device Architectures*. Switzerland: Springer, 2016. 366 p. ISBN 978-3-319-35114-8.
2. BERHE, T.A. Organometal halide perovskite solar cells: degradation and stability. *Energy Environ. Sci*., 2016, Vol. 9. p. 323–356.
3. ZHOU, D. Perovskite-Based Solar Cells: Materials, Methods, and Future Perspectives. *J. of Nanomaterials*, 2018, Vol. 2018, 15 p.
4. KOJIMA, A., TESHIMA, K., SHIRAI, Y., MIYASAKA, T. Organometal Halide Perovskites as Visible-Light Sensitizers for Photovoltaic Cells. *J. Am. Chem. Soc.*, 2009, Vol. 208, No. 17, p. 6050–6051.
5. GOTTESMAN, R., ZABAN, A. Perovskites for Photovoltaics in the Spotlight: Photoinduced Physical Changes and Their Implications. *Acc. Chem. Res*., 2016, Vol. 49, p. 320–329.
6. IM, J. H., LEE, Ch. R., LEE, J. W., PARK, S. W., PARK, N. G. 6.5% efficient perovskite quantum-dot-sensitized solar cell. *Nanoscale*, 2011, Vol. 3, p. 4088-4093.

7. YANG, D. Hysteresis-Suppressed High-Efficiency Flexible Perovskite Solar Cells Using Solid-State Ionic-Liquids for Effective Electron Transport. *Adv. Mater,* 2016, Vol. 28, p. 5206–5213.
8. DOMANSKI, K. Migration of Cations Induces Reversible Performance Losses over Day/Night Cycling in Perovskite Solar Cells, *Energy Environ. Sci*, 2017, Vol. 10, p. 604–613.
9. YAO, Y. The interface degradation of planar organic–inorganic perovskite solar cell traced by light beam induced current (LBIC). *RSC Adv*, 2017, Vol. 7, p. 42973–42978.
10. HU, J. Photovoltage Behavior in Perovskite Solar Cells under Light-Soaking Showing Photoinduced Interfacial Changes. *ACS Energy Lett*, 2017, Vol. 2, p. 950−956.
11. ZHAO, Y. Mobile-Ion-Induced Degradation of Organic Hole-Selective Layers in Perovskite Solar Cells. *J. Phys. Chem. C*, 2017, Vol. 121, p. 14517–14523.
12. DE SOUZA, E.C.C., MUCCILLO, R. Properties and Applications of Perovskite Proton Conductors. *Materials research*, 2010, Vol. 13(3), p. 385–394.
13. CHRISTIANS, J.A., MIRANDA HERRERA, P.A., KAMAT, P.V. Transformation of the excited state and photovoltaic efficiency of $CH_3NH_3PbI_3$ perovskite upon controlled exposure to humidified air. *J. Am. Chem. Soc*, 2015, Vol. 137, p. 1530–1538.
14. WANG, D., WRIGHT, M., ELUMALAI, N.K., UDDIN, A. Stability of perovskite solar cells. *Solar Energy Materials & Solar Cells*, 2016, Vol. 147, p. 255–275.
15. KHENKIN, M. Dynamics of photo-induced degradation of perovskite photovoltaics: from reversible to irreversible processes. *ACS Applied Energy Materials*, 2018, Vol. 1, p. 799–806.
16. WANGYANG, P., SUN, H., ZHU, X., YANG, D., GAO, X. Mechanical exfoliation and Raman spectra of ultrathin PbI_2 single crystal. *Materials Letters*, 2016, Vol. 168, p. 68–71.
17. LEDINSKÝ, M., LÖPER, P., NIESEN, B., HOLOVSKÝ, J., MOON, S.-J., YUM, J., DE WOLF, S., FEJFAR, A., BALLIF, C. Raman spectroscopy of organic-inorganic halide perovskites. *The journal of physical chemistry letters*, 2015, Vol. 6, p. 401–406.
18. MONTES-VALENZUELA, I., PÉREZ-SÁNCHEZ, F., MORALES-ACEVEDO, A. Structural, optical and photoluminescence properties of hybrid metal–organic halide perovskite thin films prepared by a single step solution method. *Journal of Materials Science: Materials in Electronics*, 2018, Vol. 29, p. 15404–15410.

CYSENI 2019, May 23-24, Kaunas, Lithuania
ISSN 1822-7554, www.cyseni.com

CHARACTERISATION OF ALUMINUM OXIDE THIN FILMS DEPOSITED BY SPRAY PYROLYSIS

K. D. Omotosho, A. T. Oluwabi, I. Oja Acik, A. Mere, M. Krunks
Laboratory of Thin Film Chemical Technologies
Department of Materials and Environmental Technology
Tallinn University of Technology
Ehitajate tee 5, EE-19086 Tallinn – Estonia
Email: komoto@ttu.ee

ABSTRACT

Aluminum Oxide (AlO_x) is a high-k semiconductor material with excellent optical and electrical properties, and it has been successfully used in different applications most especially as a gate insulator for thin film transistors. For the purpose of this work, an ultrasonic spray pyrolysis (USP) method was adopted. To the best of our knowledge, limited work has been done on USP deposition of AlO_x thin films. Aluminum acetylacetonate salt $Al(acac)_3$ was used as the AlO_x precursor salt. 0.05 M concentration of AlO_x precursor was prepared by dissolving Aluminum acetylacetonate in methanol, the solution was sprayed onto heated silicon wafer and quartz substrates at temperatures of 350, 450, and 550 ^{o}C. As-deposited films on quartz substrates were annealed at 500, 800, and 1000 ^{o}C for 1 hour. The microstructural, morphological and electrical properties of the films were investigated. The X-ray diffraction (XRD) studies revealed that both as-deposited and annealed AlO_x thin films were amorphous. Scanning electron microscope (SEM) images revealed that the AlO_x films were smooth, uniform, and well compacted with the absence of grain boundaries. Electrical properties of the as-deposited AlO_x thin film was accessed by constructing capacitor in a metal-insulator-structure (MIS). As revealed by the current – voltage characterization, the resistivity of the as-deposited film increases with deposition temperature from $3.07\cdot10^{4}$ Ωcm (in 350 ^{o}C as-deposited films) to $1.57\cdot10^{5}$ Ωcm (in 450 ^{o}C as-deposited film). The films have a high dielectric constant in the range of 7.4–5.6. Based on this result, USP as-deposited AlO_x film shows promising properties suitable for use in transistor application.

Keywords: Aluminum oxide, Spray pyrolysis, Dielectric, Thin films transistor, Current-voltage

1. INTRODUCTION

Aluminum Oxide (AlO_x) is considered an outstanding material for application in microelectronics, optoelectronics, sensors, water repellent coating, protective coating, gate dielectric in thin film transistors (TFTs), biomedicals and sensing layer due to the following properties: excellent dielectric constant; wide band gap; low-leakage current densities; good adhesion to glass substrate; chemical inertness; high thermal conductivity; high refractive index; and mechanical strength [1]–[5].

Amorphous AlO_x is considered as a suitable gate dielectric in TFTs to avoid leakage current through crystalline grain boundaries [2]. In order to reduce the size of metal oxide semiconductor (MOS) transistors below 50 nm for next generation electronic devices, amorphous materials that are novel with high dielectric constant, high breakdown voltage, low leakage and low interface trap density values are needed [3]. AlO_x has a band gap and dielectric constant of 9.9 eV and 10 respectively compared to SiO_2 with band gap of 9 eV and dielectric constant of 3.9 [3].

M. Aguilar Frutis et al. [5] have investigated the effect of adding water to the AlO_x spray precursor solution on the optical properties of the film formed. The thin film from the addition of water mist showed the highest refractive index (~ 1.66), and lower content of -OH and water related bonds, while the AlO_x thin film without addition of water mist has low value of refractive index with presence of water related impurities and -OH bonds.

It was reported by J. Jun et al. [6] that hydration improves the properties of AlO_x films. They discovered that increase in dipping time of AlO_x films in deionized water increases the dielectric constant from 7.8 to 11.5 with no significant increase in leakage current. This effect is due to the structural change of the film surface from aluminum oxide to pseudo-boehmite after reaction with water. J. Kolodzey et al. [7] also confirmed the effect of difference in oxidation conditions, sublayer composition and structure in the variation of current-density characteristics.

With respect to the effect of atmosphere in which dielectric measurement is carried out, N. Koslowski et al. [8] revealed that dielectric measurements done in ambient temperature increases the capacitance significantly and affect parasitic resistance due to water molecules from the atmosphere adsorbed on the film surface. It was established that AlO_x films deposited by spin coating method at high humid conditions improves the electrical properties of the film by producing a smooth film surface, very low leakage current and higher breakdown voltage. At low humid conditions, spherulite structure in form of cracks are formed on the surface of the films leading to unfavorable dielectric properties [9]. WenWen et al. in their recent study reported that increasing annealing temperature of AlO_x film decreases the leakage current density of the film and vice versa. The reduced leakage current was attributed to the decrease in oxygen defect as Al-O bonding forms, and the large leakage current was due to the presence of hydroxyl group and residual organics which form the conduction paths. They also recorded a large dielectric value of 13.8 for low temperature annealed AlO_x film, which was ascribed to the large amount of hydroxyl group revealed by the XPS result [10].

According to our review, AlO_x thin films prepared by other deposition methods such as pulsed laser deposition (PLD) [3], chemical vapor deposition (CVD) [11], [12], plasma enhanced chemical vapor deposition (PECVD) [13], and plasma enhanced atomic layer deposition (PEALD) [14], [15] have been studied extensively, however, only limited research could be found on AlO_x thin films deposited by chemical spray pyrolysis. Of all these methods, the spray pyrolysis is considered to be optimal due to its simplicity and low-cost as it does not require a vacuum [16], its ease in doping, it doesn’t require a high quality target/substrate, it also offers an easy method of adjusting the deposition rate and film thickness by altering spray parameters [17].

In this paper, we focus on the deposition of AlO_x thin film by the USP method with the aim of studying the influence of varying deposition temperature and annealing temperature on the film’s structural, morphological and electrical properties for its application as a dielectric layer in thin film transistor technology.

2. METHODOLOGY

AlO_x films were deposited onto a preheated substrate of silicon and quartz with dimension 2 cm by 1 cm by ultrasonic spray pyrolysis (USP) technique. The substrates were cleaned in methanol, ethanol and deionized water in ultrasonic bath for 5 minutes each at 60 ^oC. The precursor solution of 250 ml volume with 0.05 M concentration were prepared by dissolving 4.50 g aluminum acetylacetonate ($Al(C_5H_7O_2)_3$) powder in methanol (CH_3OH) and the solution was stirred for 15 mins with a magnetic stirrer at room temperature to ensure homogeneity. The solution was atomized by an ultrasonic generator of 1.7 MHz frequency, and the generated aerosol was transported directly to the heated substrates using air as carrier. Films were deposited by spraying 50 ml solution of AlO_x with the same molar concentration at various substrate temperatures, (Ts) of 350 ^oC, 450 ^oC and 550 ^oC in air. The carrier gas flow rate and director gas flow rate for spraying the solution were 3 L/min and 1 L/min respectively. For the deposition, spray parameters were set as 3 steps, 10 cycles. Structural studies were carried out on the quartz substrate, while electrical studies were carried out on the silicon substrate.

The as-deposited AlO_x films on quartz and silicon substrates were annealed in air at temperatures of 500 ^oC, 800 ^oC, and 1000 ^oC for 1 hour using a Nabertherm L5/11/06D furnace. X-Ray diffraction (XRD) measurement was carried out with the RIKAGU ULTIMA IV diffractometer with Cu Kα radiation ($\gamma = 1.5406$ Å, 40 kV, 40 mA) using silicon strip detector D/tex Ultra. Sample measurement were taken in the 2ϴ range from 20–60 degree with a step of 0.02^{o} and scanning speed of 5 ^{o}/min.

The surface morphology, cross-sections were investigated with the aid of Zeiss HR FESEM Ultra 55 high-resolution scanning electron microscopy (SEM). The accelerated voltage for SEM measurement was 4.0 kV.

A metal-oxide semiconductor (MIS) with structure Al/AlOx/Si-C was fabricated for the purpose of electrical measurement by evaporating Aluminum electrode contact on the surface of the films with the help of Quorum K975X vacuum evaporator. A mask with uniform area 1.7 mm^{2} was used to cover the films before deposition. Graphite paste was applied on the back side of the device to improve ohmic conductivity, and measurement was carried out through both the graphite and Al. The I-V and impedance measurements were carried out using the AUTOLAB PGSTAT 30 equipment.

3. RESULTS AND DISCUSSIONS

3.1. Surface Morphology

Figure 1 shows the surface morphology and cross-section views of AlO_x films grown at 350 ^{o}C, 450 ^{o}C and 550 ^{o}C on quartz substrate. The surface of the films deposited were homogenous, well compacted, and smooth, with the presence of some random particles of about 100 nm size. According to Alexey et al. AlO_x thin film deposited by atomic layer deposition method also show smooth surface [18].

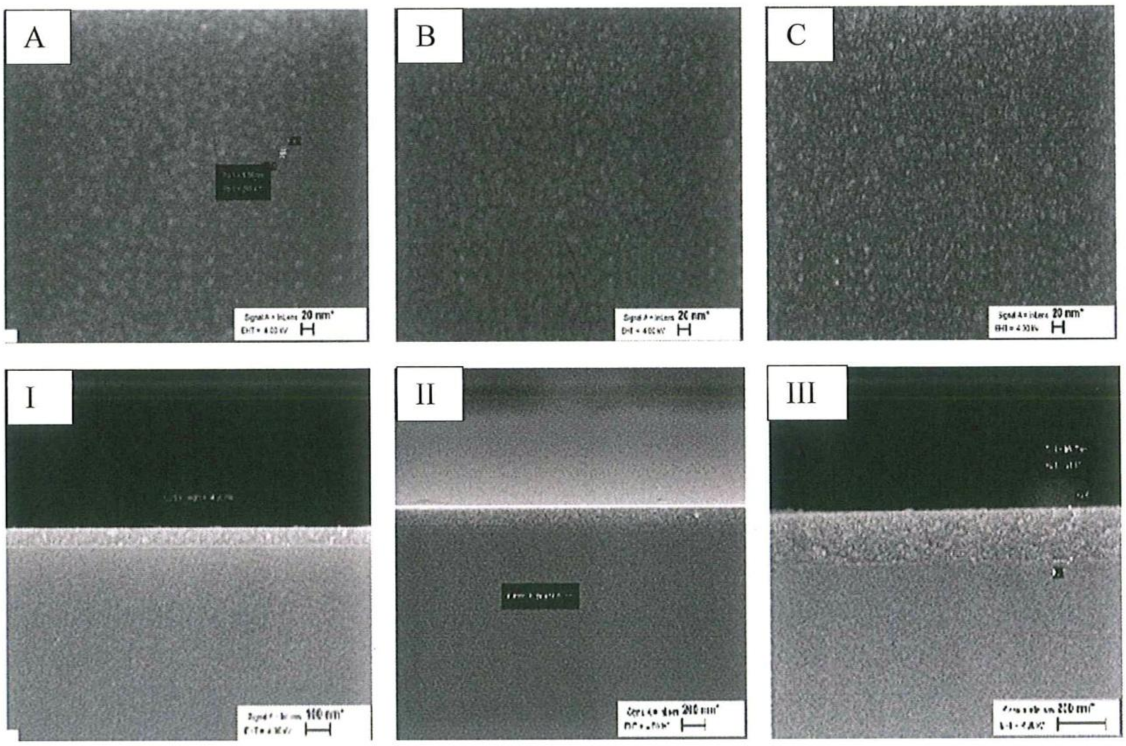

Fig. 1. SEM images with cross-section of 0.05 M concentration of AlO_x films as-deposited at 350 ^{o}C (A-I), 450 ^{o}C (B-II), and 550 ^{o}C (C-III)

The thicknesses of the films were estimated from the cross-sectional images shown in Fig. 1 (1-III). The obtained results revealed that the thicknesses of the films increase with increase in deposition temperature. The thickness of the film as-deposited at 350 ^{o}C is 54 nm, while the thickness of films as-deposited at 450 ^{o}C and 550 ^{o}C are 96 nm and 159 nm respectively.

3.2. Structural Studies

The X-ray diffractogram of AlO_x films as-deposited at 350 °C and 450 °C followed by annealing at 1000 °C on quartz substrates is shown in Figure 2. The X-ray diffractogram of the as-deposited AlO_x films and annealed AlO_x films at 500, and 800 °C show a similar pattern to the film annealed at 1000 °C below. No peaks are observed on the diffractogram, which proves that all the samples were amorphous with no degree of crystallinity in the films. Our result also corresponds with XRD measurements of AlO_x films in previous literatures that no sharp peak was observed for AlO_x film annealed until annealing temperature of 1000 °C [12], [10], [8].

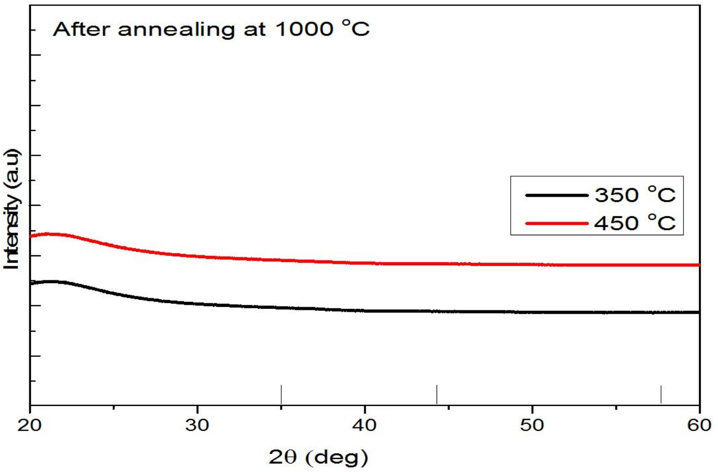

Fig. 2. X-ray diffractogram of AlO_x thin films as-deposited at 350 °C, 450 °C, and annealed at 1000 °C

3.3. Electrical Studies

3.3.1. Current-voltage characterisation

Electrical properties of the AlO_x films were characterized by constructing a capacitor of $Al/AlO_x/Si$ structure. Figure 3 shows the leakage current density in the forward bias and reverse bias regime (-2 V to +2 V). The current density at -1.0 V was estimated to be $9.5 \cdot 10^{-8}$ A/cm², $1.5 \cdot 10^{-5}$ A/cm², and $1.6 \cdot 10^{-6}$ A/cm² for AlO_x as-deposited at 350 °C, 450 °C, and 550 °C respectively. J. Jun et al. [6] reported a leakage current of $3.8 \cdot 10^{-4}$ A/cm² for as-deposited AlO_x thin film by metal organic chemical vapor deposition. Y. Koda et al. [20] also reported leakage current density of $3.6 \cdot 10^{-10}$ A/cm² for as-deposited AlO_x films. Our leakage current values are close to the values reported in previous literatures.

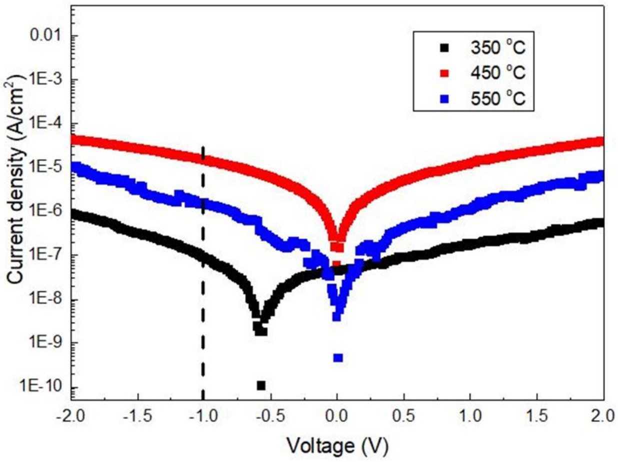

Fig. 3. Leakage current density for AlO_x thin films as-deposited at 350, 450, and 550 °C

It can be seen from the result that AlO_x thin film as-deposited at 350 ^oC has a very small leakage current. This small leakage current could be attributed to a smooth and compact surface of the sample due to the absence of grain boundaries which may act as leakage channel resulting in a large leakage current. Presence of Al-O bonding on the film surface as a result of film condensation at higher deposition temperature also decreases the leakage current of dielectric layer [10]. It also shows that 350 ^oC deposition temperature could presumably be sufficient to achieve a good dielectric with low leakage current by using USP technique.

The electrical resistivity ρ (Ω cm) of the AlO_x dielectric film was estimated from resistance R (Ω) using equation below.

$$\rho = R\,\frac{A}{L}, \tag{1}$$

where L is the thickness of the film, A is the contact area, and R is the resistance. The values for electrical conductivity was calculated by taking inverse of resistivity.

The resistivity values for the deposited AlO_x thin film at 350 ^oC, 450 ^oC and 550 ^oC are estimated to be $3.1\cdot10^4$ Ωcm, $1.6\cdot10^5$ Ωcm, and $3.9\cdot10^1$ Ωcm respectively. It can be observed that AlO_x thin films as-deposited at 350 ^oC has a large electrical resistivity among all the samples which could be as a result of its small thickness. The resistivity of the films increases with increasing deposition temperature from 350 ^oC to 450 ^oC.

3.3.2. Dielectric-characterisation

Capacitance value was extracted from the impedance and both the mean area capacitance and mean dielectric constants were estimated at different contacts for all working devices at different frequencies. The capacitance-frequency box plot for as-deposited AlO_x thin films on silicon substrates is shown in Figure 4. This plot shows the range of calculated area capacitance values for all the samples at different frequencies of 1 kHz, 10 kHz, and 100 kHz. It is seen that capacitance of AlO_x film as-deposited at 350 ^oC decreases with increase in the frequency. This phenomenon of reduced capacitance at high frequency is linked to the presence of trap states in dielectric films which prevents the film from acquiring enough speed needed to match higher frequencies [21]. On the other hand, capacitance values for AlO_x as-deposited at 450 ^oC and 550 ^oC were relatively stable across the frequency range. The variation in capacitance could be attributed to the presence of hydroxyl groups in the AlO_x films. Large amount of hydroxyl groups could lead to significant decrease in capacitance and vice versa [10]. The Capacitance (C) of the samples was estimated from equation below.

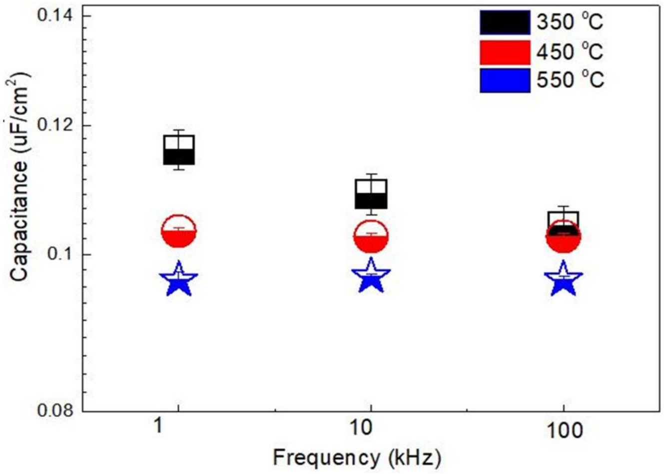

Fig. 4. Capacitance-Frequency plot for the AlO_x as-deposited on Si at 350, 450 and 550 ^oC

$$C = \frac{1}{2\pi f Z"}, \tag{2}$$

where f is the frequency, Z” is the imaginary impedance, π is a constant = 3.1415.

AlO_x film as-deposited at 350 °C, 450 °C, and 550 °C at 1 kHz exhibited mean capacitance values of 116 nF/cm^2, 57 nF/cm^2, and 36 nF/cm^2 respectively. Area capacitance reported by Wenwen et al. [10] for annealed AlO_x films were in the range of 72.2–120.6 nF/cm^2. It was also observed that the capacitance values decrease with increase in deposition temperature.

Figure 5 shows the dependence of dielectric constant on frequency for as-deposited AlO_x samples on silicon substrates. It was found that the sample as-deposited at 350 °C has a large dielectric constant value of approximately 7.4 at 1 kHz. Reported values of dielectric constant for as-deposited AlO_x films are in the range of 7–10 [22], [23]. At higher frequency dispersion, mean dielectric constant for sample as-deposited at 350 °C is almost equal to that of the sample as-deposited at 550 °C.

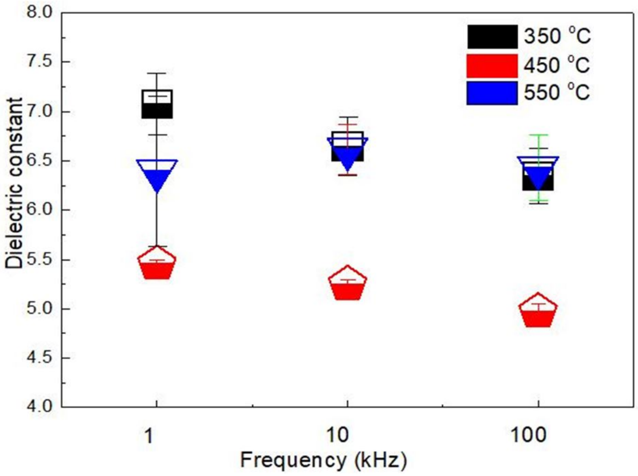

Fig. 5. Dielectric-Frequency plot for the AlO_x as-deposited on Si at 350, 450 and 550 °C

Dielectric constant, k was determined using the following equation:

$$C = \frac{\varepsilon_o k A}{d}, \tag{3}$$

where C is the capacitance, ε_o is permittivity of free space, k is the dielectric constant, A is the contact area, d is the AlO_x film thickness.

Table 1. Summary of the average dielectric constant values and area capacitance at 1kHz for all the as-deposited samples

As-deposited Samples (°C)	**Area (cm^2)**	**Mean dielectric constant @ 1kHz**	**Area Capacitance (nF/cm^2) @1kHz**
350	0.017	7.4	116
450	0.017	5.6	57
550	0.017	6.5	36

4. CONCLUSIONS

The ultrasonic spray pyrolysis method was successfully used to deposit smooth and homogenous AlO_x thin films of 0.05 M concentration at deposition temperatures of 350 °C, 450 °C and 550 °C on silicon and quartz substrates. The SEM images reveal that the AlO_x samples as-deposited were smooth, homogenous and compact. Film thickness increases with deposition temperature. XRD data shows that the as-deposited films were amorphous. Further annealing at 500 °C, 800 °C and 1000 °C shows amorphous films with no diffraction peak observed. The films were highly resistive with high dielectric constant in the range of 7.4–5.5 depending on the deposition temperature (350–550 °C). The results indicated that AlO_x thin films deposited by ultrasonic spray pyrolysis is suitable as a gate dielectric layer in thin film transistor application.

ACKNOWLEDGEMENTS

The authors acknowledge V. Mikli for SEM measurements. This study was financially supported by the Estonian Ministry of Education and Research, project IUT19-4, and by the European Union through the European Regional Development Fund, project TK141 ‘Advanced materials and high technology devices for energy recuperation systems’.

REFERENCES

1. NILAI, P., SEMBILAN, N. “International Journal of Chemical Preparation of Nanocrystalline Aluminum Oxide Thin Films : A Review,” vol. 15, no. 2, pp. 1–8, 2018.
2. CUI, J. *et al.* “Aluminum Oxide Thin Films from Aqueous Solutions: Insights from Solid-State NMR and Dielectric Response,” *Chem. Mater.*, vol. 30, no. 21, pp. 7456–7463, 2018.
3. KATIYAR, P., JIN, C., and NARAYAN, R.J. “Electrical properties of amorphous aluminum oxide thin films,” vol. 53, pp. 2617–2622, 2005.
4. GUZMAN-MENDOZA, J. et al. “Structural characteristics of Al 2 O 3 thin films prepared by spray pyrolysis Structural characteristics of Al 2 O 3 thin films prepared by spray pyrolysis,” vol. 13, no. 111, pp. 955–959, 2001.
5. AGUILAR-FRUTIS, M., GARCIA, M., FALCONY, C., PLESCH, G., and JIMENEZ-SANDOVAL, S. “A study of the dielectric characteristics of aluminum oxide thin films deposited by spray pyrolysis from Al Ž acac . 3,” pp. 200–206, 2001.
6. JUN, J. H., KIM, H. J., and CHOI, D. J. “Processing Research Effect of the hydration on the properties of an aluminum oxide film,” vol. 9, no. 1, pp. 75–78, 2008.
7. KOLODZEY, J. *et al.* “Electrical Conduction and Dielectric Breakdown in Aluminum Oxide Insulators on Silicon,” vol. 47, no. 1, pp. 121–128, 2000.
8. KOSLOWSKI, N., SANCTIS, S., and SCHNEIDER, J. “a thin film transistor device of amorphous aluminum oxide Al x O y using a molecular based precursor route †,” pp. 33–36, 2019.
9. HUH, J. *et al.* “Journal of Industrial and Engineering Chemistry Effects of process variables on aqueous-based AlO x insulators for high-performance solution-processed oxide thin- film transistors,” vol. 68, pp. 117–123, 2018.
10. XIA, W., XIA, G., TU, G., DONG, X., WANG, S., and LIU, R. “Sol-gel processed high- k aluminum oxide dielectric films for fully solution- processed low-voltage thin- film transistors,” *Ceram. Int.*, vol. 44, no. 8, pp. 9125–9131, 2018.
11. MARUYAMA, T. and ARAI, S. “Aluminum oxide thin films prepared by chemical vapor deposition from aluminum acetylacetonate Aluminum oxide thin films prepared from aluminum acetylacetonate by chemical vapor deposition,” vol. 322, no. 1992, pp. 1998–2000, 2013.
12. KIYOTO Lida. “Physical and Chemical Properties of Aluminum Oxide Film Deposited by Iida_1972_Jpn._J._Appl._Phys._11_840.pdf.” Japanese Journal of Applied Physics, 1972.
13. KALAIVANI, S. and KOTTANTHARAYIL, A. “Spray Coated Aluminum Oxide Thin Film For P-type Crystalline Silicon Surface Passivation,” pp. 8–11, 2015.
14. LALE, A., SCHEID, E., CRISTIANO, F., DATAS, L., and REIG, B. “Study of aluminium oxide thin films deposited by plasma-enhanced atomic layer deposition from tri-methyl-aluminium and dioxygen precursors : Investigation of interfacial and structural properties,”

vol. 666, no. December 2017, pp. 20–27, 2018.

15. LI, H. Y., LIU, Y. F., DUAN, Y., YANG, Y. Q., and LU, Y. N. “Method for aluminum oxide thin films prepared through low temperature atomic layer deposition for encapsulating organic electroluminescent devices,” *Materials (Basel).*, vol. 8, no. 2, pp. 600–610, 2015.
16. FALCONY, C., AGUILAR-FRUTIS, M. A., and GARCIA-HIPOLITO, M. “Spray pyrolysis technique; High-K dielectric films and luminescent materials: A review,” *Micromachines*, vol. 9, no. 8, pp. 1–33, 2018.
17. PATIL, P. S. “Versatility of Chemical Spray Pyrolysis Technique,” *Mater. Chem. Phys.*, vol. 59, pp. 185–198, 2010.
18. DRONOV, A. A, DRONOVA, D. A., KIRILENKO, E. P., TERASHKEVICH, I. M., and GAVRILOV, S. A. “Studying Composition of Al 2 O 3 Thin Films Deposited by Atomic Layer Deposition (ALD) and Electron-Beam Evaporation (EBE) upon Rapid Thermal Processing,” vol. 12, no. 4, pp. 428–433, 2017.
19. RAVINDHRANATH, K., RAMAMOORTY, M., “nano aluminum oxides as adsorbents in water remediation methods : a review,” vol. 10, no. 3, pp. 716–722, 2017.
20. KODA, Y., SUGITA, H., SUWA, T., KURODA, R., GOTO, T., TERAMOTO, A., SUGAWA, S. “Low Leakage Current Al 2 O 3 Metal-Insulator-Metal Capacitors Formed by Atomic Layer Deposition at Optimized Process Temperature and O 2 Post Deposition Annealing Y. Koda,” *E C S Trans. Electrochem. Soc.*, vol. 72, no. 4, pp. 91–100, 2016.
21. KIM, J., CHOI, S., KIM, M., HA, T., and KIM, Y. “Strontium doping e ff ects on the characteristics of solution-processed aluminum oxide dielectric layer and its application to low-voltage-operated indium-gallium-zinc-oxide thin- fi lm transistors,” *Ceram. Int.*, vol. 43, no. 16, pp. 13576–13580, 2017.
22. LEE, J., KIM, S. S., IM, S., LEE, J., KIM, S. S., and IM, S. “Electrical properties of aluminum oxide films deposited on indium-tin-oxide glasses Electrical properties of aluminum oxide films deposited on indium-tin-oxide glasses,” vol. 953, no. 2003, pp. 2–6, 2015.
23. VOIGT, M., SOKOLOWSKI, M. “Electrical properties of thin rf sputtered aluminum oxide films,” pp. 1–5, 2004.

CYSENI 2019, May 23-24, Kaunas, Lithuania
ISSN 1822-7554, www.cyseni.com

TEMPERATURE DEPENDENCE OF RAMAN SPECTRA OF $Cu_2ZnSnSe_4$ THIN FILMS

E. E. Venhlinskaya, M. S. Tivanov, O. V. Korolik
Belarusian State University
Nezavisimosti av. 4, 220030, Minsk – Belarus
Email: venglinskaya.e@gmail.com

V. F. Gremenok, A. V. Stanchik
Scientific and Practical Materials Research Centre, National Academy of Sciences,
P. Browka 19, 220072, Minsk – Belarus

R. L. Juškėnas
State Research Institute "Center for Physical Sciences and Technology",
Sauletekio av. 3, 10222 Vilnius – Lithuania

ABSTRACT

For CZTSe tetragonal structured film prepared by selenization of layer-by-layer and pre-annealed Cu-Zn-Sn metal precursor on flexible Ta substrate, temperature dependencies of the position and full width at a half maximum for the A-modes (171 and 195 cm^{-1}) were obtained in the 24–290 K temperature range and were successfully approximated by the linear and Klemens model equations. From the obtained dependencies, the coefficients of the Klemens equations, as well as the temperature coefficients for Raman shifts and peak widths were calculated.

Keywords: $Cu_2ZnSnSe_4$, CZTSe, thin film, Raman spectroscopy, temperature dependence

1. INTRODUCTION

Nowadays, copper zinc tin chalcogenides are promising materials for solar cells application. $Cu_2ZnSnSe_4$ (CZTSe) and Cu_2ZnSnS_4 (CZTS) consist of abundant and innocuous elements [1, 2]. The optical absorption coefficients of such materials are rather high and about 10^4 cm^{-1} [3]. Both CZTSe and CZTS are p-type direct band semiconductors [4]. Moreover, these materials have optimal bandgap values for solar cells application: 1.0 eV for CZTSe and 1.5 eV for CZTS [5]. The efficiency of 11.6% was obtained for CZTSe solar cells so far [6], while its theoretical efficiency is about 30% [7], which points to necessity of further development of synthesis technologies to achieve better efficiency of CZTSe.

In this work, the temperature dependent Raman spectroscopy was used to obtain fundamental knowledge on temperature behaviour of CZTSe films with tetragonal structure. This method is a unique technique to study the temperature behaviour of materials [8], for example, thermal conductivity, as thermal and electrical properties of CZTSe films are affected by anharmonic phonon-phonon interactions. The change of frequency and line width of phonon with respect to temperature can provide valuable insights regarding anharmonicity of vibration [9]. There are a few articles on temperature-dependent Raman spectroscopy of CZTSe films, so this area is still poorly investigated.

In this work, the temperature dependence of the position and full width at a half maximum (FWHM) for Raman peaks of CZTSe films were investigated in the temperature range of 24–290 K. Such range temperatures has been chosen for better aproximation and subsequent interpolation to 0 K to obtain the FWHM and peak positions for harmonic vibrations. Linear and Klemens models were used to approximate the obtained dependencies. The coefficients in equations of the Klemens model, as well as temperature coefficients for position and FWHM of Raman peaks were calculated.

2. EXPERIMENTAL

The CZTSe film was produced by selenizing Cu–Zn–Sn precursors on Ta foil substrate. The Cu–Zn–Sn precursor was deposited in the sequence of Cu/Sn/Cu/Zn layers from corresponding solutions of metal sulfates in the galvanostatic mode. Preliminary annealing was conducted in 95% Ar + 5% H_2 atmosphere (350 °C, 30 min), and the selenization process was hold in a quartz container (with a volume of 12.5 ml) with 5 mg of Se powder (580 °C, 30 min, Ar pressure of 1 bar).

The chemical composition of the CZTS film was investigated by X-ray Spectral Microanalysis (XRS) using CAMECA SX-100 setup. The phase composition of CZTSe film was analysed using X-ray diffraction (XRD) and Raman spectroscopy. An Ultima IV X-ray diffractometer (Rigaku) with monochromatic CuKα radiation (λ = 0.15406 nm) was used, scanning was done in the 25° to 70° range. Raman spectra were obtained using a Nanofinder HE (LOTIS TII) confocal spectrometer (excitation wavelength of 532 nm, incident laser power of 3 mW, laser spot diameter of 1.5 μm, spectral resolution better than 0.7 cm^{-1}). Raman spectra were measured in the range of temperatures of 24–290 K. During these measurements, the sample was placed in a vacuum temperature-controlled cell (pressure less than 5×10^{-4} Pa, temperature setting accuracy of 0.05 K).

3. RESULTS AND DISCUSSION

The results of XRS is presented in Table 1. The obtained film CZTSe is Cu-poor and Zn-rich. These conditions are favourable for CZTSe solar cells [10].

Table 1. The elemental composition of CZTSe thin film on Ta foil

Elemental composition, at. %				**Atomic ratio, arb. u.**	
Cu	Zn	Sn	Se	Cu/(Zn + Sn)	Zn/Sn
22.09	18.53	10.83	48.54	0.75	1.71

The XRD pattern of CZTSe film on flexible Ta foil (Fig. 1) shows the most intensive peak at 2θ = 27.2° of CZTSe tetragonal phase (JCPDF 52-0868) with preferred (112) orientation.

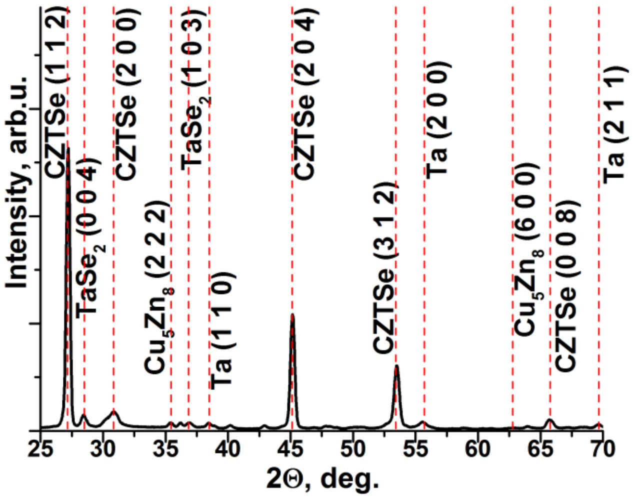

Fig. 1. XRD pattern of CZTSe thin film

The XRD analysis demonstrates that the film mainly consists of CZTSe tetragonal phase (2θ = 27.2° (112), 30.9° (200), 45.2° (204), 53.5° (312) and 65.8° (008)). Some reflexes corresponding to $TaSe_2$ (JCPDF 24-1257) at 2θ = 28.5° (004) and 36.9° (103), Cu_5Zn_8 (JCPDF 65-3157) at 2θ = 35.4° (222) and 62.9° (600), and Ta (JCPDF 89-5158) at 2θ = 38.5° (110), 55.6° (200) and 69.6° (211) are also observed.

Raman spectra reveal that the film consists of CZTSe phase (Figs. 2, 3), as two A-modes of CZTSe at 171 cm^{-1} (1A-mode) and at 195 cm^{-1} (2A-mode) [11] are observed. Modes at 80 cm^{-1} and at 235 cm^{-1} also correspond to CZTSe phase [12]. These data is in agreement with the XRD analysis.

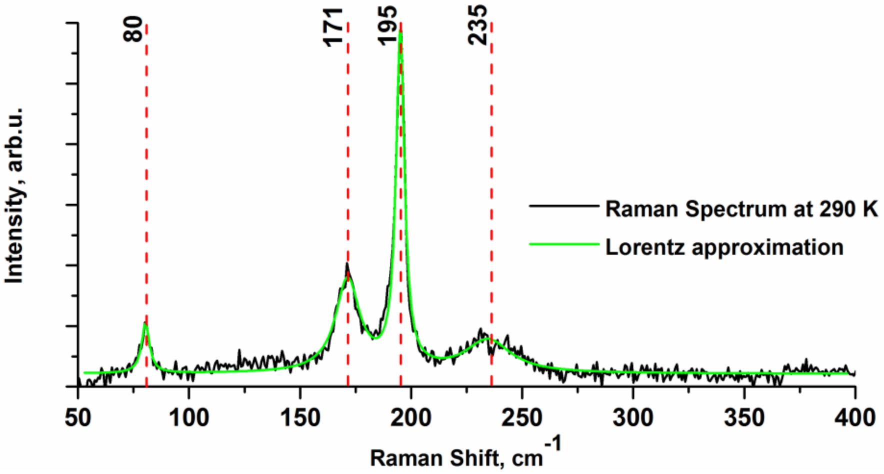

Fig. 2. Raman spectrum of CZTSe film on Ta foil at 290 K

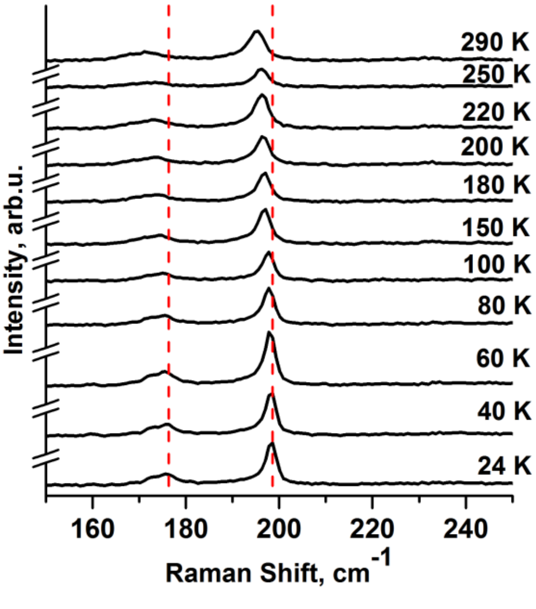

Fig. 3. Raman spectra of CZTSe film on Ta foil in the range of temperatures of 24–290 K

For precise determination of the FWHM and peak position for both A-modes, we used peak approximation with a single Lorentz function for each temperature point.

The temperature dependencies of FWHM and peak position were analyzed by the approximation with the linear model and the Klemens model equations presented below.

According to the linear model, the temperature dependencies of peak position and FWHM can be described with the equations (1) and (2) [13]:

$$\omega(T) = \omega_0 + \chi_{RS} T, \quad (1)$$

$$\Gamma(T) = \Gamma_0 + \chi_{FWHM} T, \tag{2}$$

where ω_0 is the harmonic optical phonon frequency at T = 0 K, Γ_0 is the FWHM for peak at T = 0 K, χ_{RS} and χ_{FWHM} are the temperature coefficients for Raman shift and FWHM, respectively.

The values of ω_0 and Γ_0 were obtained by extrapolation of ω and Γ temperature dependencies to T = 0 K (Fig. 4).

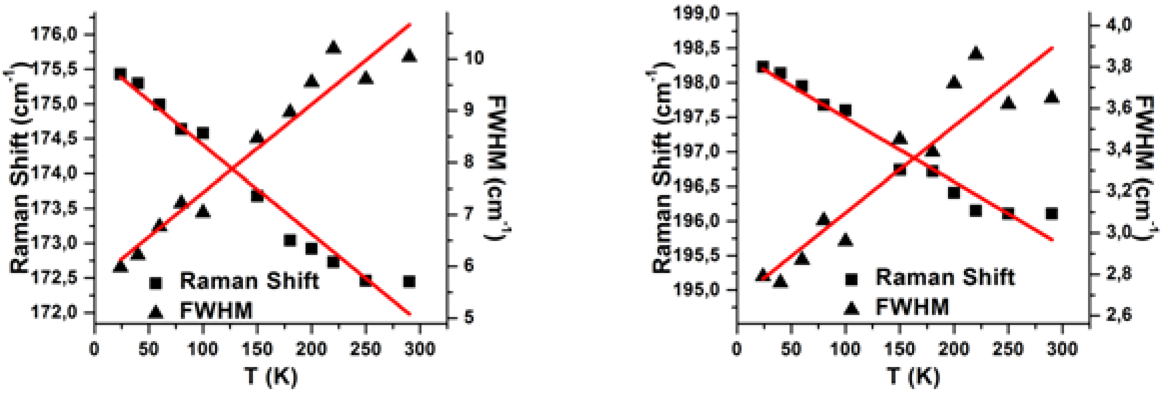

(1A) (2A)

Fig. 4. Linear approximations for temperature dependencies of peak position and FWHM in CZTSe Raman spectra for 1A and 2A modes

The temperature coefficients for Raman shift and FWHM were calculated too. Calculated values are listed in Table 2.

Table 2. The calculated values of ω_0, Γ_0, χ_{RS}, and χ_{FWHM}

Mode	**ω_0, cm^{-1}**	**Γ_0, cm^{-1}**	**χ_{RS}, cm^{-1}/K**	**χ_{FWHM}, cm^{-1}/K**
1A	175.8	5.4	-0.0128	0.0170
2A	198.5	2.6	-0.0093	0.0954

The linear approximation of FWHM and peak position temperature dependencies shows that χ_{RS} for 1A-mode is bigger than χ_{RS} for 2A one. At the same time, χ_{FWHM} is much bigger for the 2A-mode.

It is widely known that two effects influence the temperature dependency of Raman spectrum: the thermal expansion and the anharmonic coupling to phonons of other branches. Typically, the Klemens model takes into account phonon-phonon interactions and thermal expansion of the film and substrate [14]. Such calculations have been already done for graphene [15], molybdenum disulfide [16] and some other materials. We neglected the thermal expansion coefficients of the film and substrate as these layers were rather thick: CZTSe film had the thickness of about 1 µm, as it was shown in [17].

It is assumed in the Klemens model that one phonon Ph_{0i} decays into two phonons Ph_{q1} and Ph_{-q2} which satisfy the energy conservation law ($\omega_{0i} = \omega_1 + \omega_2$, $\omega_1 = \omega_2 = \omega_{0i}/2$), and the wavevectors meet the condition of $0 = q_1 + q_2$ in three phonon-process. The four-phonon process corresponds to the coupling of optical mode with three identical phonons ($\omega_1 = \omega_2 = \omega_3 = \omega_{0i}/3$) [18–20].

The temperature dependent Raman shifts $\omega_d(T)$ of 1A and 2A modes were described as

$$\omega_d(T) = \omega_0 + \Delta\omega_{ph-ph}, \tag{3}$$

where $\Delta\omega_{ph-ph}$ is the shift in peak position [15].

$$\Delta\omega_{ph-ph} = A\left[1 + \frac{2}{e^{\frac{\hbar\omega}{2k_BT}}-1}\right] + B\left[1 + \frac{3}{e^{\frac{\hbar\omega}{3k_BT}}-1} + \frac{3}{\left(e^{\frac{\hbar\omega}{3k_BT}}-1\right)^2}\right], \tag{4}$$

where A and B are the anharmonic constants related to three- and four-phonon processes, respectively, k_B is the Boltzmann constant, $\hbar$ is the reduced Planck constant, and ω is the frequency [16]. The Klemens model approximations of $\omega_d(T)$ for 1A and 2A modes are presented in Fig. 5.

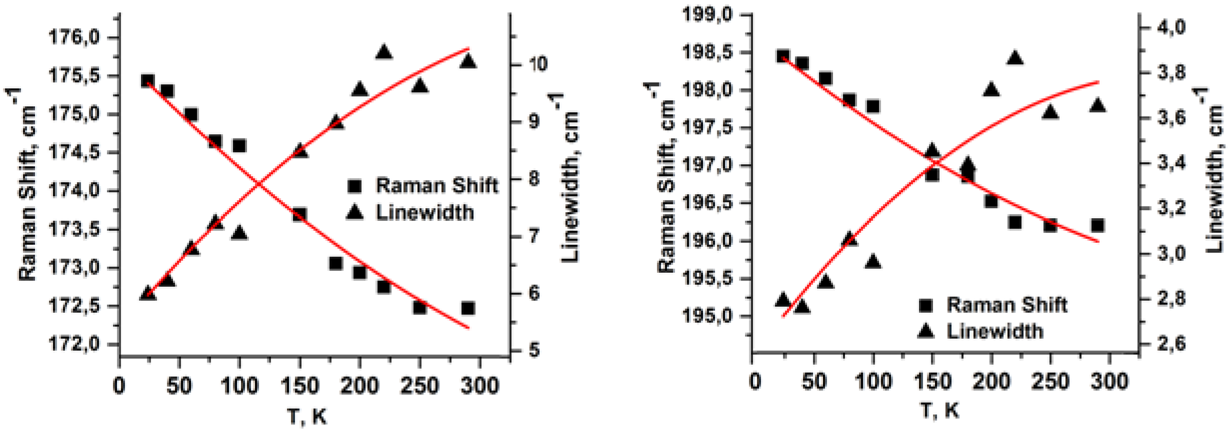

(1A) (2A)

Fig. 5. Klemens model approximations for temperature dependencies of peak position and FWHM in CZTSe Raman spectra for 1A and 2A modes

The temperature dependent Raman peak broadening was described according to the Klemens model:

$$\Gamma_d(T) = \Gamma_0 + \Delta\Gamma_{ph-ph}, \tag{5}$$

here $\Delta\Gamma_{ph-ph}$ is the peak broadening which can be calculated according to the following equation:

$$\Delta\Gamma_{ph-ph} = C\left[1 + \frac{2}{e^{\frac{\hbar\omega}{k_BT}}-1}\right] + D\left[1 + \frac{3}{e^{\frac{\hbar\omega}{3k_BT}}-1} + \frac{3}{\left(e^{\frac{\hbar\omega}{3k_BT}}-1\right)^2}\right], \tag{6}$$

where C and D are the anharmonic constants related to three- and four-phonon decay processes, respectively [9]. The Klemens model approximations of $\Gamma_d(T)$ for 1A and 2A modes are presented in Fig. 5.

The A, B, C and D coefficients calculated within the framework of the Klemens model according to equations (4) and (6) are listed in Table 3.

Table 3. The calculated values of the Klemens model coefficients

Mode	A	B	C	D
1A	-0.1354	$-2.9026 \cdot 10^{-4}$	0.0118	$5.3039 \cdot 10^{-7}$
2A	-0.1100	$-3.5612 \cdot 10^{-4}$	0.0014	$5.2566 \cdot 10^{-8}$

The values of B and D coefficients are much smaller than A and C demonstrating that three-phonon process has dominant contribution in damping and, as a consequence, in changes of Raman spectrum with temperature.

It was revealed that the temperature dependencies of Raman shift and FWHM for 1A and 2A modes of CZTSe film on Ta foil have non-linear character, as these dependencies are better approximated with the Klemens model than with the linear one.

From the results obtained it was shown that position of Raman peaks decreases, as well as their FWHM increases with temperature for both A-modes of CZTSe. The same effects were observed for CZTS in [9]. For the investigated CZTSe film, the peak shiftings were 2.12 cm^{-1} for 2A mode and 2.98 cm^{-1} for 1A mode. The broadenings were 0.86 cm^{-1} for 2A mode and 4.06 for 1A mode when the temperature changes from 24 to 290 K.

The FWHM of Raman peak is inversely proportional to the phonon lifetime/phonon relaxation time [14]. It means that the phonon lifetime or phonon relaxation time for CZTSe semiconductor decreases with temperature.

4. CONCLUSION

The temperature dependencies of position and FWHM of Raman lines were studied for CZTSe film on Ta foil in the range of 24–290 K. It was shown that the dependencies are non-linear and can be better approximated using the Klemens model for three- and four- phonon processes. The temperature coefficients of peak position and FWHM were calculated for both A-modes of CZTSe. The calculated values are negative for peak positions and positive for peak FWHM for both modes. It means that the peaks shift to the region of lower Raman shifts and their FWHM becomes higher with temperature increasing in the range of 24–290 K. For the investigated CZTSe film, the peak shifts were 2.12 cm^{-1} for 2A mode and 2.98 cm^{-1} for 1A mode. The broadenings were 0.86 cm^{-1} for 2A mode and 4.06 cm^{-1} for 1A mode. The values of the coefficients in the Klemens equations showed that three-phonon process had dominant contribution in changes of Raman spectra.

REFERENCES

1. FAN, P., Zhao, J., LIANG, G., Gu, D., Zheng, Z., Zhang, D., Cai, X., Luo, J., Ye, F. Effects of annealing treatment on the properties of CZTSe thin films deposited by RF-magnetron sputtering. *J Alloy Compd*., 2015, Vol. 625, p. 171–174.
2. GAO, S., JIANG, Z., WU, L., AO, J., ZENG, Y., SUN, Y., ZHANG, Y. Interfaces of high-efficiency kesterite $Cu_2ZnSnS(e)_4$ thin film solar cells. *Chin. Phys. B.*, 2018, Vol. 27, No. 1, p. 018803-1–018802-17.
3. GUO, T., YU, Z., LIU, L., ZHAO, Y., ZHANG, Y. Effects of both deposition and selenization temperature on the properties of one-step RF sputtered CZTSe layer. *Vacuum*, 2017, Vol. 145, p. 217–224.
4. CHANDEL, T., ZAMAN, M. Burhanuz, BASU, N., LAHIRI, J., POOLLA, R. Growth and Properties of Solvothermally derived CZTSe Nanocrystals using Elemental Precursors. *Physica B*, 2018, Vol. 545, p. 262–267.
5. CLAUWAERT, K., BINNEMANS, K., MATTHIJS, E., FRANSAER, J. Electrochemical studies of the electrodeposition of copper-zinc-tin alloys from pyrophosphate electrolytes followed by selenization for CZTSe photovoltaic cells. *Electrochimica Acta*, 2016, Vol. 188, p. 344–355.
6. PULGARÍN-AGUDELO, F.A., VIGIL-GALÁN, O., NICOLÁS-MARÍN, M.M., COUREL, M., GONZÁLEZ, R., MENDOZA-LEON, H., VELUMANI, S., ROHINI, M., ANDRADE-ARVIZU, J. A., OLIVA, F., IZQUIERDO-ROCA, V. Preparation and characterization of $Cu_2ZnSnSe_4$ and $Cu_2ZnSn(S,Se)_4$ powders by ball milling process for solar cells application. *Mater Res Express*, 2017, Vol. 4, No. 12, p. 125501-1–125501-27.

7. MALERBA, C. Cu_2ZnSnS_4 thin films and solar cells: material and device characterisation. Ph. D. Thesis, 2014, 183 p.
8. WU, Y., An, M., XIONG, R., SHI, J., Zhang, Q.M. Raman scattering spectra in the normal phase of 2H–$NbSe_2$, *J. Phys. D: Appl. Phys*., 2008, Vol. 41, p.175408-1–175408-5.
9. SARSWAT, Prashant K., FREE, Michael L., TIWARI, Ashutosh. Temperature-dependent study of the Raman A mode of Cu_2ZnSnS_4 thin films. *Phys. Status Solidi*, 2011, Vol. 248, No. 9, p. 2170–2174.
10. DAS, S., MANDAL, K.C., BHATTACHARYA, R.N., Earth-Abundant $Cu_2ZnSn(S,Se)_4$ (CZTSSe) Solar Cells. *Springer Series in Materials Science: Semiconductor Materials for Solar Photovoltaic Cells*, 2016, Vol. 218, p. 25–74.
11. DJEMOUR, R., REDINGER, A., MOUSEL, M., GUTAY, L., FONTANE, X., IZQUIERDO-ROCA, V., PEREZ-RODRIGUEZ, A., SIEBENTRITT, S. The three A symmetry Raman modes of kesterite in $Cu_2ZnSnSe_4$. *Optics Express*, 2013, Vol. 21, p. A695–A703.
12. JUSKENAS, R., NIAURA, G., MOCKUS, Z., KANAPECKAITE, S., GIRAITIS, R., KONDROTAS, R., NAUJOKAITIS, A., STALNIONIS, G., PAKSTAS, V., KARPAVICIENE, V. XRD studies of an electrochemically co-deposited Cu-Zn-Sn precursor and formation of a $Cu_2ZnSnSe_4$ absorber for thin-film solar cells. *J Alloy Compd*., 2016, Vol. 655, p. 281–289.
13. LU, D., LUO, S., LIU, S., YAO, H., REN, X., ZHOU, W., TANG, D., QI, X., ZHONG, J. Anomalous Temperature-dependent Raman Scattering of Vapor Deposited 2D Bi Thin Films. *J. Phys. Chem. C*, 2018, Vol. 122, No. 42, p. 24459–24466.
14. WANG, D., ZHAO, J., CHEN, B., ZHU, C. Lattice vibration fundamentals in nanocrystalline anatase investigated with Raman scattering. *J. Phys.: Condens. Matter*, 2008, Vol. 20, p. 085212-1–085212-8.
15. KOLESOV, Egor A., TIVANOV, Mikhail S., KOROLIK, Olga V., KAPITANOVA, Olesya O., DONG CHO, H., WON KANG, T., PANIN, Gennady N. Phonon anharmonicities in supported graphene. *Carbon*, 2019, Vol. 141, p. 190–197.
16. NAJMAEI, S., AJAYAN, Pulickel M., LOU, J. Quantitative analysis of the temperature dependency in Raman active vibrational modes of molybdenum disulfide atomic layers. *Nanoscale*, 2013, No. 5, p. 9758–9763.
17. STANCHIK, A.V., GREMENOK, V.F., BASHKIROV, S.A., TIVANOV, M.S., JUSKENAS, R.L., NOVIKOV, G.F., GIRAITIS, R., SAA, A.M. Microstructure and Raman scattering of Cu_2ZnSnS_4 thin films deposited onto flexible metal substrates. *Semiconductors*, 2018,Vol. 52, No. 2, p. 215–220.
18. LUCAZEAU, G. Effect of pressure and temperature on Raman spectra of solids: anharmonicity. *J. Raman Spectrosc.*, 2003, No. 34, p. 478–496.
19. ZHAO, Z., ELWOOD, J., CARPENTER, Michael A. Phonon Anharmonicity of PdO Studied by Raman Spectrometry. *J. Phys. Chem. C*, 2015, No. 119, p. 23094–23102.
20. TAUBE, A., ŁAPIŃSKA, A., JUDEK, J., WOCHTMAN, N., ZDROJEK, M. Temperature induced phonon behaviour in germanium selenide thin flms probed by Raman spectroscopy. J. *Phys. D: Appl. Phys*., 2016, Vol. 49, 315301-1–315301-7.

CYSENI 2019, May 23-24, Kaunas, Lithuania
ISSN 1822-7554, www.cyseni.com

CHARACTERISATION OF SPRAY PYROLYSIS SnO_2 THIN FILMS FOR PHOTOVOLTAIC APPLICATIONS

V. Nwaokolo, A. Katerski
Laboratory of Thin Film Chemical Technologies, Department of Materials Science,
Tallinn University of Technology,
Ehitajate tee 5, 19086 Tallinn – Estonia.
Email:crispviv@yahoo.com

ABSTRACT

Due to its unique electronic and optical properties, tin oxide has gained much attention in the field of photovoltaics. This research offers to determine the best conditions for the improvement of component layer in solar cell structure. SnO_2 thin films were synthesized by ultrasonic spray pyrolysis (USP) onto glass substrates at various deposition temperatures (between 300 and 500 °C) using anhydrous $SnCl_4{\cdot}4H_2O$ as a precursor. The films were investigated for structural, optical and electrical properties using X-ray diffraction (XRD), UV-VIS NIR spectrophotometry, hot probe and I-V measurement respectively. All the films display high transmittance in the visible region with average transmittance varying from 75 to 85%. XRD analysis showed the polycrystalline nature of our samples. Crystallite size increased from 1.6 nm to 36 nm with increasing deposition temperature. Resistivity decreased from $200{\cdot}10^3$ Ohmcm to $78{\cdot}10^3$ Ohmcm with increasing temperature.

Keywords: Thin films, Chemical spray pyrolysis, Spray rate, SnO_2

1. INTRODUCTION

Tin dioxide (SnO_2) has gained much attention in the field of photovoltaics and optoelectronics due to the optical bandgap (3.6 eV), electrical properties (high conductivity and mobility), useful structure, abundance, mechanical hardness, thermal stability in oxidizing environments at high temperature and chemical stability [1, 2]. They are generally regarded as an oxygen deficient n-type oxide semiconductor. Doped with fluorine SnO_2 (FTO) can be used as a transparent conductive oxide in solar cells [3]. This material is more stable and useful for electrode material in solar cells compared to Indium-Tin-Oxide (ITO) [4].

In this paper, we are looking at the various possibilities of using undoped SnO_2 to improve our glass/ITO/TiO_2/SbS_3/back contact solar cell configuration. One of such possibilities is the use of SnO_2 thin films in the window layer (TiO_2) owing to its better optical properties or as an intermediate buffer layer between the ITO/TiO_2 layer of our solar cell [5]. This is because the conductivity of SnO_2 can be easily managed. Additionally, due its useful band structure, high transmittance and stability, they could be used to replace component parts or act as a buffer layer between the front contact electron transport material (ETM) or between the ETM and absorber [6, 7]. A broad range of studies has been done in the implementation of SnO_2 thin polycrystalline films in Perovskite solar cells (PSC) [6–9]. Xiong et al noted a higher efficiency of 20.79% [6]. Hagfeldt and co-workers developed a chemical bath post- treatment SnO_2 PSCs that yielded efficiencies of close to 21%. An impressive certified record efficiency of 20.9% has been achieved by You and co-workers with SnO_2 nanoparticle planar PSCs. Due to this feat, we intend to use SnO_2 to improve our solar cell configuration.

Various types of techniques have been used for the deposition of SnO_2 such as ultrasonic spray pyrolysis (USP) [2, 10], sol-gel method [11], chemical spray pyrolysis [13]. D. Jadsadapattarakul et al reported the microstructure of SnO_2 thin films deposited by ultrasonic spray pyrolysis technique [2]. Sehrish et al investigated the photovoltaic properties of SnO_2 using sol-gel method [11] while S. Palanichamy et al have reported on the physical properties of SnO_2 thin films using nebulised spray pyrolysis [10] at different temperatures. SnO_2 thin films can be deposited using a variety of physical and chemical deposition techniques among which USP is a well-developed and economically viable method for depositing uniform thin films over large area [14]. USP is a processing technique being considered in research to prepare thin and thick films, ceramic coatings, and powders. Unlike many other film deposition techniques, it represents a very simple and relatively cost-effective processing method (especially regarding equipment costs). It offers an extremely easy technique for preparing films of any composition. USP does not require high-quality substrates or chemicals [15, 16].

The aim of this paper is to successfully deposit uniform transparent SnO_2 thin films by USP method onto different substrates (glass and glass/ITO) which are useful for photovoltaic applications and to investigate their structural and electrical properties.

2. EXPERIMENTAL DETAILS

SnO_2 thin films were deposited by ultrasonic spray pyrolysis (USP) technique using an aqueous solution containing 0.1 M tin (IV) chloride hydrate (98% Sigma-Aldridge) in 100 ml of pure water (with more than 18 MΩ·cm resistivity). Few drops of hydrochloric acid was added to prevent hydrolysis. To prepare good quality films without contamination, the soda-lime glass and glass/ITO sheets with (10 × 20 × 1 mm) dimensions were cleaned and used as a substrate on which tin oxide thin films were grown. For this experiment, thin films are defined as having 50–100 nm thickness.

The experimental setup and detailed discussion of USP technique has already been published [2, 12]. The glass substrates were then sprayed at the rate of 5 l/min for 5 minutes and 10 minutes at temperatures ranging from 300–500 ^{o}C. Optical measurements were performed by measuring total transmittance and reflectance using Jasco-V670 spectrophotometer in the wavelength range of 250 to 1500 nm. XRD patterns were obtained using ULTIMA IV Rigaku D/Max 2500 diffractometer using a Cu Ka radiation ($\lambda = 1.5406$ Å, 40 kV at 40 mA). N type conductivity was proved by using hot probe. The value of slope contact behavior and area of contact was obtained from AUTOLAB program while the thickness of the film was determined by optical measurements and used to calculate resistivity.

3. RESULTS AND DISCUSSIONS

3.1. Structural Analysis

The XRD diffraction pattern of SnO_2 thin films deposited for 5 min and 10 min are shown in Fig. 1 below. According to XRD pattern, cassiterite (ICDD: 01-077-0448$_)$ was detected which revealed the polycrystalline nature of the film having a tetragonal structure. Although, a cubic SnO_2 (ICDD: 01-071-5329) with orientation (111) was also detected for both graphs. No reflection connected to an additional phase was noticed. The film at Ts = 300 °C has an amorphous structure and crystallization of SnO_2 appears at about 400 °C and above. The peak intensity value was substantially raised at 500 °C. It can also be observed that as the deposition temperature increased from 400 to 500 °C, crystallite size increased independently from the deposition time (see Table 1). The plane (200) appears and was dominant at 500 °C. Similar observation of orientation was reported by Maio et al [18]. Furthermore, a report produced by S. Palanichamy revealed the polycrystalline nature of the SnO_2 thin films and an increase in crystallinity with substrate temperature [2].

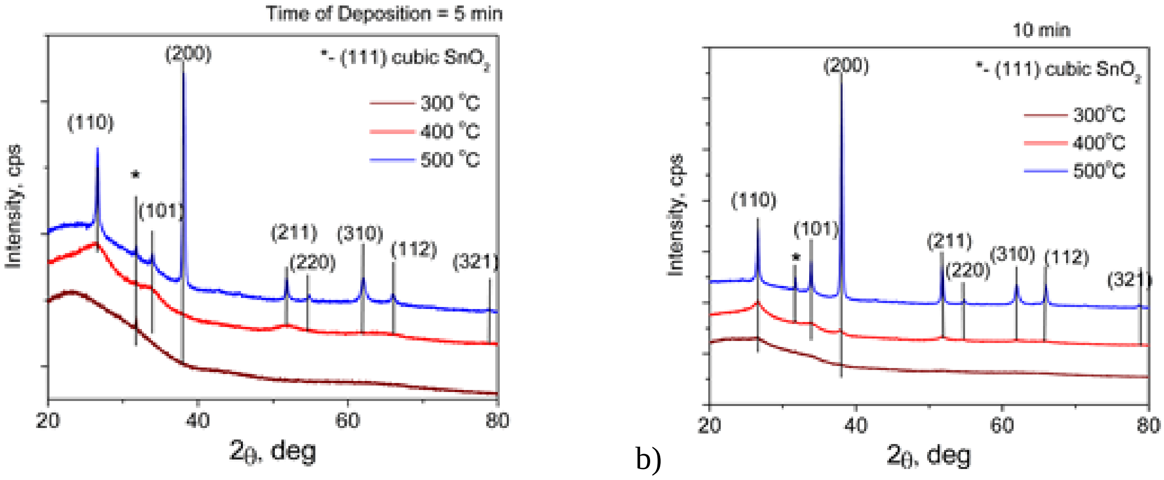

a) b)

Fig. 1. XRD plot of sprayed SnO_2 thin films deposited onto glass substrate
(a) for 5 min, (b) for 10 min

3.2. Optical Properties

The total transmittance spectra of the deposited SnO_2 thin films with different deposition temperature (T_s) recorded at wavelength range 300 to 1500 nm is displayed in Figure 2. All the films exhibit high transmittance in the visible region as well as the IR region. Average transmittance varies between 75 to 80% as deposition temperature increased from 300 to 500 ^{o}C. With increasing deposition temperature, in shorter wavelength region the soda lime glass could not transmit light and was cut from the spectrum of the SnO_2. A little shift to the band edge region for higher wavelengths was observed for different deposition times.

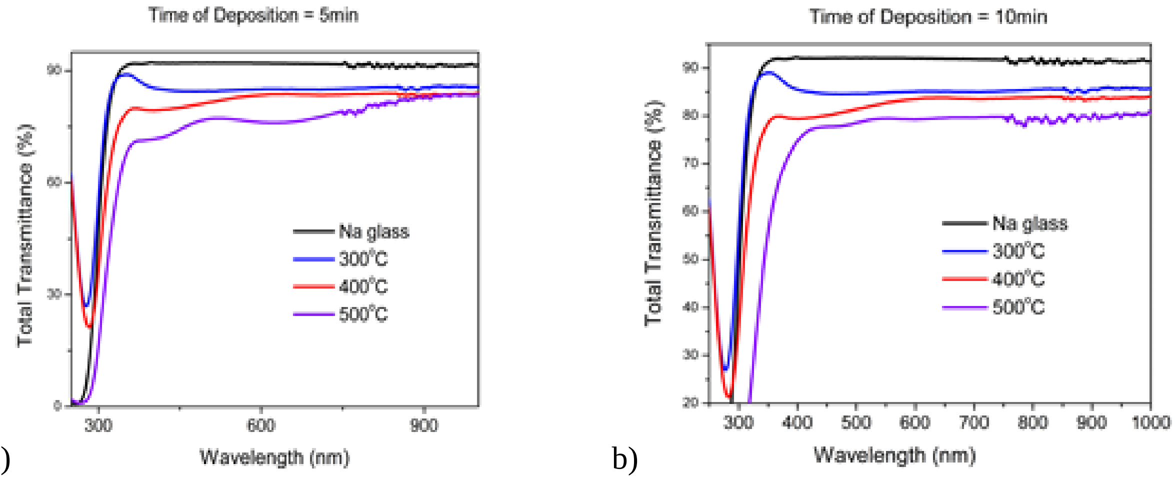

a) b)

Fig. 2. Total transmittance spectra of the deposited SnO_2 thin films on glass substrate
(a) for 5 min, (b) for 10 min

We are not able to calculate the bandgap due to used soda-lime glass substrate which intersects the signal from the SnO_2 films. In the future, we plan to use quartz substrate to overcome this difficulty.

3.3. Electrical Analysis

The electrical parameters of SnO_2 thin films as a function of deposition temperature and time was determined by measuring the resistance of substrate and calculating the resistivity of glass/ITO/SnO_2 and current density. Table 1 shows the slope, area of contact, thickness of film and resistivity while Table 2 shows average resistivity, crystallite size and contact behavior. The resistivity was calculated using the formula $\boldsymbol{\rho = R \cdot A/L, \Omega cm}$, where ρ is resistivity, $\boldsymbol{R}$ is resistance which is gotten from the Table (1/S), $\boldsymbol{A}$ is the area and $\boldsymbol{L}$ is the thickness of the film.

Table 1. Of deposition temperature, resistivity and area

ITO/Glass	**Time (min)**	**Deposition Temperature (^{o}C)**	**1/Slope (Ω)**	**Area (cm^2)**	**Thickness of film (cm)**	**Resistivity (kΩcm)**
1st Contact	5	300	27.5	0.03240	5.0E-6	178.20
2nd Contact	5	300	24.1	0.04628	5.0E-6	223.07
1st Contact	10	300	25.0	0.03697	7.0E-6	132.04
2nd Contact	10	300	25.5	0.02902	7.0E-6	105.72
1st Contact	5	400	29.6	0.02861	10.0E-6	84.69
2nd Contact	5	400	32.8	0.03324	10.0E-6	109.03
1st Contact	10	400	35.3	0.03529	12.0E-6	103.81
2nd Contact	10	400	38.9	0.01896	12.0E-6	61.46
1st Contact	5	500	42.2	0.03767	15.0E-6	105.98
2nd Contact	5	500	45.2	0.02231	15.0E-6	67.23
1st Contact	10	500	51.2	0.02371	25.0E-6	48.56
2nd Contact	10	500	73.0	0.03689	25.0E-6	107.72

Table 2. Of deposition temperature, average resistivity, crystallite size and contact behaviour

Deposition Temperature (^{o}C)	**Time (min)**	**Average Resistivity (kΩcm)**	**Crystallite size (nm)**	**Contact Behaviour**
300	5	200.63	1.600	Diode
	10	118.88	6.800	
400	5	96.86	2.600	Ohmic
	10	82.64	5.300	
500	5	86.60	33.10	Ohmic
	10	78.14	36.00	
Reference (1/s): ITO/TiO2 = $1.72 \cdot 10^5$ Ω				

Figure 3 below show the graph of average resistivity versus deposition temperature. It can be seen that electrical average resistivity of the deposited films for 5 minutes decreases from $200 \cdot 10^3$ Ωcm to $86 \cdot 10^3$Ωcm with an increase in substrate temperature, while for 10 minutes, average resistivity increased from $119 \cdot 10^3$ Ωcm to $78 \cdot 10^3$ Ωcm. Achour at al observed a similar trend while using spray pyrolysis method [22]. The decrease of electrical resistivity may be due to the increased crystallite size (See Table 1) [2].

Figure 4 shows the graph of current density versus voltage for deposition temperature. At 300 ^{o}C, we observed a curved line which indicates diode contact behavior while at 400 and 500 ^{o}C, we observed a straight line which indicates Ohmic contact behavior. We believe that adding SnO_2 at temperatures where ohmic contact is observed would help reduce the resistance loss caused by the ITO electrode and window layer.

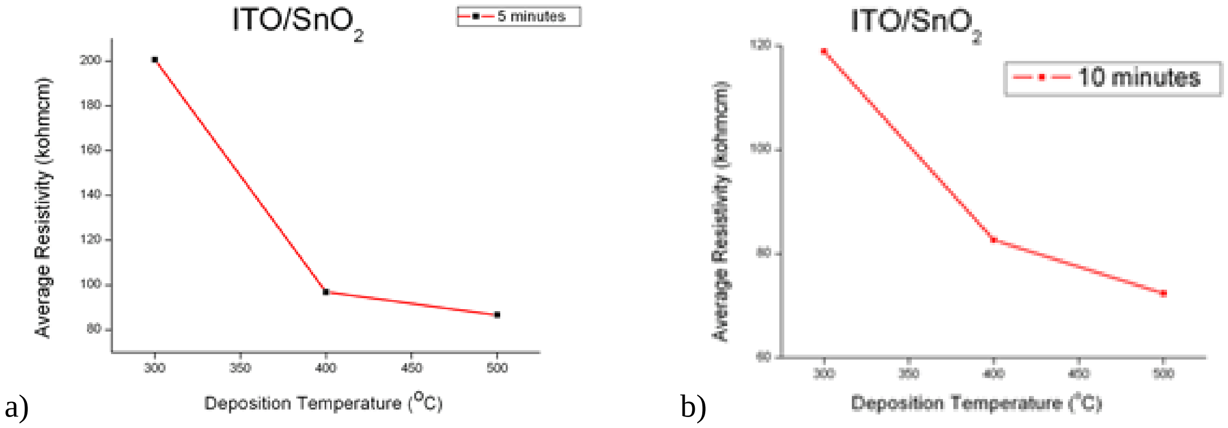

Fig. 3. Graph of average resistivity versus deposition temperature for deposition time (a) for 5 min, (b) for 10 min

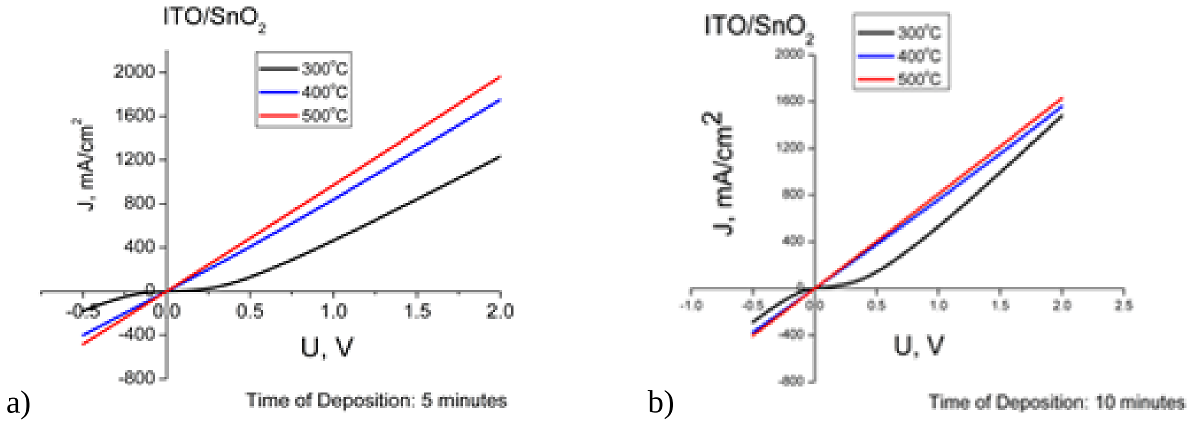

Fig. 4. Graph of current density versus Voltage for deposition temperature (a) for 5 min, (b) for 10 min

4. CONCLUSION

USP method was used to deposit uniform and homogenous SnO_2 thin films. The influence of time and temperature on deposited glass substrate was studied. XRD deposited. SnO_2 thin films showed tetragonal structure at deposition temperatures higher than 400. The thin films deposited at 300 °C displayed amorphous behavior. At T_s = 300 °C, crystallite size of films is about 1.6 nm and increases at higher deposition temperature. Additionally, this paper establishes the role of deposition temperature on electrical and optical properties as well as structure of SnO_2 thin films. It was observed that at higher deposition temperatures resistivity decreases. This implies that by using USP method, resistivity can be easily changed by varying temperature. This could be used to determine best conditions for the improvement of component layer in solar cell structure. Overall, all films exhibited high transmittance in the visible region as well as the IR region.

REFERENCES

1. MASUDAT, S. KITAMURA, Y. OKUMURA. MIYATAKE, S. TABATA, H. KAWAI, T. *Transparent thin film transistors using ZnO as an active channel layer and their electric properties* J. Appl. Phys., 93 (2003), p. 1624.
2. PALANICHAMY, J., RAJ, J., MOHAMMED, P., SATHEESH, S. KUMAR, PANDIARAJAN, S., AMALRAJ, L. *Physical properties of nebulized spray pyrolysised SnO_2 thin films at different deposition temperature. Applied physics* A [2018] 124:643.
3. THIRUMOORTHI, M. THOMAS, J. Asian Ceram. Soc. 4, 124–132 (2016).

4. NGAMSINLAPASATHIAN, SUPACHAI & SREETHAWONG, THAMMANOON & SUZUKI, YOSHIKAZU & YOSHIKAWA, SUSUMU. (2006). *Doubled layered ITO/*SnO_2 *conducting glass for substrate of dye-sensitized solar cells*. Solar Energy Materials and Solar Cells. 90. 2129-2140. 10.1016/j.solmat.2005.12.005.
5. TOSUN, B. SELIN & FEIST, REBEKAH & CAMPBELL, S.A. & AYDIL, ERAY. (2012). *Tin dioxide as an alternative window layer for improving the damp-heat stability of copper indium gallium diselenide solar cells*. Journal of Vacuum Science and Technology A: Vacuum, Surfaces and Films. 30. 10.1116/1.3692225.
6. XIONG, LIANGBIN. (2018). *Review on the Application of SnO2 in Perovskite Solar Cells.*
7. YANG, G. CHEN, C. YAO, F. CHEN, Z. ZHANG, Q. ZHENG, X. MA, J. LEI, H. QIN, P. XIONG, L. KE, W. LI, G. YAN, Y. FANG, G. Adv. Mater. 2018, 30, 1706023.
8. ANARAKI, H. KERMANPUR, A. STEIER, L. DOMANSKI, K. MATSUI, T. TRESS, W. SALIBA, M. ABATE, A. GRÄTZEL, M. HAGFELDT, A CORREA-BAENA, J. Energy Environ. Sci. 2016, 9, 3128.
9. JIANG, Q. CHU, Z. WANG, P. YANG, X. LIU, H. WANG, Y. YIN, Z. WU, J. ZHANG, J. YOU, X Adv. Mater. 2017, 29, 1703852.
10. MARIAPPAN, R. PONNUSWAMY, V. SURESH, P. ASHOK, N. JAYAMURUGAN, P. CHANDRA BOSE, A. *Superlattices Microstruct*. 71, 238–249 (2014).
11. RAJ, J. MOHAMED, SANJEEVIRAJA, C. AMALRAJ, L. Asian Ceram. Soc. 4, 191–200 (2016).
12. JADSADAPATTARAKUL, D. EUVANANONT, C. THANACHAYANONT, C. NUKEAW, J. SOOKNOI, T. *Tin oxide thin films deposited by ultrasonic spray pyrolysis* ceramics international Volume 34, Issue 4, May 2008, Pages 1051–105.
13. SVETLANA, P. *Tin Sulfide Films by Chemical Spray Pyrolysis*: Formation and Properties TALLINN UNIVERSITY OF TECHNOLOGY School of Engineering Department of Materials and Environmental Technology.
14. SEHRISH, G. ANAM, A. NAZMINA, I. SAIRA, R. SHAHZAD, N. *Tin oxide thin films prepared by sol-gel for PV applications*. International Conference on Solid State Physics 2013 (ICSSP'13) Materials Today: Proceedings 2 (2015) 5793–5798.
15. JADSADAPATTARAKUL, D. EUVANANONT, C. THANACHAYANONT, C. NUKEAW, J. SOOKNOI, T. *Tin oxide thin films deposited by ultrasonic spray pyrolysis* ceramics international Volume 34, Issue 4, May 2008, Pages 1051–1054.
16. PATIL, G. KAJALE, GAIKWAD, B. and G. H. Jain *Spray Pyrolysis Deposition of Nanostructured Tin Oxide Thin Films* International Scholarly Research Network ISRN Nanotechnology Volume 2012, Article ID 275872, 5 pages.
17. DEEPU, D. & KARTHA, C & VIJAYAKUMAR, K. 2016. *How spray rate influences the formation and properties of transparent conducting SnO2 thin films*. Journal of Analytical and Applied Pyrolysis. 121. 10.1016/j.jaap.2016.06.013.
18. DENGKUI M, QINGNAN Z, SHUO W, ZHENDONG W, XINGLIANG Z, XIUJIAN Z. *Effect of substrate temperature on the crystal growth orientation of SnO2:F thin films spray-deposited on glass substrates*, Journal of Non-Crystalline Solids, Volume 356, Issues 44–49, 2010,06.076.
19. MOCHEL, J.M. US Patent 2,564,707 (1951).
20. HILL, J.E. and CHAMBERLIN, R.R US Patent 3,148,084 (1964).
21. PRAMOD, S. PATIL *thin Film Physics Laboratory, Department of Physics, Shivaji University, Kolhapur 416004, India journal of Technology Education*. Materials Chemistry and Physics Volume 59, Issue 3, 15 June 1999, Pages 185–198.
22. ACHOUR, R. BENHAOUA, M. JLASSI, B. BENHAOUA, *Superlattices* Microstruct. 86, 403–411 (2015).

CHEMICAL AND THERMAL RESISTANCE OF PLASMA SPRAYED AL_2O_3/TIO_2 COATINGS

A. Šuopys, L. Marcinauskas R. Kėželis, M. Aikas, R. Uscila
Lithuanian Energy Institute, Laboratory of Plasma Processing
Breslaujos str. 3, LT-44403 Kaunas – Lithuania
Email: airingas.suopys@lei.lt

S. Tučkutė
Lithuanian Energy Institute, Center for Hydrogen Energy Technologies
Breslaujos str. 3, LT-44403 Kaunas, Lithuania

ABSTRACT

Nowadays a lot of attention is given to the improvement of the materials, to increase their durability, longevity, chemical and thermal resistance etc. One of the most common techniques is to form a protective coating on the material to improve its features without the need to replace it entirely. The most popular method to create a protective coating is plasma spraying. Alumina is perfect material for such cases, since it's relatively cheap and exhibits excellent thermal and chemical resistance. It's possible to achieve better results with composite coatings, addition of different materials can change properties of the coating tremendously, and different amounts of the material can modify formed coatings properties as well. Addition of titanium oxide in alumina coatings can increase the chemical resistance of material without reduction of thermal resistance. The aim of this research is to investigate the chemical and thermal resistance of alumina coatings with different addition of TiO_2. Al_2O_3, Al_2O_3-3 wt.% TiO_2 and Al_2O_3-13 wt.% TiO_2 coatings were deposited using atmospheric plasma spraying. The as-sprayed coatings were heat treated up to 500 °C with straw pellets in a furnace to imitate real working conditions of the boiler. The coatings surface morphology, structure, and elemental composition was examined by Scanning Electron Microscopy, Energy Dispersive X-Ray Spectroscopy and X-Ray Diffraction. It was determined that after heat treatment the minor changes in the elemental composition were observed. Meanwhile an additional crystalline phases of metal oxides were detected.

Keywords: Plasma spray, coating properties, alumina, titania, thermal resistance, chemical resistance

1. INTRODUCTION

The need for functional materials is ever increasing, many systems and their individual parts or sections must be durable, resistant to chemical or thermal effects and corrosion. The higher longevity can be reached – the better. One of the most effective and cost-efficient way to prolong the lifespan of certain parts or systems is to apply a protective layer of material on top. Ceramic coatings (Al_2O_3, ZrO_2, TiO_2) are widely-used in many fields, from military and medicine to aerospace industry. Coated materials exhibit superior mechanical, chemical and physical properties [1]. One of the reasons why coatings are extremely popular today, is that a thin layer of material applied on a base substrate can significantly improve features of a certain item without changing the internal structure. Plasma spray is well known coating technology, today widely used in laboratories and industry in depositing a huge variety of coatings on various surfaces and components to provide protection and improve their quality. The quality of the coating depends on several factors such as plasma temperature and flow rate, the substrate and powders that are being used. Powder composition is especially important, since different materials have different properties and greatly affect the quality of the formed coating [3-5]. One of the most widely used ceramic coating today is alumina because of its low cost, inherent attrition and corrosive resistance, excellent dielectric and thermal shock resistance. These properties allowed the construction of special surface protection of metallic components operating under severe running conditions [5]. The properties of the aluminum oxide could be improved with the addition of titanium oxide. An addition of TiO_2 in an Al_2O_3 based coating increases the wear resistance which is due to increase of the fracture toughness and decrease of the coefficient of friction [2]. Mechanical properties of the coating can also be changed with the addition of TiO_2. This was tested by authors [3] and in their study they performed characterization of alumina coatings with the addition of titanium oxide, and the effects of TiO_2 addition to Al_2O_3 base of plasma sprayed coatings. It was found that TiO_2 addition reduced the microhardness of the alumina composite coating. Similar results were obtained by other authors [4-7], they found that the increase of titania lowered the microhardness of coatings. It was also confirmed that the increase of titania decreases the coatings porosity, and increases its corrosion resistance, wear rate and elastic modulus [8]. However, the thermal insulation property of Al_2O_3-TiO_2 coatings decreases with the increase of the content of TiO_2 in powder. The possible reasons are that TiO_2 has a higher thermal conductivity than Al_2O_3, and these coatings have different porosities [9].

The aim of this paper was to deposit the alumina and alumina composite coatings and to investigate the influence of titanium oxide addition to alumina coatings resistance to thermal and chemical impact.

2. METHODOLOGY

The coatings were sprayed on steel (P265GH) substrates at atmospheric pressure using a direct current plasma torch. The plasma torch used in this experiment was developed at the Lithuanian Energy Institute [10]. The steel substrates (dimensions of 40 × 10 × 6 mm) were polished and chemically cleaned before starting the deposition process. The substrates were placed on the water-cooled sample holder and the deposition duration was ~60 s. Air was used as both the plasma forming gas (flow rate of 3.7 g/s) and the powder carrier gas (flow rate of 0.75 g/s), hydrogen was used as a secondary gas (flow rate of 0.06 g/s). The plasma torch was moving in the x-axis direction forward and back during the deposition, in order to avoid overheating the sample and ensure similar structure of the coating for all of the samples. The spraying distance was kept at 70 mm. Powders used to for the Al_2O_3 coating were MOGUL PC15, purity 99.8%, for the Al_2O_3-3 wt.% TiO_2 - ALO-105, purity 98.5%, and lastly for the third coating Al_2O_3-13 wt.% TiO_2 - MOGUL PC12. Additionally, every sample had an underlayer formed from MOGUL M3, Ni/Cr (ratio 80/30) powders.

The surface morphology of the coatings was characterized by scanning electron microscopy (SEM) using a Hitachi S-3400N, elemental composition by energy dispersive X-ray spectroscopy (EDS) using dispersive X-ray spectroscopy (Bruker Quad 5040 spectrometer, AXS Microanalysis GmbH). The measurements were performed from 1.05 mm^2 surface area at 4 different points for each sample and the mean values were presented. Structure of the coatings was analyzed using X-ray diffraction crystallography (XRD) with Bruker D8 instrument whose main parameters were: theta-theta configuration, CuKα ($\lambda = 0.154059$ nm) radiation.

Samples (together with an uncoated steel specimen Fig 1 a) were put in a metal cylinder with straw pellets (Fig. 1 b)).

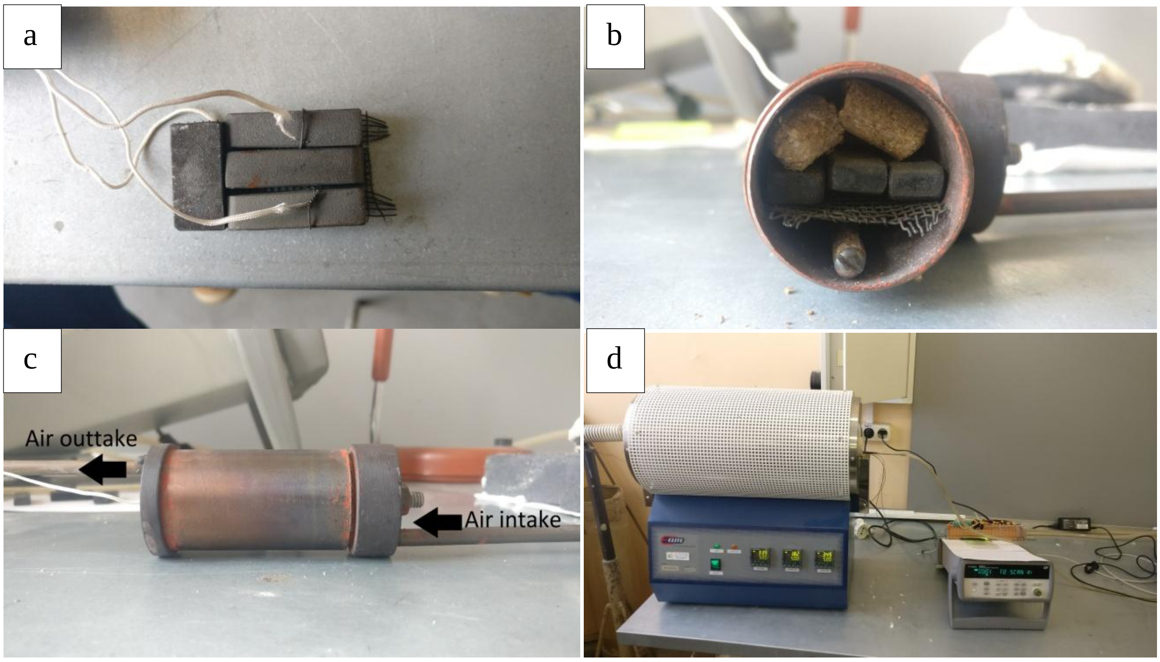

Fig. 1. a) position of the samples, b) samples in tube with grain pellets, c) metal cylinder with the samples, d) experimental setup

The cylinder had holes on each side and air was flowing through the bottom one at a constant rate (Fig. 1 c)). The furnace (model TMH12/38/500-2416 (Fig 1. d)) temperature was set to 500 °C and after the heating, the cylinder with all of the samples was left to cool down. Temperature inside the cylinder was measured by 3 thermocouples, 1st was placed under the samples, and other two were fixed on the surface of the samples (2nd on Al_2O_3-3% TiO_2 sample, 3rd on Al_2O_3-13% TiO_2 sample). The duration of one experiment was 80 minutes and this was done 10 times. After 10 cycles each of the coatings were washed using ultrasonic cleaning, then morphology, structure, and composition were examined along with the control sample of uncoated steel.

3. RESULTS AND DISCUSSION

Four different samples were used: Sample No. 1 uncoated steel sample, No. 2 – Al_2O_3 sample, No. 3 – Al_2O_3-3% TiO_2 and No. 4 – Al_2O_3-13% TiO_2.

Fig. 2 shows the temperature of one cycle measured with 3 thermocouples. The temperature of the 1st thermocouple (below the samples) is quite lower, that is due to the constant air flow from the bottom of the cylinder, and the maximum temperature is considerably lower (450-480 C°), because

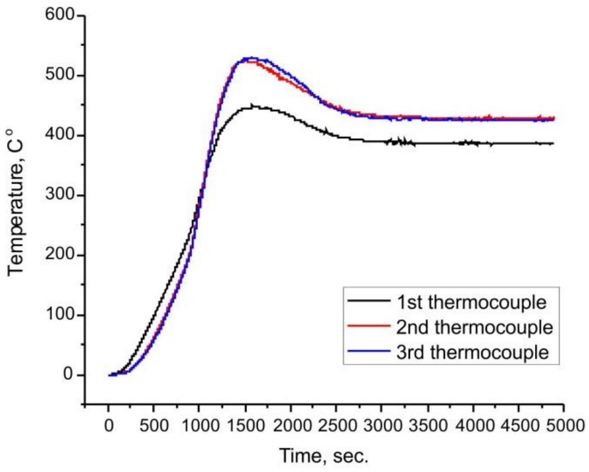

Fig. 2. Temperature graph measured by thermocouples in metal cylinder

the burning of straw pellets is happening on top of the samples. 2nd and 3rd thermocouples temperatures are quite similar. The rapid growth of temperature can be observed at 17 min mark, that is when the straw pellets start to burn, and the peak temperature is between 520-600 °C and reached at 25 min mark. The temperature when the burning is over and the temperature on the coatings surfaces starts to decrease and stabilizes at 430-470 °C.

Fig. 3 shows surface of the samples before and after 10 cycles. It can be seen that the surface of the 1st sample slightly changed 10 cycles of heating. There are more small particles on the surface, also some cavities appeared. The small particles are leftover products of straw pellets burning process, which were not washed completely before the measurement. Also during the burning process surface is being etched by the ongoing chemical reactions. And the damage done to the surface of the sample just after 10 cycles, can clearly be seen.

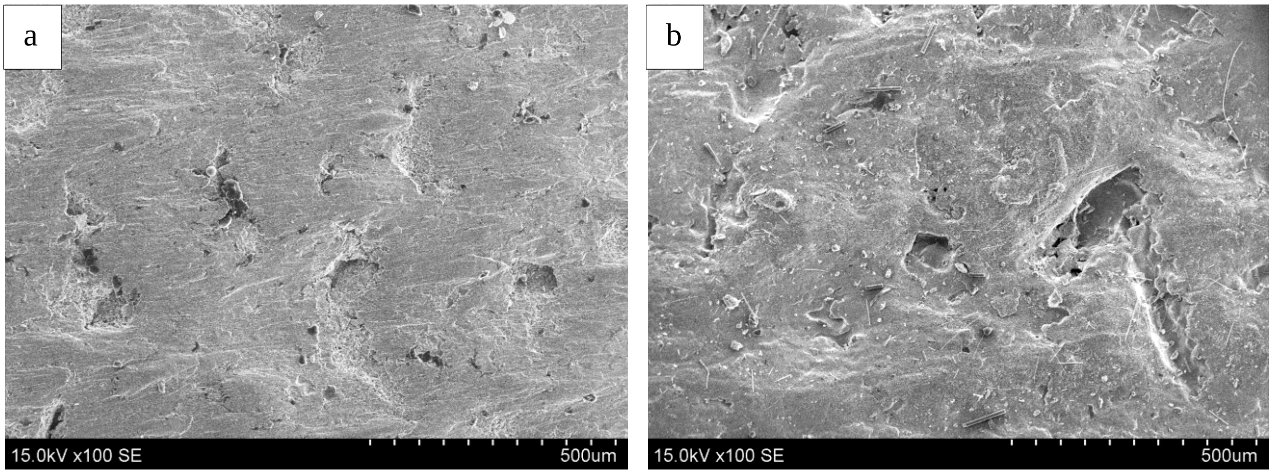

Fig. 3. SEM micrographs of steel sample, before a) and after b) 10 heating cycles

The second sample surface is shown in Fig. 4. On the untreated sample (a) the structure is typical, the coating is of lamellar structure and consists of splats and some unmolten particles, also no defects can be observed on the surface. The structure, of the same sample, after 10 cycles (Fig. 4 b)) is similar, but there are considerably more small particles on the surface. Same as in the 1st sample these particles are residues of combustion process, that cannot be washed away completely. As in the 1st sample, some cavities do form on the surface, but they are smaller and shallower. That is because the Al_2O_3 coating is much more resistant to chemical reactions than the steel substrate.

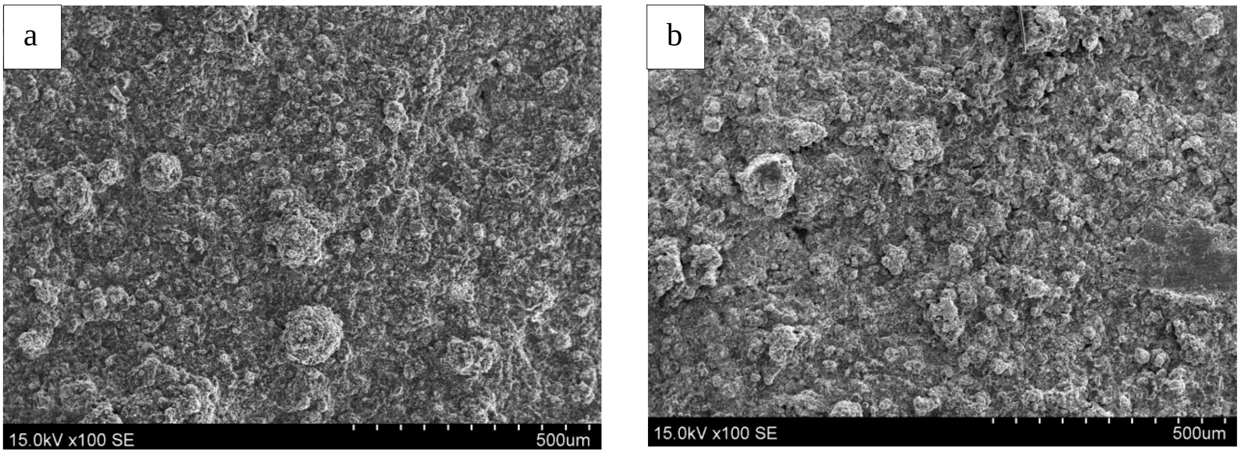

Fig. 4. SEM micrographs of Al_2O_3 sample, before a) and after b) 10 heating cycles

The surface of 3rd sample (Fig. 5) is similar 2nd coating (Fig. 4), no cracks or any other defects are observed. The main difference is that there are more small particles and the surface seems to be more porous. After 10 cycles of heating there are some residue particles of combustion process, also no visible cracks can be observed, however there are a bit hollower spaces, but the overall structure of the coating was not damaged.

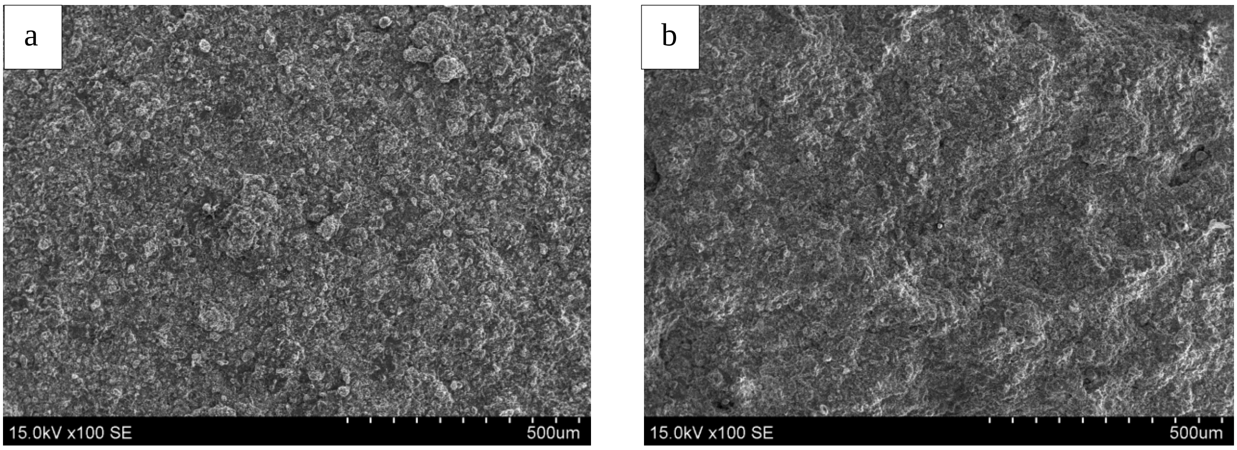

Fig. 5. SEM micrographs of Al_2O_3-3%TiO_2 sample, before a) and after b) 10 heating cycles

On the surface of 4th sample (Figure 6) there are barely any changes at all. The coatings seem almost the same. That is because of increased chemical resistance, with higher amount of titanium oxide. As in other samples, there are no visible defects even after 10 cycles of heating. This coating appears to be affected the least to the chemical and thermal impact of this test.

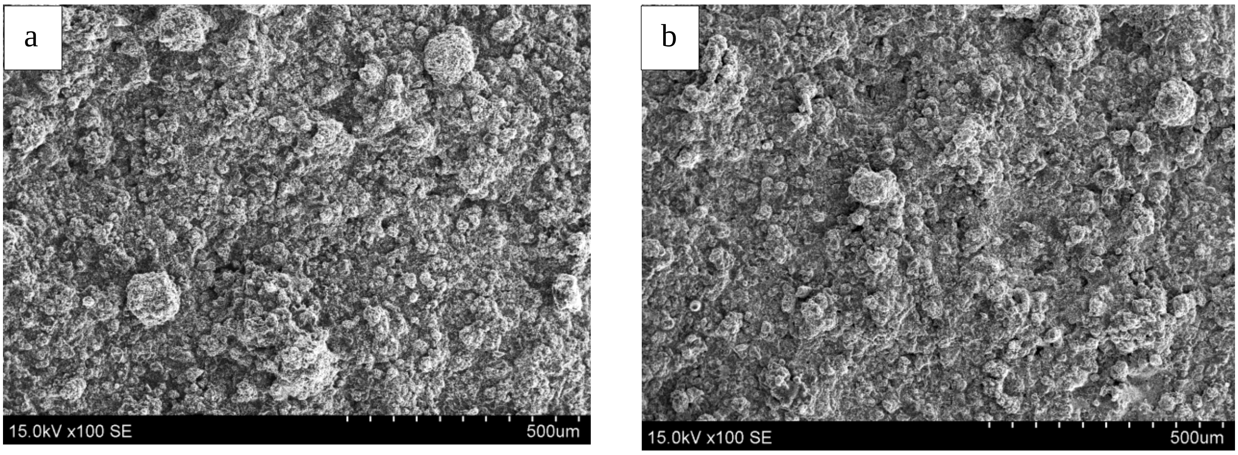

Fig. 6. SEM micrographs of Al_2O_3-13% TiO_2 sample, before a) and after b) 10 heating cycles

Elemental composition of the samples was examined before 10 heating cycles and after. 1st sample of uncoated steel consists of mostly iron (97%), oxygen (1%) and low amount of other element from impurities of the sample. The sample was greatly affected as the amount of oxygen increased by almost 42%, also other elements (silicon, potassium, calcium, sulfur) can be found, that appeared after the burning process, however their quantity is quite low. These elements can be found due to the fact, that they were not removed completely using ultrasonic cleaning.

2nd sample mainly consists of oxygen (57%) and aluminum (31%). Other elements (nickel, copper, chromium, iron, carbon and silicon) are attributed to impurities of the alumina powders and bonding layer of NiCr. After 10 cycles amount of oxygen increased by only 1% (to 58%), but aluminum decreased by 3% (to 28%). Meanwhile, the changes of other elements in the sample was negligible.

3rd sample consists of oxygen (58%), aluminum (31%) and titanium (1%). Much like in 2nd sample, low amount of the impurities (nickel, copper, chromium, iron, carbon and silicon) are found. After 10 cycles, the amount of oxygen increased by 2% (to 60%), titanium increased by 1% (to 2%) and aluminum increased by 2% (up to 33%). Minor changes of other elements concentrations (nickel, copper, silicon, chromium) was also observed, this happened due to ultrasonic cleaning was unable to completely remove the combustion products from the surface of coating and diffusion of impurities within the sample during the burning process.

As in the previous coating, the final one consists of oxygen (57%), aluminum (22%), titanium (4%) and impurities. Amount of oxygen in this sample increased by 3% (to 60%), which means the oxidation is a bit higher in Al_2O_3-13% TiO_2 coating than in Al_2O_3 and Al_2O_3-3% TiO_2. However, the amount of aluminum and titanium remained the same.

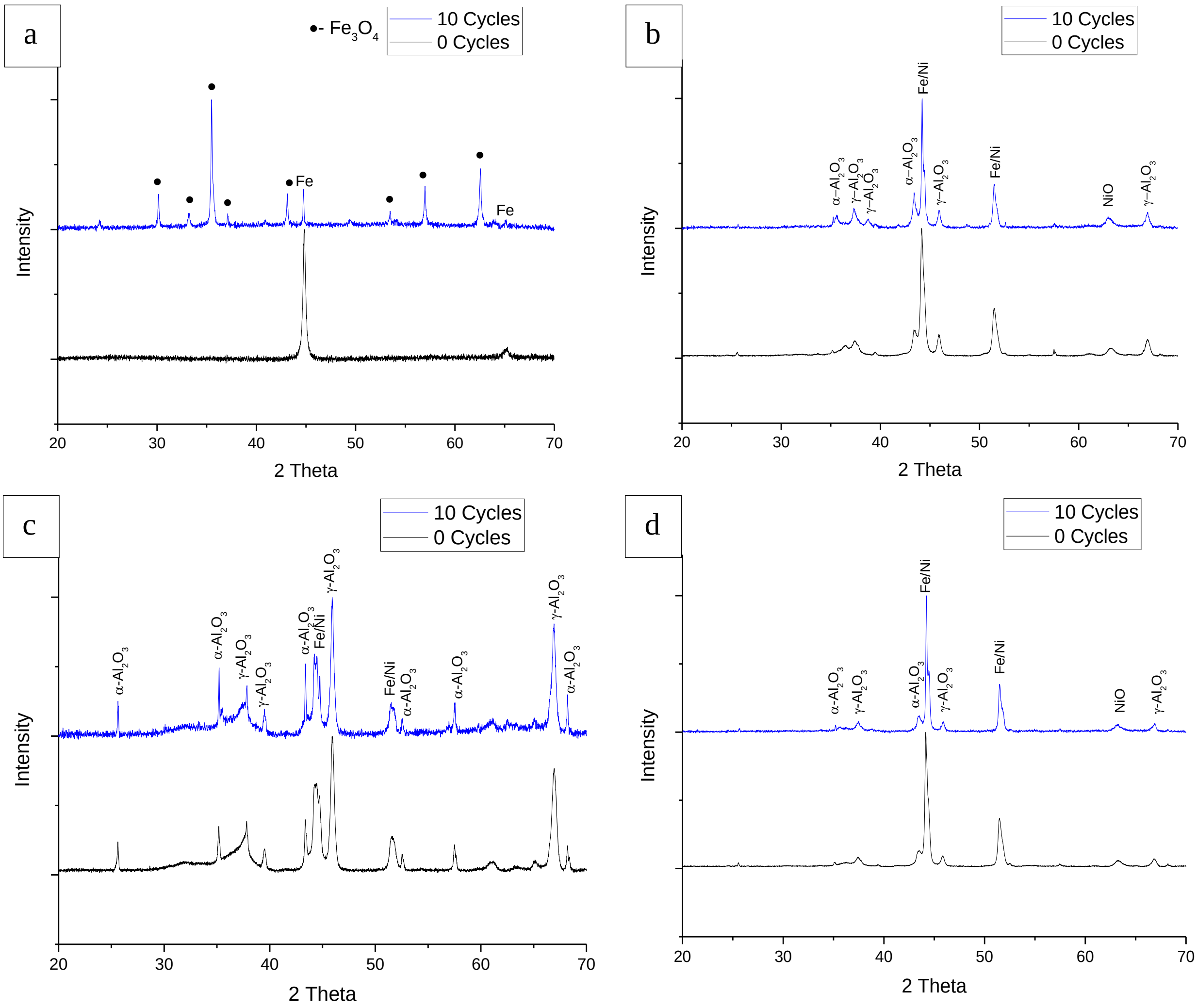

Fig. 7. X-ray diffraction patterns of samples before and after 10 heating cycles: a) Steel; b) Al_2O_3; c) Al_2O_3-3 wt.% TiO_2; d) Al_2O_3-13 wt.% TiO_2

The phase composition of as-sprayed coatings and after 10 cycles samples was identified in Fig. 7. The 1st untreated sample (Fig. 7. a) consists only of Fe phase, and after 10 cycles Fe_3O_4 becomes the dominant phase in the sample. This confirms elemental composition data, that the surface of sample experiences high level of oxidation. Phase composition of coating No. 2 (Fig. 7. b) does not change much, dominant phases are attributed to bonding layer and steel. There is a small increase of α-Al_2O_3 phase when $2\theta = 35.2°$, also the peak of α-Al_2O_3 phase narrows when $2\theta = 43.5°$. Similar results were obtained by S. Matthews [11]. In his work, he heat-treated Al_2O_3 samples in different temperatures, and observed that there are no phase composition changes in 500–700 °C temperature range. The dominant phase in sample no 3 (Fig. 7. c) is γ-Al_2O_3 when $2\theta = 37.8°$, 39.5°, 45.9° and 67.1° and their intensities do not change much. Unlike in previous sample, there is an increase of α-Al_2O_3 phase, especially when $2\theta = 35.4°$ and a smaller increase when $2\theta = 43.4$ and 57.6°. The only peak of α-Al_2O_3 phase that decreases is when $2\theta = 68.2°$. The intensity of Fe and Ni peaks when 2θ = 44.5° and 51.5° are unchanged after 10 cycles, so it can be assumed that the number of heating cycles have no effect on the amount of crystalline Fe and Ni and phase in this sample. Finally, in the sample no 4 (Fig 7. d) phase composition is much simpler. Highest intensity peaks are Fe and Ni when 2θ = 44.1° and 51.5°. Just as in 2nd sample There is a small peak of NiO, that is attributed to sublayer, when 2θ = 63.2°. The dominant phase is α-Al_2O_3 (2θ = 35.2° and 43.3°) and the only other phase is the coating is γ-Al_2O_3 (2θ = 35.1°, 45.8 and 66.8°). Since the intensity of all phase peaks varies very little, the coating remains almost the same, even after 10 heat cycles. Phase composition of Al_2O_3-TiO_2 coatings during the heat-treatment process was also investigated by S. Jia et al. [9]. The alumina and alumina composite coatings were heat-treated at 400 °C temperatures. The authors concluded that the phase composition of alumina, Al_2O_3-3% TiO_2 and Al_2O_3-13% TiO_2 coatings remained unchanged even after heat treatment at 400 °C temperatures for 4 hours.

4. SUMMARY

The Al_2O_3, Al_2O_3-3% TiO_2 and Al_2O_3-13% TiO_2 coatings were deposited by plasma spraying. The surface morphology, elemental composition and structure of the deposited and heat-treated coatings were analyzed. The SEM results indicated that the highest damaged was obtained for the steel surface. Meanwhile the coated samples (No. 2, 3, 4) after heat treatment were almost unaffected. No defects were observed, coatings did not crumble or peel off. The uncoated steel sample was heavily oxidized after the 10 cycle of heat treatment. The oxygen amount on the surface increased from 1 to 42%. Using this data, it is clear that protective layer is necessary to preserve its structural integrity. The change of elemental composition in other samples is quite low. In Al_2O_3 coating oxygen increased by less than 1% and aluminum decreased by 3%. In the Al_2O_3-3% TiO_2 coating, amount of titanium increased by less than 1%, and oxygen by 2%, but aluminum decreased by 2%. In the Al_2O_3-13% TiO_2 coating amount of oxygen increased by 3%, but aluminum and titanium remained the same. It was obtained that after 10 cycles of treatment the steel substrate is heavily oxidized and Fe_2O_3 becomes the dominant phase. The XRD results indicated that even after 10 cycles of heat treatment at 500 °C, structure of Al_2O_3, Al_2O_3-3% TiO_2 and Al_2O_3-13% TiO_2 coatings remained stable.

ACKNOWLEDGEMENT

This research was funded by the European Regional Development Fund under measure No. J05-LVPA-K “Intellect. Joint Science-Business Projects” - project No. J05-LVPA-K-01-0161 “Research and development of technologies for biofuel use efficiency increase and emissions reduction”.

REFERENCES

1. Zhang B, Wei L, Gao L, Guo H, Xu H, Microstructural characterization of PS-PVD ceramic thermal barrier coatings with quasi-columnar structures, *Surface and Coatings Technology*, Vol. 311, 2017, p. 199-205.
2. Ghazali M, Forghani S, Hassanuddin N, Muchtar A, Daud AR. Comparative wear study of plasma sprayed TiO_2 and Al_2O_3–TiO_2 on mild steels. *Tribology International*. Vol. 93, 2016, p. 681-686.
3. Yılmaz R, Kurt AO, Demir A, Tatlı Z. Effects of TiO_2 on the mechanical properties of the Al_2O_3-TiO_2 plasma sprayed coating. *Journal of the European Ceramic Society*. Vol. 27(2), 2007, p. 1319-1323.
4. Yugeswaran S, Selvarajan V, Vijay M, Ananthapadmanabhan PV, Sreekumar KP. Influence of critical plasma spraying parameter (CPSP) on plasma sprayed Alumina–Titania composite coatings. *Ceramics International*. Vol. 36(1), 2010, p. 141-149.

5. Dejang N, Watcharapasorn A, Wirojupatump S, Niranatlumpong P, Jiansirisomboon S. Fabrication and properties of plasma-sprayed Al_2O_3/TiO_2 composite coatings: A role of nano-sized TiO_2 addition. *Surface and Coatings Technology*. Vol. 204(9), 2010, p. 1651-1657.
6. Fervel V, Normand B, Coddet C. Tribological behavior of plasma sprayed Al_2O_3-based cermet coatings. *Wear*. Vol. 230(1), 1999, p. 70-77.
7. Çelik İ. Structure and surface properties of Al_2O_3–TiO_2 ceramic coated AZ31 magnesium alloy. *Ceramics International*. Vol. 42(12), 2016, p. 13659-13663.
8. Klyatskina E, Rayón E, Darut G, Salvador MD, Sánchez E, Montavon G. A study of the influence of TiO_2 addition in Al_2O_3 coatings sprayed by suspension plasma spray. *Surface and Coatings Technology*. Vol. 278, 2015, p. 25-29.
9. Jia S, Zou Y, Xu J, Wang J, Yu L. Effect of TiO_2 content on properties of Al_2O_3 thermal barrier coatings by plasma spraying. *Transactions of Nonferrous Metals Society of China*. Vol. 25(1), 2015, p. 175-183.
10. Valinčius V, Valatkevičius P, Valinčiūtė V, Marcinauskas L, *Plasma Sources Sci. Technol.* 2004, p. 199.
11. Matthews S, Taliana F, James B, Heat treatment of plasma sprayed Al_2O_3 and Al_2O_3-WO_3 coatings between 500 and 1000 °C, *Surface and coatings technology,* Vol. 212, 2012, p. 109-118.

CYSENI 2019, May 23-24, Kaunas, Lithuania
ISSN 1822-7554, www.cyseni.com

REVIEW OF RIVERINE HYDRO ENERGY RESEARCH IN LITHUANIA

G. Adžgauskas
Lithuanian Energy Institute
Breslaujos g. 3, LT-44403 Kaunas – Lithuania
Email: gintaras.adzgauskas@lei.lt

ABSTRACT

The first hydropower plant was built in Kretinga in 1890. Lithuanian hydro power resources were investigated by Henryk Merczing and Jonas Smilgevičius. Steponas Kolupaila, who is called a founder of Lithuanian hydrology, comprehensively explored Lithuanian hydropower resources and estimated their potential.

It has been determined that the potential capacity of Lithuanian rivers is 582 MW and the kinetic capacity is 82.1 MW. Hydrokinetic resources of Lithuanian rivers have been reduced due to the protected areas and comprise 13.6 MW, and the energy is 79.4 GWh/year. Riverine potential energy resources are thoroughly investigated by the scientists of Laboratory of Hydrology at the Lithuanian Energy Institute. Hydrology research is required for the development of large-scale energetics, namely for operation of Kaunas hydro energetic system (Kaunas Hydro Power Plant and Kruonis Pumped Storage Power Plant) and for selection of the site for the construction of Ignalina NPP.

The main task of this study is to review the history of the exploitation of Lithuanian hydro energy resources and to show the prospects for the development of the hydropower sector. This review shows that potential of natural resources of riverine potential energy is declining. The potential of electricity generation in Lithuanian rivers can be increased by using kinetic river flow energy. It's possible to use the kinetic energy of the riverine flow for electricity generation only in the modern hydro turbines as shows successful foreign experience.

Keywords: hydro energy, hydrology, kinetic energy

1. INTRODUCTION

Since ancient times, potential riverine hydroenergy has been used for various purposes, in the water supply and irigation systems, converting it into mechanical energy driving variuos machinery. One of the first uses of water in a water mill replacing a hand-rolled mill was described by the Greek poet Antipater of Thessalonica 20 BC [1]. It is believed that the first mentioned in written sources water mill in Lithuania, was built on the Dane River in the vicinity of Klaipėda in 1256 [2]. Therefore, water mills in Lithuania are likely to have appeared in the XII–XIII century.

Since riverine energy was started to use in economic activities, mostly in water mils, state has the need to assess and write in the chronicle utilization of riverine energy. First Lithuanian Statute has started State regulation of the water mils activity in Lithuania at 1529 [3].

First electric hydropower generator was installed in the water mil of Kretinga manor on the river Dupultis at 1890. It was first hydro power plant in Lithuania supplying electricity for the needs of manor house [3]. Riverine energy was started to use for electricity generation and supply for public needs. First hydro power plants were built without comprehensive research and evaluation of hydro resources.

2. RIVERINE HYDROENERGY RESEARCH IN LITHUANIA

2.1. Riverine Potential Hydroenergy Research

For the first time, the Lithuanian hydro power resources were thoroughly explored and investigated by the chair of the Russian Commission for the Exploration of the Water Power

Prof. Henryk Merczing in 1909, having submitted a proposal to build a power plant on the river Nemunas in Birštonas [3].

Prof. Steponas Kolupaila comprehensively studied Lithuanian hydropower resources, determined their utilization potential and suggested construction of hydroelectric power stations on the big rivers [4], [5]. In 1922 was calculated average usable Lithuanian riverine capacity equal to 149 200 kW, minimal capacity capacity was 119 360 kW and maximal capacity 373 000 kW [10].

Engineer J. Smilgevicius has proposed hydro power plants construction on the largest rivers [7].

Lithuanian Energy Committee was established in 1936 and its Water Force Commission led by S. Kolupaila performed a complex exploration of rivers hydropower resources. The hydropower calculations of the largest rivers were carried out, according to which the theoretical power of rivers during the 6 months of the average water year was 199.5 MW, and during the 9 months it was 150 MW [6]. The total power of riverine hydropower was calculated by the formula [6]:

$$N = 8QH, \tag{1}$$

where, $\eta = 0{,}815 -$ the value of the eficiency factor has already been accounted, H – river water head m, Q – water discharge m^3/s.

Statistics show that in 1926, there were 616 hydroelectric power plants in Lithuania, total power – 5966 kW, in 1939 – 640 hydroelectric power stations with an output of 8660 kW. In 1938 hydropower accounted for 2%, local resources – 28%, and imported – 70% of electricity generation [8].

Table 1. Lithuanian hydro power potential evaluation

Researchers	**Hydropower, MW**	**Hydroenergy, TWh/y**	**References**
S. Kolupaila	149,2		10
S. Kolupaila	199,5		6
“Hydroenergoprojekt” institute	118,6		10
J. Jablonskis, M. Lasinskas	689	6	10
J. Jablonskis	28,7	0,125	12

There were 355 hydro plants in Lithuania in 1948 with a total power of 12,000 kW, of which 85 – Hydro Power Plants with an installed capacity of 4000 kW [8]. Number of hydro power plants has increased until 111 Hydro Power Plants and total power reached 10.030 kW in 1958. The production of small HE in the period of 1945–1958 has increased more than 4.5 times and amounted to 20 million. kWh/y. Hydroelectric resources were explored for the development of small Hydro Power Plants, river basin districts were measured, longitudinal river profiles were made, stairs were made, and possible locations for Hydro Power Plants construction were indicated.

Hydro Power resources were started to explore in Lithuanian Energy Institute at the 1947, when a group of scientists began to take interest in hydropower issues. M.Lasinskas studied and analyzed energy indicators of Lithuanian small rivers [9]. A Hydro Power laboratory was established in 1957 and has continued the hydrology research of S. Kolupaila. The hydrology laboratory was established for the development of water resources research in 1961 and headed by academician M. Lasinskas.

Resources of small Lithuanian rivers were calculated by “Hydroenergoprojekt” institute in 1950. The power of small rivers was estimated at 118,590 kW [10].

The theoretical hydro power potential was determined of 689 MW and 6 TWh of annual hydroenergy [10]. When connecting of all settlements to the electricity grid started, the small Hydro Power Plants were abandoned and their liquidation ended in 1982. Were considered that hydropower resources of the rivers are limited and unable to meet the rapidly growing energy needs. Lithuanian electricity needs were met by thermal power plants.

The importance of hydropower and interest in its potential grew up again after Lithuania restored its independence, and after joining the European Union, the country had to fulfill its obligations to increase energy production using renewables. Therefore, since 1995, until 2005 construction of small HPP was started again.

The research results of hydropower and hydrology laboratories were used as basis to determine the most suitable locations for the construction of Ignalina NPP and Kruonis Pumped Storage Power Plant. The possibilities of the cooling pond of the nuclear power plant were investigated. The changes in the flow during operation of Kruonis Pumped Storage Power Plant were studied using the hydrodynamic modulus of the MIKE 21 model [11].

The potential energy of the Lithuanian rivers was studied by the scientists of the Lithuanian Energy Institute [12], [13]. After assessing environmental restrictions, the last one introduced in 2003, the estimated potential hydro-energy of rivers decreased from 618 million kWh down to 125 million kWh and power down to 28.7 MW [12].

2.2. Riverine Hydrokinetic Energy Research

One of the first use of Neris river water hydrokinetic power was mentioned at 1581 [14]. The first hydrokinetic power plant in Lithuania on the Merkys river was built by the inventor J. Jakaitis [15].

The kinetic energy of the Nemunas and Neris flows has been evaluated by scientists [18], [19]. The average flow rate of the Neris river is 0.8 m/s, the average power density in the cross-section is 0.30 kW/m^2 and the average power is 39 kW. Nemunas average power density was determined 0.15–0.3 kW/m^2. While in the spring flood, the kinetic power density can reach 1.4 kW/m^2.

The hydro - kinetic resources of Lithuania's medium and small rivers were determined on those sections of the river where the depth of the wag is greater than 0.5 m and the average flow velocity is higher than 0.4 m/s [16], [17]. It is estimated that the length of potentially used river segments is up to 2000 km. The relative hydrokinetic power is unevenly distributed: 54.9% of river stretches of this length have a power of less than 50 kW/km, with only 3.9% of the length stretching has value over 150 kW/km.

The hydropower of the Neris River was explored, which consists of potential and kinetic hydro-energy [20], and found that the comparative potential energy is 273,3 kW/km and the kinetic energy is 2.0 kW/km.

3. CONCLUSIONS

- From the earliest times, river energy has been used and research on riverine energy has been carried out for almost a century.
- Since 1918 in Lithuania, efforts were made to maximize the use of hydropower in an effort to replace imported fossil fuels, therefore systematic hydrological research was performed, and the average power of rivers was estimated.
- After assessing environmental restrictions, the last one introduced in 2003, the potential hydro-energy of rivers decreased from 618 million kWh down to 125 million kWh and power down to 28.7 MW.
- In assessing the hydro - kinetic energy potential of the Neris and Nemunas rivers, it is possible to find the river sections where the potential of hydro - kinetic energy can be used. The kinetic energy of the Neris river is only 0.75% of the potential energy.
- Although the potential of the potential riverine hydro-energy was reduced and the wider use of hydrokinetic energy is limited by small resources and technologies, these studies need to be developed through the advancement of the use of hydro turbines and the improvement of the ecological situation.

REFERENCES

1. JAHREN, P., TONGBO, S. How water influences our lives. Beijing (China): Chemical Industry Press/Springer, 2017. p. 285.
2. Corporate author, *Lithuanian Energetics*. Vilnius, 1982, Vol. 1, p. 192 [In Lithuanian].
3. BILYS, S., *Mirages of Hydro Power Plants in Lithuania, 1909–2009.* Vilnius, 2010. p. 152 [In Lithuanian].
4. KOLUPAILA, S., *Our white peat coal*. Lietuva, 1922, No.102 [In Lithuanian].
5. KOLUPAILA, S., River Nemunas loop. On the issue of Lithuania's electrification. *Kosmos*, 1929, No. 5, p.169-200. [In Lithuanian].
6. KOLUPAILA, S., Preliminary Lithuanian water power cadastre. *Works of Lithuanian Energy Committee.* Kaunas, 1939, Vol. 3, p.10-36. [In Lithuanian].
7. SMILGEVIČIUS, J., *Hydro power station in Pazaislis on river Nemunas*. Kaunas, 1934, p. 34. [In Lithuanian].
8. LASINSKAS, M., Hydro power in Lithuania, 1940–1990. *Power engineering*, 1991, No. 4(8), p. 41-61. [In Lithuanian].
9. LASINSKAS, M., Energy indicators of small Lithuanian rivers and their determination metodology. *Works of Kaunas Politechnical Institute*. Kaunas 1955, Vol. 4, p. 161-174. [In Lithuanian].
10. JABLONSKIS, J., LASINSKAS, M., *Cadastre of Lithuanian Rivers. (debits, slope, capacity).* Vilnius, Vol. 3, 1962, p. 640 [In Lithuanian].
11. GAILIUŠIS, B., KRIAUČIŪNIENĖ, J., RIMAVIČIŪTĖ, E., Modeling the Effect of Hydroelectric Pumped Storage Power on Regime of the Kaunas Reservoir in Lithuania. *Nordic Hydrology*, 2003, Vol. 34. No. 5, p. 507-518.
12. JABLONSKIS, J., TOMKEVIČIENĖ, A., Opportunities of the Small Lithuanian Hydropower Development. *Power Engineering*, 2004, No. 2, p. 40-46. [In Lithuanian].
13. JABLONSKIS, J., Hydropower balance of Lithuanian rivers. *Power Engineering*, 2005, No. 3, p. 40-46. [In Lithuanian].
14. BILYS et al., *Small Hydropower.* Vilnius, 2017, p. 208. [In Lithuanian].
15. PUNYS, P., VAIŠVILA, A., Run-of-the-river Hydro Power Plants. *Planning and Hydrotechnics*, 2012, 4, p. 48-57. [In Lithuanian].
16. JAKIMAVIČIUS, D., GAILIUŠIS, B., ŠARAUSKIENĖ, D., JURGELĖNAITĖ, A., MEILUTYTĖ-LUKAUSKIENĖ, D., Assessment of the riverine hydrokinetic energy resources in Lithuania. *Baltica 27 (2),* Vilnius, 2014, p. 141-150
17. GAILIUŠIS, B., JAKIMAVIČIUS, D., ŠARAUSKIENĖ, D., JURGELĖNAITĖ, A., Assessment of hydrokinetic resources of small and medium-size rivers: the Lithuanian case. *Baltica 30 (1),* Vilnius, 2017, p. 23-30.
18. PUNYS, P., MARTINAITIS, E., VYČIENĖ, G., VAIŠVILA, A., Assessment of the hydrokinetic energy characteristics of the river Neris using a one dimensional numerical HEC RAS 4.1 model. *Water Management Engineering,* 2013, 42 (62), p. 61-71.
19. PUNYS, P., ADAMONYTĖ, I., KVARACIEJUS, A., ŽILINSKAS, S., Hydraulic-geometric characteristics of the River Nemunas for the assessment of hydrokinetic resources. *Agricultural Engineering, Research Papers*, 2013, 45 (3), p. 38-50.
20. JABLONSKIS, J., MEILUTYTĖ-LUKAUSKIENĖ, D., Hydro Power Assessment of the River Neris. *Power Engineering*, 2015, Vol. 61, No. 3-4, p. 141-148. [In Lithuanian].

ACCUMULATION OF HEAVY METALS IN A COMPLEX ECOSYSTEM OF OVERGROWN LAKES ON THE EXAMPLE OF RAKOVYE LAKES IN THE LENINGRAD REGION VYBORG DISTRICT

T. S. Semyonova, N. V. Dinkelaker
Saint-Petersburg National Research University
of Information Technologies, Mechanics and Optics
Kronverkskii Pr. 4, St-Petersburg – Russia,
E-mail: little-star96@inbox.ru

N. F. J. Dinkelaker
Saint-Petersburg State Forest Technical University
Institutsky per. 5, St-Petersburg – Russia

ABSTRACT

Rakovye lakes in Leningrad Region are one of the largest lakes, which connecting with the Vuoksi River. However, after the intervention of nature and of significant changes caused by man, the lake became shallower almost 8 times and broke up into 2 small lakes.

All these transformations has changed ecosystem. Though they didn't diminish its nature protection role in the region as a main ornitological area for nesting and migrating water fowls. The lakes still play an important role as a water habitat and as the habitat of a large number of endangered species of plants and animals.

The X-ray fluorescent examination of the samples of bottom sediments showed the presence of low concentrations of heavy metals (Sr, Fe, Ni, Cr, Cu, As, Co), which have also been identified in dominant vegetation types (helophyte plants – Typha latifolia L., Typha augustifoliaL., Phragmites australis (Cav.) Trin. ex Steud., Glyceria maxima (Hartm.) Holmb.; floating plants – Nuphar lutea L., Numphaea candida J. Presl & C. Presl, Sparganium erectum L., Sparganium emersum Rehmann, Potamogen natans L.; submerged plants – Spargánium graminéum L., Myriophyllum spicatum L.).

Quiet high concentration of the lead (Pb) was fixed in all samples of the bottom sediments. The accumulation of each studied heavy metals (Sr, Pb, Fe, Ni, Cr, Cu, As, Co) in aquatic plants and their parts (leaves, roots, stems) is very low if to compare it with the bottom sediment. It has differed a few times.

Lead is the major pollutant of the ecosystem in Rakovyie lakes. The studying of the anthropogenic's transformation history of the ecosystem shows that this pollution has been causedby a very long high hunting activity in this area before the time when the area has become a nature protected area – the reservate.

Nowadays the lead which has been accumulated intto the bottom sediments for a long period of hunting on water fowls could penetrate into food chains of the lakes' ecosystem, barring into food chains over aquatic vegetation.

Keywords: ecosystem components, heavy metals, lead pollution, bottom sediments, aquatic vegetation, food chain

1. INTRODUCTION

The Rakovye lakes located on the Karelian isthmus in the Leningrad region of Russia are one of the key ornithological territories of Russia. There is one of the routes of the white sea – Baltic flight path of birds lies. Swans, geese, ducks and river ducks fly over the Rakovye lakes in thousands flocks from the Baltic and North seas to the Arctic tundra and taiga in spring and autumn back. The whole system of lakes is of great importance for the maintenance of fish resources of the Ladoga basin. Heated shallow waters are large spawning grounds for bream, roach, perch, pike and other fish species [1].

The Rakovye lakes is a system of reservoirs, which are connected both with each other and with other lakes and Vuoksa river.

The Rakovye lakes consists of a Large Rakovoe and a Small Rakovoe lakes. All lakes are shallow and subject to overgrowth to varying degrees. At the moment, the Small Rakovoe lake is completely overgrown with helophyte.

Overgrowth of water bodies is a natural process that leads to the formation of swamps. Almost all lakes are subject to this, especially those that have a weak fluidity. However, in such lakes can slow down the process of overgrowth, or, conversely, accelerate, which sometimes occurs as a result of human activity [2].

The leading role in the process of overgrowing and disappearance of lakes belongs to the highest aquatic plants. By accumulating significant biomass, they also accumulate heavy metals of both natural and man-made origin. Heavy metals can accumulate in tissues and organs, retain them during the growing season and thus exclude them from the cycle in the reservoir until their death and decomposition. Partly they precipitate in the form of carbonates, sulfates, partially adsorbed on mineral and organic sediments. As a result, the content of heavy metals in sediments is constantly increasing, and when the absorption capacity of sediments is exhausted, heavy metals enter the water. This is facilitated by an increase in water acidity, strong overgrowth of reservoirs, intensification of CO_2 release because of the activities of microorganisms [3]. Heavy metal compounds are relatively rapidly distributed over the volume of the water body. Of particular importance for aquatic ecosystems is the distribution of these pollutants in the ecosystem and their inclusion in food chains. In the case of shallow overgrown lakes, such as the Rakovye lakes, the most important is the assessment of the inclusion of heavy metals from sediments in biotic components, in which the main role is played by higher aquatic plants. Modern literature data about the contamination of the system of the Rakovye lakes by heavy metals have not been found.

Since 1994, the water area of the lakes has been included in a specially protected natural area – the nature reserve of regional importance "Rakovye lakes", but the anthropogenic load on the ecosystem has increased in the last 20 years due to the construction of the main oil pipeline in the adjacent territories and the expansion of residential areas. In this regard, the assessment of pollution of lakes with heavy metals and the prospects of their distribution in biotic components is relevant both for the conservation of lakes of high conservation value, as and for the conservation of migratory waterfowl, massively stopping on the lakes during migration. This report examines the accumulation of heavy metals in plants in overgrown lakes. Higher aquatic plants play an important role among the biotic components of aquatic ecosystems. Accumulating chemical elements, including heavy metals, in tissues and organs, they retain them throughout the growing season and thus exclude them from the cycle in the reservoir until their death and decomposition [4].

The present study was conducted to assess the modern state of accumulation of heavy metals in different species of higher aquatic plants the largest and most important lake system of the Rakovye lakes – the Big Rakovoe lake.

2. METHODS OF RESEARCH

The research was conducted in July – October of 2017 and 2018 on the lake Great Rakovoe (Karelian isthmus, Leningrad oblast, Russia). Collection of material of higher plants was carried out during land and water routes. For studies was selected as the major plant communities, among them – a representative of drop-off. The collection of plant material was carried out in spring by the method of averaged sample – from 10 to 15 plants of each species, one age group, from the same organs. The plant material was dried to an air-dry state, was crushed using a disk eraser to particle size $\leq$ 71 microns. Further preparation of samples was carried out in accordance with the requirements of the PP. 5.1-5.5 GOST ISO 11464-2015.

The study of heavy metal content in plant samples was carried out using x-ray scanning crystal diffraction spectrometer SPECTROSCAN MAX-GV by quantitative analysis.

Studies of eutrophication of water bodies was conducted on the results of geobotanical studies and indicators, which were obtained on the basis of aerial and satellite imagery of the area of the Rakovye lakes in the 1970s, the 1990s and early 2000s. Processing and interpretation of the materials made use of software packages MapInfo7, MapViewer4 methods of manual and automatic tracing.

3. RESEARCH RESULTS

The main forms of overgrowthing of the Great Rakovoe lake are the increase in the flat area of coastal dense alloys, the formation of Islands of vegetation with dense soil in the water area, the expansion of sparse zones of aquatic vegetation. Compacted alloys on the lake. B. Rakovoe is mainly represented by thickets of broadleaf cattail, narrow-leaved cattail, common reed. Sparse thickets without compacted soil formed the same types in the initial stages of settlement, as well as Sparganium emersum, Spargánium eréctum, Glycéria máxima.

The increase in the rate of overgrowth of the lake was facilitated by a decrease in the flow of water into the lake due to the dam built in 1984. By 1991, the total area of dense alloys increased by about 15%, by 1999 – by 150% compared to 1979 [5]. The year 1999 was critical for the lake's overgrowth. In the absence of measures to raise the water level of the lake could grow completely in a few years, as it is almost no sites with a depth of more than 70 cm, complicating the settlement of aquatic plants. There was a compaction and an increase in the number of Islands with vegetation, the alloys were compacted and increased in size. Continued shallowing of the Rakovye lakes, which resulted in even more growth.

However, in 2001 the dam was built on creek Holodnyi (flowing out of the lake), which has helped to increase summer water level at 40 cm. This change allowed us to slow the pace of eutrophication of lakes [6].

Inhibition of aquatic vegetation from the water level rises tracked on satellite images of 2002-2010 as a reduction in land area, defiinitely as dense alloys and reducing the area and density of the sparse thickets of higher aquatic vegetation. In the period 2010-2018, there is a gradual recovery of the area of dense alloys, which does not reach the maximum values of 1999. However, there was an intensive development of sparse macrophyte thickets throughout the lake area, which indicates the continuing threat of a new stage of lake overgrowth.

Figure 1 shows a graph of how the area of loose (dark column) and dense (light columns) alloys changed between 1979 and 2018.

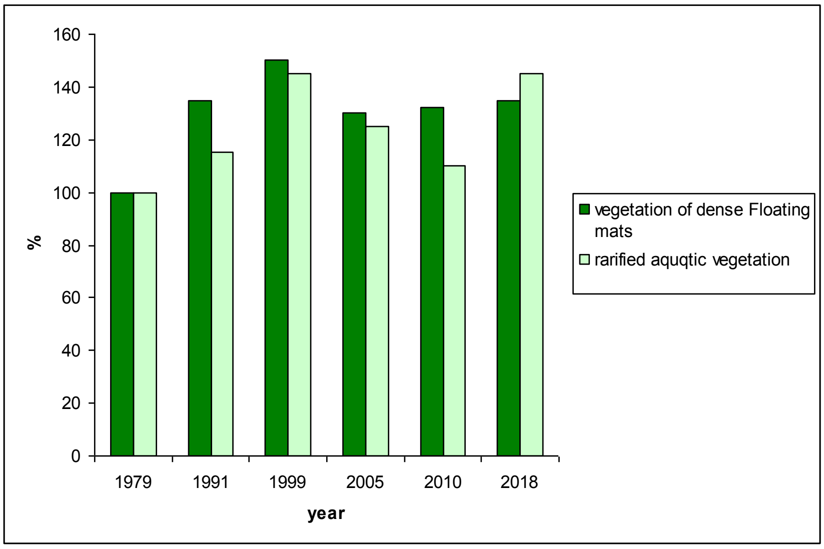

Fig. 1. Schedule of changes in the area of rafting and thickets of higher aquatic plants of the great Rakovoe lake

As the lake is overgrown with higher aquatic plants, the amount of heavy metals that accumulate in the plants and enter the reservoir after the death of the previous ones or enter the food chains of the ecosystem increases. Given the fact that heavy metals can accumulate in sediments in both mobile and little mobile forms, and the ability of plants to extract metals from sediments is different in species, it is particularly important to assess the cycle of heavy metals in the soil-plant state for different types of vegetation.

Determination of the level of accumulation of heavy metals in the soils and vegetation of a large alloys lake was performed for the bottom soil and the dominant plant species and their organs (leaves, roots, stems, fruits). Plants of different ecological groups: air-water plants and floating plants were investigated.

The study of bottom soils was carried out in the thickets of different species of aquatic plants and in the water area devoid of vegetation (Table 1).

The content of heavy metals in sediments depended little on the type of vegetation and generally had low values (Table 1). The exception was the lead content, which is slightly higher than the values typical for the water bodies of the region and the maximum permissible concentrations in the soil [7].

Table 1. The concentration of heavy metals, manganese and iron oxides in the higher aquatic vegetation of oz. B. Rakovoe

The part of the lake B. Rakovoe	**Concentration of metals in bottom sediments, mg/kg**									
	Sr	**Pb**	**As**	**Zn**	**Ni**	**Co**	**Fe**	**MnO**	**Cr**	**V**
Bottom sediments from parts of lake, overgrown with helophytes	250	18	12	66	20	4	0	558	65	50
Bottom sediments from parts of lake, overgrown with floating vegetation	189	21	11	87	23	6	4,17	656	74	58
Bottom sediments from parts of lake, overgrown with submerced vegetation	200	14	11	71	248	4,4	3,7	547	68	56
Bottom sediments from parts of lake without vegetation	180	19	10	76	21	3	4	822	70	59

The low content of heavy metals in aquatic plants of the investigated water body was revealed. We can see the results on Table 2. Distribution of accumulation of heavy metals in the water area is mosaic. There is the fact that heavy metals can accumulate in the biomass of aquatic plants.

Table 2. The concentration of heavy metals, manganese and iron oxides in the higher aquatic vegetation of the Great Rakovoe lake

Species	**Concentration of metals in dry leaves, mg/kg**									
	Sr	**Pb**	**As**	**Zn**	**Ni**	**Co**	**Fe_2O_3**	**MnO**	**Cr**	**V**
Typha latifolia L.	131	10	5	90	2	0	0.05	520	41	0
Týpha angustifólia	123	12	6	78	5	0	0.04	741	48	0
Phragmites communis Trin.	105	14	7	66	4	0	0.09	466	18	0
Sparganium ramosum Huds.	122	12	5	74	2	0	0.2	483	31	0
Glyceria maxima (Hartm.) Holmb.	117	14	3	81	3	0	0.2	754	28	0
Nuphar lutea (L.) Sm.	100	8	3	71	4	0	0.12	885	35	0
Nuphar pumila (Timm) DC.	90	9	5	80	1	0	0.16	1111	38	0
Nymphaea candida J. Presl & C. Presl	110	7	6	66	12	0	0.24	1347	40	0
Potamogeton natans L.	115	4	5	61	20	0	0.3	1567	36	4.8
Sparganium gramineum Georgi	134	3	5	105	9	0	0.2	1392	51	0
Myriophyllum spicatum L.	127	5	6	70	18	0	0.5	2015	48	0
Potamogeton perfoliatus L.	140	3	3	81	11	0	0.3	1610	43	0

We noted the effect of accumulation of strontium, lead, arsenic, chromium in aquatic plants of all studied groups. Especially effective in aquatic vegetation accumulates manganese and zinc, their concentrations in plants in some cases exceeds that in the bottom soil. At the same time, the accumulation of vanadium and cobalt in aquatic plants practically does not occur.

4. SUMMARY

At this stage of overgrowing of the lake has slowed the growth water area dense quagmire from the banks due to the artificial raising of the water level in 2001, after some degradation of the dense quagmire that occurred between 2001 and 2005, began to stabilize contours of aquatic vegetation. At this stage of growth consists of slow growth coastal pay quagmire and active capture the waters of the lake are overgrown with submerged plants.

Accumulation of heavy metals, manganese and iron oxides in the soil – plant system is quite active, but given the low content of pollutants does not pose a danger to the food chains of the ecosystem.

Different ecological groups of plants differ somewhat in their ability to extract individual heavy metals from the soil. The greatest ability to accumulate lead was observed in helophytes, strontium and zinc – in helophytes and submerged plants. The high ability of plants of all groups to accumulate manganese and zinc, most pronounced in plants with floating vegetation, is shown. Accumulation of vanadium and cobalt in the studied species of aquatic plants does not occur.

Currently, the ecosystem of the Great Rakovoe lake Is not contaminated with heavy metals, which emphasizes the importance of preserving the conservation regime of the reserve in the conditions of increasing anthropogenic load on the adjacent territories.

It is also necessary to regularly monitor the pollution of ecosystems by heavy metals, as with increasing their income accumulation in the ecosystem will be enhanced by the activities of common thickets of aquatic plants. This will lead to the rapid incorporation of these pollutants into the ecosystem. Taking into account the importance of the Rakovye lakes for fattening waterfowl during migration along the white Sea-Baltic migration route and characteristic for many species of waterfowl feeding on aquatic plants, pollution of the ecosystem will spread pollutants over long distances.

For more accurate information on heavy metals entering the soil and plants, monitoring and control of available sources of anthropogenic impact on the Rakovye lakes is necessary.

REFERENCES

1. Boch M.S., Katanskaya V.M. Cancer lakes reserve // Sketches of vegetation in specially protected natural areas of the Leningrad Region. Tr. Botanical Institute of them. V. L. Komarova RAS. SPb, 1992. Vol. 5. pp. 31−43.
2. Rast W., Thornton J.A. Trends in eutrophication research and control // Hidrological processes. 1996. V.10. P. 295–313.
3. Titov A. F., Kaznina N. M. Talanova, V. V., Heavy metals and plants. Petrozavodsk: Karelian scientific center of RAS, 2014. 194 p.
4. Rosseland B.O., Hidar A. Water, Air and Soil Pollution., 1988. Vol. 41, № 1-4, p. 165-188.
5. Popova T. A. Current state and rates of overgrowing of Karelian isthmus lakes /Ecology of the overgrown lake and problems of its restoration. SPb.: Science, 1999. 11-15 p.
6. Iovchenko N. P. Ecosystems of the reserve "Rakovye lakes": history and current state: monograph. SPb.: Ed. house SPb state University, 2011. 297 p.
7. "Norms and criteria for assessing the pollution of bottom sediments in water bodies of St. Petersburg "(Approved by the Chief state sanitary doctor of St. Petersburg 17.06.1996 and the Committee for the protection of the environment and natural resources of St. Petersburg and Leningrad region 22.07.1996).

8. Resolution of the Chief state sanitary doctor of the Russian Federation of 23.01.2006 N 1 (edition of 26.06.2017) "About introduction of hygienic standards of GN 2.1.7.2041-06" (together with "GN 2.1.7.2041-06. 2.1.7. Soil, cleaning of populated areas, waste production and consumption, sanitary protection of soil. Maximum permissible concentrations (MPC) of chemicals in soil. Hygienic standards", approved. Chief state sanitary doctor of the Russian Federation 19.01.2006) (Registered in the Ministry of justice of Russia 07.02.2006 N 7470).
9. Sadchikov A. P., Kudryashov M. A. Ecology of coastal and aquatic vegetation. Moscow: NIA Priroda, 2004. 220 p.
10. Karaskova I. L. Higher aquatic vegetation of the Eastern part of the Gulf of Finland. SPb., 1997. 158 p.

CYSENI 2019, May 23-24, Kaunas, Lithuania
ISSN 1822-7554, www.cyseni.com

A PILOT STUDY OF VIBROACOUSTIC CHARACTERISTICS OF VARTSIKHE HPP HYDROPOWER UNITS

D. DzaDzamia
Akaki Tsereteli State University
Akhalgazrdoba Avenue 98, 4600 – Georgia
Email: Datodzadzamia1@gmail.com

N. Kopaliani
Akaki Tsereteli State University
Akhalgazrdoba Avenue 98, 4600 – Georgia

Technical evaluation of hydropower units requires undertaking the pilot studies, in order to study the amplitude and frequency characteristics of vibrations in the full range of generation of vibrations. The paper describes the results of such studies using the example of hydropower units of Vartsikhe HPP. Measurements on the second unit of Vartsikhe HPP were carried out on a mounting platform. Measuring point was selected at 1 m from the shaft of the rotor to the turbine, in the standard mode of the operation in the radial, tangential and vertical directions at four points of hydropower unit. These points are – turbine, bottom bearing, top bearing and a blade-control valve. The operation mode of hydropower unit was standard, and only one unit was operational. There have been measured the sound pressure levels *dB C* and sound level *db A*, in the standard octave and third-octave bands. There were used the vibro-measuring instruments VSV-003-003 (accuracy class 1. GOST 17187-81) and the vibratory acceleration piezo sensors DN-3 (frequency range 10-4000 Hz), as well as the modern, portable vibrilometer VM 6360. During the measurements, the sections of 20-30-second vibration signals were registered using a special computer program, and then, they were processed and analyzed under laboratory conditions. The vibration signals were digitized using a special computer program as well as in a MathCad environment.

The following vibration characteristics of the taken off signals have been analyzed and generalized: forms of the vibratory acceleration signals, the root-mean-square values of signals - RMS, which are proportional to the vibrational energy of the signals).

The measurements were carried out at two-week interval. After that, there was carried out a pilot study of the acoustic characteristics of hydropower unit. There have been compared the results of the first and second measurements and relevant conclusions have been made. In pilot studies, there have been used modern methods of narrow-band, octave and tierce-octave spectral analysis (SpectraLab, MathCad). The experimental data have been processed in a MathCad environment using a special computer program, which, within several minutes, finds all vibration parameters and compares them to each other, both the results of several measurements and, if required, the results of measuring different hydropower units.

Keywords: Hydropower, Vibroacoustic characteristics, Frequency characteristics

1. INTRODUCTION

Introduction of vibrating monitoring and diagnostics tools of hydropower units requires an in-depth and thorough knowledge of their vibrational fields. To that end, it is necessary to undertake the pilot studies of vibration characteristics, in order to study the amplitude and frequency characteristics in a full range of vibration generation. The pourpose of the vibration tests is to obtain information on the current technical ststus of hydropower unit. This allows for identifying any fault immediately before the stage of its inception [8]. The paper describes the results of such study using an example of hydropower units of Vartsikhe HPP. The measurements were carried out in all three directions (vertical, tangential and radial) at four vibroactive points (at the Vartsikhe HPP) [6]. These points were as follows: turbine, bottom bearing, top bearing and a blade-control valve, as shown in Figure 1.

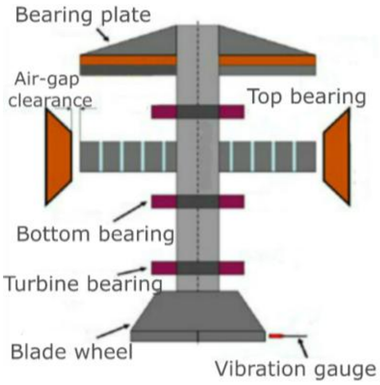

Fig. 1. The scheme of the measurement points of hydropower unit

2. RESEARCH METHODS

While solving the formulated problems, there were used the points of Theory of Machines and Mechanisms, machine dynamics, type identification, probability theory and mathematical statistics. The use of these methods allows engineers for determining any vibration signal they took off in their desired frequency band, as well as for creating a large database [7]. In the pilot studies, there were used methods of narrow-band, octave and tierce-octave spectral analysis (SpectraLab, MathCad) [3]. The methods of decision-making and type identification theory were used in developing the algorithms of diagnostics [9].

3. EXPERIMENTS

There were used the vibro-measuring instruments VSV-003 (accuracy class 1. GOST 17187-81) and the vibratory acceleration piezo sensors DN-3 (frequency range 10 -4000 Hz) (Fig. 2).

Fig. 2. Vibro-meter VSV-003 and piezo sensors DN-3

Also, there was used the modern, portable vibrilometer VM 6360 specifically bought for this expriment (Fig. 3).

Fig. 3. A portable vibrilometer VM 6360

The sensors were fixed to the measured surface uing the magnet and prism, as shown in Figure 4.

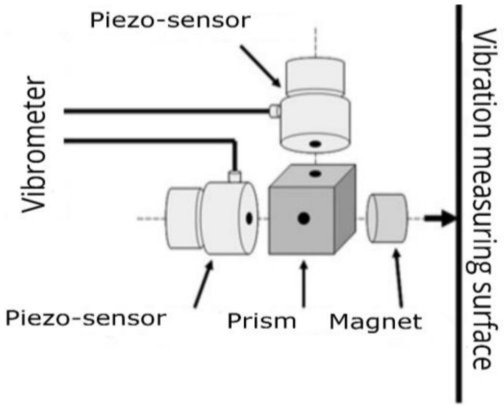

Fig. 4. Measuring instrument

The frequency of the rotor's nominal rotations at the Vartsikhe HPP (the low-rotation vertical aggregates of a Francis type) is 115.5 rpm, that is 1.923 Hz. All dynamic processes in the system are repeated with periodicity of f_0 = 1.923 Hz. This is the main frequency of the rotor's rotation rotation and the harmonics appear at the frequencies $k*f_0$, where k = 1,2,3,…

Fig. 5. Vartsikhe HPP's hydropower unit

When measuring in the vertical direction, the measuring instrument was rotated at 90 degrees to its own axis and then measured in the tangential direction. The accuracy of measurements was ± 1 *db*. The device is completely usable in measurements of relative vibrations and in the assessment measurements, especially when comparing two and several measurements with each other [10]. During the measurements, the sections of 20-30-second vibration signals were registered using a special computer program, and then, they were processed and analyzed under laboratory conditions. The vibration signals were digitized using a special computer diagnosis program created by the authors in a MathCad environment [1].

A pilot study of the acoustic properties of hydropower unit was also carried out at the Vartsikhe HPP to diagnose the technical states. The noise levels were measured in order to compare them with their reference values. There was selected the measurement point at a mounting platform at a distance of 1 m from the rotor shaft near the turbine, as shown below in Figure 6.

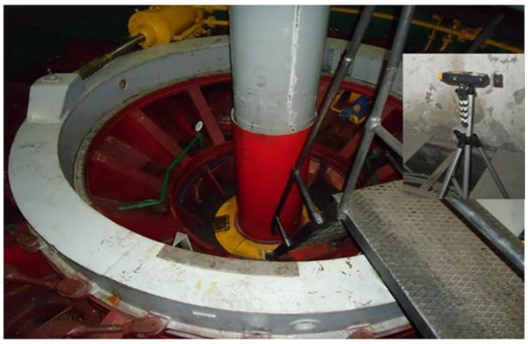

Fig. 6. Noise measurement point at a distance of 1 m from the rotor shaft near the turbine

4. PROCESSING OF SIGNALS

The following vibration characteristics of the taken off signals have been determined and analyzed:

- forms of the vibratory acceleration signals;
- the root-mean-square values of signals – RMS, which are proportional to the vibrational energy of the signals,

where RTS – is Real Time Series - the measured values of the amplitudes of vibration digital signals, i = 0,1,2, … N – the numbering of the examined points of vibrations. The growth of RMS (the root-mean-square value) indicates increasing vibration level:

$$RMS = \sqrt{\frac{1}{N-1}\sum_{i=0}^{N-1}\left[\left(RTS^{<1>}\right)_i\right]^2}\,, \tag{1}$$

$$CrestFactor = \frac{\max(RTS^{<1>})}{RMS}. \tag{2}$$

In case of large values of CrestFactor (≥ 6), the impacts are produced in the vibrating system;

- total signal levels, *db*;
- displacements with total levels on the main rotating frequency, mm;
- spectral composition of signals in the octave bands of frequencies;
- spectral composition of signals in the tierce-octave bands of frequencies;
- narrow-band spectral composition of signals (the conduction band – 0,673 Hz) in a full frequency range and the detailed analysis of constituents, using both linear and logarithmic scales of measurements;
- finding the local and global maximums with their own frequencies;
- cepstra (which indicate the perodicity in the signals);
- spectral composition of a mechanical repeater of vibor-acceleration signals; they are obtained first by finding a mechanical repeater of signal, by Hilbert transform, and then, they spectral compositions are finding by Fast Fourier Transform (FTT);
- spectral composition of a mechanical repeater of the filtered high-frequency signals [2].

All these signal characteristics are the standard functions of a MathCad package and its Extension Pack “Signal Processing”, andtheir finding in a MathCad space is carried out simply and instantaneously. The analysis of these parameters led to the localization of incepted faults. In this case, no fault will be localized as stated in the conclusion.

One of the typical digrams developed in a Mathcad environment as shown in Figure 7.

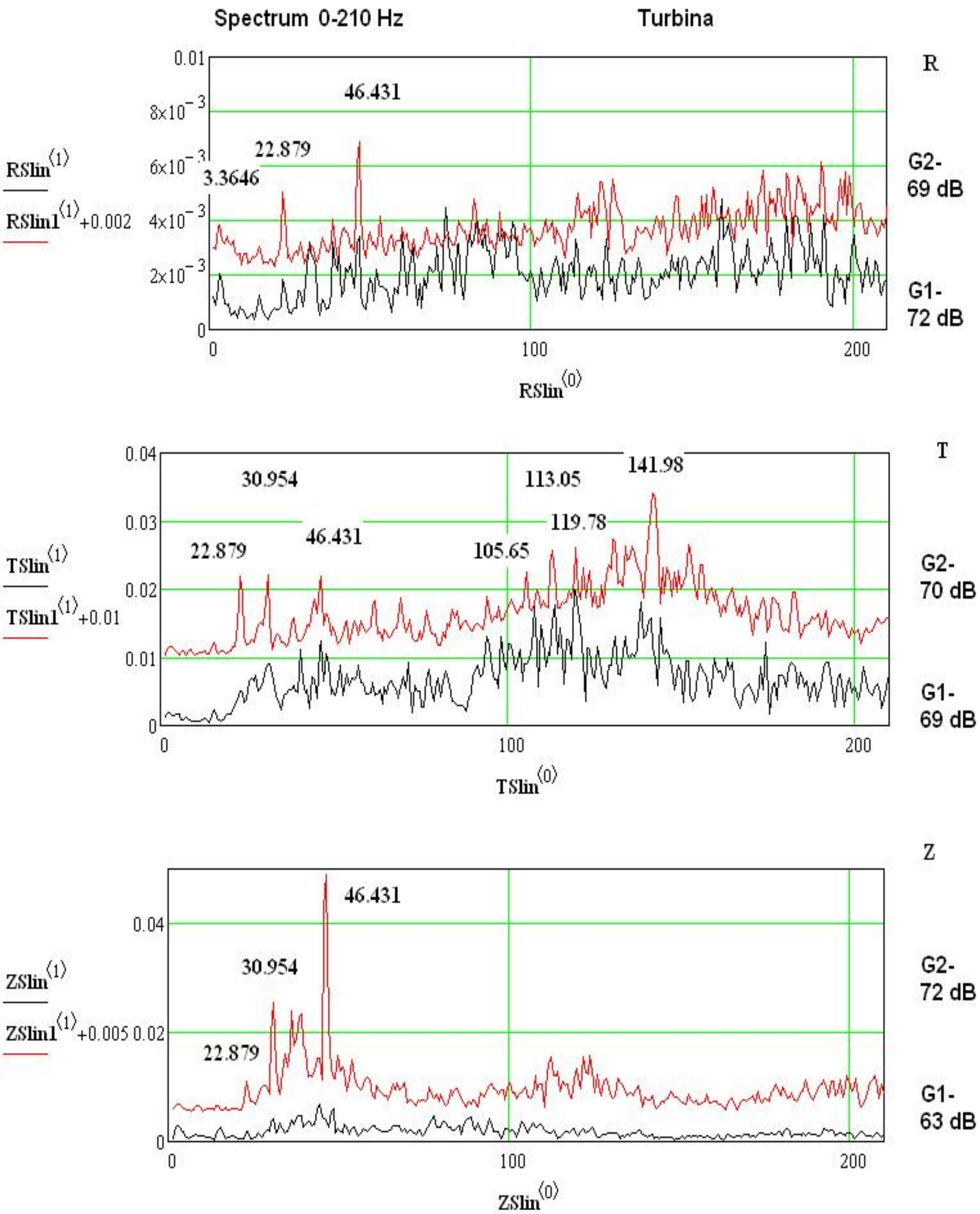

Fig. 7. Comparison of spectral constituents of G2 generator of the Vartsikhe HPP's hydropower unit in a frequency range of 0–210 Hz in vertical, tangential and radial directions

Figure 8 illustrates the comparison of the results of first and second measurements.

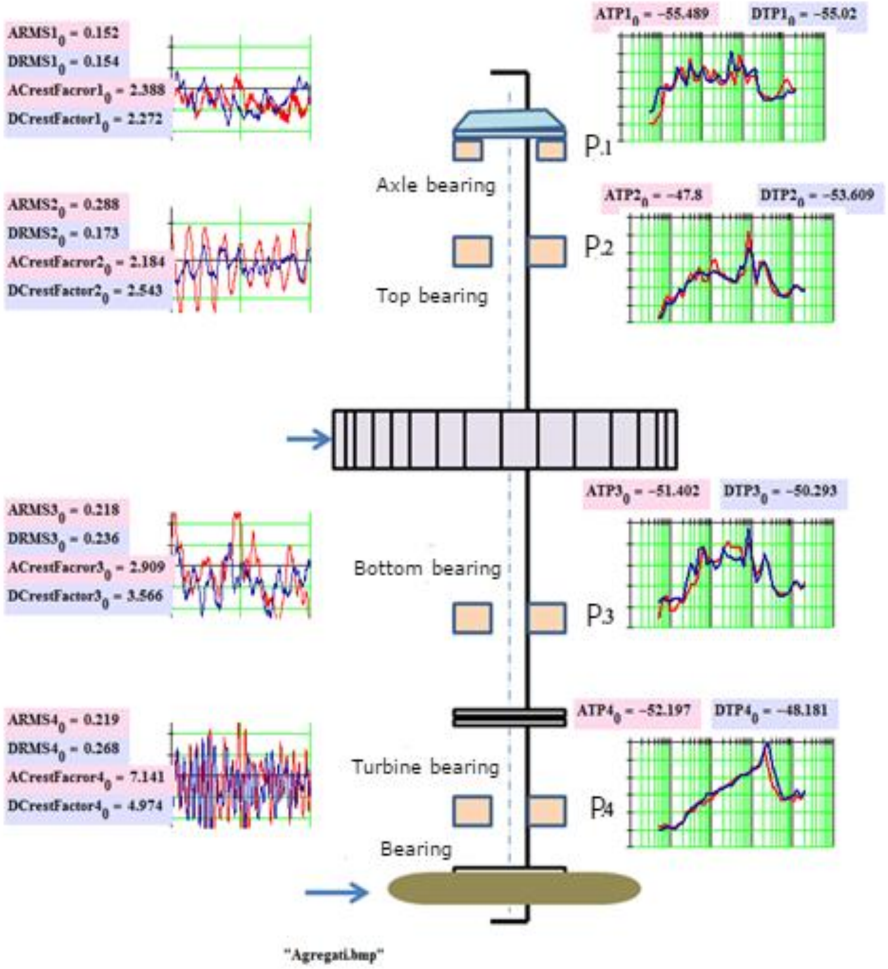

Fig. 8. Comparison of the signals of the measured ibration fields of the signals measured in radial direction (the red color designates the first measurement results, and the blue color – the second measurement results)

4.1. A pilot study of the acoustic charactersitics of the Vartsikhe HPP

Noise measurements are less common in the objectives of vibro-acoustic monitoring and diagnosis of the technical tates of energy devices. Providing a detailed and thorough analysis of a particular noise source is much more difficult in the case of other noise sources. In addition, the problem of singling out the concrete constituent of noise, which is due to the defect precipitation, is complicated as a result of possible multiple reflections and refraction of noise waves [5]. In the vicinity of the vibrating surface, there is a near diffusion field of noise with complex form pseudo-constituents, which are transformed into a simple (wave) form when removed from the source [2]. That is why noise measurements are almost always carried out at least 1 m away from the surface of the device under study. When measuring vibrations, the localization of is simplified considerably. The operational mode of hydropower unit was standard, and only one hydropower unit operated. There have been measured the sound pressure levels *dB C* and sound level *db A*, in the standard octave and tierce-octave bands [4]. The narrow-band spectral analysis was carried out by step of 0.637 Hz throughout the audible frequency range.

Figure 9 illustrates the comparison of noise levels with admissible values.

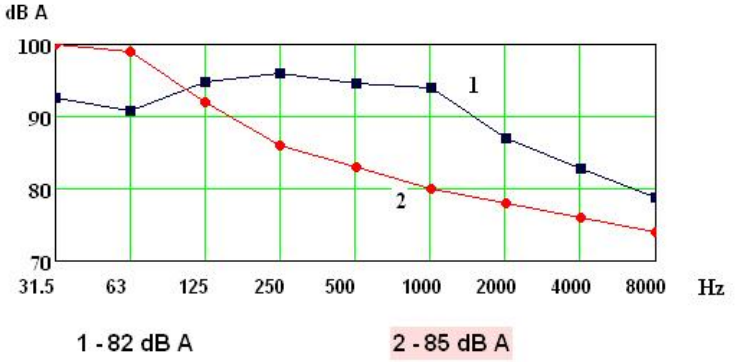

Fig. 9. Comparison of noise levels with admissible values (the red color designates the admissible level, and the blue color designates the noise level obtained as a result of measurements)

5. CONCLUSION

At the moment of measurements, except for minor deviations in the vibration characteristics of hydropower units, as far as can be judged from single measurements, there were no significant defects in the system, violation of capacity to work and hydropower units were a satisfactory technical status.

The vibrations may lead to the following possible defects: turbine (impulse wheel) malfunction; defects of its separate blades; increasing water flow turbulence; water cavitation.

None of these defects were identified during this study.

For accurate assessment of a technical status of hydropower unit, measurements should be carried out systematically, at regular intervals, and the results of previous and new measurements should be compared.

REFERENCES

1. Kopaliani, N., Kopaliani, D. The digital analyzer for vibro acoustical diagnostics of technical conditions of machines in MathCad. *Geogrian Scientific News*, 2010, No. 3, p. 26–31.
2. Norton, Michael. P. *Fundamentals of noise and vibration analysis for engineers*. Melbourne Australia: Cambridge University Press, 1999. 619 p. ISBN 0-521-34941-9.
3. Mathcad, version 14.0.0.163. Help. - Parametric Technology Corporation, 2007.
4. Digital Sound Level Meter – RadioShack, Owner's Manual. Tendy Corporation.
5. Kopaliani, N., Kopaliani, D. Development of systems with an artificial intellects for the purposes of vibroacoustical diagnostics. *Periodic scientific magazine Novation*, 2008, No. 1, p. 22-31.
6. Kopaliani, N., Kopaliani, D., Giorkhelidze, N. Digital spectral processing of vibroacoustical signals for diagnostics a technical condition of mechanical systems. *Georgian academy of sciences*, 2005, No. 8, p. 44–56.
7. Dimentberg, M. F., Frolov, K. V., Menyailov, A. l. *Vibroacoustical diagnostics for machine and structures.* Taunton, Somerset England: Research Studies Press, 1991. 630 p. ISBN 0-863-80116-1.
8. Marinescu, D. *Handbook of machine tool analysis*. Bosa Roca United States: CRC Press, 2002. 322 p. ISBN 0-8247-0704-4.
9. Kopaliani, N., Zivzivadze, O. Realization of a problem vibroacoustical diagnostics of technical conditions of hydro power units in Mathcad. *Periodic scientific magazine Novation*, 2015, No. 15, p. 232–238.
10. Kopaliani, N., Gorgodze, G., Dzadzamia, D., Purtseladze I. About one method of a digital band filtration of vibroacoustic signals. *Periodic scientific magazine Novation*, 2017, No. 19, p. 101–105.

CYSENI 2019, May 23-24, Kaunas, Lithuania
ISSN 1822-7554, www.cyseni.com

ENERGY FORECASTING VS ENERGY MODELLING
JAZZ IMPROVISATION VS SYMPHONY

M. Grajcar
HafenCity University
Überseeallee 16, 20457 Hamburg– Germany
Email: maria.grajcar@hcu-hamburg.de

ABSTRACT

Energy forecasting and energy modelling have become more than just tools mirroring general technological development; from classical mathematical relationship models based on statistics to artificial intelligence and fuzzy logic. Forecasting almost always implies modelling; this modelling exercise should not try to fit to historical records but should produce the best forecasts.

In his speech on the Global Forecasting Competition, Dr. Tao Hong listed four main issues in energy forecasting in 2014: impractical research, lack of benchmarking data, a hard-to-reproduce process, and limited educational programmes and courses. This paper addresses the issue no. 1 – impractical research, since energy forecasters devote almost all of their efforts to describing a methodology setup, leaving any interpretation of results aside. Secondly and not surprisingly, policy makers and even professionals in the energy sector do not make any distinction between energy forecasting and energy modelling; this fact is also partially responsible for the gap between the research and real needs of the energy sector.

In this paper, the relationship between energy modelling and energy forecasting is explained firstly in theory by analogy with music, and secondly in current energy models applied to natural gas forecasting. Most energy models are theoretically based on applied knowledge from macroeconomics and statistics, therefore a missing piece of social science will be explored especially with regard to the results of energy models.

Keywords: energy forecasting, energy modelling, energy infrastructure

1. INTRODUCTION/ PROBLEM SETTING

> “Change comes most of all from the unvisited No Man’s Land between the disciplines.”
> (Norbert Weiner)

Energy forecasting and modelling may either be pleasant intellectual exercises for researchers working in Computer Science or Macroeconomic Affairs departments at universities, or they may make a real change to future energy systems.

Albeit far from perfect, no matter how perfection is defined, forecasting functions and models enter the realm of policy making and may influence the security of energy supply in the future[1] as already recognised by a few authors, for example in [19].

The broader definition of energy forecasting is “forecasting in the energy industry” and covers gas and electric load forecasting, price forecasting, renewable generation forecasting etc. The term “energy” in “energy forecasting” determines the usage of forecasting methods in the respective field of interest only, as the same forecasting method may be used for various study objects; output growth forecasting, exchange rate forecasting, inflation forecasting to mention but a few.

Up until now, well-known modelling scenarios have underestimated the growth of renewable energy in developed countries and overestimated the consumption growth of natural gas in developing countries in the past and thus current energy and international policies have been based on assumptions that have not come true. Wind and solar installed capacity (and possible future

---

[1] This paper is an introduction to the research PhD project on the Security of Energy Supply with the focus on Technical Infrastructures.

production) were simply adjusted upwards afterwards in almost every forecasting report. This fact is hardly surprising to anyone unless the boom of forecasting and modelling methods is taken into consideration.

The aim of this paper is to analyse current trends in energy forecasting and modelling in relation to the energy sector. Examples of models were carefully chosen according to criteria as follows:

a) The subjects of energy forecasting and modelling are relevant for the future security of supply of a respective country or region. From this perspective, long term forecasting is of higher importance than short-time or middle-time forecasting.
b) A method used represents a current trend in the energy forecasting.

Historians may already consider writing the history of forecasting methodologies, mirroring general technological development; from classical mathematical relationship models based on statistics (linear regression, autoregressive integrated moving average) to artificial intelligence (fuzzy logic, genetic algorithms, artificial neural networks – ANNs and deep neural networks). Merkel et al. provide an overview of the last mentioned methods [1], whereas Tamba et al. conducted a fascinating literature survey on natural gas forecasting in 2018 [2].

The vastness of literature documenting forecasting methods is striking for a newcomer in the field, especially when compared to the literature on the interpretation of results for energy supply and/or future development of infrastructure. Dropping the necessity of a deep understanding of energy processes was initially regarded as a great advantage of new tools such as neural networks and fuzzy logic and led to the boom of research articles applying new tools to energy forecasting and energy modelling.

In reality, most analysts understand oil/gas prices or demand as just one of the objects of their research, to prove or validate their forecasting methodologies – without being genuinely interested in the implications of their research on the energy sector. In accordance with the nature of their discipline, they spend 95% of the space in their articles on methodology setup. To energy forecasters, the energy sector is one field of many where their knowledge is applicable, filling the missing pieces of information for the future as illustrated in Figure 1. This attitude requires an implicit core assumption that necessary information, condensed in data sets, is complete and known as well as relations among them thanks to the applied methods.

Putting forecasts under scrutiny, represented by zooming in on Figure 1, highlights the current status of the use of energy forecasting in energy sector.

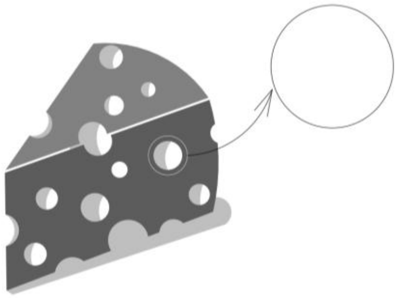

Fig. 1. Relationship between forecasts and the energy sector

As Ascher put it in his now-classical work on forecasting [3] and Overholt confirmed its timeless validity 22 years later [4], accuracy does not have to be the highest goal when producing forecasts. Forecasts ordered by public institutions set the mood in a particular decade by forecasting the future share of *renewable energy* in the energy mix, making distinctions between *smart grids* and traditional grids and promoting e.g. *Sektorkopplung* in Germany. The expressions in italics represent trendy words in chronological order (as they entered the virtual space of public debates on energy); one plays around *econometric methods, neural networks and fuzzy logic* in a similar fashion in energy forecasting. The explosion of articles in the field has the unspoken intention of enhancing the prestige of the forecaster or capturing the attention of the public and/or academic world.

2. THEORETICAL BACKGROUND OF ENERGY FORECASTING AND ENERGY MODELLING

2.1. Energy forecasting

The mere fact that energy forecasting and energy modelling are used interchangeably [5], [6], [19] reduces the use of their results in the energy sector.

Classically, energy forecasting has been based on two forecasting approaches; on the extrapolation of past historical data for predicting the future and on the modelling (simulation). The first group of methods deals with the concept of curve fitting – using multiple regression to fit a polynomial function to a series of data points. The more polynomials are chosen, the less fitting error. However, the fitting error is not the measure of the quality for the accuracy of the forecast and its reduction definitely does not increase the chances of predicting for example, oil price shocks two weeks in advance.

The main principle of forecasting is to find *a model*, whose ability for explaining historical data at best has no correlation with the quality of its predictions. As an explicit example of the logic behind the models, the Auto-Regressive Integrated Moving Average Model (ARIMA), introduced by George Box and Gwilym Jenkins in the 1970s, was chosen. Hong [7] explained the autoregressive process applied to forecasting the electric load as follows: “the current value of the electric load is often expressed as a linear combination of previous electric load values and with a random noise“. In the model-fitting process, analysts try to fit their model to the data until residuals become white noise and forecasts look reasonable[2]. Needless to say, since for example the energy forecasting of natural gas is marked by its seasonality, especially due to its use in the residential sector, researchers must use a seasonal difference while conducting long-term forecasts.

Econometric forecasting methods deliver satisfying results if the situation on the national energy market is stable as they excessively rely on history. These methods would naturally fail to predict for example the reduction of gas demand by 10% during the crisis in the Ukraine in 2013–2014. Still, regression models are the most common methodologies used in energy forecasting.

In theory, if the process (e.g. future development of the fuel consumption in one respective region, available electricity capacity of transmission system) is not known but various measurements, observations and samples exist, one may accept neural networks (NNs) as a suitable tool for energy forecasting or modelling. Rácz and Németh [8] interestingly apply neural networks, or more precisely, a method called dynamic line rating when predicting the maximum transmission capacity of the electricity grid. All theoretical conditions were fulfilled, the process is only partially known; the standard models are based on a simplified heat equation neglecting e.g. electromagnetic phenomena:

$$Pj + Ps = Pc + Pr, \tag{1}$$

where: Pj – Joule heating (J); Ps – solar heating (J); Pc – convective cooling; Pr – radiative cooling.

The above-mentioned measurements exist in the form of data for solar radiation, wind and ambient temperatures of previous years and actual current values of currents represented by the current and the temperature of the line. The model examined above-ground lines with the maximum permissible temperature of 40 °C due to the limitation of the sag. According to their results, the neural network calculated the temperature of the wire with an error of under 7%, this rate means max. 2 °C difference in a temperature, which roughly coincides with the accuracy of sensors [8].

---

[2] Similarly, forecasts based on regression analysis models per energy production site are corrected by operational staff due to their operational knowledge of the system. On the national scale this would be impossible to do.

Answering the question of maximum transmission capacity for a new technology of installing lines underground would require a new, more complex setup of a model.

2.2. Energy modelling

The concept of the modelling fits to the greater areas and to the creation of scenarios due to long-term visions as illustrated in Figure 2. Models are used for example in testing the resilience of the technical infrastructure with hypothesized shocks; showing *the way* to the goals of a low carbon energy future or testing the hypothesis of mitigation of Russian gas dependency through energy efficiency and renewable policies.

Simply put, their role is definitely not to predict.

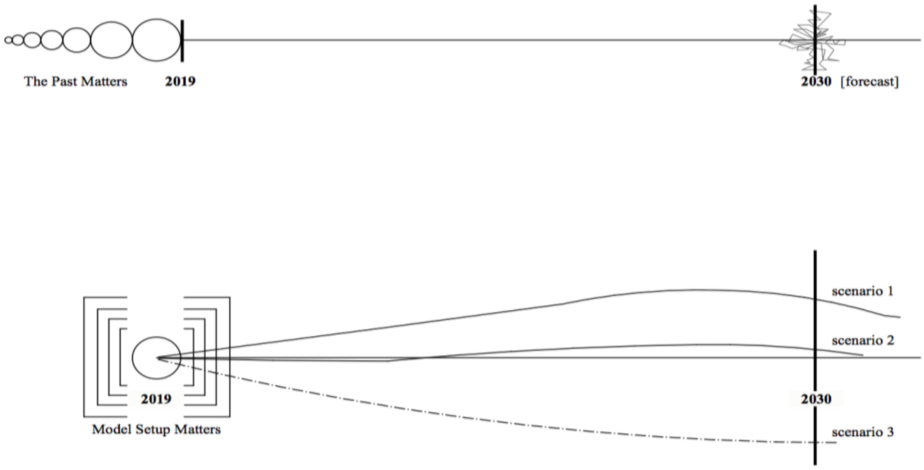

Fig. 2. Energy forecasting vs energy modelling

Henrik Lund et al. analysed the role of energy system modelling in the transition away from fossil fuels in democratic societies based on two basic archetypes: simulation vs. optimization of national energy models [9]. While the optimization approach pre-sets a goal (the lowest energy consumption or the highest reduction of carbon dioxide emissions) and searches for the lowest-cost path possible to achieve it; simulation models tend to create various scenarios for the future; ideally taking into account future technological options, fuel prices (a product of energy forecasting), and policy issues.

To conclude this part, energy models cannot promise more than the representation of an energy sector in a macroeconomic model or be a macroeconomic model itself representing national, regional or global economy. Their outcome, as shown on the example of Lund et al.'s research and in Table 1 is a projection of various scenarios without any probability distributions. Therefore, strictly speaking, their outcomes cannot be labelled as forecasts. Fragkos et al. [10] tried to solve this by incorporating uncertainty into world energy modelling in the case of the PROMETHEUS Model. This hybrid model combines structural considerations (including expert judgement) with time-series analysis for providing patterns of variation over time. Interestingly, its deterministic version[3] has been extensively used in studies of the European Commission such as EU Energy Roadmap 2050[4].

---

[3] In a deterministic version, all equation parameters are set at their mean versions [31].

[4] Shortly after, the district heating sector introduced its own Heat Roadmap of Europe as the EU Energy Roadmap 2050 anticipated the massive use of electricity in the heating sector.

Table 1. Energy forecasting vs. energy modelling with a focus on the natural gas (NG) sector

	Energy forecasting	Energy Modelling
Character	(mostly) stochastic	(mostly) deterministic
Examples of methods	a) econometric method based on input-output coefficients b) an added load method considering additions and deductions to NG demand due to new connections and efficiency improvements	Optimisation based on maximising total surplus or minimising total costs for gas infrastructure
Statistics-exogenous data	Forecast load: weather variables (temperature and humidity), heating and cooling days, temperature-humidity index	NG consumption (as a result of optimisation, it could be endogenous, too), price of natural gas and of alternative fuels (to take into account fuel-switched effects), supply constraints (e.g. pipe capacities), existing technology stock
Demand functions	(Mostly) weather responsive especially for short-term forecasting	Price responsive
Human behaviour	Implicitly in the historical data	Explicitly the own assumptions of the researchers or taken from the official national models (e.g. energy scenarios from the UK Energy Research Centre's UK Energy 2050 project)
Geographical coverage **(relevant for security of energy supply)**	Irrelevant (mostly at city or state level) "trading can take place anywhere with an internet connection"	a) global e.g. one of the first of this kind: Shell global energy model from 1974, World gas model; PROMETHEUS b) regional, national c) supranational, e.g. European Gas Market Model
Outcome	Prediction (point, interval) with a probability distribution	a) energy projection as a function of energy policies applied b) projection scenario (set of assumptions on key inputs) without a probability distribution
Evaluation of the outcome	Root Mean Squared Error (RMSE) Mean Absolute Percentage Error (MAPE) Weighted Mean Absolute Percentage Error (WMAPE)	No general evaluation standard
Client/ contracting body	Private Sector. Academic world	Public sector: federal agencies, ministries, academic world

2.3. Analogy with music. Idea experiment

At first glance, piano jazz seems like a spontaneous activity; the pianist is just listening to the jazz music in the background and a listener never knows what the final musical experience will be like. A person not familiar with computer science and statistics at a professional level (energy experts, policy makers) has the same impression when trying to understand forecasting methods as more than just a plain *black box* and inevitably wonders about the final forecasts and their relation to reality. The analogy with jazz improvisation works with the process of forecasting, not for an outcome.

On closer inspection of the jazz improvisation, one starts to question the aspect of *improvisation* in a performance – since there are certain rules (such as adapting to a rhythm, never playing the same note in a row etc.) that guide a jazz pianist when improvising. As Hatch put it, jazz performances are structured around playing the tunes, which themselves are loosely structured via partial musical arrangements called heads [11].

These rules are analogous to the classical Hubbert model, statistical methods, fuzzy logic, neural network; all methods are listed in Fig. 3 in a non-accidental order. In free jazz[5], the more experienced the jazz pianist becomes, the fewer rules are applied, with the exception of one: feeling the music. In other words, the higher we climb the ladder, the more the music loses structure, while gaining mastery of "unpredictable". The same tendency is noticed in the development of forecasting methodology: from rather rigid methods to the soft computing trying to mimic the intelligence found in nature. Thus, hidden layers in neural networks or transforming linguistically expressed knowledge (mirroring imprecise and uncertain human thinking) into workable algorithms (fuzzy logic) are placed higher up the ladder, although not achieving the climax, a paradigm change to come. In other words, single methods such as the Hubbert Curve Model, statistical models, and the Grey Prediction Model are slowly being replaced by hybrid methods such as the Bayesian Model Averaging [19], or the combination of the Autoregressive Moving Average (ARMA) method with genetic algorithms [20].

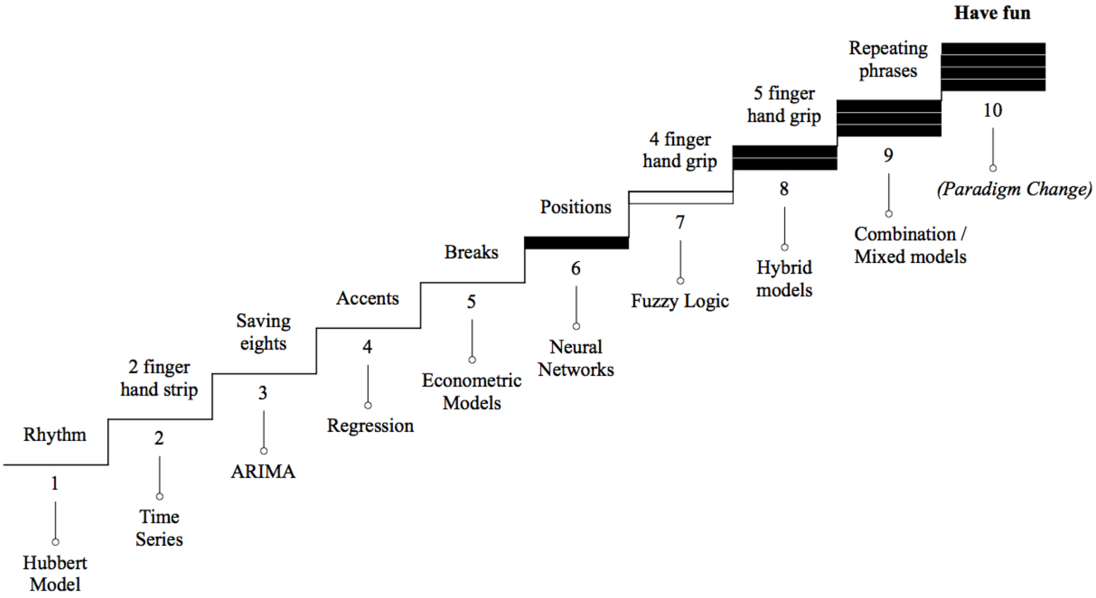

Fig 3. Parallels between steps for learning jazz piano improvisation and developing new methods for energy forecasting.
Sources: Maria Grajcar (analogy), Oliver Prehn (10 steps in piano jazz improvisation), Comfort Mosha (illustration)

---

[5] In other jazz genres, most of improvisations follow more or less strict rules. Some rules are even related to the physique of a player and the used instrument.

Symphonies such as the Symphony No. 3 D major Op. 29 *Polish* composed by Tchaikovsky are a perfect example of presenting the process of energy modelling. Taking the example of the technical infrastructure model, there is a definite number of musical instruments producing the sound (pianos as energy generation types such as combined cycle gas turbine (CCGT), coal and nuclear power plants) with their own characteristics (the note A above middle C is usually tuned to the frequency 440 Hz as well as the electrical efficiency threshold of the combined cycle gas turbine is up to 45%). During the performance of the symphony, the noise occurs (heavy breathing of a pianist, coughing of the lady in the third row), as well as during the running of the simulation. To put this another way, final results can be as unexpected as the random sounds coming from an audience in the Staatsoper Hamburg.

The choice of a master work matters, e.g. energy models comparable to symphonies composed e.g. by Scriabin with almost no repetitions have not been designed, yet. However, hybrid models would best represent the approximation of these kinds of symphonies.

2.4. Interdisciplinary Aspects

Since statistics and macroeconomic theory are inherent parts of energy forecasting and modelling, respectively; the influence of social science is illustrated in Annex 1 (Fig. 4), analogically to the identical phenomenon in music.

Because of the consequences of the state of the things in the illustration in Annex 1, Sovacool et al. [13] suggested a program-centred approach to the energy field instead of the technology-centred approach to encourage interdisciplinary depth. Although this direction is already noticeable in the calls for further research projects of national institutions in Germany, energy forecasting and modelling has not been *touched* so far. To be concrete, let us imagine analysts asking “how high will the natural gas peak demand be in Germany in 2030” instead of thinking about “how to demonstrate that neural networks are the right tool for prediction of natural gas demand in Germany in 2030.”

Regarding the interdisciplinary aspects, International Energy Relations is a discipline from a social sciences group mostly related with the original interest of this paper: energy supply security with the reliability of energy models discussed. Michael Jefferson calls the discipline “International Political Economy of Energy[6]” with its roots in the 1970s as a product of the OPEC crisis [14]. The following example demonstrates the increasing complexity of the interdisciplinary independencies having a huge impact on the outcome of energy modelling: the production quotas of OPEC countries, since December 2018 excluding Qatar, depend on the proved recoverable conventional oil reserves (field: IR – international relations). This fact caused the amendment of a definition with a shift from a 90% probability to a 50% probability, which led to the massive increase of oil reserves in the Middle East region in global statistics (field: statistics). Similarly, China, a relevant country because of its future energy demand, overestimates its own natural gas reserves due to differences in classification and definitions of gas resources/reserves between China and those accepted internationally [6].

Changed data from globally relevant information sources such as BP Statistical Review, the US Department of Energy or the IEA are used on an input side in energy models and naturally-produce quantitatively different results which stimulate discussions of “Peak Demand” instead of Peak Oil. The concept of Peak Demand has already entered the territory of energy modelling, e.g. DNV GL forecasts an oil demand peak for 2023 and gas demand peak for 2035 in its newest Energy transition outlook 2018, Oil and gas, Forecast to 2050 [15]. The industry insider and a party with its own interests in the sector uses a system dynamic model for modelling the entire world energy system based on the Stella modelling tool. Energy researchers from the DNV GL assume the continuation of current technology trends is what makes hydrogen as a special category less surprising and worth following in future analyses. Similarly, a global energy model Prometheus

---

[6] Articles of this kind are to be found in Journals such as Energy Research and Social Science, or Energy Policy.

[10] identifies 26 power generation technologies for an electricity generation module and 18 hydrogen production options in a separate hydrogen module.

3. NATURAL GAS AS SUBJECT OF ENERGY FORECASTING AND ENERGY MODELLING (EXAMPLES)

In a few examples, the research and its (im)practical use in the field of natural gas (NG) forecasting and modelling will be demonstrated, according to one single criterion: relevance of the results for either the natural gas sector and economy (forecasting) or for the energy security (modelling). This task may resemble detective work as it is not self-evident that the results of this particular scientific work shall be linked to the issues of the national economy or energy security.

Generally, most of papers follow the same structure:

1. A short justification for choosing natural gas forecasting and modelling (such as the rapid growth of natural gas consumption in a respective country, relevance of the precise forecasting for economic progress);
2. A description of the method used
3. Proof that the chosen method outperforms other methods or models by comparing MAPE and RMSE (see Table 1) or simply by naming new qualities of a suggested method (dynamic, adaptive).

The forecasting and modelling of natural gas demand or the need for further infrastructure (spatial modelling) show some peculiarities[7] inherent to the natural gas sector compared to other branches of energy forecasting and modelling (e.g., oil or electricity prices). This fact is not always considered by specialists in energy forecasting – economists and computer scientists. Secondly, if the natural gas sector is taken as just one of the sectors in a global energy system, it represents the highest uncertainty due to its unknown reserves. Starting with this very first point, Ul'yanin et al. [18] applied the balance econometric model and forecasted the depletion time of conventional natural gas reserves to 52 years (calculated from t_0 = 2015) with its consumption peak in 2029. When the unconventional natural gas reserves are included in the formulas, the depletion forecast shifts to the end of the 21st century. The outcome refers to the exhaustion of existing technological and economic possibilities as they are known now. Although the authors see the solution in nuclear bridging i.e. "the regeneration of artificial nuclear fuel plutonium -239 from uranium -238 and, possibly in the future, uranium -233 from thorium -232), the recommendation for the natural gas sector and its vast infrastructure seems to be clear: facilitation of the full deployment of power-to-gas technologies.

Gas crises in Europe in 2009 and 2014 initiated an increasing number of publications reporting on energy models set-up for testing the availability of natural gas in Europe, the level of dependency on imports and a more complex concept of energy security. Studies were mostly conducted for the most vulnerable countries in Central and South-Eastern Europe and for the United Kingdom (UK). UK researchers explored the resistance of the natural gas and electricity sector to the infrastructure failures as the country switched from natural gas exporter to importer; followed by the Netherlands for the first time ever in 2018[8] [21].

---

[7] Traditionally, short-term natural gas load (consumption) is divided into heat load, dependent mostly on temperature, and base load. The relation between the heat load and temperature is within a certain range of temperatures almost linear, as shown e.g. by Merkel et al. [1] for several Midwestern U.S. operating areas. The base load covers other usages of gas without direct dependence on the temperature, especially in the industry sector. Before massive deployment of technologies based on volatile renewable sources, the natural gas demand forecast for years to come was produced by the power generation sector without any huge variations. The same logic can be applied to the natural gas prices – without their unexpected rise – there was no need to make them a factor in forecasting methodologies. Another reason for excluding NG prices as a factor is their strong governmental regulation for final consumers (for example China).

[8] This rapid change in the NG trade deficit in the Netherlands has to do with the political decision to reduce gas extraction in Groningen, until no more gas can be extracted by 2030 due to fracking earthquakes in the region.

Chaudry et al. [16] used the combined gas and electricity network (CGEN) model for optimizing the gas and electricity infrastructure in the UK and assessing the security of natural gas supplies; based on the function of minimising the total operational and investment costs of the combined gas and electricity networks. The level of interaction between the two networks depends on the number and usage of gas turbine generators in the UK[9]. To simulate the diversity of supply, no single energy source is allowed to gain more than a 40% share of primary energy demand. Still, the decision of an operator to run a power-plant based on gas will depend on the actual electricity price, varying substantially over the day. Without considering other factors (NOx- emissions, wear-out of a turbine), this decision can be made each half an hour. Due to the possible back-up fuel, fuel-switched-effects need to be taken in account, too. Until now, only a few models have incorporated this option, one of them being Prometheus, modelling the world energy system [10]. The article has demonstrated that increasing the liquefied natural gas (LNG) capacity offers the best potential for mitigating the impacts of shocks to supply in terms of the volume of energy unserved, under two assumptions: a) flexibility of natural gas supply b) readiness to pay the market price for NG.

Selei et al. [17] went even further and combined three models for answering the question. “How far is mitigation of Russian gas dependency possible through energy efficiency and renewable policies assuming different gas market structures?” The European Gas Market model (EGMM) assumes that all producers, importers and traders are price-takers, all facilities are run at full capacities and the competitive equilibrium delivers an efficient social-welfare maximizing outcome. The setup of the model, clearly described in [17] together with assumptions, prevent extreme results from taking place. Authors accordingly claimed the demonstration of the possibility of reducing dependency on Russian natural gas “without causing an alarming rise in natural gas prices in any of the EU member countries.” Although their argument against planning more gas infrastructure as a solution for an energy supply security makes sense due to lock-in stranded assets in the sector and relying again on non-domestic energy sources in Europe, other countries such as China [6] or Germany with its NordStream 2 Project decided to rely on physical flows of the energy from abroad.

Furthermore, in 12 vulnerable countries of the EU in particular, including the Baltic States and Central and South-East Europe, natural gas, with its vast distribution network is mostly used for heating; i.e. in the sector, in which, suggested measures in [17] i.e. achieving higher energy efficiency and increasing the share of renewable energy are partially out of the scope of energy policies in respective countries.

To conclude this exemplary overview, current research on natural gas forecasting contributes to the methodology development rather than to the further knowledge gain for the natural gas sector in the respective country. If planners followed the forecasts from 2015, then China for example would be dealing with a remarkable oversupply of natural gas right now. However, it is actually the underestimation of natural gas consumption that is perceived to be linked with larger threats to the economy.

With regards to modelling and energy security, the relevance of the individual research projects is hardly accessible, as policy makers form their policies in accordance with the studies assigned by ministries and thus various research projects become secondary literature for them.

4. CONCLUDING REMARKS

The representation of the fact that most researchers do not distinguish between *energy forecasting* and *energy modelling* is comparable to a situation when a listener listening to the jazz

---

[9] Since the share of district heating networks in the UK is fewer than 2 %, it is natural that district heating networks were not considered. However, in countries like Germany, Poland or Slovakia with the high share of the use of the natural gas in the district heating network, the connection between the gas sector and heating sector would be the first to be assessed.

music or a symphony still refers to the activity as simply listening to the music. The reasons are as follows:

a) The capability of making distinctions is related to the general intelligence and the understanding of the issue thanks *to having been exposed to* them before.
b) Sharp thinking in strict mathematical terms has not been applied to the language used.
c) Although some programmes enable us to quantify relevant expressions; a word per se cannot be perceived as a number. Why not as an interval?

The advancement of energy forecasting and energy modelling requires truly interdisciplinary research of computer science with disciplines such as electrical engineering, meteorological science and international relations. Secondly, the quality of official data produced by e.g. EUROSTAT and the GDP is the Alpha and Omega of the success of current global energy models.

There is one single reality at the point of the time expressed by one single number and one unit representing for example natural gas demand in million cubic meters in Germany in 2030. The future does not offer us a space for three scenarios to take place and probably none of the scenarios known today will become reality. This one single reality is approached from various angles with their own assumptions, sometimes mirroring the wishful thinking, and the rest is done by statistical and mathematical tools. Not surprisingly, analysts do recognize shortcomings of their forecasting methods when the values violate economy theory (i.e. logic of the models) or common sense. This is usually solved by arbitrary subjective interventions or simply by ignoring these values.

Coming back to our analogy with music, listening plays a major part in piano jazz improvisation. How great (efficient) it would be, if this statement became reality for energy forecasting while addressing the needs of the energy sector? We have already mastered symphonies.

ACKNOWLEDGEMENTS

I would like to thank Comfort Mosha, M.Sc. for an unforgettable Friday afternoon (the 22nd February) spent discussing the visualisation of our ideas and Xhelona Haveriku, M.Sc. for exploring analogies between music and the natural gas sector. A special thanks goes to Jenna Arnold for ensuring the paper’s language accuracy.

REFERENCES

1. MERKEL, G.D.; POVINELLI, R.J.; BROWN, R.H. Short-Term Load Forecasting of Natural Gas with Deep Neural Network Regression. Energies 2018, 11, 2018.
2. TAMBA, J.G.; ESSIANE S.N.; SAPNKEN E.F.; KOFFI F.D.; NSOUANDÉLÉ J.L.; SOLDO B.; NJOMO D. Forecasting Natural Gas: A Literature Survey. International Journal of Energy Economics and Policy, 2018, 8(3), 216-249.
3. ASCHER, William: Forecasting: an Appraisal for Policymakers and Planners. Baltimore: Johns Hopkins University Press, 1978. 239 p. ISBN 0-8018-2273-4.
4. OVERHOLT, W.H. Ascher, William, Forecasting: an Appraisal for Policymakers and Planners. Policy Sciences (2000) 33: 101. https://doi.org/10.1023/A:1004767332251.
5. FRONTIER ECONOMICS. NG’s gas demand forecasting methodology. A report for ofgem, https://www.ofgem.gov.uk/ofgem-publications/41796/14619-117e.pdf (2006, accessed 10 February 2019) great example of the cooperation between economists and engineers.
6. SHAIKH, F., QIANG, J. Forecasting natural gas demand in China: Logistic modelling analysis. International Journal of Electrical Power & Energy Systems, 2016, 77, p. 25-32. 10.1016/j.ijepes.2015.11.013.
7. HONG, W.-C., Intelligent Energy Demand Forecasting, Lecture Notes in Energy 10, 2013. Springer-Verlag London, DOI 10.1007/978-1-4471-4968-2_2.
8. RÁCZ, L., NÉMETH, B. Investigation of dynamic electricity line rating based on neural networks. Energetika, 2018, Vol 64 No 2, p. 74-83 https://doi.org/10.6001/energetika.v64i2.3781.

9. LUND, H., ARLER, F., ØSTERGAARD P., HVELPLUND F., CONNOLLY D., MATHIESEN B., KARNØE, P. Simulation versus Optimisation: Theoretical Positions in Energy System Modelling. Energies 10, No. 7: 840.
10. FRAGKOS, P., KOUVARITAKIS, N. & CAPROS, P. Incorporating Uncertainty into World Energy Modelling: the Prometheus Model. Environ Model Assess (2015) 20: 549-569. https://doi.org/10.1007/s10666-015-9442-x
11. HATCH, M. J. Exploring the Empty Spaces of Organizing: How Improvisational Jazz Helps Redescribe Organizational Structure. Organization Studies, 1999, Vol. 20. No. 1, p. 75-100. http://doi:10.1177/0170840699201004
12. CAGE, J. 4′33″ For any instruments or combination of instruments. Piano solo arrangement. First movement. Retrieved from: https://musescore.com/peteryost/scores/3803521 on 22nd February 2019
13. SOVACOOL, B.K.; RYAN, S.E.; STERN, P.C.; JANDA, K.; ROCHLIN, G.; SPRENG D.; PASQUALETTI M.J.; WILTHITE, H.; LUTZENHISER, L. Integrating social science in energy research. Energy research and social science, 2015, Vol. 6, p. 95-99.
14. JEFFERSON, M. Energy realities or modelling: Which is more useful in a world of internal contradictions?, Energy Research & Social Science, 2016, Vol. 22, p. 1-6, https://doi.org/10.1016/j.erss.2016.08.006
15. DNV-GL, Energy Transition Outlook 2018, Oil and Gas Forecast 2050.
16. CHAUDRY, M., SKEA, J., WANG, X., JENKINS, N. Modelling UK energy system response to natural gas supply infrastructure failures. 2012. Proceedings of the Institution of Mechanical Engineers, Part A: Journal of Power and Energy, 226(4), 501–513.
17. SELEI, A., TOTH, B., RESCH, G., LÁSZLO, S., LIEBMANN, L., KADERJÀK, P. How far is mitigation of Russian gas dependency possible through energy efficiency and renewable policies assuming different gas market structures? Energy & Environment, 2017, 28, p. 54-69. 10.1177/0958305X16685471.
18. ULʼYANIN, Y.A., KHARITONOV, V.V. & YURSHINA, D.Y. Forestasting the Dynamics of the Depletion of Conventional Energy Resources. Studies on Russian Economic Development (2018) 29: 153. https://doi.org/10.1134/S1075700718020156
19. ZHANG, W., YANG J. Forecasting natural gas consumption in China by Bayesian Model Averaging. Energy Reports, 2015, p. 216-220. https://doi.org/10.1016/j.egyr.2015.11.001
20. ERVURAL, B.C., BEYCA O. F., ZAIM S. Model Estimation of ARMA using Genetic Algorithms: A Case Study of Forecasting Natural Gas Consumption. Procedia – Social and Behavioral Sciences. Volume 235, November 2016. p. 537-545. https://doi.org/10.1016/j.sbspro.2016.11.066
21. PIETERS, J. Netherlands faced first ever trade deficit in Natural Gas last year. 12th March 2019. Retrieved from https://nltimes.nl/2019/03/12/netherlands-faced-first-ever-trade-deficit-natural-gas-last-year on 17th April 2019.

Annex 1
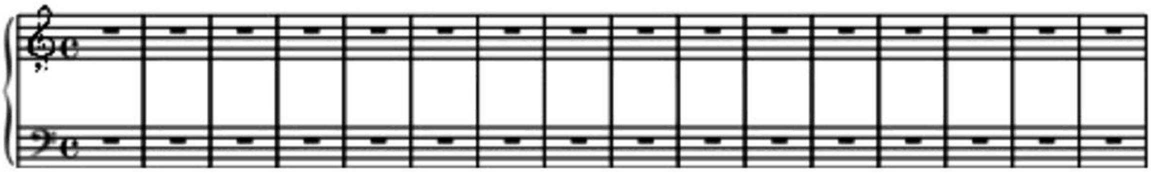
Fig. 4: Illustration of the role of social science in current energy forecasting
Source: Music note for 4′33″ Piano solo arrangement, First movement. Composed by John Cage [12]

CYSENI 2019, May 23-24, Kaunas, Lithuania
ISSN 1822-7554, www.cyseni.com

THE USE OF MULTI-PURPOSE ATOMIC COMPLEXES IN THE COUNTRIES OF MIDDLE EAST AND NORTH AFRICA

E. A. Sokolova, E. D. Fedorovich, K. Sadeghi, S. H. Ghazaie, M. V. Konushin
Peter the Great St. Petersburg Polytechnic University
Polytechnicheskaya str., 195251 – Russian Federation
Email: sokolenergo@mail.ru

S. S. Makuhin
JSC "SPbAEP"
Savushkina str., 197183 – Russian Federation

ABSTRACT

This paper presents various pre-project developments of Multi-purpose Atomic Complexes (MAC), various capacities and various types of equipment intended for the simultaneous production of electric energy, heat supply (in the form of steam and hot water) and large-scale desalination of sea water. It discusses the choice of type and capacity of nuclear reactors for the MAC, as well as desalination technology (distillation, reverse osmosis, hybrid), in relation to the needs of different countries, MAC potential customers. These are the countries of the Middle East, such as Iran, Kuwait, Saudi Arabia, United Arab Emirates, as well as the countries of North Africa: Egypt, Tunisia, Algeria. The scientific paper presents the results of the technical and economic analysis and the comparison of the MAC with various desalination technologies that are necessary to select such a MAC, that is the most suitable for a particular client country.

Keywords: multi-purpose atomic complex, nuclear desalination, water shortage in Middle East and North Africa, economic assessment of nuclear desalination in Iran

1. INTRODUCTION

The problem of ensuring the continuously growing needs of humanity for fresh water is becoming more acute in the world every year. The global shortage of fresh water, i.e. the difference between the required and available quantity is currently sensible by more than 1.2 billion people and for the future (2030), it is estimated that almost half the world's population will be living in areas of high water stress [1]. If it is not possible to significantly reduce (and even better eliminate) this deficit, then many countries of the world will be threatened by growing food shortages, rising social tensions and other difficulties, including war for water [2]. Nowadays, there is an effective way to solve this problem, namely, large-scale (in amounts of about one hundred thousandths of cubic meters per day or more) seawater desalination, which can be implemented in countries with territories in adjacent to sea or ocean. Such countries, which are considered here, are Iran, Qatar, Kuwait, Bahrain, Oman, the United Arab Emirates, Saudi Arabia, Egypt, Algeria, and Morocco.

A number of stated countries, which have great economic opportunities, already utilize powerful desalination plants for producing pure water. For example, Saudi Arabia is the leading country in production of desalinated seawater, which currently makes up more than 5,000,000 cubic meters per day. At the same time, in countries with relatively less developed economies assigned for seawater desalination technology, the situation is more critical. For instance, in Iran, the production of desalinated water is only around 420,000 cubic meters per day and it should be increased to meet the fresh water needs in future [3].

Desalination is an energy-intensive process: the amount of energy for the production of one cubic meter of fresh water range from about 4.5 to 100 kWh, depending on the desalination technology. Currently, a large amount (more than ~ 90%) of Desalination Plants (DP) mainly use fossil fuels, mainly natural gas as the source of energy. This situation can also be stated as the characteristic of the countries that we considered, most of which are rich in fossil fuels (oil, natural gas). Some of the DPs use the solar energy, the advantage of which is renewability (from an energy resource that is rapidly replaced by a natural process). The disadvantage is low power generation per square meter of installed panel, which leads to the need to extremely large areas and high capital costs for the construction of sufficiently powerful solar energy sources.

In our opinion, atomic energy source for desalination has the following indisputable advantages over the others:

- It is possible to implement any required power level - from several megawatts to several hundred, even thousands of MW.
- It is environmentally friendly: The harmful emissions (mainly CO_2) of the nuclear power is relatively low, comparing to the fossil fuel sources.
- Provision of fuel for many years. In particular, if we manage to organize an industrial scale of a closed fuel cycle with fast breeder reactors, and involve thorium fuel in nuclear power engineering.

Atomic energy source also contains some serious disadvantages. The potential hazards (in case of possible accidents in nuclear power plants) and high capital costs can be considered as the main disadvantages of nuclear power plants. Due to these difficulties, the MAC has not yet become widespread; however single desalination integrations to nuclear power plants operate in the United States, China, and Iran (in the first power unit of Bushehr NPP). Nevertheless, there can hardly be any doubt of the prospects for expanding its utilization, especially since the reserves of fossil fuels are depleting (however, new sources of fossil fuels have been proved in some regions) and their further production will be more costly.

This study discusses these perspectives in relation to the above-mentioned countries, and proposes an approach for developing recommendations on choosing the best options of equipment for MAC, considering the needs and capabilities of these countries. As a typical example, the MAC scheme with a medium-capacity nuclear water reactor (300 MW), which can be recommended for construction in a developing country, for example, in Iran is given. Our estimates show that in this case, the most appropriate desalination technology is hybrid, combining thermal desalination method of Multi-Stage Flash desalination (MSF) or Multiple-Effect desalination with the technology of Reverse Osmosis (RO).

The method proposed during the technical and economic analysis of MAC is based on the use of the DEEP programs (for economic calculations) and the DE-TOP (for thermodynamic calculations) of the main parameters and characteristics of equipment, with consideration of the MAC's specifications [4].

2. THE FRESH WATER SHORTAGE IN THE COUNTRIES OF MENA AND DEPLOYMENT OF THE MAC IN THESE REGIONS

Fig. 1 displays the water shortage status in some countries of Middle East and Northern Africa (MENA) [5]. This figure displays the grade of water stress, ranging from zero to five, in Iran, Qatar, Bahrain, Kuwait, Oman, the United Arab Emirates, Egypt, Saudi Arabia, Algeria and Morocco for 2010 and 2040. All of these countries have territories with the water of the Persian Gulf, the Oman Sea and the Mediterranean Sea (as can be seen on the map shown in Fig. 2).

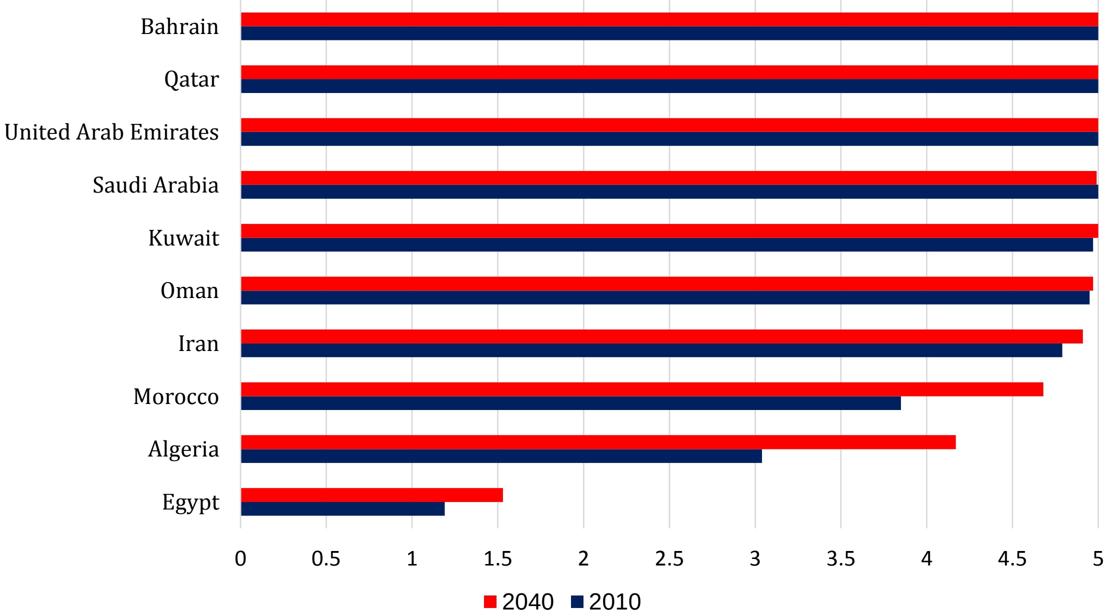

Fig. 1. Water crisis status of some MENA countries in 2010 and 2040

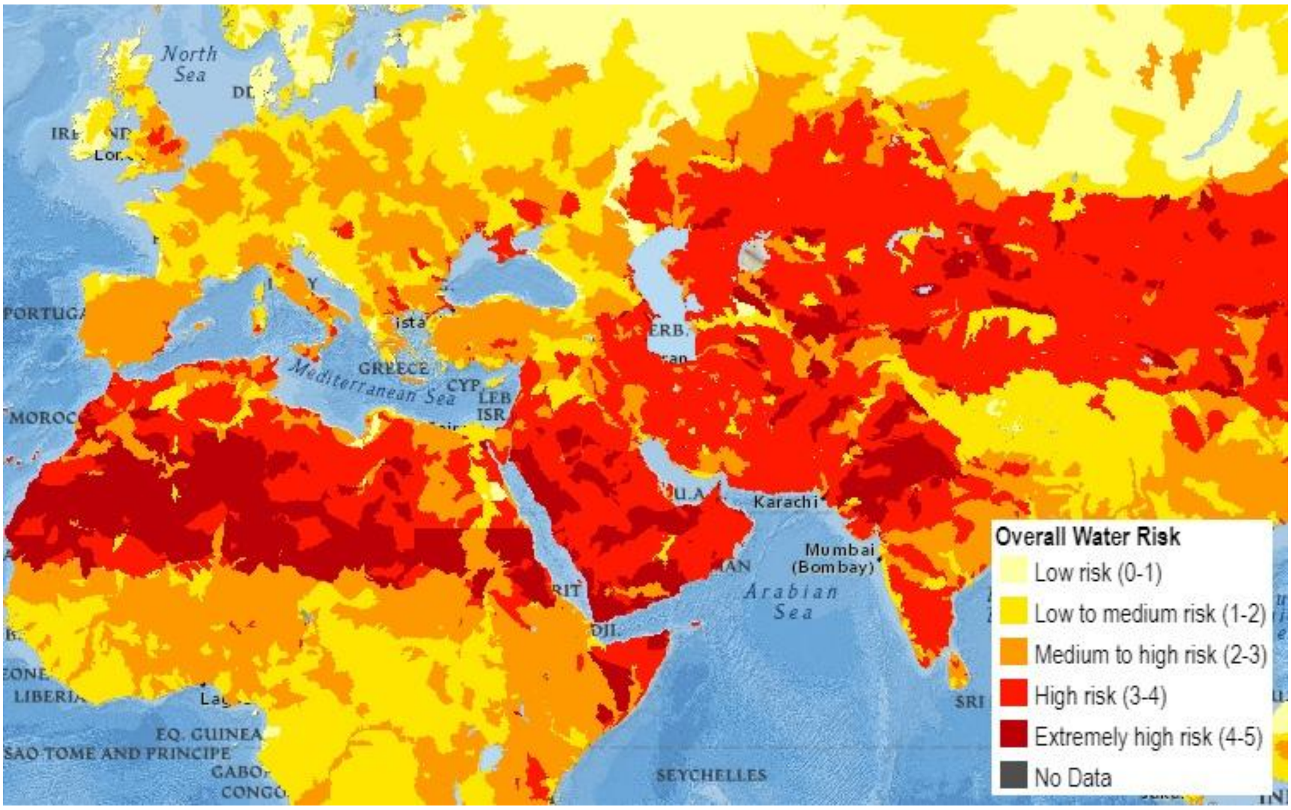

Fig. 2. Fresh water shortage in the MENA (Source: WRI Aqueduct)

The designed MAC can be constructed in these countries. Considering the potential hazards of nuclear components of the MAC, it should be located at some distance from major cities. The distance should be determined by technical and economic calculations, based on the cost of transporting the desalinated water pipeline from the MAC to the city. Then the final price of the water and energy for pumping the water to consumers can be determined. According to our estimates, the distance from the MAC to the city of the consumer will be within a few tens of kilometers. It should be noted that NPPs constructed in various countries of the world are, as a rule, at distances determined by the state and safety standards. If we talk about nuclear installations for a specific purpose, i.e. for MAC, it should be based on the need to fulfil special requirements that are more stringent than for “normal” NPPs to ensure their safety. In particular, in designing a MAC, the possibility of the leakage of radioactive substances into desalinated water should be examined in any situation and proper mechanisms must be utilized to prevent the leakage of radioactive particles into the desalinated water in accidents. Based on these considerations, we believe that the distance of several tens of kilometers from the MAC to major cities can be acceptable.

It will be easier (and less costly) to solve the problem of choosing a MAC location in cases where the purpose of water usage is just agricultural, i.e. when desalinated water will be used only for irrigation of fields, gardens and orchards. In these cases, the territory of the MAC may be sparsely populated and it is easier to handle the task of protecting people from the effects of accidents of NPP.

It is important to note that in our example of the MAC design (described in section 6) it is proposed to use a type of nuclear power technology installation that is more secure than conventional NPPs.

3. SEAWATER DESALINATION TECHNOLOGIES OF MAC

The literature on desalination of sea and brackish waters, as well as a comparison of their pros and cons, is described in the extensive literatures [6, 7]. In this relatively brief study, we are not able to represent these issues in detail and then we limit ourselves to brief conclusions, which are resulted from the analysis of the above literature. Desalination processes are known quite a lot, but the main ones, i.e. commercially available and suitable for solving the problem of large-scale desalination are only three processes: MED, MSF and RO. These methods can be used both individually and in various combinations (hybrid technologies, mainly MSF + RO and MED + RO, but sometimes MED + MSF + RO). Recently, the manufacturers are using various procedures to improve the efficiency of the main desalination technologies such as vapor compressing (Thermal Vapor Compression – TVC or Mechanical Vapor Compression – MVC) and using the heat of condensation of steam from a steam turbine to preheat the feed-water [8].

The choice of the flow rate of the seawater supply to the DP is related to the components of the concept of the hybrid in the design of the MAC and it is the goal of optimization calculations. As a result of these calculations, a MAC scheme should be developed with a specific type of reactor of a given capacity and the composition of its equipment should be determined so that the capital costs of its construction and operation are minimal compared to all other alternatives. At the same time, the requirements to ensure the specified values of electrical and thermal energy (if the MAC is three-purpose), the performance of desalinated water, the values of the specified parameters of steam (for heat supply), the specified salt concentration in desalinated water, the unconditional nuclear and radiation safety of the MAC and its reliability must be met.

4. COMPARATIVE TECHNICAL AND ECONOMIC ANALYSIS FOR CHOOSING THE MAC EQUIPMENT

Our feasibility analysis for choosing the most suitable option for a particular Country or a particular region of a country (in countries of large areas, climatic conditions and other variables may differ) is based on the use of well-known DEEP and DE-TOP, developed by the IAEA [6]. However, the results of calculations will be more accurate if some specific features of each country (such as the base unit cost, specific operation and maintenance spare parts cost, specific operation and maintenance chemical cost for pre-treatment, management salary, and etc.) are considered by modifying the parameters and formulas, which are suitable for different versions of MAC.

The DEEP software can be utilized to evaluate the cost and performance of the main desalination technologies, which are integrated to various energy sources, such as nuclear power, oil, coal, and gas. DE-TOP has been developed for thermodynamic analysis and some optimizations of the integration of nuclear power plant with the desalination technologies. It can be used to simulate different water cooled reactors or fossil fuel plants and their coupling with any other non-electrical application. These modifications mainly depend on the specific requirements (design characteristics of the MAC), types (schemes) of the MAC and the composition of its equipment as applied to the production and financial capabilities of the customer country.

Descriptions of the procedures for setting the source data of the DEEP and DE-TOP programs for performing calculation of desalination costs, environment parameters, financial costs, and etc., comprise the purpose of the assessments with these programs, which are described by these programs.

The countries that are manufacturing MAC using RO technology for desalination will either have to produce membranes, RO modules (consumables). Since the membranes eventually become clogged, tear and require replacement. The countries can also purchase membranes from other countries, if they are not capable of the production (as it is a complex process, which requires raw materials and special equipment).

Since such membranes are relatively costly, such a purchase will not be affordable for every country. For example, the opinion of Spanish manufacturers in the field of desalination; they would not recommend the wide-scale use of RO-desalination technology for Iran, thus for this purpose it is necessary to purchase membranes from another country, for example from Germany. In our opinion, this situation can be considered as temporary, because Iran's potential and capabilities in production (engineering, chemical technology and others) are such that in the future, the country will be in a position to produce its own membranes.

The advantages of RO technology in comparison with other desalination processes (such as, the reduced energy consumption, compact size and less space occupation), the developing of MAC coupling with RO technology or with hybrid desalination technology, can be regarded as an acceptable direction for the future developments.

5. AN EXAMPLE OF MAC COUPLING WITH HYBRID DESALINATION PLANT

In this section of the paper, as an example of using the methodology of technical and economic analysis, we represent a MAC plant with a 440 MW water/water power reactor coupling with MSF or MED + RO hybrid desalination technology (Fig. 3). heat and hot water for urban consumption.

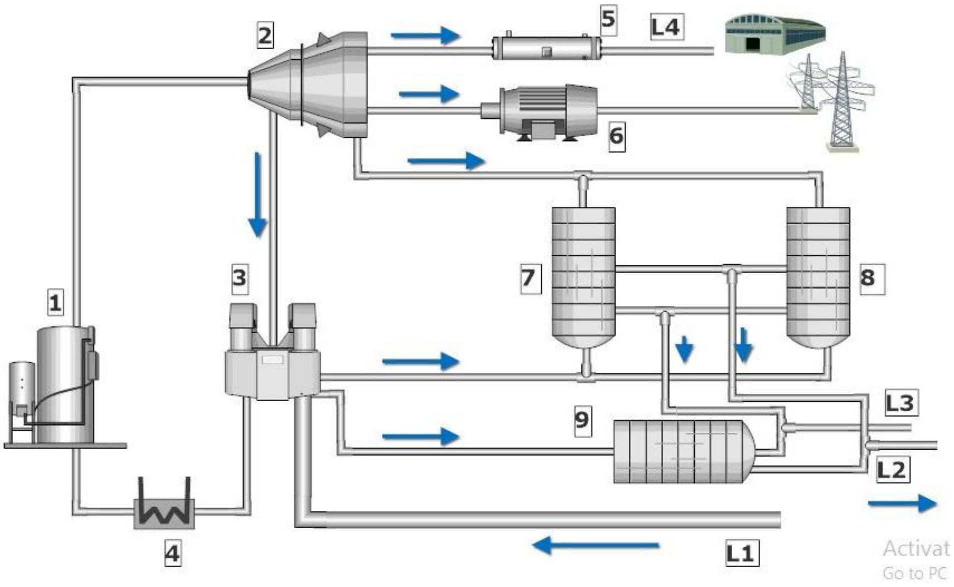

Fig. 3. The scheme of integration of the MAC with desalination systems: 1) steam generator, 2) turbine, 3) condenser, 4) pre-heater, 5) heat-exchanger, 6) generator, 7) MED unit, 8) MSF unit, 9) RO unit, L1) Intake water from the sea, L2) Freshwater, L3) Brine, L4) Hot water

In this scheme, a hot flow from the turbine enters the thermal desalination units (MED and MSF) with various temperatures (depending on the process). The intake water from the sea enters the condenser in order to be pre-heated. The total produced fresh water and brine of desalination units exit from the pipeline of L3 and L4, respectively. Furthermore, the pipeline of L4 supplies the required

According to the projects in the field multipurpose power plants (the implemented projects in China, Argentina, Mexico and other countries), we have selected a typical MAC with a medium-power nuclear water-cooled reactor (440 MW) for an analysis. Several studies about the atomic desalination complexes have been carried out: e.g. with boiling tanks (in Russia), fast neutron reactors (FN type - in Russia or FBR - fast breeder reactor) and even with the reactors, which have not been used in nuclear desalination yet, such as a high-temperature gas-cooled (HTGR or HDGR). The reasons for VVER reactors (PWR) conquest in the design of MAC systems are clear. These types of reactors were installed in many countries and have shown a high level of safety and reliability. It should be noted that the special characteristics of VK-type reactors (such as the level of power and the parameters of the steam produced) are quite appropriate for using it as the power supply of the MAC systems. In addition, they are distinguished by their simplicity of design, excellent performance and high level of reliability and safety. For example, the VK-30 industrial reactor has been successfully operated for more than forty years in the town of Meleksk, Ulyanovsk Region [9]. However, for one reason, which is very important, we would not recommend using VK (BWR) type reactors for MAC. The fact is that the probability of radioactivity entering desalinated water should be zero. The scheme of VK nuclear power plant is single-circuit. Consequently, during fuel cladding damage in result of overheating or corrosion, radioactive substances may get into boiling water, and from there into steam, and then into the condensation system of this steam, which supplies heat to the thermal desalination system (MSF or MED). Of course, a nuclear installation with a VK type reactor (BWR) should be equipped with a system for removing active products from steam during similar accidents and filtering emissions in order to prevent them from releasing into the atmosphere. However, the reliability of this system cannot be guaranteed and some radioactive particles can still get into the heating steam of the desalination plant. However, the probability of this situation to take place is low. As in the heat exchanger (hot steam - evaporating seawater) these mediums are separated by a metal wall. Nevertheless, leaks in this pipe and entering the radioactivity in drinking water is possible with catastrophic consequences. These considerations do not necessarily mean that research and development should not be carried out on designing radiation-safe MAC systems with VK-type reactors (BWRs). For example, it is theoretically possible to use MAC schemes, including an intermediate steam-water circuit that separates the reactor cycle from the heating cycle of the desalination plant. However, currently, this problem has not been solved completely and therefore, we choose the water-type nuclear reactor for our recommendations to the countries of the MENA.

By considering the safety, reliability and economic parameters as the priority requirements, we propose to use a nuclear steam supply system (NSSS) with a VVER reactor, the natural circulation of the primary coolant (NCPC) and an integral type of this installation (INSSS). In this case, loop pipelines and primary circuit circulating pumps are excluded from the NSSS, which obviously leads to a reduction in the metal used (and cost) of the NSSS and increase its reliability, since the probability of pipeline leakage and failure of circulation pumps is excluded.

The proposed NSSS-NCPC is not some kind of exotic invention. The integral principle of NSSS with natural circulation in the primary cycle is implemented in the mobile reactors [10]. It should also be noted that NPPs, which use the natural circulation of the primary coolant attract the attention of designers of low-power nuclear power plants in the several countries, especially Argentina and USA [11].

The desalination part of our proposed MAC system is based on hybrid technology (MSF or MED + RO). In this case, there is the option of combining the advantages of these technologies, the possibility of installing large-scale, relatively cheap production of fresh water using RO technology and the possibility of obtaining high quality water, using thermal processes.

The MAC design is characterized by the following parameters:

- The power of a nuclear reactor is 440 MW.
- The pressure of steam produced by its steam generators is 3.6 MPa.
- The temperature is 310 °C.
- The flow and pressure of the selected steam turbine and heating steam desalination plant is determined by the optimization calculations.
- The amount of electrical energy used by the installation of RO - is determined by the optimization calculations.
- Electricity consumption for feed water supply to the thermal and RO systems is determined according to the needs of these systems and the hydraulic resistance of pipelines and water withdrawn from the reservoir (an average value can be taken, which is based on experience from the operating of modern desalination systems).

As a result of calculations performed using the DEEP and DE-TOP programs, pressure and temperature flows of media (secondary steam, brine, fresh water) are found in all characteristic areas of the MAC concept, energy cost (thermal and electrical) corresponding to the maximum level of efficiency of MAC, i.e. the lowest capital and operating costs.

The basic economic parameters of the integrated desalination plant to the 440 MW MAC are listed in Table 1. The results of calculations by DEEP program are illustrated in the Table 2. The net electricity production of our suggested NPP is 114 MWe, the total power use for RO method and the specific power use are 5.34MWe, 3.66 KWh/m3, respectively. The electricity consumption of the thermal desalination for MED and MSF options are 1 MW and 1.3 MWe, respectively. The calculated results of table 2 indicates that the water price by the hybrid process of MED-RO is less than the water price resulted by MSF-RO combination. The total energy cost of MSF method is considerably more than the MED method. It is important to state that each method has its advantages and disadvantages, which should be compared for final decision of the desalination unit. Although the RO method provides fresh water with the least cost, it is recommended to utilize hybrid desalination technologies to take the advantages of both thermal and electrical desalination processes [12].

Table 1. The basic economic parameters of VVER-440 and desalination plant

Desalination plant specifications	**unit**	**Value**
Total desalination plant capacity	m^3/day	50,000
Total dissolved solids	ppm	40000
Feed water inlet temperature for reverse osmosis	℃	25
The lifetime of the desalination system	year	20
Interest rate	%	15
Discount rate	%	5
Electricity selling price	$/MWh	30
Water selling price	$/$m^3$	1.9

Table 2. Results of the economic evaluation of the suggested scheme

	Desalination methods	
	MED + RO	**MSF + RO**
Capital costs of the desalination plant		
Construction cost ($\$/\mathrm{m}^3$day)	1154	1154
Intermediate loop cost ($\$/\mathrm{m}^3$day)	111	111
Water plant owners cost ($\$/\mathrm{m}^3$day)	63	63
Water plant contingency cost ($\$/\mathrm{m}^3$day)	133	133
Interest during construction ($\$/\mathrm{m}^3$day)	133	133
Total capital costs($\$/\mathrm{m}^3$day)	1638	1638
Annualized capital costs (M$)	6	6
Sp. annualized cap costs ($\$/\mathrm{m}^3$)	0.41	0.41
Energy costs		
Heat cost ($\$/\mathrm{m}^3$)	0.23	0.51
Backup heat cost ($\$/\mathrm{m}^3$)	0.0	0.0
Electricity cost ($\$/\mathrm{m}^3$)	0.15	0.18
Purchased electricity cost($\$/\mathrm{m}^3$)	0.01	0.01
Total energy costs	0.39	0.7
Operation and maintenance costs		
Management cost ($\$/\mathrm{m}^3$)	0.01	0.01
Labor cost ($\$/\mathrm{m}^3$)	0.03	0.03
Material cost ($\$/\mathrm{m}^3$)	0.1	0.1
Insurance cost ($\$/\mathrm{m}^3$)	0.02	0.02
Total cost ($\$/\mathrm{m}^3$)	0.17	0.17
Total operating costs (energy +O &M)	0.56	0.86
Total annual cost (M$)	14.78	19.47
Water production cost ($\$/\mathrm{m}^3$)	0.967	1.275
Water Transport costs ($\$/\mathrm{m}^3$)	0.0	0.0
Total water cost ($\$/\mathrm{m}^3$)	**1.051**	**1.275**

6. CONCLUSION

The constantly growing shortage of the fresh water in the countries of the MENA considered in this research can be significantly diminished or even eliminated, using the large-scale nuclear desalination. Considering the development of nuclear reactors coupled to desalination systems and the great interest showed by many countries to these integrated plants, it could be understood that the nuclear desalination will have a good place in solving the electricity and potable water problems of today's world. The computational methods, which are being used in developing and integrating the desalination systems, decrease the uncertainty regarding the final cost of nuclear desalination plants. Considering the financial conditions, some of the MENA countries are the ideal candidates for constructing nuclear complexes, however different versions of MAC and some financial facilities can make these complexes purchasable by most of the nations. Due to the flexibility of the

MAC in size and mobility, after determining the required electricity and pure water capacity of each country, it can be suggested as the best option to be constructed in different regions of the world.

In this paper, the feasibility study of multi-purpose nuclear power technology complexes for producing electricity, heat, and freshwater, based on the use of DEEP and DEEP-TOP programs has been performed. Our main goal is to develope a feasible procedure, through which the countries can be provided by electricity, heat, and fresh water with considerably less environmental effects. According to our analysis, it can be stated that the nuclear desalination by the means of MAC is one of the best options for the countries, which require energy and fresh water. The economic evaluation indicates that the process of MED+RO for desalination results in less water cost in comparing to the MSF+RO method. Although, the less water cost can be achieved by using RO procedure, the use of hybrid desalination is suggested, due to the possibility of obtaining high-quality water and the capability of using the maximum amount of waste heat.

REFERENCES

1. Ahuja S. Chapter 2 - Global Water Challenges and Solutions, Advances in Water Purification Techniques. *Elsevier*, p. 17-39, ISBN 9780128147900.
2. Abdelkareem M.A., El-Haj Assad M., Taha Sayed E., Soudan B. Recent progress in the use of renewable energy sources to power water desalination plants. *Desalination*, Volume 435, 2018, p. 97-113, ISSN 0011-9164.
3. Chandrasekharam, D. Water for the millions: Focus Saudi Arabia. *Water-Energy Nexus*, Volume 1(2), 2018, p. 142-144.
4. Elaskary A.M. System Simulation for Coupling Nuclear Power Plants and Desalination in Different Scenarios. *International Journal of Scientific & Engineering Research*, Volume 4, Issue 4, April-2013 ISSN 2229-5518.
5. Luo, T., R. Young, P. Reig. Aqueduct Projected Water Stress Country Rankings. Technical Note. Washington, D.C.: World Resources Institute 2015. Available online at: www.wri.org/publication/aqueduct-projected-water-stresscountry-rankings.
6. *International Atomic Energy Agency*. TECDOC 1524 - Status of Nuclear Desalination in IAEA Member States, IAEA, Austria, January 2007. <https://www.iaea.org/publications/7584/status-of-nuclear-desalination-in-iaea-member-states>
7. Misra B.M. Seawater desalination using nuclear heat/electricity — Prospects and challenges. *Desalination*, Volume 205, 2007, p. 269–278.
8. *International Atomic Energy Agency*. IAEA -Tecdoc-1753. New Technologies for Seawater Desalination Using Nuclear Energy. Vienna, 2015.
9. Serdun N.P. Ignatenko V.I., Kitty G.S. Experimental Research Thermal Hydraulic Characteristics of the Vk-300 Reactor on Model Single Tractor Pipe. *Obninsk Institute of Atomic Energy NRNU MEPI.* 249040, Obninsk, Kaluga region, Campus, 1. 2015.
10. Antony J. Design of Experiments for Engineers and Scientists (Elsevier Insights). *Elsevier*; 2 edition (March 14, 2014).
11. *International Atomic Energy Agency*. IAEA -Tecdoc-1281. Natural Circulation Data and Methods for Advanced Water Cooled Nuclear Power Plant Designs. Vienna, 2002.
12. Megahed M. Feasibility of nuclear power and desalination on El-Dabaa site. *Desalination*, Volume 246, 2009, p. 238–256.